WILEY-VCH

Jens-Volker Kratz

Nuclear and Radiochemistry

Fundamentals and Applications

Fourth Edition

Volume 1

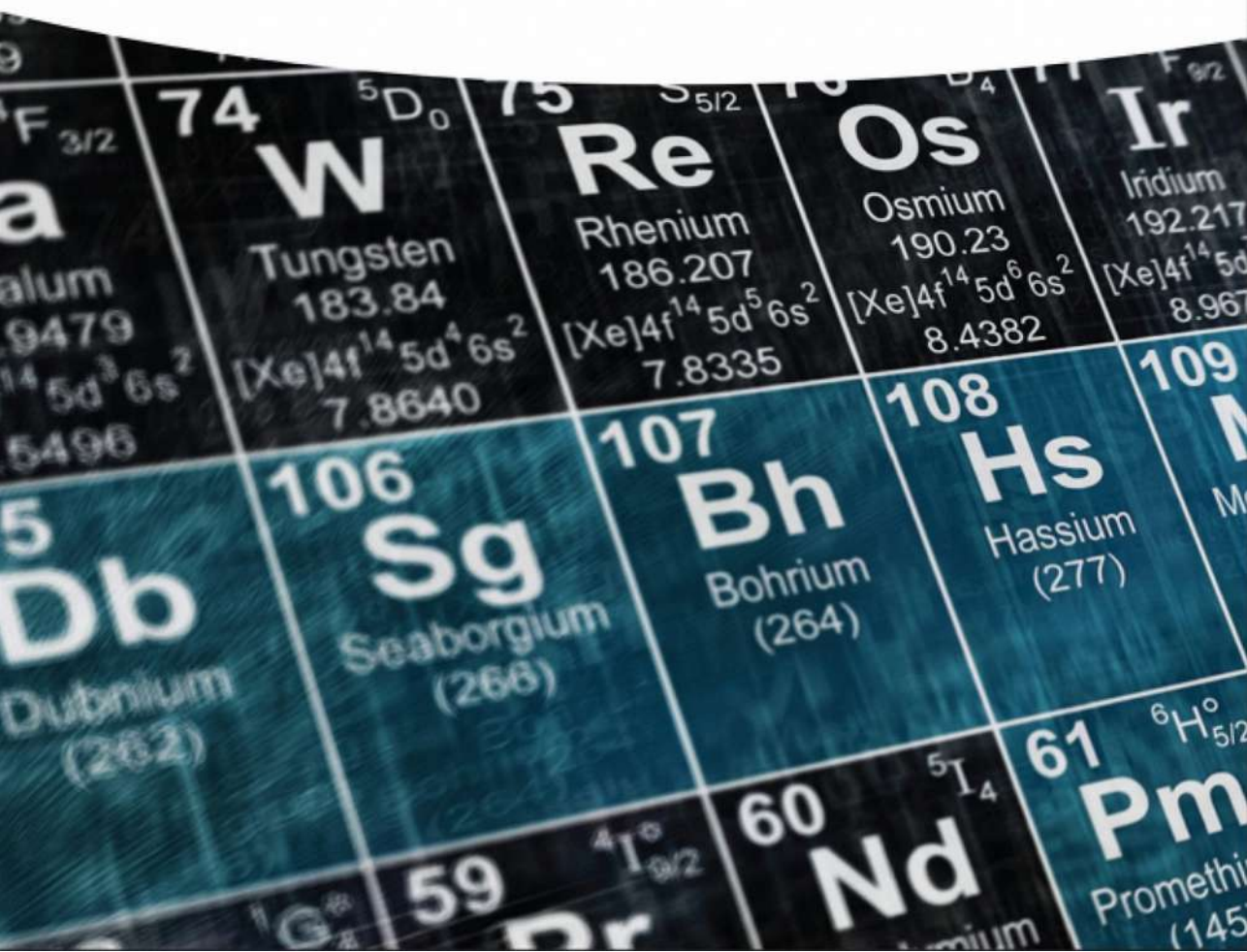

Nuclear and Radiochemistry

Fundamentals and Applications

Jens-Volker Kratz

4th Edition

Nuclear and Radiochemistry

Fundamentals and Applications

Jens-Volker Kratz

Volume 1

4th Edition

WILEY-VCH

Nuclear and Radiochemistry

Fundamentals and Applications

Jens-Volker Kratz

Volume 2

4th Edition

WILEY-VCH

Author

Jens-Volker Kratz
Department of Chemistry – TRIGA site
Johannes Gutenberg University Mainz
Fritz-Strassmann-Weg 2
55128 Mainz
Germany

Cover Design: Wiley
Cover Image: © mitya73/Shutterstock

Edition History
1st edition 1997, by K. H. Lieser
2nd edition 2001, by K. H. Lieser
3rd edition 2013, by J.-V. Kratz and K. H. Lieser

Library of Congress Card No.:
applied for

British Library Cataloguing-in-Publication Data
A catalogue record for this book is available from the British Library.

Bibliographic information published by the Deutsche Nationalbibliothek
The Deutsche Nationalbibliothek lists this publication in the Deutsche Nationalbibliografie; detailed bibliographic data are available on the Internet at <http://dnb.d-nb.de>.

Print ISBN: 978-3-527-34905-0
ePDF ISBN: 978-3-527-83193-7
ePub ISBN: 978-3-527-83195-1
oBook ISBN: 978-3-527-83194-4

Typesetting Straive, Chennai, India
Printing and Binding

Printed on acid-free paper

10 9 8 7 6 5 4 3 2 1

Contents

Contents

Preface

This textbook aims at a complete and concise description of the present knowledge of nuclear and radiochemistry and applications in various fields of the natural sciences. It is based on teaching courses and research spanning several decades. The book is mainly addressed to advanced undergraduate students and to graduate students of chemistry. Students and scientists working in physics, geology, mineralogy, biology, medicine, and other fields will also find useful information about the principles and applications of nuclear and radiochemistry.

Traditionally, nuclear chemistry has been deeply tied to nuclear physics, cooperatively called nuclear science. At the same time, a wide field of applications of nuclear and radiochemistry in other sciences has developed. Therefore, it was considered important to bring together in one textbook a detailed presentation of the physical fundamentals as well as applied aspects of nuclear chemistry ranging from nuclear structure, nuclear masses, nuclear reactions, the production of *radionuclides* and labeled compounds, the chemistry of the *radioelements*, the study of radionuclides in the environment, all the way to the nuclear and radiochemistry needed in nuclear technology. Applications also include the use of radionuclides in analytical chemistry, in geo- and cosmochemistry, dating by nuclear methods, and the use of radionuclides in the life sciences and medicine. For further reading, the relevant literature is listed abundantly at the end of each chapter. Generally, it is arranged in chronological order, beginning with the literature of historical relevance, followed by more recent work subdivided according to the subject matter into general and more specialized aspects.

After the passing of Professor Karl Heinrich Lieser, the younger author, Jens-Volker Kratz, was approached by the Lieser family and by the publisher and was motivated to prepare a generally updated third edition of this textbook. The concept and structure of the book remained largely unchanged; however, new developments and results were incorporated, including the most recent references. These updates concerned the physical properties of atomic nuclei, the nuclear force and nuclear structure, techniques in nuclear chemistry, nuclear reactions, statistical considerations in *radioactivity* measurements, physics and chemistry of the actinides and transactinides, radionuclide mass spectrometry, and modern methods of speciation of radionuclides in the environment. These have been taken from teaching courses held at the Johannes Gutenberg University over the last 30 years.

The third revised edition of Jens-Volker Kratz and Karl Heinrich Lieser "Nuclear and Radiochemistry, Fundamentals and Applications" appeared in late 2013. This successful textbook was close to being sold out in late 2019, why Wiley-VCH re-contacted Jens-Volker Kratz and asked him to prepare a fourth edition with perhaps some 20% of new contents. This was accepted after the development of a suitable concept in April 2020.

The new trend, that was already visible in the third edition, i.e. more weight on the physical aspects of modern nuclear chemistry and less on the traditional fields of radiochemistry, e.g. on radioanalysis and radiotracers in chemistry, as compared to the earlier Lieser editions, has now been even more pronounced: the standard model of particle physics is now enriched by introducing the newly discovered heavy scalar Higgs boson and the omni-present Higgs field, the statistical assessment of lifetimes in the α-decay chains of odd-Z superheavy elements is illuminated, the important use of recoil momenta and average charge states in gas-filled separators is discussed, the presentation of nuclear heavy-ion reactions is much enlarged, new methods of reprocessing and the treatment of nuclear waste are presented, new insights into the physical and chemical properties of the superheavy elements are discussed, as well as the fascinating news about neutrino masses, to name a few highlights. On the other hand, to avoid an unreasonable increase of the size of the two volumes of the fourth edition, some of the traditional Lieser chapters dealing with fields, in which today, research is no more active, have been omitted. To avoid a wrong impression, the author of the new edition along with the editors of Wiley-VCH want to clarify that the concept and the structure of the book are still basically unchanged, and we deeply appreciate that the roots planted by Karl Heinrich Lieser with the early editions of his book series are still alive and visible.

As in the previous edition, it is my pleasure to thank Mrs. Petra Sach-Muth for help and Mr. Jürgen Hubrath for professionally producing a number of new figures.

Mainz, April 2021 *Jens-Volker Kratz*

1

Fundamental Concepts

Nuclear and radiochemistry cover a wide spectrum of areas such as (i) studies of the chemical and physical properties of the heaviest human-made elements; (ii) studies of nuclear structure, nuclear reactions, and radioactive *decay*, (iii) studies of nuclear processes in the Universe, such as geochronology and cosmochemistry; and (iv) applications of radioactivity in a vast variety of fields such as *radioanalysis*, chemistry, life sciences, and industrial applications, and in the geo- and biosphere. Nuclear chemistry has ties to all traditional areas of chemistry. Nuclear chemists are involved in the preparation of radiopharmaceuticals for use in medicine. Radiometric techniques play an important role in analytical chemistry and are often used as references validating other analytical techniques. The study of the actinide and transactinide elements has traditionally involved nuclear chemists studying the limits of nuclear stability and the periodicity of the periodic table of the elements. The physical concepts at the heart of nuclear chemistry have their roots in nuclear physics. Thus, nuclear physics and nuclear chemistry overlap and are cooperatively called nuclear science. However, there are distinctions between these related fields. Besides the close ties to chemistry mentioned earlier, nuclear chemists are studying nuclear problems in different ways than nuclear physicists. Nuclear physics tends to look into the fundamental interactions between subatomic particles and fundamental symmetries. Nuclear chemists have focused on more complex phenomena where statistical properties are important. Nuclear chemists are more involved in applications of nuclear phenomena. For example, the nuclear fuel cycle or the migration of *radionuclides* in the environment is so inherently chemical that they involve nuclear chemists almost exclusively. The other term, radiochemistry, refers to the chemical applications of radioactivity and of related phenomena. Radiochemists are nuclear chemists but not all nuclear chemists are radiochemists. There are many nuclear chemists who use purely instrumental, physical techniques for their research and thus their work is not radiochemistry.

1.1 The Atom

The atom is the smallest unit a chemical element can be divided into without losing its chemical properties. The radii of atoms are on the order of 10^{-10} m (Å). The

Nuclear and Radiochemistry: Fundamentals and Applications,
Fourth Edition. Jens-Volker Kratz.

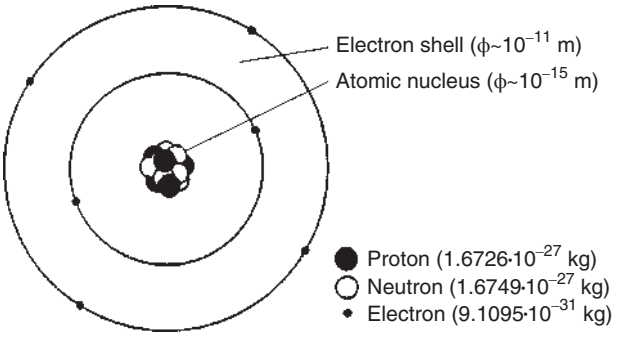

Figure 1.1 Schematic representation of the relative sizes of the atom and the nucleus.

atomic nucleus, see Figure 1.1, is a very small object with a radius on the order of $1–10 \cdot 10^{-15}$ m (femtometer, fm, called fermi) in the center of the atom and contains almost the entire mass of the atom. It contains Z protons, where Z is the atomic number of the element. Being the number of protons, Z is thus the number of positive charges in the nucleus. The nucleus also contains N neutrons, where N is the neutron number. Neutrons are uncharged particles with masses almost identical to the proton mass. Electrons surround the nucleus. Electrons are small negatively charged particles with a mass of 1/1836 of the proton mass. The electrons are bound electrostatically to the positively charged nucleus. In a neutral atom, the number of electrons equals the number of protons in the nucleus. The chemistry of the element is controlled by Z. From quantum mechanics, we know that only certain discrete energies and angular momenta of the electrons are allowed. These quantized states are schematically depicted in Figure 1.1. Later, in Chapter 5, we will see also that *nucleons* occupy orbits with discrete energies and angular momenta. However, the sizes and energies of atomic and nuclear processes are very different, allowing us to consider them separately.

1.2 Atomic Processes

In the inelastic collision of two atoms, we can anticipate (i) excitation of one or both atoms involving a change in electron configuration or (ii) ionization of one or both atoms, that is, removal of one or more electrons from the atom to form a positively charged ion. For this process to occur, an atomic electron must receive an energy exceeding its binding energy. This energy far exceeds the kinetic energies of gaseous atoms at room temperature. Thus, the atoms must have high kinetic energies as a result of nuclear decay or acceleration to eject electrons from other atoms in atomic collisions. When an electron in an outer atomic electron shell drops down to fill a vacancy in an inner electron shell, electromagnetic radiation called X-rays is emitted. In Figure 1.2, an L-shell electron is shown filling a K-shell vacancy. In the transition, a characteristic K X-ray is emitted. The energy of the X-rays is equal to the difference in the binding energies of the electrons in the two shells, which

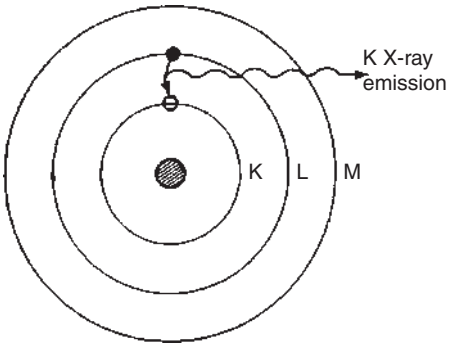

Figure 1.2 Scheme showing X-ray emission when a vacancy in an inner electron shell caused by nuclear decay is filled. An L-shell electron is shown filling a K-shell vacancy associated with K X-ray emission.

depends on the atomic number of the element. Specifically, X-rays due to transitions from the L shell to the K shell are called K_α X-rays, while X-rays due to transitions from the M to K shells are termed K_β X-rays. Refining further, $K_{\alpha 1}$ and $K_{\alpha 2}$ designate transitions from different subshells of the L shell, that is, $2p_{3/2}$ (L_{III}) and $2p_{1/2}$ (L_{II}). X-rays for transitions from M to L are L_α X-rays. For each transition, the change in orbital angular momentum $\Delta\ell$ and total angular momentum Δj must be $\Delta\ell = \pm 1$ and $\Delta j = 0, \pm 1$.

For a hydrogen-like atom, the Bohr model predicts that the transition energy ΔE is

$$\Delta E = E_\mathrm{i} - E_\mathrm{f} = R_\infty hcZ^2 \left(\frac{1}{n_\mathrm{i}^2} - \frac{1}{n_\mathrm{f}^2} \right) \tag{1.1}$$

where R_∞ is the Rydberg constant, h the Planck constant, c the speed of light, and n the principal quantum number of the electron. The X-ray energy $E_x = -\Delta E$, after inserting the physical constants, is

$$E_x = 13.6Z^2 \left(\frac{1}{n_\mathrm{f}^2} - \frac{1}{n_\mathrm{i}^2} \right) \text{ eV} \tag{1.2}$$

For K_α X-rays from hydrogen-like atoms

$$E_x = 13.6Z^2 \left(\frac{1}{1^2} - \frac{1}{2^2} \right) \text{ eV} \tag{1.3}$$

and for L_α transitions

$$E_x = 13.6Z^2 \left(\frac{1}{2^2} - \frac{1}{3^2} \right) \text{ eV} \tag{1.4}$$

In a realistic atom, Z must be replaced by $Z_{\text{effective}}$ to take care of the screening of the nuclear charge by other electrons. Henry Moseley showed the frequencies, ν, of the K_α X-rays scale as

$$\nu^{1/2} = \text{const}(Z - 1) \tag{1.5}$$

and those of the L_α X-rays scale as

$$\nu^{1/2} = \text{const}(Z - 7.4) \tag{1.6}$$

Thus, Moseley showed that the X-ray energies, hv, depend on the square of an altered, effective atomic number due to screening. The relative intensities of different X-rays depend on the chemical state of the atom, its oxidation state, complexation with ligands, and generally on local electron density. The relative intensities are, therefore, useful in chemical speciation studies. As will be discussed in Chapter 6, radioactive decays can be accompanied by X-ray production and the latter may be used to identify the decaying nucleus.

1.3 Discovery of the Atomic Nucleus

Before the discovery of radioactivity, elements were considered as unchangeable substances. In 1897, J.J. Thomson discovered the electron and concluded that the atom must have a structure. As the mass of the electron is roughly 1/2000 of the mass of hydrogen, he concluded that most of the mass of the atom must be contained in the positively charged constituents. It was assumed that negative and positive charges are evenly distributed over the atomic volume.

In 1911, Ernest Rutherford studied the scattering of α particles in thin metal foils. He found that backscattering to $\theta > 90°$ was more frequent than expected for multiple scattering from homogeneously charged atoms. This led Rutherford to postulate the existence of an atomic nucleus having mass and positive charges concentrated in a very small volume. The nucleus was supposed to be surrounded by electrons at the atomic diameter and the electrons do not contribute to the α-particle scattering. He postulated the following ansatz: the nuclear charge is Ze; that of the α particle is $Z_\alpha = 2e$. The scattering force is the Coulomb force. The nucleus is at rest in the collision, and the path of an α particle in the field of the nucleus is a hyperbola with the nucleus at the external focus. From these simplifying geometric properties and from the conservation of momentum and energy, Rutherford derived his famous scattering formula which relates the number $n(\theta)$ of α particles scattered into a unit area S at a distance r from the target foil F, see Figure 1.3, to the scattering angle θ

$$n(\theta) = n_o \frac{Nt}{16r^2} \left(\frac{ZeZ_\alpha e}{\frac{1}{2}M_\alpha v_\alpha^2} \right)^2 \frac{1}{\sin^4(\theta/2)} \tag{1.7}$$

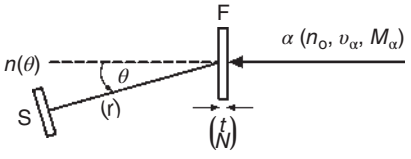

Figure 1.3 Schematic representation of the Rutherford scattering experiment. A collimated beam of α particles (n_o number of ingoing α particles with velocity v_α and rest mass M_α) hits a gold foil F (thickness t, N number of target nuclei per cubic centimeter) and is scattered to the polar angle θ under which a scintillator S at distance r from the target detects $n(\theta)$ scattered particles.

with n_0 being the number of incident α particles, t the thickness of the target foil, N the number of target nuclei per unit volume, and M_α and v_α the mass and initial velocity of the α particle.

Precision measurements by Hans Geiger and Ernest Marsden soon verified that, for sufficiently heavy scatterers, the number of scattered particles detected per unit area was indeed inversely proportional to the square of the α-particle energy and to the fourth power of the sine of half the scattering angle. In principle for all, but notably only for light target nuclei, Eq. (1.7) must be modified because the target nucleus is not at rest. This can be accommodated by inserting the center of mass energy instead of the laboratory energy and by using the reduced mass instead of the rest mass. Figure 1.4 shows the apparatus used by Geiger and Marsden. It resembled an exsiccator that could be evacuated. The upper part contained the α-particle source (in German *Emanationsröhrchen*, R) in a lead brick. The collimated beam of α particles passed a gold foil F. The α particles that, after scattering in F, interacted with the scintillator S were observed through the microscope M. The microscope together with the scintillator could be moved to different scattering angles θ by turning the flange (*Schliff*, Sch). Figure 1.5 shows the results obtained by Geiger and Marsden. They agree in an impressive way over 5 orders of magnitude with the theoretical dependence $(1/\sin^4(\theta/2))$ for pure Coulomb scattering. This way, it was possible to study systematically the magnitude of the nuclear charge in the atoms of given elements through scattering experiments since the scattered intensity depends on the square of the nuclear charge. It was by the method of α-particle scattering

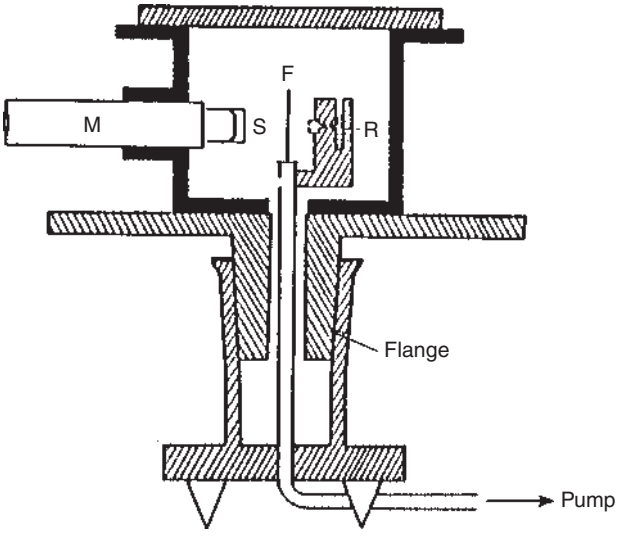

Figure 1.4 Experimental setup by Geiger and Marsden for the observation of Rutherford scattering of α particles in a gold foil F. The radioactive source R is contained in a lead housing. The scattered α particles are interacting with the scintillator S that is observed by a microscope M. The microscope together with the scintillator could be turned to variable scattering angles θ by turning the flange. Source: Geiger and Marsden (1913), figure 1 (p. 607)/Taylor & Francis.

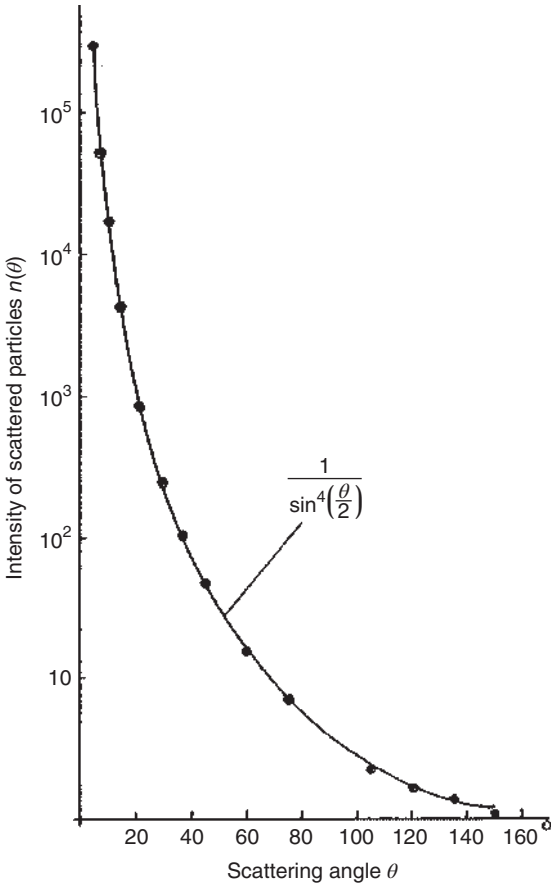

Figure 1.5 Intensity of scattered α particles measured by Geiger and Marsden as a function of scattering angle θ. The solid line represents a $1/\sin^4(\theta/2)$ function representing the theoretical dependence for pure Coulomb scattering.

that nuclear charges were determined and this led to the suggestion that the atomic number Z of an element was identical to the nuclear charge. Further understanding of atomic structure developed rapidly through the study of X-rays and optical spectra, culminating in Niels Bohr's theory of 1913 and Erwin Schrödinger's and Werner Heisenberg's quantum mechanical description of the atom in 1926.

1.4 Nuclear Decay Types

Radioactive decay involves the spontaneous emission of radiation by an unstable nucleus. While this subject will be discussed in detail in Chapter 6, we present here a general introduction. In Table 1.1, we summarize the characteristics of the various decay types. Three basic decay modes were discovered by Rutherford starting in 1899: α decay, β decay, and γ radiation. He found that α particles are completely absorbed in thin metal foils, for example, 15 μm of Al. β particles were found to be largely absorbed only in Al a 100 times thicker. An absorption equation $I = I_0 e^{-\mu d}$ was found where μ is a mass absorption coefficient (cm^{-1}) depending on Z of the

Table 1.1 Characteristics of radioactive decay modes.

Decay mode	Symbol	Emitted particle		Decay process and example (in short form)
α decay	α	Helium	${}^{4}_{2}\mathrm{He}^{2+}$	${}^{A}Z \rightarrow {}^{A-4}(Z-2) + {}^{4}_{2}\mathrm{He}^{2+}$
β decay	β^-	Electron and antineutrino	${}^{0}_{-1}\mathrm{e}^-$ $\overline{\nu}_\mathrm{e}$	${}^{1}_{0}\mathrm{n} \rightarrow {}^{1}_{1}\mathrm{p} + {}^{0}_{1}\mathrm{e}^- + {}^{0}_{0}\overline{\nu}_\mathrm{e}$ (in the nucleus) ${}^{A}Z \rightarrow {}^{A}(Z+1)$ ${}^{14}\mathrm{C}(\beta^-){}^{14}\mathrm{N}$
	β^+	Positron and neutrino	${}^{0}_{1}\mathrm{e}^+$ ν_e	${}^{1}_{1}\mathrm{p} \rightarrow {}^{1}_{0}\mathrm{n} + {}^{0}_{1}\mathrm{e}^+ + {}^{0}_{0}\nu_\mathrm{e}$ (in the nucleus) ${}^{A}Z \rightarrow {}^{A}(Z-1)$ ${}^{11}\mathrm{C}(\beta^+){}^{11}\mathrm{B}$
Electron capture (EC)	ε	Neutrino and X-ray of the daughter nuclide	ν_e	${}^{1}_{1}\mathrm{p}(\text{nucleus}) + {}^{0}_{-1}\mathrm{e}^-(\text{electron shell}) \rightarrow {}^{1}_{0}\mathrm{n} + {}^{0}_{0}\nu_e$ ${}^{A}Z \rightarrow {}^{A}(Z-1)$ ${}^{37}\mathrm{Ar}(\varepsilon){}^{37}\mathrm{Cl}$
γ transition	γ	Photon	$(h\nu)$	Electromagnetic decay of an excited nucleus
Internal conversion (IC)	e^-	Conversion electron and accompanying processes		Transfer of excitation energy to an electron in the shell ${}^{58\mathrm{m}}\mathrm{Co}(\mathrm{e}^-){}^{58}\mathrm{Co}$
Spontaneous fission	sf	Fission fragments		${}^{A}Z \rightarrow {}^{A'}Z' + {}^{A-A'}(Z-Z')$ ${}^{254}\mathrm{Cf}(\mathrm{sf})\ldots$
Proton decay	p	Proton	${}^{1}_{1}\mathrm{p}$	${}^{A}Z \rightarrow {}^{A-1}(Z-1) + {}^{1}_{1}\mathrm{p}$ ${}^{147}\mathrm{Tm}(\mathrm{p}){}^{146}\mathrm{Er}$
Cluster decay	C	Cluster		${}^{223}\mathrm{Ra} \rightarrow {}^{14}\mathrm{C} + {}^{209}\mathrm{Pb}$

absorber and d was the thickness in centimeter. γ radiation was found to be almost not absorbed (in aluminum) and a mass absorption coefficient depending on Z^5 was associated with it. Therefore, today, thick bricks of lead are commonly used in radiochemical laboratories for shielding purposes. Recognition of the character of the α and β rays as high-speed charged particles came largely from magnetic and electrostatic deflection experiments in which β particles were seen to be electrons. From the deflection of α particles, the ratio of charge to mass was found to be half that of the hydrogen ion. The suggestion that α particles were ${}^{4}\mathrm{He}^{2+}$ ions was immediately made. This was proven in 1903 by William Ramsay in an experiment in which α rays were allowed to pass through a very thin glass wall into an evacuated glass vessel. Within a few days, sufficient helium gas was accumulated in the glass vessel and was detected spectroscopically. γ radiation was found not to be deflected in the magnetic field and was recognized to be electromagnetic radiation. The difference to the atomic X-ray radiation, however, was not clear at that time.

Nuclear β decay occurs in three ways: β^-, β^+, and electron capture (EC). In these decays, a nuclear neutron or proton changes into a nuclear proton or neutron,

respectively, with the simultaneous emission of an antineutrino or an electron neutrino and an electron or positron. In EC, an orbital electron is captured by the nucleus changing a proton into a neutron with the emission of a monoenergetic neutrino. Due to the creation of a hole in the electron shell, the subsequent emission of X-rays or Auger electrons occurs. The *mass number A* remains constant in these decays while the atomic number Z is increased by 1 unit in β^- decay and decreased by 1 unit in β^+ decay and EC. In β^- and β^+ decay, the decay energy is shared between the emitted β particle, the (anti)neutrino, and the recoiling daughter nucleus.

Nuclear electromagnetic decay occurs in two ways: γ emission and internal conversion (IC). A nucleus in an excited state decays by the emission of a high-energy photon or the same excited nucleus transfers its decay energy radiation-less to an orbital electron that is ejected from the atom. As in EC, the creation of a hole in the electron shell causes accompanying processes to occur, such as X-ray emission. There is no change in the number of the nucleons.

In 1940, K.A. Petrzhak and G.N. Flerov discovered spontaneous fission of ^{238}U when they spread out a thin layer of uranium in a large area ionization chamber operated in a Moscow underground train station (to shield against cosmic radiation), observing large ionization bursts much larger than the pulse heights of the abundantly emitted α particles. A spontaneous fission half-life of 10^{16} years was estimated. It was concluded that the gain in binding energy delivers the decay energy when a nucleus with A nucleons splits into two fission fragments of roughly $A/2$.

In 1981, the emission of monoenergetic protons was discovered by S. Hofmann et al. at the GSI Helmholtz Center for Heavy Ion Research, Darmstadt. This proton radioactivity is now a widespread decay mode of very neutron-deficient nuclei. In 1984, H.J. Rose and G.A. Jones discovered cluster radioactivity in the decay of ^{223}Ra, which emits, with a probability of $8.5 \cdot 10^{-10}$ relative to the α particle emission, ^{14}C clusters and decays into ^{209}Pb. Heavier clusters are emitted from heavier nuclei with decreasing probabilities: for example, ^{238}Pu decays by emission of ^{28}Mg into ^{210}Pb and by emission of ^{32}Si into ^{206}Hg with probabilities of $5.6 \cdot 10^{-17}$ and $1.4 \cdot 10^{-16}$ relative to the α-particle emission.

In 1903 Rutherford was the first scientist to observe the laws of radioactive decay and growth of a radioactive gas emanating from a thorium salt, radon. He used an electroscope, see Figure 1.6, for these radioactivity measurements. In the electroscope, the pointer G, a gold wire, deflected from the central metal bar when the upper part of the condenser was electrically charged relative to the housing. The condenser is discharged by ionizing radiation leading to a decrease in the deflection of the pointer G with a constant speed being a measure of the "saturation current," the *activity*. Figure 1.7 shows schematically the two experiments that Rutherford conducted with 55 seconds ^{220}Rn. In version (a), the gas inlet and outlet valves in the lower part of the housing are closed. The ^{228}Th source is placed inside the electroscope and is covered so that only the ^{220}Rn emanating from the thorium salt can diffuse into the free volume and discharge the condenser, giving rise to a constant activity; see the activity vs. time diagram to the right. At a given time indicated by the arrow, the gas inlet and outlet valves are opened and the lower part of the electroscope is flushed with gas, thus removing the ^{220}Rn from the electroscope and

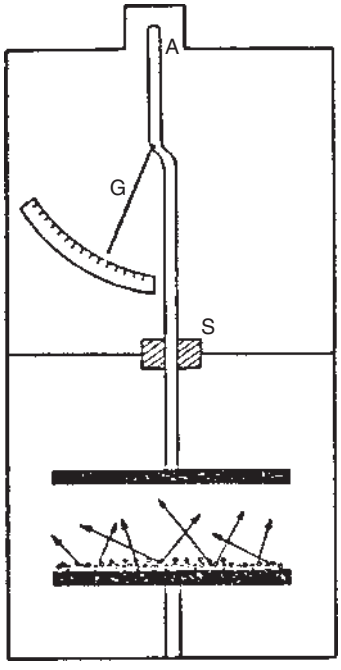

Figure 1.6 Electroscope for the measurement of radioactivity. The gold wire G strives against the strut when the upper plate of the condenser is electrically charged relative to the housing. S is an insulator. For charging the condenser, a high voltage is applied to position A. Ionizing radiation is discharging the condenser, visible by a decrease in the deflection of the gold wire from the central metal bar with a constant velocity.

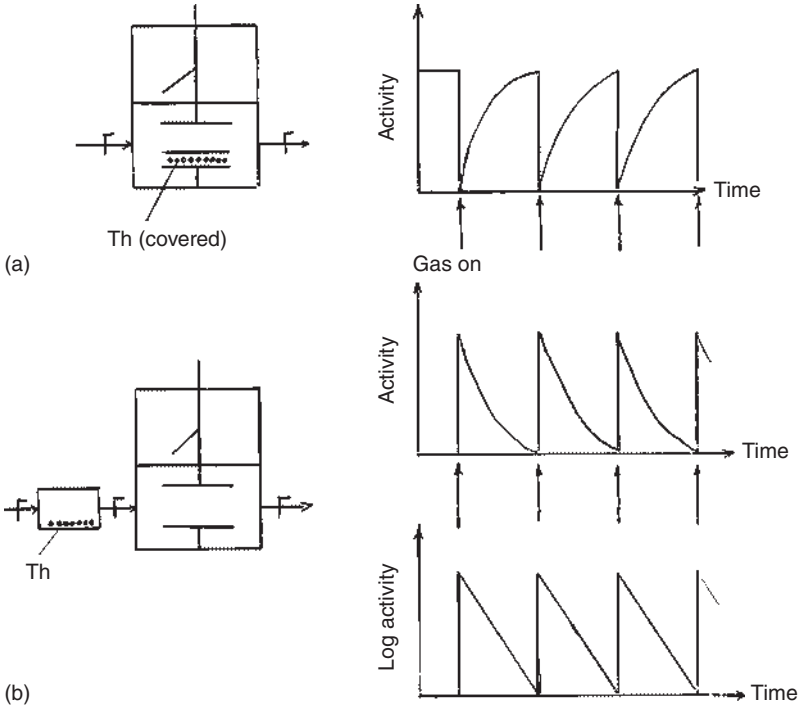

Figure 1.7 Rutherford observed the growth (a) and decay (b) of a radioactive gas (55 seconds ^{220}Rn) emanating from a Th source (1.9 years ^{228}Th).

causing the activity to fall to zero. Upon closing the valves, new ^{220}Rn grows from the ^{228}Th such that the activity discharging the condenser increases until the old saturation activity is reached. This can be repeated over and over again, showing each time the same characteristic time dependence. In version (b), the ^{228}Th source is placed in a box outside the electroscope and the activity is zero. On opening the valves and flushing ^{220}Rn into the electroscope with a carrier gas and closing the valves shortly thereafter, the ^{220}Rn decays with a characteristic time dependence. This can also be repeated over and over again. In the lower right part of Figure 1.7, the logarithm of the activity is plotted vs. time giving a linear decrease with time

$$\ln A(t) = \ln A_0 - \lambda t \tag{1.8}$$

where $A(t)$ is the activity A vs. time t, A_0 is the activity at time zero, and λ is the *decay constant*. In this way, the radioactive decay law

$$A(t) = A_0 \cdot e^{-\lambda t} \tag{1.9}$$

was discovered. The unit of activity is $1\,\text{decay}\,\text{s}^{-1} = 1\,\textit{Becquerel} = 1\,\text{Bq}$. The decay constant, λ, is characteristic for each nuclide and is related to the nuclear half-life, $t_{1/2}$, by

$$\lambda = \ln 2 / t_{1/2} \tag{1.10}$$

The activity is equal to the number of nuclei present, N, multiplied by the decay constant λ, that is, $A = \lambda N$. Therefore, the number of radioactive nuclei present will also decrease exponentially as

$$N(t) = N_0 e^{-\lambda t} \tag{1.11}$$

1.5 Some Physical Concepts Needed in Nuclear Chemistry

Some important physical concepts need to be reviewed here because we will make use of them in later discussions.

1.5.1 Fundamental Forces

All interactions in nature are the result of four fundamental forces, see Table 1.2. The weakest force is gravity. It is most significant when the interacting objects are massive, such as stars. The next stronger force is the weak interaction which acts in nuclear β decay. The electromagnetic force is next in strength, while the strong interaction is more than a hundred times stronger than the electromagnetic force. The ranges associated with the four forces are given in Table 1.2 along with their strengths relative to the strong force and with the respective force *carriers* or exchange particles. Among these, gravitons have not yet been observed but are believed to be responsible for gravity, which is not a part of the Standard Model of particle physics, see Section 1.5.6. In Chapter 6, we will see that Glashow, Salam,

Table 1.2 Fundamental forces in nature.

Force	Range (m)	Relative strength	Force carrier
Gravitational	∞	10^{-38}	Graviton?
Weak interaction	10^{-18}	10^{-5}	$W^{\pm}$, Z^0
Electromagnetic	∞	$\alpha = 1/137$	Photon
Strong interaction	10^{-15}	1	Gluon

and Weinberg introduced a unified theoretical treatment of electromagnetic and weak interactions, the electroweak interaction, in which the photon and the massive vector bosons $W^{\pm}$ and Z^0 emerge from one theory. We note in passing that the free neutron undergoes interactions with all four forces at the same time, see Chapter 8.

1.5.2 Elements from Classical Mechanics

A force is a vector that describes the rate of change of a momentum with time

$$\mathbf{F} = \frac{\mathrm{d}\rho}{\mathrm{d}t} \tag{1.12}$$

For the motion of a particle, the orbital angular momentum of the particle, l, with mass m, relative to the center of mass, is

$$\mathbf{l} = \mathbf{r} \times \mathbf{p} \tag{1.13}$$

$\mathbf{l}$ is a vector of magnitude mvr for circular motion. For motion past a stationary point, the magnitude is mvb where b is the impact parameter. The relationship between a force $\mathbf{F}$ and the potential energy V is generally

$$\mathbf{F} = \frac{-\partial V}{\partial r} \tag{1.14}$$

Thus, for example, the Coulomb force, F_C, for two charges Z_1e and Z_2e separated by the distance, r, is

$$F_C = \frac{Z_1 Z_2 e^2}{r^2} \tag{1.15}$$

where, for convenience, we set $e^2 = 1.439\,98$ MeV fm.

1.5.3 Relativistic Mechanics

When a particle moves with a velocity approaching the speed of light, according to the special theory of relativity by A. Einstein, the mass of the particle changes with speed according to

$$m' = \gamma m_0 \tag{1.16}$$

where m' and m_0 are the masses of the particle in motion and at rest and γ is the Lorentz factor

$$\gamma = (1 - \beta^2)^{-1/2} \tag{1.17}$$

and

$$\beta = \left(1 - \frac{1}{\gamma^2}\right)^{1/2}$$

where β is v/c, the velocity of the particle relative to the speed of light. The total energy of a relativistic particle is

$$E = m'c^2 \tag{1.18}$$

this being the kinetic energy, T, plus the rest mass energy equivalent m_0c^2, where

$$T = (\gamma - 1)m_0c^2 \tag{1.19}$$

For a particle at rest, the total energy is

$$E = m_0c^2 \tag{1.20}$$

For a massless particle such as the photon,

$$E = pc \tag{1.21}$$

where p is the momentum of the photon. The momentum of a relativistic particle is

$$p = \gamma m v \tag{1.22}$$

These equations demonstrate why the units MeV/c^2 for mass and MeV/c for momentum are necessary in nuclear calculations.

To give an example, we calculate the velocity, momentum, and total energy of an ^{40}Ar ion with a kinetic energy of 1 GeV/nucleon. The total kinetic energy is 40×1 GeV/nucleon = 40 GeV = 40 000 MeV. The rest mass m_0c^2 is approximately 40 atomic mass units (40 amu) or (40)(931.5) MeV, see Eq. (3.1), or 37 260 MeV. Thus, $\gamma = T/m_0c^2 + 1 = 1 + 40\,000/37\,260 = 2.07$. With Eq. (1.17), we obtain $\beta = 0.88$. So the velocity is $0.88c$ or $(0.88)(3 \cdot 10^8\ \mathrm{m\,s^{-1}}) = 2.6 \cdot 10^8\ \mathrm{m\,s^{-1}}$. We modify Eq. (1.22) to $pc = mc/(1 - \beta)^{1/2}$ and obtain (40)(931.5)(0.88)(2.07) = 67.7 GeV, that is, $p = 67.7$ GeV/c. The total energy, Eq. (1.18), is (2.07)(40)(931.5) = 77.3 GeV.

The space–time coordinates x,y,z,t in a stationary laboratory system are, in the special theory of relativity, related to the space–time coordinates in a system moving along the x axis, x',y',z',t', by

$$\begin{aligned} x' &= \gamma(x - \beta ct) \\ y' &= y \\ z' &= z \\ t' &= \gamma[t - (\beta/c)x] \end{aligned} \tag{1.23}$$

This transformation from the stationary to the moving frame is the Lorentz transformation. The inverse Lorentz transformation is obtained by reversing the sign of v giving

$$\begin{aligned} x &= \gamma(x' + \beta ct') \\ y &= y' \\ z &= z' \end{aligned}$$

$$t = \gamma[t' + (\beta/c)x']$$
$$\Delta t = \gamma[\Delta t' + (\beta/c)\Delta x]$$
$$\Delta x = \Delta x'/\gamma \tag{1.24}$$

For $\gamma > 1$, time is slowed down for the scientist in the laboratory, and the distance in the x direction is contracted. An example for the relevance of these equations in nuclear chemistry is the decay of rapidly moving particles such as muons in cosmic rays. At rest, the muon has a lifetime of 2.2 μs. At relativistic energies such as in cosmic rays, the lifetime is orders of magnitude longer. Due to this time dilatation, muons can reach the surface of the Earth.

A rule of thumb for the decision of whether the classical expressions or the relativistic expressions are to be used is $\gamma \geq 1.1$.

1.5.4 The de Broglie Wavelength

The well-known wave–particle duality says that there is no distinction between wave and particle descriptions of atomic matter; that is, associated with each particle, there is an equivalent description in which the particle is assigned a wavelength, the de Broglie wavelength,

$$\lambda = \frac{h}{p} \tag{1.25}$$

or in rationalized units

$$\lambda = \frac{\hbar}{p} \tag{1.26}$$

with $\hbar = h/2\pi$. The relativistic equivalent is

$$\lambda = \frac{\hbar c}{[E_k(E_k + 2m_0c^2)]^{1/2}} \tag{1.27}$$

Figure 1.8 shows de Broglie wavelengths for a sample of particles (electron, pion, proton, and neutron, deuteron, α particle) as a function of kinetic energy. They are largest for the lightest particles at lowest energies. The horizontal bar indicates the order of magnitude where λ becomes larger than the maximum impact parameter R for light-particle-induced reactions and from where the wavelength of the projectile influences the nuclear reaction *cross-section*, see Chapter 12.

One can also associate a wavelength to photons

$$\lambda = \frac{c}{\nu} = \frac{hc}{E_\gamma} \tag{1.28}$$

where ν is the frequency associated with the wavelength λ. A practical form of Eq. (1.28) is

$$\lambda = \frac{1.2397 \cdot 10^{-10}}{E_\gamma(\text{MeV})}\ \text{cm} \tag{1.29}$$

Treating photons as particles is useful if they are emitted or absorbed by a nucleus. Here, we have

$$E_\gamma = h\nu = pc \tag{1.30}$$

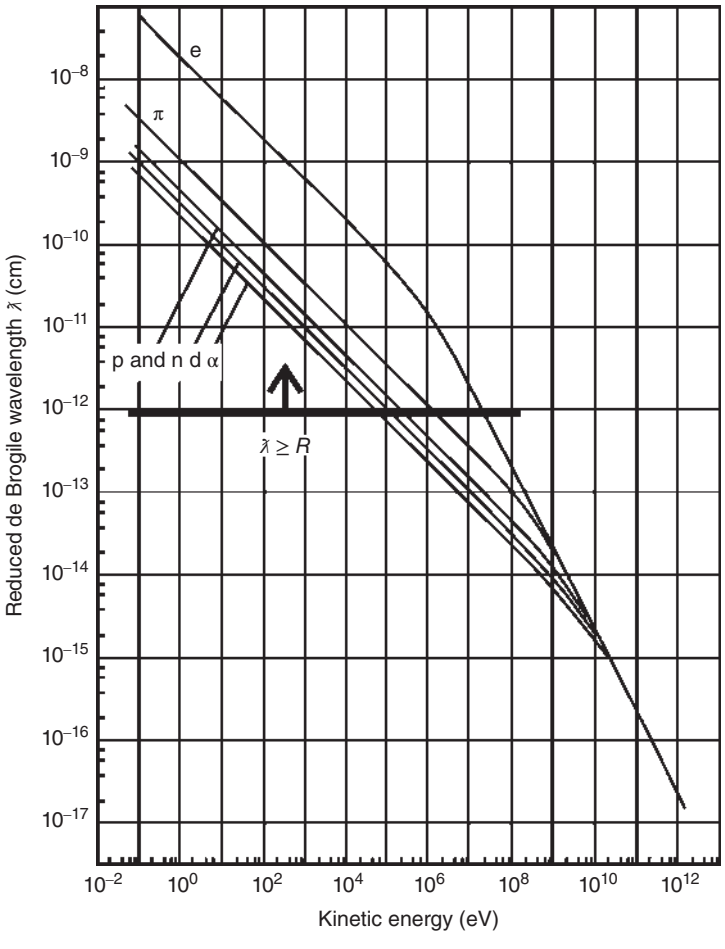

Figure 1.8 De Broglie wavelengths vs. particle kinetic energy for a few particles.

1.5.5 Heisenberg Uncertainty Principle

The Heisenberg uncertainty principle states that there are limits in our knowledge of the location of a particle and its momentum, that is,

$$\begin{aligned} \Delta p_x \cdot \Delta_x &\geq \hbar \\ \Delta p_y \cdot \Delta_y &\geq \hbar \\ \Delta p_z \cdot \Delta_z &\geq \hbar \\ \Delta E \cdot \Delta t &\geq \hbar \end{aligned} \tag{1.31}$$

where $\Delta p_i \cdot \Delta_i$ are the uncertainties in the ith component of the momentum and the location on the ith coordinate, while ΔE is the uncertainty in the total energy of the particle and Δt is its lifetime. These limits are not due to the limited resolution of our instruments; they are fundamental even with perfect instrumentation.

We will encounter a typical application in β decay, in Chapter 6, when it comes to counting the number of ways that the decay energy can be divided between the electron and the neutrino. There, with Eq. (1.31), we will see that the location and momentum of the electron and neutrino are somewhere within the volume of a spherical shell in phase space where the volume of the unit cell is h^3. The number of states of the electron with momentum between p_e and $p_e + dp_e$ is the volume of a spherical shell in momentum space $4\pi p_e^2 dp_e$. In addition, it must be found in space in a volume V. Together, this gives the phase volume $4\pi p_e^2 V dp_e$. The number of possibilities for the electron to find itself within this phase volume is obtained by normalizing the latter to the volume of the unit cell h^3, such that

$$dN_e = \frac{4\pi p_e^2 V dp_e}{h^3} \tag{1.32}$$

Similarly for the neutrino, the number of states of the free neutrino with momentum between p_ν and $p_\nu + dp_\nu$ in a volume V is

$$dN_\nu = \frac{4\pi p_\nu^2 V dp_\nu}{h^3} \tag{1.33}$$

and the total number of states $dn = dN_e\, dN_\nu$ is

$$dn = \frac{16\pi^2 V^2 p_e^2 p_\nu^2 dp_e dp_\nu}{h^6} \tag{1.34}$$

Equation (1.34) will be used in Chapter 6 to deduce the density of final states dn/dE_0 where n is the number of states per unit energy interval, the so-called statistical or phase space factor, which determines the shape of the electron momentum distribution.

1.5.6 The Standard Model of Particle Physics

Figure 1.9 depicts matter as consisting of six types, or "flavors" of quarks – called up, down, charm, strange, bottom, and top – and six light particles, the leptons, electron, muon, and tau and their three neutrino partners. The 12 particles are divided into three families of increasing mass, each family containing two quarks and two leptons. Their properties are included in Figure 1.9. Each particle also has an antiparticle of opposite electric charge. Our familiar protons and neutrons comprise three quarks: two ups and a down, and two downs and an up, respectively. The Standard Model also includes three of the four fundamental forces: the electromagnetic force and the weak and strong interactions. These are carried by exchange particles called intermediate vector bosons (or gauge bosons), that is, the photon, the W and Z bosons, and the exchange boson of the strong force, the gluon.

Particles can be classified as fermions and bosons. Fermions have antisymmetric wave functions and half-integer spins and obey the Pauli principle. Examples for fermions are neutrons, protons, and electrons. Bosons have symmetric wave functions and integer spins. They need not obey the Pauli principle. Examples are photons and the other gauge bosons. Particle groups such as fermions can be further divided into leptons and hadrons such as the proton and the neutron, the

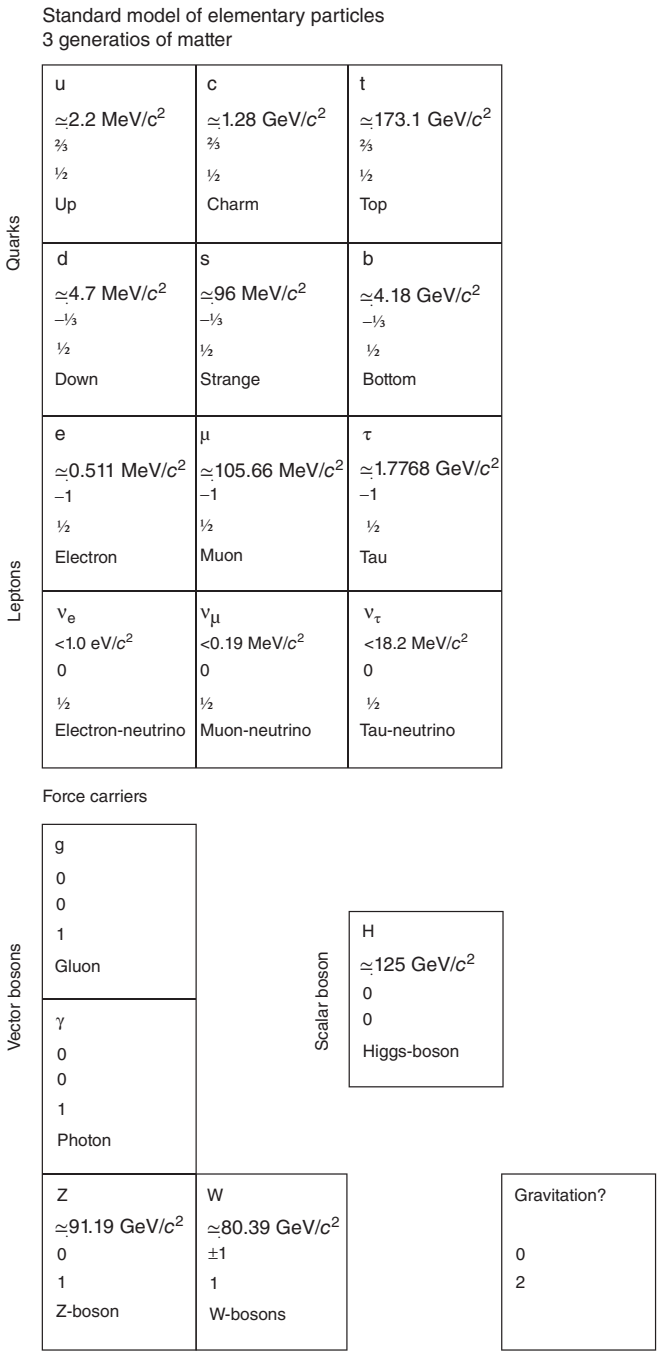

Figure 1.9 Fermions (quarks and leptons) and intermediate vector bosons and the scalar Higgs boson in the Standard Model. The bosons are the force carriers of the four fundamental interactions. Each particle is represented in one of the rectangular fields that represent, from top to bottom, the symbol of the particle, its mass (energy equivalent), its electric charge, its spin, and its name.

nucleons. Hadrons interact via the strong interaction, while leptons do not. Both particle types can interact via other forces such as the electromagnetic force. The neutrino partners of the leptons are electrically neutral and have very small rest masses. Their masses are a vital subject of current research, see Chapter 18.

The Higgs boson is an elementary particle within the standard model of elementary particle physics named after the British physicist Peter Higgs. It is electrically neutral, has spin 0, parity +1, a mass of c. 125 GeV/c^2, and disintegrates after c. 10^{-22} seconds into a bottom–antibottom pair, into two W bosons, or a tau–antitau pair, two Z bosons, or two photons, respectively. It belongs to the Higgs mechanism, a theory already suggested in the 1964 *Phys. Rev. Lett*., after which gauge bosons and fermions, except the Higgs boson itself, receive their mass by interaction with the omnipresent Higgs field.

These letters contained an explanation showing how mass could arise in local gauge theories. Gauge symmetries explain how the strong and electroweak forces arise, but such symmetries forbid vector boson mass terms. The authors showed how gauge symmetries could be spontaneously broken in such a way that the vector bosons of the theory acquire mass. These papers foresaw different aspects of this mechanism. The mechanism predicts the existence of a physical particle, known as the Higgs boson. In 2012, two experiments at the Large Hadron Collider (LHC) at CERN observed the Higgs boson, thus validating the prediction. The 2004 Wolf Prize was awarded to Englert, Brout, and Higgs for their contributions to the theories, and the 2010 APS Sakurai Prize was awarded to Englert, Brout, Higgs, Guralnik, Hagen, and Kibble. The Nobel Prize in Physics for 2013 was awarded to Englert and Higgs.

Since then, the building blocks of the standard model of particle physics let divide themselves into four groups: quarks, leptons, gauge bosons, and the Higgs boson. By the second quantization in physics, the apparent contrast between particles and waves is abolished; a particle is described as excited state of the corresponding quantum field. Thereafter, the Higgs boson corresponds to the quantum mechanical excitation of the Higgs field.

The Higgs boson, a scalar boson, is so important for particle physics because its existence related to the Higgs mechanism is predicted as a solid part of the standard model. The relevant gauge theory requires that the gauge bosons that realize the interaction between other particles are mass-less particles. Indeed, this is realized for the gauge boson of the electromagnetic interaction, the photon, and for the gauge bosons of the strong interaction, the gluons. For the gauge bosons of the weak interaction, the W- and Z-bosons, however, this is not the case. These have relatively large masses, which cause the small range, let the "weak interaction" appear so weak relatively to the electromagnetic interaction.

The Higgs mechanism shows that the mass-less W- and Z-bosons in the original equation of the theory appear in all further developed equations as particles of a certain mass. To this end, one has to let them interact with a further physical field, the Higgs field. This way, the Higgs mechanism allows one to come up with a fundamental gauge theory in which the electromagnetic and the weak interaction are unified to the electroweak interaction. By their interaction with the Higgs field, also the other masses of the elementary particles, properties that were seen before as originally

fixed, are now being interpreted as a consequence of a new kind of interaction. Only the origin of the Higgs mass itself withdraws itself from this point of view, it remains further unexplained.

Outside the standard model of elementary particles, Figure 1.9 contains another force carrier related to the gravitational force, the hypothetical gravitons, which have never been observed. The classical gravitational force as proposed by Isaac Newton is a radial field produced by mass

$$F = G \cdot \frac{m_1 \cdot m_2}{r^2} \tag{1.35}$$

with the gravitational constant $G = 6.674\,08 \cdot 10^{-11}\,\mathrm{m^3\,kg^{-1}\,s^{-2}}$. From this follows that the gravitational velocity on the earth's surface is the well-known earth gravitational acceleration $g = 9.81\,\mathrm{m\,s^{-2}}$. The ratio of the gravitational force to the electromagnetic force is 10^{-36}. Albert Einstein, in his "Allgemeine Relativitätstheorie," has seen this completely different: mass distorts space and time, the resulting gravitation is a distortion of the four-dimensional spacetime that also bends light as observed for the first time on the occasion of the total solar eclipse observed on 29 May 1919. Einstein also predicted that accelerated masses produce gravitational waves. A gravitational wave is a wave in the spacetime that is caused by accelerated mass. According to relativity theory, nothing can move faster than with the speed of light. Therefore, local changes in the gravitational field can affect distant locations only after a finite time. From this, Einstein in 1916 proposed the existence of gravitational waves. When crossing a section of space, certain distances get intermediately shrunk and stretched within the segment of space. This can be viewed as shrinkage and stretching of the space itself. As in the Newtonian gravitational theory, modifications of the sources of the gravitational field have consequences for the entire space without delay; it does not know gravitational waves. On 11 February 2016, researchers of the LIGO collaboration reported on first successful direct measurements of gravitational waves in September 2015, which were produced in the collision of two black holes. For this, in 2017, Rainer Weiss, Barry Barsh, and Kip Thome were awarded the Nobel prize in Physics.

In gravity, mass is what is the charge in electromagnetism. Other than for the electrical charge, a negative mass is not known. Therefore, dipoles of masses do not exist. Without dipoles, there cannot be dipole radiation. However, accelerated masses lead to quadrupolar radiation. The multipole expansion of the gravitational field of two circulating stars contains as lowest order the quadrupolar radiation. In a quantum field theoretical perspective in the gravitational interaction, the related gauge boson is the hypothetical graviton, a spin 2 particle in analogy to the spin 1 photon in the quantum electrodynamics. However, a formulation of the gravitation without contradictions on this basis is so far not available,

A final remark related to Figure 1.9 concerns the neutrinos, and in particular their masses. Section 18.5 of this textbook is devoted to the "Mystery of the Missing Solar Neutrinos" and its solution, which has provided a clue to physics beyond the Standard Model of particle physics. That is solid evidence for neutrino-mass fluctuations, i.e. a detector that is sensitive only to one neutrino flavor sees intensity fluctuations as a function of the mixing angle, the quadratic mass difference between

the fluctuating mass eigenstates, the distance between the source and the detector, and the neutrino kinetic energy.

In nuclear processes involving leptons, their number must be conserved. For example, in the decay of the free neutron

$$n \rightarrow p^+ + e^- + \bar{\nu}_e$$

the number of leptons on the left is zero, so the number of leptons on the right must be zero as well. We see that this is true if we assign a lepton number $L = 1$ to the electron and $L = -1$ to the $\bar{\nu}_e$ being an antiparticle. For the reaction

$$\bar{\nu}_e + p^+ \rightarrow e^+ + n + p^+ \rightarrow e^+ + n$$

which was instrumental in the discovery of the antineutrino by F. Reines and C. Cowan in 1959, $L = -1$ on both sides, and lepton conservation is fulfilled as well. As for leptons, there is a conservation law for baryons. To each baryon, we assign a baryon number $B = +1$ and $B = -1$ to each antibaryon. The total baryon number must be conserved. Take for example the reaction

$$p^+ + p^+ \rightarrow p^+ + n + \pi^+.$$

On both sides, we have $B = 2$ because the π^+ is a meson with $B = 0$. Since three quarks/antiquarks binding together make baryons/antibaryons, binding a quark with an antiquark forms mesons. The π^+ and π^- ($u\bar{d}$, $d\bar{u}$) mesons are important particles in nuclear chemistry. Mesons have integer spins and are bosons. Some mesons and baryons are listed in Table 1.3. All mesons are unstable with lifetimes up to about 10^{-8} seconds. The baryons are also unstable, with the exception of the neutron (lifetime 885.7 seconds) and the proton, which is considered to be stable.

A set of symmetries that are a sensitive probe of the Standard Model describe what happens if certain particle properties are reflected as though in a mirror. There is a charge mirror (C) changing particles into antiparticles of opposite charge, a parity mirror (P) changing the spin or handedness of a particle, and a time mirror (T) reversing a particle interaction, like rewinding a video. Surprisingly, these mirrors do not work perfectly. β particles emitted in the decay of ^{60}Co always spin in the same direction even if the spin of the cobalt nucleus is reversed. Cracks in the C and P mirrors (CP violation) also appear in the decay of exotic mesons – the kaon and the B meson. Connected to CP and T violation is the existence of permanent electric dipole moments (EDMs) in particles such as the neutron and atoms. EDMs are forbidden by P, T, and CP symmetries, but might be essential to explain the predominance of matter over antimatter in the Universe. Laboratories worldwide are actively searching for these EDMs. This is typical of high-precision measurements using nuclear particles at lowest energies to search for physics beyond the Standard Model. This way, nuclear chemists are actively involved in furthering our knowledge of fundamental interactions and symmetries.

1.5.7 Force Carriers

In Section 1.5.1, we introduced the force carriers, which are all bosons. In Section 1.5.5, we dealt with the Heisenberg uncertainty principle. Together, these

Table 1.3 Examples for hadrons.

Symbol	Quark composition	Mass (GeV/c^2)	Mean lifetime (s)
Mesons			
π^+	$\bar{d}u$	0.140	$\approx 2 \cdot 10^{-8}$
π^0	$\bar{u}u$ or $\bar{d}d$	0.135	$\approx 1 \cdot 10^{-16}$
π^-	$\bar{u}d$	0.140	$\approx 2 \cdot 10^{-8}$
ρ^+	$\bar{d}u$	0.776	
ρ^0	$u\bar{u}$ or $d\bar{d}$	0.770	
ρ^-	$\bar{u}d$	0.776	
K^-	$\bar{u}s$	0.493	$\approx 1 \cdot 10^{-8}$
K^0	$d\bar{s}$	0.498	$\approx 0.9 \cdot 10^{-10}$ to $5 \cdot 10^{-8}$
K^+	$u\bar{s}$	0.493	$\approx 1 \cdot 10^{-8}$
B^-	$u\bar{b}$	5.271	$\approx 1 \cdot 10^{-12}$
B^0	$d\bar{b}$	5.275	$\approx 1 \cdot 10^{-12}$
Baryons			
N	udd	0.9396	885.7
P	uud	0.9383	Stable
Λ	uds	1.116	$\approx 2 \cdot 10^{-10}$
Σ^+	uus	1.190	$\approx 1 \cdot 10^{-10}$
Σ^0	uds	1.192	$\approx 1 \cdot 10^{-14}$
Ξ^-	dss	1.322	$\approx 2 \cdot 10^{-10}$
Ω^-	sss	1.672	$\approx 1 \cdot 10^{-10}$

will allow us now to understand how force carriers work. For illustration, let us consider the electromagnetic force between two positively charged particles. The latter is caused by photons passing between them. One tends to think that the emission of a photon should change the energy of the emitter, but exchange of a force carrier does not. The solution is that the uncertainty principle allows the emission of virtual particles if such emission and absorption occur within a time Δt that is less than that allowed by the uncertainty principle, Eq. (1.31), saying that $\Delta t = \hbar/\Delta E$, where ΔE is the extent to which energy conservation is violated. We will come back to this in Chapter 6.

Reference

General and Historical

Geiger, H. and Marsden, E. (1913). The laws of deflexion of α particles through large angles. *Philos. Mag.* 25: 604.

Further Reading

General and Historical

Rutherford, E. and Soddy, F. (1902). The cause and nature of radioactivity I, II. *Philos. Mag.* 4 (370): 569.

Rutherford, E. and Soddy, F. (1903). Radioactive change. *Philos. Mag.* 5: 576.

Geiger, H. and Marsden, E. (1909). On a diffuse reflection of the α particle. *Proc. R. Soc. London, Ser. A* 82: 495.

Rutherford, E. (1911). The scattering of α and β particles by matter and the structure of the atom. *Philos. Mag.* 21: 669.

Moseley, H.G. (1913). The high-frequency spectra of the elements I. *Philos. Mag.* 26: 1024.

Moseley, H.G. (1914). The high-frequency spectra of the elements II. *Philos. Mag.* 27: 703.

Evans, R. (1955). *The Atomic Nucleus*. New York: McGraw-Hill.

Romer, A. (1964). *The Discovery of Radioactivity and Transmutation*. New York: Dover.

Harvey, B.G. (1965). *Nuclear Chemistry*. Englewood Cliffs, NJ: Prentice Hall.

Harvey, B.G. (1969). *Introduction to Nuclear Physics and Chemistry*, 2e. Englewood Cliffs, NJ: Prentice Hall.

Romer, A. (1970). *Radiochemistry and the Discovery of Isotopes*. New York: Dover.

Harvey, B.G. and Evans, R. (1971). *The Atomic Nucleus*. New York: McGraw-Hill.

Friedlander, G., Kennedy, J., Macias, E.S., and Miller, J.M. (1981). *Nuclear and Radiochemistry*, 3e. New York: Wiley.

Seaborg, G.T. and Loveland, W. (1982). *Nuclear Chemistry*. Stroudsberg, PA: Hutchinson-Ross.

Ehmann, W.D. and Vance, D.E. (1991). *Radiochemistry and Nuclear Methods of Analysis*. New York: Wiley.

Loveland, W. (1992). Nuclear chemistry. In: *Encyclopedia of Physical Science and Technology*, vol. 11. Orlando, FL: Academic Press.

Adloff, J.P., Lieser, K.H., and Stöcklin, G. (eds.) (1995) One hundred years after the discovery of radioactivity. *Radiochim. Acta* 70/71 (special issue).

Choppin, G.R., Liljenzin, J.O., and Rydberg, J. (2001). *Radiochemistry and Nuclear Chemistry*, 3e. Oxford: Butterworth–Heinemann.

Fényes, T. (2011). Basic properties of the atomic nucleus. In: *Handbook of Nuclear Chemistry*, 2e, vol. 1 (eds. A. Vértes, S. Nagy, Z. Klencsár, et al.), 39. Berlin: Springer-Verlag.

More Specialized

Einstein, A. (1918). Über Gravitationswellen, Königlich Preußische Akademie der Wissenschaften (Berlin), *Sitzungsberichte, Mitteilung vom 31.01.1918,* S. 154.

Englert, F. and Brout, R. (1964). Broken symmetry and the mass of gauge vector mesons. *Phys. Rev. Lett.* 13: 321.

Guralnik, G.S., Hagen, C.R., and Kibble, T.W.B. (1964). Global conservation laws and massless particles. *Phys. Rev. Lett.* 13: 585.

Higgs, P.W. (1964). Broken symmetries and the masses of gauge bosons. *Phys. Rev. Lett.* 13: 508.

Weinberg, S. (1967). A model of leptons. *Phys. Rev. Lett.* 19: 1264.

Salam, A. (1968). *Elementary Particle Theory* (ed. N. Svartholm), 367. Stockholm: Almquist and Wiksell.

Marmier, P. and Sheldon, E. (1969). *Physics of Nuclei and Particles*, vol. I and II. New York: Academic Press.

Glashow, S.L., Iliopoulos, J., and Maiani, L. (1970). Weak interactions with lepton-hadron symmetry. *Phys. Rev. D* 2: 1285.

Weinberg, S. (1972). Mixing angle in renormalizable theories of weak and electromagnetic interactions. *Phys. Rev. D* 5: 1962.

Segre, E. (1977). *Nuclei and Particles*, 2e. Reading, MA: Benjamin.

Musiol, G., Ranft, J., Reif, R., and Seeliger, D. (1988). *Kern- und Elementarteilchenphysik*. Weinheim: VCH Verlagsgesellschaft.

Frauenfelder, H. and Henley, E.M. (1991). *Subatomic Physics*, 2e. Englewood Cliffs, NJ: Prentice Hall.

Donoghue, J.F. (1994). *Dynamics of the Standard Model*. Cambridge: Cambridge University Press.

Weinberg, S. . *The Quantum Theory of Fields*. Cambridge: Cambridge University Press.1995, 2005

Heyde, K. (1999). *Basic Ideas and Concepts in Nuclear Physics*. Bristol: IOP Publishing.

Amsler, C. et al. (Particle Data Group) (2008). The review of particle physics. *Phys. Lett. B* 667: 1.

Horváth, D. (2011). The standard model of elementary particles. In: *Handbook of Nuclear Chemistry*, 2e, vol. 1 (eds. A. Vértes, S. Nagy, Z. Klencsár, et al.), 457. Berlin: Springer-Verlag.

ATLAS Collaboration (2012). Observation of a new particle in the search for the standard model Higgs Boson with the ATLAS detector at the LHC. *Phys. Lett. B* 716: 1.

CMS Collaboration (2012). Observation of a new boson at a mass of 125 GeV with the CMS experiment at LHC. *Phys. Lett. B* 716: 30.

Abbott, B.P. et al. (2016). Observation of gravitational waves from a 22-solar-mass binary black hole coalescence. *Phys. Rev. Lett.* 116: 241103.

2

Radioactivity in Nature

2.1 Discovery of Radioactivity

Radioactivity was discovered in 1896 in Paris by Antoine Henri Becquerel. He prepared crystals of uranium salts such as $K_2UO_2(SO_4)_2 \cdot 2H_2O$ and studied their phosphorescence (today we would call it fluorescence) after exposure to sunlight. On 20 February 1896, the potassium uranyl sulfate was placed on a photographic plate wrapped in tight black paper and then exposed to sunlight. Becquerel found that the phosphorescence acted on the plate even through an aluminum foil. When the plate was developed, the position of the uranium salt was clearly shown by the presence of dark spots. This experiment was reported to the Academy of Science on 24 February. A week later, Becquerel attempted to repeat the experiment. When the experiment was ready, he left it in a drawer of his desk because the weather was not sunny enough. After two days, on 26 and 27 February, Becquerel decided to start a new experiment. Before replacing the photographic plate, he developed the one that had been kept in the dark drawer in contact with the uranium. To his surprise, he found the same kind of dark spots but with an even greater intensity than when the exposure had lasted for a few hours in sunlight. Apparently, it was not necessary to irradiate the uranium salt by sunlight in order to darken the plate. The penetrating radiation was emitted spontaneously by the uranium. This key observation was reported at the Academy of Science on Monday, 2 March 1896. Another very important observation was that the "radiant activity" could render the air conducting and discharge an electroscope. Further, Becquerel found that the radiation was emitted by all types of uranium compounds and that the intensity was proportional to the mass of uranium. In a note of 23 March, he reported that phosphorescent compounds without uranium did not darken a photographic plate and that uranous sulfate, which is not phosphorescent, was blackening the plate. He also demonstrated that the radiation was independent of the physical state of the uranium and independent of whether the material was in molten, dissolved, or crystallized form. It was now clear to Becquerel that uranium itself produced the effect by the emission of penetrating radiation. In the last note in *Comptes rendues* of the year 1898, Henri Becquerel used for the first time the terms "uranic radiation" and "uranic rays."

Nuclear and Radiochemistry: Fundamentals and Applications,
Fourth Edition. Jens-Volker Kratz.

In 1898, Marie Sklodowska-Curie in France and Gerhardt C. Schmidt in Germany found independently that thorium compounds emitted an activity similar to that of uranium. Marie Curie and her husband Pierre Curie found that certain uranium minerals were more active than metallic uranium whose activity was used as a reference. The most important result was that pitchblende (*Pechblende*) was nearly four times more active than uranium. In a note by Marie Curie on this observation, we find the key sentence: "This fact is quite remarkable and suggests that these minerals may contain an element much more active than uranium." It is noteworthy that the research on radioactivity then turned from physics to chemistry. Neither Pierre nor Marie Curie was chemists. So, they hired Gustave Bémont to collaborate with them in the period from May to December 1898. The chemical analysis of pitchblende was neither particularly difficult nor innovative. The method followed the classical scheme of analysis given by Fresenius. However, the Curies were now able to follow the procedure by a new highly sensitive method involving the measurement of radioactivity of the element searched. In a biography of Pierre Curie published in 1924, Marie Curie explained

> The method we have used is a new one for chemical research based on radioactivity. (We can state today that this was the beginning of radiochemistry.) It consists of separations performed with the ordinary procedures of analytical chemistry and in the measurement of the radioactivity of all compounds separated. In this way, one can recognize the chemical character of the radioactive element sought. The latter is concentrated in fractions which become increasingly radioactive in the course of the separation.

The flow chart in Figure 2.1 shows the chemical separations which led to the discovery of polonium. The various steps were repeated and fractions with continuously increasing activities were isolated. Finally, a batch was obtained that was about 400 times more active than the metallic uranium. Shortly thereafter, another "new radioactive substance" was observed which behaved as "nearly pure barium." The Curies found that this substance could be enriched in the course of fractional crystallizations of barium chloride. The first hydrated chloride was 60 times more active than uranium. Upon dissolution in water followed by partial precipitation with alcohol, the solid was much more active than the solution. The Curies followed the progressive concentration until the activity of the chlorides was 900 times higher than that of uranium. A spectroscopic test was performed and several lines were observed that could not be assigned to any known element. The wavelength of the most intense line was 3814.8 Å (a recent value is 3814.42 Å). The intensity of the line increased with the radioactivity of the sample and the authors concluded "We think this is a very serious reason to attribute it to the radioactive part of our substance. The various reasons which we have enumerated lead us to think that the new radioactive substance contains a new element, to which we propose to give the name radium."

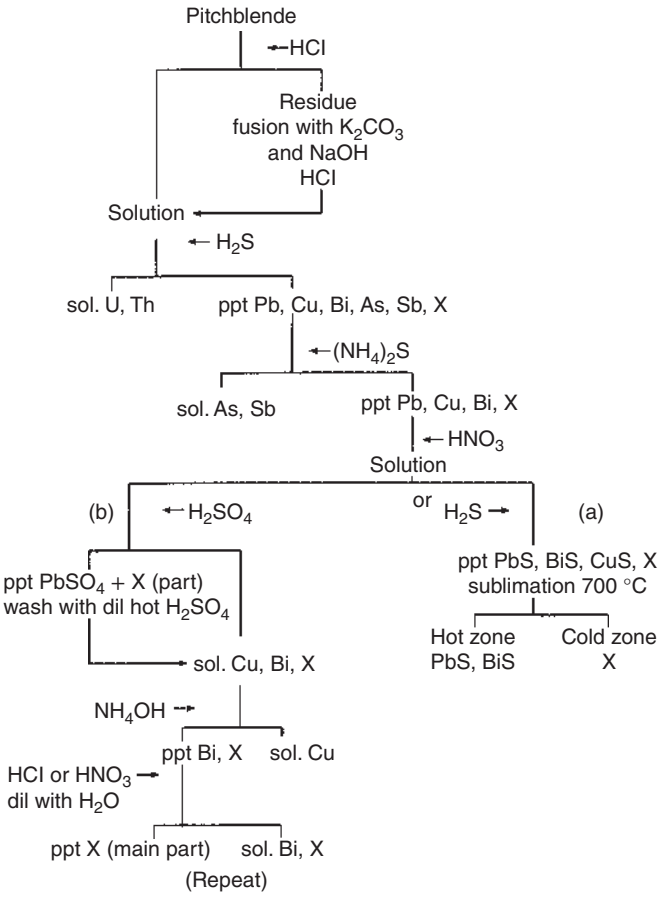

Figure 2.1 Chemical separation scheme that led to the discovery of the element X, polonium. This element was first coprecipitated with various sulfides and subsequently partially separated from bismuth and lead by sublimation (path [a]) or by an aqueous method based on the fractional precipitations of hydroxides (path [b]). Source: Adloff and MacCordick (1995), Figure 4 (p. 16)/De Gruyter.

Radioactivity, as far as we have discussed it, is a property of matter and is detected by various detectors, see Chapter 9. These detectors also indicate the presence of radiation in the absence of radioactive substances. If they are shielded by lead or other materials, the *counting rate* decreases appreciably. On the other hand, if the detectors are carried to greater heights in the atmosphere, the counting rate increases to values that are higher by a factor of about 12 at a height of 9000 m above ground level. This proves the presence of another kind of radiation that enters the atmosphere from outside. It is called cosmic radiation to distinguish it from the terrestrial radiation that is emitted by the radioactive matter on Earth. By cascades of spallation reactions (Chapter 12) with the gas molecules in the atmosphere, cosmic radiation produces a variety of particles (mesons, protons, neutrons, photons, electrons, positrons, muons, and neutrinos) as well as cosmogenic radionuclides (Chapter 18).

2.2 Radioactive Substances in Nature

Radioactive substances are widely distributed on Earth. Some are found in the atmosphere, but the majority are present in the lithosphere. Most important are the ores of uranium and thorium, including the radioactive decay products of uranium and thorium, and potassium salts. Uranium and thorium concentrations in granite are about 4 and 13 mg kg^{-1}, respectively, and the concentration of uranium in seawater is about 3 μg l^{-1}. Some uranium and thorium minerals are listed in Table 2.1. The most important uranium mineral is pitchblende (*Pechblende* in German). It was found, for example, in a formerly very rich silver mine in St. Joachimsthal in Bohemia (Jáchymov in Czech). Its occurrence in the form of black veins brought "bad luck" (*Pech* in German) to the miners at the end of the silver rush because, in the deeper formations where pitchblende appeared, silver could no longer be found. For instance, the content of U_3O_8 in pitchblende from St. Joachimsthal varied from 76% to over 80%. Other components such as Fe_2O_3, PbO, SiO_2, and CaO were present in amounts of several percent, and Bi_2O_3, As_2O_5, Na_2O, and S in amounts around 1%. The most important thorium mineral is monazite, which contains 0.1–15% Th. The measurement of natural radioactivity is an important tool for dating, for example, for the determination of the age of minerals (see Chapter 19).

Radioactive atoms with half-lives >1 day and that are found in nature are listed in Table 2.2. Table 2.2 shows that radioactivity is mainly observed with heavier

Table 2.1 Uranium and thorium minerals.

Mineral	Composition	Concentration of U (%)	Concentration of Th (%)	Deposits
Pitchblende	U_3O_8	60–90		Bohemia, Congo, Colorado (United States)
Becquerelite	$2UO_3 \cdot 3H_2O$	74		Bavaria, Congo
Uraninite		65–75	0.5–10	Japan, United States, Canada
Broeggerite	$UO_2 \cdot UO_3$	48–75	6–12	Norway
Cleveite		48–66	3.5–4.5	Norway, Japan, Texas (United States)
Carnotite	$K(UO_2)(VO_4) \cdot nH_2O$	45		United States, Congo, Russia, Australia
Casolite	$PbO \cdot UO_3 \cdot SiO_2 \cdot H_2O$	40		Congo
Liebigite	Carbonates of U and Ca	30		Austria, Russia
Thorianite	$(Th, U)O_2$	4–28	60–90	Sri Lanka, Madagascar
Thorite	$ThSiO_4 \cdot H_2O$	1–19	40–70	Norway, United States
Monazite	Phosphates of Th and rare earths		0.1–15	Brazil, India, Russia, Norway, Madagascar

Table 2.2 Naturally occurring radionuclides with half-lives >1 day (decay modes are explained in Chapter 1).

Radioactive species (radionuclides)	Half-life	Decay mode	Isotopic abundance (%)	Remarks
^{238}U	$4.468 \cdot 10^9$ yr	α, γ, e$^-$ (sf)	99.276	Uranium family
^{234}U	$2.455 \cdot 10^5$ yr	α, γ, e$^-$ (sf)	0.0055	$A = 4n + 2$
^{234}Th	24.1 d	β$^-$, γ, e$^-$		
^{230}Th (ionium)	$7.54 \cdot 10^4$ yr	α, γ (sf)		
^{226}Ra	1600 yr	α, γ		
^{222}Rn	3.825 d	α, γ		
^{210}Po	138.38 d	α, γ		
^{210}Bi	5.013 d	β$^-$, γ (α)		
^{210}Pb	22.3 yr	β$^-$, γ, e$^-$ (α)		
^{235}U	$7.038 \cdot 10^8$ yr	α, γ (sf)	0.720	Actinium family
^{231}Th	25.5 h	β$^-$, γ		$A = 4n + 3$
^{231}Pa	$3.276 \cdot 10^4$ yr	α, γ		
^{227}Th	18.72 d	α, γ, e$^-$		
^{227}Ac	21.773 yr	β$^-$, γ, e$^-$ (α)		
^{223}Ra	11.43 d	α, γ		
^{232}Th	$1.05 \cdot 10^{10}$ yr	α, γ, e$^-$ (sf)	100	Thorium family
^{228}Th	1.913 yr	α, γ, e$^-$		$A = 4n$
^{228}Ra	5.75 yr	β$^-$, γ, e$^-$		
^{224}Ra	3.66 d	α, γ		
^{190}Pt	$6.5 \cdot 10^{11}$ yr	α	0.013	Other naturally occurring radionuclides
^{186}Os	$2.0 \cdot 10^{15}$ yr	α	1.58	
^{187}Re	$5.0 \cdot 10^{10}$ yr	β$^-$	62.60	
^{174}Hf	$2.0 \cdot 10^{15}$ yr	A	0.16	
^{176}Lu	$3.8 \cdot 10^{10}$ yr	β$^-$, γ, e$^-$	2.60	
^{152}Gd	$1.1 \cdot 10^{14}$ yr	α	0.20	
^{148}Sm	$7 \cdot 10^{15}$ yr	α	11.3	
^{147}Sm	$1.06 \cdot 10^{11}$ yr	α	15.0	
^{144}Nd	$2.29 \cdot 10^{15}$ yr	α	23.80	
^{138}La	$1.05 \cdot 10^{11}$ yr	ε, β$^-$, γ	0.09	
^{123}Te	$1.24 \cdot 10^{13}$ yr	ε	0.908	
^{115}ln	$4.4 \cdot 10^{14}$ yr	β$^-$	95.7	
^{113}Cd	$9.3 \cdot 10^{15}$ yr	β$^-$	12.22	

(*Continued*)

Table 2.2 (Continued)

Radioactive species (radionuclides)	Half-life	Decay mode	Isotopic abundance (%)	Remarks
^{87}Rb	$4.80 \cdot 10^{10}$ yr	β^-	27.83	
^{40}K	$1.28 \cdot 10^{9}$ yr	β^-, ε, β^+, γ	0.0117	
^{14}C	5730 yr	β^-		Produced in the atmosphere by cosmic radiation
^{10}Be	$1.6 \cdot 10^{6}$ yr	β^-		
^{7}Be	53.3 d	ε, γ		
^{3}H	12.323 yr	β^-		

elements but is also observed for lighter ones such as ^{40}K and ^{87}Rb. ^{14}C, ^{10}Be, ^{7}Be, and ^{3}H (tritium) are produced in the atmosphere by cosmic radiation. The production of ^{14}C is about $2.2 \cdot 10^4$ atoms s^{-1} m^{-2} of the Earth's surface and that of ^{3}H about $2.5 \cdot 10^3$ atoms s^{-1} m^{-2}. Taking into account the radioactive decay and the residence time in the atmosphere, this results in a global inventory of about 63 tons of ^{14}C and about 3.5 kg of ^{3}H. A living man of 75 kg contains in his body an activity of 4000 Bq of ^{14}C and 3000 Bq of ^{40}K, 4 Bq of ^{228}Ra plus decay products, and 2 Bq of ^{226}Ra plus decay products. He inhales 220 000 Bq yr^{-1} of radon activity plus 320 000 Bq yr^{-1} of its decay products.

The measurement of the natural radioactivity of ^{14}C and ^{3}H is also used for dating. However, interference from the activities of these radionuclides in nuclear reactors and nuclear explosions has to be taken into account. The energy produced by the decay of natural radionuclides on Earth is assumed to contribute considerably to its temperature. In particular, the relatively high temperature gradient of about 30 °C per 1 km depth observed below the surface of the Earth is explained by radioactive decay taking place in the minerals, for example, in granite.

All elements found in natural sources with atomic number $Z > 83$ are radioactive. They belong to chains of successive decays and all the species in one such chain constitute a radioactive family or series of which three are observed in nature. In all of these *decay series*, only α and β^- decay are observed. The uranium series has ^{238}U as parent substance and ^{206}Pb as stable end product. Since the mass is changed by 4 units in α decay and does not change in β decay, the various mass numbers found in the family differ by multiples of 4 and a general formula for the mass numbers is $4n + 2$ where n is an integer. Figure 2.2 shows the members and transformations of the $4n + 2$ series. Thorium (^{232}Th) is the parent substance of the $4n$ or thorium series with ^{208}Pb as the stable end product. This series is shown in Figure 2.3. The $4n + 3$ or actinium series has ^{235}U (formerly known as actinouranium, AcU) as the parent and ^{207}Pb as the stable end product, see Figure 2.4. Actually, the historical names (UX_1, UX_2, …; mesothorium 1, $MsTh_1$, mesothorium 2, $MsTh_2$, …; radium A, RaA, …) have become obsolete, and the designation of the chemical element and the mass number are now standard.

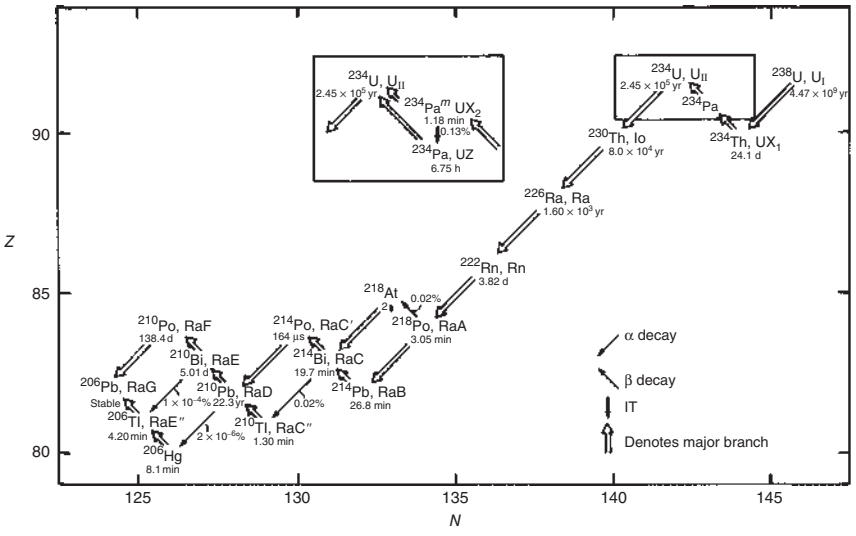

Figure 2.2 The uranium series. IT stands for isomeric transition. Source: Friedlander et al. (1981)/John Wiley & Sons.

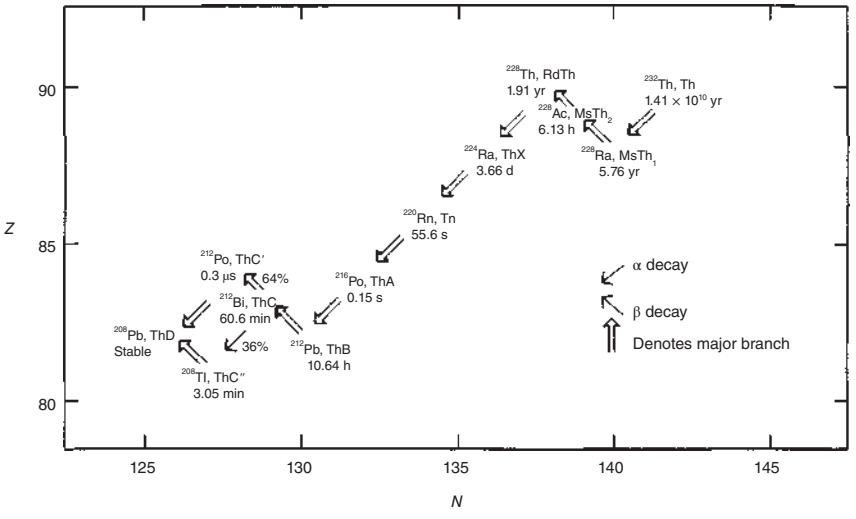

Figure 2.3 The thorium series. Source: Friedlander et al. (1981)/John Wiley & Sons.

The existence of branched decays in each of the three series should be noted. As more sensitive means for the detection of low-intensity branches became available, more branches were discovered: for example, the occurrence of astatine of mass number 219 in a $5 \cdot 10^{-3}\%$ branch of the actinium series was recognized as late as 1953. One radioactive decay series with mass numbers $4n + 1$ is missing in nature. Members of this family have been produced artificially by nuclear reactions. The parent substance of this series is ^{237}Np, *half-life* $2.144 \cdot 10^6$ years, and the stable end

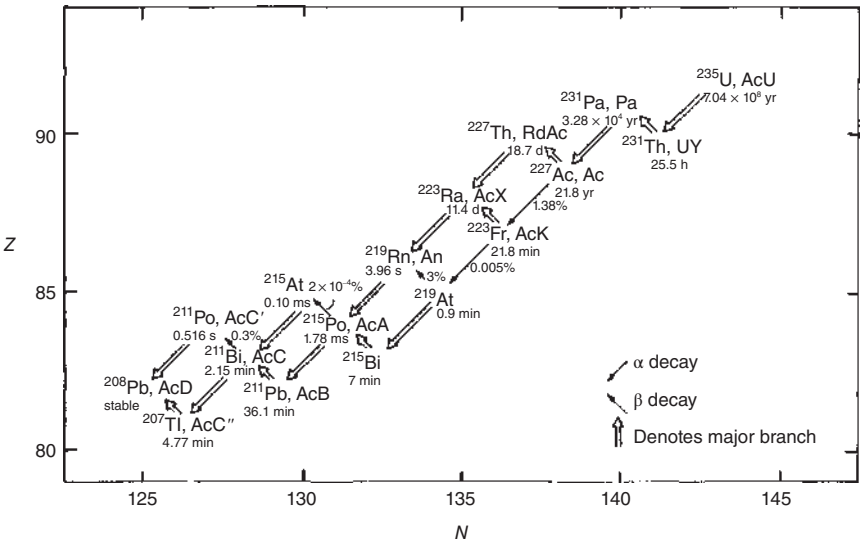

Figure 2.4 The actinium series. Source: Friedlander et al. (1981)/John Wiley & Sons.

product is ^{209}Bi. The neptunium series was probably present in nature for millions of years after the genesis of the elements some $4.5 \cdot 10^9$ years ago but decayed due to the comparatively short half-life of ^{237}Np.

One important result of the unraveling of the radioactive decay series was the conclusion reached, notably by Frederick Soddy, that different radioactive species of different mass numbers exist having identical chemical properties. This was the origin of the concept of *isotopes*, which we have already used implicitly in writing such symbols as ^{235}U and ^{238}U for uranium of mass numbers 235 and 238. Further discussion of isotopes is deferred until Section 3.2.

2.3 Nuclear Forensics

Soon after the discovery of nuclear fission (Hahn and Strassmann 1939), its potential as a powerful source of energy was realized. Within a few months, characteristic properties of the fission process were identified (Herrmann 1990), and in 1942, the first manmade self-sustaining chain reaction was achieved. As a result, nuclear research projects were initiated in the United States and in Germany. The German experiments on neutron multiplication in different uranium fuel geometries were conducted by two groups headed by W. Heisenberg at the Kaiser Wilhelm Institute for Physics (KWI), Berlin, and by K. Diebner of the Army Ordnance. The Heisenberg group with K. Wirtz used alternating layers of fuel and moderator, e.g. uranium plates, while the Diebner group used cubes. Heisenberg soon recognized the superior neutron economy of the cube design and followed this approach. The last experiment called B8 took place in March 1945 after the relocation of the KWI to Hechingen in southern Germany. Totally, 664 uranium metal cubes ($5\,\text{cm} \times 5\,\text{cm} \times 5\,\text{cm}$)

were used as fuel in a bath of heavy water (D_2O) as moderator resulting in a neutron multiplication factor of 6.7. From this, criticality was expected only for a reactor volume about 50% larger.

The majority of the uranium cubes was recovered in April 1945 by the ALSOS mission. Some 20 years later, several cubes (called "Heisenberg cubes" below) resurfaced in southern Germany. In 1998, one of them was sent to the Institute for Transuranium Elements (ITU) in Karlsruhe for nuclear forensic investigations (Mayer et al. 2015). Two years later, an uranium metal plate was retrieved at the Max Planck Institute for Nuclear Physics in Heidelberg. The material (called the "Wirtz plate") was attributed to the experiments by the Heisenberg–Wirtz group and was also sent to ITU for the same forensic investigations. These should address the following questions: What was the elemental composition of the material? When was the chemical separation of uranium from the ore? Was the uranium enriched in ^{235}U? Was the uranium exposed to some major neutron fluence? What is the origin of the uranium ore used for the production of the uranium metal?

To answer these questions, various characteristic parameters were determined, including the isotope ratios $^{230}Th/^{234}U$, $^{234,235,236}U/^{238}U$, $^{239}Pu/^{238}U$, and $^{87}Sr/^{86}Sr$, as well as the rare-earth elemental (REE) abundance pattern. Several of these data were also determined for a sample of ammonium diuranate (yellow cake) from the Hahn and Strassmann laboratory at KWI for Chemistry in Berlin (called "Hahn YC") and for uranium ore and ore concentrate (UOC) samples from Joachimsthal/Jáchimov and a mine in the former Belgian Congo as potential uranium sources.

The uranium metal samples investigated were 180 mg powder from an uranium cube, and several small pieces sawed off from the Wirtz plate. The samples were dissolved in nitric acid and chemically separated in order to concentrate the elements of interest (Sr, Th, U, and Pu) and analyzed by the following methods: thermal ionization mass spectrometry (TIMS) for $^{234,235,236,238}U$, accelerator mass spectrometry (AMS) for ^{236}U, multi-collector inductively coupled mass spectrometry (MC-ICP-MS) for strontium isotopes, sector-field ICP-MS for rare-earth elements and age determination, and resonance ionization mass spectrometry (RIMS) for ^{239}Pu.

Uranium isotope ratios were measured for the Heisenberg cube, the Wirtz plate, and the Hahn YC sample. The $^{235}U/^{238}U$ abundance ratios agreed well and corresponded to the natural value, i.e. samples were not enriched in ^{235}U. The isotopic composition of minor constituents (e.g. Sr) in uranium ores provides clues as to the geolocation of the processed natural uranium. Typically, a fraction of the minor constituents passes through mineral processing into the product material with its original isotopic composition. The $^{87}Sr/^{86}Sr$ ratios of the Heisenberg cube, the Wirtz plate, and the Hahn YC samples were 0.7037(33), 0.7078(10), and 0.7071(30), respectively, and agreed within experimental uncertainty. The $^{87}Sr/^{86}Sr$ value for the Joachimsthal ore was in the range between 0.703 and 0.707, whereas the value from the former Belgian Congo was higher, 0.711 01(8). The REE abundances for the uranium metal samples and the Hahn YC were measured in comparison to the ore samples from Joachimsthal and from the former Belgian Congo. The uranium metal samples, the Joachimsthal ore, and the Hahn YC had similar REE

patterns (pronounced Eu anomaly and lower concentrations toward the heavier REE), whereas the pattern from the former Belgian Congo was distinctly different (bell-shaped curve, no Eu anomaly). This is strong evidence that the uranium ore used for the production of the Heisenberg cube, the Wirtz plate, and the Hahn YC was mined in the Joachimsthal region.

^{236}U and ^{239}Pu are produced in reactor systems through neutron capture by ^{235}U and ^{238}U. As the ^{236}U abundances of the Heisenberg cube and the Wirtz plate were below the TIMS detection limit, small samples were measured by AMS at ANU, Canberra, and at UW, Vienna. The ^{236}U/^{238}U ratios (Table 2.3) are on the order of 10^{-10} for the cube, the plate, and the Hahn YC. The ratios are in the range typical for uranium ores between 10^{-12} and $3 \cdot 10^{-10}$. The ratios in the uranium metals and the Hahn YC indicate that ^{236}U is of natural origin.

The ^{239}Pu abundances were measured by RIMS because this method has a higher sensitivity than TIMS. The ^{239}Pu/U ratios (Table 2.3) of the cube and the plate are in excellent agreement in the range of $(1–2) \cdot 10^{-14}$.

The Joachimsthal uranium ore sample has a ^{239}Pu/U ratio of c. 10^{-13}, which is six times higher than that of the metal samples and of the same order as the ^{239}Pu/U ratios in natural uranium ores. For metal production, the uranium material was purified from decay products of uranium including thorium. It can be assumed that in the purification process, a large fraction of the plutonium was removed together with thorium, provided it was in the tetravalent state.

The age of the uranium materials, determined from the measured ^{230}Th/^{234}U ratio, reflects the time when the last chemical treatment of uranium (separation of impurities and decay products) was performed. For metal samples this will be the date of casting. In that sense, the Heisenberg cubes were produced in the second half of 1943, while the Wirtz plate was produced some three years earlier. This confirms the authenticity of the two uranium metals being used in German nuclear power projects in the early 1940s. The isotopes ^{236}U and ^{239}Pu were used as neutron fluence

Table 2.3 ^{236}U/^{238}U isotope abundance ratios and ^{239}Pu/U concentrations (g/g U) for various samples as determined by AMS and by RIMS.

Sample	^{236}U/^{238}U ($\times 10^{-10}$)	g ^{239}Pu/g U ($\times 10^{-14}$)
Heisenberg cube	0.91 ± 0.05[a)]	1.6 ± 0.8[c)]
	1.00 ± 0.04[b)]	
Wirtz plate	1.10 ± 0.05[a)]	1.4 ± 0.7[c)]
	1.11 ± 0.03[b)]	
Hahn YC	1.02 ± 0.03[b)]	
Joachimsthal ore		8.5 ± 2.8[c)]

The AMS and RIMS data are average values of two to six independent measurements.
a) Data from ANU, Canberra.
b) Data from UW, Vienna.
c) Data from UM, Mainz.
Source: Data from ANU, Canberra, UW, Vienna and UM, Mainz.

monitors. The measured abundances are consistent with natural values and do not indicate a major contribution due to a neutron fluence during reactor experiments.

References

General and Historical

Adloff, J.P. and MacCordick, H.J. (1995). The dawn of radiochemistry. *Radiochim. Acta* 70/71: 13.

Friedlander, G., Kennedy, J.W., Macias, E.S., and Miller, J.M. (1981). *Nuclear and Radiochemistry*, 3e. New York: Wiley.

Hahn, O. and Strassmann, F. (1939). Über den Nachweis und das Verhalten der bei der Bestrahlung des Urans mittels Neutronen entstehenden Erdalkalimetalle. *Naturwissenschaften* 27: 11.

Herrmann, G. (1990). 50 years ago: from the "transuranics" to "nuclear fission". *Angew. Chem. Int. Ed. Engl.* 29: 481.

Mayer, K., Wallenius, M., Lützenkirchen, K. et al. (2015). Uranium from German nuclear power projects of the 1940s – a nuclear forensic investigation. *Angew. Chem. Int. Ed.* 54: 13452.

Further Reading

General and Historical

Becquerel, H. (1896). Sur les radiations émises par phosphorescence. *C.R. Acad. Sci. Paris* 122: 420.

Becquerel, H. (1896). Sur les radiations invisibles émises par les corps phosphorescents. *C.R. Acad. Sci. Paris* 122: 501.

Becquerel, H. (1896). Sur quelques propriétés nouvelles des radiations invisibles émises par divers corps phosphorescents. *C.R. Acad. Sci. Paris* 122: 559.

Becquerel, H. (1896). Sur les radiations invisibles émises par les sels d'uranium. *C.R. Acad. Sci. Paris* 122: 689.

Becquerel, H. (1896). Émission de radiations nouvelles par l'uranium métallique. *C.R. Acad. Sci. Paris* 122: 1086.

Becquerel, H. (1896). Sur diverses propriétés des rayons uraniques. *C.R. Acad. Sci. Paris* 123: 855.

Curie, P. and Curie, M. (1898). Sur une substance nouvelle radio-active contenue dans la Pechblende. *C.R. Acad. Sci. Paris* 127: 175.

Curie, P., Curie, M., and Bémont, G. (1898). Sur une nouvelle substance fortement radioactive, contenue dans la pechblende. *C.R. Acad. Sci. Paris* 127: 1215.

Schmidt, G.C. (1898). Sur les radiations émises par le thorium et ces composés. *C.R. Acad. Sci. Paris* 126: 1264.

Schmidt, G.C. (1898). Über die vom Thorium und den Thorverbindungen ausgehende Strahlung. *Verh. Dtsch. Phys. Ges. Berlin* 17: 14.

Sklodowska-Curie, M. (1898). Rayons émis par les composés de l'uranium et du thorium. *C.R. Acad. Sci. Paris* 126: 1101.

Curie, P. (1910). *Traité de Radioactivité*. Paris: Gauthier-Villars.
Hevesy, G. and Paneth, F. (1931). *Lehrbuch der Radioaktivität*, 2e. Leipzig: Akademie Verlag.
Joliot, I. (1955). *Les carnets de laboratoire de la découverte du polonium et du radium*. Appendix to Pierre Curie, by Marie Curie. Paris: Éditions de Noël.
Ivimey, A. (1980). *Marie Curie: Pioneer of the Atomic Age*. New York: Praeger.
Ronneau, C. (1990). Radioactivity: a natural phenomenon. *Chem. Educ.* 66: 736.
Genet, M. (1995). The discovery of uranic rays: a short step for Henri Becquerel but a giant step for science. *Radiochim. Acta* 70/71: 3.
Newton, G.W.A. (1995). History of the unraveling of the natural decay series. *Radiochim. Acta* 70/71: 31.
Zeman, A. and Benes, P. (1995). St. Joachimsthal mines and their importance for the early history of radioactivity. *Radiochim. Acta* 70/71: 23.
Griffin, H.C. (2011). Natural radioactive decay chains. In: *Handbook of Nuclear Chemistry*, 2e, vol. 2 (eds. A. Vertés, S. Nagy, Z. Klencsár, et al.), 667. Berlin: Springer-Verlag.

More Specialized

Flügge, S. (ed.) (1961). *Kosmische Strahlung, Handbuch der Physik*, vol. XLV, 1/1. Berlin: Springer-Verlag.
Gmelin, L. (1979). *Gmelin's Handbook of Inorganic Chemistry*, Uranium, Supplement, 8e, vol. A1. Berlin: Springer-Verlag.
Gmelin, L. (1990). *Gmelin's Handbook of Inorganic Chemistry*, Thorium, Supplement, 8e, vol. A1. Berlin: Springer-Verlag.
Friedlander, G. and Herrmann, G. (2011). Nuclear and radiochemistry: the first 100 years. In: *Handbook of Nuclear Chemistry*, 2e, vol. 1 (eds. A. Vértes, S. Nagy, Z. Klencsár, et al.), 3. Berlin: Springer-Verlag.

3

Radioelements and Radioisotopes and Their Atomic Masses

3.1 Periodic Table of the Elements

The periodic table of the elements was invented in 1869 by Lothar Meyer and independently by Dmitri Mendeleev by ordering the elements in increasing atomic number and according to their chemical likeliness. The cover of this book shows the arrangement of the known elements in 7 horizontal periods and 18 vertical groups as recommended by the International Union of Pure and Applied Chemistry (IUPAC), Commission on the Nomenclature of Inorganic Chemistry. The periodic table initiated the discovery of new elements which can be divided into three phases, overlapping chronologically:

a. *Discovery of stable elements*: The last of this group were hafnium (discovered by D. Coster and G.C. Hevesy in 1922) and rhenium (discovered by I. and W. Noddack in 1925). With these, the group of stable elements increased to 81 (atomic numbers 1 [hydrogen] to 83 [bismuth] with the exception of elements 43 and 61). In addition, there are the unstable elements 90 (thorium) and 92 (uranium).
b. *Discovery of naturally occurring unstable elements*: Uranium had already been discovered in 1789 by Martin Klaproth and thorium in 1828 by Jöns Jakob Berzelius. The investigation of the radioactive decay of these elements initiated by Marie and Pierre Curie led to the discovery of elements with atomic numbers 84 (Po = polonium), 86 (Rn = radon), 87 (Fr = francium), 88 (Ra = radium), 89 (Ac = actinium), and 91 (Pa = protactinium).
c. *Discovery of artificial elements*: The missing elements 43 (Tc = technetium) and 61 (Pm = promethium) were synthesized in nuclear reactions. Element 85 (At = astatine) was also first produced in a nuclear reaction and later was found in the decay chains of uranium and thorium. The discovery of the transuranic elements (Chapter 17) is of special interest because this brought about a considerable extension of the periodic table. At present, 26 human-made transuranic elements are known, beginning with element 93 (Np = neptunium), then 94 (Pu = plutonium), 95 (Am = americium), and so on, ending, at this time, with 118 (Og = oganesson). According to the IUPAC, the elements beyond 112 have been fully authenticated in 2016. The first transuranic elements were discovered at Berkeley, California, by E. McMillan and P.H. Abelson (neptunium) followed

Nuclear and Radiochemistry: Fundamentals and Applications,
Fourth Edition. Jens-Volker Kratz.

by a series of discoveries by G.T. Seaborg and his group. Controversial claims for the discovery of elements 104–106 were put forward by Dubna, in Russia, and by the Berkeley group for more than 20 years. Syntheses of "superheavy elements" 107–112 were first accomplished at the GSI Helmholtz Center for Heavy-Ion Research in Darmstadt, Germany; those of element 113 at RIKEN, Japan; and claims for the discovery of elements 114–118 come from Dubna, Russia. With increasing atomic number, the nuclear stability continues to decrease giving rise to decreasing half-lives on the order of milliseconds. Locations of higher stability for deformed nuclei have been theoretically predicted and verified experimentally near atomic number $Z = 108$ and neutron number $N = 162$; however, the location of the long-predicted "island of stability" of spherical superheavy elements has long been an open question.

The radioactive elements mentioned under phases (b) and (c) are called *radioelements*. They exist only in the form of unstable nuclei and comprise the elements 43, 61, and all the elements with atomic numbers $Z \geq 84$. Thus, at this time, 38 out of 118 elements, that is, one-third of the known elements, are radioelements. This is one of the reasons why nuclear chemistry is an important branch of the natural sciences.

The radioelements were probably produced in the genesis of the heavy elements in nature and were present on the Earth in its early history. The age of the Earth is estimated to be close to $4.5 \cdot 10^9$ years. During this time, elements of shorter half-lives disappeared by nuclear decay. Radioelements with sufficiently long half-lives, such as U and Th, survived and are called primordial radioelements.

3.2 Isotopes and the Chart of Nuclides

The investigation of the natural radioelements between uranium and thallium (group b) led to the realization that the elements must exist in various forms differing from each other in their mass and their nuclear properties. In fact, about 40 kinds of atoms with different decay properties were identified, for which at most 12 places in the periodic table were available based on their chemical properties. The problem was solved in 1913 by F. Soddy who proposed to put several kinds of atoms in the same place in the periodic table. This led to the term isotope, which means "in the same place." Isotopes differ in their mass, but their chemical properties are the same if the very small influence of the mass on the chemical behavior is neglected. In 1919, F.C. Aston, who developed precision mass spectrometry, showed that most elements consist of isotopic mixtures except for a few cases such as Be, F, Na, Al, P, I, and Cs. The atomic weights of the isotopes were found to be close to a whole number, the mass number. This "whole-number rule" led to the revival of Prout's hypothesis formulated a hundred years earlier, stating that all elements are built from hydrogen. However, difficulties with this hypothesis soon arose. A nucleus with mass number A and atomic number Z, following this idea, has A protons in the nucleus giving it the mass number A and $(A - Z)$ electrons in the nucleus giving it Z as the atomic number. For example, ^{14}N has 14 protons and 7 electrons in the

nucleus giving it the atomic number 7. In order to be bound in the nucleus, the de Broglie wavelength of the electron must not be larger than the dimension of the nucleus. The kinetic energy, however, associated with such values of λ is one order of magnitude higher than the known energy of β-particles. This prompted a suggestion by Rutherford: part of the protons in the nucleus bind an electron and are present as a "neutron." The neutron was indeed discovered in 1932 by James Chadwick who observed very penetrating radiation when bombarding light target nuclei such as Be and B with α-particles. The penetrating radiation knocked protons out of paraffin with kinetic energies compatible with the supposition, consistent with all observations, that the ingoing particles were neutral particles with the mass of the proton. We know today that (α, n) reactions were taking place in the Be and B targets and, that the mass of the neutron is roughly 1.0008 times larger than that of the proton, resulting in the β^- decay of the free neutron. Werner Heisenberg interpreted Chadwick's results as follows. The neutron is not the bound state of an electron with a proton, but a neutral fermion as another constituent of atomic nuclei besides the proton. Thus, the proton–neutron model of atomic nuclei was born.

The various kinds of atoms differing from each other by their atomic number and by their mass number are called *nuclides*. Unstable, radioactive nuclides are radionuclides, and the terms radioelements for unstable elements and radionuclides for unstable nuclides are analogous. For proper identification, the chemical symbol, the atomic number, and the mass number are used. For example (cf. Table 3.1), ${}^{14}_{6}C_{8}$ is carbon with mass number $A = 14$, neutron number $N = 8$, and atomic number $Z = 6$. The atomic number can be omitted because it is defined by the chemical symbol. The neutron number $N = A - Z$. It is evident that the periodic table of the elements does not have room to include information on all the isotopes of the elements. For that purpose, the chart of nuclides was designed based on the proton–neutron model of the atomic nuclei. The number of nucleons in the nucleus is equal to the mass number, and the number of protons is equal to the atomic number. By combinations of various numbers of protons and neutrons, the atomic nuclei are formed, as shown in Table 3.1 for light nuclei. Stable nuclei in this mass region prefer equal numbers of protons and neutrons. The transfer of this information to a diagram in which the number of protons is plotted as ordinate and the number of neutrons as abscissa gives the chart of nuclides, the first part of which is shown in Figure 3.1. A modern version of the chart of nuclides (Karlsruher Nuklidkarte 2015) contains more than 4000 experimentally observed ground states and isomers; their number was continuously increasing through research at accelerators and radioactive beam facilities, see Section 11.5. About 340 nuclides are found in nature and may be subdivided into 4 groups: (i) 258 are indisputably stable; (ii) for 25 nuclides with $Z < 80$ radioactive decay has been reported but not confirmed for 7 of these due to extremely long half-lives; (iii) the main sources of radioactivity comprising 46 nuclides are members of the natural decay chains of ^{238}U, ^{235}U, and ^{232}Th; and (iv) several radionuclides are continuously produced by nuclear reactions of cosmic radiation with the Earth's atmosphere, such as ^{14}C, ^{10}Be, ^{7}Be, and ^{3}H. Radionuclides present in nature in extremely low concentrations, such as ^{244}Pu and its decay products as well as

Table 3.1 Proton–neutron model of some light nuclei (Z = number of protons, N = number of neutrons); (u) is the atomic mass unit. The atomic weight of elements containing several stable nuclides is obtained by adding their atomic masses weighed with their natural abundances.

Z	N	Nuclide	Atomic mass (u)	Natural abundance (%)	Atomic weight (u)	Remarks
1	0	^{1}H	1.007 825	99.985	1.007 97	Stable
1	1	^{2}H (D)	2.014 102	0.0155		Stable
1	2	^{3}H (T)	3.016 049			Unstable
2	1	^{3}He	3.016 030	0.000 137	4.002 60	Stable
2	2	^{4}He	4.002 603	99.999 863		Stable
2	3	^{5}He				Unstable
2	4	^{6}He	6.018 891			Unstable
3	2	^{5}Li				Unstable
3	3	^{6}Li	6.015 123	7.5	6.940	Stable
3	4	^{7}Li	7.016 004	92.5		Stable
3	5	^{8}Li	8.022 487			Unstable
3	6	^{9}Li	9.026 790			Unstable
4	3	^{7}Be	7.016 930			Unstable
4	4	^{8}Be	8.005 305			Unstable
4	5	^{9}Be	9.012 183	100.00	9.012 18	Stable
4	6	^{10}Be	10.013 535			Unstable
4	7	^{11}Be	11.021 660			Unstable
5	3	^{8}B	8.024 608			Unstable
5	4	^{9}B				Unstable
5	5	^{10}B	10.012 938	19.9	10.811	Stable
5	6	^{11}B	11.009 305	80.1		Stable
5	7	^{12}B	12.014 353			Unstable
5	8	^{13}B	13.017 780			Unstable
6	4	^{10}C	10.016 858			Unstable
6	5	^{11}C	11.011 433			Unstable
6	6	^{12}C	12.000 000	98.892	12.011 2	Stable
6	7	^{13}C	13.003 354	1.108		Stable
6	8	^{14}C	14.003 242			Unstable
6	9	^{15}C	15.010 599			Unstable
6	10	^{16}C	16.014 700			Unstable
7	5	^{12}N	12.018 613			Unstable
7	6	^{13}N	13.005 739			Unstable
7	7	^{14}N	14.003 074	99.635	14.006 7	Stable
7	8	^{15}N	15.000 108	0.365		Stable
7	9	^{16}N	16.006 099			Unstable
7	10	^{17}N	17.008 449			Unstable

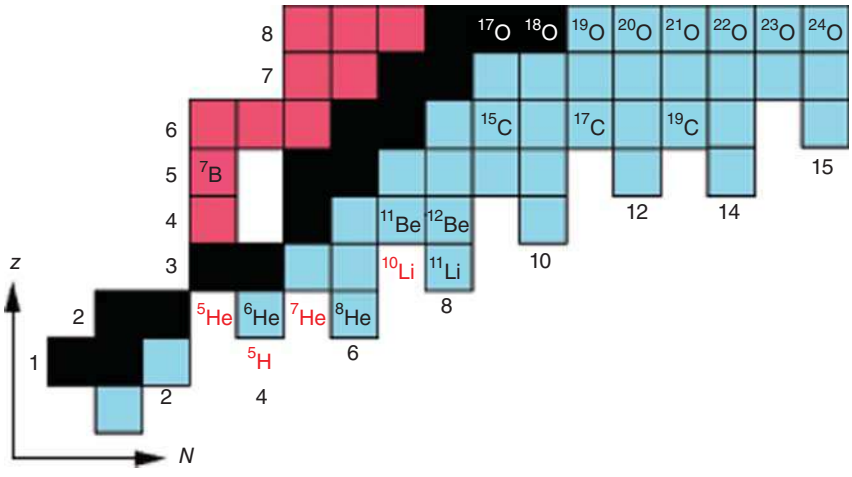

Figure 3.1 Lower part of the chart of nuclides showing the region up to the oxygen isotopes. The nuclei labeled in red are unstable nuclei existing only as short-lived resonances.

products of spontaneous fission of U and Th, are not considered in this list. Radionuclides existing from the beginning, that is, since the creation of the elements, are called primordial radionuclides. They comprise the radionuclides of group (ii) and ^{238}U, ^{235}U, ^{232}Th, and ^{244}Pu.

The following types of nuclides are distinguished:

Isotopes: equal Z

Isotones: equal N

Isobars: equal A.

The positions of these types of nuclides in the chart of nuclides are shown in Figure 3.2. For certain nuclides, different physical properties (half-lives, decay modes) are observed. These are due to different energetic states: the ground state and one or more metastable excited states of the same nuclide. These excited states are called isomeric states. Because the decay of the isomer to the ground state is "forbidden" by selection rules, isomers have their own half-lives varying from milliseconds to years. The isomers either decay into the ground state by emission of a γ-ray (isomeric transition, IT) or decay to other daughter nuclides by emission of α- or β-particles. Isomeric states are denoted by the suffix m behind the mass number A. For instance, ^{60m}Co (10.5 minutes) is an isomeric state above the ground state ^{60}Co (5.27 years). Sometimes, the ground state is explicitly denoted by the suffix g, for example, ^{60g}Co. About 400 nuclides are known to exist in isomeric states. They exist most abundantly in the vicinity of closed nucleon shells, see Section 3.4.

For light elements, as mentioned above, $N \approx Z$ is preferred. With increasing Z, however, an increasing excess of neutrons is necessary for stable nuclei. $N - Z$ is a measure for the neutron excess. For ^{4}He, the neutron excess is zero. It is 3 for ^{45}Sc, 11 for ^{89}Y, 25 for ^{139}La, and 43 for ^{209}Bi. Thus, in the chart of nuclides, the stable

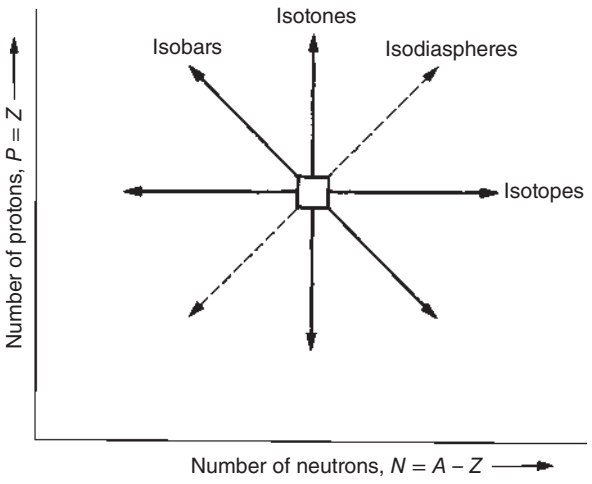

Figure 3.2 Isotopes, isotones, and isobars in the chart of nuclides.

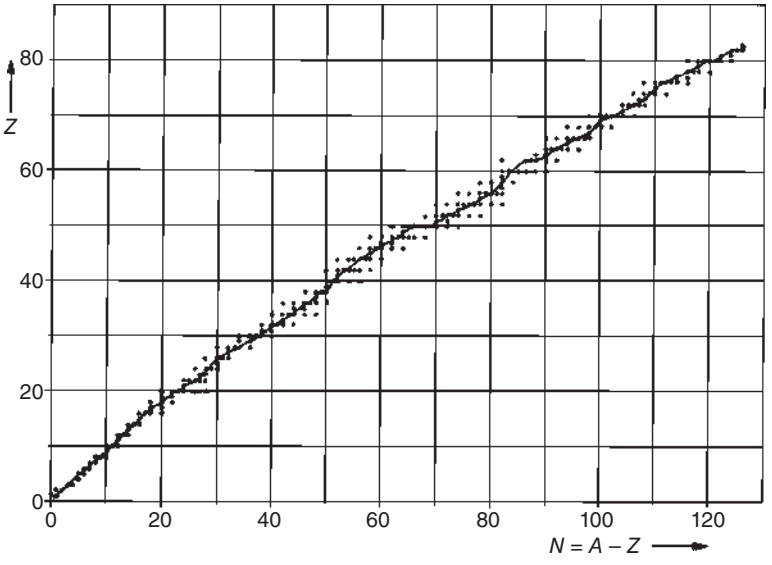

Figure 3.3 Stable nuclides and the line of β-stability.

nuclides define a mean line starting from the origin with a slope of 1 and bending smoothly to the abscissa by the increasing neutron excess with increasing Z. This is called the line of β-stability (Figure 3.3).

3.3 Nuclide Masses and Binding Energies

The mass number A of a nuclide is equal to the number of nucleons and is always an integer. The nuclide masses, on the other hand, are the absolute masses of the nuclides in atomic mass units u, and the atomic weight of an element is obtained by

adding the atomic masses of its stable isotopes by weighing them with their natural abundances.

One atomic mass unit u is equal to 1/12 of the atomic mass of the isotope ^{12}C ($M(^{12}\mathrm{C}) = 12.000\,000$ u). Nuclide masses are atomic masses and include the mass of the electrons of the neutral atom: $M =$ mass of the nucleus $+ Zm_e$, where Z is the atomic number and m_e is the mass of an electron in atomic mass units. One atomic mass unit u is $1.660\,538\,86(28) \cdot 10^{-27}$ kg. The electron rest mass is $m_e = 5.485\,799\,094\,5(24) \cdot 10^{-4}$ u, that of the hydrogen atom $M_H = 1.007\,825\,036(11)$ u, and that of the neutron $M_n = 1.008\,664\,915\,60(55)$ u. These determinations are derived from measurements by atomic mass spectrometry, see Section 3.5; hence the use of atomic masses.

According to Einstein's relation $E = mc^2$, the rest mass of a particle can be transformed into an energy equivalent by multiplying its mass by the square of the speed of light. Since $1\text{ u} = 1.660\,538\,86 \cdot 10^{-24}$ g and $c = 2.997\,925 \cdot 10^8$ m s^{-1} (30 cm ns^{-1} as an intuitive quantity), 1 u is equivalent to $1.492\,417\,89 \cdot 10^{-10}$ J. The energy unit used in nuclear science is the eV (energy gained by an electron passing in vacuo a potential of 1 V; $1\text{ eV} = 1.602\,176\,53(14) \cdot 10^{-19}$ J), keV, or MeV. Thus, the energy equivalent of an atomic mass unit is

$$1\text{ u} = 931.494\,043(80)\text{ MeV} \tag{3.1}$$

For the atomic mass of a nuclide, we have

$$M(Z,N) = ZM_H + NM_n - \delta M \tag{3.2}$$

where δM is the mass defect. It is due to the fact that the binding energy E_B of the nucleons in the nucleus results in a decrease in its mass compared to the sum of the masses of its constituents. The effect of the binding energy of the electrons is very small with respect to the binding energy of the nucleons and can be neglected. In order for a nucleus to be bound, that is, to have a positive binding energy, its mass must be smaller than the sum of the masses of its constituents. This is illustrated with the mass of ^{4}He:

$^4\mathrm{He} = 2\,^1\mathrm{H}$ atoms + 2 neutrons

(H)	2·1.0078 … u
(n)	2·1.0086 … u
	4.032 980 1 u
$M(^4\mathrm{He})$	4.002 603 3 u
δM	0.030 376 8 u

If the mass defect δM is multiplied by 931.5 MeV, we obtain the binding energy $E_B(^4\mathrm{He}) = 0.030\,376\,8 \cdot 931.5\text{ MeV} = 28.296\text{ MeV}$. Thus, we have

$$\delta M = E_B/c^2 = ZM_H + NM_n - M(Z,N) \tag{3.3}$$

If E_B is divided by the mass number, the mean binding energy per nucleon is obtained:

$$\frac{E_B}{A} = \frac{c^2}{A}(ZM_H + NM_n - M(Z,N)) \tag{3.4}$$

For our example, ^{4}He, the mean binding energy per nucleon is 7.074 MeV. The mean binding energy per nucleon is plotted in Figure 3.4 as a function of the mass number A. Figure 3.4 shows that the elements with atomic numbers around that of iron have the highest mean binding energies per nucleon. Above $A \approx 90$, the mean binding energy decreases continuously. Thus, it can be deduced immediately from Figure 3.4 that fission of heavy nuclei into two smaller ones leads to a gain in energy. The difference in the mean binding energy per nucleon of uranium atoms and two nuclides of half the mass number is about 1 MeV. Thus, roughly 200 MeV should be set free in the fission of one uranium nucleus into two smaller ones. This is the energy gained in nuclear fission in nuclear reactors. On the other hand, in the range of light atoms, the even–even nuclei ^{4}He, ^{12}C, and ^{16}O have particularly high mean binding energies of the nucleons. Values for light nuclei are plotted separately in Figure 3.5. It is obvious from Figure 3.5 that ^{4}He is a particularly stable combination of nucleons among light nuclei, and very high energies must be set free in the fusion of hydrogen to ^{4}He. This is the main energy-producing process in the Sun and is the aim of the development of fusion reactors. As the increase in the curve in Figure 3.4 in the range of light nuclides is much steeper than the decrease in the range of heavy nuclides, the energy gained per mass unit of fuel is much higher for fusion than for fission. Thus, in stellar burning processes, energy production often occurs by nuclear fusion.

Nuclear reactions and nuclear decay are always accompanied by a change in the binding energies (masses) of the participating nuclei, by the so-called Q value. The Q value is the difference in the masses of the initial states to the masses of the final states. In order to avoid calculations with very large numbers, mass tables normally do not contain atomic masses but rather mass excesses:

$$\Delta = M(Z,N) - A \cdot 931.5\,\text{MeV} \tag{3.5}$$

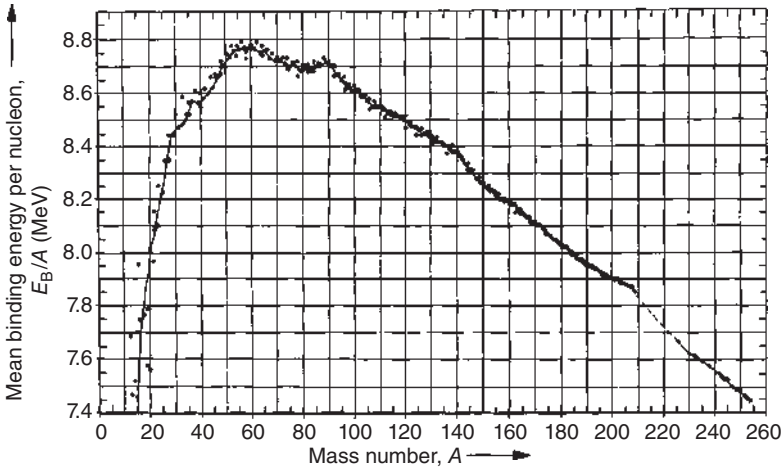

Figure 3.4 Mean binding energy per nucleon.

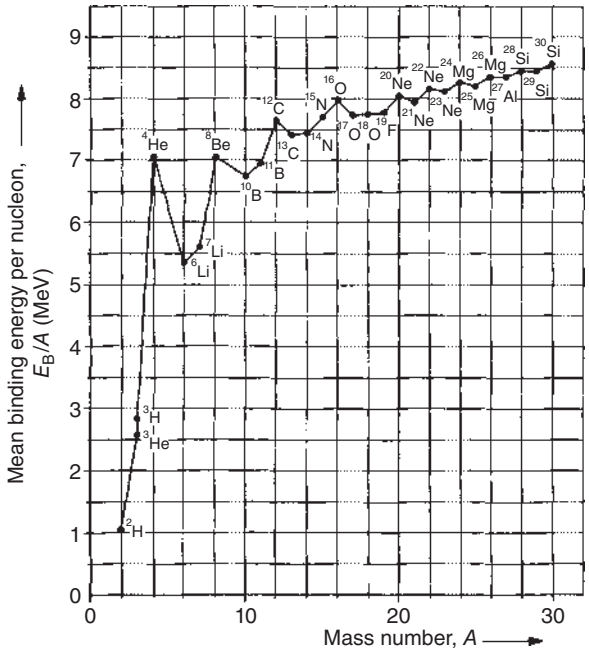

Figure 3.5 Mean binding energy per nucleon for the lightest nuclei.

that is, one subtracts the energy equivalent of the A nucleon masses from the nuclide masses. For example, the Q_α value for the α-decay of ^{238}U is derived as follows:

$$\begin{aligned}
\Delta(^{4}\mathrm{He}) &= 2.4249\ \mathrm{MeV}\\
\Delta(^{238}\mathrm{U}) &= 47.306\ \mathrm{MeV}\\
\Delta(^{234}\mathrm{Th}) &= 40.607\ \mathrm{MeV}\\
\mathrm{Q}_\alpha &= \Delta(^{238}\mathrm{U}) - [\Delta(^{234}\mathrm{Th}) + \Delta(^{4}\mathrm{He})]\\
&= 47.306 - [40.607 + 2.4249]\ \ \mathrm{MeV}\\
&= 4.274\ \ \mathrm{MeV}
\end{aligned}$$

Due to conservation of momentum and energy, the α-particle obtains from this decay energy:

$$E_\alpha = Q_\alpha \left(1 - \frac{4}{234}\right) = 4.201\ \mathrm{MeV}$$

The difference (73 keV) is the recoil energy of the daughter nucleus ^{232}Th.

Positive Q values are associated with exoergic nuclear transmutations. Note that the sign convention in nuclear science is opposite to that used in chemistry where exoergic reactions have negative enthalpies.

The abundance of stable nuclei in the chart of nuclides is as follows:

Z even, N even (even–even nuclei)	Very common (158 nuclei)
Z even, N odd (even–odd nuclei)	Common (53 nuclei)
Z odd, N even (odd–even nuclei)	Common (50 nuclei)
Z odd, N odd (odd–odd nuclei)	Rare, only 6 nuclei (^{2}H, ^{6}Li, ^{10}B, ^{14}N, ^{50}V, ^{180}Ta)

This unequal distribution does not correspond to statistics. It rather reflects the systematics of binding energies for which Carl Friedrich von Weizsäcker developed a crude theory in 1935. Its basic idea is that nuclei resemble incompressible, uniformly charged liquid drops held together by cohesive forces and by surface tension. This liquid-drop theory has evolved into what is called the "semiempirical mass equation" and describes the total binding energy of species Z, A as a sum of five energies as:

$$E_B(Z,A) = E_v + E_s + E_c + E_a \pm \delta \tag{3.6}$$

where E_v is the volume energy, E_s is the surface energy, E_c is the Coulomb energy, E_a is the asymmetry energy, and δ is the pairing energy. These energy terms have the following physical background.

Volume energy – each nucleon contributes to the total binding energy. As the nucleon–nucleon interaction is short-ranged and saturates (Chapter 5), there are not $A(A-1) \approx A^2$ bindings, but a nucleon in the interior of a nucleus is only bound to its nearest neighbors resulting in A bindings where the fit parameter a_v is the energy by which each nucleon is bound:

$$E_v = a_v A \tag{3.7}$$

Surface energy – nucleons at the surface are less bound as they have less neighbors. The surface of the nucleus is $4\pi R^2$. As $R \sim A^{1/3}$ (Chapter 4), $4\pi R^2 \sim A^{2/3}$. This term is multiplied by the parameter a_s which is also determined experimentally:

$$E_s = -a_s A^{2/3} \tag{3.8}$$

Coulomb energy – a decrease in binding energy is due to Coulomb repulsion between the protons. The Coulomb energy of a uniformly charged sphere is proportional to Z^2/R, thus,

$$E_c = -a_c \frac{Z(Z-1)}{A^{1/3}} \tag{3.9}$$

where a_c is another fit parameter.

Asymmetry energy – this term has no liquid-drop background but is of quantum-mechanical origin. It is related to the difference in binding energy of a nucleus with $N \neq Z$ and one with $N = Z$. We assume that the neutron and proton levels in the nucleus are equidistant with level spacing D and that each level is occupied by one nucleon. In order to produce the nucleus with $Z \neq N$ from a nucleus with $Z = N$, we must transform p protons into neutrons. As $N = Z = A/2$, we will have $N = p + A/2$ and $Z = A/2 - p$. This results in $p = (N-Z)/2$. Since the lowest N levels in the $N = Z$ nucleus are occupied, we must raise the p protons in energy by pD. The energy required to make the $N \neq Z$ nucleus from the $N = Z$ nucleus is $p^2D = (N-Z)^2D/4$. Further, by making $D \sim 1/A$, we take care of the fact that the level spacing gets smaller as the total number of nucleons increases. Finally, replacing $(N-Z)$ by $(A-2Z)$ gives

$$E_a = -a_a \frac{(A-2Z)^2}{A} \tag{3.10}$$

where a_a is a fit parameter.

Pairing energy – this term takes care of the special stability of completely paired nucleons in an even–even nucleus and the relatively low stability of odd–odd nuclei.

Examples of the odd–even staggering in the proton separation energies, S_p, as a function of proton number and for the neutron separation energies, S_n, as a function of the neutron number are shown in Figure 3.6. Based on this systematics, the pairing energy is parameterized as:

$$\begin{aligned} \delta &= +11/A^{1/2} && \text{for even–even nuclei} \\ \delta &= 0 && \text{for even–odd and odd–even nuclei} \\ \delta &= -11/A^{1/2} && \text{for odd–odd nuclei} \end{aligned} \tag{3.11}$$

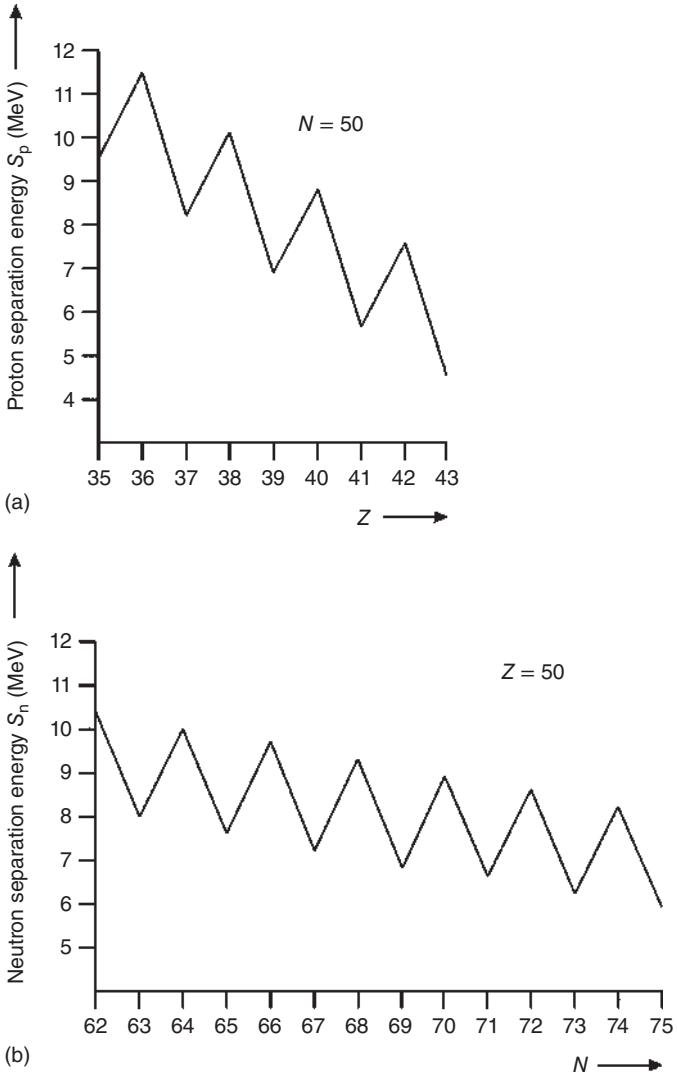

Figure 3.6 Separation energies of the outermost proton, S_p (a), and the outermost neutron, S_n (b), as a function of proton number or neutron number, respectively.

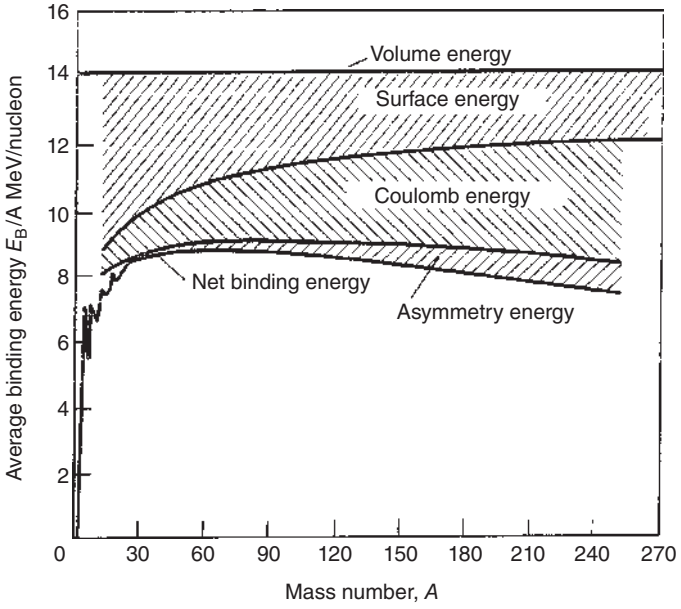

Figure 3.7 Relative contribution of the various liquid-drop model terms to the binding energy per nucleon. Source: Meyerhof (1967)/McGraw-Hill.

A classical set of parameters is $a_v = 14.1$ MeV, $a_s = 13.1$ MeV, $a_c = 0.585$ MeV, and $a_a = 19.4$ MeV. The relative contribution of each term to the binding energy per nucleon is shown in Figure 3.7. The surface energy correction to the large, constant volume energy is most significant for light nuclei where the surface is large relative to the volume. The Coulomb energy correction is most important for the heaviest nuclei. The asymmetry energy is a small effect increasing with increasing mass.

In 1966, Myers and Swiatecki introduced a modification of the semiempirical mass equation by adding an asymmetry energy correction term to the volume and surface energy terms and by a term correcting the Coulomb energy due to the diffuseness of the nuclear surface (Chapter 4) yielding the following equation:

$$E_B(Z,A) = c_1 A(1 - kI^2) - c_2 A^{2/3}(1 - kI^2) - \frac{c_3 Z^2}{A^{1/3}} + \frac{c_4 Z^2}{A} \pm \delta \tag{3.12}$$

where $I = (N - Z)/A$ is the relative neutron excess, $c_1 = 15.677$ MeV, $c_2 = 18.56$ MeV, $c_3 = 0.717$ MeV, $c_4 = 1.211$ MeV (this term corrects the Coulomb term for the surface diffuseness), $k = 1.7826$ is the symmetry energy coefficient, and $\delta = 11/A^{1/2}$. Further improvements in the treatment of the liquid-drop model, that is, the development of the droplet model of atomic nuclei and the development of folding techniques, need to be mentioned. A common feature of these models is that the average size and stability of a nucleus are described by the average binding of the nucleons to each other in a macroscopic model, while the detailed energy levels and their quantum numbers can be understood within a microscopic model, namely, the single-particle shell model that we will introduce later in Chapter 5. For completeness, we mention an independent advance in the development of techniques that solve the nuclear

many-body problem within a self-consistent mean-field approximation based on effective energy density functionals.

As can be deduced from the liquid-drop formula, Eqs. (3.6–3.11), E_B for fixed mass number A, plotted as a function of Z, gives parabolas, one parabola for odd mass numbers ($\delta = 0$) and two parabolas for even mass numbers ($\pm\delta$). Two examples are given in Figures 3.8 and 3.9. As increasing binding energies are plotted from top to bottom, the more stable nuclei are at the bottom of the curves. The unstable *isobars* are transformed stepwise, either by β^- decay from lower to higher atomic numbers, or by β^+ decay (alternatively by electron capture, EC, symbol ε) from higher to lower atomic numbers. In isobaric decay chains of odd A, the β-decay energies increase monotonically toward either side of the minimum of the "mass parabola," Z_A. In isobaric decay chains of even A, the β-decay energies alternate between small and large values. For odd mass number, the nucleus closest to Z_A is the only stable nucleus. For even mass number, more than one nucleus can be stable. In Figure 3.8, ^{64}Ni and ^{64}Zn are stable even–even nuclei. The odd–odd nucleus in between, ^{64}Cu, undergoes dual decays, 61% EC and 39% β^-. Strictly speaking, ^{64}Zn is metastable and is a candidate for double β-decay. In this case, ($\beta^+\beta^+$), (EC β^+), and (EC EC) are intelligible, all involving the emission of two electron–neutrinos; however, none of these processes has been experimentally detected so far. Double ($\beta^-\beta^-$) decay has been detected indirectly in geochemical experiments with Te- or Se-containing ores in the cases:

$$^{130}\mathrm{Te}(\beta^-\beta^-)^{130}\mathrm{Xe} \quad t_{1/2} = 2 \times 10^{21}\ \text{years}$$

and

$$^{82}\mathrm{Se}(\beta^-\beta^-)^{82}\mathrm{Kr} \quad t_{1/2} = 1 \times 10^{20}\ \text{years}$$

by detecting the noble gases mass spectrometrically.

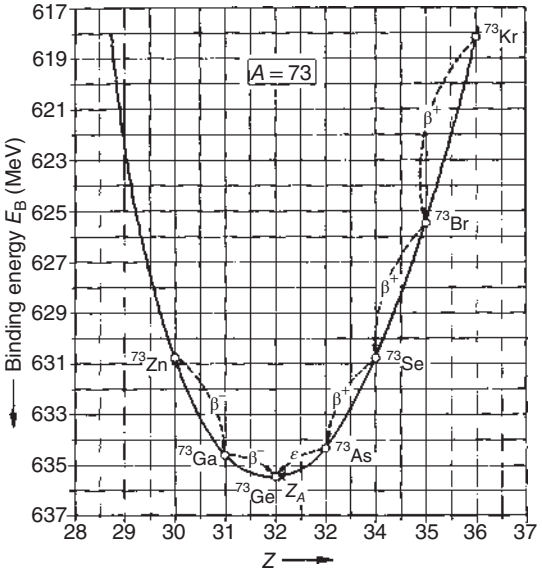

Figure 3.8 Binding energies and β-decays of nuclides with odd mass number.

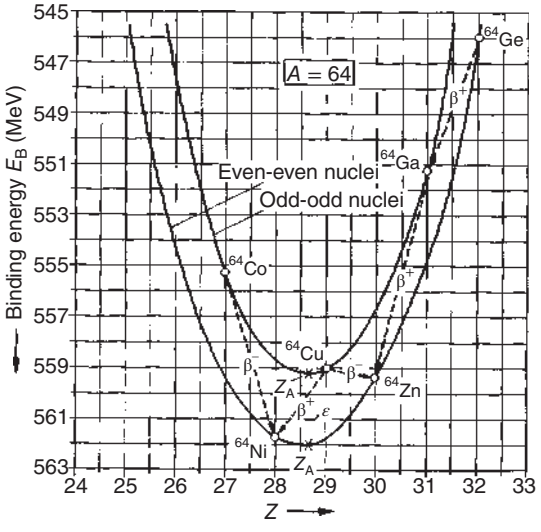

Figure 3.9 Binding energies and β-decays of nuclides with even mass number.

In 1987, double β-decay was also detected directly. An interesting idea is that of neutrino-less double β-decay which requires that the neutrino is identical with its antineutrino (Majorana neutrino).

3.4 Evidence for Shell Structure in Nuclei

As we have seen in the preceding section, the liquid-drop model correlates very well with the overall behavior of masses and binding energies. However, if the differences between experimentally determined masses and those obtained from a semiempirical mass formula such as Eq. (3.12) are plotted against the proton number or neutron number, as is done in Figure 3.10, we see that these differences are pronounced at certain values of Z and N, notably at 28, 50, 82, and 126. Nuclei with these proton and neutron numbers seem to exhibit extra stability on the order of an extra 10 MeV, which has also long been known for nuclei with Z or N values of 2, 8, and 20, although this is not readily visible in Figure 3.10. This extra stability at certain values of Z and N led, through an assumed analogy with the special stability of the atoms with closed electron shells, that is, the noble gases, to the concept of closed nucleon shells in nuclei. The first attempts by W. Elsasser, in 1934, to account for the extra stability in terms of independent nucleons in a potential well failed for N and Z values above 20 and received little attention until much more evidence for the special stability of certain configurations had been accumulated. Because the unusual properties at nucleon numbers 2, 8, 20, 28, 50, 82, and 126 remained unexplained, they became known as "magic numbers." Much of the empirical evidence for these magic numbers came from masses and binding energies, numbers of species with given N or Z, and, for example, α-particle energies. Some of these facts are given below.

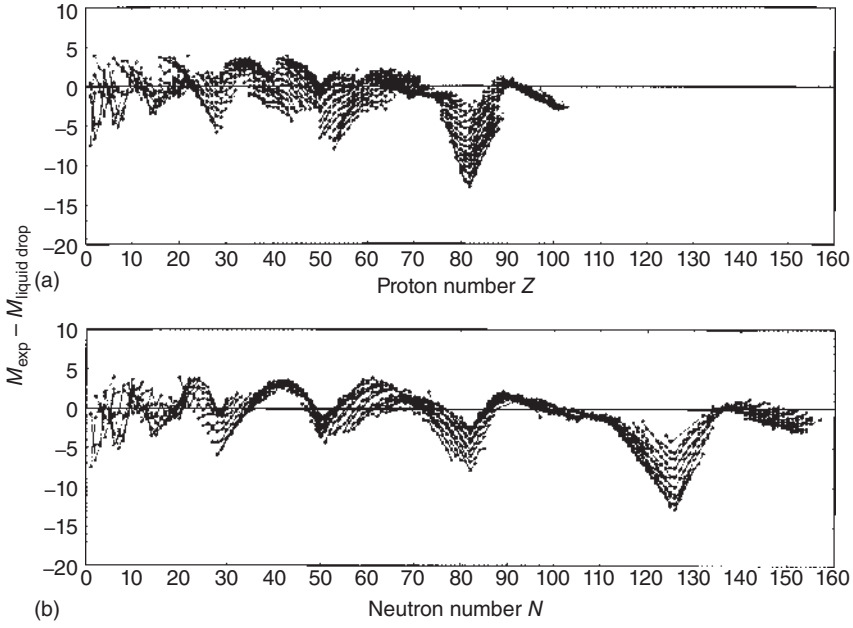

Figure 3.10 Differences between experimental atomic masses and the liquid-drop model masses as a function of proton number (a) or neutron number (b). Source: Modified from Myers and Swiatecki (1966).

For $Z > 28$, nuclides of even Z having isotopic abundances in excess of 60% are ^{88}Sr ($N = 50$), ^{138}Ba ($N = 82$), and ^{140}Ce ($N = 82$). The largest number of stable *isotones* exists for $N = 50$ (6) and for $N = 82$ (7). The largest number of stable isotopes (10) occurs for tin, $Z = 50$, and in both calcium ($Z = 20$) and tin ($Z = 50$) the stable isotopes span an unusually wide mass range. The fact that the natural radioactive decay chains end in lead ($Z = 82$) is significant, as is the neutron number of the two heaviest stable nuclides, ^{208}Pb and ^{209}Bi ($N = 126$). The particularly weak binding of the first nucleon outside a closed shell (in analogy to the low ionization potential for the valence electron in an alkali atom) is shown in Figure 3.11 for $N, Z = 51$ as examples. For nuclides with $N = 50$, 82, and 126, this is also reflected by the unusually low probabilities for the capture of neutrons. Also, in nuclei such as ^{87}Kr ($N = 51$) and ^{137}Xe ($N = 83$), one neutron is bound so loosely that it can be emitted spontaneously when these nuclei are formed in highly excited states in β^- decay of ^{87}Br and ^{137}I, respectively (β^- delayed neutron emission). Further evidence for the $N = 126$ shell comes from α-decay systematics. Q_α values are smooth functions of A for a given Z but show striking discontinuities at $N = 126$ (see Figure 6.5). The occurrence of long-lived isomeric states is correlated with magic numbers; accumulations of such isomers occur for neutron and proton numbers just below 50, 82, and 126.

By 1948, the evidence for a shell structure in nuclei had become so strong that a number of scientists sought a theoretical explanation. As discussed in detail in Chapter 5, two basic insights enabled M.G. Mayer in New York and J.H.D. Jensen et al. in Heidelberg in 1949 to arrive independently at an explanation of

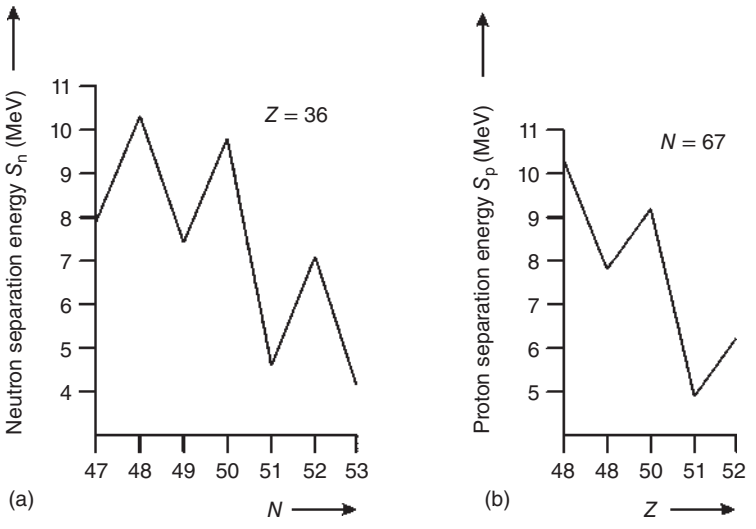

Figure 3.11 Separation energies S_p and S_n as a function of proton or neutron number at the magic numbers $Z, N = 50$, respectively. Note the particularly low separation energies at $Z, N = 51$.

the magic numbers in terms of single-particle motion. One was the realization that collisions between nucleons in a nucleus are greatly suppressed by the Pauli exclusion principle, making it plausible that an individual nucleon can move freely in an effective potential due to the presence of all other nucleons. Choosing for the nuclear potential a spherically symmetric harmonic oscillator potential and solving the Schrödinger equation for a nucleon moving in this potential, they arrived at the single-particle energy levels in the potential. The numbers of nucleons of one kind to fill all the levels up to and including the first, second, and third levels turned out to be 2, 8, and 20. Beyond the third harmonic oscillator, the numbers for completed shells deviated from the magic numbers. This was resolved by the second basic insight by Mayer and Jensen, which was the very strong effect of the spin–orbit interaction. They found that if the orbital angular momentum l and the spin of a nucleon interact such that the state with total angular momentum $j = l + 1/2$ lies at a significantly lower energy than that with $l - 1/2$, large energy gaps occur above nucleon numbers 28, 50, 82, and 126. As we will see later, the single-particle shell model predicts much more than the existence of shell closures at the magic numbers. It also predicts that the ground states of closed-shell nuclei must have zero total angular momentum and even parity and, that the ground-state total angular momenta and parities of nuclei with one nucleon above or below a closed shell are those of the extra or missing nucleon. Moreover, total angular momenta and parities of excited single-particle states can be predicted. As we will discuss in detail in Chapter 5, the single-particle shell model is an oversimplification. Even in spherical nuclei, the extreme single-particle model is too naive except in the immediate vicinity of closed shells. If several nucleons are present outside a closed shell, the residual interaction among them must be taken into account.

Various further extensions which make the shell model more widely applicable are discussed in Chapter 5.

3.5 Precision Mass Spectrometry

The experimental determination of exact atomic masses is an important tool to advance our understanding of the strong force and its consequences for nuclear structure. Traditionally, atomic masses of stable isotopes have been determined in mass spectrometers determining the mass-to-charge ratio of positive ions from the amount of deflection in a combination of electric and magnetic fields. Different arrangements have been used for bringing about velocity focusing or directional focusing, or both. Instruments that use photographic plates for recording the mass spectra are called *mass spectrographs*. Those that make use of the collection and measurement of ion currents are referred to as *mass spectrometers*. The fact that ions of the same kinetic energy and different masses require different times to traverse a given path length has been utilized in the design of several types of time-of-flight (ToF) mass spectrometers. Precisions varying between about 0.01 and 1 part in 10^5 have been achieved. For precision mass determinations, for example, in a Mattauch–Herzog mass spectrograph, the so-called doublet method has been used to advantage. This substitutes the measurement of the difference between two almost identical masses for the direct measurement of absolute masses. All measurements must eventually be related to the standard ^{12}C. But for convenience, the masses of ^{1}H, ^{2}H, and ^{16}O have been adopted as secondary standards, and for this purpose they have been carefully measured by mass determinations of the fundamental doublets:

$\left(^{12}C^{1}H_4\right)^+$ and $^{16}O^+$ at mass-to-charge ratio 16

$\left(^{12}H_3\right)^+$ and $^{12}C^+$ at mass-to-charge ratio 6

$\left(^{2}H^+\right)^+$ and $\left(^{1}H_2\right)^+$ at mass-to-charge ratio 2

With these secondary standards, molecular ion beams of the same mass number were produced as doublets, such as $(^{12}C_{14}{}^{1}H_{12})^+$ for $^{180}Hf^+$.

At the moment, atomic masses can be measured also for radioactive isotopes far away from the valley of stability at the presently existing heavy-ion accelerator and radioactive beam facilities producing exotic nuclei at the limits of stability which exhibit new features not present in stable nuclei and therefore provide deeper insight into the nature of the nuclear interaction. For this purpose, we introduce and discuss the use of Penning trap mass spectrometers, and the use of storage rings such as the experimental storage ring (ESR) at the GSI Helmholtz Center for Heavy-Ion Research.

Penning traps, Figure 3.12, are the instruments of choice for direct mass measurements on short-lived nuclides with so far unsurpassed precision. The high detection efficiency enables investigations in rarely produced species at radioactive beam facilities. By storing ions in a superposition of a strong homogeneous magnetic field that

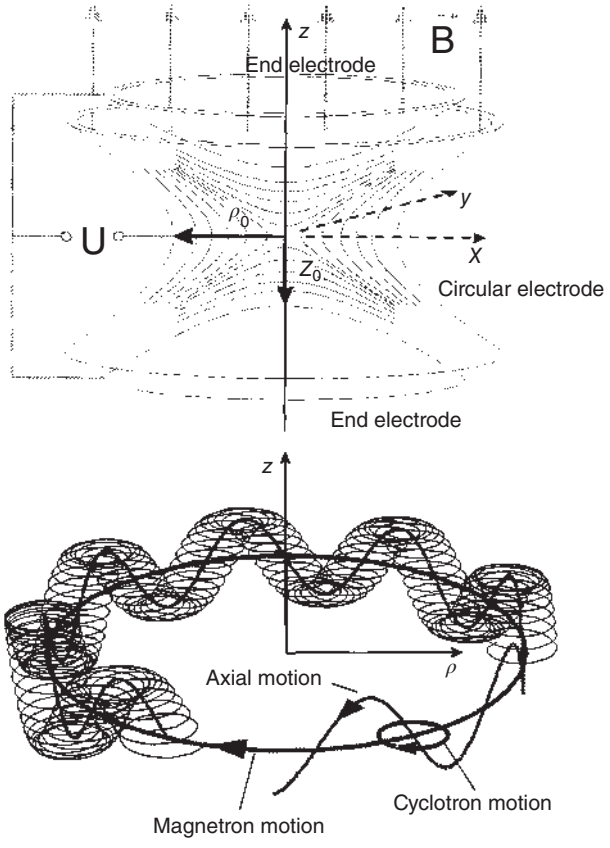

Figure 3.12 Schematic of a Penning trap (top) and ion motion (bottom).

defines the z axis, and a weak electrostatic quadrupole field, their motion separates into three independent eigenmotions with the characteristic frequencies:

$$\nu_+ = \frac{1}{2}(\nu_c + \sqrt{\nu_c^2 - 2\nu_z^2}) \tag{3.13}$$

$$\nu_- = \frac{1}{2}(\nu_c - \sqrt{\nu_c^2 - 2\nu_z^2}) \tag{3.14}$$

$$\nu_z = \frac{1}{2\pi}\sqrt{\frac{qV_0}{mD^2}} \tag{3.15}$$

Here, ν_+ is the reduced cyclotron frequency, ν_- the magnetron, and ν_z the axial frequency of an ion with a charge-to-mass ratio q/m confined in a magnetic field B and a trapping potential V_0. The parameter:

$$D = \sqrt{\frac{1}{2}\left(z_0^2 + \frac{\rho_0^2}{2}\right)} \tag{3.16}$$

is defined for the ideal hyperbolical Penning trap by the minimum distances of the end caps $2z_0$ at $\rho = 0$ and that of the ring electrode at $z = 0$, that is, $2\rho_0$. The eigenfrequencies of the ion motion are linked to the cyclotron frequency:

$$\nu_c = \frac{1}{2\pi}\frac{q}{m}B \tag{3.17}$$

by

$$\nu_c = \nu_+ + \nu_- \tag{3.18}$$

A determination of the cyclotron frequency ν_c and that of a reference ion $\nu_{c,ref}$ (carbon clusters) leads to the atomic mass of the interesting nuclide, m_{atom}. In the case of singly charged ions, the relation is given by:

$$m_{atom} = \frac{\nu_{c,ref}}{\nu_c}(m_{ref} - m_e) + m_e \tag{3.19}$$

Here, m_{ref} is the mass of the reference ion used for calibrating the magnetic field and m_e is the mass of the electron. The frequency determination of a short-lived nuclide in a Penning trap is commonly carried out via the time-of-flight-ion cyclotron resonance (ToF-ICR) method. An electric quadrupole RF field at the sum frequency $\nu_+ + \nu_-$ (cf. Eq. (3.18)) is used to couple the two radial motions, leading to a periodic energy transfer between the two harmonic oscillators. Since $\nu_+ \gg \nu_-$, the radial energy:

$$E_{rad} \approx \nu_+^2 \rho_+^2 \tag{3.20}$$

is dominated by the modified cyclotron motion. The energy E_{rad} determines an orbital magnetic moment of the stored ions which leads to a force:

$$\overline{F} = -\frac{E_{rad}}{E}\frac{\delta B}{\delta z}\overline{e}_z \tag{3.21}$$

on the ion in the magnetic field gradient when ejected from the trap. Thereby, the ToF to a detector has a minimum in case the frequency used to excite the ions in the trap equals ν_c. A plot of the ToF against the excitation frequency results in a resonance curve that determines ν_c, see Figure 3.13. Another possibility for the frequency determination is the Fourier transform-ion cyclotron resonance (FT-ICR) technique based on the image currents (mirror currents):

$$i(t) = \frac{2\pi\nu_{ion} r_{ion}(t) q}{d} \tag{3.22}$$

that the ions induce in the electrodes of the trap. In this simplified equation, ν_{ion} denotes one of the eigenfrequencies given in Eqs. (3.13–3.15), q is the charge state, and d is the electrode distance. A Fourier transformation of the time domain signal reveals the ion frequency.

The destructive ToF-ICR technique is used for short-lived nuclides with half-lives less than one second and the nondestructive FT-ICR method for very rarely produced but longer-lived species such as superheavy elements. Single-ion FT-ICR measurements are presently being developed that will eventually serve for mass mapping in the superheavy-element domain.

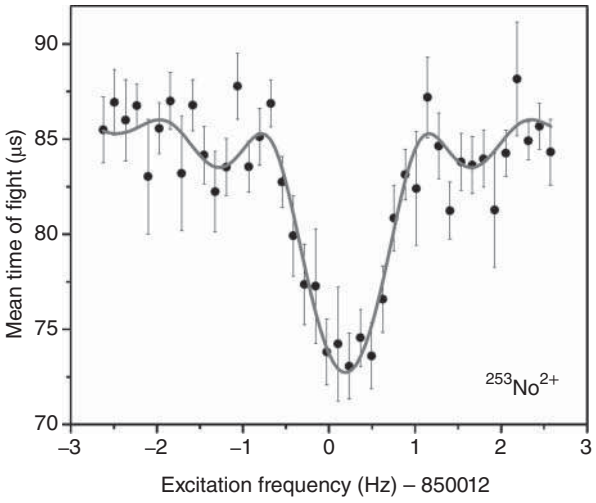

Figure 3.13 Cyclotron resonance curve for $^{253}No^{2+}$. The solid line is a fit of the theoretical line shape to the data (filled black circles). Source: Block et al. (2010)/Springer Nature.

The resolving power in a ToF mass measurement is

$$\mathfrak{R} = \frac{m}{\Delta m} = \frac{\nu_c}{\Delta \nu_c} \approx \nu_c T \tag{3.23}$$

where m is the mass, ν_c the corresponding cyclotron frequency, and $\Delta\nu_c$ the line width (FWHM) of the frequency signal. T is the excitation time in the ToF-ICR measurement and, in a FT-ICR measurement, the observation time. With an excitation period of one second and a typical cyclotron frequency in the megahertz range, $\mathfrak{R} = 10^6$ can be reached; in the case of the FT-ICR and a one second observation time, a similar resolving power is reached. The statistical error of the mass determination is given by:

$$\frac{\delta m}{m} \approx \frac{1}{\mathfrak{R}\sqrt{N_{tot}}} \tag{3.24}$$

where N_{tot} denotes either the number of ions in a ToF resonance or the number of transients in a FT-ICR measurement, each containing the signal of one ion. With 1000 ions in a ToF-ICR measurement, the statistical uncertainty for a long-lived species ($t_{1/2} \geq 1$ second) with a cyclotron frequency in the megahertz range is about $3 \cdot 10^{-8}$. When recording the image current signal, the number of repeated, successful measurement cycles will be strongly limited by the low production rates of the heavy nuclides. In this case, an accuracy of 10^{-6} to 10^{-7} is projected.

At the radioactive beam facility of the GSI Helmholtz Center for Heavy-Ion Research consisting of the heavy-ion synchrotron (SIS), the fragment separator (FRS), and the ESR, radioactive beams produced by projectile fragmentation can be used for direct mass measurements on exotic nuclei stored in the ESR. These are time-resolved Schottky mass spectrometry (SMS) and isochronous mass spectrometry (IMS). In SMS, the exotic ions separated according to their charge-to-mass ratio in the FRS are stored and electron cooled in the ESR. Thus, their velocity spread becomes negligible and the measured revolution frequencies characterize with high precision the mass-to-charge ratios of the stored ions. The frequencies are measured

with the Schottky noise technique. The principle of SMS is depicted in Figure 3.14. The peak areas in the frequency spectra, Figure 3.15, are proportional to the number of stored ions, and monitoring of their evolution in time provides half-lives. The example shown in Figure 3.15 is the discovery of the new nuclide ^{235}Ac along with its mass and half-life determination. In the IMS, the storage ring is tuned to a special ion optical mode in which the velocity spread of ions is compensated to first order by their orbit lengths. Mass-to-charge ratios of stored ions are obtained from the measured revolution times. The latter are measured with a ToF detector placed inside the ESR. The IMS does not require cooling and can be applied to nuclides with half-lives as short as a few tens of microseconds. A mass resolving power of up to 10^6 is being achieved.

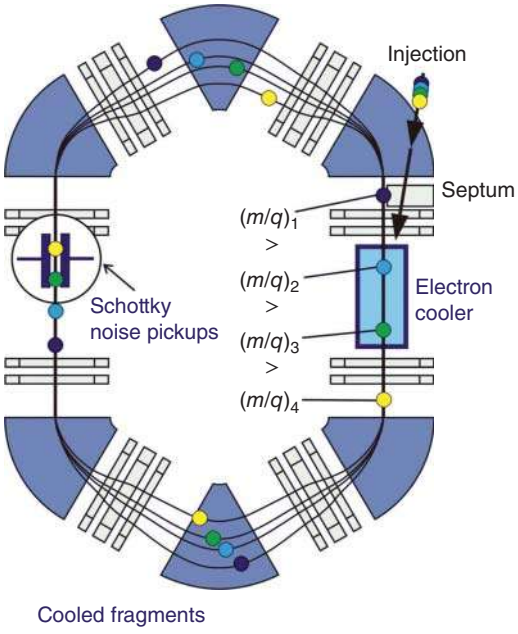

Figure 3.14 Principle of the mass determination in the experimental storage ring (ESR) consisting of six dipole magnets and six quadrupole triplets or doublets by the Schottky noise pickup (left part of the figure) technique. The motion of up to four different species characterized by their mass-to-charge ratios $(m/q)_1 > (m/q)_2 > (m/q)_3 > (m/q)_4$ is visible. The ions injected into the ESR are cooled by an electron cooler (right part of the figure) diminishing their velocity spread $\Delta v/v$ to zero. The experiments are run at energies of typically 300 MeV u^{-1} corresponding to 65% of the speed of light. The frequency of revolution is then about $2 \cdot 10^6$ s^{-1}. Source: Kluge et al. (2004)/Elsevier.

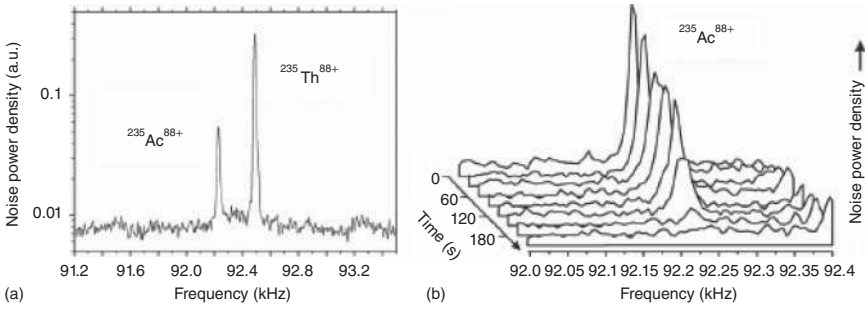

Figure 3.15 Discovery of the isotope ^{235}Ac along with its mass and lifetime measurements applying time-resolved Schottky mass spectrometry. The mass has been extracted by calibrating with the known mass of ^{235}Th (panel a), whereas the half-life has been extracted from the time evolution of the peak area (panel b). Source: Bosch et al. (2006)/Elsevier.

References

Isotopes

Chadwick, J. (1932). The existence of a neutron. *Proc. R. Soc. London, Ser. A* A136: 692.

Nuclide Masses and Binding Energies

Block, M., Ackermann, D., Blaum, K. et al. (2010). Direct mass measurements above uranium bridge the gap to the island of stability. *Nature* 463: 785.

Bosch, F., Geissel, H., Litvinov Yu. A. et al. (2006). Experiments with stored exotic nuclei at relativistic energies. *Int. J. Mass spectrom.* 251: 212.

Kluge, H.-J., Blaum, K., and Scheidenberger, C. (2004). Mass measurement of radioactive isotopes. *Nucl. Instrum. Methods Phys. Res.* A532: 48.

Meyerhof, W.E. (1967). *Elements of Nuclear Physics*. New York: McGraw-Hill.

Myers, W.D. and Swiatecki, W.J. (1966). Nuclear masses and deformations. *Nucl. Phys.* 81: 1.

von Weizsäcker, C.F. (1935). Zur Theorie der Kernmassen. *Z. Phys.* 96: 431.

Further Reading

Isotopes

Biegeleisen, J. (1953). Isotopes. *Annu. Rev. Nucl. Sci.* 3: 221.

Clewlett, G.H. (1954). Chemical separation of stable isotopes. *Annu. Rev. Nucl. Sci.* 4: 293.

Kistemacher, J., Biegeleisen, J., and Nier, A.O.C. (eds.) (1958). *Proceedings of the International Symposium on Isotope Separation*. Amsterdam: North-Holland.

London, H. (1961). *Separation of Isotopes*. London: George Newnes.

White, F.A. (1968). *Mass Spectrometry in Science and Technology*. New York: Wiley.

Romer, A. (1970). *Radiochemistry and the Discovery of Isotopes*. New York: Dover.

Newton, G.W.A. (1995). History of the unraveling of the natural decay series. *Radiochim. Acta* 70/71: 31.

Griffin, H.C. (2011). Natural radioactive decay chains. In: *Handbook of Nuclear Chemistry*, 2e, vol. 2 (eds. A. Vertés, S. Nagy, Z. Klencsár, et al.), 667. Berlin: Springer.

Nuclide Charts and Tables

Kratz, J.V. (1992). Stabile und radioaktive isotope. In: *D'Ans-Lax, Taschenbuch für Chemiker und Physiker*, 4e, vol. 1 (ed. M.D. Lechner), 59–144. Berlin: Springer.

Firestone, R.B. and Shirley, V.S. (eds.) (1996). *Table of Isotopes*, 8e. New York: Wiley.

Chu, S.Y.F., Ekström, L.P., and Firestone, R.B. (1999). WWW table of radioactive isotopes. http://ie.lbl.gov/toi/ (accessed 21 February 2013).

Firestone, R.B. (2011). Table of nuclides. In: *Handbook of Nuclear Chemistry*, 2e, vol. 2 (eds. A. Vertés, S. Nagy, Z. Klencsár, et al.), 1033. Berlin: Springer (Appendix).

Magill, J., Pfennig, G., Dreher, R., and Sótí, Z. (2015). *Karlsruher Nuklidkarte*, 9e. Nucleonica GmbH, developed under a License of the European Atomic Energy Community.

Nuclide Masses and Binding Energies

Haxel, O., Jensen, J.H.D., and Suess, H.E. (1949). On the "magic numbers" in nuclear structure. *Phys. Rev.* 75: 1766.

Mayer, M.G. (1949). On closed shells in nuclei. II. *Phys. Rev.* 75: 1969.

Haxel, O., Jensen, J.H.D., and Suess, H.E. (1950). Modellmässige Deutung der ausgezeichneten Nukleonen-Zahlen im Kernbau. *Z. Phys.* 128: 295.

Mayer, M.G. (1950). Nuclear configurations in the spin orbit coupling model. I. Empirical evidence. *Phys. Rev.* 78: 16.

Mayer, M.G. and Jensen, J.H.D. (1955). *Elementary Theory of Nuclear Shell Structure*. New York: Wiley.

Kirsten, T. (1970). Nachweis des doppelten betazerfalls. *Fortschr. Phys.* 18: 449.

Hilf, E.R., von Groote, H., and Takahashi, K. (1975). *Atomic Masses and Fundamental Constants 5*, 293. New York: Plenum Press.

Blocki, J., Randrup, J., Swiatecki, W.J., and Tsang, C.F. (1977). Proximity forces. *Ann. Phys.* 105: 427.

Myers, W.D. (1977). *Droplet Model of Atomic Nuclei*, 150. New York: IFI/Plenum Data Co.

Wapstra, A.H. and Bos, K. (1977). The 1977 atomic mass evaluation, part I, atomic mass table. *At. Data Nucl. Data Tables* 19: 177.

Quentin, P. and Flocard, H. (1978). Self-consistent calculations of nuclear properties with phenomenological effective forces. *Annu. Rev. Nucl. Part. Sci.* 28: 523.

Wapstra, A.H. and Audi, G. (1985). The 1983 atomic mass evaluation (I). Atomic mass table. *Nucl. Phys.* A432: 1.

Wapstra, A.H. and Audi, G. (1985). The 1983 atomic mass evaluation (II). Nuclear reaction and separation energies. *Nucl. Phys.* A432: 55.

Bos, K., Audi, G., and Wapstra, A.H. (1985). The 1983 atomic mass evaluation (III). Systematics of separation and decay energies. *Nucl. Phys.* A432: 140.

Wapstra, A.H., Audi, G., and Hoekstra, R. (1985). The 1983 atomic mass evaluation (IV). Evaluation of input values, adjustment procedures. *Nucl. Phys.* A432: 185.

Brown, L.S. and Gabrielse, G. (1986). Geonium theory: physics of a single electron or ion in a penning trap. *Rev. Mod. Phys.* 58: 233.

Klapdor, H.V. and Povh, B. (eds.) (1988). *Neutrino Physics*. Heidelberg: Springer.

Geissel, H., Armbruster, P. et al. (1992). The GSI projectile fragment separator (FRS): a versatile magnetic system for relativistic heavy ions. *Nucl. Instrum. Methods* B70: 286.

Audi, G., Wapstra, A.H., and Thibault, C. (2003). The AME2003 atomic mass evaluation. *Nucl. Phys.* A729: 337.

Bender, M., Heenen, P.-H., and Reinhardt, P.-G. (2003). Self-consistent mean-field models for nuclear structure. *Rev. Mod. Phys.* 75: 121.

Blaum, K. (2006). High-accuracy mass spectrometry with stored ions. *Phys. Rep.* 425 (1).

Audi, G., Kondev, E.G., Wang, M. et al. (2012). The NUBASE2012 evaluation of nuclear properties. *Chin. Phys.* C36: 1157.

Audi, G., Wang, M., Wapstra, A.H. et al. (2012). The AME2012 atomic mass evaluation (I). Evaluation of input data, adjustment procedures. *Chin. Phys.* C36: 1287.

Wang, M., Audi, G., Wapstra, A.H. et al. (2012). The AME2012 atomic mass evaluation (II). Tables, graphs and references. *Chin. Phys.* C36: 1603.

4

Other Physical Properties of Nuclei

4.1 Nuclear Radii

We have already mentioned that nuclei have dimensions on the order of several femtometers: 1 fm = 10^{-15} m. Experiments designed to measure nuclear radii lead to the conclusion that, to a crude approximation at least, nuclear radii scale is

$$R = r_0 A^{1/3} \tag{4.1}$$

where r_0 is a constant independent of A; that is, nuclear volumes are nearly proportional to the number of nucleons, and all nuclei have approximately the same density. Although nuclear densities (10^{14} g cm^{-3}) are extremely high compared with ordinary matter, nuclei are by no means densely packed with nucleons. This is an important factor for the success of the single-particle shell model. Different experimental methods lead to somewhat different values of r_0 ranging between ≈1.1 and ≈1.6 fm and also differ in the degree to which their results are fitted by Eq. (4.1). This is not surprising since different experiments measure quite different quantities. This can be the radius of the nuclear force field, the radius of the distribution of charges (protons), or the radius of the nuclear mass distribution. Measurements of the first two quantities have been available for a long time, while the third has become available only recently.

The earliest information about nuclear sizes came from Rutherford scattering with α particles from natural radioactive sources. These showed that the distance of the closest approach D of the α particles was larger than the radius of the nuclear force field, for example, D turned out to be on the order of 10–20 fm for copper and 30–60 fm for uranium. With the advent of particle accelerators, strongly interacting particles could be brought into contact with the force field of target nuclei resulting in absorption at scattering angles Θ larger than the grazing angle Θ_{gr}. Classically, if the cross section (cross sections are introduced in Chapter 12) for elastic scattering is normalized to the Rutherford or Coulomb cross section, $\sigma_{el}/\sigma_C = 1$ for small scattering angles and falls to zero at the grazing angle where absorption sets in. Due to the wave character of the ingoing and scattered particle, in reality, one observes an oscillatory structure of the quantal scattering cross section as a function of angle, which is reminiscent of optical diffraction patterns, see Figure 4.1, and the relative cross-section ratio falls off to reach 0.25 at the grazing angle. This is called the

Nuclear and Radiochemistry: Fundamentals and Applications,
Fourth Edition. Jens-Volker Kratz.

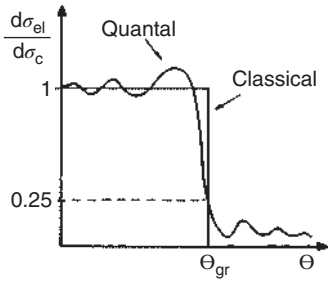

Figure 4.1 Schematic dependence of elastic scattering cross section σ_{el} normalized to the pure Coulomb scattering cross section σ_C on the scattering angle Θ in the classical and quantal representation. Source: Bass (1980)/Springer Nature.

quarterpoint. The Coulomb cross section

$$\left(\frac{d\sigma}{d\Omega}\right)_C = |f(\Theta_C)|^2 \tag{4.2}$$

is given by the absolute square of the Coulomb scattering amplitude. If, in an optical analogy, light is scattered on a black disk, the scattering amplitude is zero if the light hits the black disk; it is 0.5 if the light hits the edge of the black disk, thus the cross section goes to 0.25. Therefore, the quarterpoint recipe is used to determine the Coulomb barrier V_C from a solution of the Coulomb trajectory equation taking into account energy and angular momentum conservation via

$$\sin\frac{\Theta_{gr}}{2} = \frac{V_C}{2E_{cm} - V_C} \tag{4.3}$$

and

$$V_C = \frac{Z_1 Z_2}{R_C} e^2 \tag{4.4}$$

from which $R_C = r_0 A^{1/3}$ is deduced with r_0 being 1.35–1.6 fm.

If the whole dependence of the quantal scattering cross section on Θ at various incident energies is analyzed in a phase shift analysis, an angular momentum-dependent set of scattering phases can be deduced from the data, and these can be used to fix the parameters of the scattering potential, see Chapter 12. The most widely accepted analytical form used to describe the potential well is the one due to R.D. Woods and D.S. Saxon, obtained if a square-well potential is folded with a harmonic oscillator potential:

$$V = \frac{V_0}{1 + \exp[(r - R)/a]} \tag{4.5}$$

where V_0 is the depth of the potential (≈−50 MeV), a is a constant (≈0.5 fm), being a measure of the surface diffuseness of nuclei, and R is the distance from the center at which $V = V_0/2$. The Woods–Saxon potential is shown in Figure 4.2. Scattering experiments with hadrons result in $r_0 = 1.25$ fm and a drop-off of V/V_0 from 90% to 10% of the full potential depth, being 2 ln 9 times the constant a within a distance of ≈2.2 fm, the "skin thickness."

An entirely different class of experimental methods using probes that are not affected by nuclear forces but are sensitive to the electric charges of nuclei utilize the scattering of electrons. As the wavelength of the electrons can be chosen to be

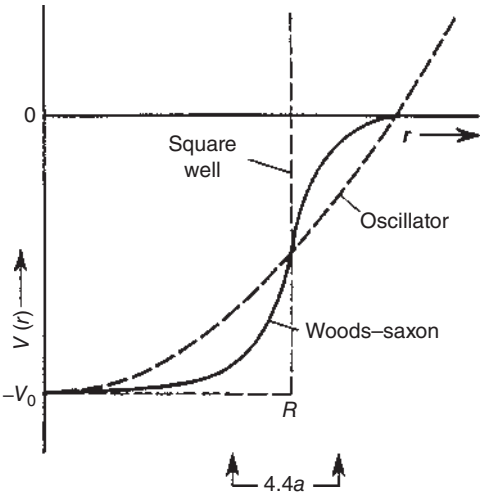

Figure 4.2 Woods–Saxon potential (solid line) in comparison to a square-well potential and a harmonic oscillator potential. The skin thickness is indicated as 4.4*a*.

rather short (500 MeV corresponds to $\lambda = 0.4$ fm), one can study charge distributions of nuclei to high resolution. The angular distribution of electrons scattered by an extended object is

$$\left(\frac{\mathrm{d}\sigma}{\mathrm{d}\Omega}\right) = \left(\frac{\mathrm{d}\sigma}{\mathrm{d}\Omega}\right)_{\text{point}} \cdot F^2(q) \tag{4.6}$$

where $F^2(q)$ is a function that can be deduced from the charge density distribution $\rho(r)$ as

$$F^2(q) = \left|\frac{1}{e}\int \rho(r)\exp[(i/\hbar)\mathbf{q}\cdot\mathbf{r}]\,\mathrm{d}\tau\right|^2 \tag{4.7}$$

Here, $\mathbf{q}$ is the momentum transfer in the scattering process. The important function $F^2(q)$ is called the form factor. It describes how the scattering from an extended object differs from the scattering from a point charge at a given q and is determined experimentally by dividing the observed cross section by that for a point charge calculated with the Mott formula. As the form factor is the Fourier transform of the charge density distribution $\rho(r)$, the latter can in principle be determined by inversion of Eq. (4.7) given that $F^2(q)$ is known in any detail. This is in most cases impossible as the momentum transfers are measured only in a finite range limited by the experiment. Rather, one is selecting a model distribution for $\rho(r)$ whose parameters are varied until the resulting form factor is in agreement with the measured one. To this end, one is using the so-called Fermi distribution, see Figure 4.3, which is closely related to the Woods–Saxon potential

$$\rho(r) = \frac{\rho_0}{1+\exp[(r-R_{1/2})/a]} \tag{4.8}$$

For $r = R_{1/2}$, the charge density falls to one-half of the central density ρ_0. The skin thickness is again $2\ln 9$ times a, that is, $4.4a$. In order to give a nuclear radius, a definition is needed to deduce it from the measured charge density distribution. Different definitions are in use. We have already defined $R_{1/2}$. Also indicated in

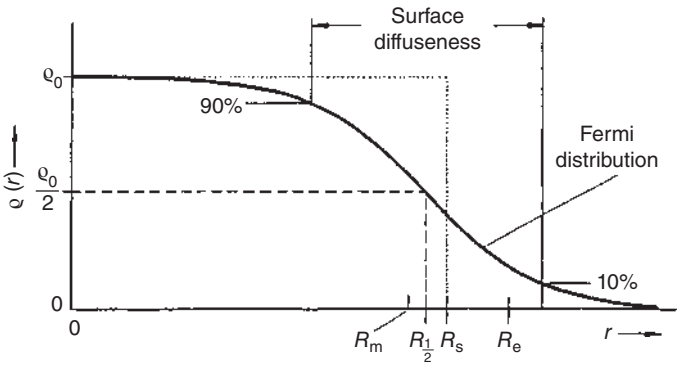

Figure 4.3 Charge distribution in a nucleus as determined by electron scattering. The various definitions of radii are indicated and are explained in the text.

Figure 4.3 is the mean square radius

$$R_m^2 = \langle r^2 \rangle = \int_0^\infty r^2 \rho(r) 4\pi r^2 \, dr \tag{4.9}$$

Instead of R_m, one finds often the equivalent radius R_e of a homogeneously charged sphere with $R_e = 1.73\,R_m$. One can also introduce the radius R_s, the equivalent sharp surface radius of a homogeneously charged sphere having the density ρ_0 everywhere. R_s is the only radius that is proportional to $A^{1/3}$. We have $R_s = 1.128\,A^{1/3}$. For the radii $R_{1/2}$ and R_e, one finds approximately $R_{1/2} = R_s - 0.89\,A^{-1/3}$ fm and $R_e = R_s + 2.24\,A^{-1/3}$ fm. The results of measurements of charge density distribution for $A > 20$ can be roughly summarized by

$$\rho(0) = \frac{Ze}{A} \text{ fm}^{-3} \tag{4.10}$$

saying that each nucleon in a medium-heavy or heavy nucleus requires a volume of 6 fm^3. With the nucleon radius of ≈0.8 fm, this underlines again that nucleons are not closely packed in nuclei.

The method of determining charge distributions by electron scattering has been advanced in particular by R. Hofstadter et al. at the Stanford Linear Accelerator. Figure 4.4 shows as an example the angular distribution of elastically scattered electrons of 420 MeV on carbon. The figure shows the fit of two different model distributions to the data. Figure 4.5 shows a survey of charge density distributions for various nuclei. The minimum in the central charge density of ^{16}O is an indication of the clustering of α particles in that nucleus, which is also known for ^{12}C.

A detailed description of the extraction of nuclear properties in atomic physics from optical transitions was given, for example, by E.W. Otten. Online laser spectroscopy allows one to study the nuclear properties of ground and isomeric states of short-lived exotic isotopes, which are available in only small quantities. The properties that can be studied are, among others, the change in the mean square radii $\delta\langle r^2 \rangle$ between isotopes. Experimental data can be determined with high accuracy, and the nuclear parameters can be extracted without using a nuclear model in long isotopic chains reaching far from the valley of stability. The difference in the charge

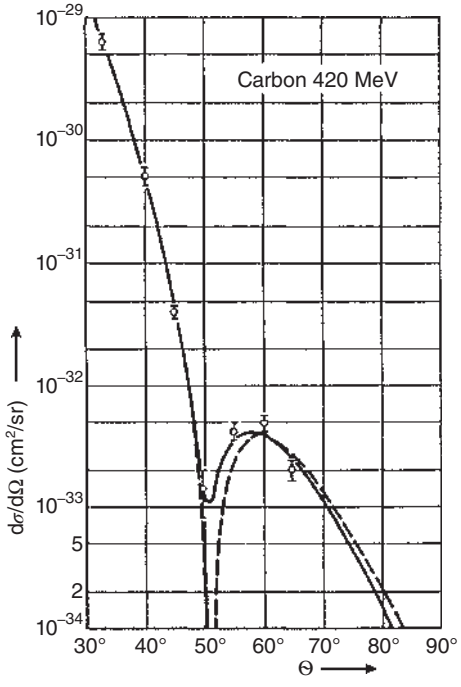

Figure 4.4 Angular distribution of elastically scattered electrons from ^{12}C at 420 MeV. Source: Hofstadter (1957)/Annual Reviews.

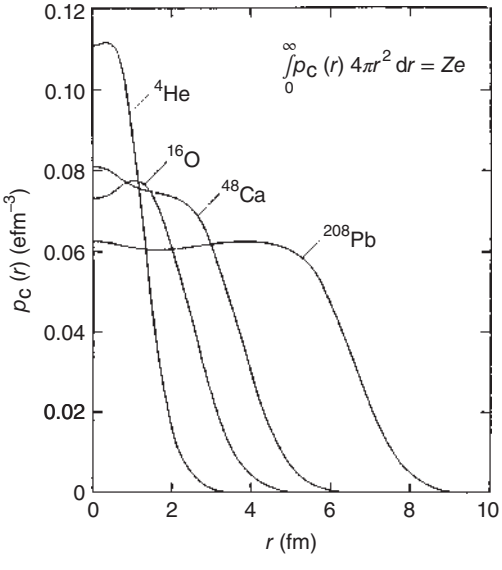

Figure 4.5 Charge distributions for a number of stable nuclei as deduced from electron scattering.

distribution gives rise to the volume or field shift (FS) with

$$\delta\nu_{\mathrm{FS}}^{MM'} = \frac{2\pi Z}{3}\Delta|\Psi(0)|^2\delta\langle r^2\rangle \tag{4.11}$$

between the isotopes with masses M and M' where $\Delta|\Psi(0)|^2$ is the change in the electron density in the nucleus in the electronic transition.

While the charge density results give information on how protons are distributed in nuclei, experimental techniques for determining the total nucleon distribution have become available only recently. Although it has been assumed that neutrons are distributed in roughly the same way as protons, there are theoretical predictions that neutron distributions may extend to larger distances from the centers than do proton distributions, and some experimental results on meson interactions with nuclear surfaces corroborated this conclusion. Recently, by measuring the spin-dipole resonance in neutron-rich isotopes, A. Krasnahorkay et al. deduced their neutron-skin thickness. By measuring electric dipole strength distributions (see Chapter 5) in neutron-rich nuclei, A. Klimkiewicz et al. observed low-lying dipole strength well below the giant dipole resonance, which was used to determine neutron-skin thicknesses $R_n - R_p$ of 0.24 ± 0.04 fm for ^{132}Sn and 0.18 ± 0.035 fm for ^{208}Pb, respectively. An alternative is to determine interaction cross sections and total charge-changing cross sections at relativistic energies (as done by L.V. Chulkov et al.) to deduce the thickness of neutron skins. Extreme examples of neutron distributions extending out to much larger radii than the proton distribution are found in light nuclei called halo nuclei. A halo nucleus is a very neutron-rich nucleus where the halo neutrons are very weakly bound. The density distribution of these weakly bound outermost neutrons extends far beyond the radius expected from the $A^{1/3}$ dependence. Examples of halo nuclei are ^{6}He, ^{8}He, ^{11}Li, ^{14}Be, and others. The best studied case is ^{11}Li where the halo neutrons are very weakly bound, making the size of ^{11}Li equal to the size of a ^{208}Pb nucleus.

Our discussion so far tacitly assumed that nuclei are spherical. As we will see later, many nuclei are in fact not spherical but exhibit deformed shapes. In those cases, our discussion of radii may be taken to apply for the mean semiaxes of these more complex shapes.

4.2 Nuclear Angular Momenta

From atomic physics, we know that the electron has an intrinsic angular momentum $s\hbar$ with $s = 1/2$. In addition, electrons occupy quantum-mechanical states that are labeled by the principal quantum number, N, which is the number of radial nodes $+1$ in the atomic wave function, with the angular momentum quantum number, l, being an integer multiple of $\hbar$ and reflecting the number of angular nodes in the wave function. Note that s and l are the maximum projections of the vectors $\mathbf{s}$ and $\mathbf{l}$ on the axis of orientation z. The eigenvalues of $\mathbf{s}$ and $\mathbf{l}$ are $|\mathbf{s}| = \sqrt{s(s+1)}\hbar$ and $|\mathbf{l}| = \sqrt{l(l+1)}\hbar$, and the projections of the latter on the z axis define the magnetic quantum numbers $m_s = \pm 1/2$ and m_l running from $-l$ via zero to $+l$. The vector $\mathbf{l}$ points at a cone around the z axis with $\cos\gamma = m_l/[l(l+1)]^{1/2}$. The atomic energy level is characterized by the total angular momentum, $\mathbf{J}$, resulting from the total orbital angular momentum, $\mathbf{L}$, and the total intrinsic spin, $\mathbf{S}$. These, in turn, result from separate electromagnetic vector couplings of the orbital angular momenta and

the spins, respectively. Except for the heaviest atoms, the electrons in the electron shell exhibit *LS* (Russel–Saunders) coupling.

That nuclei also possess angular momenta was first suggested by W. Pauli in 1924 in order to explain the hyperfine structure (hfs) in atomic spectra. The orbital angular momenta of the nuclear states are also integer multiples of $\hbar$, starting with zero. Nucleons exhibit a very strong coupling of the orbital angular momenta and the spins of individual nucleons such that $j = l + s$ is the angular momentum quantum number of the nucleon; *jj* coupling leads to the total angular momentum, I, of the nucleus. For a nucleus of even A, I must be zero or integral; for any odd-A nucleus, I must be half-integral. All nuclei of even A and even Z have $I = 0$ in their ground states. This can be understood by recalling that the nuclear force is of short range and that the nucleons are more strongly bound when they are in close proximity. The closest proximity is realized if two nucleons are in the same orbital, and if they are both neutrons and protons, their spins must be opposed to satisfy the Pauli principle. Obviously, the nuclear force tends to put pairs of nucleons into the same orbitals such that their orbital angular momenta and intrinsic spins cancel.

The coupling of the total angular momentum **J** of the electron shell with the total angular momentum of the nucleus **I** results in the total angular momentum of the atom **F**. The F states cause the hfs of the atomic spectra. For the determination of the total angular momentum of a nucleus, I, several complementary methods exist:

- One can count the number of hyperfine splitting components of a given atomic transition, which have the quantum numbers $(I + J)$, $(I + J - 1)$, …, $|I - J|$ with a multiplicity of $(2I + 1)$ if $I \leq J$, which is often the case.

One can evaluate the relative energetic distance of the hyperfine splitting components. The magnetic interaction energy for the hfs splitting is

$$\Delta E_{\mathrm{hfs}} = -\frac{A}{2}[F(F+1) - I(I+1) - J(J+1)] \tag{4.12}$$

with the interval factor

$$\frac{A}{2} = \frac{g_I \mu_{\mathrm{N}} B_0}{2IJ} \tag{4.13}$$

where g_I is the g factor of the I state, μ_{N} is the nuclear magneton (see Section 4.3), and B_0 is the magnetic field of the electron shell at the location of the nucleus, which must be calculated. One gets rid of this limitation by applying an external magnetic field.

- In a weak external magnetic field, I and J remain coupled to F, but each level splits into $(2F + 1)$ components (Zeeman effect).
- In a strong external magnetic field, I and J decouple (Paschen–Back effect), resulting in groups of levels with equal J, where each group consists of $(2I + 1)$ states.

In the preceding discussion, we used several times the term "coupling" of spins and angular momenta. Except for the very strong spin–orbit coupling $j = l + s$ of individual nucleons, which is a feature of the strong force, the other couplings, for

example, of L and S to J in the electron shell or of I and J to F in the atom, are the result of the electromagnetic interaction energy between two magnetic moments, which is proportional to the scalar product $(\boldsymbol{\mu}_L \cdot \cdot \boldsymbol{\mu}_S)$ or $(\boldsymbol{\mu}_I \cdot \cdot \boldsymbol{\mu}_J)$, respectively. We shall discuss magnetic dipole moments in Section 4.3.

An important symmetry property of the wave function of a particle or of a system of particles is parity π. If the wave function is $\boldsymbol{\psi}(r, s)$ where r stands for the position coordinates (x, y, z) and s is the spin orientation, the wave function may or may not change sign ($\pi = \pm 1$) when

$$\boldsymbol{\psi}(r, s) = \pi \boldsymbol{\psi}(-r, -s) \tag{4.14}$$

where the sign of the position coordinates is reversed as well as the direction of the spin corresponding to a reflection of the wave function at the origin. For $\pi = +1$, the system is said to have even parity; for $\pi = -1$, the system has odd parity. A second reflection needs to bring the system back into its original state, thus $\pi^2 = 1$. Two particles in states of even parity or two particles in states of odd parity can combine to form a state of even parity. A particle of even parity and one of odd parity result in a system of odd parity. This is illustrated by an example from atomic spectroscopy: allowed transitions in atoms occur only between a state of even and a state of odd parity, not between two even or two odd states. This is because the quanta of dipole radiation are of odd parity. Parity is connected with the angular momentum quantum number l through

$$\pi = (-1)^l \tag{4.15}$$

such that states with even l (s, d, g … states) have even parity; those with odd l (p, f, h … states) have odd parity.

4.3 Magnetic Dipole Moments

We know that the magnetic dipole moment due to the orbital motion of the electron with magnetic quantum number m_l is

$$\mu_{\mathrm{e}} = \frac{e\hbar}{2m_{\mathrm{e}}} m_l \tag{4.16}$$

where $e\hbar/2m_{\mathrm{e}} = \mu_{\mathrm{B}}$ is the Bohr magneton having the numerical value $5.78 \cdot 10^{-5}$ eV/T or $9.27 \cdot 10^{-21}$ erg/gauss. Extending this likewise to the nucleon leads to the definition of the nuclear magneton $\mu_{\mathrm{n}} = e\hbar/2m_{\mathrm{p}}$, which has the numerical value $3.15 \cdot 10^{-8}\,\mathrm{eV\,T^{-1}}$ or $5.50 \cdot 10^{-24}$ erg/gauss. Note that the nuclear magneton is smaller than the Bohr magneton by a factor given by the ratio of the proton to electron masses, which is ≈1836. Thus, the magnetic dipole moment of the proton is expected to be

$$\mu_l^{\mathrm{proton}} = m_l \mu_{\mathrm{N}} \tag{4.17}$$

As we will see further, because of internal currents inside the nucleons, it makes sense to rewrite the definition of the nuclear magnetic moment in terms of the

nuclear magneton by adding a constant of proportionality called the gyromagnetic ratio or simply the g factor:

$$\mu = g_l m_l \mu_N \tag{4.18}$$

where we would expect $g_l = 1$ for the orbital motion of the proton due to its charge and $g_l = 0$ for the neutron being uncharged. Additional contributions to the magnetic moment due to the intrinsic spin can be anticipated:

$$\mu = g_s m_s \mu_N \tag{4.19}$$

where $m_s = 1/2$ for fermions like the proton and neutron. For electrons, the numerical value for the spin g factor, $g_s = 2.0023$, calculated with the Dirac equation and including higher-order correction terms, is in very good agreement with the measured value. For the proton and the neutron, however, the measured values of g_s are much larger than that anticipated for a structureless particle, that is:

$g_s = +5.585\,691\,2(22)$ for the proton (magnetic moment parallel to the spin);
$g_s = -3.826\,083\,7(18)$ for the neutron (magnetic moment antiparallel to the spin).

This indicates that the magnetic moments of the nucleons are, according to the Gerasimov–Drell–Hearn (GDH) sum rule, composite quantities made up of the constituents of the nucleons with their own spins, orbital angular momenta, electric charges, and associated magnetic moments. At this time, hadron physics is far from a quantitative understanding of the magnetic moments of the nucleons.

The magnetic moment of a nucleus is

$$\boldsymbol{\mu}_I = g_I \mathbf{I} \mu_N \tag{4.20}$$

where g_I is called the nuclear g factor. All nuclei with $I = 0$ (even–even nuclei) have no magnetic moment. If the magnetic moment of a nucleus is not zero, the nucleus performs a precession in an outer magnetic field with frequency ω_L, the Lamor frequency:

$$\omega_L = g_I \mu_N \frac{B}{\hbar} \tag{4.21}$$

where B is the magnetic flux density. The Lamor frequency is in the region of radiofrequencies. The nucleus adopts $2I + 1$ energy levels differing from each other by $\Delta E = \hbar\omega_L = g_I \mu_N B$. By absorption of photons of frequency ω_L, the nucleus can pass from a given energy level to a neighboring level. This process is known as nuclear magnetic resonance (NMR) and has become an important tool in the study of chemical bonds.

For the measurement of magnetic moments, one uses their interaction with a magnetic field B. According to Eqs. (4.12) and (4.13), μ_I can be deduced from the magnitude of the hfs splitting as long as the magnetic field of the electron shell at the location of the nucleus B_0 can be calculated with sufficient precision. In an external magnetic field B, the hfs levels split. If the total angular momentum of the electron shell is $J = 1/2$, the B dependence can be given in closed form (Breit–Rabi formula). Although the influence of the magnetic field of the electron shell is dominant, one can deduce from that formula that the energy difference ΔE between a transition

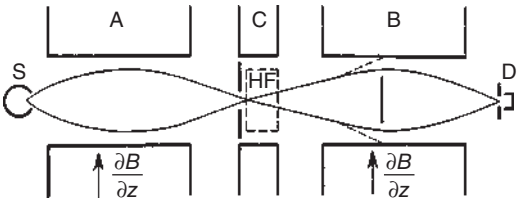

Figure 4.6 Atomic beam apparatus of I.I. Rabi (schematic).

with $\Delta F = 1$, $\Delta m = 1$ ($m_2 \rightarrow m_1$) and one with $\Delta F = 1$, $\Delta m = -1$ ($m_1 \rightarrow m_2$) depends only on the external field and magnetic moment. Such transitions were investigated in an atomic beam experiment by I.I. Rabi in 1934–1939, as an extension of the Stern–Gerlach experiment. A beam of neutral atoms evaporated from a thermal source S passes first through an inhomogeneous magnetic field A (Figure 4.6). Here, a force proportional to the z component of the magnetic moment

$$F = \mu_z \left(\frac{\partial B_z}{\partial z} \right) \tag{4.22}$$

acts on the atoms such that they fly along a curved trajectory. The magnet B at the end of the apparatus is identical to A. Thus, the particle trajectories in B are curved in the same direction as in A and the atoms are lost on the magnet poles (dashed trajectories). In between A and B there is a homogeneous magnetic field C. It does not exert a force on the atoms. In the magnet C, fed by a high-frequency (HF) generator, an HF field of frequency ω is produced. If in the magnet C at the external flux density B the exact transition energy $\Delta E = \hbar\omega_L$ is provided, induced dipole transitions occur resonantly that change the sign of μ_z. In that case, the particles are resonantly focused back to the detector D.

The NMR technique has not only been used to determine the magnetic moments of nuclei, it has also been further developed in applied sciences, of which only the most important are mentioned:

"NMR spectroscopy" has become a standard method in chemical structure research and one of the most important instruments in analytic organic chemistry. The close structural environment of a certain functional group varies in a structure-dependent way the magnetic field strength in the position of the radiofrequency, thereby leading to a "chemical shift" of the resonance frequency.

With the "NMR tomography," one can produce multiple sectional views of the human body that allow to reconstruct locally resolved 3D-images of organs that are useful to decide whether these show pathological symptoms. Alternating magnetic fields in the position of the radiofrequency excite hydrogen nuclei resonantly, and during magnetic field-off their decay induces a signal in the receiver circuit. The contrast of the images depends on the proton density and on different relaxation times in the various kinds of tissue. In addition, the proton densities in the different tissues (muscle, bone) contribute to the contrast of the images. These have also been obtained with local and time resolution showing neural processes in the brain.

4.4 Electric Quadrupole Moments

The electric potential of a uniformly charged body at a field point P due to a nonspherical charge distribution is

$$V_{\text{Coul}}(P) = k_{\text{C}} \int \frac{\rho \, \mathrm{d}v}{d} \tag{4.23}$$

where $k_{\text{C}} = 1/(4\pi\varepsilon_0)$ with the electric field constant $\varepsilon_0 = 8.854\,19 \cdot 10^{-12}\ \text{A s V}^{-1}\ \text{m}^{-1}$, ρ is the charge density, and $\mathrm{d}v$ a differential volume element. The distance d of the volume element to the field point P can be expressed in terms of r and θ and the coordinate of P on the z axis, z, by using the cosine law $d^2 = z^2 + r^2 - 2rz\cos\Theta$ giving

$$V_{\text{Coul}}(P) = k_{\text{C}} \int \frac{\rho \, \mathrm{d}v}{(z^2 + r^2 - 2rz\cos\Theta)^{1/2}} \tag{4.24}$$

which can be expanded with Legendre polynomials multiplied by $(r/z)^n$ such that

$$V_{\text{Coul}}(P) = k_{\text{C}} \int \frac{\rho}{z} \left[1 + \frac{r}{z}\cos\Theta + \frac{r^2}{2z^2}(3\cos^2\Theta - 1) + \cdots \right] \tag{4.25}$$

or

$$V_{\text{Coul}}(P) = k_{\text{C}} \int \frac{\rho}{z} \left(\sum_{n=0}^{\infty} \left(\frac{r}{z} \right)^n P_n^0(\cos\Theta) \right) \mathrm{d}v \tag{4.26}$$

Here, the terms with $n = 0, 1, 2, 3, \ldots$ are the monopole, dipole, quadrupole, octupole, etc., terms. The monopole term represented by ρ/z is the electric potential of a point charge located at the origin. For a quantum-mechanical system in a well-defined quantum state, the charge density ρ is an even function, and because the dipole moment involves the product of an even and an odd function, the corresponding integral is zero. There exists no electric dipole moment or any other odd electric moment for nuclei. The quadrupole moment

$$Q = k_{\text{C}} \int \frac{r^2}{2}(3\cos^2\Theta - 1)\rho \, \mathrm{d}v \tag{4.27}$$

will differ from zero if the nucleus is not spherical. Suppose that the nucleus has a shape produced by the rotation of an ellipsoid about the axis of symmetry. It will have a circular cross section in planes normal to that axis. Depending on the orientation of the semimajor and semiminor axes, a and b, two possible shapes can result, that is, a prolate ellipsoid having a positive quadrupole moment, and an oblate ellipsoid having a negative quadrupole moment. Defining $\overline{R} = (a + b)/2$ and $\Delta R = b - a$ results in the expression

$$Q = \frac{4}{5} Z \overline{R}^2 \left(\frac{\Delta R}{\overline{R}} \right) \tag{4.28}$$

with $(\Delta R/\overline{R})$ being the deformation parameter δ. (Note that there is another dimensionless measure of deformation, $\beta = \frac{4}{3}\sqrt{\pi/5} \cdot \delta$.) In the presence of an electrical quadrupole moment of a nucleus, the hfs lines are shifted and do not follow Eqs. (4.12) and (4.13). Therefore, quadrupole moments can be determined by

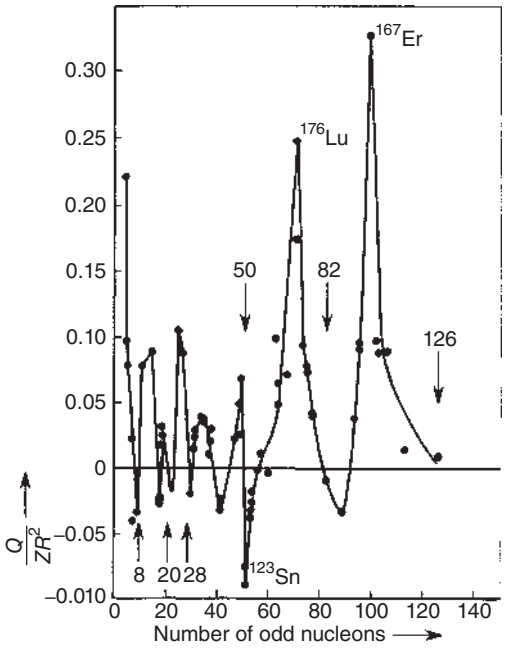

Figure 4.7 Electrical quadrupole moments as a function of the odd number of neutrons or protons.

hfs observations, for example, by microwave spectroscopy. In Figure 4.7, a number of experimental values is plotted against the number of odd nucleons. Note that nuclei with $I = 0, 1/2$ have no electric quadrupole moment. Maximum deformation is observed in the middle between closed shells. Nuclei with closed shells are spherical. The quadrupole moments given by Eq. (4.28) are so-called spectroscopic quadrupole moments. They have to be distinguished from inner quadrupole moments, which we will discuss in the context of transition probabilities (Chapter 6). Higher static electric and magnetic moments can also exist in nuclei. They are classified according to the multipole order (n in Eq. (4.26)) corresponding to a 2^n pole.

4.5 Statistics and Parity

As we have mentioned already in Section 1.5.6, all nuclei and elementary particles are known to obey one of two statistics: Bose–Einstein and Fermi–Dirac statistics. If all the coordinates describing a particle including three space coordinates and its angular momentum are interchanged with those of an identical particle in the system, the absolute magnitude of the wave function representing the system must remain the same; however, the wave function may or may not change sign. If it does not change sign, the wave function is symmetrical and Bose statistics apply. If the particle wave function does change sign with the interchange of coordinates, its wave function is antisymmetric and the particles obey Fermi statistics. In Fermi statistics, each completely specified quantum state can be occupied by only one particle, that

is, the Pauli exclusion principle applies. For particles obeying Bose statistics, no such restriction exists. A nucleus will obey Bose or Fermi statistics, depending on whether it contains an even or odd number of nucleons.

Another quantum-mechanical property connected with the symmetry properties of nuclear wave functions is parity. A system has odd or even parity according to whether or not the wave function for the system changes sign when the signs of all the space coordinates are changed. The latter corresponds to a reflection of the coordinate system at the origin (replacement of $\mathbf{r}$ by $-\mathbf{r}$). The property of the system is not allowed to change in this operation except for an arbitrary constant π, that is, $\Psi(r) = \pi\Psi(-r)$. A second reflection at the origin must lead back to the original state. Thus, $\pi^2 = 1$ or $\pi = \pm 1$. Thus, parity defines the symmetry character of the wave function upon reflection in space. Parity is a multiplicative quantum number: two particles in states of even parity ($\pi = +1$) or two particles in states of odd parity ($\pi = -1$) can combine to form a state of even parity only. A particle of even parity and one of odd parity combine to a system of odd parity. In discussing nuclear energy states, we make use of the fact that parity is connected to the angular momentum quantum number l such that states with even l (s, d, g, … states) have even parity while those with odd l (p, f, h, … states) have odd parity.

4.6 Excited States

The previous sections have dealt with the properties of the ground states of nuclei. Much of nuclear chemistry and physics are, on the other hand, concerned with excited states of nuclei, the systematization of their properties, and their

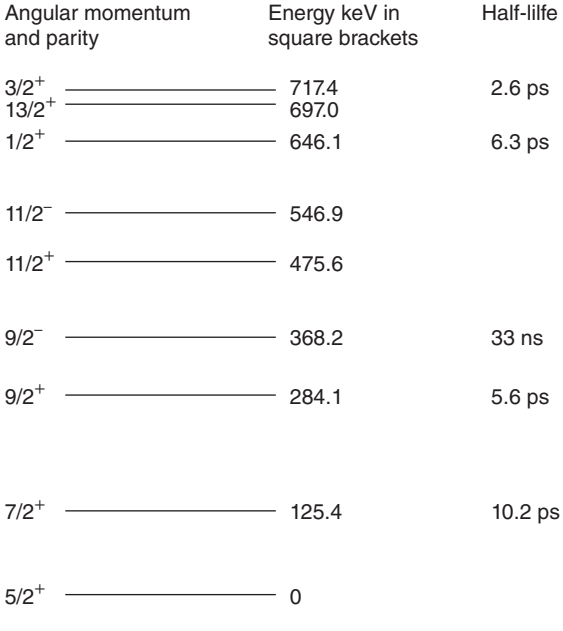

Figure 4.8 The first few energy levels of ^{185}Re.

understanding in the frame of nuclear models. Among the static properties are the excitation energies of these states, their total angular momenta, parities, and magnetic moments. Moreover, transition probabilities between excited states are of importance for the understanding of nuclear structure. These are usually given in terms of half-lives. The relative transition probabilities for transitions from a given state to two or more other states are also of fundamental interest. We will touch upon excited states and the transitions between them in the chapters on nuclear structure, decay *modes*, and nuclear reactions. Here, we merely call attention to the existence of this vast subject and, as an illustration, present in Figure 4.8 the first few excited states in ^{185}Re, their energies, total angular momenta, parities, and, where available, their half-lives.

References

Bass, R. (1980). *Nuclear Reactions with Heavy Ions*. Berlin, Heidelberg, New York: Springer-Verlag.

Hofstadter, R. (1957). Nuclear and nucleon scattering of high-energy electrons. *Annu. Rev. Nucl. Sci.* 7: 231.

Further Reading

General

Evans, R.D. (1955). *The Atomic Nucleus*. New York: McGraw-Hill.

Kaplan, I. (1964). *Nuclear Physics*, 2e. Reading, MA: Addison-Wesley.

Segré, E. (1964). *Nuclei and Particles*. New York: Benjamin.

Bohr, A. and Mottelson, B.R. *Nuclear Structure*, vol. 2. New York: Benjamin.1969 and 1975

Friedlander, G., Kennedy, J.W., Macias, E.S., and Miller, J.M. (1981). *Nuclear and Radiochemistry*, 3e. New York: Wiley.

Vertes, A. and Kiss, I. (1987). *Nuclear Chemistry*. Amsterdam: Elsevier.

Krane, K.S. (1988). *Introductory Nuclear Physics*. New York: Wiley.

Wong, S.S.M. (1998). *Introductory Nuclear Physics*, 2e. New York: Wiley.

Loveland, W.D., Morrissey, D.J., and Seaborg, G.T. (2006). *Modern Nuclear Chemistry*. Hoboken, NJ: Wiley.

Prussin, S.G. (2007). *Nuclear Physics for Applications*. Weinheim: Wiley-VCH.

More Specialized

Rabi, I.I., Kellogg, J.M.B., and Zacharias, J.R. (1934). The magnetic moment of the proton. *Phys. Rev.* 46: 157.

Rabi, I.I., Kellogg, M.B., and Zacharias, J.R. (1934). The magnetic moment of the deuteron. *Phys. Rev.* 46: 163.

Rabi, I.I., Kellogg, M.B., and Zacharias, J.R. (1936). The sign of the magnetic moment of the proton. *Phys. Rev.* 49: 421.

Rabi, I.I., Zacharias, J.R., Millman, S., and Kusch, P. (1938). A new method of measuring nuclear magnetic moment. *Phys. Rev.* 53: 318.

Rabi, I.I., Millman, S., Kusch, P., and Zacharias, J.R. (1939). The molecular beam resonance method for measuring nuclear magnetic moments. *Phys. Rev.* 55: 526.

Nilson, R., Jentschke, W.K., Briggs, G.R. et al. (1958). Investigation of excited states in ^{8}Be by alpha-particle scattering from He. *Phys. Rev.* 109: 850.

Darriulat, P., Igo, G., Pugh, H.G., and Holmgren, H.D. (1965). Elastic scattering of alpha particles by helium between 53 and 120 MeV. *Phys. Rev.* 137B: 315.

Mott, N.F. and Massey, H.S.W. (1965). *The Theory of Atomic Collisions*, 3e. Oxford: Clarendon Press.

Barrett, R.C. and Jackson, D.F. (1977). *Nuclear Sizes and Structure*. New York: Clarendon Press.

Mayer-Kuckuk, T. (1979). *Kernphysik*. Stuttgart: Teubner.

More Recent

Otten, E.W. (1989). Nuclear radii and moments of unstable isotopes. In: *Treatise on Heavy Ion Science, Nuclei Far from Stability*, vol. 8 (ed. D.A. Bromley), 515. New York: Plenum Press.

Chulkov, L.V., Bochkarev, O.V., Cortina-Gil, D. et al. (2000). Total charge-changing cross sections for neutron-rich light nuclei. *Nucl. Phys.* A674: 330.

Tanihata, I. (2002). Studies with radioactive beams, past and future. *Prog. Theor. Phys. Suppl.* 146: 1.

Jonson, B. (2004). Light dripline nuclei. *Phys. Rep.* 389: 1.

Krasnahorkay, A., Akimune, H., van den Berg, A.M. et al. (2004). Neutron-skin thickness in neutron-rich isotopes. *Nucl. Phys. A* 731: 224.

Aumann, T. (2005). Reactions with fast radioactive beams of neutron-rich nuclei. *Eur. Phys. J. A* 26: 441.

Bosch, F., Geissel, H., Litvinov, Y.A. et al. (2006). *Int. J. Mass Spectrom.* 251: 212.

Klimkiewicz, A., Paar, N., Adrich, P. et al. (2007). Nuclear symmetry energy and neutron skins derived from pygmy dipole resonances. *Phys. Rev. C* 76: 051603(R).

Ketelaer, J., Krämer, J., Beck, D. et al. (2008). TRIGA-SPEC: a setup for mass spectrometry and laser spectroscopy at the research reactor TRIGA mainz. *Nucl. Inst. Methods Phys. Res. A* 594: 162.

Fényes, T. (2011). Basic properties of the atomic nucleus. In: *Handbook of Nuclear Chemistry*, 2e, vol. 1 (eds. A. Vértes, S. Nagy, Z. Klencsár, et al.), 39. Berlin: Springer.

5

The Nuclear Force and Nuclear Structure

5.1 Nuclear Forces

Ideally, one would like to derive the properties of nuclei from the properties of the nuclear forces that govern the interactions among nucleons. This is complicated because we have only approximate techniques to solve a many-body problem. Also, it is further complicated by two additional problems:

1. The law that describes the force between two free nucleons is not exactly known.
2. There is evidence that the force exerted by one nucleon on another when they are also interacting with other nucleons may be different from the one which they exert on each other when they are free; that is, there is evidence for many-body forces.

Therefore, one is forced to make simplifying assumptions, which can lead to a variety of models, and each model may be used to describe a different aspect of the problem. This is why, in the following sections, we describe the models that have been found useful in describing a large body of nuclear data, in particular the energies, angular momenta, and parities of nuclear states as discussed briefly in Chapter 4. We start by sketching what is known about nuclear forces and their implications for the properties of complex nuclei.

Direct information about the forces existing between free nucleons can be obtained from nucleon–nucleon scattering preferably involving polarized projectiles and targets, and from the properties of the deuteron. The quantity that is more useful than the force is the potential (cf. Eq. (1.14)). The nuclear potential seems to be much more complex than other familiar potentials such as the Coulomb potential or the gravitational potential. Although it is not yet possible to write down a unique expression for the nuclear potential, several of its properties are known. The potential energy of two nucleons shows some similarity to the potential energy function that describes the stretching of a chemical bond, as follows.

1. The nuclear potential is not spherically symmetric. The directional character is determined by the angles between the angular momenta of each nucleon and the vector that connects the two nucleons. The quadrupole moment of

Nuclear and Radiochemistry: Fundamentals and Applications,
Fourth Edition. Jens-Volker Kratz.

the deuteron tells us that the potential lacks spherical symmetry. Hence, the spherically symmetric part is called the central potential, and the asymmetric part the tensor interaction.

2. The nuclear potential has a finite range and becomes large and repulsive at small distances. As stated above, there is qualitative similarity with a chemical potential but the distances are 5 orders of magnitude smaller and the energies 7 orders of magnitude larger. The nuclear potential becomes repulsive at distances smaller than 0.5 fm and vanishes exponentially when the internucleon separation exceeds 2 fm, see Figure 5.1. The long-range part of the potential is described by the Yukawa form where the nucleons exchange a π meson as the force carrier:

$$V(r) = g\frac{1}{r}\exp\left[-\left(\frac{m_\pi c}{\hbar}r\right)\right] \tag{5.1}$$

which contains g as a coupling constant and as length the Compton wavelength of the pion, $\lambda\lambda_\pi = \hbar/m_\pi c$. For smaller, intermediate distances, the heavier ρ meson is assumed to be the exchange boson, and for the repulsive part, the even heavier ω meson. In quantum chromodynamics (QCD), the force carrier is the gluon. As the exchange of a gluon between two nucleons would violate color symmetry, this is only possible if, simultaneously, a quark is exchanged. The associated Feynman graph is shown in Figure 5.2. It has been observed that the interaction between high-energy neutrons and a target of protons leads to many events (more than can be explained by head-on collisions), in which a high-energy proton is emitted in the direction of the incident neutron beam. This led to the idea that the neutron and proton, when in the range of nuclear forces, may exchange roles. This is an excellent example of what is meant by the exchange character of the nuclear potential. The exchange character of the potential, in conjunction with

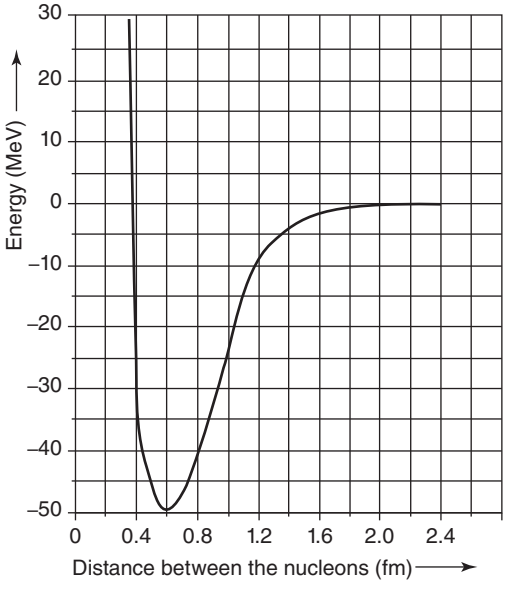

Figure 5.1 Nucleon–nucleon potential as a function of the distance between two nucleons.

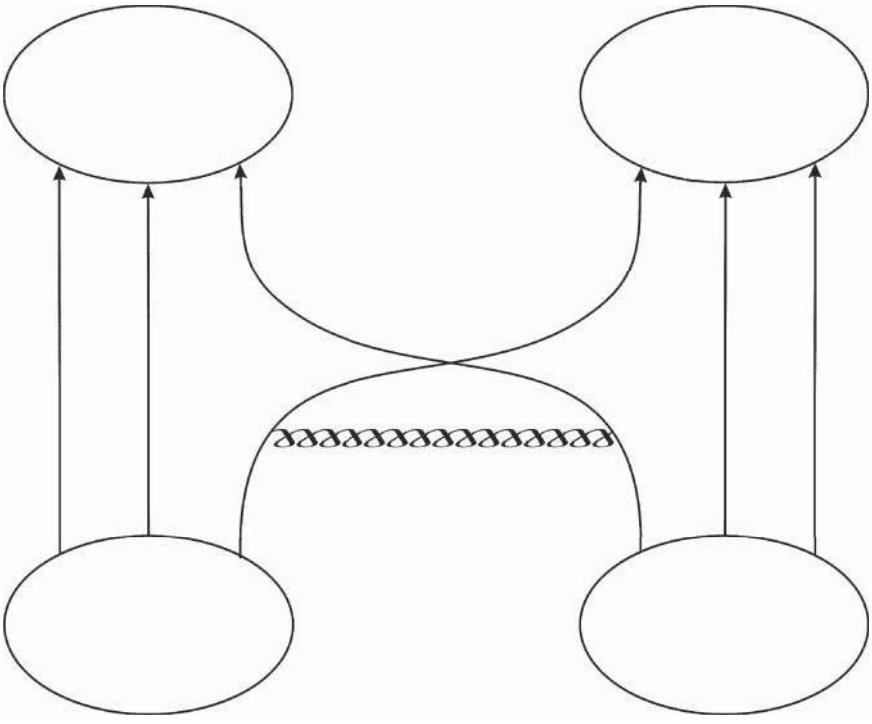

Figure 5.2 Feynman graph for the gluon exchange between two nucleons.

the requirement that the wave function describing the two-nucleon system must be antisymmetric, can give rise to the type of force described below in 3).

Deviating from the shape of the potential in Figure 5.1, the size and binding energy of the deuteron are consistent with an attractive square well potential of 25 MeV depth only and a range of about 2.4 fm. The factor of 10^7 in the relative strengths of the nuclear and chemical forces is one reason to talk about the nuclear force as the strong force.

However, in view of their extremely short range, nuclear forces appear as if they were very weak. This paradoxical behavior can be understood if we recall that, if two particles are to be confined within a distance R, they must have a de Broglie wavelength $\leq 2R$:

$$\lambda = \frac{h}{\mu v} \leq 2R \tag{5.2}$$

or

$$\mu v \geq \frac{h}{2R} \tag{5.3}$$

with $\mu = m_1 m_2/(m_1 + m_2)$ being the reduced mass. Hence, the kinetic energy of the particles is

$$\frac{1}{2}\mu v^2 \geq \frac{h^2}{8\mu R^2} \tag{5.4}$$

If the two nucleons are to remain in the range of nuclear forces, 2.4 fm, the kinetic energy must be at least

$$\frac{\left(6.626{\cdot}10^{-27}\right)^2}{8{\cdot}\frac{1}{2}\left(1.660\,56{\cdot}10^{-24}\right)\cdot\left(2.4{\cdot}10^{-13}\right)^2{\cdot}1.602{\cdot}10^{-6}} = 71\ \text{MeV} \tag{5.5}$$

which is greater than the depth of the deuteron potential. The absence of excited states of the deuteron, its low binding energy of 2.2 MeV, and its large size (the proton and neutron spend about one-half the time outside the range of the nuclear force) reflect the "weakness" of the nuclear force resulting from its small range.

3. The nuclear potential depends on the quantum state of the system. The stable state of the deuteron is the one with parallel spins of neutron and proton (triplet state). The singlet state with opposite spins is unbound. The nucleon–nucleon potential also depends on the relative angular momentum and on the orientation of the latter with respect to the intrinsic spins of the nucleons, that is, on the spin–orbit coupling. The deuteron magnetic moment, 0.857 μn, is close to the sum of the neutron and proton magnetic moments.
4. There are semiempirical formulas that can describe the nuclear potential. These are rather complex as they must contain a central part with four components to account for the effect of parallel or antiparallel spins and the evenness or oddness of the relative angular momentum. They must also contain two components each of a tensor force and spin–orbit force that occur only for parallel spins but with either odd or even relative angular momentum. This is completed by four components of a second-order spin–orbit force that can occur for both parallel and antiparallel spins.

5.2 Charge Independence and Isospin

The strong interaction between two protons or two neutrons or a neutron and a proton is the same. There are, of course, different electromagnetic forces acting in these cases, but these differences can be corrected, as we will see below. Evidence for the charge independence of the nuclear force can be found in nucleon–nucleon scattering and in the binding energies of mirror nuclei. Mirror nuclei are isobars where the number of protons in one nucleus is equal to the number of neutrons in the other nucleus. Table 5.1 lists the nuclear binding energies of some light mirror nuclei, the difference in the Coulomb energies when increasing the number of protons by one unit, and the binding energy of the $(A, Z+1)$ nucleus corrected for the mass difference between the neutron and the hydrogen atom and the Coulomb energy difference (using Eq. (3.9) with $a_c = 0.717$ MeV) between the (A, Z) nucleus and the $(A, Z+1)$ nucleus:

$$\Delta E = E(A,\ Z+1) - E(A,\ Z) = \Delta E_{\text{Coul}} - (m_n - m_H)c^2 \tag{5.6}$$

where $(m_n - m_H)c^2 = 0.782$ MeV. For example, $\Delta E = 4.907 - 0.782$ MeV $= 4.125$ MeV for the mirror nuclei ^{25}Mg and ^{25}Al, which gives for ^{25}Al a binding energy

Table 5.1 Properties of light mirror nuclei.

A	Nucleus	Binding energy (MeV)	Coulomb energy (MeV)	ΔE_{Coul} (MeV)	Corrected binding energy (MeV)
3	^{3}H	8.486	0		
	^{3}He	7.723	0.829	0.829	7.770
13	^{13}C	97.10	7.631		
	^{13}N	94.10	10.683	3.052	96.37
23	^{23}Na	186.54	23.13		
	^{23}Mg	181.67	27.75	4.62	186.29
25	^{25}Mg	205.59	26.97		
	^{25}Al	200.53	31.88	4.91	204.66
41	^{41}Ca	350.53	65.91		
	^{41}Sc	343.79	72.84	6.93	349.94

$E + \Delta E = 204.66$ MeV, very close to the binding energy of ^{25}Mg which is 205.59 MeV. The corrected binding energies $E + \Delta E$ of the $(A, Z + 1)$ nuclei in Table 5.1 are always close to those of the (A, Z) nuclei, supporting the idea of the charge independence of nuclear forces.

The charge independence of nuclear forces leads to the view (proposed by Heisenberg in 1932) that the proton and neutron are two quantum states of a single particle, the nucleon. Since only two states occur, the situation is analogous to that of the two spin states of an electron and thus the whole quantum mechanical formalism developed for the electron spins has been taken over for the charge state of nucleons. The physical property involved is called the isospin, T. Each nucleon has a total isospin of $\frac{1}{2}$ just as the electron has a total spin of $\frac{1}{2}$. The z component of the isospin, T_z, is either $+\frac{1}{2}$ or $-\frac{1}{2}$; the convention is to assign the $+\frac{1}{2}$ state to the proton and the $-\frac{1}{2}$ state to the neutron. The concept of isospin approximately carries over to complex nuclei where the corresponding quantity is the vector sum of the isospins of the constituent nucleons, which is *nearly* a good quantum number and thus *nearly* a conserved quantity. For example, ^{9}Be with five neutrons and four protons has $T_z = +\frac{1}{2}$. Two nucleons may have a total isospin of 1 or 0. For $T = 1$, T_z may be -1 (two protons), 0 (a proton and a neutron), or $+1$ (two neutrons). For a total isospin of 0, the z component can only be 0 but may have $T = 1$ or $T = 0$. Two neutrons or two protons must have $T = 1$. The Pauli principle requires that the wave function describing the dineutron and the diproton be antisymmetric. The wave function describing the system is now a function of three variables, namely, space, spin, and isospin:

$$\psi(\text{system}) = \psi(\text{space}) \quad \psi(\text{spin}) \quad \psi(\text{isospin}) \tag{5.7}$$

In the ground state of the deuteron, ψ(space) is symmetric, being a mixture of an s state and a d state, and ψ(spin) is symmetric (parallel spins), so that the isospin must

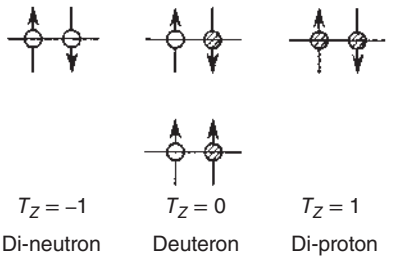

Isospin	Spin
$T = 1$ Triplet symmetric	$S = 0$ Single antisymmetric
$T = 0$ Single antisymmetric	$S = 1$ Triplet symmetric

Figure 5.3 States of the two-nucleon system with spins and isospins. Source: Mayer-Kuckuk (1979)/John Wiley & Sons.

be antisymmetric, $T = 0$; that is, the isospins are oppositely oriented. The exited state of the deuteron in which the nucleon spins are opposed (ψ(spin) antisymmetric) is the lowest one in which $T = 1$ and is unbound. The states of the two-nucleon system are shown in Figure 5.3 together with the spins and isospins. Because of the charge independence of the nuclear force, the three $T = 1$ states (isospin triplet) are all unbound, which corresponds to the experimental observation.

In the following, the implications of isospin for complex nuclei are discussed further. We have already seen that the z component of the isospin obviously determines the charge state of the nucleus, and we have

$$T_z = \frac{N-Z}{2} \quad \text{and} \quad \frac{|N-Z|}{2} \leq T \leq \frac{A}{2} \tag{5.8}$$

Except for a few odd–odd nuclei with $Z = N$, all nuclei have $T = T_z$ in their ground state; $^{235}_{92}$U in the ground state has $T = T_z = 51/2$. The other values of T are found in the excited states of the nucleus. In order to introduce the concept of isobaric analog states, we consider a nucleus (N, Z) characterized by a set of quantum numbers including T and T_z. This state is to be changed by changing T_z to $T_z - 1$ leaving all other quantum numbers, including T, the same. It now contains $Z + 1$ protons and $N - 1$ neutrons. The original state and that of the new nucleus are called isobaric analog states for the obvious reason that the two nuclei are isobars and the two quantum states are corresponding ones. T_z' of the new nucleus is $T_z - 1$, and the ground state of the new nucleus is expected to have $T' = T_z' = T_z - 1$, whereas the ground state isospin of the original nucleus is $T = T_z$. Therefore, the isobaric analog state in the nucleus $(Z + 1, N - 1)$ is an excited state with isospin 1 unit greater than that of the ground state of the isobaric analog nucleus (Z, N). It should be noted that each state of A nucleons with isospin T_0 has $2T_0 + 1$ isobaric analog states with T_z going from $+T_0$ to $-T_0$ in integer units. This is illustrated for isobaric analog states in $A = 14$ nuclei in Figure 5.4, for example, for ^{14}C, ^{14}N, and ^{14}O; ^{14}C and ^{14}O are mirror nuclei and have ground states with $T_z = \pm 1$ and are part of an isospin triplet with $T = 1$ ($T_z = 0, \pm 1$). In the $T_z = 0$ nucleus, ^{14}N, there must be a state with $T = 1$, $T_z = 0$ that is the isobaric analog state of the $T_z = \pm 1$ ground states of ^{14}C and ^{14}O. In analogy to Eq. (5.6), the energy differences between isobaric analog states are

$$E_{\mathrm{IA}}(A,\ Z+1) = E_{\mathrm{IA}}(A,\ Z) + \Delta E_{\mathrm{Coul}} - \left(m_{\mathrm{n}} - m_{\mathrm{H}}\right) c^2 \tag{5.9}$$

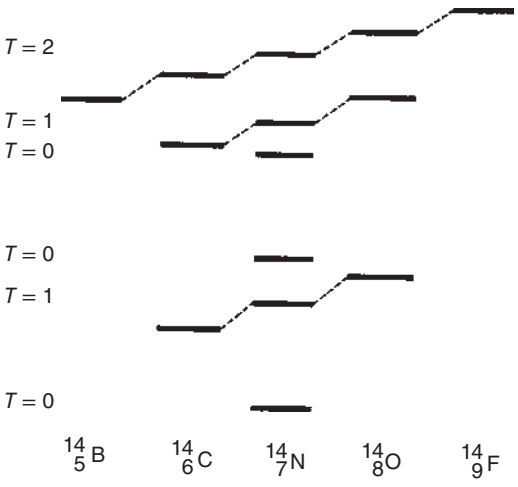

Figure 5.4 Isobaric analog states for $A = 14$ nuclei. Source: Cohen (1971)/McGraw-Hill.

Transition rates between isobaric analog states are particularly large because of the nearly perfect overlap of the space and spin parts of the wave functions. Also, β-decay transitions between mirror nuclei (superallowed transitions) belong to this phenomenon. That isospin is a *nearly* conserved quantity that will be demonstrated by the following example. In Figure 5.5, on the right-hand side, we see a nucleus (Z, N) whose ground state and low-lying states have the isospin $T_> = (N - Z)/2$. If we again change the uppermost neutron into a proton, the nucleus $(Z + 1, N - 1)$ is formed in a highly excited analog state belonging to the isospin multiplet of $T_>$. The ground state of this nucleus has the isospin $T_< = T_> - 1$. The isobaric analog states in the $(Z + 1, N - 1)$ nucleus are expected to lie in the continuum of broad overlapping excited states. They can be observed as resonances in the proton scattering on the neighboring nucleus with $(Z, N - 1)$. It has the isospin

$$\frac{(N-1)-Z}{2} = T_> - \frac{1}{2}$$

In the energy dependence of the cross section (excitation function) for the proton scattering, one observes surprisingly sharp resonances corresponding to the $T_>$ states of the (Z, N) nucleus shifted by the Coulomb energy difference. The sharpness of these states is caused by their long lifetimes because their decay probabilities are strongly reduced by isospin conservation. The most probable decay, neutron emission, cannot occur because that would lead to the nucleus $(Z + 1, N - 2)$ whose low-lying states have the isospin

$$\frac{((N-2)-(Z+1))}{2} = T_> - \frac{3}{2}$$

However, the neutron can only remove the isospin ½. On the other hand, the decay width for proton decay is reduced by the Coulomb barrier. The resulting small decay probability of the isobaric analog states leads to the remarkable sharpness of the resonances. The investigation of analog states is an important tool in nuclear spectroscopy.

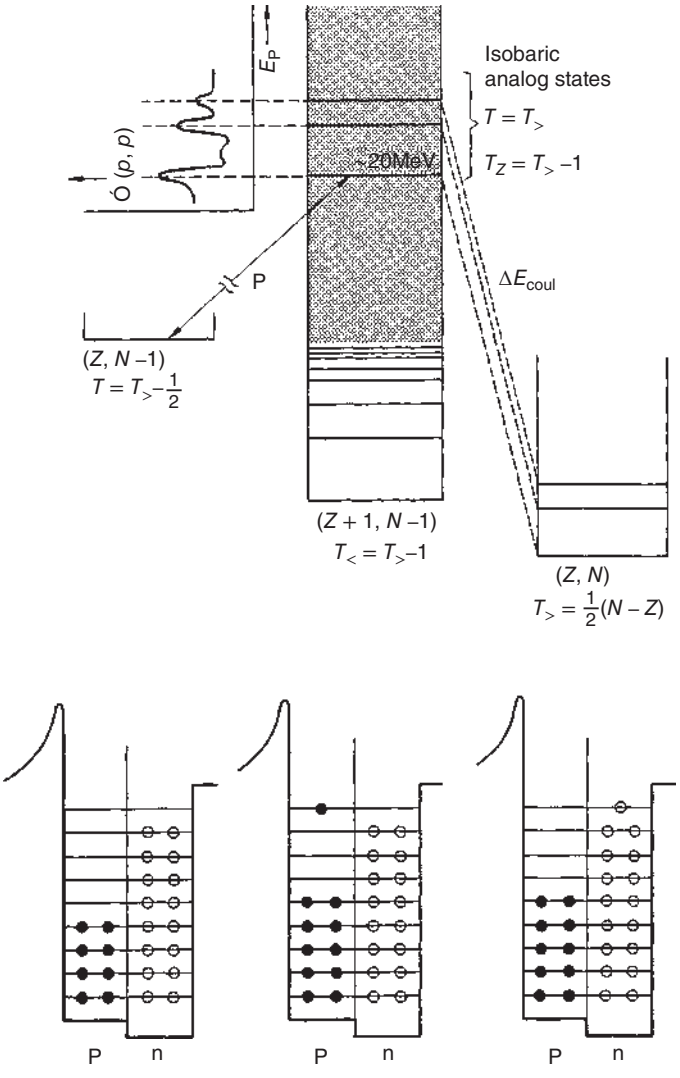

Figure 5.5 Level scheme and configurations related to the appearance of isobaric analog resonances. Source: Mayer-Kuckuk (1979)/John Wiley & Sons.

5.3 Nuclear Matter

Before we enter into the discussion of various nuclear models, we should consider the properties of infinite nuclear matter. This is a good approximation of the central region of heavy nuclei and is, therefore, a good starting point in a discussion of finite nuclei because the complexity caused by the surface of the nucleus may be ignored. Two properties of infinite nuclear matter are immediately evident from our

previous discussions. First, the average binding energies per nucleon (Section 3.3) are essentially independent of mass number, pointing to the saturation property of the nuclear force. Second, the densities are also essentially independent of mass number (Section 4.1), indicating that nuclei do not collapse until the diameter is about equal to the range of the nuclear force. Even though the density of the nucleus is very high, the nucleons are not densely packed. These two properties of nuclear matter are related and should have a common origin. Two different possible causes that have analogies in the field of chemical forces come to mind: one is the van der Waals forces between noble gas atoms in the liquid phase which are attractive and large only for nearest neighbors. There is also van der Waals repulsion which sets in when the atoms touch. The repulsion in nuclear forces at small distances would lead to the same qualitative effect. However, the density of nuclear matter is much smaller than for closely packed nucleons. Thus, there must be an additional factor. In a diamond crystal, binding energy per atom and density are also independent of its size, but the reason is different from the van der Waals example. In diamond, each carbon atom is covalently bonded to four other carbon atoms and thus interacts strongly with only these four. The first four neighbors have saturated the valency of the central carbon atom. The saturation property of the chemical bond arises from the limited number of valence electrons. The exchange character of the nuclear force also causes the interaction between nucleons to be strong only if the nucleons are in the proper states of relative motion. It is not simple to show that the repulsive core, in conjunction with the exchange character of nuclear forces, produces the approximate constancy of the average binding energy per nucleon and of density. The problem was successfully approached by K. Brueckner et al. utilizing nucleon–nucleon potentials, as touched upon briefly in Section 5.1, and that are competently described in the work by H.A. Bethe and L.C. Gomes et al. This analysis yields a binding energy per nucleon in infinite nuclear matter roughly in agreement with the volume term in Eq. (3.7) and with the central density of heavy nuclei. These calculations also provide information about the wave functions describing the motion of nucleons in nuclear matter such that nucleons move around much as free particles. The wave function for nuclear matter is an antisymmetrized product of the free-particle wave functions for each of the nearly free nucleons in a nucleus. Collisions between nucleons are quenched because, for a collision to be effective, the particles must transfer momentum to one another. But the Pauli principle forbids such momentum transfers. Thus, the properties of the nucleon–nucleon forces in conjunction with the Pauli principle cause nuclear matter to exhibit apparently contradictory behavior: there are macroscopic properties such as density and binding energies, and these resemble those of a uniformly charged liquid drop; there are at the same time microscopic properties, such as nuclear wave functions and particle motions resembling rather those of a weakly interacting gas. We have seen in Section 3.3 that the macroscopic properties have been exploited in the development of the semiempirical mass equations and these will appear again in the collective model. The microscopic properties, on the other hand, are the basis for the Fermi gas model and the independent particle model that are to be discussed next.

5.4 Fermi Gas Model

For a system of non-interacting particles in a spherically symmetric square well potential, the simplest nuclear model is the Fermi gas model. It has for $r < R$ a constant depth $-V_0$ and jumps at $r = R$ to zero. The nucleons bound inside the potential do not have enough energy to escape from this potential, that is, the potential cannot be penetrated. The nucleus is taken to be composed of a degenerate Fermi gas. The gas is degenerate because all nucleons are bound in the lowest possible states consistent with the Pauli principle. For each type of particle, the gas is characterized by the kinetic energy of the highest occupied state, the Fermi energy, E_{F}. As we have discussed in Section 1.5.5, the level density for a free particle $\mathrm{d}n/\mathrm{d}p$ is given by Eq. (1.32) and in a volume of the phase space of h^3, there exists just one particle. Integrating up to the maximum possible momentum $p_{\max}$, the Fermi momentum, yields

$$n = \frac{p_{\max}^3}{6\pi^2\hbar^3} \cdot V \tag{5.10}$$

where V is the nuclear volume. As a given state can be occupied by two particles with $s = \pm 1/2$, we have to multiply the number of n by 2 and obtain

$$n = \frac{p_{\max}^3}{3\pi^2\hbar^3} \cdot V \tag{5.11}$$

Thus, for neutrons, we have

$$p\left(3\pi^2\right)^{1/3}\left(\frac{N}{V}\right)^{1/3}_{\max} \tag{5.12}$$

and for protons

$$p\left(3\pi^2\right)^{1/3}\left(\frac{Z}{V}\right)^{1/3}_{\max} \tag{5.13}$$

With the substitution $E_F = p_{\max}^2$ and $V = \frac{4}{3}\pi r_0^3 A$, the result for the Fermi energy is

$$E_F = \left(\frac{9\pi}{4}\right)^{2/3}\frac{\hbar^2}{2m_n r_0^2}\left(\frac{N}{A}\right)^{2/3} \quad \text{for neutrons} \tag{5.14}$$

and

$$E_F = \left(\frac{9\pi}{4}\right)^{2/3}\frac{\hbar^2}{2m_p r_0^2}\left(\frac{Z}{A}\right)^{2/3} \quad \text{for protons} \tag{5.15}$$

giving with $N/A \approx 1/1.8$ and $Z/A \approx 1/2.2$ the numerical values

$E_{\mathrm{F}} = 43$ MeV for neutrons; and

$E_{\mathrm{F}} = 37$ MeV for protons.

To give the proper value for the binding energy per nucleon, about 8 MeV, this implies that the neutron gas is contained in a potential well with a central depth of about 50 MeV and that the proton gas is contained in a potential well that is about 45 MeV deep.

The Fermi gas model is not useful for the detailed prediction of the properties of low-lying nuclear states that are observed, for example, in β decay. It is useful, though, for the characterization of the momentum distribution of nucleons in the nucleus and for the thermodynamic treatment of the properties of nuclei that are excited into the continuum. This treatment is of importance in the study of nuclear reactions, see Chapter 12. As a nucleus absorbs energy, nucleons are promoted from the filled levels into the unfilled region. Each promotion leads to a specific excitation energy, and combinations of multiple excitations can lead to the same or very similar energies. The number of combinations of different promotions for a specific excitation energy grows dramatically with increasing excitation energy and gets so large that we can describe the system by a level density, $\rho(E^*, N)$, which is the number of levels per unit excitation energy for a fixed number of nucleons, N. The fact that excited nuclei, even with only a finite number of nucleons, have very dense and almost continuous distributions of levels allows us to treat their deexcitation with the help of statistical mechanics. Here, the required large number of participants in the thermodynamic equilibrium does not come from the number of nucleons but from the number of levels available to the system. For example, for the capture of a thermal neutron, the excitation energy, E^*, of the product nucleus is about 7 MeV and the level spacing, D, is on the order of 1 eV, such that $D/E \approx 10^{-7}$, or the level density $\rho(E^*, N) = 1/D \approx 10^7\,\mathrm{MeV}^{-1}$. This is large enough for thermodynamics to apply (H. Feshbach). The connection between the microscopic description of a system in terms of individual states and its macroscopic thermodynamical behavior was provided by Ludwig Boltzmann: the entropy of a system is proportional to the natural logarithm of the number of levels. Thus

$$S(E, N) = k_\mathrm{B}\rho(E, N)\Delta E \tag{5.16}$$

saying that the entropy of an excited nucleus is proportional to the level density in an energy interval ΔE. The thermodynamic temperature is related to the entropy as

$$\frac{\partial S(E^*, N)}{\partial E} = k_\mathrm{B}\frac{\partial \ln \rho(E^*, N)}{\partial E} = \frac{1}{T} \tag{5.17}$$

In nuclear physics, the convention is to give T in MeV and to set k_B equal to 1 or not to write it explicitly. The excitation energy is connected to the thermodynamic temperature by

$$E^* = aT^2 - T \tag{5.18}$$

and for large excitation energies by $E^* = aT^2$.

The level density can then be written as

$$\rho(E^*) \propto \frac{1}{E^*}\exp\left(2 \cdot \sqrt{aE^*}\right) \tag{5.19}$$

where a is the level density parameter being related to the mass number A by $a \approx A/8.5\,\mathrm{MeV}^{-1}$. Level densities can be corrected for angular momentum by including preexponential factors and by subtracting from the total excitation energy the energy involved in collective rotation, see Chapter 12. The Fermi gas level

density can be used to predict the relative probability of various decay modes, often called channels (evaporation of a neutron, or of a proton, or of an α particle, etc.) under the assumption that the nuclei are in full thermal equilibrium. Then, they will decay into different products in proportion to the number of states available at excitation energy E^* in the evaporation residue. In the statistical model, Chapter 12, the relative probability for the excited nucleus to decay into a specific channel at the residual excitation energy E^* is given by the level density, Eq. (5.19), or statistical weight of that channel divided by the sum of the statistical weights of all of the channels; that is, the excited nucleus decays preferentially into that particular evaporation residue in which the phase space is largest.

5.5 Shell Model

In the Fermi gas model, it was assumed that the nucleons move in a sharply limited volume as free particles without interaction among themselves. On the other hand, as we know from the properties of the binding energies that the nuclear force acts between pairs of nucleons, it is a priori difficult to understand how such a mean nuclear potential comes about. It is helpful to look for comparison at the situation in the electron shell. Here, the point-like nucleus provides a central Coulomb potential $-Ze^2/r$ for the electrons that is to be modified, taking into account the interaction between the evenly charged electrons. For this, one can find a mean field in a self-consistent approach to the solution of the Schrödinger equation and show that the wave function for an electron shell state can to a good approximation be written as the antisymmetrized product of single-particle wave functions for this mean field (Hartree–Fock procedure).

The essentials of this procedure will be briefly outlined. The problem is described by the Schrödinger equation for N electrons having electromagnetic interactions among themselves and with the nucleus. In the Schrödinger equation $H\psi = E\psi$, H has the form

$$H = \sum_i T_i + \sum_i V_C(r_i) + \sum_{i,j} V_{ij}(|\boldsymbol{r}_i - \boldsymbol{r}_j|) \tag{5.20}$$

with $i < j$ and with the kinetic energy

$$T_i = -\frac{\hbar^2}{2m_i}\Delta_i \tag{5.21}$$

The summation extends over all N electrons. Herein, V_C is the common central potential and V_{ij} is the interaction potential between two electrons each. Only two-body forces are considered. The summation rule in Eq. (5.20) makes sure that all possible pairings between two particles occur just once. The many-body situation in Eq. (5.20) is not solvable. Therefore, one tries to replace the sum of pair interactions, V_{ij}, that act on each particle, by the action of a mean potential, V_i; that is, one writes as a trial instead of Eq. (5.20)

$$H = \sum_i [T_i + V_C(r_i) + V_i(r_i)] \tag{5.22}$$

For each member of this sum, there is a solution function ϕ_i (single-particle wave function) with the energy eigenvalue ε_i. A special solution of Eq. (5.22) is the product of those functions

$$\Psi = \phi_1(\boldsymbol{r}_1) \cdot \phi_2(\boldsymbol{r}_2) \cdot \cdots \cdot \phi_N(\boldsymbol{r}_N)$$

Here, $E = \varepsilon_1 + \varepsilon_2 + \cdots + \varepsilon_N$. In order to obey the Pauli principle, a completely antisymmetric solution Ψ must be formed. This is done by the formation of the Slater determinant

$$\Psi = \frac{1}{\sqrt{N}} \mathrm{Det}|\phi_i(\boldsymbol{r}_k)|$$

As a starting point, one introduces into Eq. (5.22) apparently reasonable mean electrostatic potentials V_i and calculates the solution functions ϕ_i. The quantity $e|\phi_{\mathrm{i}}(\mathrm{r})|^2$ gives the charge density distribution for each electron. Inversely, one can calculate again, from the solutions ϕ_i, by averaging over the contributions of all electrons, the mean potential, V_i', acting on the ith particle. If, by chance, the latter is identical to the originally selected potential, the problem is solved. If not, one tries by variation of V_i to reach self-consistency. For the electron shell, such self-consistent solutions can in fact be found after relatively few repetitions.

In a nucleus, there is nothing that is comparable to the central Coulomb potential in the electron shell. Contrary to the repulsion between single electrons in the shell, the forces between pairs of nucleons are attractive. Anyway, one can try by a Hartree procedure to gain a mean potential. In Eqs. (5.20) and (5.22), the central potential V_{C} needs to be omitted. Instead of Eq. (5.20), we have to write

$$H = \sum_{i=1}^{A} T_i + \sum_{i,j=1}^{A} V_{ij} \tag{5.23}$$

where $i<j$ and V_{ij} is given by the nucleon–nucleon potential. One can again try to replace V_{ij} for each nucleon by a mean potential V_{i}. One looks at an arbitrarily selected nucleon, the ith one, and imagines that the interaction of the other nucleons with this particular one can approximately be averaged in a potential V_i. Eigenfunctions ϕ_i and energy states ε_i of this nucleon can be obtained from V_i. As this procedure represents only an approximation, it may be expected that residual interactions remain that cannot be included in the averaging procedure. Therefore, we split H in Eq. (5.23) in the following way:

$$H = H_0 + V_R \tag{5.24}$$

where

$$H_0 = \sum_{i=1}^{A} (T_i + V_i) = \sum h_i \tag{5.25}$$

with $h_i \equiv T_i + V_i$, and

$$V_R = \sum_{i<j} V_{ij} - \sum V_i \tag{5.26}$$

Equation (5.25) is essentially identical to Eq. (5.22). From the potential V_i, the single-particle wave functions, ϕ_i, result and obey the equation $h_i\phi_i = \varepsilon_i\phi_i$. The splitting in Eq. (5.24) is reasonable if one can show that the energies are essentially given by H_0 and that the residual interactions V_R are comparatively small. Now, in fact, it is possible to show, within a Hartree–Fock procedure that starts essentially from the nuclear forces, that this assumption is justified. It is the fundamental of the shell model. For the solutions of the Hartree–Fock equations, the existence of a repulsive core in the nucleon–nucleon potential represents a mathematical hurdle. However, one can bypass this difficulty by introducing an ad hoc selected effective potential for this region because the result depends essentially on the long-range part of the nucleon–nucleon potential whose form is well established in the meson exchange theory.

In summary, the important simplification in the shell model is to replace the nucleon–nucleon interaction inside the nucleus with an effective potential energy that acts on each nucleon as a function of its coordinates but not as a function of the coordinates of the other nucleons. The problem then reduces to solving the Schrödinger equation for a particle moving in the chosen mean-field potential.

Three potentials are usually discussed. All of them are taken to be spherically symmetric, but they differ in their radial dependence. The first is the harmonic oscillator potential,

$$V(r) = V_o\left[1 - \left(\frac{r}{R}\right)^2\right] \tag{5.27}$$

the second is the square well potential

$$\begin{aligned} V(r) &= -V_0 \quad r < R \\ V(r) &= \infty \quad r > R \end{aligned} \tag{5.28}$$

Most realistic is the Woods–Saxon potential given in Eq. (4.5). The latter, discussed in the context of nuclear charge distributions and nuclear radii, has a shape intermediate between the square well and the harmonic oscillator potentials. It is more difficult to manipulate for shell-model calculations than the other two.

The energy levels for a nucleon in the three-dimensional harmonic oscillator potential are well known:

$$\begin{aligned} \varepsilon &= \left(n_x + n_y + n_z + \frac{3}{2}\right)\hbar\omega_o = \left(\lambda + \frac{3}{2}\right)\hbar\omega_o \\ \omega_o &= \left(\frac{2V_o}{MR^2}\right)^{1/2} \end{aligned} \tag{5.29}$$

where M is the nucleon mass and n_x, n_y, n_z, and λ are the oscillator quantum numbers and phonon numbers, respectively, which are zero or positive integers. The orbital angular momentum takes on the usual values for a spherically symmetric potential

$$L\hbar = [l(l+1)]^{1/2}\hbar \tag{5.30}$$

As in atomic spectroscopy, the states with $l = 0, 1, 2, 3 \ldots$ are designated as s, p, d, f …, respectively. Because of the spherical symmetry of the potential, it is more convenient to use spherical coordinates; for the harmonic oscillator, this means that

$$\lambda = 2(n-1) + l \tag{5.31}$$

$$\varepsilon = [2(n-1) + l]\hbar\omega_o + \frac{3}{2}\hbar\omega_o \tag{5.32}$$

where $n = 1, 2, 3, \ldots$ and $\frac{3}{2}\hbar\omega_o$ is the zero-point energy of the three-dimensional harmonic oscillator, ε_0. Thus, the states are defined by the quantum numbers n and l and are identified as 3s, 1d, 2f, etc.; n is the radial quantum number giving each state $n-1$ radial nodes (not $n-l-1$ as in the usual hydrogen wave functions) $l = 0, 1, 2, 3, \ldots$, and, in addition, there is the magnetic quantum number m which takes on values from $-l$ to $+l$ such that $m\hbar$ is the projection of the angular momentum l on the space-fixed axis z. These energy levels are shown on the left-hand side in Figure 5.6. The energy levels are equidistant and are shown after

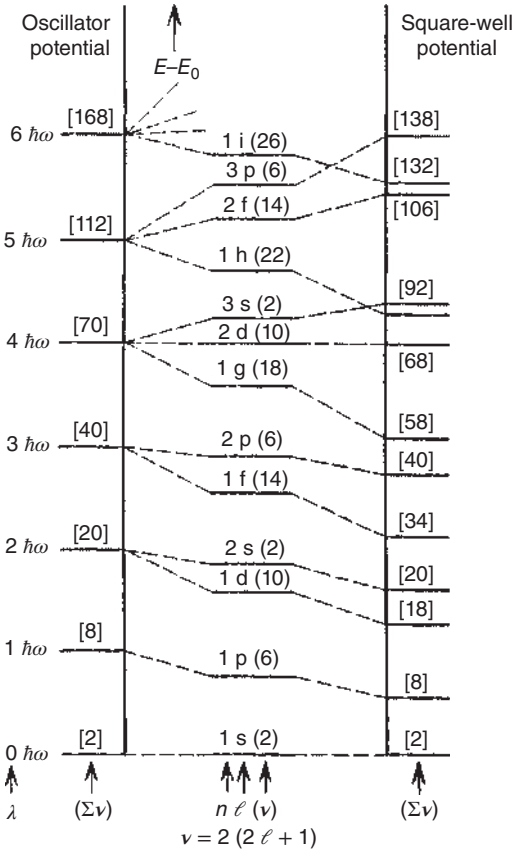

Figure 5.6 Energy levels of the three-dimensional isotropic harmonic oscillator and of the square-well potential with infinitely high walls. The numbers in parentheses are the numbers of nucleons, ν, of one kind required to fill the various levels; the numbers in square brackets, $\Sigma\nu$, are the numbers of nucleons that are required to fill the levels up to and including a given level. Source: Mayer and Jensen (1955)/John Wiley & Sons.

subtraction of the zero-point energy $\frac{3}{2}\hbar\omega_o$. We note two important properties of these levels:

1) States with the same value of $2(n-1)+l$ have the same energy and are accidentally degenerate.
2) Since the energy goes as $2(n-1)+l$, the states of a given energy must all have even or odd values of l. Hence, all degenerate states have the same parity.

We demonstrate this in Table 5.2. The pattern of the eigenstates for the square well potential on the right-hand side of Figure 5.6 is similar, but the degeneracies of the harmonic oscillator states are removed. We observe that the change from a harmonic oscillator to a square well lowers the energies of single-particle states with higher angular momentum, thus enhancing the stability of those states that concentrate particles near the edge of the nucleus. The sequence of levels in real nuclei might be expected to be somewhere between these two extremes, and this is indicated by the levels in the center of Figure 5.6.

As introduced in Section 3.4, the experimental evidence for the shell structure of nuclei points to the magic numbers 2, 8, 20, 28, 50, 82, and 126 as the number of neutrons or protons that occur at closed shells. As in the energetic sequence of the atomic numbers in chemistry, we expect large energy gaps between the energy levels of the noble gases and the next higher levels representing the alkali metals. The sequence of levels in Figure 5.6 shows the possibility of predicting the first three of the magic numbers, but the others are certainly not evident.

It was the fundamental idea of M. Goeppert-Mayer and J.H.D. Jensen et al. that, in the nuclear potential, the interaction energy between spin and angular momentum of a nucleon plays a decisive role. Such an interaction between spin and angular momentum is also evident in the atomic shell. Thus, it has electromagnetic character and leads to a relatively small fine structure splitting of the energy levels. It was a surprise to discover that the nuclear force creates a much larger spin–orbit interaction that is of a magnitude comparable to the term distances of the single-particle levels. The spin–orbit splitting in the nuclear potential is due to the exchange of ω bosons and makes states with the higher j ($j = l + 1/2$) much more stable than those with the lower j ($j = l - 1/2$). The result is (see Figure 5.7) that now also large energy gaps

Table 5.2 Examples for shell-model states in the isotopic harmonic oscillator potential.

	n	l	$\lambda = 2(n-1)+l$	$\varepsilon^{a)}$ $(\hbar\omega_o)$
1g	1	4	4	11/2
2d	2	2	4	11/2
3s	3	0	4	11/2

n is the radial quantum number, l the angular momentum quantum number, and λ the phonon number.
a) $\varepsilon - \varepsilon_o = 4\,\hbar\omega_o$.

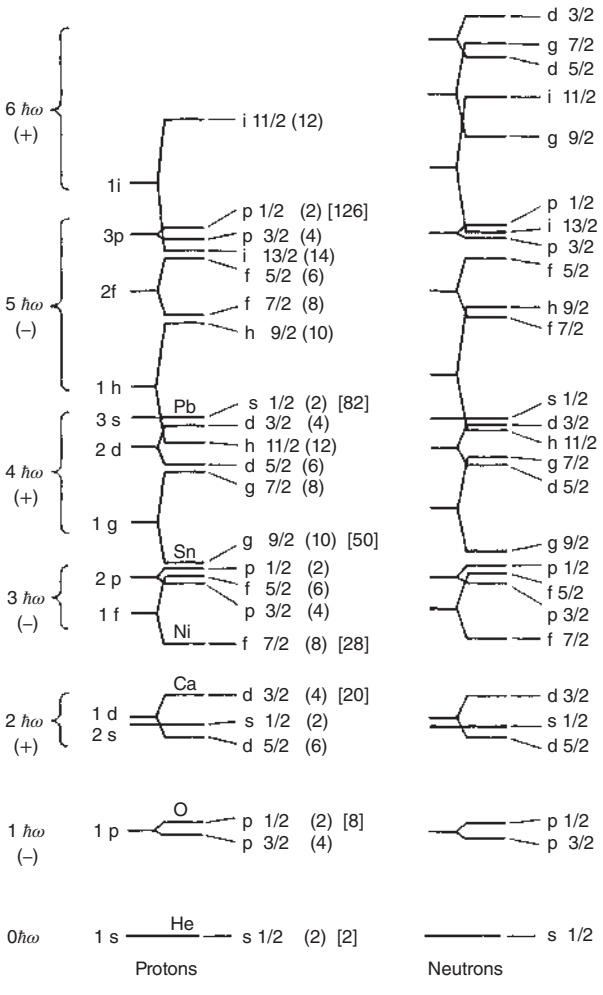

Figure 5.7 Energy levels of the shell model with spin–orbit splitting. The splitting is adjusted to experimental data. Source: Modified from Klinkenberg (1952).

occur above integral nucleon numbers 28, 50, 82, and 126 because of the splitting of the 1f, 1g, 1h, and 1i levels, respectively, and these shell closures occur exactly at the experimentally determined magic numbers.

In order to take care of the spin–orbit coupling, one has to add to the central potential $V(r)$ another energy term V_{ls} depending on the scalar product of $\boldsymbol{l}$ and $\boldsymbol{s}$, that is,

$$V_i = V(r) + V_{ls}\,(r(\boldsymbol{l}\cdot\boldsymbol{s})) \tag{5.33}$$

We can calculate the expectation value of $\boldsymbol{l}\cdot\boldsymbol{s}$ by squaring the identity $\boldsymbol{j} = \boldsymbol{l}+\boldsymbol{s}$ and find

$$(\boldsymbol{l}\cdot\boldsymbol{s}) = \frac{1}{2}[\langle j^2\rangle - \langle l^2\rangle - \langle s^2\rangle] = \frac{1}{2}\left[j(j+1) - l(l+1) - \frac{3}{4}\right] \tag{5.34}$$

For $j = l + 1/2$, we obtain $\langle \boldsymbol{l} \cdot \boldsymbol{s} \rangle = \frac{1}{2} l$ and for $j = l - 1/2$, correspondingly, $\langle \boldsymbol{l} \cdot \boldsymbol{s} \rangle = -\frac{1}{2}(l+1)$. The potential energy according to Eq. (5.33) for both cases is

$$V(r) + \frac{1}{2} V_{ls} l \quad \text{for } j = l + \frac{1}{2} \tag{5.35}$$

$$V(r) - \frac{1}{2} V_{ls}(l+1) \quad \text{for } j = l - \frac{1}{2} \tag{5.36}$$

If $V_{ls}(r)$ is negative, as is $V(r)$, the states for $j = l - 1/2$ are energetically higher than those for $j = l + 1/2$. The difference between Eqs. (5.35) and (5.36) shows that the energetic splitting of the two states is

$$\Delta E \propto l + (l+1) = 2l + 1 \tag{5.37}$$

which means that the spin–orbit splitting for each original level with angular momentum l is proportional to l.

For a simple discussion of the level sequence, we can start by setting the radial function V_{ls} constant. It is more realistic to assume that the nucleons in the flat interior of the potential find themselves in a homogeneous medium in which there is no center relative to which an angular momentum could be defined. Therefore, in V_{ls} mainly the nuclear surface should be relevant, that is,

$$V_{ls}(r) \propto \frac{1}{r} \frac{\mathrm{d}V(r)}{\mathrm{d}r} \tag{5.38}$$

in analogy to the Thomas term in the fine structure of the electron shell.

The single-particle level sequence after introduction of the spin–orbit splitting is shown in Figure 5.7 separately for protons and neutrons as the Coulomb potential for the protons causes somewhat different level sequences for the two kinds of nucleons. Figure 5.7 is easy to understand in comparison to Figure 5.6. To the left, the levels shown in the middle part of Figure 5.6 without spin–orbit splitting are shown again. For the levels after spin–orbit splitting, the values of j are added as an index, for example, $2p_{3/2}$ means $n = 2, l = 1, j = l + 1/2 = 3/2$. Each level can be filled with $2j + 1$ particles; the occupation numbers are given in parentheses. The numbers in square brackets are again the integral numbers of nucleons that are required to fill the levels up to and including a given level.

There are several important features in this energy level diagram. As the spin–orbit splitting increases in proportion to l, the $1i_{13/2}$ state is energetically lowered so much that this single-particle level no longer sits energetically in the regime of the $6\,\hbar\omega$ phonon states to which it formally belongs, but joins energetically the $5\,\hbar\omega$ phonon states. The energy gap that results from this is the reason for 126 being a magic number. The situation is very similar for the $1h_{11/2}$ state escaping from the $5\,\hbar\omega$ phonon states and joining the $4\,\hbar\omega$ phonon states, thus making 82 a magic number. Similarly, the large energy gap at nucleon number 50 is caused by the spin–orbit splitting of the 1g state. Spin–orbit splitting and shell closures are obviously closely related. If a nucleus contains 2, 8, 20, 28, 50, 82, or 126 neutrons, the level scheme in Figure 5.7 permits a prediction of the quantum states occupied by the neutrons. For example, ^{88}Sr has its 50 neutrons filling the five shells $(1s^2)$, $(1p^6)$, $(1d^{10}2s^2)$, $(1f^8_{7/2})$, $(1f^6_{5/2}2p^6 1g^{10}_{9/2})$. Similarly, the proton structure is obvious for nuclides with magic atomic numbers: He, O, Ca, Ni, Sn, and Pb. It is a well-known fact in atomic structure that filled shells are spherically symmetric and have no spin or orbital

angular momentum and no magnetic moment. In the shell model for nuclei, there is the added assumption that not only filled nucleon shells but also any even number of either protons or neutrons has zero angular momentum in the ground state. This is consistent with the observation that the ground states of all even–even nuclei have zero angular momentum and even parity. This pairing of like nucleons also results in increased binding energies as discussed in Section 3.3. Such an enhancement in the binding energy of paired nucleons suggests that, beyond the mean-field potential felt by all nucleons, there exists a residual attractive interaction between two paired nucleons when their angular momenta couple to zero. It should be noted here that the pairing force is not explicitly contained in the single-particle shell model and warrants a separate discussion below.

In any nucleus of odd mass number, all but one nucleon are considered to have their angular momenta paired off, forming an even–even core. The single odd nucleon moves independently outside this core, and the net angular momentum of the entire nucleus is given by the quantum state of this nucleon. For example, consider the nucleus ^{51}V where the odd nucleon is the 23rd proton belonging in the $1f_{7/2}$ level. The ground state of the nucleus is expected to be $f_{7/2}$. The ground state of this nucleus is indeed 7/2.

The order of levels within each shell may often be different from that in Figure 5.7, especially for two or three adjacent levels. In such a case, we conclude from the single-particle model only that several particular states are close together in energy without knowing their exact energy sequence. The extreme single-particle model is most useful in the characterization of excited states in nuclei very near to a closed shell. The low-lying states in ^{207}Pb shown in Figure 5.8 are an excellent example. The first four excited states in ^{207}Pb correspond to transitions of the neutron hole in the 126-neutron shell among the various single-particle states. Comparison of the relative stabilities of these states to the order given in Figure 5.7 shows that the states below the $N = 126$ gap do show up in ^{207}Pb; however, their sequence is not identical with the experimental one. The single-particle model, as we have presented it here, is based on finding in an approximate and purely empirical way a mean-field potential that allows us to explain the shell closures at the magic numbers. In recent years, progress has been made in replacing the empirical assumptions of the shell model by more fundamental potentials (based on meson-theoretical nucleon–nucleon potentials) derived in a Hartree–Fock procedure of self-consistent fields.

Most of the odd–odd nuclei are radioactive, and there are only very few stable ones. The assumption of pairing leaves in every case one odd proton and one odd neutron, each producing an effect on the nuclear moments. There is no universal rule to predict the resultant ground state. However, there are some guidelines for ground states and long-lived isomeric states. These were proposed by M.H. Brennan and M.N. Bernstein in 1960 and improve earlier suggestions proposed by L.W. Nordheim. For configurations in which the odd nucleons are both particles (or both holes), these coupling rules are:

i) if the so-called Nordheim number $N = j_1 + j_2 + l_1 + l_2$ is even, then $\boldsymbol{I} = |\boldsymbol{j}_1 - \boldsymbol{j}_2|$;
ii) if N is odd, then $\boldsymbol{I} = |\boldsymbol{j}_1 \pm \boldsymbol{j}_2|$;

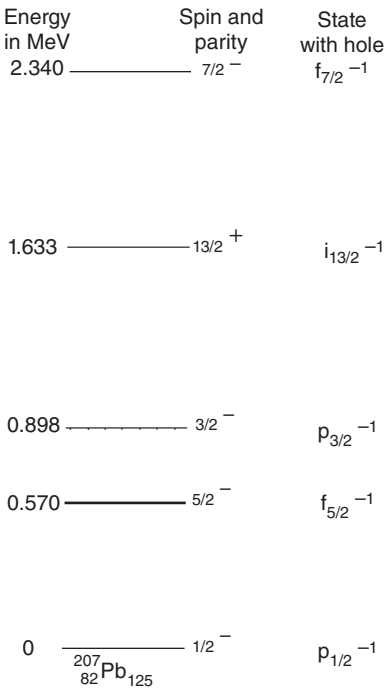

Figure 5.8 Energy levels of ^{207}Pb with energies given on the left side and angular momenta and parities on the right. The superscript −1 on the spectroscopic terms indicates a hole in any given state.

iii) the prediction for configurations in which there is a combination of a particle and a hole is $\boldsymbol{I} = \boldsymbol{j}_1 + \boldsymbol{j}_2 - 1$, which is less reliable than (i) and (ii).

An example for (i) is ^{38}Cl, for which the shell model predicts the odd proton in the $d_{3/2}$ orbital and the odd neutron in the $f_{7/2}$ state. Since N is even, $\boldsymbol{I} = 2$ is predicted with odd (−) parity since the odd nucleons are in states of opposite parity. This agrees with the measured ground-state angular momentum and parity. An example for (ii) is ^{26}Al, for which both the odd proton and neutron configurations are $d_{5/2}^{-1}$. The measured ground-state angular momentum and parity are 5^+. Finally, (iii) is illustrated by ^{56}Co ($\boldsymbol{I}^\pi = 4^+$), for which the shell model predicts for the odd proton hole $f_{7/2}^{-1}$ and for the odd neutron $p_{3/2}^{1}$.

As mentioned already in Section 3.5, there is an abundant grouping of isomers with odd Z or odd N just below the magic numbers 50, 82, and 126. This phenomenon is connected with the appearance, just below the shell closure, of a high j state ($1g_{9/2}$ before 50, $1h_{11/2}$ before 82, $1i_{13/2}$ before 126). A suitable example may be $^{113}_{48}$Cd: its odd nucleon, the 65th neutron, is assigned to the $3s_{1/2}$ state in agreement with its ground-state angular momentum $\boldsymbol{I} = 1/2$. The $1h_{11/2}$ state happens to be the first excited level in this nucleus, and the γ transition to the ground state $h_{11/2} \rightarrow s_{1/2}$ with $\Delta\boldsymbol{I} = 5$, according to the selection rules for γ decay, should be very long-lived. Actually, ^{113m}Cd decays predominantly by β-particle emission with a half-life of 14 years. The branching ratio for γ decay (isomeric transition, IT) implies a partial half-life of 1.4×10^4 years for that mode of decay.

For nuclides with either a neutron number or proton number near to half-way between magic numbers, the single-particle model is an oversimplification.

Consider ^{23}Na, which would be expected to have a $d_{5/2}$ ground state, but the measured ground state has $\boldsymbol{I} = 3/2$. This is not to be attributed to an odd proton in the $1d_{3/2}$ because $1d_{3/2}$ should definitely be higher than $1d_{5/2}$. Moreover, the magnetic moment is in disagreement with the $d_{3/2}$ assignment. Such anomalies can be caused by the interactions among all of the nucleons outside the closed shells that have not been included in the effective potential that determines the shell-model states. We shall see that these "anomalous" ground-state angular momenta have to be discussed in terms of nuclear deformation. One can try to include such residual interactions with the help of perturbation theory. Alternatively, one can use a different point of view: if the residual interactions of many nucleons add coherently, deviations from sphericity are expected, and indeed Hartree–Fock calculations for nuclei with partly filled shells do show a greater stability for deformation. In the following, we present a partly phenomenological model that deals with the dynamical consequences of deformation.

5.6 Collective Motion in Nuclei

We have already seen from the pairing term in the liquid-drop binding-energy formula and from the coupling of an even number of nucleons to total angular momentum zero that there must be an attractive force between pairs of nucleons. This force, the pairing force, is not contained in the shell-model potential and has a decisive effect on the stability of the ground state of even–even nuclei. In addition, it must be realized that there is no central source in the nucleus for a spherically symmetric potential such as the Coulomb potential that the nucleus provides in the atom. Since it is only for a closed shell that the wave function leads to a spherically symmetric potential, we anticipate that deformed potentials will be important for nuclei with partly filled shells. This was already evident in Section 4.4 when electric quadrupole moments were discussed. The nuclear potential energy is plotted in Figure 5.9 against deformation from a spherical to a deformed shape. In Figure 5.9, curve *a* represents a nucleus with no nucleons beyond a closed shell for which the spherical shape is stable. As nucleons are added, the nucleus becomes soft against deformation, curve *b*, and subsequently reaches a point, curve *c*, where the

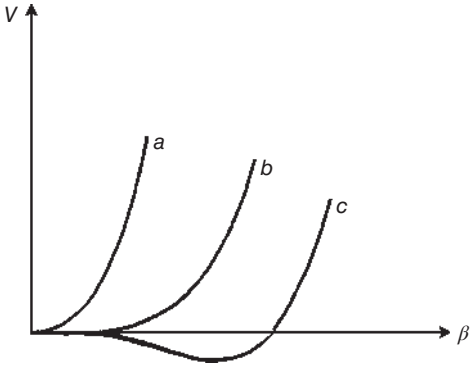

Figure 5.9 Potential energies as a function of the deformation parameter β. The curves illustrate the behavior of the nuclear potential as one moves away from a closed shell.

stable shape of the nucleus is deformed. Since the energy required for deformation is finite, it is obvious that nuclei can oscillate about their equilibrium shape and collective vibrational excitations are expected. Nuclei with stable deformed shape have distinguishable orientations in space and are expected to exhibit collective rotational excitations. Finally, the energies of the shell-model states are expected to change in a non-spherical potential and remaining degeneracies are expected to be removed. In summary, we anticipate rotational states, vibrational states, and altered single-particle states, and these are subsequently discussed below.

Evidence for the deformability of nuclei came from electric quadrupole moments of odd-A nuclei which are much larger than those expected for the odd nucleon orbiting in the field of the spherical core. Related to this enhancement of static quadrupole moments is the observation that electric quadrupole transitions ($E2$ transitions) are often orders of magnitude faster than transitions between single-particle states, Chapter 6. The enhanced quadrupole moments and the collectively enhanced quadrupolar transition rates imply that the nucleus has a spheroidal charge distribution. If all nucleons in an even–even nucleus remain paired and thus all of the angular momentum arises from collective rotation of the deformed nucleus with axial symmetry, rotational states of energy

$$E = \hbar^2 \frac{I(I+1)}{2\mathfrak{I}} \tag{5.39}$$

are expected, where $\mathfrak{I}$ is the effective moment of inertia about an axis perpendicular to the symmetry axis and $[I(I+1)]^{1/2}\hbar$ is the total angular momentum. The allowed values of I are 0, 2, 4, 6, … because of the symmetry of the spheroid with respect to a rotation of 180° and all states have positive parity. It is found that the effective moment of inertia is not that of a rigid spheroid. The implication is that only the nucleons outside of a spherical core rotate collectively around the latter. Detailed many-body calculations that include the pairing interaction show good agreement with the experimentally observed moments of inertia, which are indeed much smaller than the rigid value. The deformation is expected to be largest for nuclei half-way between closed shells; thus, the rotational bands should be most prominent for nuclei in the lanthanide and actinide region, which is actually the case. Figure 5.10 shows the ground-state rotational band of ^{242}Pu. The energies of the levels are consistent with $\hbar^2/2\mathfrak{I} = 7.3$ keV, which corresponds to a moment of inertia about half that of the rigid spheroid. The existence of states from different rotational bands of similar energies can complicate drastically the level scheme of a nucleus and can lead to dramatic alterations of the transition rates. For odd-A nuclei, the total angular momentum can be contributed by that from the intrinsic state of the odd nucleon and from the rotation of the spheroidal even–even core. As illustrated in Figure 5.11, the angular momentum of the odd nucleon, $\boldsymbol{j}$, may be in any direction, while the angular momentum from the rotation of the even–even spheroidal core, $\boldsymbol{R}$, is perpendicular to the symmetry axis of that core. The total angular momentum, $\boldsymbol{I}$, is

$$\boldsymbol{I} = \boldsymbol{R} + \boldsymbol{j} \tag{5.40}$$

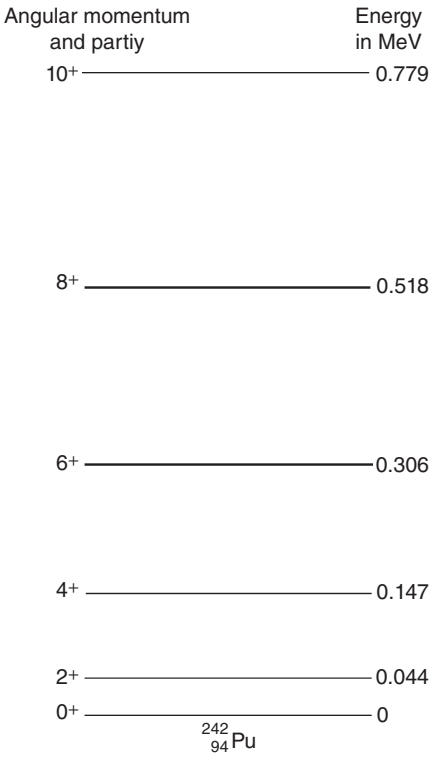

Figure 5.10 Ground-state rotational band of ^{242}Pu. Angular momenta and parities are listed on the left, energies above the ground state on the right.

The rotational energy of the core is, classically,

$$E_{\text{rot}} = \frac{\boldsymbol{R}^2}{2\mathfrak{I}} = \frac{(\boldsymbol{I}-\boldsymbol{j})^2}{2\mathfrak{I}} \tag{5.41}$$

In Figure 5.11, a coordinate system with the z axis along the symmetry axis of the spheroidal core is taken. The projections of the angular momentum vectors on the z axis are $\boldsymbol{R}_z = 0, \boldsymbol{j}_z = \boldsymbol{\Omega}, \boldsymbol{I}_z = \boldsymbol{K}, \boldsymbol{j}_z = \boldsymbol{I}_z$. Then,

$$E_{\text{rot}} = \frac{\boldsymbol{I}^2 - \boldsymbol{I}_z^2}{2\mathfrak{I}} - \frac{\boldsymbol{I}_x\boldsymbol{j}_x + \boldsymbol{I}_y\boldsymbol{j}_y}{\mathfrak{I}} + \frac{\boldsymbol{j}_x^2 + \boldsymbol{j}_y^2}{2\mathfrak{I}} \tag{5.42}$$

Then, the sum of the particle energy, $E_{\mathbf{p}}$, and the core energy, E_{rot}, is

$$E(\boldsymbol{I},\boldsymbol{K}) = \frac{[\boldsymbol{I}(\boldsymbol{I}+1) - \boldsymbol{K}^2]\hbar^2}{2\mathfrak{I}} + \left(E_p + \frac{\boldsymbol{j}_x^2 + \boldsymbol{j}_y^2}{2\mathfrak{I}}\right) - \frac{\boldsymbol{I}_x\boldsymbol{j}_x + \boldsymbol{I}_y\boldsymbol{j}_y}{\mathfrak{I}} \tag{5.43}$$

where $\boldsymbol{I} = \boldsymbol{K}+1, \boldsymbol{K}+2, \ldots$. For the ground-state band with axial symmetry, $\boldsymbol{K}$ also equals $\boldsymbol{j}_z = \Omega$. The last term in Eq. (5.43) is the Coriolis term. The Coriolis force arises when a spinning particle moves in a rotating frame of reference. Coriolis coupling analogous to the nuclear coupling in Eq. (5.43) is causing a gyrocompass to align its axis with that of the rotating earth. Equation (5.43) expresses how odd-A nuclei with spheroidal even–even cores develop bands of rotational levels, each being built

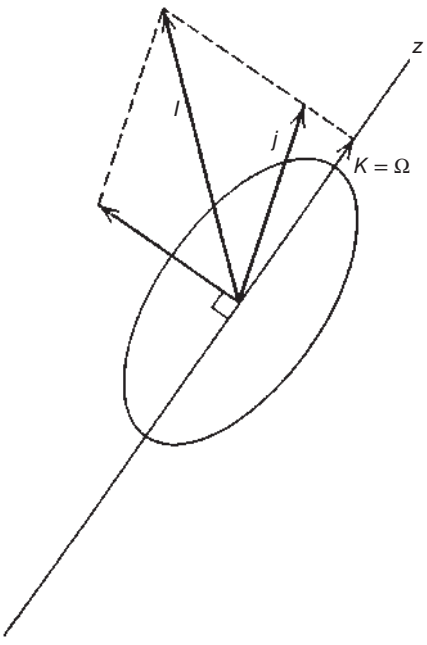

Figure 5.11 Vector diagram of the total angular momentum of a deformed nucleus. For definitions of the axes and symbols, see text.

upon a different state of the odd nucleon given by different values of $\boldsymbol{K} = \boldsymbol{\Omega} = \boldsymbol{j}_z$. An example is shown in Figure 5.12 illustrating all the energy levels of ^{25}Al up to 4 MeV excitation energy on the left. On the right, these levels have been sorted into rotational bands built on various intrinsic states of the odd proton. The example shows that different rotational bands in a given nucleus can have different moments of inertia.

With nucleon numbers nearer to those of the closed shells, the equilibrium shape of nuclei remains spherical, as illustrated by curves *a* and *b* in Figure 5.9, but the residual interaction among the nucleons outside the closed shell excludes a shell-model description of their excited states. Rather, these states are successfully described in terms of surface fluctuations about the spherical shape, that is, as vibrational excitations. This is also expected for the permanently deformed nuclei which can also oscillate about their equilibrium shape. If the vibrations are of small amplitude, they are quantized with a set of harmonic oscillators with energy quanta

$$\hbar\omega_\lambda = \hbar\left(\frac{C_\lambda}{B_\lambda}\right)^{1/2} \tag{5.44}$$

where $\hbar\omega_\lambda$ is called a phonon having parity $(-1)^\lambda$, angular momentum $[\lambda(\lambda+1)]^{1/2}\hbar$, and the projection of angular momentum on the polar axis is a multiple of $\hbar$; C_λ is the effective spring constant of the vibration in the mode λ (the second derivative of the potential), and B_λ is the effective mass. $\lambda = 1$ corresponds to a displacement of the center of mass and does not exist in the absence of external forces. $\lambda = 2$ corresponds to the quadrupolar vibration. The quantum-mechanical excitation energy spectrum of the given harmonic oscillators consists of equidistant levels of distance $\hbar\omega$. Each phonon of a quadrupolar oscillation has angular momentum $2\hbar$. For a quadrupolar

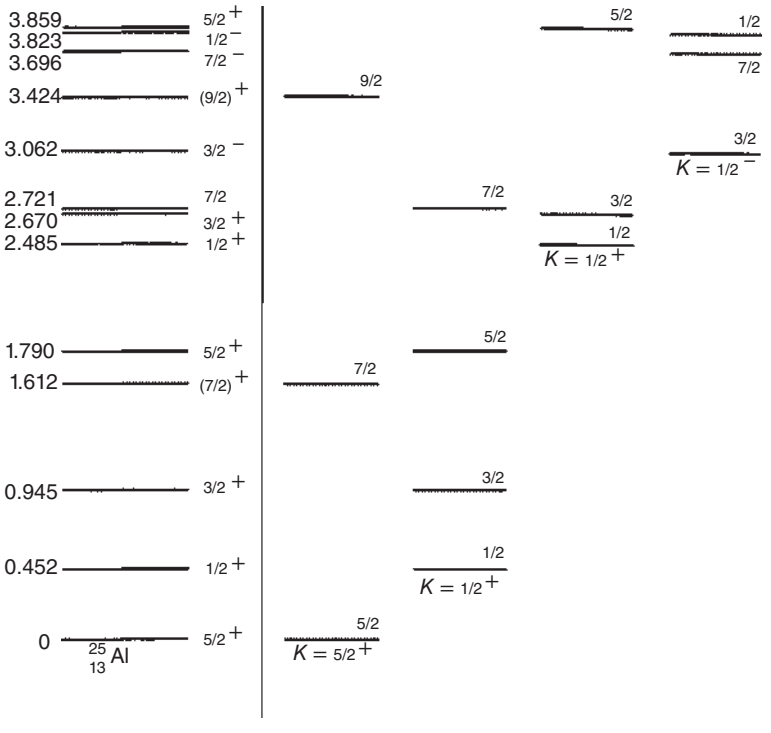

Figure 5.12 On the left are drawn all the energy levels of ^{25}Al up to 4 MeV. The angular momenta and parities of the states are also shown. On the right, these levels have been sorted into rotational bands associated with the different intrinsic states of the odd proton.

vibration, one expects the excitation energy spectrum as shown in Figure 5.13. The degeneracy of the states in a fixed value of $\hbar\omega$ is removed if the vibrations are not exactly harmonic, see for example, the two-phonon triplet in ^{76}Se in Figure 5.14. That figure shows for comparison spectra for single-particle excitation, collective vibration, and rotation. For spheroidal even–even nuclei, rotational bands built on vibrational states are often observed. The nuclear shape is parameterized in terms of the quantities β and γ. If $\gamma = 0$, the nucleus is in an axially symmetric spheroidal shape and is prolate for $\beta > 0$ or oblate for $\beta < 0$. If γ differs from zero, the nucleus assumes triaxial shapes. Nuclear vibrations are described as either β or γ vibrations, depending on whether β or γ oscillates, as shown in Figure 5.15. Octupole vibrations are also observed in certain mass regions. The energy of the rotational states built on vibrational states is given by

$$E = \frac{\hbar^2}{2\Im}[\boldsymbol{I}(\boldsymbol{I}+1) - \boldsymbol{K}^2] \tag{5.45}$$

where $\boldsymbol{K}$ is the projection of the angular momentum $\boldsymbol{I}$ on the symmetry axis. For β vibrations ($\lambda = 2$, $\boldsymbol{K} = 0$), the values of $\boldsymbol{I}^\pi$ are 0^+, 2^+, 4^+, …; for γ vibrations ($\lambda = 2$, $\boldsymbol{K} = 2$), the sequence is 2^+, 3^+, 4^+, …; for octupole vibrations ($\lambda = 3$, $\boldsymbol{K} = 1$), the sequence is 1^-, 3^-, 5^-, …. The excited levels of ^{232}U given in Figure 5.16 display this structure.

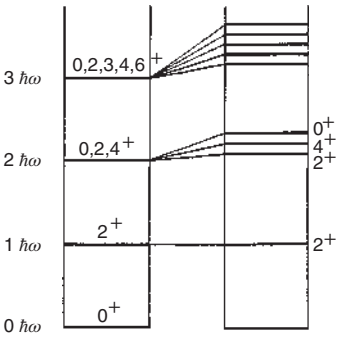

Figure 5.13 Vibrational excitations (schematic). On the right is shown the splitting of the phonon states for non-harmonic oscillations.

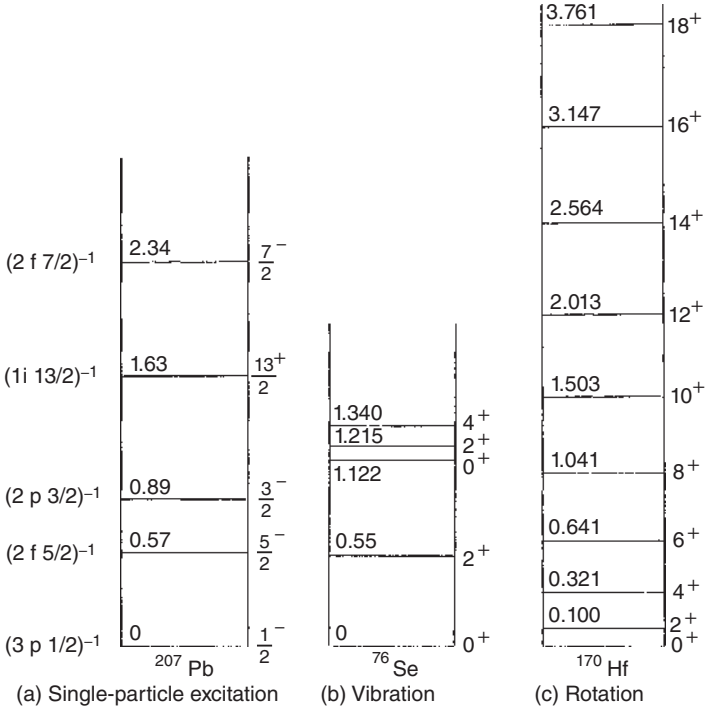

Figure 5.14 Comparison of excitation energy spectra for single-particle excitation (^{207}Pb), collective vibration (^{76}Se), and rotation (^{170}Hf).

5.7 Nilsson Model

The shell-model states are appropriate to a spherically symmetric potential. We want to ask here, how the single-particle states are changed if an axially symmetric deformed potential is used. Because, in a spheroidal nucleus, one special axis is distinguished, the degeneracy of the levels with fixed $\boldsymbol{j}$ is removed with respect to the magnetic quantum number m. For the following, the deformation axis is in the z direction. As the deformation with respect to the x–y plane is to be symmetric, there

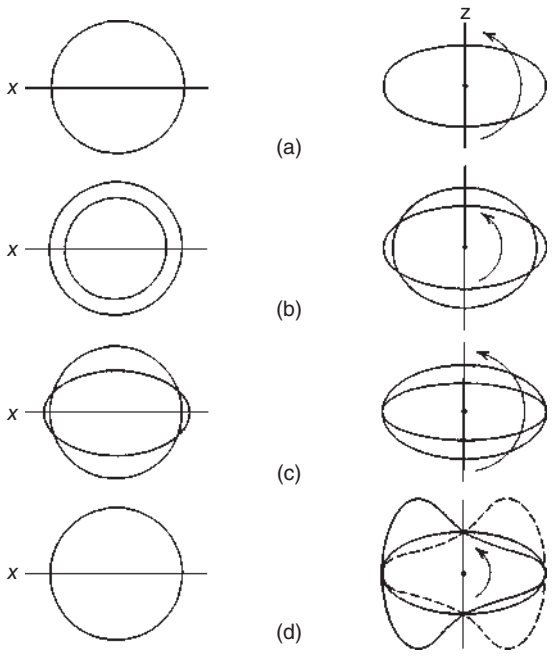

Figure 5.15 Modes of collective motion of a deformed nucleus. A cross section perpendicular to the z axis is shown on the left; a cross section in the y–z plane is shown on the right. The arrows indicate one possible mode of rotation: (a) quadrupolar rotation; (b) β vibration; (c) γ vibration; (d) octupole vibration. Source: Preston (1962)/Pearson

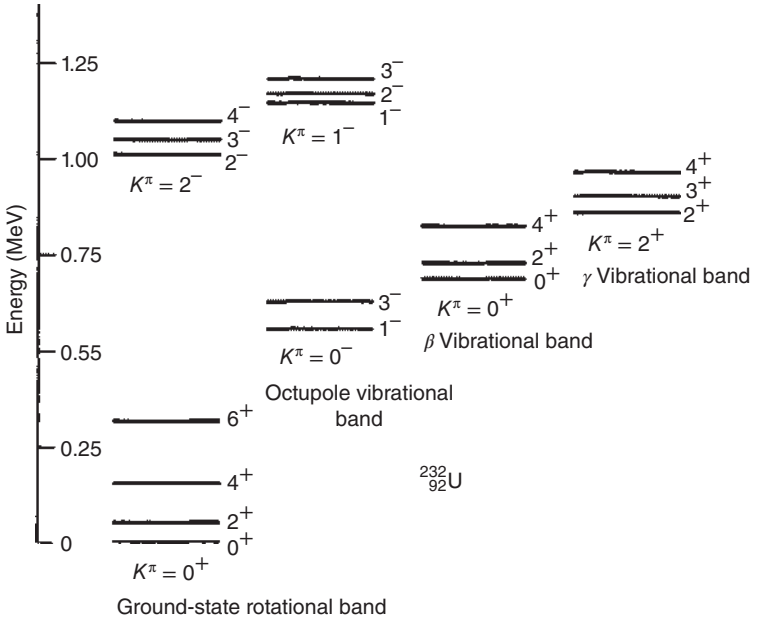

Figure 5.16 Excited levels in ^{232}U. Rotational bands, some built on vibrational states, are indicated.

is only one axis distinguished and no direction. This means that the states with $+m$ have the same energy as the states with $-m$. A level with $\boldsymbol{j} = 5/2$, for example, splits into three components with $|m| = \Omega = 5/2$, 3/2, and 1/2. Generally, a single-particle state with angular momentum $\boldsymbol{j}$ splits into $(2j+1)/2$ doubly degenerate states, and these states are characterized by the quantum number Ω running from j in integral steps down to $1/2$. According to S.G. Nilsson, one uses an oscillator potential that is no longer spherically symmetric but axially symmetric. Instead of the central potential $V(r)$ in Eq. (5.33), we write

$$V(\boldsymbol{r}) = \frac{m}{2}\left[\omega_{xy}^2(x^2+y^2) + \omega_z^2 z^2\right] \tag{5.46}$$

and we set $V_{ls}(r) = \text{const} = C$. In order to make this oscillator potential close to the Woods–Saxon potential, one can add a correction term Dl^2. The potential used by S.G. Nilsson was

$$V_i = \frac{1}{2}m\left[\omega_{xy}^2(x^2+y^2) + \omega_z^2\right] + C(\boldsymbol{l}\cdot\boldsymbol{s}) + Dl^2 \tag{5.47}$$

The two oscillator frequencies ω_{xy} and ω_z are defined with the deformation parameter δ (Eq. (4.28)),

$$\omega_z = \omega_o\left(1 - \frac{2}{3}\delta\right) \quad \text{and} \quad \omega_{xy} = \omega_o\left(1 + \frac{1}{3}\delta\right) \tag{5.48}$$

with which we take care of the constant nuclear volume. One can transform Eq. (5.47) in spherical coordinates and obtain

$$V_i = V_o(r) + V_d(\varepsilon, r)Y_2^0(\vartheta) + C(\boldsymbol{l}\cdot\boldsymbol{s}) + Dl^2 \tag{5.49}$$

Here, $V_{\text{o}}(r)$ is a central oscillator potential with frequency ω_{o} and V_{d} is a radial function

$$V_d(\varepsilon, r) = -\text{const}\delta\omega_o^2 r^2 \tag{5.50}$$

In addition,

$$Y_2^0(\vartheta) = \text{const}(3\cos^2\vartheta - 1) \tag{5.51}$$

After numerical solution of the Schrödinger equation with the potential of Eq. (5.49), one finds energy levels as a function of the deformation parameter δ. They are shown in the Nilsson diagram in Figure 5.17. To the right, prolate deformations are shown; to the left, oblate deformations. For prolate deformation, states with highest Ω lie the highest in energy, while for oblate deformation, the stability of the states increases with increasing Ω. For the characterization of the levels, one uses the quantities Ω^{π} $[N, n_2, \Lambda]$. Ω and π are good quantum numbers that correspond to the constants of the motion for the state; the terms in square brackets are the so-called asymptotic quantum numbers and describe the state which the Nilsson state approaches for large deformations. The quantity Ω is the projection of the angular momentum on the symmetry axis, $\pi = (-1)^N$ is the parity of the state, N is the total number of oscillation quanta as in the shell model, $n_z < N$ is the number of oscillation quanta along the axis of symmetry, and Λ is the component of the orbital angular momentum along the symmetry axis. As discussed earlier and illustrated by the level structure of ^{25}Al in Figure 5.12, rotational states can be

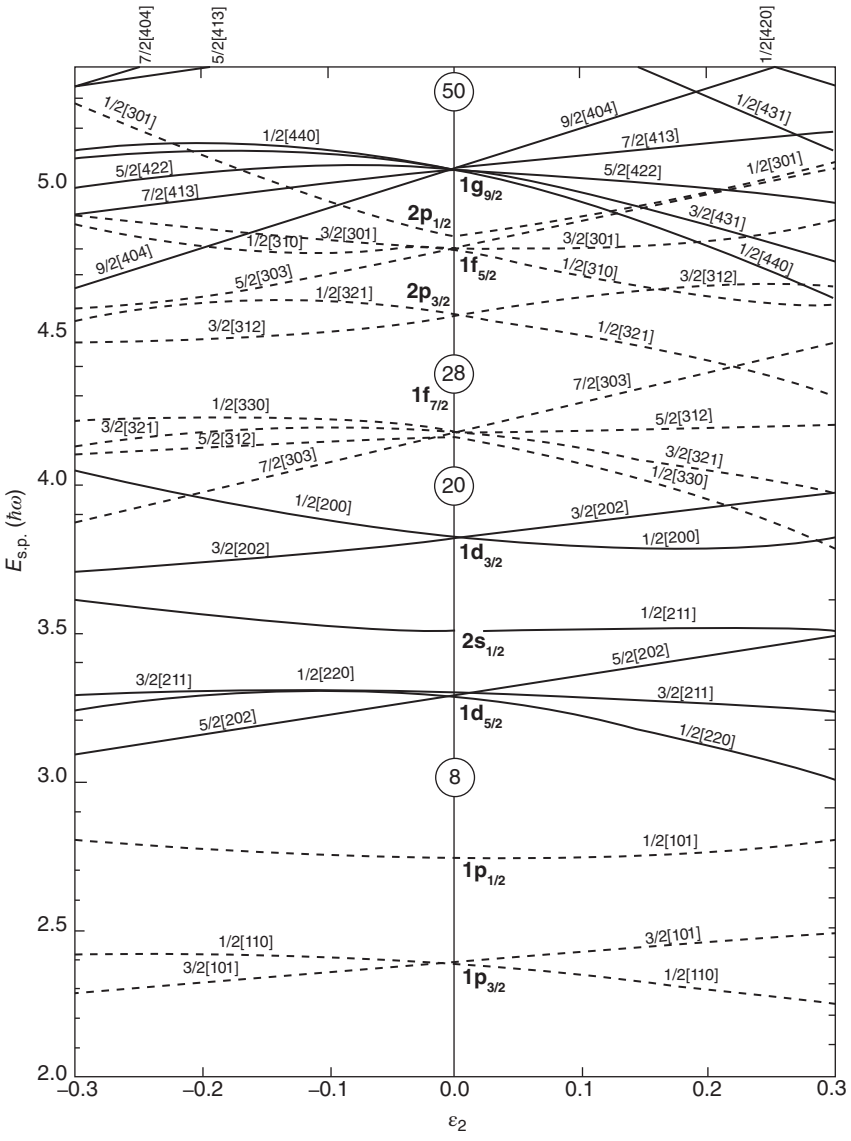

Figure 5.17 Nilsson diagram for protons or neutrons for N or $Z \leq 50$. Levels are labeled by the asymptotic quantum numbers Ω [$Nn_z\Lambda$] and at zero deformation by quantum numbers l_j. Even-parity levels are given as solid lines, odd-parity levels as dashed lines. Source: Firestone and Shirley (1996)/John Wiley & Sons.

built upon these Nilsson states. The lowest such state has I $\boldsymbol{I} = \boldsymbol{K} = \boldsymbol{\Omega}$; the excited states have $\boldsymbol{I} = \boldsymbol{K} + 1, \boldsymbol{K} + 2, \ldots$. For example, the rotational bands of ^{25}Al are built on the $5/2^+[202]$, $1/2^+[211]$, $1/2^+[200]$, and $1/2^-[200]$ single-proton intrinsic states. The model that includes these collective motions built upon appropriately modified single-particle states is sometimes called *the unified model*.

5.8 The Pairing Force and Quasi-Particles

Above, the consequences of the residual interactions among nucleons have been described phenomenologically in terms of the distortion of nuclei from spherical to spheroidal or ellipsoidal shapes. The resulting phenomena were rotational states, vibrational states, and Nilsson single-particle states. The observation that the first excited intrinsic states in even–even nuclei are much higher in energy than those of neighboring odd-A nuclei needs special attention. Also, the enhanced binding energies of the ground states of even–even nuclei are evidence of an enhanced attraction between pairs of like nucleons with angular momenta coupled to yield 0^+ states. This implies that the first excited intrinsic state of even–even nuclei would be higher than expected if only one of the nucleons in the pair was excited and the effects of pairing were destroyed. On the other hand, maintaining the pairing and raising both particles in the pair to the next higher single-particle state leads to the expectation that this state is placed about twice as high since both particles would have to be excited. The observed effect is even larger. To enlarge on this, we consider the isotopes ^{58}Ni, ^{59}Ni, and ^{60}Ni. According to the shell model, the three neutrons beyond $N = 28$ in ^{59}Ni should be in the $2p_{3/2}$ level, which is the case. The first excited state might involve raising the 31st neutron to either the $1f_{5/2}$ or the $2p_{1/2}$ state. The first excited state is a $5/2^-$ state at 339 keV. From this, it would be expected that there is an excited state in the even-mass neighbors at about 700 keV that arises from raising a pair of neutrons from the $2p_{3/2}$ state to the $1f_{5/2}$ state; however, ^{58}Ni and ^{60}Ni have 2^+ excited states at 1.45 and 1.33 MeV, and there is no state at 700 keV corresponding to the excitation of a pair of neutrons. The resulting gap in the energy spectrum requires an explanation. Obviously, it must be connected to the special features of the pairing force.

The pairing force is one consequence of the attractive nuclear forces that causes nucleons to be as close together as possible. The shell-model potential approximately accounts for the average effect of this force at distances corresponding to the average spacing between nucleons in a nucleus. There must be an additional residual attractive force between two nucleons such that they are closer to each other than to the other nucleons. The two particular single-particle states are those with the quantum numbers (n, l, j, m) and $(n, l, j, -m)$ which correspond to two particles moving in the same orbital in opposite directions consistent with the Pauli exclusion principle. In the extreme single-particle model, which neglects the residual interaction, one would fill the pairs of states up to the Fermi energy as illustrated in the left part of Figure 5.18. The residual interaction between the nucleons in each paired state alters the distribution (the right part of Figure 5.18) by removing the sharp cut-off of the occupation probability at the upper end and smearing out the distribution toward higher single-particle states. This perturbation causes the wave function to become a linear combination of unperturbed states even if they are of higher energy. Due to the partial occupation of states, a particle becomes partly a particle and partly a hole under the influence of the pairing interaction. This combination of particle and hole is known as quasi-particle. The theory developed by Bardeen, Cooper,

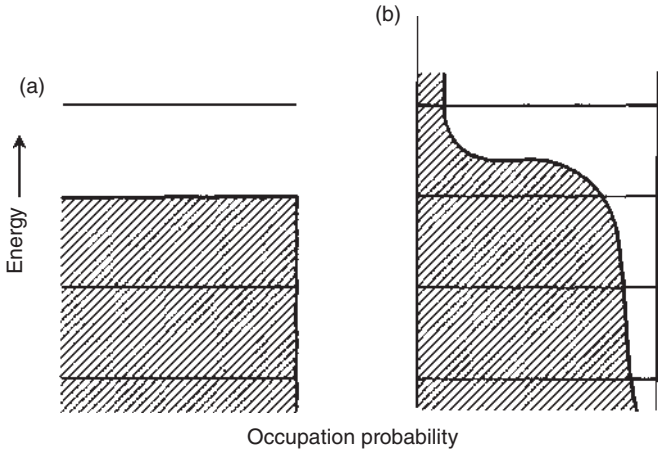

Figure 5.18 Schematic diagram of the occupation probability of nucleons in the ground state of an even–even nucleus. (a) The prediction of the extreme single-particle model. (b)The result including the pairing interaction.

and Schrieffer (BCS theory) to explain superconductivity resulting from pairing of electrons in metals was applied by Bohr, Mottelson, and Pines to the pairing of nucleons in nuclei. The resulting probability that a given pair of single-particle states will be occupied by a pair of nucleons is

$$V_i^2 = \frac{1}{2}\left(1 - \frac{\varepsilon_i - \lambda}{E_i}\right) \tag{5.52}$$

Here, ε_i is the energy of the single-particle state and λ is the Fermi energy. The quantity E_i, which plays the same role for quasi-particles as ε_i for particles in the absence of the pairing force, is given by

$$E_i = \left[(\varepsilon_i - \lambda)^2 + \Delta^2\right]^{1/2} \tag{5.53}$$

where Δ is the gap parameter being a measure of the strength of the pairing interaction, which has a value approximately equal to δ in Eq. (3.8). There are no quasi-particles present in the ground state of an even–even nucleus. Its lowest intrinsic excitation is obtained by going from zero to two quasi-particles, each of which must have an excitation energy given by Eq. (5.53). Thus, the lowest intrinsic excited state in an even–even nucleus will be approximately 2Δ, and it is this quantity that is the energy gap in the spectrum of the intrinsic energy levels of even–even nuclei. An important consequence of this energy gap for nuclear reactions, Chapter 12, is that there is no single-particle level below 2Δ in even–even nuclei, making the level density in these nuclei at a given excitation energy much smaller than in odd–odd nuclei. Nuclei with odd mass numbers have level densities intermediate between these two extremes. Nuclei with odd mass numbers contain at least one unpaired nucleon and thus contain one quasi-particle with an energy of about Δ as given by Eq. (5.53). The level density increases exponentially (Eq. (5.19)) above the energy gap.

5.9 Macroscopic–Microscopic Model

In 1967, V.M. Strutinsky proposed a hybrid model combining the liquid-drop model with a shell correction. In this method, shell effects are considered as a small deviation from a uniform single-particle energy level distribution. This deviation is then treated as a correction to the liquid-drop model energy. The dependence of the pairing strength on deformation can also be treated as another correction. The total energy is then written as a sum of the liquid-drop model energy and the shell and pairing corrections

$$E = E_{\mathrm{LMD}} + \sum_{n,p}(\delta U + \delta P) \tag{5.54}$$

where the corrections for neutrons and protons are treated separately. All quantities are functions of the deformation. The shell correction δU is the difference between the sum of the single-particle energies for two different single-particle models. The first is a realistic shell model with non-uniform level spacings and level degeneracies; the second is a uniform distribution. The shell correction is then given by

$$\delta U = U - \widetilde{U} \tag{5.55}$$

The first is

$$U = \sum_{\nu} 2\varepsilon_{\nu} n_{\nu} \tag{5.56}$$

where ε_{ν} are single-particle energies in a realistic shell-model potential and n_{ν} are the occupation numbers of these levels. For the second,

$$\widetilde{U} = 2\int_{-\infty}^{\lambda} \varepsilon \widetilde{g}(\varepsilon) d\varepsilon \tag{5.57}$$

where $\widetilde{g}(\varepsilon)$ is a uniform distribution of single-particle states, λ is the chemical potential defined by $N = 2\int_{-\infty}^{\lambda} \widetilde{g}(\varepsilon)\mathrm{d}\varepsilon$, and N is the total number of particles. The philosophy of this correction method is that any systematic errors arising from the general problem of calculating the total energy from a single-particle model will cancel, and only effects associated with special degeneracies and splitting of the levels in the particular shell-model potential will remain as a shell correction. For the uniform distribution, it is important that the averaging is done over a sufficiently large energy interval to wash out the shell effects. This averaging is done by using a weighting function

$$\widetilde{g}(\varepsilon) = (\pi\gamma)^{-1/2} \sum_{\nu} \exp\left[\gamma^{-2}(\varepsilon - \varepsilon_{\nu})^2\right] \tag{5.58}$$

The sum in Eq. (5.58) is the number of levels in the energy interval $(\pi\lambda)^{1/2}$, which is centered at the energy ε. If γ is taken to be on the order of the energy difference between major shells, $\widetilde{g}$ is not sensitive to the exact value of γ. Some examples of the shell correction δU as a function of deformation are shown in Figure 5.19. The single-particle energies used are from the Nilsson model. For spherical nuclei, the correction is negative, signaling a stronger binding for nuclei at or near closed shells. For mid-shell nuclei, the corrections are positive. At some finite deformation β of

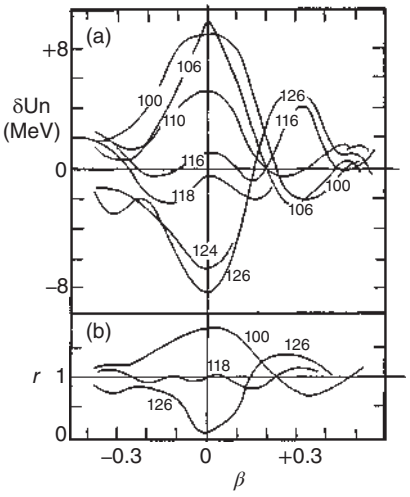

Figure 5.19 Neutron shell corrections as a function of the deformation using Nilsson single-particle energies. Curves are shown for selected neutron numbers at and below $N = 126$ (a). The ratio of the shell single-particle density to the uniform one at the Fermi energy (b). Source: Strutinsky (1967). figure 1 (p. 425)/Elsevier.

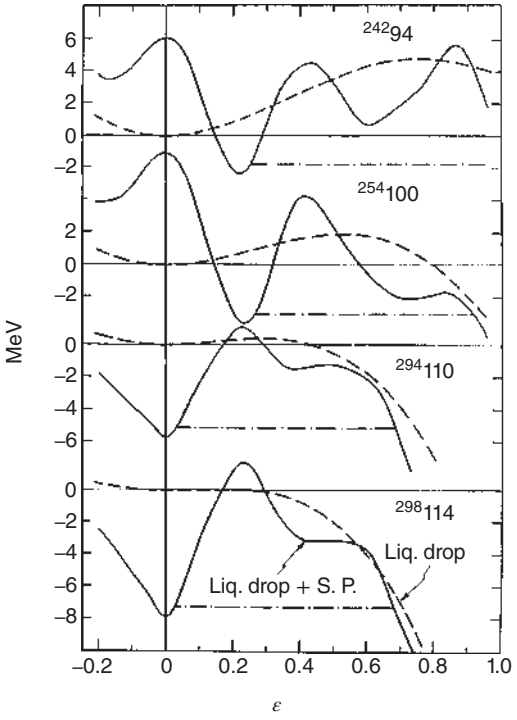

Figure 5.20 Potential energy as a function of deformation for heavy nuclei illustrating the effect of shell structure on a liquid-drop background: dashed curve, liquid-drop fission barriers; solid curve, barriers after inclusion of shell and pairing effects. Source: Tsang and Nilsson (1970). figure 7 (p. 278)/Elsevier.

about 0.3, the situation is reversed, with a positive correction for nucleon numbers close to a magic number and a negative one for mid-shell nuclei. The shell correction that favors deformed shapes for mid-shell nuclei is large enough to override the favoring of the spherical shape from the liquid-drop part of the total energy.

Examples for the total nuclear deformation energies for heavy nuclei obtained from Eq. (5.54) are shown in Figure 5.20. We will enlarge on this behavior of the

fission barriers in our discussion of fission in Chapter 12. The shell correction added to the liquid-drop fission barrier for ^{242}Pu gives a first minimum at the known deformation of the ground state and a second minimum at a ratio of the semi-major to the semi-minor axes of 2 : 1. There is evidence for the presence of such a second minimum in several nuclei from the known existence of spontaneously fissioning isomers. A highly interesting application of this model is the prediction of existence of superheavy elements. As Figure 5.20 shows, these are elements for which the liquid-drop fission barrier is zero and the stabilization against spontaneous fission is entirely due to the shell correction energy. Nilsson diagrams show a larger shell gap at $Z = 114$ than at 126 and a large shell gap at $N = 184$. Superheavy elements will be discussed in detail in Chapter 17.

5.10 Interacting Boson Approximation

Up until the mid-1970s, the two principal nuclear structure theories were the shell model emphasizing the single-particle aspects of nuclear structure along with the Pauli principle, and the collective model pioneered by Bohr and Mottelson. Subsequently, the interacting boson approximation (IBA) was proposed by A. Arima and F. Iachello based on a third approach that is group theoretical. The IBA is a model for collective behavior. It has become customary to refer to collective models of the Bohr–Mottelson type as geometric models and those of the IBA type as algebraic models. Thus today, one has a triad of models – shell, geometric, and algebraic – with which one can attack the basic features of nuclear structure. These models are not generally incompatible, although there are differences in certain important details, but rather reflect different complementary aspects of that structure.

The basic idea of the IBA is to assume that valence fermions couple in pairs only to angular momenta 0 and 2 and that the low-lying collective excitations can be described in terms of the interactions of such pairs. These fermion pairs, having integer angular momenta, are treated as bosons (called s and d bosons). The model embodies the following assumptions:

- The low-lying excitations of even–even nuclei depend only on the valence space.
- The valence nucleons are treated in pairs, as s and d bosons, with angular momenta 0 and 2.
- The number of bosons is half the number of valence protons and neutrons, both of which are counted to the nearest proton and neutron closed shells.
- The states of this boson system result from the distribution of the fermions in the s and d pairs and thus depend only on the s and d boson energies and interactions between them. These interactions are assumed to be simple, at most two-body.

A fundamental feature of the IBA is its group-theoretical structure. Since an s boson has only one magnetic substate and a d boson has five, the s–d boson system can be looked at mathematically as a six-dimensional space described by the algebraic group structure $U(6)$. This parent group has various subgroups that lead to different dynamical symmetries. There are three of these symmetries that are

physically most relevant, known by the labels U(5), SU(3), and O(6). The basic entities of the IBA are the s and d bosons which are assigned energies ϵ_s and ϵ_d. A given nucleus with N_p and N_n valence protons and neutrons each counted to the nearest closed shell has $N = (N_p + N_n)/2$ s and d bosons. For example, ^{152}Sm has $N = 6 + 4 = 10$ and both ^{144}Ba and ^{196}Pt have $N = 3 + 3 = 6$. No distinction is made on whether the valence nucleons are particles or holes. Ground and excited states are formed by distributing the bosons in different ways among s and d states and coupling them to different I. The level structures that result depend on these distributions and couplings. The formalism is phrased in terms of creation and destruction operators for the s and d bosons. The U(5) symmetry is the IBA version of a spherical vibrator. The SU(3) symmetry is that of the prolate rotor. The O(6) symmetry corresponds to a deformed, axially symmetric rotor which is γ soft. These are transition nuclei between the prolate rotor (SU(3)) and the oblate rotor ($\overline{\text{SU}}(3)$). The symmetry triangle of the IBA is shown in the center of Figure 5.21. The three corners are $\overline{\text{SU}}(3) \rightarrow 1$, U(5) $\rightarrow 2$, and SU(3) $\rightarrow 3$. The transitions between them involve the symmetry groups X(5) for spherical/prolate, O(6) for prolate/oblate, and $\overline{X}(5)$ for oblate/spherical. The symmetry triangle of the IBA suggests a periodicity of the nuclear structure that is graphically indicated by the threefold spiral in Figure 5.21. The latter assigns ^{78}Ni, ^{132}Sn, ^{208}Pb, and ^{306}122 to the spherical U(5) symmetry, ^{104}Sr,

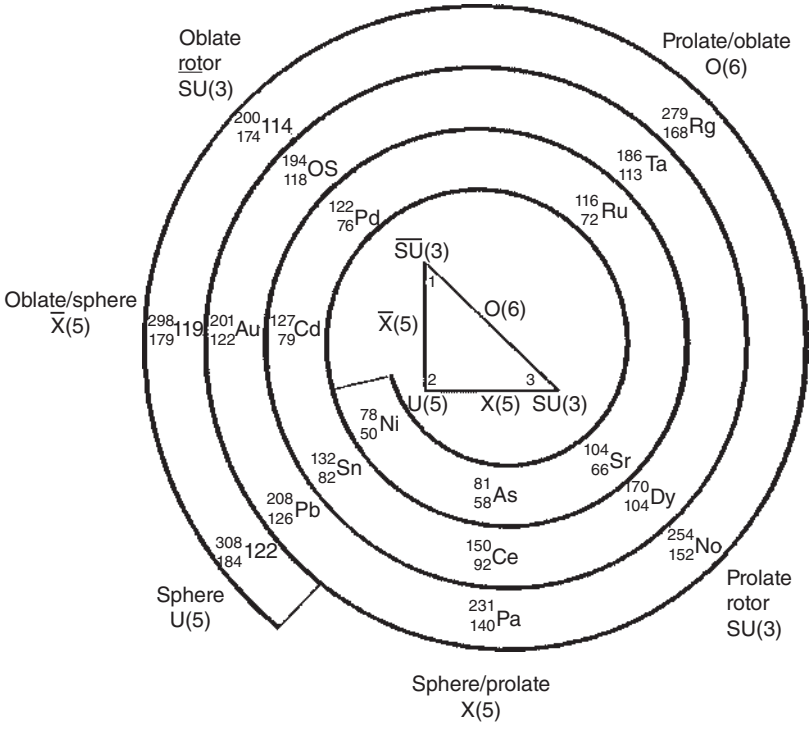

Figure 5.21 The symmetry triangle of the IBA model surrounded by a spiral with prototype nuclei suggesting a periodicity of nuclear structure. Source: Armbruster (2008). figure 2 (p. 162)/Springer Nature.

^{170}Dy, and ^{254}No to the SU(3) symmetry, and ^{122}Pd, ^{194}Os, and ^{288}114 to the $\overline{\text{SU}}(3)$ symmetry. Prototypes of the transitional nuclei between spherical and prolate are ^{91}As, ^{150}Ce, and ^{231}Pa. Prototypes for the transitional nuclei between prolate and oblate are the triaxially deformed ^{116}Ru, ^{186}Ta, and ^{279}Rg. Prototypes for the transition between oblate and spherical nuclei are ^{127}Cd, ^{201}Au, and ^{298}119. Note that the IBA periodic system would place the next spherical proton shell closure well above $Z = 114$ at $Z = 122$ in agreement with relativistic mean-field calculations.

5.11 Further Collective Excitations: Coulomb Excitation, High-Spin States, Giant Resonances

This section is intended to supplement the preceding ones with three special subjects. Coulomb excitation is a mechanism which is particularly suited for the excitation of rotational states. In so-called high-spin states (states with particularly high total angular momenta), the response of nuclei to extremely high angular momenta is studied and giant resonances are high-lying excited states of a collective nature observable as broad resonances in *excitation functions*.

Coulomb excitation is the electromagnetic excitation of a nucleus in an induction shock caused by a fast passing charged particle. This is best observed if the particle energy is below the Coulomb barrier. The colliding particles move along a Rutherford trajectory. For a simple treatment, it is important that the excitation process is sudden and not adiabatic, that is, the collision time is short compared to the oscillation period of the excitation. If υ is the projectile velocity and a is half the distance of closest approach, $a = \frac{1}{2}\, r_{\min}$, the passing time is given by a/υ. The latter is to be small compared to $1/\omega_{\text{if}} = \hbar/(E_{\text{f}} - E_{\text{i}})$ where E_{i} and E_{f} are the excitation states involved. One defines an adiabaticity parameter, ξ, as

$$\xi = \frac{a}{\upsilon}\frac{(E_f - E_i)}{\hbar} = \frac{Z_1 Z_2 e^2}{\hbar \upsilon} \cdot \frac{\Delta E}{2T} = n\frac{\Delta E}{2T} \tag{5.59}$$

Here, n is the Sommerfeld parameter (Chapter 12) and T is the kinetic energy of the projectile. If $\xi \ll 1$, the process is sudden. Under this condition, the differential cross section is given as the product of the Rutherford cross section and an excitation probability, P,

$$\frac{d\sigma}{d\Omega} = \left(\frac{d\sigma}{d\Omega}\right)_{\text{Ruth}} \cdot P \quad \text{with} \quad P = \sum |b_{\text{if}}|^2 \tag{5.60}$$

where b_{if} is an excitation amplitude which is summed over all magnetic substates. In first-order perturbation theory, the amplitudes are calculated according to

$$b_{\text{if}} = -\frac{i}{\hbar}\int_{-\infty}^{+\infty} \langle f|H'(t)|i\rangle e^{i\omega_{\text{fi}}t} dt \tag{5.61}$$

where $H'(t)$ is the time-dependent electromagnetic interaction between target and projectile. The result for the total cross section for electric multipole excitation is

$$\sigma = \left(\frac{Z_1 e}{\hbar \upsilon}\right)^2 a^{-2l+2} B(El) f(\xi) \tag{5.62}$$

Here, $B(El)$ is the reduced transition probability, see Section 6.7.2, and $f(\xi)$ is a function depending on ξ and on the multipolarity. For $E2$ transitions and $\xi \ll 1$, the value is close to 1. From the reduced transition probabilities, one can deduce the deformation properties. Equation (5.62) shows that, for example, for $l = 2$,

$$\sigma \approx \left(\frac{Z_1 e}{\hbar v}\right)^2 a^{-2} = \left(\frac{mv}{Z_2 e\hbar}\right)^2 \tag{5.63}$$

One sees that the cross section depends on the square of the projectile charge, Z_1, thus Coulomb excitation with *heavy ions* such as Pb projectiles is particularly efficient. The often-used experimental approach is to measure the γ spectrum after Coulomb excitation with a Ge detector or detector array in coincidence with the projectile scattered backward. In this setup, the observed collisions are almost central and fulfill the condition $\xi \ll 1$. In Figure 5.22, the γ spectrum is the one that has been obtained by multiple Coulomb excitation of ^{238}U by Pb ions of 5.9 MeV/A. Transitions up to $28^+ \rightarrow 26^+$ can be observed. From the electromagnetic transition probabilities, one can deduce not only the quadrupole moment ($E2$), but moreover the electric hexadecapole moment ($E4$). The resulting shape of the ^{238}U nucleus resembles that of an American football.

Fusion reactions with heavy-ion projectiles can produce very high angular momenta. The latter produce extremely strong centrifugal fields in nuclear matter, and it is not surprising that new effects result from this. In Figure 5.22, the excitation energy of a nucleus is plotted against its angular momentum I. As we have seen, for rotation with fixed moment of inertia, the rotational energy is $E_{\text{rot}} = E_{\text{rot}} = \hbar^2 I(I+1)/2\Im$. Therefore, there exists for each angular momentum I a state of minimal energy of the nucleus which corresponds just to this rotational energy. These states in Figure 5.22 lie on the so-called yrast line. The etymology of the word "yrast" is as follows. If you are rotated you get dizzy, *yr* in Swedish; if you are rotated even faster, you get more and more dizzy, up to the Swedish superlative *yrast*. Nuclei on the yrast line have no intrinsic excitation, their excitation energy is tied up entirely in rotation; they rotate cold. Above the yrast line, many states with intrinsic excitation are added. Below the yrast line, no states exist. A compound nucleus produced in a heavy-ion fusion reaction has a high angular momentum

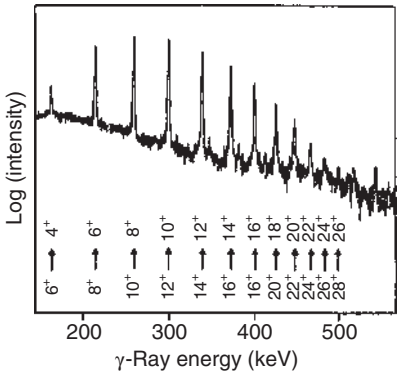

Figure 5.22 γ-Ray energy spectrum after Coulomb excitation of ^{238}U with lead ions. Source: From Mayer-Kuckuk (1979)/Springer Nature.

perpendicular to the reaction plane and a high excitation energy. This leads to the evaporation of a number of neutrons, each one cooling the compound nucleus by roughly 10 MeV. Due to their small spin, the neutrons cannot remove much angular momentum. The residual nucleus will then remove its residual excitation energy by statistical γ emission, mostly of electric dipole type, until it reaches the yrast line. From there on, the nucleus follows subsequently the rotational states down to the ground state by $E2$ transitions.

At small excitation energies and small angular momenta, in Figure 5.22 up to $I \approx 20$, we find the rotational behavior that was discussed above. The centrifugal forces are still small, and the pairing force in the nucleus is not disturbed. The moment of inertia is smaller than that of a rigid rotor but increases continuously with increasing angular momentum. For some nuclei in the region between $I = 16$ and 24, one observes a sudden change. The rotational energy from there on follows a curve corresponding to a spontaneously increased moment of inertia. The reason is that Coriolis forces break nucleon pairs. As we have discussed, the completely paired state of nuclei resembles the superconducting state in metals. The breaking of pairs corresponds to a phase transition from a supra liquid state into a normal liquid state, and the moment of inertia takes on a value that is close to that of a rigid rotor. The strong centrifugal field destroys the supra liquid state in the same way as a strong magnetic field destroys superconductivity. Effects that lead to a change in the moment of inertia become particularly visible if the experimentally determined moment of inertia is plotted against the square of the rotational frequency. The latter is determined according to

$$\omega_{\mathrm{rot}} = \left(\frac{\partial E_{\mathrm{rot}}}{\partial |\boldsymbol{I}|} \right)_{\Im \approx \mathrm{const}} \tag{5.64}$$

In Figure 5.23, the moment of inertia of ^{164}Er vs. $(\hbar\omega)^2$ is shown. At first, with increasing angular momentum, the moment of inertia increases almost linearly. This behavior reflects the gradual breaking of pairing by Coriolis forces. At $I = 14$, there is a sudden change in the slope of the curve, and at $I = 16$ and 18, the rotational frequency has decreased despite an increased angular momentum. This corresponds to a sizeable increase in the moment of inertia. The latter reaches almost the value for a rigid rotor. The level scheme in Figure 5.23a shows that we observe here the crossing of two rotational bands with different moments of inertia. As the system prefers the state with the energetically lower value, it shifts when reaching the corresponding angular momentum from the ground-state band (g band) into the Stockholm band (s band). In the case shown here, both bands can be followed a little bit further beyond the crossing point. Figure 5.23c illustrates how the jump in the moment of inertia is caused. It shows on top a rotor with arbitrary rotational axis on a rotating disk where increasing Coriolis forces eventually causes a rotational alignment (bottom) of the angular momenta of the nucleons parallel to the collective axis of rotation. If for nuclei with valence nucleons of high angular momentum j, a pair is broken at the Fermi energy, this leads to a sudden increase in the moment of inertia leading to the "backbending" visible in Figure 5.23b. In the lanthanides, this is a pair of i13/2 neutrons. By aligning the two neutrons, the nucleus gains a large amount

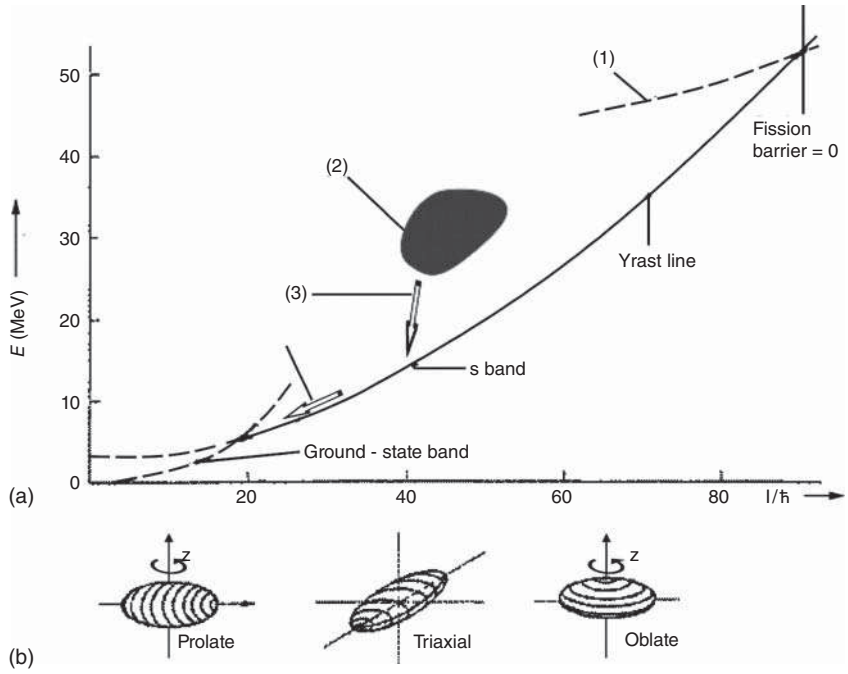

Figure 5.23 (a) Yrast line in an Energy-angular momentum plane for a deformed nucleus with $A \approx 160$, schematic. Below the yrast line, no states exist. (1) Saddle point energy for fission. (2) Typical region of excited residues after neutron evaporation from a compound nucleus formed at high angular momentum. (3) Statistical γ cascade. (b) The type of deformation in the various regions is depicted. Source: Modified from Mayer-Kuckuk (1979).

of angular momentum without spending much energy. The s band is obviously a two-quasi-particle band of aligned i13/2 neutrons.

At higher angular momenta, the prolate shape of the nuclei under the influence of strong centrifugal forces is no longer stable. Typically, a triaxial shape is observed here. At even higher angular momenta, the nucleus becomes oblate, rotating around the symmetry axis. In that case, rotational states of the type discussed above cannot occur and also the typical $E2$ transitions are missing as now, in the rotation, no changing electric field is produced. As the angular momenta are aligned in the direction of the symmetry axis, the coupling scheme is completely different from the one shown in Figure 5.11 and the electromagnetic transition probabilities resume single-particle values. Eventually, one reaches a limiting angular momentum, $l_{B_f=0}$, at which the nuclei fission spontaneously under the influence of the strong centrifugal force. These observations have all been made in the study of heavy-ion reactions.

Another type of collective excitations of nuclei is the giant resonances. These are collective vibrations of the nucleus in which an appreciable number (if not all) of the nucleons are involved and that lie at high excitation energies. The name giant resonance is connected with the history of its discovery. In photon-induced reactions of the (γ, n) type, including (γ, 2n) and (γ, 3n) at higher incident photon energies, a conspicuous resonance structure of unusual width of 3–6 MeV was observed in many

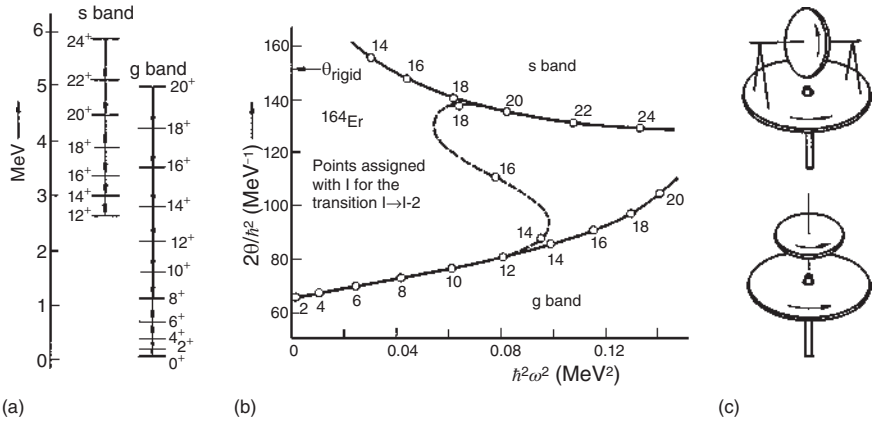

Figure 5.24 (a) Level scheme and (b) moment of inertia against $(\hbar\omega)^2$ for the nucleus ^{164}Er observed in the reaction ^{160}Gd(^{9}Be, 5n) at 59 MeV incident energy; and (c) illustration of the Coriolis interaction. Source: From Mayer-Kuckuk (1979)/Springer Nature.

nuclei. An example is shown in Figure 5.24a. The resonance energy was decreasing with $A^{1/3}$. M. Goldhaber and E. Teller explained these resonances as a vibration of all protons against all neutrons. H. Steinwedel et al. refined this picture in the sense that the shape of the nucleus does not change in these excitations. They are separator vibrations of the proton and neutron liquids whereby the symmetry energy acts as the restoring force. The types of vibration are depicted hydrodynamically in Figure 5.25. At the top of Figure 5.25b, protons and neutrons vibrate out of phase against each other. This is the electric dipole giant resonance involving an isospin change $\Delta T = 1$, therefore called an isovector resonance. The resonance energy can be parameterized by $E_{\mathrm{GDR}} = (40A^{-1/3} + 7.5)$ MeV. In a generalized hydrodynamical model, other dipole vibrations are possible in which all particles with equal angular momentum vibrate against all particles with opposite angular momentum, the magnetic dipole giant resonance shown in Figure 5.25b (bottom). This corresponds to an isoscalar resonance with $\Delta T = 0$. In inelastic scattering of protons and α particles, other vibrational modes were identified. Figure 5.25c shows at the top a compression mode, the monopole giant resonance, in which the nucleons can oscillate in phase (isoscalar $\Delta T = 0$) or out of phase (isovector $\Delta T = 1$). In Figure 5.25c, the electric giant quadrupole resonances are sketched at the bottom, again isoscalar and isovector. Their excitation energies are at $E_{\mathrm{GQR}} = 63A^{-1/3}$.

Microscopically, the response of nuclei against electromagnetic excitation is described by a transition operator depending on the electromagnetic field, that is, on a linear combination of electric (λ) and magnetic (μ) multipole fields. Of importance are the electric multipole moments $M(E\lambda)$, and these fix the reduced transition rates

$$B\left(E\lambda, I_i \to I_f\right) = \frac{1}{2I_i + 1} |\langle I_f \| M\left(E\lambda\right) \| I_i \rangle|^2 \tag{5.65}$$

The transition operator cannot yet describe the experimentally determined cross sections. For this, one needs oscillator sum rules depending on the potential energy

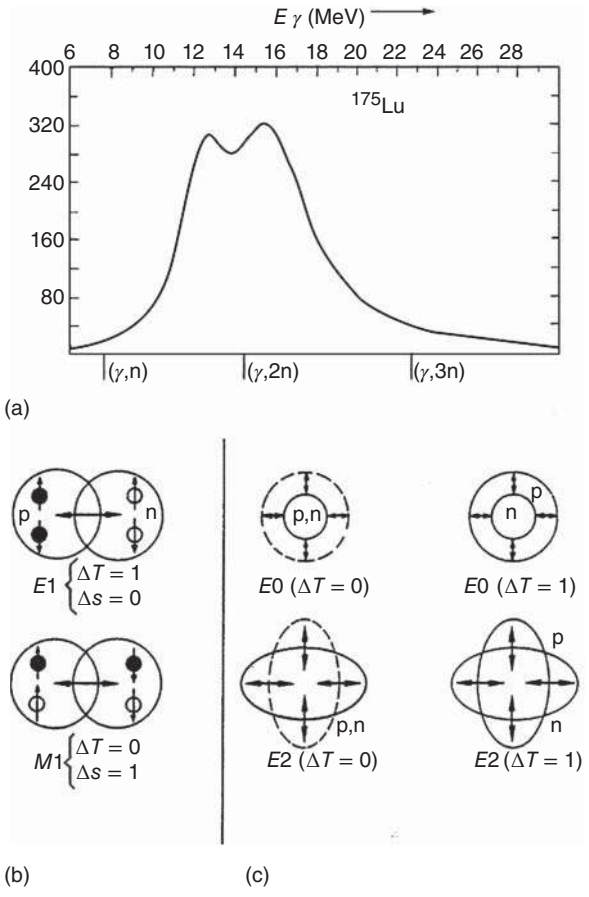

Figure 5.25 An example of a giant resonance (a) in the excitation of ^{175}Lu by bremsstrahlung quanta. For deformed nuclei, the splitting of the resonance into two bumps is characteristic as along the deformation axis there exists another vibrational frequency than in a direction perpendicular to the latter. (b, c) Illustration of giant resonances in the hydrodynamical model, (b) electric and magnetic dipole vibrations, (c) electric monopole (top) and quadrupole (bottom) vibrations. Source: Modified from Mayer-Kuckuk (1979).

of the nucleon–nucleon interaction. This oscillator strength is defined as a transition probability multiplied by the transition energy $E_a - E_0$. The sum of the oscillator strength is

$$S(M) = \sum_a (E_a - E_0)|\langle a|M|0\rangle|^2 = \frac{1}{2}\langle 0|[M,[H,M]]|0\rangle \tag{5.66}$$

where the sum runs over all states a accessible to the operator M. Equation (5.66) is known as the energy-weighted sum rule. As the electromagnetic interaction affects only the protons in the nucleus, an effective charge of $(N/A)e$ and $(-Z/A)e$ is assigned to the Z protons and N neutrons. For an $E1$ transition, this yields

$$S(E1) = \frac{9}{4\pi}\frac{\hbar^2}{2m}\frac{NZ}{A}e^2 = 14.8\frac{NZ}{A}e^2\text{MeV fm}^2 \tag{5.67}$$

which can be used to calculate the integral cross section

$$\int_0^\infty \sigma \mathrm{d}E = \frac{16\pi^3}{9\hbar c}S(E1)\text{MeV fm}^2 \tag{5.68}$$

Equation (5.68) is known as the Thomas–Reiche–Kuhn (TRK) sum rule (or energy-weighted sum rule for the $E1$ resonance). Combining Eqs. (5.67) and (5.68)

leads to a different expression for the TRK sum rule for A particles with effective charge

$$\int_0^\infty \sigma(E)\mathrm{d}E = \frac{2\pi^2\hbar e^2}{mc}\frac{NZ}{A} \cong 60\frac{NZ}{A}\mathrm{MeV\ mb} \tag{5.69}$$

In general, giant resonances exhaust the TRK sum rule. They decay rapidly into a compound nucleus which subsequently decays statistically, see Chapter 12.

References

Historical

Armbruster, P. (2008). Shifting the closed proton shell to $Z = 122$ – A possible scenario to understand the production of superheavy elements $Z = 112–118$. *Eur. Phys. J.* A37: 159.

Cohen, B.L. (1971). *Concepts of Nuclear Physics*. New York: McGraw-Hill.

Firestone, R.B. and Shirley, V.S. (eds.) (1996). *Table of Isotopes*, 8e, vol. II, H6. New York: Wiley.

Klinkenberg, P.F.A. (1952). Tables of nuclear shell structure. *Rev. Mod. Phys.* 24: 63.

Mayer, M.G. and Jensen, J.H.D. (1955). *Elementary Theory of Nuclear Shell Structure*. New York: Wiley.

Mayer-Kuckuk, T. (1979). *Kernphysik*. Stuttgart: Teubner.

Preston, M.A. (1962). *Physics of the Nucleus*. Reading, MA: Addison-Wesley.

Strutinsky, V.M. (1967). Shell effects in nuclear masses and deformations. *Nucl. Phys.* A95: 420.

Tsang, C.F. and Nilsson, S.G. (1970). Shape isometric states in heavy nuclei. *Nucl. Phys.* A140: 275.

Further Reading

Historical

Yukawa, H. (1935). On the interaction of elementary particles I. *Proc. Physico-Math. Soc. Jpn* 17: 48.

Nordheim, L.W. (1951). Nuclear shell structure and beta-decay, II. Even A nuclei. *Rev. Mod. Phys.* 23: 322.

Bohr, A. and Mottelson, B.R. (1953). Collective and individual particle aspects of nuclear structure. *Dan. Mat.-Fys. Medd.* 27: 16.

Bohr, A. and Mottelson, B.R. (1955). Collective nuclear motion and the unified model. In: *Beta and Gamma Ray Spectroscopy*, vol. 1 (ed. K. Siegbahn). Amsterdam: North-Holland.

Nilsson, S.G. (1955). Binding states of individual nucleons in strongly deformed nuclei. *Dan. Mat.-Fys. Medd.* 29: 16.

Bethe, H.A. and Morrison, P. (1956). *Elementary Nuclear Theory*. New York: Wiley.

Bardeen, J., Cooper, L.N., and Schrieffer, J.R. (1957). Theory of superconductivity. *Phys. Rev.* 108: 1175.

Bohr, A., Mottelson, B.R., and Pines, D. (1958). Possible analogy between the excitation spectra of nuclei and those of the superconducting metallic state. *Phys. Rev.* 110: 936.

Bohr, A. and Mottelson, B.R. (1960). Collective motion and nuclear spectra. In: *Nuclear Spectroscopy, Part B*, vol. 2 (ed. F. Ajzenberg-Selowe). New York: Academic Press.

Brennan, M.H. and Bernstein, A.M. (1960). jj Coupling model in odd-odd nuclei. *Phys. Rev.* 120: 927.

Kisslinger, L.S. and Sorenson, R.A. (1960). Pairing plus long range force for single closed shell nuclei. *Dan. Mat.-Fys. Medd.* 32 (9): 1–82.

Hamada, T. and Johnston, I.D. (1962). A potential model representation of two-nucleon data below 315 MeV. *Nucl. Phys. A* 34: 382.

Kisslinger, L.S. and Sorenson, R.A. (1963). Spherical nuclei with simple residual forces. *Rev. Mod. Phys.* 35: 853.

Fox, J.D., Moore, C.F., and Robson, D. (1964). Excitation of isobaric analog states in ^{89}Y and ^{90}Zr. *Phys. Rev. Lett.* 12: 198.

Nathan, O. and Nilsson, S.G. (1965). Collective nuclear motion and the unified model. In: *Alpha-, Beta- and Gamma-Ray Spectroscopy*, vol. 1 (ed. K. Siegbahn), 601. Amsterdam: North-Holland.

Baumgärtner, G. and Schuck, P. (1968). *Kernmodelle*, vol. 203. Mannheim: BI Hochschultaschenbuch.

Bohr, A. and Mottelson, B.R. (1969 and 1975). *Nuclear Structure, vol. I, Single Particle Motion, vol. II, Nuclear Deformations*. New York: Benjamin.

Wilkinson, D.H. (ed.) (1969). *Isospin in Nuclear Physics*. Amsterdam: North-Holland.

Bethe, H.A. (1971). Theory of nuclear matter. *Annu. Rev. Nucl. Sci.* 21: 93.

Cohen, B.L. (1971). *Concepts of Nuclear Physics*. New York: McGraw-Hill.

Rasmussen, J.O. (1974). Models of heavy nuclei. In: *Nuclear Spectroscopy and Reactions, Part C* (ed. J. Cerny), 97. New York: Academic Press.

Arima, A. and Iachello, F. (1975). Collective nuclear states as representations of a SU(6) group. *Phys. Rev. Lett.* 35: 1069.

Stephens, F.S. (1975). Coriolis effects and rotational alignment in nuclei. *Rev. Mod. Phys.* 47: 43.

Arima, A. and Iachello, F. (1976). Interacting boson model of collective states I, the vibrational limit. *Ann. Phys.* 99: 253.

Iachello, F. (1979). *Interacting Bosons in Nuclear Physics*. New York: Plenum Press.

Bjørnholm, S. and Lynn, J.E. (1980). The double-humped fission barrier. *Rev. Mod. Phys.* 52: 725.

McGrory, J.B. and Wildenthal, B.H. (1980). Large-scale shell model calculations. *Annu. Rev. Nucl. Part. Sci.* 30: 383.

More Recent

Feshbach, H. (1987). Small systems: when does thermodynamics apply? *Phys. Today* 40: 9.

Casten, R.F. (1990). *Nuclear Structure from a Simple Perspective*. Oxford: Oxford University Press.

Das, A. and Ferbel, T. (1994). *Introduction to Nuclear and Particle Physics*. New York: Wiley.

Hodgson, P.E., Gadioli, E., and Gadioli-Erba, E. (1997). *Introductory Nuclear Physics*. Oxford: Clarendon Press.

Heyde, K. (1999). *Basic Ideas and Concepts in Nuclear Physics*, 2e. Bristol: IOP Publishing.

Fényes, T. (2011). Basic properties of the atomic nucleus. In: *Handbook of Nuclear Chemistry*, 2e, vol. 1 (eds. A. Vértes, S. Nagy, Z. Klencsár, et al.), 39. Berlin: Springer.

6

Decay Modes

6.1 Nuclear Instability and Nuclear Spectroscopy

In Section 1.4, we introduced the various nuclear decay modes, see Table 1.1 for a summary. When presenting mass parabolas in Chapter 3, we pointed out that all but one isobar of a given mass number must be unstable toward β decay since only the isobar of lowest mass is thermodynamically stable. However, the rates of these decays can be extremely slow; for example, for double β decay, the half-lives are $\geq 10^{20}$ years, so that, for practical purposes, these nuclei may be considered stable. This holds also for all "stable" nuclides with $A \geq 140$ which are unstable toward α emission but have half-lives so long that their decay is unobservable. Likewise, nuclides with $A \geq 100$ are unstable with respect to spontaneous fission. However, because of the high Coulomb barriers for the emission of fission fragments, measurable rates of spontaneous fission are found only for the heaviest elements. Thus, it is clear that, on the one hand, the nuclear instability is closely related to the nuclear energy surface resulting from the interplay of volume, surface, Coulomb, symmetry, and pairing energy, while, on the other hand, thermodynamics tells only part of the story. We thus always ask for the decay rates or half-lives, and in this chapter, we outline the theoretical framework with which the decay rates depend not only on the decay energy, but also on the change in angular momentum, and the parity change involved in the transition. These depend on the properties of the nuclear energy levels involved, and knowledge about these properties comes from experimental nuclear spectroscopy. The latter is vital for understanding nuclear structure and is the basis for the various nuclear models discussed in Chapter 5. Conversely, the development of these models has stimulated experimental nuclear spectroscopy work performed to test model predictions.

6.2 Alpha Decay

The identity of α particles with $^4He^{2+}$ was established as early as 1903, and the monoenergetic nature of α rays was also soon recognized. When the decay takes place between the ground states of mother and daughter nuclei, the decay energy is called ground-state decay energy and is denoted by Q_α. It is obtained from the atomic

Nuclear and Radiochemistry: Fundamentals and Applications,
Fourth Edition. Jens-Volker Kratz.

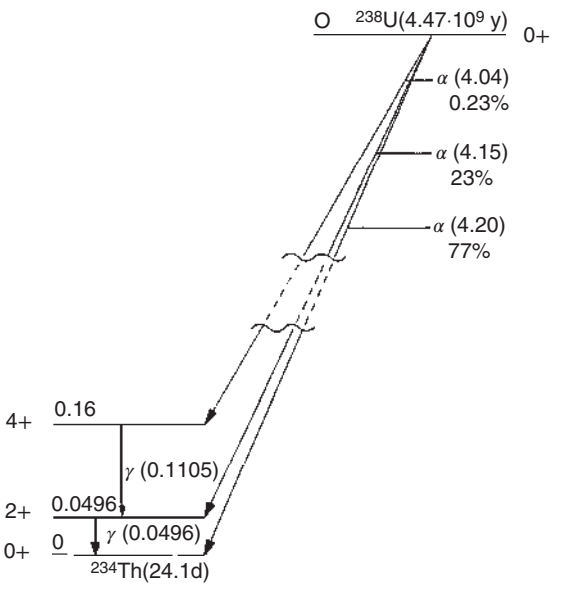

Figure 6.1 Decay scheme of ^{238}U (energies of excited states in ^{234}Th, α decays, and γ transitions in MeV). Angular momenta and parity are also indicated.

masses M_m, M_d, and M_α. The kinetic energy of the α particle is smaller than Q_α by the recoil energy of the daughter nucleus, see Chapter 3. The feeding of excited levels in the daughter, see for example Figure 6.1, leads to the so-called fine structure of α spectra. The energies of α particles range from 1.83 MeV (^{144}Nd) to 11.81 MeV (^{294}118), and most of them lie between 4 and 8 MeV. This relatively small energy range is associated with an enormous range in half-lives of roughly 30 orders of magnitude. This inverse correlation between energy and half-life was recognized in 1911 by Geiger and Nuttall (1911) who formulated for the decay constants of the α emitters in the natural decay series and the ranges R in air the relation

$$\log \lambda = a + b \log R \tag{6.1}$$

where b is a constant and a takes on different values for each of the three decay series. These relations are shown in Figure 6.2. As the range of α particles in air is a function of their energy E_α, Eq. (6.1) may also be written as

$$\log \lambda = a' + b' \log E_\alpha \tag{6.2}$$

Substitution of λ by the half-life $t_{1/2}$ gives

$$\log t_{1/2} = \overline{a} - \overline{b} \log E_\alpha \tag{6.3}$$

This relation is shown for a number of even–even nuclei in Figure 6.3.

A theoretical understanding of these relations was lacking until quantum mechanical theory developed in 1928 independently by Gamow (1928) and Gurney and Condon (1929) successfully accounted for the relationship between half-lives and energies. The Schrödinger wave equation for an α particle of energy $T = Q_\alpha = T_\alpha + T_r$ (sum of kinetic energies of α particle and recoil nucleus) inside the nuclear potential well is that of a standing wave. Its amplitude does not go abruptly to zero for $r > R_1$

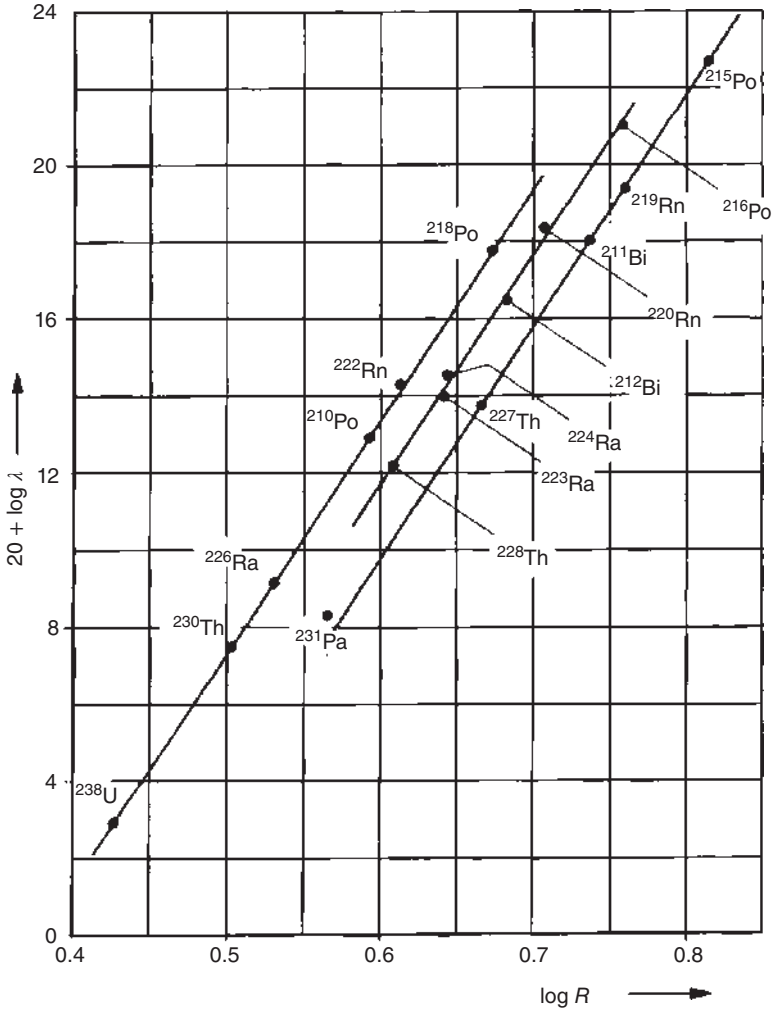

Figure 6.2 Relation between the range of α particles in air and the decay constant λ (Geiger–Nuttall rules). Source: Modified from Geiger and Nuttall (1911).

in Figure 6.4 but decreases exponentially to receive a very small amplitude outside of R_2. The approximation of the barrier by a rectangular potential and the shape of the wave functions in the three regions (1, 2, and 3) of the distance r are schematically indicated in the right part of Figure 6.4. By applying the boundary condition that the wave function and its first derivative must be continuous at R_1 and R_2 and by inserting the solutions of the Schrödinger equation in regions 1, 2, and 3, one obtains four equations for the determination of the five existing amplitudes α_1, β_1, α_2, β_2, and α_3, where α is the amplitude of an outgoing wave and β is the amplitude of the reflected wave. Most interesting is the ratio α_3/α_1 as we are interested in the transmission coefficient P. For a thick barrier (Figure 6.4a), the barrier is approximated by a histogram; that is, it is subdivided into narrow rectangles of differential

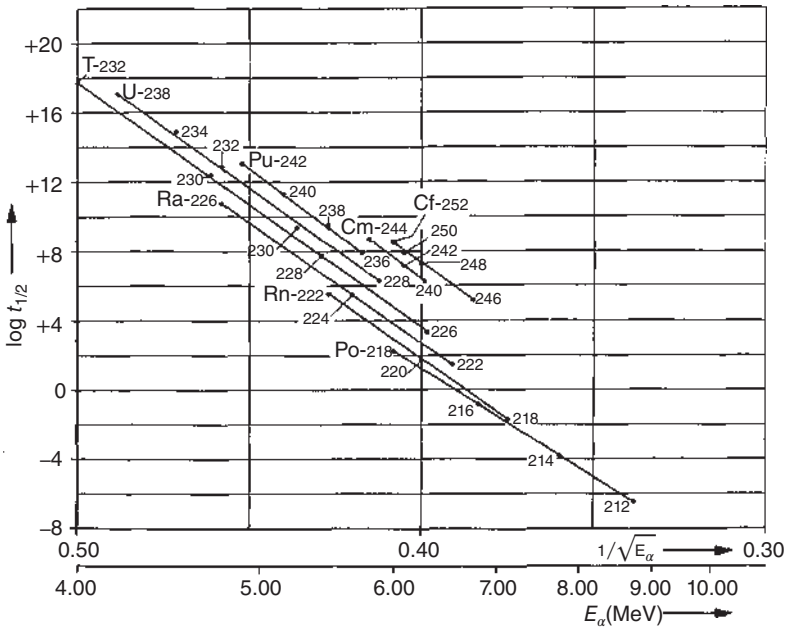

Figure 6.3 Relation between the half-life of even–even nuclei [s] and the energy of the α particles.

thickness d and the barrier penetrability factor is determined as $P = P_1 \cdot P_2 \cdot P_3 \ldots$ resulting in

$$P = \exp\left(-\frac{2}{\hbar}\sqrt{2\mu}\sum\sqrt{U(r)-T}d_i\right) \tag{6.4}$$

yielding

$$P = \exp\left(-\frac{2}{\hbar}\sqrt{2\mu}\int_{R_1}^{R_2}\sqrt{U(r)-T}\,\mathrm{d}r\right) = \mathrm{e}^{-G} \tag{6.5}$$

where

$$\mu = \frac{M_\alpha M_R}{M_\alpha + M_R}$$

is the reduced mass of the α particle and recoil nucleus and G is the so-called Gamow factor. Equation (6.5) tells us that the probability for passing the barrier decreases exponentially with increasing barrier height and width. For example, for ^{212g}Po, $E_\alpha = 8.78$ MeV, $t_{1/2} = 0.3$ µs, the barrier penetrability factor is $1.32 \cdot 10^{-13}$; for ^{144}Nd, $E_\alpha = 1.83$ MeV, $t_{1/2} = 2 \cdot 10^{15}$ year, the penetrability is $2.2 \cdot 10^{-42}$; thus, the Gamow–Gurney–Condon approach reproduces the ≈30 orders of magnitude mentioned above. The half-life is obviously inversely proportional to P, or proportional to e^G. Thus, $\log t_{1/2}$ is proportional to G, i.e. to $1/\sqrt{T}$, cf. Figure 6.3. This is an a posteriori corroboration of the Geiger–Nuttal rule.

The decay constant λ is the product of P and the frequency f with which the α particle knocks at the potential wall. That frequency can be estimated from the

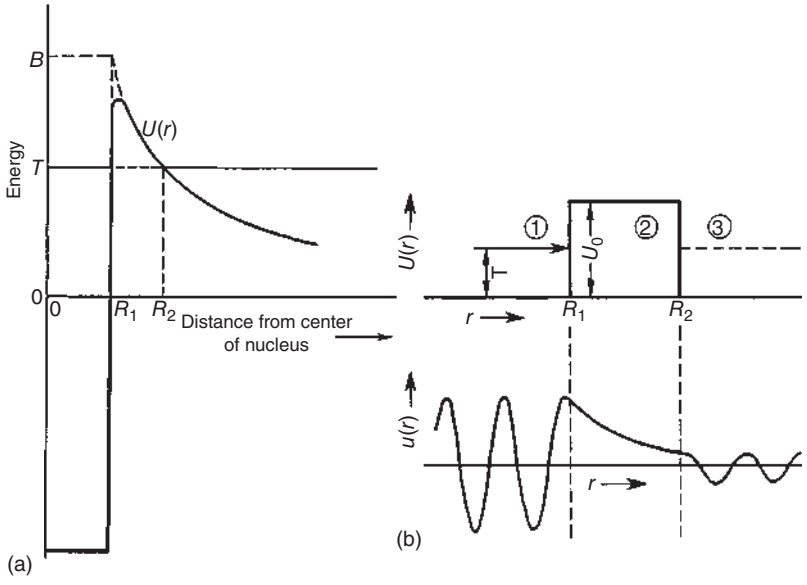

Figure 6.4 Potential energy for a nucleus–α-particle system (a). (b) Shown is a rectangular approximation of the barrier with barrier height U_0 divided into regions (1, 2, and 3) and below the shape of the wave functions $u(r)$ in these three regions.

de Broglie wavelength $h/\mu v$ of the α particle which must be on the order of R_1. Then, the velocity of the α particle is on the order of $h/\mu R_1$. If we assume that the α particle bounces back and forth between the walls of the potential, then

$$f \approx \frac{v}{2R_1} \quad \text{and} \quad f = \frac{h}{2\mu R_1^2}$$

The knocking frequency is on the order of $10^{20}\,\mathrm{s}^{-1}$ and varies only by about 30% for different nuclei. With this, the decay constant is

$$\lambda = \frac{h}{2\mu R_1^2} \exp\left(-\frac{4\pi}{h}\sqrt{2\mu}\int_{R_1}^{R_2}\sqrt{U(r)-T}\,\mathrm{d}r\right) \tag{6.6}$$

As outlined in the textbook by Friedlander et al. (1981) for simple forms of the potential energy $U(r)$, the integral in Eqs. (6.5) and (6.6) can be solved in closed form. For a square well potential of radius R_1 and a Coulomb potential $U(r) = Zze^2/r$ for $r > R_1$ (here, Z is the atomic number of the daughter nucleus, see the dashed line in Figure 6.4), the integral becomes

$$\text{Int.} = \int_{R_1}^{R_2} (Zze^2 - Tr)^{1/2}\frac{\mathrm{d}r}{r^{1/2}} \tag{6.7}$$

With the substitutions $x = r^{1/2}$ and $a^2 = Zze^2 \,/\, T$, Eq. (6.7) turns into the readily integrable form

$$\text{Int.} = 2\sqrt{T}\int_{\sqrt{R_1}}^{\sqrt{R_2}}\sqrt{a^2 - x^2}\,\mathrm{d}x$$

with the solution

$$\text{Int.} = \sqrt{T}\left[x(a^2 - x^2)^{1/2} + a^2 \arcsin\left(\frac{x}{a}\right)\right]_{\sqrt{R_1}}^{\sqrt{R_2}} \tag{6.8}$$

Values for R_1 and R_2 follow from the total kinetic energy $T = Zze^2/R_2$ and from the barrier height $B = Zze^2/R_1$. After substitution of the integration limits and some algebraic transformations, we obtain

$$\text{Int.} = \frac{Zze^2}{\sqrt{T}}\left[\arccos\left(\frac{T}{B}\right)^{1/2} - \left(\frac{T}{B}\right)^{1/2}\left(1 - \frac{T}{B}\right)^{1/2}\right] \tag{6.9}$$

Finally, remembering that $T = \frac{1}{2}\mu v^2$, substitution of Eq. (6.9) in the fundamental Eq. (6.6) gives

$$\lambda = \frac{h}{2\mu R_1^2} \exp\left\{-\frac{8\pi Zze^2}{hv}\left[\arccos\left(\frac{T}{B}\right)^{1/2} - \left(\frac{T}{B}\right)^{1/2}\left(1 - \frac{T}{B}\right)^{1/2}\right]\right\} \tag{6.10}$$

Values for decay constants calculated with Eq. (6.10) are compared in Friedlander et al. (1981) to experimental values for a number of α emitters. The calculations used for the radius $R_1 = (1.30 \cdot A^{1/3} + 1.20)$ fm with no other adjustable parameters. The agreement between calculated and measured values is remarkable, that is, within a factor of 4 in all cases except for ^{210}Po – a nucleus with 126 neutrons decaying into a nucleus with 82 protons, both tightly bound closed-shell nuclei, indicating that nuclear structure effects may not entirely be ignored – even though the values of λ extend over 27 orders of magnitude. The values of λ_{calc} depend sensitively on the nuclear radii assumed, and each increase in the nuclear radius parameter r_0 by 0.03 fm leads to a doubling of the values of λ_{calc}. The fact that Eq. (6.10) gives remarkable agreement with experimental data when r_0 is fixed at 1.30 fm should not be weighed too much as several simplifications are inherent in the approach: (i) the use of a square well potential instead of the more realistic Woods–Saxon potential; (ii) the radius of the α particle of 1.20 fm is chosen somewhat arbitrarily; and (iii) the knocking frequency f was estimated on the naive assumption that α particles preexist and oscillate in nuclei, which is termed the *one-body model*. It is remarkable that none of these simplifications strongly affects the dependence of λ on T over so many orders of magnitude, which is due to the exponential in Eq. (6.10). Even within the framework of the one-body model, much has been done in the refinement of the preexponential factor in Eq. (6.10). Alternatively, of course, f can be taken as the product of two probabilities: the probability of formation of a bound α particle inside a nucleus which should depend on the details of nuclear structure, see below, and the knocking of the α particle once formed against the potential wall.

6.2.1 Hindrance Factors

The barrier penetration theory in its simple form as discussed above applies to even–even α emitters only, and good agreement with experimental half-lives is generally found for transitions to ground states and first excited states of even–even nuclei. Other α transitions tend to be slower by factors up to 10^4 as compared to

the prediction of the simple theory. Since Eq. (6.10) was derived without considering angular momentum effects – it considers the emission of s-wave α particles only – one might be tempted to ascribe the relative slowness of other α transitions to angular momentum effects and to the need for parity conservation, which is an important selection rule for α decay. Emission of an α particle of orbital angular momentum l involves a parity change $(-1)^l$ so that $1^+ \rightarrow 0^+$ or $2^- \rightarrow 0^+$ α decays are forbidden. Also, for an α particle carrying away l units of angular momentum, one has to add a centrifugal barrier $\hbar^2 l\,(l+1)\,/\,2\mu R^2$ to the Coulomb potential $Zze^2\,/\,R$. For α decay of, for instance, ^{230}Th into levels of the ground-state rotational band of ^{226}Ra, the so-called hindrance factors, that is, the ratios of calculated (for $\Delta l = 0$) to observed transition rates, are 1 for the 0^+ ground state, 1 for the 2^+ state, 12 for the 4^+ state, and 8000 for the 6^+ state – much larger than can be accounted for by the inclusion of the centrifugal barrier in $U(r)$. There is a general trend for larger hindrance factors with increasing Δl. For even–odd, odd–even, and odd–odd nuclei, the situation is even more complex and hindrance factors up to several tens of thousands are observed with trends that are difficult to discern. Ground-state transitions for deformed odd-A nuclei are observed to be highly hindered even if there is no angular momentum change involved, while transitions to excited states are usually almost unhindered. For ^{241}Am $(5/2^-)$, α decay to the ground state and first excited state of ^{237}Np $(5/2^+, 7/2^+)$ has hindrance factors of about 500, while the more intense transition to the $5/2^-$ excited state is almost unhindered. At this point, we should not be surprised that the simple one-body theory is far from accounting for the α-decay rates in these different types of nuclei and to various kinds of excited states. It does a remarkable job of explaining the barrier penetration once the α particle is formed; however, the formation of an α particle in a nucleus should strongly depend on the nuclear structure. For example, a ground-state transition from a nucleus with an odd nucleon in the highest occupied orbital can take place only if that nucleon becomes part of the α particle. For this to occur, another nucleon pair needs to be broken. Thus, in this case, the spectroscopic factor for the formation of the α particle is much <1. On the other hand, if the α particle is formed from existing pairs, the daughter nucleus will be populated in an excited state and this may explain the "favored" transitions to excited states. Much progress has been made in calculating the probabilities for assembling α particles in different nuclei on the basis of the single-particle shell model and the collective model (see Chapter 5). Basic ideas on how to involve these models in accounting for the hindrance factors can be found in the work by H.J. Mang, I. Perlman, and others.

6.2.2 Alpha-Decay Energies

According to the liquid-drop model, the α-decay energies are expected to decrease monotonically with increasing A for a given Z, and for each series of isobars to increase with increasing Z. These expectations are indeed largely exhibited by the data shown in Figure 6.5; however, there is an abrupt interruption of the smooth trend in the vicinity of $A = 210$. If the same data had been plotted as

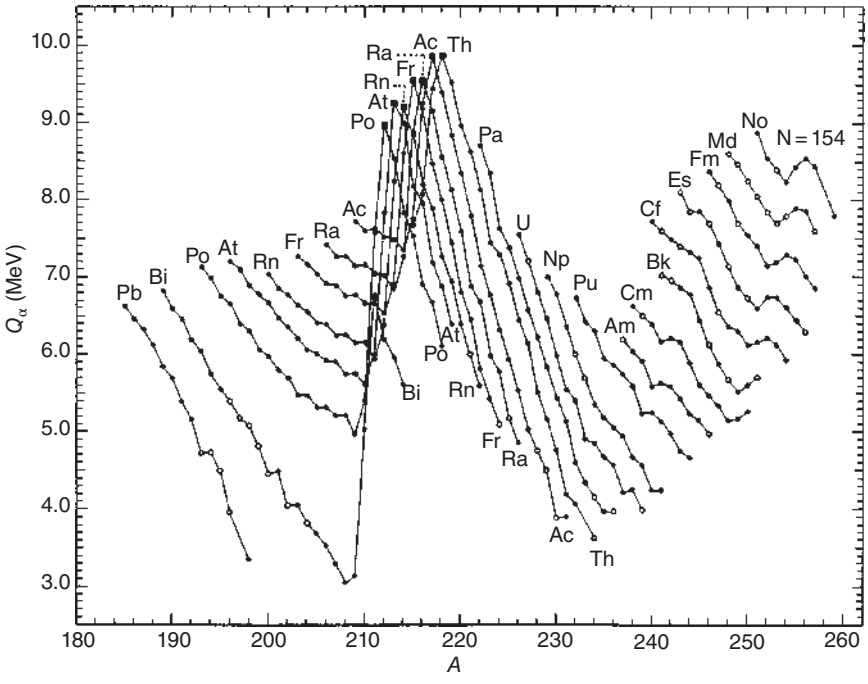

Figure 6.5 Plot of Q_α values vs. mass number for α emitters from lead to nobelium. The maxima (filled squares) with sharp drop-off to the left occur at $N = 128$. The less pronounced maxima at $N = 154$ indicate a deformed shell closure at $N = 152$. Decay energies estimated from systematics are shown as open circles. Source: Friedlander et al. (1981)/John Wiley & Sons.

a function of neutron number, which was not done because the data for different elements would be less well separated in such a plot, it would be more immediately evident that the striking drop in decay energy occurs for each element between $N = 128$ and $N = 126$. This indicates particularly high binding energies or small masses for $N = 126$ and is one of the strongest indications for a shell closure at this neutron number. In addition, the particularly large decrease in the Q_α values between the heavy polonium isotopes and the heavy bismuth isotopes reflects the closed proton shell at $Z = 82$. Likewise, the smaller peak in Q_α at $N = 154$ is an indication of a deformed neutron-shell closure at $N = 152$ which we will encounter again in the spontaneous fission half-lives. In the rare earths between ^{144}Nd and ^{155}Lu and beyond, there is another region of α emitters with the highest decay energies for emitters with $N = 84$ because the daughters are closed-shell nuclei with $N = 82$. Another island of very short-lived neutron-deficient α-emitters is located just above the doubly magic ^{100}Sn. Many other α emitters not shown in Figure 6.5 are neutron-deficient isotopes of W through Tl. The conclusion at this point is that the liquid-drop trends in the α-decay energies are as striking as the superimposed shell effects at $Z = 50$, $N = 82$, $Z = 82$, $N = 126$, $N = 152$, and, as we shall see in Chapter 17, at $N = 162$.

An empirical correlation between the α-decay half-life and the Q_α value was formulated by V.E. Viola and G.T. Seaborg:

$$\log T_\alpha(Z,n) = (aZ+b)Q_\alpha^{-1/2} + (cZ+d) + h_i \tag{6.11}$$

where h_i are the average hindrance factors for i = p, n, and pn (for odd proton, odd neutron, and odd proton and odd neutron, respectively). For even–even nuclei, $h_i = 0$. A set of newly fitted parameters is

$$a = 1.661\,75, \quad b = -8.5166, \quad c = -0.202\,28, \quad \text{and} \quad d = -33.9069$$

6.3 Cluster Radioactivity

Q values for the emission of intermediate-mass fragments called clusters from heavy nuclei where the residual nucleus is ^{208}Pb, $A_1 \rightarrow A_2 + {}^{208}$Pb, are shown in Figure 6.6. They are all positive and peak for neutron-rich species such as ^{14}C, ^{24}Ne, and ^{28}Mg. That such clusters should be emitted in a tunneling process similar to α decay was predicted in 1980 by Sandulescu et al. (1980) and experimentally detected in 1984 by Rose and Jones (1984) in the case of $^{223}\text{Ra} \rightarrow {}^{14}\text{C} + {}^{209}\text{Pb}$ with a probability of $8.5 \cdot 10^{-10}$ relative to the α-particle emission. Ever since, cluster radioactivity has rapidly evolved from the first pioneering experiments to a well-established field in nuclear science. By 1998, 20 different cluster emissions from 17 mother nuclei had been detected involving clusters from ^{14}C to ^{32}Si with probabilities down to the level of 10^{-16} relative to the α-particle emission.

Long half-lives and small branching ratios relative to α decay require detectors with unusual efficiency and selectivity. In their famous experiment, Rose and Jones were able to detect a few carbon events within an α-particle background about 10^9 times higher. Their detection system consisted simply of surface barrier silicon detectors acting as a $\Delta E - E$ telescope, with a relatively weak ^{227}Ac source containing ^{223}Ra in equilibrium placed in front of them. With this device, they

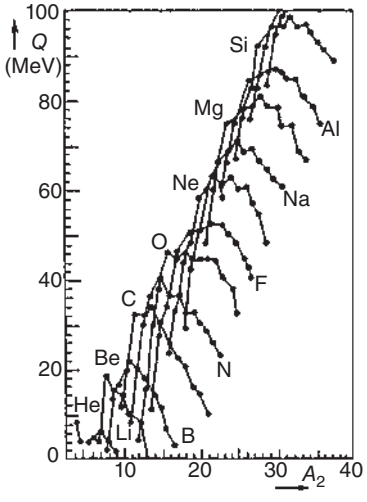

Figure 6.6 Q values for cluster radioactivity with ^{208}Pb as residual nucleus: $A_1 \rightarrow A_2 + {}^{208}$Pb.

had to search for a compromise between two conflicting conditions, efficiency and multiple pile-up rejection, and indeed they found it. However, in the second experiment they attempted, the ^{24}Ne decay of ^{232}U, the much higher flux of α particles, implied with a branching ratio that was 2 orders of magnitude smaller than in the previous case, destroyed their silicon detectors by radiation damage.

In an experiment on ^{233}U, Balysh et al. (1986) attempted in 1986 to measure ^{24}Ne radioactivity by looking at the γ decay of the daughter ^{24}Na by means of a γ-ray spectrometer. In this case, α particles were not interfering, but the low detection efficiency allowed them to infer only an upper limit for the branching ratio. It is clear from the above examples that the problem is how to avoid the highly interfering α-particle background while keeping a sufficiently high overall detection efficiency. Two possible solutions have been proposed. In the first case, the decay products are filtered by means of a magnetic field according to their magnetic rigidity. This way, clusters such as ^{14}C can be very precisely directed toward a silicon detector placed in the focal plane of a magnetic spectrometer, while rejecting the much lighter and less energetic α particles. Although characterized by an excellent background suppression and energy resolution as low as 100 keV for 30 MeV ^{14}C ions, this system has its drawback in a not particularly high efficiency, achieving a sensitivity limit of $4 \cdot 10^{-13}$ only. The second technique, by far the most widely used in cluster radioactivity research, uses solid-state nuclear track detectors (SSNTDs) to comply with both the efficiency and selectivity requirements. Here, use is made of the threshold behavior of such detectors, namely, plastic plates, which are able to register the passage of an ionizing particle in the form of a damage track only when the ionizing rate is higher than a given threshold, typical of the detector material. These detectors can be selected such that they disregard the effect of low ionizing α particles in favor of the heavier clusters searched for. After irradiation by a radioactive source, SSNTDs are etched chemically, which enlarges the damaged region from the Ångström to the micrometer scale, thus making it visible under a microscope. Minimum detectable charge numbers $\mathbf{Z}_{\min}$ range from 6 to 12 depending on the choice of the plastic material.

A landmark in cluster radioactivity research was the discovery of fine structure in the ^{14}C energy spectrum in ^{223}Ra decay. Contrary to expectations based on simple barrier penetration calculations, the 779 keV first excited state of ^{209}Pb ($11/2^+$) was found to be more strongly populated than the ground state ($9/2^+$). This has been attributed to the single-particle character of the mother–daughter wave functions. Indeed, here the ^{223}Ra Nilsson deformed wave function contains large components arising from the spherical $i_{11/2}$ neutron-shell model orbit but none from the $g_{9/2}$ state, the ground-state configuration of ^{209}Pb. In the case of α decay, it has been found in odd-*A* emitters (see Section 6.2.1) that the so-called favored transition is the one which leaves the odd proton or neutron in the same quantum state, a situation which is generally met for an excited state rather than the ground state of the daughter nucleus. Obviously, the same is true for cluster radioactivity. On the other hand, experiments performed on ^{14}C decay of the even–even isotopes ^{222}Ra and ^{224}Ra resulted in one single peak corresponding to the ground-state to ground-state transition.

6.4 Proton Radioactivity

Proton decay should involve the same physical background as α decay, that is, barrier penetration, with the simplification that there is no preformation of the particle to be considered. A necessary condition for proton radioactivity is a positive Q_p value

$$Q_p = (M_{Z+1} - M_Z - m_p - m_e)c^2 > 0 \tag{6.12}$$

M_i are the atomic masses including electrons and m_i are the masses of the proton and electron. If binding energies are used, the Q_p value is

$$Q_p = B_Z - B_{Z+1}; \quad B_Z = (ZM_H + Nm_n - M_Z)c^2 \tag{6.13}$$

The energy requirements for proton radioactivity are shown in Figure 6.7 for $N = 80$ isotones including the ^{151}Lu proton decay, the case with which this decay mode was first observed by S. Hofmann et al. According to Eq. (6.12), the Q_p values can be determined as differences in binding energies of neighboring isotones. The binding energies are theoretical values taken from a mass table. Parabolas connect the odd-A and even–even isotones; they are separated by the proton-pairing energy. As a function of the atomic number, the binding energies of isotones exhibit maximum values at $\partial B/\partial Z = 0$ and the change in the slope allows for positive Q_p values near these maxima. The quadratic Z dependence comes from the Coulomb term and the asymmetry term of the liquid-drop model. In Figure 6.7, the first proton unbound isotone is ^{149}Tm and the first candidate with a Q_p value large enough for a measurable decay branch is ^{151}Lu.

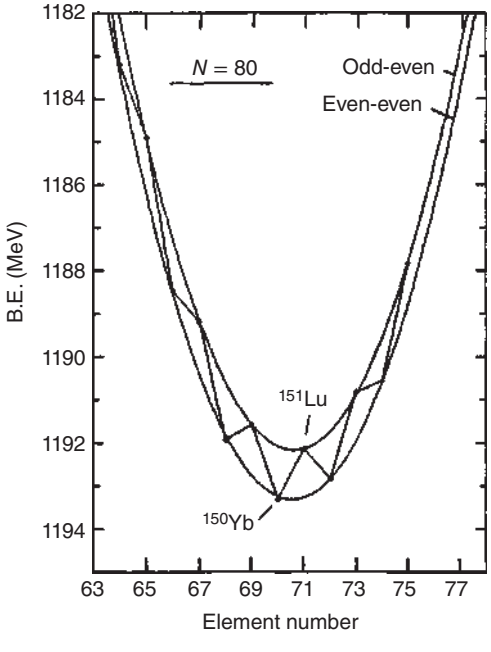

Figure 6.7 Binding energies of neutron-deficient $N = 80$ isotones. Isotonic binding energy parabolas, not to be confused with isobaric mass parabolas, connect the data points of odd–even and even–even isotones separated by the proton pairing energy Δp. Position and slope of the parabolas are mainly determined by the Coulomb and asymmetry term, both quadratic in Z, of the liquid–drop model. Source: Hofmann (1995), figure 1 (p. 94)/De Gruyter.

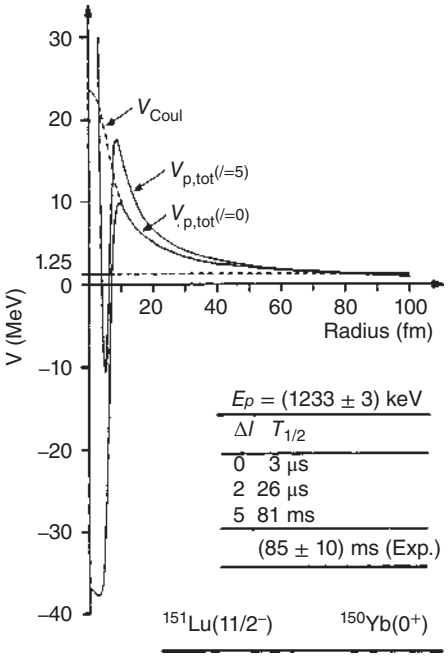

Figure 6.8 Proton–nucleus potential for the semiclassical calculation of the ^{151}Lu partial proton half-life. Source: Hofmann (1995), figure 2 (p. 95)/De Gruyter.

Following Gamow and Gurney and Condon, the decay constant is calculated as the product of a knocking frequency and the barrier penetrability. For the frequency, an expression developed by Bethe is used:

$$f = \sqrt{2}\pi^2\hbar^2[m^{3/2}R_c^3(Zze^2/R_c - Q_p)^{1/2}]^{-1} \tag{6.14}$$

yielding for ^{151}Lu a value of $6 \cdot 10^{21}$ s^{-1}. The Gamow factor is

$$G_{jl} = \sqrt{2m/\hbar^2}\int_{R_1}^{R_2}[V_{jl}(r) + V_C(r) + V_l(r) - Q_p]^{1/2} \tag{6.15}$$

with the potential being a superposition of the nuclear potential V_{jl}, the Coulomb potential V_C, and the centrifugal potential V_l. For the nuclear potential, the real part of an optical potential is used. The potential in Eq. (6.15) is shown in Figure 6.8 for the proton decay of ^{151}Lu. Figure 6.8 exhibits the very long tunneling length of ≈80 fm for decay energies around 1 MeV. Conservation of angular momentum and parity selects the allowed transitions:

$$I_i = I_f + l + s; \quad \pi_i = \pi_f(-1)^l \tag{6.16}$$

The good agreement of the calculated half-life for ^{151}Lu $(11/2^-) \rightarrow {}^{150}$Yb (0^+), $\Delta l = 5$, gives confidence in this description, although nuclear structure effects have been ignored except for the change of angular momentum and parity. An energy spectrum which shows the proton decay line of the first identified ground-state proton emitter is shown in Figure 6.9. A review article by Hofmann (1995) summarizes the details of proton radioactivity. The Chart of the Nuclides shows >60 isotopes

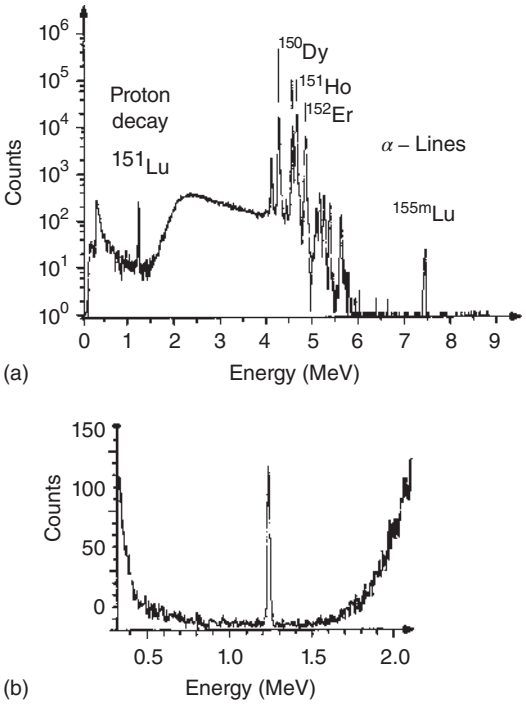

Figure 6.9 (a) Energy spectrum obtained during the irradiation of a ^{96}Ru target with 261 MeV ^{58}Ni projectiles at SHIP. The ^{151}Lu proton-decay line was observed at 1.29 MeV far below the α-decay lines of other reaction products. (b) Expanded part showing the ^{151}Lu proton-decay line. Source: Hofmann (1995), figure 5 (p. 99)/De Gruyter.

near the proton drip line that are suspiciously proton emitters, proton emitters, or even two-proton emitters in a range from ^{4,5}Li all the way up to ^{177}Tl and ^{185}Bi.

Proton emission can also occur after β^+ decay in a two-stage process. For nuclei with very high $Q_{\beta+}$ values, highly excited states with energies higher than the potential barrier, that is, proton unbound states, can be populated and decay instantaneously by emitting a proton. This two-stage process is called β^+-delayed proton emission. It is observed for β^+ emitters from ^{9}C through ^{41}Ti with $N = Z - 3$ and half-lives in the range of 1 ms to 0.5 seconds. In particular cases, β2p and βα are also observed.

For neutron-rich nuclei with very high Q_{β^-} values, neutron unbound highly excited states can be populated in β^- decay that decay instantaneously by neutron emission (β^--delayed neutron emission). This is observed frequently for nuclides such as ^{87}Br and many fission products. Delayed neutron emission is technically very important for the operation of nuclear reactors.

Stable nuclei may become unstable if their electron shell is completely stripped off; then, they will show a special kind of β^- transmutation in which the electron emitted from the nucleus occupies a free place in the empty electron shell ("bound β^- decay"). This has been observed with a half-life of 47 days in β^- decay of ^{163}Dy in the ESR (experimental storage ring) at the GSI Helmholtz Center for Heavy-Ion Research.

6.5 Spontaneous Fission

As mentioned in Section 1.4, K.A. Petrzhak and G.N. Flerov discovered in 1940 that ^{238}U undergoes fission spontaneously (symbol sf) with a half-life of about 10^{16} years, very long compared to the α-decay half-life. Since that discovery, sf rates of several dozen nuclides, all with $Z \geq 90$, have been measured and sf is thus firmly established as another radioactive decay mode in which barrier penetration plays a crucial role. The observed partial half-lives range from fractions of nanoseconds to $2 \cdot 10^{17}$ years. The height of the fission barrier, to a first approximation, is the difference between the Coulomb energy between the two fission fragments when they are just touching and the energy released in the fission process, the Q_f value. Obviously, for fission to occur spontaneously, the condition

$$Q_f \geq V_C \tag{6.17}$$

must be fulfilled. The Coulomb energy between two spherical nuclei in contact is

$$V_C = \frac{Z_1 Z_2 e^2}{R_1 + R_2} \tag{6.18}$$

and with Eq. (4.1) and $r_0 = 1.5$ fm, we obtain

$$V_C = 0.96 \frac{Z_1 Z_2}{A_1^{1/3} + A_2^{1/3}} \text{ MeV} \tag{6.19}$$

With this formula, the Coulomb energy between two nuclei in contact, each with one-half of the A and Z of ^{238}U, is 206 MeV compared to 193 MeV of energy released in the symmetric fission of ^{238}U as calculated from a semiempirical mass equation. This would indicate a fission barrier height of 15 MeV to be compared to an experimental value of 6 MeV. The Coulomb energy estimates are certainly too high because the fragments are surely not spherical at the moment of scission. Also, breakup into equal fragments does not necessarily give the greatest energy release which is, as we shall see below, much less likely than asymmetric mass splits. Thus, neither the estimates of V_C nor the estimates of Q_f in this simplistic way should be considered quantitatively significant. But what we learn this way is that the barrier height increases more slowly with increasing nuclear size than the decay energy for fission. This explains that sf is observed only for the heaviest nuclei and that the sf half-lives decrease rapidly with increasing Z.

We can pursue the energetics of fission a little further with the aid of the liquid-drop model, Eqs. (3.2) and (3.6). The energy release of a nucleus ^{A}Z into two equal fragments $^{A/2}(Z/2)$ is given by

$$Q_f = M_{Z,A} - 2M_{Z/2,A/2}$$

and with the parameters given earlier (Section 3.3 in Chapter 3), we find numerically that

$$Q_f = -3.36A^{2/3} + 0.217\frac{Z^2}{A^{1/3}} \tag{6.20}$$

Note that only the surface energy term and the Coulomb energy term do not cancel in the formation of this difference. Considering still the simple case of

breakup of the fissioning nucleus into two equal fragments, we get from Eq. (6.18) that $V_C = 0.14Z^2 / A^{1/3}$. Combining this with Eq. (6.19) and inserting into Eq. (6.16), we get, for instability against fission, a critical value of $(Z^2/A)_{crit}$ on the order of 40. The numerical value is not to be taken seriously. The important point is that, according to the liquid-drop model, there is a critical value of Z^2/A beyond which nuclei can no longer hold together for more than about 10^{-22} seconds. And we might expect that, the farther away the Z^2/A value of a nuclide is from $(Z^2/A)_{crit}$, the longer will be its half-life for spontaneous fission. Thus, the ratio

$$x = \frac{Z^2}{A} \Big/ \left(\frac{Z^2}{A}\right)_{crit} \tag{6.21}$$

where x is called the fissility parameter, should be a characteristic scaling parameter for the fissility for heavy nuclei. Measurable sf half-lives are expected for nuclei with $x < 1$.

In Figure 6.10, the logarithm of the spontaneous fission half-lives is plotted against Z^2/A. It is obvious that there is a general trend in agreement with the simple expectation of the liquid-drop model: decreasing half-lives with increasing Z^2/A. However, for even–even isotopes for each element, the sf half-lives go through a maximum

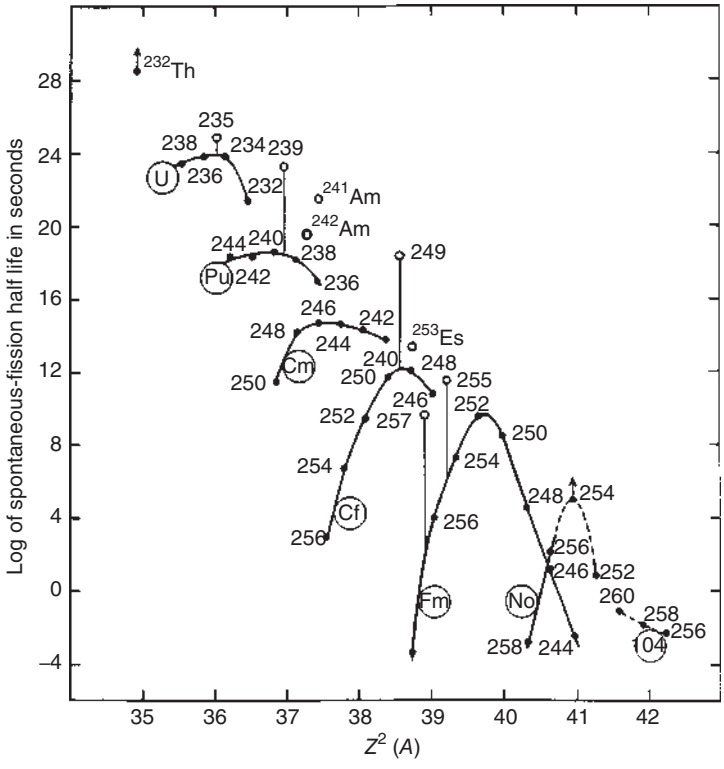

Figure 6.10 Partial half-lives for spontaneous fission vs. Z^2/A. Even–even isotopes of each element are connected. A few odd-A nuclides and the odd–odd ^{242}Am are also shown. Source: Friedlander et al. (1981)/John Wiley & Sons.

which is most pronounced for Fm isotopes ($Z = 100$), where the maximum is located at $N = 152$ which is a deformed closed shell. We have discussed the latter already in our presentation of Q_α systematics. Also, for sf, shell effects are superimposed on the smooth liquid-drop trends. Further, as with α decay, the half-lives of odd-A and odd–odd nuclei, a few of which are included in Figure 6.10, are longer by orders of magnitude than interpolation between neighboring even–even species would suggest. This indicates that odd nucleons are causing hindrance factors in analogy to α decay. It is the subtle sensitivity of barrier penetration to changes of a few megaelectronvolts in the height of the potential energy barrier and to details in nuclear structure that cause these deviations from the liquid-drop trend.

So far, we have used only static considerations. Bohr and Wheeler (1939) tried in 1938 to consider the dynamics of the fission process. Using the liquid-drop model, they treated fission in a manner analogous to transition-state theory of chemical reactions. They started visualizing the fissioning nucleus as a spherical, uniformly charged, incompressible liquid drop. Any small deformation of the drop then leads to an increase in surface area and therefore in surface energy, that is, an increase in the potential energy. At the same time, the deformation increases the average spacing between the protons, decreasing the Coulomb repulsion and thus decreasing the potential energy. As long as the change ΔE_s in the surface energy is larger than the change ΔE_C in the Coulomb energy, there is a net restoring force that tends to return the nucleus to its spherical shape. However, for some deformations, the magnitude of ΔE_C can exceed that of ΔE_s making the nucleus unstable against fission. To treat this in detail, Bohr and Wheeler parameterized the liquid-drop model shapes by a radius vector

$$R(\Theta) = R_0 \left[1 + \sum_{n=1}^{\infty} \alpha_n P_n(\cos\Theta) \right] \tag{6.22}$$

expanded in terms of multipole distortion parameters α_n and Legendre polynomials in $\cos\Theta$. For small, axially symmetric deformations, it was assumed that α_4 could already be neglected compared to the quadrupole distortion parameter $\alpha_2 = \left(\frac{5}{4}\pi\right)^{1/2} \beta_2$ and the surface and Coulomb energies were defined as

$$E_s = a_s A^{2/3} \left(1 + \frac{2}{5}\alpha_2^2 \right) \tag{6.23}$$

$$E_C = a_C A^{-1/3} \left(1 - \frac{1}{5}\alpha_2^2 \right)$$

Setting $a_s A^{2/3} = E_s^0$ and $a_C A^{-1/3} = E_C^0$, the respective energies of the sphere, they defined:

ΔE_s is the difference between E_s and that of the sphere; and
ΔE_C is the difference between E_C and that of the sphere.
They also defined a deformation or distortion energy

$$\begin{aligned} E_D = \Delta E_s + \Delta E_C &= \alpha_2^2 \left[\frac{2}{5} a_s A^{2/3} - \frac{1}{5} a_C A^{-1/3} \right] \\ &= \frac{1}{5}\alpha_2^2 (2E_s^0 - E_C^0) \end{aligned} \tag{6.24}$$

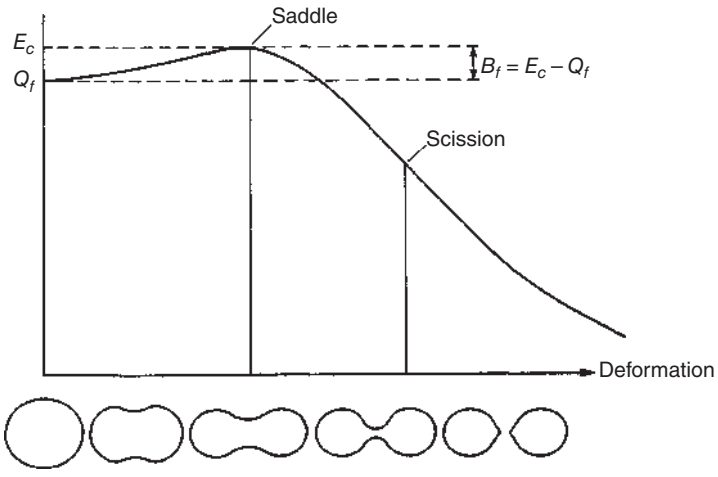

Figure 6.11 Potential energy as a function of deformation in a simple liquid-drop picture. The fission barrier B_f, the saddle point (critical deformation), and the scission point (separation into two fragments) are indicated. The distortion of an initially spherical nucleus is schematically shown beneath the potential energy diagram. Source: Friedlander et al. (1981)/John Wiley & Sons.

and a restoring force for $E_C^0 < 2E_s^0$ suggesting the definition of the fissility parameter

$$x = \frac{E_C^0}{2E_s^0} = \left(\frac{a_C}{2a_s}\right)\left(\frac{Z^2}{A}\right) = \frac{(Z^2/A)}{(Z^2/A)_{crit}} \tag{6.25}$$

meaning that $(a_C / 2a_s)^{-1}$ now stands for $(Z^2 / A)_{crit}$. More elaborate treatments of the fissility lead to

$$\left(\frac{Z^2}{A}\right)_{crit} = 50.883\left[1 - 1.7826\left(\frac{N-Z}{A}\right)^2\right] \tag{6.26}$$

containing the isospin asymmetry as introduced in Eq. (3.9) by Myers and Swiatecki.

The progress of the liquid-drop shapes and the corresponding changes in the potential energy are visualized for this simplified case in Figure 6.11. Although the original Bohr–Wheeler formalism proved qualitatively very useful, it failed in many quantitative respects. The preference for asymmetric mass splits could not be accounted for, nor could absolute barrier heights be predicted. The latter difficulty is not surprising as the distortion energy at the saddle point is due to the difference between two very large numbers, $2E_s^0$ and E_C^0, each of which has a value of several hundred million electronvolts and would have to be known extremely accurately.

Much progress has been made in recent years in refining the theory by using additional terms in the Legendre polynomial expansion and by using other expansions more suited for the transition from one distorted drop to two drops by considering shapes other than spherical ground-state shapes and saddle point shapes. For instance, saddle point shapes for various values of x are shown in Figure 6.12. One realizes that a nucleus with $x = 0.5$ can recover from a remarkable constriction near the center, while for $x = 1$, even a spherical nucleus has no chance of surviving.

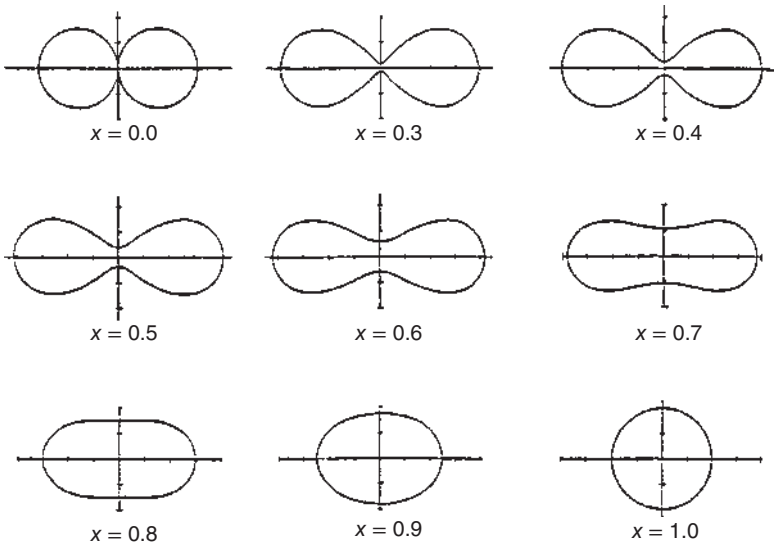

Figure 6.12 Saddle point shapes for various values of *x*. Source: Cohen and Swiatecki (1963). figure 1a (p. 416)/Elsevier.

The most significant advance, however, came from the shell-correction approach of V.M. Stutinsky that we introduced in Section 5.9. Here, we enlarge on one of its important successes: the prediction of a double-humped fission barrier in a certain region of A and Z located between isotopes of U and Bk. We have already pointed out in Section 3.4 that experimental masses deviate from masses calculated with the liquid-drop model near the magic numbers, see Figure 6.13a. These are reproduced by the Strutinsky shell corrections to the liquid-drop binding energies (Section 5.9). It was the particular merit of Strutinsky to show that shell corrections must occur not only as a function of nucleon number but also for a given nucleus, that is, at fixed number of nucleons, as a function of deformation, see Figure 6.13b. This can be visualized with the aid of Figure 6.14 in which the single-particle energies in the mean potential of all other nucleons are plotted against the deformation of the nucleus expressed in the form of the ratio of the semi-major axis to the semi-minor axis of a prolate ellipsoid. In order to simplify the reasoning, an extremely simplified potential, that of an isotropic harmonic oscillator without spin–orbit interaction, has been chosen. For spherical nuclear shapes, the calculated single-particle energies are well known to be concentrated periodically in dense groups and the resulting zones of low single-particle density correspond to the indicated magic nucleon numbers. Periodic fluctuations in the single-particle level density not only occur as a function of nucleon number but also occur for fixed nucleon number as a function of deformation. In particular, for nuclear shapes of high symmetry as given by an interger ratio of the half-axes of deformed nuclei, again zones of reduced level density occur particularly significant for a ratio of 2 : 1. The magic numbers associated with these deformations are different from those for spherical nuclei. According to this reason, a Pu nucleus with neutron number 140 should have an enhanced stability against

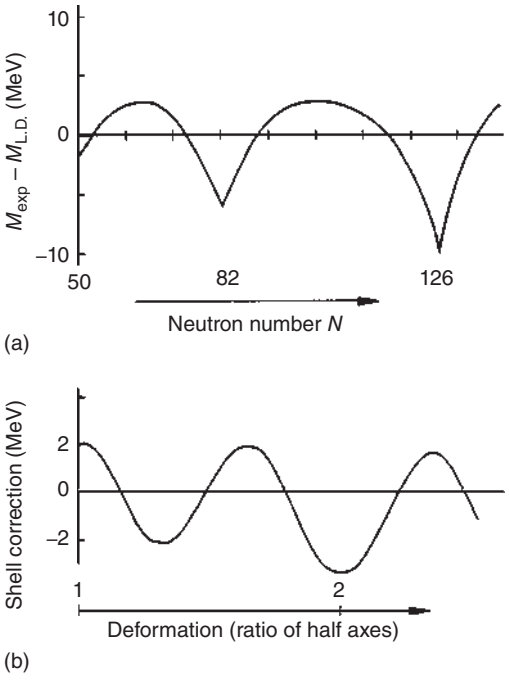

Figure 6.13 Shell-correction energies as a function of (a) neutron number (schematic, cf. Figure 3.10) and (b) deformation given by the ratio of the semi-major to the semi-minor axes. Source: Habs and Metag (1978)/John Wiley & Sons. Public Domain.

fission compared to its neighboring nuclei as long as it exhibits a ratio of half-axes of 2 : 1.

The addition of this deformation-dependent shell correction, Figure 6.13b, to the liquid-drop fission barrier in the region of elements U through Bk results in a double-humped fission barrier; see Figure 6.15b with two maxima and a deformed first minimum and a second minimum at 2–3 MeV higher energy and a ratio of the semi-major axis to the semi-minor axis of 2 : 1. The second minimum, then, was the a posteriori explanation for an observation made by Polikanov et al. (1962) at Dubna in 1962. In an attempt to synthesize new elements, they kept observing an unusually short-lived sf activity of 14 ms half-life now interpreted as fission isomer ^{242m}Am produced in incomplete fusion reactions such as

$$^{238}\mathrm{U} + {}^{22}\mathrm{Ne} \rightarrow {}^{242m}\mathrm{Am} + {}^{18}\mathrm{N}$$

or

$$^{238}\mathrm{U} + {}^{16}\mathrm{O} \rightarrow {}^{242m}\mathrm{Am} + {}^{12}\mathrm{B}$$

When measuring excitation functions (production rate or cross section vs. energy), they found that the 14 ms fission activity had an energy threshold 2.9 MeV higher than the threshold for the production of a 16 hours β activity (β^- and EC) assigned to ^{242g}Am. The 14 ms fission activity could not be an angular momentum isomer because, then, a fast γ decay was to be expected. Today, we interpret the 14 ms fission activity and more than 30 other short-lived fissioners (ns to ms), see Figure 6.16, as the respective lowest level in the second minimum of the double-humped fission

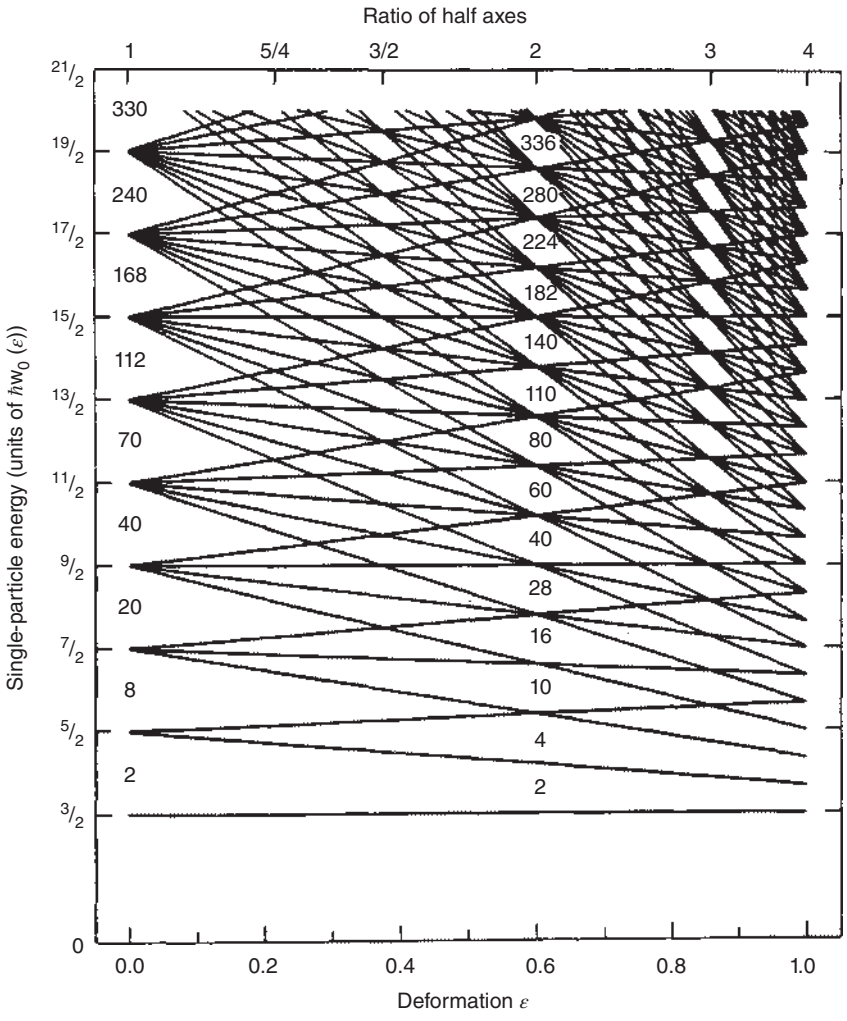

Figure 6.14 Single-particle energies in a harmonic oscillator potential for ellipsoidal prolate deformation. For simplification, no spin–orbit coupling has been taken into account. Source: Habs and Metag (1978)/John Wiley & Sons. Public Domain.

barrier (i.e. as superdeformed shape isomers). This way, the following properties are understood:

1) Their experimentally verified excitation energies of 2–3 MeV.
2) Their stability against γ decay into the ground state that is guaranteed by the existence of the inner barrier; such a decay would require a shape transformation of the nucleus.
3) The substantially shorter half-lives for sf from the isomeric state as compared to those from the ground state, since the isomer has to penetrate a much narrower barrier, for example, 14 ms for ^{242m}Am vs. 10^9 years for ^{242g}Am.

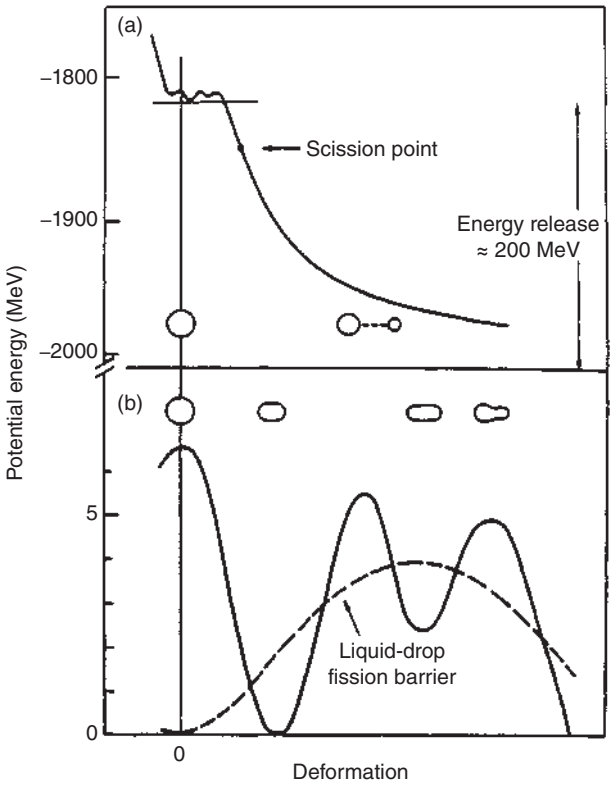

Figure 6.15 (a) Binding energy of a fissioning nucleus as a function of deformation or distance between the fission fragments, respectively. (b) Double humped fission barrier (solid line) resulting from summing the potential energy according to the liquid-drop model (dashed line) plus the shell-correction energy as a function of deformation from Figure 6.13(b). Source: Habs and Metag (1978)/John Wiley & Sons. Public Domain.

Much experimental effort has been devoted to the study of the properties of the fission isomers. Figure 6.17 shows experimentally observed rotational bands in the ground-state potential well and in the second minimum where the transitions have been measured by detecting coincidences between the electromagnetic transitions within the rotational band and the subsequent isomeric fission. These showed, see Eq. (5.39), that the rotational band on top of the fission isomer had more than twice the moment of inertia than the long-known rotational band in the ground-state well and indicated a larger deformation of the shape isomer. However, the moment of inertia is only a model-dependent function of deformation depending on how many nucleons are participating in the collective rotation. If one were to succeed in measuring the lifetimes of the rotational states, then, by use of the very well-established rotational model in the actinides (Bohr and Mottelson), one could determine the quadrupole moment of the nucleus in the fission isomeric state and deduce from that the deformation. This way was adopted by D. Habs and V. Metag in 1977. For experimental reasons, they performed this experiment with ^{239}Pu using the so-called

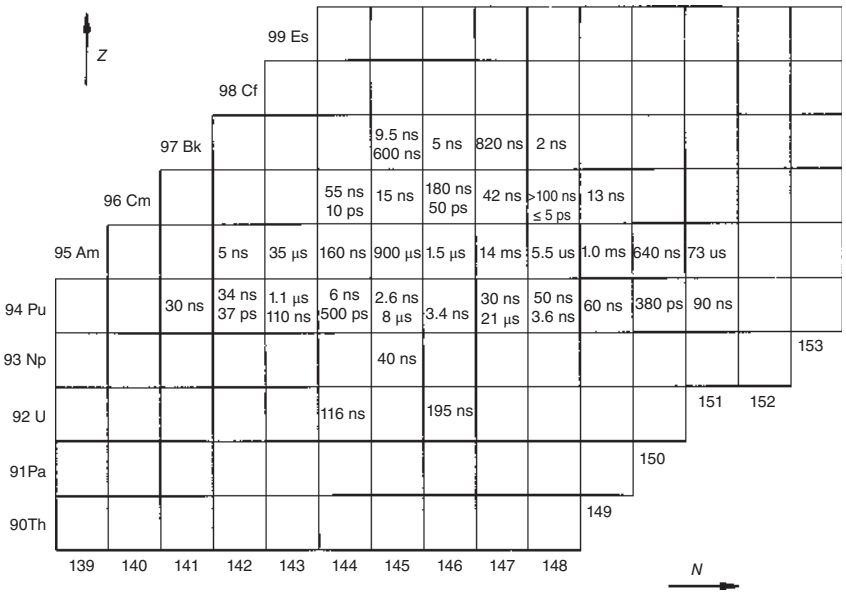

Figure 6.16 Location of the island of spontaneously fissioning isomers in the chart of nuclides with the half-lives for isomeric fission. Source: Habs and Metag (1978)/John Wiley & Sons. Public Domain.

charge plunger technique. The results are summarized in Table 6.1. The measured quadrupole moment in the second minimum of 36 barn (1 barn $= 10^{-24}$ cm) is about three times as large as the quadrupole moment in the first minimum. It represents the largest observed nuclear quadrupole moment. Theoretically calculated values [Lit.] are in very good agreement with the experimental values. In order to better visualize the quadrupole moment, one can describe the nucleus as a rotational ellipsoid with a semi-major axis c and a semi-minor axis a. For the fission isomer, this yields a ratio $(c/a)_{\mathrm{II}} = 2.0 \pm 0.1$ in contrast to $(c/a)_{\mathrm{I}} = 1.30 \pm 0.05$ in the first minimum. The measured ratio of 2 : 1 corresponds exactly to the prediction of the model discussed above and corroborates the strong shell effect for just this deformation predicted by the Strutinsky method. The modification of fission barrier heights in the liquid-drop model (solid line) by the shell correction (dashed line) throughout the periodic table is shown in Figure 6.18. The development of the fission barriers between $Z = 90$ and 114 as predicted by the macroscopic–microscopic hybrid model is shown in Figure 6.19. It is interesting to note that the contribution of the liquid-drop barrier diminishes gradually, as discussed above, and that for superheavy elements the fission barrier is solely due to the shell-correction energy resulting in very compact barrier radii.

Some concluding remarks concerning the fission process are as follows.

Because of the high neutron excess of the fissioning heavy nuclei, the fission fragments are found on the neutron-rich side of the line of β stability, as illustrated in Figure 6.20. Several neutrons ($\nu = 2$–4) are evaporated from the primary fission fragments (prompt neutrons). The evaporation residues are called fission products and

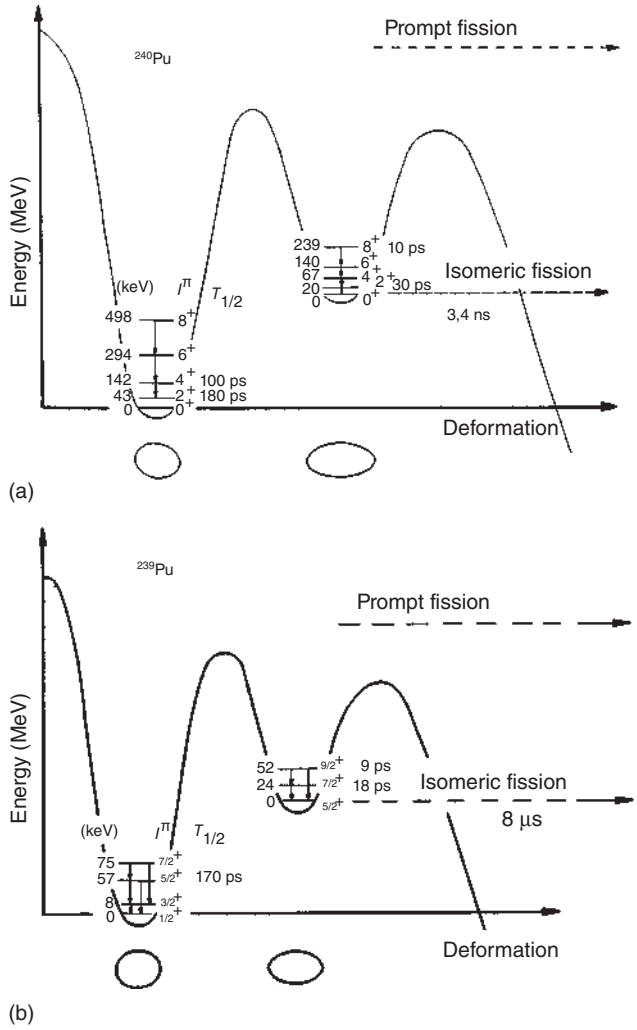

Figure 6.17 Experimentally observed electromagnetic transitions in the rotational bands in the ground-state potential well and in the shape isomeric well in (a) ^{240}Pu and (b) ^{239}Pu. Source: Habs and Metag (1978)/John Wiley & Sons. Public Domain.

decay by subsequent β^- transitions to the line of β stability. In many of these decays, β^--delayed neutrons are emitted. The subsequent steps of the fission process are depicted in Figure 6.21:

a) The nucleus oscillates between a more spherical and a more ellipsoidal shape. If, for the larger deformation, there is no restoring force, see above, the nucleus passes the barrier, there is constriction in the center of the ellipsoid, and the nucleus attains the shape of a dumbbell in which often one part has $Z \geq 50$ and $A \geq 82$.

Table 6.1 Comparison of experimental and theoretical quadrupole moments and deformations in the first and second minima of ^{239}Pu.

	1. Minimum	2. Minimum
Q_{exp}	(11.3 ± 0.5) barb	(36 ± 4) barn
Q_{theor} (^{240}Pu)		38 b (Literature)
		35 b (Literature)
$(c/a)_{exp}$	(1.30 ± 0.05)	(2.0 ± 0.1)

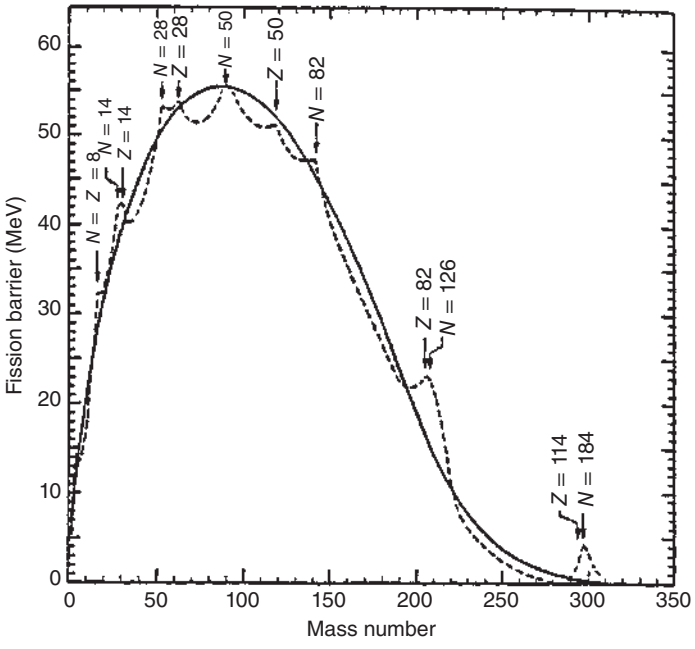

Figure 6.18 Modification of the fission barrier height in the liquid-drop model (solid line) by the shell correction (dashed line) throughout the periodic table. Source: Myers and Swiatecki (1966), figure 18 (p. 48)/Elsevier.

b) The nucleus splits into two parts. If this splitting takes place at A, two parts of nearly equal mass, but different excitation energy, are formed (symmetric fission). Most probable is the fission at B, by which two parts of different mass but similar excitation energy are formed (asymmetric fission). Scission at C leads to two parts of very different mass and excitation energy. The Coulomb repulsion energy, which has a much greater range than the nuclear force, drives both fragments apart and the fission fragments attain high kinetic energies.
c) The highly excited fission fragments evaporate prompt neutrons (from the fully accelerated fragments), sometimes also charged particles, and subsequently prompt γ radiation.

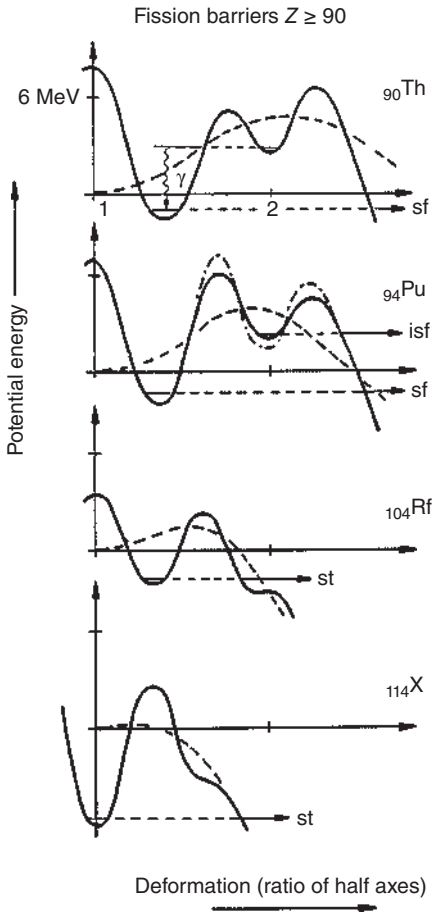

Figure 6.19 Fission barriers calculated with the macroscopic–microscopic hybrid model for nuclei with proton numbers between $Z = 90$ and $Z = 114$. The dashed barrier curves result from the liquid-drop model. The double-humped fission barrier for Pu with the magic neutron number at deformation of the second minimum is indicated by the dot–dashed curve Source: Modified from Nix (1972).

d) The resulting fission products decay by one or several β^- transformations followed by emission of γ-rays into stable products. In the case of high $Q_{\beta-}$ values exceeding the neutron separation energy in the final nucleus $(A-1, Z+1)$, β^--delayed neutron emission from a highly excited state in the emitter nucleus $(A, Z+1)$ occurs.

Partial half-lives $(t_{1/2})_i = t_{1/2}/c_i$ with c_i being the probability of that decay mode for spontaneous fission and the number of prompt neutrons set free are listed in Table 6.2. Heavier, short-lived spontaneously fissioning nuclei can be found in the Chart of Nuclides contained in the rear cover of this book. The main part of Q_f released by sf is set free promptly (about 89%) in the form of kinetic energy of the fission fragments (82%), kinetic energy of the neutrons (3%), and energy of the γ-rays (4%). The remainder appears with some delay in the form of energy of β^- particles (3%), energy of antineutrinos (5%), and energy of γ-rays (3%).

Due to the production of neutrons, spontaneously fissioning nuclides are of practical interest as neutron sources. An example is ^{252}Cf ($t_{1/2} = 2.64$ years), which is used in industrial applications and for neutron activation.

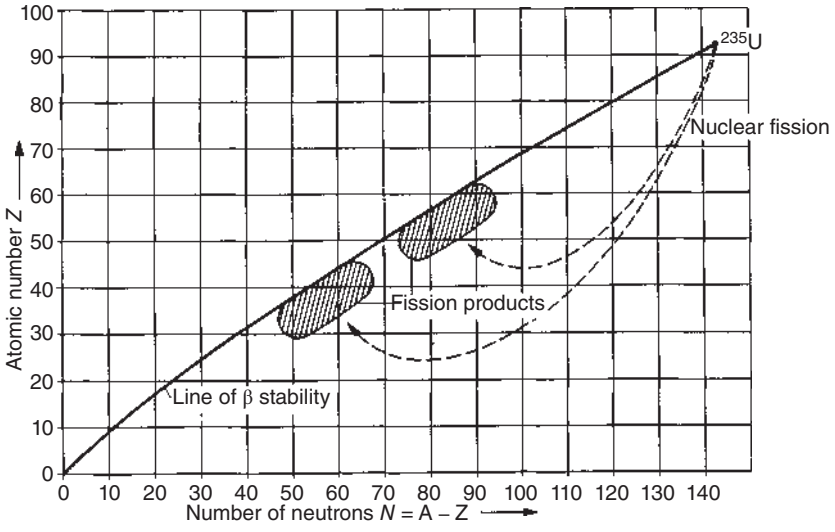

Figure 6.20 Neutron excess of the fission fragments due to the neutron excess of the heavy fissioning nuclei.

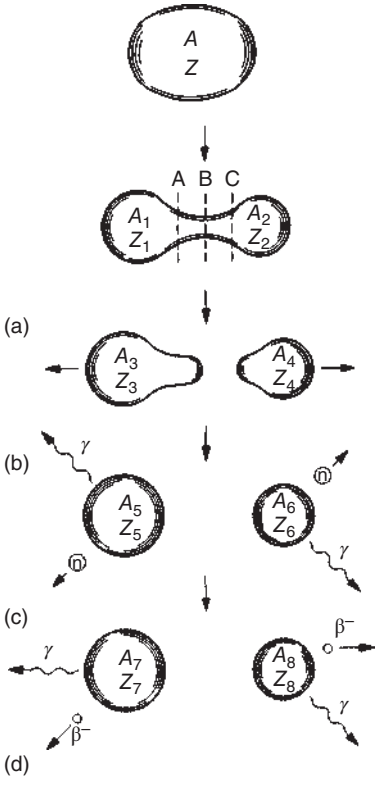

Figure 6.21 The subsequent steps of spontaneous fission. (a) Neck formatio followed by randon neck rupture. (b) accelerating prefragments. (c) Prompt deexcitation by photon emission and neutron evaporation. (d) Beta-delayed photon emission and neutron evaporation.

Table 6.2 Partial half-lives of spontaneous fission.

Nuclide	Partial half-life of spontaneous fission	Average number ν of neutrons set free	Nuclide	Partial half-life of spontaneous fission	Average number ν of neutrons set free
^{230}Th	$\geq 1.5 \cdot 10^{17}$ yr		^{249}Cf	$6.5 \cdot 10^{10}$ yr	
^{232}Th	$>10^{21}$ yr		^{250}Cf	$1.7 \cdot 10^{4}$ yr	3.53 ± 0.09
^{232}U	$\approx 8 \cdot 10^{13}$ yr		^{252}Cf	85 yr	3.764
^{233}U	$1.2 \cdot 10^{17}$ yr		^{254}Cf	60 d	3.88 ± 0.14
^{234}U	$1.6 \cdot 10^{16}$ yr		^{253}Es	$6.4 \cdot 10^{5}$ yr	
^{235}U	$3.5 \cdot 10^{17}$ yr		^{254}Es	$>2.5 \cdot 10^{7}$ yr	
^{236}U	$2 \cdot 10^{16}$ yr		^{255}Es	2440 yr	
^{238}U	$9 \cdot 10^{15}$ yr	2.00 ± 0.08	^{244}Fm	≥ 3.3 ms	
^{237}Np	$>10^{18}$ yr		^{246}Fm	≈ 20 s	
^{236}Pu	$3.5 \cdot 10^{9}$ yr	2.22 ± 0.2	^{248}Fm	≈ 60 h	
^{238}Pu	$5 \cdot 10^{10}$ yr	2.28 ± 0.08	^{250}Fm	≈ 10 yr	
^{239}Pu	$5.5 \cdot 10^{15}$ yr		^{252}Fm	115 yr	
^{240}Pu	$1.4 \cdot 10^{11}$ yr	2.16 ± 0.02	^{254}Fm	246 d	3.99 ± 0.20
^{242}Pu	$7 \cdot 10^{10}$ yr	2.15 ± 0.02	^{255}Fm	$1.2 \cdot 10^{4}$ yr	
^{244}Pu	$6.6 \cdot 10^{10}$ yr	2.30 ± 0.19	^{256}Fm	2.63 h	3.83 ± 0.18
^{241}Am	$2.3 \cdot 10^{14}$ yr		^{257}Fm	120 yr	4.02 ± 0.13
^{242m_1}Am	$9.5 \cdot 10^{11}$ yr		^{258}Fm	380 µs	
^{243}Am	$3.3 \cdot 10^{13}$ yr		^{257}Md	≥ 30 h	
^{240}Cm	$1.9 \cdot 10^{6}$ yr		^{252}No	≈ 7.5 s	
^{242}Cm	$6.5 \cdot 10^{6}$ yr	2.59 ± 0.09	^{254}No	$\geq 9 \cdot 10^{4}$ s	
^{244}Cm	$1.3 \cdot 10^{7}$ yr	2.76 ± 0.07	^{256}No	≈ 1500 s	
^{246}Cm	$1.8 \cdot 10^{7}$ yr	3.00 ± 0.20	^{258}No	1.2 ms	
^{248}Cm	$4.2 \cdot 10^{6}$ yr	3.15 ± 0.06	^{256}Lr	$> 10^{5}$ s	
^{250}Cm	$1.4 \cdot 10^{4}$ yr	3.31 ± 0.08	^{257}Lr	$> 10^{5}$ s	
^{249}Bk	$1.7 \cdot 10^{9}$ yr	3.64 ± 0.16	^{258}Lr	≥ 20 s	
^{246}Cf	$2.0 \cdot 10^{3}$ yr	2.85 ± 0.19	^{261}104	≥ 650 s	
^{248}Cf	$3.2 \cdot 10^{4}$ yr		^{261}105	8 s	

Source: Vandenbosch and Huizenga (1973), p. 66/Elsevier.

As already mentioned, asymmetric fission prevails strongly. This is illustrated for ^{242}Cm in Figure 6.22. The cumulative fission yields are in the range of several percent for mass numbers A between about 95–110 and about 130–145, and below 0.1% for symmetric fission around $A = 120$. The fission yields are the average numbers of nuclei with a given mass number produced by 100 fissions. Because two nuclei are generated, the sum of the fission yields amounts to 200%.

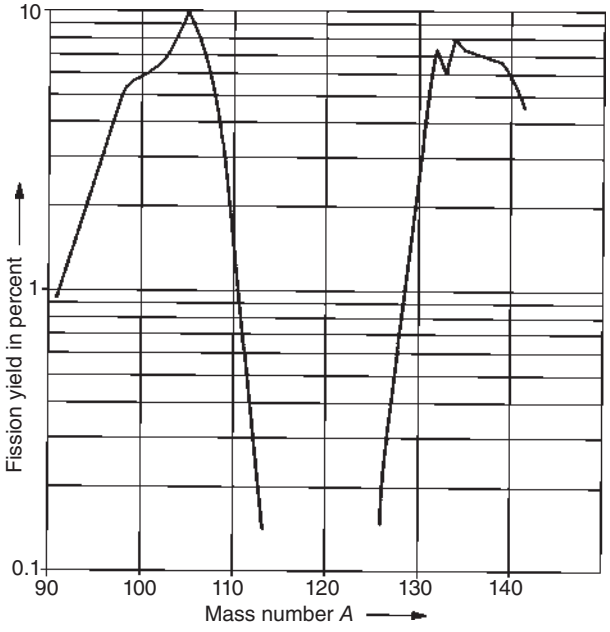

Figure 6.22 Fission yield as a function of mass number for the spontaneous fission of ^{242}Cm. Source: Modified from Steinberg and Glendenin (1954).

The mean kinetic energy of the fission fragments, according to momentum conservation, is expected to be distributed among the light (L) and heavy (H) fragments as

$$\frac{E_{\mathrm{L}}}{E_{\mathrm{H}}} = \frac{A_{\mathrm{H}}}{A_{\mathrm{L}}} \tag{6.27}$$

that is, the kinetic energies should decrease linearly with increasing mass number. However, this trend is superimposed mainly by a shell effect caused by the doubly magic ^{132}Sn for which, due to its compactness, extra kinetic energy is given. This, in turn, is the reason why in the small fraction of spontaneous fission events in which ^{132}Sn is formed, the excitation energy at $A = 132$ is so small that no neutrons are emitted from these fragments. This fraction is about 0.2% in sf of ^{252}Cf and 3% in the case of ^{235}U.

6.6 Beta Decay

Beta decay includes all decay modes in which the mass number A is conserved and the atomic number Z is changed by ± 1 unit. In β^- decay of neutron-rich nuclei, $Z \rightarrow Z+1$; in β^+ decay and electron-capture decay, $Z \rightarrow Z-1$.

6.6.1 Fundamental Processes

If we denote with m the nuclear masses and electron masses, with M the atomic masses, and with Q the decay energy, we have, for β^- decay,

$$\begin{aligned} m_z &= m_{z+1} + m_e + Q_{\beta^-} \\ +Zm_e &= Zm_e \\ \hline M_Z &= M_{Z+1} + Q_{\beta^-} \\ Q_{\beta^-} &= \Delta M \end{aligned}$$

with $Q_{\beta^-} > 0$ for $\Delta M > 0$;
for β^+-decay,

$$\begin{aligned} m_Z &= m_{Z-1} + m_e + Q_{\beta^+} \\ +Zm_e &= Zm_e \\ \hline M_Z &= M_{Z-1} + 2m_e + Q_{\beta^+} \\ Q_{\beta^+} &= \Delta M + 2m_e \end{aligned}$$

with $Q_{\beta^+} > 0$ for $\Delta M > 2m_e$;
and for EC,

$$\begin{aligned} m_Z + m_e &= m_{Z-1} + Q_{EC} \\ +(Z-1)m_e &= (Z-1)m_e \\ \hline M_Z &= M_{Z-1} + Q_{EC} \end{aligned}$$

with $Q_{EC} > 0$ for $\Delta M > 0$.

Thus, we have for β^+ decay the complication that the decay is only energetically possible if the difference in the atomic masses is in excess of $2 \cdot 511$ keV. For lower ΔM than 1022 keV, EC is the energetically allowed alternative. Q values range from 14 keV to some 15 MeV, rising with the distance from the line of β stability with shortening half-lives which become no shorter than some 10 ms; that is, the decays are relatively slow as the weak interaction is involved.

As we see in Figure 6.23, β energy spectra are continuous with $E_{max} = Q_\beta$ being reached only for an infinitesimally small fraction of the intensity and the major intensity being spread around one-third of E_{max}. This has been a puzzle for some time because, apparently, energy conservation seemed to be violated. Moreover, angular momentum conservation and the rules of statistics seemed to be violated. If an even–even nucleus decays into an odd–odd nucleus and an electron, a boson decays into a boson plus a fermion. This led W. Pauli in 1930 to postulate the emission of a second fermion in β decay, the electron neutrino, ν_e, or antineutrino, $\overline{\nu}_e$, respectively. It was supposed to carry away the missing energy and to remove the problems with angular momentum conservation. Its rest mass was assumed to be extremely small or zero, and it was assumed to carry no charge or magnetic moment. The fundamental processes in the nucleus are then

$$\beta^+ : \quad {}^1_0\mathrm{n} \rightarrow {}^1_1\mathrm{p} + {}^0_{-1}\mathrm{e} + \overline{\nu}_e \tag{6.28}$$

$$\beta^+ : \quad {}^1_1\mathrm{p} \rightarrow {}^1_0\mathrm{n} + {}^0_{+1}\mathrm{e} + \nu_e \tag{6.29}$$

$$\mathrm{EC} : \quad {}^1_1\mathrm{p} \rightarrow {}^1_0\mathrm{n} + \nu_e \tag{6.30}$$

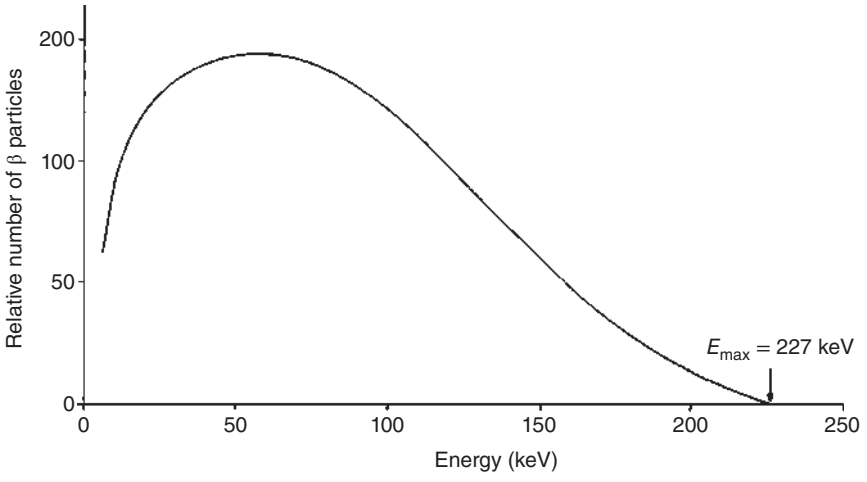

Figure 6.23 β spectrum of ^{147}Pm.

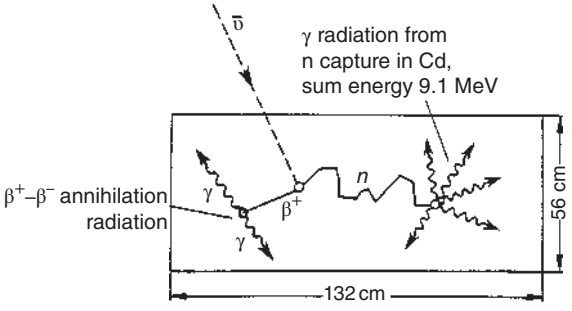

Figure 6.24 Scheme of the experiment by Cowan and Reines for the detection of electron antineutrinos.

In the case of EC, disregarding the binding energy of the captured electron, the electron neutrino receives the whole decay energy and is monoenergetic. Today's best limit for the antineutrino rest mass comes from a measurement of the shape (near E_{max}) of the β^- spectrum of ^{3}H, which is presently <1.1 eV, see Section 18.6.4. As already mentioned in Chapter 1, it took until 1959 before the first proof of the existence of the neutrino by Reines and Cowan was successful at a research reactor in which fission products emit antineutrinos. They used the inverse reaction

$$\bar{\nu}_e + {}^1_1p \rightarrow {}^1_0n + {}^0_{+1}e \tag{6.31}$$

where antineutrinos were captured in a hydrogen-containing scintillator to which a Cd compound was added inside a large tank, Figure 6.24. The produced positron annihilates after deceleration to thermal energy ($5 \cdot 10^{-12}$ seconds) after a mean lifetime of 10^{-10} seconds with an electron from the singlet state of the electron–positron pair by the emission of two 511 keV γ quanta. The neutron diffuses through the tank for some microseconds and is captured by a Cd nucleus producing a γ cascade with a sum energy of 9.1 MeV which is detected as a delayed coincidence signal. The cross

section was found to be extremely small as expected: $7 \cdot 10^{-43}$ cm^2. Attempts to detect with reactor neutrinos the reaction

$$\nu_e + {}^{37}_{17}\mathrm{Cl} \rightarrow {}^{37}_{18}\mathrm{Ar} + e^-$$

remained unsuccessful but were positive with solar neutrinos (R. Davis). Reactor neutrinos, see above, are right-handed antineutrinos, $\bar{\nu}_e$, while solar neutrinos are left-handed electron neutrinos, ν_e, produced in the hydrogen burning in the Sun. This opened a breathtaking era in nuclear astrophysics/applied radiochemistry, to which we shall return in Section 18.5.

Similar to α decay, empirical relations between the decay constant λ and the value of E_{max} were also found for β decay (by B.W. Sargent, in 1933)

$$\log \lambda = a + b \log E_{max}$$

where the values of a and b were different for light, medium-weight, and heavy nuclei. In 1934, E. Fermi formulated the probability for a β particle to be emitted in a given momentum interval

$$P(p_e)\mathrm{d}p_e = \frac{2\pi}{\hbar} |\langle \mathrm{f}|H|\mathrm{i}\rangle|^2 \frac{\mathrm{d}n}{\mathrm{d}E_0} \tag{6.32}$$

which is called Fermi's golden rule. Here, H_{if} is the Hamilton operator of weak interaction between the initial state i and the final state f. It determines the half-life. We encountered $\mathrm{d}n/\mathrm{d}E_0$ in Section 1.5.5 as a typical application of the Heisenberg uncertainty principle, see Eq. (1.34). It is called the statistical factor or phase space factor which determines the spectral shape:

$$|H_{if}|^2 = [g \cdot |\Psi_e(0)| \cdot |\Psi_\nu(0)| \cdot |M_{if}|]^2 \tag{6.33}$$

contains the residence probabilities of the leptons at the nucleus $|\Psi_e(0)|^2$ and $|\Psi_\nu(0)|^2$, the coupling constant g of the weak interaction, and the nuclear matrix element M_{if}. Thus, we have

$$P(p_e)\mathrm{d}p_e = \frac{2\pi}{\hbar} |\Psi_e(0)|^2 |\Psi_\nu(0)|^2 |M_{if}|^2 g^2 \frac{\mathrm{d}n}{\mathrm{d}E_0} \tag{6.34}$$

For s-wave emission, Fermi assumed a constancy of the lepton wave functions in space at the nuclear volume V leading to

$$P(p_e)\mathrm{d}p_e = \frac{2\pi}{\hbar} \frac{1}{V^2} |M_{if}|^2 g^2 \frac{\mathrm{d}n}{\mathrm{d}E_0} \tag{6.35}$$

Returning to Eq. (1.34) giving the total number of states $\mathrm{d}n = \mathrm{d}N_e \cdot \mathrm{d}N_\nu$, we replace p_ν by E_ν/c (Eq. (1.21)) and set

$$p_\nu = \frac{1}{c}(E_0 - E_e) \tag{6.36}$$

and

$$\mathrm{d}p_\nu = \frac{\mathrm{d}E_0}{c} \tag{6.37}$$

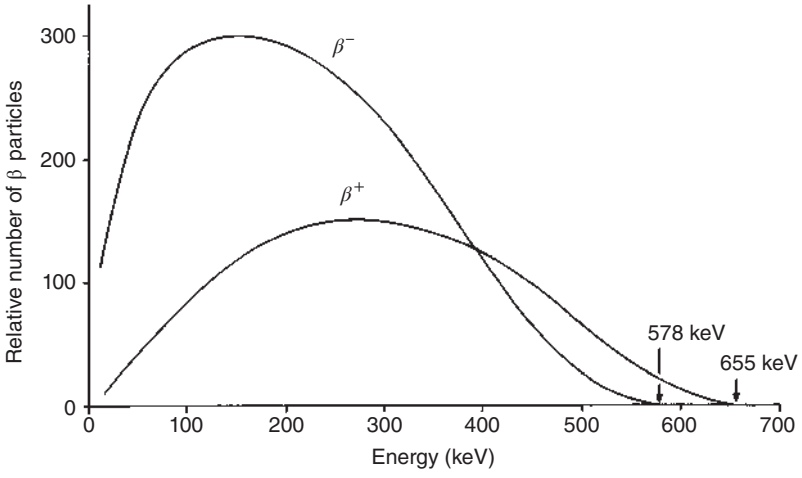

Figure 6.25 Spectra of the β^- and β^+ particles emitted by ^{64}Cu.

where dE_0 is the energy uncertainty of the decaying state, while the final state has a sharp energy. Likewise,

$$p_\nu^2 \frac{dp_\nu}{dE_0} = \frac{1}{c^2}(E_0 - E_e)^2 \frac{1}{c} = \frac{1}{c^3}(E_0 - E_e)^2 p_e^2 \, dp_e \tag{6.38}$$

With this, the statistical factor is

$$\frac{dn}{dE_0} = \frac{16\pi^2 V^2}{h^6 c^3}(E_0 - E_e)^2 p_e^2 \, dp_e \tag{6.39}$$

which no longer contains any neutrino variables and fixes the shape of the electron energy spectra. For $E_e \ll E_0$, dn/dE_0 is proportional to $p_e^2 E_0^2$, that is, proportional to p_e^2; thus, the intensity rises parabolically with p_e. On the other hand, for $E_e \approx E_0$, dn/dE_0 is proportional to $(E_0 - E_e)^2$, that is, the intensity falls parabolically toward E_{max}. In between, there is a maximum.

As we can see from Figure 6.25, there is a secondary effect on the spectral shape. The Coulomb field of the product nucleus decelerates β^- particles and accelerates β^+ particles. This is corrected by the so-called Fermi function

$$F(Z, E_e) = \frac{|\Psi_e(0)_{Coul}|^2}{|\Psi_e(0)_{free}|^2} \tag{6.40}$$

which is not solvable analytically but can be accessed via tables or computer programs. This leads us to the final expression

$$P(p_e)dp_e = \frac{64\pi^4 g^2}{h^7 c^3}|M_{if}|^2 F(Z, E_e)(E_0 - E_e)^2 p_e^2 \, dp_e \tag{6.41}$$

For a given transition, M_{if} is independent of E_e and p_e so that we can abbreviate this as

$$P(p_e)dp_e = \text{const}\, F(Z, E_e)(E_0 - E_e)^2 p_e^2 \, dp_e \tag{6.42}$$

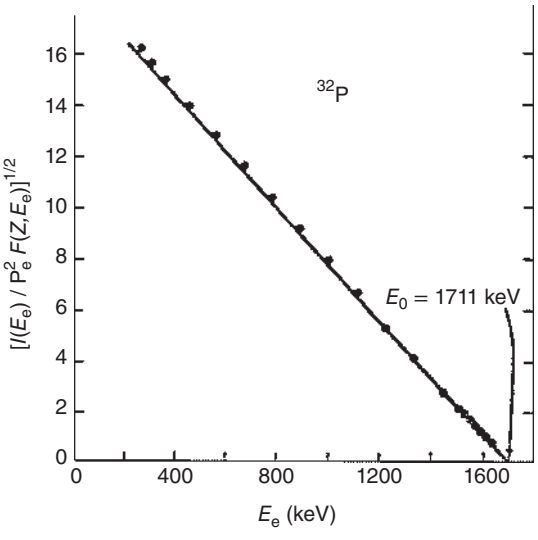

Figure 6.26 Kurie plot for β^- decay of ^{32}P.

This relation can be tested by a "Kurie plot"

$$\sqrt{\frac{P(p_e)}{p_e^2 F(Z,E_e)}} = \text{const}(E_0 - E_e) \tag{6.43}$$

For practical purposes, using the relativistic relation between p_e and E_e, a plot of

$$\sqrt{\frac{I(E_e)}{p_e^2 F(Z,E_e)}} \quad \text{vs. } E_e$$

gives a decreasing linear relation (for allowed Fermi transitions) that can be extrapolated to E_0. The Kurie plot for ^{32}P is shown in Figure 6.26. The Kurie plot is also useful for the decomposition of complex β spectra (β decay into the ground state and an excited state giving rise to two values of E_0), see Figure 6.27.

The decay constant λ is obtained by integrating Eq. (6.41) over all values of p_e:

$$\begin{aligned}\lambda &= \frac{\ln 2}{t_{1/2}} = \int_0^{p_e^{\max}} P(p_e)\mathrm{d}p_e \\ &= \frac{64\pi^4}{h^7 c^3} g^2 |M_{if}|^2 \int_0^{p_e^{\max}} F(Z,E_e) p_e^2 (E_0 - E_e)^2 \mathrm{d}p_e \end{aligned} \tag{6.44}$$

Within Eq. (6.44), the integral is abbreviated as the "integral of the Fermi function f" such that

$$\lambda = \frac{64\pi^4}{h^7 c^3} g^2 |M_{if}|^2 \cdot f \tag{6.45}$$

and

$$ft_{1/2} = \frac{h^7 c^3 \ln 2}{64\pi^4 g^2 |M_{if}|^2} \tag{6.46}$$

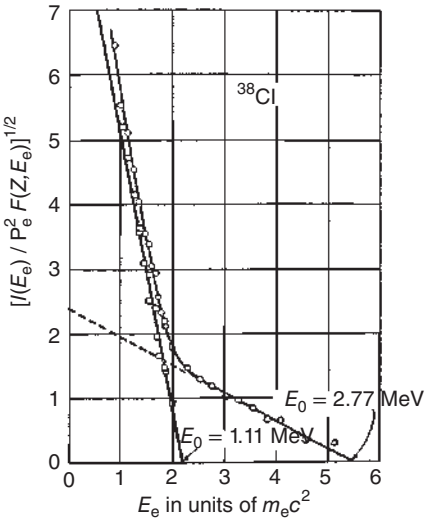

Figure 6.27 Kurie plot for β^- decay of ^{38}Cl.

For transitions of the same type (same change in angular momentum and parity), $|M_{if}|$ should be roughly constant and result in comparable *ft* values. Thus, the *ft* values are called *comparative half-lives* and are used to classify various types of β decay, see below. The *ft* values are half-lives corrected for the statistical factor and for the influence of the Coulomb field. Low *ft* values are associated with "allowed" transitions; high *ft* values are associated with "forbidden" transitions. Evaluation of the integral in Eq. (6.44) gives the following approximate values for f:

$$\log f(\beta^-) = 4.0 \log E_0 + 0.78 + 0.02Z - 0.005(Z-1) \log E_0 \tag{6.47}$$

$$\log f(\beta^+) = 4.0 \log E_0 + 0.79 + 0.007Z - 0.009(Z+1)(\log(E_0/3))^2 \tag{6.48}$$

$$\log f(\mathrm{EC}) = 2.0 \log E_0 - 5.6 + 3.5(Z+1) \tag{6.49}$$

Note that in these equations, Z, as before, is the atomic number of the product nuclide. For rapid estimates, the use of nomographs and curves such as those given in Figures 6.28 and 6.29 is practical. Here, $\log ft$ is split into $\log f_0 t + \log C$, the latter representing the influence of the Coulomb field. The example shown in Figure 6.28 is β^+ decay of ^{25}Al. Endpoint energy of 3.24 MeV and half-life of 7.6 seconds give a $\log f_0 t$ value of 3.7. Log C read off in Figure 6.29 is −0.1. Thus, $\log ft = 3.6$ is indicating a "superallowed" transition. Classification of β transmutations and selection rules is listed in Table 6.3. The lowest $\log ft$ values clustering around 3 to 3.5 are observed for mirror nuclei (Chapter 5) with "superallowed" transitions. As a general rule, transitions in which the electron and neutrino carry away no orbital angular momentum ($l = 0$) have the largest transition probabilities and are called "allowed." There is another, broader peak with $\log ft$ values between four and seven for normal allowed transitions, and the rather wide range for $\log ft$ values of this type indicates that our assumption of approximately equal $|M_{if}|^2$ for all allowed

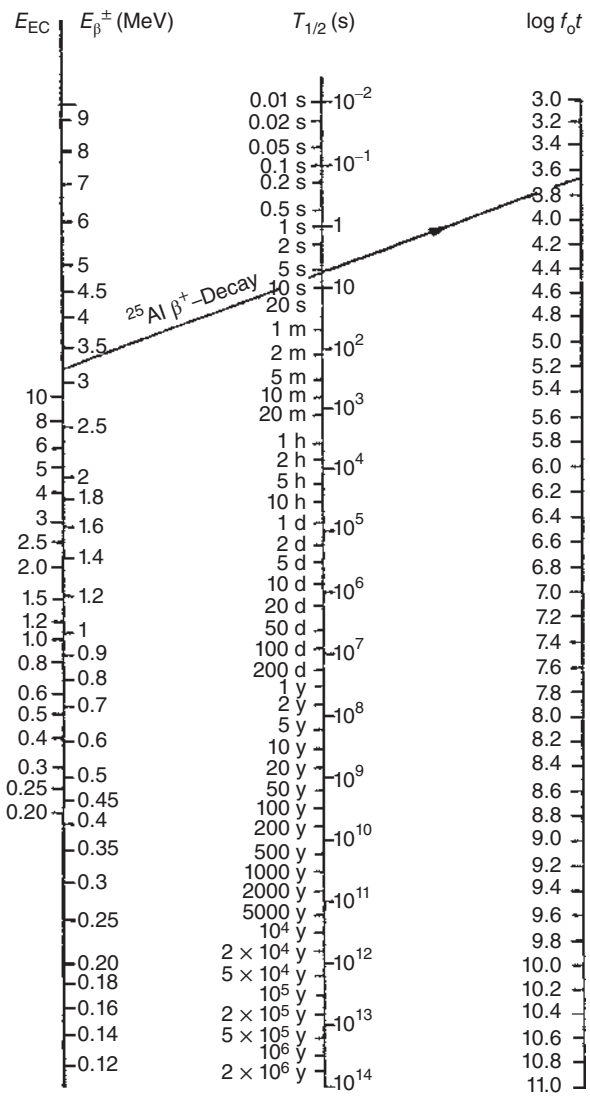

Figure 6.28 Nomograph for the graphical determination of log f_0t values. Log $ft = \log f_0t + \log C$. The example indicated is β^+ decay of ^{25}Al. Source: Moszkowski (1951), figure 2 (p. 36)/American Physical Society.

transitions is too naive. The nuclear matrix elements are evidently very sensitive to details of nuclear structure. An extreme example is the so-called *l*-forbidden decay of ^{32}P ($I = 1$) $\rightarrow$ ^{32}S ($I = 0$) with log $ft = 7.9$ because a $d_{3/2}$ neutron is transformed into an $s_{1/2}$ proton, so that $\Delta L = 2$ even though $\Delta I = 1$.

For higher l values, the magnitudes of the electron and neutrino wave functions over the nuclear volume decrease by orders of magnitude with each unit of angular momentum and, thus, β transitions with $l = 1, 2, 3$, and so on, are called first, second, third, and so on, forbidden transitions. For ^{115}In, for example, $l = 4$ and log $ft = 23$, giving that nucleus a half-life of $4 \cdot 10^{14}$ years.

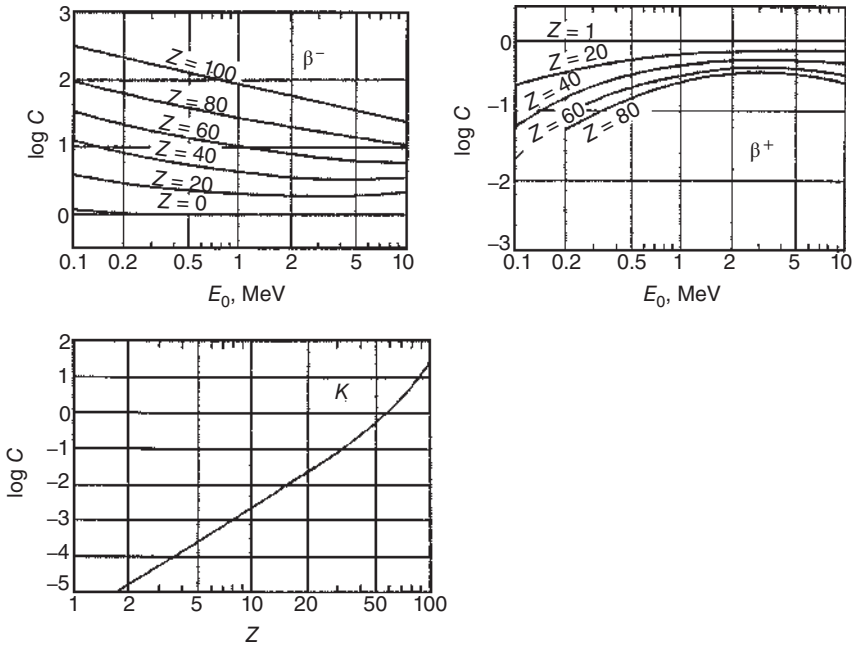

Figure 6.29 Log C as a function of E_0 and Z for β^-, β^+, and K capture decay. Z is the atomic number of the initial nucleus. Source: Moszkowski (1951), figure 2 (p. 36)/American Physical Society.

Log ft values increase by an average of 3.5 units for each unit of angular momentum or degree of forbiddenness. Such an increase in the lifetime indicates a hindrance of about $3 \cdot 10^{-4}$ for each unit of angular momentum. There is a large spread in the values, however, caused by the strong effect of the nuclear matrix element for each decay. The systematics of experimental log ft values are shown in Figure 6.30.

The β^- decay of ^{46}Sc, Figure 6.31, may be taken as an example of the application of the selection rules in Table 6.3. The half-life of ^{46}Sc is 83.8 days $= 7.24 \cdot 10^6$ seconds, and nearly 100% of ^{46}Sc is converted into the second excited state of ^{46}Ti. The ft value is calculated from Eq. (6.47) to be $\log ft = 6.3$, in good agreement with the value for allowed (normal) transitions in Table 6.3 (no change of total angular momentum, $\Delta I = 0$, no change of parity). The transition to the first excited state occurs very seldom. The half-life with respect to this transition is higher by a factor of 100/0.004 which gives $\log ft = 13.1$. This value is also in rather good agreement with the theoretical value for twofold forbidden transitions in Table 6.3 (change of total angular momentum, $\Delta I = 2$, no parity change). The direct transition to the ground state of ^{46}Ti is not observed. This would be a fourfold forbidden transition (change of total angular momentum, $\Delta I = 4$, no parity change) with $\log ft \approx 23$ according to Table 6.3, corresponding to a probability of $2 \cdot 10^{-12}$% which is too low to be detectable. The application of β-decay selection rules is an important tool for angular momentum and parity assignments in decay scheme determinations.

Table 6.3 Classification of β transitions and selection rules.

Classification	Orbital angular momentum l carried away by electron and neutrino	Change of the orbital angular momentum quantum number ΔL in the nucleus	Change of the total angular momentum ΔI in the nucleus	Change of parity	Log ft	Examples
Superallowed	0	0	0	No	2.7–3.7	n, ^{3}H, ^{6}He ($\Delta I = 1$!), ^{11}C, ^{13}N, ^{15}O, ^{17}F, ^{19}Ne, ^{21}Na, ^{23}Mg, ^{25}Al, ^{27}Si, ^{29}P, ^{31}S, ^{33}Cl, ^{35}Ar, ^{37}K, ^{39}Ca, ^{41}Sc, ^{43}Ti
Allowed (normal)	0	0	0 or 1	No	4–7	^{12}B, ^{12}N, ^{35}S, ^{64}Cu, ^{69}Zn, ^{114}In
Allowed (*or* forbidden)	0	2	1	No	6–9	^{14}C, ^{32}P
First forbidden	1	1	0 or 1	Yes	6–10	^{111}Ag, ^{143}Ce, ^{115}Cd, ^{187}W
First forbidden (unique)	1	1	2	Yes	7–10	^{38}Cl, ^{90}Sr, ^{97}Zr, ^{140}Ba
Second forbidden	2	2	2	No	11–14	^{36}Cl, ^{99}Tc, ^{135}Cs, ^{137}Cs
Second forbidden (unique)	2	2	3	No	≈14	^{10}Be, ^{22}Na
Third forbidden	3	3	3	Yes	17–19	^{87}Rb
Third forbidden (unique)	3	3	4	Yes	18	^{40}K
Fourth forbidden	4	4	4	No	≈23	^{115}In

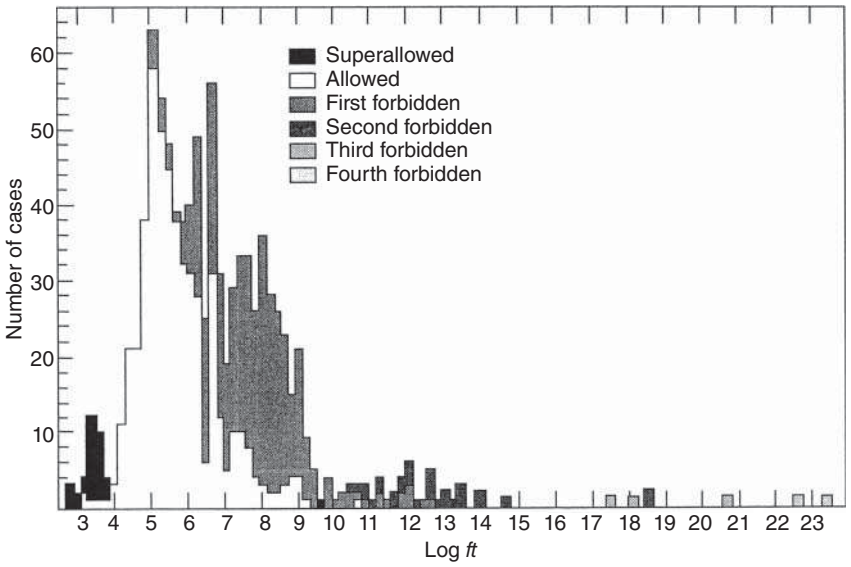

Figure 6.30 Systematics of log *ft* values. Source: Meyerhof (1967)/McGraw-Hill.

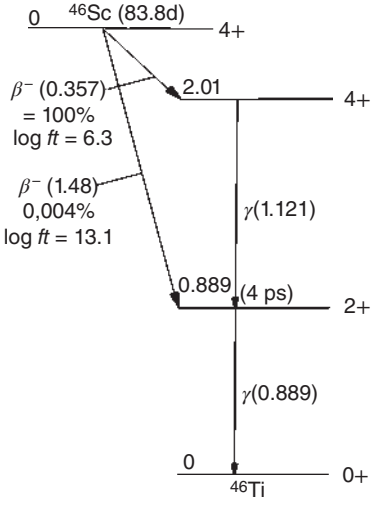

Figure 6.31 Decay scheme of ^{46}Sc.

6.6.2 Electron Capture-to-Positron Ratios

Whenever β^+ emission is energetically possible, it competes with EC. Since for the two modes of decay initial and final nuclear states are the same, the ratio $\lambda_{EC}/\lambda_{\beta+}$, at least for allowed transitions without angular momentum hindrance, is expected to be independent of $|M_{if}|^2$ and equals $f_{EC}/f_{\beta+}$. Thus, measurements of EC-to-positron branching ratios constitute a test of β-decay theory. These ratios increase with decreasing decay energy going to infinity when β^+ emission becomes impossible at decay energies $\leq 2m_e c^2$ and with increasing Z. This comes about through the

increase of the expectation value for finding orbital electrons (especially K electrons) at the nucleus and through the increasing suppression of β^+ emission by the Fermi function. Whenever energetically possible, capture of K(1s) electrons predominates over capture of electrons with higher principal quantum numbers because, of all the electron wave functions, those of the K electrons have the largest residence probability at the nucleus. For decay energies lower than the binding energy of the K electrons, EC is possible only from the L(2s + 2p) and M(3s + 3p + 3d) shells. In allowed transitions, most of the L captures take place from the $L_I(2s_{1/2})$ subshell, less from the $L_{II}(2p_{1/2})$, and zero from the $L_{III}(2p_{3/2})$ subshells. The contribution of M capture can usually be neglected. The ratio of L_I capture to K capture as a function of decay energy for allowed transitions for $Z \geq 14$ can be approximated by

$$\frac{L_I}{K} = (0.06 + 0.0011Z)\left[\frac{E_0^L(\nu)}{E_0^K(\nu)}\right]^2 \tag{6.50}$$

where the neutrino energy for capture from the L shell exceeds that for capture from the K shell by the difference between the binding energies in the two shells. At decay energies not too far in excess of the K binding energy, the ratio of neutrino energies in Eq. (6.49) is far from unity and a measurement of the L-to-K capture ratio then permits an estimate of the decay energy by using Eq. (6.50).

The only abundant radiations resulting from EC, other than the essentially undetectable neutrinos, are due to secondary processes occurring in the electron shell of the daughter. If a K-shell vacancy is filled, the difference between the K and L binding energies may be emitted as a characteristic X-ray or may be used in an internal photoelectric effect in which an additional extranuclear electron from the L, M, or other shell is emitted with kinetic energy equal to the characteristic X-ray energy minus its own binding energy. These are called Auger electrons. The whole process of readjustment in a heavy atom may involve many X-ray emissions and Auger processes in successively higher shells. The fraction of vacancies in a given shell that is filled with accompanying X-ray emission is called fluorescence yield. The K-shell fluorescence yield ω_K increases with increasing Z as shown in Figure 6.32. ω_L varies with Z in a similar manner but is several times smaller than the K yield for a given Z. Another secondary process accompanying EC is the emission of inner bremsstrahlung. This is the emission of a continuous spectrum of electromagnetic radiation of very low intensity associated with the deceleration of the captured relativistic electron in the nucleus. The bremsstrahlung quanta take over a part of the decay energy that is normally taken over by the neutrino. The measurement of the endpoint of the bremsstrahlung spectrum is the only way to determine Q_{EC} directly.

6.6.3 Nuclear Matrix Elements

Because, in β decay, relativistic electrons are produced, the matrix elements need to be formulated within the Dirac theory. As in the fundamental processes, for example, in the β^- decay of the neutron, four particles are involved, the ansatz for the Hamilton function, Eq. (6.32), is to construct for the energy density a bilinear quantity of the form $(\Psi_p^* \Omega \Psi_n)(\Psi_e^* \Omega \Psi_\nu)$ with suitable Dirac operators Ω. The symbol Ψ^* stands

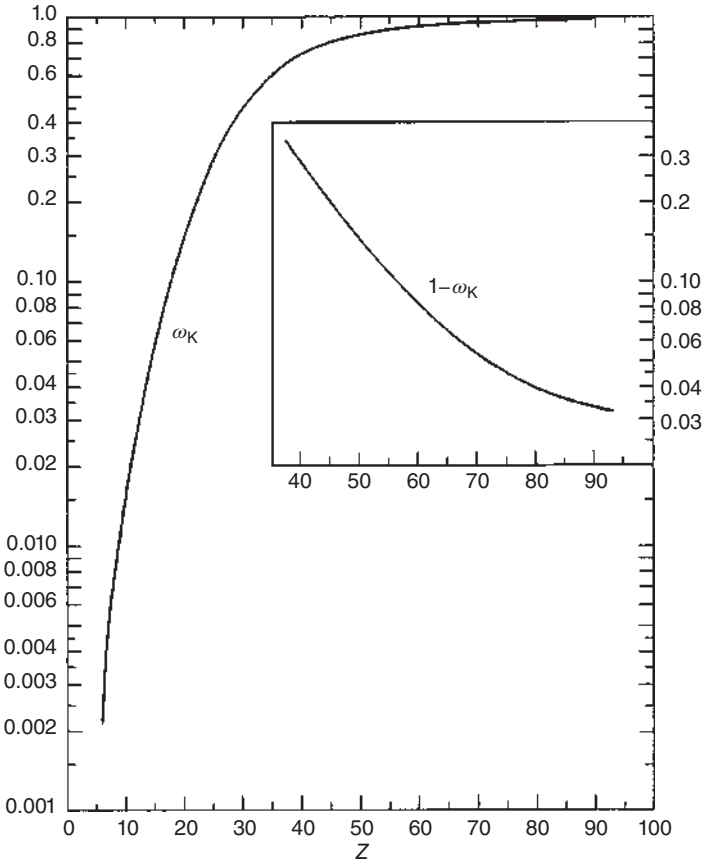

Figure 6.32 K-shell fluorescence yield ω_K as a function of Z. At high Z a curve of $1-\omega_K$ is shown. Source: Friedlander et al. (1981)/John Wiley & Sons.

for the hermitic adjunct wave function. As there are 16 linear independent Dirac matrices and, as in the above expression, the two factors must not necessarily contain the same operator, there are $16^2 = 256$ mathematically possible bilinear forms. Their number is dramatically reduced by Fermi's requirement of a Lorentz-invariant linear point interaction, and there remain five possibilities if, in addition, we require that in both factors we have the same operators. Then, for the Hamilton function of the neutron decay,

$$H = \int \sum_k g_k (\Psi_p^* \Omega_k \Psi_n)(\Psi_e^* \Omega_k \Psi_\nu) d\tau \tag{6.51}$$

there are five Dirac matrices with the transformation properties k = S, P, V, A, T and five different coupling strengths. The intergration is over the nuclear volume. The transformation properties are those of a scalar S, pseudoscalar P, polar vector V, axial vector A, and that of a tensor T. In order to decide which of these interactions are realized in nature, it is insufficient to observe the spectral shape and the half-life. To this end, polarization experiments are required. It was possible, in particular, to

investigate the decay of the free neutron in much detail and to determine the correlation between the direction of β^- emission and the spin orientation in the decay of polarized neutrons. This experimentally allows for a unique conclusion about the nature of the interaction. Of the five possibilities, indeed only two contribute, having the transformation properties V and A. With realistic approximations, that is, constancy of the lepton wave functions in space over the nuclear volume, Eq. (6.35), and non-relativistic approximation of the nucleon wave functions, we obtain two simple matrix elements:

$$\Omega_V \rightarrow M_F = (\Psi_p^* 1 \Psi_n) \mathrm{d}\tau \tag{6.52}$$

for the Fermi matrix element; and

$$\Omega_A \rightarrow M_{\mathrm{GT}} = (\Psi_p^* \vec{\sigma} \Psi_n) \mathrm{d}\tau \tag{6.53}$$

for the Gamow–Teller matrix element.

The operator in the Fermi matrix element is the unit matrix **1**; in the Gamow–Teller matrix element, it is the spin operator $\boldsymbol{\sigma}$. The unit matrix keeps the spin orientation of the decaying neutron, and the resulting proton equals so that the spins of the electron and antineutrino must be antiparallel (singlet state, $\Sigma s = 0$) and the associated selection rule is $\Delta I = 0$, $\Delta \pi = 0$. The spin operator reverses the spin orientation of the proton relative to that of the neutron so that the spins of the leptons must be parallel (triplet state, $\Sigma s = 1$). The selection rule for Gamow–Teller transitions is $\Delta I = 0$ or ± 1, no. $0 \rightarrow 0$, $\Delta \pi = 0$.

Returning to Eq. (6.46), we have thus to rewrite it by taking into account that β decay involves a linear combination of V and A interaction (V–A current–current interaction) where

$$ft_{1/2} = \frac{h^7 c^3 \ln 2}{64\pi^4 (g_{\mathrm{V}}^2 M_{\mathrm{F}}^2 + g_{\mathrm{A}}^2 M_{\mathrm{GT}}^2)} \tag{6.54}$$

It is interesting to ask what the values are of the coupling constants g_{V} and g_{A}. The simplest way would be to determine them from experimental *ft* values for a pure Fermi transition and a pure Gamow–Teller transition because then, $M_{\mathrm{GT}} = 0$ and $M_{\mathrm{F}} = 0$, respectively. In principle, this is possible, as we know from the selection rules that a $0 \rightarrow 0$ transition must be a pure Fermi transition and a $\Delta I = 1$ transition must be a pure Gamow–Teller transition. Of course, only decays are suitable for which the nuclear matrix elements are safely known. For the determination of the Fermi coupling constant, the decay $^{14}\mathrm{O} \rightarrow {}^{14}\mathrm{N}$ is a good candidate for a $0 \rightarrow 0$ transition. The Fermi matrix element can be calculated reliably; it is $M_{\mathrm{F}}^2 = 2$. The measured half-life is 70.6 seconds; the Q_β value is 1810.6 ± 1.5 keV. With these values, Eq. (6.54) gives

$$g_{\mathrm{V}} = 0.88 \cdot 10^{-4} \ \mathrm{MeV\,fm^3} \tag{6.55}$$

(In particle physics, the coupling constants are often given in units of the reciprocal proton mass, e.g. the universal coupling constant (Fermi constant derived from muon decay) $G_{\mathrm{F}} = 1.026 \cdot 10^{-5} m_{\mathrm{p}}^{-2}$.) In a corresponding way, the coupling constant g_{A} should be accessible. An example would be the decay $^6\mathrm{He} \rightarrow {}^6\mathrm{Li}$ ($0^+ \rightarrow 1^+$, $Q_\beta = 3.5$ MeV, $t_{1/2} = 0.8$ seconds). Here, unfortunately, the calculated Gamow–Teller

matrix element depends on special assumptions about the nuclear structure. $M_{GT}^2 = 6$ is possible but uncertain. On the other hand, there is no doubt about the matrix elements in the decay of the free neutron. Here, the simple expressions in Eqs. (6.52) and (6.53) are valid. In that case,

$$M_F^2 = \left| \int (\Psi_p^* 1 \Psi_n) \, d\tau \right|^2 = 1 \tag{6.56}$$

$$M_{GT}^2 = \left| \int (\Psi_p^* \boldsymbol{\sigma} \Psi_n) \, d\tau \right|^2 = 3 \tag{6.57}$$

In 2006, the Particle Data Group (PDG) evaluated the world's average value for the lifetime of the neutron as 885.7 ± 0.8 seconds. The decay energy (782 keV) results from the neutron–proton mass difference. From this, the *ft* value can be deduced and as the ratio of the matrix elements is known, the ratio of the coupling constants can be determined as

$$\lambda = \frac{g_A}{g_V} = -1.2695 \pm 0.0029 \tag{6.58}$$

6.6.4 Parity Non-Conservation

In Section 4.5, we introduced the concept of parity, which is the response of the wave function to an operation in which the signs of the spatial coordinates are reversed. As we indicated in Section 6.2, parity conservation forms an important selection rule for α decay. In general, we find that parity is conserved in strong and electromagnetic interactions.

The possibility that conservation of parity does not hold for weak interactions was suggested in 1956 by Lee and Yang (1956) as an explanation for what appeared to be two different decay modes of the same particle, the K^+ meson, one to a two-pion (even-parity) final state and another one to a three-pion (odd-parity) final state. They pointed out that no then-existing data proved parity conservation in weak interactions and suggested some experimental tests. The first experimental verification of non-conservation of parity in weak interactions came in the historical experiment by C.S. Wu et al. in 1956 in which the emission of β^- particles from polarized ^{60}Co nuclei whose angular momenta were aligned by a magnetic field at very low temperatures to suppress thermal motion was found to be preferentially along the direction opposite to the angular momentum vector. The experimental situation is depicted in Figure 6.33. The measured angular distribution of the electrons had the shape

$$I(\Theta) = 1 - \frac{\boldsymbol{\sigma}\mathbf{P}}{E} = 1 - \frac{v}{c} \cos\Theta \tag{6.59}$$

Here, $\boldsymbol{\sigma}$ is the unit vector in the direction of the angular momentum of the nucleus, $\mathbf{P}$ and E are the momentum and energy of the electron, respectively, and Θ is the angle of emission relative to the angular momentum vector. In the β^- transition of ^{60}Co, the orbital angular momentum of the ν–e pair is zero. As $\Delta I = 1$, the spins of the electron and antineutrino must be parallel to the direction of the magnetic field. For the intensity maximum at $\Theta = \pi$, the electron is polarized with a left screw sense

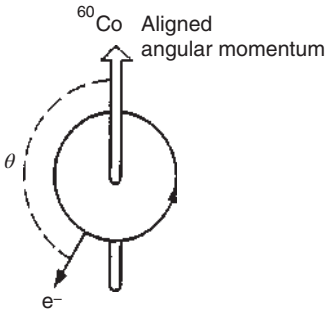

Figure 6.33 Direction of the aligned nuclear angular momentum and direction of the emitted electron in β^- decay of ^{60}Co. Source: Musiol et al. (1988)/John Wiley & Sons.)

(left-handed). The polarization of the electron along the direction of its momentum is called helicity H. We have

$$H = \frac{I_+ - I_-}{I_+ + I_-} = -\frac{v}{c} \tag{6.60}$$

where I_+ and I_- are the intensities of the electrons in the direction of $\boldsymbol{\sigma}$ parallel and antiparallel to $\mathbf{P}$. The helicity is the eigenvalue of the helicity operator

$$H = \frac{\boldsymbol{\sigma}\mathbf{P}}{E} \tag{6.61}$$

The helicity of the electrons could be demonstrated in a number of weak decays. One always found, for e^-,

$$H = -\frac{v}{c} \quad \text{(left-handedness)} \tag{6.62}$$

and, for e^+,

$$H = +\frac{v}{c} \quad \text{(right-handedness)} \tag{6.63}$$

These experiments showed not only a violation of parity conservation but also a violation of the invariance of charge conjugation C. Only the combined invariance under operation CP is conserved in the weak interaction. In these weak decays, there also appears a neutrino or antineutrino. If we apply Eqs. (6.62) and (6.63) to the neutrinos with rest mass zero, we obtain fully polarized neutrinos of helicity $H_\nu = -1$ and antineutrinos with $H_{\bar{\nu}} = +1$.

Our understanding of the implications of parity non-conservation may be improved by considering the properties of different quantities under space inversion. Polar vectors, such as linear momentum, velocity, or electric field, change sign under this operation, whereas axial vectors, such as angular momentum or magnetic field which are characterized by direction and by a screw sense, do not change sign. A quantity that is the scalar product of two polar vectors or of two axial vectors will be invariant under space inversion. Such quantities are called scalars. A quantity that is the scalar product of one polar vector and one axial vector changes sign under space inversion. The occurrence of such quantities, called pseudoscalars, is prohibited by the requirement of parity conservation. The Wu experiment was specifically designed to look for a pseudoscalar quantity, namely a component of β-particle intensity proportional to the product of nuclear angular momentum

(an axial vector) and the electron velocity (a polar vector). The asymmetry found established the existence of this pseudoscalar component and thus proved that parity was not conserved in β decay. Since then, many other experiments have corroborated non-conservation of parity in all weak interactions. They have shown that the neutrinos accompanying electron capture and β^+ decay are left-handed, that is, they have their spins antiparallel to their direction of motion. Positrons then must be right-handed, electrons left-handed, and the antineutrinos accompanying β^- decay right-handed.

It is worthwhile to emphasize that everything in this section about spectrum shapes and lifetimes in β decay is unaffected by the overthrow of parity conservation because only scalar quantities are involved. Thus, Fermi's theory is largely unaffected except for the need to include some additional parity-non-conserving coupling constant in the interaction. If we rewrite the Hamilton function for the V–A interaction with γ matrices, this is done by the projection operator $P = (1 + \gamma_5)$, namely,

$$H_\beta = \frac{1}{\sqrt{2}} \int \{g_V(\psi_p^* \Omega_V \psi_n)(\psi_e^* \Omega_V P \psi_\nu) + g_A(\psi_p^* \Omega_A \psi_n)(\psi_e^* \Omega_A P \psi_\nu)\} \mathrm{d}\tau \quad (6.64)$$

$$H_\beta = \frac{1}{\sqrt{2}} \int \{g_V[\bar{p}\gamma_\mu n][\bar{e}\gamma_\mu(1+\gamma_5)\nu] + g_A[\bar{p}\gamma_5\gamma_\mu n][\bar{e}\gamma_\mu(1+\gamma_5)\nu]\} \mathrm{d}\tau \quad (6.65)$$

The discovery of parity non-conservation has stimulated whole new classes of experiments involving the observation of (i) asymmetry of β emission from polarized nuclei and polarized neutrons, (ii) polarization of β particles, (iii) correlations between β particles and polarized γ-rays.

6.6.5 Massive Vector Bosons

In Chapter 1, we briefly mentioned the unified electroweak theory of Glashow, Salam, and Weinberg requiring four gage bosons: the photon and the charged and neutral massive vector bosons $\mathbf{W}^\pm$ and Z_0. Within the SU(2) × U(1) gage group, there is a triplet of massive vector bosons, $\mathbf{W}^+$, $\mathbf{W}^-$, and $\mathbf{W}^0$, and a singlet B^0. The W couples with the leptons, the so-called multiplets of the weak isospin, the B^0 with the same particles and with the electromagnetic charge. W^0 and B^0 are no eigenstates of the mass matrix, but their linear combinations correspond to real physical particles, the photon and the Z^0 boson,

$$\gamma = \cos\Theta_w B^0 + \sin\Theta_w W^0 \quad (6.66)$$

and the orthogonal combination

$$Z^0 = -\sin\Theta_w B^0 + \cos\Theta_w W^0 \quad (6.67)$$

where Z^0 corresponds to the neutral current as a transmitter of the weak force. The angle Θ_w is the weak mixing angle. Its experimentally determined value is $\sin^2\Theta_w = 0.215 \pm 0.014$. The massive vector bosons $\mathbf{W}^\pm$ and Z^0 were detected in 1983 at the Proton–Antiproton Collider of the European Research Center, CERN in Geneva with masses

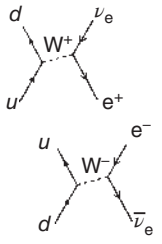

Figure 6.34 Feynman diagrams of the β^- decay and β^+ decay according to Eqs. (6.69) and (6.70).

$$m_W = 82.1 \pm 1.7\text{GeV} \quad \text{and} \quad m_Z = 93.0 \pm 1.7\text{GeV} \tag{6.68}$$

for which the Nobel Prize in Physics 1984 was awarded jointly to Carlo Rubbia and Simon van der Meer "for their decisive contributions to the large project, which led to the discovery of the field particles W and Z, communicators of weak interaction."

The charged vector bosons decay into either a pair of leptons or a pair of quarks. The number of possible decays of the Z^0 is much larger, but the final states are also either a pair of leptons or a pair of quarks. Thus, the vector bosons couple not only with the leptons but also with the quarks. Therefore, it is more fundamental to rewrite the "fundamental process" of $\beta^\pm$ decay, Eqs. (6.28) and (6.29), rather as

$$d \rightarrow u + e^- + \bar{\nu}_e \tag{6.69}$$

$$u \rightarrow d + e^+ + \nu_e \tag{6.70}$$

The respective Feynman diagrams are shown in Figure 6.34.

6.6.6 Cabibbo–Kobayashi–Maskawa Matrix

The weak interaction occurs in two different ways involving: (i) charged weak currents and the charged vector bosons $W^\pm$ and (ii) neutral weak currents and the neutral vector boson Z^0. The interactions caused by the charged weak currents are phenomenologically divided into several classes, among others into:

1) Leptonic processes in which only charged leptons and neutrinos are involved, for example, muon decay, $\mu^- \rightarrow e^- + \overline{\nu}_e + \overline{\nu}_\mu$.
2) Semileptonic processes without violation of the strangeness quantum number S in which both leptons and hadrons participate. Examples are neutron β^- decay $n \rightarrow p + e^- + \overline{\nu}_e$, pion decay $\pi^+ \rightarrow \mu^+ + \nu_\mu$, and elastic neutrino–nucleon scattering $\nu_\mu + n \rightarrow \mu^- + p$.
3) Semileptonic processes with change of S such as Λ hyperon decay $\Lambda \rightarrow p + e^- + \overline{\nu}_e$.

The cross sections and lifetimes of the weak interaction are given by the universal coupling constant G_F, the Fermi constant. We had already seen that in weak interactions, four fermions are always involved, and it is straightforward to describe the interaction term in the Hamilton operator in the form of a current–current coupling. Let us look at the muon decay $\mu^- \rightarrow e^- + \overline{\nu}_e + \overline{\nu}_\mu$ or the equivalent

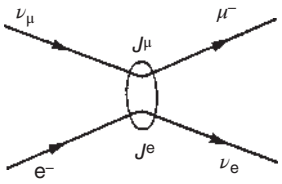

Figure 6.35 Scattering of the muon neutrino on an electron as current–current interaction. Source: Musiol et al. (1988)/John Wiley & Sons.

neutrino–electron scattering $\nu_\mu + e^- \to \mu^- + \nu_e$. We imagine this interaction as the result of the interaction between a muon current J^μ and an electron current J^e, see Figure 6.35, with the currents

$$J^\mu = \Psi^*_\mu \gamma_\mu (1 + \gamma_5) \Psi_{\nu_\mu} \quad \text{and} \quad J^e = \Psi^*_e \gamma_\mu (1 + \lambda_5) \Psi_{\nu_e} \tag{6.71}$$

giving the Hamilton operator

$$H_\mu = \frac{G_F}{\sqrt{2}} J^e \bar{J}^\mu \tag{6.72}$$

Semileptonic processes are more complicated. Leptons are point-like elementary particles, whose properties are completely reflected by theory. On the other hand, hadrons are complex particles with an inner structure resulting from strong interaction. Let us select as a prototype neutron β^- decay or the equivalent neutrino–neutron scattering $\nu_e + n \to e^- + p$. This can be described by the interaction of a hadronic current J^N with a lepton current J^e

$$H_n = \frac{G_F}{\sqrt{2}} J^N \bar{J}^e \tag{6.73}$$

where, in the hadronic current, the coupling constants g_V and g_A occur. If the weak interaction of the hadrons was to be identical to the weak interaction of the leptons, we would have $G_F = g_V = g_A = 1$. It is remarkable that g_V (see the Cabibbo–Kobayashi–Maskawa (CKM) matrix element V_{ud} below) deviates only by a few percent from the Fermi constant G_F and that $g_V \approx 1$ and $g_A \approx 1.25$. This means that, despite their inner structure, the nucleons in semileptonic processes behave nearly equal to the leptons. The weak interaction has a nearly universal form for all fermions. It appears that the hadron structure is nearly irrelevant for at least the vector part of the interaction. One formulates this fact with the hypothesis of the "conserved vector current." The axial vector current, however, is significantly different for leptons and hadrons. But as g_A does not deviate very much from unity, one is here formulating the hypothesis of "partially conserved axial vector currents."

Another complication arises if we consider a weak interaction involving a change in the strangeness quantum number S. Instead of the Λ hyperon decay into $p + e^- + \nu_e$, we consider again the equivalent neutrino reaction together with the corresponding reaction without change in strangeness

$$\begin{aligned} \bar{\nu}_e + p &\to n + e^+ \\ \bar{\nu}_e + p &\to \Lambda + e^+ \end{aligned} \tag{6.74}$$

considering that hadrons are composed of three constituent quarks: p = uud, n = udd, and Λ = uds. Thus, reactions (6.74) can be characterized as transitions of a u quark in a d or an s quark carrying the strangeness quantum number

$$\begin{aligned} \overline{\nu}_e + u &\rightarrow d + e^+ \\ \overline{\nu}_e + u &\rightarrow s + e^+ \end{aligned} \tag{6.75}$$

It was N. Cabibbo who suggested that the relative probabilities for these two transitions $u \rightarrow d$ and $u \rightarrow s$ be described by an angle θ_C. This angle is now called the Cabibbo angle. With this, the hadronic current in Eq. (6.73) is changed into

$$J^N = \Psi_u^* \gamma_\mu (1 + \gamma_5)(\cos\theta_C \Psi_d + \sin\theta_C \Psi_s) \tag{6.76}$$

where $\cos^2\theta_C$ and $\sin^2\theta_C$ measure the relative probabilities for the two transitions and $\cos^2\theta_C + \sin^2\theta_C = 1$. Experimentally, the Cabibbo angle is rather small ($\sin^2\theta_C = 0.05$), which means that the transition probability for the strangeness changing processes is about a factor of 20 smaller than for the strangeness-conserving processes. This also means that the vector coupling constant g_V in semileptonic β decays is $\cos^2\theta \cdot G_F^2 \approx 0.95 G_F^2$.

For the purely hadronic weak processes, the complications are even much larger than for the semileptonic ones and we do not go into these details.

The Cabibbo theory which relates to two quark generations ud and sc, see Figure 1.9, contains one single mixing parameter, the Cabibbo angle θ_C. In 1973, Kobayashi and Maskawa (1973) extended the theory to three quark generations. The resulting CKM matrix is a 3×3 matrix that describes in the frame of the Standard Model, Section 1.5.6, in which the quarks of three flavor generations (i.e. u-type quarks of charge $\frac{2}{3}e$ and d-type quarks of charge $-\frac{1}{3}e$) can be changed into other quarks of the same charge by interaction with a charged W boson. The CKM matrix therefore is also called the quark-mixing matrix. If a u-type quark of a given flavor u_i is changed by interaction with a W^+ boson into a d-type quark, the square of the matrix element $|V_{ij}|^2$ corresponds to the transition probability to a quark of flavor d_j. The value of $|V_{ij}|^2$ also corresponds to the probability for the transition of a quark d_j to a quark u_i by interaction with a W^- boson. This means that the CKM matrix describes the connection between the quark flavors of a given initial state and of a corresponding final state where the transition is caused by flavor-changing charged currents (the W bosons). The matrix equations in which the nine CKM matrix elements and the flavor eigenstates of the six quarks are given explicitly are depicted in Figure 6.36 for an initial state $|D_{init}\rangle$ containing exclusively d-type quarks and likewise for an initial state $|U_{init}\rangle$ containing exclusively u-type quarks. It is a safe experimental fact that the CKM matrix is different from a unit matrix, $V_{UD} \neq 1^{3\times3}$.

The nine CKM matrix elements correspond to three real mixing angles and a complex phase. Therefore, the transition probabilities of the quarks are not completely independent of each other but obey certain relationships reflecting the different quark masses. The importance of the complex phase lies in the CP violation of the weak interaction within the Standard Model. It is noteworthy that only by beginning with a dimension of three can a complex phase exist, that is, CP violation requires at least three quark generations. For their prediction, based on this reasoning, of a third

$$\begin{bmatrix} V_{ud} & V_{us} & V_{ub} \\ V_{cd} & V_{cs} & V_{cb} \\ V_{td} & V_{ts} & V_{tb} \end{bmatrix} \begin{bmatrix} \langle d | D_{init} \rangle \\ \langle s | D_{init} \rangle \\ \langle b | D_{init} \rangle \end{bmatrix} = \begin{bmatrix} \langle u | U_{end} \rangle \\ \langle c | U_{end} \rangle \\ \langle t | U_{end} \rangle \end{bmatrix}$$

$$\begin{bmatrix} \langle u | U_{init} \rangle \\ \langle c | U_{init} \rangle \\ \langle t | U_{init} \rangle \end{bmatrix} = \begin{bmatrix} V_{ud} & V_{us} & V_{ub} \\ V_{cd} & V_{cs} & V_{cb} \\ V_{td} & V_{ts} & V_{tb} \end{bmatrix} \begin{bmatrix} \langle d | D_{end} \rangle \\ \langle s | D_{end} \rangle \\ \langle b | D_{end} \rangle \end{bmatrix}$$

Figure 6.36 Matrix equations in which the nine CKM matrix elements and the flavor eigenstates of the six quarks are given explicitly.

$$\begin{bmatrix} V_{ud} & V_{us} & V_{ub} \\ V_{cd} & V_{cs} & V_{cb} \\ V_{td} & V_{ts} & V_{tb} \end{bmatrix} =$$

$$\begin{bmatrix} \langle u | u_w \rangle \langle u | c_w \rangle \langle u | t_w \rangle \\ \langle c | u_w \rangle \langle c | c_w \rangle \langle c | t_w \rangle \\ \langle t | u_w \rangle \langle t | c_w \rangle \langle t | t_w \rangle \end{bmatrix} \begin{bmatrix} \langle d_w | d \rangle \langle d_w | s \rangle \langle d_w | b \rangle \\ \langle s_w | d \rangle \langle s_w | s \rangle \langle s_w | b \rangle \\ \langle b_w | d \rangle \langle b_w | s \rangle \langle b_w | b \rangle \end{bmatrix}$$

Figure 6.37 CKM matrix as the product of two unitary transformation matrices that represent, separately for the u-type quarks and for the d-type quarks, the connection between the system of eigenstates of the electroweak interaction, and the system of quark mass eigenstates.

$$\begin{bmatrix} |d'\rangle \\ |s'\rangle \\ |b'\rangle \end{bmatrix} = \begin{bmatrix} V_{ud} & V_{us} & V_{ub} \\ V_{cd} & V_{cs} & V_{cb} \\ V_{td} & V_{ts} & V_{tb} \end{bmatrix} \begin{bmatrix} |d\rangle \\ |s\rangle \\ |b\rangle \end{bmatrix}$$

Weak eigenstates — Mass eigenstates

Figure 6.38 The d-type quark mass eigenstates being transformed by the CKM matrix into eigenstates of the electroweak interaction.

generation of quarks, Kobayashi and Maskawa together with Y. Nambu received the 2008 Nobel Prize in Physics.

The fact that the electroweak interaction mixes the three quark generations has led to the consideration of a system of eigenstates of the electroweak interaction $|d_w\rangle$, $u_w\rangle$, and $s_w\rangle$, also sometimes denoted $|d'\rangle$, $|u'\rangle$, and $|s'\rangle$, and the matrix equation has been rewritten as the product of two unitary transformation matrices A_{U_wU} and A_{D_wD}, respectively, that separately for u- and d-type quarks represent the connection between the system of the eigenstates of the electroweak interaction and the system of the quark mass eigenstates as shown in Figure 6.37. In compact form, this matrix product is

$$V_{UD} = A^*_{U_wU} A_{D_wD} \tag{6.77}$$

For the system of the d-type quarks, one often finds the notation given in Figure 6.38, where the quark mass eigenstates, under the weak interaction represented by the CKM matrix, are transformed into weak eigenstates.

In a theoretical sense, within the Standard Model, the CKM matrix is unitary. In an experimental sense, it must not necessarily fulfill the unitarity condition. The test of unitarity is a vivid subject of actual research. If the unitarity should be found to be violated, this would be a hint for physics beyond the Standard Model. For the first

row of matrix elements, $|V_{ud}|^2$ can be deduced from the lifetime of the free neutron or from the ft_0 values of superallowed $0^+ \rightarrow 0^+$ Fermi transitions or from pion β decay; $|V_{us}|^2$ can be determined from the semileptonic decay of K mesons; and $|V_{ub}|^2$ from the decay of the B meson. The present state is as follows.

From the decay of the free neutron which is presently best studied in storage experiments with ultracold neutrons (UCNs), we have

$$\tau^{-1} = \text{const}\, G_F^2 |V_{ud}|^2 (1 + 3|\lambda|^2) \tag{6.78}$$

and

$$|V_{ud}|^2 = \frac{(4908 \pm 4)\text{s}}{\tau \cdot (1 + 3|\lambda|^2)} \tag{6.79}$$

With the world average of the neutron lifetime $\tau = 885.7(7)$ s and the value for λ derived from a recent measurement of the β asymmetry in the decay of polarized neutrons

$$W_\beta(\Theta) = 1 + \frac{v_\beta}{c} A P_n \cos\Theta$$

where P_n is the degree of neutron polarization

$$A = \frac{2\lambda(\lambda + 1)}{1 + 3\lambda^2} = -0.1189\,(7)$$

$$\lambda = \frac{g_A}{g_V} = -1.2739\,(9)$$

we obtain $|V_{ud}| = 0.9717(13)$ from neutron decay. Together with the values for $|V_{us}| = 0.2196(23)$ from kaon decay and $|V_{ub}| = 0.0036(9)$ from B meson decay, the deviation from unitarity

$$\Delta = |V_{ud}|^2 + |V_{us}|^2 + |V_{ub}|^2 - 1 \tag{6.80}$$

$$\Delta = 0.0084 \pm 0.0028$$

according to Abele et al. (2002), which is a 3σ deviation from zero. If the values for nuclear β decay and pion decay

$$|V_{ud}| = 0.973\,8(4) \quad (0^+ \rightarrow 0^+)$$

$$|V_{ud}| = 0.972\,8(30) \quad \text{(pion)}$$

are combined with the neutron value (Abele et al. 2004), a deviation of

$$\Delta = 0.0040 \pm 0.0012$$

remains. The situation is depicted in Figure 6.39. A more recent value for the neutron lifetime reported by A. Serebrov et al. in 2005, $\tau = 878.5 \pm 0.8$ seconds, resulted in a deviation of

$$\Delta = -0.003\,8(28)$$

Thus, the present situation is unsatisfactory, and more high-precision measurements of the neutron lifetime in which nuclear chemists are heavily involved are urgently needed.

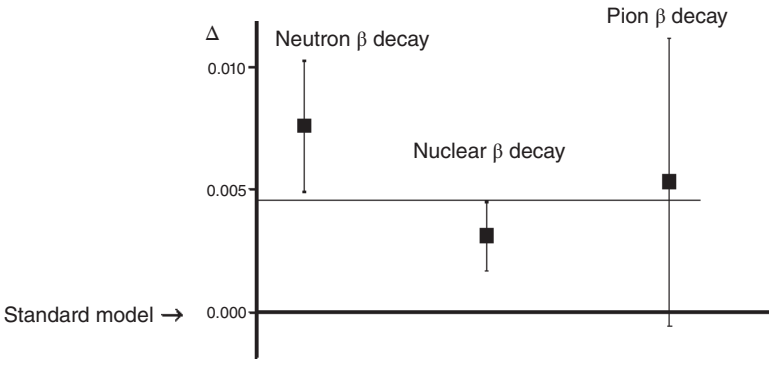

Figure 6.39 Deviations Δ from unitarity of the CKM matrix derived from the neutron β^- decay, nuclear β decay, and pion β decay.

6.7 Electromagnetic Transitions

Radioactive decay processes may leave the product nucleus in its ground state or, more frequently, in an excited state. Excited states are also populated in Coulomb excitation, in nuclear resonance absorption, and in nuclear reactions. In this chapter, we deal with the phenomena that occur in the deexcitation of excited states. Excited states can be of single-particle nature (particle–hole states) or collective vibrational or rotational states. A nucleus in an excited state may give away its excitation energy in a variety of ways. The most common transition is by emission of electromagnetic radiation called γ radiation. γ-Rays have a frequency ($>10^{20}$ Hz) determined by the decay energy $E = h\nu$ being in the kilo- to megaelectronvolt regime. Frequently, the transition does not proceed directly from the excited state to the ground state but may go in several steps involving intermediate excited states. As an example, the decay scheme of ^{198}Au is plotted in Figure 6.40. With 98.7% probability, ^{198}Au decays by β^- decay into the first excited state in ^{198}Hg, 0.412 MeV above the ground state, with 1.3% probability into the second excited state at 1.087 MeV above the ground state, and with 0.025% into the ground state of ^{198}Hg. Accordingly, three γ transitions are observed; the second excited state decays with 20% probability directly into the ground state and with 80% probability into the first excited state at 0.412 MeV, resulting in the following intensities relative to the total β^- intensity: γ(1.087) $1.3 \cdot 0.2 = 0.26\%$; γ(0.676) $1.3 \cdot 0.8 = 1.04\%$; γ(0.412) $98.7 + 1.3 \cdot 0.8 = 99.74\%$. All γ-rays are monoenergetic. Because the recoil energies given to the nucleus in a γ transition are very small compared to the energies of the γ-rays, the latter are practically equal to the excitation energies or the differences in excitation energies of the nuclei. γ-Ray emission may be accompanied, or even replaced, by the emission of internal conversion (IC) electrons.

In *internal conversion*, the decay energy of the nucleus is electromagnetically transferred to an extranuclear electron leading to the emission of an electron with a kinetic energy equal to the difference between the energy of the nuclear transition involved and the binding energy of the electron in the atom.

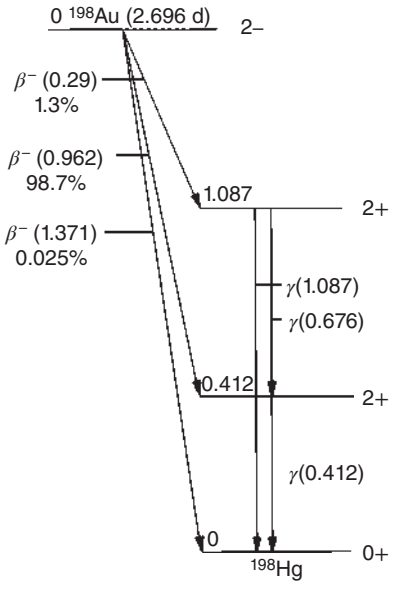

Figure 6.40 Decay scheme of ^{198}Au. The 1.087 MeV transition is $E2$, the 0.676 MeV transition is $E2 + 45\%\ M1$, the 0.412 MeV transition is $E2$.

A third process for the deexcitation of a nucleus is possible if the decay energy exceeds 1022 keV, the rest mass of two electrons. Then, it is possible for the nucleus to create an electron–positron pair and to emit them with kinetic energies that total the excitation energy minus 1022 keV. This is an uncommon mode of deexcitation. All these processes are characterized by a change in energy without change in Z and A.

The overwhelming majority of electromagnetic transitions take place on a time scale too short for direct measurements, that is, in $<10^{-12}$ seconds, an order of magnitude that would be expected for a dipole of nuclear dimensions and unit charge. As was indicated in Chapter 5, electromagnetic processes are of importance in all types of radioactivity measurements and in the establishment of nuclear level schemes whether or not their lifetimes can be measured. In particular cases, that is, for small decay energies E and for large differences in the initial and final nuclear angular momentum ΔI, electromagnetic transitions can be retarded by orders of magnitude, which is the case in the decay from isomeric states. An example of a much-retarded isomeric transition (IT) is the decay of ^{186m}Re with a half-life of $2 \cdot 10^5$ years with a decay energy of 59 keV and a transition from an 8^+ state to a 1^- state.

6.7.1 Multipole Order and Selection Rules

Electromagnetic transitions are associated with a change in the charge or current distribution in nuclei. As charge distributions give rise to electric moments and current distributions to magnetic moments, the transitions are classified as electric (E) and magnetic (M). They are described by solutions of the Maxwell equations for the radiation field of an oscillating charge or current distribution and expressed as an expansion in spherical harmonics of order 1, 2, 3, 4 ... , called multipole order.

The successive terms in this multipole expansion are transitions in which the radiation field carries off 1, 2, 3, 4 ... units of angular momentum. We see that, as in β decay, transition probabilities fall off rapidly with increasing angular momentum changes. The accepted nomenclature is to refer to radiation carrying off $l = 1, 2, 3, 4$ ... units of $\hbar$ as dipole, quadrupole, octupole, hexadecapole (i.e. 2^l pole) radiation. The shorthand notation for an electric 2^l pole transition is El and for a magnetic 2^l pole transition Ml. Thus, $E2$ means electric quadrupole, $M4$ magnetic hexadecapole. The electric and magnetic multipole transitions differ in their parity properties. If we denote even and odd parity of the radiation by +1 and −1, electric 2^l pole radiation has parity $(-1)^l$ and magnetic 2^l pole radiation has parity $(-1)^{l+1}$. As a γ-ray must carry away at least $1\hbar$, γ emission is not possible for $E0$ transitions where only internal conversion is possible.

From what was said above about angular momenta associated with 2^l pole transitions, it follows that $l \geq |I_i - I_f|$. Consideration of the vector addition of the angular momenta involved leads to the further restriction that l cannot exceed $I_i + I_f$ so that the selection rule for the total angular momenta of the initial and final state and the angular momentum carried away by the radiation field l is

$$I_i + I_f \geq l \geq |I_i - I_f| \tag{6.81}$$

for both electric and magnetic transitions. If the initial and final states have the same parity, electric multipoles of even l and magnetic multipoles of odd l are allowed. Equation (6.81) tells us that, if the transition is between a 4^+ and a 2^+ state, multipole orders l can range from 2 to 6, but because the parity rules $E2$, $M3$, $E4$, $M5$, and $E6$ are the only transitions possible. The actual situation is much simpler because, as a rule, only the lowest multipole order or sometimes the lowest two contribute appreciably to the intensity. This is because the transition probability is proportional to $(R/\lambda)^{2l}$ where R is the nuclear radius and λ is the wavelength of the emitted radiation divided by 2π. λ is always large compared to nuclear dimensions (for a 1 MeV photon, $\lambda \approx 2{\cdot}10^{-11}$ cm) so that the next higher multipole order will be reduced in intensity by several orders of magnitude. Exceptions to this rule occur when the lowest transition is magnetic dipole ($M1$); here, $E2$ transitions can often compete favorably. This is in line with the fact that current densities in nuclei giving rise to magnetic multipoles are smaller than the charge densities producing electric multipoles by $(v/c) \cong 10^{-2}$, where v represents the speed of the charges (protons) in the nucleus. Accordingly, we expect $E(l+1)$ transitions to compete with Ml transitions, particularly for $l = 1$.

The selection rules are summarized in Table 6.4. Significant special cases are $0 \rightarrow 0$ transitions which cannot take place by single-photon emission because a photon must remove at least 1 unit of angular momentum. This condition can always be fulfilled for $\Delta I = 0$ transitions by proper orientation of the vectors $\mathbf{I}_i$ and $\mathbf{I}_f$. If there is no change in parity in a $0 \rightarrow 0$ transition, deexcitation may only occur by internal conversion. If $\Delta E \geq 1022$ keV, the transition may involve the simultaneous emission of an electron–positron pair. The former mode is observed for transitions to the 0^+ ground states from other 0^+ states in ^{82}Ge ($\Delta E = 0.691$ MeV; $t_{1/2} = 0.42\,\mu$s) and in ^{214}Po ($\Delta E = 1.415$ MeV; partial $t_{1/2} = 0.8$ ns). Pair emission is observed, for example, from the first excited state in ^{16}O ($\Delta E = 6.05$ MeV; $t_{1/2} = 0.05$ ns) and from a 1.84 MeV

Table 6.4 Selection rules for electromagnetic transitions.

ΔI	$0^{a)}$	$0^{a)}$	1	1	2	2	3	3	4	4	…
$\Delta\Pi$	No	Yes	No	Yes	No	Yes	No	Yes	No	Yes	
Transition	$M1$	$E1$	$M1$	$E1$	$E2$	$M2$	$M3$	$E3$	$E4$	$M4$	
	$E2$		$E2^{b)}$			$(E3)^{b)}$	$(E4)^{b)}$			$(E5)^{b)}$	

a) The selection rule (Eq. (6.81)) excludes any single-photon transition when $I_i = I_f = 0$. For transitions between two $I = 1/2$ states of equal parity, $E2$ is forbidden, but $M1$ is allowed.

b) When one of the states involved in a transition has $I = 0$ and the allowed transition of lowest order is a magnetic multipole, the next higher electric multipole is strictly forbidden by Eq. (6.81).

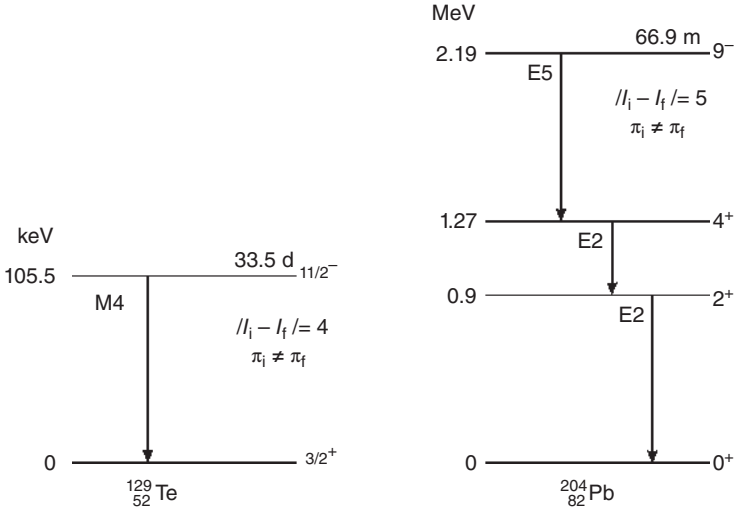

Figure 6.41 Examples of the application of the selection rules for electromagnetic transitions (Table 6.4) to isomeric states in ^{129}Te and ^{204}Pb.

state in ^{42}Ca ($t_{1/2} = 0.33$ ns). Transitions between two $I = 0$ states of opposite parity cannot take place by any single-photon transition; it would require the simultaneous emission of two γ quanta or two conversion electrons, which has not been observed.

Examples for the application of the selection rules are given in Figure 6.41 where the $11/2^- \rightarrow 3/2^+$ transition in ^{129}Te has to be assigned to a $M4$ transition and the $9^- \rightarrow 4^+$ transition in ^{204}Pb is identified with an $E5$ transition. In both cases, the high multipole orders lead to long lifetimes of the decaying state, that is, to isomeric states.

6.7.2 Transition Probabilities

In this section, we want to return to a more quantitative discussion of transition probabilities for γ transitions with the aim of comparing theoretical predictions to experimental observations. It has already been stated that the transition probability for emission of 2^l pole radiation of wavelength λ from a nucleus of radius R should be

roughly proportional to $(R/\lambda)^{2l}$. Since $R \propto A^{1/3}$ and $E_\gamma = \hbar c/\lambda$ (or $E_\gamma \lambda = 197$ MeV fm), we get an estimate for the transition probability or partial decay constant for γ emission

$$\lambda_\gamma \propto E^{2l} A^{2l/3} \tag{6.82}$$

A more detailed analysis gives an E^{2l+1} dependence, and both the A and E dependence become steeper with increasing multipole order.

To calculate absolute transition probabilities, one needs to make more specific assumptions about the charge and current distributions in nuclei, that is, one has to select a particular nuclear model. The simplest model for this purpose is the extreme single-particle model, see Section 5.5, where one assumes that the λ transition can be described as the transition of a single proton from one quantum state to another, whereby the rest of the nucleus is represented as the mean-field potential. In this framework, V.F. Weisskopf derived expressions for decay constants for electric and magnetic 2^l pole transitions. The transition probability is

$$\lambda(\sigma, l, m) = \frac{8\pi(l+1)}{l\hbar[(2l+1!!)]^2}\left(\frac{\omega}{c}\right)^{2l+1}|M^\sigma_{lm}|^2 \tag{6.83}$$

where 5!! stands for 1·3·5 and 6!! stands for 2·4·6, and so on. $\sigma = E$, M stands for the multipole character. M is the transition matrix element $M_{l,m} = \langle\psi_2|M_{\mathrm{op}}|\psi_1\rangle$ that is being formed between the proton states ψ_1 and ψ_2 with the multipole operator M_{op}. For $l = 1$, $\sigma = E$ ($E1$ transition), Eq. (6.83) gives the radiated power $\lambda \cdot \hbar\omega \propto (\omega^4 / c^3)D^2$ where D stands for the dipole matrix element. This corresponds to the classical formula for a Hertz dipole with the dipole moment D. The matrix elements $M_{l,m}$ can be calculated in a central mean potential. One integrates separately over the spherical harmonics in ψ. The result for the transition probability for electric multipole radiation is

$$\lambda(El) = \frac{2(l+1)\omega}{l[2(2l+1)!!]^2}\left(\frac{e}{\hbar c}\right)^2\left(\frac{R}{\lambda}\right)^{2l} S|M_{El}|^2 \tag{6.84}$$

The corresponding equation for $\lambda(Ml)$ contains the additional factor $10(\hbar m_{\mathrm{p}} cR)^2$. One is averaging here over the unobserved magnetic substates. The matrix element depends only on the radial wave functions. S is a statistical factor depending on I_{i}, I_{f}, and l and stems from the integrals over the spherical harmonics. S is usually not much different from 1. A simple estimate of the matrix elements is obtained by assuming the radial wave functions to be constant over the nuclear volume. One then obtains, for example,

$$M_{El} = \frac{3}{3+l} \tag{6.85}$$

One often gives transition probabilities in units of the values calculated with Eqs. (6.84) and (6.85), which are called Weisskopf units and are extreme single-particle units. Practical variants of the Weisskopf formulas are

$$\lambda(El) = \frac{4.4(l+1)10^{21}}{l[(2l+1)!!]}\left(\frac{3}{3+l}\right)^2\left(\frac{E_\gamma}{197}\right)^{2l+1} R^{2l}\ \mathrm{s}^{-1} \tag{6.86}$$

$$\lambda(Ml) = \frac{1.9(l+1)10^{21}}{l[(2l+1)!!]}\left(\frac{3}{3+l}\right)^2\left(\frac{E_\gamma}{197}\right)^{2l+1} R^{2l-2}\,\mathrm{s}^{-1} \tag{6.87}$$

If the transition occurs between more complicated configurations, the matrix element in Eq. (6.83) must be replaced by an averaging over the initial states and a summation over the final states of the following form:

$$B(\sigma l, I_1 \to I_2) = \frac{1}{2I_1+1}\sum_{m_1,m_2,m}\left|\sum_p M_{l,m}(p)\right|^2 \tag{6.88}$$

which is called reduced transition probability. The sum with the index p is a sum of single-particle matrix elements over all participating nucleons. The reduced transition probabilities are important in the case of transitions between states that are due to collective excitations. In particular for collective $E2$ transitions, the $B(E2)$ transition probabilities can be 10–100 times larger than the single-particle matrix elements. A survey of the existing lifetimes of electromagnetically decaying states will be given below.

The results of the calculations mentioned above are transition probabilities for γ-ray transitions. From these, we obtain immediately the average lifetime $\tau = 1/\lambda$ for the excited state, given the fact that it decays exclusively by γ radiation. For the examination of nuclear model concepts that enter into the calculation of the matrix elements, one needs comparisons to experimental lifetimes. The most important methods for the determination of lifetimes are the following:

a) Direct measurement of the lifetime. For ITs, one can measure the decay curve and deduce from it the half-life. For shorter-lived states, the electronic determination by delayed coincidences is applicable over a wide range of lifetimes. For this, one needs a start signal that can be delivered either by the nuclear reaction populating the interesting state or by a preceding radioactive decay. This works down to lifetimes on the order of 10^{-10} seconds.
b) Doppler shift methods. An excited nucleus that is produced in a nuclear reaction in a thin target leaves the target with a given velocity that results from momentum conservation. The energy of a γ-ray emitted in flight is shifted relative to the energy of the γ-ray emitted at rest by the Doppler effect. One can, for example, stop the excited reaction products after a selectable flight distance in a catcher foil, the so-called plunger. Those nuclei that reach the plunger in the excited state deliver after stopping an unshifted γ-ray line, while those that decay earlier show the Doppler shift. If one plots the intensity ratio of the two lines as a function of the distance of the plunger from the target, the lifetime of the excited state can be deduced.

Even shorter lifetimes can be observed if the excited recoil nucleus is directly implanted in a catcher. If the lifetime of the excited level is on the order of the time required for the deceleration process in the solid, one can again make use of the Doppler effect. In the forward direction, emissions occurring at the beginning of the deceleration process give a shifted γ-ray line, those at the end an unshifted one. Because, during emission, all velocities are present, one observes a continuum

between the extreme energies. In practice, this results in a broadening of the γ line and in a shift of its centroid. A broadened but unshifted γ line is observed under 90° relative to the beam direction because, in this direction, momentum components of both signs are equally abundant. The deduction of a lifetime from the line shift requires detailed knowledge of the time dependence of the deceleration in matter. This Doppler shift attenuation method is applicable in the range of $5 \cdot 10^{-12}$ to 10^{-13} seconds. Application of the Doppler shift attenuation method has only become feasible with the advent of high-resolution Ge semiconductor detectors as the line width delivered by the spectrometer must be smaller than the Doppler shift.

c) Measurement of the natural line width. The natural line width can in some cases be determined by Mössbauer spectroscopy, from which the average lifetime results immediately.
d) Determination by Coulomb excitation where a nucleus is excited by the time-dependent Coulomb field of a passing ion. From the intensity of the γ-ray line (or from the cross section), the reduced transition probabilities can be deduced, see Section 5.11. The accessible lifetimes are in the range of $\tau > 10^{-13}$ seconds.

We return now to a survey of the existing lifetimes. The single-particle transition probabilities that are obtained under the simplifying assumptions of Eqs. (6.84) and (6.85) as well as from corresponding equations for magnetic transition rates are depicted in Figure 6.42 as a function of γ-ray energy. The calculations have been done for $A = 100$, $S = 1$, $r_0 = 1.2$ fm. It is evident, for example, for $E_\gamma = 0.5$ MeV, that the decay constants λ vary between 10^{14} s^{-1} (for $E1$) and 10^{-8} s^{-1} (for $E5, M5$). These estimates can only be a rough approximation of the true processes inside a nucleus. If one compares the single-particle transition probabilities to experimental values, one finds the following behavior: $E1$ transitions are normally slower by factors of 10^3 to 10^7, and most of the $E2$ transitions are roughly a factor of 10^2 faster than the Weisskopf estimates. For the other transitions, the transition rates are approximately of the correct order of magnitude or larger.

The small transition probabilities for electric dipole transitions are understandable according to the shell model as most of the $E1$ transitions at low energy occur between very complicated configurations. For "collective dipole transitions," the total charge of the nucleus would have to oscillate. Within the liquid-drop model, this would require the vibration of the entire proton liquid against the neutron liquid. For this, a very large excitation energy is required. Such transitions are indeed observed in the energy range of giant resonances, Section 5.11. On the other hand, the particularly large transition probability for $E2$ transitions is indeed correlated with collective excitations. We take this opportunity to come back to the electromagnetic transition probabilities between rotational states that we touched upon in Sections 5.6 and 5.11. Because the inner wave function of the nucleus in these transitions is not supposed to change, we see here transitions between various rotating deformed charge distributions that rotate with different frequencies. It is natural that this involves the deformation, that is, the electric quadrupole moment,

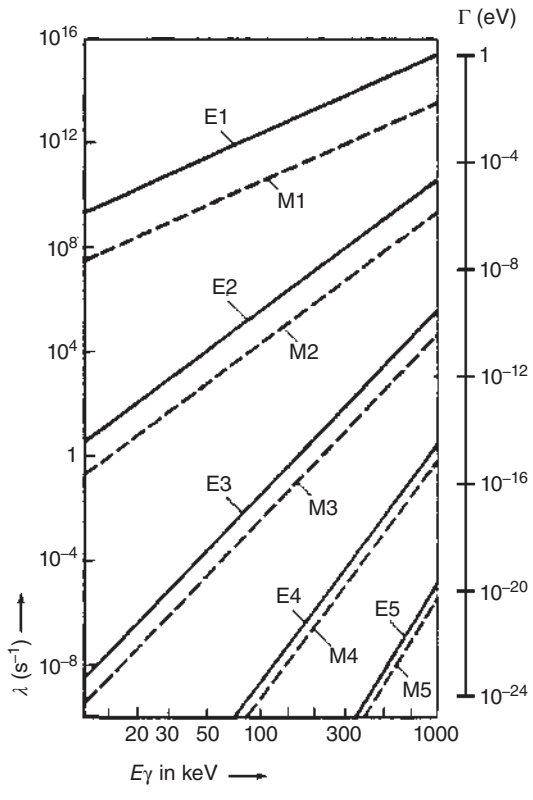

Figure 6.42 Single-particle γ-transition probabilities λ for various multipole orders against γ-ray energy. The calculations were performed for $A = 100$, $S = 1$, and $r_0 = 1.2$ fm. To the right, the respective decay widths $\Gamma = \hbar/\tau$ are indicated.

Section 4.4. We have to distinguish here between the spectroscopic quadrupole moment, Eq. (4.28), as it is observed in the laboratory system (x, y, z) and an "inner" quadrupole moment Q_0 of a nucleus that is relevant in the body-fixed coordinate system (1, 2, 3). In the latter, we look at a classical system that is deformed in the three directions. For this, we can calculate an "inner" quadrupole moment in the (1, 2, 3) system. The quadrupole moment Q_β, on the other hand, refers to a z axis that is rotated against the axis of deformation of the nucleus by an angle θ and we obtain

$$Q_\beta = \frac{1}{2}(3\cos^2\beta - 1)Q_0 \tag{6.89}$$

For a quantum system, Q_β corresponds to the spectroscopic quadrupole moment for small deformations. For a body-fixed "inner" quadrupole moment for the nucleus in the (1, 2, 3) system, we have

$$Q_0 = \langle\chi|Q_{\text{op}}|\chi\rangle \tag{6.90}$$

where χ is the inner wave function in the deformed potential and Q_{op} is the quadrupole operator

$$Q_{\text{op}} = \frac{1}{e}\int r^2(3\cos^2\Theta - 1)\rho(r)\mathrm{d}\tau \tag{6.91}$$

applied in the body-fixed system. For a given model for the angular momentum coupling such as in Figure 5.11, one can deduce the spectroscopic quadrupole moment Q from Q_0 according to

$$Q = \frac{3K^2 - I(I+1)}{(I+1)(2I+3)} Q_0 \tag{6.92}$$

which is analogous to the classical Eq. (6.89). For $K = I = 0$ or $K = I = 1/2$, the first factor in Eq. (6.92) is 0. Therefore, the quantity Q_0 is not observable for the ground state of even–even nuclei, but it is relevant for transition probabilities between different rotational states. In order to find these transition probabilities, we have to make use of the matrix element for reduced transition probabilities, Eq. (6.88). Because for a quadrupole transition between two rotational levels, only the eigenfunction for the rotation of the entire nucleus is changed, but not the eigenfunction for the inner structure of the nucleus, the reduced matrix element is of a relatively simple form

$$B(E2, I_1 \to I_2) = \frac{5}{16\pi} e^2 Q_0^2 \langle I_1, K, 2, 0 \mid I_2, K\rangle^2 \tag{6.93}$$

in which the last term is a Clebsch–Gordon coefficient which is a general normalization coefficient for the angular momenta and the angular momentum projections that can be found in standard references. For transitions between states of a rotational band, $K = 0$, $I_1 = I$, and $I_2 = I - 2$, the coefficient only contains values of I:

$$\langle I_1, K, 2, 0 \mid I_2 K\rangle^2 = \langle I, 0, 2, 0 \mid (I-2)0\rangle^2 = \frac{3I(I-1)}{2(2I+1)(2I-1)}$$

so that the reduced transition probability is

$$B(E2, I_1 \to I_2) = \frac{15}{32\pi} e^2 Q_0^2 \frac{I(I-1)}{(2I+1)(2I-1)} \tag{6.94}$$

As the quadrupole moment Q_0 is much larger in a deformed nucleus than that in a single-particle model for a single nucleon, Eq. (6.94) predicts much larger transition probabilities than for single-particle transitions. However, a change in the quantum number K corresponds to a change in the inner nuclear structure and, therefore, the transition rates between states belonging to different K bands are only on the order of single-particle transition rates. Furthermore, one can show that for $E2$ transitions, the selection rule is $\Delta K = 0, \pm 1, \pm 2$. In summary, from the observed transition probabilities or lifetimes, relations such as Eq. (6.94) serve to deduce inner quadrupole moments Q_0.

6.7.3 Internal Conversion Coefficients

Internal conversion (IC) is a competing process to γ-ray emission. In this case, the excited nucleus interacts electromagnetically with an orbital electron and transfers radiationless the nuclear excitation energy to the electron. The kinetic energy of the IC electron, E_{IC}, is equal to the difference between the energy of the nuclear transition and the binding energy of the electron in the atom. For the 0.412 MeV transition in the β^- decay of ^{198}Au (Figure 6.40), the spectrum of emitted IC electrons is depicted in Figure 6.43 showing lines for the ejection of electrons from the

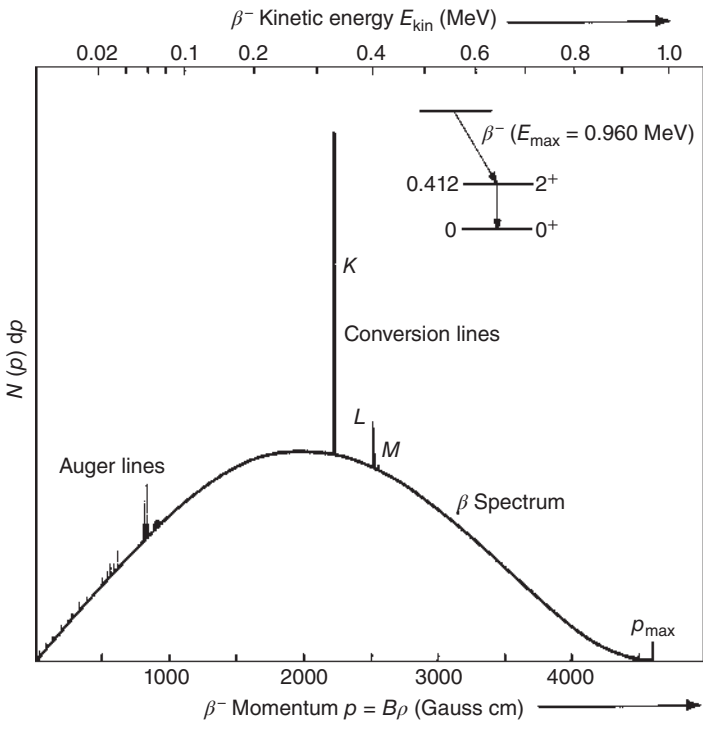

Figure 6.43 Internal conversion electron spectrum for a 412 keV transition in ^{198}Hg. Source: Marmier and Sheldon (1969)/Elsevier.

K, L, and M shells with the principal quantum numbers of 1, 2, or 3, respectively. The IC process leaves the atom with a vacancy in one of these shells leading, as in EC, to the emission of X-rays and Auger electrons. Superimposed on this spectrum is the accompanying spectrum of β^- particles from the β decay that feeds the excited state. The ratio of the rate of the IC process to the rate of γ emission is known as the conversion coefficient α, having values between zero and infinity. Separate coefficients for internal conversion in the K, L, and M shells (α_K, α_L, α_M) and even in the subshells (α_{LI}, α_{LII}, α_{LIII}) may be measured as well as computed. In general, the coefficients for any shell increase with decreasing energy, increasing multipolarity, and increasing Z. This is shown in Figure 6.44 separately for electric and magnetic transitions. Note that the decay constant

$$\lambda = \lambda_{IC} + \lambda_\gamma = \lambda_\gamma(1 + \alpha) \tag{6.95}$$

and

$$\alpha_{total} = \alpha_K + \alpha_L + \alpha_M + \cdots \tag{6.96}$$

The internal conversion coefficient depends on the density of the atomic electrons at the nucleus and can be calculated using principles from atomic physics. Large

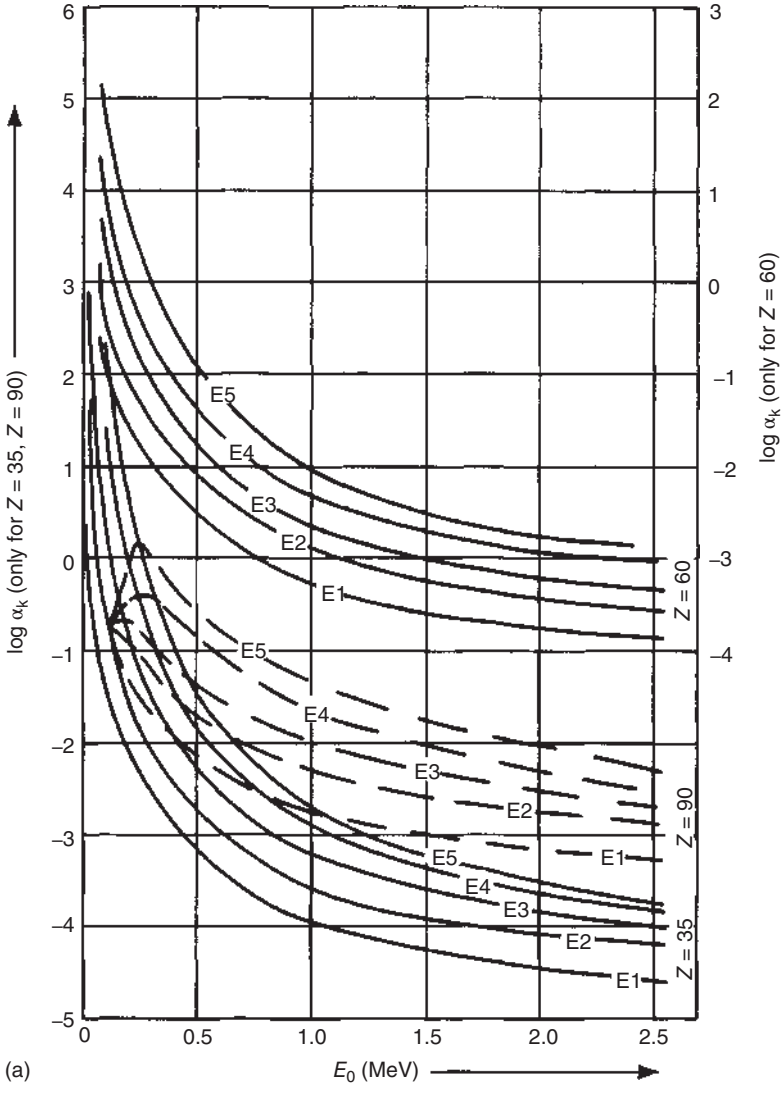

Figure 6.44 Semilogarithmic plots of K conversion coefficients for (a) electric and (b) magnetic multipole transitions in nuclei with atomic numbers $Z = 35$, 60, and 90, using data tabulated by Sliv and Band, in terms of the transition energy E_0. Source: Marmier and Sheldon (1969)/Elsevier.

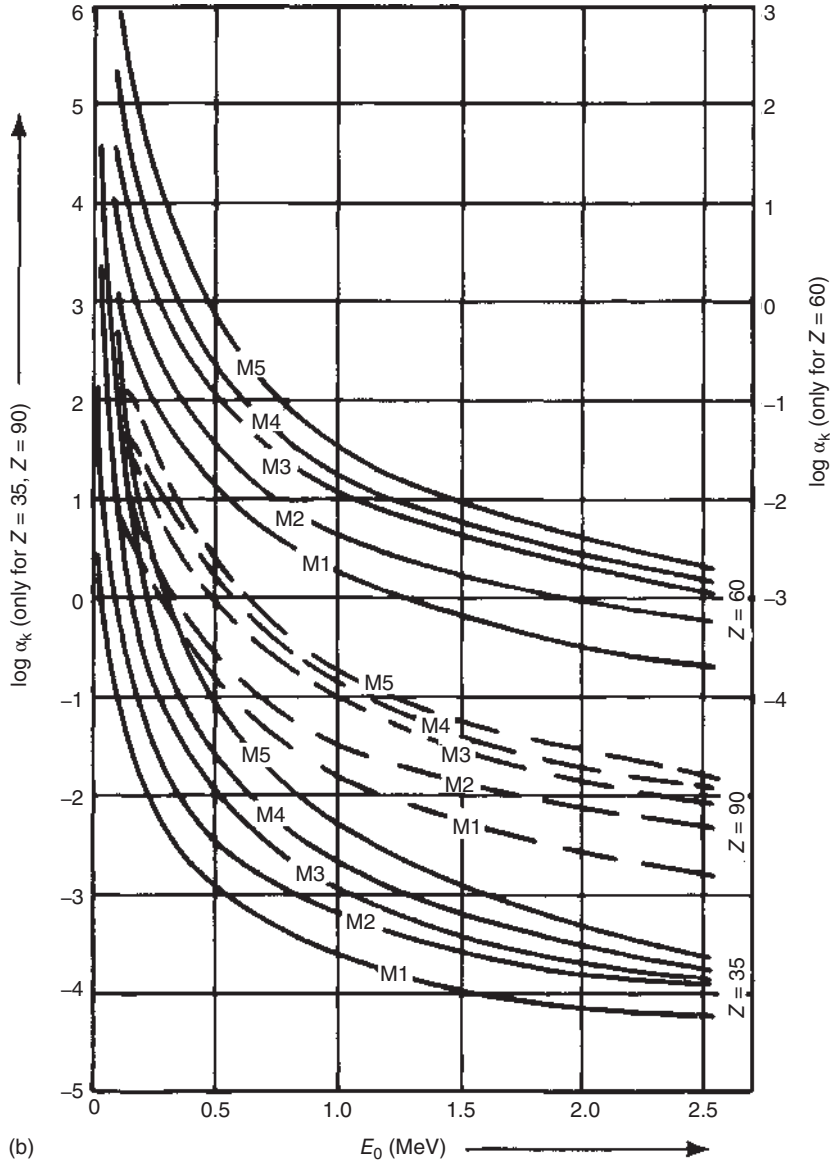

Figure 6.44 (*continued*)

tables and nomographs (Figure 6.44) of IC coefficients are available. Rough approximations for the coefficients are

$$\alpha(El) = \frac{Z^3}{n^3}\left(\frac{l}{l+1}\right)\left(\frac{e^2}{4\pi\varepsilon_0\hbar c}\right)^4\left(\frac{2m_e c^2}{E}\right)^{l+5/2} \tag{6.97}$$

$$\alpha(Ml) = \frac{Z^3}{n^3}\left(\frac{e^2}{4\pi\varepsilon_0\hbar c}\right)^4\left(\frac{2m_e c^2}{E}\right)^{l+3/2} \tag{6.98}$$

Table 6.5 Comparison of the experimental and calculated conversion coefficient ratios for the decay of a 124 keV level in ^{173}Lu.

		Calculated			
	Experimental	***E*1**	***E*2**	***M*1**	***M*2**
α_K/α_L	4.88	3.6	$6 \cdot 10^{-2}$	4.2	1.0
α_{LI}/α_{LII}	3.57	2.3	$2.2 \cdot 10^{-2}$	12	11
$\alpha_{LII}/\alpha_{LIII}$	0.87	0.8	0.9	6.5	0.25

where n is the principal quantum number of the electron and $e^2/4\pi\epsilon_0\hbar c$ is the fine-structure constant 1/137. The α_K/α_L ratio is approximately 8 due to the n^3 factor.

Experimental determination of absolute conversion coefficients is difficult, since it entails the measurement of conversion electron and γ-ray intensities, both with known detection efficiencies. In practice, it is much easier to determine in an electron spectrograph the relative intensities of two or more conversion electron lines belonging to the same transition and to compare these ratios to theoretical values. Such ratios can be used to great advantage to characterize the multipole order of the transition and thus ΔI and $\Delta\pi$. This is an important tool in nuclear spectroscopy. An example is given in Table 6.5 for the conversion of a 124 keV level in ^{173}Lu being fed in the EC decay of ^{173}Hf. The best agreement between the experimental conversion coefficient ratios and the calculated ones is given for an $E1$ transition between the $5/2^-$ state and the $7/2^+$ ground state in ^{173}Lu.

6.7.4 Angular Correlations

We have tacitly assumed in our previous discussion of the various techniques for identification of the multipole order of electromagnetic transitions – half-lives and conversion coefficients – that the γ-rays themselves bear no sign of the multipole interaction. This is the case under normal circumstances. However, the solutions of the Maxwell equations are multipole fields giving rise to different angular distributions of the emitted radiation with respect to the direction of the nuclear angular momentum. We normally deal with sources that contain randomly oriented nuclei, and therefore, the observed angular distribution of γ-rays is isotropic. In the case of the Wu experiment, we have already encountered one method for obtaining the alignment of nuclear angular momenta by the application of a strong external magnetic field near 0 K. This technique is costly and has found limited but important applications.

A more widely applied method for obtaining partially oriented nuclei is to observe a γ-ray in coincidence with a preceding radiation which may be an α or β particle or a preceding γ radiation. By selecting a particular direction of emission for this first radiation, the first particle provides the reference axis, but it must also introduce an unequal population of the magnetic substates of the intermediate state in order for

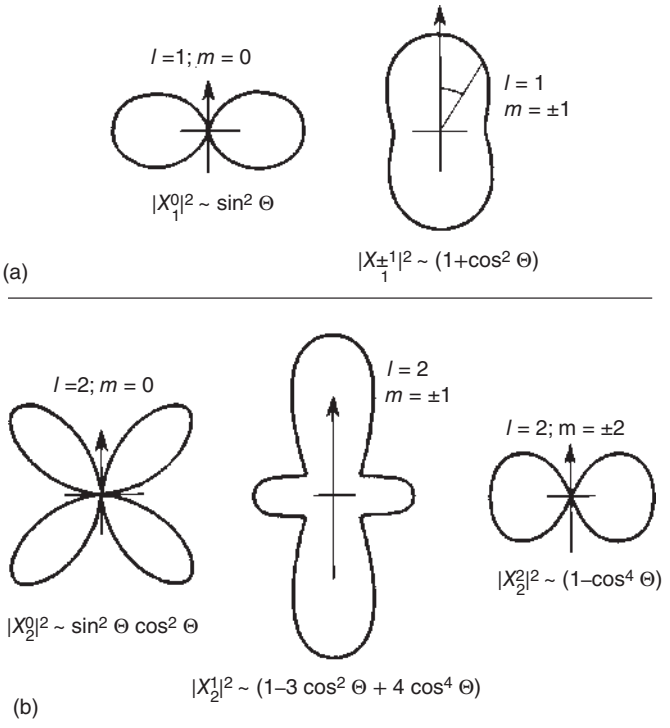

Figure 6.45 Angular distribution $|X_l^m(\Theta)|^2$ for (a) dipole and (b) quadrupole transitions. Source: Mayer-Kuckuk (1979)/John Wiley & Sons.

the second transition to have an anisotropic angular distribution. This way, we select a preferred direction of the angular momentum of the intermediate nucleus provided the lifetime of this state is short enough for the orientation to be preserved until the second γ-ray is emitted. The direction of the γ-ray emission will be correlated with the direction of emission of the preceding radiation if a coincidence experiment is done in which the angle θ between the two sample detector axes is varied and the coincidence rate is determined as a function of θ.

The angular distribution of the multipole radiation is directly related to the properties of the normalized spherical harmonics $\mathbf{X}_l^m(\Theta, \phi)$. The intensity relative to the quantization axis z is directly proportional to $|\mathbf{X}_l^m|^2$. In Figure 6.45, the resulting distributions are depicted for dipole and quadrupole transitions. These functions are cylindrically symmetric. Thus, there is no asymmetry in the radiation from systems with only two substates, namely, $I = 1/2$, $m_I = \pm 1/2$. The intensity of $m = 0$ for dipole radiation is zero along the z axis because the sine function becomes zero. Conversely, for $l = 1$, $m = \pm 1$ most quanta are emitted in the z direction and the distribution has non-zero minima perpendicular to the z axis.

It is worthwhile to consider the case of a dipole–dipole cascade involving levels with angular momenta 0, 1, and 0 as depicted in Figure 6.46. The direction of the source S to the detector D_1 for the first γ quantum γ_1 defines the z axis. As $\Delta I = 1$, we have a dipole transition. Of the two possible angular distributions, $|X_1^0|^2$ and $|X_1^{\pm 1}|^2$,

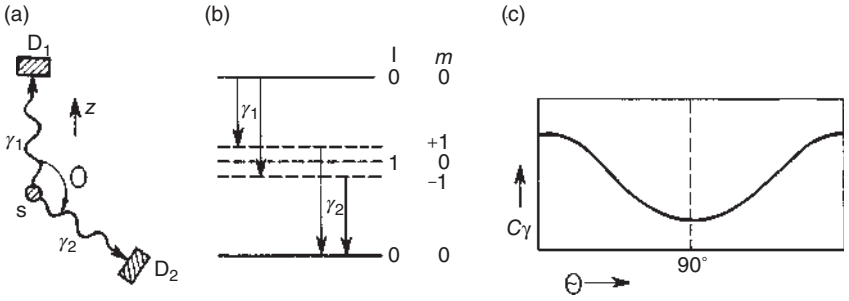

Figure 6.46 Angular correlation of a $0 \rightarrow 1 \rightarrow 0$ dipole–dipole cascade: (a) experimental principle; (b) level scheme and γ transitions; (c) coincidence rate C_γ as a function of the angle θ between detectors D_1 and D_2. Source: Mayer-Kuckuk (1979)/John Wiley & Sons.

only $|X_1^{\pm 1}|^2$ emits quanta in the z direction. With respect to the quantization axis defined by detector D_1, only the states with magnetic quantum numbers $m = +1$ and $m = -1$ can be occupied in the intermediate level. In Figure 6.46, the substates are depicted separately even though they have the same energy. It is evident from Figure 6.46 that the second γ quantum γ_2 must again cause a change of $\Delta m = \pm 1$ with respect to the z direction. This corresponds to the distribution $|X_1^{\pm 1}|^2$ in Figure 6.45 that is observed if the coincidence rate C_γ is plotted against the angle θ between D_2 and D_1. C_γ varies between 0° (180°) and 90° by 2 : 1.

Generally, the angular correlations are analyzed in terms of a power series of even Legendre polynomials

$$W(\Theta) = 1 + A_2 P_2(\cos\Theta) + A_4 P_4(\cos\Theta) + \cdots \tag{6.99}$$

The coefficients A are compared to tabulated values for given sequences of angular momenta. Only even polynomials are required as, in the emission, parity is conserved. This causes an angular distribution symmetric about 90°.

The example described above becomes even clearer if we suppose that a dipole quantum in the direction of emission carries angular momentum +1 or −1; that is, that the angular momentum vector is either parallel or antiparallel to the momentum of the quantum. Therefore, after the $0 \rightarrow 1$ transition, the nuclear angular momentum must be either antiparallel or parallel to the direction of emission. Relative to that direction, the second quantum is emitted with the dipole distribution for $\Delta m = \pm 1$. If we now apply a magnetic field perpendicular to the plane defined by the two detectors, the angular momentum of the intermediate state will rotate with the Larmor frequency ω_L given by Eq. (4.21) until the second emission occurs. If the average lifetime of the intermediate state is not too short, one observes a rotation of the angular distribution by a mean angle of precession. One observes a precession if the lifetime $\tau > \hbar/E$ where E is the interaction energy. For a known magnetic flux density and a known average lifetime, this allows the magnetic moment of the intermediate state to be determined. As one is determining the product of the g factor and the magnetic field, one needs to know the contribution of the electron shell to the magnetic field at the location of the nucleus. Conversely, one can draw conclusions about the magnetic field of the electron shell if one carries out the

experiment in different chemical environments. This application of a fundamental nuclear phenomenon to applied research in condensed matter has been called perturbed angular correlation (PAC) and is discussed in Section 14.3.

References

Alpha Decay

Geiger, H. and Nuttall, J.M. (1911). The ranges of α particles from various radioactive substances and a relation between range and period of transformation. *Philos. Mag.* 22: 613 and 23: 439 (1912); *Z. Phys.* 8: 45.

Gamow, G. (1928). Zur Quantentheorie des Atomkerns. *Z. Phys.* 51: 204.

Gurney, R.W. and Condon, E.U. (1928). Quantum mechanics and radioactive disintegration. *Nature* 122: 439 and *Phys. Rev.* 33: 127 (1929).

Friedlander, G., Kennedy, J.W., Macias, E.S., and Miller, J.M. (1981). *Nuclear and Radiochemistry*, 3e. New York: Wiley.

Cluster Radioactivity

Sandulescu, A., Poenaru, D.N., and Greiner, W. (1980). New type of decay of heavy nuclei intermediate between fission and α decay. *Sov. J. Part. Nucl.* 11: 528.

Rose, H.J. and Jones, G.A. (1984). A new kind of natural radioactivity. *Nature* 307: 245.

Balysh, A.Y., Gurov, A.A., Demekhin, A.V. et al. (1986). Radiochemical search for the decay of ^{233}U with the emisssion of ^{24}Ne using a low-background semiconductor gamma-ray spectrometer. *Sov. Phys. JETP* 64: 21.

Proton Radioactivity

Hofmann, S. (1995). Proton radioactivity. *Radiochim. Acta* 70/71: 93.

Spontaneous Fission

Bohr, N. and Wheeler, J.A. (1939). The mechanism of nuclear fission. *Phys. Rev.* 56: 426.

Cohen, S. and Swiatecki, W.J. (1963). *Ann. Phys. (N.Y.)* 22: 406.

Habs, D. and Metag, V. (1978). Messung Extremer Kerndeformation von Spaltisomeren. *Phys. Bl.* 12: 647.

Polikanov, S.M., Druin, V.A., Karnaukov, V.A. et al. (1962). Spontaneous fission with anomalously short period. I. *Sov. Phys. JETP* 15: 1016.

Myers, W.D. and Swiatecki, W.J. (1966). Nuclear masses and deformations. *Nucl. Phys.* 81: 1.

Vandenbosch, R. and Huizenga, J.R. (1973). *Nuclear Fission*. New York: Academic Press.

Beta Decay

Steinberg, E.P. and Glendenin, L.E. (1954). Radiochemical investigation of the spontaneous fission of Cm^{242}. *Phys. Rev.* 195: 437.

Moszkowski, S.A. (1951). Rapid method of calculating Log(*ft*) values. *Phys. Rev.* 82: 35.

Lee, T.D. and Yang, C.N. (1956). Question of parity conservation in weak interactions. *Phys. Rev.* 104: 254.

Nix, J.R. (1972). Calculation of fission barriers for heavy and superheavy nuclei. *Annu. Rev. Nucl. Sci.* 22: 65.

Kobayashi, M. and Maskawa, T. (1973). CP-violation in the renormalizable theory of weak interactions. *Prog. Theor. Phys.* 49: 652.

Abele, H., Astruc Hoffmann, M., Baeβler, S. et al. (2002). Is the unitarity of the quark-mixing CKM matrix violated in neutron β- decay? *Phys. Rev. Lett.* 88: 211801.

Abele, H., Barberio, E., Dubbers, D. et al. (2004). Quark mixing, CKM unitarity. *Eur. Phys. J.* C33: 1.

Further Reading

Alpha Decay

Perlman, I., Ghiorso, A., and Seaborg, G.T. (1950). Systematics of alpha radioactivity. *Phys. Rev.* 77: 26.

Mang, H.J. (1957). Zur Theorie des α-Zerfalls (Insbesondere der Kerne in der Umgebung von ^{208}Pb). *Z. Phys.* 148: 582.

Hanna, G.C. (1959). Alpha radioactivity. In: *Experimental Nuclear Physics*, vol. III (ed. E. Segre), 54. New York: John Wiley & Sons, Inc.

Mang, H.J. (1960). Calculation of α-transition probabilities. *Phys. Rev.* 119: 1063.

Mang, H.J. (1964). Alpha decay. *Annu. Rev. Nucl. Sci.* 14: 1.

Viola, V.E. and Seaborg, G.T. (1966). Lifetimes for alpha, beta and spontaneous fission decay. *J. Inorg. Nucl. Chem.* 28: 741.

Fliessbach, T. and Mang, H.J. (1976). On absolute values of α-decay rates. *Nucl. Phys.* A263: 75.

Roeckl, E. (1995). Alpha radioactivity. *Radiochim. Acta* 70/71: 107.

Cluster Radioactivity

Poenaru, D.N. and Ivascu, M. (eds.) (1989). *Particle Emission from Nuclei*, vol. 2. Boca Raton, FL: CRC Press.

Hourany, E., Berrier-Rousin, G., Elayi, A. et al. (1995). ^{223}Ra spectroscopy in ^{14}C cluster radioactivity. *Phys. Rev.* C52: 267.

Bonetti, R. and Guglielmetti, A. (1999). Measurements on cluster radioactivity – present experimental status. In: *Heavy Elements and Related New Phenomena*, vol. II (eds. W. Greiner and R.K. Gupta), 643. Singapore: World Scientific.

Gupta, R.K. (1999). Collective description of exotic cluster decays and shell structure effects of parent/daughter nuclei. In: *Heavy Elements and Related New Phenomena*, vol. II (eds. W. Greiner and R.K. Gupta), 730. Singapore: World Scientific.

Mirea, M. and Gupta, R.K. (1999). Fine structure in cluster radioactivity. In: *Heavy Elements and Related New Phenomena*, vol. II (eds. W. Greiner and R.K. Gupta), 765. Singapore: World Scientific.

Poenaru, D.N. and Greiner, W. (1999). Numerical and analytical super-asymmetric fission model for exotic cluster decays. In: *Heavy Elements and Related New Phenomena*, vol. II (eds. W. Greiner and R.K. Gupta), 673. Singapore: World Scientific.

Proton Radioactivity

Hofmann, S. (1996). Proton radioactivity. In: *Nuclear Decay Modes* (ed. D.N. Poenaru). Bristol: IOP Publishing.

Spontaneous Fission

Blatt, J.M. and Weisskopf, V.E. (1952). *Theoretical Nuclear Physics*. New York: Wiley.

Strutinsky, V.M. (1967). Shell effects in nuclear masses and deformations. *Nucl. Phys.* A95: 420.

Tsang, C.F. and Nilsson, S.G. (1970). Shape isomeric states in heavy nuclei. *Nucl. Phys.* A140: 275.

Habs, D., Metag, V., Specht, H.J., and Ulfert, G. (1977). Quadrupole moment of the 8-μs fission isomer in ^{239}Pu. *Phys. Rev. Lett.* 38: 387.

Vandenbosch, R. (1977). Spontaneous fission isomers. *Annu. Rev. Nucl. Sci.* 27: 1.

Beta Decay

Fermi, E. (1934). Versuch einer Theorie der β-Strahlen. *Z. Phys.* 88: 161.

Kurie, F.N.D., Richardson, J.R., and Paxton, H.C. (1936). The radiation emitted from artificially produced radioactive substances, I. The upper limit and shapes of the β-ray spectra from several elements. *Phys. Rev.* 49: 368.

Rose, M.E. and Jackson, J.L. (1949). The ratio of L_1 to K capture. *Phys. Rev.* 76: 11540.

Wu, C.S., Ambler, E., Hayward, R.W. et al. (1957). Experimental test of parity conservation in beta decay. *Phys. Rev.* 105: 1413.

Reines, F. (1960). Neutrino interactions. *Annu. Rev. Nucl. Sci.* 10: 1.

Cabibbo, N. (1963). Unitary symmetry and leptonic decays. *Phys. Rev. Lett.* 10: 531.

Cabibbo, N. and Chilton, F. (1965). Hyperon production by neutrinos in a SU(3) model. *Phys. Rev.* 137: B1628.

Konopinsky, E.J. (1966). *The Theory of Beta Radioactivity*. London: Clarendon Press.

Siegbahn, K. (ed.) (1966). *Alpha-, Beta- and Gamma-Ray Spetroscopy*, vol. 2. Amsterdam: North-Holland.

Wu, C.S. and Moszkowski, S.A. (1966). *Beta Decay*. New York: Interscience.

Rubinson, W. (1971). The correction for atomic excitation energy in measurements of energies of electron capture decay. *Nucl. Phys.* A169: 629.

Wolfenstein, L. (1983). Parametrization of the Kobayashi-Maskawa matrix. *Phys. Rev. Lett.* 51: 1945.

Raman, S. and Gove, N.B. (1995). Rules for spin and parity assignmentsbased on logft values. *Phys. Rev.* C7: 1973.

Amsler, C., Particle Data Group et al. (2008). CKM quark-mixing matrix. *Phys. Lett.* B667: 1. http://pdg.lbl.gov/2008/reviews/kmmixrpp.pdf.

Electromagnetic Transitions

Goldhaber, M. and Sunyar, M.J. (1951). Classification of nuclear isomers. *Phys. Rev.* 83: 906.

Blatt, J.M. and Weisskopf, V.F. (1952). *Theoretical Nuclear Physics*, 583. New York: Wiley.

Wilkinson, D.H. (1960). Analysis of gamma decay data. In: *Nuclear Spectroscopy, Part B* (ed. F. Ajzenberg-Selove), 852. New York: Academic Press.

Ambler, E. (1963). Nuclear orientation. In: *Methods of Experimental Physics: Nuclear Physics*, vol. 5B (eds. L.C.L. Yuan and C.S. Wu), 162. New York: Academic Press.

Frauenfelder, H. (1963). Angular correlations. In: *Methods of Experimental Physics: Nuclear Physics*, vol. 5B (eds. L.C.L. Yuan and C.S. Wu), 129. New York: Academic Press.

de Groot, S.R., Tolhock, H.A., and Huiskamp, W.J. (1966). Orientation of nuclei at low temperatures. In: α-, β-, *and* γ-*Ray Spectroscopy*, vol. 2 (ed. K. Siegbahn), 1199. Amsterdam: North-Holland.

Hagström, S., Nordling, C., and Siegbahn, K. (1966). Tables of electron binding energies and kinetic energy vs. magnetic rigidity. In: α-, β-, *and* γ-*Ray Spectroscopy*, vol. 1 (ed. K. Siegbahn), 845. Amsterdam: North-Holland.

Way, K. and Hurley, F.W. (1966). Directory to tables and reviews of angular-momentum and angular-correlation coefficients. *Nucl. Data* 1: 473.

Taylor, H.W. et al. (1971). A tabulation of γγ directional-correlation coefficients. *At. Data Nucl. Data Tables* A9: 1.

Band, I.M., Trzhaskovskaya, M.B., and Listengarten, M.A. (1976). Internal conversion coefficients for $Z \leq 30$. *At. Data Nucl. Data Tables* 18: 433.

Band, I.M., Trzhaskoskaya, M.B., and Listengarten, M.A. (1978). Internal conversion coefficients for E5 and M5 nuclear transitions, $30 \leq Z \leq 104$. *At. Data Nucl. Data Tables* 21: 1.

Rösel, F., Fries, H.M., Alder, K., and Pauli, H.C. (1978). Internal conversion coefficients for all atomic shells with $30 \leq Z \leq 104$. *At. Data Nucl. Data Tables* 21: 89.

7

Radioactive Decay Kinetics

7.1 Law and Energy of Radioactive Decay

Radioactive decay follows the laws of statistics. If a sufficiently large number of radioactive atoms are observed for a sufficiently long time, the law of radioactive decay is found to be

$$-\frac{\mathrm{d}N}{\mathrm{d}t} = \lambda N \tag{7.1}$$

where N is the number of atoms of a certain radionuclide, $-\mathrm{d}N/\mathrm{d}t$ is the disintegration rate, and λ is the *disintegration* or decay constant (dimension s^{-1}). It is a measure of the probability of radioactive decay. The law of radioactive decay describes the kinetics of the reaction

$$A \rightarrow B + x + Q \tag{7.2}$$

where A denotes the radioactive mother nuclide, B is the daughter nuclide, x is the particle emitted, and Q is the energy set free by the decay process, which is called the Q value. Equation (7.2) represents a first-order reaction and is in the present case a mononuclear reaction.

Radioactive decay is only possible if $Q > 0$. The Q value can be determined by comparison of the atomic masses. We have

$$Q = \Delta M c^2 = [M_A - (M_B + M_x)]c^2 \tag{7.3}$$

Even if $Q > 0$, the question of the probability of a radioactive decay process is still open. It depends, as we have discussed in Chapter 6, on the decay energy, but also on the change in angular momentum and parity, and on the existence of a potential barrier that must be penetrated by quantum-mechanical tunneling.

Integration of Eq. (7.1) gives

$$N = N_0 \mathrm{e}^{-\lambda t} \tag{7.4}$$

where N_0 is the number of radioactive atoms at time $t = 0$. Instead of the decay constant λ, the half-life $t_{1/2}$ is frequently used. This is the time after which half the

Nuclear and Radiochemistry: Fundamentals and Applications,
Fourth Edition. Jens-Volker Kratz.

radioactive atoms have decayed: $N = N_0/2$. Introducing the half-life $t_{1/2}$ in Eq. (7.4), it follows that

$$t_{1/2} = \frac{1\mathrm{n}2}{\lambda} = \frac{0.693}{\lambda} \tag{7.5}$$

and

$$N = N_0\left(\frac{1}{2}\right)^{t/t_{1/2}} \tag{7.6}$$

From this equation, it is seen immediately that the number of radioactive atoms has decreased to one-half after one half-life, to 1/128 (less than 1%) after seven half-lives, and to 1/1024 (about 0.1%) after 10 half-lives. If the time t is small compared with the half-life of the radionuclide ($t \ll t_{1/2}$), the following approximation may be used:

$$\begin{aligned} \mathrm{e}^{-\lambda t} &= 1 - \lambda t + \frac{(\lambda t)^2}{2} - \cdots \\ &= 1 - (\ln\ 2)\left(\frac{t}{t_{1/2}}\right) + \frac{(\ln\ 2)^2}{2}\left(\frac{t}{t_{1/2}}\right)^2 - \cdots \end{aligned} \tag{7.7}$$

The average lifetime τ is obtained by the usual calculation of an average value

$$\tau = \frac{1}{N_0}\int_0^\infty N\,\mathrm{d}t = \int_0^\infty \mathrm{e}^{-\lambda t}\,\mathrm{d}t = \frac{1}{\lambda} \tag{7.8}$$

From Eq. (7.4) it follows that after the average lifetime τ, the number of radioactive atoms has decreased from N_0 to N_0/e ($\tau = t_{1/2}/(\ln 2)$).

Generally, the half-life of a radionuclide does not depend on pressure, temperature, state of matter, or chemical bonding. However, in some special cases in which low-energy transitions occur, these parameters have been found to have a small influence (Section 14.2).

The activity A of a radionuclide is given by its disintegration rate

$$A = -\frac{\mathrm{d}N}{\mathrm{d}t} = \lambda N = \frac{\ln 2}{t_{1/2}}N \tag{7.9}$$

The dimension is s^{-1}, and the unit is called the becquerel (Bq): $1\,\mathrm{Bq} = 1\,\mathrm{s}^{-1}$. An older unit is the *Curie* (Ci). It is still used sometimes, related to the activity of 1 g of ^{226}Ra, and defined as $1\,\mathrm{Ci} = 3.700 \cdot 10^{10}\,\mathrm{s}^{-1} = 37\,\mathrm{GBq}$. Smaller units are 1 millicurie (mCi) = 37 MBq, 1 microcurie (μCi) = 37 kBq, 1 nanocurie (nCi) = 37 Bq, and 1 picocurie (pCi) = 0.37 Bq; 1 Ci is a rather high activity, which cannot be handled directly but needs special installations, such as hot cells. Activities of the order of several millicuries are applied in medicine for diagnostic purposes, activities of the order of 1 μCi are usually sufficient for the investigation of the behavior of radionuclides, and activities of the order of 1 nCi are measurable without special efforts.

As the activity A is proportional to the number N of radioactive atoms, the exponential law, Eq. (7.4), holds also for the activity:

$$A = A_0\mathrm{e}^{-\lambda t} \tag{7.10}$$

The mass m (in g) of the radioactive atoms can be calculated from their number N and their activity A:

$$m = \frac{N \cdot M}{N_{Av}} = \frac{A \cdot M}{N_{Av}\lambda} = \frac{A \cdot M}{N_{Av} \ln 2} t_{1/2} \tag{7.11}$$

where M is the nuclide mass and N_{Av} is Avogadro's number ($6.022 \cdot 10^{23}$).

In laboratory experiments with radionuclides, knowledge of the mass of the radioactive substances is very important. For example, the mass of 1 MBq of ^{32}P ($t_{1/2} = 14.3$ days) is only about 10^{-10} g, and that of 1 MBq of ^{99m}Tc ($t_{1/2} = 6.0$ hours) is only about $5 \cdot 10^{-12}$ g. If there is no carrier present in the form of a large excess of inactive atoms of the same element in the same chemical state, these small amounts of radionuclides may easily be lost, for instance, by adsorption on the walls. Whereas in the case of radioisotopes of stable elements, the condition of the presence of carriers is often fulfilled due to the ubiquity of most stable elements, it is not fulfilled in the case of short-lived isotopes of radioelements, and extraordinary behavior may be observed (Section 11.1).

The ratio of the activity to the total mass m of the element (the sum of radioactive and stable isotopes) is called the specific activity A_s:

$$A_s = \frac{A}{m} \text{ (Bq g}^{-1}\text{)} \tag{7.12}$$

Sometimes, high or well-defined specific activities are required, for instance, in the case of the application of radionuclides or labeled compounds in medicine, or as tracers in other fields of research.

7.2 Radioactive Equilibria

Genetic relations between radionuclides, as in the decay series, can be written in the form

$$\text{nuclide 1} \rightarrow \text{nuclide 2} \rightarrow \text{nuclide 3} \tag{7.13}$$

In words, nuclide 1 is transformed by radioactive decay into nuclide 2, and the latter into nuclide 3. Nuclide 1 is the mother nuclide of nuclide 2, and nuclide 2 the daughter nuclide of nuclide 1. At any instant, the net production rate of nuclide 2 is given by the decay rate of nuclide 1 diminished by the decay rate of nuclide 2:

$$\frac{dN_2}{dt} = -\frac{dN_1}{dt} - \lambda_2 N_2 = \lambda_1 N_1 - \lambda_2 N_2 \tag{7.14}$$

With the decay rate of nuclide 1, it follows that

$$\frac{dN_2}{dt} + \lambda_2 N_2 - \lambda_1 N_1^0 e^{-\lambda_1 t} = 0 \tag{7.15}$$

where N_1^0 is the number of atoms of nuclide 1 at time 0. The solution of the first-order differential equation, Eq. (7.15), is

$$N_2 = \frac{\lambda_1}{\lambda_2 - \lambda_1} N_1^0 (e^{-\lambda_1 t} - e^{-\lambda_2 t}) + N_2^0 e^{-\lambda_2 t} \tag{7.16}$$

N_2^0 is the number of atoms of nuclide 2 present at $t = 0$. If nuclides 1 and 2 are separated quantitatively at $t = 0$, the situation becomes simpler and two fractions are obtained. In the fraction containing nuclide 2, this nuclide is no longer produced by the decay of nuclide 1, and for the fraction containing nuclide 1, it follows that, with $N_2^0 = 0$,

$$N_2 = \frac{\lambda_1}{\lambda_2 - \lambda_1} N_1^0 (e^{-\lambda_1 t} - e^{-\lambda_2 t}) \tag{7.17}$$

Rearranging,

$$N_2 = \frac{\lambda_1}{\lambda_2 - \lambda_1} N_1 [1 - e^{-(\lambda_2 - \lambda_1)t}] \tag{7.18}$$

or, after substitution of the decay constants λ by the half-lives $t_{1/2}$,

$$N_2 = \frac{t_{1/2}(2)/t_{1/2}(1)}{1 - t_{1/2}(2)/t_{1/2}(1)} N_1 \left[1 - \left(\frac{1}{2}\right)^{t_{1/2}(2) - t_{1/2}(1)}\right] \tag{7.19}$$

The term in the exponent of $\frac{1}{2}$ in Eq. (7.19) may be rewritten to show the influence of the ratio of the half-lives $t_{1/2}(1)/t_{1/2}(2)$:

$$\frac{t}{t_{1/2}(2)} - \frac{t}{t_{1/2}(1)} = \left[1 - \frac{t_{1/2}(2)}{t_{1/2}(1)}\right] \frac{t}{t_{1/2}(2)} \tag{7.20}$$

The time necessary to attain radioactive equilibrium depends on the half-life of the daughter nuclide as well as on the ratio of the half-lives. This is seen in Figure 7.1. After a sufficiently long time, the exponential function in Eq. (7.18) becomes zero and radioactive equilibrium is established:

$$N_2 = \frac{\lambda_1}{\lambda_2 - \lambda_1} N_1 = \frac{t_{1/2}(2)/t_{1/2}(1)}{1 - t_{1/2}(2)/t_{1/2}(1)} N_1 \tag{7.21}$$

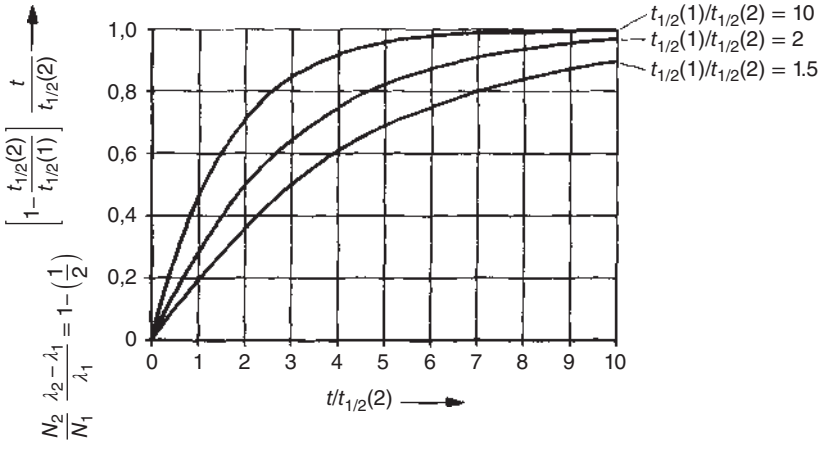

Figure 7.1 Attainment of radioactive equilibrium as a function of $t/t_{1/2}(2)$ for different ratios of the half-lives of the mother and daughter nuclides.

In radioactive equilibrium, the ratio N_2/N_1, the ratio of the masses, and the ratio of the activities are constant. It should be mentioned that this is not an equilibrium in the sense used in thermodynamics and chemical kinetics, because it is not reversible, and in general, it does not represent a stationary state.

Four cases can be distinguished:

a) The half-life of the mother nuclide is much longer than that of the daughter nuclide, $t_{1/2}(1) \gg t_{1/2}(2)$.
b) The half-life of the mother nuclide is longer than that of the daughter nuclide, but the decay of the mother nuclide cannot be neglected, $t_{1/2}(1) > t_{1/2}(2)$.
c) The half-life of the mother nuclide is shorter than that of the daughter nuclide: $t_{1/2}(1) < t_{1/2}(2)$.
d) The half-lives of the mother nuclide and the daughter nuclide are similar: $t_{1/2}(1) \approx t_{1/2}(2)$.

These four cases are considered in the following sections in more detail, because they are of practical importance in radiochemistry.

7.3 Secular Radioactive Equilibrium

In secular radioactive equilibrium ($t_{1/2}(1) \gg t_{1/2}(2)$), Eq. (7.18) reduces to

$$N_2 = \frac{\lambda_1}{\lambda_2} N_1 (1 - e^{-\lambda_2 t}) \tag{7.22}$$

Assuming that mother and daughter nuclides are separated from each other at time $t = 0$, the growth of the daughter nuclide in the fraction of the mother nuclide and the decay of the daughter nuclide in the separated fraction are as plotted in Figure 7.2. The logarithms of the activities are plotted in Figure 7.3. The solid curves can be measured directly in the two fractions after chemical separation, whereas the dashed curves are found by extrapolation or by subtraction, respectively.

After $t \gg t_{1/2}(2)$ (in practice, after about 10 half-lives of nuclide 2), radioactive equilibrium is established and the following relations hold:

$$\frac{N_2}{N_1} = \frac{\lambda_1}{\lambda_2} = \frac{t_{1/2}(2)}{t_{1/2}(1)} \tag{7.23}$$

$$A_1 = A_2 \tag{7.24}$$

The activities of the mother nuclide and of all the nuclides emerging from it by nuclear transformation or a sequence of nuclear transformations are the same, provided that secular radioactive equilibrium is established.

Secular radioactive equilibrium has several practical applications:

a) Determination of the long half-life of a mother nuclide by measuring the mass ratio of daughter and mother nuclides, provided that the half-life of the daughter nuclide is known. Examples are the determinations of the half-lives of ^{226}Ra and ^{238}U, which cannot be obtained directly by measuring their radioactive decay,

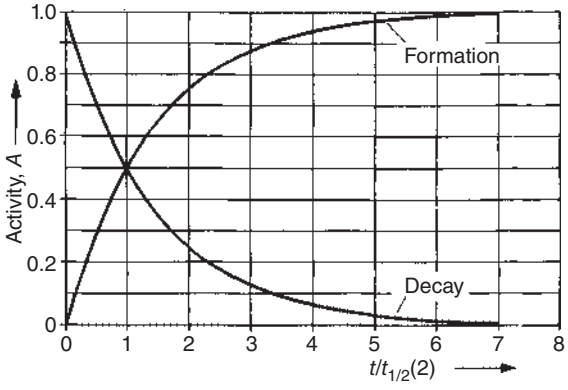

Figure 7.2 Decay of the daughter nuclide and its formation from the mother nuclide in the case of secular equilibrium as a function of $t/t_{1/2}(2)$.

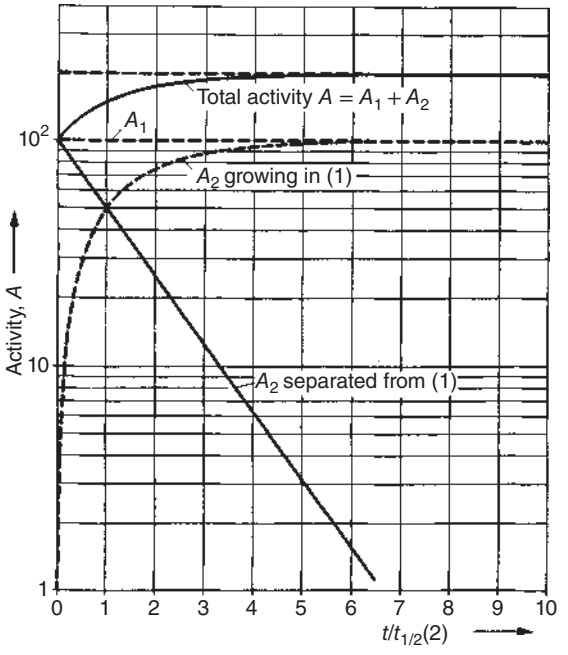

Figure 7.3 Secular equilibrium: activities of mother and daughter nuclides as a function of $t/t_{1/2}(2)$.

because of the long half-lives. The half-life of ^{226}Ra is obtained by measuring the absolute activity of the daughter nuclide ^{222}Rn in radioactive equilibrium with ^{226}Ra, and its half-life. From the activity and the half-life, the number of radioactive atoms of ^{222}Rn is calculated by using Eq. (7.9), and the half-life of ^{226}Ra is obtained from Eq. (7.23). The half-life of ^{238}U is determined by measuring the mass ratio of ^{226}Ra and ^{238}U in a uranium mineral. With the known half-life of ^{236}Ra, that of ^{238}U is calculated by application of Eq. (7.23).

b) Calculation of the mass ratios of radionuclides that are in secular radioactive equilibrium. From the half-lives, the masses of all radionuclides of the natural decay series in radioactive equilibrium with the long-lived mother nuclides can be calculated by using Eq. (7.11).

c) Calculation of the mass of a mother nuclide from the measured activity of a daughter nuclide. For example, the amount of ^{238}U in a sample can be determined by measuring the activity of ^{234}Th or of ^{234m}Pa. The latter emits high-energy β^- radiation and can therefore be measured easily. The mass of ^{238}U is obtained by application of Eq. (7.11) with $A_1 = A_2$:

$$m_1 = \frac{M_1}{N_{Av}} \frac{A_2}{\ln 2} t_{1/2}(1) \tag{7.25}$$

where m_1 is the mass and M_1 is the nuclide mass of the long-lived mother nuclide, and N_{Av} is Avogadro's number.

d) Finally, the previous application can be reversed inasmuch as a sample of U or U_3O_8 can be weighed to provide a source of known activity of ^{234m}Pa. The α radiation of ^{238}U is filtered from the high-energy β^- radiation of ^{234m}Pa by covering the sample with thin aluminum foil. From Eq. (7.11), it follows with $A_1 = A_2$ that 1 mg of ^{238}U is a radiation source emitting 740 β^- particles from ^{234m}Pa per minute. Such a sample may be used as a β^- standard.

7.4 Transient Radioactive Equilibrium

The attainment of a transient radioactive equilibrium is plotted in Figure 7.4 for $t_{1/2}(1)/t_{1/2}(2) = 5$. Now $t_{1/2}(2)$ alone does not regulate the attainment of radioactive equilibrium; its influence is modified by a factor containing the ratio $t_{1/2}(1)/t_{1/2}(2)$, as already explained in Section 7.2. Again, as in Figure 7.3, the solid curves can be

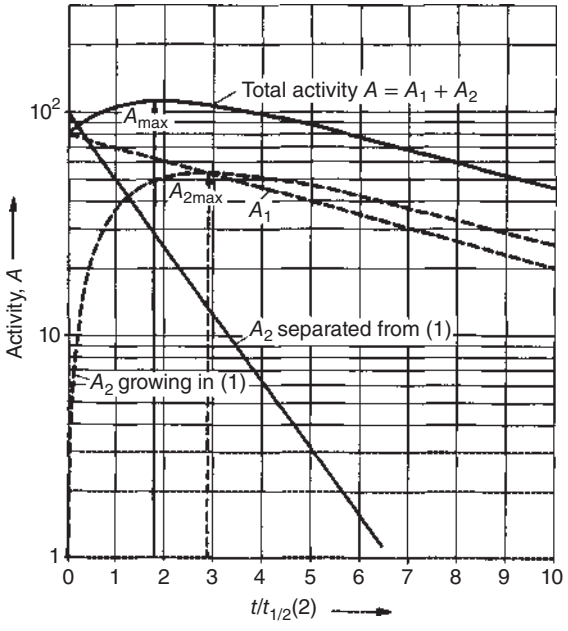

Figure 7.4 Transient equilibrium: activities of mother and daughter nuclides as a function of $t/t_{1/2}(2)$ ($t_{1/2}(1)/t_{1/2}(2) = 5$).

measured experimentally, and the dashed curves are obtained by extrapolation or by subtraction, respectively.

After attainment of radioactive equilibrium, Eq. (7.19) is valid. Introducing the half-lives, this equation becomes

$$\frac{N_2}{N_1} = \frac{t_{1/2}(2)}{t_{1/2}(1) - t_{1/2}(2)} \tag{7.26}$$

whereas in secular radioactive equilibrium, the activities of the mother and the daughter nuclide are the same, in transient radioactive equilibrium, the daughter activity is always higher:

$$\frac{A_1}{A_2} = \frac{\lambda_1 N_1}{\lambda_2 N_2} = 1 - \frac{\lambda_1}{\lambda_2} = 1 - \frac{t_{1/2}(2)}{t_{1/2}(1)} \tag{7.27}$$

The possibilities of application of transient radioactive equilibrium are similar to those explained for secular radioactive equilibrium. Instead of Eq. (7.25), the following equation holds:

$$m_1 = \frac{M_1}{N_{\mathrm{Av}}} \frac{A_2}{\ln 2} [t_{1/2}(1) - t_{1/2}(2)] \tag{7.28}$$

7.5 Half-Life of Mother Nuclide Shorter than Half-Life of Daughter Nuclide

In this case, the mother nuclide decays faster than the daughter nuclide, and the ratio between the two changes continuously, until the mother nuclide has disappeared and only the daughter nuclide is left. The situation is plotted in Figure 7.5. No radioactive equilibrium is attained.

7.6 Similar Half-Lives

As the difference between the half-lives of mother nuclide and daughter nuclide becomes smaller and smaller, the attainment of radioactive equilibrium is more and more delayed, as can be seen from Eq. (7.20) and from Figure 7.1, provided that $t_{1/2}(1) > t_{1/2}(2)$. In this situation, the following questions are of practical interest:

a) How much time must elapse before the decay curve of the longer-lived radionuclide can be observed?
b) At which time after the separation of mother and daughter nuclide does the daughter nuclide reach maximum activity?

In answering question (a), it is assumed that an error ε can be accepted in measuring the decay curve:

$$\varepsilon = \mathrm{e}^{-(\lambda_2 - \lambda_1)t} \quad \text{if } \lambda_1 < \lambda_2 \tag{7.29a}$$

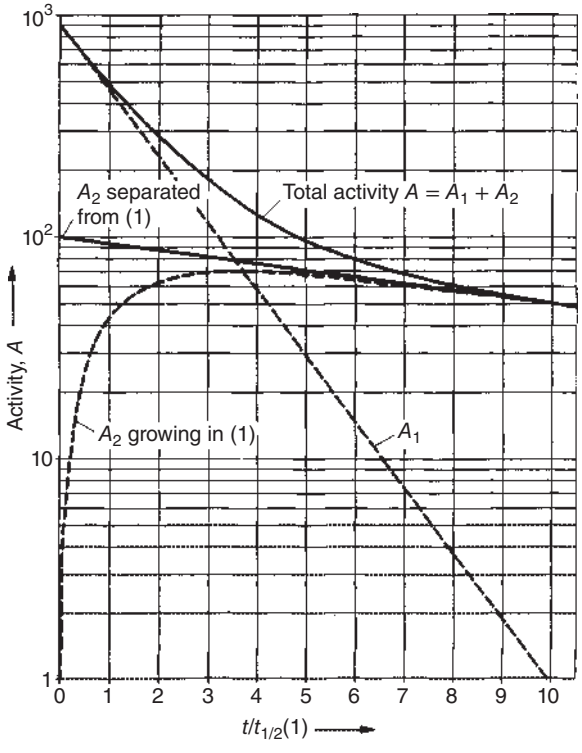

Figure 7.5 Half-life of mother nuclide shorter than that of daughter nuclide – no radioactive equilibrium ($t_{1/2}(1)/t_{1/2}(2) = 0.1$).

or

$$\varepsilon = e^{-(\lambda_1 - \lambda_2)t} \quad \text{if } \lambda_1 > \lambda_2 \tag{7.29b}$$

By introducing the half-lives, the following equations are obtained for the time after which the decay curve of the longer-lived radionuclide is observed with an error ε:

$$t \geq \frac{\log(1/\varepsilon)}{\log 2} \frac{t_{1/2}(1)t_{1/2}(2)}{t_{1/2}(1) - t_{1/2}(2)} \quad \text{if } t_{1/2}(1) > t_{1/2}(2) \tag{7.30a}$$

or

$$t \geq \frac{\log(1/\varepsilon)}{\log 2} \frac{t_{1/2}(1)t_{1/2}(2)}{t_{1/2}(2) - t_{1/2}(1)} \quad \text{if } t_{1/2}(1) < t_{1/2}(2) \tag{7.30b}$$

Application of this formula to the case of the sequence of radionuclides

$$^{135}\text{I} \xrightarrow[6.6 \text{ hours}]{\beta^-} {}^{135}\text{Xe} \xrightarrow[9.1 \text{ hours}]{\beta^-} {}^{135}\text{Cs}$$

gives the result that 160 hours elapse before the half-life of the longer-lived ^{135}Xe can be observed in the decay curve with an error of 1%. This is a very long time compared with the half-lives, and the activity of ^{135}Xe will have decreased by 5 orders of magnitude.

In order to answer question (b), Eq. (7.17) is differentiated with respect to time and dN_2/dt is set equal to zero. The resulting equation is

$$t_{max}(2) = \frac{1}{\lambda_2 - \lambda_1} \ln \frac{\lambda_2}{\lambda_1} \tag{7.31}$$

In the sequence $^{135}I \rightarrow {}^{135}Xe \rightarrow {}^{135}Cs$, the maximum activity of ^{135}Xe is reached after 11.1 hours.

7.7 Branching Decay

Branching decay is often observed for odd–odd nuclei on the line of β stability. For example, ^{40}K, which is responsible for the natural radioactivity of potassium, decays into ^{40}Ca with a probability of 89.3% by emission of β^- particles and into ^{40}Ar with a probability of 10.7% by electron capture. Branching decay is also observed in the decay series, as already mentioned in Section 2.2.

For a certain radionuclide A showing branching decay into a nuclide B and a nuclide C,

$$B \overset{\lambda_b}{\leftarrow} A \overset{\lambda_c}{\rightarrow} C$$

the two probabilities of decay, given by the decay constants, may be denoted by λ_b and $\lambda_{c,}$ respectively. As these two probabilities are independent of each other, the decay constant λ_A of the radionuclide A is given by the sum of λ_b and $\lambda_{c,}$ and the decay rate of A is

$$-\frac{dN_A}{dt} = \lambda_b N_A + \lambda_c N_A = \lambda_A N_A \tag{7.32}$$

Integration of this equation gives

$$N_A = N_A^0 e^{-(\lambda_b + \lambda_c)t} \tag{7.33}$$

The rates of production of the nuclides B and C are

$$\frac{dN_B}{dt} = \lambda_b N_A \quad \text{and} \quad \frac{dN_C}{dt} = \lambda_c N_A \tag{7.34}$$

and the decay rates of these nuclides are

$$-\frac{dN_B}{dt} = \lambda_B N_B \quad \text{and} - \frac{dN_c}{dt} = \lambda_C N_C \tag{7.35}$$

The net rate of production of B is

$$\frac{dN_B}{dt} = \lambda_b N_A - \lambda_B N_B \tag{7.36}$$

or, introducing Eq. (7.33),

$$\frac{dN_B}{dt} + \lambda_B N_B - \lambda_b N_A^0 e^{-(\lambda_b + \lambda_c)t} = 0 \tag{7.37}$$

Integration of this equation with $N_B = 0$ at $t = 0$ gives

$$N_B = \frac{\lambda_b}{\lambda_B - (\lambda_b + \lambda_c)} N_A^0 [e^{-(\lambda_b+\lambda_c)t} - e^{-\lambda_B t}] \tag{7.38}$$

A similar relation holds for nuclide C. In the case of secular equilibrium ($\lambda_b + \lambda_c \ll \lambda_B$), it follows that

$$\frac{N_B}{N_A} = \frac{\lambda_b}{\lambda_B} \quad \text{and} \quad \frac{N_C}{N_A} = \frac{\lambda_c}{\lambda_C} \tag{7.39}$$

whereas there are two probabilities in branching decay, λ_b and λ_c, there is only one half-life:

$$t_{1/2}(A) = \frac{\ln 2}{\lambda_A} = \frac{\ln 2}{\lambda_b + \lambda_c} \tag{7.40}$$

In the case of secular equilibrium, two partial half-lives may be formally distinguished:

$$t_{1/2}(A)_b = \frac{\ln 2}{\lambda_b} \quad \text{and} \quad t_{1/2}(A)_c = \frac{\ln 2}{\lambda_c} \tag{7.41}$$

Introduction of these partial half-lives leads to the relations

$$\frac{N_B}{N_A} = \frac{t_{1/2}(B)}{t_{1/2}(A)_b} \quad \text{and} \quad \frac{N_C}{N_A} = \frac{t_{1/2}(C)}{t_{1/2}(A)_c} \tag{7.42}$$

which are analogous to Eq. (7.23).

If the daughter nuclides are longer-lived or even stable (as in the case of the decay of ^{40}K), the following equations are valid:

$$N_B = \frac{\lambda_b}{\lambda_b + \lambda_c} N_A [e^{(\lambda_b+\lambda_c)t} - 1] \tag{7.43a}$$

$$N_C = \frac{\lambda_c}{\lambda_b + \lambda_c} N_A [e^{(\lambda_b+\lambda_c)t} - 1] \tag{7.43b}$$

and

$$\frac{N_B}{N_C} = \frac{\lambda_b}{\lambda_c} \tag{7.44}$$

If the time t is small compared with the half-life of the mother nuclide A ($t \ll t_{1/2}(A)$), it follows from Eq. (7.1) that

$$\frac{N_B}{N_A} = \lambda_b t \quad \text{and} \quad \frac{N_C}{N_A} = \lambda_c t \tag{7.45}$$

7.8 Successive Transformations

In the previous sections, radioactive equilibrium between a mother nuclide and a daughter nuclide according to Eq. (7.13) has been considered. This can be extended to a longer sequence of successive transformations:

$$(1) \rightarrow (2) \rightarrow (3) \rightarrow (4) \rightarrow \cdots \rightarrow (n) \cdots \tag{7.46}$$

For such a sequence, Eq. (7.14) can be written in a more general form

$$\frac{\mathrm{d}N_n}{\mathrm{d}t} = \lambda_{n-1}N_{n-1} - \lambda_n N_n \tag{7.47}$$

Solution of the series of differential equations with $n = 1, 2, 3, 4, \ldots, n$, for the initial conditions $N_1 = N_0^1, N_2 = N_3 = \cdots = N_n = 0$, gives for the number of atoms $N_n(t)$ of nuclide number n in the series at the time t

$$N_n = c_1 \mathrm{e}^{-\lambda_1 t} + c_2 \mathrm{e}^{-\lambda_2 t} + \cdots + c_n \mathrm{e}^{-\lambda_n t} \tag{7.48}$$

The coefficients in this equation are

$$\begin{aligned} c_1 &= \frac{\lambda_1 \lambda_2 \ldots \lambda_{n-1}}{(\lambda_2 - \lambda_1)(\lambda_3 - \lambda_1)\ldots(\lambda_n - \lambda_1)} N_1^0 \\ c_2 &= \frac{\lambda_1 \lambda_2 \ldots \lambda_{n-1}}{(\lambda_1 - \lambda_2)(\lambda_3 - \lambda_2)\ldots(\lambda_n - \lambda_2)} N_1^0 \\ c_n &= \frac{\lambda_1 \lambda_2 \ldots \lambda_{n-1}}{(\lambda_1 - \lambda_n)(\lambda_2 - \lambda_n)\ldots(\lambda_{n-1} - \lambda_n)} N_1^0 \end{aligned} \tag{7.49}$$

By use of these equations, the number of atoms in any series of transformations can be calculated. For the daughter nuclide 2, Eq. (7.17) is obtained.

In some practical cases, the equations for $n = 3$ are useful:

$$N_3 = \lambda_1 \lambda_2 N_1^0 \left[\frac{\mathrm{e}^{-\lambda_1 t}}{(\lambda_2 - \lambda_1)(\lambda_3 - \lambda_1)} + \frac{\mathrm{e}^{-\lambda_2 t}}{(\lambda_1 - \lambda_2)(\lambda_3 - \lambda_2)} + \frac{\mathrm{e}^{-\lambda_3 t}}{(\lambda_2 - \lambda_3)(\lambda_1 - \lambda_3)} \right] \tag{7.50}$$

If nuclide 3 is stable ($\lambda_3 = 0$), the increase of N_3 is given by

$$N_3 = N_1^0 \left[1 - \frac{\lambda_2}{\lambda_2 - \lambda_1} \mathrm{e}^{-\lambda_1 t} - \frac{\lambda_1}{\lambda_1 - \lambda_2} \mathrm{e}^{-\lambda_2 t} \right] \tag{7.51}$$

With the decay law for nuclide 1 and Eq. (7.17), it follows that

$$N_3 = N_1^0 - N_1 - N_2 \tag{7.52}$$

That is, the number of atoms of the stable end product is given by the number of atoms of the mother nuclide 1 at the beginning, diminished by the number of atoms 1 that are still present and the number of atoms of the intermediate 2.

If the half-life of the mother nuclide is much longer than those of the succeeding radionuclides (secular equilibrium), Eq. (7.43b) becomes much simpler, provided that radioactive equilibrium is established. As in this case $\lambda_1 \ll \lambda_2, \lambda_3, \ldots, \lambda_n$, all terms are small compared with the first one, giving

$$N_n = c_1 \mathrm{e}^{-\lambda_1 t} \tag{7.53}$$

and

$$c_1 = \frac{\lambda_1}{\lambda_n} N_1^0 \tag{7.54}$$

Furthermore, under these conditions, the following relations are valid:

$$\frac{N_n}{N_1} = \frac{\lambda_1}{\lambda_n} \quad \text{or} \quad \frac{N_n}{N_1} = \frac{t_{1/2}(n)}{t_{1/2}(1)} \tag{7.55}$$

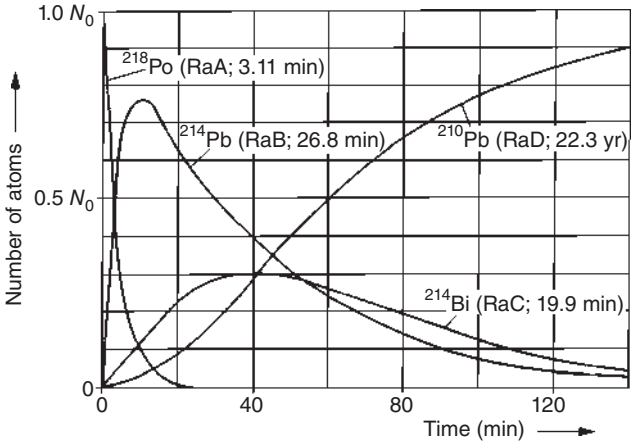

Figure 7.6 Several successive transformations: decay of ^{218}Po. Source: Based on Rutherford et al. (1930).

and

$$A_n = A_1 \tag{7.56}$$

These equations are the same as those derived for radioactive equilibrium between mother and daughter nuclide (Eqs. (7.23) and (7.24)); that is, in secular equilibrium the relations in Section 7.3 are not only valid for the directly succeeding daughter nuclide, but also for all following radionuclides of the decay series. This has already been applied in the examples given in Section 7.3.

If secular equilibrium is not established, the activities of succeeding radionuclides can also be calculated by using the equations given in this chapter. An example is the decay of the naturally occurring ^{218}Po ($^{218}\text{Po} \xrightarrow{\alpha} {}^{214}\text{Pb} \xrightarrow{\beta^-} {}^{214}\text{Bi} \xrightarrow{\alpha} {}^{210}\text{Pb}\ldots$). The activities of ^{218}Po and its first decay products are plotted in Figure 7.6 as a function of time (according to Rutherford et al. 1930).

Reference

General

Rutherford, E., Chadwick, J., and Ellis, C.D. (1930). *Radiation from Radioactive Substances*. Cambridge: Cambridge University Press.

Further Reading

General

Evans, R.D. (1955). *The Atomic Nucleus*. New York: McGraw-Hill.

Segré, E. (ed.) (1959). Radioactive decay. In: *Experimental Nuclear Physics*, vol. III. New York: Wiley.

Kaplan, I. (1964). *Nuclear Physics*, 2e. Reading, MA: Addison-Wesley.

Friedlander, G., Kennedy, J.W., Macias, E.S., and Miller, J.M. (1981). *Nuclear and Radiochemistry*, 3e. New York: Wiley.

Browne, E. and Firestone, R.B. (1986). *Table of Radioactive Isotopes* (ed. V.S. Shirley). New York: Wiley.

More Specialized

Bateman, H. (1910). The solution of a system of differential equations occurring in the theory of radioactive transformations. *Proc. Cambridge Philos. Soc.* 15: 423.

Lieser, K.H. (1991). *Einführung in die Kernchemie*, 3e. Weinheim: Wiley-VCH.

Nagy, S. (2011). Kinetics of radioactive decay. In: *Handbook of Nuclear Chemistry*, 2e, vol. 1 (eds. A. Vértes, S. Nagy, Z. Klenczár, et al.), 333. Berlin: Springer-Verlag.

8

Nuclear Radiation

8.1 General Properties

Knowledge of the properties of nuclear radiation is needed for the measurement and identification of radionuclides and in the field of radiation protection. The most important aspect is the interaction of radiation with matter.

Charged high-energy particles or photons, such as α particles, protons, electrons, positrons, γ-ray or X-ray photons, set off ionization processes in gases, liquids, or solids:

$$M \rightarrow M^+ + e^- \tag{8.1}$$

where M is an atom or a molecule. Any kind of radiation that is able to produce ions according to Eq. (8.1) is called *ionizing radiation*. The arrow → indicates a reaction induced by ionizing radiation. Excited atoms or molecules M^* may also be produced:

$$M \rightarrow M^* \tag{8.2}$$

The chemical reactions induced by ionizing radiation in gases, liquids, and solids are the field of radiation chemistry, whereas the concern of photochemistry is the chemical reactions induced by light (visible and ultra violet [UV]).

The minimum energy needed for ionization or excitation of atoms or molecules is on the order of several electronvolts, depending on the nature of the atoms or molecules. The photons of visible light have energies varying between about 1 eV ($\lambda = 1240$ nm) and 10 eV ($\lambda = 124$ nm). If their energy is high enough, as in the case of UV radiation, they lose it by one ionization process. Particles with energies on the order of 0.1–10 MeV, however, produce a large number of ions and electrons and of excited atoms or molecules. The products of the reactions (8.1) and (8.2) are accumulated in the track of the high-energy particle or photon. Heavy particles, such as α particles or protons, lead to a high density of the reaction products in the track, whereas their density is low in the track of electrons or γ-ray photons.

The ions M^+ and the excited atoms or molecules M^* produced in the primary reactions (8.1) and (8.2), respectively, give rise to further (secondary) reactions:

$$M^+ \rightarrow R^+ + R \text{ (dissociation)} \tag{8.3}$$

$$M^+ + e^- \rightarrow M^* \text{ (recombination)} \tag{8.4}$$

Nuclear and Radiochemistry: Fundamentals and Applications,
Fourth Edition. Jens-Volker Kratz.

$$M^+ + X \rightarrow Y^+ \text{ (chemical reaction)} \tag{8.5}$$

$$M^+ + X \rightarrow M + X^+ \text{ (charge transfer)} \tag{8.6}$$

$$M^+ \rightarrow M^{n+} + (n-1)e^- \text{ (emission of Auger electrons)} \tag{8.7}$$

$$M^* \rightarrow M + h\nu \tag{8.8}$$

$$M^* \rightarrow 2R \text{ (dissociation into radicals)} \tag{8.9}$$

$$M^* \rightarrow R^+ + R^- \text{ (dissociation into ions)} \tag{8.10}$$

$$M^* + X \rightarrow Y \text{ (chemical reaction)} \tag{8.11}$$

$$M^* + X \rightarrow M + X^* \text{ (transfer of excitation energy)} \tag{8.12}$$

Many of these secondary reactions are very fast and occur within 10^{-10}–10^{-7} seconds. Reactions (8.4), (8.8), and (8.9) are relatively frequent. Recombination is favored in liquids and solids.

The concentration of the reaction products in the track is proportional to the energy lost by the ionizing particles per unit distance traveled along their path, which is called linear energy transfer (LET). For example, in water, the LET value of 1 MeV α particles is 190 eV nm^{-1}, and for 1 MeV electrons it is 0.2 eV nm^{-1}. This means that the concentration of reaction products in the track is higher by a factor of about 10^3 for α particles. In air, the ionizing radiation loses 34.0 (electrons) to 35.1 eV (α particles) per ion pair produced according to Eq. (8.1). Because this value is about twice the ionization energy of N_2 (15.6 eV) and O_2 (12.1 eV), it follows that about half of the energy given off by the particles is used in the production of excited atoms and molecules, respectively, according to Eq. (8.2).

If particles, in particular α particles, protons or photons, have sufficiently high energy, they may also give rise to nuclear reactions. Electrons entering the force field of nuclei give off part of their energy in the form of photons (bremsstrahlung). If their energy is on the order of 1 MeV (e.g. β^- radiation), these photons have the energy of X-rays (X-ray bremsstrahlung), and at energies above 10 MeV, the photons have the energies of γ-rays.

Neutrons may lose their energy in steps by collisions with other particles or they may induce nuclear reactions. In contrast to particles, photons mostly give off their energy in one step.

The behavior of various kinds of radiation in a magnetic field is shown in Figure 8.1: γ radiation is not deflected, β^+ and β^- radiation are deflected in different directions, and the influence of the magnetic field on α particles is much smaller because the deflection depends on e/m (e is the charge and m the mass).

Whereas α radiation is easily absorbed (e.g. by one sheet of paper), for quantitative absorption of β radiation materials of several millimeters or centimeters thickness (depending on the energy) and for absorption of γ radiation either lead walls or

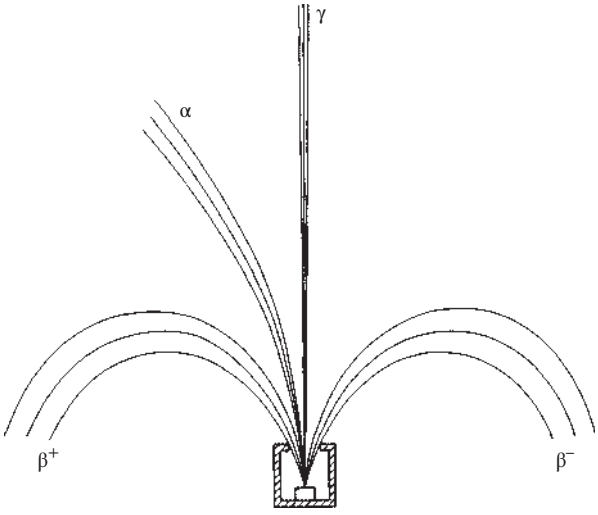

Figure 8.1 Behavior of various kinds of radiation in a magnetic field.

thick walls of concrete are needed. At the same energy, the ratio of the absorption coefficients for α, β, and γ radiation is about $10^4 : 10^2 : 1$. Furthermore, it has to be taken into account that α and β particles can be absorbed quantitatively, whereas the absorption of γ-ray photons is governed by an exponential law, and therefore only a certain fraction can be held back.

8.2 Heavy Charged Particles ($A \geq 1$)

The limited range of α radiation can be seen in Figure 8.2. The range depends on the energy of the α particles and amounts to several centimeters in air. Their course is practically not influenced by the collisions with electrons. Occasionally an α particle collides with a nucleus and is strongly deflected, or it is captured by a nucleus and induces a nuclear reaction.

The specific ionization of α particles in air is shown in Figure 8.3: the number of ion pairs produced per millimeter of air increases strongly with the distance and falls

Figure 8.2 α-rays in a cloud chamber.

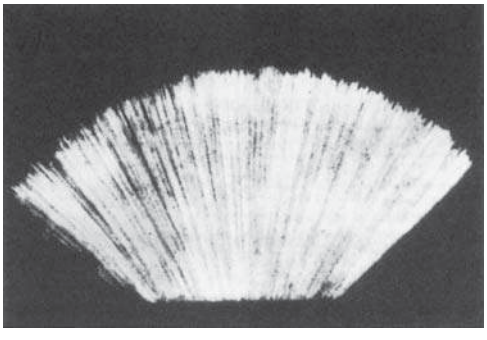

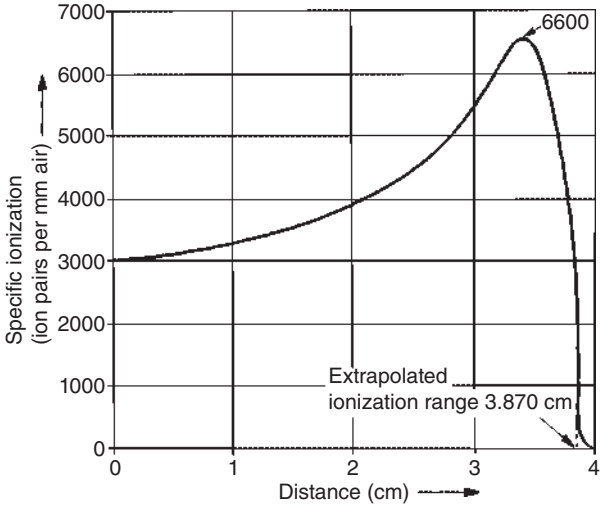

Figure 8.3 Specific ionization of the α particles of ^{210}Po in air.

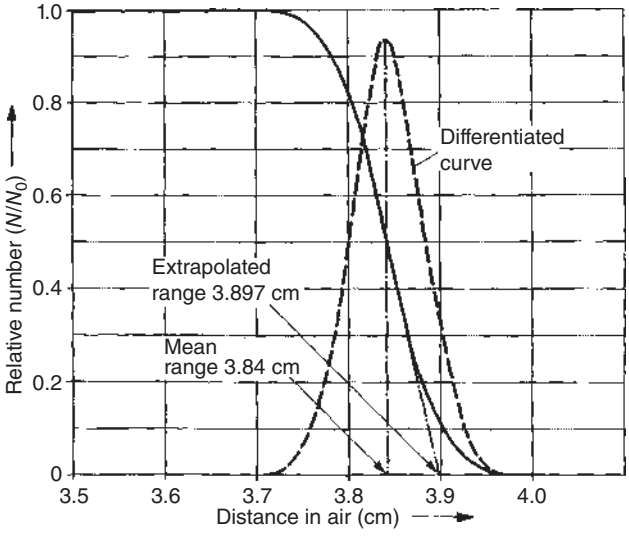

Figure 8.4 Relative number of the α-particles from ^{210}Po as a function of the distance.

off rather sharply near the end of the range of the α particles. The increase is due to the decreasing velocity of the α particles. As the energy decreases by about 35 eV per ion pair generated, an α particle with an initial energy of 3.5 MeV produces about 10^5 ion pairs. At the end of its path it forms a neutral He atom.

The relative number of α particles is plotted in Figure 8.4 as a function of the distance from the source. The variation of the range is caused by the statistical variation of the number of collisions. Exact values of the range in air are obtained by

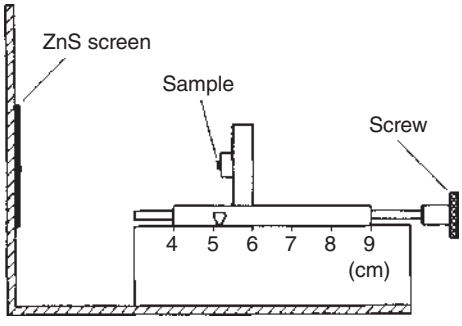

Figure 8.5 Device for the determination of the range of α-particles in air.

Table 8.1 Range of the α particles of ^{214}Po ($E = 7.69$ MeV) in various substances.

Substance	Extrapolated range (cm)	Density (g cm^{-3})	Range (mg cm^{-2})
Air	6.95	0.001 226	8.5
Mica	0.003 6	2.8	10.1
Lithium	0.012 91	0.534	6.9
Aluminum	0.004 06	2.702	11.0
Zinc	0.002 28	7.14	16.3
Iron	0.001 87	7.86	14.7
Copper	0.001 83	8.92	16.3
Silver	0.001 92	10.50	20.2
Gold	0.001 40	19.32	27.0
Lead	0.002 41	11.34	27.3

extrapolating or by differentiating the curve in Figure 8.4 (extrapolated range or average range, respectively). A simple device for the determination of the range of α particles in air is shown in Figure 8.5: ZnS emits light as long as it is being hit by α particles. At a certain distance between the ZnS screen and the α source, the emission of light decreases very quickly, indicating the range of the α particles in air. By application of this method, curves of the kind shown in Figure 8.4 can be obtained.

The range of α particles in various substances is listed in Table 8.1. Multiplication of the range in cm by the density of the substance (g cm^{-3}) gives the range in g cm^{-2}. Table 8.1 shows that the ranges in mg cm^{-2} are similar for very different substances; they increase markedly at higher atomic numbers.

As a measure of the absorption properties of a substance, the stopping power is used; it is defined as the energy lost per unit distance traveled by the particle

$$S(E) = -\frac{\mathrm{d}E}{\mathrm{d}x} \tag{8.13}$$

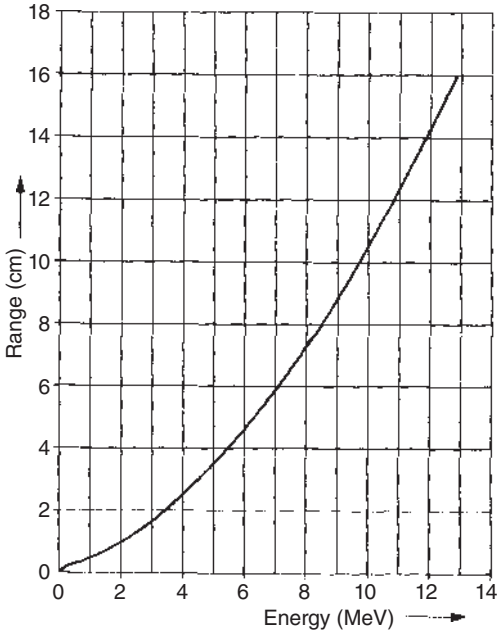

Figure 8.6 Range of α-particles as a function of their initial energy. Source: Modified from Jesse and Sadanskis (1950).

The stopping power depends on the energy of the particle, just as the specific ionization does. The range of the particles is given by

$$R = \int_0^{E_0} \frac{\mathrm{d}E}{S(E)} \tag{8.14}$$

where E_0 is the initial energy.

In Figure 8.6 the range of α particles in air is plotted as a function of their initial energy. The curve can be used to determine the energy of α particles. Most α particles have ranges between about 3 and 7 cm in air, and for these the approximate relation $R\,(\mathrm{cm}) = 0.318E^{3/2}$ (E in MeV) is valid.

In general, the stopping power for heavy charged particles is made up from the electronic stopping power and the nuclear stopping power

$$-\frac{\mathrm{d}E}{\mathrm{d}x} = S_{\text{electronic}} + S_{\text{nuclear}} \approx S_{\text{electronic}} \tag{8.15}$$

The electronic stopping power is much larger than the nuclear stopping power. Nuclear reactions do take place but they are rare. The stopping powers are functions of mass, charge, and velocity of the ion, and the atomic number and the density of the stopping material. Niels Bohr estimated the energy loss rate in a simple way as resulting from a series of impulses given to bound electrons by the ion. A net impulse to the electron occurs in the direction perpendicular to the ion's trajectory. The energy lost by the ion in one encounter with an electron depends on the impact parameter, b, as

$$\Delta E(b) = \frac{2q^2e^4}{m_e v^2 b^2} \tag{8.16}$$

with q being the charge of the ion, υ its velocity, and m_e the electron mass. Multiplying by the electron number density N_e, times the volume element dV, gives the differential expression

$$-dE(b) = \Delta E(b) N_e dV = \Delta E(b) N_e 2\pi \, db \, dx \tag{8.17}$$

Integration should be done over the range b_{min} to b_{max} where b_{min} corresponds to a collision in which a maximum of energy is transferred to the electron. Thus,

$$\Delta E(b_{min}) = \frac{2q^2e^4}{m_e \upsilon^2 b_{min}^2} = 2\gamma^2 m_e \upsilon^2 \tag{8.18}$$

with the Lorentz factor γ (Eq. (1.17)) giving

$$b_{min} = \frac{qe^2}{\gamma m_e \upsilon^2} \tag{8.19}$$

To deduce the maximum impact parameter, one has to consider that the ion rapidly passes the bound electron orbiting with its own characteristic frequency. In order for the collision to be rapid, the time for the ion to pass the atom should be given by the ratio of the impact parameter to the ion's velocity, and the latter, in turn, should be less than the time for an electron orbit, that is,

$$\frac{b_{max}}{\gamma \upsilon} \leq \frac{R_e}{\upsilon_e} \tag{8.20}$$

where, clearly, R_e/υ_e is a function, $f(Z)$, of the atomic number of the stopping material. Combining these two limits into the expression for the energy loss rate results in Bohr's classical equation

$$\left(-\frac{dE}{dx}\right)_{Bohr} = \frac{4\pi q^2 e^4}{m_e \upsilon^2} N_e \ln \frac{\gamma^2 m_e \upsilon^3 f(Z)}{qe^2} \tag{8.21}$$

In a quantum-mechanical correct formalism derived by Bethe and Bloch, with an expanded form of the electron number density, we have

$$\left(-\frac{dE}{dx}\right)_{Bethe-Bloch} = 4\pi N_A r_e^2 m_e c^2 \rho \frac{Zq^2}{A\beta^2} \left[\ln \frac{2m_e c^2 (\gamma\beta)^2}{I} - \beta^2\right] \tag{8.22}$$

where N_A is Avogadro's number, r_e is the radius of the electron, and ρ is the density of the stopping material with atomic number Z, mass number A, and ionization potential I.

Modern versions of the Bethe–Bloch formula include further corrections. One applies these at high energies where polarization of electrons by the Coulomb field of the ion shields more distant electrons. This correction, δ, tends to decrease the electron density. Another correction termed shell correction, C, depends on the orbital velocities of the electrons and is also subtractive. The resulting form is

$$\left(-\frac{dE}{dx}\right)_{Bethe-Bloch} = 0.3071 \ \text{MeV cm}^2 \ \text{g}^{-1} \ \rho \frac{Zq^2}{A\beta^2} \left[\ln \frac{2m_e c^2 (\gamma\beta)^2}{I} - \beta^2 - \frac{\delta}{2} - \frac{C}{Z}\right] \tag{8.23}$$

with the dimension MeV cm^{-1} when the density is in g cm^{-3}. In practice, several computer codes and stopping power tables are available. The website www.srim.org

and the references therein represent the largest compilation on the stopping of energetic ions in matter. The program describing the stopping power and ranges of ions in matter (SRIM) and tutorial about the use of SRIM (TRIM) found there are used widely to estimate stopping powers, ranges, and range straggling.

It is common to divide through by the density, ρ, and to report the mass stopping power

$$-\frac{1}{\rho}\frac{\mathrm{d}E}{\mathrm{d}x}$$

in the dimension $\mathrm{MeV\,cm^2\ g^{-1}}$ which is convenient for combining different materials. The stopping power of a compound or any mixture of materials will depend on the overall density and the relative numbers of atoms of each chemical element. The stopping power is then given by Bragg's rule using the following averaging procedure:

$$\left(\frac{1}{\rho}\frac{\mathrm{d}E}{\mathrm{d}x}\right)_{\text{total}} = \frac{w_1}{\rho_1}\left(\frac{\mathrm{d}E}{\mathrm{d}x}\right)_1 + \frac{w_2}{\rho_2}\left(\frac{\mathrm{d}E}{\mathrm{d}x}\right)_2 + \frac{w_3}{\rho_3}\left(\frac{\mathrm{d}E}{\mathrm{d}x}\right)_3 + \cdots \tag{8.24}$$

where the w_i refer to the mass fraction of element i in the mixture.

The equations for stopping power all have a part that depends on the ion and another that depends on the material. Looking at the part that depends on the ion, it appears that

$$-\frac{\mathrm{d}E}{\mathrm{d}x} \propto \frac{q^2}{v^2}\ln(\gamma^2 v^2) \tag{8.25}$$

in which we can convert v^2 into kinetic energy, E, by applying factors of $m_{\text{ion}}/2$. The resulting expression shows that the energy loss rate is proportional to the mass of the ion and inversely proportional to the kinetic energy:

$$-\frac{\mathrm{d}E}{\mathrm{d}x} \propto \frac{Aq^2}{2E}\ln\frac{\gamma^2 2E}{A} \tag{8.26}$$

At low kinetic energy, the $\ln(\gamma^2 2E/A)$ term is approximately constant and

$$-\frac{\mathrm{d}E}{\mathrm{d}x} \propto \frac{Aq^2}{E} \tag{8.27}$$

indicating that a more energetic ion is losing energy at a lower rate than a less energetic ion. Note that particles with $\beta \approx 0.96$ are called *minimum ionizing particles*. The rate at which kinetic energy is dissipated is relatively constant over most of the ion's path and slowly increases as the ion penetrates into the material, as can be seen in Figure 8.7. Simultaneously, the kinetic energy of the ion uniformly decreases as it moves through the material. Two sudden changes occur as the velocity of the ion approaches the Bohr velocity of the atomic electrons: the energy loss rate increases dramatically as $\beta \to 0$; and the ionic charge decreases as the ion captures orbital electrons causing the rate to drop rapidly. The ion rapidly loses energy at the end of its range and stops suddenly. All particles of a given type follow the same energy loss curve in a given material. The example shown in Figure 8.7 started with 8 GeV ^{40}Ar ions in Be. However, these curves display the expected result for all ^{40}Ar ions with kinetic energies less than 8 GeV. The energy loss of an ion with 3 GeV or 3 MeV can

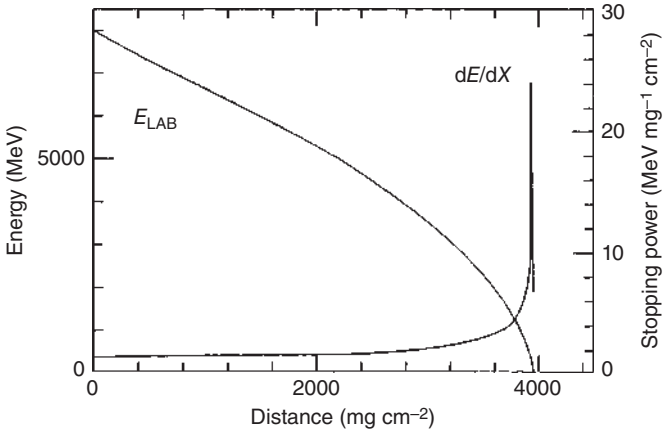

Figure 8.7 Energy loss rate as a function of thickness for a ^{40}Ar projectile in metallic beryllium (scale to the right) for an ion that enters the foil at an energy of 8 GeV. The remaining kinetic energy of the ion is shown on the left scale. Source: Loveland et al. (2006), figure 02 (p. 115)/John Wiley & Sons.

be read off the graph by finding the position where the residual energy of the ion is equal to the required energy. This means that all ions will follow exactly the same energy loss pattern, within statistical limits if we ignore nuclear Coulomb scattering. The latter does occur and is called *energy straggling*. It is represented by a Gaussian distribution

$$\frac{N(E)\,\mathrm{d}E}{N} = \frac{1}{\alpha\sqrt{\pi}} \exp\left[-\frac{(E-\overline{E})^2}{\alpha^2}\right] \tag{8.28}$$

where the straggling parameter α, which is the half-width at $1/e$ height, is given as

$$\alpha^2 = 4\pi q^2 e^4 N_e x_0 \left[1 + \frac{kI}{m_e v^2} \ln \frac{2m_e v^2}{I}\right] \tag{8.29}$$

where the thickness of the material that the ion has penetrated is ρx_0 and k is about 4/3.

In the approximation where the ion follows a straight-line trajectory, the range for a given kinetic energy, $R(E)$, is given by the integral

$$R(E) = \int_0^E -\left(\frac{\mathrm{d}E}{\mathrm{d}x}\right)^{-1} \mathrm{d}E \tag{8.30}$$

There are difficulties inherent in this simple integral: the ions suffer a different number of collisions with atomic electrons and undergo scattering from the Coulomb fields of the atomic nuclei. Thus, the ion's trajectory is made up of a series of straight-line segments. The projection of the range onto the initial velocity vector of the ion will not be a single value but consist of a statistical distribution of ranges, an effect called *range straggling*. Note that the range of an ion and its fluctuations are integral quantities, while the energy loss and its fluctuations are differential quantities.

A word is in order concerning the practical point of calculating the amount of energy deposited in a relatively thin foil, for example, in a target backing. The proper technique relies on determining the ranges of ions in graphs or tables of ranges as follows. Let an ion with energy E_0 pass that foil of thickness t. The particle emerges from the foil with energy E_1 which we want to determine. We find the total range of the ion in the material from tables, R_0. The particles emerging from the foil have the residual range $R_0 - t$. We can then use the range table to determine E_1 that corresponds to the range $R_1 = R_0 - t$. Here, the slowing down by the energy loss rate which is not linear will be contained in the range function and does not have to be evaluated explicitly.

8.3 Beta Radiation

As already mentioned in Section 8.1, the interaction of β radiation with matter is much weaker than that of heavy charged particles. Whereas a 3 MeV α particle has a range of about 1.7 cm in air and produces several thousand ion pairs per millimeter, a β particle of the same energy covers a distance of about 10 m in air and produces only about four ion pairs per millimeter. On the other hand, the electrons are markedly deflected by collisions with other electrons, in contrast to the heavy charged particles, and they therefore exhibit a zigzag course.

The absorption of the β particles of ^{32}P by aluminum is plotted in Figure 8.8. The form of the absorption curve is due to the continuous energy distribution of the β particles and the scattering of the β radiation in the absorber. At the end of the absorption curve a nearly constant intensity of bremsstrahlung (X-rays) is observed.

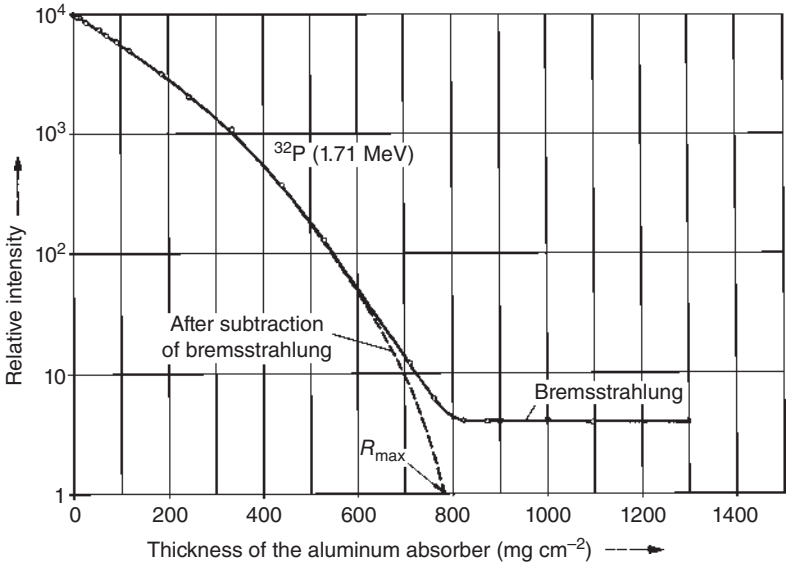

Figure 8.8 Absorption of the β particles of ^{32}P in aluminum.

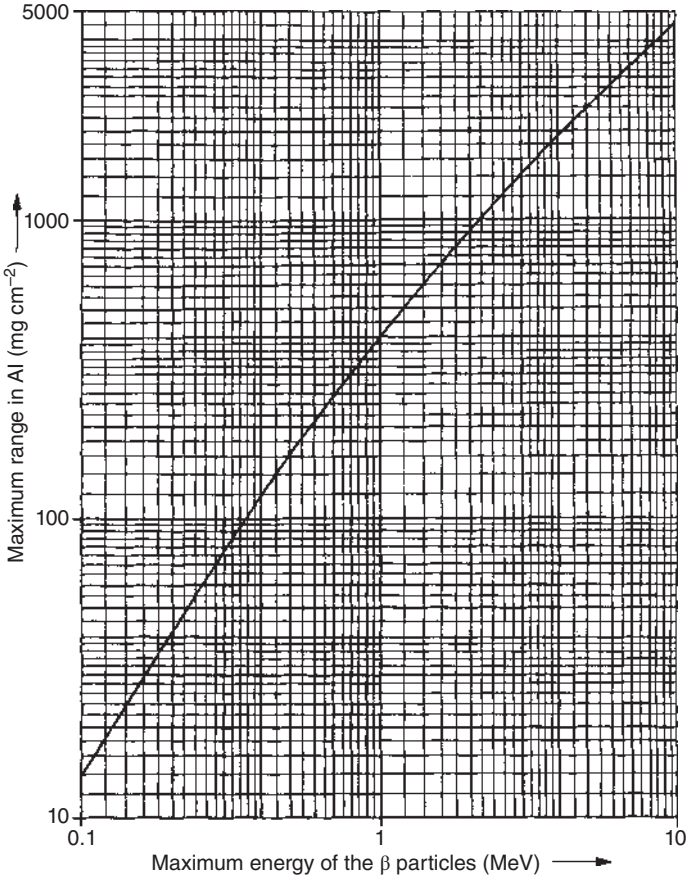

Figure 8.9 Maximum range R_{max} of β particles as a function of their maximum energy E_{max}. Source: Modified from Katz and Penfold (1952).

By extrapolation of the absorption curve, the maximum range R_{max} of the β particles can be found. In practice, this extrapolation is carried out by subtraction of the bremsstrahlung and extension of the curve to $10^{-4}I_0$ (Figure 8.8).

Absorption curves of β^- and β^+ radiation are very similar. By use of the calibration curve in Figure 8.9, the maximum energy E_{max} of β particles can be determined from their maximum range R_{max}.

Conversion electrons are monoenergetic and exhibit a nearly linear absorption curve (Figure 8.10), if their energy is more than 0.2 MeV. At energies below 0.2 MeV, the absorption curve deviates from linearity. To obtain the effective range of conversion electrons, the linear part of the absorption curve is extrapolated to the intensity $I = 0$.

β radiation interacts with matter in three different ways:

a) Interaction with electrons leads to excitation of the electron shell and ionization. The important parameter for this interaction is the electron density in the

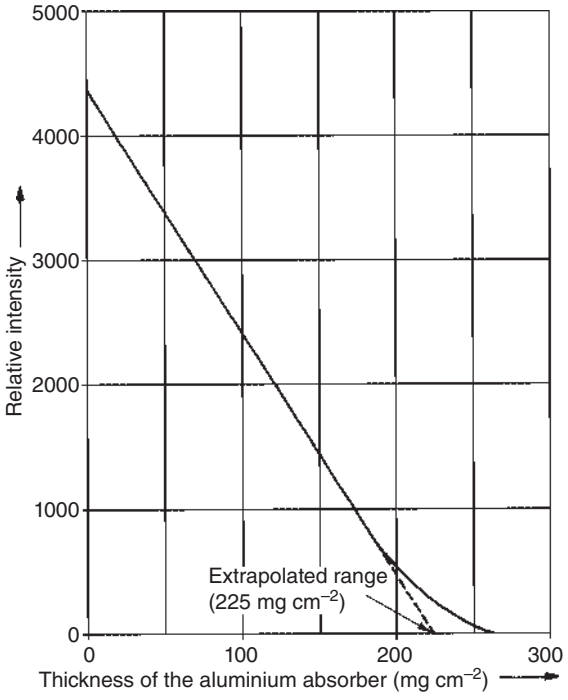

Figure 8.10 Absorption of the conversion electrons of ^{137m}Ba.

absorber, that is, the number of electrons per mass unit given by Z/A. This is given in Table 8.2 for three different energies E_{max} of β particles and different absorbers. The electronic stopping power of electrons is derived in a very similar way as the stopping power of heavy charged particles.

b) Interaction with atomic nuclei increases with the energy of the β radiation. In the electric field of a nucleus, high-energy electrons emit X-rays of continuous energy distribution (bremsstrahlung) and lose their energy in steps. The ratio of energy loss by emission of bremsstrahlung (radiative stopping power) and energy loss by ionization is approximately given by

$$\frac{E(\text{bremsstr.})}{E(\text{ioniz.})} = \frac{E_{max} \cdot Z}{800} \tag{8.31}$$

where E_{max} is the maximum energy of the β radiation in MeV and Z the atomic number of the absorber. Equation (8.31) indicates that the radiative contribution becomes significant for high values of Z and high electron energies (several hundred megaelectronvolts). As β-particle energies are much smaller, the radiative contribution to the stopping power of β particles is small.

c) Backscattering can be measured by the method shown in Figure 8.11. It also depends on the energy E_{max} of the β radiation and the atomic number Z of the absorber, as shown in Figure 8.12 for three different energies E_{max} as a function of Z.

Studies of range distributions of β^- particles were important before solid-state detectors were available. These measurements have shown that the combination

Table 8.2 Maximum range of β particles of three different energies in various substances.

Maximum energy (MeV)	Substance	*Z/A*	Maximum range (mg cm^{-2})
0.156 (^{14}C)	Water	8/18 = 0.44	34
	Aluminum	13/27 = 0.48	28
1.71 (^{32}P)	Water	0.44	810
	Aluminum	0.48	800
1.0	Aluminum	0.48	400
	Gold	79/197 = 0.40	500

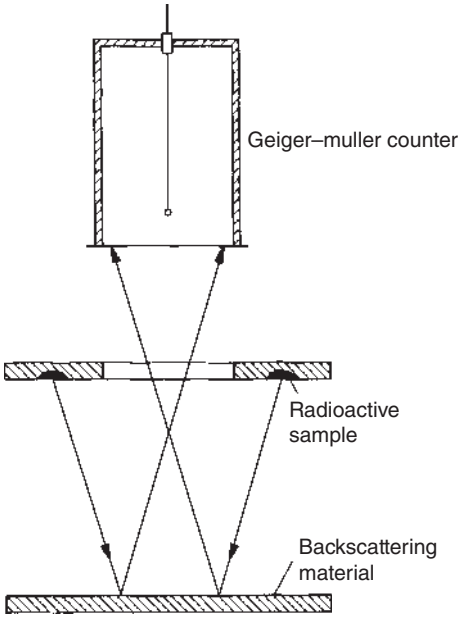

Figure 8.11 Setup for the measurement of backscattering.

of the Fermi energy distribution with the sloping range distribution leads to an approximately exponential attenuation of the β-decay electrons as

$$N_t = N_0 e^{-\mu t} \tag{8.32}$$

where N_t is the number of β particles transmitted through a thickness t; μ can be associated empirically with the energy E_{max} as

$$\mu(\mathrm{m^2\ kg^{-1}}) = 1.7 E_{max}^{-1.14} \tag{8.33}$$

where E_{max} is given in MeV.

In the case of absorption of β^+ radiation, emission of γ-ray photons is observed: positrons are the antiparticles of electrons (Section 1.5.6). After having given off

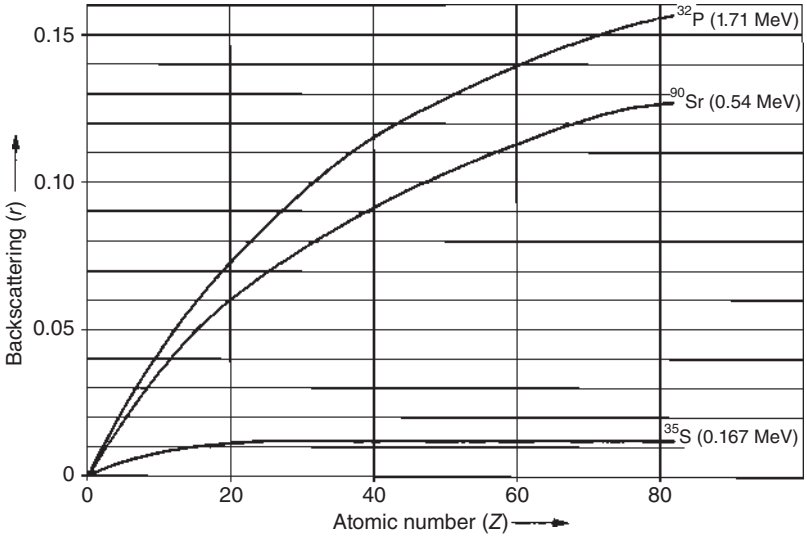

Figure 8.12 Backscattering of β radiation of various energies as a function of the atomic number Z of the absorber.

their energy by the interactions (a)–(c), they react with electrons by annihilation and emission of predominantly two γ-ray photons with an energy of 511 keV each in opposite directions (conservation of momentum). The energy of $2 \cdot 511 = 1022$ keV is equivalent to the sum of the masses of the electron and the positron. This annihilation radiation allows identification and measurement of β^+ radiation.

The maximum energy of β^+ radiation can be determined by plotting an absorption curve as shown in Figure 8.8, or, more accurately, by use of a magnetic spectrometer, as in the case of, for instance, α particles, where the relation between the velocity and the magnetic flux density B is $\upsilon = \mathrm{B}\ \rho Ze/m$, but (for β particles) at much lower flux density B, because of the higher e/m value. At the same energy, the velocity υ of electrons is much higher than that of α particles, which makes relativistic correction necessary:

$$\upsilon = B\rho\frac{e}{m_0}\sqrt{1-\left(\frac{\upsilon}{c}\right)^2} \tag{8.34}$$

where ρ is the radius of the β particles in the spectrometer, e their charge, m_0 their rest mass, and c the velocity of light. An example of a β spectrum is given in Figure 6.23.

Charged particles moving in a substance with a velocity which is higher than the velocity of light in that substance emit Cerenkov radiation. Thus, deep-blue Cerenkov radiation is observed if β radiation passes through a transparent substance, such as water, because the condition $\upsilon \geq c/n$ (n is the refractive index of the substance) is already fulfilled for β particles at relatively low energies, in contrast with α particles of the same energy. The electrons can be compared to a source of sound moving faster than the velocity of sound and carrying with it a Mach cone.

With respect to radiation protection, absorbers of low atomic numbers Z are already useful for absorption of β radiation, for instance, aluminum of about 1 cm thickness.

8.4 Gamma Radiation

X-rays and γ-rays have similar properties and are distinguished by their origins: X-rays are emitted from the electron shell of atoms, if electrons are passing from states of higher energy to those of lower energy (characteristic X-rays) or if electrons are slowed down in the field of nuclei (bremsstrahlung); γ-rays are emitted from nuclei, if these decay from excited states to states of lower energy. The energy range of X-rays varies from about 100 eV to 150 keV (range of wavelengths about 10 nm to 10 pm), and that of γ-rays from about 10 keV to 10^4 MeV (range of wavelengths about 0.1 to 10^{-7} nm). That means there is an overlap in the energy ranges of X-rays and γ-rays. Electrons with energies above 10 MeV striking a substance of high atomic number induce the emission of very energetic ("hard") bremsstrahlung, which is also called γ radiation, because of its high energy. In contrast to the γ-rays emitted from nuclei, this bremsstrahlung shows a continuous energy distribution. Monoenergetic bremsstrahlung, "tagged photons," can be produced behind a "radiator" at electron accelerators by measuring the energy of the scattered electron in a magnetic spectrometer, thus defining the energy of the produced photon.

The absorption of γ-rays and X-rays is, in principle, different from that of charged heavy particles or β-rays. While the latter lose their energy by a succession of collisions, γ-ray photons give off their energy mostly in one process. Because they do not carry a charge, their interaction with matter is small. For the absorption of γ-rays an exponential law is valid:

$$I = I_0 \mathrm{e}^{-\mu d} \tag{8.35}$$

(μ is the absorption coefficient and d the thickness of the absorber). The exact validity of this exponential law is restricted to monoenergetic γ radiation, a narrow pencil of γ-rays, and a thin absorber.

The relation between the energy of γ radiation and its absorption is characterized by the half-thickness $d_{1/2}$, that is, the thickness of the absorber by which the intensity of the γ radiation is reduced to half of it. Introducing $I = I_0/2$ in Eq. (8.35) gives

$$d_{1/2} = \frac{\ln 2}{\mu} \tag{8.36}$$

Instead of the linear absorption coefficient, the mass absorption coefficient μ/ρ ($\mathrm{cm^2\ g^{-1}}$) is often used:

$$I = I_0 \mathrm{e}^{-\mu d/\rho} \tag{8.37}$$

In this equation, d is in units of $\mathrm{g\,cm^{-2}}$. The absorption of the γ radiation of ^{137}Cs as a function of d in $\mathrm{g\,cm^{-2}}$ is plotted in Figure 8.13.

Due to the exponential absorption law, the intensity $I = 0$ is not attained. By $7d_{1/2}$ the initial intensity is reduced to about 1%, and by $10d_{1/2}$ to about 1%. For the purpose

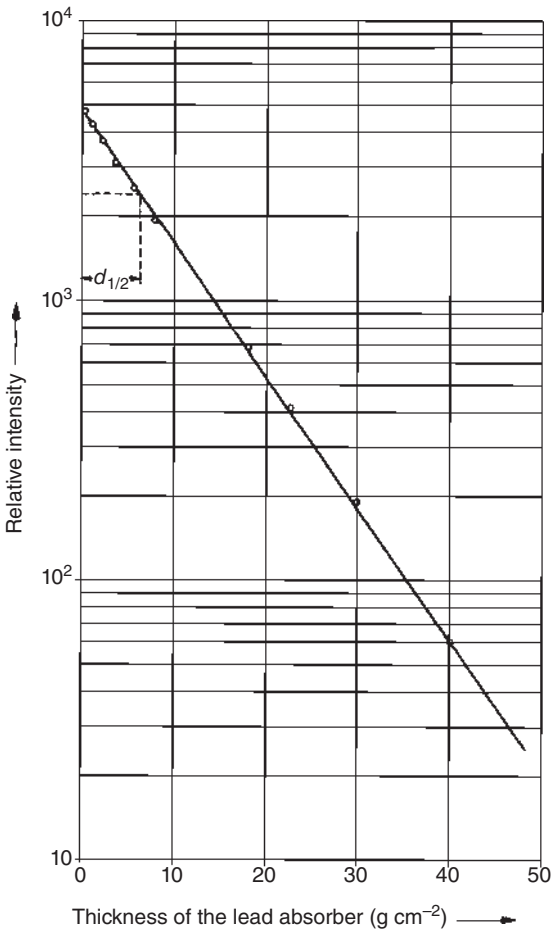

Figure 8.13 Absorption of the γ radiation of ^{137}Cs.

of radiation protection, it is useful to know that the intensity of 1 MeV γ radiation is reduced to about 1% by 5 cm of lead or 25 cm of concrete.

In the first place, the absorption of γ radiation depends on the density of the absorber, similar to the absorption of α or β radiation. Table 8.3 lists the mass absorption coefficients for various absorbers and various energies of γ radiation.

The half-thickness of γ radiation in lead can be used as a measure of the energy (Figure 8.14). The fact that, at higher energies, two values are found for the same half-thickness is due to the coexistence of several different absorption mechanisms. These are due to interactions of the photons with the nuclei or with the shell electrons. Table 8.4 lists the types of interactions of photons (X-rays and γ radiation) with matter as well as the dependence of the cross-section of the interaction on the atomic number, Z, of the medium. Figure 8.15 shows the cross-sections as a function of photon energy:

Table 8.3 Mass absorption coefficient μ/ρ (g cm^{-2}) for γ-rays of different energy.

E_γ (MeV)	Nitrogen	Water	Carbon	Sodium	Aluminum	Iron	Copper	Lead
0.1022	0.1498	0.165	0.1487	0.1532	0.1643	0.3589	0.4427	5.30
0.2554	0.1128	0.1255	0.1127	0.1086	0.1099	0.1186	0.1226	0.558
0.5108	0.0862	0.096	0.0862	0.0827	0.0833	0.0824	0.0814	0.149
1.022	0.0629	0.0697	0.0629	0.0603	0.0607	0.0590	0.0580	0.0682
2.043	0.0439	0.0488	0.0438	0.0422	0.0427	0.0420	0.0414	0.0442
5.108	0.0270	0.0298	0.0266	0.0271	0.0286	0.0312	0.0315	0.0434
10.22	—	0.0216	—	—	0.0226	—	—	0.0537

Source: Modified from Davisson and Evans (1952).

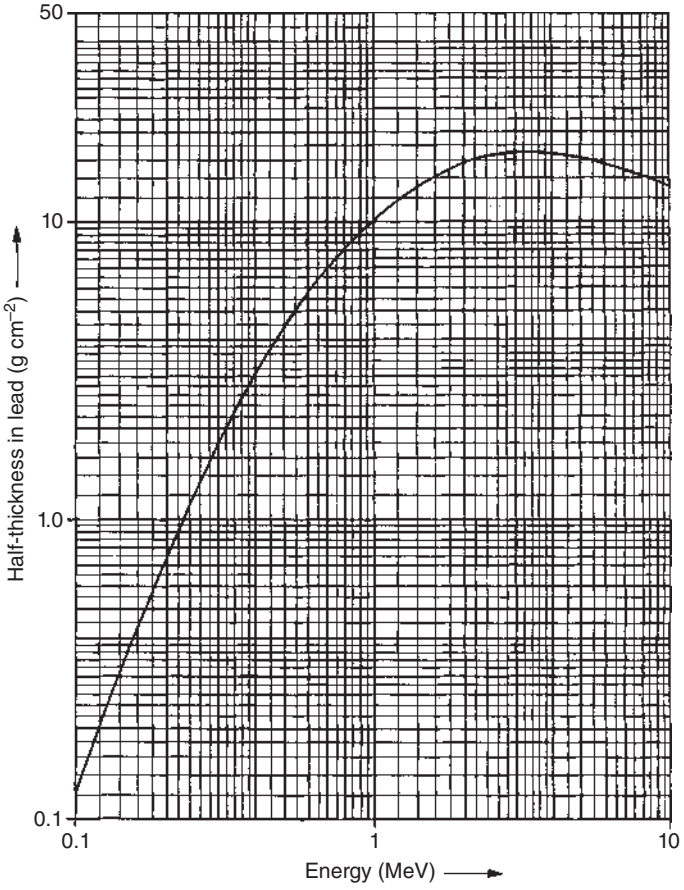

Figure 8.14 Half-thickness of γ radiation in lead as a function of the energy. Source: Modified from Davisson and Evans (1952).

Table 8.4 Types of interactions of photons (X-rays and γ radiation) in matter.

Reacting constituent	Absorption	Scattering	
		Elastic	Inelastic
Shell electrons	Photoelectric effect $\sigma \propto Z^4$	Rayleigh scattering $\sigma \propto Z^2$ Thomson scattering $\sigma \propto Z$	Compton effect $\sigma \propto Z$
Atomic nuclei	Photonuclear reaction (γ,n), (γ,p), etc., $\sigma \propto Z$ resonance absorption	(γ,γ) scattering $\sigma \propto Z^2$	(γ,γ′) scattering
Coulomb field of nuclei	Pair production $\sigma \propto Z^2$		

The Z dependence of the cross-section of the interaction is also shown 5.

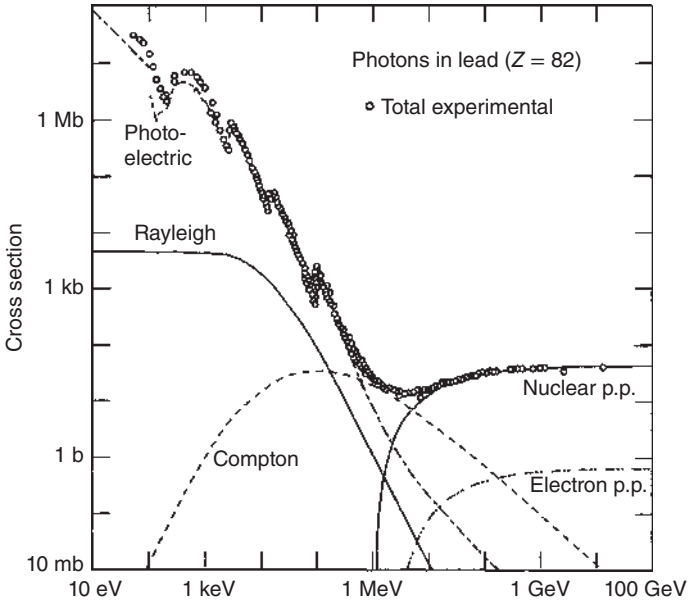

Figure 8.15 Total cross-section in barn of photon interactions in lead as a function of photon energy. The contributions by the photoelectric effect, Rayleigh and Compton scattering, and pair production in the field of the nucleus (nuclear p.p.) and of the shell electrons (electron p.p.) are depicted. Note the resonances ("edges" as they are called) in the photoelectric effect. Source: Horváth and Vértes (2011), figure 03 (p. 70)/Springer Nature.

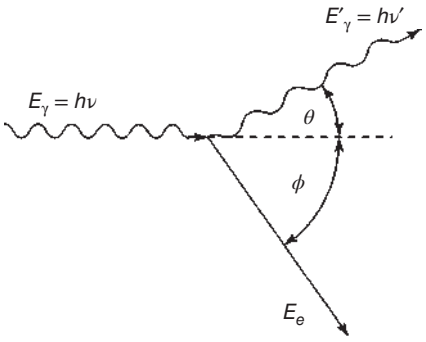

Figure 8.16 Compton effect. Source: Horváth and Vértes (2011), figure 04 (p. 70)/Springer Nature.

a) By the photoelectric effect, a γ-ray photon transfers its energy to a bound electron, which is emitted as a photoelectron. The energy of the photoelectron is

$$E_e = E_\gamma - E_B \tag{8.38}$$

E_γ is the energy of the γ-ray photon and E_B the binding energy of the electron. Momentum conservation prohibits the photoelectric effect on free electrons; the atom has to absorb the recoil momentum. The recoil energy of the resulting ion can be neglected, because of the small mass of the electron compared to the mass of the ion. E_B is, in general, also relatively small compared to E_γ.

b) By the Compton effect, a γ-ray photon gives off only a part of its energy to an electron, which is emitted. According to the law of conservation of momentum, the γ-ray photon changes its frequency ν and its direction, as shown in Figure 8.16. Since the binding energy of the electron is negligible compared to E_γ, we assume the electron to have been free before the collision. The energy of the scattered γ-ray photon is

$$E'_\gamma = \frac{E_\gamma}{1 + \frac{E_\gamma}{m_e c^2}(1 - \cos\theta)} \tag{8.39}$$

where E_γ is the initial energy of the photon, θ the angle of scattering, m_e the rest mass of the electron, and c the velocity of light. The energy of the emitted electron is

$$E_e = E_\gamma \frac{(1 - \cos\theta)}{1 + \frac{E_\gamma}{m_e c^2}(1 - \cos\theta)} \tag{8.40}$$

The maximum energy of the emitted electron occurs for $\theta = 180°$ and is, for $E_\gamma / m_e c^2 \gg 1$, roughly $E_\gamma - m_e c^2/2 = E_\gamma - 255\,\text{keV}$ where a sharp drop of the continuum energy spectrum of the Compton effect is observed, which is called the Compton edge.

c) Pair production is observed at energies $E_\gamma \geq 2 m_e c^2 = 1.022\,\text{MeV}$. For energy–momentum conservation, pair production requires a third body, so pairs are usually created in the Coulomb field of an atomic nucleus. In the electric field of nuclei, the γ-ray photon is transformed into an electron and a positron, provided that the energy is at least equivalent to the sum of the masses of the electron and the positron. Thus, pair formation is the reverse of annihilation. Its

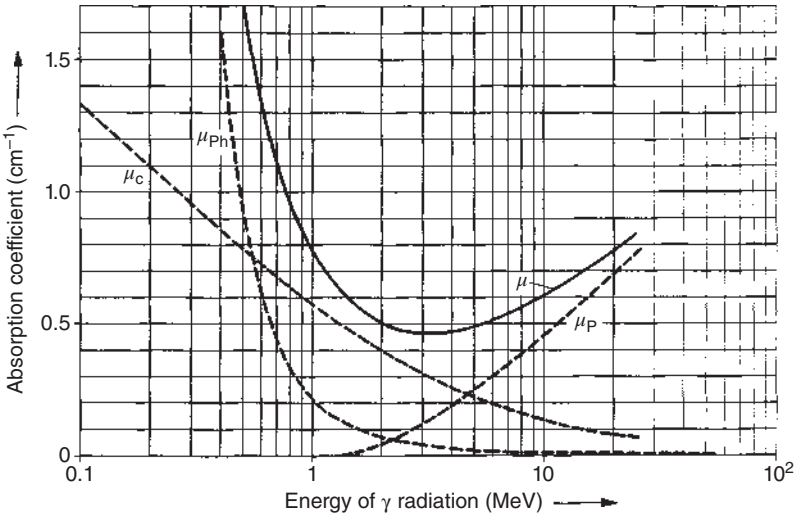

Figure 8.17 Total absorption coefficient μ and partial absorption coefficients of γ radiation in lead as a function of the energy. Source: Modified from Davisson and Evans (1952).

probability increases sharply with increasing energy of the γ-ray photons and represents the majority of the absorption processes at energies $E_\gamma = 10\,\text{MeV}$. Furthermore, pair production increases with the square of the atomic number Z of the absorber. Similar to bremsstrahlung, pair production can also occur in the field of the atomic electrons and, to approximately include this mechanism in the cross-section, the Z^2 dependence should be replaced by a $Z(Z+1)$ dependence.

The total absorption coefficient μ is given approximately by the sum of the partial absorption coefficients due to the photoeffect (μ_{Ph}), the Compton effect (μ_{C}), and pair formation (μ_{P}):

$$\mu = \mu_{\text{Ph}} + \mu_{\text{C}} + \mu_{\text{P}} \tag{8.41}$$

The contributions of these partial absorption coefficients to the absorption of γ radiation in lead are plotted in Figure 8.17 as a function of the initial energy of the γ radiation. The strong increase in the contribution of pair formation at higher energies leads to the bending of the curve for the total absorption coefficient μ in Figure 8.17.

In Figure 8.18, the total absorption coefficient for photon interactions of γ radiation in Pb, Cu, Fe, and Al is plotted as a function of the energy of the γ radiation. Besides the main absorption processes (a) to (c), several other processes are of minor influence. At low energies of the γ radiation, elastic scattering by the atoms of the absorber is observed, as in the case of X-rays. Here, no energy is transferred to the atoms; they are neither ionized nor excited – just the direction of the photon is changed. The electromagnetic field of the propagating photon

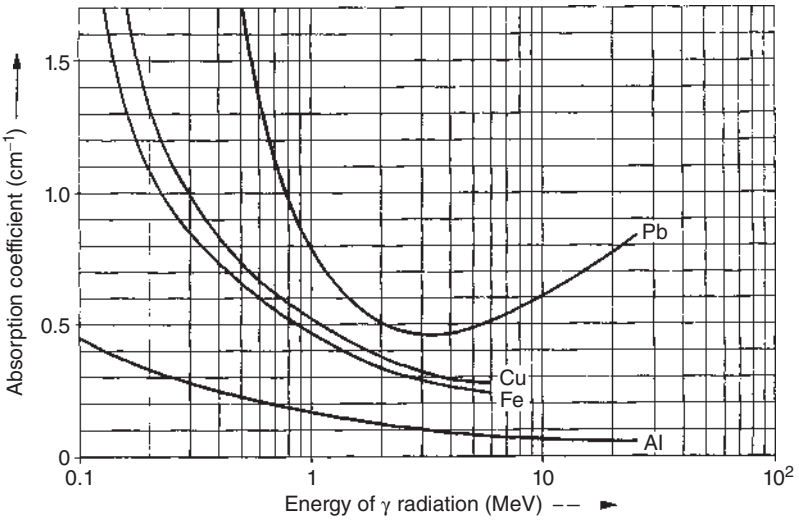

Figure 8.18 Total absorption coefficient of γ radiation in various materials as a function of the energy. Source: Modified from Davisson and Evans (1952).

polarizes the atoms of the medium and induces electric dipoles on which the photon is scattered by the atom as a whole, and we speak of Rayleigh or coherent scattering, cf. Figure 8.15. At very low energies, we have elastic scattering on free electrons (Thomson scattering). At moderate energies, photons do not interact with each other. A very high-energy photon ($E_\gamma > 1$ GeV), on the other hand, can convert into a virtual particle–antiparticle pair for very short times and distances, as allowed by the Heisenberg uncertainty principle. Thus, a high-energy photon can interact with the virtual constituents of another photon (photon–photon interaction). At high energies of the γ radiation, nuclear reactions are induced (photonuclear reactions).

The energy of γ radiation can be found roughly from the half-thickness $d_{1/2}$ by use of the curve in Figure 8.14. The more accurate method of determination of γ-ray energies and of identification of radionuclides is γ-ray spectrometry by means of solid-state detectors. In the γ-ray spectra obtained by this method, sharp photopeaks are observed which allow determination of the energy according to Eq. (8.38).

Absorption of γ radiation for the purpose of radiation protection requires lead walls or thick walls of concrete, as already mentioned in Section 8.1.

8.5 Neutrons

Neutrons are emitted by spontaneously fissioning heavy nuclei. They play an important role in nuclear reactions, in particular in nuclear fission (Section 12.7.6). High fluxes of neutrons are available in nuclear reactors (Chapter 15).

Neutrons are the most penetrating radiation for the simple reason that their only significant interaction is with nuclei via the strong force. Because neutrons are electrically neutral, their interaction with electrons through their magnetic

dipole moment is very small and primary ionization by neutrons is negligible. The probability for interaction of fast neutrons with matter is very small as it is practically confined to the very small nuclei. On the other hand, neutrons cause significant radiation damage because all of their interactions cause nuclear recoil and many lead to nuclear transmutation.

The contributions of the different kinds of interaction depend on the energy of the neutrons. The following energy ranges are distinguished:

<335 neV: Ultracold neutrons (UCNs), velocities around 6 m s^{-1}.
<0.1 eV: Thermal neutrons (the energy distribution is comparable to that of gas molecules at ambient temperature corresponding to a mean kinetic energy of 0.025 eV corresponding to a velocity of 2200 m s^{-1}).
0.1–100 eV: Slow neutrons (neutrons with energies on the order of 1 eV to 1 keV are also called resonance neutrons, because maxima of absorption are observed in this energy range).
0.1–100 keV: Neutrons of intermediate energies.
0.1–10 MeV: Fast neutrons.

Neutrons are termed ultracold (UCN) when they are slow enough to be confined in traps. Such traps may be formed by (i) the strong material optical (Fermi) potential V_F in suitable material bottles (V_F (^{58}Ni) ≈ 335 neV), (ii) magnetic potential walls (60 neV T^{-1}), and (iii) the potential energy of the Earth's gravitational field (100 neV m^{-1}). At this time, "superthermal sources" produce the highest UCN densities, for example, by down-scattering in solid deuterium (sD_2 at 5 K) of cold neutrons into the UCN regime where the kinetic energy of the incoming neutron leads to phonon excitations of the solid state. The strong interaction potential introduced by Fermi is an effective potential that corresponds for a positive scattering length (Chapter 12) to a repulsive interaction

$$V_F = \frac{2\pi\hbar}{m} Na \tag{8.42}$$

where m is the neutron mass, N the number density of nuclei in the material, and a the coherent scattering length of the bound nucleus. The wave function of a neutron reflected from a material surface represented by a step V in potential energy is shown in Figure 8.19, indicating that a small fraction W, due to quantum-mechanical tunneling, is also penetrating the surface and is absorbed in the material. A few relevant numbers are given in Table 8.5.

In contrast to protons, deuterons, α particles, and other particles carrying positive charges, neutrons do not experience Coulomb repulsion by nuclei. Low-energy neutrons are very effectively absorbed by a great number of nuclei, giving rise to nuclear reactions. Elements such as B, Cd, Sm, Eu, Gd, and Dy are used as excellent neutron absorbers.

Fast neutrons lose their energy mainly in elastic and inelastic collisions. The energy given off in one elastic collision depends on the angle of collision and is at maximum $4AE_0/(A+1)^2$ in the case of central collisions, where E_0 is the energy of the neutron before the collision and A is the mass number of the target nucleus. The lighter the nucleus, the higher the energy loss of the neutron. Hydrogen-containing

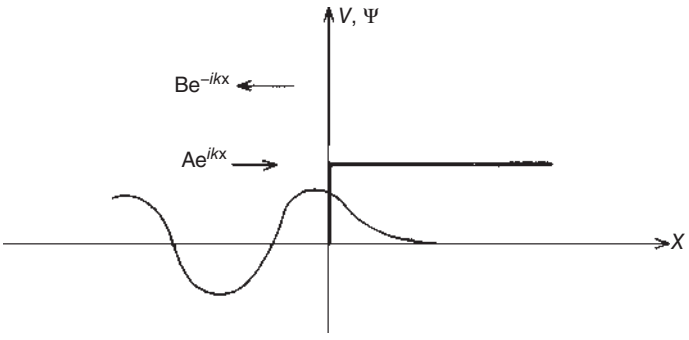

Figure 8.19 Wavefunction of the neutron reflected from a material surface represented by a step V in potential energy indicating that a small fraction W is also penetrating the surface and gets lost.

Table 8.5 UCN properties of a few selected materials.

Element or isotope	ρ (g cm^{-3})	N (cm^{-3}) · 10^{22}	a_{coh}^{bound} (cm) · 10^{-13}	V (neV)	σ_{tot} (barn)	$f = W/V \cdot 10^{-5}$
^{58}Ni	8.8	9.0	14.4	335	44	8.6
Ni	8.8	9.0	10.6	252	48	12.5
Be	1.83	12.3	7.75	252	1.4	0.5
^{65}Cu	8.5	8.93	11.0	244	28	7.0
Fe	7.9	8.5	9.7	210	30	8.5
C	2.0	10.0	6.6	180	1.4	0.6
Cu	8.5	8.93	7.6	168	43.5	15.5
Pb	11.3	3.29	9.6	83	2.0	0.6
Al	2.7	6.02	3.45	54	2.8	2.25

f = UCN loss factor.

substances such as water or paraffin are the most effective media to reduce the energy of neutrons.

In the elastic scattering of neutrons with energies below 10 MeV, all energy transfers between zero and the limit $4AE_0/(A+1)^2$ are equally probable. The probability for a neutron of energy E_0 to get a residual energy between E and $E + \mathrm{d}E$ is

$$P(E)\mathrm{d}E = \frac{\mathrm{d}E}{4AE_0/(A+1)^2} \tag{8.43}$$

and the average energy will be

$$\begin{aligned}\overline{E} &= \int_{E_0[1-4A/(A+1)^2]}^{E_0} P(E)E\,\mathrm{d}E = \frac{(A+1)^2}{4AE_0}\int_{E_0[1-4A/(A+1)^2]}^{E_0} E\,\mathrm{d}E \\ &= E_0\left[1 - \frac{2A}{(A+1)^2}\right]\end{aligned} \tag{8.44}$$

which means that the average value of E/E_0 is independent of E_0. This means that the average value of E/E_0 after n collisions is

$$\frac{\overline{E}_n}{E_0} = \left[1 - \frac{2A}{(A+1)^2}\right]^n \tag{8.45}$$

Note that this distribution of energies is strongly skewed. The probability for a neutron of initial energy E_0 to get an energy between E_n and $E_n + \mathrm{d}E_n$ after n elastic collisions with hydrogen nuclei is obtained from the recursion relation

$$P_n(E_n)\mathrm{d}E_n = \int_{E_n}^{E_0} [\mathrm{d}E_{n-1} P_{n-1}(E_{n-1})] \left[\frac{\mathrm{d}E_n}{E_{n-1}}\right] \tag{8.46}$$

where the term in the first square bracket is the probability of obtaining an energy between E_{n-1} and $E_{n-1} + \mathrm{d}E_{n-1}$ in $n-1$ collisions, and the term in the second square bracket is the probability of going from the interval $E_{n-1} \to E_{n-1} + \mathrm{d}E_{n-1}$ to the interval $E_n \to E_n + \mathrm{d}E_n$ in the nth collision. The integration is performed over the variable E_{n-1}. Ignoring thermal motion, Eq. (8.46) has the solution

$$P_n(E_n) = \frac{1}{(n-1)!E_0}\left(\ln\frac{E_0}{E_n}\right)^{n-1} \tag{8.47}$$

The average number of collisions required to slow down a neutron of initial energy E_0 to an energy E is another interesting quantity. To this end, we write the energy after n collisions

$$E = E_0 f_1 f_2 \cdots f_i \cdots f_n \tag{8.48}$$

where

$$f_i = \frac{E_i}{E_{i-1}} \tag{8.49}$$

A solution can be obtained by taking the logarithm of both sides of Eq. (8.48):

$$\ln\left(\frac{E}{E_0}\right) = \ln(f_1 f_2 \cdots f_i \cdots f_n) = \sum_{i=1}^{n} \ln f_i$$

and by defining $x_i = -\ln f_i$ so that

$$\ln\left(\frac{E_0}{E}\right) = \sum_{i=1}^{n} x_i \tag{8.50}$$

As for a gas molecule, the average number of collisions is the distance traveled divided by the mean free path. The number of collision-free segments of its path is then

$$\overline{n} = \frac{\ln(E_0/E)}{\overline{x}} + 1 = \frac{\ln(E_0/E)}{\overline{\ln(E_{i-1}/E_i)}} + 1 \tag{8.51}$$

where the quantities with bars denote mean values. The mean value of $\ln(E_{i-1}/E_i)$ is obtained in the same way as $\bar{E}$ in Eq. (8.44) resulting in

$$\overline{\ln\left(\frac{E_{i-1}}{E_i}\right)} = 1 - \frac{(A-1)^2}{2A}\ln\left(\frac{A+1}{A-1}\right) \tag{8.52}$$

Substituting Eq. (8.52) in Eq. (8.51) gives

$$\overline{n} = \frac{\ln(E_0/E)}{1 - [(A-1)^2/2A]\ln[(A+1)/(A-1)]} + 1 \tag{8.53}$$

For the particular case of collisions with protons, the denominator in Eq. (8.53) becomes unity, and we obtain

$$E_n = E_0 e^{1-\overline{n}} \tag{8.54}$$

Equation (8.54) tells us that about 20 collisions with protons are necessary to slow down a neutron of several megaelectronvolts to thermal energies. For this purpose, paraffin about 20 cm thick is sufficient. Graphite is also used as slowing-down (moderating) material for neutrons. About 120 collisions with the nuclei of carbon atoms are necessary to have the same effect as 20 collisions with protons. After having lost the main part of their energy, the neutrons are captured by nuclei, giving rise to nuclear reactions. Thus, neutron attenuation follows an exponential law similar to that for photons with an energy-dependent attenuation length μ_{E} as

$$I = I_0 \mathrm{e}^{-\mu_{\mathrm{E}} x} \tag{8.55}$$

where x is the penetration depth and I_0 the incident intensity. The attenuation length is the inverse of the mean free path, λ, which is proportional to the total nuclear reaction cross-section

$$\mu_{\mathrm{E}} = \frac{1}{\lambda_{\mathrm{E}}} = N_0 \sigma_{\mathrm{tot}}(E) \tag{8.56}$$

Here, N_0 is the total number of nuclei per unit volume in the material. The total nuclear reaction cross-section, σ_{tot}, is characteristic of each isotope in the absorbing material. The most important neutron interactions are:

- elastic scattering;
- inelastic scattering (to undergo inelastic scattering, the neutron must have sufficient energy, typically above 1 MeV);
- radiative capture, that is, (n, γ) reactions (for low-energy neutrons, the cross-section follows a $1/\upsilon$ dependence);
- neutron-induced fission, which occurs at all energies where the excitation energy brought in by the neutron exceeds the height of the fission barrier;
- knockout reactions, such as (n, p) and (n, α) reactions, which are common at neutron energy in excess of thermal energy.

Thus, the total interaction cross-section is

$$\sigma_{\mathrm{tot}}(E) = \sigma_{\mathrm{elastic}} + \sigma_{\mathrm{inelastic}} + \sigma_{\mathrm{capture}} + \sigma_{\mathrm{fission}} + \cdots \tag{8.57}$$

Obviously, not all thermal neutrons have the same energy. After neutrons are slowed down to energies comparable to thermal agitation energies, they may either loose or gain energy in subsequent collisions inside the moderator, resulting in a Maxwellian distribution of velocities with the fraction of neutrons with velocities between υ and $\upsilon + \mathrm{d}\upsilon$ being

$$F(\upsilon)\mathrm{d}\upsilon = 4\pi^{-1/2}\left(\frac{M}{2kT}\right)^{3/2} \upsilon^2 \mathrm{e}^{-M\upsilon^2/2kT}\,\mathrm{d}\upsilon \tag{8.58}$$

Here, M is the neutron mass, T the temperature, and k Boltzmann's constant. The most probable velocity is

$$v_{\mathrm{m}} = \left(\frac{2kT}{M}\right)^{1/2} \tag{8.59}$$

and the average velocity is

$$\overline{v} = \left(\frac{8kT}{\pi M}\right)^{1/2} = \frac{2v_{\mathrm{m}}}{\sqrt{\pi}} \tag{8.60}$$

and the average kinetic energy is

$$\overline{E} = \frac{3}{2}kT \tag{8.61}$$

That is, the average kinetic energy of the neutrons depends on the temperature of the moderator. At very low temperatures, the Maxwellian distribution function becomes a poor approximation because of discrete energy levels of the medium.

The velocity distribution that is significant for cross-section calculations is

$$F'(v)\mathrm{d}v = 2\left(\frac{M}{2kT}\right)^2 v^3 \mathrm{e}^{-Mv^2/2kT}\,\mathrm{d}v \tag{8.62}$$

which is different from Eq. (8.58) in the preexponential term because the velocity distribution in a medium and that felt by a sample placed in the medium are different. This is because the probability that a neutron will strike the sample in a given time is proportional to v. It is the weighted distribution denoted here by $F'(v)\mathrm{d}v$ that is significant for any transmutation.

Detection of neutrons is based on ionization processes caused by the products of their interactions (nuclear reactions or collisions) with nuclei.

8.6 Short-Lived Elementary Particles in Atoms and Molecules

Absorption of short-lived particles, such as positrons, muons, pions, kaons, or σ particles, may lead to formation of unusual (exotic) kinds of atoms or molecules. A proton in a hydrogen atom may be substituted by a positively charged short-lived elementary particle, such as a positron or a positive muon, or an electron in the electron shell of an atom or molecule may be substituted by a negatively charged short-lived particle, such as a negative muon, a negative pion, or an antiproton. Some kinds of hydrogen-like atoms containing short-lived elementary particles are listed in Table 8.6. The lifetime of these species varies between about 10^{-9} and 10^{-6} seconds. However, during this time their properties can be studied by application of fast and sensitive electronic methods.

A positronium atom ($\mathrm{e}^+\mathrm{e}^- = \mathrm{Ps}$) is comparable to a hydrogen atom and can be considered to represent the lightest form of an atom, in which e^+ and e^- rotate around a common center of gravity. Positronium atoms have half the reduced mass of hydrogen, half the ionization potential of hydrogen (6.8 eV), and twice the Bohr radius.

Table 8.6 Properties of hydrogen and hydrogen-like atoms containing short-lived elementary particles.

Atom	Binding energy (eV)	Rest mass (u)
(p^+e^-) hydrogen (H)	13.6	1.007 8
(e^+e^-) positronium (Ps)	6.8	0.001 097 2
(μ^+e^-) muonium	13.5	0.114 95
$(p^+\mu^-)$ muonic atom	2 531	1.121 7
$(p^+\pi^-)$ pionic atom	3 236	1.271 7
(p^+K^-)	8 618	1.537 3
(p^+p^-)	12 498	2.014 6
$(p^+\Sigma^-)$	14 014	2.284 3

Positronium atoms are formed by absorption of positrons in matter. For instance, about 30% of the positrons absorbed in argon yield Ps:

$$e^+ + Ar \rightarrow Ps + Ar^+ \tag{8.63}$$

Two ground states of Ps are known, a triplet (ortho) state (*o*-Ps, $^3S_1$, parallel spins of e^+ and e^-, lifetime $1.4 \cdot 10^{-7}$ seconds) and a singlet (para) state (*p*-Ps, $^1S_0$, antiparallel spins of e^+ and e^-, lifetime $1.25 \cdot 10^{-10}$ seconds); *o*-Ps annihilates by emission of three γ-ray photons, *p*-Ps annihilate by emission of 2511 keV photons. In the absence of a chemical environment, there should be three times more triplet Ps than singlet Ps. The annihilation of the unbound e^+ occurs with the same lifetime as the decay of *p*-Ps. Thus, the occurrence of the long-lived component (*o*-Ps) proves the existence of bound Ps.

The lifetime of Ps is strongly affected by the interaction with molecules. Thus, Ps has been used as chemical probe, see Chapter 14.

Muonium atoms (μ^+e^-) are formed by absorption of positively charged muons in matter. They show similarities to positronium atoms.

Muonic atoms (e.g. $p^+\mu^-$), on the other hand, are obtained by absorption of negatively charged muons. In these atoms, μ^- replaces an electron in the electron shell. Due to the relatively high mass of μ^- compared to that of e^-, their interaction with the nucleus is rather strong, and muons serve as probes to study the properties of nuclei. As the ratio of the atomic orbit is inversely proportional to the mass of the orbiting particle, the μ^- orbitals begin to enter the nuclei of muonic atoms with increasing atomic number and consequently the residence time of the muon in the nucleus increases, too. For instance, the "Bohr radius" of μ^- in muonic Pb is only about 4 fm, whereas the radius of the nucleus is about 7 fm. Finally, the muon may be captured by the nucleus or it may decay as a free particle. The influence of the charge distribution in nuclei on muons is also greater than that on electrons, and X-rays emitted by muonic atoms, in particular from inner orbitals, give information about the charge distribution and surface structure of nuclei. The influence of

electron densities and chemical bonds has been studied by use of pionic atoms, such as $p^+\pi^-$.

Finally, another interesting aspect should be mentioned: it is expected that in muonic molecular ions the reactions between nuclei are favored, because of their smaller distance apart, for instance, $d^+d^+\mu^- \rightarrow {}^4He^+ + \gamma$ or $d^+t^+\mu^- \rightarrow {}^4He^+ + n + \gamma$. This kind of reaction would offer the possibility of fusion at relatively low temperatures ("cold fusion") of about 10^3 K in contrast to "hot fusion" at about 10^8 K (Section 15.10).

References

Interaction with Matter

Davisson, C.M. and Evans, R.D. (1952). *Rev. Mod. Phys.* 24: 79.

Horváth, D. and Vértes, A. (2011) Interaction of radiation with matter, in *Handbook of Nuclear Chemistry*, 2nd(eds. A. Vértes, S. Nagy, Z. Klencsár, R.G. Lovas, and F. Rösch), Springer-Verlag, Berlin, p. 363.

Jesse, W.P. and Sadanskis, J. (1950). *Phys. Rev.* 78: 1.

Katz, L. and Penfold, A.S. (1952). *Rev. Mod. Phys.* 24: 28.

Loveland, W., Morrissey, D.J., and Seaborg, G.T. (2006). *Modern Nuclear Chemistry*. Hoboken, NJ: Wiley.

Further Reading

General

Rutherford, E., Chadwick, J., and Ellis, C.D. (1930). *Radiation from Radioactive Substances*. Cambridge: Cambridge University Press (reprinted 1951).

Compton, A.H. and Allison, S.K. (1935). *X-rays in Theory and Experiment*. London: Van Nostrand.

Segrè, E. (ed.) (1953). *Experimental Nuclear Physics*, vol. 1. New York: Wiley.

Draganic, I.G., Draganic, Z.D., and Adloff, J.P. (1990). *Radiation and Radioactivity on Earth and Beyond*. Boca Raton, FL: CRC Press.

Interaction with Matter

Bohr, N. (1913). On the theory of the decrease of velocity of moving electrified particles on passing through matter. *Philos. Mag.* 25: 10.

Dienes, G.J. and Vineyard, G.H. (1957). *Radiation Effects in Solids*. London: Interscience.

Whaling, W. (1958). The energy loss of charged particles in matter. In: *Encyclopedia of Physics*, vol. 34 (ed. E. Flügge). Berlin: Springer-Verlag.

Lindhard, J., Scharff, M., and Schiøtt, H.E. (1963). Range concepts and heavy ion ranges. *K. Dan. Vidensk. Selsk. Mat.-Fys. Medd.* 33 (14): 1–42.

Northcliffe, L.C. and Schilling, R.F. (1970). Ranges and stopping power tables for heavy ions. *Nucl. Data Tables* 7A: 233.

Betz, H.-D. (1972). Charge states and charge-changing cross sections of fast heavy ions penetrating through gaseous and solid media. *Rev. Mod. Phys.* 44: 465.

Neutrons, UCN

Golub, R. and Pendlebury, J.M. (1975). Super thermal sources of ultracold neutrons. *Phys. Lett.* A53: 133.

Steyerl, A., Nagel, H., Schreiber, F.-X. et al. (1986). A new source of cold and ultracold neutrons. *Phys. Lett.* A116: 347.

Ignatovich, V.K. (1990). *The Physics of Ultracold Neutrons*. Oxford: Clarendon Press.

Frei, A., Sobolev, Y., Altarev, I. et al. (2007). First production of ultracold neutrons with a solid deuterium source at the pulsed reactor TRIGA Mainz. *Eur. Phys. J.* A34: 119.

9

Measurement of Nuclear Radiation

9.1 Activity and Counting Rate

The activity (disintegration rate) A as defined in Section 1.4 is a property of radioactive matter and can be measured by various devices which give a certain counting rate I', which depends on the activity A, the overall counting efficiency η of the device, and the background counting rate I_0:

$$I' = I + I_0 = \eta A + I_0 \tag{9.1}$$

Usually, the counting rate is measured in counts per minute (cpm). $I = I' - I_0$ is the (net) counting rate caused by the radioactive sample to be measured. I_0 is the reading in the absence of a radioactive sample. It is due to the radiation emitted by the surrounding material and cosmic radiation. At low radioactivity of the sample, the background counting rate I_0 may contribute appreciably to I' and special measures are taken to minimize I_0.

The overall counting efficiency η depends on the properties of the radionuclides and the measuring device. The various factors contributing to η will be discussed in detail later in this chapter.

At constant η, the net counting rate $I = I' - I_0$ is proportional to the activity A, and for many purposes, such as determination of half-lives or application of radionuclides as tracers, measurement of the relative activity, given by I at constant η, is sufficient.

In Figure 9.1, the logarithm of the net counting rate I is plotted as a function of time t. The curve obtained is called the decay curve and is used for the determination of half-lives.

The counting rate I of a radioactive sample which contains several radionuclides is given by the sum of the counting rates of the individual radionuclides:

$$I' = I_1 + I_2 + \cdots = \eta_1 A_1 + \eta_2 A_2 + \cdots \tag{9.2}$$

If the number of radionuclides present in the sample is low, the decay curve can be separated by subtraction into individual decay curves of the radionuclides, either graphically or arithmetically, as shown in Figure 9.2. The analysis of decay curves is of practical importance for the investigation of radionuclide purity. As examples,

Nuclear and Radiochemistry: Fundamentals and Applications,
Fourth Edition. Jens-Volker Kratz.

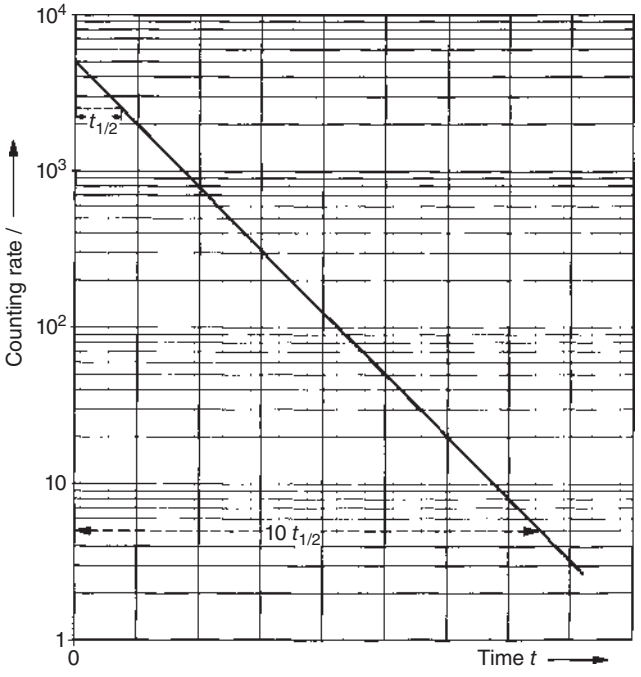

Figure 9.1 Counting rate as a function of time (determination of half-lives).

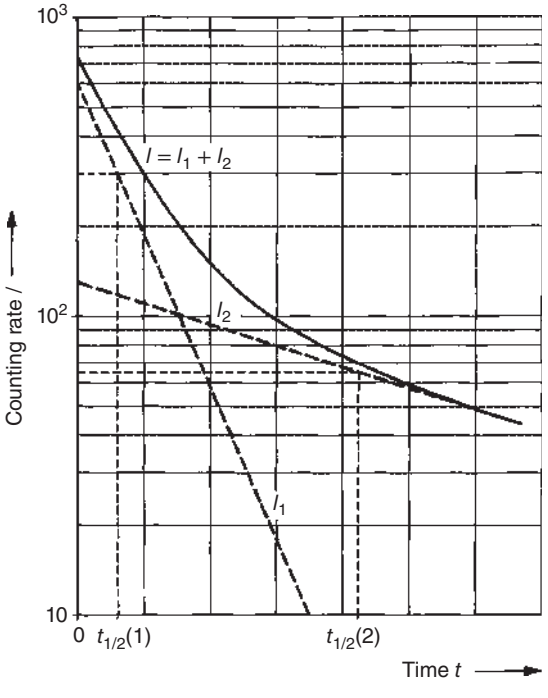

Figure 9.2 Counting rate of a mixture of two radionuclides.

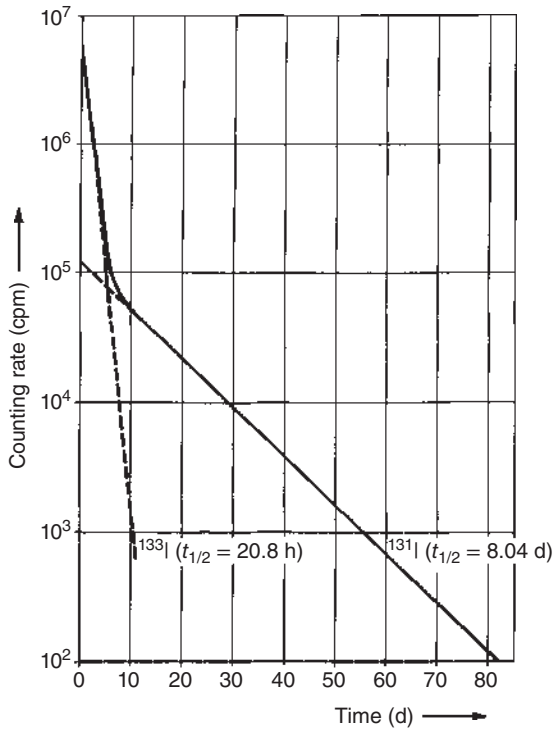

Figure 9.3 Short-lived impurity (^{133}I in ^{131}I).

contamination of a sample by a short-lived impurity is shown in Figure 9.3, and contamination by a long-lived impurity in Figure 9.4.

The overall counting efficiency η in Eq. (9.1) depends on the frequency H of the decay mode measured in relation to the activity, the self-absorption S of the radiation in the radioactive sample, the contribution B of backscattered radiation, the geometrical arrangement G of the sample with respect to the counter, the absorption W of the radiation in the air and in the window of the counter, the internal counting efficiency η_i of the counter, and the correction D for the dead time of the counter:

$$\eta = H \cdot (1 - S) \cdot (1 + B) \cdot G \cdot (1 - W) \cdot \eta_i \cdot (1 - D) \tag{9.3}$$

By self-absorption, absorption in the air and the window, and dead time of the counter, η is reduced, whereas it increases by the influence of backscattering.

The overall counting efficiency η may vary between about 0.01 and 1, depending on the kind of radiation and its energy and the type of counter used. Self-absorption S in the sample is high for α and low-energy β radiation, but negligible for γ radiation. As an example, the self-absorption S of the β^- radiation of ^{45}Ca in samples of $CaCO_3$ is plotted in Figure 9.5 as a function of the thickness of the sample. Backscattering may contribute appreciably to the counting rate in the case of β radiation, if the sample is placed on materials of high atomic number Z, as is evident from Figure 8.11.

The influence of the geometrical arrangement is shown in Figure 9.6. G is given by the solid angle $\Omega/4\pi$. Absorption W in the air and the window of the counter

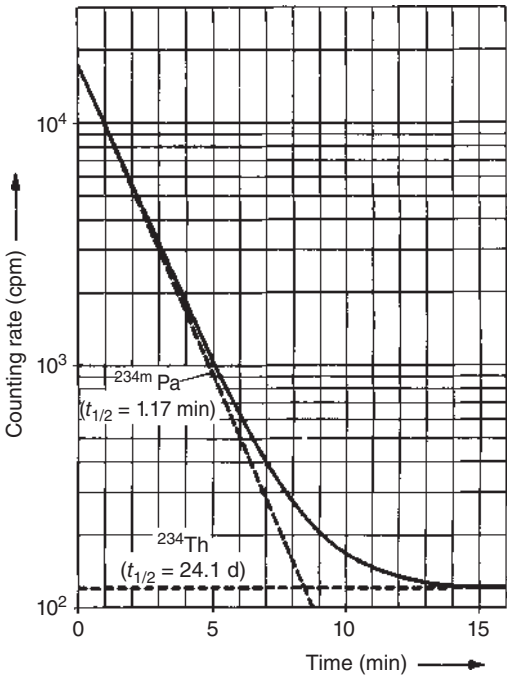

Figure 9.4 Long-lived impurity (^{234}Th in ^{234m}Pa).

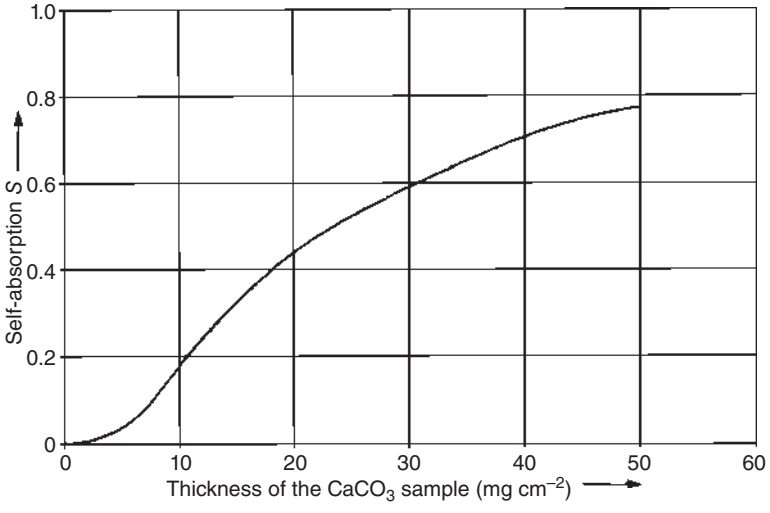

Figure 9.5 Self-absorption S of the β^- radiation of ^{45}Ca in $CaCO_3$ as a function of the thickness of the sample.

is very high for α and low-energy β radiation, like self-absorption S in the samples, and thin windows or windowless counters are needed for the measurement of these kinds of radiation. The internal counting efficiency η_i varies appreciably between about 0.01 and 1.0 with the kind of radiation and the type of counter. The dead time

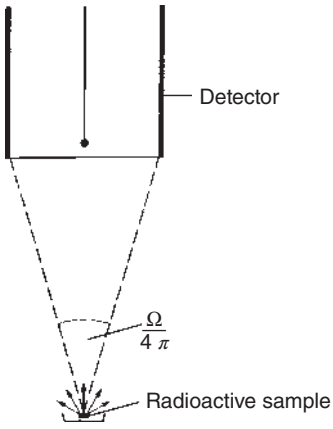

Figure 9.6 Influence of the geometrical arrangement (factor G given by the solid angle $\Omega/4\pi$).

of the counters is due to the fact that they need some time for recovery with the result that, during a certain period, the dead time, registration of a following event is not possible. Relatively long dead times of the order of 100–500 μs are found for Geiger–Müller counters. The number of non-counted events is given by

$$I - I^* = \frac{I^{*2}t}{1 - I^*t} \tag{9.4}$$

I is the "true" counting rate for the dead time $t = 0$, and I^* is the counting rate measured. $I - I^*$ increases appreciably with the number of counted events and with the dead time, as shown in Figure 9.7.

9.2 Gas-Filled Detectors

Gas-filled detectors have been in use since the beginning of radiochemistry. Ionizing radiation passing through a gas creates a trail of ion pairs (positive ions and free electrons). If an electric field is applied, the ions and the electrons move in opposite directions. The motion of the charged particles gives rise to a current that can be measured in an external circuit. A simple arrangement of a gas-filled ionization detector connected to a suitable circuit is shown in Figure 9.8. Commonly, the detector consists of a cathode and an anode placed in a gas-filled chamber. At typical distances of a few centimeters, it takes a few microseconds for the electrons to reach the anode and a few milliseconds for the slower-moving positive ions to reach the cathode. The total number of ion pairs arriving at the electrodes and hence the height of the pulse observed in the circuit depend on the electric field strength or the voltage, respectively, applied to the detector. Either steady-state currents or pulses resulting from individual ionizing events may be measured, depending on the time constant of the device. The time constant RC of the circuit is the time required for an initial charge on the capacitor of capacitance C to be reduced to $1/e$ of its value when the capacitor is short-circuited with a resistance R. If RC is long compared to the time between ionizing events, a steady state is reached and a direct current (or a voltage developed across a known resistor through which this current flows)

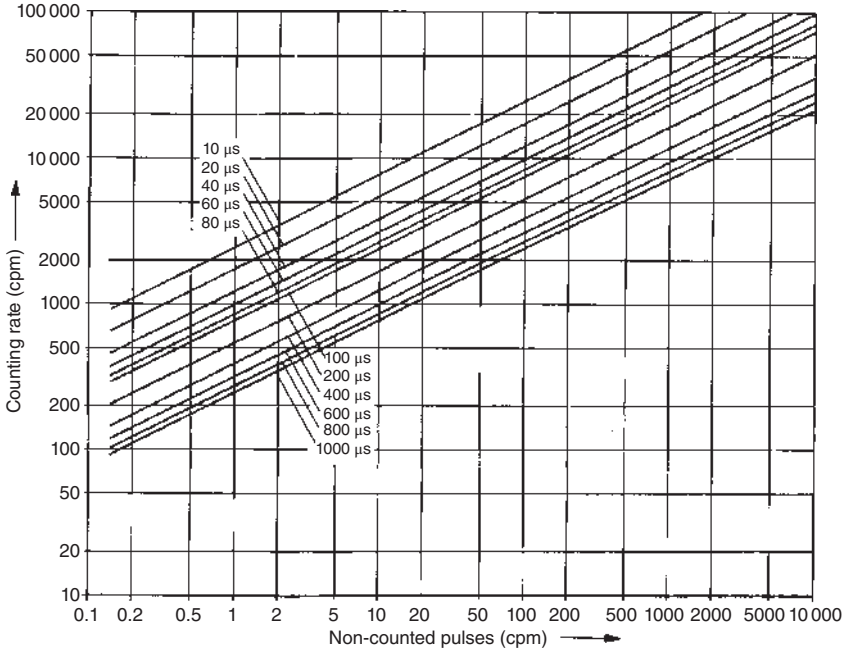

Figure 9.7 Non-counted pulses at different dead times of the detectors.

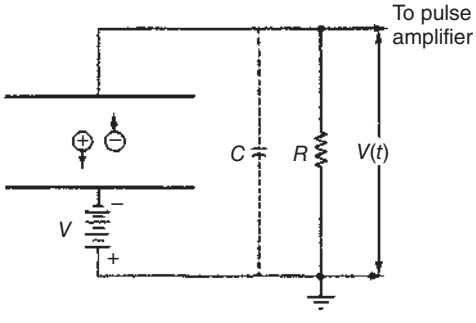

Figure 9.8 Schematic representation of a parallel-plate ionization chamber and its electronic circuit.

may be measured. On the other hand, if RC is small compared to the time between ionizing events, the charges collected during individual events or the corresponding voltages may be measured by means of appropriate alternating current circuitry. In Figure 9.9, the pulse height is plotted as a function of the voltage. At low voltages, the electrons recombine with the ions (region of partial recombination). With increasing voltage, nearly all the electrons are collected at the anode and a saturation current is observed. This is the range of operation of ionization chambers. Because the specific ionization is appreciably higher in the case of α particles than in the case of β particles, an α particle produces a much higher pulse in an ionization chamber, as indicated in Figure 9.9.

In general, an α particle gives off its energy while passing through an ionization chamber and produces $N = E_\alpha/E_1$ ions, where E_α is the energy of the α particle

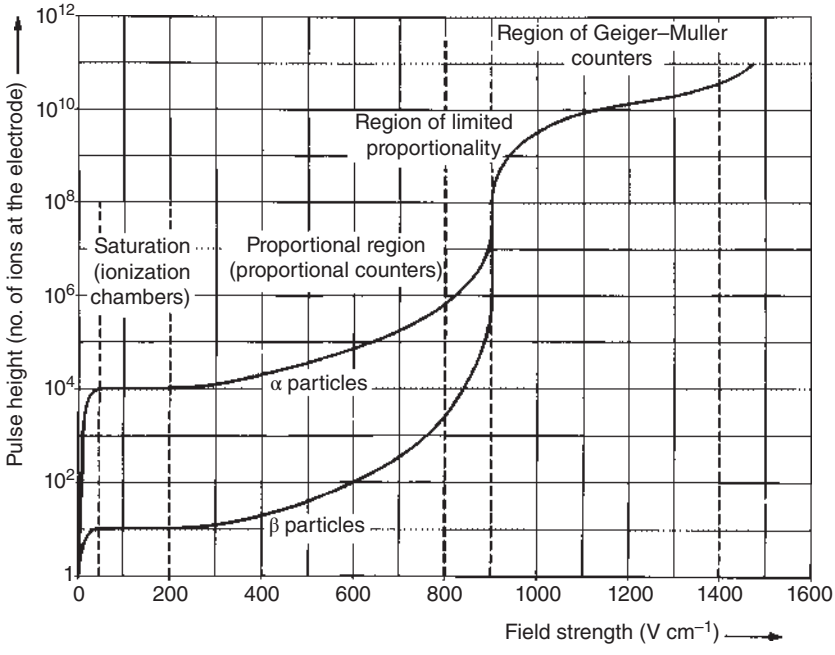

Figure 9.9 Pulse height as a function of the field strength.

and E_1 is the energy used for the production of one ion pair. As in air $E_1 = 35\,\text{eV}$ (Section 8.1), it follows that an α particle with $E_\alpha = 3.5\,\text{MeV}$ produces about 10^5 ion pairs, corresponding to a pulse of approximately $10^{-14}\,\text{A s}$, which can be measured by means of an efficient amplifier. In contrast to α particles, the pulses produced by β particles in an ionization chamber are smaller by a factor of the order of 10^3 and can hardly be measured.

Further increase of the voltage in the gas-filled detector also leads to an increase of the pulse height (Figure 9.9). Under these conditions, the electrons are accelerated on their way to the anode and gain so much energy that they are able to produce secondary free electrons by collisions with the gas molecules (gas amplification). Over a wide voltage range, the output pulse increases with the voltage applied. This is the range of operation of proportional counters. These are always coupled with pulsed operation (small *RC* values). The cathode is most often a cylinder, and the anode is an axial thin wire of 20–50 µm diameter used to obtain high field strengths. In a practical case, the voltage gradients at wall and wire are on the order of $200\,\text{V cm}^{-1}$ and $5 \cdot 10^4\,\text{V cm}^{-1}$. The multiplication factor, given by the ratio of secondary and primary electrons, depends on the voltage and field gradient, respectively, and varies as shown in Figure 9.10 in argon and methane as a function of the applied voltage. It is seen that relatively small admixtures of argon lower the operating voltages of methane-filled proportional counters appreciably. On the other hand, the presence of methane in argon-filled counters decreases the dependence of F on the applied voltage and thus improves the stability of operation with respect to voltage variations. In a given gas, the functional dependence of the

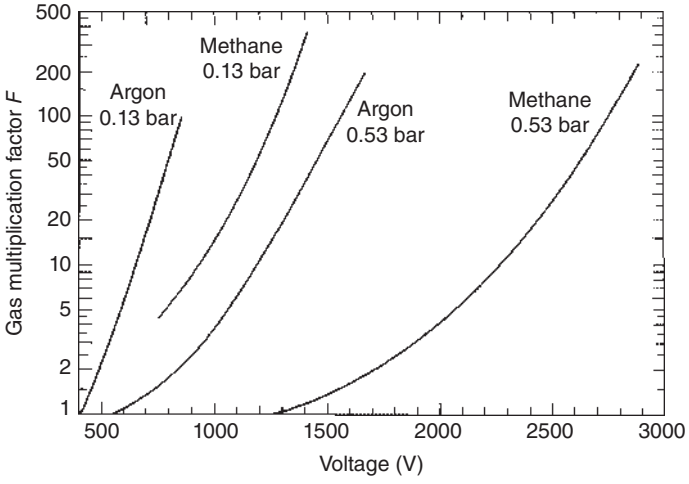

Figure 9.10 Multiplication factors in argon and methane as a function of the applied voltage. Wire radius $r = 0.13$ mm, cathode radius $R = 11$ mm. Source: Friedlander et al. (1981), figure 4 (p. 121)/John Wiley & Sons.

multiplication factor M on wire radius r, cathode radius R, pressure p, and voltage V is of the form

$$F = f\left[\frac{V}{\ln(R/r)}, (pr)\right] \tag{9.5}$$

Because the specific ionization is much higher in the case of α particles, they give higher pulse heights than β particles at the same multiplication factor and α radiation can be measured in the presence of β radiation, as in ionization chambers. α radiation is measured at low voltages and β radiation at high voltages. The pulse heights measured with proportional counters are usually on the order of several millivolts. As the number of primary electrons is proportional to the energy of the particles, this energy can be determined.

If the voltage applied in the gas-filled detector is further increased, the number of electrons collected at the cathode becomes independent of the number of initial ion pairs produced by the incident radiation. This is the operation range of Geiger–Müller counters (Figure 9.9). Under the operating conditions of these counters, a single ionization produced in the gas by any kind of radiation leads to a discharge spreading out over the whole counter by a sequence of secondary ionization processes and giving a relatively high pulse of several volts that can be measured directly without amplification. At still higher voltages, continuous discharge takes place without the influence of radiation.

9.2.1 Ionization Chambers

Ionization chambers are constructed in various ways, for instance, as grid ion chambers, guard ring chambers, current ion chambers, or integrating ion chambers. Usually, the electrodes are parallel plates and enclosed in a gas-tight chamber,

filled with air or a noble gas. Because of the low pulse heights to be measured, good electrical insulation of the electrodes is of great importance. The effect of the slowly moving positive ions is troublesome because, as they move to the cathode, they induce a charge on that electrode. If no correction is made for this induced charge, the size of the output pulse will depend on the position of the particle track. An efficient way to eliminate the positive ion induction is the addition of, for example, a grid to the ionization chamber. The grid positioned parallel to the collecting electrode is charged positively with respect to the cathode but less positive than the anode. It shields the collecting electrode from the effects of the positive ions.

As mentioned above, in certain applications, instead of recording pulses of individual particles, the charge from several events is integrated. For example, if an α particle produces 10^5 ion pairs and 10^6 α particles per second enter the chamber, they produce 10^{11} ion pairs corresponding to a current of 10^{-8} A, which can be easily measured. The current from the chamber is then measured as a function of time to determine a decay curve.

Devices with segmented anodes are able to take samples of the rate of ionization dE/dx of charged particles and are used to identify particles from nuclear reactions. A time projection chamber (TPC) is a large, gas-filled cylinder with a negative high-voltage electrode at its center and an external magnetic field. When ionizing radiation passes through the TPC, the produced electrons drift toward the end of the cylinder under the influence of the axial magnetic and electric fields. Multiple anode wires measure the position of the electrons at the end of the chamber. The arrival time of the electrons and the total charge collected are also recorded. The particle trajectory through the chamber is reconstructed from this information.

Ionization chambers are primarily used to measure α emitters, in particular, radioactive gases such as radon, and fission fragments. They are applied for the calibration of radioactive sources, radiation monitoring, and dosimetry in radiation protection.

9.2.2 Proportional Counters

Proportionality between pulse height and primary ionization requires that the avalanches produced by individual primary electrons be essentially independent of one another; that is, each avalanche must be confined to a small region of the central wire. In the course of an avalanche, excitation of molecules can lead to the emission of UV light which in turn is able to produce photoelectrons. With any reasonable value of F, the pulse size is almost entirely determined by the amount of avalanche ionization and therefore essentially independent of the location of the primary track. Because of the small volume of the multiplicative region, the avalanche electrons travel through only a small part of the potential difference applied to the counter and most of the pulse height is therefore contributed by the positive ions moving away from the central wire. Although the total time for the positive ions to reach the cathode is of the order of 1 ms, the variation of field gradient with radius is such that initially the pulse rises very rapidly and then

approaches its final height slowly. If the total collection time is t, the time at which half the final pulse height is reached is about $(r/R)\ t$, or typically on the order of 1 μs. Amplifier circuits with time constants of this order are therefore used to clip the pulses from proportional counters. Even with sharp clipping, proportionality is preserved because the pulse shape is independent of pulse height. With a clipping circuit, a proportional counter is ready to accept a new event within ≤1 μs after a count and proportional counters can thus be used at higher counting rates than Geiger–Müller counters, see below. These are also generally more stable and have better plateau characteristics. A voltage plateau is a region where the counting rate – not the pulse height – caused by a constant radioactive source is independent of the applied voltage. Proportional counters have plateaus of typically several hundred volts with slopes of ≤1% per 100 V. The onset and length of the plateau depend on the setting of the discriminator, an electronic device that prevents pulses below a given pulse height from being registered and that is needed to cut out pulses due to electronic noise. Figure 9.11 shows the response of a proportional counter to a source of both α and β particles as a function of voltage. The counter exhibits two plateaus, one in which only the α particles are registered, and a second one in which both types of particles are detected. Proportional counters usually consist of a sealed cylinder serving as the cathode, a thin wire as the anode, and a thin window, but they are often constructed as flow counters, as shown in Figure 9.12. In this type of counter, a gas, preferably methane or a mixture of argon and methane, flows through the counter during operation and the sample is brought into the counter. Windowless proportional counters are well suited to measure α and low-energy β radiation. High and well-defined values of G in Eq. (9.3) are obtained with 2π and 4π counters, which are shown in cross section in Figure 9.13.

In 2π counters, half of the total radiation emitted by the sample is recorded, whereas 4π counters are equipped with two anode wires and the radiation emitted by the sample can be counted quantitatively. These types of counters are used

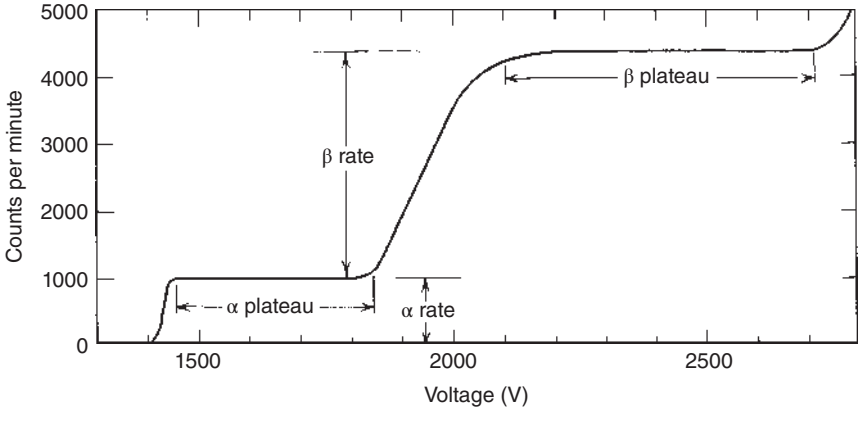

Figure 9.11 Counting rate as a function of applied voltage for a proportional counter exposed to a source emitting both α and β particles. Source: Friedlander et al. (1981), figure 5 (p. 121)/John Wiley & Sons.

Figure 9.12 Flow counter.

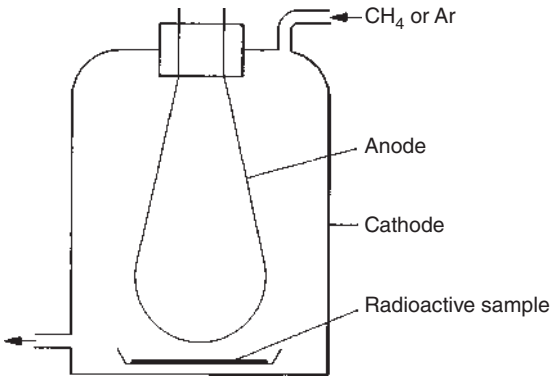

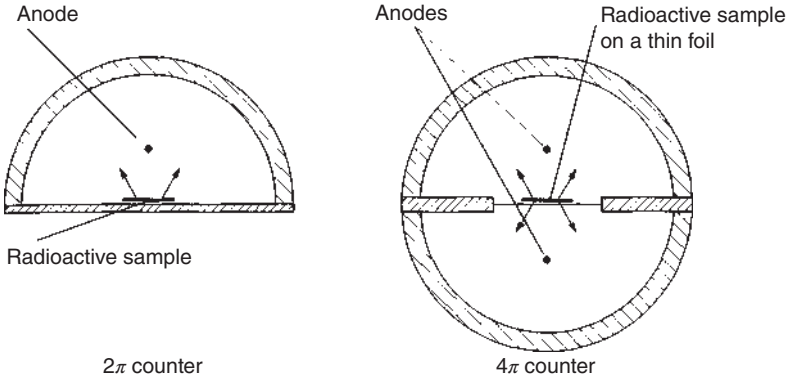

Figure 9.13 Cross sections of 2π and 4π counters.

for the measurement of the absolute activity A of radioactive samples because an overall counting efficiency $\eta = 1.0$ in Eq. (9.3) can be obtained.

As proportional counters have low internal counting efficiency for γ radiation (about 1%), they are not suited to measure γ radiation. However, proportional counters of special design and operating at high gas pressure are applied in X-ray and low-energy γ-ray spectrometry.

An extension of the proportional counter is the multiwire proportional counter, now widely used in nuclear reaction studies. It consists of a plane of parallel wires, spaced one to several millimeters apart, and mounted between two parallel electrodes in a gas such as argon–pentane. Excellent spatial and time resolution has been obtained with such proportional chambers.

9.2.3 Geiger–Müller Counters

Geiger–Müller counters are operated at relatively high voltages of several kilovolts. The avalanche-like spreading of the ionization processes leads to the production of a great number of positive ions which are moving more slowly than the electrons. The neutralization of the electrons at the anode wire gives rise to the emission

of photons, which react with the gas by emission of photoelectrons. These trigger further avalanches, and the processes continue until the build-up of the positive ion sheath in the vicinity of the anode wire reduces the electric field strength so far that no more events can be counted. It takes about 100–500 μs for the ions to reach the cathode, where they can cause secondary electron emission from the surface, thus triggering a new discharge. Therefore, measures must be taken to eliminate the negative influence of the positive ions.

Usually, the processes are stopped by addition of a quench gas to the main filling gas. Vapors of polyatomic molecules such as ethanol, ether, ethyl formate, methane, bromine, or chlorine may be applied. Because of the lower ionization energy of these molecules, the positive charge of the ions is transferred to the molecules and these dissipate their energy by dissociation or predissociation. Chlorine and bromine exhibit strong absorption of the photons emitted; they dissociate, recombine, and return to the ground state via a series of low-energy excited states.

As already mentioned, the dead time of Geiger–Müller counters varies between about 100 and 500 μs and therefore the number of non-counted events is relatively high at high counting rates (Figure 9.7). Organic quench gases are gradually consumed after about 10^8–10^9 counts. The advantages of Geiger–Müller counters are their simplicity and the fact that further amplification is not needed. Halogen-quenched counters exhibit longer lifetimes, lower dead times, and lower operational voltages. Most Geiger–Müller counters are equipped with windows and are therefore inexpedient for measuring α and low-energy β radiation. Energy discrimination is not possible. γ radiation can be counted with a low internal counting efficiency η_i of about 1%.

Various types of Geiger–Müller counters are shown in Figure 9.14. The end-window counter equipped with mica windows of about 1.5–3 mg cm^{-2} is a very simple instrument and very frequently used. The immersion counter and the counter with the ring-like glass beaker are used to measure liquids, and the gas counter is used for the determination of the activity of gases. Geiger–Müller counter plateaus are shorter and have more of a slope than proportional counters. Until reliable high gain amplifiers became available, the large pulse sizes from Geiger–Müller counters made them preferable to proportional counters; now, the advantages are strongly in the other direction.

9.3 Scintillation Detectors

The main parts of a scintillation counter are sketched schematically in Figure 9.15. In the transparent crystal or liquid, the radiation is absorbed and photons are emitted. At the photocathode of the photomultiplier tube, the photons release electrons which are multiplied by the dynodes of the multiplier to give pulses of several millivolts. Some examples of solid and liquid scintillators are listed in Table 9.1.

Scintillation counters are applied primarily for measuring γ radiation and low-energy β radiation. If γ radiation is to be measured, thick scintillating crystals of high density are used in order to absorb as much γ radiation as possible. NaI

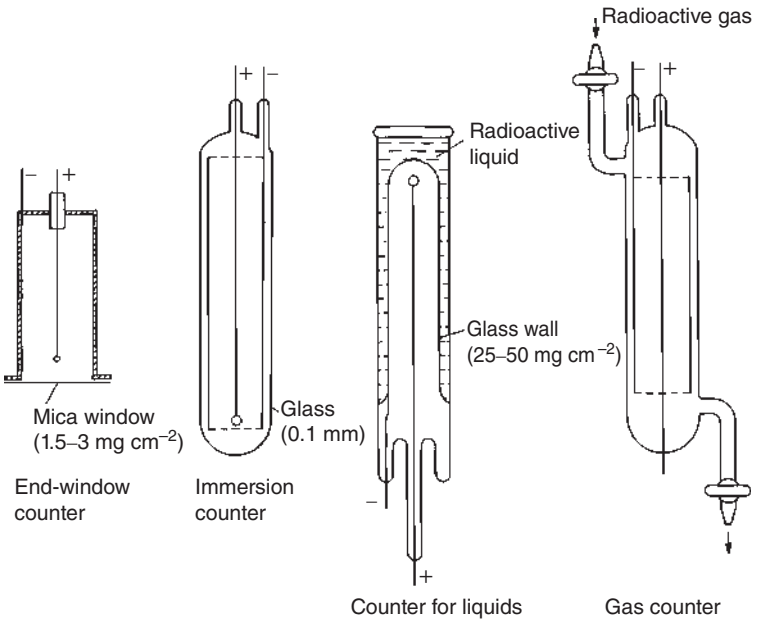

Figure 9.14 Various types of Geiger–Müller counters.

Figure 9.15 Scintillation detector (schematically).

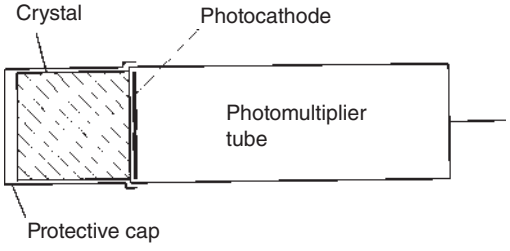

or CsI crystals doped (activated) by the addition of small quantities of Tl are well suited, and at a size of 1–2 in. (2.5–5 cm), they give an internal counting efficiency η_i of 15–30%. This counting efficiency is appreciably higher than that obtained with gas counters for γ radiation. Well-type crystals offer a nearly 4π geometry. Approximately 30 eV of energy deposition in an NaI(Tl) crystal is required to produce one light photon, and it takes about 10 photons to release one photoelectron at the photocathode of the photomultiplier. These photoelectrons are accelerated by a potential of the order of 100 V to the first dynode where each one produces n secondary electrons. These secondary electrons are similarly accelerated to and multiplied n-fold at the second dynode, and so forth. With 10 dynodes, and with n being 3–4, the total multiplication factor is n^{10}, that is, on the order of 10^5 or 10^6. Thus, a 0.3 MeV γ-ray absorbed in an NaI(Tl) crystal produces 10^4 light photons, giving 10^3 photoelectrons and leading eventually to an output pulse of 10^8 electrons or $1.6 \cdot 10^{-11}$ C. In an output circuit of 10^{-10} F capacitance, this would be a pulse of 0.16 V requiring further amplification. With careful regulation of dynode voltages,

Table 9.1 Some properties of solid and liquid scintillators.

Scintillator	Density ($g\,cm^{-3}$)	λ_{max} (nm)	Relative pulse height	Decay time (μs)	Suitability
Inorganic crystals					
NaI(Tl) crystals	3.67	410	210	0.23	For γ radiation
CsI(Tl) crystals	4.51	500	338	0.8	For γ radiation
BGO crystals	7.13	480	46	0.3	For γ radiation
BaF_2 crystals	4.88	310			For γ radiation
Slow			57	0.6	
Fast			8	0.0008	
ZnS(Ag)	4.09	450	100	7	For α radiation
Organic crystals					
Anthracene	1.25	440	100	0.022	
trans-Stilbene	1.16	410	60	0.004	For β radiation
p-Terphenyl	1.23	400	40	0.004	
Liquids					
p-Terphenyl (5 g) in 1 l toluene	—	355	35	0.0015	For low energy
2,5-Diphenyloxazole (3 g) in 1 l toluene	—	382	40	0.0021	β radiation

there is good proportionality between the energy absorbed in the crystal and the height of the output pulse. The energy resolution of NaI(Tl) detectors is rarely better than 6% for the 1332 keV γ-ray of ^{60}Co as compared to the 0.13% resolution of Ge detectors. Pulse-height spectra taken with NaI(Tl) detectors have the same basic characteristics as those taken with Ge detectors, that is, photopeaks, Compton distributions, and annihilation radiation escape peaks, see Section 9.4; however, an additional feature in NaI(Tl) spectra is the so-called iodine escape peak about 28 keV below the photopeak. It results from absorption of a γ-ray near the surface of the detector and subsequent escape of a K X-ray of iodine. Other inorganic scintillators in common use are bismuth germanate ($Bi_4Ge_3O_{12}$, BGO) which is a high-density material. Its low light output (20% of that of NaI(Tl)) limits its use to cases where a high efficiency with poorer resolution is of primary interest. Barium fluoride (BaF_2) is a material with very fast light output but reduced light yield. It is used where fast timing is important.

For counting low-energy β radiation, the crystal is substituted by a scintillating liquid and the sample is dissolved in the liquid (internal source liquid scintillation counting). The method is also used to measure α-particle and weak X-ray and γ-ray emitters. The different types of radiation can be distinguished by pulse shape discrimination. Self-absorption of the radiation in the sample, absorption of the

radiation in the air and the window of the detector, and backscattering of β particles are avoided.

The scintillating liquid is prepared by dissolving a primary and, if necessary, a secondary scintillator in a suitable solvent and adding a solution containing the radioactive sample. A secondary scintillator (or wavelength shifter) is needed, if the primary scintillator (e.g. 2,5-diphenyloxazole, PPO) emits photons with a wavelength that is too short for the photomultiplier. In this case, the secondary scintillator (e.g. 1,4-bis[2-(5-phenyloxazolyl)]benzene, POPOP) or di-methyl-POPOP shifts the wavelength to lower values so that the photomultiplier responds. As solvents, mainly organic compounds are used, for example, toluene, benzene, *p*-xylene, or dioxane. If the sample is added in the form of an aqueous solution, solvents that are miscible with water are applied. However, the sample may also be introduced as an emulsion or a suspension, or even pieces of paper carrying the sample may be added.

Foreign substances, such as water, that are introduced with the sample into the scintillator often reduce the light output and the counting efficiency. The shape of the spectrum may also be changed. This effect is known as quenching. It limits the amount of sample that can be added.

The sample container or vial must be transparent at the wavelength of the scintillator used and resistant to the solvent. Preferably, it is put between two photomultipliers to obtain higher counting efficiency. Using this arrangement, the thermal noise of the photomultipliers can be reduced to a minimum by means of an anticoincidence circuit: thermal electrons which are the major source of thermal noise are emitted at random and are registered only by one photomultiplier, whereas the events counted in both photomultipliers are due to the radioactive decay in the sample. The main advantage of liquid scintillation counting is the relatively high counting efficiency, which can amount to about 100%.

Transparent organic crystals, such as anthracene, may also be used as scintillators (Table 9.1). They can be used to measure β radiation of medium or high energy, but they exhibit no special advantages. Plastic scintillators are also commercially available. They are produced by mixing scintillator (e.g. PPO or *p*-terphenyl), wavelength shifter (e.g. POPOP), and a monomer such as styrene, and then polymerizing the mixture. Large plastic scintillators are often used as anticoincidence counters surrounding low-level detectors. All organic scintillators are characterized by short fluorescence lifetimes, typically 2–4 ns. Thus, they are suitable in high count rate situations or for fast time measurements. The light output is 10–50% of that of NaI(Tl) crystals.

9.4 Semiconductor Detectors

Semiconductor detectors are sometimes referred to as solid-state ionization chambers to distinguish them from gas-filled detectors, but they differ from other solid-state detectors, such as solid scintillation or solid track detectors, by their semiconductor properties. Condensed phases have higher densities than gases

and provide more efficient stopping of the radiation per unit length. Metals allow rapid recombination of the electron–positive ion pairs, and insulators inhibit the collection of the charge. Therefore, only semiconductors have been used extensively for radiation detectors, in particular for γ- and X-ray spectrometry and as particle detectors. The way of working is similar to that of ion chambers or proportional counters: the radiation is measured by means of the number of charge carriers set free in the detector, which is arranged between two electrodes. Ionizing radiation produces free electrons and holes. If the energy of the electrons is high enough, they are able to produce new electron–hole pairs. This process takes about 1–10 ps. The number of electron–hole pairs depends on the energy transmitted by the radiation to the semiconductor. As a result, a certain number of electrons are transferred from the valence band to the conduction band and an equivalent number of holes are left behind in the valence band. Under the influence of an electric field, electrons as well as holes travel to the electrodes, where they give rise to a pulse that can be measured in an outer circuit.

Part of the energy of the incident radiation is used up by the production of electron–hole pairs, and another part by excitation of lattice vibrations, similar to the situation in gases, where some energy is used for excitation and dissociation processes (Section 9.2).

The materials most frequently used as detectors for nuclear radiation are silicon and germanium. The energy levels of silicon are shown in Figure 9.16. The energy levels of the valence electrons are so close together that they form a nearly continuous band of energies, the valence band. In pure silicon, there is a region of energies above the valence band in which there are no allowed energy levels. This is called *the forbidden gap*. Just above the forbidden gap is the conduction band, another band of energies that allows electron migration through the crystal. At room temperature, the energy gap between the valence and conduction bands is 1.08 eV for Si and 0.79 eV for Ge, whereas the total energy required for production of electron–hole pairs and excitation of lattice vibrations is $E = 3.6$ eV for Si and $E = 2.8$ eV for Ge at room temperature, and about 0.2 eV more at 77 K. Compared to the energy used for production of an ion pair in gas detectors (≈35 eV), this energy is very low and the number of charge carriers produced in a semiconductor is appreciably higher. Consequently, in semiconductor detectors, the statistical variation of the pulse height is smaller and the energy resolution is higher. Therefore, these detectors are particularly suitable for energy determination of all kinds of nuclear radiation and charged particles. The time resolution is also very good. It depends on the size and the properties of the individual semiconductor detector and varies between about 0.1 ns and 1 μs. Compared to gas ionization detectors, the density of semiconductor detectors is higher by a factor on the order of 10^3 and charged particles of high energy can give off their energy in a semiconductor detector of relatively small dimensions. The specific energy loss, $-\mathrm{d}E/\mathrm{d}x$, can also be determined by using semiconductor detectors and, by arranging a very thin and a thick semiconductor detector one behind the other (detector telescope), charged particles can easily be identified. For measurement of γ radiation, relatively large crystals are needed because of the low specific ionization of this kind of radiation.

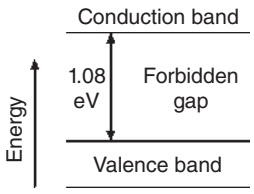

Figure 9.16 Schematic diagram of the energy levels of crystalline silicon.

The requirements of high-energy resolution are well met by Si and Ge. The photoelectric effect increases with Z^4–Z^5, where Z is the atomic number of the substance, and the linear absorption coefficient for 100 keV γ-rays in Ge is higher than in Si by a factor of about 40. Therefore, Ge crystals are better suited for measuring γ radiation. Semiconductors with still higher atomic numbers, such as CdTe and HgI_2, have been investigated with respect to their suitability as detector materials, but they are not commonly used.

In the application of semiconductor detectors, two influences have to be considered, one caused by temperature and the other by impurities or lattice defects. The energy gap between the valence and the conduction bands is on the order of 1 eV and small enough to be surmounted by thermal excitation, resulting in thermal noise which increases strongly with temperature. At room temperature, the thermal conductivity of Si is about $4 \cdot 10^{-4}\,\mathrm{S\,m^{-1}}$ and that of Ge about $1 \cdot 10^{-2}\,\mathrm{S\,m^{-1}}$. To avoid high thermal noise, the detectors are operated at low temperatures (liquid nitrogen). This is of special importance in the case of Ge detectors because, for these, the energy gap is lower than for Si detectors (0.79 eV compared to 1.08 eV at room temperature). At the temperature of liquid nitrogen, the thermal conductivity of pure Si and Ge is negligible compared to that due to impurities.

Impurities lead to the presence of charge carriers (electrons in the conduction band or holes in the valence band) in the absence of an incident radiation and cause a leakage current. For instance, an element of group 15 of the periodic table, such as P or As, introduces additional electrons into the lattice of Si or Ge and has the effect of an electron donor. The donor level is indicated in Figure 9.17. Because of the negative charges, this kind is called an n-type semiconductor. On the other hand, the presence of an element of group 13 of the periodic table, such as B or Ga, gives rise to electron holes and has the effect of an electron acceptor. The acceptor level is indicated in Figure 9.18. Due to the positive charges, this kind is called a p-type semiconductor. Additional acceptor or donor levels may be present because of lattice defects. Crystals with defined contents of foreign atoms may be obtained by doping, that is, by introducing measured amounts of foreign atoms.

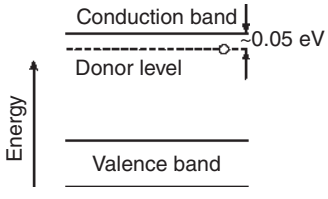

Figure 9.17 Energy levels of crystalline silicon with a donor level.

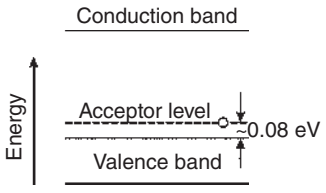

Figure 9.18 Energy levels of crystalline silicon with an acceptor level.

The influence of impurities can be ruled out in two ways: by preparation of high-purity crystals or by elimination of the influence of the charge carriers introduced by the impurities.

High-purity Ge crystals containing only one foreign atom per 10^{10} Ge atoms or less can now be prepared and offer optimal conditions for measuring γ-rays. They are referred to as intrinsic Ge (i-Ge) or high-purity Ge (Hp-Ge) and are operated at liquid nitrogen temperature, in order to avoid thermal noise. For the purpose of cooling, the crystals are enclosed in a vacuum cryostat. The nuclear radiation entering the crystals produces electron–hole pairs that are collected at the electrodes within microseconds. The charge transported through the crystal is proportional to the energy absorbed. Hp-Ge detectors are highly sensitive and exhibit excellent energy resolution (up to about 0.2–0.5 keV at energies of about 10–100 keV, respectively). This makes these detectors very attractive for γ spectrometry.

Various geometrical configurations of Ge detectors are available: planar, coaxial, and well-type detectors. The latter are widely used because they offer very good geometrical conditions.

The influence of impurities can be eliminated by compensation of the surplus charge carriers or by introducing a p–n barrier, respectively. A p–n barrier is the combination of two zones of semiconductor material, one of the p-type and the other of the n-type. This gives a diode with a p–n junction, see Figure 9.19. At the junction, the mobile charge carriers diffuse from regions of higher concentration to those of lower concentration. Thus, electrons move from the n-type to the p-type region and combine there with the positive holes. As a result, a depletion layer of high resistance is formed in which there are no charge carriers. This depletion layer is also called an intrinsic (i) layer, and it represents the sensitive (active) volume of the detector which comprises three zones, p–i–n. The depletion zone can be increased by application of a reverse bias (positive electrode on n-type, negative electrode on p-type). For use as nuclear radiation detectors, it is important that the depleted layer of the

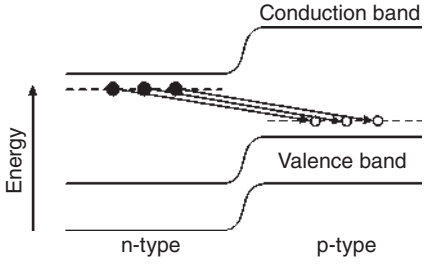

Figure 9.19 Schematic diagram of a p–n junction.

semiconductor has high sensitivity. p–n junction detectors containing a depleted layer can be prepared by controlled diffusion, ion implantation, or formation of a surface barrier (SSB). By thermal diffusion, small concentrations of P or As may be introduced into Si or Ge to produce n-type regions or small concentrations of B or Ga may be added to obtain p-type regions. As an example, a slab of p-type Si is taken as the base material and at one surface of the slab a thin layer (0.1–1 μm) of n-type Si is produced by introducing a small concentration of P. By application of a reverse bias and a field of the order of 10^3 V cm^{-1}, a depleted layer is produced, the thickness of which depends on the magnitude of the applied field.

Ion implantation is carried out by bombarding one surface of the semiconductor with ions accelerated to energies of several hundred kiloelectronvolts. Monoenergetic ions have a well-defined range in the semiconductor material, and controlled depth profiles of implanted ions can be obtained. The advantage of these kinds of detectors is their great stability.

SSB detectors, Figure 9.20, are prepared from n-type Si. On one side, the surface is etched and exposed to air to produce an oxide layer that forms the semiconductor junction (barrier) and a thin gold layer is deposited for electrical contact. By this procedure, a p-layer is obtained with a thickness of <1 μm. During use, these detectors must be shielded from visible light as electron–hole pairs can be created by photons that enter the silicon through the thin gold contact. The gold and oxide layers are also thin to reduce the amount of kinetic energy lost by the particle before it enters the active silicon region. These layers make up a dead layer that can be significant in α spectroscopy. Recently, SSBs with very thin and uniform dead layers have been produced with ion-implanted junctions. A thin layer of B is implanted near the surface of n-type Si to form the junction. Ruggedized detectors are available in which the radiation enters the Si through the thicker and light-tight Al contact. The bulk of the material is p-type Si, and a negative bias is applied to the Au contact so that the entry window can remain at ground potential. SSB detectors are mainly used for charged-particle spectrometry and for α and β spectrometry. Optimal energy resolution for α and β radiation is obtained with thin detectors of small surface area. For instance, at surface areas of about 1–4 cm^2, the energy resolution for α and β radiation is about 10–30 keV.

Fully depleted Si detectors in which the zone of depletion extends over the whole crystal are also available. The energy loss, $-\mathrm{d}E/\mathrm{d}x$, in this kind of detector can be determined by means of another detector which is placed behind the first one and in which the remaining energy is measured.

Si p–i–n diodes are a more recent class of detectors. They are made up with a p-type layer on one side of an intrinsic Si wafer and an n-type layer on the opposite,

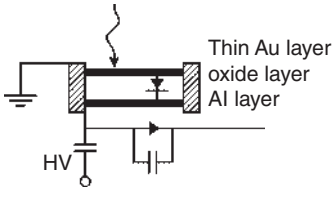

Figure 9.20 Representation of a simple surface barrier detector.

therefore a p–i–n sandwich. These detectors are available in much larger ranges of sizes and shapes than SSB detectors.

To obtain high counting efficiencies for γ- or X-rays, thick depleted layers (thick intrinsic regions) are needed. These are obtained by drifting Li into crystals of Ge or Si. Ge(Li) crystals are used as detectors for γ-rays because of the high density of Ge, and Si(Li) crystals as detectors for X-rays. Li atoms act as donor atoms, and Li^+ ions are very mobile in the lattice of Ge or Si, moving from one interstitial site to another. In the process of drifting, an excess of Li is introduced by diffusion into a p-type crystal of Ge or Si producing an n-type region of about 0.01–1 mm. By application of a reverse bias and raising the temperature, the Li^+ ions are pulled into the p-type region of the crystal where they compensate for the acceptor atoms. In this way, three zones are created: one of n-type, an intrinsic one (i), and a p-type region, as indicated in Figure 9.21. The intrinsic region extends up to about 15–20 mm and exhibits high sensitivity. It defines the active volume of the detector, and the voltage applied is effective across this region. Because of the high mobility of Li in the lattice of Ge at room temperature, Ge(Li) detectors must be cooled permanently by liquid nitrogen. If the γ-rays enter the detector through the n-type layer, low-energy γ-rays and X-rays may get absorbed, or at least severely attenuated, in that insensitive layer. The more recently developed intrinsic Ge detectors avoid this problem of an insensitive layer and, furthermore, are not adversely affected by being warmed up to room temperature.

A typical γ-ray spectrum taken with a Ge detector is shown in Figure 9.22. Because of the different mechanisms of γ-ray absorption (Section 8.4), γ-ray spectra show several contributions. A photopeak and a broad Compton continuum are always observed. The photopeak is used for identification because it gives the full energy of the γ-rays. The Compton continuum shows an edge at an energy below that of the photopeak. At energies above 1.02 MeV, additional contributions are found. The positrons originating from pair production are generally annihilated within the detector, but one or both of the annihilation photons may escape from

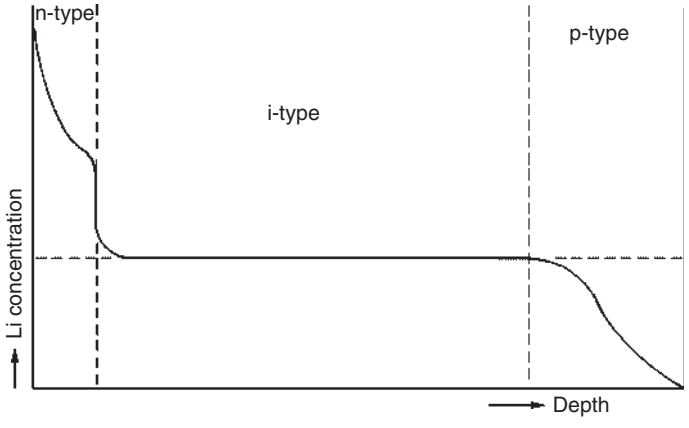

Figure 9.21 Lithium concentration in a Ge(Li) crystal.

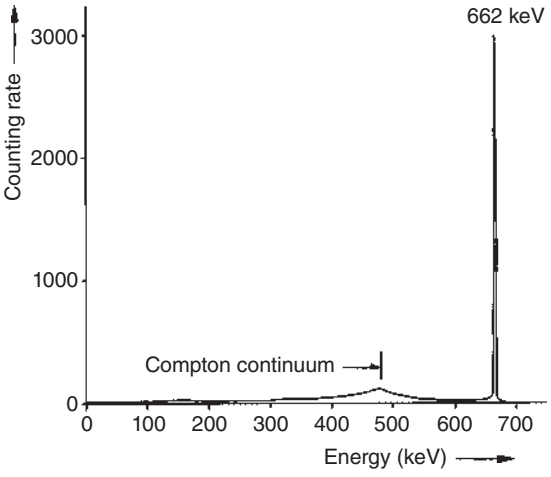

Figure 9.22 γ-ray spectrum of ^{137}Cs taken with a Ge(Li) detector (the γ-rays are emitted by the metastable ^{137m}Ba).

the detector without interaction, depending on the size of the detector. These photons give rise to a "single escape peak" at $E = -0.511$ MeV and a "double escape peak" at $E = -1.022$ MeV, where E is the energy of the photopeak produced by the residual photon after pair production. Additional peaks may be observed at energies above the photopeaks, if two γ-rays or a γ-ray and an X-ray are emitted in cascade, resulting in a small "sum peak." Sum peaks can be distinguished from photopeaks by varying the distance between sample and detector: whereas the intensity of photopeaks varies linearly with the solid angle between sample and detector, the intensity of sum peaks varies with the square of that angle.

9.5 Choice of Detectors

The suitability of the detectors described in Sections 9.2–9.4 for the measurement of α, β, and γ radiation is compiled in Table 9.2.

Gaseous samples are preferably measured in ionization chambers (α radiation), proportional counters, or Geiger–Müller gas counters. The samples are introduced into the counters or passed through with a gas stream (flow counters).

For the measurement of liquid samples containing α emitters or low-energy β emitters, the liquid scintillation technique is most favorable. High-energy β emitters or γ emitters in liquid samples can be counted by means of Geiger–Müller counters, but in the case of γ emitters, the use of NaI(Tl) scintillation counters is much more favorable because of the higher counting efficiency.

Solid samples containing high-energy β emitters can be measured with end-window Geiger–Müller counters, whereas proportional counters are suitable for the measurement of α and β emitters. Self-absorption of α- and β-rays in solid samples may play an important role and requires special attention in the case of α and low-energy β radiation. Very thin and homogeneous layers can be obtained by electrolytic or vapor deposition of the radionuclides to be measured or by solvent extraction and subsequent evaporation of the solvent.

Table 9.2 Suitability of detectors for the measurement of various kinds of radiation.

Kind of radiation	Ionization chambers	Proportional counters	Geiger–Müller counters	Scintillation detectors	Semiconductor detectors
α radiation	Favorable	Flow counters very favorable	Unfavorable	Liquid scintillation favorable	Si barrier detectors favorable
High-energy β radiation (>1 MeV)	Unsuitable	Suitable	Favorable	Organic crystals favorable	Si barrier detectors suitable
Low-energy β radiation (<0.5 MeV)	Unsuitable	Favorable	Unfavorable	Liquid crystals very favorable	Si barrier detectors favorable
High-energy γ radiation (>0.1 MeV)	Unsuitable	Unsuitable	Unfavorable	NaI(Tl), CsI(Tl) crystals very favorable	i-Ge, Ge(Li) detectors very favorable
Low-energy γ radiation (<0.1 MeV) and X-rays	Unsuitable	Suitable	X-ray counters favorable	NaI(Tl), CsI(Tl) crystals favorable	Si(Li) detectors very favorable

SSB detectors are very useful for the detection and measurement of α particles. The internal counting efficiency for α particles is $\eta_i = 1.0$. If the geometry G of the arrangement of an α source and detector is well defined and self-absorption S in the sample can be neglected, absolute activities of α emitters can be determined. The performance of SSB detectors is conventionally tested by recording the spectrum of a calibration source, for example, a ^{241}Am source.

For the measurement of γ emitters in solids, NaI(Tl) scintillation detectors or Ge detectors are most suitable, depending upon whether high counting efficiency or high-energy resolution is required. For comparison, the spectra of ^{60}Co taken with a NaI(Tl) scintillation detector and with a Ge(Li) detector are plotted in Figure 9.23.

X-rays and γ-rays with energies below 50 keV are usually measured with Si(Li) detectors encapsulated in a cryostat with a Be window about 20 μm thick. The samples may also be introduced into a windowless vacuum chamber. The internal counting efficiency attains values of about 1.0, if the active layer of the detector is thick enough, and the energy resolution is in the range of about 100–200 eV at energies of about 4–10 keV. This energy resolution is sufficient to distinguish the characteristic X-rays of light elements with neighboring atomic numbers Z, such as the K_α rays of Al and Si.

Proportional counters may also be applied for the detection and measurement of X-rays, provided that the energy is low enough to interact effectively with the gas filling. For energies of a few kiloelectronvolts, a mixture of He and methane is often used, whereas at higher energies Ar, Kr, or Xe is preferable.

Combinations of chemical separation and counting techniques are frequently used in radiochemistry. For instance, activity measurements in an ionization

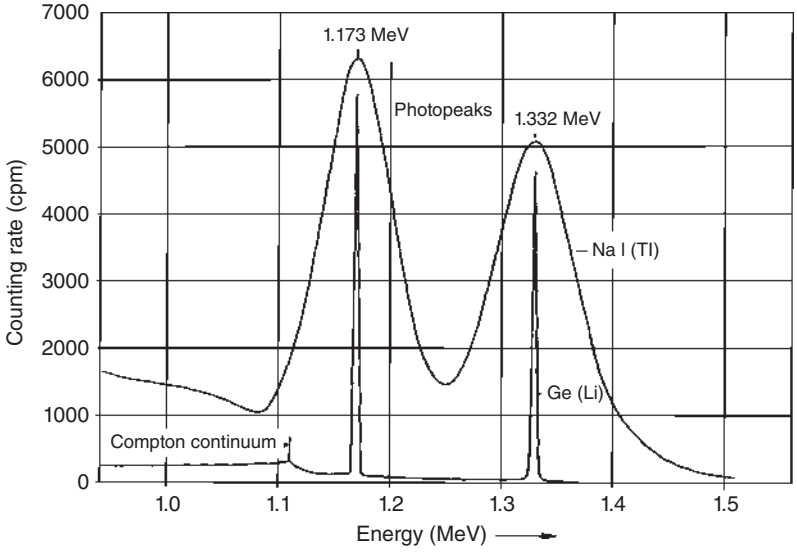

Figure 9.23 γ-ray spectra of ^{60}Co taken with an NaI(Tl) scintillation detector and a Ge(Li) semiconductor detector.

chamber, a proportional counter, or a scintillation detector can be made online after a gas chromatographic separation. This combination is known as radio–gas chromatography. A carrier gas flows continuously through the system, and a suitable counting gas is added before the gas stream enters the counter. The simplest method of operation is to use methane as the carrier and counting gas in the proportional counter. After chemical separation of radioactive substances by paper or thin-layer chromatography, the activity distribution on the paper or thin-layer chromatogram can be directly measured, for example, by scanning the chromatogram with a proportional counter and recording the activity.

9.6 Spectrometry

γ-ray and α-ray spectrometry are important tools of nuclear and radiochemistry. They are mainly used for the identification of radionuclides. Because of the continuous energy distribution of β radiation, β-ray spectrometry is less frequently applied.

For γ-ray spectrometry, i-Ge or Ge(Li) detectors are most suitable because they offer the highest energy resolution (about 0.2–0.4 keV at energies on the order of 100 keV). The disadvantages of Ge detectors are their low internal counting efficiency η_i and the fact that they have to be operated at low temperatures (liquid-nitrogen cooling). A schematic diagram of a simple pulse-height analysis system is shown in Figure 9.24. In general, the detectors are combined with a preamplifier, an amplifier, and a multichannel analyzer, in which the pulses are sorted according to their pulse heights. Frequently, the multichannel analyzer is

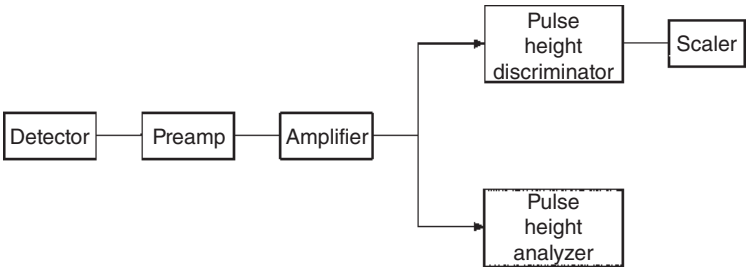

Figure 9.24 Schematic diagram of a simple pulse-height analysis system.

Table 9.3 Some γ-ray standards.

Nuclide	γ-ray energy (keV)	Frequency *H* (number of γ-rays per disintegration)	Half-life
^{241}Am	26.345	0.024	432.7 yr
	59.536	0.357	
^{57}Co	122.061	0.855	271.8 d
	136.473	0.107	
^{203}Hg	279.188	0.815	46.6 d
^{51}Cr	320.084	0.098 3	27.7 d
^{137}Cs	661.66	0.852 1	30.0 yr
^{54}Mn	834.83	0.999 75	312.2 d
^{60}Co	1 173.24	0.999 0	5.271 yr
	1 332.50	0.999 8	
^{22}Na	1 274.53	0.999 4	2.602 yr
	511.0	1.81	
^{88}Y	898.07	0.927	106.6 d
	1 836.08	0.993 5	

operated by a computer and a program for peak search, peak net area calculation, energy calibration, and radionuclide identification. To identify unknown γ emitters, the pulse-height scale must be calibrated by means of γ-ray sources of known energy. Some γ emitters suitable for calibration are listed in Table 9.3.

Scintillation detectors with NaI(Tl) crystals may also be used for γ spectrometry. Because NaI(Tl) crystals can be made in larger size than Ge crystals and because the atomic number of I is larger than that of Ge, the internal counting efficiency of NaI(Tl) detectors for γ-rays is higher than that of Ge crystals, as already discussed in Section 9.5. On the other hand, the energy resolution is appreciably lower (5–7% for γ energies on the order of 100 keV). Scintillation detectors are operated in a way similar to that used with Ge detectors, but without cooling.

For α spectrometry, Si SSB detectors are most suitable. They are operated at room temperature in a vacuum chamber to avoid energy losses. The α particles are stopped within a thin depleted region of the detector, and the number of electron–hole pairs is directly proportional to the energy of the α particles. The charge pulses are integrated in a charge-sensitive amplifier. Some α emitters used as α sources for the purpose of calibration are listed in Table 9.4. For β spectrometry, semiconductor detectors with a thickness of the intrinsic region exceeding the maximum penetration distance of the electrons to be counted are suitable. Because of the continuous energy distribution of β particles, the spectrum of a pure β emitter is a curve with a maximum at medium energies and extending to a maximum energy E_{max} (Figure 6.23), whereas conversion electrons give relatively sharp peaks. Some pure β emitters are listed in Table 9.5.

X-ray spectrometry is generally carried out with Si(Li) detectors. The setup is similar to that applied in γ-ray spectrometry with i-Ge or Ge(Li) detectors: cooling of the detector in a cryostat, operation in combination with a preamplifier, an amplifier, and a multichannel analyzer. The energy resolution is very good and makes it possible to distinguish the characteristic X-rays of neighboring elements. Some X-ray emitters that may be used for calibration purposes are listed in Table 9.6.

The same equipment as for X-ray spectrometry is used for X-ray fluorescence analysis (XFA). In this method, emission of characteristic X-rays is induced by excitation with X-ray sources (X-ray tubes or X-ray emitting radionuclides) or with charged particles (PIXE, i.e. particle-induced X-ray emission).

Neutron spectrometry will be considered in Section 9.10.

9.7 Determination of Absolute Disintegration Rates

As indicated in Section 9.1, measurements of relative and absolute activities are to be distinguished. For the determination of relative activities, the overall counting efficiency η in Eq. (9.3) must be constant, but it needs not to be known, whereas η must be known exactly for the determination of absolute activities. The overall counting efficiency can either be calculated or be determined by calibration. In both cases, all factors in Eq. (9.3) must be considered.

If the radionuclides in the sample to be measured and in the calibration source are different, differences in the frequency E of the decay mode have to be taken into account. Self-absorption S of the radiation in the sample is, in general, negligible for γ-rays, but it may play an important role in the case of α- and low-energy β-rays, and it cannot be neglected for thick samples in the case of high-energy β-rays and X-rays. The contribution of backscattering can be avoided by elimination of material of high atomic number Z in the vicinity of the sample. The geometrical factor G may be calculated from the distance between the sample and the window of the counter and the dimensions of both. In 2π or 4π counters, the geometrical conditions are well defined. For the absorption of the radiation in the air and in the window of the counter, the same is valid as for the self-absorption S. However, the influence of W can be avoided by using windowless counters (e.g. 2π or 4π counters).

Table 9.4 Some α standards.

Nuclide	Energy of the α particles (MeV)	Frequency *H* (number of α particles per disintegration)	Half-life
^{148}Gd	3.182 787	1.00	75 yr
^{232}Th	3.952	0.23	$1.405 \cdot 10^{10}$ yr
	4.010	0.77	
^{230}Th	4.621 1	0.234	$7.54 \cdot 10^{4}$ yr
	4.687 6	0.763	
^{238}U	4.147	0.23	$4.468 \cdot 10^{9}$ yr
	4.196	0.77	
^{235}U	4.395 2	0.55	$7.037 \cdot 10^{8}$ yr
^{234}U	4.723 8	0.275	$2.454 \cdot 10^{5}$ yr
	4.776 1	0.725	
^{236}U	4.445	0.26	$2.342 \cdot 10^{7}$ yr
	4.994	0.74	
^{231}Pa	4.950 5	0.228	$3.276 \cdot 10^{4}$ yr
	5.013 1	0.254	
	5.029 2	0.20	
	5.058 7	0.11	
^{239}Pu	5.104 7	0.106	$2.411 \cdot 10^{4}$ yr
	5.142 8	0.151	
	5.155 5	0.732	
^{240}Pu	5.123 66	0.263 9	$6.563 \cdot 10^{3}$ yr
	5.168 15	0.735	
^{243}Am	5.234 3	0.11	$7.380 \cdot 10^{3}$ yr
	5.276 6	0.88	
^{210}Po	5.304 38	1.00	138.376 d
^{241}Am	5.443 01	0.128	432.7 yr
	5.485 70	0.852	
^{238}Pu	5.456 47	0.283	87.74 yr
	5.499 21	0.716	
^{244}Cm	5.762 84	0.236	18.11 yr
	5.804 96	0.764	

Table 9.5 Some pure β emitters.

Nuclide	E_{max} (MeV)	Half-life
^{3}H	0.0186	12.33 yr
^{14}C	0.156	5730 yr
^{32}P	1.710	14.28 d
^{33}P	0.248	25.34 d
^{35}S	0.167	87.51 d
^{36}Cl	0.714	$3.01 \cdot 10^5$ yr
^{45}Ca	0.252	163.8 d
^{63}Ni	0.067	100.1 yr
^{90}Sr/^{90}Y	0.546/2.27	28.5 yr/3.19 d
^{99}Tc	0.292	$2.13 \cdot 10^5$ yr
^{147}Pm	0.224	2.623 yr
^{204}Tl	0.766	3.78 yr

Table 9.6 Some X-ray emitters.

Nuclide	Characteristic X-rays	Energies (keV)	Half-life
^{57}Co	Fe K	6.391; 6.404; 7.058	271.77 d
^{109}Cd	Ag K	21.99; 22.16; 24.93	1.2665 yr
^{153}Gd	Eu K	40.40; 41.54; 47.00; 48.50	241.6 d
^{241}Am	Np L	11.87; 13.93; 15.86; 17.61; 21.00	423.7 yr

In many detectors, the internal counting efficiency η_i depends on the energy of the radiation. This must also be taken into account if sources containing other radionuclides are used for calibration. Generally, calibration curves $\eta_i = f(E)$ are determined for the detectors used under defined conditions by application of different radionuclides of known activity as radiation sources.

Finally, the influence of the dead time (D in Eq. (9.3)) has to be taken into account, particularly if the dead time of the detector is high (as in the case of Geiger–Müller counters) and if the counting rates of the sample and the calibration source are markedly different.

With respect to the influence of the factors S, B, and W in Eq. (9.3), the determination of the absolute activity A of α and β emitters may cause problems and thin samples and windowless counters are preferable for these radiations. Thin samples are obtained by electrical or vapor deposition on thin metal sheets or thin polymer foils. By use of windowless 2π or 4π proportional counters, the influence of W can be neglected. The determination of absolute activities of γ-ray emitters involves fewer problems because the influence of the factors S, B, and W is, in general, negligible.

Absolute activities of radionuclides may also be determined by coincidence measurements, provided that the decay scheme is relatively simple, for example, only one β transition followed immediately by the emission of one or more γ-ray photons. The principles of the use of coincidence circuits are discussed in Section 9.8.

9.8 Use of Coincidence and Anticoincidence Circuits

Many nuclear processes occur one after the other within a very short time on the order of picoseconds or less – for instance, α or β decay followed by γ-ray emission or emission of a cascade of γ-rays. The events are practically coincident, and for many purposes, it is of interest to know whether two particles or photons are emitted practically at the same time or not. For the detection and measurement of coincident events, two detectors and a coincidence circuit are used. The detectors are chosen according to the coincidences to be measured, for example, α–γ, β–γ, γ–γ, X–γ, β–e^-, or other types of coincidences, and the coincidence circuit records only events occurring within a given short time interval. Scintillation counters and semiconductor detectors are commonly used for these measurements.

On the other hand, by application of an anticoincidence circuit, only those events are recorded that are not in coincidence with others.

Coincidence studies are very useful for detailed investigation of decay schemes. For that purpose, in both detectors, the pulse heights are determined simultaneously, giving the energies of the coincident particles or photons, respectively.

An application of anticoincidence circuits is the anti-Compton spectrometer. The Compton continuum in γ spectra can be reduced relative to the photopeaks by placing the Ge detector inside a second detector, usually a scintillation detector, connected in anticoincidence, so that only pulses in the central detector that are not coincident with those in the outer detector are recorded. Anti-Compton spectrometers are very useful for measurements of γ-rays of very high energy.

9.9 Low-Level Counting

If samples of very low activity are to be measured, the contribution of the background to the counting rate and hence the errors of the measurement are relatively high. The influence of the background can be reduced by improving the detector shielding and by coincidence or anticoincidence circuits.

Usually, detectors are shielded by housings of lead or of lead outside and steel inside. Steel is used to absorb the radiation from radioactive impurities in lead. In order to absorb more background radiation, thicker walls may be used for these housings. With regard to the use of lead and steel as shieldings, it has to be taken into account that freshly prepared Pb contains ^{210}Pb, and steel produced after 1940 may contain ^{60}Co. Therefore, old lead and steel produced before 1940 are preferable as shielding materials.

As γ-rays of the radioactive source to be measured may induce X-ray fluorescence in the lead housing, it is advantageous to line the housing inside with sheets of tin of 3 mm thickness which are able to absorb the lead K X-rays. Sn K X-rays can be absorbed by further lining the housing inside with sheets of copper of 1 mm thickness.

In addition, low counting rates may be measured in underground locations to reduce the contribution of high-energy cosmic radiation. To reduce airborne radioactivity (e.g. ^{222}Rn), the space between the shielding and detector may be filled with paraffin. Cadmium and copper may be added to the shielding as neutron absorbers. Because (n, γ) reactions in these materials give rise to a secondary γ-ray background, the detector may be surrounded by mercury, which absorbs γ-rays very effectively and may be cleaned by distillation.

By coincidence or anticoincidence methods, the background of a detector may by decreased by a factor of about 100 or more. The application of an anticoincidence circuit is the same as in an anti-Compton spectrometer.

9.10 Neutron Detection and Measurement

Neutron detection and measurement are based largely on the production of secondary ionizing radiation by the neutrons. Low-energy (slow) neutrons, in particular thermal neutrons, are measured with high efficiency by means of the charged particles emitted in neutron-induced reactions, such as (n, p) or (n, α) reactions, or nuclear fission. High-energy (fast) neutrons are detected via recoiling ions, preferably spallation protons, produced by collisions of the high-energy neutrons with converter materials of preferably high density. The charged particles created in the converter, mostly protons, can be measured in gas-filled detectors, scintillation detectors, or semiconductor detectors. An example is the Large Area Neutron Detector (LAND) in operation at the GSI Helmholtz Center for Heavy Ion Research at Darmstadt. It consists of a large number of $10 \times 10 \times 200$ cm paddles built from alternating layers of 5 mm iron and 5 mm plastic scintillator, where the charged particles produced in the iron layers produce light in the scintillator layers that is read out by photomultipliers mounted at both ends of the paddles. The difference in arrival time of the light in the two photomultipliers serves to localize the position where scintillation light was produced by the secondary charged particles in a paddle; the mean time provides time-of-flight information. In all, 20 paddles constitute one layer of $2 \times 2\,\mathrm{m}^2$ and a total of 20 layers where consecutive layers are oriented orthogonally to each other results in a total depth of 1 m. An energy resolution of $\Delta T_n/T_n = 5\%$ for a flight path of 15 m and an overall efficiency of close to 100% are achieved for a neutron with $T_n = 1$ GeV. Thus, neutron momenta (or energies) can be measured with high resolution.

Thermal neutrons are most frequently detected by means of the nuclear reactions ^{10}B(n, α)^{7}Li, ^{3}He(n, p)^{3}H, or neutron-induced fission of ^{235}U. For this purpose, ionization chambers are covered on the inner surface with a thin layer of material containing ^{10}B or ^{235}U or they may be filled with $^{10}BF_3$ or ^{3}He. Fast neutrons can be

detected by use of a filling gas containing hydrogen; the recoiling protons produced by collisions of the neutrons with the hydrogen nuclei are measured. With these kinds of ionization chambers, integral fluxes can be determined at high neutron fluxes over large ranges of intensity. The ionization chambers are operating even at high γ-ray intensities because the internal counting efficiency for γ-rays is very low. Gridded ionization chambers filled with ^{3}He are applied as neutron spectrometers in the energy range of about 10 keV–2 MeV.

Proportional counters filled with $^{10}BF_3$ or ^{3}He are used for integral measurement of thermal and epithermal neutrons. Fluxes and spectra of neutrons of intermediate or high energy can be measured with proportional counters filled with ^{3}He or H_2. Instead of H_2, solid hydrogen-containing compounds such as polyethylene can be used.

In scintillators, the counting efficiency for neutrons is relatively high, but the discrimination against γ-rays is low. Slow neutrons may be detected via the $^{6}Li(n, \alpha)^{3}H$ or the $^{10}B(n, \alpha)^{7}Li$ reactions. ^{6}Li or ^{10}B is incorporated in a ZnS scintillator or in liquid or glass scintillators. Crystals of ^{6}LiI are also used. Fast neutron spectra can be measured via proton recoil in large organic solid or liquid scintillators. Very low neutron fluxes can be determined with scintillators containing Gd by measuring the total energy of the γ-rays from the interaction of the neutrons with Gd.

Semiconductor detectors are used as neutron counters by deposition of a suitable "converter" material on the surface of a semiconductor. For instance, a compound containing ^{6}Li or ^{235}U may be deposited by evaporation, or ^{3}He may be sealed into the vacuum-tight detector housing. Advantages of these detectors are their small size and their high counting efficiency for thermal neutrons. However, they are not applicable at high neutron fluxes because of high leakage currents and deterioration.

Instead of direct counting, neutron fluxes can also be determined by activation methods. Activation by (n, γ) reactions and subsequent measurement of the induced activity is a widely used technique. Au, In, and Co are frequently applied as flux monitors. The presence of epithermal neutrons makes corrections necessary. Epithermal neutrons may be measured independently by wrapping the flux monitors in Cd or Gd, which absorb the thermal neutrons.

9.11 Track Detectors

9.11.1 Photographic Emulsions and Autoradiography

The oldest track detectors are photographic plates. They led to the detection of radioactivity by Becquerel in 1896. Photographic emulsions on plates or films indicate the position of radionuclides (*autoradiography*). The main advantage of autoradiography is the possibility of exact localization of radionuclides emitting α- or β-rays.

Smooth surfaces are required for autoradiography. The samples can be metals, polished surfaces of minerals, paper chromatograms, or thin sections of tissues of biological or medical origin. Autoradiography is often used in mineralogy and biology. It may also be applied for studying chemical processes. As an example, the

Figure 9.25 Autoradiograph of a sheet of iron showing the very early stage of corrosion at the edge of a drop of water by labeling with ^{59}Fe.

autoradiograph of an iron surface is shown in Figure 9.25, indicating the deposition by corrosion of extremely small amounts of iron hydroxide labeled with ^{59}Fe in a drop of water.

The local resolution of an autoradiograph depends on the thickness of the layer containing the radionuclide, the distance between that layer and the photographic emulsion, the thickness of the photographic emulsion, and the radiation emitted by the radionuclide. The influence of the distance between the radioactive layer and the photographic emulsion is illustrated in Figure 9.26. The thickness of the photographic emulsion should not be >10 μm. Fine-grain emulsions are preferable, but they need longer exposure. Special nuclear emulsions are available. Short-range radiation such as α or low-energy β radiation gives good contrast. The influence of the energy of β radiation is shown in Figure 9.27. At lower energy of the β particles, the autoradiograph is appreciably sharper.

Autoradiographs may be obtained by pressing a photographic plate or film onto the surface of the sample or by the stripping film or liquid emulsion techniques. In these techniques, a strip of a thin photographic layer or a liquid emulsion is directly placed on the surface of the sample. After exposure and developing,

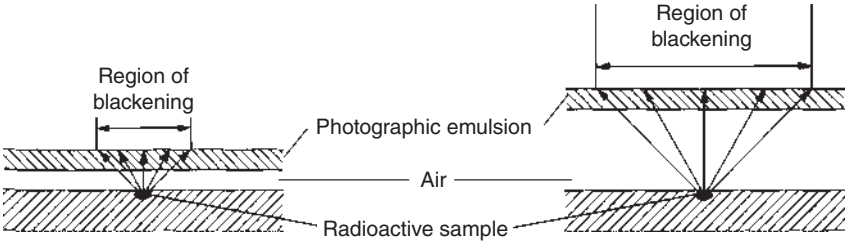

Figure 9.26 Autoradiography: influence of the distance between a radioactive sample and the photographic emulsion.

Figure 9.27 Autoradiograph of two β emitters of different energies: (a) ^{35}S (E_{max} = 0.167 MeV); (b) ^{32}P (E_{max} = 1.71 MeV).

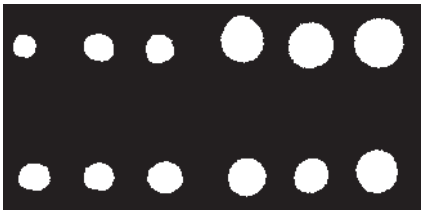

sample and photographic emulsion can be investigated by means of a microscope (microautoradiography).

The time of exposure depends on the activity and the energy of the radionuclide and on the sensitivity of the photographic emulsion. At activities on the order of 10^5 Bq cm^{-2}, several hours may be needed. However, the most favorable exposure times have to be found in separate experiments.

Photographic films with nuclear emulsions are used successfully in order to record very rare events induced by cosmic radiation. For this purpose, light-shielded packages of films have been carried by balloons to high altitudes. Some elementary particles, for example, the positron and the π meson, have been detected by using photographic emulsions.

9.11.2 Dielectric Track Detectors

Heavy ionizing particles produce tracks of radiation damage in insulating or semiconducting solids. The tracks have the shape of a cylindrical channel with dimensions of about 1–10 nm. Without further treatment, they can only be observed in an electron microscope, but after etching (e.g. by hydrofluoric acid [HF]), they are visible under an optical microscope. This is due to the fact that chemical attack is much faster in the region where the material is damaged by the ions than in undamaged regions. Various etching procedures have been developed, and tracks of heavy particles have been studied in many materials, such as minerals, glasses, inorganic crystals, and plastic materials. Mica is frequently applied. Each material can be characterized by a certain value of linear energy transfer (LET, given by dE/dx) below which tracks are not observed. For instance, this value related to the density is $(1/\rho)(dE/dx) = 13$ MeV mg^{-1} cm^2 for mica, which means that mica does not register ions with an atomic mass A less than about 30, and fission fragments can be detected by mica even in the presence of much higher fluxes of lighter ions, for example, α particles. It has been found that the density of ions and excited atoms along the track is directly related to the specific ionization of the radiation which increases with the atomic number Z of the ions that have produced the tracks. As the rate of etching depends on the density of ionization, the atomic number Z of the particles can be identified. Information about the mass number A may also be obtained. Solid track detectors have found application in the investigation of spontaneous fission of transuranic nuclides, of cluster radioactivity, of cosmic radiation at high altitudes on the order of 20 km, and in dating of minerals by counting the number of tracks.

Another application of track detectors is dosimetry of particles and neutrons. For neutron dosimetry, the track detectors may be covered with uranium foils in which the neutrons induce fission. Alternatively, the detectors may be covered with a foil containing B or Li, see Section 9.10.

Since tracks caused by radiation damage are very stable, they can be investigated after very long periods of time. Many minerals contain a record of damage by fission products or cosmic rays that have been conserved over millions of years. This makes track detectors very valuable for geochemistry and space science.

9.11.3 Cloud Chambers

In cloud chambers (Wilson chambers), the tracks of ionizing particles are visible by condensation of droplets. The gas in the chamber is saturated with the vapor of water, alcohol, or other volatile liquids. By sudden expansion, supersaturation is obtained and condensation occurs along the ion tracks. Dust or other condensation centers must be eliminated, to avoid interferences. Cloud chambers can be operated in cycles by a piston or diaphragm (expansion chamber) or by diffusion of a saturated vapor into a colder region (diffusion cloud chamber).

9.11.4 Bubble Chambers

The bubble chamber makes use of the fact that liquids can be heated for short times above their boiling points without actually boiling. Charged particles passing through such a superheated liquid induce the formation of vapor bubbles along their tracks. Because superheated liquids are not stable for long periods of time, bubble chambers are operated intermittently by variation of the pressure. At normal pressure, the liquid is just below the boiling point, and by reducing the pressure, supersaturation is obtained.

The advantage of bubble chambers is the higher density compared to that in cloud chambers. This makes them particularly useful for the detection of high-energy particles produced in high-energy accelerators. Bubble chambers with volumes of several cubic meters have been built. They are preferably operated with liquid hydrogen.

9.11.5 Spark Chambers

Spark chambers contain a system of parallel plates or wires that are alternately at a positive high voltage and at earth potential. The chamber is filled with a noble gas. An ionizing particle crossing the gap between two plates or wires causes the production of a spark near its trajectory. The high voltage is applied in short pulses which are triggered by counters surrounding the chambers. In this way, the chambers are sensitive only for selected types of events. The detection efficiency of spark chambers is very high, and the resolution is very good. The selective operation is a great advantage over bubble chambers. Wire spark chambers with dimensions of many meters containing on the order of 10^5 wires have been constructed.

9.12 Detectors Used in Health Physics

For monitoring personnel radiation exposures, measuring radioactive contamination, and surveying laboratories and equipment, and for the detection of radionuclides incorporated in the human body, various detectors and instruments are used. The principles of operation of these detectors have been discussed in the previous sections of this chapter.

9.12.1 Portable Counters and Survey Meters

The dose rate in a given radiation field can be determined by means of sensitive portable detectors such as Geiger–Müller counters or ionization chambers in combination with batteries and compact DC amplifiers. A movable shield may be used to distinguish between hard and soft radiation. The same types of instruments are suitable for surveying laboratories and instruments. Geiger–Müller counters have higher sensitivity and may trigger audible signals. They are preferably used for rapid surveys and detection of small amounts of high-energy β radiation. In the usual form as end-window counters, they are not suitable for the detection of α or low-energy β radiation. Ionization chambers can be equipped with thin windows ($<3\,\mathrm{mg\,cm^{-2}}$) or open screens for the detection of α and low-energy β radiation. As monitors for γ-rays, portable scintillation counters are the most sensitive.

9.12.2 Film Badges

People who are handling radioactive material or are exposed to nuclear radiation should wear badge-type holders containing a photographic film which records the general exposure to radiation over a certain period of time (usually one month). X-ray film is generally used for β and γ dosimetry. Information about the type and energy of the radiation is obtained by placing various filters (plastic, aluminum, and cadmium foils) over certain areas of the film. Exposure to thermal neutrons is measured with boron-loaded films. Track counters are used as monitors of fast neutrons and radiation of very high energy.

9.12.3 Pocket Ion Chambers

Pocket ionization chambers are small enough to be worn like a ball pen. They are charged by a temporary connection to a voltage source, and the residual charge after exposure is read on the scale of an electrometer fitted in the ionization chamber. Pocket ion chambers are not sensitive to α and low-energy β radiation.

9.12.4 Thermoluminescence Dosimeters

In certain crystals such as LiF or CaF_2 containing Mn as impurity, the electrons and holes produced by nuclear radiation are trapped on the impurities. In this way, energy is stored in the crystals. It can be released in the form of light by heating the crystals. This property of thermoluminescence can be used for radiation dosimetry. The crystals are heated electrically and the light output is measured by means of a photomultiplier. In the case of LiF(Mn) crystals, the response is nearly independent of the energy in the range between about 30 keV and 3 MeV and the effective atomic number of LiF is similar to that of soft tissue. On the other hand, Li(Mn) is only suitable for doses $\geq$10 mrad, whereas CaF_2(Mn) is sensitive down to about 0.1 mrad.

9.12.5 Contamination Monitors

Contamination on the hands can be detected with Geiger–Müller or proportional counters. For detection and measurement of airborne contamination, filters may be used. The activity on the filters can be measured continuously by passing the filters through a proportional counter.

Radioactive contamination on laboratory benches, instruments, or floors can be detected by the simple method of wiping: the surface to be checked for contamination is wiped with a piece of filter paper, and the filter paper is measured with a suitable detector for α, β, or γ activity.

9.12.6 Whole-Body Counters

Whole-body counters consist of a heavily shielded space. The person to be examined is placed inside and surrounded by a large number of scintillation detectors. In this way, γ-emitting radionuclides in the body can be detected with high sensitivity and identified. In the absence of contamination by artificial radionuclides, the γ radiation from ^{40}K is observed. The uptake of small amounts of artificial γ-ray emitters such as ^{137}Cs can be determined effectively, whereas pure α or β emitters cannot be detected in the body.

Reference

Friedlander, G., Kennedy, J.W., Macias, E.S., and Miller, J.M. (1981). *Nuclear and Radiochemistry*, 3e. New York: Wiley.

Further Reading

General

Overman, R.T. and Clark, H.M. (1960). *Radioisotope Techniques*. New York: McGraw-Hill.

Yuan, L.C.L. and Wu, C.S. (eds.) (1961). *Methods of Experimental Physics, Nuclear Physics*, vol. 5A. New York: Academic Press.

O'Kelley, G.D. (1962). Detection and Measurement of Nuclear Radiation. *NAS-NS 3105*. Washington, DC.

Snell, A.H. (ed.) (1962). *Nuclear Instruments and their Uses*. New York: Wiley.

Price, W.J. (1964). *Nuclear Radiation Detection*. New York: McGraw-Hill.

Siegbahn, K. (ed.) (1966). *Alpha-, Beta- and Gamma-Ray Spectroscopy*, 2 vols. Amsterdam: North-Holland.

Bächmann, K. (1970). *Messung Radioaktiver Nuklide* (ed. K.H. Lieser). Weinheim: Verlag Chemie.

Hamilton, J.H. (ed.) (1972). *Radioactivity in Nuclear Spectroscopy, Modern Techniques and Applications*, vols. I and II. New York: Gordon and Breach.

Krugers, J. (ed.) (1973). *Instrumentation in Applied Nuclear Chemistry*. New York: Plenum Press.
Cerny, J. (ed.) (1974). *Nuclear Spectroscopy and Reactions*, vols. A, B, and C. New York: Academic Press.
Ouseph, P.J. (1975). *Introduction to Nuclear Radiation Detection*. New York: Plenum Press.
Mann, W.B., Ayres, R.L., and Garfinkel, S.B. (1980). *Radioactivity and its Measurement*, 2e. Oxford: Pergamon.
Tait, W.H. (1980). *Radiation Detection*. London: Butterworths.
Faires, R.A. and Boswell, G.G.J. (1981). *Radioisotope Laboratory Techniques*, 4e. London: Butterworths.
Knoll, G.F. (2000). *Radiation Detection and Measurement*, 3e. New York: Wiley.

More Specialized

Rossi, B.B. and Staub, H.H. (1949). *Ionization Chambers and Counters*, National Nuclear Energy Series V, vol. 2. New York: McGraw-Hill.
Yagoda, H. (1949). *Radioactive Measurements with Nuclear Emulsions*. New York: Wiley.
Wilkinson, D.H. (1950). *Ionization Chambers and Counters*. Cambridge: Cambridge University Press.
Blau, M. (1961). Photographic emulsions. In: *Methods of Experimental Physics, Nuclear Physics*, vol. 5A (eds. L.C.L. Yuan and C.S. Wu). New York: Academic Press.
Barkas, W.H. (1963). *Nuclear Research Emulsions*. New York: Academic Press.
Schram, E. and Lombaert, R. (1963). *Organic Scintillation Detectors*. Amsterdam: Elsevier.
Birks, J.B. (1964). *The Theory and Practice of Scintillation Counting*. Oxford: Pergamon.
Bertolini, G. and Coche, A. (eds.) (1968). *Semiconductor Detectors*. Amsterdam: North-Holland.
Brouns, R.J. (1968). Absolute Measurement of Alpha Emissions and Spontaneous Fission. *NAS-NS 3112*, Washington, DC.
Ewan, G.T. (1968). Semiconductor spectrometers. In: *Progress in Nuclear Techniques and Instrumentation*, vol. III (ed. F.J.M. Farley). Amsterdam: North-Holland.
Chiang, H.H. (1969). *Basic Nuclear Electronics*. New York: Wiley.
Adams, F. and Dams, R. (1970). *Applied Gamma-Ray Spectrometry*, 2e. Oxford: Pergamon.
Bransome, E.D. (ed.) (1970). *Scintillation Counting*. New York: Grune and Stratton.
Crouthamel, C.A., Adams, F., and Dams, R. (1970). *Applied Gamma-Ray Spectrometry*. Oxford: Pergamon.
Kowalski, E. (1970). *Nuclear Electronics*. Berlin: Springer-Verlag.
Deme, S. (1971). *Semiconductor Detectors for Nuclear Radiation Measurement*. London: Adam Hilger.
Dyer, A. (ed.) (1971). *Liquid Scintillation Counting*, vol. 1. London: Heyden.
Fischer, H.A. and Werner, G. (1971). *Autoradiography*. Berlin: Walter de Gruyter.
Quittner, P. (1972). *Gamma-Ray Spectroscopy with Particular Reference to Detector and Computer Evaluation Techniques*. London: Adam Hilger.

Goulding, F.S. and Pehl, R.H. (1974). Semiconductor radiation detectors. In: *Nuclear Spectroscopy and Reactions*, vol. A (ed. J. Cerny), 290. New York: Academic Press.

Horrocks, D.L. (1974). *Applications of Liquid Scintillation Counting*. New York: Academic Press.

Neame, K.D. and Homewood, C.A. (1974). *Liquid Scintillation Counting*. New York: Wiley.

Yolanda, Z. (1974). Users Guide for Radioactivity Standards. NAS-NS 3115, Washington, DC.

Fleischer, R.L., Price, P.B., and Walker, R.M. (1975). *Nuclear Tracks in Solids*. Berkeley, CA: University of California Press.

Morinaga, H. and Yamazaki, T. (1976). *In-Beam Gamma-Ray Spectroscopy*. Amsterdam: North-Holland.

Erdtmann, G. and Soyka, W. (1979). *The Gamma Rays of the Radionuclides* (ed. K.H. Lieser). Weinheim: Verlag Chemie.

Dyer, A. (1980). *Liquid Scintillation Counting Practice*. London: Heyden.

Reus, U. and Westmeier, W. (1983). Catalog of gamma rays from radioactive decay. *At. Data Nucl. Data Tables* 29 (1 + 2): 193–406.

Leo, W.R. (1987). *Techniques for Nuclear and Particle Physics Experiments*. Berlin: Springer-Verlag.

Debertin, K. and Helmer, R.G. (1988). *Gamma- and X-Ray Spectrometry with Semiconductor Deterctors*. Amsterdam: North-Holland.

deFilippis, S. (1990). Activity analysis in liquid scintillation counting. *Radioact. Radiochem. I* 4: 22.

Firestone, R.B. and Shirley, V.S. (eds.) (1996). *Table of Isotopes*, 8e. New York: Wiley.

Chu, S.Y.F., Ekström, L.P., and Firestone, R.B. (1999). WWW Table of Radioactive Isotopes. http://ie.lbl.gov/toi/ (accessed 27 February 2013).

L'Annunziata, M.F. (ed.) (2003). *Handbook of Radioactivity Analysis*, 2e. San Diego, CA: Academic Press.

Griffin, H.C. (2011). Radiation detection. In: *Handbook of Nuclear Chemistry*, 2e, vol. 5 (eds. A. Vertés, S. Nagy, Z. Klencsár, et al.), 2259. Berlin: Springer-Verlag.

Kanyár, B. and Köteles, G.J. (2011). Dosimetry and biological effects of ionizing radiation. In: *Handbook of Nuclear Chemistry*, 2e, vol. 5 (eds. A. Vertés, S. Nagy, Z. Klencsár, et al.), 2213. Berlin: Springer-Verlag.

MacLaughlin, W.L., Miller, A., Kovács, A., and Mehta, K.K. (2011). Dosimetry methods. In: *Handbook of Nuclear Chemistry*, 2e, vol. 5 (eds. A. Vertés, S. Nagy, Z. Klencsár, et al.), 2287. Berlin: Springer-Verlag.

10

Statistical Considerations in Radioactivity Measurements

The nuclear decay law, Chapter 7, describes the average activity of a sample of radioactive nuclei as a function of time. However, in measurements of radioactive decay, we observe fluctuations about the average behavior predicted by the decay law. Thus, in this chapter, we need to describe the applications of statistical methods to radioactivity measurements.

10.1 Distribution of Random Variables

As a practical introduction, we consider a set of data obtained with a Geiger–Müller counter measuring in 10 successive one minute intervals a long-lived radioactive source. The data are compiled in Table 10.1. We see that the counting rate obviously fluctuates and ask the question: What is the most probable value? It is straightforward to calculate the arithmetic mean and assume it to be the true counting rate. Here, we are assuming that our data reflect the probability distribution of an infinite number of measurements called the "parent population," which is obviously not the case. Anyway, it makes sense to start with determining the arithmetic mean as

$$\bar{x} = \frac{1}{N_0} \sum_{i=1}^{i=N_0} x_i \tag{10.1}$$

where N_0 denotes the number of measurements. For the values in Table 10.1, $\bar{x} = 103$, and this is the best estimate that we can make of the true average $\bar{x}_t$ which is the average of the parent population. The distribution of the count rates about $\bar{x}_t$ is a measure of the precision and can be described by giving "moments" of the distribution

$$\frac{1}{N_0} \sum_{i=1}^{i=N_0} (x_i - \bar{x}_t)^n \tag{10.2}$$

The first moment ($n = 1$) vanishes because of the definition of $\bar{x}_t$.The other odd moments, Eq. (10.2), vanish also if the distribution is symmetric about $\bar{x}_t$. Often, just the second moment ($n = 2$), called the "variance," is given and denoted σ_x^2.

Nuclear and Radiochemistry: Fundamentals and Applications,
Fourth Edition. Jens-Volker Kratz.

Table 10.1 Fluctuations of the counting rate of a steady radioactive source.

Measurement	Counts x_i (min^{-1})	$(x_i - x)$	$(x_i - x)^2$
1	93	−10	With the first measurement, one cannot yet define an average
2	100	−3	9
3	106	+3	9
4	87	−16	256
5	122	+19	361
6	99	−4	16
7	109	+6	36
8	89	−14	196
9	110	+7	49
10	115	+12	144
Totals	1030	0	1076

The square root of the variance is the "standard deviation" σ_x. With these, we can describe a "normal distribution"

$$P(x)\,\mathrm{d}x = \frac{1}{\sqrt{2\pi\sigma_x^2}} \exp\left[\frac{-(x-\bar{x}_t)^2}{2\sigma_x^2}\right] \mathrm{d}x \tag{10.3}$$

which is expected to describe the distribution of experimental results with statistical fluctuations. In the data of Table 10.1, which contains only a limited number of observations, we do not know $\bar{x}_t$: we have only an estimate of it, $\bar{x}$, and the estimate of the variance is

$$\sigma_x^2 = \frac{1}{N_0 - 1} \sum_{i=1}^{i=N_0} (x_i - \bar{x})^2 \tag{10.4}$$

For the data in Table 10.1, we have $\sigma_x^2 = 1076/9 = 119.56$ and $\sigma_x = 10.93$. The difference between Eqs. (10.2) and (10.4) comes about because we have estimated $\bar{x}$ from N_0 observations. This leaves only $(N_0 - 1)$ independent quantities for the estimation of the variance. If $N_0 = 1$, no variance can be estimated, see top position in the most right column of Table 10.1. On the other hand, if N_0 is large, the interval $\bar{x} \pm \sigma_x$ will include ≈68% of the observations, $\bar{x} \pm 2\sigma_x$ will include ≈95%, and $\bar{x} \pm 3\sigma_x$ will include ≈98% of the observations.

Further, we have to consider two more quantities. These are:

i. the distribution of the values of $\bar{x}$ for various sets of measurements each with a finite N_0 and
ii. the distribution of the values of σ_x^2 obtained from the same sets of measurements.

The solution of these problems can be found in standard texts and is contained in the *t*-test of the reliability of $\bar{x}$ as an estimate of $\bar{x}_t$, the χ^2-test of the randomness of the data, and the *F*-test of the reliability of σ_x^2 as an estimate of the true variance of the distribution. As to the reliability of $\bar{x}$ which is our main interest, a measure of

this is the variance of a mean defined as

$$\sigma_{\bar{x}}^2 = \frac{1}{N_0(N_0-1)} \sum_{i=1}^{i=N_0} (x_i - \bar{x})^2. \tag{10.5}$$

$\sigma_{\bar{x}}^2$ is our best estimate of the variance of the distribution of average values found from an infinite number of sets of experiments, each containing N_0 measurements of which Table 10.1 is one example. The value of $\sigma_{\bar{x}}$ from Table 10.1 is $\sqrt{119.6/10} = 3.46$. The significance of this number for a normal distribution is the probability of observing a value of $\bar{x}$ between $\bar{x}$ and $\bar{x} + \mathrm{d}\bar{x}$ given by

$$P(\bar{x})\mathrm{d}\bar{x} = \frac{1}{\sqrt{2\pi\sigma_{\bar{x}}^2}} \exp\left[\frac{-(\bar{x}-\bar{x}_t)^2}{2\sigma_{\bar{x}}^2}\right] \mathrm{d}\bar{x} \tag{10.6}$$

In the previous discussion, only uncertainties in the experimental data due to statistics were considered. But there may also be a systematic error that contributes to the overall uncertainty, for example, if a detector or counting system is not working properly at times. A criterion helping us to search for such malfunctions is

$$\chi^2 = \frac{\sum_{i=1}^{i=N_0} (x_i - \bar{x})^2}{\bar{x}} \tag{10.7}$$

For the data in Table 10.1, $\chi^2 = 1076/103 = 10.45$; that is, chi-squared per degree of freedom is 1.045, which is acceptable. A systematic error would be indicated by a value above 1.7 or below 0.6.

10.2 Probability and Probability Distributions

Given a set of N_0 objects containing n_1 objects of the first kind, n_2 objects of the second kind, and n_i objects of the ith kind, the probability p_i that an object is of the ith kind is $p_i = n_i/N_0$. For example, the probability that one card drawn from a full deck will be an ace is 4/52. If we rewrite the definition of the average value $\bar{x}$ of a number of quantities x_i, taking into account that any particular value may appear n_i times, we have

$$\bar{x} = \frac{1}{N_0} \sum n_i x_i = \sum p_i x_i \tag{10.8}$$

Generalizing, the average value of any function of x is

$$\overline{f(x)} = \sum p_i f(x_i) \tag{10.9}$$

and

$$\sigma_x^2 = \sum p_i (x_i - \bar{x})^2 = \overline{x^2} - \bar{x}^2 \tag{10.10}$$

In a large number K of measurements, we find the ith result k_i times. Note that, now, the ratio k_i/K is not the probability p_i of the ith result as defined earlier, but k_i/K approaches p_i as K becomes larger and larger:

$$\lim_{K\to\infty} \frac{k_i}{K} = p_i \tag{10.11}$$

When we look at the compounding probabilities, we utilize the addition theorem and the multiplication theorem. We consider the former theorem first. If we have N_0 objects containing n_i objects of the kind a_i and if the kinds a_1, a_2 through a_i have no members in common, the probability that one of the N_0 objects belongs to a combined group $a_1 + a_2 + \cdots + a_i$ is $\sum_{i=1}^{i=j} p_i$. This means, for two mutually exclusive events with probabilities p_1 and p_2, the probability of one or the other occurring is $p_1 + p_2$. For example, if one card is drawn from a full deck, the chance of its being either a 5 or a 10 is $4/52 + 4/52 = 2/13$. The other type of compounding probabilities is described by the multiplication theorem. If the probability of an event i is p_i and if after i has happened the probability of another event j is p_j, the probability that first i and then j happens is $p_i \times p_j$. For example, if two cards are drawn from a full deck, the probability of two aces is $4/52 \times 3/51$. The probability of four aces in four cards is $4/52 \times 3/51 \times 2/50 \times 1/49$.

The binomial distribution law treats a rather general case of compounding probabilities involving both the addition theorem and the multiplication theorem. Consider a very large set of objects in which the probability of an object with the property w is p. If n objects are withdrawn from the set, the probability $W(r)$ that r of the objects have the property w is

$$W(r) = \frac{n!}{(n-r)!r!} p^r (1-p)^{n-r} \tag{10.12}$$

We try to explain this in the following. Let us consider just r of the n objects. That the first of these has the property w has the probability p. That the first and the second have the property w has the probability p^2, and so on. Thus, the probability that all r objects have the property w is p^r. If r of the n objects happen to be of this kind, the other $n - r$ objects must have another property. This probability is $(1-p)^{n-r}$. For a given choice of r objects out of the n objects, the probability of finding exactly r with the property w is $p^r(1-p)^{n-r}$. But this particular choice is not the only one. The first of the r objects can be chosen from the n existing objects in n different ways, the second in $n-1$ ways, the third in $n-2$ ways, and the rth in $n-r+1$ ways. The product of these terms $n(n-1)(n-2)\ldots(n-r+1)$ is $n!/(n-r)!$. However, this term is too large because it not only gives the total number of arrangements of the objects in the way required but also includes the number of arrangements that differ only in the order of selection of the r objects. This can be repaired by dividing by the number of permutations of r objects, which is $r!$, leading finally to the coefficient $n!/(n-r)!r!$. This is what is inherent in Eq. (10.12). The latter is called the binomial distribution law because the coefficient is nothing more than the coefficient $x^r y^{n-r}$ in the binomial expansion of $(x+y)^n$. Because in Eq. (10.12)

$$x + y = p + (1-p)$$

we obtain

$$\sum_{r=0}^{n} W(r) = 1$$

by which the binomial distribution is normalized. In the application of the binomial distribution law for radioactive disintegrations, we ask for the probability $W(m)$ of

obtaining m disintegrations in a time t from a sample of N_0 radioactive nuclei. Here, N_0 is the number n in the above derivation of the binomial distribution law and m replaces the number r that is to have a certain property, – namely, that of decaying in a given time t. Thus, for this case, the binomial distribution law takes the form

$$W(m) = \frac{N_0!}{(N_0 - m)!m!} p^m (1-p)^{N_0 - m} \tag{10.13}$$

Obviously, the probability for a nucleus not to decay in time t, $1-p$ in Eq. (10.13), is just the ratio of the number N that survive the time interval t to the initial number N_0:

$$\frac{N}{N_0} = \mathrm{e}^{-\lambda t}$$

Then, $p = 1 - \mathrm{e}^{-\lambda t}$, and we can rewrite $W(m)$ in the form

$$W(m) = \frac{N_0!}{(N_0 - m)!m!} (1 - \mathrm{e}^{-\lambda t})^m (\mathrm{e}^{-\lambda t})^{N_0 - m} \tag{10.14}$$

With this, we can describe the distribution of time intervals between successive disintegrations. The probability $P(t)\,\mathrm{d}t$ is the product of the probability of no disintegration between 0 and t and the probability of a disintegration between t and $t + \mathrm{d}t$. The first of these two probabilities is given by Eq. (10.14) for $m = 0$ as

$$W(0) = \frac{N_0!}{N_0!0!} (1 - \mathrm{e}^{-\lambda t})^0 (\mathrm{e}^{-\lambda t})^{N_0} = \mathrm{e}^{-N_0 \lambda t} \tag{10.15}$$

Here, $0! = 1$, and the probability of any one of the N_0 nuclei to decay in the time $\mathrm{d}t$, from the addition theorem, is $N_0 \lambda\, \mathrm{d}t$. Thus,

$$P(t)\,\mathrm{d}t = N_0 \lambda \mathrm{e}^{-N_0 \lambda t}\,\mathrm{d}t \tag{10.16}$$

This has been proven experimentally. From the binomial law, Eq. (10.12), we can also derive the average disintegration rate by making use of Eq. (10.9) as

$$\bar{r} = \sum_{r=0}^{r=n} r W(r) = \sum_{r=0}^{r=n} r \frac{n!}{(n-r)!r!} p^r (1-p)^{n-r}$$

To proceed from here, we need the binomial expansion of $(px + (1-p))^n$ which is

$$(px + (1-p))^n = \sum_{r=0}^{r=n} \frac{n!}{(n-r)!r!} p^r x^r (1-p)^{n-r} = \sum_{r=0}^{r=n} x^r W(r)$$

Differentiating with respect to x yields

$$np(px + (1-p))^{n-1} = \sum_{r=0}^{r=n} r x^{r-1} W(r) \tag{10.17}$$

With $x = 1$, we arrive at the desired expression

$$np = \sum_{r=0}^{r=n} r W(r) = \bar{r} \tag{10.18}$$

meaning that the average number $\bar{r}$ of the n objects having the property w is just n times the probability for any one of the objects to have the property w. Applied

to radioactive disintegrations, n needs to be replaced by N_0 and p needs to be set equal to $1-\mathrm{e}^{-\lambda t}$. Then, the average number of nuclei disintegrating in the time t is $N_0(1-\mathrm{e}^{-\lambda t})$. For times short compared to the half-life, the approximation $(1-\mathrm{e}^{-\lambda t}) = \lambda t$ can be used so that the average number of nuclei disintegrating in the time t is $N_0\lambda t$. The disintegration rate to be expected is $N_0\lambda t/t$ which is $N_0\lambda$. This corresponds to the familiar expression $-\mathrm{d}N/\mathrm{d}t = \lambda N$.

Differentiating Eq. (10.17) again with respect to x, we obtain

$$n(n-1)p^2(px+(1-p))^{n-2} = \sum_{r=0}^{r=n} r(r-1)x^{r-2}W(r)$$

With $x = 1$, we have

$$n(n-1)p^2 = \sum_{r=0}^{r=n} r(r-1)W(r) = \sum_{r=0}^{r=n} r^2W(r) - \sum_{r=0}^{r=n} rW(r)$$

which we can abbreviate to

$$n(n-1)p^2 = \overline{r^2} - \overline{r}$$

Recalling from Eq. (10.10) that the variance is

$$\sigma_r^2 = \overline{r^2} - \overline{r}^2$$

we have

$$\sigma_r^2 = n(n-1)p^2 + \overline{r} - \overline{r}^2$$

and with $\overline{r} = np$, Eq. (10.18), we have

$$\sigma_r^2 = n^2p^2 - np^2 + np - n^2p^2 = np(1-p)$$

For nuclear decay, this becomes

$$\sigma^2 = N_0(1-\mathrm{e}^{-\lambda t})\mathrm{e}^{-\lambda t} \tag{10.19}$$

As the counting interval is usually short compared to the half-life, we can often use the approximation $\sigma = \sqrt{m}$.

This demonstrates a very important property of the binomial distribution. There is a simple relationship between the mean and the variance of the distribution, that is, a single observation from a distribution that is expected to be binomial gives an estimate of both the mean and the variance of the distribution. If a reasonably large number of counts has been accumulated, this count rate may be used to estimate σ. Thus, if 100 counts are recorded in one minute, the expected standard deviation is $\sigma \approx \sqrt{100} = 10$ and the counting rate might be written as 100 ± 10 cpm. If 1000 counts are registered in 10 minutes, the standard deviation is $\sqrt{1000} = 32$ and the counting rate is $(1000 \pm 32)/10 = 100 \pm 3.2$ cpm. This shows that for a given counting rate, the standard deviation is inversely proportional to the square root of the time of measurement.

On the other hand, if the counting time is long compared to the half-life, $\mathrm{e}^{-\lambda t} \to 0$ and in this limit $\sigma = 0$. The explanation is obvious: we start with N_0 nuclei and wait for all of them to decay; thus, the number of decays is exactly N_0. However, in

practice, we do not observe the number of decays but that number times a coefficient η representing the efficiency of the detection system. In this limiting case, the proper representation of $\sigma = \sqrt{np(1-p)}$ is

$$\sigma = \sqrt{N_0\eta(1-\eta)}$$

If $\eta \ll 1$, then $\sigma = \sqrt{N_0\eta}$. When $\lambda t \approx 1$ and η is neither unity nor very small, a more exact analysis of $\sigma = \sqrt{np(1-p)}$ is in order resulting in

$$\sigma = \sqrt{N_0\lambda t\eta(1-\eta+\eta e^{-\lambda t})}.$$

At this point, the question arises of why it is not necessary to take account of the detection efficiency in the more familiar case where λt is small, where we have written $\sigma = \sqrt{m}$. If we do consider η in this case, we have

$$\sigma = \sqrt{N_0(1-e^{-\lambda t})\eta(1-\eta+\eta e^{-\lambda t})}$$

and for λt small and with the same approximations as before,

$$\sigma = \sqrt{N_0\lambda t\eta}$$

which is the square root of the number of counts recorded. This is just the conclusion we had reached without bothering about the detection efficiency.

If we impose the restrictions $\lambda t \ll 1$, $N_0 \gg 1$, $m \ll N_0$, onto the binomial distribution, that is, if we consider a large number of decaying nuclei observed for a time short compared to the half-life, we arrive at a more convenient form of the binomial distribution, the Poisson distribution. To derive it, we make use of the mathematical approximation

$$\ln(1+x) \approx x - \frac{x^2}{2} \cdots \quad \text{if } x \ll 1 \tag{10.20}$$

The average value of the distribution in Eq. (10.14) is defined as

$$M = N_0(1-e^{-\lambda t})$$

The binomial distribution may then be written as

$$W(m) = \frac{N_0!}{(N_0-m)!m!}\left(\frac{M}{N_0}\right)^m\left(1-\frac{M}{N_0}\right)^{N_0}\left(1-\frac{M}{N_0}\right)^{-m}$$

We rewrite the term

$$\frac{N_0!}{(N_0-m)!} = N_0(N_0-1)\ldots(N_0-m+1) = N_0^m\left(1-\frac{1}{N_0}\right)\ldots\left(1-\frac{m-1}{N_0}\right)$$

For $m \ll N_0$, this may be approximated by taking its logarithm and using the first term of Eq. (10.20) with the result

$$\frac{N_0!}{(N_0-m)!} \approx N_0^m \exp\left[-\frac{m(m-1)}{2N_0}\right] \tag{10.21}$$

The term $[1-(M/N_0)]^{N_0}$ may also be estimated by using Eq. (10.20) since $M/N_0 \ll 1$ as

$$\ln\left(1-\frac{M}{N_0}\right)^{N_0} = N_0\ln\left(1-\frac{M}{N_0}\right) \approx -M - \frac{M^2}{2N_0}$$

Therefore,

$$\left(1-\frac{M}{N_0}\right)^{N_0} \approx \mathrm{e}^{-M}\mathrm{e}^{-M^2/2N_0} \tag{10.22}$$

This time, two terms of the expansion have been used because $M^2/2N_0$ is not very small even for $M/N_0 \ll 1$. Again from Eq. (10.20), we can deduce a third approximation

$$\begin{aligned} \ln\left(1-\frac{M}{N_0}\right)^{-m} &\approx \frac{mM}{N_0} \\ \left(1-\frac{M}{N_0}\right)^{-m} &\approx \mathrm{e}^{mM/N_0} \end{aligned} \tag{10.23}$$

We insert the three approximate results from Eqs. (10.21)–(10.23) into the binomial distribution in Eq. (10.14) and obtain

$$W(m) = \frac{M^m e^{-M}}{m!}[\mathrm{e}^{-(M-m)^2/2N_0}\mathrm{e}^{m/2N_0}] \tag{10.24}$$

Here, $W(m)$ is now the probability of obtaining the particular number of counts m when M is the average number. The first factor in Eq. (10.24) is the famous Poisson distribution

$$W(m) = \frac{M^m \mathrm{e}^{-M}}{m!} \tag{10.25}$$

The second term in square brackets is a correction factor indicating how well the Poisson distribution in Eq. (10.25) is approximating the binomial distribution in Eq. (10.14). To give an example, if $N_0 = 100$ and $M = 1$, both the Poisson and binomial distributions give $W(0) = 0.37$, but the binomial distribution gives $W(10) = 0.7 \cdot 10^{-7}$, while the Poisson distribution gives $W(10) = 1.0 \cdot 10^{-7}$. The corrected Poisson distribution in Eq. (10.24) gives $0.7 \cdot 10^{-7}$.

A few particular features of the Poisson distribution should be noted. The probability of obtaining $m = M - 1$ is equal to the probability of obtaining $m = M$ or $W(M) = W(M-1)$. For large M, the distribution is nearly symmetrical about $m = M$ if values of m very far from M are excluded. For the data in Table 10.1, we had calculated a standard deviation according to Eq. (10.4), $\sigma_x = 10.93$. With $\sigma = \sqrt{m}$ we obtain a value of 10.15. This illustrates that the distribution functions are models and, when they are applied to finite data sets, their predictions may deviate from each other.

A further approximation of the distribution law can be made for large values of m and for $|M-m| \ll M$. With these further restrictions and with the appropriate expansion

$$\ln\left(1+\frac{M-m}{m}\right) = \frac{M-m}{m} - \frac{(M-m)^2}{2m^2}$$

and with the use of Stirling's approximation

$$x! = \sqrt{2x}x^x\mathrm{e}^{-x}$$

we can modify the Poisson distribution to obtain the Gaussian distribution

$$W(m) = \frac{1}{\sqrt{2\pi M}} \exp\left[\frac{-(M-m)^2}{2M}\right] \tag{10.26}$$

which is symmetric about $m = M$. For both the Poisson and the Gaussian distributions we may derive $\sigma = \sqrt{M}$. This functional dependence is a necessary condition for the Poisson distribution but not for the Gaussian distribution. The general form for the Gaussian is

$$W(m) = \frac{1}{\sqrt{2\pi\sigma^2}} \exp\left[\frac{-(M-m)^2}{2\sigma^2}\right]$$

where there is not necessarily a fixed relation between M and σ. The relationship between M and σ for the Gaussian distribution of counting rates is a consequence of the particular source of random error: the fluctuation in the decay rate consistent with a decay probability per unit time that is independent of time.

10.3 Maximum Likelihood

So far, we have discussed a priori probability, that is, the probability that a given event will occur prior to any experimental observation. In practice, we are often concerned with a different concept of probability. We often wish to deduce from a limited set of observations the probability that some particular distribution of events gave rise to these observations. We wish to determine which of several hypotheses best accounts for our limited results. This is called *statistical inference* and deals with the a posteriori probability of a given result which is the probability of that result after the result has been obtained. To distinguish a posteriori probability from a priori probability, the term likelihood is substituted for the former. A set of results x_i has been determined and we wish to know which of several hypotheses best accounts for these results. For each of the hypotheses, a likelihood function $L(x_i|H)$ is defined, where H stands for hypothesis A, B, C, … and $L(x_i \mid A) = \prod_{i=1}^{n} P(x_i \mid A)$ with $P(x_i|A)$ being the a posteriori probabilities for the values x_i under hypothesis A. The method of maximum likelihood then consists in choosing from the likelihood functions for all the different hypotheses the one that has the maximum value. This maximization is done by expressing the different hypotheses in terms of some parameter choice and taking the first and second derivatives of the likelihood function with respect to that parameter. If the value of a parameter is to be deduced from a series of measurements, the "best" value is the one that gives the maximum value of the likelihood function for these measurements. This sounds complicated and is best illustrated by an example. We want to demonstrate how the maximum likelihood can be used to determine the "goodness" of a fit to experimental data. We consider data that can be described by the linear relationship

$$y(x) = a + bx \tag{10.27}$$

and assume for simplicity that the data follow a Gaussian distribution. Then for any value of $x = x_i$ we can calculate the a posteriori probability P_i for making the observed measurement y_i with a standard deviation σ_i of observations around the actual value $y(x_i)$

$$P_i = \frac{1}{\sigma_i\sqrt{2\pi}} \exp\left[-\frac{1}{2}\left(\frac{y_i - y(x_i)}{\sigma_i}\right)^2\right] \tag{10.28}$$

and the likelihood function of the observed set of measurements for any values of a and b is

$$L(y \mid a, b) = \prod P_i = \prod\left(\frac{1}{\sigma_i\sqrt{2\pi}}\right) \exp\left[-\frac{1}{2}\sum\left(\frac{\Delta y_i}{\sigma_i}\right)^2\right] \tag{10.29}$$

where the product $\prod$ is taken for i from 1 to N. The terms $\Delta y = y_i - a - bx$ are the deviations between each of the observed values y_i and the corresponding calculated values. If the measurements came from the parent distribution of Eq. (10.27) rather than from any other distribution, the method of maximum likelihood says that the best estimates for a and b are those that maximize the probability in Eq. (10.29). This is done by minimizing the sum in the exponential called χ^2:

$$\chi^2 = \sum\left(\frac{\Delta y_i}{\sigma_i}\right)^2 = \sum \frac{1}{\sigma^2}(y_i - a - bx_i)^2 \tag{10.30}$$

with the optimum fit to the data being that which minimizes the weighted sum of squares of deviations (method of least squares).

10.4 Experimental Applications

When a derived quantity is calculated, there is the question of the relationship between the precision of the computed value and the precision of the input, for example, a background counting rate is to be subtracted from an observed counting rate. Consider the independent measurements of two quantities x and y which lead to the result that the probability of observing a value of x between x and $x + \mathrm{d}x$ is $X(x)\,\mathrm{d}x$, and similarly for y. Then, the independence of the measurements tells us that the probability of having a result with x between x and $x + \mathrm{d}x$ while y is between y and $y + \mathrm{d}y$ is

$$P(x, y)\,\mathrm{d}x\,\mathrm{d}y = X(x)Y(y)\,\mathrm{d}x\,\mathrm{d}y \tag{10.31}$$

If we ask for the best estimate of some quantity f which is a function $f(x, y)$ of the variables x and y, what is the precision of the estimate of f? The answer is given by Eq. (10.9): the best estimate of $f(x, y)$ is its average value

$$\overline{f(x,y)} = \iint X(x)Y(y)f(x,y)\,\mathrm{d}x\,\mathrm{d}y \tag{10.32}$$

It is instructive to investigate the properties of Eq. (10.32) by making a Taylor expansion of $f(x, y)$ about the point $\overline{x}, \overline{y}$ that is our best estimate of $\overline{x}_t, \overline{y}_t$:

$$\overline{f(x,y)} = \iint X(x)Y(y) \begin{bmatrix} f(\overline{x},\overline{y}) + (x-\overline{x})f_x(\overline{x},\overline{y}) + (y-\overline{y})f_y(\overline{x},\overline{y}) \\ +\frac{1}{2}(x-\overline{x})^2 f_{xx}(\overline{x},\overline{y}) + \frac{1}{2}(y-\overline{y})^2 f_{yy}(\overline{x},\overline{y}) \\ +(x-\overline{x})(y-\overline{y})f_{xy}(\overline{x},\overline{y}) + \dots \end{bmatrix} \mathrm{d}x\,\mathrm{d}y \quad (10.33)$$

where $f_x(\overline{x},\overline{y})$, $f_{xx}(\overline{x},\overline{y})$, $f_{xy}(\overline{x},\overline{y})$, and so on mean partial derivatives $\partial f/\partial x$, $\partial^2 f/\partial x^2$, $\partial^2 f/\partial x \partial y$, and so on and are evaluated at $\overline{x}, \overline{y}$. If $f(x, y)$ is a slowly varying function near $\overline{x}, \overline{y}$, so that higher derivatives can be neglected, then

$$\overline{f(x,y)} = f(\overline{x},\overline{y}) \quad (10.34)$$

where $f(\overline{x},\overline{y})$ is the quantity that is sought. This is so because

$$\iint X(x)Y(y)(x-\overline{x}) = \overline{x} - \overline{x} = 0 \quad \text{and} \quad \iint X(x)Y(y)(y-\overline{y}) = \overline{y} - \overline{y} = 0$$

For the three elementary arithmetic operations of addition, subtraction, and multiplication, the Taylor series terminates after a finite number of terms and we obtain

$$\overline{x+y} = \overline{x} + \overline{y} \quad (10.35)$$

$$\overline{x-y} = \overline{x} - \overline{y} \quad (10.36)$$

$$\overline{xy} = \overline{x}\,\overline{y} \quad (10.37)$$

The estimate of the variance is

$$\sigma_f^2 = \left[\overline{f(x,y) - \overline{f(x,y)}}\right]^2 = \iint X(x)Y(y)\left[f(x,y) - \overline{f(x,y)}\right]^2 \mathrm{d}x\,\mathrm{d}y \quad (10.38)$$

If again a Taylor expansion is used and the higher order terms are neglected,

$$\sigma_f^2 = f_x^2(\overline{x},\overline{y})\sigma_x^2 + f_y^2(\overline{x},\overline{y})\sigma_y^2 + \cdots \quad (10.39)$$

and exact expressions result for the variance of three of the elementary arithmetic operations:

$$\sigma^2_{\overline{x+y}} = \sigma_x^2 + \sigma_y^2 \quad (10.40)$$

$$\sigma^2_{\overline{x-y}} = \sigma_x^2 + \sigma_y^2 \quad (10.41)$$

$$\frac{\sigma^2_{\overline{xy}}}{\overline{x}^2\overline{y}^2} = \frac{\sigma^2_{\overline{x}}}{\overline{x}^2} + \frac{\sigma^2_{\overline{y}}}{\overline{y}^2} + \frac{\sigma^2_{\overline{x}}\sigma^2_{\overline{y}}}{\overline{x}^2\overline{y}^2} \quad (10.42)$$

The last term in Eq. (10.42) may usually be neglected. Also, the first two terms of Eq. (10.39) are a good approximation for the variance of other functions x and y.

Let the background counting rate of a counter be 300 counts in 15 minutes. With a sample in place, the total counting rate is measured to be 800 counts in 10 minutes. We require the net counting rate of the sample and its standard deviation. The background rate R_b is

$$R_\mathrm{b} = \frac{300 \pm \sqrt{300}}{15} = 20 \pm 1.15 \text{ cpm}$$

and the total rate R_t is

$$R_t = \frac{800 \pm \sqrt{800}}{10} = 80 \pm 2.83 \text{ cpm}$$

The net rate $R_n = 80 - 20 = 60$ cpm, its standard deviation is $\sigma_n = \sqrt{1.15^2 + 2.83^2} = 3.05$, and $R_n = 60 \pm 3.05$ cpm.

Another example is the calculation of the average of two numbers, both of which have an uncertainty given by their standard deviations σ_1 and σ_2. We require weighted average x_m given by

$$x_m = \left(\frac{x_1}{\sigma_1^2} + \frac{x_2}{\sigma_2^2}\right) / \left(\frac{1}{\sigma_1^2} + \frac{1}{\sigma_2^2}\right)$$
$$x_m = \frac{x_1 + wx_2}{1 + w}$$

where $w = (\sigma_1/\sigma_2)^2$, that is, each number is weighted by the inverse of its standard deviation squared. For the weighted average of N values, x_i, with standard deviation σ_1, we have

$$x_m = \frac{\sum_{i=1}^{N}(x_i/\sigma_i^2)}{\sum_{i=1}^{N}(1/\sigma_i^2)}$$

The standard deviation of x is given by

$$\sigma_{x_m} = \left(\frac{1}{\sum_{i=1}^{N}(1/\sigma_i^2)}\right)^{1/2}$$

For two independent measurements of activity, we have count rates R_n of 70 ± 8.37 cpm and 50 ± 7.07 cpm. The weighted average is

$$w = (8.37/7.07)^2 = 1.40$$

$$x_m = \frac{(70) + (1.4(50))}{1 + 1.4} \approx 58.33 \text{ cpm}$$

The standard deviation of the weighted average is

$$\sigma_{x_m} = \left(\frac{1}{\frac{1}{70} + \frac{1}{50}}\right)^{1/2} = 5.4$$

Thus, the average counting rate was 58.33 ± 5.4 cpm.

10.5 Statistics of Pulse-Height Distributions

In proportional, scintillation, and semiconductor spectrometers, the pulse heights have a normal distribution for a monoenergetic radiation. The energy resolution is

expressed in terms of the full width at half maximum (FWHM) of the pulse-height distribution around the most probable pulse height H. The pulse height $h_{1/2}$ at the half maximum of the distribution is obtained from the ratio of probabilities

$$\frac{W(h_{1/2})}{W(H)} = \exp\left[\frac{-(H-h_{1/2})^2}{2\sigma_h^2}\right] = 0.5 \tag{10.43}$$

Then $(H-h_{1/2})^2/2\sigma_h^2 = \ln 2$ and the FWHM is

$$\frac{2|H-h_{1/2}|}{H} = 2\sqrt{2\ln 2}\frac{\sigma_h}{H} = \frac{2.355\sigma_h}{H}$$

The spread in pulse heights for monoenergetic radiation in a proportional counter arises from statistical fluctuations in the number of ion pairs formed and the statistical fluctuations in the gas multiplication factor. The pulse height is proportional to the product of the gas multiplication and the number of ion pairs, and therefore, the fractional standard deviation of the pulse height equals the square root of the sum of the squares of the fractional standard deviations of the two quantities. As an example, consider the pulse-height spectrum produced by the interaction of Mn K X-rays in a proportional counter filled with 90% argon and 10% methane operating with a gas multiplication factor $F = 1000$. The energy per ion pair is about 27 eV and the number of ion pairs formed by a 5.95-keV X-ray is $5950/27 = 220 \pm \sqrt{220}$. If the numbers of ions collected per initial ion pair have a Poisson distribution, the fractional standard deviation in the gas multiplication is $\sqrt{1000}/1000$. Thus,

$$\frac{\sigma_h}{H} = \sqrt{\frac{220}{220^2} + \frac{1000}{1000^2}} = \sqrt{0.004\,55 + 0.001\,00} = 0.0745$$

and the FWHM is $2.355 \times 0.0745 = 0.175$ or 17.5%.

If the gas multiplication factor is made sufficiently large, the fluctuations in the number of ion pairs alone determine the resolution, and, in that case, the resolution of a proportional counter is inversely proportional to the square root of the energy of the ionizing radiation.

In a scintillation counter, the statistical fluctuations in pulse heights arise from several sources. The conversion of the radiation into photons, the electron emission at the photocathode, and the electron multiplication at each dynode are subject to statistical variations. For most practical purposes, Poisson distributions are applicable. With this, the standard deviation of the pulse height for a monoenergetic radiation is

$$\sigma_h \approx H\sqrt{\frac{\overline{n}}{E\overline{q}f\overline{p}(\overline{n}-1)}} \tag{10.44}$$

where H is the most probable pulse height for an energy E in keV, $\overline{q}$ are the number of photons emitted per 1 keV, f is the light collection efficiency at the photocathode, $\overline{p}$ is the mean value of the photocathode efficiency, that is, the number of photoelectrons arriving at the first dynode for each photon arriving at the photocathode, and $\overline{n}$ is the average electron multiplication per dynode. In practice, f can be made almost unity, $\overline{p}$ is on the order of 0.1, $\overline{n}$ is between 3 and 5, and $\overline{q}$ is on the order of 30 for NaI(Tl),

15 for anthracene, and 7 for stilbene and for liquid scintillators. For example, the resolution for the 662-keV photopeak of ^{137}Cs in a NaI(Tl) scintillation crystal can be estimated as

$$\frac{\sigma_h}{H} = \sqrt{\frac{4}{662 \times 30 \times 1 \times 0.1 \times 3}} = 0.026$$

The FWHM is $2.355 \times 0.026 = 0.061$ or 6.1%, which is not far from the best resolution obtained in a NaI(Tl) counter.

In a semiconductor detector, pulse-height fluctuations arise from the sharing of energy between ion pair formation and lattice excitation. For fixed energy E, the relative standard deviation is

$$\frac{\sigma_h}{H} = \sqrt{\frac{F\varepsilon}{E}} \tag{10.45}$$

where F is the Fano factor, that is, the ratio of the energy that goes into phonons to the total energy absorbed in the semiconductor, and ε is the average energy required to produce an electron–hole pair. An empirical value for the Fano factor is 0.12 for silicon and large germanium detectors and 0.08 for the best small-volume germanium detectors. The value of ε at 90 K is 3.76 eV for silicon and 2.96 eV for germanium. The FWHM for 1 MeV γ-rays in germanium at 90 K is $2.355 \times \sqrt{0.12 \times 2.96/10^6} = 1.4 \cdot 10^{-3}$ or $1.4 \cdot 10^3$ eV. The absolute value of the FWHM increases with increasing energy, but the percent resolution decreases as E increases. For example, the FWHM for 10 MeV photons in germanium is $4.4 \cdot 10^3$ eV or 0.04%, whereas for 0.1 MeV photons, it is $4.4 \cdot 10^2$ eV or 0.4%.

10.6 Statistical Assessments of Lifetimes in α-Decay Chains of Odd-*Z* Heavy Elements

The low-lying nuclear structure of odd-Z nuclei is usually complex, with several states of various spins and different parities, some of which might be isomeric. This translates into complex α-decay sequences, where different lifetimes and decay energies can be observed in transitions between a particular pair of mother and daughter nuclei. Interestingly, however, for the description of many of the published $Z \geq 113$ decay chains, it appears to suffice to consider just one type of decay sequence, i.e. that the decay of each isotope always proceeds with the same decay mode and from the same state, be it $^{287-289}$115 by Oganessian et al. (2013) or ^{293,294}117 by Khuyagbaatar et al. (2014). For example, element 115 chains have been grouped by Oganessian et al. (2013) according to their length. The observed four two-α-long chains were observed at low excitation energy and were assigned to the new isotope ^{289}115, while all five-α-long chains seen at the same excitation energy were assigned to the isotope ^{288}115. However, in three of the four chains, the observed decay times were very similar to the ones in the long chains. This suggested that those chains might actually originate from the isotope ^{288}115 which would then imply the presence of either SF or EC decay in ^{284}113 or ^{280}Rg. This would suggest that the length of an α-decay chain

is not a good descriptor to define the reaction channel and that more complex decay sequences of $^{288,289}115$ must be considered.

A better descriptor might be derived from a rigorous statistical assessment of the lifetimes in the decay chains of $^{288}115$ and the proposed $^{289}115$. To assess whether distributions of experimental correlation times are compatible with the assumption that each step can be described by one single half-life, a relatively "new test for random events of an exponential distribution" developed by Schmidt was applied by Forsberg et al. (2016b) to the 96 five-α-long chains associated with the isotope $^{288}115$. The method relies on the fact that the standard deviation σ_θ for a distribution of logarithms of lifetimes, $\theta = \ln(t)$, has strictly a fixed value if the lifetimes originate from an exponential decay, however dependent on the number of available lifetimes. The 90% confidence intervals $[\sigma_{\theta,\text{low}}, \sigma_{\theta,\text{high}}]$ have been calculated for different numbers of data points by Monte Carlo techniques. A small value of σ_θ suggests that the lifetimes do not originate from an exponential distribution, and a large value indicates that decays from more than one species are present. The results tell that there is no need to assume the decay of more than one radioactive species for any of the decay steps of these 96 chains, and they can serve as reference for the 3n evaporation channel $^{288}115$. The focus lies now on the interpretation of the 14 short chains, 4 from Oganessian et al. (2013), 7 from Forsberg et al. (2016a), and 3 from Gates et al. (2015). To this end, a more robust figure of merit (FoM) was developed by Forsberg et al. (2016a).

A $\text{FoM}_j^{(n)}$, defined for each correlation time $t_j^{(n)}$ in decay step $j = 1, 2, 3$ of the chain identified by the number n, is calculated as the value of a probability density function for a reference data set. The geometric mean of $\text{FoM}_j^{(n)}$ over all available steps j in chain n defines the $\text{FoM}_{\text{geom}}^{(n)}$ for that chain. The arithmetic mean of $\text{FoM}_{\text{geom}}^{(n)}$ over all N chains defines the FoM for the data set with respect to the interpretation under consideration.

The reference data set can be the one to examine. In this case, the task of the test is to provide a measure of the internal congruence of the data set; each chain is evaluated with respect to the averages of the entire data set. If the individual chains all deviate strongly from the average data, the FoM will be low. If the chains are all too similar to their average, the FoM will be high. Such a test is similar to the one proposed by Schmidt. Note, however, that a low σ_θ corresponds to a large FoM and vice versa.

The probability density function for a selected reference data set is constructed from N reference chains. Presumably, these reference chains originate from an exponential distribution characterized by an average lifetime τ. This τ is not known precisely but has an uncertainty. The probability density function used when evaluating the FoM should take this uncertainty into account, which leads to a smearing. The smeared probability function is constructed as follows (Forsberg et al., 2016a).

1. For each step j, the average experimental lifetime $\bar{t}_j$ is calculated, and the number of available lifetimes N_j is noted.
2. For each step j, the likelihood function for the true lifetime τ_j, given by N_j and $\bar{t}_j$, is determined.

3. For each step j, a τ_j is selected with a probability governed by the likelihood function for τ_j, and then a set of N_j lifetimes are generated from the exponential distribution defined by this τ_j. This procedure is repeated until a smooth histogram emerges.

The corresponding analytic expression for the smeared probability function for step j, using a reference data set with N_j data points and average lifetime $\bar{t}_j$ in step j,

$$f(t) = t(N_j - 1)\frac{(N_j\bar{t}_j)^{N_j-1}}{(N_j\bar{t}_j + t)^{N_j}} \tag{10.46}$$

is obtained by weighting an exponential distribution $g(t) = \frac{t}{\tau}\,\mathrm{e}^{-\frac{t}{\tau}}$ with the normalized likelihood function for τ

$$h(\tau) = \frac{N^{N-1}}{(N-2)!}\,\frac{\bar{t}^{N-1}}{\tau^N}\,\mathrm{e}^{-\frac{N\bar{t}}{\tau}} \tag{10.47}$$

To decide whether an FoM indicates congruence or not, it is compared to the distribution of FoM values that result when the same method is applied to a very large number of sets of chains generated by a Monte Carlo method to mimic the basic properties of the set of 14 short chains. One method would be to generate sets of 14 random numbers from exponential distributions $g(t)$ characterized by the values $\bar{t}_j$. However, it was decided to take into account the uncertainties in $\bar{t}_j$ also when generating sets of chains. The chains were generated in the following way:

1. For the first decay step, a random τ_1 was picked according to the τ likelihood function $h(\tau)$. Fourteen random lifetimes from the exponential distribution $g(t)$ defined by this τ_1 were generated.
2. For the second decay step, a random τ_2 was picked according to the τ likelihood function $h(\tau)$. Fourteen random lifetimes from the exponential distribution $g(t)$ defined by this τ_2 were generated.
3. For the third decay step, a random τ_3 was picked according to the τ likelihood function $h(\tau)$. Ten random lifetimes from the exponential distribution $g(t)$ defined by this τ_3 were generated.
4. The generated lifetimes were collected in 14 chains – 10 with 3 lifetimes, and 4 with 2 lifetimes.

In this way, 10^5 sets of chains with similar characteristics as the experimental 14 short chains were created. The FoM for the generated sets of chains were evaluated in the same way as the experimental data. The FoM distribution for these simulated chains and the corresponding upper and lower 90% confidence limits were plotted. They were compared to the $\mathrm{FoM}_{\mathrm{geom}}$ distribution for a single chain with the corresponding lower 90% limit to demonstrate the effect of low statistics. This was done for two different cases – for recoil-α-SF and recoil-α-α-SF chains. The conclusions based on this exercise are presented in Forsberg et al. (2016b) and here in Chapter 17. In our opinion, they have removed the alleged genetic link between $^{293}117$ and $^{289}115$ proposed by Oganessian et al. (2013) that IUPAC carelessly did not question, when it approved the names for elements 115 and 117.

10.7 Setting Upper Limits when no Counts Are Observed

The simplest answer to an experiment that failed to detect the decay being sought is to give the "one-event upper limit." The assumption is made that one event had been detected, and one is calculating the decay rate or cross-section taking into account target thickness, beam intensity, detection efficiency, and so forth.

By using the properties of the Poisson distribution, a more sophisticated answer can be given. The probability of observing m events if the mean value is M is

$$W\left(\frac{m}{M}\right) = \frac{M^m}{m!} = \mathrm{e}^{-M}$$

The probability of observing no events in a time t for a decay rate λ is

$$W\left(\frac{0}{\lambda t}\right) = \mathrm{e}^{-\lambda t}$$

The upper limit on the count rate when zero counts are observed, λ_0, is given by

$$\lambda_0 = -\frac{1}{t}\ln(1 - \mathrm{CL})$$

where CL is the confidence limit that is to be attached to the upper limit. For a limit with 95% confidence, CL = 0.95. Consider a decay process that should produce one event per week, yet no counts are observed at $\eta = 1$ in five weeks. Then, the upper limit on the decay rate is

$$\lambda_0 = -\frac{1}{5}\ln(1 - 0.95) = 0.6 \text{ per week}$$

References

Forsberg, U., Rudolph, D., Andersson, L.-L. et al. (2016a). Recoil-α-fission and recoil-α-α-fission events observed in the reaction ^{48}Ca + ^{243}Am. *Nucl. Phys.* A953: 117.

Forsberg, U., Rudolph, D., Fahlander, C. et al. (2016b). A new assessment of the alleged link between element 115 and element 117 decay chains. *Phys. Lett.* B760: 293.

Gates, J.M., Gregorich, K.E., Gothe, O.R. et al. (2015). Decay spectroscopy of element 115 daughters: ^{280}Rg → ^{276}Mt and ^{276}Mt → ^{272}Bh. *Phys. Rev.* C92 (R): 021301.

Khuyagbaatar, J., Yakushev, A., Düllmann, Ch.E. et al. (2014). Study of the ^{48}Ca + ^{249}Bk fusion reaction leading to element Z =117: long-lived α-decaying ^{270}Db and discovery of ^{256}Lr. *Phys. Rev. Lett.* 112: 172501.

Oganessian, Yu.Ts, Abdullin, F.Sh., Dmitriev, S.N. et al. (2013). Investigation of the ^{243}Am + ^{48}Ca reaction products previously observed in the experiments on elements 113, 115, and 117. *Phys. Rev.* C87: 014302.

Further Reading

Feller, W. (1950). *Probability Theory and its Applications*. New York: Wiley.

Breitenberger, E. (1955). Scintillation-spectrometer statistics. In: *Progress in Nuclear Physics*, vol. 4 (ed. O.R. Frisch), 56. London: Pergamon.

Brownlee, K.A. (1960). *Statistical Theory and Methodology in Science and Engineering*. New York: Wiley.

Bevington, P.R. (1969). *Data Reduction and Error Analysis for Physical Sciences*. New York: McGraw-Hill.

Rényi, A. (1970). *Foundations of Probability*. San Francisco, CA: Holden-Day.

Goulding, F.S. and Landis, D.A. (1974). Semiconductor detector spectrometer electronics. In: *Nuclear Spectroscopy and Reactions, Part A* (ed. J. Cerny), 414. New York: Academic Press.

Meyer, S.L. (1975). *Data Analysis for Scientists and Engineers*. New York: Wiley.

Schmidt, K.-H., Sahm, C.C., Pielenz, K., and Clerc, H.G. (1984). Some remarks on the error analysis in the case of poor statistics. *Z. Phys.* A316: 19.

Barlow, R.J. (1989). *Statistics – A Guide to the Use of Statistical Methods in the Physical Sciences*. Chichester: Wiley.

Michel, R. and Kirchhoff, K. (1999). *Nachweis-, Erkennungs- und Vertrauensgrenzen bei Kernstrahlungsmessungen*. Fachverband für Strahlenschutz e.V, TÜV-Verlag, Cologne.

Schmidt, K.H. (2000). A new test for random events of an exponential distribution. *Eur. Phys. J.* A8: 141.

Brüchle, W. (2003). Confidence intervals for experiments with background and small numbers of events. *Radiochim. Acta* 91: 71.

Nagy, S. (2011). Stochastics and nuclear measurements. In: *Handbook of Nuclear Chemistry*, 2e, vol. 1 (eds. A. Vertés, S. Nagy, Z. Klencsár, et al.), 395. Berlin: Springer-Verlag.

11

Techniques in Nuclear Chemistry

In this chapter, we intend to deal with techniques established in the production and isolation of radionuclides for various purposes, for example, production of radiotracers for application in various fields of research like chemistry, analytics, life sciences, geology, biology, and so forth, production of exotic nuclei and study of their nuclear properties such as half-lives and decay schemes, all the way through in-beam nuclear reaction studies. We start this chapter with some basic remarks on the unique aspects of the chemistry of radionuclides.

11.1 Special Aspects of the Chemistry of Radionuclides

11.1.1 Short-Lived Radionuclides and the Role of Carriers

The most important aspects of the chemistry of short-lived radionuclides are that:

- the mass of the radionuclides is small; and
- chemical procedures have to be fast.

The mass of a radionuclide is proportional to its half-life:

$$m = A\frac{M}{\ln 2 N_{\mathrm{Av}}} t_{1/2} \tag{11.1}$$

where A is the activity in Bq (s^{-1}), μ is the mass of the nuclide in atomic mass units (u), and N_{Av} is the Avogadro's number. This relation is illustrated in Table 11.1 for the activity of 10 Bq and radionuclides of various half-lives. At short half-lives, the masses of the radionuclides are considerably smaller than the masses usually handled in chemical operations. Traces of the order of 10^{-10} g or less are, in general, only detectable on the basis of their radioactivity, and handling of those traces requires special attention. The following aspects have to be considered:

- the mass of the radionuclide to be handled;
- the presence of isotopic carriers;
- the presence of non-isotopic carriers.

Nuclear and Radiochemistry: Fundamentals and Applications,
Fourth Edition. Jens-Volker Kratz.

Table 11.1 Number of atoms and mass of various radionuclides corresponding to 10 Bq.

Radionuclide	Half-life	Number of atoms	Mass (g)	Concentration if dissolved in 10 ml (mol l^{-1})
^{238}U	$4.468 \cdot 10^9$ yr	$2.0 \cdot 10^{18}$	$8.0 \cdot 10^{-4}$	$3.4 \cdot 10^{-4}$
^{226}Ra	1600 yr	$7.3 \cdot 10^{11}$	$2.7 \cdot 10^{-10}$	$1.2 \cdot 10^{-10}$
^{227}Ac	21.77 yr	$9.9 \cdot 10^{9}$	$3.7 \cdot 10^{-12}$	$1.6 \cdot 10^{-12}$
^{60}Co	5.272 yr	$2.4 \cdot 10^{9}$	$2.4 \cdot 10^{-13}$	$4.0 \cdot 10^{-13}$
^{210}Po	138.38 d	$1.7 \cdot 10^{8}$	$6.0 \cdot 10^{-14}$	$2.9 \cdot 10^{-14}$
^{32}P	14.26 d	$1.8 \cdot 10^{7}$	$9.5 \cdot 10^{-16}$	$3.0 \cdot 10^{-15}$
^{24}Na	14.96 h	$7.7 \cdot 10^{5}$	$3.1 \cdot 10^{-17}$	$1.3 \cdot 10^{-16}$
^{251}Md	4.0 mo	$3.5 \cdot 10^{3}$	$1.4 \cdot 10^{-18}$	$5.5 \cdot 10^{-19}$
^{258}Lr	3.9 s	$5.6 \cdot 10$	$2.4 \cdot 10^{-20}$	$0.9 \cdot 10^{-20}$

Carriers are elements or compounds with identical or very similar chemical properties to the radionuclide. With respect to the suitability as carriers, the chemical state is decisive. Carriers are often added to ensure normal chemical behavior of radionuclides. For that purpose, they must be in the same chemical state as the radionuclide considered.

In the case of radioisotopes of stable elements, such as ^{60}Co, ^{32}P, and ^{24}Na, small amounts (traces) of these elements are always present, due to their ubiquity. The masses are, in general, higher than the masses of short-lived radioisotopes, and the omnipresent traces act as isotopic carriers of the short-lived radionuclides, provided that they are in the same chemical state. In the case of isotopes of radioelements, such as ^{226}Ra, ^{227}Ac, ^{210}Po, ^{251}Md, or ^{258}Lr, however, stable nuclides are absent and the masses of the radionuclides are identical with the masses of the elements, provided that the presence of longer-lived radioisotopes can be excluded.

Traces of elements or compounds of other elements with similar properties may serve as non-isotopic carriers for radioisotopes of stable elements as well as for isotopes of radioelements. The influence of non-isotopic carriers depends on the nature of the compounds and the chemical operation. For example, in precipitation reactions, non-isotopic carriers, or hold-back carriers, may play a major role.

Separation of short-lived radionuclides requires application of fast methods. The time needed for the separation procedure should not exceed the half-life. Precipitation, including filtration or the usual ion-exchange methods followed by elution, and chromatographic methods require up to several minutes. Solvent extraction involving slow complexation reactions may take too much time.

For fast filtration, the device used by Otto Hahn (Figure 11.1) is well suited. The filter with the precipitate can easily be removed and measured. The same device may be used for fast separation by ion exchange on thin layers. For example, short-lived radioisotopes of iodine may be separated rather effectively on a thin layer of AgI (or AgCl) by means of the ion-exchange reaction $AgI(AgCl) + {}^*I^- \rightarrow Ag{}^*I + I^-(Cl^-)$ (Figure 11.2).

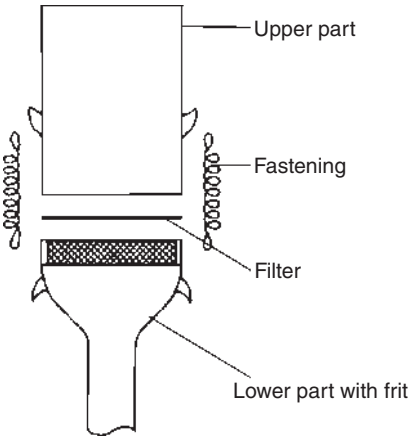

Figure 11.1 Hahn's suction frit.

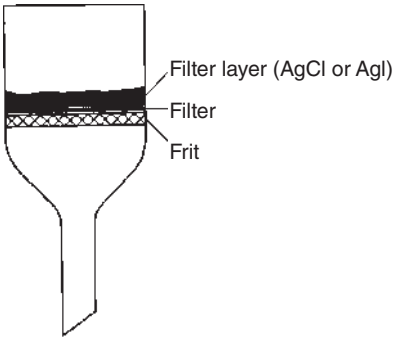

Figure 11.2 Filter layer for separation of carrier-free iodine (I_2 or I^-) by exchange.

Thermochromatography using a quartz glass column is applied for the separation of volatile compounds (Section 11.1.3). Aerosols may be injected for transportation of the radionuclides and a reactive gas (e.g. Cl_2) may be added to form special compounds or to investigate the chemical behavior of the radionuclides, in particular radionuclides of heavy elements.

11.1.2 Radionuclides of High Specific Activity

In the absence of stable isotopes, the specific activity of radionuclides is given by

$$\frac{A}{m} = \frac{\ln 2}{t_{1/2}} \frac{N_{\mathrm{Av}}}{M} \tag{11.2}$$

where A, m, $t_{1/2}$, and M are the activity, mass, half-life, and atomic mass of the radionuclide, respectively, and N_{Av} is Avogadro's number. Even for longer-lived radionuclides such as ^{14}C ($t_{1/2} = 5730$ years), the specific activity is rather high and the mass of the substance is very small, if stable isotopes are absent. For example, 1 GBq ^{14}C (≈27 mCi) corresponds to a mass of only 6.06 mg ^{14}C and a specific activity of 165 GBq per gram of ^{14}C. Due to the presence of small amounts of stable isotopes of carbon, specific activities of up to about 100 GBq ^{14}C per gram of carbon

are obtained in practice. Synthesis of ^{14}C-labeled carbon compounds of this specific activity means handling milligram amounts and requires small pieces of equipment and special precautions. Reactions in closed systems, use of vacuum lines, and cooling traps are favorable.

The term carrier-free is often used to indicate the absence of stable isotopes or longer-lived radioisotopes of the radionuclide considered. However, due to the omnipresence of most stable elements, carrier-free radioisotopes of stable elements are, in general, not available. The presence of stable isotopes or longer-lived radioisotopes has to be taken into account, and the specific activity is smaller than calculated by Eq. (11.2). As long as the presence of such other isotopes cannot be excluded, it is more correct to distinguish "no-carrier-added" (n.c.a.) and "carrier-added" radionuclides. On the other hand, radioisotopes of radioelements are carrier-free if longer-lived radioisotopes are absent.

11.1.3 Microamounts of Radioactive Substances

From the previous sections it is evident that radionuclides of high specific activity often represent very small amounts (microamounts, non-weighable amounts <1 μg) of matter, especially if the half-lives are short. Handling such microamounts requires special precautions because in the absence of measurable amounts of carriers the radionuclides are microcomponents and their chemical behavior may be different from that observed for macrocomponents. This aspect is of special importance if the system contains liquid/solid, gas/solid, or liquid/liquid interfaces. The percentage of radionuclides sorbed on the walls of a container depends on the chemical form (species) of the radionuclide, its concentration, and specific activity, and on the properties of the container material. At high specific activity of a radionuclide in solution, the surface of a glass beaker generally offers an excess of surface sorption sites.

Glass surfaces have an ion-exchange capacity on the order of 10^{-10} mol cm^{-2} ($\approx 10^{14}$ ions cm^{-2}) and a similar number of sorption sites is available for chemisorption. Thus, 100 ml glass beakers have an ion-exchange capacity of about 10^{-8} mol corresponding to a concentration of 10^{-7} mol l^{-1} in 100 ml. Therefore, sorption on glass walls may be marked at concentrations below 10^{-6} mol l^{-1}. By comparison with Table 11.1 it is obvious that, in the absence of carriers, even long-lived radionuclides may easily be sorbed on glass walls by ion exchange or chemisorption.

Chemisorption is very pronounced if the radionuclide is able to react with the surface. An example is the sorption of hydroxo complexes of tri- and tetravalent elements by the silanol groups on glass surfaces. Sorption increases with the formation of mononuclear hydroxo complexes in solution and decreases with the condensation to polynuclear complexes at higher pH values. Several measures may be taken to suppress ion exchange or chemisorption of traces of radionuclides on glass surfaces:

- high concentration of H^+ to suppress ion exchange and hydrolysis;
- high concentration of non-isotopic cations, anions, or other substances to suppress ion exchange and adsorption of the radionuclides considered;

- hydrophobization of the glass surface (e.g. by silanizing with trichlorosilane) to prevent ion exchange and chemisorption.

  The surfaces of plastic materials, such as polyethylene, polypropylene, or Perspex, do not exhibit ion exchange, but adsorption may be pronounced, in particular adsorption of organic compounds including organic complexes of radionuclides.

  Sorption of radionuclides on particulates in solution is frequently observed. The particles may be coarsely or finely dispersed. Their surface properties (surface layer, charge, ion-exchange, and sorption properties) play a major role. In general, they offer a great number of sorption sites on the surface, and microamounts of radionuclides may be found on the surface of these particles instead of in solution. Sorption of radionuclides on colloidal particles leads to the formation of *radiocolloids* (carrier colloids, Section 11.4).

  Reactions at gas/solid interfaces may lead to sorption of radionuclides from the gas phase or they may cause loss of activity of solid samples by interaction with the gas phase. For example, $Ba^{14}CO_3$ exhibits loss of $^{14}CO_2$ to moist air due to the isotope exchange $^{14}CO_3^{2-}(s)/^{12}CO_2(g)$ in the presence of water vapor. The specific activity of solid samples may be reduced appreciably by such reactions.

  Separation of nonweighable amounts of radioactive substances requires application of suitable techniques. Precipitation is, in general, not possible because the solubility product cannot be exceeded. Coprecipitation may be used after addition of a suitable carrier. An isotopic carrier must be in the same chemical state as the radionuclide and leads to marked lowering of the specific activity. A non-isotopic carrier must coprecipitate the radionuclide efficiently and it must be separable from the radionuclide after coprecipitation.

  According to Hahn, two possibilities are distinguished in the case of coprecipitation or cocrystallization:
- coprecipitation (cocrystallization) by isomorphous substitution; and
- coprecipitation (cocrystallization) by adsorption.

  Radionuclides that are able to form normal or anomalous mixed crystals with the macrocomponent are incorporated at lattice sites. In most cases, the distribution in the lattice is heterogeneous, that is, the concentration of the microcomponent varies with the depth. If the solubility of the microcomponent is lower than that of the macrocomponent, it is enriched in the inner parts of the crystals. Heterogeneous distribution may even out over longer periods of time by diffusion or recystallization.

  For homogeneous distribution of a microcomponent (i) and a macrocomponent (ii) in a solid phase (s) and a liquid phase (l), Nernst's distribution law is valid and the following relation is obtained:

$$\frac{(c_1/c_2)_s}{(c_1/c_2)_l} = \frac{(n_1/n_2)_s}{(n_1/n_2)_l} = K_h \tag{11.3}$$

where c_1 and c_2 are the concentrations and n_1 and n_2 are the mole numbers. K_h is called the homogeneous distribution coefficient.

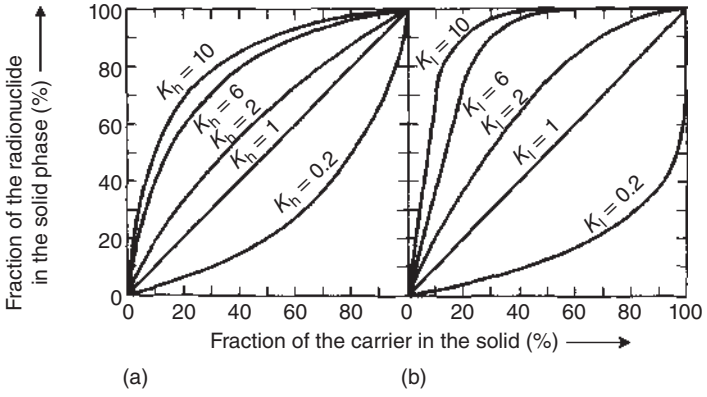

Figure 11.3 Fraction of the radionuclide in the solid phase as a function of fractional precipitation or crystallization. (a) Homogeneous distribution and (b) heterogeneous distribution.

In the case of heterogeneous distribution, Nernst's distribution law holds only for the respective surface layer in equilibrium with the solution and the relation is

$$\frac{\log n_1^o/(n_1^o - n_2)}{\log n_2^o/(n_2^o - n_2)} = K_1 \tag{11.4}$$

where n_1 and n_2 are the mole numbers of the microcomponent and the macrocomponent in the solid and n_1^o and n_2^o are the total numbers of moles present. K_1 is called the logarithmic distribution coefficient.

These relations have been verified for the distribution of ^{226}Ra as a microcomponent in $BaSO_4$. At elevated temperature, a homogeneous distribution is obtained after some hours, whereas a heterogeneous distribution is observed at low temperature and fast separation of solid and solution. A heterogeneous distribution is also found after crystallization by slow evaporation of the solvent.

The fraction of a radionuclide present as the microcomponent that is separated in the cases of homogeneous and heterogeneous distribution by coprecipitation or cocrystallization is plotted in Figure 11.3 as a function of the precipitation or crystallization of the macrocomponent for various values of homogeneous and logarithmic distribution coefficients. Knowledge of these values is important for separation by fractional precipitation or crystallization. Figure 11.3 shows that separation is more effective in the case of a heterogeneous distribution, provided that $K_1 > 1$. For example, at a distribution coefficient of 6, precipitation of 50% of the macrocomponent leads to coprecipitation of 98.4% of the microcomponent in the case of a heterogeneous distribution and only to coprecipitation of 86% in the case of a homogeneous distribution. Therefore, fast precipitation or slow evaporation at low temperature is most effective for separation of radionuclides by fractional precipitation or crystallization, respectively.

Coprecipitation of microamounts of radioactive substances by adsorption depends on the surface properties such as the surface charge and the specific surface area of the solid. For instance, cationic species are preferably sorbed on surfaces carrying

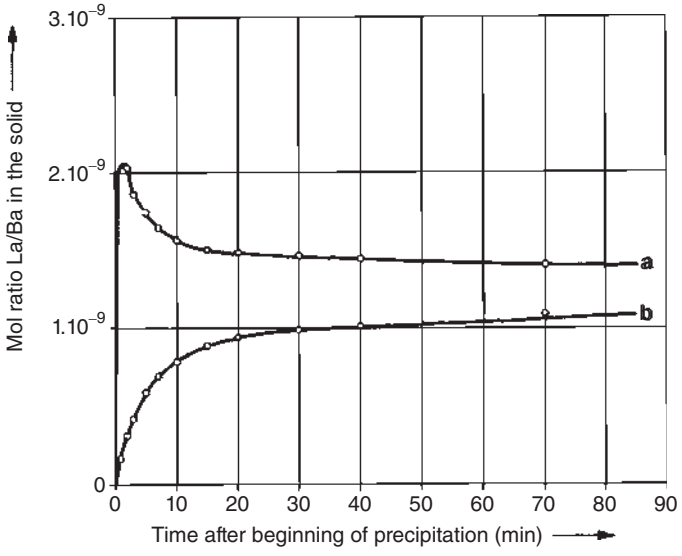

Figure 11.4 Coprecipitation of carrier-free La with $BaSO_4$: (a) La occluded; (b) La adsorbed at the surface. Source: Lieser and Wertenbach (1962), figure 02 (p. 75)/De Gruyter.

negative surface charges, and hydroxides are very effective sorbents because of their high specific surface area. Microcomponents adsorbed on particles formed in the early stages of precipitation or crystallization are partly occluded in the course of crystal growth (inner adsorption). As an example, coprecipitation of n.c.a. ^{140}La with $BaSO_4$ by adsorption is shown in Figure 11.4 as a function of time after the beginning of precipitation. The amount of ^{140}La occluded in the $BaSO_4$ crystals decreases with time, mainly due to Ostwald ripening, whereas the amount of ^{140}La adsorbed at the surface of the $BaSO_4$ crystals increases.

If macroamounts of other elements are to be separated from microamounts of radioactive substances by precipitation, isotopic or non-isotopic hold-back carriers may be added to suppress coprecipitation of the radioactive substances.

In ion-exchange and chromatographic procedures, microamounts of radioactive substances may be lost by sorption on the ion exchangers or sorbents or on the walls of the columns. Small amounts of impurities in the materials used may be responsible for unexpected reactions and losses.

The most favorable separation method for microamounts is solvent extraction because the number of possible ion-exchange and sorption sites on solid surfaces is relatively small. However, small amounts of impurities in the organic or aqueous phases may also lead to unexpected behavior of microcomponents.

Many effects described in this section increase with decreasing amounts of the radioactive substance. If the number of atoms or molecules becomes very small ($\ll$100), the usual thermodynamic descriptions are no longer applicable. The distribution of one or several atoms of an element or of several molecules in a system is no longer defined because the law of mass action, partition functions, and thermodynamic functions, such as chemical potential, Gibbs free energy, and

entropy, are based on the properties of a multitude of atoms or molecules of the same kind.

The rate of reaction between two microcomponents (i) and (ii) is $R = kc_1c_2$, and if both concentrations c_1 and c_2 are extremely small, R is also extremely small, and the microcomponents (i) and (ii) cannot be assumed to be in equilibrium.

Single-atom chemistry is of particular importance if only single atoms are available for chemical studies, as in the case of the heaviest elements. The short-lived isotopes of these elements can only be produced at a rate of one atom at a time, and the investigation of their chemical properties requires special considerations.

The equilibrium constant K of a chemical reaction $A + B \leftrightarrow C + D$ is given by $K = (a_C \cdot a_D)/(a_A \cdot a_B)$, where a_A, a_B, a_C, and a_D are the chemical activities. However, if only one atom is present, it cannot exist at the same time in the form of A and C and a_A or a_C must be zero. Consequently, in single-atom chemistry, K is no longer defined. The same holds for $\Delta G = -RT \ln K$, the free enthalpy of the reaction. In order to overcome this problem, in single-atom chemistry, the probabilities of finding the single atom in the form of A or C are introduced instead of the chemical activities or concentrations, respectively, and by use of these probabilities, equilibrium constants, and single-particle free enthalpies can be defined.

An example is the distribution equilibrium of a single atom between two phases, where the distribution coefficient K_d is defined by the probabilities of finding the single atom in one phase or in the other. If a one-step partition method is applied, K_d must be measured repeatedly many times, in order to obtain a statistically relevant result. Much more favorable is the use of a multistage method, particularly a chromatographic method, in which the partition of the single atom is taking place many times successively.

In chemical experiments with short-lived single atoms, it is necessary to take into account the time that is necessary to obtain chemical equilibrium. In this respect, chromatographic methods comprising fast adsorption and desorption processes are also very favorable.

Moreover, the half-life of a single radioactive atom cannot be measured, and even if the half-life is known, the instant at which the atom will undergo disintegration cannot be predicted. Radioactive decay, chemical kinetics, and chemical equilibria are governed by the laws of probability and many measurements with single atoms are necessary to establish the statistics and to obtain relevant results. With regard to chemical properties, it is important that all the atoms are present in the same chemical form (same species).

The chemical behavior of small numbers of atoms in interstellar space, that is, in an environment that is virtually free of matter, also exhibits some special features. Because energies cannot be transmitted to or from other atoms or molecules, exothermic reactions lead to immediate decomposition and endothermic reactions are not possible.

11.1.4 Radiocolloids

Radiocolloids are colloidal forms of microamounts of radioactive substances. Their formation was first observed in 1913 by Friedrich Paneth in his research on the

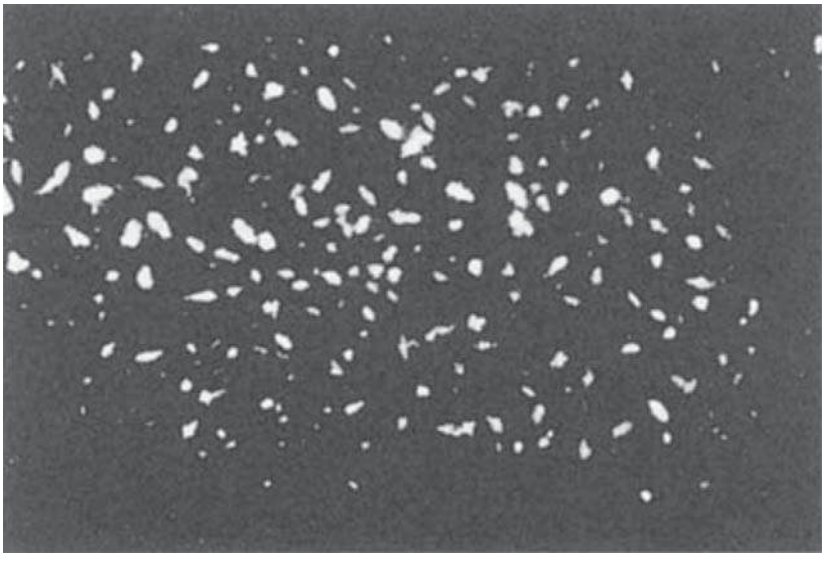

Figure 11.5 Autoradiograph of a radiocolloid (^{234}Th, pH ≈ 3).

separation of ^{210}Bi and ^{218}Po. Radiocolloids can be separated from aqueous solutions by ultrafiltration, centrifugation, dialysis, and electrophoresis. They can be detected with high sensitivity by autoradiography. As an example, the autoradiograph of a radiocolloid of ^{234}Th is shown in Figure 11.5.

In order to understand the nature of radiocolloids, knowledge of the general properties of colloids is needed. Colloids are finely dispersed particles in a liquid phase, a gas phase, or a solid phase. The size of colloidal particles is in the range between that of molecules or ions and that of particles visible by means of a light microscope, that is, between about 1 nm and about 0.45 μm. The upper value corresponds to the mean wavelength of visible light. Large molecules, in particular polymers and biomolecules, approach or exceed the upper value and may also form colloids.

Like ions and small molecules, colloids are considered to be components of the phase in which they are suspended. In general, the metastable colloidal state exists for longer periods of time (up to several months) and colloidal particles may be transported with water or air over long distances.

Small particles have a large specific surface area and a relatively large specific surface energy. Therefore, they have the tendency to form particles of lower specific surface energy, that is, they are metastable with respect to larger particles. The main feature of colloids is that aggregation to larger particles is prevented by mutual repulsion, for example, in water by electric charges of the same sign in the case of hydrophobic colloids, or by shells of water molecules in the case of hydrophilic colloids.

A colloidal solution is also called a sol, in contrast to a gel, which exhibits the properties of a solid but contains large amounts of solvent and is amorphous. Typical examples are a sol and a gel of silicic acid (silica gel). Colloidal particles of inorganic

hydroxides ($Fe_2O_3 \cdot xH_2O$, $Al_2O_3 \cdot xH_2O$, $TiO_2 \cdot xH_2O$, $ThO_2 \cdot xH_2O$, and others) often carry positive charges. By the addition of ions with opposite charge, neutralization and coagulation may occur. Therefore, colloids of this kind are sensitive toward electrolytes. Other hydrophilic colloids, such as colloidal polysilicic acid, are stabilized by a shell of water molecules and are less sensitive to the presence of electrolytes. Hydrophobic colloids may be stabilized by surface-active substances in such a way that the hydrophobic part of these substances is bound on the surface, whereas the hydrophilic part is directed to the outside and leads to mutual repulsion of the particles.

Many organic molecules are large enough to form colloids, and organic colloids are frequently encountered in the life sciences. Humic substances are found in natural waters and may form complexes with radionuclides.

Generally, radiocolloids may be generated in two ways:

a. The radionuclide or the labeled compound may form an intrinsic colloid (*Eigenkolloid*, sometimes also called a "real colloid").
b. The radionuclide or the labeled compound may be sorbed on an already existing colloid which serves as carrier (carrier colloid, *Fremdkolloid*, sometimes also called a "pseudocolloid").

   Formation of an intrinsic colloid is only possible if the solubility of the radionuclide or the labeled compound is exceeded. If an isotopic or a non-isotopic carrier is present, the radionuclide or the labeled compound will be incorporated if the solubility of the carrier is exceeded. In this case, a carrier colloid is formed containing the radionuclide or the labeled compound in a homogeneous or heterogeneous distribution. A carrier colloid is also formed if the radionuclide or the labeled compound is sorbed on an already existing colloid. This may be an inorganic colloid such as polysilicic acid or colloidal iron(III) hydroxide, or an organic colloid such as humic acid. Because colloids have a high specific surface area, the probability of formation of carrier colloids by sorption of radionuclides or labeled compounds is high if colloids are present. This probability increases with increasing concentration of colloids and with decreasing concentration of radionuclides or labeled compounds and their carriers. Both kinds of carrier colloids are real colloids, not "pseudocolloids."

It is obvious that the formation of radiocolloids will be observed:

a) if colloids of other origins are present; or
b) if the solubility of the radionuclide, the labeled compound, or a suitable carrier is exceeded.

   Colloids are found in many systems, for example, in natural waters and in the air. Traces of colloids formed by dust particles or by particles given off from the walls of containers are practically omnipresent. They can only be removed by careful ultrafiltration. If a radionuclide or a labeled compound enters such a system, there is a high probability that it will be sorbed on the colloids, provided that the competition from other ions or molecules is not too strong. Only if the presence of colloids from other origins is excluded, and if the solubilities of relevant

species are not exceeded, can the formation of radiocolloids by microamounts of radionuclides be neglected.

In aqueous solutions, generation of radiocolloids is favored by hydrolysis of the radionuclide considered. Mononuclear hydroxo complexes may form colloids by condensation to polynuclear complexes if their concentration is high enough or they may be sorbed on the surface of colloids from other origins. Formation of radiocolloids of these kinds can be prevented by a low pH or addition of complexing agents. For instance, addition of F^- ions prevents formation of radiocolloids of ^{95}Zr.

Commonly, a distinction is made between genuine solutions containing only matter in molecular dispersion (ions, molecules) and colloidal solutions containing colloidal particles. As already mentioned, colloids are also considered to be components of the phase in which they are suspended.

Like normal colloids, radiocolloids show different behavior from that of ions or molecules. For instance, they are generally not sorbed on ion exchangers or chromatographic columns.

It should be emphasized that the (metastable) colloidal state cannot be described by thermodynamic functions. Consequently, a thermodynamic description of a system fails in the presence of colloids. For example, the solubility product is well defined for certain (in general crystalline) solids and takes into account the ions in equilibrium with these solids. Nonionic and colloidal forms, however, are not taken into account.

11.1.5 Tracer Techniques

Tracer techniques comprise all methods in which microamounts (traces) of radionuclides or labeled compounds are added to a system, in order to pursue (trace) the fate, transport, or chemical reaction of a certain element or compound in that system. Radioactive tracers are preferably used because they can be detected and measured in very low concentrations and with high sensitivity, as is evident from Table 11.1. With a measuring period of 10 minutes and an overall counting efficiency of 20%, 10 Bq can be determined with a statistical error of about 3%.

The prerequisite of tracer techniques is that the radionuclide is in the same chemical form as the species to be investigated. At least, it must exhibit the same behavior, for instance, in the study of transport processes. The same chemical behavior can be assumed in the case of isotopic tracers, provided that isotope effects can be neglected. However, isotope effects are only marked for light atoms, in particular hydrogen, for which kinetic and equilibrium isotope effects have to be taken into account in the case of substitution of H by D or T.

Tracer techniques offer the unique possibility of studying the kinetics of chemical reactions in chemical equilibria in which one isotope is exchanged for another (isotopic exchange reactions, reaction enthalpy $\Delta H \approx 0$, reaction entropy $\Delta S \neq 0$). Isotopic exchange reactions have found broad application for kinetic studies in homogeneous and heterogeneous systems.

Besides the investigation of isotopic exchange reactions, tracer techniques are applied in various fields of science and technology:

- radioanalysis;
- investigation of bonding and reaction mechanisms in chemistry and biochemistry;
- measurement of diffusion and self-diffusion;
- study of pathways of elements or compounds in biological systems, in the human body, and in the environment;
- application for diagnostic purposes in nuclear medicine;
- investigation of transport processes in industrial equipment;
- study of corrosion and wear.

11.2 Target Preparation

In our discussion of the techniques used in the production of radioisotopes, the targets are the next point of interest. The techniques used to prepare targets for nuclear bombardments depend on the type of experiment and on the nature of the irradiation. In the following, we discuss separately targets for reactor irradiations, thick-target accelerator targets, thin accelerator targets, and the measurement of the homogeneity of the thin targets and their target thickness.

Sample preparation for reactor irradiations is generally rather straightforward, though some special considerations are necessary. These concern the containers for samples to be exposed and depend on the neutron flux and the length of bombardment. For irradiations on the order of minutes to hours in the modest fluxes of many research reactors, plastic vials are often satisfactory and give rise to rather low activity levels. For longer irradiations and higher fluxes, samples are often sealed in quartz glass vessels. After irradiation, these must often be allowed to cool for some time to let the intense 2.6 hours ^{31}Si activity decay. Thought must also be given to the arrangement for opening these vessels without undue hazards to personnel and contamination hazards. The thermal stability of the substance to be irradiated is another problem to be considered. Some reactors have special water-cooled irradiation facilities. The irradiation of aqueous solutions creates special problems; the radiation decomposition of water can build up dangerous pressures and provisions are necessary for venting or catalytically recombining the gases. Self-shielding may be a problem for substances with high neutron capture cross sections. As an example, consider a 0.1 mm layer of gold where the neutron capture cross section for thermal neutrons is 100 barn. Here the flux depression is already 6%.

In accelerator bombardments, the variety of targeting problems is so large that only a few general remarks can be made. When the production of the radionuclide is the only goal without the need to characterize quantitatively the nuclear reaction involved, it is adequate to use a thick target in which the bombarding particles are appreciably degraded in energy. For example, if a 40 MeV beam of ^{4}He ions is available, and if we intend to produce a radionuclide in an (α, n) reaction, we would use a target thick enough to degrade the beam to the (α, n) threshold to maximize the

yield of the desired radionuclide. On the other hand, if it were desirable to produce the (α, n) product with minimal contamination by the (α, 2n) product, we would not use the 40 MeV ^{4}He ions but would first degrade the beam with degrader foils below the threshold of the (α, 2n) reaction.

Because, in accelerator bombardments, the energy dissipation in the target can become on the order of a kilowatt over an area of a square centimeter, metal targets soldered to a water-cooled backing plate are useful. If nonmetallic elements or compounds need to be irradiated, targets can be made by pressing powders into grooves on a cooled backing plate. Cooling can be assisted by blowing helium over the target surface. Liquid or gas targets, either stationary or flowing, are also used in some applications.

In the largest variety of accelerator experiments, thin targets are needed. The appropriate target thickness depends on the particular information that is sought. In experiments designed to measure excitation functions (cross sections as a function of incident energy), the target must be thin enough so that the energy degradation of the bombarding particle in the target will not cause a significant change in the cross section, typically a milligram per square centimeter. If the spectra of ejectiles produced in a reaction are to be measured, the criterion for maximum target thickness will be set by the energy loss of these secondaries in the target. Likewise, if an experiment is aiming at the determination of momenta and angular distributions of the recoil nuclei, the targets need to be so thin that these recoiling reaction products will not undergo appreciable scattering or degradation on their way out of the target. This may require targets of no more than a few micrograms per square centimeter.

The need to suppress secondary reactions caused by particles produced in the primary interactions, if the products of such secondary reactions interfere with the measurement, may be another limitation on target thickness. The product of a (p, pπ^+) reaction with high-energy protons, for example, is the same as that of an (n, p) reaction on the same target. Thus, in an attempt to measure the tiny cross section (10^{-4} barn) of a (p, pπ^+) reaction, the targets used must be thin enough so that the (n, p) reactions caused by low-energy neutrons produced in the target do not swamp the sought for effect. The problematic may depend on the number of secondaries per primary interaction, on the ratio of primary to secondary cross sections, and on the angular distribution of the secondaries. In practice, it may be necessary to irradiate targets of several different thicknesses and to extrapolate the results to zero target thickness.

For the production of thin targets, in principle, whenever suitable foils are commercially available they offer the simplest solution. However, not many metals are available in thicknesses below a milligram per square centimeter; among those are aluminum, nickel, and gold. Vacuum evaporation has been used to prepare targets of a large variety of metals, some nonmetallic elements, and some compounds. The method is wasteful of material, but has occasionally been used to make separated isotope targets. The evaporated films are deposited on a variety of backing materials (metal foils, plastic films). Plastic films for target backings are usually prepared by letting a few drops of a suitable solution of the plastic spread on distilled water and,

after evaporation of the solvent, picking up the film on a metal frame. Useful plastics are Formvar, soluble in chloroform, collodium, soluble in amyl acetate, and a tough resin called VYNS, a polyvinyl acetate–polyvinyl chloride copolymer, soluble in cyclohexanone. Film thicknesses are usually 5–10 $\mu g\,cm^{-2}$. If an unsupported target is required, techniques are available for stripping off or dissolving the backing. Probably the most useful is evaporation on a layer of water-soluble material such as $BaCl_2$, NaCl, or glucose on glass, followed by gentle dissolution of this intermediate layer in water, where the desired film is floated off. Self-supporting foils with thicknesses down to about 10 $\mu g\,cm^{-2}$ have been prepared in this way. For the deposition of small amounts of material with high efficiency, cathodic sputtering has been used as well.

A widely used method for target preparation is electrodeposition. It is not restricted to the deposition of metals, but can be used for cathodic deposition of hydroxides or other compounds. Electrodeposition can be made nearly quantitative and is therefore suitable for use with enriched isotopes. Molecular plating, that is, electrodeposition of molecular species from organic solvents, has been widely used. This is the method that has been applied in the preparation of actinide targets used in hot fusion reactions with beams of ^{18}O through ^{48}Ca to produce transactinide elements up to $Z = 118$ at this time, see Chapter 17. Materials such as ^{238}U, $^{242,244}Pu$, ^{243}Am, ^{248}Cm, ^{249}Bk, and ^{249}Cf have been deposited at the cathode by molecular plating in the form of hydroxides on thin metal foils such as $\approx 2\,\mu m$ Ti mounted on supporting frames. In the heavy-ion beam, these targets are "baked in" by bombarding them for typically 10 minutes at a rather low beam intensity and by increasing the beam intensity every 10 minutes until the maximum tolerable beam intensity is reached. This way, the amorphous hydroxide deposits are transformed into an oxide layer. To cope with the heat load during bombardment, rotating target wheels have been used for some time, where the heated target spot is continuously rotated out of the beam and allowed to cool by heat radiation before it is again hit by the beam. The target wheel is mounted in a special box together with the target wheel drive and fiber glass optics for rotation speed control. Thus, the rotating target is confined in a nearly closed container in order to protect the beam line and the experimental apparatus against contamination by the highly radioactive target material. Such a cassette with the target wheel inside is used in the TransActinide Separator and Chemistry Apparatus (TASCA), a newly installed gas-filled separator at the GSI Helmholtz Center for Heavy-Ion Research. The target wheel consists of four individual target segments with 6 cm^2 area each, necessitating about 12 mg of target material to obtain average target thicknesses of 0.5 $mg\,cm^{-2}$. The wheel rotates at 2250 revolutions min^{-1} (rpm) and is synchronized with the beam macrostructure. Each beam pulse illuminates one single target, which subsequently cools during 75 ms before being hit again. Before entering the target wheel, the beam passes a carbon stripper foil wheel, which is mounted upstream of the target wheel and carries four 50 $\mu g\,cm^{-2}$ carbon foils. This foil serves to increase the charge state of the beam, which is beneficial for keeping the background due to primary beam in the TASCA focal plane minimal, even in the potential case when there are pin-holes in the target backing. The two wheels are driven by a common stepper motor. The position of the wheel is monitored by optical sensor technology

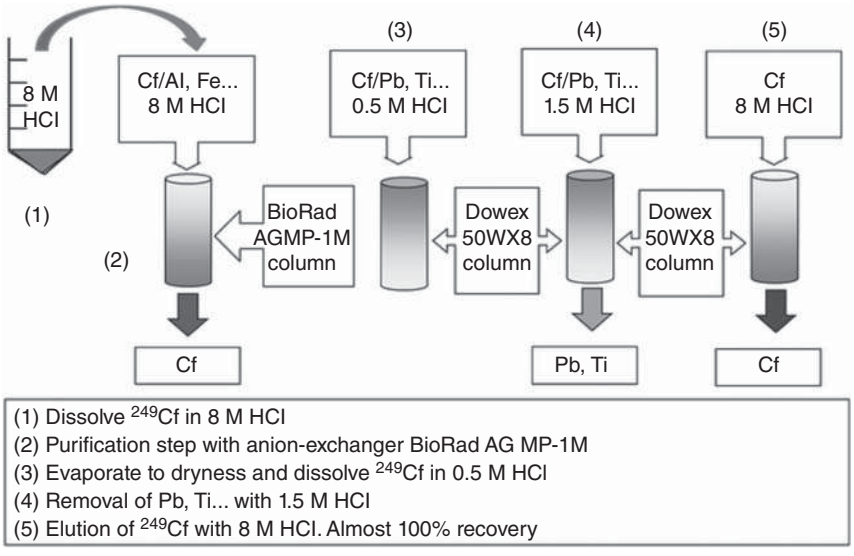

Figure 11.6 Example for the purification procedure of target materials. Source: Runke et al. (2014), figure 05 (p. 110)/Springer Nature.

(optical fiber sensors). The synchronization of the wheel with the UNILAC timing structure along with the necessary control of the stepper motor is performed using a PLC algorithm. If the system detects an asynchronous state, the beam is switched off within 1 ms.

The extremely precious target materials must be purified before they can be used for the production of new transactinide activities. The purification of, e.g. ^{249}Cf from used material is being performed by ion chromatography as illustrated in Figure 11.6. The ^{249}Cf is available in the form of the oxide, chloride, or nitrate and is dissolved in 8 M HCl. This solution is fed onto an anion-exchange column, Bio Rad AG MP-1 M, kept at a temperature of 55 °C for the first purification step. With 8 M HCl, ^{249}Cf is eluted from the column while impurities like Fe and Al remain on the anion-exchange column. The ^{249}Cf eluate is evaporated to dryness and redissolved in 0.5 M HCl. This solution is passed through a cation-exchange column, DOWEX 50 WX 8 ($T = 55$ °C). After a washing step with 1.5 M HCl to elute Pb and Ti, ^{249}Cf is eluted with 8 M HCl. After evaporation of the eluate, the ^{249}Cf chloride is converted into the nitrate by evaporation with 8 M HNO_3. The recovery yield over all purification steps was almost 100%.

For subsequent molecular plating (MP), aliquots of the purified actinide stock solution (typically in 8 M HNO_3) are evaporated to dryness in a Teflon beaker by means of a heating plate and an infrared lamp. The residue is dissolved in 100 µl 0.1 M HNO_3 and the solution is transferred to the plating cell. After washing the Teflon beaker three times with 1 ml isopropanol and transferring the solution into the plating cell, in the last step, 51 ml isobutanol are added. The plating cell consisted of polyether-etherketone (PEEK). On one side, the target backing, a thin (~2 µm) Ti-foil glued on an Al frame is mounted, and the Ti-foil acts as the cathode. As an

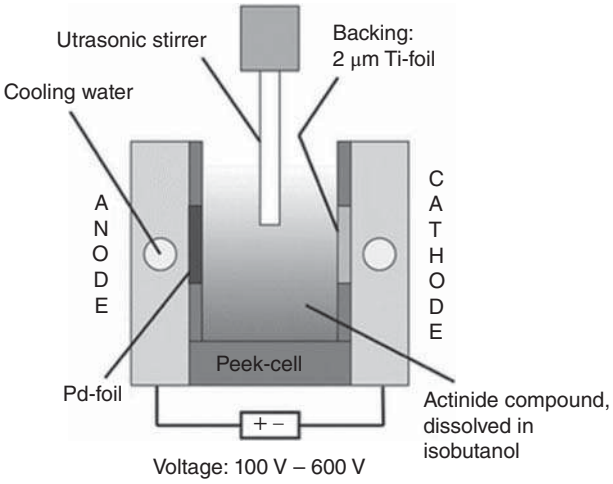

Figure 11.7 Plating cell for the molecular plating of actinide targets for the TASCA target wheel. Source: Runke et al. (2014), figure 06 (p. 110)/Springer Nature.

Table 11.2 Details of the plating procedures of various target materials. MP was performed at constant current resulting in a variable voltage.

Isotope	Solvent	Plating time (h)	Voltage (V)	Current density (mA cm^{-2})
^{243}Am	Isobutanol	6.0	150–200	0.2–0.3
^{244}Pu	Isobutanol	6.0	150–200	1.1
^{248}Cm	Isobutanol	3.0	150–300	0.7
^{249}Bk	Isobutanol	3–4	300–600	0.3
^{249}Cf	Isobutanol	4–5	300–600	0.2

anode, a Pd-foil in the same geometry as the target frame is used. The plating cell is clamped between two water cooled Ti blocks. For the mixing of the actinide solution, an ultrasonic stirrer is applied. Depending on the target material, current densities ranging from 0.3 to 1.1 mA cm^{-2} are used, resulting in voltages of 100–600 V. The plating time varies between three and six hours. A schematic of the setup for MP is shown in Figure 11.7. The details of the plating procedures are summarized in Table 11.2 and Figure 11.8.

The ^{249}Bk target segments mounted on the rotating target wheel are shown in Figure 11.9. The total weight of the ^{249}Bk targets is about 12 mg, corresponding to a ß $^{-}$ activity of $7 \cdot 10^{11}$ Bq. Handling activities of this order of magnitude requires particular care. Because in this special case, an enormous electrical charge is quickly deposited in the electrolyte, it is recommendable to connect it to ground.

Subsequent to the molecular plating, the target thickness is determined indirectly by neutron activation analysis (Section 20.3) by measuring the residual concentration of the actinide element in the electrolyte solution. An aliquot of 1 ml is transferred into a PE tube for the irradiation. A standard sample of the

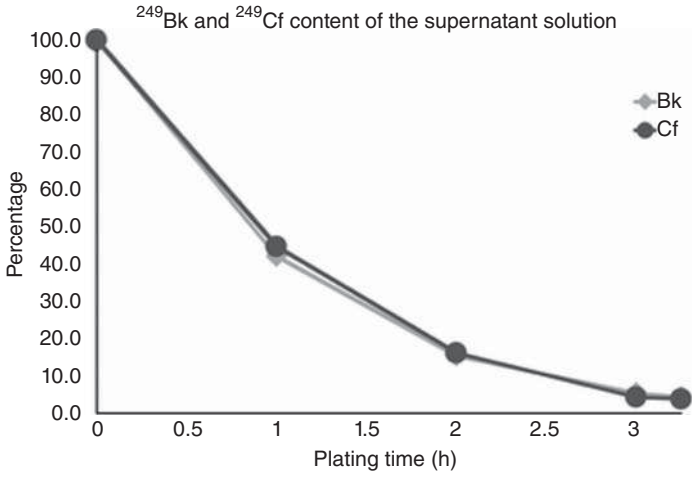

Figure 11.8 Measurement of the ^{249}Bk and ^{249}Cf activities in solution during MP. Source: Runke et al. (2014), figure 07 (p. 110)/Springer Nature.

Figure 11.9 Target wheel with four segments carrying each ≈500 μg cm^{-2} of ^{249}Bk deposited by molecular plating on ≈2 μm Ti-backings. Source: Runke et al. (2014), figure 08 (p. 110)/Springer Nature.

same actinide is irradiated together with the samples in order to be independent of possible variations in the neutron flux. Prior to the determination of the residual actinide concentration in the electrolyte by γ-ray spectroscopy, the samples are allowed to cool down with respect to short-lived interfering activities. The surface morphology of the deposited layers is investigated by scanning electron microscopy (SEM). In addition, energy dispersive X-ray spectrometry (EDS) gives information about the chemical composition of the deposited layer. This yields the information that the actinide is not deposited in the form of its nitrate in which it was present in the electrolyte, but as the hydroxide. The target thickness is also controlled by α-particle spectroscopy. The shift of the spectral line to lower energies when a foil is interposed between source and detector is a measure of the average foil thickness over the area of the beam.

Other methods include weighing an accurately measured area, which is often the method of choice for self-supporting targets. It can also be supplied to backed targets

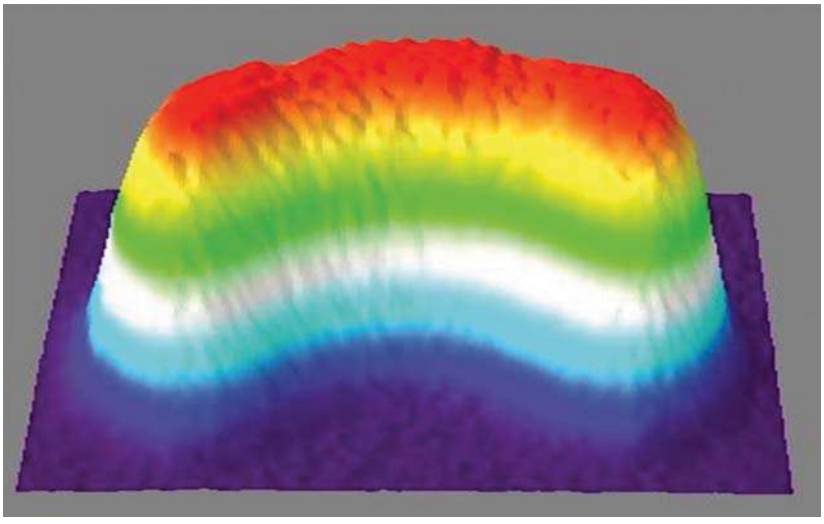

Figure 11.10 Photo-stimulated luminescence picture of an actinide target for the TASCA target wheel. Source: Courtesy K. Eberhardt.

if the backing material is weighed separately before target deposition and if the ratio of target weight to backing weight is not too small. In experiments performed in external beams with particle detectors, it is sometimes practical to determine target thicknesses by means of Rutherford scattering, see Section 20.12. This requires measurement of both the primary beam and scattered beam intensities and accurate knowledge of the beam energy and scattering angle. This can be used, by the way, as a very useful on-line monitoring of the target integrity during the course of an experiment. Occasionally, it may be practical to determine the target thickness after an irradiation. This may be done by dissolving the target and analyzing the solution for the target material.

Radiographic imaging (RI) can provide important information about the homogeneity and the thickness of radioactive targets on thin backings. The FLA7000 apparatus from FUJIFILM Corporation uses reusable imaging plates (IPs). Different IPs are available for β and γ emitters and for α emitters. The IP consists of crystallites with sizes of 25 or 50 μm which will be excited into a stable excited state by radiation. During the reading process by a 650 nm laser, the amount of emerging luminescence light is graded into grayscale levels which are converted to the arbitrary unit photo-stimulated luminescence (PSL). Figure 11.10 shows the PSL picture of an actinide target; it is seen that this target is acceptably homogeneous.

11.3 Measuring Beam Intensity and Fluxes

A measure of the yield of a radionuclide produced in a nuclear reaction induced by charged particles is the cross section, σ (cm^2), given as

$$\sigma = \frac{A}{N\phi(1 - e^{-\lambda t})} \tag{11.5}$$

where N is the number of target atoms per square centimeter, ϕ is the projectile flux (s^{-1}), λ is the decay constant (s^{-1}), and A is the produced activity (s^{-1}). Thus, to determine a cross section, we need to measure the projectile beam intensity. The most common technique for measuring the intensity of a charged particle beam is through the use of a Faraday cup. The beam is stopped in an electrically isolated section of beam pipe, Figure 11.11, and the collected charge is measured with a current integrator. The beam intensity is the current divided by the charge on each ion. As the beam will liberate secondary electrons in the material in which it stops, care must be taken regarding the loss of these secondary electrons from the Faraday cup. If these electrons escape, their positive ion partners will add to the positive charges of the stopped beam particles causing an overestimate of the beam current. Therefore, the Faraday cup is made as a long cylinder to inhibit electron escape geometrically, and a magnetic field produced by permanent magnets surrounding the cylinder is applied to the cup along with a suppressing high voltage (−1.5 kV) to further prevent electron loss.

When the energy of the beam is too large to be stopped in a Faraday cup, the beam intensity is monitored by a secondary ionization chamber having thin entrance and exit windows. They measure the energy loss when the beam traverses them, and they must be calibrated to give absolute beam intensities. If the beam intensity is less than 10^6 particles s^{-1}, individual particles can be counted, for example, in a plastic scintillator detector.

When performing irradiations with neutrons, the flux (ϕ in Eq. (11.5) is given in neutrons cm^{-2} s^{-1} and N is the total number of target atoms) is measured using a monitor reaction. A thin foil of a pure element, most commonly a gold foil, is placed in the irradiating flux near the target and irradiated simultaneously with the target. Then both the reaction products from the target and in the monitor foil are counted by γ-ray spectroscopy using a Ge detector. The flux is calculated using the known

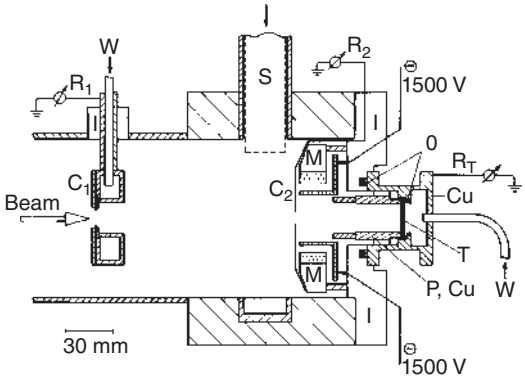

Figure 11.11 Faraday cup for high-intensity bombardments of water-cooled production targets or beam dumps at the UNILAC accelerator: C_1 and C_2, circular beam collimators; Cu, copper parts; I, insulator; W, deionized cooling water; M, magnet (magnetic field 1 kG); O, O-ring; P, screw cylinder pressing the target, T, into the copper holder; R, current readings; S, slider valve. The space between S and T can be evacuated or ventilated separately. Source: Schädel et al. (1978), figure 03 (p. 75)/De Gruyter.

cross section for the monitor reaction. Given the fact that the target and the monitor foil have been exposed to the same flux, we have for the activity of the reaction products from the target and in the monitor foil, A_{target} and A_{monitor}, respectively, at the end of the irradiation

$$A_{\text{target}} = N_{\text{t}}\sigma_{\text{t}}\phi(1 - \text{e}^{-\lambda_{\text{t}}t})$$
$$A_{\text{monitor}} = N_{\text{m}}\sigma_{\text{m}}\phi(1 - \text{e}^{-\lambda_{\text{m}}t})$$

where the cross section for the reaction of interest, substituting ϕ in terms of the monitor reaction, is

$$\sigma_{\text{t}} = \frac{A_{\text{target}}}{A_{\text{monitor}}} \cdot \frac{N_{\text{t}}}{N_{\text{m}}} \cdot \frac{(1 - \text{e}^{-\lambda_{\text{m}}t})}{(1 - \text{e}^{-\lambda_{\text{t}}t})} \cdot \sigma_{\text{m}}$$

The same procedure is applicable for high-energy protons. Here typical monitor reactions are $^{27}\text{Al} \rightarrow {}^{24}\text{Na}$, $^{27}\text{Al} \rightarrow {}^{22}\text{Na}$, $^{27}\text{Al} \rightarrow {}^{18}\text{F}$, $^{12}\text{C} \rightarrow {}^{7}\text{Be}$, where the arrows indicate a complex reaction path. The loss of recoils from the monitor or target foils can be corrected for by irradiating a stack of three identical foils and only counting the center foil.

The measurement of neutron fluxes by foil activation is more complicated because the monitor cross sections are energy dependent. The simplest case is monitoring thermal neutron fluxes. Thermal neutron activation monitors with odd-A isotopes with large thermal (n, γ) cross sections are selected. The (n, γ) activation cross sections vary as $1/\upsilon$, although some nuclides have resonances in the capture cross sections for neutrons with energies between 1 and 1000 eV. A correction for resonance capture can be made by irradiating the monitor foils with and without a Cd cover. The (n, γ) cross section for Cd below 0.4 eV is very large and is small for energies above this. Thus, very few low-energy neutrons will penetrate the Cd. Irradiation of the foil without the Cd cover will cause reactions with thermal neutrons and resonance neutrons, while the Cd-covered monitor foil will just respond to resonance neutrons. So-called threshold monitor foils where the activating reaction has an energy threshold such as (n, p), (n, α), and (n, 2n) reactions are also in use. By irradiating a set of threshold monitor foils with different thresholds with neutrons, one can determine the relative amounts of different energy groups in the neutron energy spectrum. Details can be found in Knoll (2000) and Tsoufanidis (1995).

11.4 Neutron Spectrum in Nuclear Reactors

As we briefly indicated in the preceding section, the neutron spectrum from a nuclear reactor is typically divided into two components: a thermalized flux with a Maxwell–Boltzmann energy distribution and an epithermal flux whose energy distribution is proportional to the reciprocal neutron energy, $1/E_{\text{n}}$.

11.4.1 Thermal Neutrons

In most nuclear reactors, neutrons that are in thermal equilibrium with the moderator, at room temperature, have by far the highest flux. The velocity of

thermal neutrons exhibits a Maxwell distribution where the number of neutrons having a velocity between υ and $\upsilon + \mathrm{d}\upsilon$ is expressed in terms of the total number of neutrons, temperature, and velocity. Neutron density per unit velocity is given by

$$\frac{\mathrm{d}n}{\mathrm{d}\upsilon} = 4\pi\left(\frac{m}{2\pi kT}\right)^{3/2}\upsilon^2 \exp\left(-\frac{m\upsilon^2}{2kT}\right) \tag{11.6}$$

where m is the neutron mass, T is the absolute temperature, k is the Boltzmann's constant, and n is the total number of neutrons per unit volume, obtained by summing $\mathrm{d}n$ over all possible velocities between zero and infinity

$$n = \int_{\upsilon=0}^{\upsilon=\infty} \mathrm{d}n(\upsilon) \tag{11.7}$$

The most probable velocity, υ_{mp}, corresponding to the maximum of the probability curve determined from the condition $\mathrm{d}n/\mathrm{d}\upsilon = 0$, is $(2kT/m)^{1/2}$. At room temperature, 293.6 K, the most probable velocity is 2200 m s^{-1}, corresponding to a kinetic energy of 0.025 eV and a wavelength of $1.8 \cdot 10^{-10}$ m. By substituting υ_{mp}^2 for $(2kT/m)$, Eq. (11.6) can be rewritten as

$$\frac{\mathrm{d}n}{\mathrm{d}\upsilon} = \frac{4}{\sqrt{\pi}}\frac{\upsilon^2}{\upsilon_{\mathrm{mp}}^3}\exp\left(-\frac{\upsilon^2}{\upsilon_{\mathrm{mp}}^2}\right) \tag{11.8}$$

Tables of thermal cross sections typically contain values for monoenergetic neutrons of 0.025 eV rather than cross sections averaged over the whole Maxwell distribution. In practice, however, thermal cross sections are measured not for a single velocity, but for the entire Maxwell distribution. For calculations of production rates of radionuclides in nuclear reactors, however, the monoenergetic neutron flux (ϕ_0) at 0.025 eV is most useful.

The velocity distribution given by Eqs. (11.6) and (11.8) can be converted to an energy distribution by replacing υ and $\mathrm{d}\upsilon$ by E and $\mathrm{d}E$, using the relationship $E = m\upsilon^2/2$. Thus, the neutron density per unit energy is

$$\frac{\mathrm{d}n}{\mathrm{d}E} = 2\pi n\left(\frac{1}{\pi kT}\right)^{3/2}\exp\left(-\frac{E}{kT}\right)\sqrt{E} \tag{11.9}$$

The most probable energy, E_{mp}, at room temperature is $E_{\mathrm{mp}} = 0.0126$ eV. The energy-dependent thermal neutron flux can be obtained by substituting $n(E)$ from Eq. (11.9) in the following equation:

$$\begin{aligned}\phi_{\mathrm{th}}(E) &= \frac{\mathrm{d}n(E)}{\mathrm{d}E}\frac{\mathrm{d}\upsilon(E)}{\mathrm{d}E} \\ &= n(E)\upsilon(E) \\ &= \frac{2\pi n}{(\pi kT)^{3/2}}\left(\frac{2}{m}\right)^{1/2}\exp\left(-\frac{E}{kT}\right)\end{aligned} \tag{11.10}$$

where m is the neutron mass and $\upsilon(E) = (2E/m)^{1/2}$. The one-group thermal flux, ϕ_{th}, is then given by

$$\phi_{\mathrm{th}} = \int_{\mathrm{th}} \phi_{\mathrm{th}}(E)\mathrm{d}E \tag{11.11}$$

where the integration is done over the "thermal range," defined to be from 0 to 5 times kT ($5kT = 0.1$ eV). Eq. (11.10) decreases to very small values above $5kT$ so that the integration can be taken to infinity as well, and by combining Eqs. (11.10) and (11.11) one obtains

$$\phi_{\text{th}}(E) = \frac{2\pi n}{(\pi kT)^{3/2}}\left(\frac{2}{m}\right)^{1/2}\int_0^{\infty}\exp\left(-\frac{E}{kT}\right)\mathrm{d}E = \frac{2n}{\sqrt{\pi}}\left(\frac{2kT}{m}\right)^{1/2} \tag{11.12}$$

If E_T is the neutron energy corresponding to kT, and υ_T is the associated velocity, $E_T = kT = m\upsilon_T^2/2$, and the numerical values of E_T and υ_T are $8.617\,T \cdot 10^{-5}$ eV and $1.284\,T \cdot 10^4$ cm s^{-1}, respectively. Now, from Eq. (11.12), one can deduce the useful relations between $\boldsymbol{\Phi}_{\text{th}}$ and $\boldsymbol{\Phi}_0$

$$\frac{\phi_{\text{th}}}{\phi_0} = \frac{2}{\sqrt{\pi}}\left(\frac{\upsilon_T}{\upsilon_0}\right) = \frac{2}{\sqrt{\pi}}\left(\frac{T}{T_0}\right)^{1/2} \tag{11.13}$$

which depends on the temperature. If $T = T_0$, this ratio is $2\pi^{-1/2} = 1.128$, that is, $\boldsymbol{\Phi}_{\text{th}}$ will exceed the monoenergetic $\boldsymbol{\Phi}_0$ by 12.8%.

11.4.2 Epithermal Neutrons and Resonances

Epithermal neutrons are distinguished from thermal neutrons as many neutron resonances (Section 12.7.2, Figure 12.18) are observed in the epithermal region. It is generally assumed that the thermal neutron flux goes to zero when the neutron energy is above $5kT$. In fact, due to the exponential decrease of the Maxwellian function, only 1.7% of the Maxwellian neutrons are more energetic than $5kT$. In practice, an effective cutoff determined by the neutron spectrum transmitted through a cadmium filter is used, see above. The epithermal flux is to a good approximation proportional to $1/E$ for moderators containing hydrogen, for example, H_2O, from 1 to 2 MeV, the average neutron energies from fission, down to 1 eV. The cutoff, however, is not sharp and depends on the thickness of the cadmium absorber. For infinitely dilute or very small samples, the so-called resonance integrals are given by Stoughton and Halperin (1959) as

$$I = \int \sigma\left(E\frac{\mathrm{d}E}{E}\right) \tag{11.14}$$

where the integration is usually taken from $5kT$ or E_{Cd} (the effective cadmium cutoff) to ≈1 MeV. The lower limit is rather important while the upper limit is not. Thus,

$$I_0 = \int_{E_{\text{Cd}}}^{1\text{ MeV}}\frac{\sigma(E)}{E}\mathrm{d}E \quad \text{and} \quad I_0' = \int_{5kT}^{1\text{ MeV}}\frac{\sigma(E)}{E}\mathrm{d}E \tag{11.15}$$

These integrals are called the infinitely dilute resonance integrals, the difference depending on the lower limit of integration. In Eq. (11.15), it is assumed that the resonance flux varies as $1/E$ down to $5kT$ and vanishes below this energy. Values of these resonance integrals can be computed by putting values of $\sigma(E)$, obtained from the Breit–Wigner formula (Section 12.7.2), into Eq. (11.15) and carrying out the integration from E_{Cd} (or $5kT$) to infinity over a particular resonance. Further

simplifications can be made by letting $E = E_r$ and then integrating from zero to infinity. The resultant value

$$I_0 \approx I_0' \approx \frac{\pi \sigma_{r\gamma} \Gamma}{2E_r} \tag{11.16}$$

provides a reasonable approximation of the integral under the $\sigma_\gamma(E)$ vs. $\ln E$ curve at and near a particular resonance "r." In Eq. (11.16), $\sigma_{r\gamma}$ is the maximum value of the radiative capture cross section at a particular resonance energy E_r and Γ is the width of the resonance at half maximum. The contributions to I_0 from all known resonances must be added to obtain the resonance integral.

11.4.3 Reaction Rates in Thermal Reactors

In a reactor, both neutron flux and cross section are functions of neutron energy. The general equation describing the reaction rate is given by

$$R = \int \frac{\mathrm{d}(\phi\sigma)}{\mathrm{d}E} \mathrm{d}E \tag{11.17}$$

The two-group theory discussed above suggests dividing Eq. (11.17) into the contributions from thermal and epithermal neutrons:

$$R = \int_0^{5kT} \frac{\mathrm{d}(\phi\sigma)}{\mathrm{d}E} \mathrm{d}E + \int_{5kT}^{\infty} \frac{\mathrm{d}(\phi\sigma)}{\mathrm{d}E} \mathrm{d}E \tag{11.18}$$

11.5 Production of Radionuclides

11.5.1 Production in Nuclear Reactors

Many radionuclides used in science and technology are produced in nuclear reactors because neutrons are available with high flux densities $\Phi \approx 10^{10}$ to 10^{15} cm^{-2} s^{-1} and because the cross sections of (n, γ) reactions are relatively high. In general, research reactors are applied for the production of radionuclides because they are mostly equipped with special installations for that purpose. Power reactors may also be used, preferably for the production of greater amounts of long-lived radionuclides, such as ^{60}Co as a radiation source. Larger reactors offer more space for introducing a greater number of samples without affecting the neutron flux too much. As the activity increases with Φ, high neutron flux densities are required for the production of high activities, particularly in the case of long-lived radionuclides.

The samples used for irradiation must withstand the temperature and the radiation in the reactor without decomposition. In general, they are encapsulated in aluminum cans or in quartz ampoules which are introduced in irradiation tubes or directly into special positions within the reactor core.

Some research reactors are equipped with a so-called thermal column of about 1 m × 1 m × 1 m, consisting of blocks of graphite and installed near the reactor core. Due to the moderator properties of graphite, only thermal neutrons are present in such a column.

Fast pneumatic transport systems are needed for the investigation of short-lived radionuclides. They can be operated over distances of several meters and the samples can be brought, within 0.1 to 1 seconds, directly from the place of irradiation to the counter.

A survey of neutron-induced reactions used for the production of radionuclides is given in Table 11.2; (n, γ) reactions are preferably induced by thermal neutrons giving isotopic products of limited specific activity.

As an example, irradiation of 1 g NaCl at a thermal neutron flux density $\Phi = 10^{13}\ \mathrm{cm^{-2}\ s^{-1}}$ may be considered:

$$\begin{aligned}
&^{23}\mathrm{Na(n,\gamma)^{24}Na} \quad (\sigma = 0.53\ \mathrm{b};\ t_{1/2} = 14.96\ \mathrm{hours})\\
&^{35}\mathrm{Cl(n,\gamma)^{36}Cl} \quad (\sigma = 0.43\ \mathrm{b};\ t_{1/2} = 3.0{\cdot}10^{5}\ \mathrm{years})\\
&^{35}\mathrm{Cl(n,\gamma)^{35}Cl} \quad (\sigma = 0.49\ \mathrm{b};\ t_{1/2} = 87.5\ \mathrm{days})\\
&^{37}\mathrm{Cl(n,\gamma)^{38}Cl} \quad (\sigma = 0.43\ \mathrm{b};\ t_{1/2} = 37.10\ \mathrm{minutes})
\end{aligned} \tag{11.19}$$

The activities obtained after an irradiation time of 24 hours are $3.7 \cdot 10^{10}$ Bq ^{24}Na ($2.2 \cdot 10^{12}\ \mathrm{Bq\,mol^{-1}}$), $2.1 \cdot 10^{4}$ Bq ^{36}Cl ($1.2 \cdot 10^{6}\ \mathrm{Bq\,mol^{-1}}$), $1.1 \cdot 10^{10}$ Bq ^{38}Cl ($6.4 \cdot 10^{10}\ \mathrm{Bq\,mol^{-1}}$), and $3.0 \cdot 10^{8}$ Bq ^{35}S. The activities as well as the specific activities increase with the neutron flux density and the irradiation time. Whether the specific activity is sufficient or not depends on the purpose for which the radionuclides are used. For medical applications, high specific activities are mostly required. The specific activity of ^{35}S depends on the presence of sulfur impurities in the sample. In general, the specific activity of non-isotopic products is high, provided that no carrier is added.

With respect to high specific activity, (n, γ) reactions followed by relatively quick β^- decay are favorable. This is illustrated by the production of ^{131}I by neutron irradiation of Te. The following reactions have to be considered:

$$\begin{aligned}
&^{130}\mathrm{Te(n,\gamma)^{131m}Te} \xrightarrow{\mathrm{IT,30\ hours}} {}^{131}\mathrm{Te} \xrightarrow{\beta^-,\gamma,\mathrm{25\ minutes}} {}^{131}\mathrm{I} \xrightarrow{\beta^-,\gamma,\mathrm{8.02\ days}}\\
&(H = 0.338)\\
&^{128}\mathrm{Te(n,\gamma)^{129m}Te} \xrightarrow{\mathrm{IT,33.6\ days}} {}^{129}\mathrm{Te} \xrightarrow{\beta^-,\gamma,\mathrm{69.6\ minutes}} {}^{129}\mathrm{I} \xrightarrow{\beta^-,\gamma,1.57\cdot10^{7}\ \mathrm{years}}\\
&(H = 0.317)\\
&^{126}\mathrm{Te(n,\gamma)^{127m}Te} \xrightarrow{\mathrm{IT,109\ days}} {}^{127}\mathrm{Te} \xrightarrow{\beta^-,\mathrm{9.35\ hours}} {}^{127}\mathrm{I\ (stable)}\\
&(H = 0.189)
\end{aligned} \tag{11.20}$$

The (n, γ) reactions lead partly to the isomeric states and partly to the ground states, and the isomeric states change partly first into the ground states and partly directly to the daughter nuclides. From Eq. (11.20) it follows that after irradiation a decay time of several days is favorable in order to increase the yield of ^{131}I. Longer decay times are unfavorable because of the decay of ^{131}I and the formation of increasing amounts of ^{129}I. In general, I is separated from Te by distillation. More recently, ^{125}I has gained increased importance. Reactor production of ^{125}I involves neutron irradiation of ^{124}Xe followed by post-irradiation decay time to allow the 16.9 hours ^{125}Xe to decay to 59.4 days ^{125}I. The latter

decays by 100% electron capture to the first excited state of ^{125}Te (35.5 keV, 1.49 ns). Deexcitation from this level to the ground state of stable ^{125}Te is highly converted. The 35.5 keV emission is just above the 33.2 keV K absorption edge of iodine. The energy averaged over all photons (X- and γ-rays) in the decay of ^{125}I is 26.4 keV. ^{125}I is now widely used as a tracer in biology and medicine. Current applications include biodistribution studies of ^{125}I-labeled drugs, peptides, and antibodies, and the use of ^{125}I-labeled nucleic acid precursors in cell-targeted therapeutics. In this case, the radiotoxicity is due to the fact that the decay of ^{125}I is followed by a shower of short-range secondary electrons of only a few hundred electronvolts and 1 μm path length in tissue. Thus, a significant fraction of the decay energy is deposited in microscopic volumes in the vicinity of DNA, leading to multiple strand breaks. Such molecular lesions have been shown to have profound biological consequences. Recently, permanent implants into the prostate with ^{125}I seeds have become increasingly popular. Typical implant seeds (1 mCi of ^{125}I per seed) are designed to deliver a dose of 160 Gy during the full decay.

Szilard–Chalmers reactions may also be applied to obtain radionuclides of high specific activity after (n, γ) reactions (Section 13.6).

Some radionuclides can be produced by (n, p) and (n, α) reactions with thermal neutrons, for example,

$$^{3}\mathrm{He(n,p)}^{3}\mathrm{H} \quad (\sigma = 5327\ \text{barn}; \quad t_{1/2} = 12.323\ \text{years}) \tag{11.21}$$

$$^{14}\mathrm{N(n,p)}^{14}\mathrm{C} \quad (\sigma = 1.81\ \text{barn}; \quad t_{1/2} = 5730\ \text{years}) \tag{11.22}$$

$$^{6}\mathrm{Li(n,\alpha)}^{3}\mathrm{H} \quad (\sigma = 940\ \text{barn}; \quad t_{1/2} = 12.323\ \text{years}) \tag{11.23}$$

$$^{40}\mathrm{Ca(n,\alpha)}^{37}\mathrm{Ar} \quad (\sigma = 0.0025\ \text{barn}; \quad t_{1/2} = 35.0\ \text{days}) \tag{11.24}$$

As the product nuclides are non-isotopic, their separation from the target nuclides does not cause problems. Production of ^{14}C according to (11.22) is of great practical interest. The long half-life of ^{14}C requires a long irradiation time (≥1 year) to obtain sufficient yield. Therefore, the nitrogen compound used as target must be heat and radiation resistant. Nitrides, such as AlN or Be_3N_2, are most suitable. After irradiation, they are heated in a stream of oxygen; ^{14}C escapes as $^{14}CO_2$ and is bound by $Ba(OH)_2$ as $Ba^{14}CO_3$. The specific activity is of the order of 2 GBq mmol^{-1} (2.3 GBq mmol^{-1} if free from impurities and up to 1.6 GBq mmol^{-1} in practice). Because of the long irradiation time, $Ba^{14}CO_3$ is rather expensive (about US$10 000 per gram). $Ba^{14}CO_3$ and $^{14}CO_2$, respectively, are used for the preparation of a great variety of ^{14}C-labeled organic compounds by chemical or biochemical methods. Short synthetic routes and high yields are preferred to keep the losses as small as possible.

Tritium is produced on a large scale according to (11.23) by irradiation of Li or its compounds in nuclear reactors. Due to the high cross section of this reaction and the relatively short half-life of *T* compared to that of ^{14}C, the yield is relatively high and the costs of T production are relatively low. *T* is obtained as a gas containing about 90% *T* and can be oxidized to tritiated water (T_2O) for further use; 1 Ci ($3.7 \cdot 10^{10}$ Bq)

Table 11.3 Parameters of the produced targets.

Isotope	Target area (cm^2)	Target thicknesses ($\mu g\ cm^{-2}$)	Deposition yield (%)
^{243}Am	6.00	534 ± 27–824 ± 41	79–99
^{244}Pu	1.44	390 ± 20–790 ± 40	79–96
^{248}Cm	2.90	371 ± 19–465 ± 23	91–100
^{249}Cf	6.00	454 ± 23–537 ± 27	88–97
^{249}Bk	6.00	354 ± 18–508 ± 25	88–96

of T is about 0.104 mg and as T_2 gas it has a volume of 0.38 cm^3 under normal temperature and pressure. T is mainly used for controlled thermonuclear fusion experiments. It has also been produced for application in nuclear weapons (Section 15.11). Relatively small amounts of T are used for labeling of organic compounds.

Pulsed research reactors, such as reactors of the TRIGA type, are especially designed for production and investigation of short-lived radionuclides. In these reactors, the neutron flux is increased for about 30 ms to about $10^{15}\ cm^{-2}\ s^{-1}$ by taking out the pulse rod (Section 15.5). Due to the prompt negative temperature coefficient of the zirconium–uranium–hydride fuel elements, the outburst of power causes a sudden temperature increase to about 300 °C where the fission neutrons are no longer thermalized and the chain reaction is stopped automatically. After about 10 minutes, the fuel moderator elements have cooled down to room temperature and a new pulse can be started. The activities of radionuclides of various half-lives obtained with pulsed reactors are compared in Table 11.3 to those produced at constant neutron flux densities. The table shows that pulsed reactors are useful for the production and investigation of radionuclides with half-lives below 10 seconds.

A great number of radionuclides are produced in nuclear reactors by fission. Some of these fission products may be separated for practical applications. For this purpose, either special separation procedures may be included in the course of reprocessing or samples of enriched uranium may be irradiated in nuclear reactors and reprocessed separately with the aim of isolating the desired radionuclides. The main problems with fission products are the high activities to be handled, and the fact that their application requires careful purification procedures to reach acceptable radionuclide purity. Long-lived radioactive impurities, in particular actinides, have to be separated effectively. Radionuclide purity is of special importance in the case of medical applications, for example, the application of fission ^{99}Mo in radionuclide generators.

Reactions with fast neutrons, such as (n, 2n), (n, p), and (n, α) reactions, are only of minor importance for the production of radionuclides in nuclear reactors. However, special measures may be taken for irradiation of samples with high-energy neutrons. For instance, the samples may be irradiated in special fuel elements of ring-like cross section as shown in Figure 11.12, or they may be irradiated in a receptacle made of enriched uranium. In both cases, the fast neutrons originating from the fission of

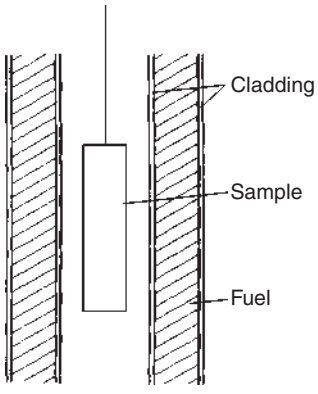

Figure 11.12 Irradiation in a ring-like fuel element.

^{235}U enter the samples directly and their flux density is higher by about 1 order of magnitude than that at other places in the reactor.

Another possibility is the generation of fast neutrons by mixing the sample with LiD or introducing LiD together with the sample into the reactor. Fast neutrons with energies of about 14 MeV are produced in LiD by the successive reactions ^{6}Li(n, α)t and d(t, n)α. The flux density of 14 MeV neutrons is smaller by a factor of about 10^4 than that of thermal neutrons.

If activation by epithermal or fast neutrons is to be favored over activation by thermal neutrons, the flux of thermal neutrons can be suppressed by wrapping the samples in foils of cadmium, which has a high neutron absorption cross section for thermal neutrons ($\sigma_a = 2520$ barn). This possibility is also used in activation analysis.

The high intensity of γ radiation in nuclear reactors may be reduced by shielding the samples with Pb or Bi. The absorption coefficients of these metals are μ_γ (Pb) = 0.8 cm^{-1} and μ_γ (Bi) = 0.7 cm^{-1} for 1 MeV γ-rays and μ_n (Pb) = $0.56 \cdot 10^{-2}$ cm^{-1} and μ_n (Bi) = $0.93 \cdot 10^{-3}$ cm^{-1} for thermal neutrons. By application of 2 cm Pb or Bi, the intensity of γ radiation can be reduced by a factor of about 5 and 4, respectively, whereas the neutron flux is not markedly diminished. Table 11.4 lists examples of reactor-produced radionuclides important to nuclear medicine. It gives the production reaction, the cross section for thermal neutrons, as well as the resonance integral for epithermal neutrons defined by Eq. (11.14). The most relevant examples in Table 11.4 are

- ^{99}Mo produced preferentially by fission.
- ^{131}I produced by fission and neutron capture reactions followed by β^- decay.
- ^{114m}In produced by neutron capture reactions.
- ^{177}Lu produced by neutron capture reactions.
- ^{125}I produced by neutron capture followed by β^- decay.
- ^{188}W produced by double neutron capture.
- ^{117m}Sn produced by neutron inelastic scattering.
- ^{67}Cu produced by fast neutron-induced reactions.

For fabrication of ^{99}Mo/^{99m}Tc generators, the principal issue that differentiates fission-produced ^{99}Mo from the neutron capture route is specific activity.

Table 11.4 Neutron-induced reactions in nuclear reactors (survey).

Reaction	Decay modes of the products	Remarks
(n, γ)	Predominantly β^-; rarely β^+ or ε	Generally applicable; high yields with thermal neutrons
(n, 2n)	Predominantly β^+; sometimes β^-	Strongly endoergic; high-energy neutrons (>10 MeV) required
(n, p)	Nearly always β^-	Mostly endoergic (exceptions: ^{14}N(n, p)^{14}N, ^{35}Cl(n, p) ^{35}S, and some others); frequently at small mass numbers ($A < 40$)
(n, α)	Predominantly β^-	Mostly endoergic (exceptions ^{6}Li(n, α)^{3}H and ^{10}B(n, α)^{7}Li); predominantly at small mass numbers
(n, f)	Fission with thermal neutrons: always β^-; fission with high-energy neutrons: also β^+ or ε	Nuclides with atomic numbers $A > 90$; fission of ^{233}U, ^{235}U, and ^{239}Pu with thermal neutrons

Commercial manufacturers of ^{99}Mo/^{99m}Tc generators require a specific activity of 37–74 GBq mg^{-1}. Fission-produced ^{99}Mo has a specific activity of $2.6 \cdot 10^3$ GBq mg^{-1}, whereas the specific activity of neutron capture produced ^{99}Mo, even in the highest available neutron flux, is approximately 1.9–3.7 GBq mg^{-1}, 10–20 times lower than required for the traditional single-stage generator system. In the most widely used generator, ^{99}Mo is loaded onto a column of alumina and ^{99m}Tc is eluted from the column with normal saline. The radioactive isotopes of iodine have played a major role in nuclear medicine and in the radioiodination of various biological molecules. Three isotopes that are in common use are ^{125}I, ^{131}I, and ^{123}I. Two other isotopes, ^{122}I and ^{124}I, both positron emitters, are also of interest as sources for positron emission tomography (PET). ^{114m}In is a potential radionuclide for radioimmunotherapy and a potential source for brachytherapy. ^{177}Lu attached to biological targeting molecules such as tumor-associated antibodies and peptides is under active investigation for radioimmunotherapy. ^{188}W produced by double neutron capture in highly enriched ^{186}W decays by β^- decay with a half-life of 69.78 days into ^{188}Re which is used for various medical applications. The convenient half-life of 17 hours and 100% β^- emission with high energies make ^{188}Re an attractive candidate for radiotherapy of tumors. ^{117m}Sn has been used in clinical trials for the palliation of pain caused by breast and prostate cancer metastasized to bone. Finally, ^{67}Cu is of interest in exploring its therapeutic applications (Tables 11.5 and 11.6).

11.5.2 Production by Accelerators

The various types of accelerators offer the possibility of applying a great variety of projectiles of different energies. The most frequently used projectiles are protons, deuterons, and α particles. Some features of the reactions induced by these particles

Table 11.5 Activities of radionuclides of various half-lives obtained in pulsed reactors of the TRIGA type compared to those obtained at constant flux densities (activities in MBq g^{-1} for $\sigma_{n,\gamma} = 1$ barn, $H = 1$ and $M = 100$).

Half-life	Pulsed reactor	Activities at constant neutron flux (saturation activity)		
	($\Phi_{max} = 10^{16}$ cm^{-2} s^{-1}; 10 ms)	$\Phi = 10^{11}$ cm^{-2} s^{-1}	$\Phi = 10^{12}$ cm^{-2} s^{-1}	$\Phi = 10^{13}$ cm^{-2} s^{-1}
0.01 s	$3.0 \cdot 10^7$			
0.1 s	$4.0 \cdot 10^6$			
1 s	$4.2 \cdot 10^5$			
10 s	$4.2 \cdot 10^4$			
1 min	$7.0 \cdot 10^3$	$6.0 \cdot 10^2$	$6.0 \cdot 10^3$	$6.0 \cdot 10^4$

are summarized in Table 11.7. Neutrons may be produced indirectly by nuclear reactions, γ-rays are generated as bremsstrahlung in electron accelerators, and heavy ions are available in heavy-ion accelerators. Deuterons are often preferred as projectiles because of the relatively high cross sections obtained with them. Some examples of radionuclides produced by d-induced reactions are listed in Table 11.8.

Several positron emitters are of practical importance in nuclear medicine for PET. Some are listed in Table 11.9. Protons or deuterons with energies varying between about 4 and 40 MeV are produced at small cyclotrons. The smallest machine is a baby cyclotron that accelerates deuterons only up to 4 MeV. It is used exclusively in hospitals to produce ^{15}O. The next level of accelerator is a single-particle negative ion machine for production of ≤11 MeV protons. It can produce the four major β^+ emitters, namely, ^{11}C, ^{13}N, ^{15}O, and ^{18}F, although the absence of a deuteron beam is disadvantageous for the production of ^{15}O and gives a low yield for ^{13}N. The next higher level of cyclotrons are two-particle machines with proton beam energies ≤20 MeV and deuteron beam energies ≤10 MeV. These are ideally suited for the production of the commonly used PET radionuclides. Even higher energy machines (≤40 MeV) often make available, besides p and d, also ^{3}He and ^{4}He beams. These offer the possibility to produce many more radionuclides such as ^{123}I, ^{81}Rb/^{81}Kr, ^{67}Ga, ^{111}In, ^{201}Tl, ^{22}Na, ^{57}Co, ^{44}Ti, ^{68}Ge, ^{72}As, and ^{140}Nd. When energies in excess of 100 MeV are considered for spallation reactions, only proton beams are of interest.

(γ, n) reactions are applied for the production of isotopic neutron-deficient nuclides. Some examples are listed in Table 11.10. The cross sections of these reactions vary between about 1 and 100 mb. They increase with E_γ, the energy of the γ-ray photons, and decrease again at higher values of E_γ, as illustrated in Figure 11.13 for the reaction ^{141}Pr(γ, n)^{140}Pr. The contribution of (γ, 2n), (γ, 3n), and (γ, 4n) reactions increases with E_γ. For example, by irradiation of rubidium salts, ^{83}Rb can be produced which decays by electron capture into ^{83m}Kr:

$$^{85}\mathrm{Rb}(\gamma, 2\mathrm{n})^{83}\mathrm{Rb} \xrightarrow[\epsilon]{86.2\ \text{days}} {}^{83\mathrm{m}}\mathrm{Kr} \xrightarrow[\mathrm{IT}]{1.83\ \text{hours}} \tag{11.25}$$

Table 11.6 Examples of reactor-produced radionuclides of current interest to nuclear medicine.

		Reaction cross section (b)	
Radionuclide ($t_{1/2}$)	**Production reaction**	σ	I_0
^{64}Cu (12.7 h)	^{63}Cu(n, γ)	4.50 ± 0.02	4.97 ± 0.08
^{67}Cu (26 d)	^{67}Zn(n, p)	Fast neutrons: $(1.07 \pm 0.11) \cdot 10^{-3}$	
^{90}Y (64.00 h)	^{90}Sr(β$^-$, 28.79 yr)	—	—
	^{89}Y(n, γ)	1.28 ± 0.02	1.0 ± 0.1
	^{90}Zr(n, p)	Fast neutrons: $0.175 \cdot 10^{-3}$	
^{99}Mo (66 h)	^{235}U(n, f) (6.07%)	582.6 ± 1.1	144 ± 6
	^{98}Mo(n, γ)	0.13 ± 0.06	6.9 ± 0.3
^{103}Pd (16.99 d)	^{102}Pd(n, γ)	3.4 ± 0.3	10.0 ± 2.0
^{114m}In (49.51 h)	^{113}In(n, γ)	8.1 ± 0.8	220 ± 15
^{117m}Sn (14.0 d)	^{116}Sn(n, γ)	$(5.8 \pm 1.2) \cdot 10^{-3}$	$(3.50 \pm 0.53) \cdot 10^{-1}$
	^{117}Sn(n, n′)	Epithermal neutrons: $(2.22 \pm 0.16) \cdot 10^{-1}$	
^{125}I (59.4 d)	^{124}Xe(n, γ)^{125}Xe(β$^-$, 16.9 h)	165 ± 20	$(3.6 \pm 0.7) \cdot 10^3$
^{131}I (8.02 d)	^{235}U(n, f) (2.89%)	582.6 ± 1.1	144 ± 6
	^{130}Te(n, γ)^{131g}Te(β$^-$, 25.0 min)	0.27 ± 0.06	0.46 ± 0.05
^{153}Sm (46.28 h)	^{152}Sm(n, γ)	206 ± 6	2970 ± 100
^{166}Ho (26.8 h)	^{165}Ho(n, γ)	61.2 ± 1.1	650 ± 22
	^{164}Dy(n, γ)^{165}Dy (β$^-$, 2.33 h)	$(2.65 \pm 0.10) \cdot 10^3$	$(3.4 \pm 0.2) \cdot 10^2$
	^{165}Dy(n, γ)^{166}Dy(β$^-$, 81.5 h)	$(3.6 \pm 0.3) \cdot 10^3$	$(2.2 \pm 0.3) \cdot 10^4$
^{169}Yb (32.0 d)	^{168}Yb(n, γ)	$(2.3 \pm 0.17) \cdot 10^3$	$(2.13 \pm 0.1) \cdot 10^4$
^{177}Lu (6.7 d)	^{176}Lu(n, γ)	$(2.09 \pm 0.07) \cdot 10^3$	$(1.09 \pm 0.04) \cdot 10^3$
	^{176}Yb(n, γ)^{177}Yb(β$^-$, 1.9 h)	2.85	6.3
^{186}Re (3.72 d)	^{185}Re(n, γ)	112 ± 2	1717 ± 50
^{188}Re (17.0 h)	^{187}Re(n, γ)	76.4 ± 1.0	300 ± 20
^{188}W (69.78 d)	^{186}W(n, γ)^{187}W	36.48	290.3
	^{187}W(n, γ)	14.5	398
^{191m}Ir (4,94 s)	^{190}Os(n, γ)^{191}Os(β$^-$, 15.4 d)	13.1 ± 0.3	30 ± 1
^{194}Ir (19.28 h)	^{192}Os(n, γ)^{193}Os(β$^-$, 30.11 h)	2.0 ± 0.1	4.6 ± 0.2
	^{193}Os(n, γ)^{194}Os(β$^-$, 6.0 yr)	38 ± 10	Unknown
^{195m}Pt (4.02 d)	^{194}Pt(n, γ)	$(4.2 \pm 0.8) \cdot 10^{-2}$	$(5.26 \pm 0.79) \cdot 10^2$
	^{195}Pt(n, n′)	Epithermal neutrons: $(2.87 \pm 0.20) \cdot 10^{-1}$	
^{199}Au (75.3 d)	^{198}Pt(n, γ)^{199}Pt(β$^-$, 31 min)	3.66 ± 0.19	54 ± 4
	^{197}Au(n, γ)^{198}Au	98.7 ± 0.1	1550 ± 28
	^{198}Au(n, γ)	$(2.51 \pm 0.04) \cdot 10^4$	Unknown
^{223}Ra (11.43 d)	^{226}Ra(n, γ)^{227}Ra(β$^-$, 42.4 min)^{227}Ac(β$^-$, 21.8 y)^{227}Th(β$^-$, 18.7 d)	12.8 ± 1.5	280

σ: thermal neutron cross section; I_0: resonance integral for epithermal neutrons.

Table 11.7 Production of radionuclides by accelerators (survey).

Reaction	Decay modes of the products	Remarks
(p, γ)	β^+ or ε, rarely β^-	Sharp resonances with light nuclei; (p, n) reactions may compete
(p, n)	β^+ or ε, sometimes β^-	Mostly endoergic; threshold energy 2–4 MeV
(p, α)	—	Very seldom
(d, n)	β^+ or ε, sometimes β^-	Exoergic; high yields
(d, 2n)	β^+ or ε, rarely β^-	Threshold energy 5–10 MeV; at higher energies (d, 3n) and (d, 4n) reactions
(d, p)	Mostly β^-	Generally relatively high yields; with 14 MeV deuterons practically applicable for all elements
(d, α)	β^+ or β^-	Mostly exoergic; frequently observed with light nuclei, e.g. ^{6}Li(d, α)α
(α, n)	β^+ or ε, rarely β^-	Applied for production of neutrons; yields decrease with increasing atomic number; at higher energies (α, 2n) and (α, 3n) reactions
(α, p)	Mostly β^-, sometimes β^+ or ε	Relatively high threshold energies (like other reactions with α particles); reactions with nuclides of high atomic number require high energy of the α particles
(γ, n)	β^+, sometimes β^-	High-energy γ-rays available as bremsstrahlung; always endoergic; threshold energy given by the binding energy of the neutron; at higher energies increasing contributions of (γ, 2n) and (γ, 3n) reactions

^{83m}Kr is of interest for practical application and can be obtained from an ^{83}Rb/^{83m}Kr radionuclide generator.

In accelerator production of radionuclides, the cross section data play an important role. To predict the yield with reasonable accuracy, the full excitation function needs to be known. This is equally true for the competing reaction channels. The expected yield of a product nuclide in a certain energy range and target thickness can be calculated by using the expression

$$Y = \frac{N_{\mathrm{Av}} H}{M} I(1 - \mathrm{e}^{-\lambda t}) \int_{E_1}^{E_2} \left(\frac{\mathrm{d}E}{\mathrm{d}(\rho x)} \right)^{-1} \sigma(E) \mathrm{d}E \tag{11.26}$$

where Y is the produced activity in Bq, N_{Av} Avogadro's number, H is the enrichment or isotopic abundance of the target nuclide, M is the mass number of the target isotope, I is the projectile beam intensity (s^{-1}), $\mathrm{d}E/\mathrm{d}(\rho x)$ is the stopping power, $\sigma(E)$ is the cross section at energy E, λ is the decay constant of the product nucleus, and t is the irradiation time. Non-isotopic impurities can be removed by chemical

Table 11.8 Reactions with deuterons applicable to production of radionuclides.

		Yield (kBq μA^{-1} h^{-1}) (thick targets)		
Target	**Nuclear reaction**	**8 MeV**	**14 MeV**	**19 MeV**
Li, LiF, $LiBO_2$	$^{6}Li(d, n)^{7}Be$	—	Low	74
B_2O_3	$^{10}Be(d, n)^{11}C$	$1.85 \cdot 10^4$	$1.79 \cdot 10^4$	—
Mg, MgO	$^{24}Mg(d, \alpha)^{22}Na$	—	39–67	—
Cr	$^{50}Cr(d, \alpha)^{48}V$	—	Low	—
Cr	$^{52}Cr(d, 2n)^{52}Mn$	—	$2.96 \cdot 10^3$	—
Fe	$^{56}Fe(d, \alpha)^{54}Mn$	—	37	—
Mn alloy	$^{55}Mn(d, 2n)^{55}Fe$	—	26	0.74
Fe	$^{56}Fe(d, 2n)^{56}Co$	—	High	—
Fe	$^{56}Fe(d, n)^{57}Co$	—	High	185
Fe	$^{57}Fe(d, n)^{58}Co$	—	High	—
Cu	$^{65}Cu(d, 2n)^{65}Zn$	—	130	—
Ge alloy	$^{74}Ge(d, 2n)^{74}As$	—	74	370
As alloy	$^{75}As(d, 2n)^{75}Se$	—	High	—
NaBr	$^{79}Br(d, 2n)^{79}Kr$	—	High	—
$SrCO_3$	$^{88}Sr(d, 2n)^{88}Y$	—	$1.41 \cdot 10^3$	—
Pd	$^{107}Pd(d, n)^{106}Ag$	—	Average	—
Te	$^{130}Te(d, 2n)^{130}I$	—	$3.3 \cdot 10^4$	—
NaI	$^{127}I(d, 2n)^{127}Xe$	—	Average	—
Au	$^{197}Au(d, 2n)^{197}Hg$	—	$3.0 \cdot 10^4$	—

separations; isotopic impurities can be reduced by using enriched isotopes as target material and by careful selection of the bombarding energy range inside the target.

The commonly employed radioisotope 13.2 hours ^{123}I, for example, can be produced via various nuclear reactions. The $^{124}Te(p, 2n)^{123}I$ reaction is a good example of the importance of the cross section data. To reduce the level of isotopic impurities, it is essential to use highly enriched ^{124}Te as target material. Due to the $^{124}Te(p, n)^{124}I$ reaction, it is not possible to avoid completely a 4.2 days ^{124}I impurity. Figure 11.14 depicts that the suitable proton energy window is $25 \rightarrow 18$ MeV; that is, the incident proton energy should be 25 MeV and the thickness of the tellurium target should be adjusted such that the target degrades the proton energy down to 18 MeV. Then, the yield of ^{123}I is 560 MBq μA^{-1} h^{-1}, and the yield of ^{124}I is limited to 1%. As ^{124}I gains significance in PET, Figure 11.12 indicates that the suitable energy window for the production of rather pure ^{124}I is $12 \rightarrow 8$ MeV, where the yield of ^{124}I is 16 MBq μA^{-1} h^{-1}.

Table 11.9 Production of positron emitters used in nuclear medicine.

Radionuclide	Half-life	Mode of decay ($E_{\beta^+(max)}$)	Nuclear reactions	Yields (thick targets) (MBq μA^{-1} h^{-1}) (Particle energies [MeV])
^{11}C	20.38 min	β^+ (99.8%)	$^{14}N(p, \alpha)^{11}C$	≈3800 (13)
		(0.96 MeV)	$^{11}B(p, n)^{11}C$	≈3400 (10)
			$^{10}B(d, n)^{11}C$	≈2500 (10)
^{13}N	9.96 min	β^+ (100%)	$^{12}C(d, n)^{13}N$	≈2000 (8)
		(1.19 MeV)	$^{16}O(p, \alpha)^{13}N$	≈1700 (16)
^{15}O	2.03 min	β^+ (99.9%)	$^{14}N(d, n)^{15}O$	≈2400 (8)
		(1.72 MeV)	$^{16}O(p, pn)^{15}O$	≈3700 (25)
^{18}F	109.7 min	β^+ (97%)	$^{20}Ne(d, \alpha)^{18}F$	≈1100 (14)
		(0.635 MeV)	$^{18}O(p, n)^{18}F$	≈3000 (16)[a]
			$^{16}O(^3He, p)^{18}F$	≈500 (40)
^{38}K	7.6 min	β^+ (100%)	$^{35}Cl(\alpha, n)^{38}K$	≈260 (20)
		(2.68 MeV)	$^{38}Ar(p, n)^{38}K$	≈800 (16)
			$^{40}Ca(d, \alpha)^{38}K$	≈200 (12)
^{73}Se	7.1 h	β^+ (65%)	$^{75}As(p, 3n)^{73}Se$	≈1400 (40)
		(1.32 MeV)	$^{75}As(d, 4n)^{73}Se$	≈650 (45)
^{75}Br	1.6 h	β^+ (75.5%)	$^{76}Se(p, 2n)^{75}Br$	≈3700 (30)
		(1.74 MeV)	$^{76}Se(d, 3n)^{75}Br$	≈3000 (35)[a]
			$^{75}As(\alpha, 4n)^{75}Br$	≈250 (60)
^{76}Br	16.0 h	β^+ (57%)	$^{76}Se(p, n)^{76}Br$	≈290 (16)[a]
		(3.90 MeV)	$^{77}Se(p, 2n)^{76}Br$	≈250 (25)[a]

a) Using highly enriched isotopes.
Source: From Stöcklin and Pike (1993).

It may be noted that indirect formation of ^{123}I via the production of ^{123}Xe leads to higher radionuclide purity. Several reactions are feasible:

$$
\begin{aligned}
&^{122}Te(\alpha, 3n)^{123}Xe\\
&^{123}Te(\alpha, 4n)^{123}Xe\\
&^{124}Te(\alpha, 5n)^{123}Xe\\
&^{122}Te(^3He, 2n)^{123}Xe \xrightarrow{\beta^+(1.505),EC(0.149),2.08\ hours} {}^{123}I\\
&^{123}Te(^3He, 3n)^{123}Xe\\
&^{124}Te(^3He, 4n)^{123}Xe\\
&^{127}I(p, 5n)^{123}Xe\\
&^{127}I(d, 6n)^{123}Xe
\end{aligned}
\qquad (11.27)
$$

Table 11.10 Examples of the production of radionuclides by (γ, n) reactions.

Target	Radionuclide produced by (γ, n) reaction	Half-life	Resonance energy (MeV)	Cross section at the resonance energy (barn)
TiO_2	^{45}Ti	3.08 h	—	—
$Co(NO_3)_2 \cdot 6H_2O$	^{58}Co	70.86 d	16.9	0.13
$AgNO_3$	^{106m}Ag	8.3 d	14.0	0.24
KIO_3 or LiI	^{126}I	13.11 d	15.2	0.45
Cs_2CO_3	^{132}Cs	6.47 d	—	—
$TINO_3$	^{202}TI	12.23 d	≈17	0.092
$Pb(NO_3)_2$	^{203}Pb	51.9 h	—	—

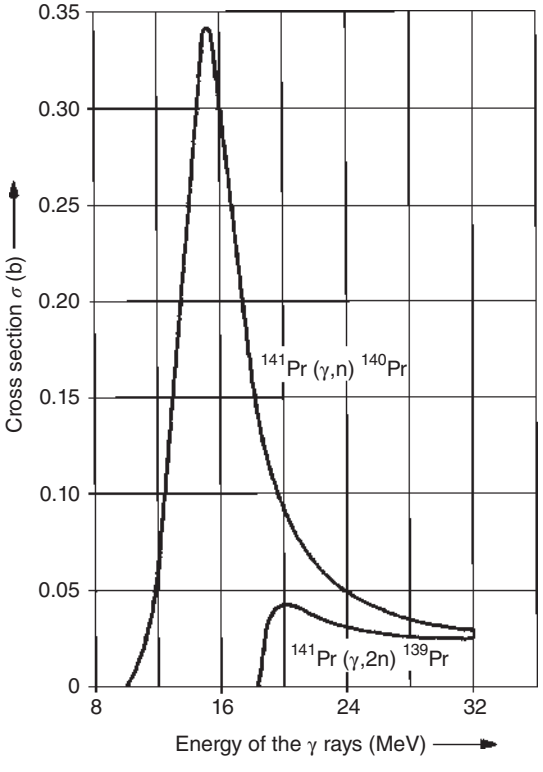

Figure 11.13 Cross sections of the reactions $^{141}Pr(\gamma, n)^{140}Pr$ and $^{141}Pr(\gamma, 2n)^{139}Pr$ as a function of the photon energy. Source: Carver and Turchinetz (1959), figure 03 (p. 55)/IOP Publishing.

If 50 MeV protons are available, the (p, 5n) reaction with ^{127}I is the most favorable because iodine has only one stable nuclide. However, measurable amounts of ^{125}Xe are produced by the (p, 3n) reaction. The volatile products formed by irradiation of I_2, LiI, NaI, KI, or CH_2I_2 are transferred by He. In a first trap, cooled to −79 °C, directly formed iodine and iodine compounds are separated, and, in a second trap, cooled to −196 °C, ^{123}Xe and ^{125}Xe are collected. The second trap is taken off and after about

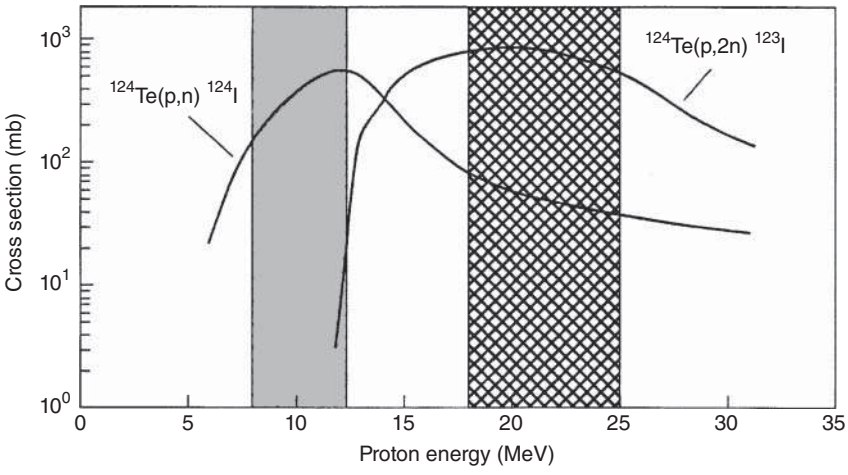

Figure 11.14 Excitation functions of ^{124}Te(p, n)^{124}I and ^{124}Te(p, 2n)^{123}I reactions. The suitable energy window for the production of ^{123}I is 25 → 18 MeV (after Qaim (2001)). The same data can be used for the production of pure ^{124}I. The suitable energy window is then 12 → 8 MeV. Source: Qaim (2001), figure 6 (p. 66)/De Gruyter.

five hours the iodine formed by decay of ^{123}Xe is dissolved in dilute NaOH. During this time, ^{123}Xe has largely decayed, but ^{125}Xe ($t_{1/2} = 16.9$ hours) only to some extent. The yields are on the order of 100–500 MBq μA^{-1} h^{-1}, and the relative activity of ^{125}I is on the order of 0.1%.

The samples may be irradiated inside or outside the accelerator. In both cases, heat is generated by the deceleration of the charged particles. Due to the use of high beam currents (e.g. 50 μA), the heat deposited in the target is rather high, up to a few kilowatts per square centimeter, and an efficient heat transfer is of prime importance in target construction. Other criteria for an optimum target design are (i) ease of chemical separation of the radioactive product; (ii) chemical reactivity and specific activity of the product; (iii) recovery of the target material; and (iv) high yield of the product. The chemical reactivity of the product is most important for the labeling of a pharmaceutical with the radionuclide. The chemical state of the latter is often influenced by the chemical state of the target and in situ reactions within the target. For example, in the ^{20}Ne(d, α)^{18}F reaction, a mixture of Ne + 0.1% F_2 as target filling leads to $[^{18}F]F_2$, but to $^{18}F^-_{aq}$ if a mixture of Ne + H_2 is used and the target is rinsed with water after irradiation. $[^{18}F]F_2$ is used for electrophilic labeling, whereas $^{18}F^-_{aq}$ is used for nucleophilic substitution.

Considerable effort has been devoted to the targetry used in the production of the four major β^+ emitters, namely, ^{11}C, ^{13}N, ^{15}O, and ^{18}F. Pressurized gas targets are used for production of ^{11}C and ^{15}O. The produced activity is removed from the target by expansion and leading the gas to vessels in which conversion to other chemical forms known as primary precursors is achieved. The chemical form of the activity leaving the target depends upon the additive given to the N_2 gas in the target and, in the case of ^{11}C, on the radiation dose in the target. The resulting ^{15}O from an $N_2(O_2)$ target in the ^{14}N(d, n)^{15}O reaction is $[^{15}O]O_2$. In the ^{14}N(p, α)^{11}C reaction, at

high radiation dose, mostly $^{11}CO_2$ is obtained; at lower radiation doses, ^{11}CO. The standard route to ^{15}O makes use of a deuteron beam at the cyclotron. If that is not available, the $^{15}N(p, n)^{15}O$ reaction on highly enriched ^{15}N may be utilized, requiring an efficient recovery system for the enriched target gas.

The production of electrophilic ^{18}F also involves bombardment of a gas target. The removal of the activity from the target requires the addition of some F_2 carrier. In the $^{20}Ne(d, \alpha)$ reaction, the 0.1% F_2 is directly mixed with the Ne gas. In the $^{18}O(p, n)^{18}F$ reaction, two subsequent steps are required. First, highly enriched gaseous ^{18}O is bombarded with protons, and the ^{18}F deposits on the inner target surface. After cryogenic recovery of the ^{18}O target gas, a mixture of F_2 and Kr is introduced into the target. Second, in a subsequent short proton bombardment, an isotopic exchange between the deposited ^{18}F and the gaseous F_2 occurs, leading to the recovery of the ^{18}F in the gas phase as $[^{18}F]F_2$. The specific activity of ^{18}F is much higher in the $^{18}O(p, n)$ reaction than in the $^{20}Ne(d, \alpha)$ reaction. Water targets are used for the production of ^{13}N and ^{18}F. In the $^{16}O(p, \alpha)^{13}N$ reaction, natural $H_2{}^{16}O$ is used at a proton energy range of $16 \rightarrow 7$ MeV. In the $^{18}O(p, n)^{18}F$ reaction, enriched $H_2{}^{18}O$ is employed at a proton energy range of $16 \rightarrow 3$ MeV. At high currents, $^{13}NO_3^-$ and nucleophilic $^{18}F^-_{aq}$ are produced. In the latter case, the irradiated water is transferred to an anion exchange column where the $^{18}F^-_{aq}$ activity is sorbed. The enriched water passes through and is collected and recycled. The ^{18}F activity is eluted from the column in 0.1 M Na_2CO_3. The yield per batch amounts to 70 GBq. The radionuclidic and chemical purity of all four "organic" positron emitters is more than 99%. Thus, the production techniques of the commonly used PET radionuclides are well established.

The number of nonstandard positron emitters with applications in nuclear medicine is large. They are rather regarded as research tools and their relative importance has been changing. The following categories can be distinguished: (i) alkali metals (e.g. ^{38}K, ^{81}Rb); (ii) longer-lived positron emitters consisting of halogens and other elements suitable for labeling of organic compounds (e.g. $^{75,76}Br$, ^{124}I, ^{73}Se); (iii) metals forming complexes with suitable organic ligands (e.g. ^{52}Fe, ^{53}Co, ^{64}Cu); (iv) β^+ emitting analogs of single-photon emission computer tomography (SPECT) and therapeutic radionuclides (e.g. ^{94m}Tc for ^{99m}Tc, ^{86}Y for ^{90}Y, $^{120,124}I$ for ^{123}I and ^{131}I, etc.). The production of typical radionuclides in each of these groups has been reviewed by Qaim (2011). A large number of γ-ray emitting radionuclides are applied in diagnostics by SPECT. The most commonly used SPECT radionuclide, 6.0 hours ^{99m}Tc, is commercially available via the $^{99}Mo/^{99m}Tc$ generator. The four other major SPECT radionuclides, namely, ^{67}Ga, ^{111}In, ^{123}I, and ^{201}Tl, are also discussed by Qaim (2001). Cyclotron-produced therapeutic radionuclides include β^-, α, and Auger electron emitters, and the most commonly used ones are ^{67}Cu, ^{103}Pd, ^{186}Re, ^{211}At, and ^{225}Ac. Their major production routes and properties are also reviewed by Qaim (2001).

11.5.3 Separation Techniques

The task of quantitative and effective separation of small amounts of radionuclides has appreciably enhanced the development of modern separation techniques. High

radionuclide purity is of great importance for applications in nuclear medicine as well as for sensitive measurements. In this context, impurities of long-lived radionuclides are of particular importance because their relative activity increases with time. For example, if the activity of ^{90}Sr is only 0.1% of that of ^{140}Ba after fresh separation, it will increase to 11.5% in three months.

The most frequently used separation techniques are

- crystallization, precipitation, or coprecipitation
- electrolysis
- distillation
- solvent extraction
- ion exchange
- chromatography.

Fractional crystallization was one of the first methods used in radiochemistry by Marie and Pierre Curie to separate $^{226}RaCl_2$ from $BaCl_2$. Precipitation is only applicable if the solubility product is exceeded, that is, if the concentration of the radionuclide to be separated is high enough. If the concentration is too low, coprecipitation may be applied by addition of a suitable carrier, such as stable compounds of identical or very similar chemical properties. Application of isotopic carriers is very effective, but it leads to a decrease in specific activity. Therefore, non-isotopic carriers with suitable chemical properties are preferred. Hydroxides such as iron(III) hydroxide or other sparingly soluble hydroxides give high coprecipitation yields because of their high sorption capacity. Coprecipitation of actinides with LaF_3 is an important example. Coprecipitation by the formation of anomalous solid solutions (anomalous mixed crystals), for example, coprecipitation of actinides(III) and (IV) with $BaSO_4$ or $SrSO_4$ in the presence of K^+ or Na^+ ions, respectively, is also possible.

If coprecipitation of radionuclides present in ultralow concentrations is to be avoided, hold-back carriers are added. Isotopic carriers are most effective for this purpose, but they lead to low specific activity.

For filtration, Hahn's suction frits are convenient (Figure 11.1). They allow easy removal of the filter for further operations or subsequent measurements.

Electrolytic deposition of radionuclides is frequently applied. It gives thin samples and is well suited for the preparation of standard samples. For instance, Po, Pb, or Mn can be deposited with high yields on anodes of Cu, Pt, or Ag and by the electrolysis of the nitrates or chlorides of Th and Ac in acetone or ethanol solutions these elements can be separated on cathodes. The preparation of thin samples by electrolytic deposition is of special interest for the measurement of α emitters, such as isotopes of Pu or other actinides.

Separation of radionuclides by distillation is applicable if volatile compounds are formed. Separation of ^{131}I from irradiated Te has already been mentioned in Section 11.5.1. Other examples are separation of Ru as RuO_4 under oxidizing conditions, and volatilization of Tc as Tc_2O_7 from concentrated H_2SO_4 at 150–250 °C. ^{32}P may be purified by volatilization as PCl_5 in a stream of Cl_2.

Solvent extraction is widely used for separation of radionuclides because this technique is simple, fast, and applicable in the range of low concentrations.

Table 11.11 Examples for the separation of radionuclides by extraction.

Element	Extractant	Remarks
Fe	(a) isopropylether	Extraction from HCl solutions as $HFeCl_4$
	(b) cupferron in $CHCl_3$	Quantitative extraction from HCl solution
Br	CCl_4	Extraction of Br_2 from HNO_3 solution
Sr	TTA[a)]	At pH > 10
Y	(a) D2EHPA[b)] in toluene	Separation from Sr in HCl solution
	(b) TBP[c)]	Effective separation from rare earth elements at high HNO_3 concentration
Zr	(a) TBP[c)]	Strong HCl or HNO_3 solution
	(b) DBP[d)] in dibutyl ether	Quantitative extraction from acid solution
Tc	Tetraphenylarsonium chloride in $CHCl_3$	Extraction from neutral or alkaline solutions in the presence of H_2O_2 as $(C_6H_5)_4AsTcO_4$
I	CCl_4	Extraction from acid solution
Cs	Sodium tetraphenylborate in amyl acetate	Selective extraction as $Cs(C_6H_5)_4B$ from buffered solution
Ce	(a) Ether	Separation of Ce(IV) from lanthanides(III)
	(b) TBP[c)]	Extraction of Ce(IV); separation from lanthanides(III)
Ac	TTA[a)] in benzene	At pH 6 from aqueous solution
Th	(a) Methyl isobutyl ketone	From HNO_3 solution
	(b) TTA[a)] in benzene	From acid solution
	(c) TBP[c)] in kerosine	From $HNO_3/NaNO_3$ solution
U	(a) Ether	Selective extraction of UO_2^{2+} under certain conditions
	(b) TBP[c)] in kerosine	Extraction of UO_2^{2+} from HNO_3 solutions
Pu	TBP[c)] in kerosine	Extraction of Pu(VI) and Pu(IV) from HNO_3 solutions
Am, Cm	TTA[a)] in benzene	Quantitative extraction of Am(III) and Cm(III) at pH 4
Bk	D2EHPA[b)] in heptane	Extraction of Bk(IV) from strong HNO_3 solution in presence of $KBrO_3$ – possibility of separating Bk from Cm and Cf

a) α-thenoyltrifluoroacetone.
b) Di(2-ethylhexyl)phosphoric acid.
c) Tri-*n*-butyl phosphate.
d) Di-*n*-butylphosphoric acid.

Addition of a carrier is not required. Some examples of the separation of radionuclides by solvent extraction are given in Table 11.11. Solvent extraction plays an important role in reprocessing, Section 15.7. Tributyl phosphate (TBP), methyl isobutyl ketone (Hexon), and trilaurylamine (TLA) are preferred complexing agents for the separation and purification of U and Pu.

Ion-exchange procedures have also found broad application in radiochemistry. The selectivity S is measured by the difference in the logarithms of the distribution coefficients $K_d(1)$ and $K_d(2)$: $S = \log K_d(1) - \log K_d(2)$. Commercial ion-exchange resins exhibit relatively low selectivities. Higher values of S are obtained by use of organic ion exchangers carrying chelating groups of high selectivity (preferably "tailor-made") as anchor groups or by application of inorganic ion exchangers. Highly selective organic ion exchangers are synthesized on the basis of polystyrene, cellulose, or other substances as matrices. High selectivity with commercial ion-exchange resins is also obtained by the addition of complexing agents, such as α-hydroxycarboxylic acids (lactic acid, α-hydroxy-iso-butyric acid, and others) to the solution. Under these conditions, the selectivity is determined by the difference in the logarithms of the stability constants K_S of the complexes: $S = \log K_S(1) - \log K_S(2)$.

Inorganic ion exchangers comprise a great variety of compounds: hydrous oxides (e.g. $Al_2O_3 \cdot xH_2O$, $SiO_2 \cdot xH_2O$, $TiO_2 \cdot xH_2O$, $ZrO_2 \cdot xH_2O$, $Sb_2O_5 \cdot xH_2O$), acid salts (e.g. phosphates of Ti, Zr, hexacyanoferrates of Mo), salts of heteropoly acids (e.g. ammonium molybdophosphate), and clay minerals. Many ionic inorganic compounds also exhibit ion-exchange properties (e.g. $BaSO_4$, AgCl, CuS) and offer the possibility of highly selective separations (e.g. I^- and I_2 on AgCl). The main disadvantage of inorganic ion exchangers is the relatively slow equilibration. Examples of the separation of radionuclides by ion exchange are listed in Table 11.12.

Chromatographic separation techniques are based on adsorption, ion exchange, or partition between a stationary and a mobile phase. Gas chromatography (GC) is applied for the separation of volatile compounds. Thermochromatography (using a temperature gradient) or isothermal GC is frequently used for the study of the properties of small amounts of radionuclides. For the investigation of radionuclides of extremely short half-life the chromatographic column, usually a quartz glass tube, may be operated on-line with the production of the radionuclide by an accelerator, aerosols may be added as carriers, and chemical reactions may be initiated by injection of reactive gases into the column.

For the separation of radionuclides in aqueous solution, high-performance liquid chromatography (HPLC) or ion-exchange chromatography may be applied. Reversed-phase partition chromatography (RPC) offers the possibility of using organic extractants as the stationary phase in a multistage separation. On-line extraction techniques are also available.

Some specific effects of the radiation from radioactive substances on the separation procedures need to be noted. At very high activity levels, say at 10^{12} β disintegrations per minute per milliliter of solution, decomposition of water and other solvents and heat effects may affect the procedures. At the same time, the person carrying out the separation can receive dangerous doses of radiation unless protected by shielding or distance. Even at lower activity levels, where the health hazards from radiation are minimal, special care is still required to prevent the spread of radioactive contamination that could seriously raise counter backgrounds and interfere with low-level experiments. The degree of precaution

Table 11.12 Examples of the separation of radionuclides by ion exchange.

Elements to be separated	Ion exchanger[a)]	Eluant
Cs/Rb	Zirconium tungstate	1 M NH_4Cl
Cs/Rb, K	Duolite C-3	0.3 M HCl (Rb, K, ...), 3 M HCI (Cs)
Cs/Rb/K/Na	Titanium hexacyanoferrate	l M HCl
Alkaline earths	Dowex 50	1.5 M ammonium lactate, pH 7
Cs/Ba/rare earths	Dowex 50	$LiNO_3$ solution
Ba/Ra	Dowex 50	0.32 M ammonium citrate, pH 5.6
Rare earths	Dowex 50	5% ammonium citrate, pH 3–3.5, or 0.2–0.4 M α-hydroxyisobutyric acid, pH 4.0–4.6, or 0.025 M ethylene-diaminetetraacetic acid (EDTA)
Mn/Co/Cu/Fe/Zn	Dowex 1	HCl of decreasing concentration
Zr/Nb	Dowex 50	1 M HCl + H_2O_2 (Nb); 0.5% oxalic acid (Zr)
Zr/Pa/Nb/Ta	Dowex 1	HCl/HF solutions
Actinides/lanthanides	Dowex 50	20% ethanol, saturated with HCl (actinides are first eluted)
Actinides	Dowex 50	5% ammonium citrate, pH 3.5, or 0.4 M ammonium lactate, pH 4.0–4.5
Th/Pa/U	Dowex 1	10 M HCl or 9 M HCl/1 M HF

a) Instead of the ion exchangers listed, others with similar properties may be applied.

needed to prevent contamination and hazardous radiation exposure depends on the amount of activity handled, on the type and energy of the radiation, the half-life of the radionuclide, and possibly on its chemical properties. Radiation protection is discussed explicitly in Chapter 25.

11.5.4 Radionuclide Generators

Application of short-lived radionuclides has the advantage that the activity vanishes after relatively short periods of time. This aspect is of special importance in nuclear medicine. Short-lived radionuclides may be produced by irradiation in nuclear reactors or by accelerators, but their supply from irradiation facilities requires the matching of production and demand, and fast transport. These problems are avoided by application of radionuclide generators containing a longer-lived mother nuclide from which the short-lived daughter nuclide can be separated.

The mother nuclide must be present in such a chemical form that the daughter nuclide can be separated repeatedly by a simple operation, leaving the mother nuclide quantitatively in the generator. After each separation, the activity of the daughter nuclide increases again, and the daughter nuclide can be separated

repeatedly at certain intervals of time. For example, after three half-lives of the daughter nuclide, 87.5% of its saturation activity is reached and separation may be repeated with a relatively high yield. Fixation of the mother nuclide and simple separation of the daughter nuclide are achieved by use of separation columns containing a suitable ion exchanger or sorbent from which the daughter nuclide can be eluted.

Since the separation can be repeated many times, radionuclide generators are sometimes called "cows" and the separation procedure is called "milking." Some mother/daughter combinations used in radionuclide generators are listed in Table 11.13. They are very useful if the short-lived radionuclides are applied frequently and have gained great practical importance in nuclear medicine, mainly for diagnostic purposes, where the main advantage of the application of short-lived radionuclides is the short radiation exposure. High radionuclide purity is an essential prerequisite and needs careful examination, in particular with respect to the presence of long-lived α emitters.

The radionuclide generators with potential medical application can be classified into the following categories: (i) generators releasing positron emitting radionuclides for PET; (ii) generators releasing photon emitters for SPECT; (iii) generators releasing therapeutic radionuclides; and (iv) in vivo generators. Key examples of category (i) include the mother/daughter pairs 9.26 hours ^{62}Zn/9.74 minutes ^{62}Cu, 270.8 days ^{68}Ge/68 minutes ^{68}Ga, and 25.6 days ^{82}Sr/1.273 minutes ^{82}Rb. Key examples of category (ii) include the pairs 4.58 hours ^{81}Rb/13 seconds ^{81m}Kr, 66.0 hours ^{99}Mo/6.0 hours ^{99m}Tc (involved in 90% of all diagnostic procedures), 21.5 days ^{178}W/9.31 minutes ^{178m}Ta, 15.4 days ^{191}Os/4.94 seconds ^{191m}Ir, and 1.73 days ^{195m}Hg/30.5 seconds ^{195m}Au. Key examples of category (iii) include 28.6 years ^{90}Sr/64.1 hours ^{90}Y, 3.4 days ^{166}Dy/1.12 days ^{166}Ho, 69 days ^{188}W/16.9 hours ^{188}Re, 10 days ^{225}Ac/45.6 minutes ^{213}Bi, 3.66 days ^{224}Ra/10.64 hours ^{212}Pb, and 21.77 days ^{227}Ac/11.43 days ^{223}Ra. The concept of in vivo generators involves the labeling of various molecular carriers with intermediate half-life generator parents which, after accumulation in the desired tissue, generate much shorter-lived daughter radionuclides. The latter can either act as an imaging source or as a therapeutic emitter of α, β^-, or Auger electrons. The most intensively studied pair is ^{166}Dy/^{166}Ho. The in vivo concept for tumor therapy focuses on ^{225}Ac/^{213}Bi. Details on all of these mother/daughter pairs in the four categories just mentioned, their production, and application can be found in Rösch and Knapp (2011).

Some radionuclide generators have also found application in chemical laboratories and in industry. An example is the ^{137}Cs/^{137m}Ba generator. ^{137m}Ba has a relatively short half-life (2.55 minutes) and decays by isomeric transition (IT) and emission of 662 keV γ-rays into the stable ground state ^{137}Ba. The γ radiation can easily be detected and measured. The "milking" procedure can be repeated after several minutes. The long half-life of the mother nuclide ^{137}Cs (30.17 years) makes it possible to use this generator for long periods of time. However, ^{137}Cs must be bound so firmly that its migration within the time of use of the generator can be excluded. ^{137}Cs is produced in nuclear reactors as a fission product with a rather high yield (6.18%) and can be fixed quite firmly in thin layers of hexacyanoferrates generated on the surface of small pieces of metals (e.g. Fe, Mo).

Table 11.13 Examples of mother and daughter nuclides suitable for use in radionuclide generators.

Mother nuclide			Daughter nuclide		
Nuclide	**Half-life**	**Decay mode**	**Nuclide**	**Half-life**	**Decay mode**
^{28}Mg	20.9 h	β^-, γ	^{28}Al	2.246 min	β^-, γ
^{42}Ar	33 yr	β^-	^{42}K	12.36 h	β^-, γ
^{44}Ti	6.04 yr	ε, γ	^{44}Sc	3.92 h	β^+, ε, γ
^{60}Fe	$1.5 \cdot 10^6$ yr	β^-, γ	^{60m}Co	10.5 min	β^-, IT γ
^{66}Ni	54.6 h	β^-	^{66}Cu	5.l min	β^-, γ
^{62}Zn	9.13 h	ε, β^+, γ	^{62}Cu	9.74 min	β^+, ε, γ
^{72}Zn	46.5 h	β^-, γ	^{72}Ga	14.1 h	β^-, γ
^{68}Ge	270.8 d	ε	^{68}Ga	67.63 min	β^+, ε, γ
^{72}Se	8.5 d	ε, γ	^{72}As	26.0 h	β^+, ε,γ
^{83}Rb	86.2 d	ε, γ	^{83m}Kr	1.83 h	IT
^{82}Sr	25.34 d	ε	^{82}Rb	1.27 min	β^+, ε, γ
^{90}Sr	28.64 yr	β^-	^{90}Y	64.1 h	β^-, γ
^{87}Y	80.3 h	ε, β^+, γ	^{87m}Sr	2.81 h	IT
^{99}Mo	66.0 h	β^-, γ	^{99m}Tc	6.0 h	IT
^{103}Ru	39.35 d	β^-, γ	^{103m}Rh	56.1 min	IT
^{100}Pd	3.7 d	ε, γ	^{100}Rh	20.8 h	α, γ
^{103}Pd	16.96 d	ε, γ	^{103m}Rh	56.1 min	β^-, γ
^{112}Pd	21.1 h	β^-, γ	^{112}Ag	3.12 h	α, γ
^{115}Cd	53.38 h	β^-, γ	^{115m}In	4.49 h	β^-, α, γ
^{115m}Cd	44.8 h	β^-, γ	^{115m}In	4.49 h	β^-
^{111}In	2.81 d	ε, γ	^{111m}Cd	49 min	α, γ
^{113}Sn	115.1 d	ε, γ	^{113m}In	99.49 min	α, γ
^{127}Sb	3.85 d	β^-, γ	^{127}Te	9.35 h	β^-, α, γ
^{118}Te	6.0 d	ε	^{118}Sb	3.5 min	α, γ
^{132}Te	76.3 h	β^-, γ	^{132}I	2.30 h	β^-, γ
^{137}Cs	30.17 yr	β^-, γ	^{137m}Ba	2.55 min	β^-, γ (IT)
^{128}Ba	2.43 d	ε, γ	^{128}Cs	3.8 min	α, γ
^{140}Ba	12.75 d	β^-, γ	^{140}La	40.27 h	β^-, γ
^{134}Ce	75.9 h	ε	^{134}La	6.67 min	β^-, γ (IT)
^{144}Ce	284.8 d	β^-, γ	^{144}Pr	17.3 min	β^-, γ
^{178}W	22 d	ε	^{178}Ta	2.45 h	β^-, γ
^{188}W	69 d	β^-, γ	^{188}Re	16.98 h	β^-, γ

Table 11.13 (Continued)

Mother nuclide			Daughter nuclide		
Nuclide	**Half-life**	**Decay mode**	**Nuclide**	**Half-life**	**Decay mode**
^{189}Re	24.3 h	β^-, γ	^{189m}Os	6.0 h	$\varepsilon, \beta^+, \gamma$
^{194}Os	6.0 yr	β^-, γ	^{194}Ir	19.15 h	IT
^{189}Ir	13.3 d	ε, γ	^{189m}Os	6.0 h	β^-, γ
^{188}Pt	10.2 d	ε, γ	^{188}Ir	41.5 h	IT, β^-, γ
^{200}Pt	12.5 h	β^-	^{200}Au	48.4 min	IT, β^-, γ
^{194}Hg	520 yr	ε	^{194}Au	38.0 h	IT
^{195m}Hg	40 h	IT, ε, γ	^{195m}Au	30.5 s	IT
^{210}Pb	22.3 yr	β^-, γ	^{210}Bi	5.01 d	β^-, γ
^{204}Bi	11.22 h	ε, γ	^{204m}Pb	67.2 min	β^+, γ
^{211}Rn	14.6 h	$\varepsilon, \alpha, \gamma$	^{211}At	7.22 h	β^-, γ
^{224}Ra	3.66 d	α, γ	^{220}Rn	55.6 s	IT
^{224}Ra	3.66 d	α, γ	^{212}Pb	10.64 h	$\beta^+, \varepsilon, \gamma$
^{226}Ra	1600 yr	α, γ	^{222}Rn	3.825 d	β^-, γ
^{228}Ra	5.75 yr	β^-, γ	^{228}Ac	6.13 h	$\beta^+, \varepsilon, \gamma$
^{225}Ac	10.0 d	α, γ	^{221}Fr	4.9 min	β^-, γ
^{225}Ac	10.0 d	α, γ	^{213}Bi	45.59 min	$\varepsilon, \beta^+, \gamma$
^{225}Ac	10.0 d	α, γ	^{209}Pb	3.25 h	β^-, γ
^{226}Ac	29 h	$\beta^-, \varepsilon, \gamma$	^{226}Th	31 min	IT
^{227}Ac	21.77 yr	β^-, α, γ	^{227}Th	18.72 d	β^-, γ
^{227}Ac	21.77 yr	β^-, α, γ	^{223}Fr	21.8 min	IT
^{228}Th	1.913 yr	α, γ	^{224}Ra	3.66 d	$\varepsilon, \beta^+, \gamma$
^{229}Th	7880 yr	α, γ	^{225}Ra	14.8 d	β^-, γ
^{234}Th	24, 10 d	β^-, γ	^{234m}Pa	1.17 min	$\varepsilon, \beta^+, \gamma$
^{230}U	20.8 d	α, γ	^{226}Th	31 min	IT
^{238}U	$4.468 \cdot 10^9$ yr	α, γ	^{234}Th	24.10 d	β^-, γ
^{240}U	14.1 h	β^-, γ	^{240m}Np	7.22 min	IT
^{245}Pu	10.5 h	β^-, γ	^{245}Am	2.05 h	$\varepsilon, \alpha, \gamma$
^{246}Pu	10.85 d	β^-, γ	^{246m}Am	25 min	α, γ
^{254}Es	276 d	α, γ	^{250}Bk	3.22 h	β^-, γ

11.6 Use of Recoil Momenta

If an intermediate mass nucleus of $A = 100$ makes a complete fusion reaction with a 100 MeV α particle, the recoil energy of the compound nucleus is approximately 4 MeV. Complete fusion of an $A = 100$ nucleus with a 100 MeV ^{16}O projectile gives

the resulting compound nucleus a recoil energy of 13.8 MeV. Compared to chemical binding energies, these energies are extremely large and the recoils will escape from a thin target ($<500\,\mu g\,cm^{-2}$). Thus, the recoiling nuclei can be collected by physical or radiochemical techniques. Physical techniques can involve electromagnetic separators to isolate the so-called "evaporation residues" from unwanted background. Radiochemical techniques can make use of implantation of the recoils in suitable catcher foils that may be used directly for radioactivity measurements, or may be used for chemical separations with the goal of isolating the desired product nuclei and measuring their decay properties free of background radiation.

In intermediate energy and relativistic nuclear collisions, the momentum transfer to the target nucleus is much less, and the energy of the recoiling nucleus is typically about 5 to 100 keV/nucleon. Such recoils are called "heavy residues." In reactions studied in inverse kinematics, with a heavy projectile striking a lighter target nucleus, the momentum of the recoiling heavy nucleus is approximately the same as the momentum of the projectile. There are a variety of ways to collect the heavy residues. One traditional radiochemical technique applied in normal reaction kinematics is the so-called thick-target–thick-catcher technique. Here, a target whose thickness exceeds the average range of the recoils is surrounded by C or Al catcher foils whose thickness exceeds the range of the recoiling product nucleus. The average range of the recoiling nucleus $\langle R \rangle$ which relates to its kinetic energy is

$$\langle R \rangle = \frac{N_e W}{N_e + N_r}$$

where N_e is the number of recoils that escape from the target, N_r is the number that remains in the target, and W is the thickness of the target. The fraction of the recoils that is caught in the forward catcher foil, F, and the fraction that is caught in the backward catcher foil, B, can be used to obtain some information about the relative velocity υ of the recoiling nucleus, and the isotropic velocity V received by it in the sequential particle-emission steps. The quantity $\eta = \upsilon/V$ relates to F and B as

$$\eta = \frac{(F/B)^{1/2} - 1}{(F/B)^{1/2} + 1}$$

Thus, the thick-target–thick-catcher method delivers some crude information about the kinematics of the nuclear reaction at intermediate energy and relativistic energies.

For the study of recoils at low beam energies, thin targets need to be used. The energy loss of the recoils in these targets is calculable and tolerable. The catcher foil mentioned above can also take the form of a tape or wheel that can transport the collected activity to a low-background location for counting. The catcher foil can also take the form of a stack of thin foils that, upon disassembly and counting, can be used to reconstruct a differential range distribution. Stacks of foils can be mounted at various angles to measure angular and energy distributions. Catcher-foil techniques are used to advantage to study reactions with very low cross sections. The catcher can also take the form of a jet of rapidly moving gas, a helium jet. The gas contains an

aerosol with over 10^6 particles cm^{-3}, typically an alkali halide or carbon clusters, to which the recoils attach themselves. The helium jet can be transported over substantial distances in thin capillaries. The aerosol particles and the attached radionuclides then escape through a small orifice into vacuum, with the gas achieving sonic velocity, and are collected by impaction on a collector surface. The resulting deposit can be counted directly or can be dissolved for chemical processing. The principal limitation of devices such as tapes, wheels, and jets is that the recoils must be stopped and mechanically transported to the detectors, restricting their use to studies of nuclei with $t_{1/2} > 0.5$ seconds. For the detection and identification of radionuclides with shorter half-lives, instruments based on direct magnetic and/or electrostatic deflection of target recoils are suitable. Such devices use the ionic charge and momentum of the recoiling fusion evaporation residues (EVRs) to achieve their spatial separation from the projectiles and other reaction products. The separation times are determined by the recoil velocities and the lengths of the separators. They are typically in the range of 1–2 μs. Two types of recoil separators have been developed:

1. Wien filters or velocity separators use the specific kinematic properties of the fusion–evaporation products. A very successful example is the velocity filter *SHIP* (Separator for Heavy-Ion reaction Products). EVRs produced in complete fusion reactions emerge from the target and pass through a thin carbon foil that has the effect of equilibrating the ionic charge distribution of the residues. The ions then pass through two filter stages consisting of electric deflectors, dipole magnets, and a quadrupole triplet for focusing. The length of the separator is 11 m. The solid angle of acceptance is 2.7 msr. Since the EVRs have very different velocities and angular distributions than target-like transfer and deep inelastic products and projectiles, SHIP with its ±5% velocity acceptance and narrow angular acceptance separates the EVRs from the other reaction products and the beam. The residues then pass through a large-area time-of-flight (ToF) detector and are implanted in an array of position-sensitive silicon detectors. From their time of flight and the implantation energy signal, a rough estimate of their mass is obtained. Identification of the EVRs is achieved by observing time correlations between the implantation signal and its position and subsequent decay signals from the same position due to α or SF decay and signals from γ- or X-ray detectors placed close to the silicon detector array. This device, see Chapter 17, was instrumental in the discovery of elements 107–112.
2. The gas-filled separators use the different magnetic rigidities of the recoils and projectiles traveling through a low-pressure (about 1 mbar) gas-filled volume in a magnetic field. Mostly He or H_2 or mixtures thereof are used. EVRs emerging from the target undergo a sequence of charge-changing collisions with the gas and quickly equilibrate to a common average charge state. The charge equilibration allows a very efficient collection of the recoils in the focal plane. The trajectory of the ions through the gas-filled separator is determined by their magnetic rigidity, $B\rho = mv/qe$. B denotes the magnetic flux density, ρ the radius of curvature of the ion trajectory, m and v the mass and velocity of the ion, respectively, q_{av},

its average ionic charge. The appropriate magnetic rigidity, $B\rho$, for collection of a given product nucleus can be roughly estimated by

$$B\rho = \frac{mv}{q_{av}} = \frac{mv}{(v/v_0)Z^{1/3}} = \frac{0.0227A}{Z^{1/3}}Tm \tag{11.28}$$

where m, Z, and v are the mass, atomic number, and velocity of the recoil, and v_0 is the Bohr velocity ($2.19 \cdot 10^6$ m s^{-1}), the velocity of the electron in Bohr's model of the hydrogen atom. The projectiles are separated from the recoils right after the target in the dipole magnet. This dipole is followed by two quadrupole magnets that focus the EVRs onto the focal-plane detector. For the detection of heavy-element residues, collection efficiencies of up to 60% are achieved.

Equation (11.28) shows the two important first-order properties of gas-filled separators: $B\rho$ is independent of the velocity and of the initial charge distribution of the EVRs. It also allows a rough estimation of the separation properties of a gas-filled separator. For a symmetric target–projectile combination, the ratio of rigidities is 1 : 0.6 : 0.6 for EVRs, scattered target atoms, and projectiles. For an asymmetric system like ^{48}Ca + ^{248}Cm, the ratios are 1 : 0.9 : 0.3, that is, the high-intensity beam is well separated and the EVRs and the scattered target atoms are still separated by 10%.

In practice, q_{av} turns out to be a sensitive function of the electron shell structure of the recoiling ion and the gas. Figure 11.15 shows experimental $B\rho/A$ values in He as a function of Z which, according to Eq. (11.28), for a constant velocity, reflect mainly the dependence on q_{av}. The electron-shell configurations as a function of the number of remaining electrons $N_e = Z - q_{av}$ are shown for two velocity ranges $v/v_0 = 4$ and $v/v_0 = 2.2$, respectively. The configurations on top apply to the neutral atoms. The following conclusions can be drawn from Figure 11.15. The general trend of the Z dependence for both velocities is given by straight lines proportional to $Z^{-1/3}$. Contrary to Eq. (11.28), there is a velocity dependence of $B\rho$. Imposed on the smooth trends are fluctuations which are obviously correlated with the shell structures. The maxima in $B\rho/A$ correspond to high ionization energies of the next electron to be removed. The shell effects seem to decrease with increasing Z and with higher velocities. Extrapolation beyond $Z = 102$ shown for $v = 2.2v_0$ by the dashed line is based on the similarities of the 4f–5d shell of the lanthanides and the 5f–6d shell of the actinides. The uncertainty at $Z = 116$ is $\Delta B\rho/B\rho = \pm 5\%$. Based on additional systematic measurements of average charges, Gregorich et al. (2005) have made a global fit to the average charge in He, including a sinusoidal correction for the shell structure of the stripped ion:

$$q_{av} = mx + b + d\sin\left\{\frac{2\pi}{32}[Z - (mx + b) - f]\right\} \tag{11.29}$$

$$x = \frac{v}{v_0}Z^{1/3} \quad \text{for } Z \geq 45$$

The best fit was obtained for $m = 0.641$, $b = -0.235$, $d = 0.517$, and $f = 74.647$. The sinusoidal correction is based on an estimate of the number of electrons, $Z - (mx + b)$, remaining on the ion. It has an amplitude $d = 0.517$, of approximately half a charge unit and a period of 32, the length of the sixth and seventh period of

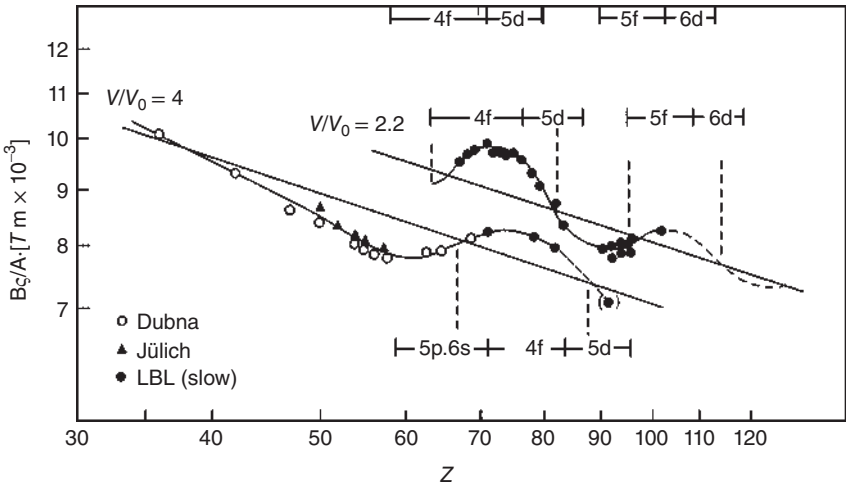

Figure 11.15 Experimental values for $B\rho/A$ as a function of Z. The smooth lines through the data points are to guide the eye. The straight lines are fits to the data to show the $\sim Z^{-1/3}$ trend. Uncertainties in the data are of the size of the data points. Source: Ghiorso et al. (1988), figure 01 (p. 3)/Elsevier.

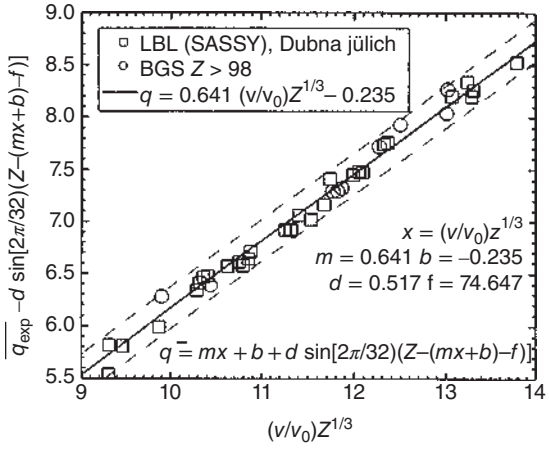

Figure 11.16 Average charges of heavy ions passing through dilute He gas. The ordinate shows the average charges with the sinusoidal correction for the electronic shell structure of the stripped ions. The best fit is shown by the solid line. The dashed lines indicate the $\pm 2\sigma$ deviations about the fit. Source: Gregorich et al. (2005), figure 03 (p. 25)/American Physical Society.

the periodic table. In Figure 11.16, a plot of ρ_{av} minus the sinusoidal correction vs. $(\upsilon/\upsilon_0)Z^{1/3}$ is shown to give a linear correlation. The fit in the region $9 \leq x \leq 14$ is especially good with a standard deviation of 0.1 charge units.

Khuyagbaatar et al. (2012) have measured the average charge state of ^{188}Pb and ^{252,254}No ions in dilute helium gas at the gas-filled separator TASCA. Hydrogen gas was also used as a filling gas for measurements of the average charge state of ^{254}No. Helium and hydrogen gases at pressures from 0.2 mbar to 2.0 mbar were used and a strong dependence of the average charge state on the pressure of the filling gases was observed. This was interpreted by Khuyagbaatar et al. by looking at some general

aspects of charge-exchange collisions. The charge state distribution of heavy ions passing a gas can be described in terms of the fractions of the heavy ions $F_i(x)$ in charge state I, where x refers to the number of gas atoms or molecules per square centimeter traversed by the heavy ion ($\sum_i F_i(x) = 1$). The variation of the charge state fractions is described by a system of differential equations

$$\frac{dF_i(x)}{dx} = \sum_{j \neq i} \left[\sigma_{ij} \cdot F_j(x) - \sigma_{ji} \cdot F_i(x) \right] \tag{11.30}$$

where σ_{ij} and σ_{ji} are the cross sections for electron capture and loss processes. At larger values of x, the variation of the fractions decreases and may vanish completely, $dF_i(x)/dx \to 0$. This means that the electron capture and electron loss processes between the heavy ions and gas species compensate each other and the fraction of each ith charge state (hereafter F_i) in the heavy ions will not change any more. This situation gives the distributions of equilibrated charge states of heavy ions. From this point of view, the equilibrated charge state is determined as

$$\overline{q} = \sum_i q_i \cdot F_i \tag{11.31}$$

Bohr assumed that a heavy atom moving rapidly through a gas retains all of its electrons that have orbital velocities exceeding that of the atom relative to the medium. Applying the Thomas-Fermi model for the structure of the atom, he then obtained the well-known dependence of the equilibrated average charge state $\overline{q}$ of a heavy ion of atomic number Z on its velocity v, $\overline{q} = (v/v_0) \cdot Z^{1/3}$ that is contained in Eq. (11.28).

In principle, these relatively simple concepts of the equilibrated average charge state are valid when the time between two subsequent collisions between the heavy ion and gas particles is long enough that all excited electrons de-excite to the ground state. However, this is true only at low gas pressures with the number of collisions between the heavy ions and gas particles being rare. The probability of collisions between excited heavy ions and species of the filling gas is not negligible in a wide range of gas pressures. This becomes more significant as the time between subsequent collisions becomes comparable to the lifetime of the excited states in the atomic shell. Heavy ions in excited atomic states are losing more easily an electron in a collision with the medium, which leads to an increase in the equilibrated average charge state with increasing gas pressure. Thus, the real average charge state (hereafter average charge state) of heavy ions ($\overline{q}_r$) in the gas will be different from the equilibrated one ($\overline{q}$), and it can be determined as the sum of $\overline{q}$ and a correction term of the so-called "density effect" ($\overline{q}_r = \overline{q} + \Delta q$).

Khuyagbaatar et al. have decided to represent the correction term for the "density effect" by an exponential function

$$\Delta q = C_0 \cdot \overline{q} \cdot e^{-\Delta t/\tau} \tag{11.32}$$

as an analogy to the radioactive decay law because this effect is related to the de-excitation of the electrons from excited states. C_0 is a constant that can in principle be directly determined as 0.2 according to an old estimation by Bohr and Lindhard. However, the authors preferred to keep this as a free parameter that was

fixed empirically. T is an average lifetime of excited states in the heavy ions, which was assumed to be a constant value, and Δt, the time between subsequent collisions, was assumed to be $\Delta t \sim {}^{1}/_{(vP)}$, where v is the velocity of the heavy ion and P is the gas pressure. Mbar was used as unit for the gas pressure and the dimensionless value of (v/v_0) for the velocity which is often used at gas-filled separators. Thus, the average charge state of a heavy ion including the "density effect" turned out as

$$\overline{q}_r = \overline{q}(1 + C_0 \cdot e^{-C_1/(v/v_0)}) \tag{11.33}$$

Here the constants C_0 and C_1 are being fixed empirically. This expression provides the influence of the "density effect" relative to the equilibrated average charge state. The average charge state was deduced from the measured distributions of ERs in the focal plane detector. The ERs were identified through their characteristic α decays. The ER distribution in the focal plane is Gaussian like in both the horizontal and vertical direction. The experimental distributions of ^{252}No in the focal plane detector as a function of the He gas pressure in TASCA are shown in Figure 11.17.

The actual magnetic rigidity can be determined from the position of the center of the horizontal distribution. If this is off center on the detector, indicating that the magnetic rigidity is different from the value preset at the separator, the real magnetic rigidity of the detected ERs can be estimated using the following expression

$$(B\rho)_r = (B\rho)_0 \cdot \left(1 + \frac{X}{100 \cdot D}\right) \tag{11.34}$$

where $(B\rho)_0$ is the value of the magnetic rigidity of the separator set for the given experiment, and D is the dispersion at the focal plane of TASCA in mm per 1 % change in $(B\rho)_0$ (Ghiorso et al. 1988). The average charge state of the ERs can be found from the following expression (Ghiorso et al. 1988) using the $(B\rho)_r$ value:

$$(B\rho)_r = 0.0227 \frac{A\left(\frac{v}{v_0}\right)}{\overline{q}_r} \tag{11.35}$$

where A is the atomic number of the ERs. This equation and further developments of it describe the experimental distributions of ERs over a wide pressure range well. The results also describe the width of the ER distributions well.

In Khuyagbaatar et al. (2012), the average charge state of heavy ions in gas mixtures was also investigated. First of all, the "density effect" was also observed in gas mixtures. Khuyagbaatar et al. considered the formalism of charge exchange collisions in terms of charge state fractions $F_i(x)$. In the case of pure He (H_2) gas, the equilibrated charge state is reached at large values of x, and their distribution is determined by fractions $F_i^{He}(x)$ and $F_i^{H_2}(x)$. In the case of different types of gas particles, each fraction of the ith charge state of heavy ions will have a probability $p(He) = n_{He}/(n_{H_2} + n_{He})$ and $p(H_2) = n_{H_2}/(n_{H_2} + n_{He})$ to collide with He atoms or H_2 molecules, respectively, with $p(He) + p(H_2) = 1$. Then, the fraction of the ith charge state of heavy ions ($\sum_i F_i^m = 1$) in gas mixtures of He and H_2 will be determined by

$$F_i^m = F_i^{He} \cdot p(He) + F_i^{H_2} \cdot p(H_2) \tag{11.36}$$

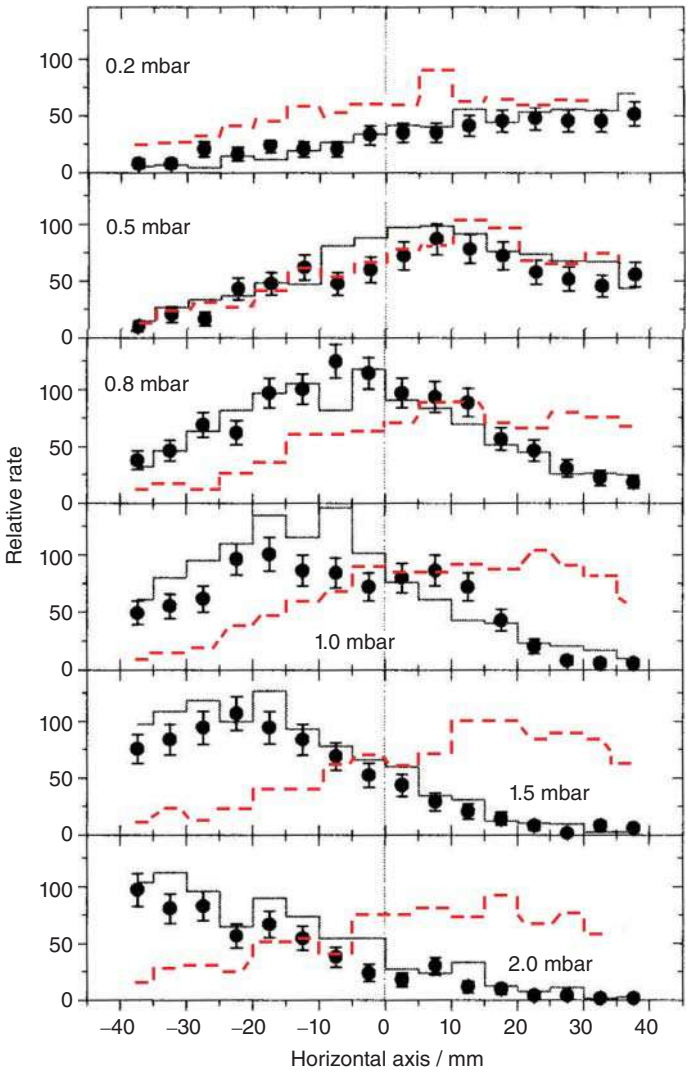

Figure 11.17 Experimental distributions of ^{252}No in the focal plane detector as a function of the He gas pressure in TASCA. The separator was always set to the same magnetic rigidity of $(B\rho)_0 = 2.07$ Tm. Only statistical error bars are shown. Lines are the calculated distributions according to Eq. (11.33) using the average charge state prediction from Gregorich et al. (2005) (dashed red) and including the "density effect" (solid black). Source: Redrawn from Khuyagbaatar et al. (2012).

Assuming the equilibration of charge states in gas mixtures, the following expression can be derived from expressions (11.31) and (11.36):

$$\bar{q}^{m} = \bar{q}^{He} \cdot p(He) + \bar{q}^{H_2} \cdot p(H_2) \tag{11.37}$$

where $\bar{q}^{He}$ and $\bar{q}^{H_2}$ are the equilibrated average charge states of No ions in pure He and H_2 at a given pressure P, respectively. This expression is just a weighted mean

value of the two equilibrated average charge states in pure He and pure H_2. However, this expression cannot be used directly to obtain the average charge state, as no correction terms for the "density effect" are included. In Khuyagbaatar et al. (2012), to this end, the assumption was made that the ratio $\Delta q/\overline{q}$ is constant for He and H_2 pressures P within (0.2–2.0) mbar based on results from the previous subsection on the dependence of the average charge state on the gas pressure. Then, the following expression is valid:

$$\overline{q}_{\mathrm{r}}^{\mathrm{m}} = \overline{q}_{\mathrm{r}}^{\mathrm{He}} \cdot \mathrm{p(He)} + \overline{q}_{\mathrm{r}}^{\mathrm{H_2}} \cdot \mathrm{p(H_2)} \tag{11.38}$$

Using this equation, the resulting values of $\overline{q}_{\mathrm{r}}^{\mathrm{m}}$ describe well the average charge states of ^{254}No ions in the gas mixtures over a wide range of gas pressures.

11.7 Preparation of Samples for Activity Measurements

Careful consideration must be given to the chemical and physical form in which samples are to be measured. α emitters are usually counted in the form of thin deposits, preferably prepared by electrodeposition and placed inside a proportional counter or near a Si detector. Nuclides that emit soft radiations such as soft β radiation, X-rays, conversion electrons, or Auger electrons may be assayed for activity if they can be prepared in the form of a gas suitable as part of a counter-gas mixture. Typically, ^{14}C compounds may be burned to CO_2 and added to the counting-gas mixture that is introduced into a proportional counter. Close to 100% counting efficiency can be obtained for CO_2 partial pressures up to 5 mbar, but a good gas handling and purification system is mandatory. Much in use for the measurement of weak β emitters such as ^{3}H and ^{14}C are liquid scintillation counters, especially for applications in organic and biochemistry. Ready-to-use scintillator cocktails are commercially available. They can hold up to 20% water without appreciable quenching.

In nuclear research, β active nuclides are prepared as thin solid samples and measured preferably with thin-window counters. Sorption and self-absorption can be troublesome and need attention. If a sample emits both β- and γ-rays, γ assay is the method of choice. In order to avoid troublesome consequences of effects such as backscattering, self-scattering, and self-absorption (Chapter 9) in measurements of β activities, weightless samples should be mounted on nearly weightless supports (plastic films of less than 0.1 mg cm^{-2}) and assayed in a 4π counter.

Among the various sample mounting techniques, evaporation of a solution to dryness is one of the simplest techniques. Normally, this leaves a rather nonuniform deposit with most of the residue in a ring around the edge. To avoid this, the preparation of a hydrophobous surface can be useful. Another trick is the addition of a wetting agent (e.g. tetraethylene glycol), or precipitation and settling of the radioactive material prior to evaporation. Coprecipitation and filtering by using a Hahn suction frit and subsequent drying of the deposit could be an alternative way of preparing uniform samples for measurement. Whenever possible, these should be covered by a thin film of Formvar or Mylar to avoid contamination of the counter. The preparation

of extremely thin ("weightless") samples can be done by electrodeposition. Samples for 4π counting and for measurements of β-spectral shapes must not only be thin themselves but also be mounted on equally thin backings. Because an insulating film of plastic can become highly charged as a result of the emission of charged particles from the source, the potential building up can seriously distort the spectrum of emitted particles. Therefore, films used for β-spectrometer samples should always be rendered conducting by evaporation of a thin (μg) metal coating, and grounded. Further techniques familiar from target preparation such as volatilization and electrospray are sometimes in use as well. For radionuclides that are themselves formed by radioactive decay, preferably by α decay, recoil techniques have been particularly useful. Similarly, the recoil energy imparted by a nuclear reaction can be used to deposit the desired product nuclei on a suitable catcher foil, Section 11.5. These techniques have gained particular importance in the investigation of transuranic nuclei produced in accelerator bombardments.

11.8 Determination of Half-Lives

The enormous range of experimentally accessible half-lives requires various measurement techniques, representative cases of which we want to introduce in this chapter.

For very long half-lives, the activity may not change measurably in a reasonable counting time. Then, the decay constant λ may be obtained from $\lambda N = -\mathrm{d}N/\mathrm{d}t = A/\eta$, provided the activity A can be determined in an absolute way through knowledge of the counting efficiency η, and N is known or can be determined, for example, mass spectrometrically, by the isotope-dilution technique, see Section 20.7. Alternatively, the disintegration rate may be obtained from the measurement of the equal disintegration rate of a daughter in secular equilibrium. For example, determinations of the half-life of ^{235}U were based on the α-particle counting rate of ^{231}Pa obtained in a known yield from old uranium ores. This was of advantage because the α particles of ^{235}U could not be measured due to the much larger rate of α decays of ^{238}U and ^{234}U.

Half-lives of years to hundreds of years can be determined by differential measurements. Here, one compares as a function of time the activity of a sample having the half-life to be determined to that of a sample that is practically nondecaying. The technique involves the measurement of the ratio of the two activities as a function of time in a single counter. Thereby, the samples must be counted always under exactly the same conditions. If the decay constant of the reference source is negligible compared to the decay constant λ to be determined, the ratio $R = c\ \mathrm{e}^{-\lambda t}$ with c being a constant. With 10^7 to 10^8 counts per measurement, the half-life can be determined to an accuracy of 5–10% within measurements over a period of $\frac{1}{100}\ t_{1/2}$.

Half-lives in the range of seconds to years are determined by measuring a decay curve and plotting log A vs. time, see Figures 9.1–9.4. Multiple components of different half-lives can be fitted to the data by the least-squares procedure. It is always advantageous to use energy-selective detectors such as semiconductor detectors to measure separately the activities of several radionuclides present in the sample.

More sophisticated techniques are required as the half-lives get shorter. Either the time dependence or the decay rate is still the observed quantity. The lower limit to the half-life is then determined by the dead time of the detector, but in practice often by the transport time of the activity from the production site to the detector. In the other type of experiment, rather the distribution of time intervals between formation and decay of a radionuclide is used, which is given by the exponential decay law.

In experiments of the type addressed first, the short-lived radioisotope is the product of a nuclear reaction and recoils out of the target. It is caught on a rapidly moving conveyor and transported to a detector which measures the decay curve. In the second type of experiments, one needs a start signal when the radionuclide is formed and a stop signal when it decays. The two signals are sent to an electronic circuit that records the distribution in elapsed time between the two signals. In a recoil separator, for instance, the start signal is from the implantation of the EVR in the position-sensitive focal-plane detector. The stop signal is the α- or sf decay recorded at the same position. If the time distances between the start and stop signals are treated on a logarithmic time scale, the frequency distribution of decay times $\mathrm{d}N/\mathrm{d}t = N\lambda \mathrm{e}^{-\lambda t}$ is changed to the following form, where the substitution $\ln(t) = \vartheta$ is used:

$$\frac{\mathrm{d}N}{\mathrm{d}\vartheta} = N\lambda \mathrm{e}^{\vartheta}\mathrm{e}^{-\lambda \mathrm{e}^{\vartheta}} \tag{11.39}$$

In this representation, the ideal radioactive decay curve becomes a peak with a universal shape, and the number of counts N and the lifetime τ determine the height and position of this peak. An example is shown in Figure 11.18. It is taken from an experiment performed at the gas-filled separator TASCA at the GSI Helmholtz Center for Heavy-Ion Research in which the ^{244}Pu(^{22}Ne, 4n)^{262}Rf reaction was investigated at a beam energy of 109 MeV in the center of the target (cot). In all, 10 EVR implantation events with energies between 1.4 and 3.3 MeV correlated with SF events at the same positions in the detector array in time intervals $\Delta t_{\mathrm{EVR\text{-}SF}}$ between 46 and 684 ms were recorded and assigned to the 4n EVR ^{262}Rf. In addition, 15 implantation signals with higher energies of 4–15 MeV, typical for target-like transfer products, followed at the same detector positions by SF with correlation times below 4 ms were recorded and assigned to decays of 0.9 ms $^{244\mathrm{m}}$Am and 73 µs $^{246\mathrm{m}}$Am fission isomers (dashed curves in Figure 11.17). The time analysis resulted in a half-life for the newly identified ^{262}Rf of 190^{+100}_{-50} ms (solid line in Figure 11.17). The data allowed for a clear distinction between EVR-SF correlations from EVRs of the complete fusion reaction and Am fission isomers due to significant differences in correlation times and implantation energies. Previous values for the half-life of ^{262}Rf were either 47 ms or 2.1 seconds. The 47 ms is the result of an experiment in which Am fission isomers and the 4n EVR could not be distinguished. The 2.1 seconds is the half-life of $^{261\mathrm{b}}$Rf, the 5n EVR, erroneously assigned to the 4n channel.

For short-lived γ emitters, we have discussed in Section 6.7.1, Doppler shift methods using a plunger, the Doppler shift attenuation method, and the use of the natural line width ΔE where $\Delta E \cdot \Delta t = \hbar$.

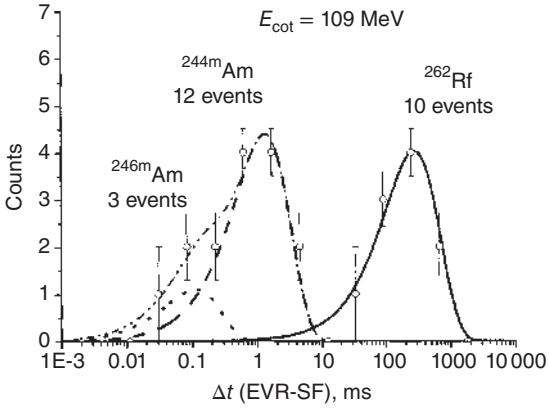

Figure 11.18 Correlation times Δt(EVR-SF) of products from the ^{244}Pu(^{22}Ne, 4n) reaction at 109 MeV (cot) producing 190 ms ^{262}Rf (10 events, fit: solid line), and of the transfer products 0.9 ms ^{244m}Am (12 events, fit: dot–dashed line) and 73 μs ^{246m}Am (3 events, fit: dotted line). The sum of the latter two contributions is also indicated. Source: Gorshkov et al. (2008). Elsevier.

11.9 Decay-Scheme Studies

Much but not all of our knowledge about nuclear structure has been obtained in decay-scheme studies. These are one branch of nuclear spectroscopy in which radioactive decay populates excited levels up to some energy determined by the Q value of the decay, that is, in a limited energy window. Even in this energy range, not all levels may be populated because of selection rules. There are many radionuclides whose level schemes are not accessible through decay studies but can be investigated by other techniques such as Coulomb excitation, inelastic scattering, nuclear reactions, and in-beam γ-ray spectroscopy. Some of these topics were touched upon in Section 5.11, others will be covered in Chapter 12, and some in-beam techniques will be mentioned at the end of this chapter.

A complete decay scheme includes all modes of decay of a radionuclide, the energies and transition rates of the radiations, their sequence, half-lives of intermediate states, and the quantum numbers, in particular angular momenta and parities of the levels involved. The amount of detail available depends on the instrumentation and techniques used in the experiments. Even when the decay scheme of a nuclide is under investigation, it may not be available free from other radioactive isotopes. Then, measurements have to be made as a function of time to sort out those radiations associated with the nuclide of interest. First, the half-life needs to be established. Then, the decay modes are identified through use of selective detectors for, for example, α, β, and γ radiation, conversion electrons, X-rays, and fission fragments. Determinations of the energy spectra of these radiations are obtained with the energy-sensitive detectors described in Chapter 9. Questions about the sequence in which the radiations are emitted are answered by coincidence measurements. Coincidence techniques are helpful in energy determinations also. Imagine a low-intensity, low-energy β branch in the presence of an intense high-energy ground-state transition. In that case, the former may escape detection in a β-spectrographic measurement. However, as the high-energy β spectrum is not coincident with γ-rays, but the low-energy branch is, a β measurement in coincidence with γ-rays will detect the low-energy component. With a β spectrometer

and a Ge detector in coincidence, the β spectrum coincident with each of several γ radiations may be observed.

To illustrate the techniques of decay-scheme studies, a relatively simple example is presented in the following. It encompasses the same general principles that would be encountered in much more common and much more complicated decay-scheme studies. A useful simple example is the decay of ^{198}Au with a half-life of 2.696 days. It was thought to decay by emission of a single β^- group with $Q_\beta = 0.96$ MeV and allowed spectrum shape to the first excited state at 412 keV in ^{198}Hg (see Figures 6.40 and 6.43). The energy of the subsequent γ decay has been determined with high precision, for example, by magnetic spectrometer measurements of conversion electrons, and is given as $411.804\,41 \pm 0.000\,15$ keV and the internal conversion coefficients are $\alpha_K = 0.0300 \pm 0.0003$, $\alpha_K/\alpha_L = 2.79 \pm 0.05$, and $\alpha_{L_I}/\alpha_{L_{II}}/\alpha_{L_{III}} = 2.2/2.2/1.0$ establishing $E2$ multipolarity for the 412 keV transition. As the ground state of ^{198}Hg is 0^+, the angular momentum and parity of the 412 keV level must be 2^+. Careful measurements of the spectral shape of the 0.961 MeV β spectrum showed that a correction factor was required to linearize the Kurie plot and the transition was thus identified as nonunique first forbidden in agreement with the log *ft* value of 7.4. The angular momentum and parity of ^{198}Au could thus be 1^-, 2^-, or 3^-, with 1^- excluded immediately because this would make the β transition rate to the ground state of ^{198}Hg have the same order as that to the 412 keV level, which is not the case. With scintillation counters, two additional weak γ transitions in the decay of ^{198}Au were identified. Their energies were subsequently determined with high precision through conversion electron spectroscopy as 0.675 88 and 1.087 67 MeV. Their intensities relative to the 412 keV transition are $1.1 \cdot 10^{-2}$ and $2.4 \cdot 10^{-3}$, respectively. The energies of the three γ transitions suggest that there is a second excited state in ^{198}Hg at 1.088 MeV with decays to the ground state and to the 412 keV level. The 0.676 MeV transition is in coincidence with the 0.412 MeV transition, and the 1.088 MeV transition is not coincident with other γ-rays. Internal conversion coefficients for the 0.676 MeV transition are $\alpha_K = 0.022 \pm 0.002$ and $\alpha_K/\alpha_L = 5.7 \pm 0.5$ pointing at an $M1$–$E2$ mixture. For the 1.088 MeV transition $\alpha_K = 0.0045 \pm 0.0003$ and $\alpha_K/\alpha_L = 6.3 \pm 0.5$, an $E2$ assignment is appropriate. The 1.088 MeV state is then 2^+ as is the first excited state at 0.412 MeV. More detailed information about the $M1$–$E2$ mixing ratio came from angular correlation measurements. Coincidence experiments showed that the 0.676 MeV γ-ray is coincident with the conversion electrons of the 0.412 MeV transition and with a β^- spectrum of endpoint energy 0.290 ± 0.015 MeV and an intensity of 1.3%. Another β^- transition of 0.025% intensity and an endpoint energy of 1.37 MeV was found in a magnetic spectrometer and represents the ground-state transition; the log *ft* value of approximately 12 corroborates this assignment. Finally, the lifetime of the 0.412 MeV level has been determined by delayed coincidences to be 23 ps. This is to be compared to single-particle estimates of 0.5 ns for $E2$ and 0.3 ps for $M1$, respectively. The magnetic moment of the 0.412 MeV state was measured by observing the precession of the angular correlation in an external magnetic field. Additional low-lying states in ^{198}Hg not populated in ^{198}Au decay have been found in the decay of ^{198}Tl and in nuclear reaction studies.

As we indicated above, the particular decay scheme just discussed in detail is unusually simple. It was presented in order to illustrate some essential features that would be equally applicable to more complex decay-scheme studies. To indicate what a more typical decay scheme looks like, we show in Figure 11.19 the level scheme of ^{99}Tc as deduced from the β^- decay of ^{99}Mo. We refrain here from discussing it, but mention that, as pointed out in Section 11.4.3, the couple ^{99}Mo/^{99m}Tc is used in the most frequently used radionuclide generator from which 6.01 hours ^{99m}Tc is milked, which is the workhorse in nuclear medicine. The isomer ^{99m}Tc (142.6833 keV, $1/2^-$) decays by a 2.1726 keV $E3$ transition to a $7/2^+$ level at 140.511 keV whose γ transition ($M1 + E2$) to the ground state of ^{99}Tc ($9/2^+$) is used for imaging. Because of the extremely long half-life of ^{99}Tc, the latter does not cause any health physics problems.

11.10 In-Beam Nuclear Reaction Studies

With the exception of the recoil-separation techniques using gas-filled separators or Wien filters, the techniques used to produce and to handle radionuclides that were presented in the preceding sections were "off-line" techniques. We now proceed to "on-line" or in-beam studies in which particles (anything from γ quanta to fission fragments) and recoil nuclei are detected within an ongoing nuclear reaction.

The identification of particles emitted in a reaction requires the simultaneous measurement of specific ionization and at least two of the following observables: kinetic energy, momentum, and velocity.

Kinetic energy, for modest energies, is obtained by stopping the particle completely in a gas ionization chamber or semiconductor detector in which a pulse proportional to the kinetic energy is detected. Nonrelativistic momenta are determined by magnetic deflection where the radius of curvature ρ of a particle of momentum m and charge q in a magnetic field B is m/Bq. Energy loss $\mathrm{d}E/\mathrm{d}x$ lets the particle pass through a semiconductor, proportional counter, or ionization chamber that is thin compared to its range and a variety of particle identification schemes are based on this technique. They involve a counter telescope, in which one or more thin transmission detectors measure $\Delta E/\Delta x$, and a total absorption detector. Particle identification was first done by using an electronic circuit that forms the product of E and $\mathrm{d}E/\mathrm{d}x$ which, according to the Bethe–Bloch equation, is proportional to Mq^2. By plotting the number of events against this product, a particle identifier spectrum is obtained. By using algorithms somewhat more complicated than $E \times (\mathrm{d}E/\mathrm{d}x)$, individual isotopes can be resolved up to $q \sim 10$, see Figure 11.20, and individual elements up to $Z \leq 50$ with the upper limit depending on the energy. Velocity is determined from a ToF measurement. Two detectors a distance d apart provide start and stop signals and a time-to-amplitude converter converts the time interval Δt into a pulse height. Obviously, $v = d/\Delta t$. The start and stop signals are often provided by the secondary electrons emitted from very thin carbon foils in the path of the particle where the electrons are detected by a channel plate. ToF measurements can be combined with E and $\mathrm{d}E/\mathrm{d}x$ measurements by using

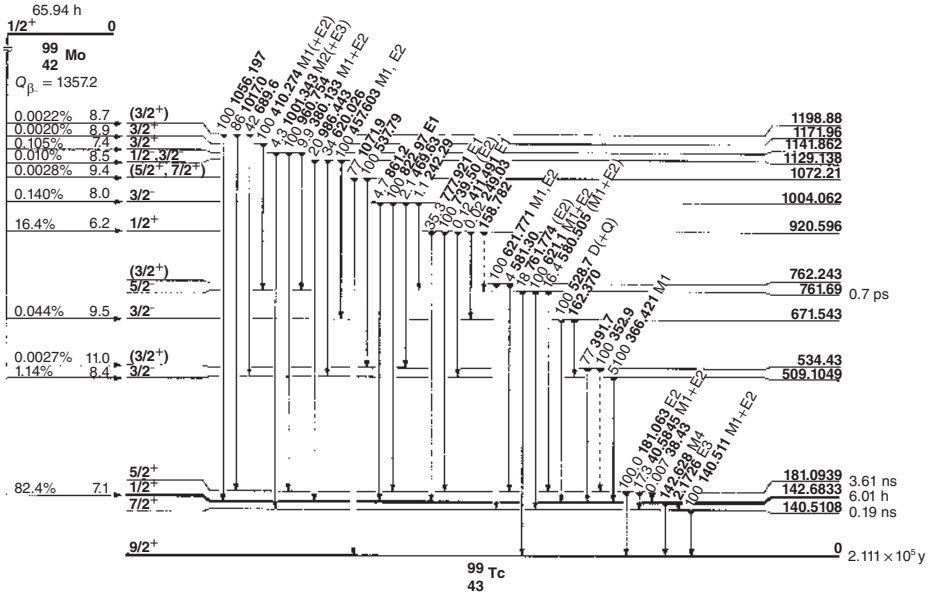

Figure 11.19 Level scheme of ^{99}Tc as deduced from studies of the β^- decay of ^{99}Mo. Source: Firestone and Shirley (1996), figure 03 (p. 50)/John Wiley & Sons.

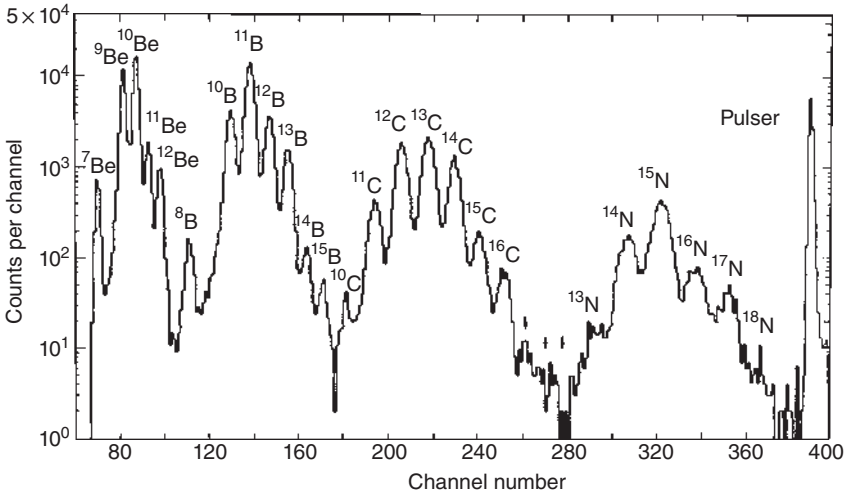

Figure 11.20 Particle identifier spectrum obtained in energy loss measurements in semiconductor detectors in the interaction of 5.5 GeV protons with ^{238}U. Source: Poskanzer et al. (1968), figure 02 (p. 5)/Elsevier.

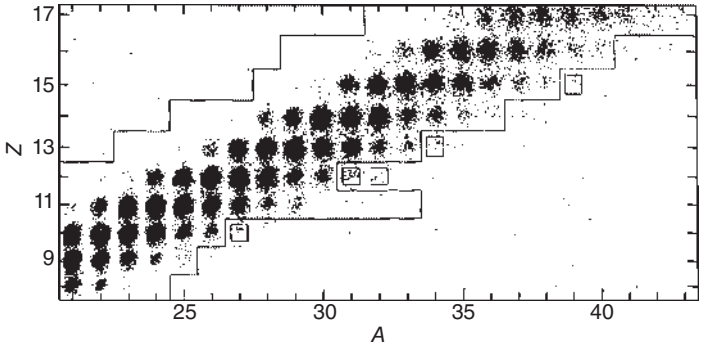

Figure 11.21 *Z*–*A* distribution of fragments from the interaction of 800 MeV protons with ^{238}U identified by a combination of $\Delta E/\Delta x$ and ToF measurements. The boxes indicate the new nuclides ^{27}Ne, ^{31,32}Mg, ^{34}Al, and ^{39}P. The solid lines enclose the region of previously known nuclei. Source: Butler et al. (1977), figure 04 (p. 15)/American Physical Society.

the distance between the ΔE and E detectors as the flight path. The combination of velocity and kinetic energy information gives in principle unambiguous mass identification. However, instrumental limitations make isotopic resolution difficult for $q \geq 15$ unless high kinetic energies are present where resolution up to $Z \approx 40$ can be achieved. The combination of E, dE/dx, and ToF measurements has been used for the identification of new isotopes as illustrated in Figure 11.21.

In studies of fission, spallation reactions, and heavy-ion reactions, mass analysis of reaction products is a powerful tool. One such device is the LOHENGRIN separator at the high-flux reactor at Grenoble in France, where unslowed fission products are separated according to their charge-to-mass ratios by a focusing mass spectrograph

of moderately high resolution. Kinetic energy spectra of mass-separated fission products can be determined as well as the dependence of fission yields along a mass chain on kinetic energy. In heavy-ion reactions, direct mass analysis of unslowed reaction products by magnetic deflection has been combined with ToF, dE/dx, or energy measurements. More widely used is the mass analysis of stopped reaction products: on-line isotope separators, so-called ISOL facilities, have been installed at accelerators and reactors. The principle is schematically depicted in Figure 11.22. A particularly prolific one is ISOLDE, belonging to CERN's accelerator complex (http://cern.ch/isolde). The facility has been in operation since 1967 and is presently receiving protons from the PS-Booster accelerator. The typical proton energy is 1.4 GeV, which can be lowered to 1 GeV on request. Depending on the isotopes of interest and possible isobaric contamination, the target material and the subsequent ion source are chosen to match the experimental requirements, namely, production yield and purity. More than 25 different target materials are offered with uranium carbide being the most versatile. The target material is kept at an elevated temperature, in the case of uranium carbide at 2000 °C, so that the produced exotic atoms diffuse out of the target into an adjacent ion source. The ionization takes place in a hot plasma, on a hot surface, or by laser excitation. The resonance ionization laser ion source (RILIS) is particularly selective through stepwise resonant excitation of atoms to above the ionization threshold. With a careful combination of target material and ion source type, chemical selectivity may be obtained, thus resulting in the selective production of more than 70 of the chemical elements. There is continuous target and ion source development going on. With REX-ISOLDE isotopes as heavy as radon have been post-accelerated to 3 MeV per nucleon with efficiencies reaching up to 10%. The multiply charged ions needed for post-acceleration are produced by stopping the singly charged ions from ISOLDE in a Penning trap, transferring them to an electron beam ion source where they are brought to mass-to-charge ratios between $A/q = 3$ and 4.5 before magnetic separation and acceleration. The main user of the post-accelerated beams is the MINIBALL γ array. It consists of eight cryostats each containing three individual Ge crystals that are mounted in close geometry around the target position. In Coulomb excitation experiments, the spherical target and detection chamber are equipped with a double-sided silicon strip detector (DSSSD) to detect projectile and/or target particles. The DSSSD allows one to determine the energy (velocity) and scattering angle of the detected particles, which is necessary for the Doppler correction of the γ-ray spectrum. It is also possible to investigate one or two neutron transfer reactions.

Atomic beam experiments with radioactive ions were pioneered at ISOLDE and still provide important and model-independent information on nuclear ground-state properties such as charge radius, spin, magnetic dipole moment, and electric quadrupole moment. Most studies involve collinear laser spectroscopy. COLLAPS uses different detection techniques to obtain information on hyperfine splitting and isotope shifts. Most common is the classical collinear laser spectroscopy where fluorescence light emitted by the excited atoms is detected. The ISOLTRAP Penning trap mass spectrometer is used for high-precision measurements of atomic masses, see Section 3.5. The WITCH experiment aims at a test of the Standard Model by

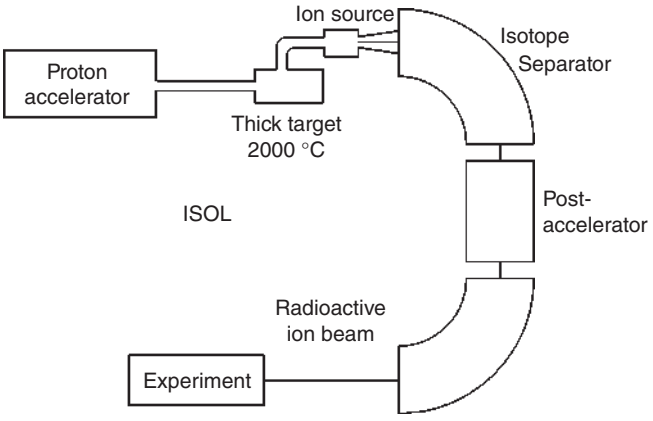

Figure 11.22 Schematic view of the ISOL technique for generating radioactive beams.

probing the recoil energy spectrum after β decay of selected isotopes in order to search for scalar or tensor contributions to the weak interaction. The NICOLE experiment aims at the measurement of magnetic dipole moments by use of oriented nuclei at low temperatures and on-line β-NMR. This brief facility portrait cannot provide a complete overview of all recent ISOLDE experiments. We note in passing that there is also an active solid-state physics program going on. The next major upgrade is the HIE-ISOLDE project in which the post-acceleration will be increased up to 10 MeV u^{-1}.

A powerful alternative to ISOL facilities are the accelerator facilities producing relativistic radioactive beams by projectile fragmentation. The scheme of such a facility is depicted in Figure 11.23. One example, among several others, is the heavy-ion synchrotron (SIS) in combination with the fragment separator (FRS), see Chapter 16, at the GSI Helmholtz Center for Heavy-Ion Research. The SIS can accelerate all ions, from hydrogen to uranium, to a maximum magnetic rigidity of 18 Tm, which corresponds to energies of 1–4.5 GeV u^{-1}. Secondary beams of radioactive isotopes can be produced (typically in a 2 g cm^{-2} Be target) via projectile fragmentation and can be efficiently separated in flight by the FRS. The FRS is an achromatic magnetic forward spectrometer with a momentum resolving power of 1500 for an emittance of 20π mm mrad. Heavy-ion beams with magnetic rigidities up to 18 Tm can be analyzed by the device. The system has four independent stages, each consisting of a 30° dipole magnet and a set of quadrupoles before and after the dipole to fulfill first-order focusing conditions. The ion optical system can be corrected for second-order aberrations by using sextupole magnets in front of and behind each dipole magnet. In practice, it is necessary that the selected radioactive beam is spatially separated from all other reaction products. Due to the relativistic velocities of the projectile fragments, a separation by A and Z is not possible using only magnetic sector fields. Therefore, a combination of magnetic rigidity analysis and energy loss of the fragments in matter was chosen. The principle of separation as adapted to the FRS is schematically presented in Figure 11.23. The keys to isotopic separation are an achromatic ion optical system characterized by a high momentum resolution and a profiled energy degrader

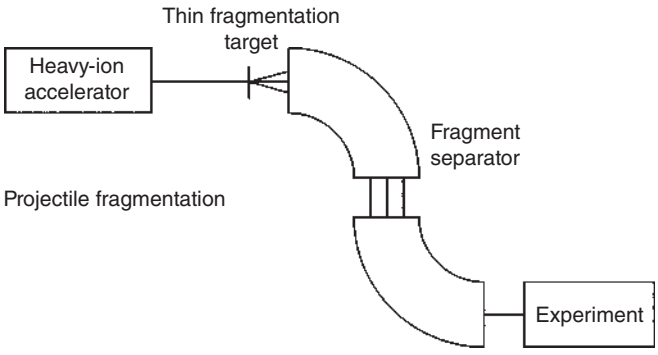

Figure 11.23 Scheme of a projectile fragmentation facility for the production of relativistic radioactive beams.

placed at the dispersive focal plane. The first two dipole stages of the FRS perform an A/Z selection for fully ionized reaction products; that is, the fragments with the same magnetic rigidity are focused on the same position of the energy degrader. The different energy loss of the ions penetrating the degrader provides the additional selection needed for the separation of a selected nuclide ($B\rho - \Delta E - B\rho$ method). An experimental result demonstrating the separation method is presented in the lower part of Figure 11.24. In this experiment, the FRS was tuned for ^{18}F produced by fragmentation of 500 MeV u^{-1} ^{40}Ar in a 2 g cm^{-2} Be target. With magnetic separation only (without the achromatic degrader) the FRS delivers a beam cocktail of fragments with approximately the same A/Z ratio. Radioactive beams from the FRS can either be injected into the experimental storage ring (ESR) (mentioned in Section 3.5) for high-resolution mass measurements, for example, or it can be transported to one of the experimental setups dedicated for reaction studies and nuclear spectroscopy. The experimental techniques used there will be illustrated in the following by selecting the ALADIN-LAND experiments as an example.

The experimental method applied by the *LAND* (Large-Area Neutron Detector) collaboration consists of producing high-energy radioactive beams with kinetic energy typically a few hundred mega-electronvolts per u and a kinematically complete measurement of breakup reactions in secondary targets ("breakup spectroscopy"). The measurement is exclusive or kinematically complete in the sense that all reaction products with velocities close to the beam velocity and γ-rays are detected. A schematic drawing of the detection setup is depicted in Figure 11.25. The experimental results exemplified in the following paragraphs utilized radioactive beams produced by fragmentation of primary ^{40}Ar and ^{18}O beams delivered by the SIS. Typical primary-beam intensities were 10^{10} ions s^{-1}. Fragment beams were selected by the FRS according to their magnetic rigidity only. Thus, mixed secondary beams with similar A/Z ratio were transported to the experimental area. The incident projectiles were uniquely identified on an event-by-event basis by utilizing energy loss and ToF measurements. An example is shown in the upper left panel of Figure 11.25 where the composition of a mixed beam of ^{40}Ar fragments can be seen. The settings of the FRS and the beam line were optimized for the

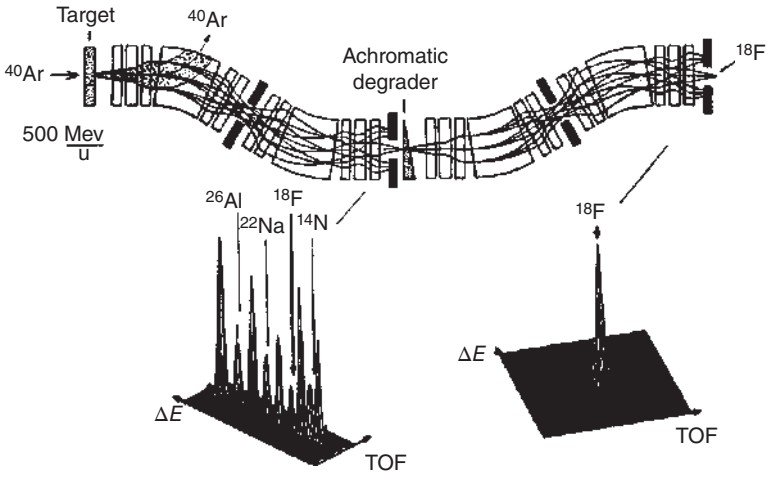

Figure 11.24 The isotopic separation principle of the FRS illustrated by measured fragment distributions produced by ^{40}Ar projectiles. The goal of this experiment was to demonstrate the separation and implantation of ^{18}F ions. Source: Geissel et al. (1992), figure 02 (p. 100/Elsevier.

transport of ^{22}O. In a similar manner, the fragments produced in the reaction target are identified. Here, the magnetic rigidity is determined from three position measurements defining the trajectories of the charged projectile residues in the magnetic field of ALADIN (A Large-Aperture DIpole magNet) placed behind the target. Additional energy loss and ToF measurements allow unique identification of the outgoing fragments and determination of their momenta. The lower right panel of Figure 11.25 shows an example of identified fragments produced in the breakup of ^{20}O in a carbon target.

Neutrons emitted from the excited projectile or excited projectile-like fragments are kinematically focused in the forward direction and are detected with high efficiency (∼90%) in LAND (Section 9.10). The momenta of the neutrons are determined from the ToF and position information. The angular range for fragments and neutrons covered by the detectors corresponds to a 4π measurement of the breakup in the rest frame of the projectile for fragment-neutron relative energies up to 5.5 MeV (at 500 MeV u^{-1} beam energy).

At the high beam energies used, the γ-rays must be detected with good angular resolution in order to minimize Doppler broadening effects. In Figure 11.25, the crystal ball spectrometer consisting of 160 NaJ(Tl) detectors is shown. The breakup target is positioned in the center of it. The excitation energy prior to breakup is obtained by reconstructing the Lorentz-invariant mass combining the results of the measurements described above. The resolution in excitation energy depends on the relative fragment-neutron kinetic energy and on the resolution for measuring the γ sum energy in the projectile rest frame in the case of the population of excited states. It changes from about 200 keV close to the threshold to a few megaelectronvolts in the region of the giant dipole resonance (GDR) (at excitation energies around

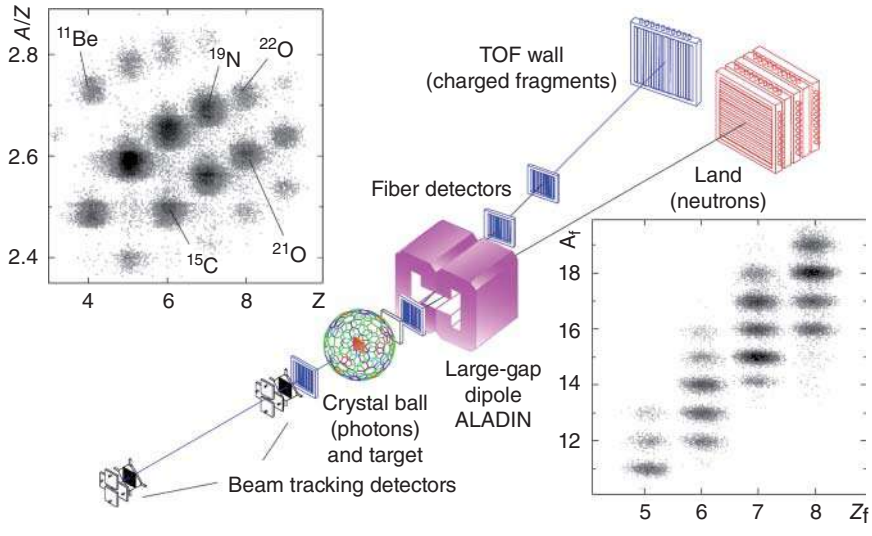

Figure 11.25 Schematic drawing of the LAND detection setup (not to scale). Shown are the beam and fragment detectors, the crystal ball photon spectrometer, the large-aperture dipole magnet ALADIN, and the neutron detector LAND placed about 11 m downstream from the target. The upper left panel shows the composition of the mixed radioactive beam impinging on the secondary target positioned in the center of the crystal ball. The lower right panel displays the fragment identification for reactions of ^{20}O in a carbon target. Source: Aumann (2005), figure 03 (p. 25)/Springer Nature.

15 MeV). In order to extract the electromagnetic excitation (Coulomb excitation) cross section, breakup in a lead target is used and the nuclear contribution is determined from a measurement with a carbon target and scaled accordingly before subtraction. Among the halo nuclei (Section 4.1), two-neutron halo nuclei have attracted particular interest due to their three-body character with their two-body subsystems both being unbound. Because of this property, they were named "Borromean" nuclei. For the study of two-neutron halo nuclei, various information about their nuclear structure can be gained in breakup spectroscopy:

i. the momentum distribution of the fragments and of the neutrons contains direct information about the ground-state wave function of the projectile;
ii. the reconstruction of the invariant mass allows the reconstruction of the excitation energy spectra of unbound intermediate states (resonances) through which the halo nucleus decays;
iii. the angular correlation between the direction of the momentum of the intermediate state and the relative momentum of the decay products gives information about angular momentum and the parity of the intermediate state;
iv. the structure of the halo continuum can be investigated by electromagnetic excitation; and
v. correlations between the halo neutrons can be investigated.

In the following, we shall look at the one-neutron knockout reactions with ^{6}He, ^{8}He, and ^{11}Li halo nuclei illustrating items (i)–(iii) listed above.

The transverse momentum distribution of the recoiling unbound ^{5}He after one-neutron knockout from 240 MeV u^{-1} ^{6}He projectiles in a carbon target (as reconstructed from α and neutron momenta) is displayed in the left frame of Figure 11.26. The dashed curve corresponds to the full Fourier transformation of the theoretical three-body wave function. After introducing a radial cutoff in order to account for the peripheral nature of the reaction process (the experiment requires the detection of an intact ^{4}He core), perfect agreement with the experimental data is achieved (solid curve) indicating an intermediate state with $l = 1$. The sensitivity to the angular momentum of the halo neutron ($p(^5\mathrm{He}) = -p(\mathrm{n})$) becomes evident by looking at the much narrower dot–dashed curve that holds for an s state ($l = 0$). The invariant-mass spectrum of ^{5}He (α–n relative kinetic energy distribution) after one-neutron knockout from ^{6}He in a carbon target is shown in the right frame of Figure 11.26. A prominent peak coinciding with the energy of the known $p_{3/2}$ ground-state resonance in ^{5}He (0.89 MeV above the α + n + n state which is separated from the ^{6}He ground state by $S_{2n} = 0.97$ MeV) is visible. The dotted curve shows the ^{5}He ground-state resonance in a Breit–Wigner parameterization which, after convolution with the experimental resolution (solid histogram), accounts for most of the measured cross section. This is consistent with a two-step process: one-neutron knockout leading to the unbound ^{5}He resonance with a comparatively long lifetime which subsequently decays into α + n far away from the reaction zone.

The presence of the intermediate ^{5}He resonance can also be seen in the angular correlation observed between the direction of the ^{5}He momentum and the decay direction, that is, the α + n relative momentum

$$p_{\alpha n} = \frac{m_\alpha m_n}{m_\alpha + m_n}\left(\frac{p_\alpha}{m_\alpha} - \frac{p_n}{m_n}\right).$$

(The angular momentum vector of ^{5}He is aligned perpendicular to the plane that is defined by the projectile momentum vector and the ^{5}He momentum vector.) The distribution on this angle $\vartheta_{\alpha n}$ is shown in the lower left panel of Figure 11.26 exhibiting an anisotropy characteristic of a relative angular momentum $l_n = 1$. The solid histogram which describes the data very well results from a Monte Carlo calculation assuming an angular correlation function $W \sim 1 + 1.5\cos^2(\vartheta_{\alpha n})$. Experimental effects are taken into account in the Monte Carlo simulation. A two-step process involving only the $p_{3/2}$ resonance, however, would yield a correlation function $W \sim 1 + 3\cos^2(\vartheta_{\alpha n})$, with an anisotropy twice as large as the observed one. The experimental result can be understood quantitatively by assuming a 7% admixture only of the higher-lying $p_{1/2}$ resonance in ^{5}He. An energy diagram showing the states involved and the observed reaction paths is shown in Figure 11.27. It is important to note that the presence of the angular correlation between the ^{5}He momentum and the decay direction shows that the (α + n) center-of-mass motion is indeed correlated with the initial momentum of the halo neutron prior to the knockout reaction, and thus carries the information on the projectile wave function.

A similar experiment utilizing a 227 MeV u^{-1} ^{8}He beam was performed to study states in the unbound nucleus ^{7}He after one-neutron knockout in a carbon target.

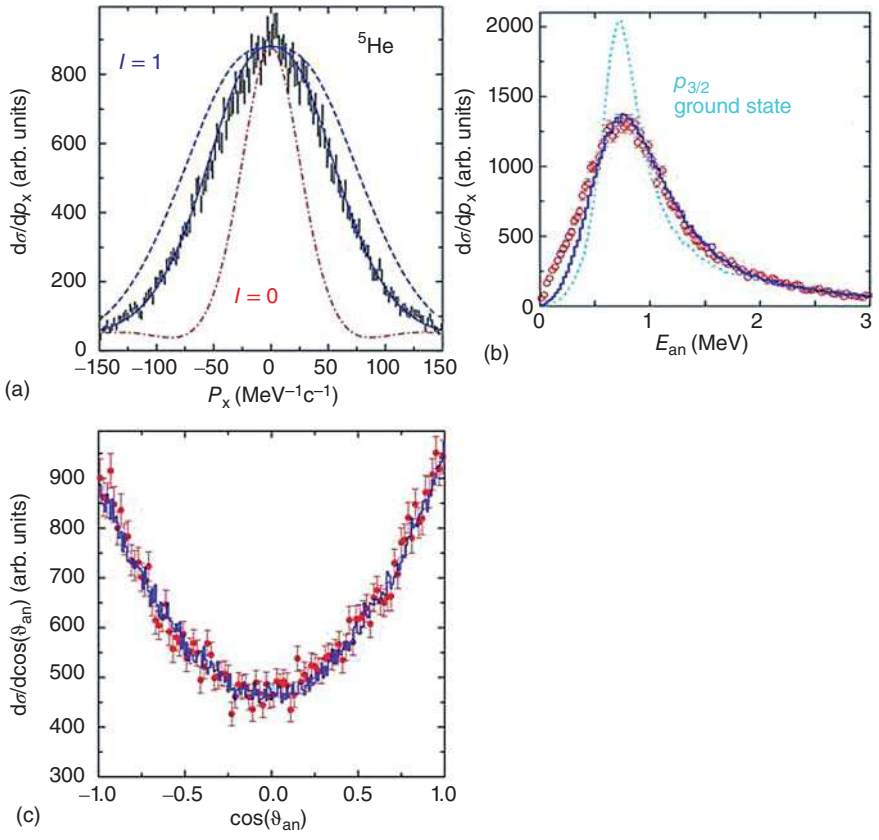

Figure 11.26 One-neutron removal reaction from ^{6}He (240 MeV u^{-1}) on a C target measured with the LAND reaction setup at GSI. (a) Transverse momentum distribution of ^{5}He compared to calculations for $l = 1$ with (solid curve) and without (dashed curve) taking into account the peripheral nature of the reaction. To demonstrate the sensitivity of the distribution to the angular momentum, the distribution for $l = 0$ (dot–dashed curve) is also indicated. (b) α–n relative energy distribution. The dotted curve shows the ^{5}He ground-state resonance, which after convolution with the instrumental response (solid histogram) accounts for most of the measured cross section. (c) Angular correlation in the decay of ^{5}He, see text. Source: T. Aumann.

The ^{6}He–n relative energy spectrum shown in Figure 11.28 exhibits a narrow resonance around 400 keV corresponding to the known $p_{3/2}$ ground state of ^{7}He. The shape of the spectrum at higher excitation energies can be well described by a fit assuming a second resonance with resonance energy $E_r = 1.0(1)$ MeV and a width $\Gamma = 0.75$ MeV interpreted as the $p_{1/2}$ spin–orbit partner of the ground state, see the proposed level scheme inset in Figure 11.28. This implies a small splitting of the $p_{3/2}$ and $p_{1/2}$ states of 0.6 MeV only, which should be compared to the lowest possible estimate of this energy difference in ^{5}He, which is 1.2 MeV. Thus, a considerable decrease of the spin–orbit splitting is found when approaching the neutron drip line. This reduction might be related to the fact that the spin–orbit force, which

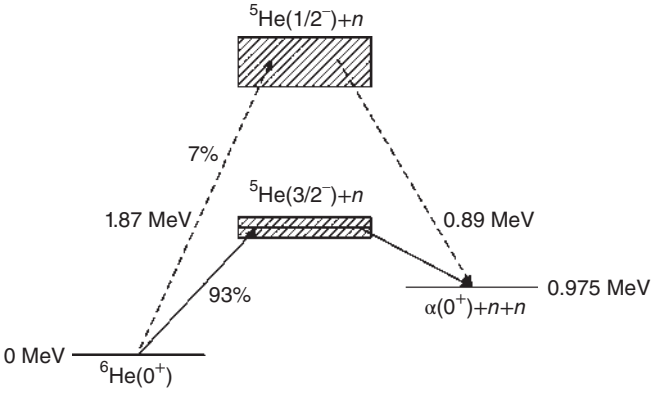

Figure 11.27 Energy level diagram of the states and reaction paths involved in the one-neutron removal reaction of ^{6}He in a C target. Source: T. Aumann.

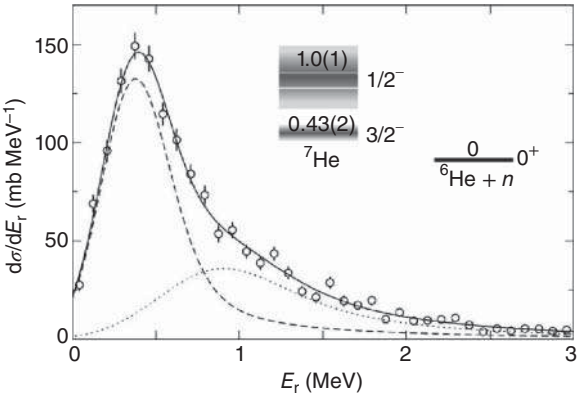

Figure 11.28 Relative energy spectrum of the ^{6}He–n system measured after breakup of a 227 MeV ^{8}He beam in a C target. The spectrum is described by a fit (solid curve) assuming two resonances. Also shown is the proposed level scheme of ^{7}He. Source: T. Aumann.

is proportional to $-(1/r)\,\mathrm{d}V/\mathrm{d}r$, becomes smaller due to the difference in size and diffuseness between stable nuclei of normal nuclear density and the more and more diluted nuclear structure when adding excessive numbers of neutrons. As the occurrence of shell gaps in the sequence of single-particle energy levels, Section 5.5, is closely related to the large spin–orbit splitting in stable nuclei, the strongly decreasing spin–orbit splitting in nuclei with increasing isospin may be related to the observed phenomenon of a "quenching" of shell effects in nuclei far from β stability.

It is interesting to compare the results obtained in the one-neutron knockout reactions with ^{6,8}He to the ^{11}Li case. Here, the knockout reaction populates unbound states in ^{10}Li. The left frame in Figure 11.29 shows the ^{10}Li invariant-mass spectrum for a 287 MeV u^{-1} ^{11}Li beam impinging on a carbon target. The spectrum can be described by assuming two states in ^{10}Li populated with about equal intensity corresponding to the knockout from the $(s_{1/2})^2$ or $(p_{3/2})^2$ components in ^{11}Li, respectively. This interpretation is supported by the transverse momentum distribution of ^{10}Li shown in the right frame of Figure 11.29. A fit to the distribution

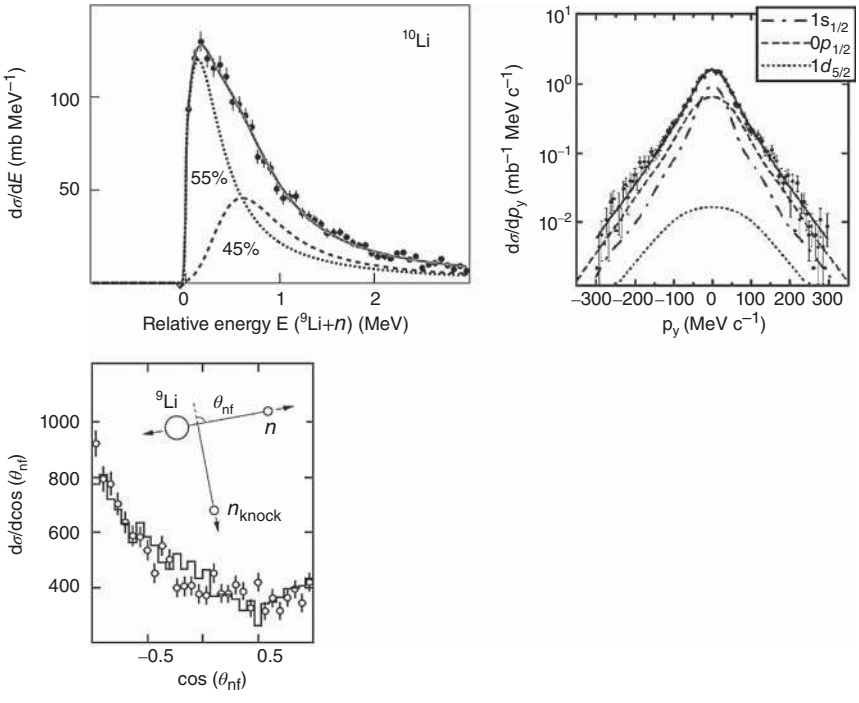

Figure 11.29 One-neutron removal reaction of 287 MeV u^{-1} ^{11}Li in a C target measured with the LAND reaction setup at GSI. Left panel: ^{10}Li invariant-mass spectrum. Right panel: ^{10}Li transverse momentum distribution. Bottom panel: Angular correlation in the decay of ^{10}Li. The spectra are consistent with a mixture of $(s_{1/2})^2$ and $(p_{3/2})^2$ with about equal intensity in the ^{11}Li ground state. Source: Aumann (2005)/Springer Nature.

yields $l = 0$ and $l = 1$ components with similar cross sections. Bertulani and Hansen (2004) extracted corresponding spectroscopic factors of 33(2) and 64(5) for the two components, respectively. They also included a d component in the fit, which turns out to be very small, 4(3)%, see Figure 11.29. The angular correlation shown in the bottom panel gives independent evidence of a mixture of s and p states in the ^{11}Li wave function. There is not only anisotropy but also an asymmetric shape. The asymmetry comes from the interference between the two different decay paths populating different-parity states in ^{10}Li: the ground state (s state) and exited states with $l = 1$.

In summary, the breakup reaction of 2n halo nuclei on light targets is dominated by a two-step process, see Figure 11.30: knockout of one of the halo neutrons populating states in the unbound $A-1$ nucleus which subsequently decay into core +n. The states in the daughter nucleus are identified by the invariant-mass method, and the angular momentum l of the knocked-out neutron is determined from the momentum distribution of the core +n recoiling system. Further information on the quantum numbers of the states involved is obtained with high sensitivity from the angular correlations. The new quality inherent in the breakup spectroscopy as

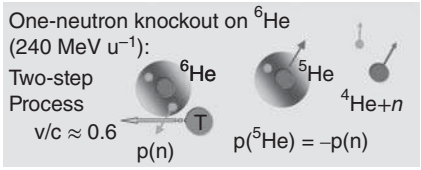

Figure 11.30 Pictorial representation of the one-neutron knockout reaction of a two-neutron halo nucleus (^{6}He as an example) as a two-step process. The target nucleus knocks out one of the halo neutrons of the projectile with momentum p(n). The unbound intermediate state, here ^{5}He, is emitted with momentum $p(^5\text{He}) = -p(\text{n})$. The angular momentum vector of the intermediate state is aligned perpendicular to the plane that is defined by the projectile momentum vector and the momentum vector of the intermediate state. In the subsequent decay of the unbound intermediate state, this gives rise to an angular correlation between the direction of the core momentum and the core-n relative momentum. Source: T. Aumann.

compared to decay-scheme studies, Section 11.9, is the unequivocal, direct access to the wave functions.

Electromagnetic dissociation of halo nuclei in lead targets with large cross sections can be explained by nonresonant transitions to the continuum due to a large overlap between the tail of the neutron wave function and continuum wave functions with large wave lengths, that is, small relative momenta. Dipole strengths and energy-weighted sum rules are obtained this way, containing information on the splitting of the dipole motion into that of the core, that of the halo neutrons, and that of the relative motion between core and halo. We refrain from going into more detail at this point.

In peripheral heavy-ion collisions at energies of 1 GeV u^{-1}, collective nuclear states at high excitation energies are excited with large cross sections. Due to the high velocity and Lorentz contraction, the mutual electromagnetic field contains high frequencies up to several tens of megaelectronvolts per $\hbar$ and is of transverse nature. A measure of the maximum excitation energy is the "adiabatic cutoff"

$$E_{\max} = \frac{\hbar}{\tau} = \frac{\hbar c \gamma \beta}{b} \tag{11.40}$$

with γ and β being the relativistic Lorentz factor and the velocity, respectively, and b the impact parameter. With a typical minimum impact parameter of $b_{\min} = 14$ fm for a medium heavy nucleus impinging on a lead target, 25 MeV is estimated as the maximum excitation energy for a beam energy of 1 GeV u^{-1}. With this, the excitation of the GDR becomes dominant reaching cross sections of the order of 1 barn. The electromagnetic excitation of the GDR induced by high-energy beams on targets of high nuclear charge was studied systematically in a series of experiments exploring the multiphonon states of the dipole resonance (see the review by Aumann et al. (1998)). Due to a large excitation probability reaching 30% for heavy nuclei at grazing impact, two-step excitations of the second phonon of the GDR vibration (2-ph GDR) become possible with large cross sections. The measurements with stable nuclei have demonstrated that the (γ, n) cross sections and thus the $B(E1)$ strength distribution can be reliably extracted from the measured cross sections. It was also shown that the only free parameter entering into the semiclassical

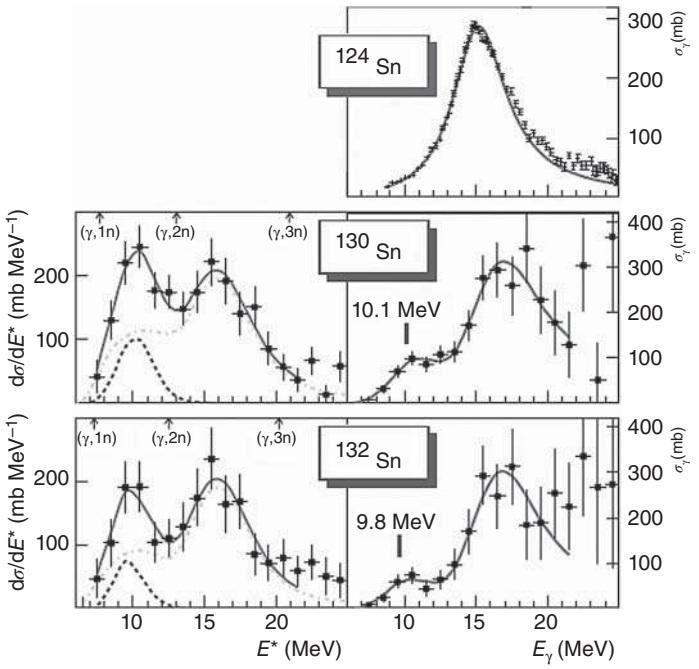

Figure 11.31 Left frames: differential cross sections for the electromagnetic excitation of ^{130,132}Sn in a lead target at about 500 MeV u^{-1}. Right panels: corresponding photoneutron cross sections. The solid curves are the result of a fit of a Lorentzian (GDR region) plus a Gaussian (low-lying peak) including convolution with the instrumental response. The dot dashed and dashed curves represent the individual contributions. Upper right frame: for comparison, photoneutron cross sections for the stable isotope ^{124}Sn measured in a real-photon experiment. Source: Adrich et al. (2005), figure 02 (p. 32)/American Physical Society.

calculations, the minimum impact parameter $b_{\min}$, is well determined from systematics. With this background, the evolution of the dipole strength distribution as a function of neutron-to-proton ratio was investigated systematically. We restrict our discussion here to the electromagnetic excitation of heavy neutron-rich Sn isotopes produced as a mixed secondary beam including ^{132}Sn produced by fission of a ^{238}U beam with an energy around 600 MeV u^{-1}. The differential cross section for the electromagnetic excitation of ^{130,132}Sn (∼500 MeV u^{-1}) on a lead target is displayed in Figure 11.31 (left frames). The right frames display the corresponding photo-absorption (γ, n) cross sections. The upper right panel shows the result of a real-photon experiment for the stable isotope ^{124}Sn for comparison. The spectrum is dominated by the excitation of the GDR. A fit of a Lorentzian plus Gaussian parameterization for the photo-absorption cross sections of ^{130,132}Sn (solid curves) yields positions and widths of the GDR comparable to those known for stable nuclei in this mass region. The GDR almost exhausts the energy-weighted TRK sum rule (Section 5.11). It should be noted that the spectrum shown for ^{132}Sn was obtained from a measurement with a rather low beam intensity of about 10 ^{132}Sn ions s^{-1}

only. An additional peak structure is clearly visible below the GDR energy region. The position around 10 MeV is close to the predicted energy of a soft collective mode (Pygmy resonance) by a relativistic quasi-particle random-phase approximation (QRPA). The Pygmy resonance is thought to be a collective vibration of the neutron skin (Section 4.1) against the core of the nucleus and the experimentally observed strength in this peak corresponds to 4% of the TRK sum rule, also in good agreement with QRPA predictions. The existence of low-lying $E1$ Pygmy resonance strength was shown to have a striking impact on the astrophysical r-process abundance distribution.

References

Target Preparation

Lieser, K.H. and Wertenbach, H. (1962). *Z. Phys. Chem.* 34: 1.

Runke, J., Düllmann, Ch.E., Eberhardt, K. et al. (2014). Preparation of actinide targets for the synthesis of heaviest elements. *J. Radioanal. Nucl. Chem.* 299: 1081.

Measuring Beam Intensities and Fluxes

Schädel, M. et al. (1978). Chemical separations of actinides from irradiated uranium targets. *Radiochim. Acta* 25: 111.

Knoll, G.F. (2000). *Radiation Detection and Measurement*, 3e. New York: Wiley.

Tsoufanidis, N. (1995). *Measurement and Detection of Radiation*, 2e. Washington, DC: Taylor & Francis.

Radionuclide Production at Reactors and Accelerators

Stöcklin, G.V. and Pike, W. (eds.) (1993). *Radiopharmaceuticals for Positron Emission Tomography*. Dordrecht: Kluwer Academic.

Carver, J.H. and Turchinetz, W. (1959). *Proc. Phys. Soc.* 73: 110.

Qaim, S.M. (ed.) (2001). Nuclear data for medical applications. *Radiochim. Acta* 89: 279.

Qaim, S.M. (2011). Cyclotron production of medical radionuclides. In: *Handbook of Nuclear Chemistry*, 2e, vol. 4 (eds. A. Vértes, S. Nagy, Z. Klencsár, et al.), 1903. Berlin: Springer-Verlag.

Generators

Rösch, F. and Knapp, F.F. (2011). Radionuclide generators. In: *Handbook of Nuclear Chemistry*, 2e, vol. 4 (eds. A. Vértes, S. Nagy, Z. Klencsár, et al.), 1935. Berlin: Springer-Verlag.

Recoil Techniques

Ghiorso, A., Yashita, S., Leino, M.E. et al. (1988). Sassy, a gas-filled magnetic separator for the study of fusion reaction products. *Nucl. Instrum. Methods Phys. Res.* A269: 192.

Gregorich, K.E., Loveland, W., Peterson, D. et al. (2005). Attempt to confirm superheavy element production in the $^{48}Ca+^{238}U$ reaction. *Phys. Rev.* C72: 014605.

Khuyagbaatar, J., Ackermann, D., Andersson, L.-L. et al. (2012). Study of the average charge states of ^{188}Pb and ^{252,254}No ions at the gas-filled separator TASCA. *Nucl. Instrum. Methods Phys. Res.* A689: 40.

General

Gorshkov, A. et al. (2012). *Study of the Average Charge States of 188Pb and 252,254No Ions at the Gas-filled Separator TASCA*. Elsevier.

Firestone, R.B. and Shirley, V.S. (eds.) (1996). *Table of Isotopes*, 8e. New York: Wiley.

In-Beam Nuclear Reaction Studies

Adrich, P. et al. (2005). Evidence for Pygmy and giant dipole resonances in ^{130}Sn and ^{132}Sn. *Phys. Rev. Lett.* 95: 132501.

Aumann, T. (2005). Reactions with fast radioactive beams of neutron-rich nuclei. *Eur. Phys. J.* A26: 441.

Aumann, T., Bortignon, P.F., and Emling, H. (1998). Multiphonon giant resonances. *Annu. Rev. Nucl. Part. Sci.* 48: 351.

Bertulani, C.A. and Hansen, P.G. (2004). Momentum distributions in stripping reactions of radioactive projectiles at intermediate energies. *Phys. Rev.* C70: 034609.

Butler, G.W., Perry, D.G., Remsberg, L.P. et al. (1977). Observation of the new nuclides ^{27}Ne, ^{31}Mg, ^{32}Mg, ^{34}Al, and ^{39}P. *Phys. Rev. Lett.* 38: 1380.

Geissel, H., Armbruster, P., Behr, K.H. et al. (1992). The GSI projectile fragment separator (FRS); a versatile magnetic system for relativistic heavy ions. *Nucl. Instrum. Methods Phys. Res.* B70: 286.

Poskanzer, A.M., Butler, G.W., Hyde, E.K. et al. (1968). Observation of the new isotope ^{17}C using a combined time-of-fligjt particle-identification technique. *Phys. Lett.* 27B: 414.

Radionuclide Production at Reactors and Accelerators

Stoughton, R.W. and Halperin, J. (1959). *Nucl. Sci. Eng.* 6: 100.

Further Reading

General

Hahn, O. (1936). *Applied Radiochemistry*. Ithaca, NY: Cornell University Press.

Wahl, A.C. and Bonner, N.A. (1951). *Radioactivity Applied to Chemistry*. New York: Wiley.

Garrison, W.M. and Hamilton, J.G. (1951). Production and isolation of carrier-free radioisotopes. *Chem. Rev.* 49: 237.

Cook, C.B. and Duncan, J.F. (1952). *Modern Radiochemical Practice*. Oxford: Clarendon Press.

Whitehouse, W.J. and Putman, J.L. (1953). *Radioactive Isotopes – An Introduction to their Preparation, Measurement and Use*. Oxford: Clarendon Press.

Meinke, W.W. (ed.) (1959–1962). *Monographs on the Radiochemistry of the Elements, Subcommittee on Radio-Chemistry*, Nuclear Science Series, NAS-NS 3001–3058. Washington, DC: National Academy of Sciences. National Research Council.

Meinke, W.W. (ed.) (1960–1965). *Monographs on Radiochemical Techniques, Subcommittee on Radio-Chemistry*, Nuclear Science Series, NAS-NS 3101–3120. Washington, DC: National Academy of Sciences, National Research Council.

Haissinsky, M. (1964). *Nuclear Chemistry and its Applications*. Reading, MA: Addison-Wesley.

International Atomic Energy Agency (1971). Radioisotope Production and Quality Control. IAEA Technical Reports Series No. 128. Vienna.

McKay, H.A.C. (1971). *Principles of Radiochemistry*. London: Butterworths.

Maddock, A.G. (1972). Radiochemistry. In: *International Review of Science, Inorganic Chemistry*, vol. 7. London: Butterworths [and vol. 8 (1975)].

Faires, R.A. and Parks, B.H. (1973). *Radioisotope Laboratory Techniques*, 3e. London: Butterworths.

Evans, E.A. and Muramatsu, M. (eds.) (1977). *Radiotracer Techniques and Applications*. New York: Marcel Dekker.

Malcolme-Lawes, D.J. (1978). *Introduction to Radiochemistry*. London: Macmillan.

Geary, W. (1986). *Radiochemical Methods*. New York: Wiley.

Ehmann, W.D. and Vance, D.E. (1991). *Radiochemistry and Nuclear Methods of Analysis*. New York: Wiley.

Adloff, J.P. and Guillaumont, R. (1993). *Fundamentals of Radiochemistry*. Boca Raton, FL: CRC Press.

L'Annunziata, M.F. (ed.) (2003). *Handbook of Radioactivity Analysis*. San Diego, CA: Academic Press.

Eberhardt, K., Brüchle, W., Düllmann Ch.E. et al. (2008). Preparation of targets fort the gas-filled separator TASCA by electrochemical deposition and design of the TASCA target wheel assembly. *Nucl. Instrum. Methods Phys. Res.* A590: 134.

Liebe, D., Eberhardt, K., Hartmann, W. et al. (2008). The application of neutron activation analysis, scanning electron microscopy, and radiographic imaging fort the characterization of electrochemically deposited layers of lanthanide and actinide elements. *Nucl. Instrum. Methods Phys. Res.* A590: 145.

Special Aspects of the Chemistry of Radionuclides

Zvara, I. (1976). One atom at a time chemical studies of transactinide elements. In: *Transplutonium Elements* (eds. W. Müller and R. Lindner), 11. Amsterdam: North-Holland.

Herrmann, G. and Trautmann, N. (1976). Rapid chemical separation procedures. *J. Radioanal. Chem.* 32: 533.

Beneš, P. and Majer, V. (1980). *Trace Chemistry of Aqueous Solutions*. Amsterdam: Elsevier.

Guillaumont, R., Chevallier, P., and Adloff, J.P. (1987). Identification of oxidation states of ultra-trace elements by radiation detection. *Radiochim. Acta* 40: 191.

Guillaumont, R., Adloff, J.P., and Peneloux, A. (1989). Kinetic and thermodynamic aspects of tracer scale and single atom chemistry. *Radiochim. Acta* 46: 169.

Guillaumont, R., Adloff, J.P., Peneloux, A., and Delamoye, P. (1991). Sub-tracer scale behaviour of radionuclides, application to actinide chemistry. *Radiochim. Acta* 54: 1.
Guillaumont, R. and Adloff, J.P. (1992). Behaviour of environmental plutonium at very low concentration. *Radiochim. Acta* 58: 53.

Target Preparation

Parker, W.C. and Slätis, H. (1965). Sample and window techniques. In: *Alpha-, Beta-, and Gamma-Ray Spectroscopy*, vol. 1 (ed. K. Siegbahn), 379. Amsterdam: North-Holland.
Adair, H.L. and Kobisk, E.H. (1984). Heavy-ion targets. In: *Treatise on Heavy-Ion Science*, vol. 7 (ed. D.A. Bromley), 119. New York: Plenum Press.

Radionuclide Production at Reactors and Accelerators

McMillan, E.M. (1959). Particle accelerators. In: *Experimental Nuclear Physics*, vol. III (ed. E. Segre), 639. New York: Wiley.
Livingstone, M.S. and Blewett, J.P. (1962). *Particle Accelerators*. New York: McGraw-Hill.
Blewett, M.H. (1963). The electrostatic (Van de Graaff) generator. In: *Methods of Experimental Physics*, vol. 5B (eds. L.C.L. Yuan and C.S. Wu), 584. New York: Academic Press.
Lapostolle, P.M. and Septier, L. (1970). *Linear Accelerators*. Amsterdam: North-Holland.
Wolf, A.P. and Jones, W.B. (1983). Cyclotrons for biomedical radioisotope production. *Radiochim. Acta* 34: 1.
Humphries, S. (1986). *Principles of Charged Particle Accelerators*. New York: Wiley.
Scharf, W. (1986). *Particle Accelerators and their Uses*. New York: Harwood.
Mirzadeh, S., Mausner, L.F., and Garland, M.A. (2011). Reactor-produced medical radionuclides. In: *Handbook of Nuclear Chemistry*, 2e, vol. 4 (eds. A. Vértes, S. Nagy, Z. Klencsár, et al.), 1857. Berlin: Springer-Verlag.

Separation Procedures

Kraus, K.A. and Nelson, F. (1957). Radiochemical separations by ion exchange. *Annu. Rev. Nucl. Sci.* 7: 31.
Freiser, H. and Morrison, G.H. (1959). Solvent extraction in radiochemical separations. *Annu. Rev. Nucl. Sci.* 9: 221.
Stary, J. (1964). *The Solvent Extraction of Metal Chelates*. Oxford: Pergamon.
Marcus, Y. and Kertes, A.S. (1969). *Ion Exchange and Solvent Extraction of Metal Complexes*. New York: Wiley.
Korkisch, J. (1969). *Modern Methods for the Separation of Rarer Metal Ions*. Oxford: Pergamon.
De, A.K., Khopar, S.M., and Chalmers, R. (1970). *Solvent Extraction of Metals*. London: Van Nostrand.
Braun, T. (1975). *Radiochemical Separation Methods*. Amsterdam: Elsevier.
Trautmann, N. and Herrmann, G. (1976). Rapid chemical separation procedures. *J. Radioanal. Chem.* 32: 533.
Marinsky, J.A. and Marcus, Y. (eds.) (1981). *Ion Exchange and Solvent Extraction*, A Series of Advances, vol. 1–8. New York: Marcel Dekker.

Korkisch, J. (1989). *Handbook of Ion Exchange Resins: Their Application to Inorganic Analytical Chemistry*, vol. I–VI. Boca Raton, FL: CRC Press.

Lehto, J. and Hou, X. (2010). *Chemistry and Analysis of Radionuclides – Laboratory Techniques and Methodology*. Weinheim: Wiley-VCH.

Generators

Spitsyn, V.I. and Mikheev, N.B. (1971). Generators for the production of short-lived radioisotopes. *At. Energy Rev.* 9: 787.

Lieser, K.H. (1976). Chemische Gesichtspunkte fur die Entwicklung von Radionuklidgeneratoren. *Radiochim. Acta* 23: 57.

Lambrecht, R.M. (1983). Radionuclide generators. *Radiochim. Acta* 34: 9.

Knapp, F.F. Jr. and Butler, T.A. (eds.) (1984). *Radionuclide Generators*, ACS Symposium Series. Washington, DC: American Chemical Society.

Boyd, R.E. (1987). Technetium generators; status and prospects. *Radiochim. Acta* 41: 59.

Recoil Techniques

Harvey, B.G. (1960). Recoil techniques in nuclear reactions and fission studies. *Annu. Rev. Nucl. Sci.* 10: 235.

Alexander, J.M. (1968). Studies of nuclear reactions by recoil techniques. In: *Nuclear Chemistry* (ed. L. Yaffe), 273. New York: Academic Press.

Semchenkov, A., Brüchle, W., Jäger, E. et al. (2008). The transactinide separator and chemistry apparatus (TASCA) at GSI – optimization of ion-optical structures and magnet designs. *Nucl. Instrum. Methods Phys. Res.* B266: 4153.

In-Beam Nuclear Reaction Studies

Klapisch, R. (1974). On-line mass separation. In: *Nuclear Spectroscopy and Reactions*, vol. A (ed. J. Cerny), 213. New York: Academic Press.

MacFarlane, R.D. and McHarris, W.C. (1974). Techniques for the study of short-lived nuclei. In: *Nuclear Spectroscopy and Reactions*, vol. A (ed. J. Cerny), 244. New York: Academic Press.

Goulding, F.S. and Harvey, B.G. (1975). Identification of nuclear particles. *Annu. Rev. Nucl. Sci.* 25: 167.

Münzenberg, G. (1992). The separation techniques for secondary beams. *Nucl. Instrum. Methods Phys. Res.* B70: 265.

Zhukov, M.V., Danilin, B.V., Fedorov, D.V. et al. (1993). Bound state properties of borromean halo nuclei: 6He and 11Li. *Phys. Rep.* 231: 151.

Goriely, S. (1998). Radiative neutron captures by neutron-rich nuclei in the r-process nucleosynthesis. *Phys. Lett.* B436: 10.

Paar, N., Ring, P., Niksic, T., and Vretenar, D. (2003). Quasiparticle random phase approximation based on the relativistic Hartree-Bogoliubov model. *Phys. Rev.* C67: 034312.

Jonson, B. (2004). Light dripline nuclei. *Phys. Rep.* 389: 1.

12

Nuclear Reactions

A nuclear reaction is a process in which a nucleus reacts with a proton or another nucleus, an elementary particle, or a photon to produce one or more other nuclei and possibly other particles. The nuclear states that can be investigated in the decay of radioactive isotopes as discussed in Section 11.9 are limited to a relatively low energy range. A much larger energy range is accessible through nuclear reactions. It is of great principle and practical importance to understand the various reaction mechanisms that occur in nuclear collisions.

The phenomenon of nuclear reactions was discovered by Rutherford in 1919 when he observed that, in the bombardment of nitrogen with the 6.69 MeV α particles of ^{214}Po, scintillation of a zinc sulfide screen persisted even when enough material to absorb all the α particles was interposed between the nitrogen and the screen. Further experiments showed that the long-range particles causing the scintillation were protons and Rutherford's first reaction may be written as

$$^{14}_{7}\mathrm{N} + {}^{4}_{2}\mathrm{He} \rightarrow {}^{17}_{6}\mathrm{O} + {}^{1}_{1}\mathrm{H}$$

with the shorthand notation ^{14}N(α,p)^{17}O where, as indicated here, atomic numbers are commonly omitted. Most nuclear reactions are studied by inducing a collision between two nuclei where one of the nuclei is at rest, the target nucleus, and the other nucleus, the projectile, is in motion. In a nuclear reaction, there is conservation of the total number of nucleons A, charge, energy, momentum, angular momentum, statistics, and parity. Nuclear reactions, like chemical reactions, are always accompanied by a release or absorption of energy, and this is expressed by adding the term to the right-hand side of the equation. Thus, a more complete statement of Rutherford's first reaction is

$$^{14}\mathrm{N} + {}^{4}\mathrm{He} \rightarrow {}^{17}\mathrm{O} + {}^{1}\mathrm{H} + Q$$

The quantity Q is the energy of the reaction or simply the reaction Q value. Other than in chemistry, the convention is to assign positive Q values to energy-releasing reactions (exoergic reactions) and negative Q values to energy absorption (endoergic reactions). Another important difference between chemical reactions and nuclear reactions must be pointed out. In chemical reactions, macroscopic amounts of material undergo transmutation and heats of reaction are given per mole of the reactants. In nuclear reactions, single processes are considered

Nuclear and Radiochemistry: Fundamentals and Applications,
Fourth Edition. Jens-Volker Kratz.

and the Q values are therefore given per nucleus transformed. For example, the reaction ^{14}N(α,p)^{17}O has a Q value of -1.190 MeV or $-1.190\,66 \cdot 10^{-6}$ ergs or $-4.56 \cdot 10^{-14}$ cal per ^{14}N atom transformed. To convert 1 mol of ^{14}N to ^{17}O would require an energy of $6.022 \cdot 10^{23} \cdot 4.56 \cdot 10^{-14}$ cal $= 2.75 \cdot 10^{10}$ cal. This is 5 orders of magnitude larger than the largest values observed for heats of chemical reactions. The Q value is calculated with tabulated mass excesses, see Eq. (3.5), as $Q = \Delta(^{14}\text{N}) + \Delta(^{4}\text{He}) - (\Delta(^{17}\text{O}) + \Delta(^{1}\text{H})) = 2.863 + 2.425 - (-0.811 + 7.289\,03)$ MeV $= -1.190$ MeV. Does that mean that the reaction can actually be produced by α particles whose kinetic energies are just over 1.19 MeV? The answer is no for two reasons. First, in the collision, conservation of momentum requires that at least 4/18 of the kinetic energy of the α particle must be retained by the products as kinetic energy. Thus, only 14/18 of the α particle's kinetic energy is available for the reaction. The threshold energy of α particles for the ^{14}N(α, p)^{17}O reaction is $18/14 \times 1.19$ MeV $= 1.53$ MeV. The second reason why the α particles must have higher energies than the Q value is the Coulomb repulsion between the α particle and the ^{14}N nucleus, Eq. (1.15),

$$V_C = 1.44 \frac{Z_1 Z_2}{R_1 + R_2} \text{MeV}$$

Setting $R = 1.5A^{1/3}$ fm, we get a value of about 3.4 MeV for the Coulomb barrier between the α particle and the ^{14}N nucleus. Thus, classically, an α particle must have $18/14 \times 3.4 = 4.4$ MeV kinetic energy for the (α, p) reaction to occur even though the energetic threshold for the reaction is only 1.53 MeV. In the quantum mechanical treatment of the problem, there exists a finite probability for barrier penetration, but the probability is extremely small as we saw in the discussion of α decay in Section 6.2.

12.1 Collision Kinematics

Generalizing the above discussion, and using the notation $A_1 + A_2 \rightarrow A_3 + A_4$, we can describe the situation before the collision in the laboratory system by

$$E_{\text{lab}} = \frac{m}{2} A_1 v_\infty^2 \tag{12.1}$$

$$P_{\text{lab}} = m A_1 v_\infty \tag{12.2}$$

where m is the nucleon mass, A_1 is the mass number of the projectile, and v_∞ is the velocity at infinite distance with

$$v_\infty = \sqrt{\frac{2E_{\text{lab}}}{mA_1}} = 1.389 \sqrt{\frac{E_{\text{lab}}}{A_1}} \text{ cm ns}^{-1} \tag{12.3}$$

In the center-of-mass system, Figure 12.1, before the collision, both ions move toward the center of mass, S, with

$$v_1 = \frac{A_2}{A_1 + A_2} v_\infty$$

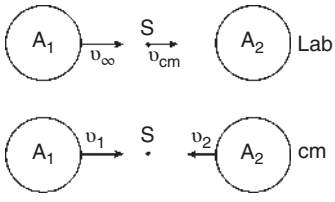

Figure 12.1 Laboratory and center-of-mass system before the collision.

$$v_2 = \frac{A_1}{A_1 + A_2} v_\infty \tag{12.4}$$

The kinetic energy and momentum in the center-of-mass system are

$$E_{\text{cm}} = \frac{m}{2}(A_1 v_1^2 + A_2 v_2^2) = \frac{\mu}{2} v_\infty^2 \tag{12.5}$$

$$P_{\text{cm}} = m(A_1 v_1 + A_2 v_2) = \mu v_\infty$$

where μ, the reduced mass, equals

$$m\frac{A_1 A_2}{A_1 + A_2} = mA_{12}$$

Only the center-of-mass energy E_{cm} and the relative momentum P_{cm} are available for the reaction. The remainder is translational energy (recoil energy) of the total system

$$E_{\text{trans}} = \frac{A_1}{A_1 + A_2} E_{\text{lab}} \tag{12.6}$$

and

$$E_{\text{cm}} = E_{\text{lab}} - E_{\text{trans}} \tag{12.7}$$

The translational velocity of the center of mass relative to the laboratory system is

$$v_{\text{cm}} = \frac{A_1}{A_1 + A_2} v_\infty = v_2 = \sqrt{\frac{2E_{\text{trans}}}{m(A_1 + A_2)}} = 1.389\sqrt{\frac{E_{\text{trans}}}{A_1 + A_2}} \text{ cm ns}^{-1} \tag{12.8}$$

Another useful energy variable is the laboratory energy per nucleon

$$\epsilon = \frac{E_{\text{lab}}}{A_1} = \frac{E_{\text{cm}}}{A_{12}} = \frac{m}{2} v_\infty^2 \tag{12.9}$$

After the collision, the situation is as depicted in Figure 12.2. In the center-of-mass system, the product A_3 is emitted with velocity v_3 under the center-of-mass angle Θ. It is common to look explicitly at the projectile-like product A_3; for the target-like fragment, the corresponding variables result from trivial transformation. Figure 12.2 also shows the situation in the laboratory system: vector addition of v_3 and v_{cm} yields $v_{3\text{lab}}$ under laboratory angle $\vartheta_{3\text{lab}}$. The connection between $\vartheta_{3\text{lab}}$ and Θ_{cm} is

$$\tan \vartheta_{3\text{lab}} = \frac{v_3 \sin \Theta}{v_3 \cos \Theta + v_{\text{cm}}} = \frac{\sin \Theta}{\cos \Theta + \frac{v_{\text{cm}}}{v_3}} \tag{12.10}$$

and vice versa

$$\Theta = \vartheta_{3\text{lab}} + \arcsin \frac{v_{\text{cm}} \sin \vartheta_{3\text{lab}}}{v_3}$$

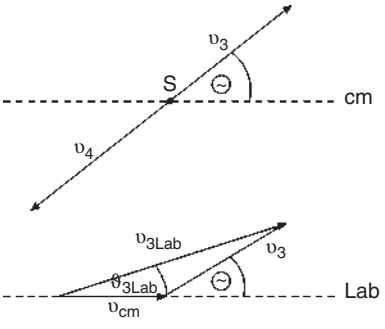

Figure 12.2 Center-of-mass and laboratory system after the collision.

It is customary to introduce the kinematic variable $\gamma_3 = \upsilon_{cm}/\upsilon_3$. For elastic scattering, $\upsilon_3 = \upsilon_1$ and $\gamma_3 = A_1/A_2$. For two colliding ions of equal mass, $\gamma_3 = 1$ and $\vartheta_{3lab} = \Theta/2$. In the general case of a two-body reaction, the quantity γ_3 is given by

$$\gamma_3 = \left(\frac{A_1 A_3}{A_2 A_4}\frac{E_{cm}}{E_{cm}+Q}\right)^{1/2} \tag{12.11}$$

where the Q value can also be determined as the difference of the kinetic energies after and before the reaction as $Q = E_f^\infty - E_i^\infty$ equal to the total kinetic energy loss $\mathrm{TKEL} = \mathrm{TKE_i} - \mathrm{TKE_f} = -Q$. The ∞ sign indicates that the particles need to be separated far enough from each other so that the interaction potential is no longer acting. Because of the conservation of the total energy, the Q value at the same time corresponds to the difference of the rest masses of the initial and final state (Eq. (3.5)).

12.2 Coulomb Trajectories

Figure 12.3 shows the classical trajectories of two colliding ions in the center-of-mass system. The distance of closest approach between the two centers of gravity, D, and the scattering angle Θ is related by

$$D = a\left(1 + \csc\frac{\Theta}{2}\right) \quad \text{with} \quad \csc\frac{\Theta}{2} = \frac{1}{\sin\frac{\Theta}{2}} \tag{12.12}$$

where the parameter a is defined as one-half the distance of closest approach in a head-on collision ($\Theta = 180°$):

$$a = \frac{Z_1 Z_2 e^2}{\mu \upsilon_\infty^2} \tag{12.13}$$

Together with the asymptotic wavelength of relative motion at large separation, $\lambda = \hbar/\mu\upsilon_\infty$, we obtain the Sommerfeld parameter

$$n = \frac{a}{\lambda} = \frac{Z_1 Z_2 e^2}{\hbar \upsilon_\infty} \quad \text{or} \quad n = a \cdot k = 0.157\frac{Z_1 Z_2}{\sqrt{\epsilon}} \tag{12.14}$$

where large values of n correspond to nearly classical motion ($\lambda \ll R$). Coulomb trajectories are completely specified by the two kinematic parameters D and Θ. It is often more convenient to use instead two constants of motion, the total energy

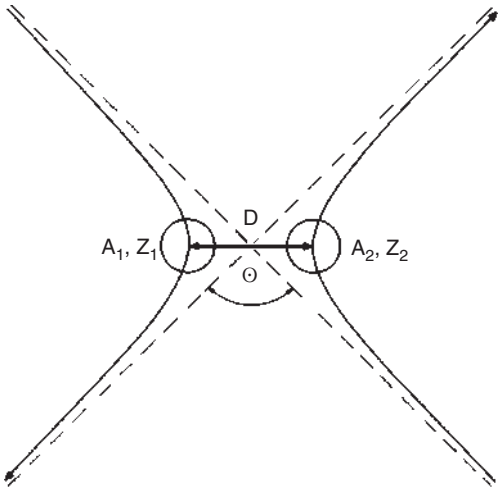

Figure 12.3 Coulomb trajectories in the center-of-mass system.

$E_{\mathrm{cm}} = \frac{1}{2}\mu v_\infty^2$ and the classical angular momentum $L\hbar$ which is related to the quantized angular momentum $l\hbar$ by $L^2 = l(l+1)$. The requirement of energy conservation from infinity to the point of closest approach leads to

$$E_{\mathrm{cm}} = V_{\mathrm{C}}(D) + V_{\mathrm{rot}}(D) = \frac{Z_1 Z_2 e^2}{D} + \frac{L^2\hbar^2}{2\mu D^2} \tag{12.15}$$

which can be rearranged with the previously introduced Sommerfeld parameter as

$$L^2 = kD(kD - 2n) \tag{12.16}$$

This is an important relation between the distance of closest approach and the angular momentum for Coulomb trajectories. Inserting Eq. (12.12) into Eq. (12.16) yields

$$\sin\frac{\Theta}{2} = \frac{n}{kD - n} \tag{12.17}$$

At $D = R_1 + R_2 = R_{\mathrm{C}}$, nuclear reactions start to occur and we have the classical threshold

$$E_{\mathrm{C}} = \frac{Z_1 Z_2 \mathrm{e}^2}{R_{\mathrm{C}}} = A_{12}\epsilon_{\mathrm{C}} \tag{12.18}$$

Because of the diffuse surface of nuclei and the finite range of the nuclear force, R_{C} is always somewhat larger than $R_1 + R_2$ and we have the empirical relation

$$R_{\mathrm{C}} = 1.16(A_1^{1/3} + A_2^{1/3} + 2)\ \mathrm{fm} \tag{12.19}$$

The onset of nuclear reactions defines the "grazing trajectory" and the corresponding Coulomb scattering angle Θ_{gr} for which we have

$$\sin\frac{\Theta_{\mathrm{gr}}}{2} = \frac{n}{kR_{\mathrm{C}} - n} = \frac{\epsilon_{\mathrm{C}}}{2\epsilon - \epsilon_{\mathrm{C}}} \tag{12.20}$$

where we have made use of the identity

$$kR_{\mathrm{C}} = 2n\frac{\epsilon}{\epsilon_{\mathrm{C}}}$$

We can write as well

$$\sin\frac{\Theta_{\rm gr}}{2} = \frac{E_{\rm C}}{2E_{\rm cm} - E_{\rm C}} \tag{12.21}$$

and

$$\Theta_{\rm gr} = 2\arcsin\left(\frac{E_{\rm C}}{2E_{\rm cm} - E_{\rm C}}\right) \tag{12.22}$$

According to Eq. (12.16), the grazing trajectory is associated with

$$L_{\rm gr}^2 = (kR_{\rm C})^2\left(1 - \frac{\epsilon_{\rm c}}{\epsilon}\right) \tag{12.23}$$

and the grazing angular momentum vanishes for $(\varepsilon = \varepsilon_{\rm C})$ where grazing implies a head-on collision. At higher energies, $L_{\rm gr}$ rises proportional to $(\varepsilon - \varepsilon_{\rm C})^{1/2}$. For charged particles, the impact parameter $b_{\rm gr}$ is smaller than $R_{\rm C}$ because the Coulomb potential deflects the projectile, see Figure 12.4, and we have $L_{\rm gr} = P_{\rm cm} x\mathbf{b}_{\rm gr}$ with the relative momentum

$$P_{\rm cm} = \mu v_\infty = \sqrt{2\mu\frac{\mu}{2}v_\infty^2} = \sqrt{2\mu E_{\rm cm}}$$

Thus, at the point of contact, where the kinetic energy is reduced to $E_{\rm cm} - E_{\rm C}$, we have

$$P_{\rm cm} = (2\mu(E_{\rm cm} - E_{\rm C}))^{1/2}$$

which we can rewrite as

$$P_{\rm cm} = (2\mu E_{\rm cm})^{1/2}\left(1 - \frac{E_{\rm C}}{E_{\rm cm}}\right)^{1/2} \tag{12.24}$$

where the first factor is the relative momentum at large distance and the second factor corrects for the ascent to the Coulomb barrier. Likewise, we have at the point of contact

$$L_{\rm gr} = R_{\rm C}(2\mu E_{\rm cm})^{1/2}\left(1 - \frac{E_{\rm C}}{E_{\rm cm}}\right)^{1/2}$$

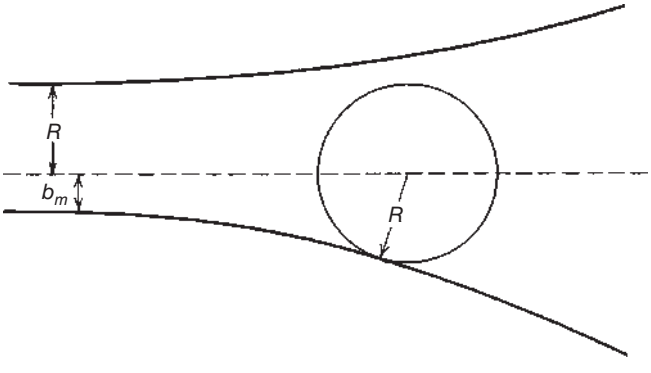

Figure 12.4 Classical trajectories for charged particles with impact parameters R and $b_{\rm m}$.

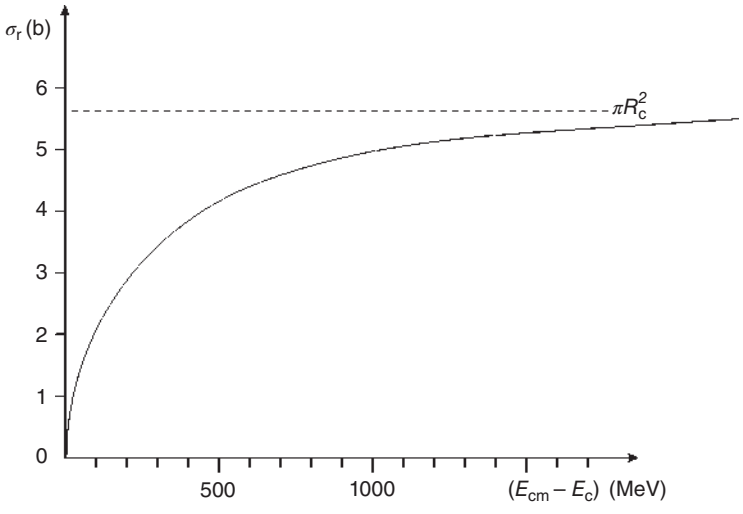

Figure 12.5 Energy dependence of the reaction cross section as a function of $(E_{cm} - E_C)$. The geometrical limit is reached asymptotically for large values of E_{cm}. The data are calculated for the reaction of ^{48}Ca with ^{208}Pb where $R_C = 13.41$ fm and $E_C = 176.12$ MeV.

and at large distance $L_{gr} = b_{gr}(2\mu E_{cm})^{1/2}$ giving together

$$b_{gr} = R_C\left(1 - \frac{E_C}{E_{cm}}\right)^{1/2} \tag{12.25}$$

Then, the reaction cross section $\sigma_r = \pi b_{gr}^2$ becomes

$$\sigma_r = \pi R_C^2\left(1 - \frac{E_C}{E_{cm}}\right) \tag{12.26}$$

which is shown in Figure 12.5 to reach asymptotically the geometric limit $\sigma_r = \pi R_C^2$ for large values of E_{cm}. For neutrons, the factor $1 - (E_C/E_{cm})$ does not apply. Here, for small energies, we do not have $\lambda \ll R$ but λ can take large values (see Figure 1.8), and the reaction cross section becomes

$$\sigma_r = \pi(R + \lambda)^2 \tag{12.27}$$

and in the limit of very large de Broglie wavelengths, $\lambda \gg R$,

$$\sigma_r = \pi\lambda^2 \tag{12.28}$$

12.3 Cross Sections

If we associate with each scattering center an area σ (which can be deduced geometrically or quantum mechanically) and if the centroid of the projectile hits this area, we assume we get a nuclear reaction. The current density j of the incoming particles is equal to the number of particles that hit the area A in time dt. In this

area, we have $\omega{\cdot}A$ scattering centers each with an area σ, so that the area covered by scattering centers is $\omega A\sigma$; then

$$\frac{\text{number of reactions}}{\mathrm{d}t} = \omega \cdot \sigma \cdot A \cdot j \tag{12.29}$$

where $\omega{\cdot}\sigma$ is the fraction of the target area that is covered by the scattering areas, which is equal to the probability for a reaction $W = \omega{\cdot}\sigma$. Even in the case when W is determined quantum mechanically, that is, σ has nothing in common with a scattering area, we have the definition

$$\begin{aligned}\sigma &= \frac{\text{number of reactions per time unit}}{\text{current density } j \times \text{number of scattering centers}} \text{ (area)} \\ &= \frac{\text{number of reactions per scattering center/s}}{\text{current density } j} \text{ (cm}^2\text{)}\end{aligned}$$

Reactions of a special type, for example, reactions in which a specific product is emitted into the solid angle element $\mathrm{d}\Omega$ under polar angle ϑ, are assigned a differential cross section per unit solid angle

$$\left(\frac{\mathrm{d}\sigma}{\mathrm{d}\Omega}\right)_\Theta = \frac{\begin{array}{c}\text{number of particles scattered} \\ \text{in the solid angle element } \mathrm{d}\Omega/\text{s}\end{array}}{\text{current density } j} \text{ (mb sr}^{-1}\text{)}$$

relative to one scattering center. If $\Omega = 1$ sr (steradian), the solid angle element normalized to the surface of a sphere is 1. Instead of a solid angle element $\mathrm{d}\Omega$ at a given polar angle ϑ, one can look at a given polar angle interval between ϑ and $\vartheta + \mathrm{d}\vartheta$. The particles then run into a ring-shaped solid angle element $\mathrm{d}R$ and the differential cross section is then

$$\begin{aligned}\left(\frac{\mathrm{d}\sigma}{\mathrm{d}\Theta}\right)\mathrm{d}\Theta &= \int_{\phi=0}^{2\pi}\left(\frac{\mathrm{d}\sigma}{\mathrm{d}\Omega}\right)_\Theta \mathrm{d}\Omega = \left(\frac{\mathrm{d}\sigma}{\mathrm{d}\Omega}\right)_\Theta \cdot \int_{\phi=0}^{2\pi} \sin\Theta\,\mathrm{d}\Theta\,\mathrm{d}\phi \\ &= \left(\frac{\mathrm{d}\sigma}{\mathrm{d}\Omega}\right)_\Theta 2\pi \sin\Theta\,\mathrm{d}\Theta\end{aligned} \tag{12.30}$$

and

$$\left(\frac{\mathrm{d}\sigma}{\mathrm{d}\Theta}\right) = 2\pi \sin\Theta\left(\frac{\mathrm{d}\sigma}{\mathrm{d}\Omega}\right)_\Theta \tag{12.31}$$

The situation is depicted in Figure 12.6 which shows that particles coming through a ring of impact parameters between b and $b + \mathrm{d}b$ around the symmetry axis are scattered into the solid angle element $\mathrm{d}R$. Due to the conservation of the particle number,

$$j \cdot 2\pi b\,\mathrm{d}b = j\,\mathrm{d}R\left(\frac{\mathrm{d}\sigma}{\mathrm{d}\Omega}\right) = j \cdot 2\pi \sin\Theta\,\mathrm{d}\Theta$$

or

$$\left(\frac{\mathrm{d}\sigma}{\mathrm{d}\Omega}\right)_\Theta = \frac{b}{\sin\Theta}\left|\frac{\mathrm{d}b}{\mathrm{d}\Theta}\right| \tag{12.32}$$

In a classical collision process, each impact parameter is associated with a fixed scattering angle Θ. We have just cut the incoming particle current in ring zones with radii b and $b + \mathrm{d}b$, and we have associated the particles that entered this ring

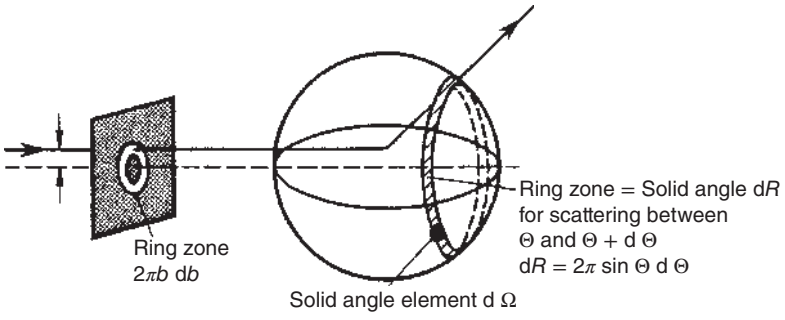

Figure 12.6 Geometrical situation in a scattering process. Source: Mayer-Kuckuk (1979), figure 01 (p. 11)/John Wiley & Sons.

Figure 12.7 The incident beam is perpendicular to the plane of the figure. The particles with a given l are considered to strike within the designated ring zone.

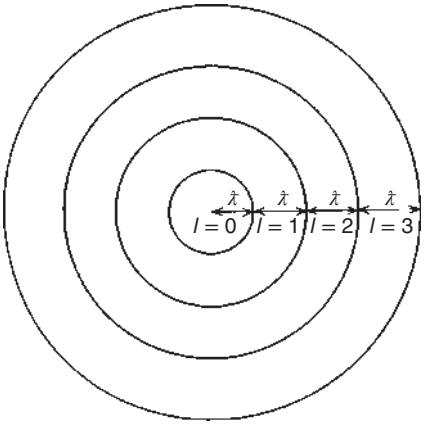

zone with an increment of scattering angles. A similar procedure offers itself for the quantum mechanical case. We parameterize the incoming particles according to angular momenta, a constant of motion. An incoming particle has the momentum $P = \hbar k = \hbar/\lambda$. A particle coming in at distance $b = l \cdot \lambda$ has the angular momentum $P \cdot b = Pl\,\lambda = l\hbar$. This is equivalent to cutting the beam in ring zones perpendicular to the beam direction, and the associated circles have radii $\lambda, 2\lambda, 3\lambda \ldots$, see Figure 12.7. This means that the impact parameter does not take discrete values but ranges for which we have

$$l\lambda \leq b \leq (l+1)\lambda$$

and the cross section σ_1 associated with the lth zone is equal to the area of the ring zone

$$\sigma_l = (l+1)^2\lambda^2 \cdot \pi - l^2\lambda^2 \cdot \pi = (2l+1)\pi\lambda^2 \tag{12.33}$$

So far, this is only a qualitative approach. In order to arrive at a quantitative picture, the incoming plane wave e^{ikz} must be decomposed into angular momentum

eigenfunctions and their interaction with the outgoing scattered wave must be considered. This leads to

$$\sigma_l = \pi\lambda^2(2l+1)\cdot T_l \tag{12.34}$$

where T_l is the so-called transmission coefficient which contains all the information about the potential and the resulting "scattering phases." Before we set off on our adventure to deduce T_l, we want to return to some practical aspects that we touched on briefly in Section 11.4. The rate of production of a nuclear reaction product is

$$R_i = I \cdot N_\mathrm{t} \cdot \sigma_i \tag{12.35}$$

with

R_i = number of reactions in channel i per s
I = number of beam particles per s
N_t = number of target atoms per cm^2
σ_i = cross section for reaction i in cm^2

The natural order of magnitude for a cross section (corresponding to the geometrical nuclear area) is 10^{-24} cm^2 called 1 b "barn" defined in the "Manhattan project". Thus, we have

1 b = 10^{-24} cm^2
1 mb = 10^{-27} cm^2
1 μb = 10^{-30} cm^2
1 nb = 10^{-33} cm^2
1 pb = 10^{-36} cm^2
1 fb = 10^{-39} cm^2

We use an example to show how to deal with this in practice: Consider a one hour irradiation of a 10 mg cm^{-2} target of Mn with 1 μA of 35 MeV α particles: ^{55}Mn(α,2n)^{57}Co; $\sigma = 200$ mb; $t_{1/2} = 270$ days. How many ^{57}Co nuclei are being formed? Now,

$$1\ \mathrm{A} = 6.24\cdot 10^{18}\ \text{charges per s};\ 1\ \mu A = 3.12\cdot 10^{12}\ {}^4\mathrm{He}^{2+}\ \text{ions per s}$$

$$R_\mathrm{i} = 3.12\cdot 10^{12}\cdot \frac{10\cdot 10^{-3}\cdot 6.022\cdot 10^{23}}{55}\cdot 200\cdot 10^{-27} = 6.8\cdot 10^{7}\ \mathrm{s}^{-1}$$

In one hour, we have $3600\cdot 6.8\cdot 10^7 = 2.4\cdot 10^{11}$ ^{57}Co nuclei produced, if the decay during bombardment is neglected. The decay rate of these nuclei is

$$-\frac{\mathrm{d}N}{\mathrm{d}t} = \lambda\cdot N = \frac{0.693}{270\cdot 24\cdot 3600}\cdot 2.4\cdot 10^{11} = 7.2\cdot 10^{3}\ \mathrm{Bq}$$

Thus,

$$-\frac{\mathrm{d}N}{\mathrm{d}t} = \lambda\cdot N = R_i\cdot\lambda_i\cdot t \quad \text{for } t \ll t_{1/2}$$

If the decay of the product during bombardment cannot be neglected, we have

$$-\frac{\mathrm{d}N}{\mathrm{d}t} = \lambda\cdot N = I\cdot N_\mathrm{t}\cdot\sigma_i - \lambda\cdot N$$

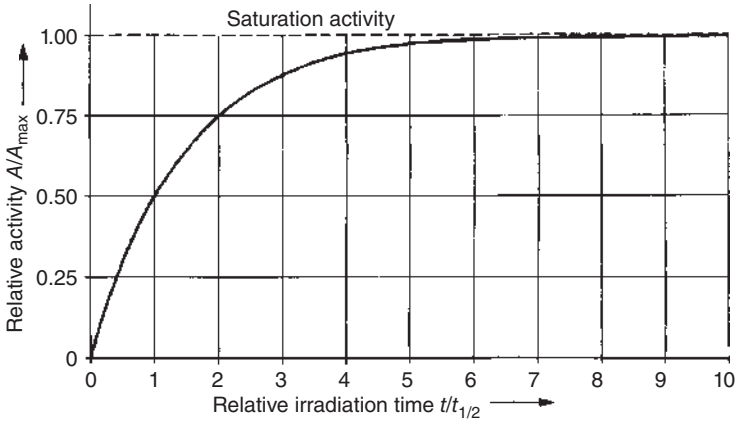

Figure 12.8 Activity as a function of irradiation time.

and if the flux is constant within the target and N_t does not change appreciably with time, integration of the latter equation gives

$$-\frac{dN}{dt} = \lambda \cdot N = I \cdot N_t \cdot \sigma_i(1 - e^{-\lambda t}) \tag{12.36}$$

and only for $t \ll t_{1/2}$ does $(1 - e^{-\lambda t})$ behave as λt. The influence of the irradiation time on activation is illustrated in Figure 12.8. For the production of radionuclides, irradiation times of a few half-lives are usually sufficient. About 99% of the saturation activity is obtained after seven half-lives.

12.4 Elastic Scattering

The quantum mechanical scattering formalism to be discussed here gives for pure Coulomb scattering the classical Rutherford scattering formula; there will be deviations from the latter if the nuclear force (absorption) is added. Therefore, the measurement of elastic scattering is suited to determining the reaction cross section, see Section 12.5. Moreover, a detailed measurement of the angular distribution of the elastic scattering cross section allows us to determine the parameters of the potential.

We consider an incoming plane wave with a sharply defined linear momentum $\mathbf{P}_z = \hbar \cdot \mathbf{k}$. Because of the uncertainty principle, there is a large expansion in the z direction and the scattering process becomes stationary for a given time; hence,in the plane wave with wave function $\exp[i(\mathbf{kr} - \omega t)]$, the time-dependent factor can be omitted in the stationary treatment and we have $\exp[i\mathbf{kr}] = \exp(ikz)$. The outgoing wave is a spherical wave with $(1/r)\exp(ikr)$, where $1/r$ makes sure that the current density falls off with $1/r^2$ which guarantees particle number conservation. The amplitude of the outgoing wave depends on Θ so that the total wave function takes the form

$$\Psi_T(\mathbf{r}) = A[e^{ikz} + f(\Theta)e^{ikr}/r] \tag{12.37}$$

with

$$\left(\frac{\mathrm{d}\sigma}{\mathrm{d}\Omega}\right)_{\Theta} = |f(\Theta)|^2 \tag{12.38}$$

The next step is the expansion of the plane wave in terms of angular momentum eigenfunctions with the solution of the radial equation for a free particle $R(r) = j_l(kr)$, a spherical Bessel function, which results in

$$\Psi_{\text{plane}} = \mathrm{e}^{\mathrm{i}kz} = \sum_{l=0}^{\infty}(2l+1)i^l j_l(kr)P_l(\cos\Theta) \tag{12.39}$$

If a potential is switched on, the outgoing wave is modified by the scattering process. For elastic scattering, the wave number k cannot be changed, though the amplitude and the phase can. This is taken care off by multiplying the outgoing spherical wave with a factor η_l which in the general case is a complex number. Thus, we have

$$\Psi_{\text{scat}} = f(\Theta)\mathrm{e}^{\mathrm{i}kr}/r = \Psi_{\text{T}} - \Psi_{\text{plane}}$$

resulting in

$$f(\Theta) = \frac{\mathrm{i}}{2k}\sum_{l=0}^{\infty}(2l+1)(1-\eta_l)P_l(\cos\Theta) \tag{12.40}$$

and with Eq. (12.38), we have

$$\left(\frac{\mathrm{d}\sigma}{\mathrm{d}\Omega}\right)_{\Theta} = \frac{1}{4k^2}\left|\sum_{l=0}^{\infty}(2l+1)(1-\eta_l)P_l(\cos\Theta)\right|^2 \tag{12.41}$$

which contains the interference terms between different P_l causing asymmetric angular distributions with constructive and destructive interferences. Integration over the total solid angle results in

$$\sigma_{\text{s}} = \pi\lambda^2\sum_{l=0}^{\infty}(2l+1)|1-\eta_l|^2 \tag{12.42}$$

and

$$\sigma_{\text{s},l} = \pi\lambda^2(2l+1)|1-\eta_l|^2 \tag{12.43}$$

containing $|1-\eta_l|^2$ as a correction factor relative to the simple ring zone picture. We can now allow for the possibility that a reaction (absorption) takes place and obtains

$$\sigma_{\text{r},l} = \pi\lambda^2(2l+1)(1-|\eta_l|^2) \tag{12.44}$$

The reaction cross section is zero when $|\eta_l| = 1$. This is immediately obvious as, for $|\eta_l| = 1$, there is no change in the amplitude of the outgoing wave. The largest reaction cross section is obtained for $\eta_l = 0$. Then,

$$\sigma_{\text{r},l}^{\max} = \sigma_{\text{s},l} = \pi\lambda^2(2l+1) \tag{12.45}$$

Note that, for each reaction, there is also a scattering wave. The largest scattering cross section is obtained for $\eta_l = -1$, that is,

$$\sigma_{\text{s},l}^{\max} = 4\pi\lambda^2(2l+1) \tag{12.46}$$

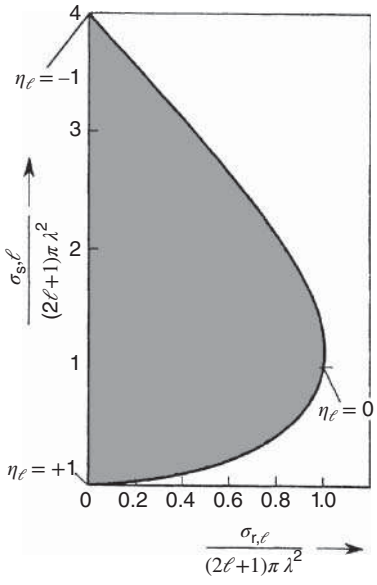

Figure 12.9 Possible values of the scattering cross section for a given reaction cross section. Source: Blatt and Weisskopf (1952)/Dover Publications.

It is four times as large as the largest reaction cross section. This comes about because, in elastic scattering, the incoming and outgoing waves can interfere coherently. For positive interference, the amplitudes can be doubled and the cross section can be increased by a factor of 4. In Figure 12.9, the values that the variable η_l and the cross sections can take according to Eqs. (12.44)–(12.46) are shown graphically. Only within the shaded area are scattering and reaction processes possible. On the limiting line, η is real.

At this point, comparison to Eq. (12.34) shows that the transmission coefficient T_l is given as

$$T_l = (1 - |\eta_l|^2) \tag{12.47}$$

For pure elastic scattering ($|\eta_l| = 1$), one often uses another, more illustrative notation

$$\eta_l = \mathrm{e}^{2\mathrm{i}\delta_l} \tag{12.48}$$

where the real angle δ_l is called the "phase shift" or "scattering phase." Starting from Eq. (12.38) and with a transformation deduced from Euler's formula, $\mathrm{e}^{\mathrm{i}\delta} \sin\delta = \frac{1}{2}\mathrm{i}(1 - \mathrm{e}^{2\mathrm{i}\delta})$, we obtain

$$\begin{aligned} f(\Theta) &= \frac{\mathrm{i}}{2k}\sum_l (2l+1)(1 - \mathrm{e}^{2\mathrm{i}\delta})P_l(\cos\Theta) \\ &= \lambda\sum_l (2l+1)\mathrm{e}^{\mathrm{i}\delta_l}\sin\delta_l P_l(\cos\Theta) \end{aligned} \tag{12.49}$$

and in analogy to Eq. (12.42)

$$\sigma_s = \int |f(\Theta)|^2 \mathrm{d}\Omega = 4\pi\lambda^2 \sum_l (2l+1)\sin\ \Theta^2 \tag{12.50}$$

If we allow, in addition to the long-range Coulomb interaction, the short-range nuclear interaction also, $\eta_l = \eta_l(\text{Coulomb}) \cdot \eta_l(\text{nuclear})$, and in Eq. (12.48) δ is to be replaced by $\sigma + \delta$ where σ is the Coulomb scattering phase and δ is the nuclear scattering phase, then we obtain

$$\begin{aligned} f(\Theta) &= \frac{i}{2k}\sum_l (2l+1)(1-e^{2i(\sigma_l+\delta_l)})P_l(\cos\Theta) \\ &= \frac{i}{2k}\sum_l (2l+1)[(1-e^{2i\sigma_l}) + e^{2i\sigma_l}(1-e^{2i\delta_l})]P_l(\cos\Theta) \\ &= \frac{i}{2k}\sum_l (2l+1)(1-e^{2i\sigma_l})P_l(\cos\Theta) + \frac{i}{2k}\sum_l (2l+1)e^{2i\sigma_l}(1-e^{2i\delta_l})P_l(\cos\Theta) \end{aligned} \tag{12.51}$$

The first term is $f_{\text{Coul}}(\Theta)$, the scattering amplitude associated with the Coulomb field alone outside the range of the nuclear potential, and it alone contributes for large values of l. The second term contains both scattering phases σ and δ and thus contains interferences from both phases.

A simple special case is the scattering of particles with $l = 0$ (s-wave scattering). As $P_0(\cos\Theta) = 1$, it follows from Eq. (12.49), (12.38) that

$$f_0 = \lambda e^{i\delta_0}\sin\delta_0 \tag{12.52}$$

and

$$\left(\frac{d\sigma}{d\Omega}\right) = |f_0|^2 = \lambda^2 \sin^2\delta_0 \tag{12.53}$$

In this case, the cross section is isotropic. The total cross section is

$$\sigma_0 = 4\pi\lambda^2\sin^2\delta_0 = 4\pi|f_0|^2 \tag{12.54}$$

which means that the scattering center acts like a sphere of radius f_0. The limit of $-f_0$ for very large wavelengths of the incoming particles is called the "scattering length" a

$$\lim(-f_0) = a \tag{12.55}$$

It is an important quantity for neutron scattering, see Section 8.5.

An illustrative exercise is to calculate the differential cross section for a given scattering potential. We mentioned above that the cross section is given by a set of phase shift angles δ_l. For simplicity, we select the case of s-wave scattering from a square well potential, that is, we search for the relation between δ_0 and the parameters of the potential. Let its depth be $-V_0$ and its range R_0. Let E be the kinetic energy of the incoming particle. What we need are solutions of the Schrödinger equation for $r < R_0$ and $r > R_0$, and at $r = R_0$, the boundary condition must hold that the wave function and its first derivative are continuous.

For $r < R_0$, and for $l = 0$, the Schrödinger equation takes the form

$$u'' + \frac{2m}{\hbar^2}[E - V(r)]u = u'' + k^2 u = 0 \tag{12.56}$$

$$k^2 = \frac{2m}{\hbar^2}[E - V]; \quad k = \frac{1}{\hbar}\sqrt{2m[E-V]}$$

having solutions of the form

$$u_{\text{in}} = \alpha e^{ikr} + \beta e^{-ikr} \tag{12.57}$$

representing the incoming wave with amplitude α and the reflected wave with amplitude β. The wave number inside the potential is

$$k_{\text{in}} = \frac{1}{\hbar}\sqrt{2m[E - V_0]}$$

so that with Eq. (12.57)

$$u_{\text{in}} = \alpha(\cos k_{\text{in}} r + \text{i} \sin k_{\text{in}} r) + \beta(\cos k_{\text{in}} r - \text{i} \sin k_{\text{in}} r) \tag{12.58}$$

with the boundary condition $u_{\text{in}} = 0$ at $r = 0$. Inserting $r = 0$ gives $\alpha + \beta = 0$, so that with $\beta = -\alpha$, Eq. (12.58) takes the form

$$u_{\text{in}} = 2\alpha \,\text{i} \sin k_{\text{in}} r \tag{12.59}$$

For $r \geq R_0$, that is, outside of the potential,

$$k_{\text{out}} = \frac{1}{\hbar}\sqrt{2mE}$$

our familiar expression

$$\Psi_T(r) = A[e^{ikz} + f(\Theta)e^{ikr}/r]$$

gives with $\eta_0 = e^{2i\delta_0}$ and $P_0(\cos\Theta) = 1$

$$u_T = r\Psi_T = \frac{\text{i}}{2k_{\text{out}}}[e^{-ik_{\text{out}}r} - e^{2i\delta_0} e^{ik_{\text{out}}r}] \tag{12.60}$$

and with the substitution $\frac{1}{2}\text{i}(1 - e^{2i\delta}) = e^{i\delta}\sin\delta$,

$$u_{\text{T}} = r\Psi_{\text{T}} = \frac{e^{i\delta_0}}{k_{\text{out}}} \sin(k_{\text{out}} r + \delta_0) = \frac{e^{i\delta_0}}{k_{\text{out}}} \sin k_{\text{out}} \left(r + \frac{\delta_0}{k_{\text{out}}} \right) \tag{12.61}$$

Functional values and first derivatives of u_{in} and u_{out} at $r = R_0$ must be equal, yielding the equations

$$\frac{e^{i\delta_0}}{k_{\text{out}}} \sin(k_{\text{out}} R_0 + \delta_0) = 2\alpha \,\text{i} \sin k_{\text{in}} R_0 \tag{12.62}$$

$$e^{i\delta_0} \cos(k_{\text{out}} R_0 + \delta_0) = 2\alpha \,\text{i}\, k_{\text{in}} \cos k_{\text{in}} R_0 \tag{12.63}$$

By dividing Eq. (12.62) by Eq. (12.63), we obtain

$$\left(\frac{1}{k_{\text{out}}} \right) \tan(k_{\text{out}} R_0 + \delta_0) = \left(\frac{1}{k_{\text{in}}} \right) \tan k_{\text{in}} R_0 \tag{12.64}$$

or, resolved for δ_0,

$$\delta_0 = -k_{\text{out}} R_0 + \text{arcrtan} \left\{ \left(\frac{k_{\text{out}}}{k_{\text{in}}} \right) \tan k_{\text{in}} R_0 \right\} \tag{12.65}$$

This is the desired connection, as δ_0 is now uniquely determined by R_0, by E via k_{out}, and by V_0 via k_{in}. And with the known δ_0, the differential cross section is given

by Eq. (12.53). This exercise provides an illustrative demonstration of the action of the "phase shift." The incoming wave for $l = 0$ is

$$u_{\text{plane}} = \frac{\mathrm{i}}{2k_{\text{out}}}\left[\mathrm{e}^{-\mathrm{i}k_{\text{out}}r} - \mathrm{e}^{\mathrm{i}k_{\text{out}}r}\right] = \frac{1}{k_{\text{out}}}\sin k_{\text{out}}r \tag{12.66}$$

This is the solution in the absence of a potential. If the potential is switched on, the total wave, u_{T}, results according to Eq. (12.61), and the sine wave is shifted along the r axis by the amount δ_0/k_{out}. This is illustrated in Figure 12.10. By the attractive potential, the wave is pulled toward the potential border R_0. Figure 12.10 shows that this phase shift is required in order to obtain the continuous connection to u_{in}. According to Eq. (12.59), u_{in} is also a sine wave, but because of the higher energy inside the potential, its wavelength $\lambda = 1/k_{\text{in}}$ is shorter than outside the potential.

As the wavelength inside the potential depends on the depth of the potential and on the kinetic energy of the particle, it is possible, for certain energies, that the continuous connection at $r = R_0$ happens to occur with a horizontal tangent. As is shown by Figure 12.11a, the wave inside the potential, in this particular case, has a particularly large amplitude leading to a particularly large cross section; we call this "resonance scattering." Conversely, the case shown in Figure 12.11b can occur when the continuous connection at $r = R_0$ is close to where the sine wave goes through the zero characteristic for "potential scattering." Relative to the potential scattering, the phase shift δ_0 for resonance scattering amounts to 90°.

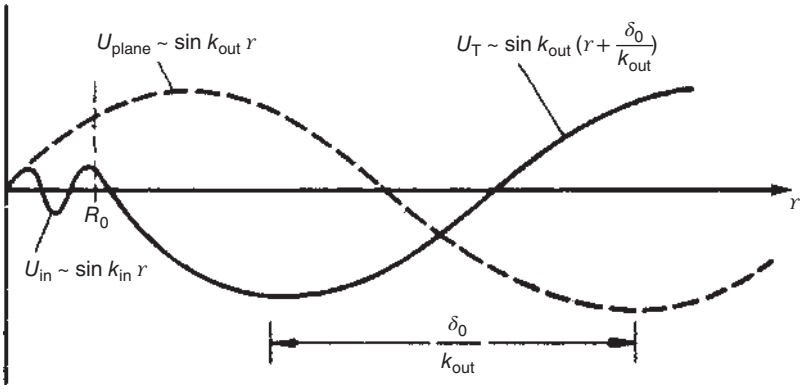

Figure 12.10 Illustration of the phase shift δ_0/k_{out} by an attractive potential. Source: Mayer-Kuckuk (1979), figure 03 (p. 14)/John Wiley & Sons.

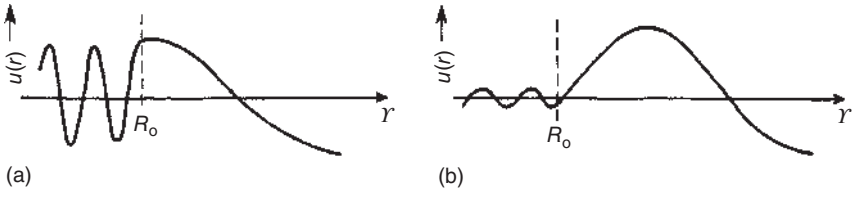

Figure 12.11 (a) Continuous connection of the wave function at $r = R_0$ in the case of resonance scattering where the connection occurs with a horizontal tangent; (b) in the case of potential scattering. Source: Mayer-Kuckuk (1979), figure 04 (p. 14)/John Wiley & Sons.

How does one proceed in scattering experiments with true nuclei? A prerequisite is that angular distributions for elastic scattering are measured for a number of different incident energies. One then tries to find, in a numerical iteration process, the set of values of δ_l that best describes the measured data. This way, one obtains the scattering phases as a function of the energy. One then tries to obtain, for a realistic form of the scattering potential, a determination of the potential parameters such that the found set of δ_l results as a solution of the Schrödinger equation. In principle, one proceeds as in the case of the square well potential presented above; however, the solutions generally require numerical methods on a computer. As a practical example, we present the α-particle scattering from ^{4}He (gas target). Figure 12.12 shows the angular distributions for elastic scattering at a number of incident energies with fits to the differential cross sections given by the phase shifts. The differential cross sections were analyzed in terms of complex phase shifts $\mathrm{Re}(\delta_l) + \mathrm{i}\,\mathrm{Im}(\delta_l)$ Darriulat et al. (1965). The real parts of the phase shifts, Figure 12.13, vary smoothly as a function of energy. Resonances are identified at E_{res} equal to the channel energies where $\delta_l = 90°$. In the scattering of identical 0^+ particles, only even values of l can occur. The resonances are members of a rotational band with $I^\pi = 0^+, 2^+, 4^+, 6^+, 8^+, 10^+$ in unbound ^{8}Be. δ_0 jumps from 0° to 180° in close vicinity to 0 MeV, defining a resonance at $E_{\mathrm{res}} = 0.096$ MeV, representing the unbound 0^+ ground state in ^{8}Be. δ_2 goes through 90° close to 6 MeV, representing the 2^+ state at 2.9 MeV. δ_4 goes through 90° near 23 MeV, representing the 4^+ state at $E_{\mathrm{res}} = 11.4$ MeV. E_{res} for the 6^+ and 8^+ states is at 29 and 57 MeV, respectively. The resulting potential is dependent on l, and the imaginary parts of the phase shifts are appreciable at all energies involving the reseparation channels ^{7}Li + p, ^{7}Be + n, ^{4}He + t + p, ^{4}He + ^{3}He + n, ^{3}He + ^{5}He, and so forth, with increasing energy thresholds. The real parts of the phase shifts all start positive at an energy corresponding to an impact parameter of 5 fm indicating the size of the attractive potential. δ_0 and δ_2 become negative at energies corresponding to impact parameters of 1–2 fm where the potential is repulsive.

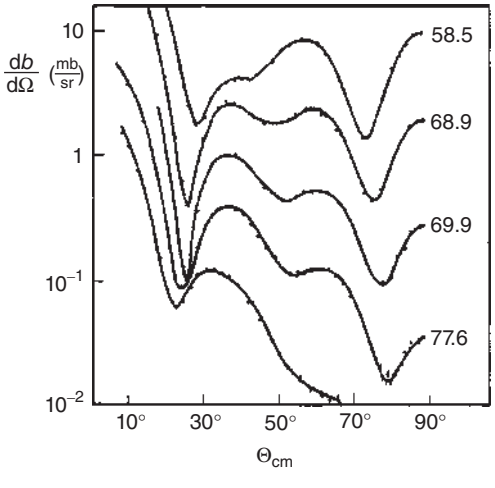

Figure 12.12 Angular distributions for elastic scattering of α particles by ^{4}He at various laboratory bombarding energies given in MeV. The lines are fits to the differential cross sections given by the phase shifts obtained in a phase-shift analysis by Darriulat, P. et al. Source: Modified from Darriulat et al. (1965).

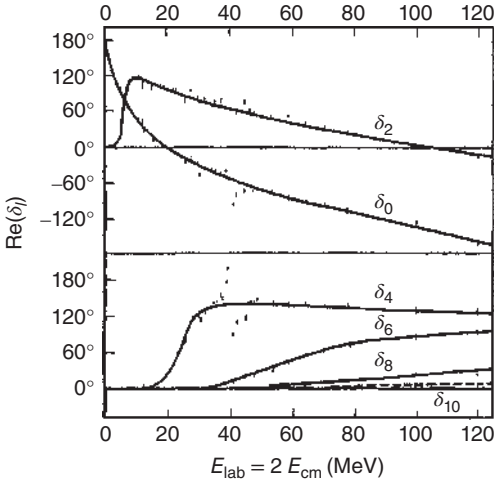

Figure 12.13 Real parts of the phase shifts Re(δ_l) plotted as a function of energy. The solid curves are fits using the potential parameters deduced from the analysis by Darriulat et al. Source: Darriulat et al. (1965), figure 03 (p. 11)/American Physical Society.

12.5 Elastic Scattering and Reaction Cross Section

The strength of the nuclear force and its short range make absorption from the elastic channel quite probable as soon as the nuclei get close to R_C, where the transition is expected to occur in a narrow range. Classically, we have

$$\begin{aligned} \frac{d\sigma}{d\Omega} &= \frac{d\sigma_C}{d\Omega} \quad \text{for } \Theta \le \Theta_{gr} \\ &= 0 \qquad \text{for } \Theta > \Theta_{gr} \end{aligned}$$

$$\begin{aligned} \sigma_r &= \pi R_C^2 \left(1 - \frac{\epsilon_C}{\epsilon}\right) \text{ for } \epsilon > \epsilon_C \\ &= 0 \qquad\qquad\quad \text{for } \epsilon \le \epsilon_C \end{aligned}$$

This led J.S. Blair in 1954 to the quantum mechanical sharp-cut-off model in which the sharp cut-off is introduced in the angular momentum space:

$$\eta_l = 1 \text{ for } l > l_{max}$$
$$\eta_l = 0 \text{ for } l \le l_{max}$$

Then, for $\varepsilon > \varepsilon_C$, we have, as deduced above,

$$\frac{d\sigma}{d\Omega} = \left| f_{Coul}(\Theta) + \frac{i}{2k} \sum_{l=0}^{l_{max}} (2l+1) e^{2i\sigma_l} (1 - e^{2i\delta_l}) P_l(\cos\Theta) \right|^2$$

and

$$\sigma_r = \pi \lambda^2 \sum_{l=0}^{l_{max}} (2l+1)$$

As can be seen from Figure 12.14, the Blair model gives qualitative agreement with the angular distribution but fails in detail. The discrepancies disappear by and

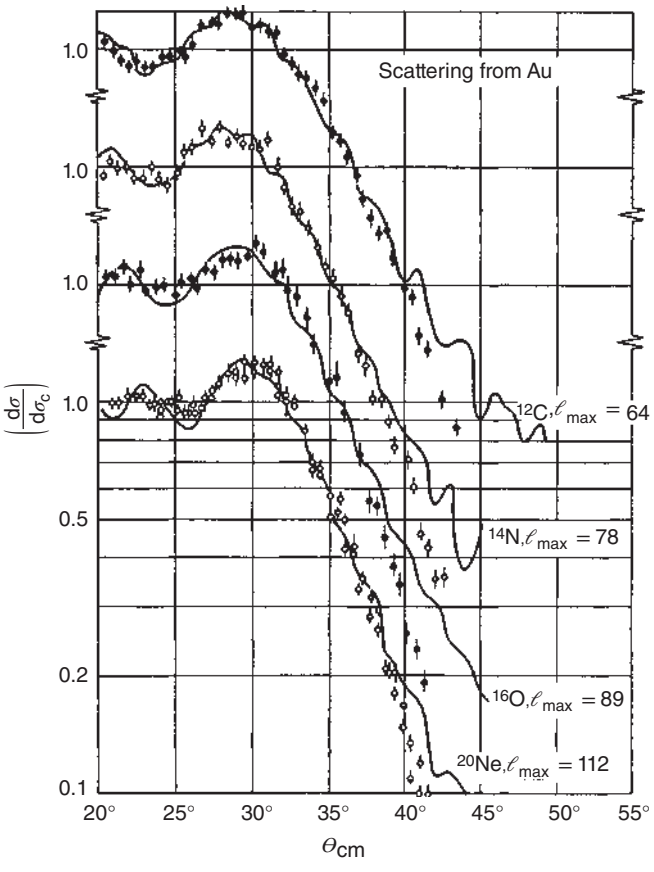

Figure 12.14 Comparison of experimental angular distributions for heavy-ion elastic scattering with Blair model predictions. Source: Zucker (1960), figure 02 (p. 15)/Annual Reviews, Inc.

large if the sharp cut-off in l is replaced by a smooth l dependence of η_l (or δ_l) taking into account the diffuse nuclear surface and the exponentially decreasing depth of the nuclear potential. J.A. McIntyre's ansatz, developed in 1960, uses a smoothing function

$$\eta_l = g_\eta(l)$$

$$\delta_l = \delta(1 - g_\delta(l))$$

with the functions

$$g_i(l) = \left\{1 + \exp\left(\frac{l_i - l}{\Delta_i}\right)\right\} \quad (i = \eta, \delta)$$

Here, l_i is the cut-off parameter and Δ_i stands for the diffuseness in angular momentum space. The dependence of l on the scattering parameters in the smooth-cut-off model is shown schematically in Figure 12.15. With this parameterization, the

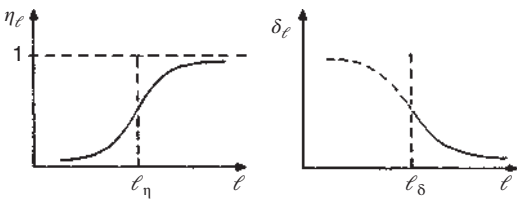

Figure 12.15 Schematic representation of the scattering parameters η_l and δ_l as a function of l in the smooth cut-off model.

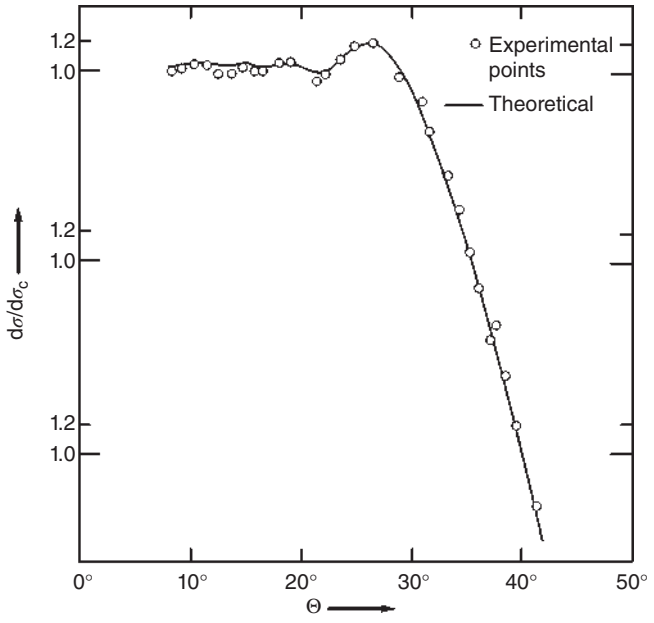

Figure 12.16 Comparison of the experimental angular distribution for $^{12}C + Ta$ elastic scattering with a fit of the smooth cutoff model. Source: Modified from Alster and Conzett (1964).

description of the angular distribution is much improved, see Figure 12.16, and is used to fix the parameters l_i and Δ_i. On physical grounds, it is clear that the angular momentum cut-off parameters l_i are closely related to the grazing angular momentum and thus to the Coulomb radius R_C of the interaction region. Semiclassically, from Eq. (12.16), one expects

$$l_i(l_i + 1) = kR_C(kR_C - 2n) \tag{12.67}$$

which has been used extensively to extract R_C and the reaction cross section.

A final remark is in order with respect to the different diffraction patterns observed experimentally. If the Coulomb effects on the particle trajectories are small, and if the projectile can be described by an incoming plane wave, this means that from the wave field, a spherical piece is cut out. This leads to a diffraction pattern that is known in optics as Fraunhofer diffraction. For Fraunhofer diffraction, the light source and the screen are at infinity. We expect this pattern for $n < 1$ and $E \gg V_C$. In the other limit, we have rather that for heavy ions, $n \gg 1$ and the particle bundle in

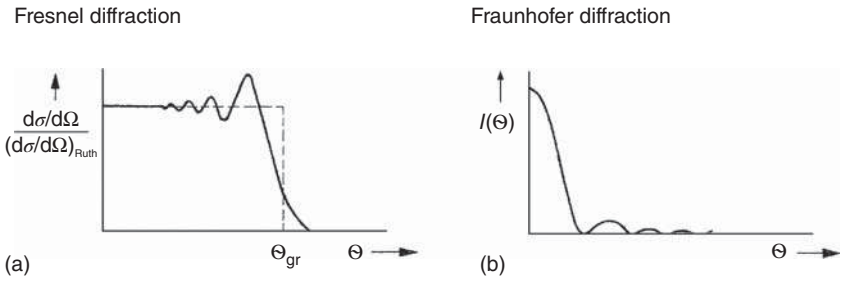

Figure 12.17 Schematic representation of the shape of angular distributions in the case of (a) Fresnel diffraction with $l_{gr} \cdot \sin\Theta_{gr} \ll 1$ (Eq. (12.68)) applying for heavy-ions, and (b) Fraunhofer diffraction with $l_{gr} \cdot \sin\Theta_{gr} \geq 1$ (Eq. (12.69)) applying rather for light-ion scattering. Source: Modified from Mayer-Kuckuk (1979).

the Coulomb field becomes strongly divergent. The optical analogy is the diffraction pattern that a divergent light bundle causes on a disk of radius a; this pattern being called Fresnel diffraction. Here, the light source and the screen are at a finite distance from the scattering object. If we call the larger of these distances d, the condition for Fresnel diffraction is

$$\frac{a}{\lambda} \cdot \frac{a}{d} \ll 1$$

Further, if we identify the radius, a, of the scattering object with the impact parameter for the grazing collision, $a = b_{gr}$, according to Section 12.3, we have $\lambda_{gr} = b_{gr}/l_{gr}$ so that the condition for Fresnel diffraction can be written as

$$\frac{b}{b_{gr}/l_{gr}} \cdot \frac{b_{gr}}{b_{gr}/\sin\Theta_{gr}} = l_{gr} \cdot \sin\Theta_{gr} \ll 1 \tag{12.68}$$

whereas, conversely, for Fraunhofer diffraction, we have

$$l_{gr} \cdot \sin\Theta_{gr} \geq 1 \tag{12.69}$$

The angular distributions for the two types of diffraction are schematically depicted in Figure 12.17. Obviously, the heavy-ion examples that we have shown in Figures 12.14 and 12.16 are of the Fresnel type. The Fraunhofer type (not shown) is rather expected for light-ion scattering.

12.6 Optical Model

In Section 12.4, we saw that, for elastic scattering,

$$|\eta_l| = 1 = e^{2i\delta_l}$$

$$\begin{aligned} f(\Theta) &= \frac{i}{2k}\sum_l (2l+1)(1-e^{2i\delta})P_l(\cos\Theta) \\ &= \lambda\sum_l (2l+1)e^{i\delta_l}\sin\delta_l P_l(\cos\Theta) \end{aligned} \tag{12.49}$$

and

$$\sigma_s = \int |f(\Theta)|^2 \, d\Omega = 4\pi\lambda^2 \sum_l (2l+1)\sin^2\Theta \tag{12.50}$$

With Eqs. (12.49) and (12.50), we can deduce another useful relation. We can replace $e^{i\delta_l}$ in Eq. (12.49) by $\cos\delta_l + i\sin\delta_l$ and recall that for $\Theta = 0$ (forward scattering), $P_l(\cos\Theta) = 1$. This means that

$$\mathrm{Im}\, f(0) = \lambda \sum_l (2l+1)\sin^2\delta_l = \frac{\sigma_s}{4\pi\lambda} \tag{12.70}$$

that is, the imaginary part of the scattering amplitude in the forward direction, representing absorption, is related to the total cross section for elastic scattering; this is called the optical theorem. The name comes from the fact that $\mathrm{Im}\, f(0)$ is related to the imaginary part of the diffraction index n that the scattering medium has for the incoming wave:

$$\mathrm{Im}\, f(0) = \frac{k^2}{2\pi}\mathrm{Im}\, n \tag{12.71}$$

This leads to another view of the scattering process in terms of the diffraction of the incoming wave when entering another medium. We have discussed that the wavelength of an s-wave particle inside the potential is shorter than outside, thus

$$\begin{aligned} n &= \frac{\lambda_{out}}{\lambda_{in}} = \frac{k_{in}}{k_{out}} \\ n &= \frac{\frac{1}{\hbar}\sqrt{2m(E+V_0)}}{\frac{1}{\hbar}\sqrt{2mE}} \\ n &= \sqrt{1+\frac{V_0}{E}} \end{aligned} \tag{12.72}$$

for a real square well potential. The occurrence of reactions corresponds to the absorption of the wave in the nucleus. We can take care of that by introducing a complex diffraction index

$$n' = n(1 - i\chi)$$

where χ is the absorption coefficient, or, by introducing a complex potential, the optical potential

$$U(r) = V(r) - iW(r) \tag{12.73}$$

This describes the excitation functions for nuclear reactions after averaging over the single resonances (transition from η_l to $\langle\eta_l\rangle$) and has the character of a single-particle interaction with a mean potential; that is, the potential $U(r)$ that delivers the average scattering function $\langle\eta_l\rangle$ for the scattering wave function is the optical potential. It is usually given a radial dependence according to the Woods–Saxon potential, Eq. (4.5),

$$f(r) = \{1 + \exp[(r-R)/a]\}$$

with a skin thickness $d = 2a\ln 9$ (decrease from 90% to 10%) = 2.2 fm and $a = 0.5$ fm. The single-particle potential also contains a spin–orbit coupling term so that

$$V(r) = -V_0(r) + V_{ls}h(r)\mathbf{l}\cdot\mathbf{s}$$

with

$$h(r) = (\hbar/m_\pi c^2)\frac{1}{r}\frac{\mathrm{d}f(r)}{\mathrm{d}r}$$

which contains a rough ansatz for the range of the nuclear force via the Compton wavelength of the pion. For $W(r)$, we find empirically that for low energies $\leq$20 MeV, absorption occurs essentially in the surface (W_0) and for higher energies, there is predominantly volume absorption (V_0). The optical potential depends on a number of parameters such as V_0, W_0, W_V, V_ls, W_ls, r_0, a which are not uniquely defined but must be determined empirically. Typical values are $-V_0 = 50$ MeV, $W_0 = 2$ to 10 MeV, $r_0 = 1.2$ fm, $a = 0.5$ fm. V_0 becomes repulsive for very high energies. The optical potential serves for the calculation of an averaged η_l (we have demonstrated the principle for the real square well potential) and is thus used to predict cross sections for elastic scattering, for their angular distributions, and for the total reaction cross sections. It delivers no information about competing reaction channels.

12.7 Nuclear Reactions and Models

Because even nucleon–nucleon scattering is not yet completely understood, there is no unique, exact theory for nucleon–nucleus or nucleus–nucleus collisions other than several simplifying models that apply for different classes of nuclear reactions. We shall introduce briefly here those different classes that evolve with various degrees of inelasticity when nuclear contact is reached:

a. Inelastic scattering, that is, transfer of energy to a bound nucleon leading to particle–hole excitation, also called quasi-particle, see Section 5.8.
b. Collective excitation, that is, vibrational excitation, rotational excitation, and excitation of giant resonances, see Section 5.11.
c. Direct reactions such as (d, p) or (^{3}He, ^{4}He) reactions.
d. Compound nucleus (CN) reactions. Neither the projectile nor the constituents of the target leave the combined system. In a complicated process, the incoming energy is subsequently distributed among many to all nucleons. This statistical distribution changes as long as, randomly, after a long time, one particle gets so much energy that it is evaporated from the surface of the compound nucleus in thermal equilibrium.
e. Precompound decay preferentially observed at higher energies. Here, the incoming energy is dissipated in only a few collisions, and particles are emitted preferentially in a forward direction before a thermal equilibrium is reached.
f. High-energy reactions. In a fast first collision phase, the incoming particle(s) cause an intranuclear cascade leading to particle emission. The excited residual nucleus subsequently evaporates particles in a second slow reaction phase.

This mechanism is called spallation. In central collisions, an explosive emission of particles from a hot compressed collision zone (phase transition) leads via coalescence to the formation of intermediate mass fragments (IMFs) and is called multifragmentation.

12.7.1 Investigation of Nuclear Reactions

The investigation of nuclear reactions comprises the identification of the product nuclei, determination of the cross sections σ, measurement of the energy spectra of the products, the angular distributions, and the determination of excitation functions $\sigma = f(E)$ as shown in Figure 12.21 in Section 12.7.2. Many of the techniques used in investigations of nuclear reactions have been touched upon in Chapter 11. Nuclear chemists will usually detect the radioactive decay of the reaction products after or without chemical separation using Eq. (12.36). For example, in the Goshal experiment discussed in Section 12.7.2, this involves the measurement of characteristic γ transitions in the decay of 38 minutes ^{63}Zn (670, 962 keV), of 9.1 hours ^{62}Zn (41, 597 keV), and of 3.4 hours 61Cu (283, 656 keV). From the tabulated line intensities (number of γ quanta per decay) and the measured decay rates, and knowledge of the projectile flux and target thickness, the cross sections can be calculated. The advantage is that there is a unique Z and A assignment. Flux densities have to be determined in a Faraday cup or by using monitor foils of which the cross sections are well known. Sample and monitor have to be irradiated under exactly the same conditions. Sandwich arrangements and stacks of sample and monitor foils may be advantageous. If the energy loss of the projectiles in a given target thickness is known, irradiation of a stack of targets can allow the determination of a whole excitation function in one bombardment.

Nuclear physics techniques are manifold and may, for example, make use of a magnetic spectrometer or a combination of a measurement of time-of-flight (ToF) and (ΔE,E) measurement where the ToF determines the velocity v of the product nucleus, ΔE is used to determine Z, and $(\Delta E + E) = \frac{1}{2} mAv^2$ is used to determine A. Very good resolutions for Z and A are, for example, in the reaction of ^{136}Xe with ^{56}Fe,

$$\frac{\Delta Z(\mathrm{FWHM})}{Z} = \frac{0.8}{54} \quad \text{and} \quad \frac{\Delta A(\mathrm{FWHM})}{A} = \frac{2.5}{136}$$

that is, the resolution is limited.

12.7.2 Compound Nucleus Model

The compound-nucleus model was introduced in 1936 by Bohr (1936) and turned out to be very successful. In this model, it is assumed that the incident particle amalgamates with the target nucleus such that its kinetic energy in the center of mass, which is increased by the depths of the potential, is distributed randomly among the nucleons. The resulting excited quasi-stationary state has an unusually long lifetime of 10^{-14} to 10^{-19} seconds compared to the time for a nucleon to traverse the nucleus (10^{-22} seconds) due to statistical fluctuations in the energy distribution among the nucleons, until enough energy is concentrated on one nucleon or

a cluster of nucleons to allow it to escape. The most probable fluctuations are those that concentrate only part of the excitation energy on the escaping particle so that its kinetic energy will be less than the maximum possible and that the residual nucleus is still in an excited state, leading to the sequential emission of several particles from the compound nucleus. The similarity to the escape of molecules from a hot liquid has caused the emission of particles from the compound nucleus to be called evaporation. In the compound-nucleus model, two independent steps are distinguished:

i. Capture of the projectile followed by random sharing of the energy among the nucleons in the compound nucleus reaching thermal equilibrium.
ii. Evaporation of particles from the compound nucleus.

The independence of the two stages means that the compound nucleus can be formed in different entrance channels, but its subsequent decay into evaporation residues is independent of its mode of formation. The excitation energy of the compound nucleus is given by

$$U = \frac{M_A}{M_A + M_a} E_a + B_a \tag{12.74}$$

where M_A and M_a are the masses of the target and projectile, E_a is the laboratory kinetic energy of the projectile, and B_a is the binding energy of particle a in the compound nucleus. The excitation energy of a compound nucleus formed by the capture of a slow neutron is expected to be only slightly higher than the binding energy of the neutron so that it takes a very long time before enough energy is concentrated on a neutron, again through thermal fluctuations, to allow it to be evaporated from the compound nucleus. Therefore, the probability for deexcitation by γ emission is much higher and the main reaction with slow neutrons is the (n,γ) reaction. The excitation function for slow-neutron reactions with silver for the energy range 0.01–100 eV is shown in Figure 12.18. Three important features can be noted:

i. The cross sections fluctuate in a very small energy interval, that is, resonances are apparent.
ii. The widths of the resonances are extremely small.
iii. The distances between the resonances are large compared to their widths.

For the 5.19 eV resonance in ^{109}Ag, for example, the width for neutron emission is $\Gamma_n = 12.5$ meV and the width for γ emission is $\Gamma_\gamma = 136$ meV. If the resonances were single-particle resonances, their widths should be on the order of the depth of the imaginary part of the optical model potential, that is, megaelectronvolts. This is off by more than 7 orders of magnitude. The small widths led Bohr to the conclusion, by use of the Heisenberg uncertainty principle, that the resonances are long-lived states with lifetimes of 10^{-14} to 10^{-15} seconds representing a quasi-stationary state, the compound nucleus. The fact that the average spacing between the resonances was more than 100–1000 times smaller than expected for single-particle levels prompted the idea that the quasi-stationary excited state of the compound nucleus must involve the excitation of many particles. For this reason, the optical model is

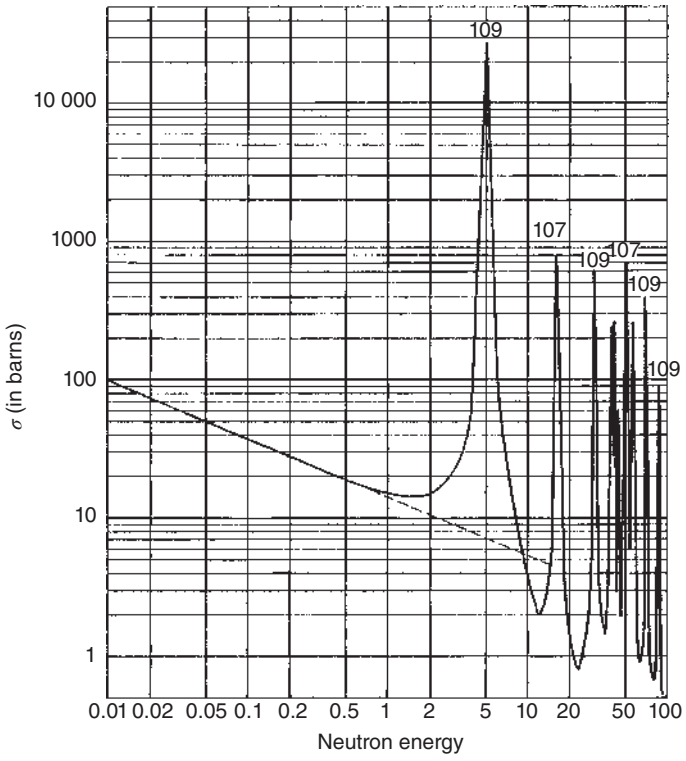

Figure 12.18 Excitation function for reactions of slow neutrons with silver. The data are for silver of natural isotopic abundance; however, each resonance has been assigned to one of the two isotopes as indicated by mass number for a few of the peaks. Source: From Friedlander et al. (1981)/John Wiley & Sons, Inc.

not directly applicable to slow-neutron reactions; however, there is a connection between optical model parameters and the average over many resonances. In view of the two independent stages of the compound-nucleus reactions, the relative amount of γ-ray emission and neutron emission was postulated to be the same when nucleus ${}^{A}_{Z}X$ is irradiated with neutrons and ${}^{A}_{Z-1}X$ is irradiated with protons, provided the energies of the projectiles are such that the same non-overlapping resonant state is populated. This is known as Bohr's "independence hypothesis." We shall return to it again in the discussion of overlapping resonances.

In Section 12.4, we pointed out that resonances occur if the continuous connection of the wave functions at $r = R_0$ occurs with a horizontal tangent. One can show that the behavior of the slope of the tangent f near the resonance determines the width of the resonance. If $\mathrm{d}f/\mathrm{d}E$ is large close to the resonance energy E_{res}, the resonance width is small and the lifetime is large. If $\mathrm{d}f/\mathrm{d}E$ close to the resonance is small, the resonance is broad and the lifetime is small. Based on the relation $\Gamma_{\mathrm{Aa}} \sim (\mathrm{d}f/\mathrm{d}E)^{-1}$ for the general reaction

$$\mathrm{A} + \mathrm{a} \rightarrow \mathrm{C} \rightarrow \mathrm{B} + \mathrm{b} \tag{12.75}$$

G. Breit and E. Wigner arrived at a general expression for the dimensionless resonance amplitude

$$A_{\text{res}} = \frac{\mathrm{i}\Gamma_{\text{Aa}}}{(E - E_{\text{res}}) + i\Gamma/2} \tag{12.76}$$

with Γ_{Aa} being the particle width in the entrance channel, and Γ the total width of the level. The cross section for the particular (12.75) should be written

$$\sigma_{\text{A}\to\text{C}\to\text{B}} = \sigma_{\text{A}\to\text{C}} \cdot W_{\text{B}} \tag{12.77}$$

where $\sigma_{\text{A}\to\text{C}}$ is the cross section for formation of the compound nucleus, and W_{B} is the probability that the compound nucleus decays into channel Bb according to (12.75). The factorization in Eq. (12.77) explicitly represents the independence hypothesis. Then, the Breit–Wigner treatment gives the expression

$$\sigma_{\text{A}\to\text{C}} = \pi\lambda_{\text{Aa}}^2 \frac{2I_{\text{C}} + 1}{(2I_{\text{A}} + 1)(2I_{\text{a}} + 1)} \cdot \frac{\Gamma_{\text{Aa}}\Gamma}{(E - E_{\text{res}})^2 + (\Gamma/2)^2} \tag{12.78}$$

where λ_{Aa} is the relative wavelength in the entrance channel, Γ is the total width of the level, and Γ_{Aa} is the partial width for decay into channel Aa. Generally, $\Gamma_J/\hbar$ is the probability per unit time that the compound nucleus decays into channel J. The total width is $\Gamma = \sum_J \Gamma_J$ and $W_{\text{B}} = \Gamma_{\text{Bb}}/\Gamma$. By inserting Eq. (12.78) and W_{B} into Eq. (12.77), we obtain the famous one-level Breit–Wigner formula

$$\sigma_{\text{A}\to\text{C}\to\text{B}} = \pi\lambda_{\text{Aa}}^2 \frac{2I_{\text{C}} + 1}{(2I_{\text{A}} + 1)(2I_{\text{a}} + 1)} \cdot \frac{\Gamma_{\text{Aa}}\Gamma_{\text{Bb}}}{(E - E_{\text{res}})^2 + (\Gamma/2)^2} \tag{12.79}$$

Applied to the (n,γ) reaction, we obtain

$$\sigma_{(\text{n},\gamma)} = \pi\lambda^2 = \frac{2I_{\text{C}} + 1}{2(2I_{\text{A}} + 1)} \cdot \frac{\Gamma_{\text{n}}\Gamma_{\gamma}}{(E - E_{\text{res}})^2 + (\Gamma/2)^2} \tag{12.80}$$

where Γ_{n} and Γ_{γ} are the partial widths for the neutron and γ emission. Transforming Eq. (12.79) for $E_{\text{res}} = 0$ reveals best the shape of the cross section as a Lorentz curve, see Figure 12.19. At half the maximum cross section, the resonance has the width Γ. Setting $E = E_{\text{res}}$ and $\Gamma = \Gamma_{\text{Aa}}$ (total rescattering of the projectile), the maximum cross section is

$$\sigma_{\text{s,res}}^{\max} = 4\pi\lambda^2$$

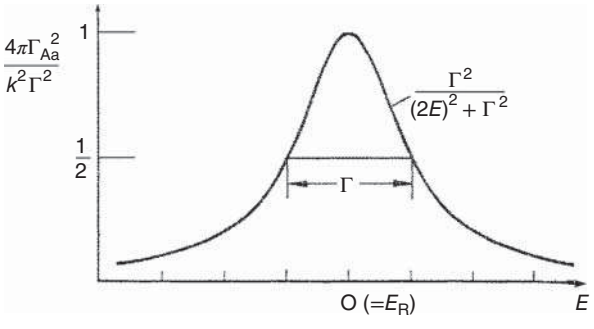

Figure 12.19 Shape of the scattering resonance (Lorentz curve).

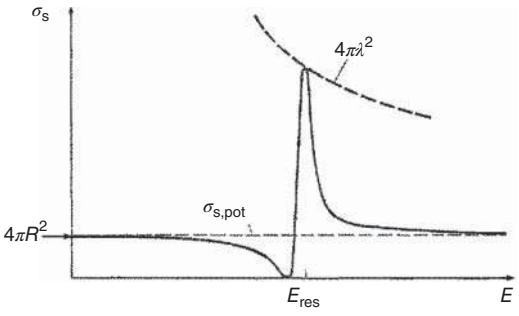

Figure 12.20 Cross section for elastic scattering for l = 0 close to a resonance fluctuating between $4\pi R^2$ and $4\pi\lambda^2$ with destructive and constructive interferences. Source: Modified from Mayer-Kuckuk (1979).

For $|E - E_{res}| \gg \Gamma$, $\sigma_{s,res} \to 0$; here is the potential scattering that we neglected above. We have $\sigma_{s,pot} = 2\pi/k^2(1 - \cos 2kR)$, and for $l = 0$ and $\lambda \gg R$, and with the approximation $\cos x = 1 - x^2/2$, we obtain

$$\sigma_{s,pot} = \frac{2\pi}{k^2}\frac{4k^2R^2}{2} = 4\pi R^2 \tag{12.81}$$

For energies between $E = E_{res}$ and $|E - E_{res}| \gg \Gamma$, the amplitudes for potential scattering and resonance scattering can be on the same order of magnitude. For $E < E_{res}$, we have opposite signs causing destructive interference. For $E > E_{res}$, there is constructive interference. Figure 12.20 shows the resulting shape of the resonance.

In Figure 12.18, for the lowest energies below the resonance region, the cross section falls off with increasing energy following a $1/v$ law. Here, the dominant term in the denominator of Eq. (12.80) is E_{res}, making the denominator essentially constant. Then, the energy dependence of the cross section depends on three remaining factors:

i. $\lambda^2 \sim 1/v^2$;
ii. $\Gamma_n \sim v$;
iii. Γ_γ being independent of changes in neutron energy in the electronvolt range since the energy of the γ-ray is several megaelectronvolts. Thus, the three factors make $\sigma_{(n,\gamma)} \propto 1/v$.

As the energy of the bombarding particle is increased significantly, use of the one-level Breit–Wigner formula becomes problematic. First, the widths of the levels become larger because more exit channels become available. Second, the energy spacing between levels becomes smaller. The result is that resonances begin to overlap. Under these conditions, the various states of the compound nucleus taking part in the reaction do not behave independently and interferences between them are to be expected. These interferences could have the following consequences. The angular distribution of the evaporated particles would not be symmetric about a plane normal to the beam direction, as it must be if a single non-overlapping quantum state rotating in the reaction plane decays statistically. Asymmetry (see the angular correlation in the decay of ^{10}Li, Section 11.10) can arise from interferences between particles emitted with, for example, $l = 0$ and $l = 1$ having different parities. Further, interferences would affect the relative probabilities for emission of various kinds of particles depending on the entrance channel, and the independence between entrance

and exit channels would no longer be true. Problems caused by interferences and by fluctuating partial widths could be removed if the following statistical assumptions are made. The interference terms, being either positive or negative, have random signs and cancel out. This leads to a symmetrical angular distribution. Further, it is assumed that the overlapping states have essentially the same partial widths for the competing decay channels. This leads to the independence hypothesis. Thus, the statistical assumptions allow us to extend the Bohr model to the region of overlapping resonances, that is, to the continuum, and this may be tested by the measurement of angular distributions of evaporated particles and by experimental tests of the independence hypothesis.

It has been verified many times that the angular distribution of particles emitted by compound nuclei at excitation energies up to several tens of megaelectronvolts are perfectly symmetric, indicating that the statistical assumptions just mentioned have some validity. Deviations are observed for some particles of relatively high energy that are emitted preferentially in a forward direction; see the section on precompound decay.

Tests of the independence hypothesis mostly involve the measurement of excitation functions for the production of several radionuclides via a compound nucleus that has been produced in different entrance channels. Named after the author of the first such experiment, S.N. Goshal, these important tests are referred to as "Goshal experiments." Goshal investigated the decay of an excited ^{64}Zn compound nucleus produced in the reactions $^{4}\mathrm{He} + {}^{60}\mathrm{Ni}$ and $^{1}\mathrm{H} + {}^{63}\mathrm{Cu}$. The decay channels investigated were $^{63}\mathrm{Zn} + \mathrm{n}$, $^{62}\mathrm{Zn} + 2\mathrm{n}$, and $^{62}\mathrm{Cu} + {}^{1}\mathrm{H} + \mathrm{n}$. The cross sections for these three exit channels are compared in Figure 12.21, where the energy scales for the helium ion and proton bombardments are adjusted to give

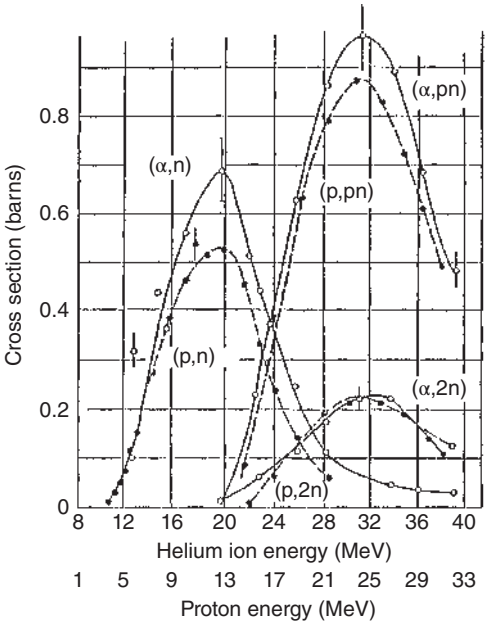

Figure 12.21 Comparison of the decay of the compound nucleus ^{64}Zn formed by $^{60}\mathrm{Ni} + \alpha$ and $^{63}\mathrm{Cu}$ + proton. The relative position of the helium ion and proton energy scales is adjusted to give compound nuclei of the same excitation energy. Source: Goshal (1950), figure 02 (p. 25)/American Physical Society.

compound nuclei of the same excitation energy. The fair agreement of the cross sections for the α-induced and p-induced reactions shows that the independence hypothesis seems to be confirmed. It is common to plot ratio curves as a function of compound-nucleus excitation energy such as

$$\frac{\sigma(\alpha, \mathrm{pn})}{\sigma(\alpha, 2\mathrm{n})} = \frac{W(\mathrm{pn})}{W(2\mathrm{n})} = \frac{\sigma(\mathrm{p}, \mathrm{pn})}{\sigma(\mathrm{p}, 2\mathrm{n})}$$

With these, it is often found that a ratio curve for α-particle-induced reactions has a shape similar to that of the corresponding proton-induced reactions but is displaced on the energy scale, usually to higher energies. Such a displacement can be rationalized when it is realized that, to reach the same excitation energy of the compound nucleus, the α particles bring in more angular momentum than the protons and that the rotational energy component of the excitation energy does not contribute to particle emission. In fact, to be truly in the same state, two compound nuclei must have not only the same energy but also the same angular momentum. Correcting angular momentum effects by shifting energy scales is only approximately correct. More stringent tests of the independence hypothesis involve the measurement of differential cross sections $\mathrm{d}^2\sigma/\mathrm{d}\Omega\mathrm{d}E$ for the emission of particles as a function of angle and energy. Such differential experiments have also shown the independence hypothesis to be valid when angular momentum effects are properly taken into account. Thus, the statistical assumption has proved to be successful for the description of a very large body of reactions with energies up to 50 MeV. These qualitative remarks can be given quantitative expression because the statistical assumption implies that statistical equilibrium exists during a compound-nucleus reaction. Statistical equilibrium implies in turn that the numbers of compound nuclei and of sets of particles that correspond to the various decay channels are determined by their relative state densities (Section 5.4). These concepts are incorporated into the "statistical model." It is able to predict the energy spectrum of the evaporated particles as well as excitation functions for various products in terms of average nuclear properties, as detailed in the following paragraphs.

We consider the decay of compound nucleus C (formed by capture of projectile a) at excitation energy E into the evaporation residue B at excitation energy U and ejectile b with kinetic energy ϵ_{Bb} relative to B according to

$$\mathrm{C}(E) \overset{\epsilon_{\mathrm{Bb}}}{\rightarrow} \mathrm{B}(U) + \mathrm{b} \tag{12.82}$$

and apply to it the principle of detailed balance demanding that statistical equilibrium be maintained by reactions proceeding forward and backward at precisely the same rate. The energetics are depicted in Figure 12.22 together with the energy spectrum of the evaporated particles. By equating the probabilities per unit time for the forward and backward reactions and expressing these in terms of the densities of states, an expression can be derived for the energy spectrum of emitted particles b:

$$I(\epsilon_{\mathrm{Bb}})\mathrm{d}\epsilon_{\mathrm{Bb}} = \frac{\mu_{\mathrm{Bb}}}{\pi^2\hbar^3}\sigma_{\mathrm{Bb}}\epsilon_{\mathrm{Bb}}\frac{\omega_B(U)}{\omega_C(E)} \tag{12.83}$$

where $I(\varepsilon_{\mathrm{Bb}})\mathrm{d}\varepsilon_{\mathrm{Bb}}$ is the probability per unit time of the compound nucleus to emit particle b with relative kinetic energy between $\varepsilon_{\mathrm{Bb}}$ and $\varepsilon_{\mathrm{Bb}} + \mathrm{d}\varepsilon_{\mathrm{Bb}}$, μ_{Bb} is the reduced

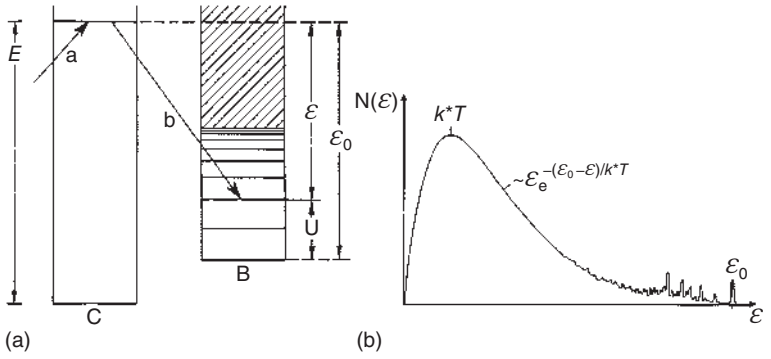

Figure 12.22 (a) Energy scheme in the formation and decay of compound nuclei. (b) Energy spectrum of the evaporated particles (schematic). Source: From Mayer-Kuckuk (1979)/Springer Nature.

mass, σ_{Bb} is the cross section for the reaction of nucleus B at excitation energy U with particle b at kinetic energy $\varepsilon_{\mathrm{Bb}}$ (the inverse cross section), and $\omega_{\mathrm{B}}(U)$ and $\omega_{\mathrm{C}}(E)$ are the densities of states of B and C at their respective excitation energies. The maximum of the energy spectrum at relatively low kinetic energy occurs because, although $\varepsilon_{\mathrm{Bb}}$ obviously increases with kinetic energy, U simultaneously decreases and the density of states $\omega_{\mathrm{B}}(U)$ decreases in an approximately exponential way as discussed below. For the use of Eq. (12.83), we need expressions for the inverse cross section σ_{Bb} and for the densities of states. The inverse cross section is

$$\sigma_{\mathrm{Bb}} = \pi\lambda^2 \sum_l (2l+1)(1 - |\langle\eta_l\rangle|^2)$$

where $|\langle\eta_l\rangle|^2$ is calculated in the frame of the optical model. It is evident that densities of states are of great importance to calculations in evaporation theory. We follow the usual convention of discussing this topic in terms of level densities rather than state densities, the difference being that a level of angular momentum J has $2J+1$ states. We have discussed that the excitation energy E of the compound nucleus is randomly distributed among its nucleons. The number of possibilities to distribute the energy among A nucleons at a given energy is identical to the level density, $\rho(U)$, which is of central importance in the statistical model. The simplest assumption about $\rho(U)$ is that the energy levels above the Fermi energy are equidistant with a distance D_0. If a given energy is selected, one can count the number of possibilities to associate the number of nucleons with the available levels such that the excitation energy U results. The solution of this combinatorial exercise is

$$\rho(U) \propto \frac{1}{U} \mathrm{e}^{2\sqrt{aU}} \quad \text{with } a = \frac{\pi^2}{6D_0} \tag{12.84}$$

where a is called the level density parameter. Improved treatments of the level density are available by replacing the model of equidistant levels by the Fermi gas model. The level density parameter is proportional to A and associates the excitation energy with a thermodynamic temperature, see Eq. (5.18) in Section 5.4.

According to the energy diagram shown in Figure 12.22, we can replace U by $(\varepsilon_0 - \varepsilon)$. Returning to Eq. (12.83) and using Eq. (12.84) for the level density, as well as Eq. (5.18), we see that the spectrum of evaporated particles has the form

$$I(\epsilon) \propto \sigma \epsilon e^{-(\epsilon_0 - \epsilon)/T} \tag{12.85}$$

which is the shape of a Maxwell–Boltzmann distribution. A plot of $\ln[I(\varepsilon)/\sigma\varepsilon]$ vs. $(\varepsilon_0 - \varepsilon)^{1/2}$ allows us to linearize the evaporation spectrum and to evaluate the level density parameter a and the nuclear temperature T.

Equation (12.84) can be modified by taking into account that the level density depends on the angular momentum as

$$\rho(U, I) \propto \frac{1}{U^2}(2I+1)\mathrm{e}^{2\sqrt{aU}} \cdot \mathrm{e}^{-E_{\mathrm{rot}}/T} = \frac{1}{U^2}(2I+1)\exp\left\{2\sqrt{aU} - \frac{I(I+1)}{2\sigma^2}\right\} \tag{12.86}$$

where we have set for the rotational energy

$$E_{\mathrm{rot}} = \frac{I(I+1)\hbar^2}{2\Im} = \frac{I(I+1)}{2\sigma^2}$$

with $\sigma^2 = \Im T/\hbar^2$ being the so-called angular momentum cut-off parameter. In Figure 12.23, the dependence of the level density on U and I is shown graphically. In the U–I plane, the yrast line, known from Section 5.11, cuts the plane into an allowed and a forbidden area. The trivial reason is that the rotational energy eats

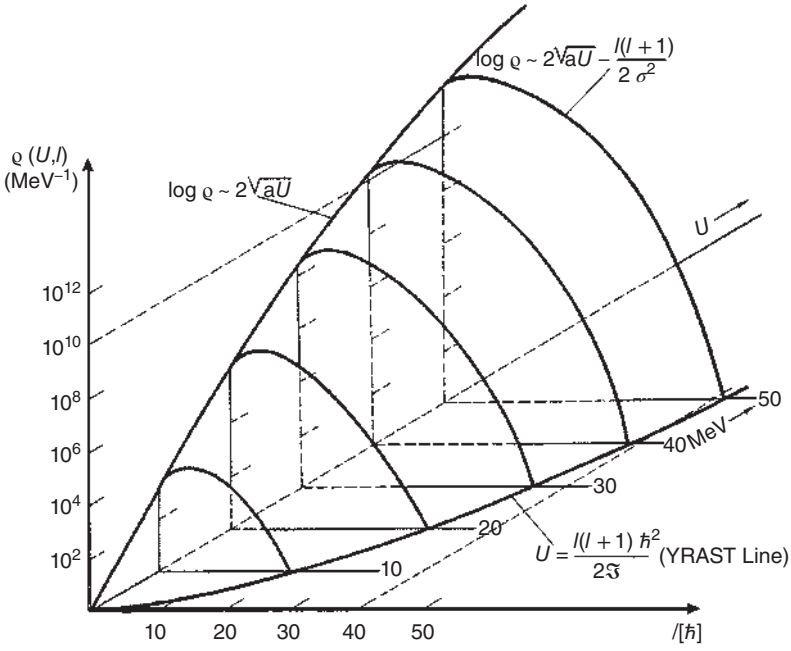

Figure 12.23 Level density as a function of U and I calculated for ^{65}Zn. Source: From Mayer-Kuckuk (1979)/Springer Nature.

up a fraction of the energy U that is needed for cold rotation and this part does not contribute to the level density.

Interesting observations can be made when looking at the systematics of level densities. A hint for these observations is already contained in Figure 12.21. Here, it is obvious that the cross sections for the (α,2n) and (p,2n) reactions leading to $^{62}_{30}$Zn, an even–even nucleus, are much smaller than the cross sections for the (α,pn) and (p,pn) reactions leading to $^{62}_{29}$Cu, an odd–odd nucleus. As the cross sections for competing evaporation channels depend on the different level densities, this is a hint for the fact that level densities in even–even nuclei are smaller than that in odd–odd nuclei. We have seen in Chapter 3 that nuclei with even numbers of protons or neutrons are stabilized by the pairing energy. The mass parabolas for even–even and odd–odd nuclei are two times the pairing energy apart from each other (Figure 3.9), and for even–even nuclei, there is no single-particle state below the mass parabola for the odd–odd nuclei, that is, within the pairing gap. It is also well known from experimental data that at least up to the region explored by neutron resonances, even–even nuclei have level spacings larger than those of their odd-Z or odd-N neighbors. These pairing effects on the level density become less marked with increasing excitation, as might be expected from the rapidly increasing nucleon configurations that can lead to a total excitation energy. Average level spacings deduced from the mean energy intervals between slow-neutron resonances are shown in Figure 12.24, illustrating the tendency for the spacing in even–even nuclei slightly to exceed those of even–odd and odd–even nuclei and appreciably to

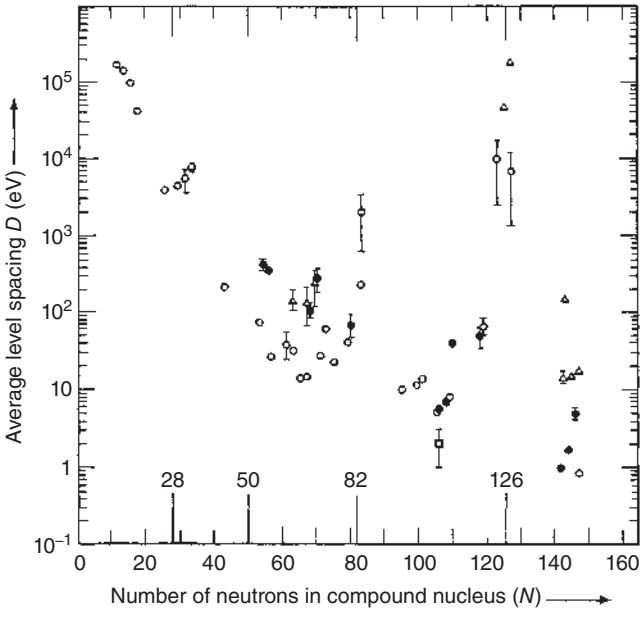

Figure 12.24 Level spacing for even–even •, even–odd △, odd–even □, and odd–odd nuclei ○. Note the particularly large level spacing for closed-shell nuclei. Source: Newton (1956), figure 04 (p. 35)/Canadian Science Publishing.

exceed those in odd–odd nuclei. In addition, the data reveal discontinuities at the magic numbers where the ground-state masses are decreased by the shell correction energies.

The pairing effect must be taken into account in the expressions for level density, and in view of the energy dependence noted above, this may be done by introducing a fictitious ground state that the nucleus would have in the absence of enhanced stability due to pairing. This leads to the expression

$$\rho(U) = C \exp[2a^{1/2}(U - \delta_{\mathrm{n}} - \delta_{\mathrm{p}})^{1/2}] \tag{12.87}$$

in place of Eq. (12.84). The quantities δ_{n} and δ_{p} are zero for odd neutron and odd proton numbers and are positive for even neutron and proton numbers. Thus, the level density of an odd–odd nucleus at a given excitation energy is indeed greater than that of an adjacent even–odd or odd–even nucleus, which, in turn, is greater than that of an adjacent even–even nucleus. Our example from Figure 12.21 is remarkable as the (α,pn) and (p,pn) cross sections are considerably greater than those for the emission of two neutrons despite the fact that the Coulomb barrier for proton emission serves to diminish proton emission. Considerable success in the interpretation of excitation functions has been achieved with Eq. (12.87), for example, by Dostrovsky et al.

Apart from the level densities, we need the probabilities for particles of a given kinetic energy to penetrate the potential border of the nucleus. In Eq. (12.83), we had already considered the probabilities per unit time for the forward and backward reactions and expressed these in terms of the densities of states. The total probability per unit time for the emission of particle b is obtained by integrating Eq. (12.83) over the whole spectrum,

$$P_{\mathrm{b}} = \int_0^{E-S_{\mathrm{b}}} I(\epsilon_{\mathrm{Bb}}) d\epsilon_{\mathrm{Bb}} \tag{12.88}$$

where the upper limit of the integral is given by the excitation energy of the compound nucleus minus the separation energy S_{b} of particle b. To go from Eq. (12.88) to the fraction of all compound nuclei decaying into channel Bb, we must divide the integral in Eq. (12.88) by the sum of all such integrals for all decay channels. The cross section for a reaction such as Eq. (12.75) is then obtained by multiplying that fraction by the formation cross section of the compound nucleus. The calculation of cross sections for reactions involving the sequential emission of several particles becomes complicated in that it requires the evaluation of multiple integrals, which is usually done by Monte Carlo methods.

For compound-nucleus fission, the anisotropic angular distributions of the fission fragments indicate that formation and decay are not completely independent; there is angular momentum coupling between the entrance and exit channels. Also, there is another important peculiarity for compound-nucleus fission. According to D.L. Hill and J.A. Wheeler, in 1953, the fission properties are not determined by the final state level densities as in particle evaporation, but by the level density at the saddle point ("fission channels"). Fission probabilities and fission fragment angular distributions are determined by the saddle point transition-state model.

Before we go into this, we want to answer the question on how anisotropy comes about. If there were complete independence of entrance and exit channels, the angular distribution would be isotropic, $(d\sigma/d\Omega)_\Theta = \text{const}$. On the contrary, if the compound nucleus rotates with high angular momentum in the entrance channel reaction plane with the angular momentum vector perpendicular to that plane, one may expect that elongation of the compound nucleus toward the saddle point occurs in that reaction plane and the fission fragments are emitted in that plane. Then, the tips of the fission fragment momentum vectors lie on a circle in that reaction plane yielding an isotropic distribution in the reaction plane. Since we can have as many reaction planes as we like, rotationally symmetric around the beam direction, there is a circle in each of these reaction planes such that the circles touch each other at $\Theta = 0°$ and at $\Theta = 180°$. The density of these circles is at a minimum at $\Theta = 90°$, and it can be shown that under these assumptions the angular distribution is

$$\left(\frac{d\sigma}{d\Omega}\right)_\Theta \propto \frac{1}{\sin\Theta} \tag{12.89}$$

According to Eq. (12.31), this gives

$$\left(\frac{d\sigma}{d\Theta}\right) = \text{const}$$

In reality, fission does not always occur in the entrance channel reaction plane because there is coupling of the total angular momentum with one of the six normal modes of intrinsic rotation in a fissioning system, that is, with the tilting mode. The latter tilts the deformed nucleus out of the entrance channel reaction plane. Qualitatively, tilting disperses the cross section away from 0° and 180°. The angular momentum coupling scheme is shown in Figure 12.25. The experimental scattering angle Θ is the vector sum of the internal scattering angle in the entry plane Θ_i and the tilting angle φ between the entry plane and the exit plane. According to J.A. Wheeler, the probability of emitting a fission fragment at an angle Θ from a transition-state nucleus characterized by **I**, **K**, and **M** is

$$P^{\mathrm{I}}_{\mathrm{M,K}} = \frac{(2I+1)}{4\pi R^2} |d^{\mathrm{I}}_{\mathrm{M,K}}(\Theta)|^2 2\pi R^2 \sin\Theta \, d\Theta \tag{12.90}$$

where $d^{\mathrm{I}}_{\mathrm{M,K}}(\Theta)$ is a symmetric top wave function tabulated by A.N. Behkami (1971). The basic assumptions are that the angular momentum quantum numbers are

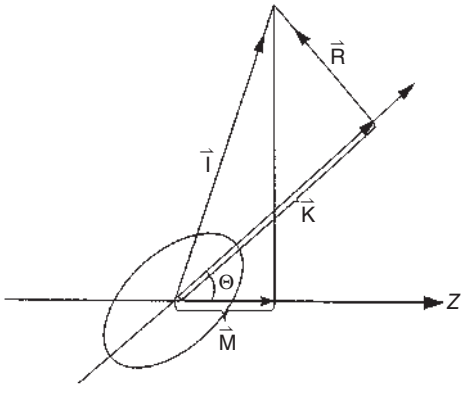

Figure 12.25 Angular momentum coupling scheme for a deformed nucleus.

frozen in at the saddle point and that the nucleus is a rigid rotor. In low-energy fission, individual saddle point transition states are populated and the angular distributions change from forward to sideward to backward peaking, reflecting the quantum numbers involved. For higher excitation energies and higher angular momenta where $M \sim 0$, one again uses a statistical model considering a level density of transition states with total angular momentum **I** and projection **K** on the symmetry axis

$$\rho(\mathbf{I}, \mathbf{K}) \propto \exp[(E - E_{\text{rot}})/T] \tag{12.91}$$

where E is the total excitation energy, $E_{\text{rot}}^{I,K}$ is the energy bound in collective rotation at the saddle point, T is the thermodynamic temperature, and $(E - E_{\text{rot}}^{I,K})$ is the fraction of the available energy that causes level density. Explicitly,

$$E_{\text{rot}}^{I,K} = \frac{\hbar^2}{2\mathfrak{I}_\perp} R^2 + \frac{\hbar^2}{2\mathfrak{I}_\parallel} K^2 \tag{12.92}$$

where $\mathfrak{I}_\perp$ and $\mathfrak{I}_\parallel$ are moments of inertia about axes perpendicular and parallel to the symmetry axis, respectively, and $R^2 = I^2 - K^2$. The resulting transition-state level density is

$$\rho(I, K) \propto \exp\{(E/T) - (\hbar^2 I^2/2\mathfrak{I}_\perp) - (\hbar^2 K^2/2\mathfrak{I}_\parallel)[(1/\mathfrak{I}_\parallel) - (1/\mathfrak{I}_\perp)]\} \tag{12.93}$$

meaning that if I is fixed (by the cross section), $\rho(K)$ depends only on the moments of inertia at the saddle point as

$$\rho\,(K) \propto \exp\left\{-\left(\hbar^2 K^2/2T\right)\left[\left(1/\mathfrak{I}_\parallel\right) - \left(1/\mathfrak{I}_\perp\right)\right]\right\} \tag{12.94}$$

This equation is equivalent to a Gaussian distribution introduced by Halpern and Strutinsky

$$\rho(K) \propto \exp(-K^2/2K_0^2) \quad \text{for } K \leq I$$

$$\rho(K) = 0 \quad \text{for } K > I$$

Here, K_0^2 is the standard deviation squared (the variance) of the Gaussian and relates to the temperature and the moments of inertia as

$$K_0^2 = T/\hbar^2[(1/\mathfrak{I}_\parallel) - (1/\mathfrak{I}_\perp)] \tag{12.95}$$

If $[(1/\mathfrak{I}_\parallel) - (1/\mathfrak{I}_\perp)]$ is replaced by $1/\mathfrak{I}_{\text{eff}}$, we have

$$K_0^2 = \frac{T \cdot \mathfrak{I}_{\text{eff}}}{\hbar^2} \tag{12.96}$$

which tells us that by measuring the fission fragment angular distribution close to 0° and close to 180°, this will allow us to learn about the shape of the fissioning nucleus at the saddle point. We will come back to this fascinating perspective shortly. In turn, the fission fragment angular distribution $W(\Theta)$, after some approximation, takes the form

$$W(\Theta) \propto \sum_{I=0}^{\infty} (2I+1) T_I \sum_{K=-I}^{I} \frac{(2I+1)|d_{M=0,K}^{I}(\Theta)|^2 \exp(-K^2/2K_0^2)}{\sum_{K=-I}^{I} \exp(-K^2/2K_0^2)} \tag{12.97}$$

with T_I the transmission coefficient for the formation of the compound nucleus with angular momentum I. This leads us to the shorthand notation

$$W(\Theta) \propto \sum_{I=0}^{\infty} \frac{(2I+1)^2 T_I \exp\left[\left(-I+\frac{1}{2}\right)^2 \sin^2\Theta/4K_0^2\right] J_0\left[i\left(I+\frac{1}{2}\right)^2 \sin^2\Theta/4K_0^2\right]}{\operatorname{erf}\left[\left(I+\frac{1}{2}\right)/(2K_0^2)^{1/2}\right]} \tag{12.98}$$

In Eq. (12.98), J_0 is the zero-order Bessel function with imaginary argument and $\operatorname{erf}\left[\left(I+\frac{1}{2}\right)/(2K_0^2)^{1/2}\right]$ is the error function defined by

$$\operatorname{erf}(x) = (2/\pi^{1/2}) \int_0^x \exp(-t^2)\, \mathrm{d}t$$

Examination of experimental anisotropies, for example, $W(174°)/W(90°)$, shows (Vandenbosch and Huizenga 1965) that the anisotropies increase with increasing I/K_0^2, see Eq. (12.98), and that K_0^2 increases with $\sqrt{E}$, see Eq. (12.96), in both cases as expected. The anisotropy decreases with increasing Z^2/A of the compound nucleus, indicating that it decreases with decreasing saddle point deformation but not quantitatively as predicted by the liquid–drop model. Saddle or transition-state deformations computed from first-chance fission anisotropies as a function of Z^2/A are shown in Figure 12.26 where they are compared to theoretical predictions based on the charged liquid–drop model calculations using $(Z^2/A)_{\text{crit}} = 50.1$ by Cohen

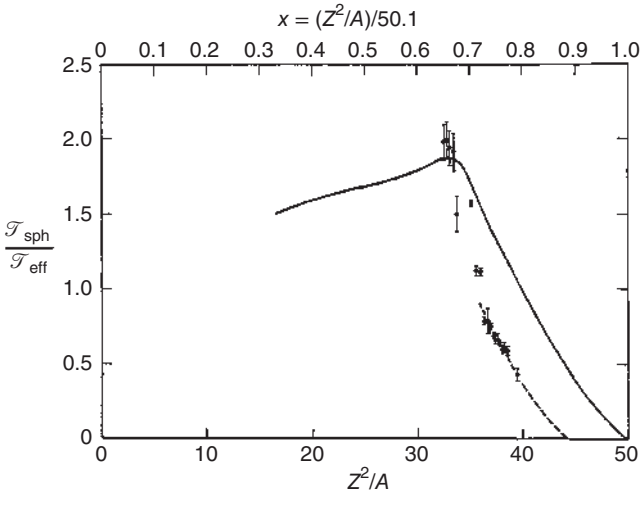

Figure 12.26 Transition-state deformation calculated from first-chance fission anisotropies as a function of Z^2/A for the compound nucleus. Theoretical predictions based on liquid–drop model calculations using $(Z^2/A)_{\text{crit}} = 50.1$ by Cohen and Swiatecki (solid line). Extrapolation from ^{231}Pa and heavier nuclei to zero saddle deformation give a revised estimate of $(Z^2/A)_{\text{crit}} = 45$ (dashed line). The extrapolated curve is based on $a = A/8$ for the level density parameter of the compound nucleus. Source: Reising, Bate, and Huizenga (1966), figure 05 (p. 35)/American Physical Society.

and Swiatecki. This indicates problems with the liquid–drop saddle point shapes. This led to the introduction of the rotating liquid–drop model (RLDM) by Cohen et al. in 1974 (Cohen, Plasil, and Swiatecki 1974). In Section 6.5, we introduced the liquid–drop model fissility parameter x (Eq. (6.25)) as resulting from the interplay between the restoring surface energy and the repulsive Coulomb energy. The fundamental assumption in the RLDM is that, in addition to the Coulomb force, a centrifugal force has to be considered and these two repulsive forces are similar in their action. Thus, an angular momentum-dependent fissility parameter, $x(l)$, was introduced:

$$x(l) = x(0) + \eta(x) \cdot y \tag{12.99}$$

The quantity $x(l)$ is defined as the fissility at which a non-rotating system has the same saddle point deformation – expressed in terms of $\mathfrak{I}_{\text{sph}}/\mathfrak{I}_{\text{eff}}$ – as the considered rotating system. With this one defines the equality

$$\frac{\mathfrak{I}_{\text{sph}}}{\mathfrak{I}_{\text{eff}}}(x(l), I = 0) = \frac{\mathfrak{I}_{\text{sph}}}{\mathfrak{I}_{\text{eff}}}(x, \langle I^2 \rangle)$$

In Eq. (12.99), the two dimensionless parameters are

$$x(0) = \frac{E_{\text{C}}^0}{2E_{\text{s}}^0} = \frac{1}{50.883(1 - 1.7826I^2)} \cdot \frac{Z^2}{A} \approx \frac{Z^2}{50A} \tag{12.100}$$

$$y = \frac{E_{\text{rot}}^0}{E_{\text{s}}^0} = \frac{1.9249}{(1 - 1.7826I^2)} \cdot \frac{l^2}{A^{7/3}} \approx \frac{2l^2}{A^{7/3}}$$

The quantity $I = (N - Z)/A$ is the isospin asymmetry as introduced in Eq. (3.12) by Myers and Swiatecki. The x parameter is a measure of the ratio of the disruptive Coulombic repulsion to the surface attractive force. The y parameter is the newly introduced ratio of centrifugal repulsive force to surface attractive force. The fission barriers in the RLDM are the differences between ground-state and saddle point energies as calculated in terms of the x and y parameters for idealized liquid–drop nuclei with sharp surfaces. Figure 12.27 shows some nuclear shapes predicted by the RLDM as a function of the x and y parameters. The saddle point shapes can be described in terms of compactness (the ratio of the median semi-minor axis to semi-major axis) and the "necking in," which refers to how small the cross-sectional area of the neck is with respect to the cross-sectional area of, for example, a cylinder-like shape (as at $x = 0.8$, $y = 0$ in Figure 12.27). It is evident that, for a given value of x, the compactness of the saddle point shapes increases with increasing y. Another prediction of the RLDM is the critical angular momentum at which the fission barrier vanishes as a function of mass number as shown in Figure 12.28. This quantity is often designated as $l_{B_{\text{f}}=0}$, and it is seen to be largest for nuclei around $A = 100$ and to decrease dramatically for heavier nuclei.

Values of $\mathfrak{I}_{\text{sph}}/\mathfrak{I}_{\text{eff}}$ deduced from the anisotropies of the angular distributions in a variety of fusion reactions as a function of $x(l)$ are plotted in Figure 12.29. The ^{4}He-, ^{12}C-, and ^{16}O-induced reactions require only a small renormalization by $\Delta x(l) = -0.03$ to follow the predicted trend by the RLDM. For higher products

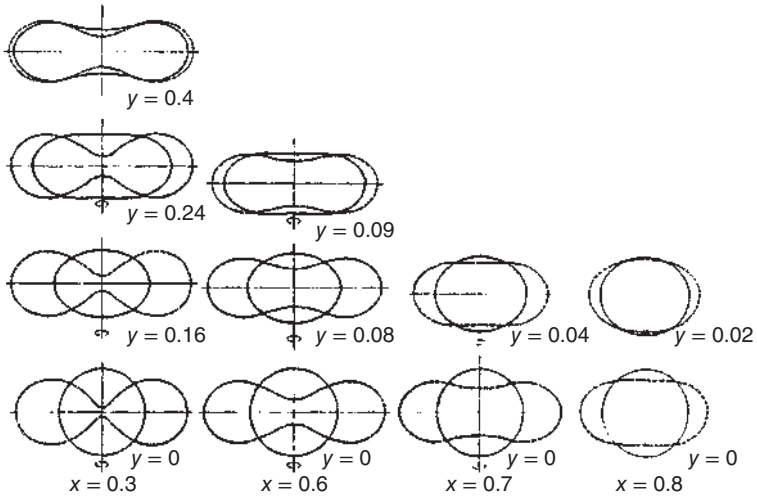

Figure 12.27 Shape projections vs. x (fissility) and y (angular momentum) parameters for the rotating liquid–drop model. The dashed curves represent saddle point shapes and the solid curves represent equilibrium ground-state shapes. The vertical axes are the axes of rotation. Source: Cohen, Plasil, and Swiatecki (1974), figure 5 (p. 38)/Elsevier.

Figure 12.28 The critical angular momentum $l_{B_f=0}$ for the vanishing of the fission barrier as a function of the mass number. The hatched region corresponds to l values where the binding energy of the neutrons becomes equal to the fission barrier. Source: Plasil (1974)/Oak Ridge National Laboratory. Public Domain.

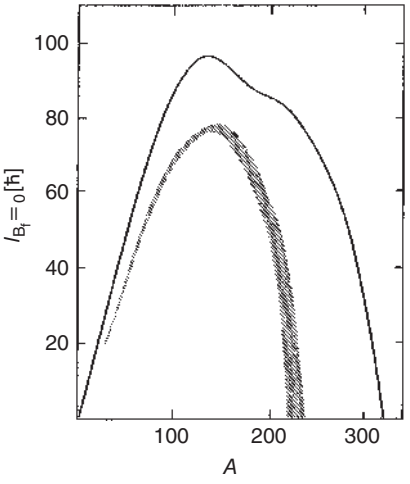

of $Z_1 \cdot Z_2$, the anisotropies are much too large. Speculation about possible reasons included the validity of approximations within the saddle point transition-state model (the use of $\langle I \rangle$ and a constant temperature, the RLDM knowing only $K = 0$ and symmetric mass divisions), as well as about K breaking between saddle and scission and the need for scission point models. As we shall detail in Section 12.8.1, the obvious explanation is rather that for the heavier collision systems, compound-nucleus formation is dynamically hindered and the observed fission fragments originate from preequilibrium "quasi-fission" in which the tilting mode does not reach thermal equilibrium.

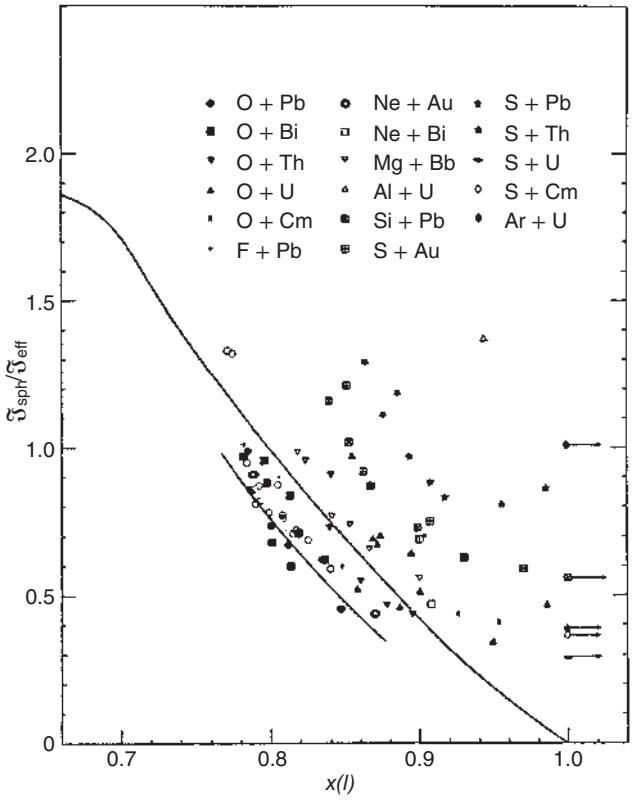

Figure 12.29 Values of $\mathfrak{I}_{sph}/\mathfrak{I}_{eff}$ vs. $x(l)$ for a number of compound nucleus fission reactions. The data for $\alpha + Th$ are depicted by open circles; the other symbols are assigned to the reactions in the figure. The data are compared to the prediction of the RLDM (solid line). The ^{4}He, ^{12}C, ^{16}O, ^{19}F induced reaction data call for a renormalization by $\Delta x(l) = -0.03$. For the data of the heavier systems, see text. Source: Back et al. (1985), figure 03 (p. 25)/American Physical Society.

12.7.3 Precompound Decay

The frequent observation of high-energy tails on the bell-shaped excitation functions for compound-nucleus evaporation reactions called for a model that explained these continuous spectra at energies too high to be accounted for by the statistical theory. This model assumes that these high-energy particles are emitted prior to the attainment of statistical equilibrium, hence the name precompound decay. See the review by Blann (1975). Figure 12.30 shows as an example the proton spectrum from the reaction $^{54}Fe(p,p')$ induced by 62 MeV protons, which exhibits three components: an evaporation peak at low energies; some sharp resonances close to the beam energy produced by direct reactions to be discussed below; and a broad continuum in between that is the signature of precompound decay. The associated angular distributions are generally forward peaked. Precompound decay has been described by the exciton model of Griffin. In this model, based on the observation that an incoming

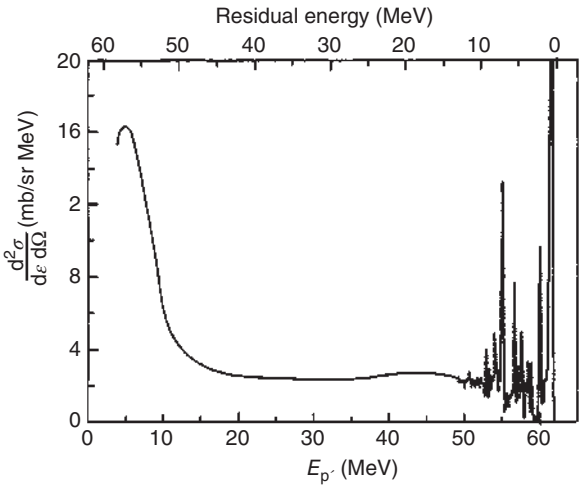

Figure 12.30 Proton spectrum at 35° in a 62 MeV bombardment of ^{54}Fe. Source: Blann (1975), figure 04 (p. 45)/Annual Reviews, Inc.

nucleon and a bound nucleon create an additional excited nucleon and a nucleon hole, the focus is on the total number of "excitons" (particle–hole states). With each subsequent collision, the number of excitons either stays constant or increases by two and the possibilities in which the excitation energy can be shared by excited particles and holes grow rapidly with the exciton number. For a given exciton number, every particle–hole configuration including those with unbound particles has equal probability. On this basis, the number of states with unbound particles is calculated as well as the energies of these escaping particles. By summing over the exciton numbers, one can obtain energy spectra. Intranuclear transition rates are obtained from mean free paths of nucleons in nuclear matter using the imaginary part of the optical potential.

12.7.4 Direct Reactions

In direct reactions (see the high-energy part of the energy spectrum in Figure 12.30), the wave functions of the entrance and exit channels largely overlap such that the transition is fast and occurs with a minimum of rearrangement within the nucleus. The typical example for a direct reaction is a (d, p) reaction in which the neutron of the deuteron is caught by the target nucleus and the proton is scattered away without much energy loss. This is called *a stripping reaction*. The inverse case occurs in the (^{3}He, α) reaction where a neutron is taken from the target nucleus in a pickup reaction. Generally, the exchange of one or a few nucleons is called quasi-elastic transfer reaction. These reactions are further characterized by asymmetric angular distributions, mostly forward peaked, that exhibit diffraction patterns similar to those observed in elastic scattering. In order to make the relation between angular distribution and transferred momentum intelligible, we briefly look at a crude model for a (d, p) reaction. The deuteron is assumed to collide with the target nucleus A in a grazing collision. The neutron is caught with orbital angular momentum l_n under formation of the product nucleus B, whereas the proton escapes under angle Θ. The

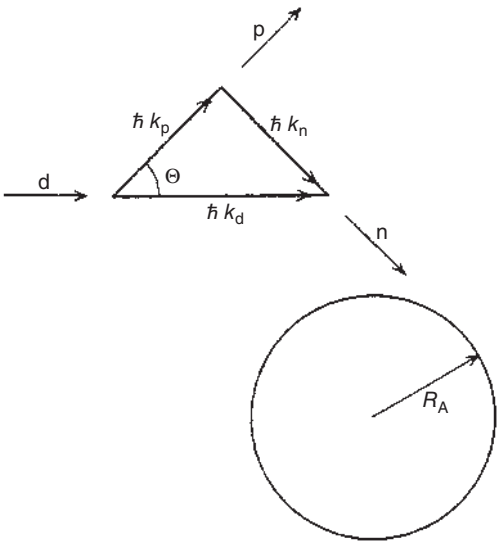

Figure 12.31 Momentum diagram for a (d, p) reaction with the proton emitted at an angle Θ and the neutron captured with impact parameter R_A.

target nucleus must be heavy enough so that the lab and cm coordinates are practically identical. Then, the momentum diagram shown in Figure 12.31 is valid. The deuteron approaches with momentum $\hbar k_d$ and the proton goes off with momentum $\hbar k_p$, at an angle Θ. The momentum of the captured neutron is obtained from the conservation of momenta:

$$k_n^2 = k_d^2 + k_p^2 - 2k_d k_p \cos\Theta \tag{12.101}$$

If R_A is the interaction radius, the orbital angular momentum carried in by the captured neutron is classically given by $l_n = R_A \cdot \hbar k_n$, or quantum mechanically by

$$\hbar\sqrt{l_n(l_n+1)} = R_A \hbar k_n \tag{12.102}$$

Combining Eqs. (12.101) with (12.102), we get

$$\frac{l_n(l_n+1)}{R_A^2} = k_d^2 + k_p^2 - 2k_d k_p \cos\Theta$$

or

$$\cos\Theta = \frac{k_d^2 + k_p^2 - l_n(l_n+1)/R_A^2}{2k_d k_p} \tag{12.103}$$

Since k_d and k_p are measured quantities, there is a definite relation between l_n and Θ. In the quantum mechanical treatment, we obtain a distribution instead of this simple relation. Nevertheless, Eq. (12.103) reproduces the position of the main maximum. This is shown in Figure 12.32 for the reaction ^{76}Se(d,p)^{77}Se where the 43rd neutron is built in the target nucleus. According to Figure 12.32, the $^1g_{9/2}$ ($l=4$) or the $^2p_{1/2}$ ($l=1$) levels are candidates. If we use Eq. (12.103) with $E_d = 7.8$ MeV and $E_p = 13$ MeV to calculate the angles belonging to $l=4$ and $l=1$, we obtain 64° and 19°, respectively, showing that the $^2p_{1/2}$ single-particle state is likely to be populated. The simplest quantum mechanical treatment of the data in Figure 12.32 can

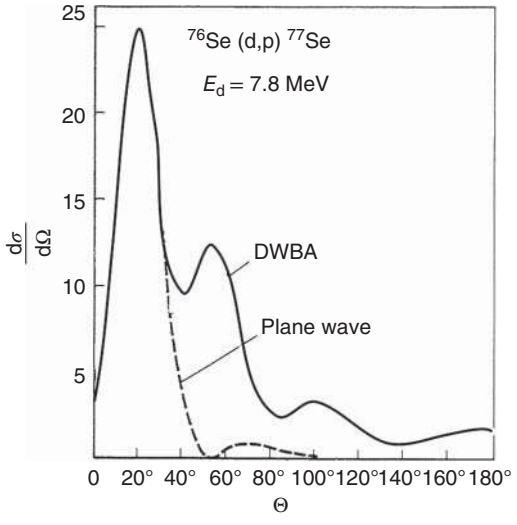

Figure 12.32 Angular distribution of a (d, p) reaction on ^{76}Se with theoretical descriptions using the Born approximation for plane waves and the distorted-wave Born approximation DWBA. Source: Modified from Mayer-Kuckuk (1979).

be done with the Born approximation for plane waves. An improved reproduction of the data is obtained if the plane waves are replaced by waves distorted by the effective nuclear potential (distorted wave Born approximation, DWBA). The cross section for a single-particle transfer to a given level with angular momentum transfer l_j has the following form:

$$\left(\frac{d\sigma}{d\Theta}\right)^{l_j}_{\text{experiment}} = S_{l_j}\left(\frac{d\sigma}{d\Omega}\right)^{l_j}_{\text{DWBA}} \tag{12.104}$$

Here, $(d\sigma/d\Omega)^{l_j}_{\text{DWBA}}$ represents the kinematical part of the cross section depending on the incident energy, the Q value, angular momentum transfer l, angular momentum j of the single-particle state, and angle Θ. By comparing the experimental cross section to the DWBA cross section, the spectroscopic factor S_{l_j} can be determined. The experimental determination of spectroscopic factors is an important tool for testing nuclear models.

12.7.5 Photonuclear Reactions

In 1934, J. Chadwick and M. Goldhaber observed the first nuclear reaction induced by photons, the photodisintegration of the deuteron by the 2.61 MeV γ-rays of a ^{208}Tl source. From their measurement of the kinetic energy of the protons produced, they deduced a rather accurate value of the neutron mass.

Reactions of bremsstrahlung photons produced at electron accelerators are dominated by the excitation of the isovector giant dipole resonance (GDR), see Section 5.11. The energy of the resonance varies smoothly with the target mass number decreasing from 24 MeV in ^{16}O to 13 MeV in ^{209}Bi. The peak cross sections are 100–300 mb. The Goldhaber–Teller model makes some simple predictions about the magnitude and A dependence of the cross sections as $0.06NZ/A$ MeV b and the peak energies as $aA^{-1/3}$ where a varies from 60 MeV for the lightest to

80 MeV for the heaviest targets. The competition between (γ,n), (γ,p), (γ,2n), and photofission reactions (in heavy nuclei) is consistent with statistical considerations of compound-nucleus deexcitation. From 30 to about 140 MeV, the absorption cross sections are roughly constant at about one-tenth of the peak cross section of the GDR. At these and still higher energies, the absorption of the photon occurs by a neutron–proton pair and is called the *quasi-deuteron mechanism*. Since pairs of like nucleons do not have dipole moments, they are not effective for photon absorption. In the interaction with a quasi-deuteron, the two nucleons fly apart in nearly opposite direction. In light nuclei, they have a high probability of escaping from the nucleus. In heavy nuclei, the probability to interact with other nucleons in a cascade increases. The quasi-deuteron model is consistent with the angular distributions and energy spectra of the escape protons. Above the pion threshold, photon absorption cross sections increase. Pions created inside a nucleus are reabsorbed and distribute their energy among nucleons.

12.7.6 Fission

Even though we have already dealt with spontaneous fission as one of the decay modes in Section 6.5, it is appropriate to return to fission at this point because fission is another important mode of deexcitation of an excited compound nucleus and competes with the evaporation of mostly neutrons in the region of high atomic numbers. Whereas spontaneous fission is a tunneling process, induced fission occurs when enough excitation energy is available for the compound nucleus to surmount the fission barrier. Fission by thermal neutrons has gained enormous practical importance resulting from the large energy release of close to 200 MeV per fission and from the fact that in each neutron-induced fission, several neutrons are emitted, thus making a divergent chain reaction possible. Fission cross sections $\sigma_{n,f}$ for nuclear fission by thermal neutrons are compiled in Table 12.1. Heavy nuclei with an odd number of neutrons such as ^{233}U, ^{235}U, ^{239}Pu, and ^{242}Am are fissioned by thermal neutrons with high cross sections of 530, 586, 752, and 2100 barn, respectively, because the captured neutron is paired and the pairing energy results in an excitation energy exceeding the fission barrier. In contrast, heavy nuclei with even neutron number such as ^{226}Ra, ^{232}Th, ^{231}Pa, and ^{238}U capture an unpaired neutron so that the total excitation energy does not exceed the fission barrier. They can undergo fission with fast neutrons with reaction thresholds of 0.2–1.7 MeV. For heavy nuclei with an odd number of neutrons in the region up to −0.1 eV, the fission cross sections, in Figure 12.33, follow the $1/v$ law. Then, at energies up to −1000 eV, they exhibit sharp resonances like (n,γ) reactions. At still higher neutron energies, $\sigma_{n,f}$ becomes rather constant at 1–2 barn. As shown in Figure 12.34 for the case ^{238}U + n, $\sigma_{n,f}$ rises steeply from threshold to a plateau, then another steep rise close to 6 MeV occurs followed by another plateau, followed by further increases alternating with plateaus. This comes about through second- and higher-chance fissions: when the excitation energy of the compound nucleus, ^{239}U, is high enough, the residual nucleus after evaporation of a neutron, ^{238}U, can still be sufficiently excited to undergo fission. This process is designated as a (n,nf) reaction. At still higher energies, the evaporation of a second neutron can

Table 12.1 Cross sections $\sigma_{n,f}$ of nuclear fission by thermal neutrons (energy around 0.025 eV) and mean number $\overline{\nu}$ of neutrons set free by fission.

Nuclide	$\sigma_{n,f}$ (b)	$\overline{\nu}$	Nuclide	$\sigma_{n,f}$ (b)	$\overline{\nu}$
Th-227	≈200		Am-241	3.1	
228	<0.3		242	2100	3.22 ± 0.04
229	30		$242m_1$	7000	
230	≤0.0005	2.08 ± 0.02	243	0.074	3.26 ± 0.01
232	0.000 003		244	2200	
233	15		244 m	1600	
234	<0.01		Cm-242	≈5	2.65 ± 0.09
Pa-230	1500		243	620	
231	<0.020		244	1.1	3.43 ± 0.05
232	≈700		245	2100	
233	<0.1		246	0.16	3.83 ± 0.03
234	<5000		247	82	
234m	<500		248	0.36	
U-230	≈25		249	≈1.6	
231	250		Bk-250	1000	
232	74		Cf-249	1700	
233	530	3.13 ± 0.06	250	<350	
235	586	2.432 ± 0.066	251	4500	
238	0.000 003		252	32	3.86 ± 0.07
239	15		253	1300	
Np-234	≈900		Es-254	2000	
236	2600		254m	1800	
237	0.020		Fm-255	3300	
238	2100		257	2950	
239	<1				
Pu-236	160	2.30 ± 0.19			
237	2300				
238	17	2.33 ± 0.08			
239	752	2.874 ± 0.138			
240	≈0.044	2.884 ± 0.007			
241	1010	2.969 ± 0.023			
242	<0.2	2.91 ± 0.02			
243	200				

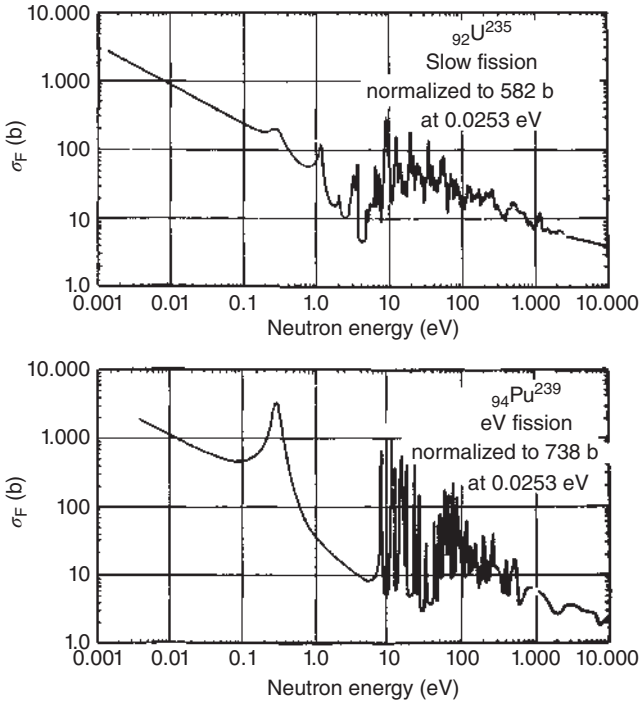

Figure 12.33 Fission cross sections for neutron-induced fission of ^{235}U and ^{239}Pu as a function of neutron energy. Source: From Friedlander et al. (1981)/John Wiley & Sons, Inc.

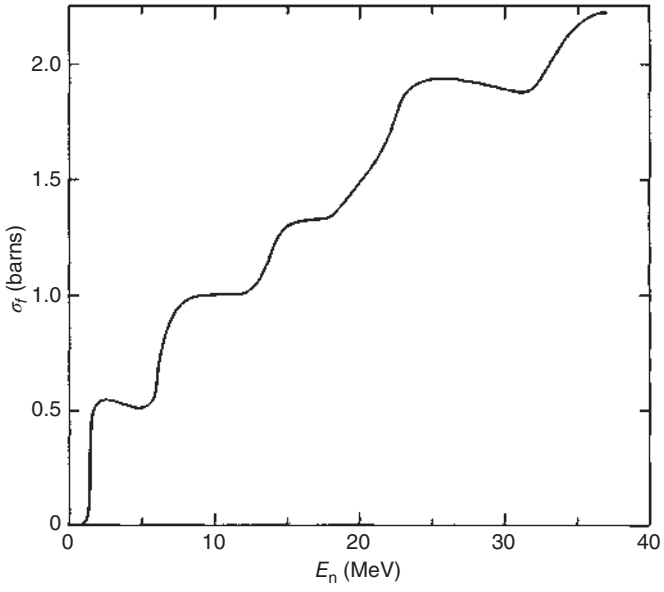

Figure 12.34 Fission cross sections of ^{238}U for neutrons up to 37 MeV. Source: From Friedlander et al. (1981)/John Wiley & Sons, Inc.

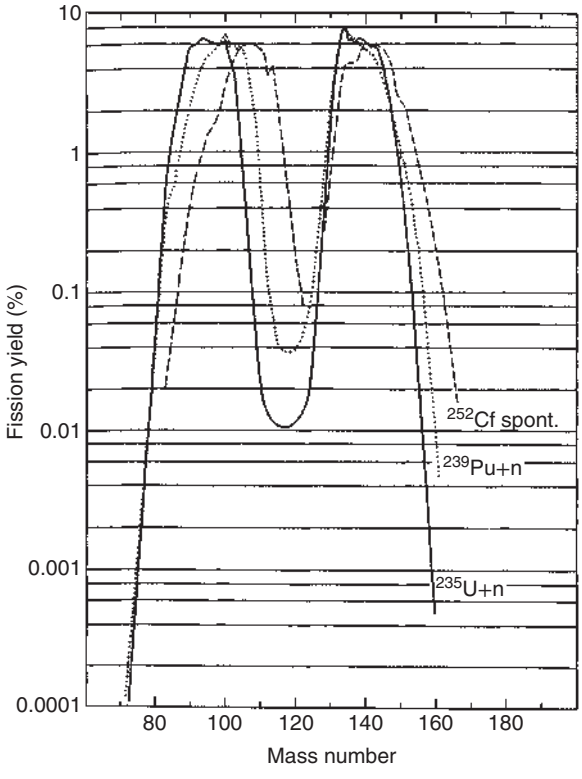

Figure 12.35 Fission product mass distributions for the thermal neutron-induced fission of ^{235}U and ^{239}Pu and the spontaneous fission of ^{252}Cf. Source: From Friedlander et al. (1981)/John Wiley & Sons, Inc.

be followed by fission of ^{237}U in a (n,2nf) reaction, and so forth. Fission can also be induced by protons, deuterons, helium ions, and γ-rays. In bombardments with charged particles, the low-energy behavior of the cross sections is largely determined by the Coulomb barrier. With increasing bombarding energies, fission in lighter and lighter elements becomes possible.

In thermal neutron-induced fission of most nuclei, an asymmetric mass distribution with a ratio of the heavy to light mass of about 1.4 is much more likely than a symmetric mass split. Mass distributions for thermal neutron-induced fission of ^{235}U and ^{239}Pu are shown in Figure 12.35 along with that for spontaneous fission of ^{252}Cf. The distributions are approximately symmetrical about the minima corresponding to equal mass splits. The left-hand edge of the heavy-mass peak is at the same position for different fissioning nuclei, which is caused by the shell closures at $Z = 50$ and $N = 82$, while the low-mass peak shifts. Shell effects are also causing the fine structure in the fission yields near the maxima due to preferential formation of primary fission fragments with closed shells as well as post-fission neutron emission from fragments containing 51 or 83 neutrons. With increasing neutron energy, that is, increasing excitation energy, the fission-yield curve fills in so that, for example, the peak-to-valley ratio which is 600 for thermal neutrons becomes only about 6 for 14 MeV neutrons, see Figure 12.36. When the bombarding energy is about 50 MeV, the mass distributions for the highly fissile elements near uranium exhibit single

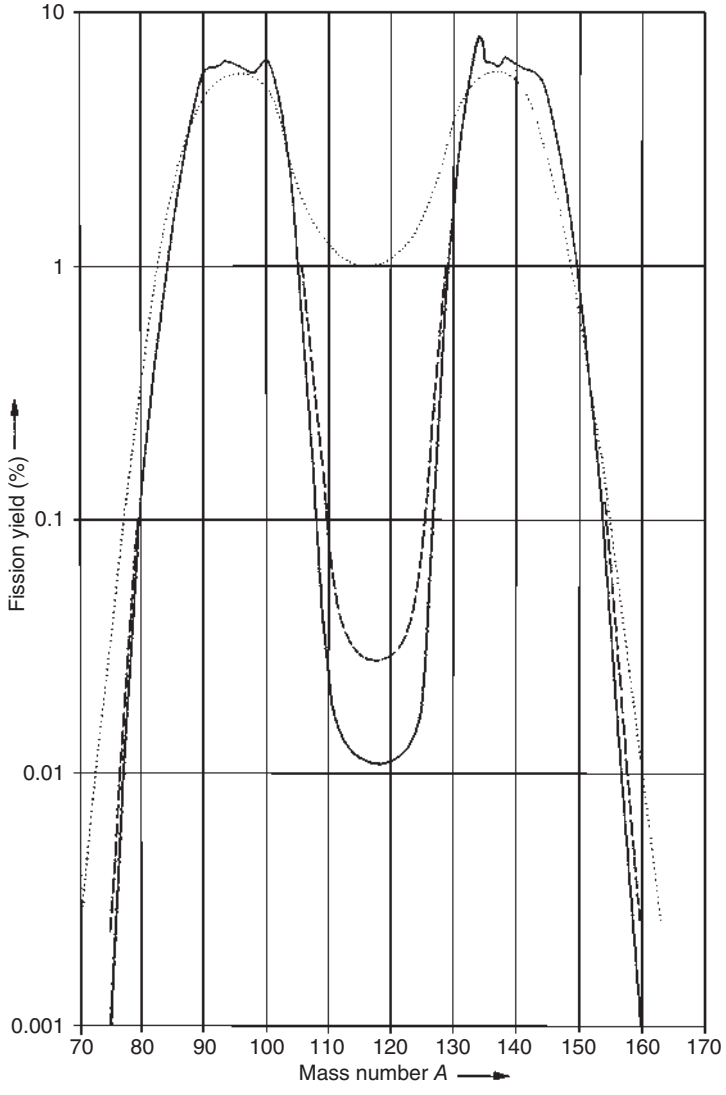

Figure 12.36 Fission yields for the fission of ^{235}U by neutrons of various energies: solid line, thermal neutrons; dashed line, neutrons produced by fission; dotted line, 14 MeV neutrons. Source: Flynn and Glendening (1970), figure 07 (p. 25)/U.S Department of Energy/Public domain.

broad humps. Fission of lead and bismuth leads to much narrower single-peaked distributions that become broader with increasing excitation energies. Fission of intermediate elements like radium leads to a triple-humped distribution. For the thermal neutron fission of ^{257}Fm, broad symmetric fission is observed. Narrow symmetric mass distributions are also observed in spontaneous fission of ^{258}Fm, ^{259}Fm, ^{260}Md, and ^{262}No. In electromagnetically induced fission of ^{238}U projectile fragments, the transition region between double-humped, triple-humped, and

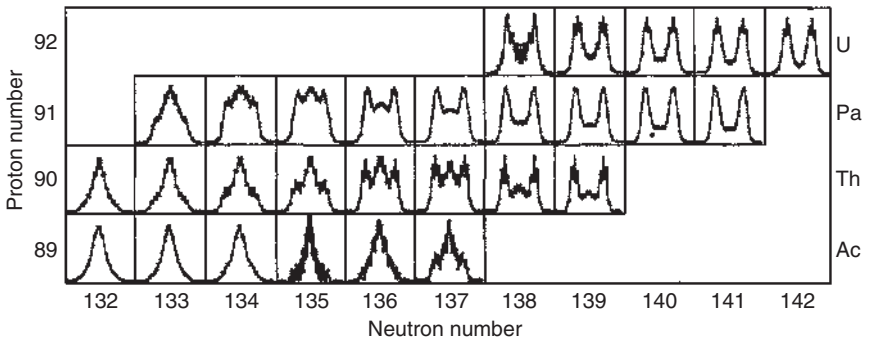

Figure 12.37 Atomic number (Z) distributions for the electromagnetically induced fission of several Ac, Th, Pa, and U nuclei produced by projectile fragmentation of a ^{238}U beam. Source: Schmidt et al. (1998), figure 03 (p. 45)/World Scientific Publishing.

single-peaked distributions can be mapped as is shown by the atomic number (Z) distributions in Figure 12.37. As nuclear matter is not very polarizable, the protons will divide to first order like the neutrons. Since the high-Z elements that undergo fission have neutron-to-proton ratios that are much larger than the stable isotopes in the fission product region, the primary fission fragments are always on the neutron-rich side of the β stability line. After neutron evaporation, each of the emerging fission products decays in a series of β^- processes to its stable isobar. Beginning with the discovery by O. Hahn and F. Strassmann on 17 December 1939, that ^{139}Ba resulted from reactions of uranium with thermal neutrons, which constituted the discovery of fission, an enormous amount of radiochemical work has been devoted to the identification and characterization of several hundreds of fission products, that is, about 90 mass chains with several members each. Even today, work on fission product characterization continues. Mass yields of a given A are best determined by mass spectrometry or by radioassay of the last, usually fairly long-lived, member of a β^- decay chain. The independent yields of the members along the decay chains must be rapidly separated from their radioactive precursors. Several independent yields along a given mass chain have now been determined, and such data exist for many mass numbers. They show that the yields of even-Z products are systematically higher than those of odd-Z products by ±25%. The independent yields, after correction for this odd–even effect, are consistent with a Gaussian distribution of isobaric yields around a most probable charge Z_p with a width that is approximately independent of A. For a given mass number, the distribution in Z is

$$P(Z) = \frac{1}{\sqrt{c\pi}} \exp\left[-\frac{(Z - Z_p)^2}{c}\right] \tag{12.105}$$

where the parameter $c = 0.79 \pm 0.14$ for fission of ^{235}U with thermal neutrons, corresponding to a FWHM of 1.50 ± 0.12 charge units. The values of Z_p are usually discussed in terms of their displacements from the charge Z_{UCD} that would be attained if the postulate of an unchanged charge density prevailed, saying that the primary fragments had the same charge-to-mass ratio as the compound nucleus. However,

the data for the light-mass peak cluster around $Z_p - Z_{UCD} = +0.5$ and those for the heavy-mass peak at $Z_p - Z_{UCD} = -0.5$. Among the possibilities to describe the values of Z_p theoretically, the calculation of the minimum potential energy for a double nuclear system including pairing corrections deserves to be mentioned.

The energy released in fission is determined by the difference between the mass of the compound nucleus and the sum of the masses of the fission fragments. Part of this energy goes into internal excitation of the fission fragments causing evaporation of prompt neutrons, but most of it is released as kinetic energy of the fission fragments. The average total kinetic energy is somewhere between 160 and 190 MeV and varies for different fissioning systems as $Z^2/A^{1/3}$. The actual kinetic energy release varies with the mass split. It is largest for mass splits in which the spherical doubly magic ^{132}Sn is emitted. From momentum conservation, we expect a ratio of kinetic energies of the light fission fragment (L) to the heavy fission fragment (H) as $E_L/E_H = M_H/M_L$. The average fission fragment kinetic energy as well as the total kinetic energy as a function of the fragment mass for fission of ^{239}Pu by thermal neutrons is shown in Figure 12.38. Table 12.2 gives an account of the total energy released in thermal neutron-induced fission of ^{235}U and ^{239}Pu showing that the usable energy is 195 and 202 MeV, respectively.

Mass distributions can also be deduced from the measurement of the velocities v_L and v_H of coincident fragments by time-of-flight techniques. Because neutron emission from the fragments is isotropic, it does not change the velocities on average; thus "kinematic coincidence" experiments determine the fragment masses prior to neutron emission. By comparing the mass distributions obtained from such physical measurements to those determined radiochemically (i.e. fission product mass distributions after the emission of prompt neutrons), one can determine the average number of prompt neutrons emitted from the primary fission fragments as a function of fragment mass. One such comparison of primary fission fragment mass distribution prior to prompt neutron emission with the secondary fission product

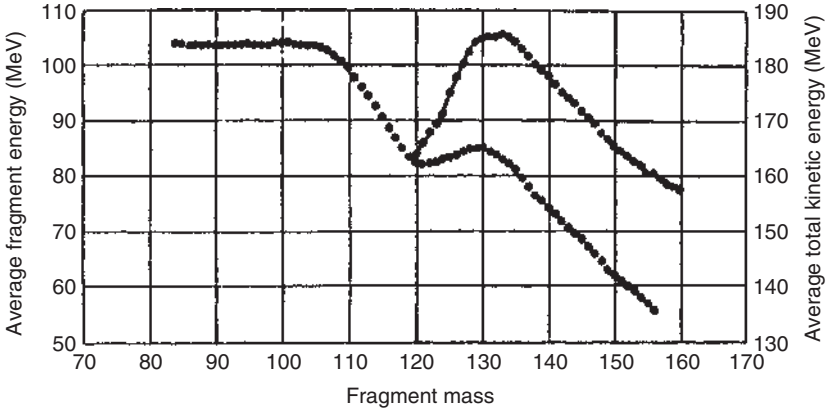

Figure 12.38 Average single-fragment and total pre-neutron-emission kinetic energy in ^{235}U thermal neutron fission. Source: Schmitt et al. (1965), figure 04 (p. 47)/World Scientific Publishing.

Table 12.2 Total energy release (in MeV) in the fission of $^{235}_{92}$U and $^{239}_{94}$Pu by thermal neutrons.

	H	$^{235}_{92}$U	
Kinetic energy	Light fragments	99.8	101.8
	Heavy fragments	68.4	73.2
Prompt radiation	Neutrons	4.8	5.8
	γ radiation	7.5	~7
Deexcitation of fission products	β^- radiation	7.8	~8
	γ radiation	6.8	~6.2
Neutrinos (not usable)		~12	~12
Usable energy		195	202

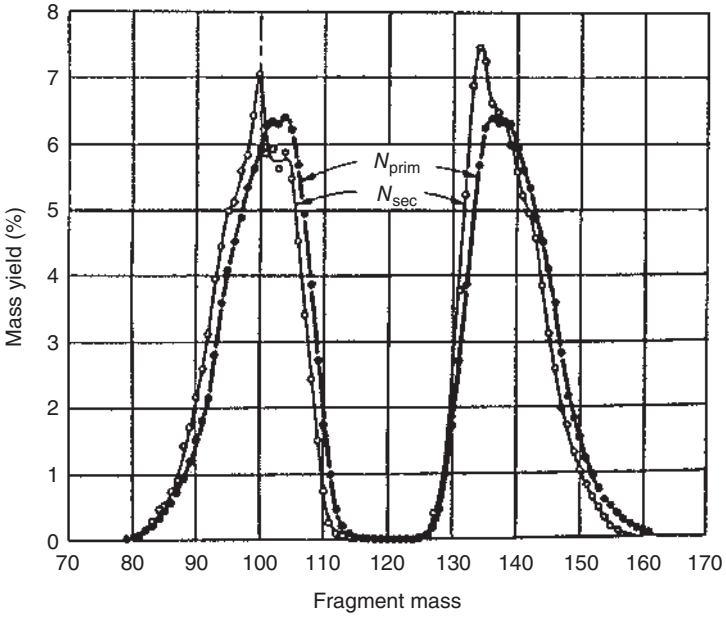

Figure 12.39 Pre-neutron-emission mass distribution, N_{prim}, and post-neutron-emission mass distribution, N_{sec}, in ^{235}U thermal neutron fission. Source: Schmitt et al. (1965), figure 05 (p. 49)/World Scientific Publishing.

distribution after neutron evaporation is shown in Figure 12.39 for the fission of ^{239}Pu with thermal neutrons. The average numbers $\overline{\nu}$ of neutrons per fission for thermal neutron-induced fission are also compiled in Table 12.1. The actual values of ν for individual fission events are distributed around $\overline{\nu}$ in approximately a normal distribution with a width of slightly more than one neutron. The value of $\overline{\nu}$ increases with increasing bombarding energy, and higher values of $\overline{\nu}$ are found for fissioning nuclides with higher atomic numbers, for example, 3.86 for ^{252}Cf and 4.02 for ^{257}Fm.

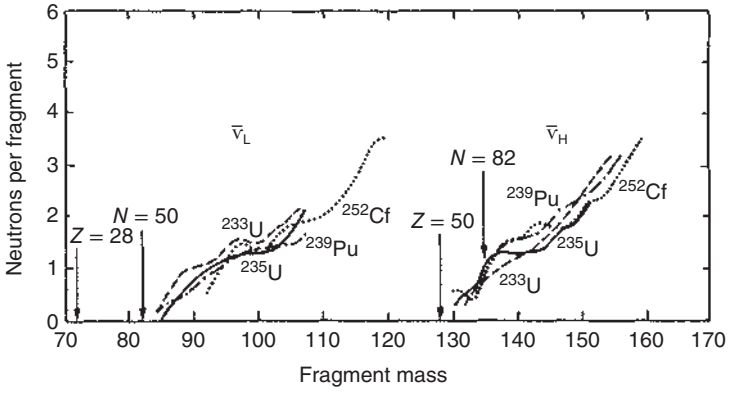

Figure 12.40 Summary of neutron yields derived from a comparison of cumulative mass yields with primary mass yields as functions of the initial fragment mass. The approximate initial fragment masses corresponding to various magic numbers are indicated. Source: Terrell (1965), figure 02 (p. 22)/International Atomic Energy Agency/Public domain.

Angular correlations of fission neutrons with fission products show that −90% of them originate from fully accelerated fission fragments in flight, while the remainder are emitted prior to full acceleration. Studies of the type shown in Figure 12.37 show that $\bar{\nu}$ is a strong function of the fragment mass with a plot of $\bar{\nu}$ vs. A, see Figure 12.40, exhibiting a "sawtooth" shape which is similar in various fission reactions. Most striking is the value of $\bar{\nu}$ close to zero for $A = 132$ which correlates with the particularly high kinetic energy of the spherical ^{132}Sn as fission fragment.

The energy spectra of fission neutrons in the frame of the moving fragment are very nearly Maxwellian, see Figure 12.22, and average neutron energies in the laboratory system are on the order of 2 MeV.

In about 1 fission event out of 400, the fissioning nucleus splits into three charged particles. In most cases, the third particle is an α particle. It is likely that these third particles stem from the neck of the scission configuration, which is strongly suggested by the angular distribution of the fragments. The third particles are focused in a direction of about 90° with respect to the axis formed by the two fission fragments. The focusing is not exactly 90° but somewhat more inclined toward the light fragment because the Coulomb reflection of the larger fragment is stronger. Fragments heavier than α particles are also emitted with yields decreasing with increasing Z relative to ^{4}He down to 10^{-7}%. These extend to atomic numbers of 10 in ^{233}U(n_{th}, f) and 14 in ^{249}Cf(n_{th}, f). These numbers apparently represent a measure of the size of the neck in a dumbbell shape of the nucleus at scission (Denschlag 2011) where random neck rupture occurs due to a Rayleigh instability Brosa, Grossmann, and Müller (1990).

In Section 5.9, we introduced the macroscopic–microscopic shell-correction approach by Strutinsky. It is based on using the liquid–drop model to account for the smooth, average properties of nuclei and correcting these by the separately evaluated single-particle effects that account for the non-uniform distribution of nucleons in phase space. Within this approach, in order to account for the details of

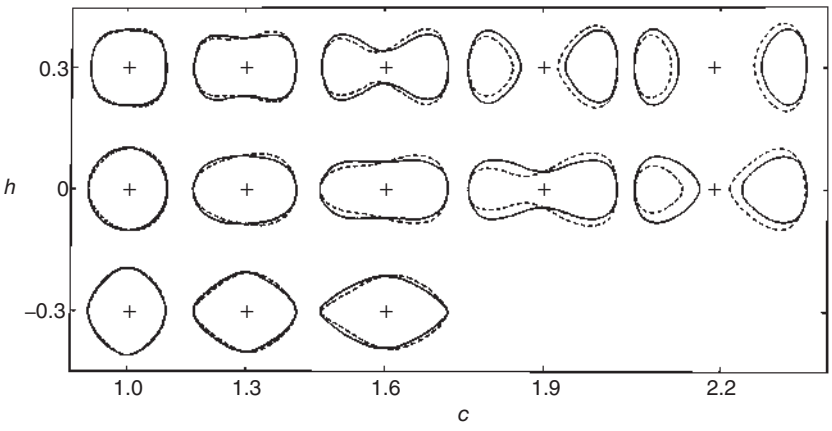

Figure 12.41 Some nuclear shapes in the (c, h) parameterization. The solid lines show symmetric shapes ($\alpha = 0$); the dashed lines represent shapes with an asymmetry parameter $\alpha = 0.2$. Source: Brack et al. (1972), figure 03 (p. 38)/American Physical Society.

the fission process, the task is to map the potential energy surfaces (PESs) from the ground state all the way to the separated fragments. This involves calculation of the potential energy as a function of deformation, mass and charge asymmetry, and for some functional form of the potential such as a Woods–Saxon potential generalized to non-spherical shapes. For practical computations, the deformed shapes must be describable in terms of a small set of parameters, typically three. A convenient description involves an elongation parameter c defined as the ratio of the length of the deformed nucleus to the diameter of the sphere of equal volume and a parameter h that defines the neck thickness at any given elongation. In addition, asymmetry in the elongation direction needs to be considered and is expressed in terms of a parameter α. Some typical shapes in this parameterization are shown in Figure 12.41. A spherical nucleus has $c = 1$, $h = 0$, and $\alpha = 0$.

When energies calculated for an actinide nucleus in the liquid–drop model are mapped in the (c, h) parameterization, a surface with a well-developed valley along the $h = 0$ line from $c = 1$ over a saddle point at $c \sim 1.5$ is seen, which then slopes down to $c = 1.7$, where the energy surface suddenly drops toward increasing h (neck formation), and eventually leads to two separate fragments. The results for a shell-correction calculation are depicted in Figure 12.42, where, in the upper right frame, a contour plot of the liquid–drop energy of ^{240}Pu shows the features just discussed. In the left-hand frames of the figure, we see the separate shell-correction energies for 94 protons (a) and 146 neutrons (b). The lower right frame shows the sum of the other three maps. We see that the sphere is no longer a stable configuration and that the ground state is deformed ($h = -0.15$, $c = 1.2$). An important feature is the appearance of a second minimum at $h = 0$ and $c = 1.4$ (already introduced in Section 6.5 in connection with the existence of fission isomers) about 2 MeV higher than the ground state and separated from it by a barrier about 6 MeV high. This is followed, at $c = 1.6$, by a second slightly lower saddle. This outer potential well has its origin in the neutron shell correction: $N = 146$ is a magic number for

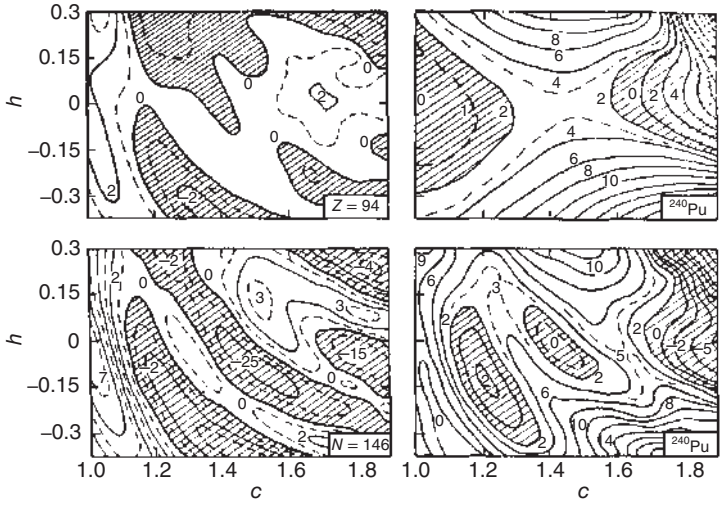

Figure 12.42 Contour maps, in the (c, h) plane, of the potential energy of ^{240}Pu. The left-hand side shows the shell-correction energies for 94 protons (top) and 146 neutrons (bottom). The upper right-hand map shows the liquid–drop energy of ^{240}Pu normalized to 0 MeV for the spherical shape ($h = 0$, $c = 1$). The lower right-hand map is the sum of the other three and represents the total deformation energy of ^{240}Pu. The contour lines are drawn at 2 MeV intervals, and regions with potential energies below 2 MeV are shaded. In the lower right map, the shaded area centered at $h = -0.15$, $c = 1.2$ represents the ground state, the other at $h = 0$, $c = 1.4$ the second minimum, with the first saddle in between. The second saddle is located at $h = 0$, $c = 1.6$. Source: Brack et al. (1972), figure 04 (p. 40)/American Physical Society.

a deformation of $c \sim 1.5$. The PES for ^{240}Pu is typical for all lighter actinides which have a deformed ground state with c between 1.12 and 1.22 and a second minimum at $c = 1.4$ corresponding to a ratio of axes of 2 : 1. The relative heights of the first and second barriers change gradually with the second barrier decreasing from ~8 MeV in ^{228}Ra with increasing A until it essentially disappears in ^{252}Fm. Thus, at the lower mass numbers, the outer barrier is the rate-determining one, whereas this role is shifted to the inner barrier for larger values of A. Another important feature emerges when minimization of the total deformation energy with respect to α is performed. It is found that asymmetry, in particular that corresponding to the observed mass asymmetries in the fission product mass distributions, significantly lowers the height of the second saddle (by about 2 MeV for ^{240}Pu). This comes about by shell effects of the nascent fragments in which the doubly magic ^{132}Sn plays a dominant role. This is schematically shown in Figure 12.43 and is the obvious reason for the observation of asymmetric mass distributions for $Z < 100$ (and symmetric mass distributions at $Z \sim 100$).

12.7.7 High-Energy Reactions

For the investigation of high-energy reactions, photographic emulsions or other track detectors have been applied. These are selected according to their sensitivity

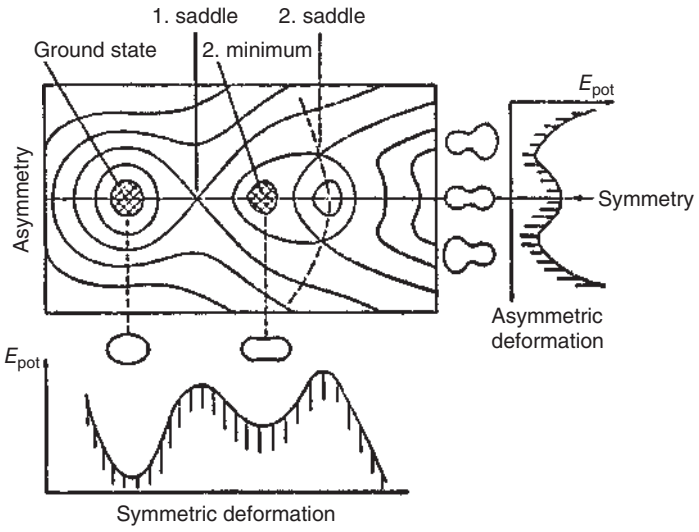

Figure 12.43 Schematic representation of the potential energy surface of an actinide nucleus as a function of asymmetry and deformation. In the left part of the map, shell effects of the fissioning nucleus are responsible for the existence of two minima and two saddle points. The right part of the figure indicates that, beyond the second saddle, shell effects of the nascent fragments determine the potential energy. The energetically preferred path to scission is to circumvent the symmetric second saddle and to descend toward scission in a mass asymmetric valley where the mass asymmetry is fixed by the doubly magic ^{132}Sn.

to ionizing radiation of various LET values. By means of this technique, charges, masses, kinetic energies, and angles with respect to the beam direction have been determined at relatively low beam intensities. Mass spectrometry is another valuable method, in particular if an on-line arrangement is used such that the reaction products are immediately transported from the target into the mass spectrometer. The transport may be combined with a chemical separation. Activation techniques have also been widely applied and were often combined with the thick target–thick catcher technique, Section 11.6. Examples of monitor reactions that are applied in high-energy proton bombardments are ^{12}C(p,pn)^{11}C and ^{27}Al(p,3pn)^{24}Na. Cross sections for these reactions in the energy range between 50 MeV and 30 GeV are listed in Table 12.3.

At incident nucleon energies $\leq$50 MeV where the compound-nucleus model accounts for most of the observations, direct reactions and preequilibrium emission are already competing reaction channels. Their importance increases with increasing bombarding energy, and above 100 MeV, nuclear reactions proceed almost completely by direct interactions. Figure 12.44 shows mass–yield curves for proton-induced reactions at 40, 400, and 4000 MeV with ^{209}Bi targets. At 40 MeV, where the reactions are dominated by the formation of the compound nucleus, only products with mass numbers close to the target mass are observed. At 400 MeV, there is a wide distribution of products which is divided into two groups. The one reaching from the target mass down to products with $A = 150$ is called the

Table 12.3 Cross sections of the monitor reactions $^{12}C(p,pn)^{11}C$ and $^{27}Al(p,3pn)^{24}Na$ for various proton energies.

Proton energy (MeV)	$^{12}C(p,pn)^{11}C$ σ (mb)	$^{27}Al(p,3pn)^{24}Na$ σ (mb)
50	86.4	6.2
60	81.1	8.7
80	70.5	10.0
100	61.3	10.2
150	45.0	9.4
200	39.0	9.3
300	35.8	10.1
400	33.6	10.5
600	30.8	10.8
1 000	28.5	10.5
2 000	27.2	9.5
3 000	27.1	9.1
6 000	27.0	8.7
10 000	26.9	8.6
28 000	26.8	8.6

spallation products. The term spallation is derived from the verb to spall, which means to chip or to break up. The other group ranging from $A = 60$ through 150 is associated with fission. At 4000 MeV, there is a broad distribution of products with no evident division between spallation and fission. New is the increased yield for $A < 30$ products (IMFs) for which the term fragmentation has been coined. The probability for fragmentation increases markedly with a further increase in bombarding energy.

At the higher bombarding energies, one is obviously producing a large array of products of different sizes associated with a broad spectrum of excitation energies from zero up to the maximum possible. Among the emitted particles, some were found to be of high energy close to that of the incident particle and to be forward peaked. In an attempt to explain the observed phenomena, R. Serber suggested in 1947 that if the energy of the incident proton is significantly larger than the interaction energy of nucleons in the nucleus, and if its wavelength is shorter than the average distance between the nucleons, then the incident proton will collide with nucleons in a collision cascade. The cross section and angular distribution for each collision will be nearly the same and resemble that for collisions with free nucleons. From the density of nuclear matter and the nucleon–nucleon cross section, Serber estimated for the mean free path of the proton at a few hundred megaelectronvolts a value of ~3 fm and reasoned that a high-energy proton may make only a

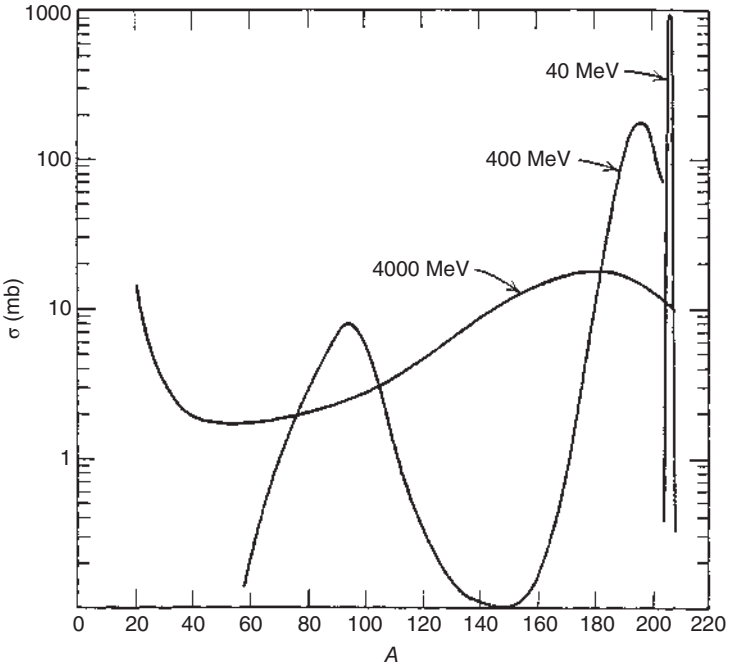

Figure 12.44 Comparison of the mass distributions of the products of reactions of 40, 400, and 4000 MeV protons with ^{209}Bi. Source: Friedlander et al. (1981), figure 02 (p. 15)/John Wiley & Sons.

few collisions while penetrating a target nucleus, leaving behind only a fraction of its energy and sometimes ejecting a nucleon with which it collides. In this way, an intranuclear cascade is created. At energies above 350 MeV, the cascade must include pions that can be created in nucleon–nucleon collisions. The pions help enhance the deposited energy in the nucleus because they have short mean free paths in nuclei. Production and interaction of pions could be the cause of a rapid change of the mass yields for lower A above ~400 MeV bombarding energy. The emerging model for spallation is schematically depicted in Figure 12.45. A cascade nucleon may either immediately escape from the nucleus as is shown for a neutron and a proton, or be slowed down such that it is captured by the nucleus and contributes its energy to the total excitation energy. At the end of the intranuclear cascade taking ~10^{-22} seconds, during which several particles may be ejected, the product nucleus remains in an excited state. A spectrum of cascade products with a wide distribution in A, Z, and excitation energy remains. In a second step occurring on a much longer time scale, these cascade products deexcite by particle evaporation. Monte Carlo methods have been successful in accounting for the distribution of cascade products as well as the energy spectra and angular distributions in the first step followed by deexcitation in the same process as the second stage in compound-nucleus reactions, the difference being that we deal here with a whole spectrum of excited nuclei and a spectrum of excitation energies.

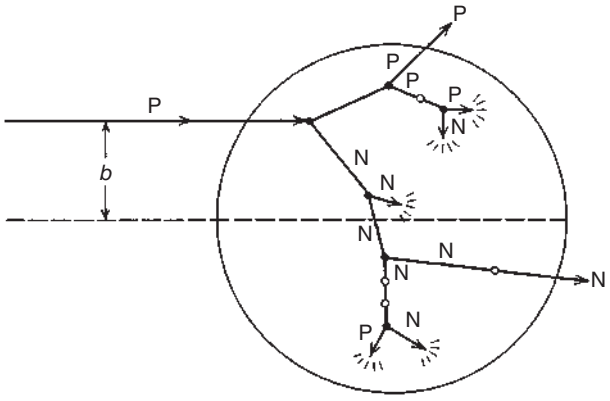

Figure 12.45 Schematic representation of an intranuclear cascade generated by a proton with impact parameter *b*. The filled circles indicate positions of collisions. The open circles represent collisions forbidden by the Pauli exclusion principle. The short arrows ending within the nucleus indicate captured nucleons that contributed to the total excitation energy. Source: Friedlander et al. (1981), figure 03 (p. 17)/John Wiley & Sons.

The double-humped mass distribution known for thermal neutron-induced fission is replaced as we have seen in Figure 12.44 by a single broad peak centered below half the mass of the target nuclide which is, at 400 MeV, still well separated from the distribution of spallation products. In the gigaelectronvolt energy range, this separation is lost. However, experiments in which two fragments in coincidence are detected show that fission still accounts for a large fraction of the total cross section. From angular correlations, it can be inferred that these binary fission processes result from cascades in which only tens of megaelectronvolts have been deposited. The fragments from these true fission events are on the neutron-rich side of the β stability line, and the kinetic energies reflect a binary breakup. The more neutron-deficient "fission products" involve deposited energies of hundreds of megaelectronvolts, have lower kinetic energies, and do not appear to have partners of comparable mass. It is likely that they do not arise from fission processes but rather from deep spallation or fragmentation (see Section 11.6).

The high yield of products with $A \leq 30$ in the gigaelectronvolts bombarding-energy range and especially their recoil properties cannot be accounted for by the two-stage spallation mechanism. The term fragmentation was introduced above. Excitation functions for these IMFs rise steeply above a few hundred megaelectronvolts. The observation that neutron-deficient products in the fission-product mass region have very similar excitation functions has led to the speculation that the two types of products may represent partners of the same breakup process. The mechanism for their production has not been clearly elucidated in proton-induced reactions. A clue to its mechanistic understanding may be the recent observation of a liquid–gas-phase transition in relativistic heavy-ion collision (RHIC), where a hot nuclear vapor is created at a critical temperature that subsequently condenses into droplets of IMFs.

12.8 Nuclear Reactions Revisited with Heavy Ions

The first nuclear reactions induced by heavy ions were reported in 1950, but it was not until several years later that accelerators and experimental techniques suitable for detailed heavy-ion reaction studies became available. In the 1960s and 1970s, an almost explosive growth of activities occurred in this field and it has since become a forefront area in nuclear research. By using heavy-ion reactions to synthesize exotic nuclei, one can explore nuclear structure at its limits. A very rich field of study is the dynamics of collisions of heavy nuclei. The exploration of the nuclear equation of state (EOS) is of great importance. The observations of phase transitions from the liquid phase to the gas phase and to the quark–gluon plasma are phenomena that are accessible only in heavy-ion collisions. Accelerators capable of producing intense beams of ions up to uranium at energies up to several megaelectronvolts per nucleon are now in operation (see Chapter 16). The variety of experimental possibilities is enormous and makes for a very attractive field of study.

The various impact parameters and trajectories in a heavy-ion reaction close to the barrier are indicated in Figure 12.46. Distant collisions lead to elastic scattering (EL) and Coulomb excitation (CE) (see Section 5.11). Grazing collisions lead to inelastic scattering and the onset of nucleon exchange in quasi-elastic transfer reactions (QE). Head-on collisions lead to fusion of the colliding nuclei and compound-nucleus formation (CN). Fusion of heavy nuclei is dynamically hindered, giving rise to reseparation channels that have previously not been observed in reactions with light projectiles. For near-head-on collisions, quasi-fission (QF) is a reaction with substantial mass, charge, and energy exchange between the reaction partners, but without full amalgamation characteristic of compound-nucleus formation. For intermediate impact parameters between head-on and grazing collisions, a dynamically very interesting new type of nuclear reaction, deep inelastic collision

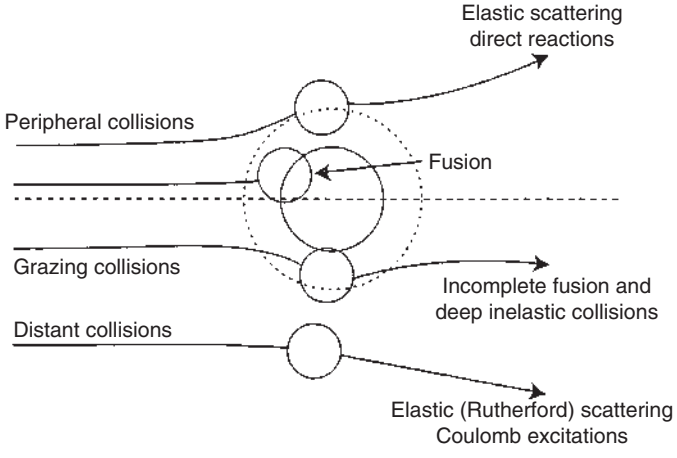

Figure 12.46 Classification of heavy-ion collisions based on impact parameter. Source: Hodgson, Gladioli, and Gladioli-Erba (1997), figure 03 (p. 50)/Oxford University Press.

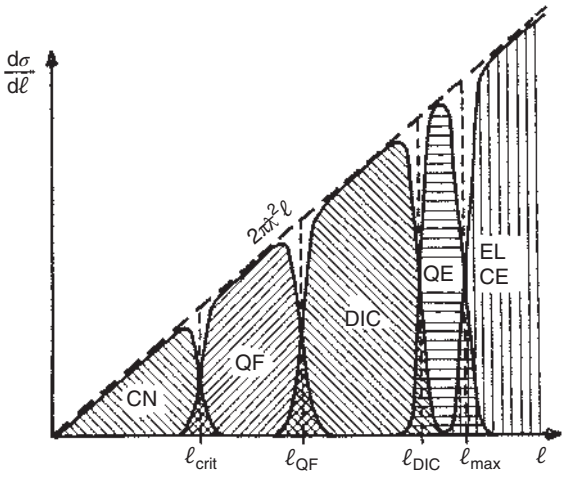

Figure 12.47 The l dependence of the partial cross sections for compound nucleus formation (CN), quasi-fission (QF), deep inelastic collisions (DICs), quasi-elastic transfer (QE), Coulomb excitation (CE), and elastic scattering (EL). Source: Schröder and Huizenga (1984)/Springer Nature.

(DIC), is observed. The new reseparation channels make their appearance because, in such heavy di-nuclear systems, the repulsive centrifugal and Coulomb forces are overwhelming and the attractive nuclear force is too weak to accomplish complete fusion. Thus, the reaction partners reseparate before forming a compound nucleus. If, as we just stated, the reaction mechanisms are separated from each other by the ranges of impact parameters in which they occur, it is obvious that they are also separated in angular momentum space, see Figure 12.47. In CE and EL, we have the highest values of the angular momentum l, exceeding $l_{\max}$ where nuclear contact is first established. DIC corresponds to intermediate values of l. CN formation occurs for $l=0$ up to l_{crit} where the attractive pocket in the potential disappears. Slightly more peripheral collisions lead to quasi-fission where the di-nuclear system is getting close to the compound nucleus, but as it stays outside of the unconditional saddle (the fission barrier), many degrees of freedom do not reach equilibrium.

12.8.1 Heavy-Ion Fusion Reactions

According to Eq. (12.34), fusion cross sections should emerge from a simple one-dimensional potential energy picture in which the total potential $V(r)=Z_1Z_2e^2/r+V_{\text{N}}(r)+V_l(r)$ has a pocket, see Figure 12.48, between $l=0$ and l_{crit}. For these partial waves, fusion occurs for center-of-mass energies exceeding the fusion barrier V_{B}, else tunneling is calculated using the WKB method, that is,

$$T_l = (1+t_l)^{-1} \tag{12.106}$$

with

$$t_l = \exp\left[2\int_{r_{\text{i}}}^{r_{\text{o}}}\sqrt{\frac{2\mu}{\hbar}|V(r)-E_{\text{cm}}|}\,\mathrm{d}r\right]$$

Figure 12.49 shows experimental fusion cross sections for the $^{40}\text{Ar}+^{122}\text{Sn}$ reaction that are compared to a calculation with the above-mentioned one-dimensional

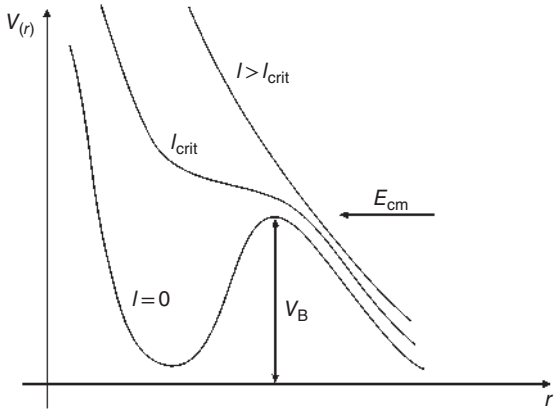

Figure 12.48
One-dimensional potential energy $V(r)$ for rigid spheres (schematic) as a function of the distance of the charge centers r.

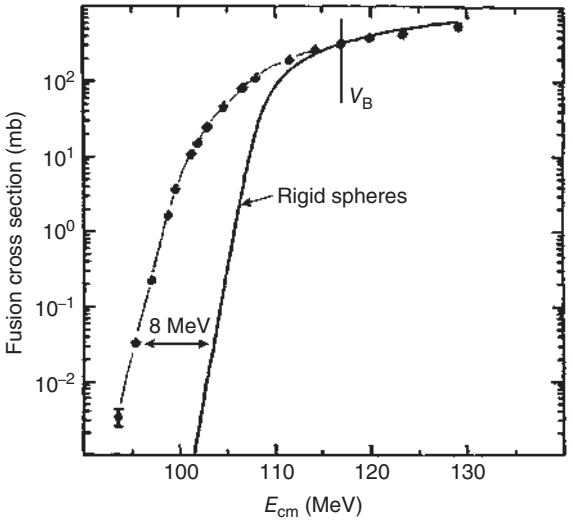

Figure 12.49 Fusion cross sections for $^{40}Ar + ^{122}Sn$. The solid line is a calculation for rigid spheres with the one-dimensional potential. Below the barrier, tunneling is calculated with the WKB method, see text. Source: Reisdorf et al. (1985), figure 02 (p. 5)/Elsevier.

rigid spherical potential. Other than for proton-induced fusion reactions, this calculation fails to reproduce the experimental data below the fusion barrier, for example, near 100 MeV, by 4 orders of magnitude. The discrepancy can alternatively be expressed in terms of an "asymptotic barrier shift" which is 8 MeV in the present case. One talks about a "sub-barrier enhancement" of fusion below the "classical" region. Figure 12.50 shows measured excitation functions for the fusion of ^{40}Ar with various Sn and Sm targets. In this figure, global size effects have been removed by a so-called proximity scaling and by comparing the fusion cross section to that of a reference isotope yielding "reduced" fusion cross sections

$$\sigma_{\mathrm{fus}}^{\mathrm{red}}(E_{\mathrm{cm}}) = \frac{R_{\mathrm{Bref}}^2}{R_{\mathrm{B}}^2}\sigma_{\mathrm{fus}}\left(E_{\mathrm{cm}}\frac{V_{\mathrm{Bref}}}{V_{\mathrm{B}}}\right) \tag{12.107}$$

Two conspicuous phenomena emerge when this type of scaling is used: (i) the Sn data merge at all energies, while the Sm data merge only in the "classical" region ($E/B \geq 1.04$); (ii) single-barrier penetration calculations for rigid spheres

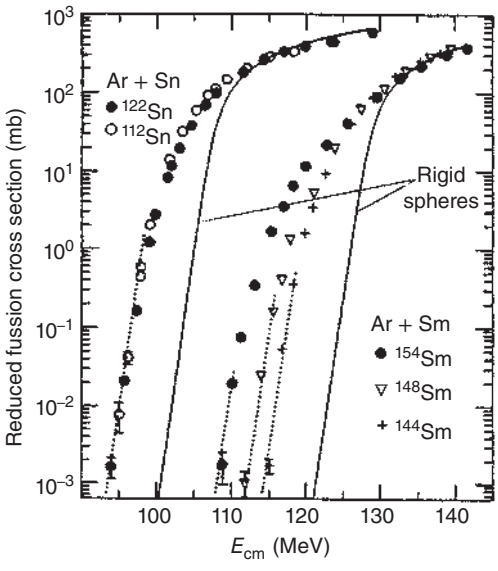

Figure 12.50 Reduced (due to proximity scaling) fusion cross sections for $^{40}Ar + {}^{112,122}Sn$ and $^{40}Ar + {}^{144,148,154}Sm$. Source: Reisdorf et al. (1985), figure 03 (p. 5)/Elsevier.

using the WKB method (solid curves) reproduce the data only in the classical region. Phenomenologically, and staying within a barrier penetration picture, one can bridge the "classical" region and the "pure tunneling" region by introducing a normalized barrier "fluctuation" or "distribution" $D(B)$ and by calculating the fusion cross section from

$$\sigma_{\text{fus}}(E_{\text{cm}}) = \int D(B)\sigma(B, E_{\text{cm}})\text{d}B \tag{12.108}$$

This allows one to correlate sub-barrier fusion cross sections with nuclear structure which is strongly suggested by Figure 12.50. The different behavior of the Sm isotopes (showing different asymptotic barrier shifts) as compared to the Sn isotopes, both spanning the same increase in neutron number, is correlated with nuclear spectroscopy. In the approach phase, projectile and target are subject to mutual Coulomb excitation, Section 5.11, populating collective rotational and vibrational states. Thus, at contact, projectile and target are not in their spherical ground states. Figure 12.51 illustrates what this means, for example, for the ^{154}Sm target nucleus for which there is a high probability of excitation into low-lying rotational states. Their static deformation gives rise to a variation of $\pm 7\%$ in the barrier height and of ± 1.2 fm in the surface-to-surface distance, which we might call "orientational" fluctuations. This comes about because the standard nuclear potential

$$V_{\text{N}}(r, s) = -V_0 \frac{R_1 R_2}{R_1 + R_2} \exp[1.33(R_1 + R_2 - r)/a] \tag{12.109}$$

depends exponentially on the distance of the nuclear surfaces $-s = (R_1 + R_2 - r)$. Here, $R_1R_2/(R_1 + R_2)$ is the radius of curvature describing the adhesion between two curved surfaces, 1.33 fm stands for the range of the nuclear force, and a is the surface diffuseness introduced in Section 4.1. As the picture in the upper left corner indicates, the surface distance s depends on the angle of orientation of the deformed

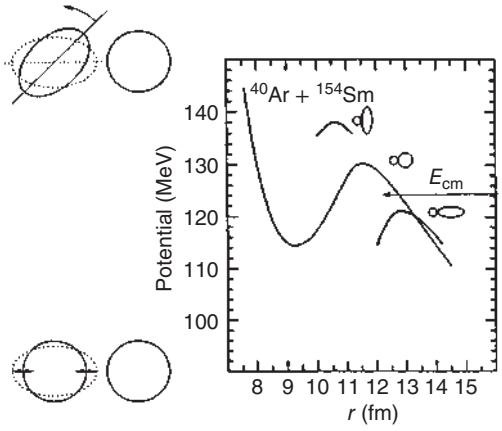

Figure 12.51 Schematic representation of barrier fluctuations in the fusion of ^{40}Ar with ^{154}Sm. The static deformation of ^{154}Sm in low-lying excited states gives rise to a variation of ±7% in the barrier height and ±1.2 fm in the surface-to-surface distance. In the upper left corner, the "orientational fluctuations" are schematically depicted. Moreover, one expects "vibrational fluctuations" (lower left corner) due to the excitation of low-lying quadrupole and octupole vibrations.

nucleus Θ and we have to rewrite

$$\sigma_{\text{fus}} = \pi\lambda^2 \sum_{l=0}^{l_{\text{crit}}} (2l+1) \int_0^{\pi/2} T_l(\Theta) \sin\Theta \, \mathrm{d}\Theta \tag{12.110}$$

where $T_l(\Theta) = (1 + t_l(\Theta))^{-1}$ and with

$$t_l(\Theta) = \exp\left[2\int_{r_i}^{r_o} \sqrt{\frac{2\mu}{\hbar}|V_l(r,s) - E_{\text{cm}}|}\, \mathrm{d}r\right]$$

In the Sm isotopes, as one goes from the spherical nucleus (^{144}Sm) to stable deformation (^{154}Sm), the transition is rather gradual, hence the intermediate asymptotic barrier shift for ^{148}Sm in Figure 12.50. Moreover, one expects "vibrational" fluctuations due to the excitation of low-lying quadrupole and octupole vibrations representing momentary deformations. These are seen by the fusing system because fusion acts like a fast snapshot camera. The asymptotic shift for the spherical Sn isotopes (as well as for ^{144}Sm) which are closed-shell nuclei with $Z = 50$ and $N = 82$, respectively, is due to such "vibrational" fluctuations. In summary, these considerations suggested the description of heavy-ion fusion cross sections with a distribution of potentials generated from a Gaussian distribution of the radius parameter r_0 with a standard deviation $\sigma(r_0)/r_0$ (4.3% for the Sn data, and 6.4% for the ^{154}Sm data) but cut-off at 2.5 times the standard deviation. The truncation is necessary because of the existence, suggested by the data, of an "adiabatically" lowest barrier. Figure 12.52 shows the results of such a three-parameter description of the fusion excitation functions for ^{40}Ar + ^{154}Sm and ^{144}Sm. The dotted curves are again calculations without barrier fluctuations. The double-headed arrows span the energy region between the fitted average barrier location and the low-energy limit of the fluctuation range, the adiabatic barrier. Below that energy, tunneling is required.

Coupled-channel calculations where one couples to the barrier–transmission process, the low-energy collective states that are known to be strongly excited by inelastic scattering reactions such as (p,p′) or (α,α′) are a more ab initio approach to

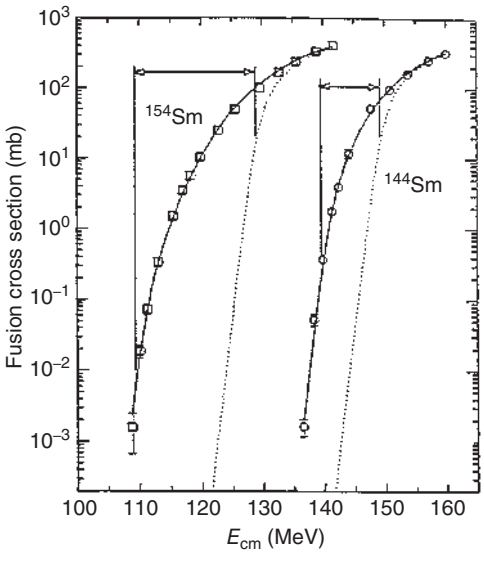

Figure 12.52 Three-parameter fits (solid lines) to the fusion cross sections of ^{40}Ar with ^{154}Sm and ^{144}Sm (the latter shifted by 20 MeV) with a Gaussian distribution of the radius parameter with the fit parameters r_0, $\sigma(r_0)/r_0$, and a truncation parameter $t/\sigma(r_0)$. The dotted lines are calculations with the same potential but without barrier fluctuations. The double arrows indicate the energy region between the average barrier and the low-energy limit of the fluctuation range corresponding to the adiabatic barrier. Below that energy, tunneling is required. Source: Reisdorf et al. (1985), figure 04 (p. 6)/Elsevier.

describe fusion excitation functions. In the Schrödinger equation

$$\left[-\frac{\hbar^2}{2\mu}\frac{\mathrm{d}^2}{\mathrm{d}R^2} + V(R) - E\right]\chi_i(R) = -\sum_j M_{ij}\chi_j(R) \tag{12.111}$$

the coupling matrix M_{ij} between the radial wave functions χ_i and χ_j in the pedagogical case of two levels, the ground state and one excited state, is

$$M_{ij} = \begin{pmatrix} 0 & F \\ F & Q \end{pmatrix}$$

where F is the collective model coupling strength related to the isoscalar transition rate in the inelastic scattering reaction and Q is the excitation energy of the excited state. Diagonalization leads to the eigenvalues

$$\lambda_{\pm} = (-Q \pm \sqrt{4F^2 + Q^2})/2$$

which means, as shown graphically in Figure 12.53, that the original barrier splits into two. Realistic cases are shown in Figure 12.54 where the data for ^{40}Ar + ^{122}Sn and ^{144}Sm are compared to coupled-channel calculations for 16 collective states below 4 MeV that are taken into account together with their collective model coupling strengths. In the case of the dashed curve, only the ^{40}Ar levels are coupled. The dotted curves represent the no-coupling limit. Figure 12.55 shows the distribution of eigenvalues for ^{40}Ar + ^{144}Sm as an example. The eigenvalue 0 corresponds to the unperturbed barrier location. The distribution corresponds to a theoretical barrier distribution. In modern fusion evaporation codes, channel coupling is included in the calculation of the compound-nucleus formation cross section.

A final remark relates to the energy region below the adiabatic barrier where tunneling is required. In Figure 12.56, the logarithmic slope of the ^{90}Zr + ^{90}Zr cross sections is steeper than predicted by the WKB method. This indicates that the inertial

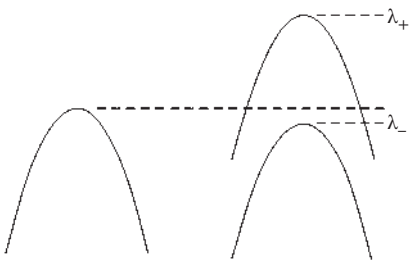

Figure 12.53 Schematic representation of the splitting of the original barrier by channel coupling into two energy eigenvalues λ_+ and λ_- in the simplified case of one of the reaction partners being excited from its ground state to one excited state.

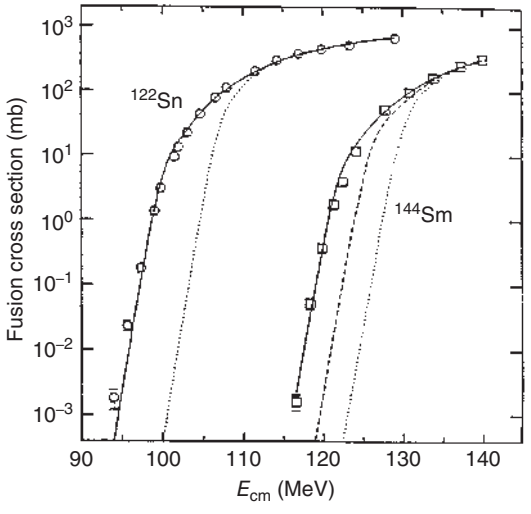

Figure 12.54 Coupled-channel calculations (solid curves) for $^{40}Ar + {}^{122}Sn$ and $^{40}Ar + {}^{144}Sm$ where 16 excited states (2^+, 3^-, 4^+, 5^-) below 4 MeV which are strongly excited in (p,p′) reactions are taken into account with their collective-model form factors: dashed curve, only the ^{40}Ar levels are coupled; dotted curves, no coupling limit. Source: Reisdorf et al. (1985), figure 05 (p. 6)/Elsevier.

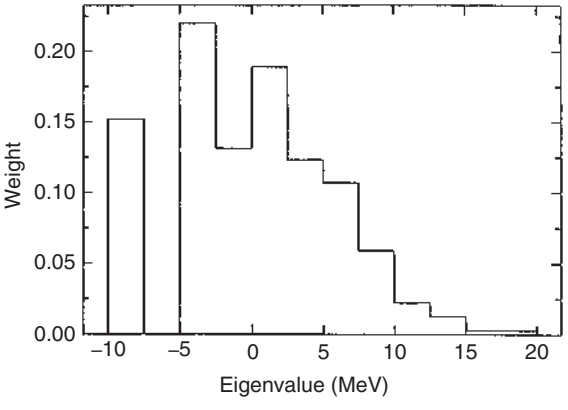

Figure 12.55 Theoretical barrier distribution function for $^{40}Ar + {}^{144}Sm$. The eigenvalue 0 corresponds to the unperturbed barrier location. Source: Reisdorf et al. (1985), figure 06 (p. 7)/Elsevier.

mass parameter, usually taken to be equal to the reduced mass, needs to be increased by a factor of 2. For $^{90}Zr + {}^{89}Y$, where the latter contains a proton hole in comparison to ^{90}Zr, the logarithmic slope is even steeper. This reminds us of the odd-particle hindrance of another tunneling process: spontaneous fission.

For $Z_1 \cdot Z_2 \geq 1600$, a new phenomenon is replacing the sub-barrier enhancement of the fusion cross sections. We have already discussed in Section 12.7.2, in connection

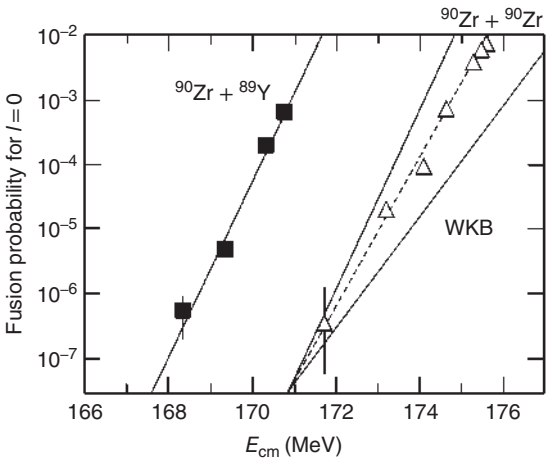

Figure 12.56 Comparison of P_{fus} for ^{90}Zr + ^{89}Y (squares) and ^{90}Zr + ^{90}Zr (triangles). The three lines arbitrarily merging near 171 MeV have the slope of the ^{89}Y data (left), of the ^{90}Zr data (middle), and of the WKB calculation (right) using the Bass potential.

with the RLDM, that for very heavy compound nuclei, the balance of forces becomes very critical for the attractive nuclear force relative to the overwhelming repulsive Coulomb and centrifugal forces so that the fission saddle points are significantly influenced. If this is so, one expects this also for the reverse process: heavy-ion fusion. The resulting phenomenon is a fusion hindrance for massive systems. The fusion probability is defined as

$$P_{\text{fus}}(E,l) = \sigma_{\text{evr}}/\pi\lambda^2 \sum_l (2l+1)W(E+Q,l) \tag{12.112}$$

where σ_{evr} is a measured cross section for an evaporation residue and $W(E+Q,l)$ is the survival probability as a function of excitation energy. As for sufficiently heavy systems, fission acts as a central collision filter ($l < 15\hbar$), one essentially extracts information on $P_{\text{fus}}(E,l \approx 0)$. One adopts the energy where $P_{\text{fus}}(E) = 0.5$ as the experimental dynamical barrier. The consequence of dynamically hindered fusion is characterized in Figure 12.57 for the system ^{124}Sn + ^{96}Zr. At the standard barrier (B_{Bass}), the fusion probability is not 0.5, but is reduced by several orders of magnitude. The difference in energy between the standard barrier and the $P_{\text{fus}} = 0.5$ point is larger than 20 MeV. The barrier is dynamically shifted by the "extrapush." The second characteristic feature, the very gradual rise of the excitation function, is characterized by a standard width σ_{B} which is much larger than the standard deviation σ_{cc} due to channel coupling at the unperturbed barrier, which is an indication that the way of the fusing system from the contact point to the compound nucleus is now accompanied by friction. According to the dissipation–fluctuation theorem, we have $\sigma_{\text{B}}^2 = \sigma_{\text{cc}}^2 + \sigma_{\text{diss}}^2$ and the tiny evaporation residue cross section at the standard barrier is entirely due to fluctuations. Actually, according to W.J. Swiatecki, the system moves on a macroscopic PES defined by a separation variable, a neck opening variable, and an asymmetry variable under the influence of friction and encounters three "milestones," see Figure 12.58. The first one is the contact point. The second one is the conditional saddle where projectile and target have developed a neck at the condition of frozen entrance channel mass asymmetry. To overcome the conditional

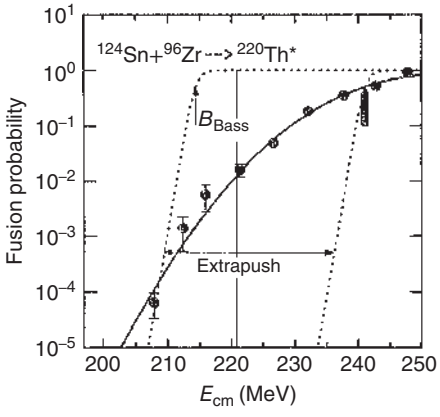

Figure 12.57 Fusion probability as a function of energy for the $^{124}Sn + {}^{96}Zr$ system. The solid curve is the fit of an error function to the data. The thick (thin) arrow indicates the dynamical barrier and the standard barrier (B_{Bass}). The dotted curves are from WKB calculations using either B_{Bass} or the dynamically shifted barrier. The extrapush energy is indicated. Source: Reisdorf (1994)/IOP Publishing.

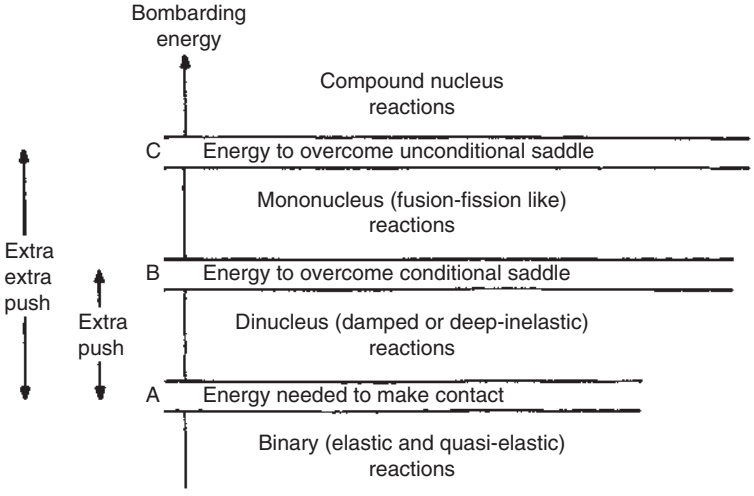

Figure 12.58 Schematic illustration of the three "milestones" in the potential energy surface separating QE, DIC, QF, and CN reactions. Source: Bjørnholm and Swiatecki (1982), figure 02 (p. 75)/Elsevier.

saddle, the system needs to compensate frictional losses by additional kinetic energy, the extrapush. If the conditional barrier is not overcome, DICs show up as the first reseparation channel. The third "milestone" is the unconditional saddle, the fission barrier of the compound nucleus. To overcome the latter, the system needs an extra-extrapush of kinetic energy. If the unconditional saddle is not overcome, the system reseparates in a quasi-fission (QF) reaction. The need for an extrapush to reach the QF regime and the need for an extra-extrapush to reach the compound nucleus are supported by experimental evidence.

The systematics of measured differences between the dynamical barriers and the standard barriers ($B_{Bass)}$ for surviving evaporation residues are shown in Figure 12.59. The data refer to nearly symmetric systems with $Z_pZ_t = 1500–2000$

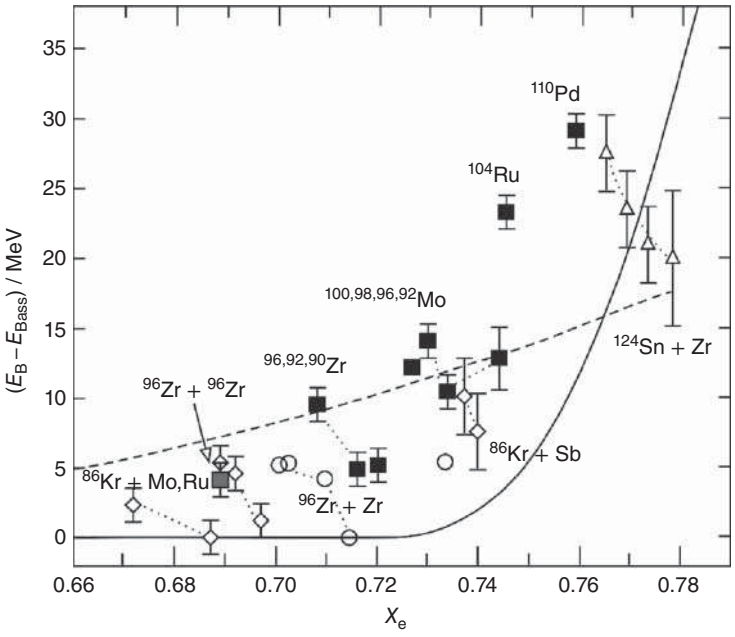

Figure 12.59 Measured barrier shifts relative to B_{Bass} and the predictions of the extrapush model by Blocki et al. and the surface friction model by Fröbrich. Data points for isotopic chains are connected by dotted lines. Source: Quint et al. (1993)/Springer Nature.

still having fission barriers of several megaelectronvolts. The abscissa in Figure 12.54 is a measure of the effective fissility x_e as defined by Bjørnholm and Swiatecki (1982):

$$x_e = (Z^2/A)_{eff}/(Z^2/A)_{crit} \tag{12.113}$$

with

$$(Z^2/A)_{crit} = 50.883/[1 - 1.7826I^2]$$

and

$$(Z^2/A)_{eff} = \frac{4Z_pZ_t}{A_p^{1/3}A_t^{1/3}(A_p^{1/3} + A_t^{1/3})}$$

This is up to a factor of 1.2 an estimate of the ratio of Coulomb to nuclear forces for two spherical nuclei with sharp surfaces in contact using the radial parameter and the surface energy constant of the 1967 Myers and Swiatecki mass formula. Although there is a global trend as a function of this liquid–drop-like scaling, it is obvious that the straggling of the data points is quite large, indicating the necessity for an additional ordering parameter. As the deviations of the individual barrier shifts from the liquid–drop scaling obviously correlate with the nuclear structure of the colliding nuclei, it is necessary to come up with an alternative scaling as shown in Figure 12.60, where a structural parameter v_{min}, being the minimum distance

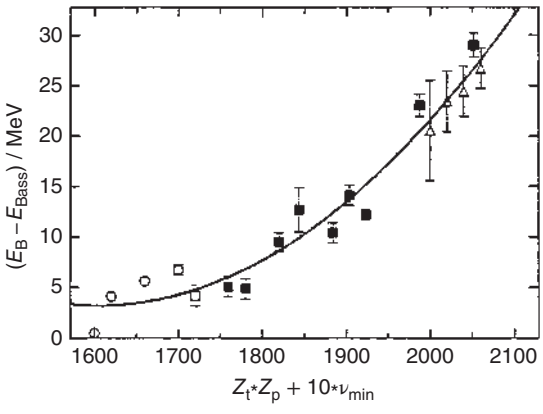

Figure 12.60 Demonstration of an improved scaling law for the observed barrier shifts for the systems indicated in Figure 12.59. The solid line is a parabolic fit to the data. The structural parameter v_{min} is the minimum distance to the next closed shells. Source: Quint et al. (1993)/Springer Nature.

to the next closed shells, is used. For the fusion probability at the standard barrier, expressions of the form

$$p(B_{\text{Bass}}) = 0.5 \exp[-c(x - 0.72)] \tag{12.114}$$

are in use, with modifications in the definition of x, for example, taking into account the fast N/Z equilibration in the entrance channel and averaging between the entrance channel fissility and the compound-nucleus fissility.

12.8.2 Quasi-Fission

A schematic illustration of the three reaction channels in strongly dissipative heavy-ion reactions is shown in Figure 12.61. The sequence of shapes in the middle of the figure clarifies that, in quasi-fission reactions, the mass asymmetry degree of freedom is (almost) equilibrated but reseparation occurs on a relatively short time scale because there is no stabilizing fission barrier. Figure 12.62 shows for $^{238}\text{U} + ^{27}\text{Al}$ and $^{238}\text{U} + ^{48}\text{Ca}$ contour plots of double differential cross sections as a function of the total center-of-mass kinetic energy (TKE) and mass number A for binary events integrated over all angles. The numbers on the contour lines give the cross sections in mb/(u MeV). The two large peaks centered at the initial energy and mass are from quasi-elastic transfer reactions. The distributions extending from the peaks toward lower TKE are skewed toward smaller mass asymmetry because sequential fission removes their counterparts, extending toward larger mass asymmetry. The parabolic dashed lines represent the expected TKE release in fission following the Viola systematics. Thus, at first sight, the central part of the cross sections is reminiscent of typical fission signatures. Figure 12.63 shows contour plots of double-differential cross sections as a function of center-of-mass scattering angle and the mass number A of binary events, intergrated over all values of TKE. In diagram (a), there is a clean separation between scattering events and fission. At first sight, the fission fragment angular distribution looks symmetric around 90° for all masses, but a more careful study of the contour lines reveals a forward–backward asymmetry of the angular distribution at fixed mass

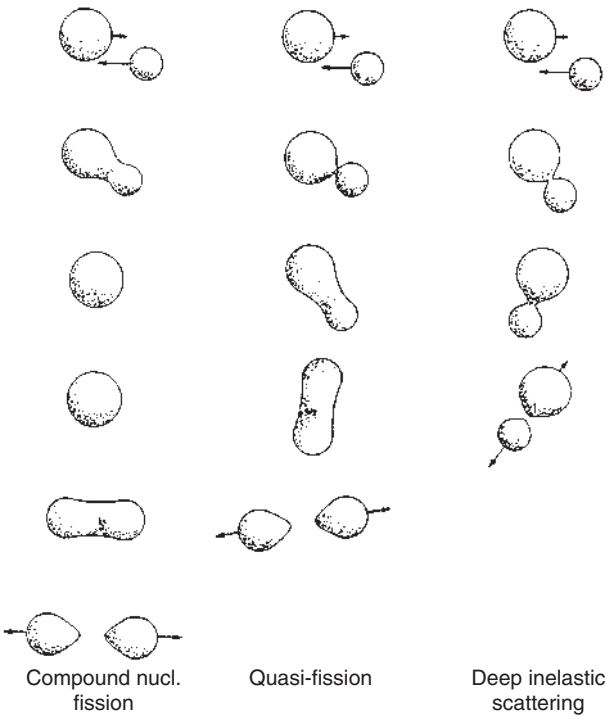

Figure 12.61 Sequence of shapes in compound-nucleus fission (left), quasi-fission (middle), and deep inelastic scattering (right). Source: Töke et al. (1985), figure 02 (p. 15)/Elsevier.

number even in the reaction $^{238}\mathrm{U} + {}^{27}\mathrm{Al}$. In (b), the non-equilibrium nature of the quasi-fission reactions becomes even more apparent through massive mass–angle correlations. The cross sections for the projectile-like fragments cluster at forward angles, whereas the cross sections for the target-like fragments cluster at backward angles. The angular distributions depend on the mass number, and the mass distribution depends on the scattering angle. Töke et al. (1985) have deduced reaction times from the angles of rotation $\Delta\Theta$ and have investigated the average mass drift $\langle \Delta A \rangle = A_\mathrm{p} - \langle A \rangle$, where $\langle A \rangle$ is the centroid of the mass distribution and $A_\mathrm{p} = 238$ is the projectile mass. Assuming that the maximum mass drift possible is to symmetry, that is, $\Delta A_\mathrm{max} = 1/2(A_\mathrm{p} - A_\mathrm{t})$, where A_t is the target mass, they calculated a normalized mass drift $\langle \Delta A \rangle / A_\mathrm{max}$ as a function of reaction time for three bins of excitation energies of the combined systems $E^* < 40\,\mathrm{MeV}$, $40 < E^* < 80\,\mathrm{MeV}$, and $80 < E^* < 120\,\mathrm{MeV}$, respectively, as shown in Figure 12.64. The solid lines are fits to the data using the parameterization

$$\langle \Delta A \rangle / A_\mathrm{max} = 1 - \exp[-(t_\mathrm{reac} - t_0)/\tau] \tag{12.115}$$

where t_0 is a time lag of about $1 \cdot 10^{-21}$ seconds needed for the contact, formation, and rupture of a neck, and τ is the 1/e relaxation time of the mass drift mode found to be equal to $(5.3 \pm 1) \cdot 10^{-21}$ seconds independent of excitation energy E^*. The driving

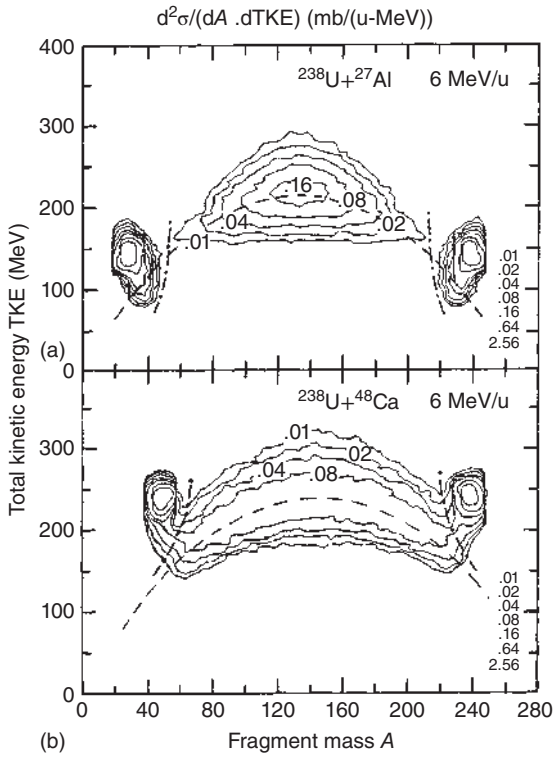

Figure 12.62 Contour plots of double-differential cross sections as a function of total kinetic energy TKE and mass A for binary events, intergrated over all angles. The numbers on the contour lines and in the inserted columns are cross sections in mb/(u MeV). The parabolic dashed lines are the expected TKE release in fission according to the Viola systematics. Source: Töke et al. (1985), figure 03 (p. 15)/Elsevier.

force is

$$F_{\mathrm{C}} = \frac{\mathrm{d}U}{\mathrm{d}\langle A\rangle} = -k(\langle A\rangle - A_{\mathrm{sym}})$$

where k is a force constant estimated in the liquid–drop model, that is, the second derivative of the mass asymmetry potential, $k = 0.0035\,\mathrm{MeV\,u^{-2}}$. In an overdamped motion, there is an equal counteracting friction force

$$F_{\mathrm{d}} = \frac{1}{m}\frac{\mathrm{d}\langle A\rangle}{\mathrm{d}t}$$

where m is the mobility that could, in principle, depend on the temperature T. The relaxation time in Eq. (12.115)

$$\tau = \frac{1}{m \cdot k}$$

being constant and independent of the temperature signals that the exchanged nucleons during mass asymmetry relaxation have a large mean free path and interact with the surface or with the overall potential. This type of friction is called "one-body dissipation." The universal mass drift relaxation time tells us that there is temperature-independent friction, which is a signature of one-body friction.

Lützenkirchen et al. (1986), by investigating the angular distributions of quasi-fission reactions near 0° and 180°, determined the variance of the tilting mode and found that the values of K_0^2 do not correspond to the equilibrium values

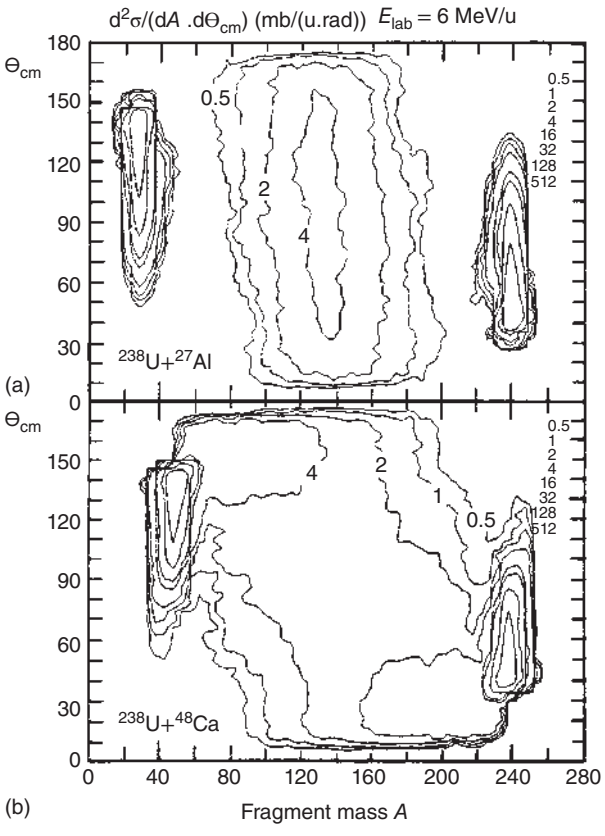

Figure 12.63 Contour plots of double-differential cross sections as a function of center-of-mass angle and the mass *A* for binary events, integrated over all values of TKE. Source: Töke et al. (1985), figure 04 (p. 15)/Elsevier.

according to Eq. (12.96) but develop dynamically with time. It appears that the relaxation time is longer at lower bombarding energy, that is, at lower orbital angular momenta.

Keller et al. (1987) studying reactions of ^{50}Ti, ^{54}Cr, and ^{58}Fe with ^{208}Pb at the barrier were able to measure with radiochemical methods the average isotope masses of complementary charged fragments. Typically, for a fragment with charge 35, one expects a pre-evaporation mass around 86 u on account of the minimum potential energy. If the total kinetic energy of such products is assumed to be given by the Viola systematics, and if an excitation energy sharing according to the mass ratio (thermal equilibrium) is assumed, one obtains a post-evaporation mass number of about 83. The measured average mass number, however, was 77.8. This indicated that the acceptor of the neck nucleons obtained nearly the full excitation energy. The complete trend with charge division suggests that donor nuclei are cold, while acceptor nuclei are hot.

More complete radiochemical studies by Klein et al. (1997) and Wirtz et al. (2001) confirmed these observations for the system ^{51}V + ^{197}Au at the Bass-model barrier,

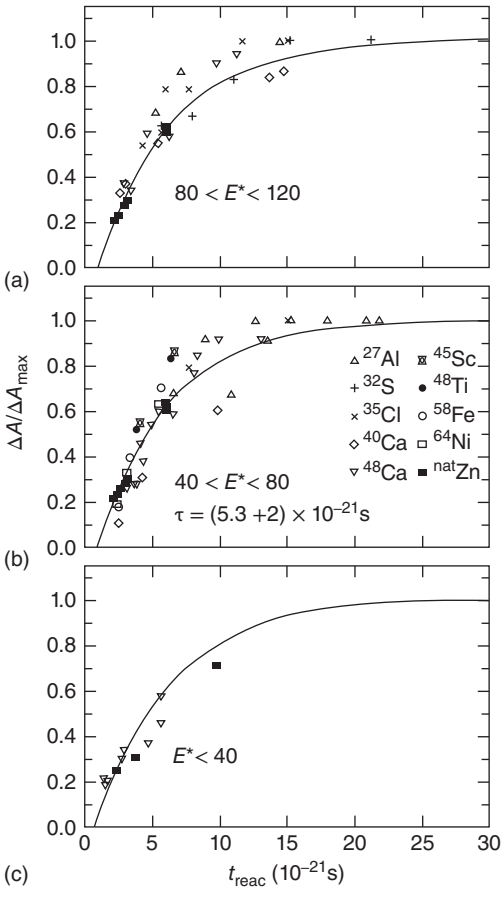

Figure 12.64 Normalized mass drift as a function of reaction time. The solid lines are fits to the data with Eq. (12.115) yielding a universal mass drift relaxation time of $\tau = (5.3 \pm 1) \cdot 10^{-21}$ seconds. Source: Töke et al. (1985), figure 04 (p. 15)/Elsevier.

Figure 12.65. The extreme acceptor–donor asymmetry at the barrier changes toward equipartition of the excitation energy only 25 MeV above the barrier energy, $E_{cm} = B + 25$ MeV, and develops toward a near temperature equilibrium at $E_{cm} = B + 75$ MeV, where the excitation energies of the fragments are expected to scale with the mass numbers:

$$\frac{E_3}{E_4} = \frac{a_3}{a_4}\frac{T^2}{T^2} = \frac{a_3}{a_4} = \frac{8.5 \cdot A_3}{A_4 \cdot 8.5} = \frac{A_3}{A_4}$$

This is in accordance with the observations reviewed by Töke and Schröder (Bock 1979–1982) at higher energy at modest kinetic energy losses.

Figure 12.65 indicates that, at a bombarding energy corresponding exactly to the Coulomb barrier, $E = B$, there is a conspicuous dependence of excitation energies on the direction of the mass flow. In the reaction of $^{51}V + ^{197}Au$, fragments with mass numbers below 197 are cold and fragments with mass numbers above 51 are hot. On the other hand, fragments above the Au target take over most of the excitation energy available, whereas fragments below the V projectile are formed without much excitation. This extreme donor–acceptor asymmetry changes toward equipartition of the excitation energy only 25 MeV above the barrier energy, $E = B + 25$ MeV,

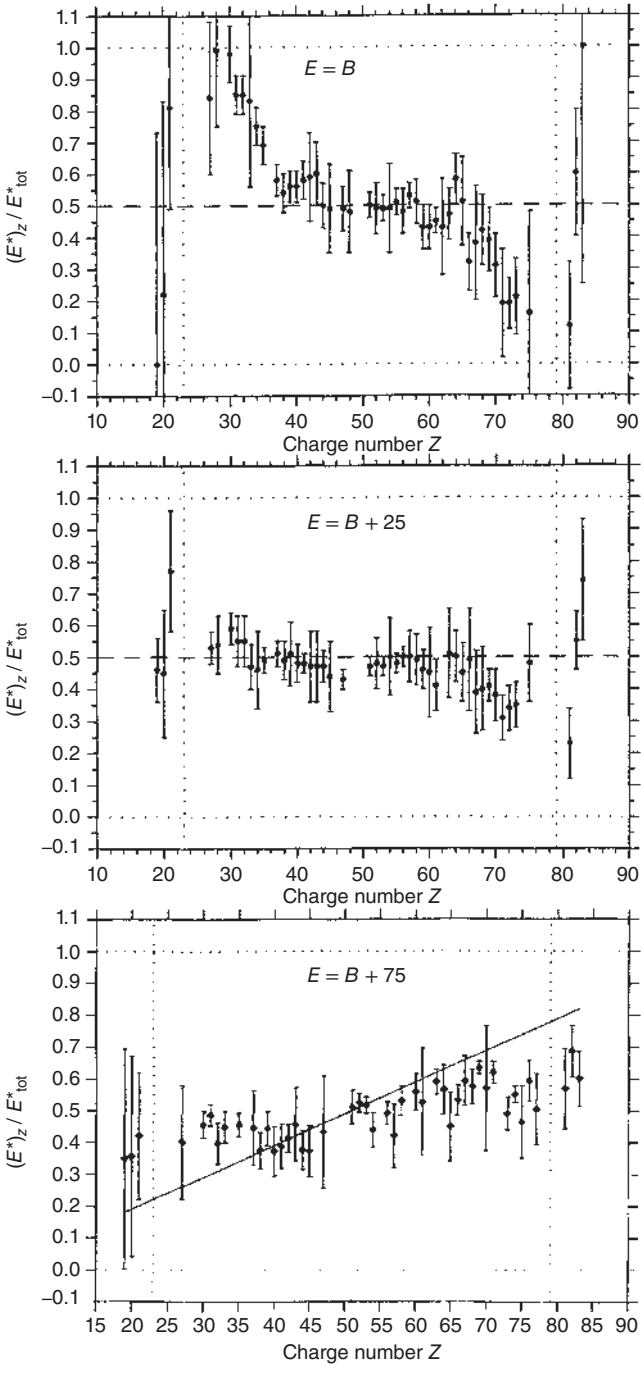

Figure 12.65 Fractional excitation energies as a function of fragment charge in the $^{51}V + ^{197}Au$ reaction at three different bombarding energies relative to the barrier. Source: Wirtz et al. (2001), figure 03 (p. 50)/De Gruyter.

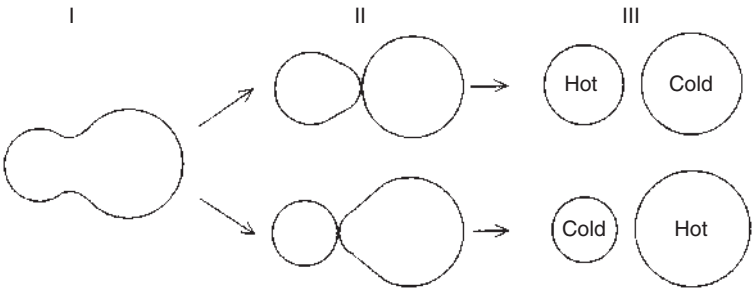

Figure 12.66 Schematic illustration of random neck rupture leading to hot acceptor nuclei and cold donor nuclei.

and develops toward a near temperature equilibrium at $E = B + 75$ MeV. The extreme donor–acceptor asymmetry at the barrier is in agreement with the random neck ruture model of Brosa, Grossmann, and Müller (1990) where nuclear scission happens due to a hydrodynamical instability triggered by random surface vibrations. At the barrier, where the velocity of the reaction partners at contact is zero, the system heals a neck and the acceptor of the neck is deformed, and the deformation energy shows up as excitation energy. Figure 12.66 illustrates how a slightly asymmetric double nuclear system can split so that the acceptor of the neck is formed hot and the donor is formed cold. With increasing bombarding energy over the Coulomb barrier, according to the nucleon exchange model to be discussed in Section 12.8.3, there is, for short interaction times, an equipartition of the dissipated energy that develops gradually, for longer interaction times and larger dissipated energies, into a thermal equilibrium. The data in Figure 12.65 are consistent with this expectation.

12.8.3 Deep Inelastic Collisions

Looking back at Figure 12.58, we now discuss the second reseparation channel, the DICs, in which, after making close contact and healing a neck, target and projectile dissipate TKE all the way down to the Coulomb barrier energy V_C, dissipate orbital angular momentum by tangential friction, and exchange nucleons. The measured cross section extends continuously in TKE, angle, and charge. Masses are often not measured directly but are inferred from the nuclear charge Z. Figure 12.67 illustrates for the reaction $^{86}\mathrm{Kr} + {}^{166}\mathrm{Er}$ at 8.18 MeV/u that the three variables TKE, angle Θ_{cm}, and nuclear charge Z are not correlated sharply: strong fluctuations exist around their slowly shifting mean values. The ridge of the cross section shifts with increasing dissipated energy from the grazing angle to forward angles, Figure 12.67a, and seems to pass through 0° to negative angles. Because the experiment cannot distinguish positive and negative scattering angles, the branch representing negative scattering angles appears like a foot extending up to 80° on the side of the positive angle scattering. Because of the elongation of the fragments at scission, a considerable part of the cross section extends below the energy limit V_C for touching spheres and follows the Viola systematics. Figure 12.68 explains the Wilczynski diagram. Part (a) sketches in an energy against scattering angle

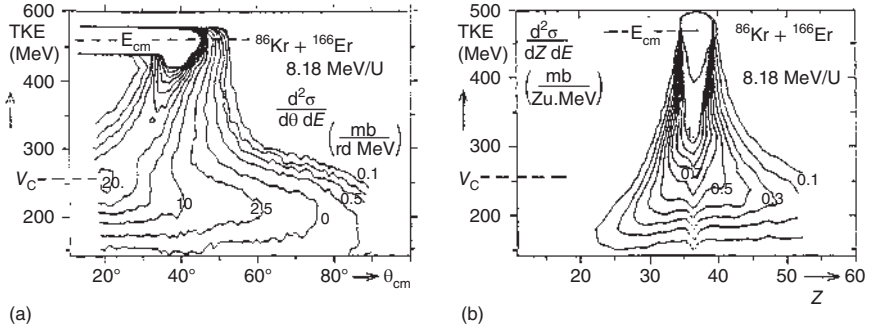

Figure 12.67 Contour plots for the Wilczynski diagram (a) and for the diffusion plot (b) of the $^{86}Kr + ^{166}Er$ collisions. Source: Bock (1979–1982), figure 04 (p. 23)/North-Holland Publishing.

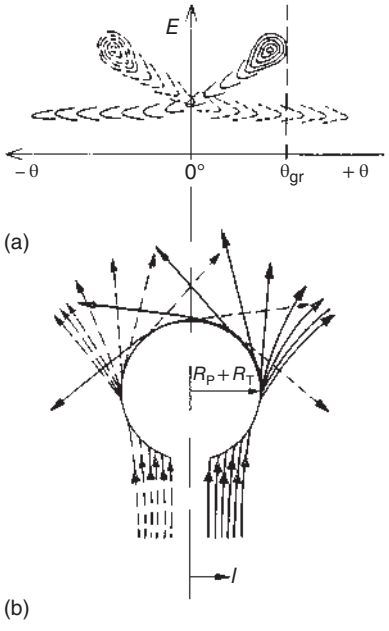

Figure 12.68 Wilczynski diagram: (a) energy vs. scattering angle plot; (b) trajectories leading to the energy–angle correlation of part (a). Source: Bock (1979–1982), figure 05 (p. 23)/North-Holland Publishing.

plot of the contour lines of constant cross section. In a reaction plane defined by the beam axis and by the detection angle, two components are visible: for impact parameters on the right-hand side of the beam axis (solid lines) and on the left-hand side (dashed lines). Part (b) of the figure illustrates the corresponding trajectories leading to the energy–angle correlation of part (a). The ingoing angular momentum is denoted by l. The mean charge, Figure 12.67b, is practically constant, but the width of the distribution widens considerably.

A number of simple features of the reaction are already visible in the one-dimensional projections in Figure 12.69 where the same data as in Figure 12.67 are presented as a function of energy (a), nuclear charge of the projectile-like fragment (b), and as a function of angle (c). The large energy damping associated

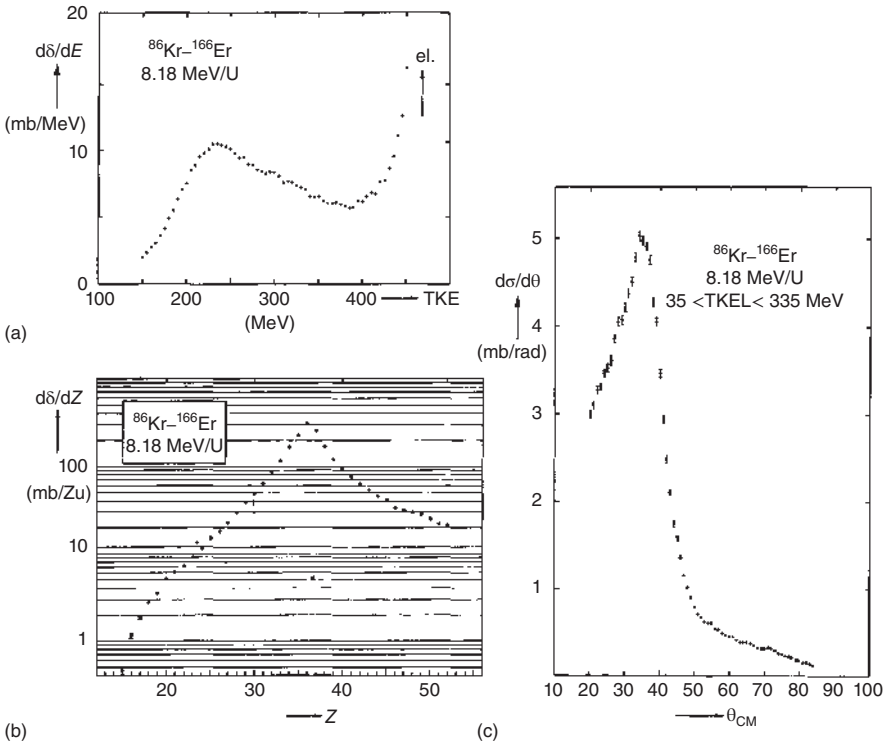

Figure 12.69 One-dimensional projection of all inelastic events with TKEL > 35 MeV as a function of energy (a), charge (b), and scattering angle (c). Same data as in Figure 12.67. Source: Bock (1979–1982), figure 06 (p. 23)/North-Holland Publishing.

with DIC is well illustrated in part (a) of the figure. The charge distribution is very broad. The probability of producing elements far away from the projectile charge decreases with a factor of 1.5–2 per Z unit. For elements heavier than the projectile, the yields are higher than for elements lighter than the projectile. As we shall see later, this is associated with a finite drift velocity that displaces the centroid of the distribution toward charge symmetry. The angular distribution is about 30° wide with a skewness toward smaller angles. The maximum is located about 5° to 10° forward of the quarter-point angle, see Section 4.1. At angles larger than 50°, a tail emerges with a rather flat slope; this is identical with the foot in Figure 12.67 that is associated with negative angle scattering.

More Wilczynski diagrams gained as scatterplots in overview types of experiments are shown in Figure 12.70. The evolution of the shape of the "deflection function" scales with the reduced Sommerfeld parameter (cf. Eq. (12.14)) $n' = Z_1 Z_2 e^2/\hbar v_{\mathrm{CB}}$ where v_∞ is replaced by the relative velocity v_{CB} at the Coulomb barrier. These values are 310 for (a), 380 for (b), 450 for (c), and 770 for (d). To characterize the shape of the deflection function of (a), one talks about "orbiting," which is still indicated also for (b). The shape of (c) is called "focusing," and the shape of (d) is called "Coulomb trajectory."

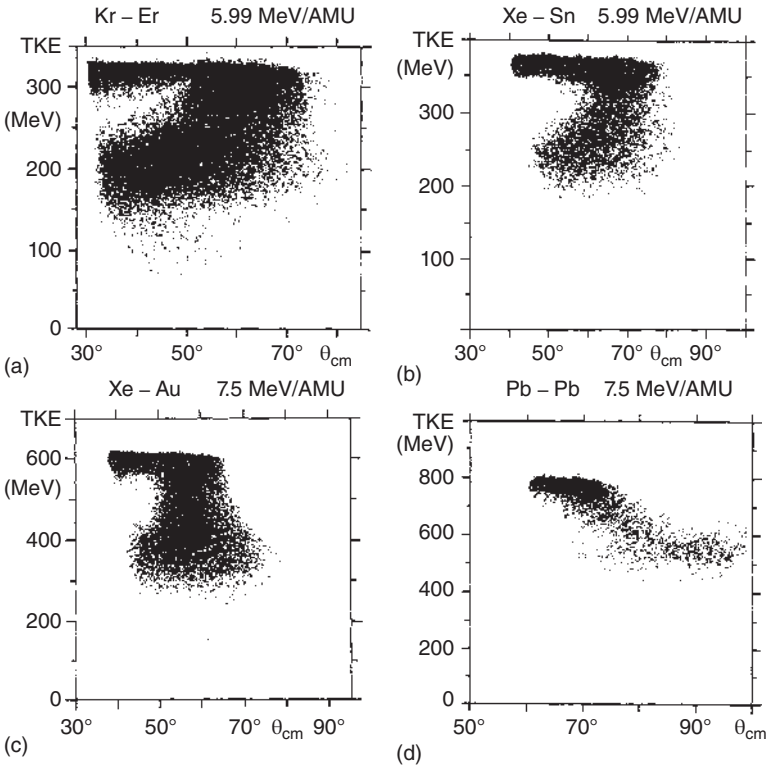

Figure 12.70 Wilczynski from different target–projectile combinations. Source: Bock (1979–1982), figure 07 (p. 23)/North-Holland Publishing.

In the study of mass transfer and other relaxation phenomena, it is important to define an observable which is closely related to the interaction time. In the original studies of light systems in which orbiting occurs, the scattering angle was used as the relevant parameter. The frequency of rotation of the di-nuclear system $\Delta\Theta/\mathrm{d}t$ must be given by the ratio of the angular momentum to the moment of inertia. Thus with some model-dependent assumptions about the latter, the interaction time

$$\tau_{\mathrm{int}} \propto (\Theta_{\mathrm{gr}} - \Theta)/I_{\mathrm{gr}} \tag{12.116}$$

can be estimated. Later, in the study of heavier systems, since no angular dependence was observed (focusing in the case of Xe + Au, Bi), it was natural to select the TKEL as the relevant parameter; in fact, the strongest evolution of the element distribution was observed as a function of the dissipated energy as shown in Figure 12.71. In order to elucidate which of the two parameters, TKEL or scattering angle, is most relevant, Rudolf et al. have analyzed in detail, see Figure 12.72, the triple-differential cross sections $\mathrm{d}^3\sigma/\mathrm{d}E\ \mathrm{d}\Theta\mathrm{d}Z$ for the Kr + Er collision. This reaction is well suited for such an analysis as the ridge of the cross section for the partly damped events changes as a function of scattering angle as well as TKEL. Six adjacent domains were selected in angle for an energy window of 50 MeV. The element distributions of the six domains were then compared to each other in part (b) of the figure, and

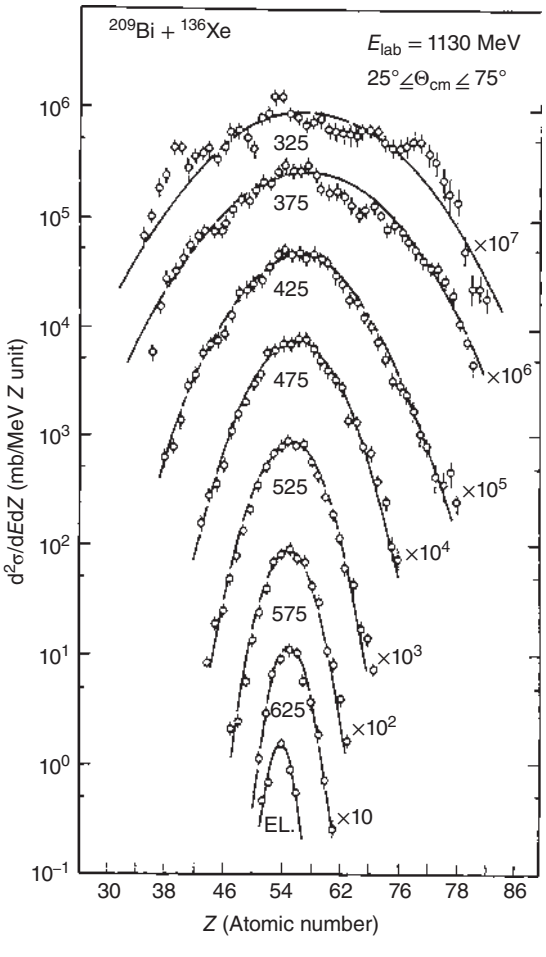

Figure 12.71 Element distributions as a function of TKE indicated at the top of each curve. The TKE bins are 50 MeV wide. The curves represent Gaussian fits. Source: Schröder and Huizenga (1984)/Springer Nature.

no significant dependence on the center-of-mass scattering angle was observed for a selected energy loss, while the distributions displayed a definite change as a function of energy similar to what is evident in Figure 12.71. This latter figure suggests a description of the probability for the population of an element Z at time t as a Gaussian distribution

$$P(Z,t) = \frac{1}{\sqrt{2\pi\sigma_Z^2}} \exp\left\{-\frac{(Z-Z_0)^2}{2\sigma_Z^2}\right\} \tag{12.117}$$

that widens with increasing TKEL. As we shall see later, within the diffusion model, the same probability is given as

$$P(Z,t) = \frac{1}{\sqrt{4\pi D_Z t}} \exp\left\{-\frac{(Z-Z_0-vt)^2}{4D_Z t}\right\} \tag{12.118}$$

In both equations, Z_0 is the centroid of the charge distribution. In Eq. (12.118), D_Z is the diffusion coefficient, v is the drift velocity, and t is the interaction time. A

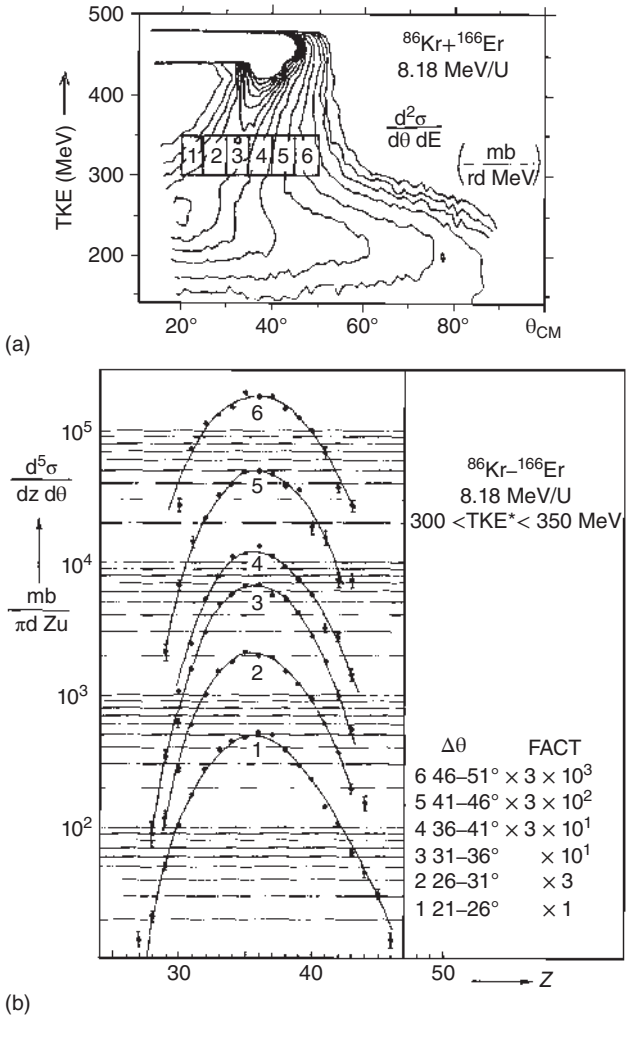

Figure 12.72 Analysis of the element distributions as a function of energy loss and scattering angle: (a) Wilczynski diagram with bins 1 through 6 for which the element distributions are displayed in part (b). Source: Bock (1979–1982), figure 08 (p. 35)/North-Holland Publishing.

comparison of Eqs. (12.117) and (12.118) tells us that

$$\sigma_Z^2 = 2D_Z t \tag{12.119}$$

Thus, the widening of σ_Z^2 with increasing TKEL is a better possibility for selecting impact parameters or interaction times than the scattering angle.

If TKEL is the central variable, and if TKEL is caused by one-body friction as discussed above, then it is obvious that the energy loss should be ascribed to the recoil momentum associated with each nucleon exchange. The friction force per nucleon

exchange is

$$F_{\text{ex}} = -k_{\text{ex}}|\dot{r}|$$

where $|\dot{r}| = v$ is the velocity of relative motion (neglecting the Fermi momentum of the exchanged nucleon). Then, the momentum transfer per nucleon exchange is

$$\Delta p = m|\dot{r}|$$

The system must counteract with an equal recoil momentum so that

$$\delta E_{\text{ex}} = \frac{m}{\mu} E_{\text{av}}$$

Here, the nucleon mass $m = 1$, μ is the reduced mass of the system, and $E_{\text{av}} = E_{\text{cm}} - V_{\text{C}} - \text{TKEL}$ is the available kinetic energy at each instant of the interaction. This gives the famous recoil formula

$$-\frac{\mathrm{d}E_{\text{av}}}{\mathrm{d}N_{\text{ex}}} = \frac{E_{\text{av}}}{\mu} \tag{12.120}$$

saying that the dissipated energy per exchange step N_{ex} is proportional to the available energy before that exchange step. The number of exchange steps, in a model of a flat source (flat PES, no drift), is $N_{\text{ex}} = \sigma_A^2$ where

$$\sigma_A^2 = \sigma_Z^2 + \sigma_N^2 + 2\rho_{NZ}\sigma_Z\sigma_N \tag{12.121}$$

is the variance of the mass distribution and ρ_{NZ} is the correlation coefficient between the proton and neutron exchange steps. In the case of uncorrelated exchange ($\rho = 0$), we have $\sigma_N^2 = (N/Z)\sigma_Z^2$ where the factor (N/Z) reflects the abundance of neutrons and protons in the total system. Measurements of N/Z populations in DIC, however, indicate strong correlations. The products lie in a narrow valley with a slope $\mathrm{d}N/\mathrm{d}Z$ given by the PES such that $\rho = 1$ and $\sigma_N = (\mathrm{d}N/\mathrm{d}Z)\sigma_Z$. Thus, the correlation term in Eq. (12.121) becomes $2(\mathrm{d}N/\mathrm{d}Z)\sigma_Z^2$ and hence

$$\begin{aligned}\sigma_A^2 &= \sigma_Z^2(1 + (\mathrm{d}N/\mathrm{d}Z)^2 + 2(\mathrm{d}N/\mathrm{d}Z)) \\ &= \sigma_Z^2(1 + (\mathrm{d}N/\mathrm{d}Z))^2 \\ &= (\mathrm{d}A/\mathrm{d}Z)^2\sigma_Z^2\end{aligned}$$

If we set $(\mathrm{d}A/\mathrm{d}Z)$ roughly equal to (A/Z), we arrive at the often used equation

$$\sigma_A^2 = (A/Z)^2\sigma_Z^2 \tag{12.122}$$

Equation (12.120) suggests that we should expect a universal dissipated energy curve if TKEL is plotted against σ_A^2 or σ_Z^2, independent of the Z and A of projectile and target; however, as is emphasized by Figure 12.73, large differences in the behavior of individual systems are observed, indicating pronounced nuclear structure dependencies in the variances at given values of TKEL.

These systematic deviations from Eq. (12.120) have led to a modified ansatz by Dakowski et al. which, besides the recoil term of Eq. (12.120), contains an additive term DE depending on the excitation energy and on the nuclear structure of the nuclei involved:

$$-\frac{\mathrm{d}E_{\text{av}}}{\mathrm{d}\sigma_A^2} = \frac{E_{\text{av}}}{\mu} + \text{DE(TKEL)} \tag{12.123}$$

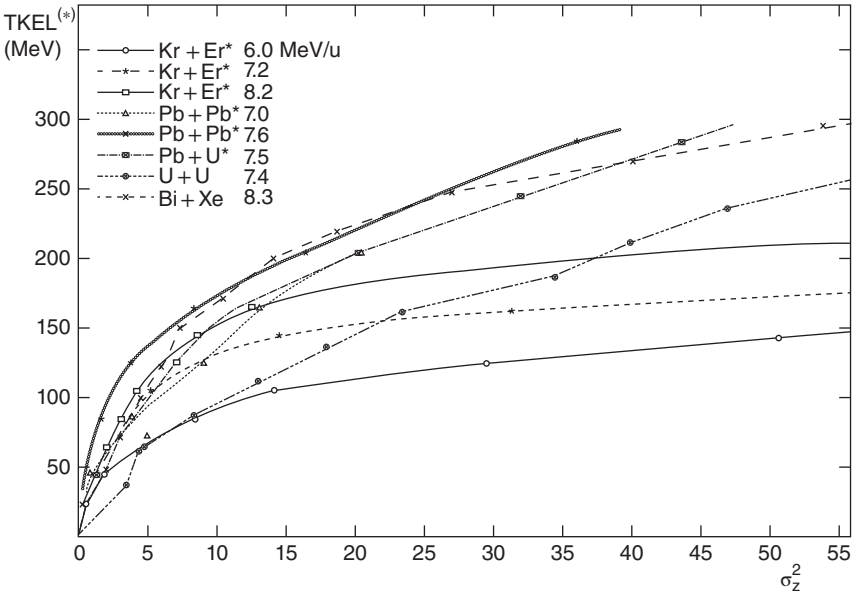

Figure 12.73 TKEL vs. σ_Z^2 correlations for different heavy systems. Source: Bock (1979–1982), figure 08 (p. 35)/North-Holland Publishing.

In order to extract DE(TKEL) from the data, one subtracts the recoil energy $E_{\mathrm{av}}/\mu = \mathrm{RE}$ from the data, see Figure 12.74, and finds that DE for a given system (Kr + Er) is independent of the bombarding energy and decays away rapidly with increasing TKEL (Figure 12.74a). Moreover, one finds that DE is, in particular in the first bin of $5 \leq \mathrm{TKEL} \leq 45$ MeV, extremely structure dependent with a maximum value of DE_0 for $^{208}\mathrm{Pb} + ^{208}\mathrm{Pb}$ and a minimum value of DE_0 for $^{238}\mathrm{U} + ^{238}\mathrm{U}$. In Figure 12.75, DE_0 is compared to other structure-dependent quantities for the studied systems. Part (a) shows the correlation with the sum of energies of the 2^+ states for projectile and target $E(2^+)$. As an additional structure quantity to be compared to DE_0, there are the ground-to-ground Q values Q_{gg} for two-nucleon transfer reactions

- two-neutron transfer from target to projectile $Q_{\mathrm{gg}}(1)$ and vice versa $Q_{\mathrm{gg}}(2)$
- two-proton transfer from target to projectile $Q_{\mathrm{gg}}(3)$ and vice versa $Q_{\mathrm{gg}}(4)$

which are averaged in

$$\mathrm{d}S = \frac{1}{4}\sum_{i=1}^{4} Q_{\mathrm{gg}}(i)$$

The correlation between $\mathrm{d}S$ and DE_0 is shown in Figure 12.75b. The correlations in Figure 12.75 show that DE_0 reflects the intrinsic structure properties of the colliding nuclei. Three regions can be distinguished in the DE plots of Figure 12.74:

- region A characterized by strong nuclear structure effects of the colliding nuclei;

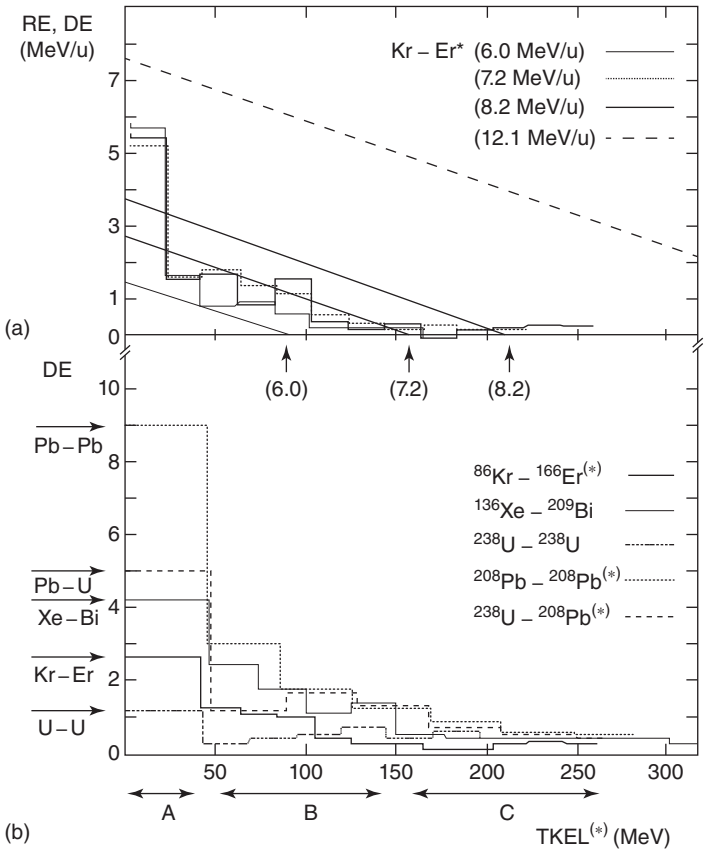

Figure 12.74 (a) RE and DE as a function of TKEL for Kr + Er at four different bombarding energies. (b) Comparison of the DE values for different systems. Source: Bock (1979–1982), figure 08 (p. 35)/North-Holland Publishing.

- region B showing how fast the shell structure is dissolved in a DIC;
- region C representing the effect of the deformability of the di-nuclear system.

Equation (12.123) can be thought of as an extension of the one-body dissipation approach. For each nucleon exchange, in addition to the recoil energy, a structure energy needs to be dissipated since the nucleons are, in the beginning of the DIC, transferred to unoccupied levels above the Fermi energy of the colliding nuclei. As the DIC proceeds, several nucleons are promoted to higher orbits by inelastic excitation and by nucleon exchange. In this later stage, the nucleons can be exchanged between such higher orbits without particle–hole creation. Considerably less structure energy is then needed.

Experiments in which both charge and mass numbers were determined have investigated N/Z equilibration and the role of the PES for the evolution of charge and mass flow in DIC. Schüll et al. (1981) used a magnetic spectrometer to measure first and second moments of nuclide distributions for Xe-like products

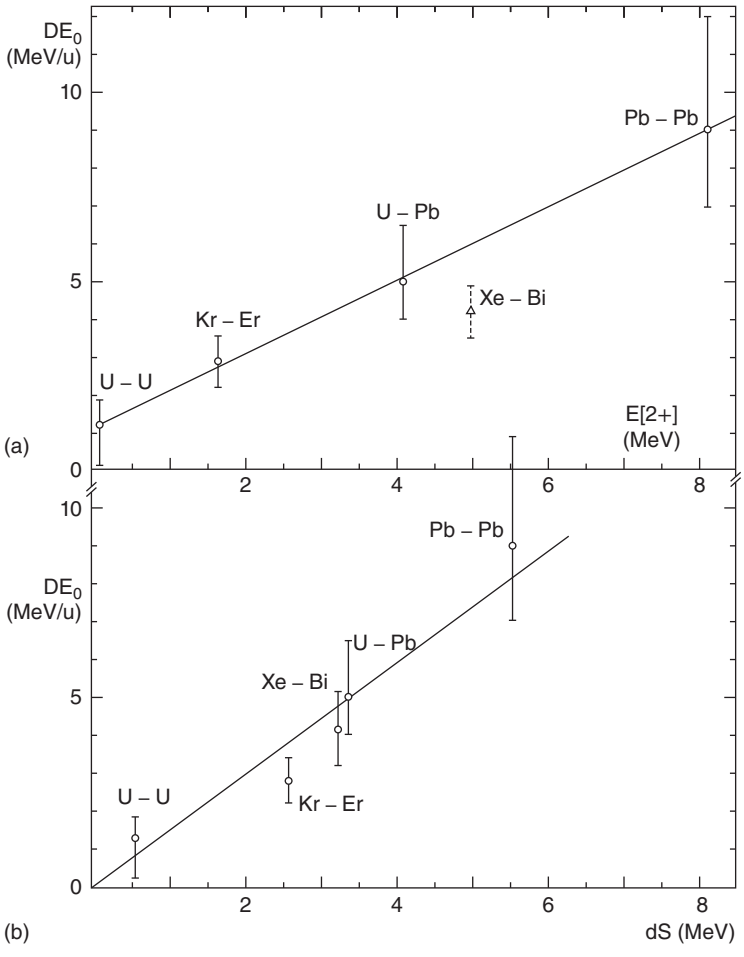

Figure 12.75 DE_0 correlations with nuclear structure quantities: (a) with the energy of the lowest collective 2^+ state; (b) with the averaged Q_{gg} value for two-nucleon transfer dS. Source: Bock (1979–1982), figure 08 (p. 35)/North-Holland Publishing.

from 5.9 MeV u^{-1} ^{136}Xe incident on a ^{56}Fe target at $\Theta_{lab} = 14°$ where the maximum cross section for DIC occurs. For small excitations, neutron transfer from ^{136}Xe to ^{56}Fe predominates. With increasing excitation energy, the distribution spreads out and moves away from the injection point, evolving along $A = \text{const}$ toward a larger charge asymmetry and then, reaching a stretched ellipsoidal shape, drifts toward mass symmetry. This can be described quantitatively by the first and second moments of the nuclide distributions which reflect the drift and diffusion properties of the system. In Figure 12.76, the drift of the centroids is shown in the N–Z plane together with a contour plot of the PES calculated using shell-corrected liquid–drop binding energies for a near-grazing partial wave ($l = 150\,\hbar$) at an interaction distance of 12.8 fm. One can appreciate the importance of the neutron evaporation corrections by comparing the paths of the first moments of both the uncorrected

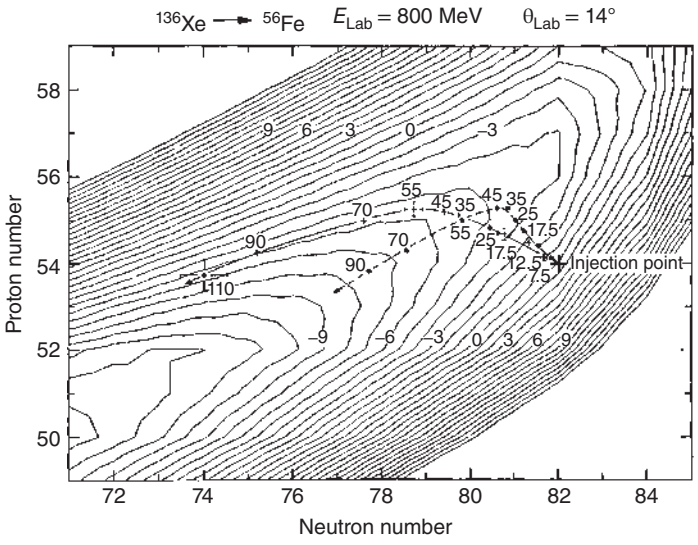

Figure 12.76 PES for ^{136}Xe + ^{56}Fe with the drift path of the first moments of the projectile-like nuclide distributions (crosses, uncorrected; heavy dots, corrected for neutron evaporation; numbers, total excitation energy in MeV). The PES contour lines are spaced by 1 MeV and include ground-state shell corrections. Source: Schüll et al. (1981), figure 03 (p. 25)/Elsevier.

and the corrected data in Figure 12.76. The tendency to minimize the potential energy by following almost exactly the gradient of the PES is clearly recognized. Starting from an initial N/Z ratio of 1.52, the neutron excess of the projectile is relaxed to a value of 1.46 which corresponds to the minimum of an $A = 136$ cut through the PES. If ground-state shell effects are omitted from the PES calculation, the minimum of the PES would shift to $Z \approx 56$, $N \approx 79$ which would be in conflict with the data. Therefore, they clearly demonstrate the importance of shell effects on mass and charge flow in partially damped collisions.

It has been suggested that N/Z ratios of the fragments from damped collisions equilibrate faster than the mass asymmetry. Indeed, Figure 12.76 suggests that the initial drift associated with N/Z equilibration precedes the drift in the mass asymmetry coordinate. That charge equilibration at fixed mass asymmetry might be intrinsically faster than mass asymmetry relaxation dates back to Hill and Wheeler who, already in 1953, had pointed out that the charge distributions in fission might be due to a collective isovector mode in analogy to the Steinwedel–Jensen model of GDRs. In such a hydrodynamical description, the fluctuations in the division of charge are expected to be associated with the quantum mechanical zero-point motion even if there is no excitation energy. The driving force for such a collective mode originates from the liquid–drop potential which, for fixed mass asymmetry, gives to a good approximation

$$V(Z_3)\big|_{A_3} = \frac{1}{2}c(Z_3 - \overline{Z}_3)^2 + \text{const} \tag{12.124}$$

If this harmonic oscillator is weakly damped through coupling to the intrinsic degrees of freedom of the system which constitute a heat bath of temperature T, the eigenvalues of the mode are known from quantum mechanics to be

$$\epsilon(T,\omega) = \frac{1}{2}\hbar\omega + \frac{\hbar\omega}{\exp(\hbar\omega/T) - 1} \tag{12.125}$$

where the collective frequency, ω, and the stiffness, c, are related through the inertial parameter B as $c = \mathrm{B}\omega^2$, and B is assumed to be constant. Using the harmonic oscillator eigenfunctions, one determines the charge variance at fixed mass asymmetry to be

$$\sigma^2_{Z_3}\Big|_{A_3} = \frac{1}{c}\left(\frac{1}{2}\hbar\omega + \frac{\hbar\omega}{\exp(\hbar\omega/T) - 1}\right) \tag{12.126}$$

Two extreme predictions can be derived from Eq. (12.126) depending on the relative magnitude of the phonon energy $\hbar\omega$ compared to the temperature T. If $\hbar\omega \gg T$, the zero-point motion dominates and

$$\sigma^2_{Z_3}\Big|_{A_3} = \hbar\omega/2c \tag{12.127}$$

In that case, the charge fluctuations are purely quantal. In the other extreme $\hbar\omega \ll T$,

$$\sigma^2_{Z_3}\Big|_{A_3} = T/c \tag{12.128}$$

One is then dealing with classical statistical fluctuations.

Of the many experimental studies, we show one as an example. This was the measuring of differential recoil ranges for Au-like products in the reaction of 900 MeV ^{132}Xe with ^{197}Au using γ-ray spectroscopy and determining a cross-sectional surface $\sigma(Z,A_{\mathrm{prim}},E_x)$. Among other moments, this primary yield surface defined the conditional variances $\sigma^2_{Z_3}\Big|_{A_3}$ as a function of the total excitation energy, which are shown in Figure 12.77. The solid line in this figure is calculated with Eq. (12.128) using a stiffness of 2.7 MeV and the temperature $T = \sqrt{8E_x/A_{\mathrm{tot}}}$. The dashed line corresponds to the equilibrium variance for quantal fluctuations. The phonon energy was estimated as $\hbar\omega = 78\ \mathrm{MeV}/(A_1^{1/3} + A_2^{1/3}) = 7.2$ MeV. The disagreement of the experimental data with the predicted conditional variance of 1.35 does not necessarily exclude quantal fluctuations. If a considerably increased inertia associated with the $E1$ mode is assumed for the di-nuclear complex made up of a Xe-like fragment touching an Au-like fragment is assumed, as compared to a normal spherical nucleus, the resulting variance of the quantal fluctuations could be much smaller. Updegraff and Onley have shown for the photofission of ^{238}U that the dipole vibration energy decreases for increasing deformation and is at least four times reduced for the very constricted shape of the fissioning nucleus at scission. This would invalidate the condition $\hbar\omega \gg T$ for zero-point motion and explain the classical statistical behavior of the fluctuations.

It was realized by Nörenberg that the picture of a distribution that broadens as time grows has a similarity with a diffusion process which can be described classically by a transport equation of the Fokker–Planck type

$$\frac{\partial f(y,t)}{\partial t} = -\frac{\partial}{\partial y}(vf) + \frac{\partial^2}{\partial y^2}(Df) \tag{12.129}$$

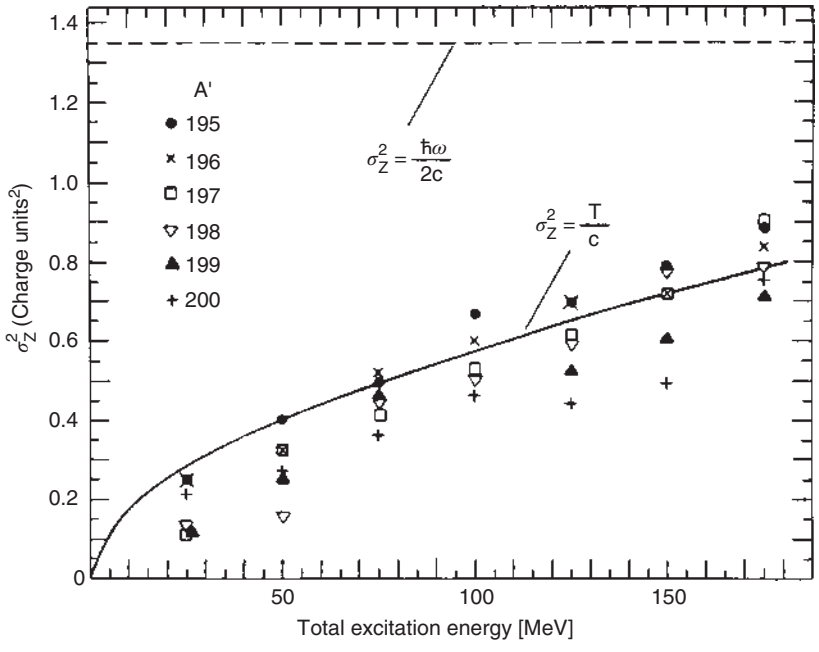

Figure 12.77 Charge variances at fixed mass asymmetry for the ^{132}Xe + ^{197}Au reaction at 900 MeV. The dashed curve indicates the expected variance due to quantal fluctuations. The solid curve is calculated for classical fluctuations. Source: Poitou et al. (1979), figure 04 (p. 35)/Elsevier.

where f is the probability of finding the system at time t with the property y; v and D are transport coefficients, the drift velocity and the diffusion coefficient, respectively. The solution has the form

$$f(y,t) = \frac{1}{\sqrt{4\pi Dt}} \exp\left\{-\frac{(y-vt)^2}{4DT}\right\} \tag{12.130}$$

with $\sigma_y^2 = 2Dt$.

Applied to element distributions by Riedel and Nörenberg (1979), this yields Eqs. (12.118) and (12.119). Their application to reproduce experimental element distributions is shown in Figure 12.78 to illustrate charge drift and diffusion as a function of time. In the (U + U) collision, the dissipative cross sections (open circles) have been reconstructed from the two-body events (filled circles) by taking sequential fission into account.

12.8.3.1 The ^{238}U + ^{238}U Reaction

Multi-nucleon transfer reactions between two ^{238}U nuclei at energies close to the Coulomb barrier were studied in the late 1970s (i) to investigate the gross features of the reaction by measuring product charge, total kinetic energy, and angular distributions (Hildenbrand et al. 1977; Freiesleben et al. 1979), (ii) to learn about the prospects of synthesizing very heavy actinide isotopes and possibly superheavy elements in their ground states in these damped collisions (Schädel et al. 1978), and

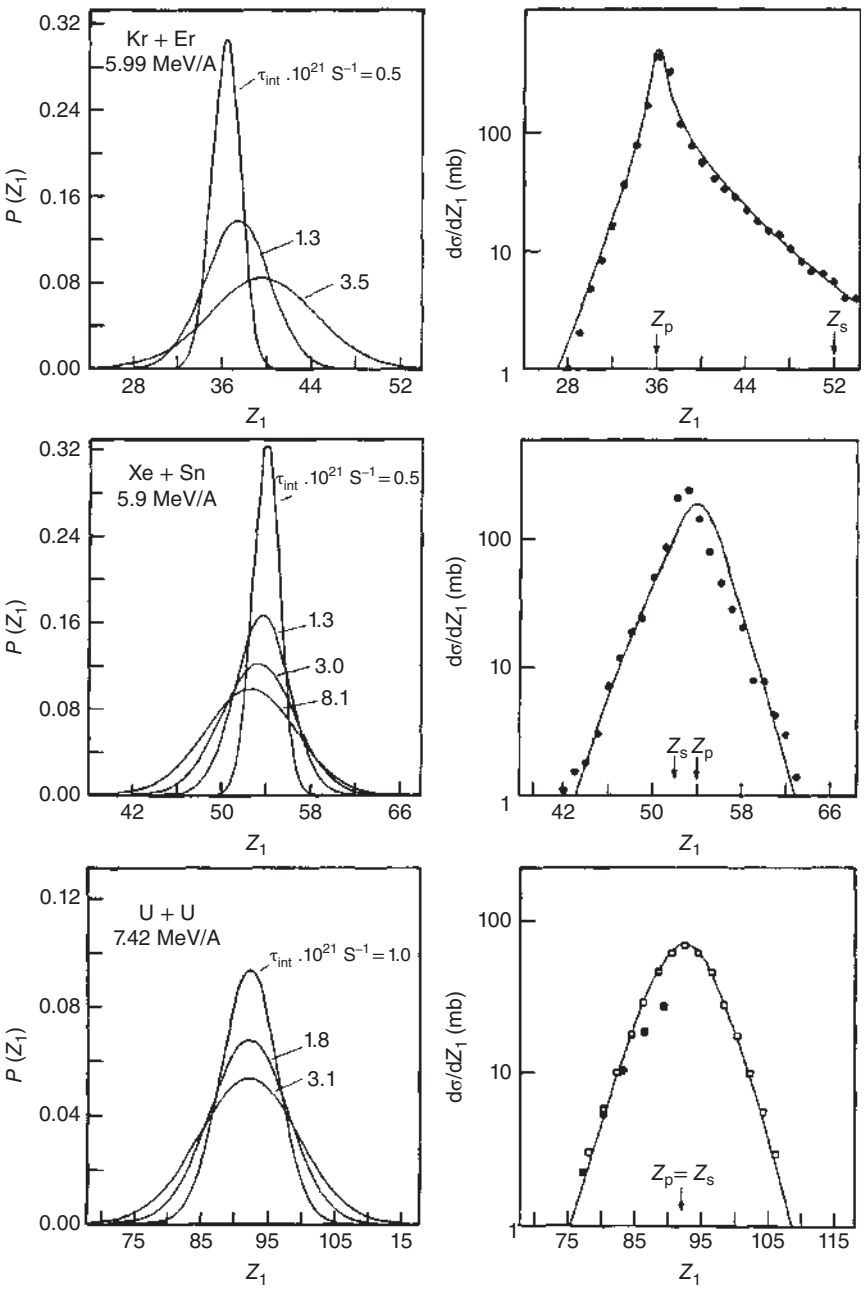

Figure 12.78 Element distributions for DIC. The fitted values for the drift and diffusion coefficients are (in units of 10^{-22} s) $v = 0.3$, $D = 1.9$ for Kr + Er, $v = -0.1$, $D = 1.6$ for Xe + Sn, and $v = 0$, $D = 7.5$ for U + U. Source: Bock (1979–1982), figure 09 (p. 40)/North-Holland Publishing.

(iii) to study fission phenomena (Hildenbrand et al. 1977) of such heavy fragments with atomic numbers up to $Z = 116$. These experiments showed that fission of one or both of the colliding nuclei is the dominant process. However, for a given energy dissipation, more particle diffusion was reported (Hildenbrand et al. 1977; Freiesleben et al. 1979) than previously observed in other collision systems, a feature highly desirable for the syntheses of very heavy elements. In qualitative agreement with this observation, cross sections for surviving heavy actinides were found to exceed those in Ar + U, Kr + U, and Xe + U reactions by typically 1 order of magnitude (Schädel et al. 1978). Analyses of the survival probabilities of these highly fissionable nuclei revealed (Schädel et al. 1978) that their formation is associated with the low-energy tails of the excitation-energy distributions. Exclusive investigations of the three-body exit channels using kinematic coincidences with large-area ionization chambers revealed (Glässel et al. 1979) that this reaction channel has to be interpreted as a two-step mechanism with fission following the deep-inelastic collision with minimum scission-to-scission times of 10^{-20} seconds even for intermediate nuclei with $Z > 110$. The studies by Schädel et al. (1978) used radiochemical techniques based on bombardments of thick targets at various incident energies, chemical separations, and nuclide identification by α-particle spectroscopy, sf counting, and γ-ray spectroscopy. These studies and those of the $^{238}U + ^{248}Cm$ reaction (Schädel et al. 1982) have recently been revisited and published in detail by Kratz, Schädel, and Gäggeler (2013).

12.8.3.2 Isotope Distributions at Fixed Z Below $Z = 92$

The integral cross section integrated over all values of total kinetic energy for individual isotopes of a given Z is used to define a Gaussian distribution whose centroids and widths vary smoothly with Z. This is so for products below $Z = 92$ down to about $Z = 79$ representing the survivors of deep-inelastic collisions followed further down in Z by a symmetric product distribution peaking at $Z = 46$ and extending down to $Z = 23$, resulting from sequential fission of highly excited fragments from damped collisions. For fission products with atomic numbers $33 \leq Z \leq 43$ and $50 \leq Z \leq 61$, the yield distributions are incompatible with a single Gaussian. Here, in agreement with previous results in ^{40}Ar-, ^{56}Fe-, ^{86}Kr-, and ^{136}Xe-induced reactions with ^{238}U targets, an additional component (Kratz et al. 1976; Reus et al. 1977; Kratz, Norris, and Seaborg 1974; Otto et al. 1976) is observed in the isotope distributions. This component is characterized by much narrower widths and more neutron-rich centroids compatible with its assignment to sequential fission of only moderately excited fragments from quasi-elastic collisions giving rise to a double-humped fission-product mass distribution. A rather complete yield surface between atomic numbers 23 and 100 including isotopes with half-lives from 23 minutes to 7.4×10^3 years is shown in Figure 12.79. It was obtained (Schädel et al. 1978) in the bombardment of a thick ^{238}U target with ^{238}U projectiles of $\leq 7.50\,\mathrm{MeV\,u^{-1}}$. Note here that the cross sections presented in publication (Schädel et al. 1978) were "integral cross sections" for projectile-like and target-like products. Apart from the data contained in Figure 12.79a,b, the data presented in this work for the $^{238}U + ^{238}U$ reaction have been divided by 2 to make them compatible with all other reactions involving

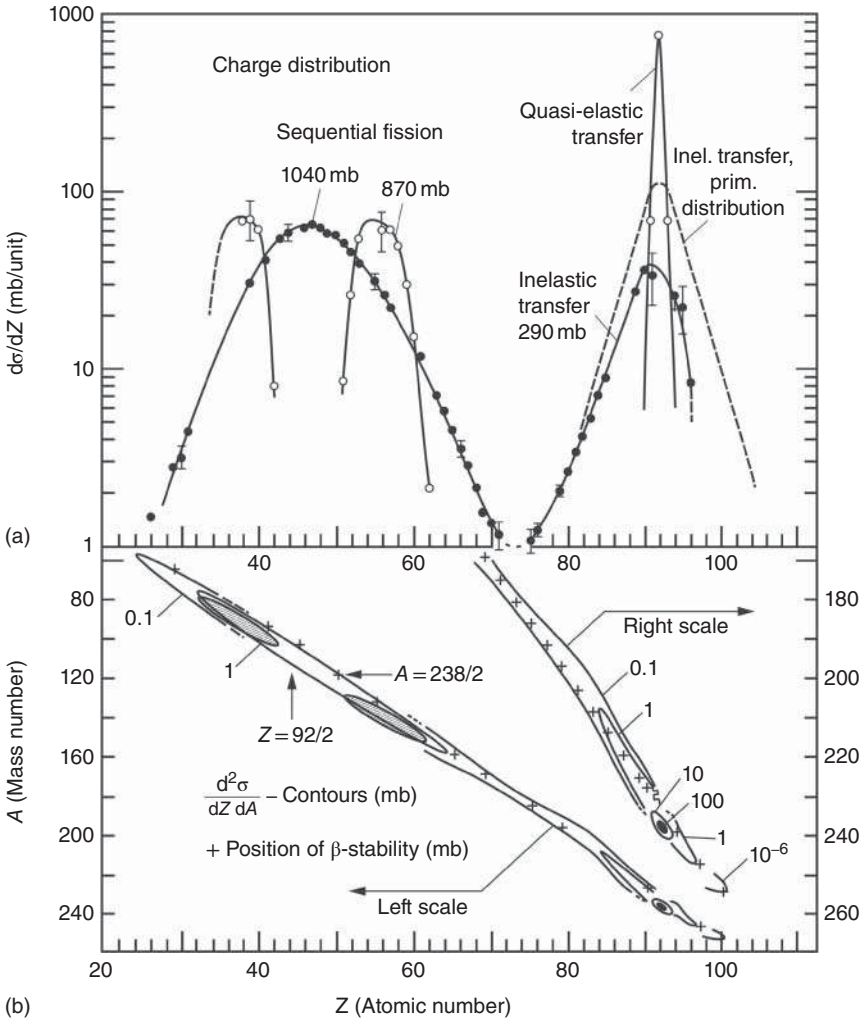

Figure 12.79 Element distribution for ≤7.50 MeV u^{-1} $^{238}U + ^{238}U$. (a) Yields for quasi-elastic transfer and sequential fission at low excitation energies (open symbols) and for damped collisions with the associated sequential fission process (closed symbols). The dashed line represents the reconstructed primary yield distribution for the damped collision process. (b) Independent yield isopleths in the *Z*–*A* plane. The location of the ß-stability line is indicated for comparison. Source: Schädel et al. (1978)/American Physical Society.

^{238}U. The systematics of yield dispersions in Figure 12.79 suggest to interpret the distribution to be attributable to four components: Quasi-elastic transfer residues, deep-inelastic transfer residues, sequential fission after quasi-elastic collisions, and sequential fission after deep-inelastic collisions.

From the experimental centroids $\overline{A}_Z$ for the survivors of the damped collisions below $Z = 92$ and from model predictions of the most probable primary mass numbers $\overline{A}'_Z$ based on the minimization of the potential energy for the dinuclear system

at the scission point, one can estimate the average number of neutrons evaporated from the primary fragments. The minimum potential energy (MPE) concept is justified by phase space considerations relating the most probable transfer to the highest level density in the intermediate complex. The highest level density is associated with the maximum available energy E^* (or the minimum potential energy) in the dinuclear system. ΔE^* can be calculated if the potential energy is normalized to the entrance channel potential energy. Then, the change in liquid–drop energies between entrance and exit channels is the conventional ground state Q value, Q_{gg}, and

$$\Delta E^* = Q_{\mathrm{gg}} + \Delta V_C + \Delta V_N + \Delta V_l - \delta_n - \delta_p \tag{12.131}$$

where V_C, V_N, V_l are the Coulomb, nuclear, and centrifugal potentials, respectively, and δ_n and δ_p are corrections of the available energy owing to breaking of neutron and proton pairs in the diffusion process, respectively (Volkov 1974). Omission of these corrections would correspond to the unrealistic assumption that nucleons are transferred from the ground state of the donor nucleus to the ground state of the acceptor nucleus which would lead to an overestimate of the available energy ΔE^* and consequently to an overestimate of the level density in the intermediate complex. In practice, for the predictions of primary mass distributions at fixed Z, δ_p can be omitted, whereby Eq. (12.131) is termed Volkov's generalized Q_{gg} systematics including non-pairing corrections δ_n. $\Delta E^*(Z)$ can then be used to estimate the average number of evaporated neutrons $\overline{\nu}_Z$, see Figure 12.80a. These data make it possible to estimate the average fragment excitation energies $\overline{E}_Z$ with the help of statistical evaporation calculations. In Figure 12.80, bottom, the resulting average total excitation energies $\overline{E}_{\mathrm{tot}}$ and the values of $\overline{\mathrm{T}}\,\overline{\mathrm{K}}\,\overline{\mathrm{E}}\,\overline{\mathrm{L}}$ are shown as a function of the atomic number by taking into account the values of Q_{gg}.

These data have been used to calculate (Schädel et al. 1978) isotope populations for the heaviest actinide elements observed in the $^{238}\mathrm{U} + ^{238}\mathrm{U}$ reaction at $\leq$7.50 MeV.

12.8.3.3 Bombarding-Energy Dependence of the Deep-Inelastic Collisions

In addition to the measurement of the element distribution at 7.50 MeV u^{-1} incident energy, such measurements are also available (Kratz et al. 1979) for elements with $68 \leq Z \leq 100$ at 6.49 and 8.30 MeV u^{-1} incident energies. The target thicknesses in these experiments define ranges of projectile energies $B \leq E \leq 6.49$ MeV u^{-1}, $B \leq E \leq 7.50$ MeV u^{-1}, and $7.65 \leq E \leq 8.30$ MeV covered inside the targets. The element yields of uranium-like fragments are shown in Figure 12.81 and are compared to diffusion-model predictions (Zagrebaev and Greiner 2008). The most striking feature of the data is the large reduction in the deep-inelastic product cross sections for the lowest energy bin. Large reductions in the mass and charge diffusion at near-barrier energies have also been reported elsewhere (Kratz et al. 1979; Essel et al. 1979; Rehm et al. 1981). Apparently, there is a threshold behavior for massive charge and mass transfers close to the barrier which is not predicted by the diffusion model (Zagrebaev and Greiner 2008).

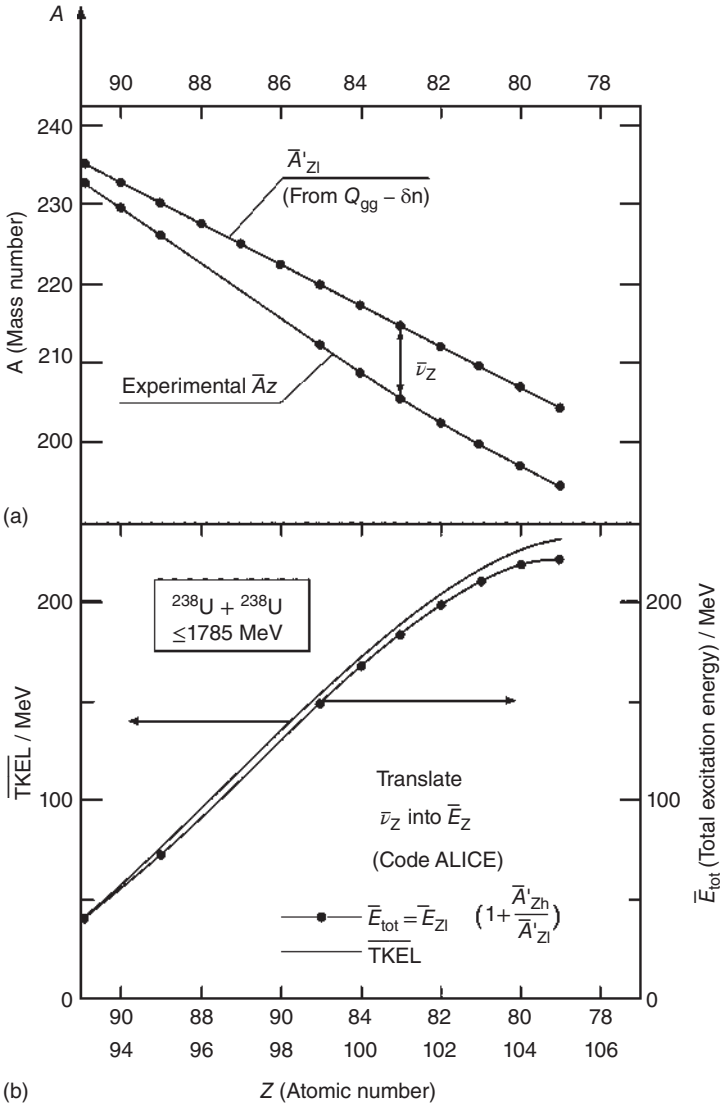

Figure 12.80 (a) Primary mass numbers $\overline{A}'_Z$ for the light uranium-like fragments for $Z \leq 91$ obtained by minimization of the potential energy for two touching liquid drops including corrections δ_n for the breaking of neutron pairs in the nucleon exchange process. Comparison with the experimental mean product mass number $\overline{A}_Z$ for ≤ 7.50 MeV u^{-1} $^{238}U + ^{238}U$ gives the average number of neutrons $\overline{\nu}_Z$ evaporated from the primary fragments. (b) Their mean excitation energy $\overline{E}_Z$ is determined with a statistical evaporation code. The mean total excitation energy $\overline{E}_{tot}$ as a function of Z is indicated, involving the assumption of a partition of the excitation energy between complementary fragments in proportion to their primary masses. The values of the total kinetic energy loss $\overline{TKEL}$ result from $\overline{E}_{tot}$ by adding Q_{gg}. Source: Kratz, Schädel, and Gäggeler (2013)/American Physical Society.

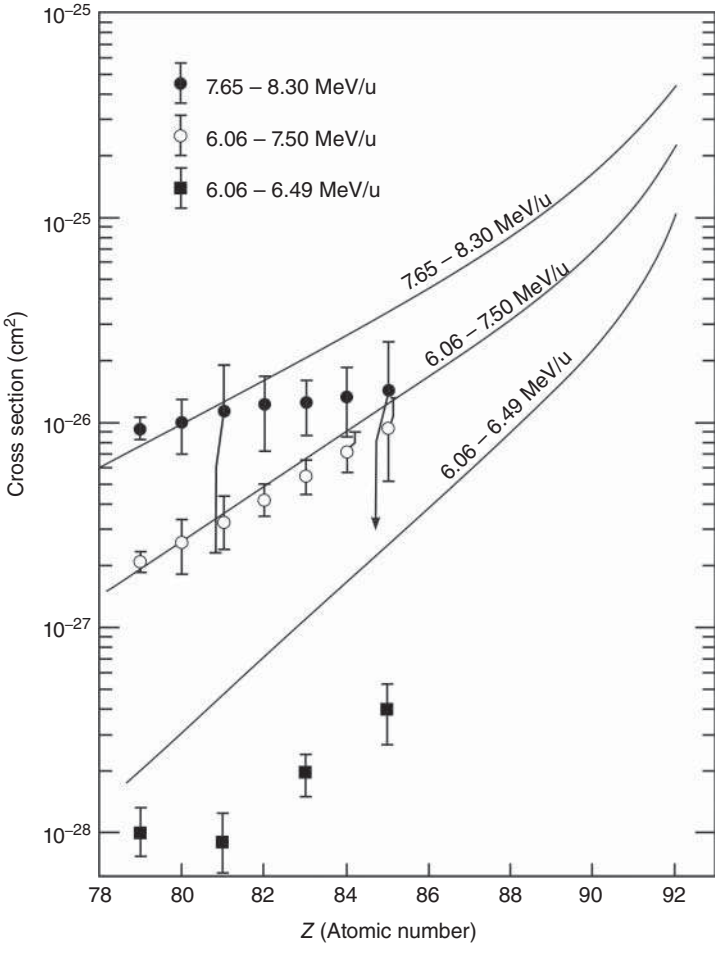

Figure 12.81 Element yields of uranium-like fragments in three different bins of laboratory energies (in MeV u^{-1}) defined by the incident projectile energy and the effective target thickness. For the higher energy bins and for the higher atomic numbers, the data are increasingly depleted by sequential fission. The solid lines are the results of diffusion-model predictions (Plasil 1974), see Section 2.5. Source: Kratz, Schädel, and Gäggeler (2013)/American Physical Society

The estimates for the relative contribution of deep-inelastic collisions to the total reaction cross sections are

$$\mathrm{DIR}_{\mathrm{prim}}/\sigma_r \approx 0.20 \text{ at } B \leq E \leq 6.49 \text{ MeV u}^{-1}$$
$$\mathrm{DIR}_{\mathrm{prim}}/\sigma_r \approx 0.38 \text{ at } B \leq E \leq 7.50 \text{ MeV u}^{-1}$$
$$\text{and } \mathrm{DIR}_{\mathrm{prim}}/\sigma_r \approx 0.55 \text{ at } 7.65 \leq E \leq 8.30 \text{ MeV u}^{-1}.$$

These estimates indicate that quasi-elastic collisions are the most dominant reaction mechanism near the barrier and that their relative importance decreases continuously as the beam energy is increased. In terms of absolute cross sections, this

means that the cross section for the damped collision process raises steeper with increasing incident energy than the total reaction cross section. Consequently, for reactions with very large mass transfer, e.g. for the reaction

$$^{238}\mathrm{U} + {}^{238}\mathrm{U} \rightarrow {}_{114}\mathrm{X} + {}_{70}\mathrm{Yb}$$

for which a cross section of 10^{-28} cm^2 can be extrapolated from the data at $\leq$7.50 MeV u^{-1} (see below, Figure 12.87), the cross sections are dramatically reduced at near-barrier energies. At $B \leq E \leq 6.49$ MeV u^{-1}, the primary yield for $Z_h = 114$, $Z_l = 70$ is of the order of 10^{-30} cm^2 only. The folding of this primary yield with estimated survival probabilities for the emission of three neutrons leads to estimates of the cross sections for evaporation residues of 10^{-39} to 10^{-40} cm^2 which are not accessible experimentally.

12.8.3.4 Isotope Distributions at Fixed Z Above $Z = 92$

As an example, isotopic distributions of the complementary elements Rn and Cf from the $^{238}\mathrm{U} + {}^{238}\mathrm{U}$ reaction at a bombarding energy of $\leq$8.65 MeV u^{-1} (Gäggeler et al. 1980) are shown in Figure 12.82. This figure is a very suitable and impressive introduction to this section. The arrow at $A = 224.1/251.9$ indicates the location of the most probable primary mass number calculated with the generalized Q_{gg} systematics including non-pairing corrections δ_n. The differences between the measured maxima $\overline{A}_Z$ and the most probable primary mass numbers $\overline{A}'_Z$ are a measure for the number of evaporated neutrons. For Rn, this number is ≈ 10, and for Cf, it is ≈ 3.5, indicating extremely different average excitation energies, large dissipated energies in the case of Rn, and much lower dissipated energies in the Cf nuclei. While the integral cross section for Rn is close to the primary yield, the yield of the Cf isotopes is depleted by sequential fission by many orders of magnitude. Thus, it is evident from Figure 12.82, that surviving evaporation residues of the heavy actinides are associated only with the low-energy tails of the excitation-energy distributions.

To investigate the dependence of the actinide production rates on incident energy, several thick-target bombardments were carried out (Kratz, Schädel, and Gäggeler 2013) with projectile energies varying from 6.49 to 8.65 MeV u^{-1}. In contrast to the mean cross sections for the light complements Ra through Bi (Figure 12.81), the actinide cross sections do not increase by orders of magnitude with increasing projectile energy. As an example, Figure 12.83 shows the thick-target cross sections for the ${}_{98}$Cf isotopes. The data are compatible with the same variance of the Gaussian distribution and the same centroid $\overline{A}_Z = 249.3$ at all incident energies. Similar observations hold for the other actinide elements. This indicates that the survivors of the heavy actinides are formed in identical dissipated-energy tails independent of the bombarding energy. From the differences between $\overline{A}'_Z$ and $\overline{A}_Z$, we know that the average number of neutrons evaporated from the primary actinide fragments is 3–4. Statistical evaporation calculations yield an average excitation energy carried away per emitted neutron of 9 MeV. Thus, average excitation energies of 35 MeV for the survivors of the actinide fragments were estimated (Schädel et al. 1978; Kratz, Schädel, and Gäggeler 2013) for all bins of projectile energies.

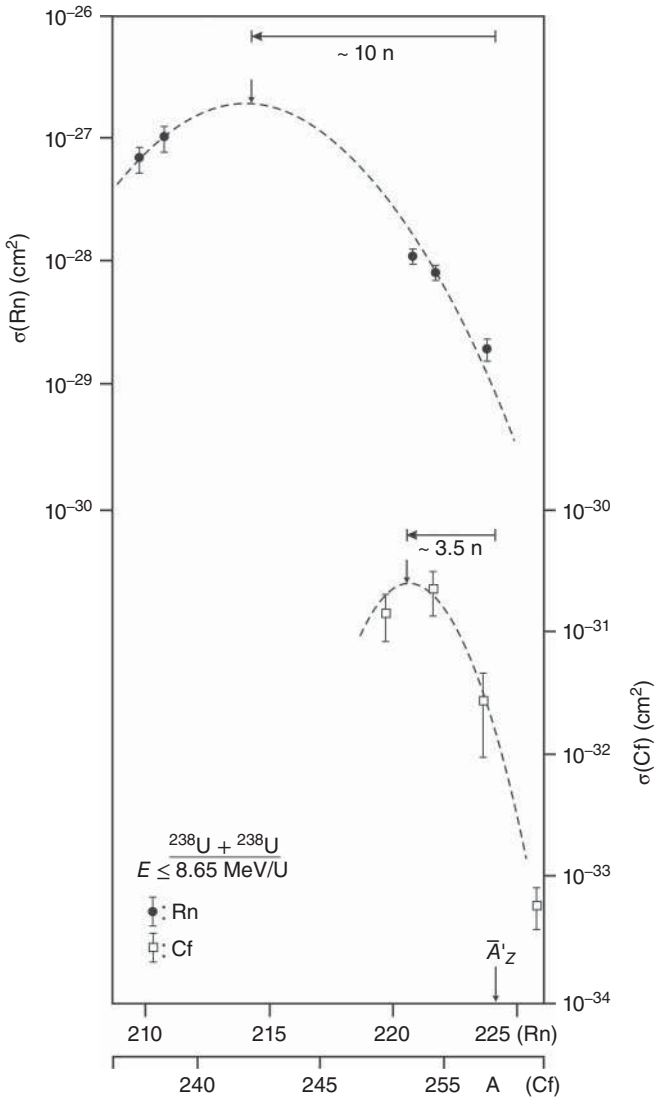

Figure 12.82 Isotope distributions of the complementary elements $_{86}$Rn and $_{98}$Cf in the $^{238}U + ^{238}U$ reaction at ≤8.65 MeV/u. $\overline{A}'_Z$ is the most probable primary mass number calculated within the generalized Q_{gg} systematics including corrections for the breaking of neutron pairs. Source: Kratz, Schädel, and Gäggeler (2013)/American Physical Society.

Due to the similarity of the isotope distributions independent of incident energy, it appeared to be sufficient to try to illuminate the mechanism for the formation of the surviving actinides at one incident energy, i.e. at ≤ 7.50 MeV u^{-1} where information on the average dissipated energies, Figure 12.80, is available.

To investigate the mechanism responsible for the formation of the surviving actinides, the measured product populations for the complementary elements

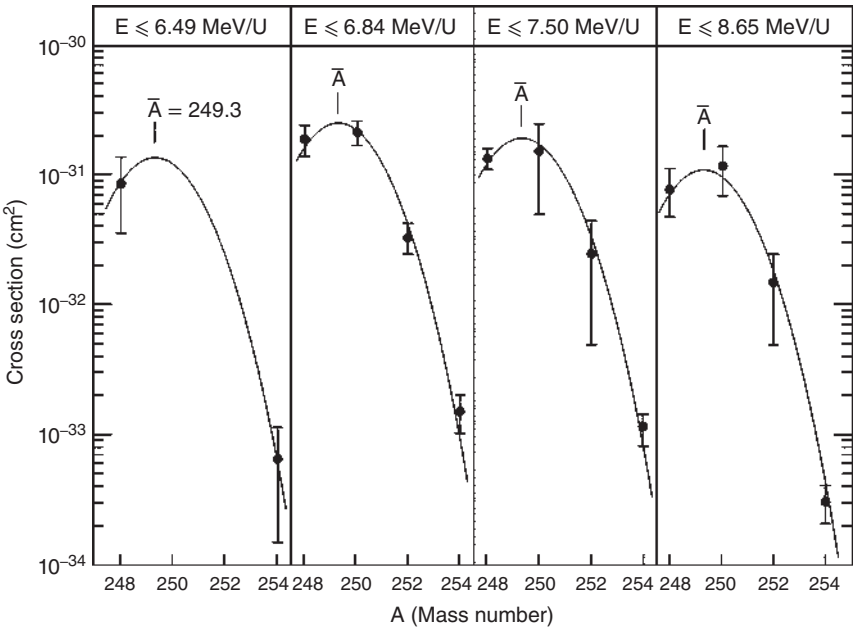

Figure 12.83 Thick-target cross sections for $_{98}$Cf isotopes at four different incident energies in the ^{238}U + ^{238}U reaction. The low-energy threshold is 6.06 MeV u^{-1} corresponding to the Coulomb barrier, calculated with the interaction radius of 16.89 fm (Hoffman et al. 1985; Gäggeler et al. 1986). The solid lines are Gaussians centered at $\overline{A}_Z = 249.3$ at all incident energies with a constant width of 3.3 u (FWHM). Source: Kratz, Schädel, and Gäggeler (2013)/American Physical Society.

$_{84}$Po–$_{100}$Fm, $_{85}$At–$_{99}$Es, and $_{86}$Rn–$_{98}$Cf were reconstructed with the following assumptions (Schädel et al. 1978; Kratz, Schädel, and Gäggeler 2013):

(i) The isotope distributions of the light complements $_{84}$Po, $_{85}$At, and $_{86}$Rn are not significantly influenced by fission.

(ii) The most probable mass number of primary fragments $\overline{A}'_Z$ can be deduced with the generalized Q_{gg} systematics including corrections δ_n for the pair breaking of the transferred neutrons. Comparison of $\overline{A}'_Z$ with A_Z gives the average number of neutrons ν_Z evaporated from the primary light fragments and their mean excitation energy. The mean total excitation energy $\overline{E}_{tot}$ for the light and heavy fragments is deduced by assuming a partition of the energy between the two fragments in proportion to their initial masses.

(iii) The measured variance $\sigma^2(A)$ of the isotope distributions for fixed Z results from the superposition of three dispersions:

$$\sigma^2(A) = \sigma^2(A') + \sigma^2(E^*) + \sigma^2(\nu) \tag{12.132}$$

Here, $\sigma^2(A')$ represents the variance of the primary fragment isotope distribution around $\overline{A}'_Z$, $\sigma^2(E^*)$ accounts for the broad range of total excitation energies (Poitou et al. 1979; Riedel and Nörenberg 1979) associated with the formation of a given primary fragment A'_Z which leads to a broad range of final products A_Z in the

neutron-evaporation process, and $\sigma^2(\nu)$ reflects the fluctuations in the number of evaporated neutrons from a given fragment A'_Z at fixed excitation energy.

The measured isotope distribution for polonium corresponds to $\sigma^2(A) = 6.9\,\mathrm{u}^2$. The variance $\sigma^2(\nu)$ is not larger than $0.5\,\mathrm{u}^2$ in the present experiments, as follows from evaporation calculations with the code ALICE. For $\sigma^2(E^*)$, a value of $\approx 4.5\,\mathrm{u}^2$ is estimated from the Q-value dispersions (Hildenbrand et al. 1977; Freiesleben et al. 1979) of about 100 MeV FWHM. We note here that the dispersion in the excitation energy is the dominant contribution in the U + U reaction. If we neglect the dependence of $\sigma^2(A')$ and $\sigma^2(\nu)$ on excitation energy, the variance of the primary fragment isotope distributions in the Po – Fm region is $\sigma^2(A') = 2.1\,\mathrm{u}^2$ (FWHM = 3.4 u).

We can now describe the population $Y(A;Z)$ of a given actinide isotope by starting from such a narrow primary fragment distribution around the centroid $\overline{A}'_Z$ as derived from values of $Q_{\mathrm{gg}} - \delta n$ by simulating the evaporation of $x = A' - A$ neutrons:

$$Y(A,Z) = P_x(E) \sum_{i=1}^{x} \left(\frac{\Gamma_n}{\Gamma_n + \Gamma_f} \right)^i Y(A',Z) \tag{12.133}$$

where $P_x(E)$ is the probability (extracted from ALICE code calculations) of emitting x and only x neutrons from primary fragment (A',Z). $\Gamma_n/(\Gamma_n + \Gamma_f)$ corrects for the fission competition in the evaporation chain using an empirical approach (Sikkeland, Ghiorso, and Nurmia 1968), based on fusion-evaporation data for light-mass projectile-induced reactions where the angular momenta of the fusion products are low. While the most abundant $_{86}$Rn, $_{85}$At, and $_{84}$Po isotopes are predominantly formed in collisions where energies close to the mean value are deposited in the system, the calculations show that the *surviving* transcurium isotopes originate exclusively from the low-energy tails of the excitation-energy distributions. In Figure 12.84, the measured $_{98}$Cf, $_{99}$Es, and $_{100}$Fm isotope cross sections are compared with the calculated populations using Eq. (12.133) and parameters derived from the experimental light-product isotope distributions as indicated in the figure. The values of $\overline{E}_{\mathrm{tot}}$ for Cf, Es, and Fm are read from Figure 12.80. The dotted curve in Figure 12.84 represents the Fm case where the total excitation energy is shared between the fragments in proportion to their primary masses. Since isotopes close to $\overline{A}'_Z$ are not observed experimentally and the centroid of the curve is too neutron rich, we conclude first that the energy distributions fall off steeper than with a Gaussian shape at the lowest excitation energies. We take care of this steeper decrease by approximating it by a sharp energy cut-off. An energy cut-off of 35 MeV yields the dashed curves in Figure 12.84 which reproduce the position and width of the experimental distributions, but still fail to reproduce the absolute cross sections by 1 order of magnitude. This discrepancy may be explained by (i) shell effects, (ii) lower Γ_n/Γ_f values as compared to the empirical systematics (Sikkeland, Ghiorso, and Nurmia 1968) due to angular momentum effects, or (iii) by non-statistical processes leading to non-equilibrium states in the exit channel. Assuming (i) may be correlated with the simultaneous formation of a nearly magic, spherical light fragment with $Z = 82$ or $N = 126$ which does not take up much excitation energy and leads, hence, to an increased depletion by fission of the heavy

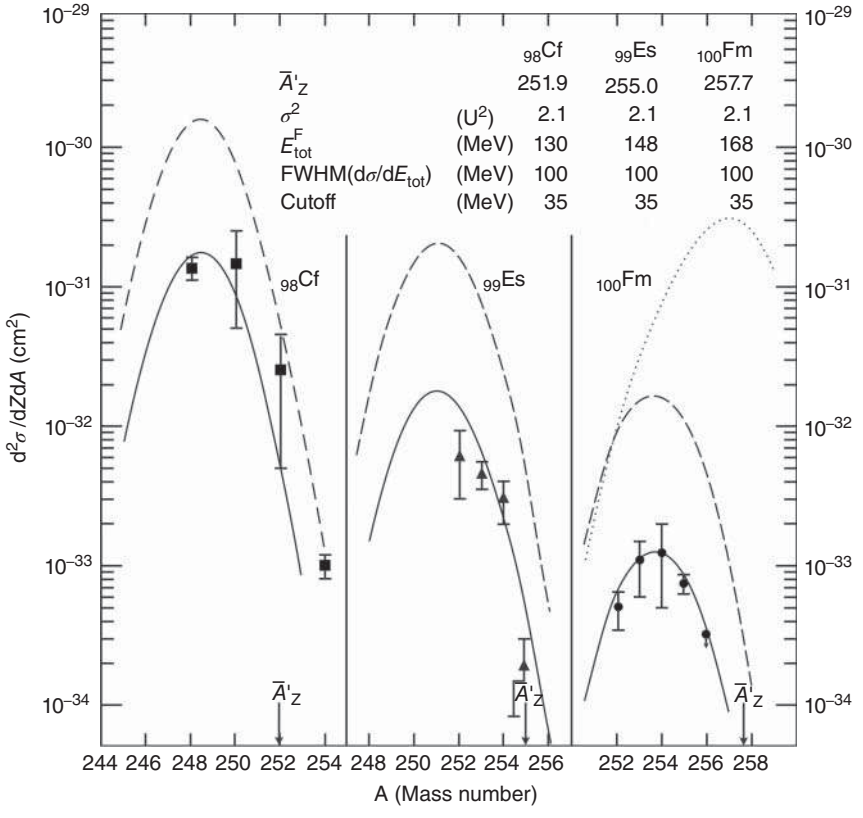

Figure 12.84 Comparison of measured (symbols) and calculated isotope distributions (curves) for the heaviest actinide elements observed in the $^{238}U + ^{238}U$ reaction at $\leq$7.50 MeV u^{-1}. The calculations are outlined in the text. Source: Schädel et al. (1978)/American Physical Society.

fragments. Agreement between experiment and our estimates is indeed obtained, see solid curves in Figure 12.84, if, starting with $Z_h = 98$, it is assumed that the total excitation energy in the low-energy collisions is concentrated in the heavy fragment. Independent of shell closures, a general tendency for the acceptors of mass and charge in damped collisions to carry the total excitation energy and for the donors to stay cold was observed by Klein et al. (1997) and Wirtz et al. (2001) in the $^{51}V + ^{197}Au$-damped collisions. This could be a general handicap for the attempt to produce heavy elements in $^{238}U + ^{238}U$ or ^{248}Cm collisions. Ad (ii): Based on the RLDM, Γ_n/Γ_f can be expressed (Schmidt et al. 1979) as

$$\left(\frac{\Gamma_n}{\Gamma_f}\right)_l = \left(\frac{\Gamma_n}{\Gamma_f}\right)_{l=0} \times \exp - \left(\frac{l^2}{l^2_{\lim}}\right) \tag{12.134}$$

were $l_{\lim}$ is a limiting angular momentum which is a function of the temperature of the nucleus and its moment of inertia in the ground state and at the saddle point. Assuming an evaporation cascade with $n = 4$ and theoretical fragment spins (Riedel and Nörenberg 1979), one obtains again a reduction of the cross sections by about 1

order of magnitude. Ad (iii): The theoretical approach is valid only if the fragments in the exit channel are fully equilibrated. However, it has been shown (Glässel et al. 1979) that for very heavy fragments in the $^{238}U + ^{238}U$ reaction, such an assumption might not be valid. Fragment deformations to shapes more elongated than the respective saddle point shapes might be associated with large charge transfers.

12.8.3.5 The $^{238}U + ^{248}Cm$ Reaction

The formation cross sections for transcurium isotopes in the $^{238}U + ^{248}Cm$ reaction at $\leq 7.40\,MeV\,u^{-1}$ (Schädel et al. 1982) are shown in Figure 12.85. They are compared with thick-target cross sections for the $^{238}U + ^{238}U$ reaction at $7.50\,MeV\,u^{-1}$ incident energy. The approximate independence of the cross sections of the survivors of the primary heavy actinide isotopes from the projectile energies discussed above for the $^{238}U + ^{238}U$ reaction tells us that the cross sections for $_{98}Cf$, $_{99}Es$, and $_{100}Fm$ are three to 4 orders of magnitude higher than in the $^{238}U + ^{238}U$ reaction due to the

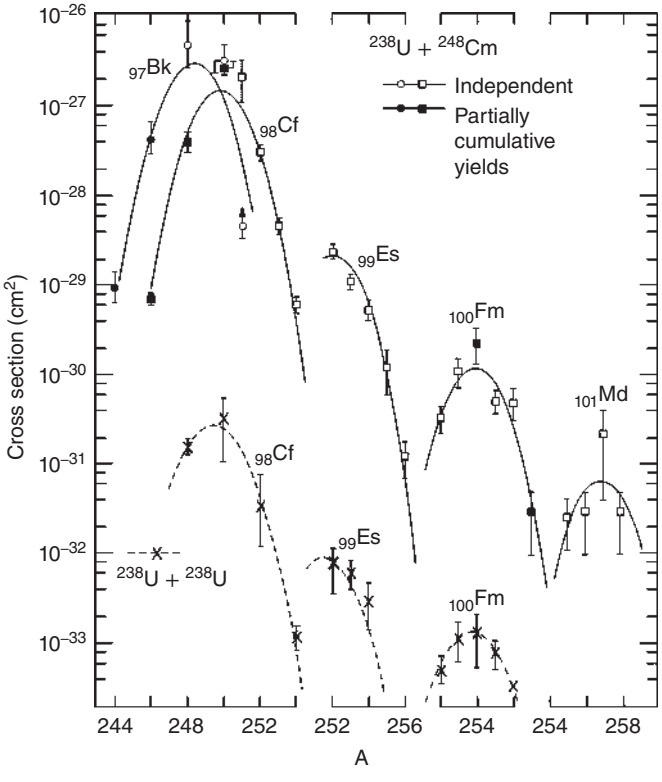

Figure 12.85 Cross sections for the formation of target-like transcurium isotopes in the $^{238}U + ^{248}Cm$ reaction at $\leq 7.40\,MeV\,u^{-1}$. For comparison, the data for the $^{238}U + ^{238}U$ reaction at $\leq 7.50\,MeV\,u^{-1}$ are also shown. The curves are drawn to guide the eye. The lower limit for the yield of ^{251}Bk is based on γ-ray intensities of $\leq 70\%$ at 177 keV and $\leq 30\%$ at 153 keV. Source: Schädel et al. (1982)/American Physical Society.

reduced number of protons to be transferred from the target. For ^{259}No, the measured upper cross-sectional limit is 30 nb (Schädel et al. 1982; Kratz, Schädel, and Gäggeler 2013).

The measured cross sections for the much less fissile projectile-like fragments $_{84}$Po and $_{85}$At are about the same in the ^{238}U + ^{248}Cm reaction and in the ^{238}U + ^{238}U reaction indicating that the integral, primary actinide yield distribution is nearly the same in both reactions. This suggests that also the primary actinide yields before fission are about the same for a given (ΔZ, ΔN) transfer in both systems.

The experimental observation of largely different cross sections for the surviving evaporation residues of target-like fragments from the same (ΔZ, ΔN) channels could either indicate differences in the reaction mechanism (which is unlikely), or simply reflect the different survival probabilities of the different product nuclei. In order to test the latter hypothesis, we assume that for the same (ΔZ, ΔN) channels, excitation energies and angular momenta are the same. Then, it is reasonable to approximate the *ratios* of cross sections $\sigma(\mathrm{U}+\mathrm{U})/\sigma(\mathrm{U}+\mathrm{Cm})$ for a given channel by the ratio of relative neutron decay widths

$$\prod_{i=1}^{x}\langle\Gamma_n/\Gamma_{\mathrm{tot}}\rangle_{i(\mathrm{U+U})}/\prod_{i=1}^{x}\langle\Gamma_n/\Gamma_{\mathrm{tot}}\rangle_{i(\mathrm{U+Cm})}, \tag{12.135}$$

using angular-momentum independent, effective values of Γ_n/Γ_f averaged over x deexcitation steps, such as the empirical values of Sikkeland, Ghiorso, and Nurmia (1968). Inherent in this approach is the assumption that modifications of the fission probabilities by excitation energy and angular momentum cancel to a good approximation. Starting from the measured yields for $_{95}$Am ($\Delta Z = 3$) through $_{97}$Bk ($\Delta Z = 5$) in the ^{238}U + ^{238}U reaction (Schädel et al. 1978), cross sections for $_{99}$Es ($\Delta Z = 3$) through $_{101}$Md ($\Delta Z = 5$) in the ^{238}U + ^{248}Cm reaction (Schädel et al. 1982) were calculated for given values of x. The results, Figure 12.86, show that an average of $x = 3$–4 evaporated neutrons is consistent with the data for the heavier actinides implying average excitation energies of about 30–40 MeV in the surviving heavy fragments. This is also consistent with the difference between the observed mass numbers $\overline{A}_Z$ and the primary mass numbers calculated by minimization of the potential energy (Schädel et al. 1982; Kratz, Schädel, and Gäggeler 2013; Kratz et al. 1979) for two touching nuclei, where $\overline{A}'_Z - \overline{A} = x$. The values of $x = 3$–4 are also consistent with our conclusions arrived at in the discussion of Figure 12.84 (i.e. the energy cut-off of 35 MeV), where, however, additional assumptions were required to arrive at the absolute cross sections. The virtue of the present analysis is that it is free from such additional assumptions.

It is interesting, at this point, to look forward at Section 12.8.4, where a barrier for neck formation in the system ^{238}U + ^{197}Au was determined as 676 MeV (cm) to be compared to an interaction barrier of 644 MeV saying that neck formation in this system requires a dissipated energy of more than 30 MeV. Thus, it is tempting to interpret the energy cut-off of roughly 35 MeV with the requirement for neck formation for multi-nucleon transfer in the heaviest systems.

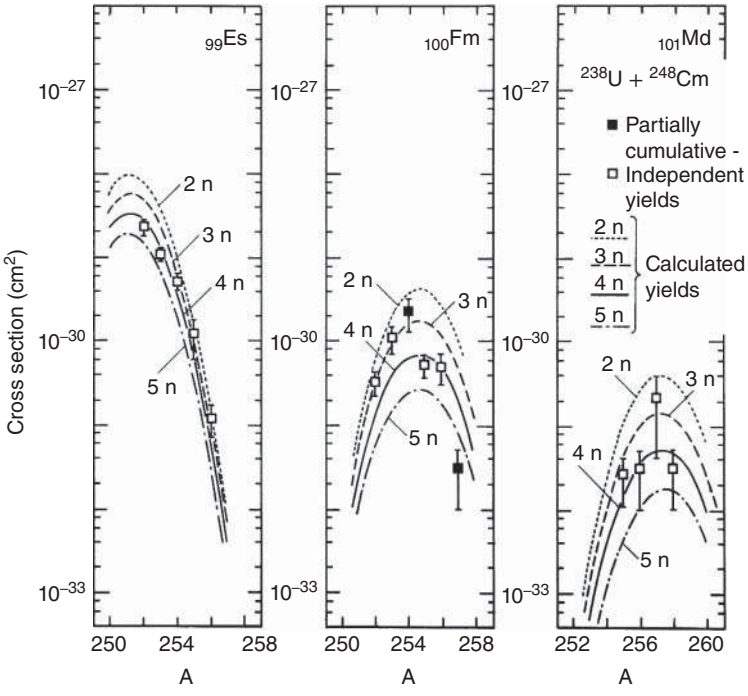

Figure 12.86 Comparison of the measured (symbols) and calculated (curves) for the isotope distributions in the $^{238}U + ^{248}Cm$ reaction. The calculations for the 2n – 5n reactions are outlined in the text. Source: Schädel et al. (1982)/American Physical Society.

12.8.3.6 Comparison of the Element Yields with Diffusion-Model Predictions

In the theoretical work by Riedel and Nörenberg (1979), the phenomenological model (Wolschin and Nörenberg 1978; Ayik, Wolschin, and Nörenberg 1978; Riedel, Wolschin, and Nörenberg 1979; Schmidt and Wolschin 1980) for the analysis of dissipative heavy-ion collisions has been extended to also treat cases where thick targets are used. In the interval between the maximum incident energy E_{m} and the Coulomb barrier V_{C}, the loss of energy of the ^{238}U beam in the thick target is proportional to the distance from the target surface. Therefore, the energy-averaged element distribution is given by

$$\frac{\mathrm{d}\overline{\sigma}}{\mathrm{d}Z} = \frac{1}{E_m - V_C}\int_{V_C}^{E_m} \mathrm{d}E \frac{\mathrm{d}\sigma(E)}{\mathrm{d}Z}. \tag{12.136}$$

In the phenomenological model, the element distribution for a given sharp incident energy E is determined by

$$\frac{\mathrm{d}\sigma(E)}{\mathrm{d}Z} = \frac{2\pi}{k^2}\int_0^{l_{\mathrm{gr}}(E)} \mathrm{d}l \cdot l \cdot P(Z, \tau(l)) \tag{12.137}$$

with the solution

$$P(Z, \tau(l)) = [4\pi D_Z \tau(l)]^{-1/2} \cdot \exp\{-(Z - Z_p)^2 / 4D_Z \tau(l)\} \tag{12.138}$$

of a Fokker–Planck equation for a constant diffusion coefficient D_Z and zero drift velocity. $\tau(l)$ is the interaction time as a function of incident angular momentum l. The analysis of various heavy-ion collisions has taught that for a given projectile-target combination, the interaction time is a function of the impact variable $x = l/l_{gr}$ for different incident energies. Therefore, the approximation

$$\tau(E, l) \equiv \tau(l/l_{gr}) = \tau(x) \tag{12.139}$$

is used for interaction times corresponding to different incident energies in a thick target. Using an average diffusion coefficient D_Z for the energy interval $[V_C, E_m]$, one obtains according to Eq. (18) for the element distribution in a thick-target experiment

$$\frac{d\overline{\sigma}}{sZ} = \frac{1}{E_m - V_C}\int_{V_C}^{E_m} \sigma_R(E)dE \cdot \int_0^1 p(x)P(Z, \tau(x))dx = \overline{\sigma}_R p_1(Z). \tag{12.140}$$

Here, the notion $\sigma_R(E) = \pi l_{gr}^2(E)/k^2$ for the reaction cross section as a function of E and $p(x) = 2x$ for the probability distribution of the impact variable x $(0 \le x \le 1)$ have been introduced. Because of the energy averaging in a thick target experiment, the probability distributions of various quantities are considerably different from those for a thin target with a sharp incident energy. These have been worked out in detail (Riedel and Nörenberg 1979).

In Figure 12.87, the calculated element distribution (Eq. (12.143)) with an average diffusion coefficient $D_Z = 0.9 \cdot 10^{22}$ s^{-1} is compared with the experimental data (Schädel et al. 1978) at ≤ 7.50 MeV u^{-1} incident energy. The theoretical results for

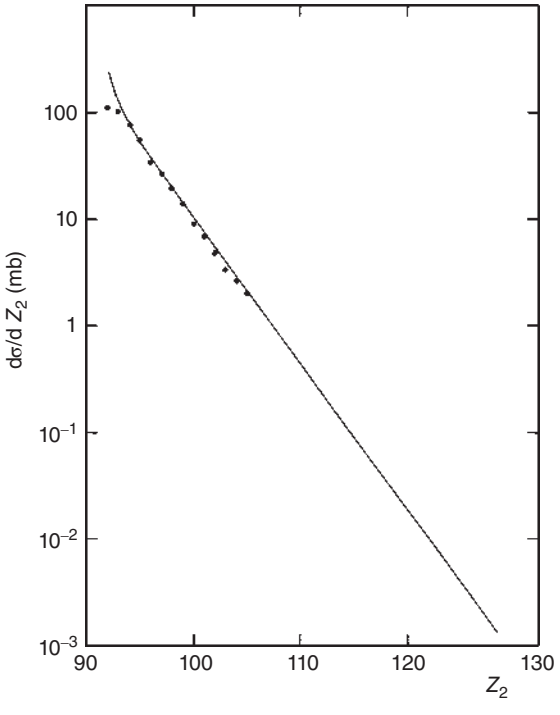

Figure 12.87 Element distribution for $^{238}U + ^{238}U$ at ≤ 7.50 MeV u^{-1} in a fit of the diffusion coefficient to the experimental data. Source: Riedel and Nörenberg (1979)/Springer Nature.

$p_1(Z)$ have been normalized to the experimental reaction cross section of ≈1 barn. Deviations from the experimental points close to the target charge $Z = 92$ are due to the upper limit unity in the second integral in Eq. (12.143). This was not adjusted to improve the agreement in this region of Z. The excellent reproduction of the experimental element yields more distant from the symmetric charge gave some confidence for the extrapolation of the theoretical calculations into the region of heavier fragments. Probabilities of, e.g. $p(E^*, Z)$ were calculated up into the region of $Z = 120$ which are 3 orders of magnitude smaller as compared to $Z = 100$. Compared to the energy thresholds of about 35 MeV associated with the production of heavy actinides (Schädel et al. 1978), the theoretical thresholds are systematically too low, e.g. a threshold of 35 MeV is associated with the production of $Z = 116$ and not with $Z = 98–100$ which is required by the experimental data. Therefore, there has been no attempt (Schädel et al. 1978) to reproduce the experimental $_{98}$Cf, $_{99}$Es, and $_{100}$Fm data on the basis of the theoretical probabilities $p(E^*,Z)$. Rather, the integral element yields below $Z = 92$ were compared (Schädel et al. 1978) with the theoretical predictions which, in this region, should be less dependent on low-energy thresholds. Figure 12.81 indicates that there is agreement of the theoretical predictions with the experimental cross sections at 7.65–8.30 MeV u^{-1} and at 6.06–7.50 MeV u^{-1}. At 6.06–6.49 MeV u^{-1}, i.e. in the energy bin closest to the Coulomb barrier, there is a marked disagreement between the experimental element yields and the diffusion-model prediction with the former being a factor of about five lower than theory. This is associated with the choice of a constant impact variable $x = l/l_{gr} = 0.7$ at all incident energies which results in a constant ratio of cross sections $DIR_{prim}/\sigma_r = 0.51$ independent of bombarding energy. Experimentally, this is clearly not the case as is shown in Section 12.8.3.3 that the ratios DIR_{prim}/σ_r for $^{238}U + ^{238}U$ collisions are 0.20 in the energy bin 6.06–6.49 MeV u^{-1}, 0.38 at ≤7.50 MeV u^{-1}, and 0.55 in the energy bin 7.65–8.30 MeV u^{-1}, i.e. depend markedly on the incident energy. As we have stated already in Section 12.8.3.3, large reductions of mass and charge diffusion at near-barrier energies were also reported elsewhere (Kratz et al. 1979; Essel et al. 1979; Rehm et al. 1981).

In the much more recent theoretical work by Zagrebaev and Greiner (Zagrebaev et al. 2006; Zagrebaev and Greiner 2007a,b; Zagrebaev and Greiner 2008), mass transfer is treated in a Langevin-type equation for the mass asymmetry η

$$\frac{d\eta}{dt} = \frac{2}{A_{CN}} D_A^{(1)}(\eta) + \frac{2}{A_{CN}} \sqrt{D_A^{(2)}(\eta)\Gamma(t)} \tag{12.141}$$

which has been derived from the corresponding master equation for the distribution function. The contribution of Zagrebaev and Greiner is to emphasize the role of shell effects in these transfer reactions. For example, in the reaction of ^{238}U with ^{248}Cm, at a modest energy above the barrier (1.1 V_B), the calculations show a net particle transfer from ^{238}U to ^{248}Cm, forming ^{208}Pb from ^{238}U and adding 30 nucleons to ^{248}Cm. This calculation, when applied to the reaction of $E_{cm} = 800$ MeV $^{238}U + ^{248}Cm$, reproduced the previous measurements of Schädel et al. (1982) and predicted the formation at pb levels of new n-rich isotopes of Sg (Figure 12.88). Neutron and proton transfers are treated separately, and sequential transfer is allowed. A time-dependent

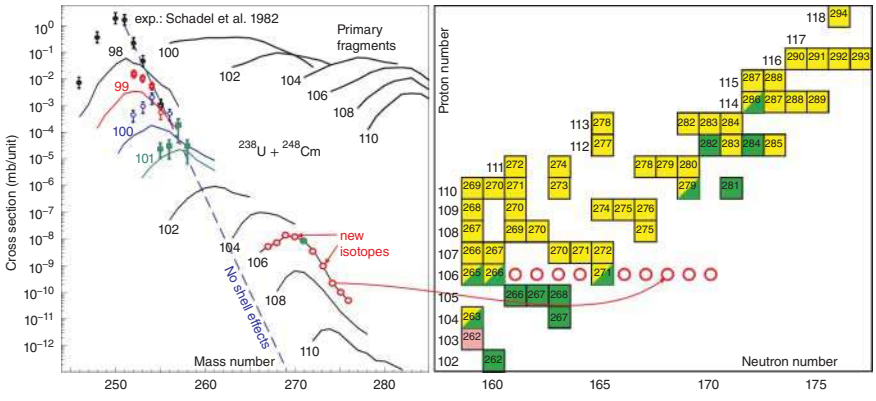

Figure 12.88 Predicted yields of superheavy nuclei in collisions of 800 MeV (cm) $^{238}U + ^{248}Cm$. Source: Zagrebaev and Greiner (2008)/American Physical Society.

potential energy, which transforms, after contact, from a diabatic to an adiabatic potential, is used to describe the motion of the colliding nuclei. The potential energy depends on the distance between the ions, their deformations and the neutron and proton asymmetries of each ion. The cross sections are calculated for the primary fragments and their de-excitation by particle emission and fission is then calculated. Details are given in (Kratz, Loveland, and Moody 2015).

Both the diffusion models by Riedel and Nörenberg (1979) and by Zagrebaev and Greiner (Zagrebaev et al. 2006; Zagrebaev and Greiner 2007a,b; Zagrebaev and Greiner 2008) give little hope to reach superheavy elements close to $Z = 114$ with measurable cross sections in reactions such as $^{238}U + ^{248}Cm$. However, Figure 12.88 suggests that a search for hitherto undiscovered neutron-rich isotopes in the region of elements 105 through 108 with cross sections >1 pb (Zagrebaev and Greiner 2008; Kratz, Loveland, and Moody 2015) might be attractive. For longer-lived isotopes of elements 104 through 108, this might even be possible with chemical separations as the chemical properties of these elements are well known (Kratz 2011). For short-lived isotopes, magnetic separators such as large-aperture solenoids are under discussion and might eventually open the way to many interesting new isotopes. In (Kratz, Loveland, and Moody 2015), these and other perspectives are discussed in detail.

12.8.4 "Simple" (Quasi-elastic) Reactions at the Barrier

Quasi-elastic reactions are treated in time-dependent semi-classical theory for one-step processes giving probability amplitudes introduced by Broglia, Pollarolo, and Winther (1981) of the type

$$c_{\mathrm{fi}} = \frac{1}{i\hbar}\int_{-\infty}^{\infty} \mathrm{d}t \langle f|V_t|i\rangle \exp\frac{i\varphi_{\mathrm{fi}}t}{\hbar} \tag{12.142}$$

with f final, i initial state, V_t being the interaction causing the transfer and the phase φ_{fi} being given by

$$\varphi_{fi}t = (E_f - E_i)t + \int_0^t [L_f(t') - L_i(t')]\mathrm{d}t' \tag{12.143}$$

Here, $E_f - E_i$ is the Q-value and

$$L_{f,i} = T_{f,i} - V_{f,i}(r_{fi}) \tag{12.144}$$

are the Lagrange functions for the nucleus–nucleus system (T kinetic, V potential energy) along the classical trajectory. "Orbit matching" occurs when the phase $\varphi_{fi}t$ is stationary in the region where the matrix $\langle f|V_t|i\rangle$ is maximal which is usually the case around the distance r_{cl} of closest approach. Disregarding for simplicity, the recoil terms and changes in orbital momenta coming from the kinetic energies in the Lagrangians lead to the well-known matching condition

$$Q_{\mathrm{eff}} = Q + V_i(r_{cl}) - V_f(r_{cl}) = 0. \tag{12.145}$$

For neutrons, $V_i - V_f$ is ignored and for protons, only the Coulomb part of $V_i - V_f$ is usually considered.

Compilations by van den Berg et al. (1987) and Rehm et al. (1990) of angle and energy-integrated one-neutron transfer cross sections in heavy-ion reactions, some 20–30% above the barrier fit well into a smooth systematics if the influence of the available Q value window and of the neutron binding energy is removed. It was proposed by van den Berg et al. (1987) that the latter could be done by switching to reduced cross sections $\sigma_t x(B_i B_f)^{1.1}$, where $B_{i,f}$ are the neutron separation energies. This is shown in Figure 12.89. The smooth curve (Rehm et al. 1990) is an error

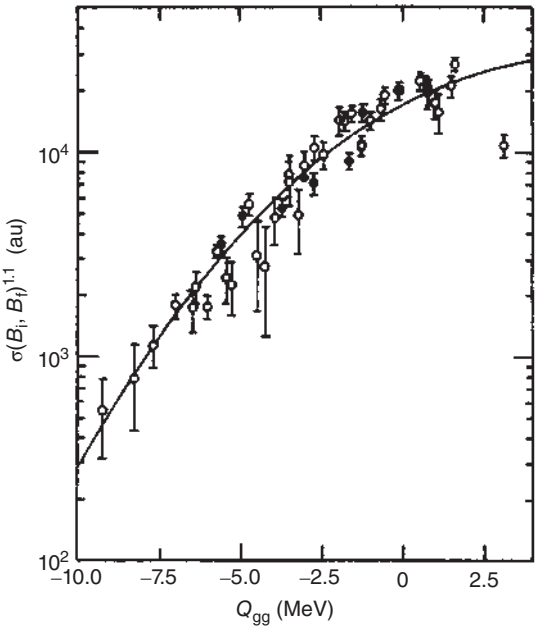

Figure 12.89 Reduced cross sections for one-neutron transfer as a function of the ground-state Q value at incident energies 20–30% above the Coulomb barrier. The full curve is a fit to the data by Wolfs et al. (Kratz, Loveland, and Moody 2015). Source: Kratz, Loveland, and Moody (2015)/Elsevier.

function derived from a Gaussian with a standard width $\sigma = 4.1$ MeV. According to Broglia, Pollarolo, and Winther (1981), this width is inversely proportional to the collision time in first-order perturbation theory. One has approximately

$$\sigma^2 = 20 \left(\frac{E}{A} \right) / r_{\mathrm{cl}} \,\mathrm{MeV}^2 \tag{12.146}$$

yielding the value $\sigma \approx 3.5$ MeV for the systematics in Figure 12.89, somewhat smaller than the value fitted to the data, where E/A is the energy per nucleon in MeV u^{-1}, and r_{cl} is the distance of closest approach in fm.

The smooth systematics suggested that aside from the Q value and separation-energy dependence, nuclear structure is essentially averaged out when integrated cross sections are considered. On the other hand, Reisdorf (1994) has compiled one-neutron transfer data from the literature, limiting those to a narrow energy band ($0.97 \leq E/B \leq 1.06$) around the Bass potential barrier. The result is shown in Figure 12.90. The very large scatter of the cross sections which is not correlated with E/B is in striking contrast to the smooth systematics at higher energies. As for fusion reactions, one is witnessing here also for the "simple" one-neutron transfer reactions an increased complexity in measured cross sections at or below the barrier as compared to the behavior at energies well above the barrier. Reisdorf (1994) suggested that channel coupling to complex reactions causes this phenomenon at barrier energies when saturation, i.e. limitation by absorption, has not yet been reached.

Whether an experimental cross section σ_{exp} has to be judged as large or small, can be decided by comparing values of

$$\sigma' = \sigma_{\mathrm{exp}} (B_i B_f)^{1.1} / f(Q_{\mathrm{gg}}) \tag{12.147}$$

where

$$f(Q_{\mathrm{gg}}) = 1 + \mathrm{erf} \left(\frac{Q_{\mathrm{gg}} - Q_{\mathrm{opt}}}{\sqrt{2}\sigma} \right). \tag{12.148}$$

At the Coulomb barrier, $\sigma = 3.5$ MeV is chosen.

For example, in the $^{86}\mathrm{Kr} + {}^{130}\mathrm{Te}$ reaction (Figure 12.92), one finds in arbitrary units for the neutron pickup $\sigma'_{+1n} = 12\,700$, to be compared with $\sigma'_{-1n} = 4500$ for the neutron stripping reaction. Likewise, for the proton transfers, one finds

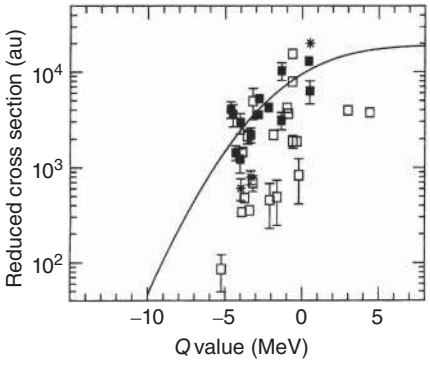

Figure 12.90 Systematics of one-neutron transfer cross sections close to the Coulomb barrier energy. Full squares: systems with $Z_p Z_t \geq 1800$, open squares: systems with $Z_p Z_t < 1200$, asterisks: intermediate systems. The smooth curve with arbitrary normalization corresponds to a Q window 15% narrower than in Figure 12.1. Source: Reisdorf et al. (1992/Springer Nature).

$\sigma'_{+1n} = 1600$ and $\sigma'_{-1n} = 13\,700$. In both cases, the effective Q values, neglecting the nuclear polarization part, differ by 1 MeV or less, but the values of σ' are markedly different. A look at Figure 12.92 suggests how this could be associated with nuclear polarization. In this figure, the smooth curves represent the "complex" reactions. The one-nucleon transfer channels ($\pm$1n, $\pm$1p) are large when the corresponding isotope is close to the maximum of the complex-reaction channels and small when the contrary is the case. This strongly suggests that the coupling to the macroscopic trend (coupling to a multitude of channels) followed by the complex reactions creates a polarization field that favors matching even for relatively negative Q values. It should be noted that the two-neutron transfer is also affected by this: σ_{+2n} is larger than $\sigma_{-1n.}$

Reisdorf (1994) suggested that in the matching Eq. (12.145), one cannot neglect changes in the nuclear parts of the potential which are just due to polarization. Due to the narrow Q window in slow collisions, a polarization potential of 3 MeV near the barrier boosts the cross section for a $Q = -4$ MeV transition by as much as a factor of 3. Such a shift has to be seen on the scale of the maximum possible "macroscopic polarization" at fixed mass asymmetry. This is nothing else than the difference between the potential barrier and the conditional saddle point on the PES. For symmetric systems with $Z_p Z_t$ between 1000 and 2000, this is on the order of 20 MeV. Nuclear polarization will also lower the surface-to-surface distance, favoring transfer of nucleons even further.

For large internuclear distances, a simple exponential Ansatz for the transfer form factor $F_{fi}(r)$ and the absorptive potential W, neglecting the effect of nuclear attraction on the classical trajectories, and expanding the time-dependent radial separation $r(t)$ around the distance of closest approach, allows one to write the transfer cross section in the semiclassical approximation as a product of four terms

$$\sigma_{fi}(\Theta) = P_t P_{abs} P_Q \sigma_{ruth}(\Theta) \tag{12.149}$$

where σ_{ruth} is the Rutherford cross section. Following Landowne and Pollarolo (1990), the absorption probability can be written as

$$P_{abs} = \exp\left[2\left(\frac{2\pi a_w}{\hbar^2 \ddot{r}_{cl}}\right)^{1/2}\right] W(r_{cl}) \tag{12.150}$$

where a_w is the diffuseness of $W(r)$ and $\ddot{r}_{cl}$ is the acceleration at the point of closest approach. For the Q_{fi}-value dependence, we have

$$P_Q = \exp\left(-\frac{a_f Q_{fi}^2}{\hbar^2 \ddot{r}_{cl}}\right), \tag{12.151}$$

and the transfer probability is

$$P_t = \frac{2\pi a_f}{\hbar^2 \ddot{r}_{cl}} F_{fi}(r_{cl})^2 \tag{12.152}$$

where a_f is the diffuseness of F_{fi}. To a good approximation, one has for Coulomb trajectories

$$P'_t = P_t / \sin(\Theta/2) \approx \exp(-2r_{cl}/a_f) \text{ with } a_f = \hbar(2\mu)^{-1/2}(B_i B_f)^{-1/4} \tag{12.153}$$

where μ is the reduced nucleon mass. Failure of experimental data to follow the exponential slope given by Eq. (12.156) has been termed "slope anomaly." Slope anomalies can be expected whenever quantum mechanical effects play a role. For relatively light systems, this could be dispersive or refractive effects (Wuosmaa et al. 1991). Another source of anomalies is interference effects between amplitudes from different orientations of deformed nuclei (Guidry et al. 1981). Such effects have also been predicted by coupled-channels calculations (Landowne, Price, and Esbensen 1988).

We shall focus here on a one-neutron transfer case, linking one of the possible origins of the slope anomaly to a coupled-channels effect. Landowne, Price, and Esbensen (1988) have claimed with the use of the above formulae that a good understanding of the measured (Wirth et al. 1991; Wirth et al. 1986) one-neutron transfer cross sections in the systems $^{238}\mathrm{U} + {}^{238}\mathrm{U}$, $^{197}\mathrm{Au}$ could be achieved. Reisdorf (1994) has used the same formalism avoiding to neglect the contribution of the orbital angular momentum for $\ddot{r}_{\mathrm{cl}}$ and refraining from varying the strength of the form factor with energy. The results for P_t' are shown in Figure 12.91 (left panel) using as abscissa the reduced distance of closest approach $d_0 = r_{\mathrm{cl}}/(A_p^{1/3} + A_t^{1/3})$. For the reaction $^{238}\mathrm{U} + {}^{197}\mathrm{Au}$, there is precise equivalence of angular distributions at fixed energy with the excitation function at fixed angle. The data for the transfer product $^{198g}\mathrm{Au}$ covered large angular ranges and 13 energies between 88% and 109% of the interaction barrier B_I. An excellent reproduction of the data is obtained without varying the strength of the form factor, using $a_f = 1.70\,\mathrm{fm}$ (from Eq. (12.156), one gets 1.822) and $a_w = 0.9$ which is larger than the standard value used by Landowne and Pollarolo. Due to optical model ambiguities, Reisdorf (1994) did not draw any

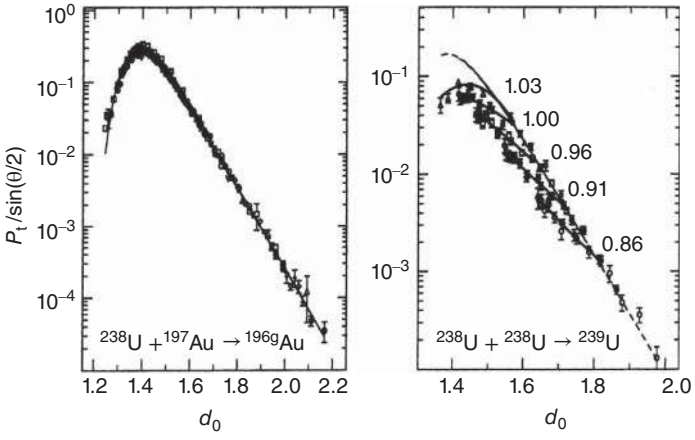

Figure 12.91 Reduced transfer probabilities P_t' vs. the reduced distance of closest approach. The data are from Wirth et al. (1991) and Funke (1990). Left panel: reaction $^{238}\mathrm{U}(^{197}\mathrm{Au},{}^{198g}\mathrm{Au})$ at 13 different energies (see text). The smooth curve is a theoretical fit. Right panel: reaction $^{238}\mathrm{U}(^{238}\mathrm{U},{}^{239}\mathrm{U})$. The smooth broken dashed curve is a theoretical fit to the data. The full curves branching out are to guide the eye for five different energies. The branching out occurs at different distances depending on the indicated energy (given in units of the barrier energy). Source: Reisdorf (1994)/IOP Publishing.

conclusion from the absorptive parameters. In agreement with other studies (Funke 1990), it was concluded that absorption sets in at $d_0 = 1.55$ fm.

In contrast, for the reaction $^{238}U + ^{238}U$ leading to the transfer product ^{239}U, the data for different energies do not superimpose, see Figure 12.91 (right panel), thus one learns that absorption sets in at distances that vary with the incident energy. This striking effect cannot be reproduced by the above formalism, unless one introduces new parameters for each energy. One cannot invoke deformation in a simple way to explain the difference between the two systems because the deformed ^{238}U occurs at least once in both systems. The broken line in the figure was obtained using the same absorption parameters as for $^{238}U + ^{197}Au$ and $a_f = 1.65$ fm.

Funke (1990) has found a correlation of these effects with the ground-state Q value for transfer. In the reaction $^{238}U + ^{197}Au$, the ground-state Q value for transfer is 0.43 MeV, while for the reaction $^{238}U + ^{238}U$, it is -1.35 MeV. There seems to be an analogy with the coupled-channels effects studied by Thompson et al. (1988) for the reaction $^{17}O + ^{208}Pb \rightarrow ^{209}Pb$. They found that back-angle cross sections for angular momentum and/or energy-mismatched transfer reactions were depleted if a coupling of the first excited state in ^{17}O to both the ^{17}O ground state and the transfer states was included, an effect that could not be reproduced by DWBA calculations. It is tempting to invoke the coupling to rotational bands in ^{238}U to explain the present anomalies as well. This means, deformation is seen only in mismatched transfer reactions. Coupled-channels calculations should be performed.

12.8.5 "Complex" Transfer Reactions

The observation of complex reactions at barrier and sub-barrier energies is rather recent. One study by Reisdorf et al. (1992) looked at increasingly heavy systems using the very sensitive radiochemical detection methods: $^{86}Kr + ^{76}Ge$, $^{86}Kr + ^{104}Ru$, and $^{86}Kr + ^{130}Te$, spanning $Z_p Z_t = 1152$–1872 at energies quite close to the Bass-model barriers. The observed reseparation channels go well beyond the traditional one or two nucleon transfers, even for the lightest system. The increasing complexity is documented by the measured mass distributions, Figure 12.92. The existence of a distinct new component in the reaction channels is revealed by the isotopic distributions around the projectile-target charges, see Figure 12.92. Gaussian peaks appear as smoothly behaved complex-reaction background under a narrow quasi-elastic peak dominated by one and two nucleon transfers. The "simple" quasi-elastic channels are understood as resulting from peripheral trajectories reflected from the combined nuclear, Coulomb, plus centrifugal potential. The complex channels result from a massive exchange of mass and charge between the two partners made possible by neck formation and leading to an isotope peak position and width heavily influenced by the gradients and curvature of the binuclear PES.

Information on what happens if the injection point is not close to the valley of optimum charge density was obtained by Gäggeler et al. (1986) studying the reaction $^{48}Ca + ^{248}Cm$ close to the Bass-model barrier. They found essentially constant cross sections of 1–2 mb for the elements U ($\Delta Z = 4$) through Rn ($\Delta Z = 10$) below the target. The situation became spectacular by the addition of data for $^{40,44}Ca + ^{248}Cm$

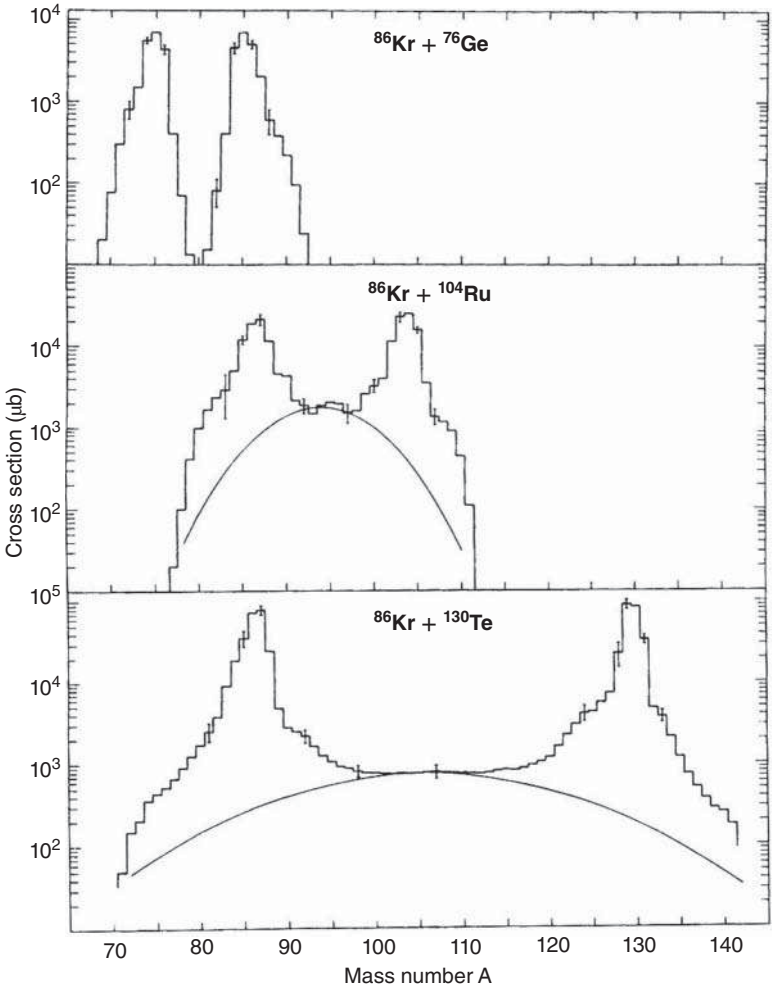

Figure 12.92 Mass distributions for ^{86}Kr + ^{76}Ge (a), ^{104}Ru (b), and ^{130}Te (c) at $E_{cm} = 129.1$, 178.6, and 203.0 MeV, respectively. Source: Reisdorf et al. (1992)/Springer Nature.

by Türler et al. (1992). Below the target, the yields differ by more than 2 orders of magnitude between the ^{48}Ca and the ^{40}Ca-induced reactions with an intermediate behavior for the ^{44}Ca projectile, see Figure 12.93. In the ^{40}Ca case, one is injecting into the PES at a point that is 20 MeV above the optimum charge-density configuration, whereas in the ^{48}Ca case, one is within 1 MeV of this optimum, see Figure 12.94. N/Z equilibration through the neck will lead to a larger asymmetry in the ^{40}Ca case; in combination with ^{248}Cm, the optimum charge is 17 with the consequence that there is much less drift to the light-mass side of the target and more yield is going to the heavy side of the target allowing a more copious production of heavier elements leading also, presumably, to more fusion than in the ^{48}Ca-induced reaction, since larger charge asymmetry lowers the repulsive Coulomb forces.

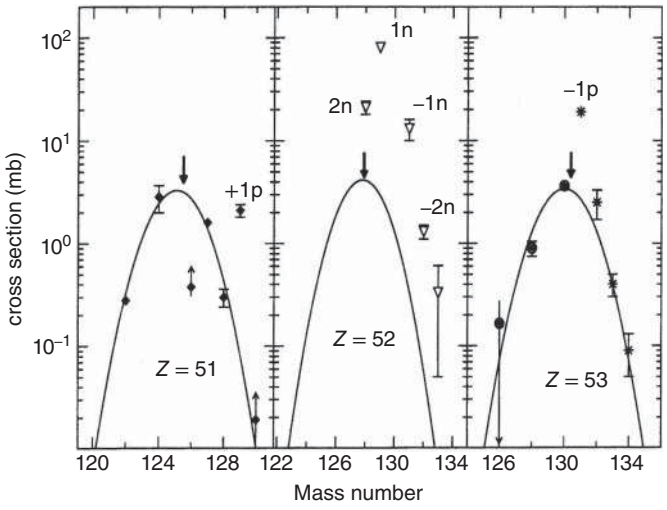

Figure 12.93 Yields for Sb, Te/Kr, and I ejectiles in the reaction $^{86}Kr + ^{130}Te$ at $E_{cm} = 203.0$ MeV. The Gaussian curves were obtained by fits taking into account the yields for a total of about sixty detected nuclides, but leaving out the predominantly quasi-elastic channels that are indicated in the figure. The arrows close to the top of the curves indicate the most favored mass at fixed charge from potential energy considerations. Source: Reisdorf et al. (1992)/Springer Nature.

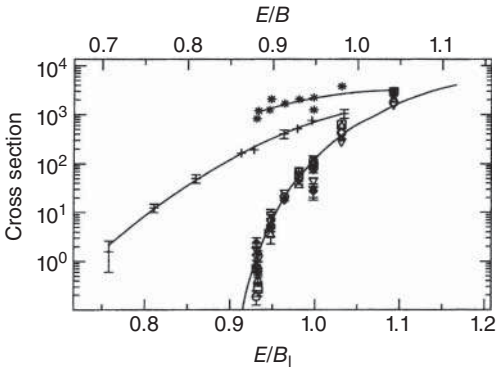

Figure 12.94 Comparison of excitation functions for one-neutron transfer, massive transfer, and fusion. Crosses, one-neutron transfer (in mb) for $^{238}U + ^{238}U$; asterisks: one-neutron transfer (to ^{237}U in mb) for $^{238}U + ^{197}Au$. All other symbols stand for complex transfer channels (in μb) ($^{223-225}Ra$, $^{225-226}Ac$, ^{227}Th) in the system $^{238}U + ^{197}Au$. The cross sections for each isotope have been renormalized with an energy-independent factor to agree best with the values for ^{224}Ra, in order to stress the common shape of the excitation functions. While the smooth curves going through the neutron-transfer data are just to guide the eye, the curve going through the complex transfer data represents the measured fusion cross section for $^{40}Ar + ^{154}Sm$ scaled down by a factor of 100 and shifted towards 5% higher E/B_I (see the upper abscissa). The transfer data are from Funke et al. (1991). B_I is the interaction barrier, B is the adjusted neck formation barrier. Source: Reisdorf (1994/IOP Publishing.

Complex reactions have also been observed by Funke et al. (1991) in very heavy systems such as $^{238}U + ^{238}U$, ^{197}Au at and below the Coulomb barrier. For such systems, the Bass-model potential no longer has a pocket; nevertheless, rather exotic transfer reactions leading to products such as ^{227}Th (a net two-proton and nine-neutron transfer) were observed. This can be qualitatively understood by assuming that a neck has formed between the two nuclei, possibly taking advantage of a favorable tip-to-tip orientation, and a massive nucleon exchange took place leading to approximately Gaussian isotope distributions peaking close to the minimum of the PES. For Th, this can be estimated to be around mass 228–230 for the studied systems, hence not too far, considering the finite widths of the observed distributions (about 2.5 u FWHM), from the observed ^{227}Th. The analogy of the excitation function for such a neck formation with fusion excitation functions is shown in Figure 12.95, where a comparison is made with the fusion data for $^{40}Ar + ^{154}Sm$, Reisdorf et al. (1985), which, like $^{197}Au + ^{238}U$, is a combination of a medium soft spherical nucleus with a well-deformed nucleus. One finds that the barrier for neck formation is 676 MeV (cm). Clearly, sub-barrier fusion physics continues all the way to $^{238}U + ^{238}U$, except that now, in principle, one can study more directly the coupling of the "simple" to the "complex" channels that lead to fusion in lighter systems. The lifetime of the necked configuration seems to be short: the angular distributions of the complex reaction products were found (Funke et al. 1991) to be sharply backward peaked.

Neck formation at barrier energies is also evidenced by another phenomenon concerning the way the total excitation energy is shared at separation. The excitation energy division in collisions well above the barrier has been discussed in a review by Töke and Schröder (1992) primarily in terms of the one-body dissipation model and one of its ingredients, Randrup (1978) version of the stochastic nucleon exchange model. The processes at higher energies are dominated by heat generating deceleration. As is known from low-energy fission, the separation of two fragments which were transiently linked by a neck can lead to a rather peculiar sharing of the excitation energy: one fragment appears to be cold, while the partner is hot, giving rise to the famous sawtooth for the average number of emitted neutrons vs. mass. The relevant physics lies in the way how the neck is ruptured, i.e. in the way the neck nucleons are shared at separation, cf. the random neck rupture model by Brosa, Grossmann, and Müller (1990).

Keller et al. (1987) studying reactions of ^{50}Ti, ^{54}Cr, and ^{58}Fe with ^{208}Pb at the barrier were able to measure with radiochemical methods the average isotope masses of complementary charged fragments. From this study mentioned in Chapter 12.8.2, the complete trend with charge division suggested that donor nuclei are cold, whereas acceptor nuclei are hot.

More complete radiochemical studies by Klein et al. (1997) and Wirtz et al. (2001) confirmed these observations for the system $^{51}V + ^{197}Au$ at the Bass-model barrier. The extreme acceptor–donor asymmetry at the barrier changes toward equipartition of the excitation energy only 25 MeV above the barrier energy, $E_{cm} = B + 25$ MeV, and develops toward a near temperature equilibrium at $E_{cm} = B + 75$ MeV in

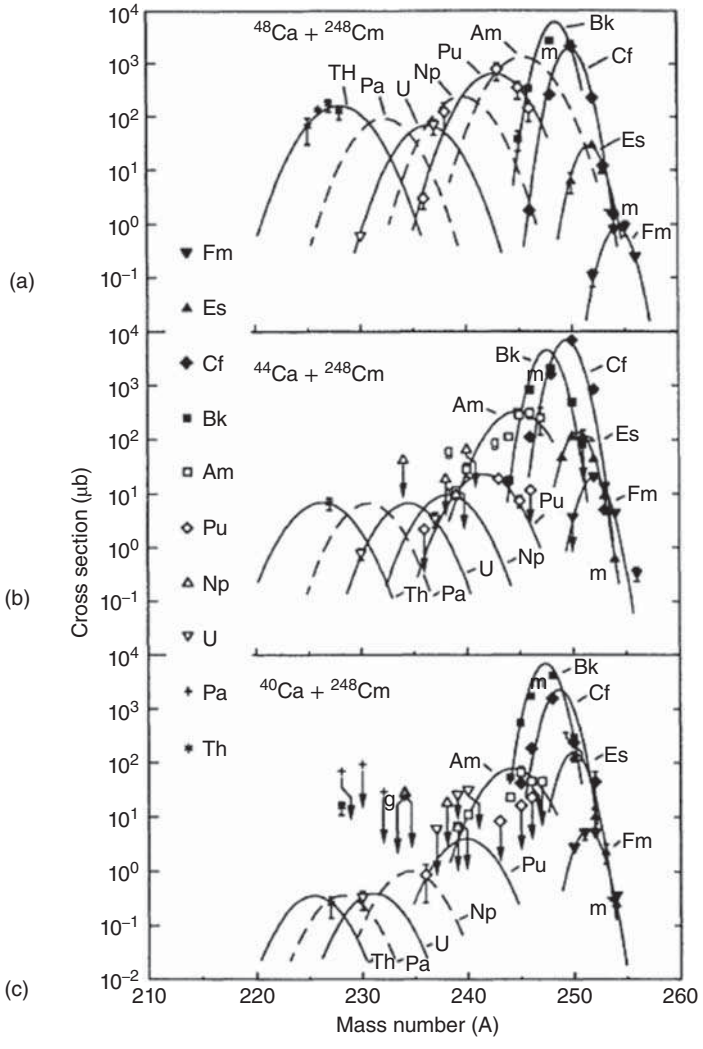

Figure 12.95 Isotope distributions of target-like fragments in reactions of Ca projectiles with ^{248}Cm. Ground-state isomers or metastable isomers are denoted with "g" or "m," respectively. Arrows indicate detection limits. (a): Reactions of 247–263 MeV ^{48}Ca projectiles with ^{248}Cm Refs. (Hoffman et al. 1985; Gäggeler et al. 1986). (b): Reactions of 251–257 MeV ^{44}Ca projectiles with ^{248}Cm (Türler et al. 1992). (c): Reactions of 251–257 MeV ^{40}Ca projectiles with ^{248}Cm (Hoffman et al. 1985). Source: Hoffman et al. (1985), Gäggeler et al. (1986), and Türler et al. (1992).

accordance with the observations reviewed by Töke and Schröder (1992) at higher energy at modest kinetic energy losses.

For obvious reasons that will become clear below, the kinematics of multi-nucleon transfer reactions in $^{48}Ca + ^{248}Cm$ collisions at 262 MeV (center of target) was investigated by Götz et al. (2017) by using a stacked-foil technique and chemical separations of trans-curium elements. Trans-curium isotopes were identified

by α-particle spectroscopy. For Fm isotopes, by comparing the centroids of the measured post-neutron emission isotope distributions with the most probable primary mass number predicted by Volkov's generalized Q_{gg} systematics, the missing mass (number of evaporated neutrons) is estimated. The latter is compared with that deduced from the measured centroid of the laboratory angular distribution peaked closely to the grazing angle and the centroid of the range distribution, being used to determine the average TKEL and the average excitation energy. The latter agrees within the uncertainties with the missing mass so that a consistent picture of the reaction mechanism emerges. For products closer to the target Z, e.g. Cf and Bk, the distributions of kinetic energies are much broader than for Fm, reflecting the fact that in the former, values of TKEL reach from quasi-elastic scattering all the way to deep inelastic scattering. The measured laboratory angular distribution and the average laboratory kinetic energy of the Fm isotopes, being the prototypes for multi-nucleon transfer products, are benchmark values for the design of electromagnetic separators to be constructed for the separation and detection of unknown

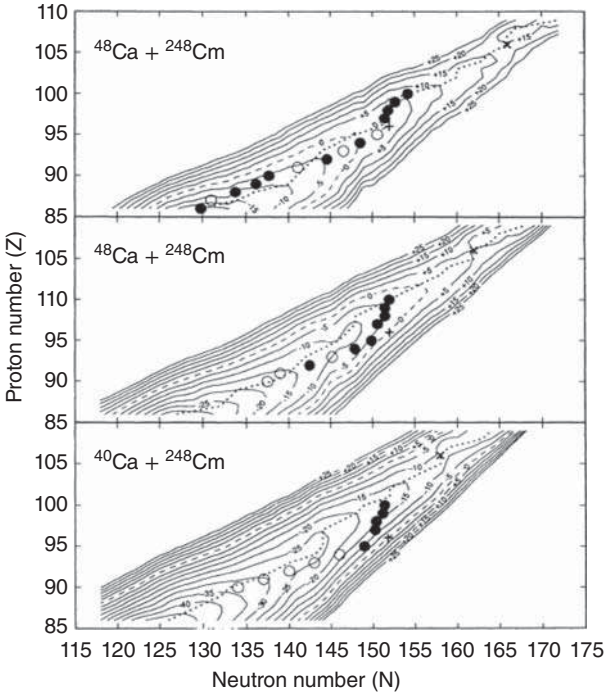

Figure 12.96 Contour map representation of the calculated PES for the reactions of ^{40,44,48}Ca projectiles with ^{248}Cm at an angular momentum of $l = 0\hbar$. The dashed lines denote the equipotential contour lines at 0 MeV. The injection points (^{248}Cm) are represented by +. The dotted lines connect the minima of the potential energies calculated for each Z. The Businaro–Gallone saddle point is indicated by x. The filled circles represent the position of the experimentally determined maxima of the isotope distributions for each Z, whereas the open circles represent estimated maxima. ^{48}Ca data from (Hoffman et al. 1985; Gäggeler et al. 1986), ^{44}Ca data from (Türler et al. 1992), ^{40}Ca data partly from (Hoffman et al. 1985). Source: Hoffman et al. (1985), Gäggeler et al. (1986), and Türler et al. (1992).

neutron-rich transactinides produced in this nuclear reaction type. For Fm, the angular distributions are peaked closely to the laboratory grazing angle $\theta gr = 27°$ with a width of $\pm 12°$. The laboratory kinetic energies are close to 80 MeV. These values can serve as benchmarks for the design of a large acceptance electromagnetic separator for the separation and detection of neutron-rich transactinide evaporation residues produced in multi-nucleon transfer reactions (Figure 12.96).

This work (Götz et al. 2017) picks up on studies performed about 30 years ago where also transfer reaction products in the reaction $^{48}Ca + ^{248}Cm$ was investigated using radiochemical methods (Hoffman et al. 1985; Gäggeler et al. 1986; Türler et al. 1992). The novelty of (Götz et al. 2017) is the successful attempt to obtain information about the reaction kinematics using a stacked-foil technique. Formerly (Gäggeler et al. 1986; Türler et al. 1992), it was argued that due to the FWHM of about 2.5 amu of the above-target isotopic distributions and of about 5 amu for below-target isotopic distributions, the above-target isotopic distributions (Bk, Cf, Es, Fm) were the result of quasi-elastic processes, while the below-target isotopic distributions due to their much larger widths contained a significant share of deeply inelastic reactions. It was speculated that these were missing in the above-target isotopic distributions. The work by Götz et al. (2017) now suggests that for Fm, high TKEL of 70 MeV occurs and that for, e.g. Cf, a broad distribution of recoil energies and thus TKEL is observed. Thus, the work of Götz et al. suggests some revision of the old, rather simplistic interpretation (Gäggeler et al. 1986; Türler et al. 1992). The narrower FWHM for above-target isotopic distributions is shown in Götz et al. (2017) to be the result of fission of the most highly excited trans-target fragments associated with large TKEL, while for the below-target fragments at large TKEL, the survival probability is high. This corresponds to interpretations contained in Kratz, Schädel, and Gäggeler (2013) and Kratz, Loveland, and Moody (2015), see Figure 12.82.

12.8.6 Relativistic Heavy-Ion Collisions, the Phases of Nuclear Matter

Nuclear matter can exist in a wide range of temperatures and densities. In heavy-ion collisions in the GeV u^{-1} regime, nuclear matter can be heated and compressed. This way, one can explore the phase diagram of nuclear matter. We present here three observations: the liquid-to-gas transition of nuclear matter; the measurement of hadron properties in the nuclear medium; and the phase transition to the quark–gluon plasma.

A liquid-to-gas transition is what we observe every day when we boil water. The average distance between water molecules is of the order of 0.1 nm as a result of an attractive interaction at large distances and a strong repulsion at short distances. The underlying potential is shown in Figure 12.97 (top left). When we heat water by transferring energy to its molecules, the temperature increases until we reach 100 °C. At this point, the temperature stays constant, although we keep transferring energy. This energy is used to break the bonds between the water molecules; thereby water is converted to vapor. The temperature increases again only after all water has been evaporated.

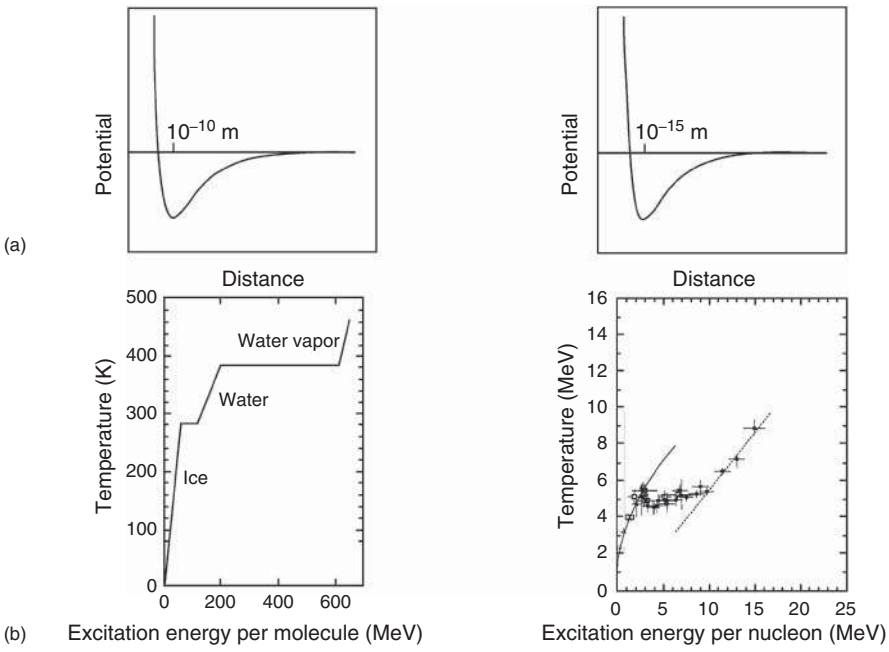

Figure 12.97 Liquid-to-gas-phase transition for water (a) and nuclear matter (b).

The force between two nucleons in a nucleus shows a very similar dependence on the distance, see Figure 12.97 (top right). However, the scale is changed by 5 orders of magnitude leading to a density 15 orders of magnitude higher than that of normal matter. As we discussed in Section 3.3, that nuclei in their ground state behave very similar to a liquid. A liquid-to-gas transition of nuclear matter was observed in 600 MeV u^{-1} $^{197}Au + ^{197}Au$ collisions by the ALADIN-LAND collaboration, where LAND was used as a calorimeter measuring via the neutron multiplicity the total excitation energy per nucleon in the system. The temperature was derived from isotopic ratios of He and Li isotopes. As is shown in Figure 12.97 (bottom right), when nuclear matter is heated in a nuclear collision, one first observes an increase of the temperature followed by a plateau-like behavior corresponding to the breaking of bonds between nucleons at $T_{\mathrm{HeLi}} \approx 5$ MeV, that is, one observes the evaporation of nuclear matter. The resulting observation is multifragmentation where a hot nuclear vapor is formed which subsequently condenses into droplets of IMFs near the critical temperature. Only after completion of the evaporation does the temperature rise again, Figure 12.97 (bottom right).

In the almost parallel work by Blaich et al., the system $^{197}Au + ^{197}Au$ was also investigated, but at 15 MeV u^{-1}, where the available energy is of the same order of magnitude as the value determined in the work by Pochodzalla et al., but target and projectile approached each other with a velocity well below the Fermi velocity. The question was whether this condition was sufficient to also create a liquid-to-gas transition where a hot nuclear vapor is formed which subsequently condenses into droplets of IMFs. To this end, a radiochemical catcher-foil experiment was

performed in which the reaction products were accumulated in foil stacks and assayed by means of X-ray and Υ-ray spectroscopy. This method allows for easy coverage of large solid angles and yields inclusive double-differential cross sections $d^2\sigma/dvd\theta$, when stacks of thin foils are used such that range distributions in different intervals of scattering angle are measured. By measuring differential ranges in the vicinity of ^{197}Au ($Z \geq 50$), their deflection was obtained at 15 MeV u^{-1}. Four irradiations at 9, 11, 13, and 15 MeV u^{-1} provided excitation functions of IMFs. The third type of irradiation at the highest energy used stacks of up to 13 foils to measure differential range distributions of selected IMFs. These foil stacks translate via range-velocity relations in a grid $v_{\text{perpendicular}} - v_{\text{parallel}}$ – plane which is different for each isotope.

For gold-like fragments, narrow peaks were observed at the grazing angle for all values of TKEL up to 1 GeV. The excitation function of ^{24}Na as a function of total kinetic energy was compared to a compilation of ^{24}Na-production in ^{197}Au bombardments with protons and light ions, i.e. ^{12}C and ^{20}Ne. If IMF production is a universal channel that opens up at a given excitation energy, the production cross sections should be factorized, i.e. at the same energy, they should scale with the geometrical cross section for different target-projectile combinations. All the data with light projectiles fall on a smooth line that saturates toward E_{cm} approaching 8 GeV. However, the data for the ^{197}Au projectile are not factorized, but exhibit much higher cross sections and a different energy dependence. This is a hint that we are looking here at a different reaction mechanism.

The experimental distributions in the $v_{\text{perpendicular}} - v_{\text{parallel}}$ – plane for $Z \leq 50$ exhibit a "Coulomb ridge" which is a clear signature of fission events and becomes very clear for the lighter fragments. The radius of the ring-like ridge is on the order of 1 cm ns^{-1} and increases with decreasing mass in close agreement with the Viola systematics. For the very light fragments, the radius becomes so large that several kinematical solutions start to overlap. Thus, the location of the ^{24}Na fragments originating from very asymmetric fission of the projectile-like fragment is superimposed by the corresponding fragment where scattering occurred on the opposite side of the target nucleus. In addition, there are two Coulomb ridges at smaller v_{parallel} resulting from sequential fission of the target-like fragments. Results of four-body trajectory calculations describe these data quite well. The main feature, the Coulomb ridges in the velocity distribution is well described, confirming the message that the ^{24}Na is formed via sequential fission. From the existence of the "Coulomb ridge," we see clearly that the light elements are formed in a two-step process: In the first, deep-inelastic step, a projectile-like fragment is scattered at the grazing angle for all energy losses, as can be seen from the deflection function. In the second step, the excited projectile-like fragment and/or target-like fragment undergo fission. The fission cross section is not isotropically distributed along the semi-circular Coulomb ridge but shows preferential emission of the light fission fragments along an axis connecting the projectile-like and target-like pre-fragments toward the latter. This is consistent with the light fragments from the second reaction step being the remnants of the neck connecting the two Au-like fragments in the first, deep-inelastic reaction step.

Similar data have been obtained for the system $^{129}Xe + ^{122}Sn$ at 12.5 MeV u^{-1} by Glässel et al. Here also, it was found that the fragments of the fissioning nucleus are emitted collinearly with the axis through the two partners of the first step and that their relative velocities depend on the direction of emission. This demonstrates that dynamically induced sequential fission happens on a very fast time scale in these systems (≈ 1–10^{-21} seconds). Thus, the production mechanism of IMFs is very different from the liquid-to-gas phase transition. A plausible explanation for this change might be the slow velocity of projectile and target at 15 MeV u^{-1}. This still allows for collective phenomena like neck formation leading to larger deformations of the residues of the first step which results in a large probability for pre-equilibrium sequential fission with an extremely broad mass distribution and fragment trajectories influenced by final-state Coulomb interaction.

Let us return to the liquid-to-gas phase transition in nuclear matter, e.g. at 600 Mev u^{-1} $^{197}Au + ^{197}Au$ collisions. The high energy density in the collision zone between projectile and target nuclei can also be used to create new particles, for example, positively and negatively charged kaons (antikaons). The complex evolution of a nuclear collision at relativistic energies in space and time is described in transport-model calculations related to the restoration of chiral symmetry – one of the fundamental symmetries of quantum chromodynamics (QCD) predicting that the mass of hadrons is modified in compressed nuclear matter. Figure 12.98 shows in a schematic way the predicted change of the K^+ and K^- mass as a function of nuclear density where density 1 corresponds to normal nuclear matter density. K^+ and K^- production was studied experimentally in proton–proton collisions as a function of collision energy, and the K^- yield was always found to be at least 1 order of magnitude smaller than the K^+ yield. In contrast, in heavy-ion collisions, the production probability for the K^+ and K^- mesons was found to be nearly the same when plotted as a function of the energy above the threshold, see Figure 12.98. Compared to the proton–proton reaction, the K^- production is enhanced in nucleus–nucleus

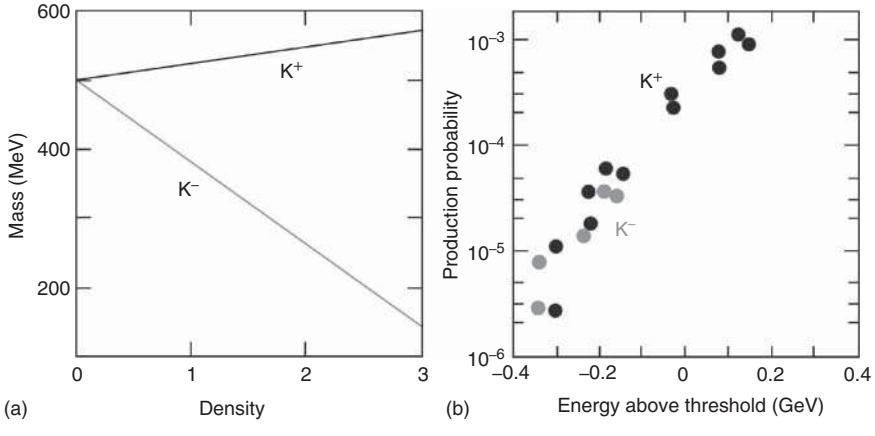

Figure 12.98 Kaon mass as a function of nuclear density (schematic, a) and kaon production probability as a function of the energy above threshold (GeV) (b). Source: Modified from Böttcher et al. (2004).

collisions. If the mass of the K^- meson is indeed lowered in the compressed nuclear medium as predicted theoretically, then it takes less energy to produce such a K^- meson, and for a given energy, one can produce more K^- particles compared to the proton–proton collision. This experimental result is therefore taken as evidence that the kaon masses are indeed modified in dense nuclear matter.

If we further increase the temperature in nucleus–nucleus collisions, we expect nuclear matter to undergo another phase transition to the so-called quark-gluon plasma (QGP). If one performs heavy-ion collisions at ultrarelativistic energies ($>5\,\mathrm{GeV\,u^{-1}}$), energy densities in the collision zone reach values sufficiently high that quarks and gluons are liberated, forming a plasma of free-moving particles. The quasi-free quarks and gluons in the collision zone show their color charges, while at the periphery of the collision, the energy density is not sufficient for quark–gluon plasma formation. Here, the nucleons remain intact. In the final phase of the reaction, one can determine the temperature and density of the matter. Various results obtained at the Super Proton Synchrotron (SPS) at CERN indicate that in the initial phase of the collision, the phase boundary was surpassed. The experimental signatures of a phase transition include (i) a suppression of the production of the heavy vector mesons J/Ψ and Ψ' and the upsilon states; (ii) the creation of a large number of ss quark-antiquark pairs; and (iii) the momentum spectra, abundance, and direction of emission of di-lepton pairs. This observation is of utmost relevance for understanding the strong interaction, but it also provides an important contribution to our understanding of the evolution of the Universe which started with the Big Bang. Ever since, the Universe has expanded and cooled down from this initial phase of near-infinite energy density and temperature. A few microseconds after the Big Bang, the whole Universe was a QGP until, in the millisecond range, quarks and gluons were confined and formed nucleons and later on nuclear matter.

In experiments, we have now managed to go backward in this evolution and a detailed investigation of the questions related to the evolution of the early Universe will be the research line at the RHIC and at LHC with the ALICE detector. There have been runs at the LHC with lead-ion collisions at a cm energy, $\sqrt{s}$, of 2.76 TeV per nucleon pair starting in 2010. Often, comparison was done with the corresponding results from Brookhaven's Relativistic Heavy-Ion Collider RHIC, where the energy is ∼14 times lower. The J/ψ meson is composed of a heavy quark-antiquark pair with the two objects orbiting at a relative distance of about 0.5 fm, held together by the strong color interaction. However, if such a state were to be placed inside a QGP, it turns out that its binding could be screened by the huge number of color charges (quarks and gluons) that make up the QGP freely roaming around it. This causes the binding of the quark and antiquark in the J/ψ to become weaker so that ultimately, the pair disintegrates and the J/ψ disappears – i.e. it is "suppressed". Theory has shown that the probability of dissociation depends on the temperature of the QGP, so that the observation of a suppression of the J/ψ has been seen as a way to place a "thermometer" in the medium itself. Such a J/ψ suppression was first predicted in 1986 and was thoroughly investigated over the following years in experiments with heavy-ion collisions. In particular, Pb–Pb

interactions were studied at CERN's SPS at a cm energy, $\sqrt{s}$, of around 17 GeV per nucleon pair, and then Au–Au collisions were studied at $\sqrt{s}$=200 GeV at RHIC. As predicted by the theory, a suppression of the J/ψ yield was observed with respect to what would be expected from a mere superposition of production from elementary nucleon–nucleon collisions. However, the experiments also made some puzzling observations. In particular, the size of the suppression (about 60–70% for central, i.e. head-on nucleus–nucleus collisions) was found to be approximately the same at the SPS and RHIC, despite the jump in the cm energy of more than 1 order of magnitude, which would suggest higher QGP temperatures at RHIC. Ingenious explanations were suggested but a clear-cut explanation of this puzzle proved impossible. At the LHC, extremely interesting developments were expected. In particular, a much higher number of charm–anticharm pairs are produced in the nuclear interaction, thanks to the unprecedented cm energies. As a consequence, even a suppression of the J/ψ yield in the hot QGP phase could be more than counterbalanced by a statistical combination of charm–anticharm pairs happening when the system, after expansion and cooling, finally crosses the temperature boundary between the QGP and a hot gas of particles. If the density of heavy quark pairs is large enough, this regeneration process may even lead to an enhancement of the J/ψ yield – or at least to a much weaker suppression with respect to the experiments at lower energies. The observation of the fate of the J/ψ in nuclear collisions at the LHC constituted one of the goals of the ALICE experiment and was among its main priorities during the first runs of the LHC with lead beams.

In a comparison of the J/ψ suppression between RHIC (PHENIX) and the LHC (ALICE), the ALICE results showed a strikingly smaller suppression, in particular for head-on collisions despite the much larger cm energy. Therefore, despite the higher temperatures attained in the nuclear collisions at the LHC, more J/ψ mesons were detected in the ALICE experiment. Such an effect is likely to be related to a regeneration process occurring at the temperature boundary between the QGP and a hot gas of hadrons ($T \approx 160$ MeV).The picture that arises from these observations is consistent with the formation, in Pb–Pb collisions at the LHC, of a deconfined system (QGP) that can suppress the J/ψ meson, followed by a hadronic system in which a fraction of the charm–anticharm pairs coalesces and ultimately gives a J/ψ yield larger than that observed at lower energies.

References

Alster, J. and Conzett, H.E. (1964). Elastic scattering of ^{13}C ions from Fe, Ni, ^{107}Ag, In, and Ta. *Phys. Rev.* 136: B1023.

Ayik, S., Wolschin, G., and Nörenberg, W. (1978). *Z. Phys.* A286: 71.

Back, B.B., Betts, R.R., Gindler, J.E. et al. (1985). Angular distributions in heavy-ion-induced fission. *Phys. Rev.* C32: 195.

Behkami, A.N. (1971). *Nucl. Data Tables* 10: 1.

van den Berg, A.M., Rehm, K.E., Kovar, D.G. et al. (1987). Systematics of quasi-elastic neutron transfer cross sections for heavy-ion induced reactions. *Phys. Lett. B* 194: 334.

Bjørnholm, S. and Swiatecki, W.J. (1982). Dynamical aspects of nucleus-nucleus collisions. *Nucl. Phys.* A391: 471.

Blann, M. (1975). Preequilibrium decay. *Annu. Rev. Nucl. Sci.* 25: 123.

Blatt, J. and Weisskopf, V. (1952). *Theoretical Nuclear Physics*. New York: Wiley.

Bock, R. (ed.) (1979–1982). *Heavy Ion Collisions*, vol. 3. Amsterdam: North-Holland.

Bohr, N. (1936). Neutron capture and nuclear constitution. *Nature* 137: 344.

Böttcher, I., Förster, A., Grosse, E. et al. (2004). K^+ and K^- production in heavy-ion collisions at SIS energies. *J. Phys. G: Nucl. Part. Phys.* 30: S393.

Brack, M., Damgaard, J., Jensen, A.S. et al. (1972). Funny hills: the shell correction approach to nuclear shell effects and its application to the fission process. *Rev. Mod. Phys.* 44: 320.

Broglia, R.A., Pollarolo, G., and Winther, A. (1981). On the absorptive potential in heavy ion scattering. *Nucl. Phys.* A361: 307.

Brosa, U., Grossmann, S., and Müller, A. (1990). Nuclear scission. *Phys. Rep.* 197: 167.

Cohen, S., Plasil, N., and Swiatecki, W.J. (1974). Equilibrium configurations of rotating charged or gravitating liquid masses with surface tension. II. *Ann. Phys.* 82: 557.

Darriulat, P., Igo, G., Pugh, H.G., and Holmgren, H.D. (1965). Elastic scattering of alpha particles by helium between 53 and 120 MeV. *Phys. Rev.* 137: B315.

Denschlag, J.O. (2011). Nuclear fission. In: *Handbook of Nuclear Chemistry*, 2e, vol. 1 (eds. A. Vértes, S. Nagy, Z. Klenczár, et al.), 223. Berlin: Springer-Verlag.

Essel, H., Hartel, K., Henning, W. et al. (1979). Charge and mass transfer in the reaction ^{136}Xe+^{208}Pb at energies close to the coulomb barrier. *Z. Phys.* A289: 265.

Flynn, K.F. and Glendening, L.E. (1970). *Report ANL-7749*. Argonne, IL: Argonne National Laboratory.

Freiesleben, H., Hildenbrand, K.D., Pühlhofer, F. et al. (1979). The reaction ^{238}U + ^{238}U at 7.42 MeV/u. *Z. Phys.* A292: 171.

Friedlander, G., Kennedy, J.W., Macias, E.S., and Miller, J.M. (1981). *Nuclear and Radiochemistry*, 3e. New York: Wiley.

Funke, F. (1990). Doctoral thesis. Johannes Gutenberg University Mainz, GSI Report 90-10.

Funke, F., Kratz, J.V., Trautmann, N. et al. (1991). Cross sections for nuclear reactions in collisions of ^{238}U +^{238}U and ^{238}U +^{197}Au near and below the Coulomb barrier. *Z. Phys.* A340: 303.

Gäggeler, H., Trautmann, N., Brüchle, W. et al. (1980). Search for superheavy elements in the ^{238}U + ^{238}U reaction. *Phys. Rev. Lett.* 45: 1824.

Gäggeler, H., Brüchle, W., Brügger, M. et al. (1986). Production of cold target-like fragments in the reaction of ^{48}Ca +^{248}Cm. *Phys. Rev.* C33: 1983.

Glässel, P., von Harrach, D., Civelecoglu, Y. et al. (1979). Three-particle exclusive measurements of the reactions ^{238}U + ^{238}U and ^{238}U + ^{248}Cm. *Phys. Rev. Lett.* 43: 1483.

Goshal, S.N. (1950). An experimental verification of the theory of compound nucleus. *Phys. Rev.* 80: 939.

Götz, M., Götz, S., Kratz, J.V. et al. (2017). Radiochemical study of the kinematics of multi-nucleon transfer reactions in ^{48}Ca + ^{248}Cm collisions 10% above the Coulomb barrier. *Nucl. Phys.* A961: 1.

Guidry, M.W., Nichols, T.L., Neese, R.E. et al. (1981). Two-nucleon transfer reactions in deformed nuclei using very heavy ions. *Nucl. Phys.* A361: 275.

Hildenbrand, K.D., Freiesleben, H., Pühlhofer, F. et al. (1977). Reaction between ^{238}U and ^{238}U at 7.42 MeV/Nucleon. *Phys. Rev. Lett.* 39: 1065.

Hodgson, P.E., Gladioli, E., and Gladioli-Erba, E. (1997). *Introductory Nuclear Physics*. Oxford: Clarendon Press.

Hoffman, D.C., Fowler, M.M., Daniels, W.R. et al. (1985). Excitation functions for production of heavy actinides from interactions of ^{40}Ca and ^{48}Ca ions with ^{248}Cm. *Phys. Rev.* C31: 1763.

Keller, H., Bellwied, R., Lützenkirchen, K. et al. (1987). Unusual excitation-energy division in quasi-fission reactions between ^{50}Ti, ^{54}Cr, and ^{58}Fe and ^{207,208}Pb at the barrier. *Z. Phys.* A328: 255.

Klein, P., Kratz, J.V., Gober, M.K. et al. (1997). Excitation energy division in ^{51}V + ^{197}Au collisions near the Coulomb barrier. *Z. Phys.* A357: 193.

Kratz, J.V. (2011). Chemistry of transactinides. In: *Handbook of Nuclear Chemistry*, Chapter 20, 2e, vol. 2 (eds. A. Vértes, S. Nagy, Z. Klencsár, et al.), 926–1004. Springer Science+Business Media B.V.

Kratz, J.V., Norris, A.E., and Seaborg, G.T. (1974). Mass-yield distributions in the reaction of ^{84} Kr ions with ^{238}U. *Phys. Rev. Lett.* 33: 502.

Kratz, J.V., Liljenzin, J.O., Norris, A.E., and Seaborg, G.T. (1976). Charge and mass distributions in the reaction of ^{40}Ar ions with ^{238}U. *Phys. Rev.* C13: 2347.

Kratz, J.V., Brüchle, W., Franz, G. et al. (1979). Study of the NZ ratios of light and heavy fragments from collisions of ^{129}Xe, ^{132}Xe, and ^{132}Xe with ^{197}Au near the interaction barrier. *Nucl. Phys.* A332: 477.

Kratz, J.V., Schädel, M., and Gäggeler, H.W. (2013). Reexamining the heavy-ion reactions ^{238}U + ^{238}U and ^{238}U + ^{248}Cm and actinide production close to the barrier. *Phys. Rev.* C88: 054615.

Kratz, J.V., Loveland, W., and Moody, K.J. (2015). Syntheses of transuranium isotopes with atomic numbers $Z \leq 103$ in multi-nucleon transfer reactions. *Nucl. Phys.* A944: 117.

Landowne, S. and Pollarolo, G. (1990). Single neutron transfer in ^{238}U + ^{238}U collisions. *Phys. Lett. B* 241: 313.

Landowne, S., Price, C., and Esbensen, H. (1988). Two-particle transfer reactions with heavy-deformed nuclei. *Nucl. Phys.* A484: 98.

Lützenkirchen, K., Kratz, J.V., Wirth, G. et al. (1986). Angular distributions in quasi-fission reactions. *Nucl. Phys.* A452: 351.

Mayer-Kuckuk, T. (1979). *Kernphysik*. Stuttgart: Teubner.

Newton, T.D. (1956). *Can. J. Phys.* 34: 804.

Otto, R.J., Fowler, M.M., Lee, D., and Seaborg, G.T. (1976). Mass yield distributions in the reaction of ^{136}Xe ions with ^{238}U. *Phys. Rev. Lett.* 36: 135.

Plasil, N. (1974). *Proceedings International Conference on Reactions Between Complex Nuclei*, vol. 2, 107. Amsterdam: North-Holland.

Poitou, J., Lucas, R., Kratz, J.V. et al. (1979). Second moments of N/Z-distributions in damped collisions of ^{132}Xe with ^{197}Au. *Phys. Lett. B* 88: 69.

Quint, A.B., Reisdorf, W., Schmidt, K.-H. et al. (1993). Investigation of the fusion of heavy nearly symmetric systems. *Z. Phys.* A346: 119.

Randrup, J. (1978). Mass transport in nuclear collisions and (1979) *Nucl. Phys. A* 307: 319 and (1979). *Nucl. Phys. A* 327: 516.

Rehm, K.E., Essel, H., Sperr, P. et al. (1981). Dissipative collisions of heavy ions at energies close to the Coulomb Barrier. *Nucl. Phys.* A366: 477.

Rehm, K.E., Beck, C., van den Berg, A.M. et al. (1990). Systematic behavior of one- and two-nucleon transfer reactions induced by medium-weight projectiles. *Phys. Rev.* C42: 2497.

Reisdorf, W. (1994). Heavy-ion reactions close t the Coulomb barrier. *J. Phys. G: Nucl. Part. Phys.* 20: 1297.

Reisdorf, W., Hessberger, F.P., Hildenbrand, K.D. et al. (1985). Fusion near the threshold: a comparative study of the systems $^{40}Ar + ^{112,\,116,\,122}Sn$ and $^{40}Ar + ^{144,\,148,\,154}Sm$. *Nucl. Phys.* A438: 212.

Reisdorf, W., Kratz, J.V., Bellwied, R. et al. (1992). Competition between binary reactions and fusion in heavy-ion collisions at the Coulomb barrier. *Z. Phys.* A342: 411.

Reising, R.F., Bate, G.L., and Huizenga, J.R. (1966). *Phys. Rev.* 141: 1161.

Reus, U., Habbestad-Wätzig, A.M., Esterlund, R.A. et al. (1977). Mass-yield distributions in the reaction of ^{56}Fe ions with ^{238}U. *Phys. Rev. Lett.* 39: 171.

Riedel, C. and Nörenberg, W. (1979). Theoretical estimates of the production of transuranium elements in heavy-ion collisions. *Z. Phys.* A290: 385.

Riedel, C., Wolschin, G., and Nörenberg, W. (1979). Relaxation times in dissipative heavy-ion collisions. *Z. Phys.* A290: 47.

Schädel, M., Kratz, J.V., Ahrens, H. et al. (1978). Isotope distributions in the reaction of ^{238}U with ^{238}U. *Phys. Rev. Lett.* 41: 469.

Schädel, M., Brüchle, W., Gäggeler, H. et al. (1982). Actinide production in collisions of ^{238}U with ^{248}Cm. *Phys. Rev. Lett.* 48: 852.

Schmidt, R. and Wolschin, G. (1980). Mass transport in anharmonic potentials. *Z. Phys.* A296: 215.

Schmidt, K.H., Faust, W., Münzenberg, G. et al. (1979). *Proceedings of the International Conference on Physics and Chemistry of Fission*, Jülich 1979, IAEA-SM/241-C8.

Schmidt, K.-H. et al. (1998). *Heavy Ion Physics* (eds. Yu.T. Oganessian and R. Kalpakchieva). Singapore: World Scientific.

Schmitt, H.W. et al. (1965). *Phys. Rev.* 141: 1146.

Schröder, W.U. and Huizenga, J.R. (1984). Damped nuclear reactions. In: *Treatise on Heavy-Ion Science*, vol. 2 (ed. D.A. Bromley), 242. New York: Plenum Press.

Schüll, D., Shen, W.C., Freiesleben, H. et al. (1981). The influence of the potential energy surface on neutron excess and mass equilibration in the $^{136}Xe + ^{56}Fe$ system. *Phys. Lett. B* 102: 116.

Sikkeland, T., Ghiorso, A., and Nurmia, M. (1968). Analysis of excitation functions in Cm(C,xn)No reactions. *Phys. Rev.* 172: 1232.

Terrell, J. (1965). *Proceedings of the IAEA Symposium on the Physics and Chemistry of Fission, Salzburg*, vols. 2, 3. Vienna: IAEA.

Thompson, I.J., Nagarajan, M.A., Lilley, J.S., and Fulton, B.R. (1988). Evidence of projectile polarisation effects on the reaction ^{208}Pb(^{17}O, ^{16}O)^{209}Pb. *Nucl. Phys.* A487: 141.

Töke, J. and Schröder, W.U. (1992). Excitation energy division in dissipative heavy-ion collisions. *Annu. Rev. Nucl. Part. Sci.* 42: 491.

Töke, J., Bock, R., Dai, G.X. et al. (1985). Quasi-fission – the mass-drift mode in heavy-ion reactions. *Nucl. Phys.* A440: 327.

Türler, A., von Gunten, H.R., Leyba, J.D. et al. (1992). Actinide production from the interactions of ^{40}Ca and ^{44}Ca with ^{248}Cm and a comparison with the ^{48}Ca +^{248}Cm system. *Phys. Rev.* C46: 1364.

Vandenbosch, R. and Huizenga, J.R. (1973). *Nuclear Fission*. New York: Academic Press.

Volkov, V.V. (1974). *Proceedings of the International Conference on Reactions between Complex Nuclei, Nashville 1974*, vol. II, 363. Amsterdam: North Holland.

Wirth, G., Brüchle, W., Brügger, M. et al. (1986). Sub-Coulomb transfer in ^{238}U +^{238}U collisions. *Phys. Lett. B* 177: 282.

Wirth, G., Funke, F., Brüchle, W. et al. (1991). One-neutron transfer in ^{238}U + ^{197}Au collisions. *Phys. Lett. B* 253: 28.

Wirtz, C., Kratz, J.V., Brüchle, W. et al. (2001). Excitation energy division in ^{51}V + ^{197}Au collisions 75 MeV above the barrier. *Radiochim. Acta* 89: 689.

Wolschin, G. and Nörenberg, W. (1978). Analysis of relaxation phenomena in heavy-ion collisions. *Z. Phys.* A284: 209.

Wuosmaa, A.H., Rehm, K.E., Glagola, B.G. et al. (1991). Neutron transfer at large distances in the system ^{36}S+^{92}M. *Phys. Lett. B* 255: 316.

Zagrebaev, V. and Greiner, W. (2007a). Shell effects in damped collisions: a new way to superheavies. *J. Phys. G: Nucl. Part. Phys.* 34: 2265.

Zagrebaev, V. and Greiner, W. (2007b). Superheavy nuclei and giant quasi-atoms. *Nucl. Phys. A* 787: 363.

Zagrebaev, V. and Greiner, W. (2008). Synthesis of superheavy nuclei: a search for new production reactions. *Phys. Rev.* C78: 034610.

Zagrebaev, V.I., Oganessian, Yu. Ts., Itkis, M.G., and Greiner, W. (2006). Superheavy nuclei and quasi-atoms produced in collisions of transuranium ions. *Phys. Rev. C* 73: 031602®.

Zucker, A. (1960). Nuclear interactions of heavy ions. *Annu. Rev. Nucl. Sci.* 10: 27.

Further Reading

General

Evans, R.D. (1955). *The Atomic Nucleus*. New York: McGraw-Hill.

Myers, W.D. and Swiatecki, W.J. (1966). Nuclear masses and deformations. *Nucl. Phys.* 81: 1.

Meyerhof, W.E. (1967). *Elements of Nuclear Physics*. New York: McGraw-Hill.

Jackson, D.F. (1970). *Nuclear Reactions*. London: Methuen.

Hodgson, P.E. (1971). *Nuclear Reactions and Nuclear Structure*. Oxford: Clarendon Press.

Cerny, J. (ed.) (1974). *Nuclear Spectroscopy and Reactions, Parts A, B, C*. New York: Academic Press.

Hodgson, P.E. (1978). *Nuclear Heavy-Ion Reactions*. Oxford: Clarendon Press.

Rudolf, G., Gobbi, A., Stelzer, H. et al. (1979). Energy loss and nucleon exchange in the reaction of ^{86}Kr with ^{166}Er. *Nucl. Phys.* A330: 243.

Gorbachev, V.M., Zamyatnin, Y.S., and Lbov, A.A. (1980). *Nuclear Reactions in Heavy Elements*. Oxford: Pergamon.

Freiesleben, H. and Kratz, J.V. (1984). N/Z equilibration and nucleon exchange in dissipative heavy-ion collisions. *Phys. Rep.* 106: 1.

Rehm, K.E. (1991). Quasi-elastic heavy-ion collisions. *Ann. Rev. Nucl. Part. Sci.* 41: 429.

Wolfs, F.L.H., Rehm, K.E., Ma, W.C. et al. (1992). Elastic scattering and quasielastic transfer in the system ^{76,82}Se + ^{192,198}Pt. *Phys. Rev.* C45: 2283.

Wong, S.S.M. (1998). *Nuclear Physics*, 2e. New York: Wiley.

Sagaidak, R.N., Kniajeva, G.N., Itkis, I.M. et al. (2003). Fusion suppression in mass-asymmetric reactions leading to Ra compound nuclei. *Phys. Rev.* C68: 014603.

Zagrebaev, V. and Greiner, W. (2010). New ideas on the production of heavy and superheavy neutron rich nuclei. *Nucl. Phys. A* 834: 366c.

Sobotka, L.G. and Viola, V.E. (2011). Nuclear reactions. In: *Handbook of Nuclear Chemistry*, 2e, vol. 1 (eds. A. Vértes, S. Nagy, Z. Klenczár, et al.), 143. Berlin: Springer-Verlag.

More Specialized

Fernbach, S., Serber, R., and Taylor, T.B. (1949). The scattering of high-energy neutrons by nuclei. *Phys. Rev.* 75: 1352.

Nilson, R., Jentschke, W.K., Briggs, G.R. et al. (1958). Investigation of excited states in ^{8}Be by alpha-particle scattering from He. *Phys. Rev.* 109: 850.

Huizenga, J.R. and Igo, G. (1962). Theoretical reaction cross sections for alpha particles with an optical model. *Nucl. Phys.* 29: 462.

Griffin, J.J. (1966). Statistical model of intermediate structure. *Phys. Rev. Lett.* 17: 478.

Hodgson, P.E. (1967). The optical model of nucleus-nucleus interaction. *Annu. Rev. Nucl. Sci.* 17: 1.

Porile, N.T. (1968). Low-energy nuclear reactions. In: *Nuclear Chemistry*, vol. I (ed. L. Yaffe). New York: Academic Press.

Firk, F.W.K. (1970). Low-energy photonuclear reactions. *Annu. Rev. Nucl. Sci.* 20: 39.

Mcfarlane, M.H. and Schiffer, J.P. (1974). Transfer reactions. In: *Nuclear Spectroscopy and Reactions, Part B* (ed. J. Cerny). New York: Academic Press.

Perey, F.G. (1974). Elastic and inelastic scattering. In: *Nuclear Spectroscopy and Reactions, Part B* (ed. J. Cerny). New York: Academic Press.

Fuller, E.G. and Hayward, E. (eds.) (1976). *Photonuclear Reactions*. New York: Dowden, Hutchinson and Ross.

Broglia, R.A. and Winter, A. (1981). *Heavy Ion Reactions*. London: Benjamin/Cummings.

Satchler, G.R. (1983). *Direct Nuclear Reactions*. Oxford: Clarendon Press.

Nuclear Fission

Hahn, O. and Strassmann, F. (1939). Über den Nachweis und das Verhalten der bei der Bestrahlung des Urans mittels Neutronen entstehenden Erdalkalimetalle. *Naturwissenschaften* 27: 11.

Halpern, I. and Strutinsky, V.M. (1958). *Proceedings of the UN International Conference on Peaceful Uses of Atomic Energy, 15, 408, P/1513*. New York: United Nations.

Terrell, J. (1962). Neutron yields from individual fission fragments. *Phys. Rev.* 127: 880.

Wahl, A.C. (1962). Nuclear charge distribution in low-energy fission. *Phys. Rev.* 126: 1112.

Cohen, S. and Swiatecki, W.J. (1963). The deformation energy of a charged drop: Part V: Results of electronic computer studies. *Ann. Phys. (New York)* 22: 406.

Wheeler, J.A. (1963). *Fast Neutron Physics*, Part II (eds. J.B. Marion and J.L. Fowler), 2051. New York: Interscience.

Herrmann, G. (1964). 25 Jahre Kernspaltung. *Radiochim. Acta* 3: 169 and (1965) 4: 173.

International Atomic Energy Agency (1965, 1969, 1973). *Physics and Chemistry of Fission*. Vienna: IAEA.

Viola, V.E. (1965). Correlation of fission fragment kinetic energy data. *Nucl. Data Sheets* A1: 391.

Viola, V.E. and Seaborg, G.T. (1966). Lifetimes for alpha, beta and spontaneous fission decay. *J. Inorg. Nucl. Chem.* 28: 741.

Strutinsky, V.M. (1967). Shell effects in masses and deformations. *Nucl. Phys.* A95: 420.

Updegraff, W.E. and Onley, D.S. (1971). Dynamic collective model of photofission. *Nucl. Phys.* A161: 191.

Nix, J.R. (1972). Calculation of fission barriers for heavy and superheavy nuclei. *Annu. Rev. Nucl. Sci.* 22: 65.

Hoffman, D.C. and Hoffman, M.M. (1974). Post-fission phenomena. *Annu. Rev. Nucl. Sci.* 24: 151.

Specht, H.J. (1974). Nuclear fission. *Rev. Mod. Phys.* 46: 773.

Cuninghame, J.G. (1978). Status of fission product yield data. In: *Fission Product Nuclear Data – 1977*, IAEA Report 213, vol. I, 351. Vienna: International Atomic Energy Agency.

Denschlag, J.O. (1978). Prediction of unmeasured fission yields by nuclear theory or systematics. In: *Fission Product Nuclear Data – 1977*, IAEA Report 213, vol. II, 421. Vienna: International Atomic Energy Agency.

Wahl, A.C. (1989). Nuclear charge and mass distributions from fission. In: *Fifty Years with Nuclear Fission* (eds. J.W. Behrens and A.D. Carlson), 525. La Grange Park, IL: American Nuclear Society.

Herrmann, G. (1990). Fifty years ago: from the "transuranics" to "nuclear fission". *Angew. Chem. Int. Ed. Engl.* 29: 481.

Gönnenwein, F. (1991). Mass, charge, kinetic energy of fission fragments. In: *The Nuclear Fission Process* (ed. C. Wagemans), 287. Boca Raton, FL: CRC Press.

Wagemans, C. (1991). Spontaneous fission. In: *The Nuclear Fission Process* (ed. C. Wagemans), 35. Boca Raton, FL: CRC Press.

Herrmann, G. (1995). The discovery of nuclear fission – good solid chemistry got things on the right track. *Radiochim. Acta* 70/71: 51.

Denschlag, J.O. (1997). Fission fragment mass, charge, and energy distributions. In: *Experimental Techniques in Nuclear Physics* (eds. D.N. Poenaru and W. Greiner), 535. Berlin: Walter de Gruyter.

Compound Nucleus Reactions

Shapiro, M.M. (1943). Cross sections for the formation of the compound nucleus by charged particles. *Phys. Rev.* 90: 171.

Feshbach, H., Porter, C.E., and Weisskopf, V.F. (1954). Model for nuclear reactions with neutrons. *Phys. Rev.* 96: 448.

Friedman, F.L. and Weisskopf, V.F. (1955). The compound nucleus. In: *Niels Bohr and the Development of Physics* (ed. W. Pauli). New York: McGraw-Hill.

Dostrovsky, I., Fraenkel, Z., and Friedlander, G. (1960). Monte Carlo calculations of nuclear evaporation processes III. Applications to low-energy reactions. *Phys. Rev.* 116: 683.

Ericson, T. (1960). The statistical model and nuclear level densities. *Philos. Mag. Suppl.* 9 (36): 425.

Huizenga, J.R. and Moretto, L.G. (1972). Nuclear level densities. *Annu. Rev. Nucl. Sci.* 22: 427.

Brosa, U. and Grossmann, S. (1982). In the exit channel of nuclear fission. *Z. Phys.* A310: 177.

Feshbach, H. (1987). Small systems: when does thermodynamics apply? *Phys. Today* 40: 9.

High-Energy Nuclear Reactions

Serber, R. (1947). Nuclear reactions at high energies. *Phys. Rev.* 72: 1114.

Hudis, J. (1968). High-energy nuclear reactions. In: *Nuclear Chemistry*, vol. I (ed. L. Yaffee). New York: Academic Press.

Beg, K. and Porile, N.T. (1971). Energy dependence of the recoil properties of products from interaction of ^{238}U with 0.45–11.5 GeV protons. *Phys. Rev.* C3: 1631.

Bertini, H.W. (1972). Nonelastic interactions of nucleons and π mesons with complex nuclei at energies below 3 GeV. *Phys. Rev.* C6: 631.

Harp, G.D. (1974). Extension of the isobar model for intranuclear cascades to 1 GeV. *Phys. Rev.* C10: 2387.

Goldhaber, A.S. and Heckman, H.H. (1978). High-energy interactions of nuclei. *Annu. Rev. Nucl. Sci.* 28: 161.

Heavy-Ion Reactions

Kaufmann, R. and Wolfgang, R. (1961). Nuclear transfer reactions in grazing collisions of heavy ions. *Phys. Rev.* 121: 192.

Wilczinski, J. (1973). Nuclear molecules and nuclear friction. *Phys. Lett.* 47B: 484.

Schröder, W.U. and Huizenga, J.R. (1977). Damped heavy ion collisions. *Annu. Rev. Nucl. Sci.* 27: 465.

Olmi, A., Sann, H., Pelte, D. et al. (1978). Multiplicity of γ rays in the reactions ^{86}Kr-^{120}Sn and ^{86}Kr-^{166}Er. *Phys. Rev. Lett.* 41: 688.

Dakowski, M. (1979). *Proceedings of the International School in Physics "Enrico Fermi"*, Varenna, Italy.

Bass, R. (1980). *Nuclear Reactions with Heavy Ions*. Berlin: Springer-Verlag.

Glässel, P., Harrach, D.v., Specht, H.J., and Grodzins, L. (1983). Observation of proximity and non-equilibrium effects in ternary heavy ion reactions. *Z. Phys.* A310: 189.

Bromley, D.A. (ed.) (1984–1989). *Treatise on Heavy-Ion Science*, 8 vols. New York: Plenum Press.

Fröbrich, P. (1984). Fusion and capture of heavy ions above the barrier: analysis of experimental data with the surface friction model. *Phys. Rep.* 116: 337.

Blocki, J.P., Feldmeier, H., and Swiatecki, W.J. (1986). Dynamical hindrance to compound-nucleus formation in heavy-ion reactions. *Nucl. Phys.* A459: 145.

Pochodzalla, J., Möhlenkamp, T., Rubehn, T. et al. (1995). Probing the nuclear liquid–vapor phase transition. *Phys. Rev. Lett.* 75: 1040.

Blaich, Th., Kratz, J.V., Schmoll, R., and Wirth, G. (1996). Dynamical intermediate-mass fragment production in ^{197}Au + ^{197}Au collisions at energies $\leq$ 15 MeV/u. *Z. Phys.* A356: 49.

Zagrebaev, V. and Greiner, W. (2007). Shell effects in damped collisions: a new way to superheavies. *J. Phys. G: Nucl. Part. Phys.* 34: 2265.

13

Chemical Effects of Nuclear Transmutations

13.1 General Aspects

The chemical binding energies between atoms vary between about 40 and 400 kJ mol^{-1}, corresponding to about 0.4–4 eV (1 eV $\approx$ 96.5 kJ mol^{-1}). The energies involved in nuclear reactions are on the order of several megaelectronvolts, and parts of these energies are transmitted to the atoms in the form of recoil and excitation energy. Therefore, chemical bonds are strongly affected by nuclear transmutations. High kinetic energy of single atoms does not mean high temperature, because the temperature of a system is given by the mean kinetic energy of all the atoms or molecules, $E_{\text{kin}} = \frac{3}{2} k_{\text{B}} T$ (for three degrees of freedom). However, deviating from the usual concept of temperature, the temperature equivalent of a single particle may be related to its kinetic energy by the equation

$$T = E_{\text{kin}}/k_{\text{B}} = 1.16 \times 10^4 E_{\text{kin}} \quad (\text{K eV}^{-1}) \tag{13.1}$$

Because energies on the order of 1 eV^{-1} MeV are transmitted to the atoms by nuclear transmutations, corresponding to temperature equivalents on the order of 10^4–10^{10} K, these atoms are called "*hot atoms*" and their chemistry is called "*hot-atom chemistry*," or "recoil chemistry" if the recoil effects are considered.

Chemical effects of nuclear transmutations were first observed by L. Szilard and T.A. Chalmers in 1934 (Szilard and Chalmers 1934) when irradiating ethyl iodide with neutrons. They found several chemical species containing ^{128}I that are produced by the chemical effects of the nuclear reaction ^{127}I(n, γ)^{128}I. In the following years, the chemical effects of radioactive decay were observed in gaseous compounds, liquids, and solids. The chemical effects of nuclear reactions can be divided into primary effects taking place in the atom involved in the nuclear reaction, secondary effects in the molecules or other associations of atoms, and subsequent reactions. Primary and secondary effects are observed within about 10^{-11} seconds after the nuclear reaction.

Primary effects comprise recoil of the nucleus and excitation of the electron shell of the atom. The excitation may be due to recoil of the nucleus, change of atomic number Z, or emission of electrons from the electron shell. Secondary effects and subsequent reactions depend on the chemical bonds and the state of matter. Chemical bonds may be broken by recoil or excitation. In gases and liquids, mainly the

Nuclear and Radiochemistry: Fundamentals and Applications,
Fourth Edition. Jens-Volker Kratz.

bonds in the molecules are affected. The range of recoil atoms is relatively large in gases and relatively small in condensed phases (liquids and solids). Fragments of molecules are mobile in gases and liquids, whereas they may be immobilized in solids on interstitial sites or lattice defects and become mobile if the temperature is increased.

The chemical reactions taking place after nuclear reactions may be distinguished as "hot," "epithermal," and "thermal" reactions. Hot reactions proceed at high energies of the atoms in a statistical way, that is, without preference for certain bonds or reaction partners. In epithermal reactions, certain bonds or reaction partners are preferred, but the reactions exhibit unusual chemical features. Hot and epithermal reactions are comparable to reactions induced by ionizing radiation; ions and radicals play an important role. Thermal reactions proceed at relatively low energies (<1 eV) and are similar to chemical reactions observed at temperatures up to several hundred degrees Celsius. Recoiling atoms of high energy break their bonds, leave their position as ions, and give off their energy in a cascade of hot, epithermal, and thermal reactions.

The fraction of the atoms produced in a nuclear reaction and found in the form of the original chemical compound is called *retention*. Retention can be due to the nonbreaking of chemical bonds (primary retention) or to the breaking of bonds followed by recombination or substitution reactions (secondary retention).

13.2 Recoil Effects

The Q value of a nuclear reaction is shared between the reaction products according to the law of conservation of momentum

$$E_1 m_1 = E_2 m_2 \tag{13.2}$$

E_1 and m_1 are the energy and mass of the recoiling atom, and E_2 and m_2 are the energy and mass of the particle emitted in the course of the nuclear reaction. If the velocity of the emitted particle approaches the velocity of light, the increase of m_2 according to Eq. (1.16) has to be taken into account and the recoil energy E_1 is

$$E_1 = \frac{m_2^0}{m_1} E_2 + \frac{E_2^2}{2 m_1 c^2} \tag{13.3}$$

By inserting the nuclide masses M and the value of E_2 in MeV, the following relation is obtained:

$$E_1 = \frac{E_2}{M_1}(M_2 + 5.37 \times 10^{-4} E_2) \tag{13.4}$$

The second term in the parentheses on the right-hand side is negligible if $M_2 \geq 1$ u. In the case of emission of electrons or positrons, Eq. (13.4) becomes

$$E_1 = \frac{E_2}{M_1}(5.49 + 5.37 E_2) \times 10^{-4} \tag{13.5}$$

(M_1 in u, energies in MeV).

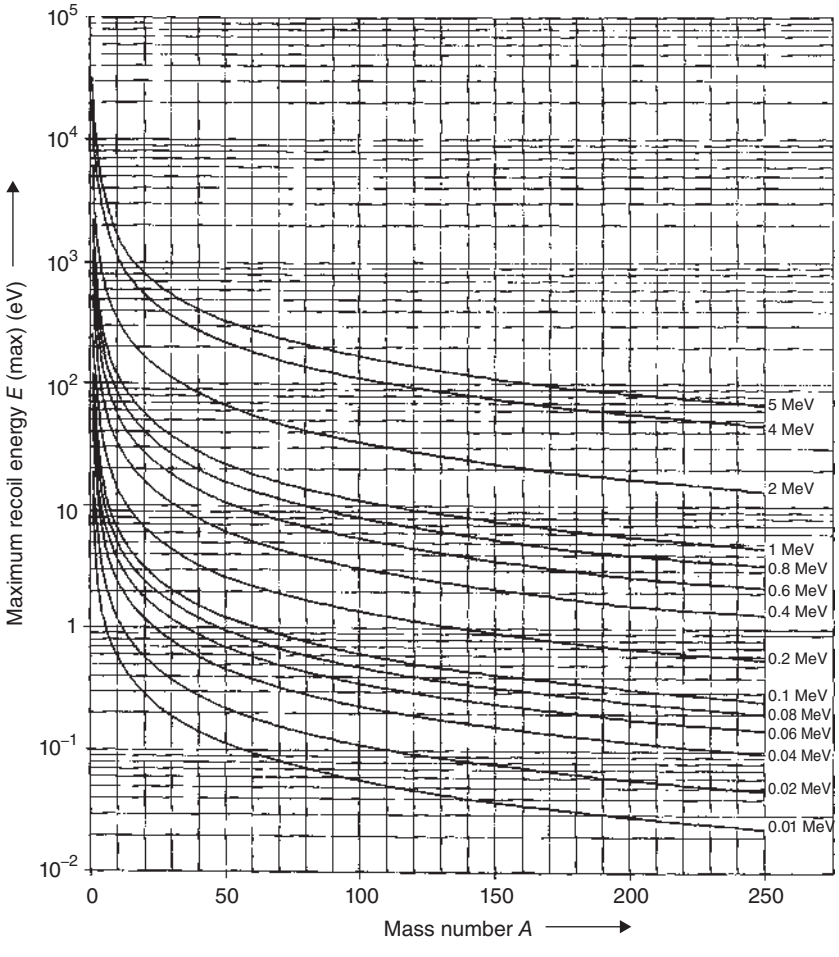

Figure 13.1 Recoil energy due to the emission of β particles as a function of the mass number for various energies of the β particles.

In Figure 13.1, the recoil energy for β decay is plotted as a function of the mass number for various energies of the β particles.

If a γ-ray photon is emitted, the law of conservation of momentum gives

$$m_1 v_1 = \frac{E_\gamma}{c} \tag{13.6}$$

and the energy of the recoiling atom is

$$E_1 = 5.37 \times 10^{-4} \frac{E_\gamma^2}{M_1} \tag{13.7}$$

(M_1 in u, energies in MeV).

The recoil energy for emission of γ-ray photons of various energies is plotted in Figure 13.2 as a function of the mass number.

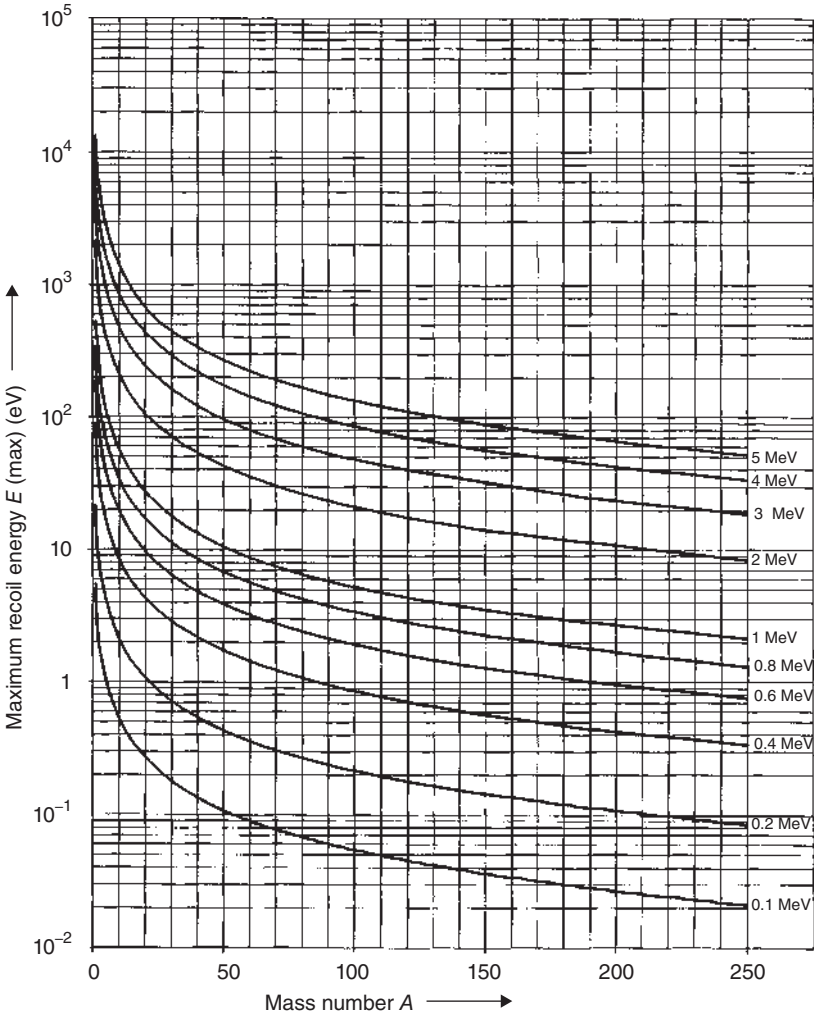

Figure 13.2 Recoil energy due to the emission of γ-ray photons of various energies as a function of the mass number.

Application of Eqs. (13.2)–(13.7) is illustrated by some examples:

a) *α decay of* ^{212}Po: The energy of the α particles is $E_2 = 8.785$ MeV, and the recoil energy is $E_1 = 0.169$ MeV. As the recoil energy due to α decay is always many orders of magnitude higher than the energy of chemical bonds, α decay will always cause breaking of chemical bonds.
b) β^- *decay of* ^{90}Sr: The energy of the β^- particles (electrons) varies between zero and the maximum value of 0.546 MeV. Together with the electron, an antineutrino $\overline{\nu}$ is emitted ($E_e + E_{\overline{\nu}} = 0.56$ MeV). The recoil energy of the daughter nuclide ^{90}Y depends on the masses of the electron and the neutrino and on the angle under which they are emitted (Figure 13.3). The maximum recoil

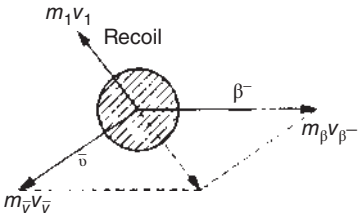

Figure 13.3 Recoil effect due to the emission of a β^- particle and an antineutrino.

energy calculated by Eq. (13.5) is $E_1(\max) = 5.11$ eV. This value is greater than the energy of chemical bonds. However, most frequently the recoiling atom will have only a part of $E_1(\max)$ and the chemical bonds may not be broken. Generally, the following statement can be made in the case of β decay: with decreasing energy of β decay, the probability increases that chemical bonds are not broken by recoil effects.

c) *Emission of γ-ray photons in isomeric transition*: In isomeric transition, only γ-ray photons are emitted – in the case of isomeric transition of ^{80m}Br, photons of 0.049 and 0.037 MeV. Equation (13.7) gives $E_1 = 0.016$ eV for the recoil energy due to emission of 0.049 MeV photons, which is not sufficient to break chemical bonds. This holds for all isomeric transitions in which low-energy photons are emitted.

d) *Emission of γ-ray photons immediately after α or β decay or emission of several γ-ray photons*: In this case, the recoil effects overlap as indicated in Figure 13.4.

e) *Emission of γ-ray photons in nuclear reactions*: The Q value of the exoergic reaction ^{37}Cl (n, γ)^{38}Cl is 6.11 MeV. By absorption of thermal neutrons, negligible amounts of kinetic energy are transmitted by the neutrons. The excitation energy is given off by emission of one or several γ-ray photons, and by applying Eq. (13.7), the maximum recoil energy due to the emission of one 6.11 MeV photon is calculated to be $E_1(\max) = 528$ eV. This energy is appreciably higher than the energy of chemical bonds, and even fractions of this energy resulting from the emission of several photons are high enough to break chemical bonds. Therefore, in most (n, γ) reactions, chemical bonds will be broken. In Szilard–Chalmers reactions, this recoil effect is used to separate isotopic product nuclides from target nuclides.

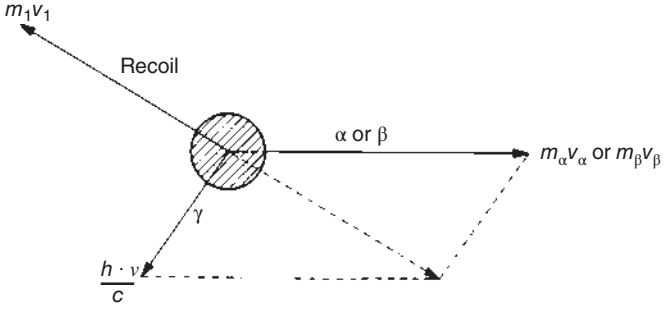

Figure 13.4 Recoil effect due to the simultaneous emission of an α or β particle, respectively, and a γ-ray photon.

f) *Emission of protons, neutrons, or α particles in nuclear reactions*: The Q value of the exoergic reaction $^{14}N(n, p)^{14}C$ is $\Delta E = 0.626$ MeV. If the kinetic energy of the neutrons is neglected, the Q value is shared among the reaction products, and from Eq. (13.2), it follows that

$$E_1 = \frac{m_2}{m_1}(Q - E_1) = 0.042 \text{ MeV}$$

This recoil energy is appreciably higher than the energy of any chemical bond. Generally, emission of protons, neutrons, or α particles leads to the breaking of chemical bonds.

Recoil energies due to emission of α particles, protons, neutrons, β particles, and γ-ray photons are listed in Table 13.1 for various mass numbers and various energies of the emitted particles. It is evident from this table that by emission of particles with $M \geq 1$, chemical bonds will be broken, whereas recoil energies due to emission of electrons, positrons, or γ-ray photons may be higher or lower than the energies of chemical bonds.

Table 13.1 Recoil energy due to emission of α particles, protons, neutrons, electrons, and γ-ray photons.

Energy of the particle emitted (MeV)	Mass number *A*	Recoil energy			
		α (keV)	p or n (keV)	β	γ
0.1	10	40	10	6.0 eV	0.54 eV
	50	8	2	1.2 eV	0.11 eV
	100	4	1	0.6 eV	0.05 eV
	200	2	0.5	0.3 eV	0.03 eV
0.3	10	120	30	21.3 eV	4.83 eV
	50	24	6	4.3 eV	0.97 eV
	100	12	3	2.1 eV	0.48 eV
	200	6	1.5	1.1 eV	0.24 eV
1.0	10	400	101	109 eV	53.7 eV
	50	80	20	22 eV	10.7 eV
	100	40	10	11 eV	5.4 eV
	200	20	5	5 eV	2.7 eV
3.0	10	1201	302	648 eV	483 eV
	50	240	60	130 eV	97 eV
	100	120	30	65 eV	48 eV
	200	60	15	32 eV	24 eV
10.0	10	4003	1008	5.92 keV	5.4 keV
	50	800	202	1.18 keV	1.1 keV
	100	400	101	0.59 keV	0.5 keV
	200	200	50	0.30 keV	0.3 keV

Effects similar to recoil effects are observed if nuclei are bombarded with high-energy projectiles. The momentum transmitted to the target nucleus results in a kinetic energy given by

$$E_1 = E_x \frac{M_x}{M_A + M_x} = E_x - E^* \text{ MeV} \tag{13.8}$$

where E_x is the energy of the projectile and E^* the excitation energy of the product nucleus. Neutrons, protons, or α particles with energies of about 1 MeV hitting a nucleus transmit energies on the order of several kiloelectronvolts up to several hundreds, with the result that chemical bonds are always broken. On the other hand, the energies transmitted by absorption of low-energy photons will not rupture chemical bonds.

13.3 Excitation Effects

Electron shells are influenced by nuclear transmutations in various ways:

- excitation due to recoil;
- excitation due to change of the atomic number;
- excitation due to electron capture or internal conversion.

These effects overlap and lead to ionization, emission of electrons from the electron shell, and fluorescence. They may cause secondary reactions in molecules and subsequent reactions of the ions or excited atoms or molecules produced by these effects.

If a nucleus suffers a recoil, parts of the electron shell, in particular valence electrons, may be stripped off and stay behind, resulting in ionization of the atom. This ionization depends on the recoil energy, the strength of the chemical bonds, and the state of matter. Ions carrying from 1 to about 20 positive charges have been observed.

α Decay leads to a decrease of the atomic number by two units, $Z' = Z - 2$, and causes an expansion of the electron shell, as illustrated in Figure 13.5 for the α decay of radioisotopes of Bi. Differences in the binding energies are marked for electrons in the inner shells. Furthermore, there are two surplus electrons after α decay. However, in the case of α decay, the excitation effects due to the change of the atomic number are relatively small compared to the recoil effects that have been discussed in the previous chapter, with the result that the recoil effects dominate.

In the case of β decay, on the other hand, the effects due to the change of the atomic number may be significant, in particular if the energy of the β particles is low. β^- decay leads to an increase in the atomic number by 1 unit, $Z' = Z + 1$, and to a contraction of the electron shell, as illustrated in Figure 13.6 for β^- decay of radioisotopes of Sr. Furthermore, one electron is missing after β^- decay. Immediately after β^- decay, all the electrons of the atom are at energy levels that are higher than those corresponding to the new atomic number, which means that all the electrons are in an excited state. The total excitation energy of the electron shell amounts to many electronvolts (e.g. 107 eV in the case of β^- decay of a radioisotope of tin [$Z = 50$]). It is

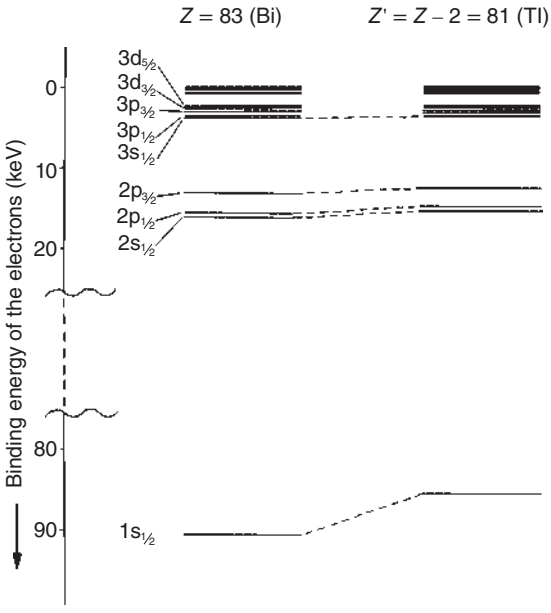

Figure 13.5 Expansion of the electron shell due to α decay.

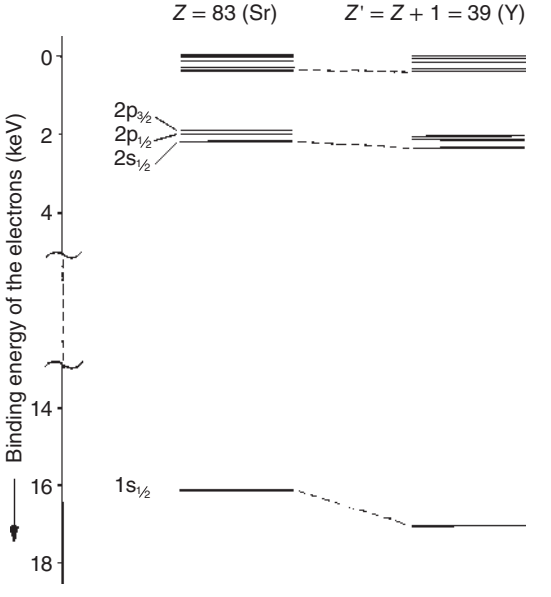

Figure 13.6 Contraction of the electron shell due to β^- decay.

given off by emission of electrons from the electron shell. These electrons are called *Auger* electrons. The remaining vacancies in the inner orbitals are filled by other electrons, and X-ray photons are emitted that are characteristic of the new atomic number.

In contrast to β^- decay, β^+ decay, just as α decay, leads to an expansion of the electron shell, the electrons take up energy from neighboring atoms, and the excitation effects discussed for β^- decay are not observed.

Another effect due to the change of the atomic number has to be considered in case of β decay, in particular if the recoil energy is lower than the energy of the chemical bonds. The chemical properties of the isobaric daughter nuclide resulting from β decay are, in general, different from those of the mother nuclide. If the recoil energy is not sufficient to break the chemical bonds, the daughter nuclide stays in the same position, but in an unusual chemical surrounding. Examples are

$$\begin{aligned} {}^{14}CH_3 - CH_3 &\overset{\beta^-(0.156)}{\rightarrow} ({}^{14}NH_3 - CH_3)^+ \\ &\rightarrow {}^{14}NH_3 + CH_3^+ \\ &\text{or} \rightarrow {}^{14}NH_2^+ + CH_4 \end{aligned} \tag{13.9}$$

and

$$\begin{aligned} {}^{35}SO_2Cl_2 &\overset{\beta^-(0.167)}{\rightarrow} \left({}^{35}ClO_2Cl_2\right)^+ \\ &\rightarrow {}^{35}ClO_2^+ + Cl_2 \\ &\text{or} \rightarrow {}^{35}ClO_2 + Cl_2^+ \end{aligned} \tag{13.10}$$

Occasionally, after β^- decay, the daughter nuclide is in a chemically stable state:

$${}^{212}Pb^{2+} \overset{\beta^-}{\rightarrow} {}^{212}Bi^{3+} \tag{13.11}$$

$${}^{14}CO \overset{\beta^-}{\rightarrow} {}^{14}NO^+ \tag{13.12}$$

With respect to the lifetime of the excited states resulting from changes in the atomic number, isothermal and adiabatic decay may be discussed. All the experimental results indicate an adiabatic decay, which means transfer of the excitation energy to all the electrons, resulting in a certain lifetime of the excited state of the daughter nuclide on the order of about 1 μs.

Ionization and excitation of daughter nuclides due to β^- decay have been proved by experimental results. For example, in the case of β^- decay of ^{85}Kr, 79.2% of the resulting ^{85}Rb was found in the form of Rb^+, 10.9% in the form of Rb^{2+}, and the remainder in the form of Rb ions with higher charges up to 10^+. Decay of ^3HH gives a yield of 90% $^3HeH^+$, and recoil effects cannot be responsible for formation of these ions, because the maximum recoil energy is 0.82 eV, whereas the ionization energy is ≈2 eV.

By electron capture (ε) or internal conversion, electrons are taken away from inner orbitals and the vacancies are filled with electrons from outer orbitals with resulting emission of characteristic X-rays. Electrons may also be emitted by an internal photoeffect. Finally, at least one electron is missing, and this may also cause breaking of the chemical bond. As electron capture leads also to a change of the atomic number ($Z' = Z - 1$), it is not possible to distinguish the effects due to the capture of an electron from those that are caused by the change of Z. In internal conversion, however, the atomic number is not changed, and the chemical effects observed in this case can be due either to recoil or to disappearance of the electron. With respect to the chemical effects, the isomeric transition of ^{80m}Br has been investigated in detail:

$${}^{80m}Br \overset{IT(0.049,0.037)}{\rightarrow} {}^{80}Br \tag{13.13}$$

The energies of isomeric transition are only 49 and 37 keV, and the conversion coefficients are 1.6 and ≈ 300, respectively. The recoil energy due to emission of a 49 keV γ-ray photon is only 0.016eV (Section 13.2). It is too low to break a C—Br bond (247 kJ ≈ 2.6 eV). The recoil energy due to emission of an electron from the 1s orbital (0.45 eV) is also too small to break the C—Br bond. Actually, breaking of the C—Br bond due to isomeric transition of ^{80m}Br is observed, for instance, if butyl bromide labeled with ^{80m}Br is shaken with water. In this experiment, the main fraction of ^{80}Br is found to be free of ^{80m}Br in the aqueous phase. Results of experiments with various compounds labeled with ^{80m}Br are compiled in Table 13.2. The high retention in the case of solid $(NH_4)_2[PtBr_6]$ is due to the fact that, in the solid state, the missing electron is quickly substituted.

The effects due to the vacancies in the inner orbitals after β^- decay, electron capture, or internal conversion can be summarized as follows. The vacancies are filled with electrons from outer orbitals and characteristic X-ray photons are emitted. These photons may transmit their energy or a part of their energy to electrons in the same electron shell by an internal photo- or Compton effect, respectively, and these electrons leave the atom as Auger electrons. The resulting vacancies are filled again with electrons from outer orbitals, and additional X-rays are emitted. This process is called *internal fluorescence*. The photons may again liberate Auger electrons by an internal photoeffect and so forth. The ratio of the number of Auger electrons to the number of photons emitted depends on the atomic number of the atom. The number of K X-rays emitted per vacancy in the K shell is called the fluorescence yield ω_K, and $1 - \omega_K$ is the Auger yield for the K shell. The fluorescence yields and the Auger yields for the K shell and the L shell are plotted in Figure 13.7 as a function of the atomic number Z.

The result of an Auger effect is always an ionization of the atom. For example, due to the isomeric transition of ^{131m}Xe, ions of ^{131}Xe are found to carry on average a charge of 8.5^+.

Table 13.2 Breaking of bonds due to internal conversion of ^{80m}Br.

Compound	Free ^{80}Br (%)	Retention (%)
HBr (g)	75	25
CF_3Br (g)	99	1
CH_3Br (g)	94	6
$CH_3Br + Br_2$ (l)	94	6
$CC1_3$ Br (g)	93	7
$CC1_3Br + Br_2$ (l)	87	13
$C_6H_5Br + Br_2$ (l)	87	13
$[Co(NH_3)_5Br]^{2+}$ (aq)	100	0
$[Co(NH_3)_5Br]\,(NO_3)_2$ (s)	86	14
$[PtBr_6]^{2-}$ (aq)	47	53
$(NH_4)_2\,[PtBr_6]$ (s)	0	100

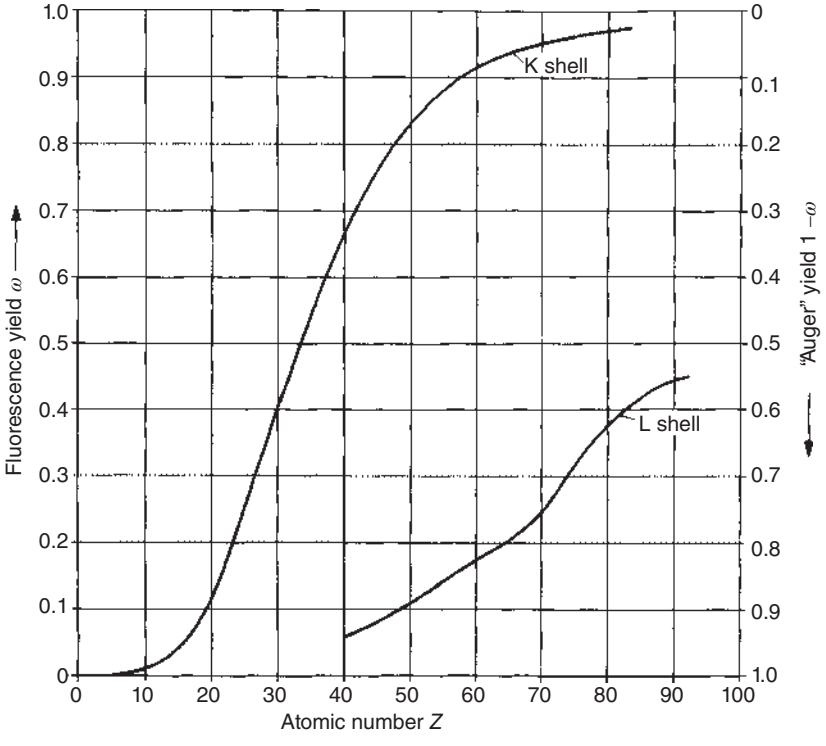

Figure 13.7 Fluorescence yield ω and "Auger" yield $1 - \omega$ for the K and L shells as a function of the atomic number. Source: Burshop (1952), figure 02 (p. 15)/Cambridge University Press.

13.4 Gases and Liquids

In gases and liquids, intramolecular bonds are only affected to a certain degree by the recoil due to a nuclear reaction occurring in an atom of a molecule or by the kinetic energy transmitted to an atom by an incident projectile. Molecules in gases and liquids are mobile, and the intermolecular binding forces are small, provided that the pressure is not too high.

The situation in a gas molecule is illustrated schematically in Figure 13.8. The effect of the recoil of the atom (1) on the bond between that atom and the rest of the molecule (R) depends on the direction of the recoil and the inertia of R. If the recoil of 1 is not in the direction toward R, the recoil energy E_1 is split up into the kinetic energy of the molecule and the energy E_B affecting the chemical bond:

$$E_1 = E_B + \frac{m_1 + m_R}{2} v_s^2 \tag{13.14}$$

Figure 13.8 Recoil effect in a gas molecule: x, particle or photon emitted; 1, nucleus suffering recoil; R, rest of the molecule.

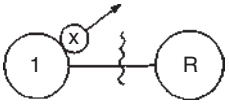

where v_s is the velocity of the center of gravity of the molecule. Application of the law of conservation of momentum gives

$$E_B = E_1 \left(1 - \frac{m_1}{m_1 + m_R}\right) = E_1 \frac{m_R}{m_1 + m_R} \tag{13.15}$$

This equation shows that the influence of the recoil on the chemical bond increases with the mass of the rest *R*.

If the recoil is in the direction toward *R*, part of the kinetic energy E_1 may be transformed by inelastic collision into excitation energy of the recoiling atom 1 and the rest *R*:

$$E_1 = E_1' + E_R + E_1^* - E_R^* \tag{13.16}$$

E_1' and E_R are the kinetic energies, and E_1^* and E_R^* the excitation energies of 1 and *R*, respectively. In this case, the effect of the recoil on the chemical bond depends on the kinetic energy E_R transmitted to *R* and on the excitation energies E_1^* and E_R^*.

If liquids are considered, intermolecular forces have to be taken into account. These forces cause a greater inertia of R, apparently greater values of m_R, and greater values of E_B (Eq. (13.15)). In the limiting case, the rest R is so strongly bound to neighboring molecules that $m_R \gg m_1$ and $E_B \approx E_1$.

Chemical effects of nuclear reactions in gases are preferably investigated by use of mass spectrometry. For example, radioactive decay of tritium in ^{3}H-labeled ethane leads to the formation of ethyl ions (≈80%) and fragments of ethane (≈20%). Because the recoil energy is too low to break C—C bonds, fragmentation of the ethane molecule must be due to excitation effects.

The charge distributions of the ions found after β^- decay of ^{133}Xe and after isomeric transition of ^{131m}Xe are plotted in Figure 13.9. The rather similar curves found for the ions of ^{133}Cs and of ^{131}Cs result mainly from excitation effects.

The observation that the decay of *T* in $C_6H_5CH_2T$ and in $C_6H_4TCH_3$ gives very similar spectra of products is explained by the fact that tropylium ions ($C_7H_7^+$) are formed as intermediates.

The chemical effects of nuclear reactions in liquids have been investigated in great detail with alkyl halides. As mentioned earlier, the first example was studied by Szilard and Chalmers in 1934. They irradiated ethyl iodide with neutrons and were able to extract about half of the ^{128}I produced by the nuclear reaction ^{127}I(n, γ)^{128}I into an aqueous phase. Similar results are obtained in the case of (d, p), (n, 2n), and (γ, n) reactions and other alkyl or aryl halides; appreciable amounts of the radioisotopes of iodine or other halogens obtained by these reactions can be extracted into aqueous solutions.

The chemical effects of the nuclear reaction ^{127}I(n, γ)^{128}I are explained as follows. In the first stage (primary effect), the chemical bond between ^{128}I and C is broken by the recoiling "hot" ^{128}I atom, which loses its energy in a sequence of collisions with other molecules ("hot reactions"). By these reactions, various fragments of the molecules are produced, which are difficult to detect because their concentration is extremely small and because they disappear quickly by subsequent

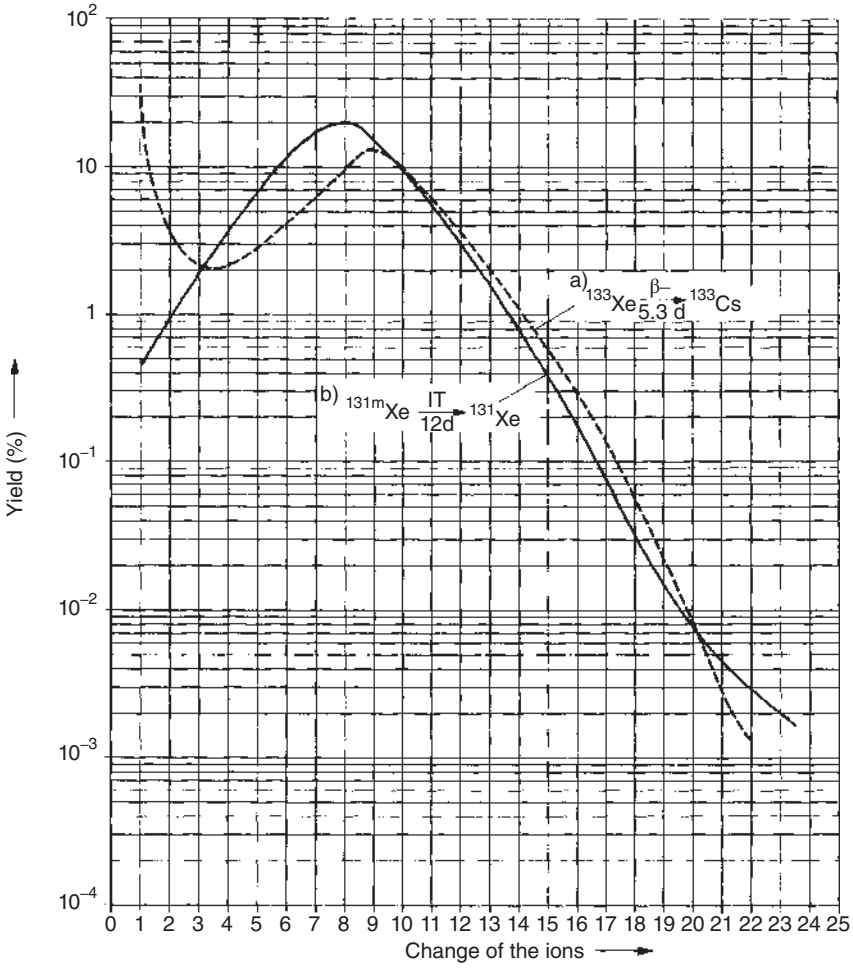

Figure 13.9 Charge distribution of the ions: (a) after β^- decay of ^{133}Xe; (b) after isomeric transition of ^{131m}Xe. Source: Snell et al. (1961), figure 04 (p. 50)/International Atomic Energy Agency/Public domain.

reactions. After the "hot" atom has given off the main part of its kinetic energy by hot and epithermal reactions, various thermal reactions are possible, in particular recombination or substitution reactions:

$$C_2H_5{}^{127}I + {}^{128}I\cdot \rightarrow C_2H_5\cdot + {}^{128}I\cdot + {}^{127}I\cdot \tag{13.17}$$

$${}^{127}I\cdot + {}^{128}I\cdot \rightarrow {}^{127}I^{128}I \tag{13.18}$$

$$C_2H_5\cdot + {}^{128}I\cdot \rightarrow C_2H_5{}^{128}I \tag{13.19}$$

$$C_2H_5{}^{127}I + {}^{128}I\cdot \rightarrow C_2H_5{}^{128}I + {}^{127}I\cdot \tag{13.20}$$

or, less frequently,

$$C_2H_5{}^{127}I + {}^{128}I\cdot \rightarrow CH_2{}^{128}ICH_2{}^{127}I + H\cdot \tag{13.21}$$

$$C_2H_5{}^{127}I + {}^{128}I\cdot \rightarrow CH_3CH^{127}I^{128}I + H\cdot \tag{13.22}$$

Free iodine produced by reaction (13.18) can be extracted. ^{128}I-labeled ethyl iodide is formed by reactions (13.19) and (13.20). The substitution products can be separated by gas chromatography.

The chemical effects observed after neutron irradiation of ethyl iodide have found great practical interest, because they allow general application to various compounds and chemical separation of isotopic products of nuclear reactions. In particular, isotopic nuclides of high specific activity can be obtained by Szilard–Chalmers reactions (Section 13.6).

For the investigation of "hot"-atom-induced reactions, the technique of scavenging is often applied. In this method, small amounts of reactive compounds (scavengers) are added, which react preferentially with atoms or radicals produced by the chemical effects of nuclear reactions. Whereas "hot" reactions are not influenced by the presence of scavengers, scavengers are highly selective in the range of thermal reactions.

13.5 Solids

In general, atoms or ions in solids are not mobile. They are bound rather strongly to neighboring atoms or ions, as indicated in Figure 13.10. The strong embedding of atoms in crystalline solids leads to an apparently high mass m_1. Two possibilities may be distinguished:

a) The momentum transmitted is high enough to break all bonds with neighboring atoms and the atom involved in the reaction is pushed out of its position in the lattice.
b) The momentum is too small for a rupture of chemical bonds, and the atom stays in its place without suffering a recoil ($m_1 \rightarrow \infty$, $E_1 \rightarrow 0$). Excitation energy transmitted to the atom will quickly be distributed among neighboring atoms in the lattice within about 10^{-11} seconds.

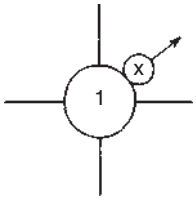

Figure 13.10 Recoil effect in a crystalline solid: x, particle or photon emitted; 1, atom bound in the solid.

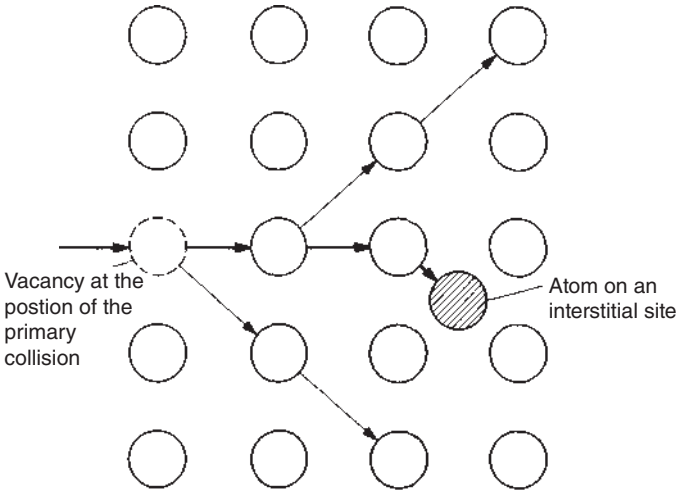

Figure 13.11 Generation of disorder in solids by a cascade of collisions (schematically).

At high recoil energies or high energies transmitted by incident particles or photons, the "hot" atoms collide with other atoms, pushing them from their lattice sites and producing a series of lattice defects (vacancies and atoms on interstitial sites), as indicated for a simple lattice in Figure 13.11. In the course of these subsequent reactions, the "hot" atom gives off its kinetic energy and stays on a lattice site or on an interstitial site. The range of a recoiling atom and the number of lattice defects produced depend on the recoil energy, the mass of the recoiling atom, and the density of the solid. The range of recoil atoms in aluminum is plotted in Figure 13.12 as a function of the recoil energy. This range is short after (n, γ) reactions (0.5–5 nm) and long after (n, α), (n, p), (d, p), and (γ, n) reactions (50–1000 nm). The lattice defects in the solid may cause remarkable changes in the properties of the solid (conductivity, volume, reactivity).

After the recoil atoms have come to rest, subsequent reactions are stopped. Further reactions including recombination of reactive atoms or molecular fragments are possible after diffusion of the reactive species or after dissolution of the solid. Diffusion can be enhanced by increasing the temperature (thermal annealing) or by irradiation with γ-rays or electrons (radiation annealing). Dissolution may lead to recombination, reaction with other species, or reaction with the solvent. Due to these processes, secondary retention may increase or decrease. As an example, the retention of ^{35}S in the form of sulfate after neutron irradiation of ammonium sulfate and dissolution is plotted in Figure 13.13 as a function of the time of thermal annealing at 180 °C. Major proportions of the ^{35}S atoms are found in the form of sulfur and of sulfite.

Because of the low concentrations of the products of primary and secondary reactions, their identification is only possible in some cases and by application of special techniques, such as Mössbauer spectroscopy, Section 14.4.

Table 13.3 Radioactive products found after nuclear reactions.

Irradiated compound	Nuclear reaction	Reaction products
Perchlorates	$^{37}Cl(n, \gamma)^{38}Cl$	ClO_3^-, Cl^-
Periodates	$^{127}I(n, \gamma)^{128}I$	I^-, IO_3^-
Chlorates	$^{37}Cl(n, \gamma)^{38}Cl$	Cl^-
Bromates	$^{79}Br(n, \gamma)^{80m}Br$ $^{81}Br(n, \gamma)^{82}Br$	Br^-, Br_2
Iodates	$^{127}I(n, \gamma)^{128}I$	I^-
Sulfates	$^{34}S(n, \gamma)^{35}S$	S, SO_3^{2-}, S^{2-}
Phosphates	$^{31}P(n, \gamma)^{32}P$	PO_3^- and others
Permanganates	$^{55}Mn(n, \gamma)^{56}Mn$	$Mn^{2+}(MnO_2)$
Chromates	$^{50}Cr(n, \gamma)^{51}Cr$	Cr^{3+}(mono-, bi-, and polynuclear)
Ferrocene	$^{58}Fe(n, \gamma)^{59}Fe$ $^{54}Fe(n, \gamma)^{55}Fe$	Fe^{2+}
Copper phthalocyanine	$^{63}Cu(n, \gamma)^{64}Cu$	Cu^{2+}

Source: Based on Müller (1967).

With respect to chemical separation of isotopic nuclides from target nuclides after (n, γ) reactions, changes in the valence state and of complexation are of special interest. Some examples are listed in Table 13.3. All nuclides produced by (n, γ) reactions are found in appreciable amounts in lower valence states and free from complexing ligands, respectively.

Several models have been put forward to explain the chemical effects of nuclear reactions in solids. Elastic collisions of the recoiling atom with surrounding atoms have been assumed by Libby (1947) in his billiard ball model: the "hot" atom loses its energy in steps, and after its last collision, it is in a reaction cage, from which it may either escape as a free atom if its energy is high enough or recombine with the fragments in this cage with resulting secondary retention. However, some experimental results cannot be explained by this model. In the "hot zone" model (Harbottle and Sutin 1959), distribution of the kinetic energy of the recoiling atom over neighboring atoms by collisions within about 10^{-11} seconds is assumed with the resultant formation of a molten hot zone in which chemical reactions (e.g. exchange and substitution reactions) take place. The molten zone cools down quickly and contains many dislocations. The disorder model (Müller 1967) has been developed for crystalline solids. In this model, the formation of a great number of dislocations is assumed instead of the formation of a hot zone.

The fact that atoms in crystalline solids do not suffer a recoil at low energies (<100 keV) of emitted or incident particles is made use of in Mössbauer spectroscopy (recoilless γ-ray resonance absorption; Section 14.4).

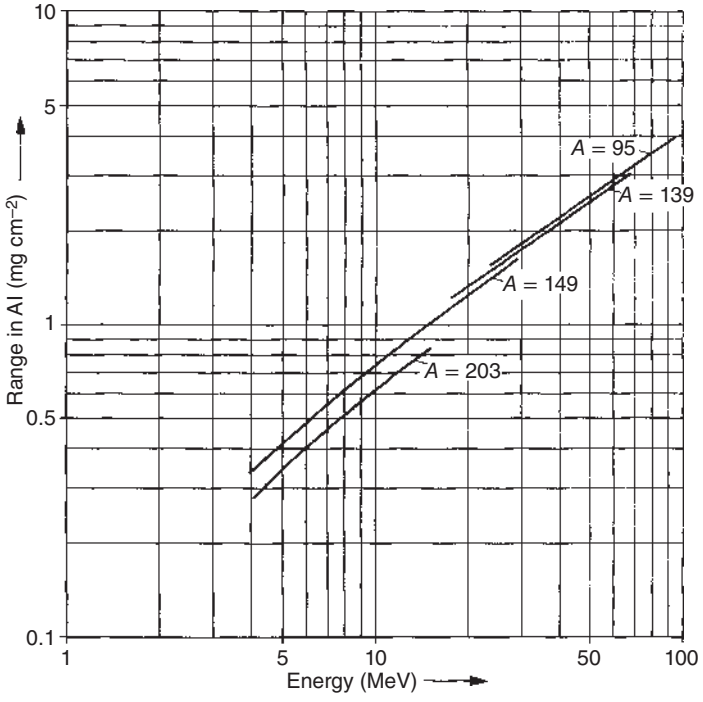

Figure 13.12 Range of recoiling atoms of various mass numbers *A* as a function of the recoil energy. Source: Adapted from Harvey (1960) and Alexander and Gazdik (1960).

Figure 13.13 Thermal annealing of ammonium sulfate: relative activity of ^{35}S in the form of sulfate (retention) as a function of the time of annealing at 180 °C.

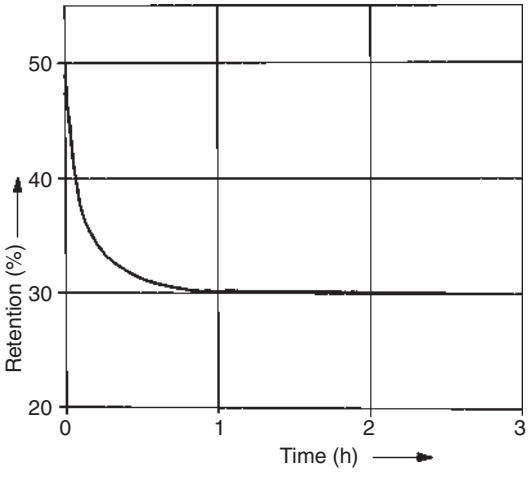

13.6 Szilard–Chalmers Reactions

The background of Szilard–Chalmers reactions has already been mentioned in Section 13.4. Isotopic nuclides produced by nuclear reactions can be separated by chemical methods from the target nuclides due to the chemical effects of the nuclear reactions, such as changes in the oxidation state or other changes of chemical bonds. The specific activity of the product nuclides may be high, but it depends on the degree of radiation decomposition of the compound containing the target nuclide. The possibility of separation of isotopic products from target nuclides by Szilard–Chalmers reactions is preferably used in the case of (n, γ) reactions, but it may also be applied for (γ, n), (n, 2n), and (d, p) reactions. If the product nuclide does not contain inactive isotopes, it is called "carrier-free." However, due to the ubiquity of stable elements and long-lived natural radioelements, the presence of small amounts of carriers must always be taken into account.

Szilard–Chalmers reactions are applicable to elements existing in different stable oxidation states or forming substitution-inert complexes. Exchange reactions between the oxidation states or with the complexes should not take place during irradiation and chemical separation, because they would cause a decrease in the specific activity. Therefore, substitution-labile complexes are not suitable.

Szilard–Chalmers reactions are characterized by the enrichment factor (i.e. the ratio of the specific activity of the radionuclide considered after separation to the average specific activity before separation) and by the yield (i.e. the ratio of the activity of the radionuclide obtained after separation to its total activity). Enrichment factors of up to about 1000 or more may be obtained, and yields of about 50–100% are of practical interest.

Examples of Szilard–Chalmers reactions are given in Table 13.4. Radionuclides of the halides may be obtained in high specific activities by neutron irradiation of alkyl or aryl halides or of the salts of the oxoacids. Radionuclides of other elements may also be produced in high specific activities by neutron irradiation of covalent compounds.

Szilard–Chalmers reactions are of special interest for the investigation of nuclear isomers, because they offer the possibility of separating isomeric nuclides.

13.7 Recoil Labeling and Self-labeling

Chemical effects of nuclear transmutations not only cause rupture of chemical bonds, but also lead to the formation of new chemical bonds, a result that may be used for the preparation of labeled compounds. Recoil labeling and self-labeling both involve radiation-induced reactions and also belong to the field of radiation chemistry.

Recoil labeling was first observed by A.F. Reid in 1934. After neutron irradiation of a mixture of ethyl iodide and pentane, ^{128}I-labeled amyl iodide was found. It is produced by substitution of an H atom by a "hot" ^{128}I atom.

Table 13.4 Yield and retention for some Szilard–Chalmers reactions.

Irradiated compound	Nuclear reaction	Yield (%)	Retention (%)
CH_3CH_2I	$^{127}I(n, \gamma)^{128}I$	54	46
$LiIO_3$		34	66
$NaIO_3$		33	67
KIO_3		33	67
NH_4IO_3		78	22
CH_2Br_2	$^{81}Br(n, \gamma)^{82}Br$	57	43
$CHBr_3$		53	47
$NaBrO_3$		90	10
$KBrO_3$		91	9
C_6H_5Cl	$^{37}Cl(n, \gamma)^{38}Cl$	65	35
$NaClO_3$		98	2
Li_2CrO_4	$^{50}Cr(n, \gamma)^{51}Cr$	34	66
Na_2CrO_4		26	74
$Na_2Cr_2O_7$		20	80
K_2CrO_4		39	61
$K_2Cr_2O_7$		10	90
$(NH_4)_2CrO_4$		82	18
$(NH_4)_2Cr_2O_7$		68	32
$LiMnO_4$	$^{55}Mn(n, \gamma)^{56}Mn$	91	9
$NaMnO_4$		91	9
$KMnO_4$		77	23
Na_3PO_4	$^{31}P(n, \gamma)^{32}P$	50	50
Na_2HPO_4		55	45
$Na_4P_2O_7$		42	58
Na_3AsO_3	$^{75}As(n, \gamma)^{76}As$	10	90
Na_2HAsO_4		40	60

Source: Based on Harbottle and Sutin (1959).

T- and ^{14}C-labeled compounds are of special interest in organic chemistry. T and ^{14}C can be produced with relatively high yields by the following reactions:

$$^{6}Li(n, \alpha)^{3}H \quad \sigma = 940\,b; \quad E_1(T) = 2.74\,MeV \tag{13.23}$$

$$^{3}He(n, p)^{3}H \quad \sigma = 5327\,b; \quad E_1(T) = 0.190\,MeV \tag{13.24}$$

$$^{14}N(n, p)^{14}C \quad \sigma = 1.81\,b; \quad E_1(^{14}C) = 0.042\,MeV \tag{13.25}$$

(E_1 is the recoil energy.) The range of tritium atoms produced by reaction (13.23) is relatively long (about 40 μm in organic compounds), and a heterogeneous mixture

of fine-grained organic substance and a lithium compound is suitable for labeling the compound. Reaction (13.24) may be used for T-labeling in the gaseous phase. For recoil labeling with ^{14}C by means of reaction (13.25), a homogeneous mixture is needed because of the short range of the ^{14}C recoil atoms.

Substantial disadvantages of recoil labeling are the multitude of labeled compounds produced and the radiation decomposition due to the "hot" recoil atoms and the incident radiation, which require careful chemical separation. Furthermore, the yield of a certain labeled compound is relatively small. For example, recoil labeling with ^{14}C leads to a great variety of substitution products in which any carbon atom in the molecule may be substituted by ^{14}C and products containing additional carbon atoms. These products due to substitution and the addition of carbon atoms contain about 0.1–10% of the ^{14}C produced. The remainder of the ^{14}C is found in the form of degradation products and polymers. Recoil labeling with T leads to the formation of simple compounds such as HT and CH_3T. The specific activity is limited by the radiation decomposition. Values on the order of about 10^{11} Bq g^{-1} may be obtained in the case of recoil labeling with T and values on the order of about 10^8 Bq g^{-1} in the case of recoil labeling with ^{14}C.

Self-labeling of organic compounds with tritium was first described in detail by K.E. Wilzbach and is also called *Wilzbach labeling*. In this method, the organic compound is stored together with tritium gas in a closed vial for about one week. Labeling proceeds by reactions with "hot" atoms and by radiation-induced reactions: on the one hand, the ions $^3HeT^+$ and T^+ produced by the decay of T_2 react with the organic compound; and on the other hand, the β^- particles emitted by T cause ionization of the organic compounds and formation of radicals followed by reaction with T_2. The radiation-induced reactions can be enhanced by the addition of a chemically inert β^- active radionuclide such as ^{85}Kr or by electric discharges.

For self-labeling with T, high partial pressures of tritium gas and gaseous or finely dispersed organic compounds are favorable. The products can be separated by gas chromatography or other chromatographic methods. Specific activities on the order of about 10^{12} Bq g^{-1} are obtained.

Self-labeling with ^{14}C by use of $^{14}CO_2$ or $^{14}C_2H_2$ is of little practical importance, because of the low specific activities of the products.

References

Alexander, J. and Gazdik, M.F. (1960). Recoil properties of fission products. *Phys. Rev.* 120: 874.

Burshop, E.H.S. (1952). *The Auger Effect and other Radiationless Transitions*. London: Cambridge University Press.

Harbottle, G. and Sutin, N. (1959). The Szilard-Chalmers reaction in solids. In: *Advances in Inorganic Chemistry and Radiochemistry*, vol. 1 (eds. H.J. Emeleus and A.G. Sharpe). New York: Academic Press.

Harvey, B.G. (1960). Recoil techniques in nuclear reaction and fission studies. *Annu. Rev. Nucl. Sci.* 10: 235.
Libby, W.F. (1947). Chemistry of energetic atoms produced in nuclear reactions. *J. Am. Chem. Soc.* 69: 2523.
Müller, H. (1967). Chemische Folgen von Kernumwandlungen in Festkörpern. *Angew. Chem.* 79: 128.
Snell, A.H., Pleasonton, F., and Carlson, T.A. (1961). *Chemical Effects of Nuclear Transformations*, Proceedings Series, vol. I, S. 147. Vienna: IAEA.
Szilard, L. and Chalmers, T.A. (1934). Chemical separation of the radioactive element from its bombarded isotope in the Fermi effect. *Nature* 134: 462.

Further Reading

McKay, H.A.C. (1950). The Szilard–Chalmers process. In: *Progress in Nuclear Physics*, vol. I (ed. O.R. Frisch). Oxford: Pergamon.
Willard, J.E. (1953). Chemical effects of nuclear transformations. *Annu. Rev. Nucl. Sci.* 3: 193.
Spinks, J.W.T. and Woods, R.J. (1964). *An Introduction to Radiation Chemistry*. New York: Wiley.
Harbottle, G. (1965). Chemical effects of nuclear transformations in inorganic solids. *Annu. Rev. Nucl. Sci.* 15: 89.
Wolfgang, R. (1965). Hot atom chemistry. *Annu. Rev. Phys. Chem.* 16: 15.
Maddock, A.G. and Wolfgang, R. (1968). The chemical effects of nuclear transformations. In: *Nuclear Chemistry*, vol. II (ed. L. Yaffe), 185. New York: Academic Press.
Stöcklin, G. (1969). *Chemie heiβer Atome, Chemische Reaktionen als Folge von Kernprozessen*, Chemische Taschenbücher, vol. 6. Weinheim: Verlag Chemie.
Baumgärtner, F. and Wiles, D.R. (1972). Radiochemical transformations and rearrangements in organo-metallic compounds. *Fortschr. Chem. Forsch.* 32: 63.
Newton, G.W.A. (1972). Chemical effects of nuclear transformations. In: *Radiochemistry*, Specialist Periodical Reports, vol. 1. London: The Chemical Society.
Carlson, T.A. (1975). *Photoelectron and Auger Spectroscopy*. New York: Plenum Press.
Glentworth, P. and Nath, A. (1975). Recoil chemistry of solids. In: *Radiochemistry*, Specialist Periodical Reports, vol. 2. London: The Chemical Society.
Urch, D.S. (1975). Nuclear recoil chemistry in gases and liquids. In: *Radiochemistry*, Specialist Periodical Reports, vol. 2. London: The Chemical Society.
Harbottle, G. and Maddock, A.G. (eds.) (1979). *Chemical Effects of Nuclear Transformations in Inorganic Systems*. Amsterdam: North-Holland.
Tominaga, T. and Tachikawa, E. (1981). *Modern Hot Atom Chemistry and Its Application*. Berlin: Springer-Verlag.
Matsuura, T. (ed.) (1984). *Hot Atom Chemistry*. Tokyo/Amsterdam: Kodansha/Elsevier.
Lieser, K.H. (1991). *Einführung in die Kernchemie*, 3e. Weinheim: Wiley-VCH.
Adloff, J.P., Gaspar, P.P., Imamura, M. et al. (eds.) (1992). *Handbook of Hot Atom Chemistry*. Tokyo/Weinheim: Kodansha/Wiley-VCH.

Adloff, J.P. and Guillaumont, R. (1993). *Fundamentals of Radiochemistry*. Boca Raton, FL: CRC Press.

Maddock, A.G. (1995). Radioactivity and the nuclear environment. *Radiochim. Acta* 70/71: 323.

Yoshihara, H.K. (1995). X-rays and radiochemistry. *Radiochim. Acta* 70/71: 333.

Wojnárovits, L. (2011). Radiation chemistry. In: *Handbook of Nuclear Chemistry*, 2e, vol. 3 (eds. A. Vertés, S. Nagy, Z. Klencsár, et al.), 1265. Berlin: Springer-Verlag.

Yoshihara, H.K. and Sekine, T. (2011). Hot atom chemistry. In: *Handbook of Nuclear Chemistry*, 2e, vol. 3 (eds. A. Vertés, S. Nagy, Z. Klencsár, et al.), 1333. Berlin: Springer-Verlag.

14

Influence of Chemical Bonding on Nuclear Properties

14.1 Survey

In Chapter 13, the chemical effects of nuclear transmutations were discussed. Conversely, the electronic structure, in particular chemical bonds, may also affect nuclear properties. However, because the binding energies of the electrons are smaller by a factor on the order of 10^3–10^6 than the binding energies of the nucleons, the influence of chemical bonding on nuclear properties is, in general, relatively small.

The most drastic change in the properties of a nucleus is obtained if all the electrons are stripped off, and such a nucleus, which is stable in the presence of its electron shell, may become unstable. This was discussed in Section 6.4. Special conditions exist if the nuclides have only one electron in their electron shell, for example, a nucleus of ^{238}U with one electron. The investigation of such "hydrogen-like" ions will give valuable information about quantum electrodynamics.

As far as the nuclei are concerned, low-energy excited states are most sensitive to changes in chemical bonding. This is the field of Mössbauer spectroscopy, which has become a very important tool for the investigation of chemical bonding. It will be discussed in Section 14.4.

Interaction between the magnetic field of the electrons and the nuclear spin is the basis for various techniques that are broadly applied in chemistry, atomic physics, nuclear physics, and solid-state physics. The magnetic field of the electrons is due to their spin and orbital angular momentum and is much larger than the magnetic field of the nucleus. Consequently, the nuclear spin is oriented in relation to the field produced by the electron shell. This leads to hyperfine spectra that can be resolved by means of optical spectrometers of very high resolution.

Nuclear magnetic resonance (NMR) is observed if an atom is placed in an external magnetic field of varying field strength B so that decoupling of J and I (the total angular momentum of the atom and the angular momentum of the nucleus) is obtained. The vector $\boldsymbol{\mu}_I$ of the nuclear magnetic moment precesses around the direction of the field in such a way that the components in the direction of the field are restricted to

Nuclear and Radiochemistry: Fundamentals and Applications,
Fourth Edition. Jens-Volker Kratz.

$$\boldsymbol{\mu}_I = g_I B_\mathrm{n} m_I \tag{14.1}$$

where g_I is the nuclear g-factor, B_n is the nuclear magneton, and m_I is the quantum number of the magnetic angular momentum. In the external field, the states with different m_I have slightly different energies. The potential magnetic energy of the nucleus is given by

$$E_\mathrm{magn} = -\boldsymbol{\mu}_I \mathbf{B} = -g_I B_\mathrm{n} m_I B \tag{14.2}$$

and the energy spacing between two adjacent levels with $m_I = \pm 1$ is

$$\Delta E = g_I B_\mathrm{n} B \tag{14.3}$$

These relations can be used to calculate the nuclear magnetic moment if I is known, or vice versa. The nuclear field experienced by the nucleus is not exactly equal to the external field because of the shielding effect of the electron shell, which depends on the electron structure. Although this shielding effect is very small, it can easily be measured by use of NMR spectrometers.

NMR techniques are broadly applied in chemistry, but the interactions between nuclear magnetic moment and the electronic structure including the NMR techniques are not discussed here in detail because they are not considered to be part of nuclear chemistry.

14.2 Dependence of Half-Lives on Chemical Bonding

As already mentioned, changes of *transmutation* properties are observed if electrons of the electron shell are involved in the transmutations, as in the case of electron capture (ε) or in the emission of conversion electrons (e^-). The rate of both processes depends on the electron density at the nucleus. Consequently, the half-life of electron capture and the probability of emission of conversion electrons vary to a small degree with the number and the distribution of the electrons, in particular K electrons, in the electron shell.

An influence of chemical bonding on the half-life of electron capture has been measured for light nuclides such as ^{7}Be. In metallic ^{7}Be, the density of the ls electrons at the nucleus is somewhat higher than in $^7Be^{2+}$ ions. The relative changes of the decay constants of ^{7}Be in various compounds compared to that in metallic ^{7}Be are listed in Table 14.1. It is seen that the relative changes are generally below the 1% level. The data scale linearly with the electron densities at the nucleus in the various compounds. A world record is achieved with the half-lives of ^{7}Be inside C_{60} fullerenes (^{7}Be@C_{60}) at $T = 5$ and 293 K, which are 52.47 ± 0.04 and 54.65 ± 0.04 days as compared to the half-life of ^{7}Be in Be metal which is 53.25 ± 0.04 days. In these studies, ^{7}Be recoils from nuclear reactions were implanted in fullerenes. After irradiation, the sample was dissolved in CS_2 and filtered through a Millipore filter to remove insoluble material. The soluble fraction was fed onto a chromatographic column containing pentabromobenzyl groups on an inert support, and elution curves were recorded with a γ-ray spectrometer to detect the 478 keV quanta in the decay

Table 14.1 Relative changes of the decay constants of ^{7}Be $(\Delta\lambda/\lambda) \cdot 100$ (%) compared to that of ^{7}Be in Be metal for various compounds of ^{7}Be.

Compound	$(\Delta\lambda/\lambda) \cdot 10^2$ (%)
$^{7}Be@C_{60}$ (5 K)	+1.49
$^{7}Be@C_{60}$ (293 K)	+0.99
$^{7}Be_4O(CH_3COO)_6$	+0.058
$[^{7}Be(H_2O)_4]^{2+}$	+0.023
^{7}Be metal	±0
^{7}BeO	−0.014
$^{7}BeF_2$ hexagonal	−0.078
$^{7}Be(C_5H_5)_2$	−0.094
$^{7}BeF_2$ amorphous	−0.12
$^{7}BeBr_2$	−0.16

of ^{7}Be and a UV detector to follow the elution of the fullerenes. A clear correlation between the γ counting rate and the UV chromatogram of the fullerenes indicated that the endohedral $^{7}Be@C_{60}$ eluted in the fullerene position showing that the atom-doped fullerene was indeed produced by nuclear recoil implantation. Using quantum-chemical calculations of the electron densities at the ^{7}Be nucleus position inside the C_{60}, the relatively large changes in the half-lives could be reproduced.

Application of external pressure also leads to an increase of the decay constant of ^{7}Be: $\Delta\lambda/\lambda \approx 2.2 \cdot 10^{-5}$ per kilobar for ^{7}BeO.

An influence of chemical bonding on the emission of conversion electrons has been observed for ^{99m}Tc, ^{90m}Nb, ^{125m}Te, and ^{235m}U. ^{99m}Tc ($t_{1/2}$ = 6.0 hours) decays in 0.8% directly from the metastable state at 142.66 keV into the ground state ^{99}Tc ($t_{1/2} = 2.13 \cdot 10^5$ years) and in 99.2% via an excited state at 140.49 keV. The 2.17 keV transition is practically fully converted by emission of electrons from the M and N shells which are involved in chemical bonding. Correspondingly, changes $\Delta\lambda/\lambda$ of about 10^{-3} have been observed for Tc metal, Tc_2S_7, and $KTcO_4$.

Relatively large effects have been found for ^{235m}U ($t_{1/2}$ = 26.1 minutes). The energy of the isomeric state is 68 eV higher than that of the ground state of ^{235}U. At these low energy differences, only conversion of electrons in the 6s, 6p, 5f, 6d, and 7s orbitals is possible, and because these electrons are engaged in chemical bonding, an appreciable influence of chemical bonding on the probability of isomeric transition is to be expected. Accordingly, $\Delta\lambda/\lambda \approx 0.3\%$ has been found for ^{235m}UC compared to ^{235m}U metal and ≈10% for $^{235m}UO_2$ ($t_{1/2}$ = 24.7 minutes) compared to ^{235m}U implanted in Ag ($t_{1/2}$ = 27.1 minutes).

An influence of temperature on the probability of transmutation of *nuclear isomers* is expected at temperatures of several hundred million kelvin, but these influences have not yet been measured.

14.3 Dependence of Radiation Emission on the Chemical Environment

The emission of K_α- and K_β-X-rays after electron capture depends on the electron density in the 2p and 3p orbitals, respectively. If these orbitals are affected by changes in chemical bonding, the ratio of the intensities of K_α- and K_β-X-rays may also change. For instance, in the case of ^{51}Cr, this ratio is about 10% higher for Cr(VI) compared to Cr(0).

Changes in the angular correlation between particles or γ-rays emitted in immediate succession have been observed for some nuclides. These nuclides have a magnetic moment and an electric quadrupole moment which interact with the surrounding field. If this field is influenced by variations in chemical bonding, the angular correlation may also be affected. In Section 6.7.4, we introduced the method of γγ correlations and pointed out that either or both of these nuclear moments will interact with the existing fields in the substance containing the intermediate nucleus and will cause the angular momentum vector to precess about the local field direction. This requires that, in order to measure a perturbation of the angular correlation, the condition $\tau > \hbar/E$ must be fulfilled, where τ is the mean lifetime of the intermediate state and E is the interaction energy of the nuclear moment with the local field. The critical lifetime is on the order of 10^{-11} seconds. For the resulting perturbed angular correlations (PACs), the correlation function exhibits a time dependence given by

$$W(\Theta, t) = A_k G_k(t) P_k(\cos\Theta) \tag{14.4}$$

Here, G_k is the perturbation factor carrying all the information about interactions of the intermediate state with the extranuclear environment. At $t = 0$, $G_k(t) = 1$. The experimental arrangement for the determination of an angular correlation involves the measurement of a coincidence rate as a function of the angle defined by the two detectors and the source. To measure time-dependent perturbations, it is necessary to measure the coincidence rate as a function of time after emission of the first transition. The most commonly used source in PAC studies is 42.4 days ^{181}Hf. Other sources that have been widely used are 2.83 days ^{111}In, 48.6 minutes ^{111m}Cd, and 7.45 days ^{111}Ag, all of which populate the 121 ns, 247 keV state ($5/2^+$) in ^{111}Cd. One area in which the PAC technique has been quite successful is the study of macromolecules in solution to determine rotational correlation times, conformation changes, binding constants, metal–protein interactions, and the chemical structure of metal-ion binding sites on proteins. The in vivo mode of the technique makes it possible to observe directly chemical changes in living organisms: for example, it has been shown with PAC that $^{111m}Cd^{2+}$ binds at the active region (the Zn^{2+} position) of the enzyme carbonic anhydrase. This provided evidence that PAC reflects the effective molecular rotational correlation time at the metal binding site and thus ^{111m}Cd can be used as a "rotational tracer" to label biological macromolecules.

More recently, at heavy-ion accelerators such as Vicksi in Berlin, the PAC technique has been replaced by implantation of polarized nuclei into condensed matter. In heavy-ion fusion reactions such as ^{181}Ta(^{14}N, 5n)^{180}Hg, the angular momentum

vectors of the evaporation residues are automatically oriented perpendicular to the beam axis (alignment). By making use of their recoil momentum, these evaporation residues are implanted into the condensed matter to be investigated. The slowing-down process takes about 10^{-12} seconds. If the lifetime of excited states in the evaporation residue that decay by γ-ray emission is more than 10^{-8} seconds, it is sufficient to detect hyperfine interactions with the chemical environment. To detect magnetic fields, probes with a magnetic moment are used. To detect electric field gradients, probes with an electric quadrupole moment are being used. The experimental arrangement is schematically indicated in Figure 14.1. A pulsed heavy-ion beam hits the target and the produced probes are stopped inside the substrate. The anisotropic γ radiation is detected by two detectors. A transverse magnetic field causes a precession of the probes (γ spin rotation, γSR) visible in the time spectra shown in the middle part of Figure 14.1. One observes clearly the intensity modulation superimposed on the exponential decay. In the lower part, the γSR spectrum is shown as it is produced by division of the two time spectra. The frequency reflects the strength of the magnetic hyperfine interaction, which is a measure of the magnetic hyperfine field. The decreasing amplitude is a measure of the number of oriented nuclear probes, and the damping is due to relaxation phenomena (spin fluctuations) caused by radiation damage, molecular motion, and diffusion. Figure 14.2 shows the γSR spectrum due to an electric hyperfine interaction measured during implantation of ^{125}Xe in Cd. Here, several frequencies are superimposed producing a complex structure; this is because each spin has its own frequency. Figure 14.3 results from the implantation of probes of Cd, In, Sn, Sb, I, and Xe in Cd and shows the dependence of the deduced electric field gradient as a function of the filling of the sp shell. Elements below Sb see in Cd a positive electrical field gradient, elements above Sb see a negative field gradient; at Sb, the shell is half occupied. Magnetic γSR spectra in metals and nonmetallic compounds of the same element show different Lamor frequencies named "Knight shift." In metals, the frequencies are higher by about 1% because of the magnetic shift by an additional magnetic field at the nucleus caused by s electrons in the conduction band. Conversely, p electrons can cause a negative contribution to the Knight shift. Our examples in Figure 14.4 are the γSR spectra of ^{210}At in liquid and solid Bi. In liquid Bi, a positive Knight shift is observed, in solid Bi a negative Knight shift. This is indicative of a temperature-dependent change of the electron configuration.

Another probe of the chemical environment is positron annihilation. The energy corresponding to the annihilation of a positron and electron is usually released in the form of two γ quanta, although a very much rarer mode involving the emission of three quanta is also known. The two-quantum annihilation occurs after the positron has been slowed down to thermal energies ($5 \cdot 10^{-12}$ seconds). Momentum conservation demands that the two γ quanta have equal and opposite momenta; each carries off an energy of $mc^2 = 511\,\text{keV}$. The chemical environment can grossly affect the mean lifetime of the positron as well as the fraction of the annihilations that emit three photons instead of two. The slowed positrons collide thermally with electrons and have an annihilation probability that depends on the relative orientation of the spins of the positron and of the electron: annihilation of the singlet state (opposed

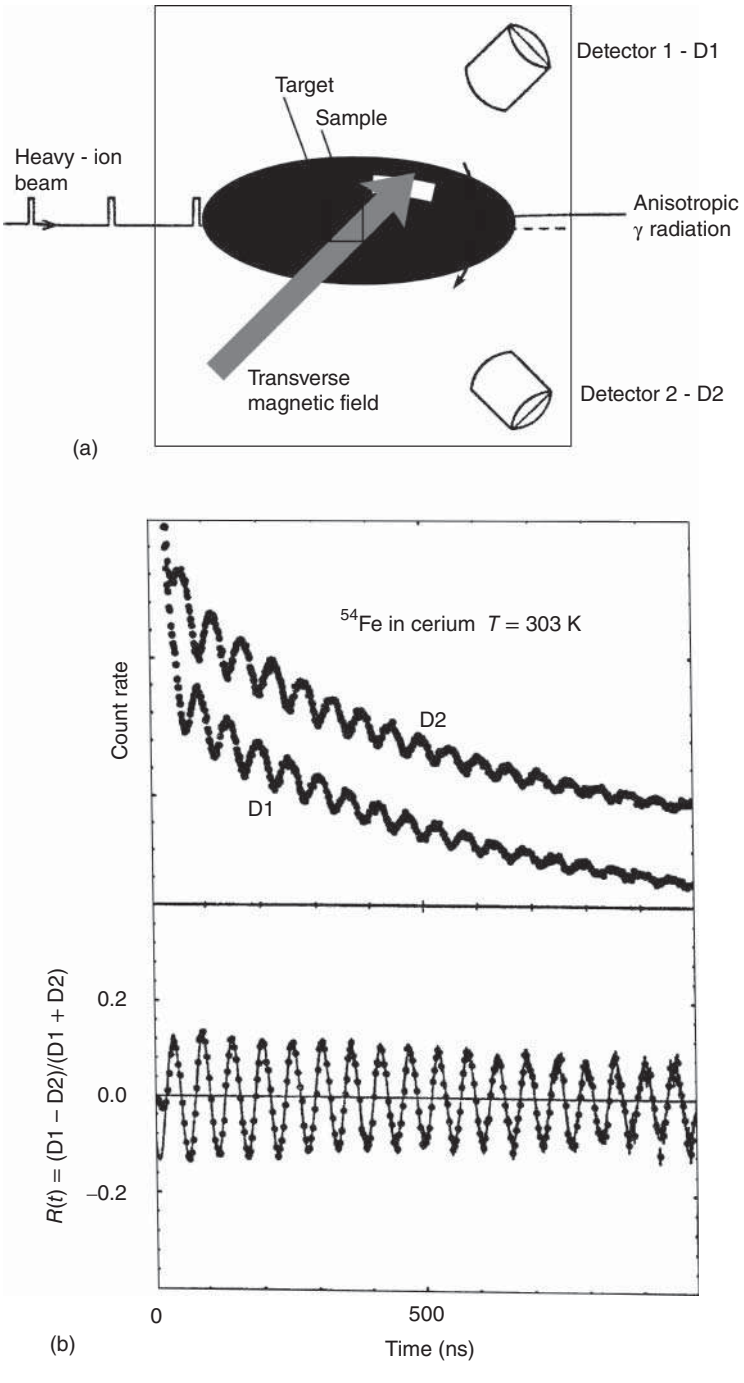

Figure 14.1 (a) A pulsed heavy-ion beam hits a target and the polarized probe nuclei produced by a fusion reaction are implanted in the condensed matter substrate. The anisotropic γ radiation is measured by two detectors. Middle: the two time spectra of the two detectors are shown. An intensity modulation superimposed on the exponential decay of the signal can be clearly seen. (b) The magnetic γSR (γ spin rotation) spectrum obtained by division of the two time spectra.

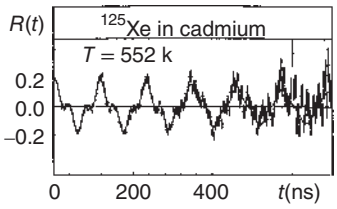

Figure 14.2 Example of a γSR spectrum caused by electrical hyperfine interaction.

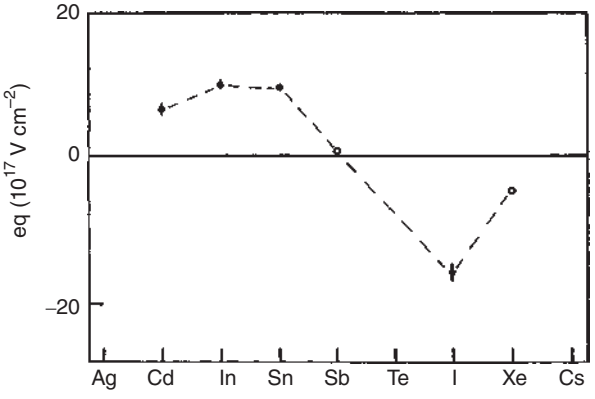

Figure 14.3 Various probe nuclei of the elements Cd, In, Sn, Sb, I, and Xe were implanted into Cd, and the electric field gradients deduced from the respective γSR spectra are plotted as a function of the filling of the sp shell.

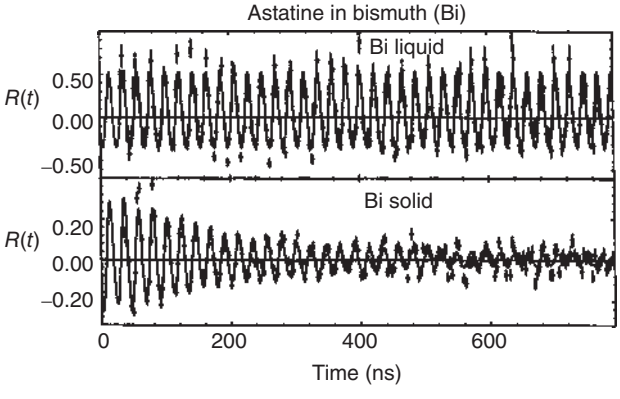

Figure 14.4 Example of the "Knight shift" between the Lamor frequencies in a metal and a non-metallic compound of the same element: magnetic γSR spectra of ^{210}At in Bi; by counting the periods, one can see that in liquid Bi, a higher field acts at the location of the probe nucleus than in metallic Bi.

spins) is about 1115 times more probable than annihilation of the triplet state (parallel spins). Moreover, because each photon must be emitted with at least $1\hbar$ of angular momentum and has only two states of polarization, annihilation in the singlet state gives two photons, whereas that in the triplet state gives three. It is this difference in multiplicity that causes the large difference between the probabilities of singlet and

triplet annihilation. If the relative spins of the positron and electron were randomly oriented in each collision, the triplet-state collisions would be three times as frequent as singlet-state collisions and the ratio of two-photon to three-photon annihilation would be $1115/3 = 372$.

It is also possible that the collision of a thermalized positron and an electron leads to the formation of a bound system, an atom of positronium (e^+e^-), before annihilation occurs. Positronium, Ps, is a light isotope of hydrogen with half the reduced mass and half the ionization potential (6.8 eV) and twice the Bohr radius. If Ps were left undisturbed after being formed, there would be three times more triplet Ps (*ortho*-Ps) than singlet Ps (*para*-Ps). And since the lifetime for annihilation of the *para*-Ps is about 10^{-10} seconds and that for *ortho*-Ps is about 10^{-7} seconds, one-quarter of the annihilation would occur with a mean lifetime of 10^{-10} seconds and three-quarters with 10^{-7} seconds. In the absence of Ps formation, the mean lifetime would be 10^{-10} seconds with no long-lived component. Thus, the longer mean lifetime for annihilation proved the existence of Ps. Interestingly, the formation probability of Ps depends on the stopping medium. Ps is formed 36% of the time in water and 57% in benzene; the remainder annihilates in collisions as free positrons. This is understood when it is realized that a positron must have at least an energy of $V - 6.8$ eV to form Ps with an electron from a molecule of ionization potential V. If the energy is much higher than V, the collision leads merely to ionization of the molecule without the formation of Ps. Since previous collisions are likely to leave the positron with an energy between zero and V, an upper limit to the probability of positronium formation may be close to $6.8/V$. Because the formation rate of Ps may be inhibited by interactions between the positron and substrate molecules, chemical information can be obtained from the formation process. However, it is from the *reactions* of *ortho*-Ps that the most useful information about the chemical environment may be obtained. Its lifetime can be quenched by interaction with the substrate molecules. Three main processes are shortening the o*rtho*-Ps lifetime resulting in rapid two-photon annihilation. These are (i) electron pickoff in which a bound Ps annihilates with an electron other than the one to which it is bound; (ii) spin conversion from triplet Ps (ortho) to singlet Ps (para) states in the presence of external magnetic fields or paramagnetic species, for example,

$$^{T}\mathrm{Ps}(\uparrow\uparrow) + \mathrm{NO}(\downarrow) \rightarrow \mathrm{NO}(\uparrow) + {}^{S}\mathrm{Ps}(\uparrow\downarrow) \rightarrow \mathrm{NO}(\uparrow) + 2\gamma$$

and (iii) chemical reactions with the substrate molecules. These can be demonstrated with the following examples:

Addition reactions $\mathrm{Ps} + (\mathrm{CF_3})_2\mathrm{NO} \rightarrow (\mathrm{CF_3})_2\mathrm{NO} \cdot \mathrm{Ps} \rightarrow 2\gamma$
Exchange reactions $\mathrm{Ps} + \mathrm{Cl_2} \rightarrow \mathrm{Cl} + \mathrm{PsCl} \rightarrow 2\gamma$
Oxidation reactions $\mathrm{Ps} + \mathrm{Fe^{3+}} \rightarrow \mathrm{Fe^{2+}} + \mathrm{e^+} \rightarrow 2\gamma$
Reduction reactions $\mathrm{Ps} + \mathrm{e^-} \rightarrow \mathrm{Ps^-} \rightarrow 2\gamma$

In each case, the Ps senses a more electron-rich environment leading to its annihilation. The outcome is a shortened lifetime and the chemical information comes from the determination of the rate of conversion of the long-lived *ortho*-Ps to either

the short-lived *para*-Ps or free positrons because this rate is related to the electron density in the medium.

Positrons are usually obtained from a ^{22}Na source. ^{22}Na emits a 1.28 MeV γ-ray after β^+ decay. The positron annihilation lifetime is deduced from the time delay between the 1.28 MeV photon and one of the 511 keV annihilation γ-rays. The decay curve is resolved into two components. The shorter-lived component is from the decay of free positrons, *para*-Ps, and reacting *ortho*-Ps. The longer-lived component is due to thermalized *ortho*-Ps. A quantitative kinetic description of *ortho*-Ps conversion has been used to calculate the chemical rate constants for reactions between Ps and various substrates. The reaction of *ortho*-Ps (σ-Ps) with a diamagnetic substrate M can be written

$$2\gamma \overset{\lambda_p}{\leftarrow} o-\mathrm{Ps} + \mathrm{M} \underset{k_2}{\overset{k_1}{\rightleftharpoons}} \mathrm{PsM} \overset{\lambda_c}{\rightarrow} 2\gamma \tag{14.5}$$

where k_1 and k_2 are the rate constants for formation and decomposition of the complex PsM, λ_c is the rate constant for positronium annihilation in the complex, and λ_p is the rate constant for positronium annihilation with the solvent. This assumes that, even if oxidation of Ps takes place, PsM complex formation is the rate-limiting step. A set of kinetic equations can be solved for these reactions, allowing the calculation of the time-dependent 2γ rate ($R_{2\gamma}$) from lifetime measurements:

$$R_{2\gamma} = A\exp(-\lambda_1 t) + B\exp(-\lambda_2 t) \tag{14.6}$$

Here, A and B are scaling factors and λ_1 and λ_2 are the decay constants for the short- and long-lived components of the experimental decay curve, respectively. λ_2 can be expressed in terms of the constants defined in Eq. (14.5):

$$\lambda_2 = \lambda_p + \frac{k_1\lambda_c}{k_2+\lambda_c}[\mathrm{M}] \tag{14.7}$$

For dilute solutions, λ_p approximately equals λ_2 (measured in pure solvent); thus the observed rate constant, $k_{obs} = k_1\lambda_c/(k_2+\lambda_c)$ in Eq. (14.7), can be written as

$$k_{obs} = \frac{\lambda_2 - \lambda_p}{[\mathrm{M}]} \tag{14.8}$$

The reactivity of Ps with a number of diamagnetic compounds is given in Table 14.2. It can be concluded that compounds having high electron affinities show strong reactivity with Ps. Another area in which positronium annihilation is used to great advantage is the study of vacancies in solids. In a perfect lattice, Ps is delocalized. On the other hand, Ps tends to localize lattice defects as regions of low electron density. This results in a measurable decrease in the annihilation rate. Applications are studies of the annealing of radiation damage and of the temperature and pressure dependence of equilibrium vacancy concentrations in metals.

The muon is another particle that is useful as a chemical probe in condensed matter. It interacts with nuclei through the electromagnetic field and its creation and decay occur through events in which parity is not conserved. It is formed in the decay

Table 14.2 Reactivity of various compounds with thermal positronium.

Strong interaction $k_{obs} > 10^8\ M^{-1}\ s^{-1}$	Weak interaction $k_{obs} < 10^8\ M^{-1}\ s^{-1}$
Nitroaromatics	Simple aliphatic or aromatic hydrocarbons: alkanes, benzene, anthracene, etc.
Quinones	
Maleic anhydride	Aniline, phenol, haloalkanes
Tetracyanoethylene	Halobenzenes, aliphatic nitro compounds
Halogens	Phthalic anhydride, benzonitrile
Inorganic ions in solution ($E_0 > -0.9$ eV)[a)]	(Diamagnetic) inorganic ions in solution ($E_0 < -0.9$ eV)
Organic ions in solution	

a) E_0 is the standard redox potential.

of the π meson which is created in high-energy nuclear collisions, for example, by cosmic radiation in the Earth's atmosphere:

$$\begin{aligned} \pi^+ &\rightarrow \mu^+ + \nu_\mu \\ \pi^- &\rightarrow \mu^+ + \bar{\nu}_\mu \end{aligned} \qquad t_{1/2} = 2.6 \cdot 10^{-10} \text{ seconds}$$

Subsequently, the muon decays into an electron, a neutrino, and an antineutrino:

$$\begin{aligned} \mu^+ &\rightarrow e^+ + \nu_e + \bar{\nu}_\mu \\ \mu^- &\rightarrow e^- + \bar{\nu}_e + \nu_\mu \end{aligned} \qquad t_{1/2} = 1.5 \cdot 10^{-6} \text{ seconds}$$

Non-conservation of parity in these two weak decay processes has the following consequences:

a) Muons from pion decay are polarized along their direction of motion and there are more muon spins pointing in one direction than in the opposite direction.
b) In muon β decay, the angular distribution of the electrons is not symmetric about a plane perpendicular to the spin of the muon.

Item (a) above means that the muon spin is aligned along the direction of motion. If the muon beam is stopped in an absorber and the angular distribution of the decay electrons is measured, item (b) means that the number of electrons measured at an angle θ relative to the original direction of motion of the muons is different from the number of electrons observed at $180° - \theta$. This is the experiment originally carried out by Garwin et al. (1957) demonstrating the violation of parity in the two decay processes given above. Implicit in this experiment is the assumption that the muons are not depolarized in the absorber. However, the magnetic moment of the muon will cause it to interact with any magnetic fields it may encounter in the stopping material and the muon polarization would then be lost. This depolarization was first observed in experiments in which the observed asymmetry in the β decay of the muon was seen to decrease by a factor of ≈ 2 when the stopping material was changed from graphite to a photographic emulsion containing AgBr. This dependence of the depolarization on the chemical environment makes the muon a chemical probe.

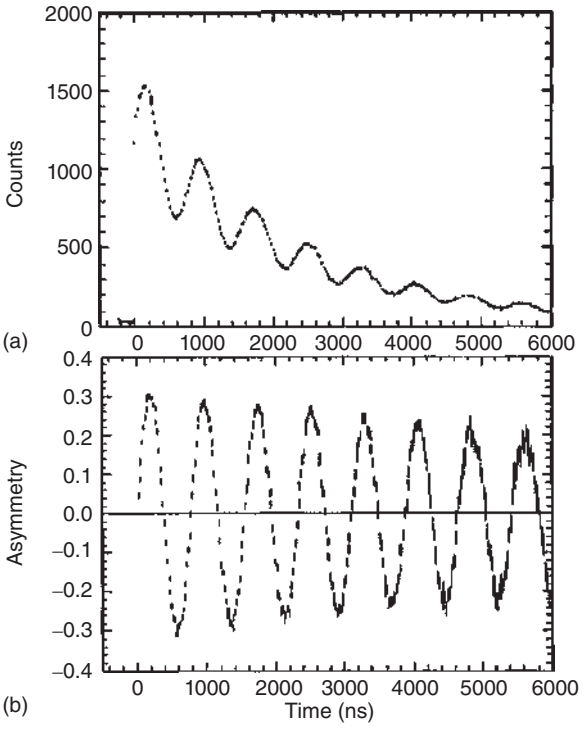

Figure 14.5 Typical μSR spectrum (number of detected positrons as a function of muon lifetime). The exponential muon decay is superimposed (a) by a signal oscillating with the muon precession frequency in a transverse magnetic field. The lower spectrum (b) shows the slowly relaxing oscillation amplitude with the exponential removed. Source: Percival (1979), figure 05 (p. 11)/De Gruyter.

Positive muons lose energy in matter, first by scattering with electrons down to about 3 keV, followed by capture of electrons. Thus, muonium atoms, Mu, are formed as μ^+ are stopped in nearly all materials. This correlates with the fact that muonium has a higher ionization potential than most other atoms. Thermalized muonium can be of importance in various chemical studies such as kinetic *isotope effects* and structural isotope effects. Chemical information can be extracted from the degree of residual polarization of the muon as it is stopped in condensed matter.

The muon spin depolarization is often measured with the transverse field muon spin rotation (μSR) technique in which a B field perpendicular to the original muon spin is applied. The time delay between the stopping of a muon in the sample and the emission of a positron in the forward direction is measured with a timing circuit. A typical decay curve is shown in Figure 14.5 in which the oscillation in the detection of the e^+ is superimposed by the exponential decay of the muon. These oscillations reflect the preferential emission of the e^+ along the spin direction of the muon with an angular frequency

$$\omega = \mu_\mu \frac{B}{\hbar}$$

where μ_μ is the magnetic moment of the muon, which is 3.18 times the proton magnetic moment. The time dependence of the positron intensity reflects the average depolarization due to interactions with the medium. The advent of a number of meson factories has spurred interest in muon chemistry. Much activity has been

devoted to thermal muon kinetics in gases and liquids, and μ^+SR spectroscopy in metals, superconductors, and insulators.

Muonium formation is not possible with the μ^-. Also, the negative charge diminishes depolarization of the μ^-. However, it causes the formation of another interesting class of substances in which the μ^- is captured into a stable atomic or molecular orbital. Evidence for these new chemical species comes from the X-rays emitted as the μ^- cascades down to the 1s state. The fact that the muon is 207 times as heavy as the electron causes the energy of a transition to increase by a factor of 207 and the radius of an orbit to decrease by a factor of 207. In muonic atoms, depolarization of the μ^- can occur through interactions with electrons during capture but also through interaction of the μ^- in the atomic 1s state with the nuclear magnetic moment if one exists. The capture of the μ^- into molecular and, finally, atomic orbitals may also provide interesting chemical information. The probabilities that a μ^- will be captured by various kinds of atoms are proportional to the product of the atom fraction and the atomic number, which has been verified for alloys. For other substances, the valence electronic structure of the elements involved affects the capture probabilities.

14.4 Mössbauer Spectrometry

Mössbauer spectrometry has already been mentioned in discussing the chemical effects of nuclear reactions in solids (Section 13.5). Electrons in the inner orbitals of atoms have a finite probability of entering the nucleus, interacting with the nuclear charge distribution and thereby affecting the nuclear energy levels and γ transitions. The probability of the interaction of the electrons with the nucleus varies with the properties of the electron orbitals and consequently with chemical bonding. A γ-ray photon emitted from an isomeric state of an atom bound in a certain chemical compound will have a slightly different energy compared to that of a photon emitted by the same atom bound in another compound. This energy difference is called an isomer shift. It is extremely small – only about 10^{-10} of the energy of the γ-ray emitted.

In order to be able to measure such small energy differences, several effects have to be taken into account. The natural line width $\Gamma = \Delta E$ of γ-rays is given by the Heisenberg uncertainty principle,

$$\Gamma \cdot \tau = h/2\pi \tag{14.9}$$

where τ is the mean lifetime of the excited state. Values of τ between about 10^{-9} and 10^{-7} seconds are the most suitable for Mössbauer spectrometry because they ensure sufficient resolution. At higher values of τ the line width is too small and at lower values of τ it is too large to be measured without experimental problems.

The most frequently used Mössbauer nuclide is ^{57}Fe, originating from the Mössbauer source ^{57}Co by electron capture (Figure 14.6). Source and Mössbauer nuclide form a Mössbauer pair. The half-life of the first excited state of ^{57}Fe at $E^* = 14.4$ keV is 98 ns ($\tau = 1.4 \cdot 10^{-7}$ seconds), and the natural line width is $\Gamma = 4.6 \cdot 10^{-9}$ eV.

In the case of free atoms of ^{57}Fe, the recoil energy is $E_1 = 1.95 \cdot 10^{-3}$ eV (Eq. (13.7)), and the same kinetic energy is transferred to a free ^{57}Fe atom by an incident γ-ray

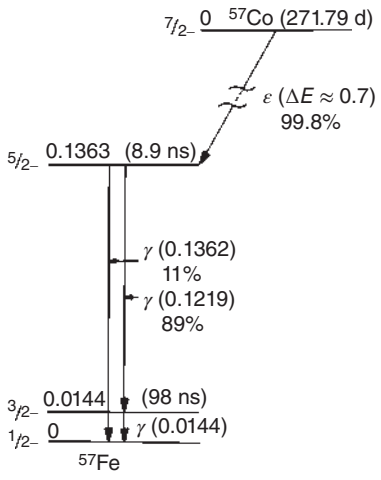

Figure 14.6 Transmutation of ^{57}Co (Mössbauer source) into ^{57}Fe (Mössbauer nuclide); Mössbauer level at 0.0144 MeV (excitation energy).

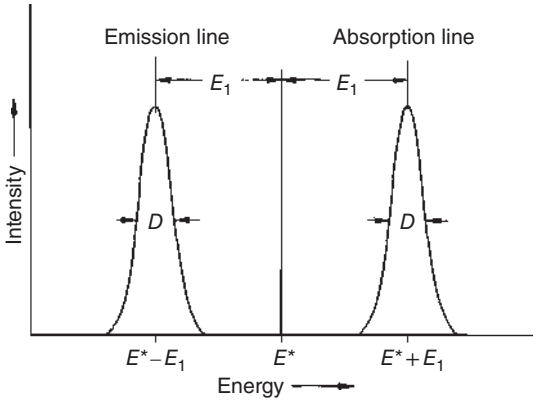

Figure 14.7 Absorption of γ-ray photons by free atoms; E^* = excitation energy; E_1 = recoil energy; D = line broadening by the Doppler effect.

photon of the energy E_1. Due to the energy E_1 transmitted to the nuclei by recoil or absorption, the emission line is shifted to lower energies, $E = E^* - E_1$, and the absorption line to higher energies, $E = E^* + E_1$, as shown in Figure 14.7.

In crystalline solids, however, the atoms are firmly bound to neighboring atoms, the whole system behaves like a rigid block of high mass, and the ^{57}Fe atoms emitting the 14.4 keV γ-ray photons do not suffer a recoil, and photons take away the full energy of the electromagnetic transition, as explained in Section 13.5. On the other hand, by absorption of the 14.4 keV γ-ray photon, a ^{57}Fe atom embedded in a crystalline solid does not receive measurable amounts of kinetic energy, and the energy of the photon is quickly distributed among the neighboring atoms.

Another effect is due to the vibration of atoms in solids. At room temperature, this vibration leads to a Doppler effect and line broadening on the order of $D \approx 10^{-2}$ eV. To obtain sufficient resolution, this line broadening has to be suppressed by cooling to the temperature of liquid nitrogen. Thus, the emitting and absorbing atoms have to be embedded in solids and both have to be kept at low temperatures, in order to measure recoilless resonance absorption of γ-rays. These are essential conditions for Mössbauer spectrometry.

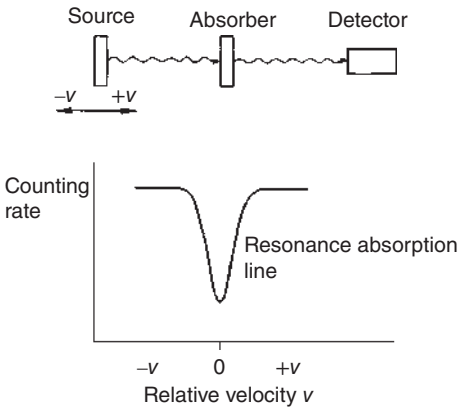

Figure 14.8 Mössbauer experiment (schematically).

The original Mössbauer experiment was carried out with ^{191}Os as source and an iridium foil as absorber in an arrangement shown schematically in Figure 14.8. The Mössbauer nuclide is ^{191}Ir. Some of the 129 keV γ-rays emitted after β^- decay of ^{191}Os from the first excited state of ^{191}Ir are absorbed by the atoms of ^{191}Ir in the foil, exciting these atoms from the ground state to the first excited state (resonance absorption). The latter decays with a half-life of 0.13 ns to the ground state, reemitting 129 keV γ-ray photons at random. As a result, a decrease in the intensity is measured by the detector.

If source and absorber are in different chemical states, the nuclear energy levels of the atoms in the source and in the absorber differ by a small amount ΔE_{elec}, as mentioned above, and resonance absorption is obtained by moving the source with a velocity v, in order to change the kinetic energy of the photons by adding or subtracting this small amount ΔE_{elec}. In this way, a Mössbauer spectrum of a certain compound relative to a reference compound is obtained. The location of the absorption maximum is the chemical shift δ (on the order of mm s^{-1}) which is characteristic of the compound.

ΔE_{elec} is due to the electric monopole interaction between the electrons in the nucleus. To a good approximation, we have

$$\Delta E_{\text{elec}} = 2/5\pi Ze^2(\bar{r}_{\text{ex}}^2 - \bar{r}_{\text{gr}}^2)[|\Psi_{\text{e}}(0)|^2 - |\Psi_{\text{a}}(0)|^2] \tag{14.10}$$

where $\bar{r}_{\text{ex}}^2$ and $\bar{r}_{\text{gr}}^2$ are the mean square nuclear radii in the excited state and in the ground state, respectively, and $|\Psi_{\text{e}}(0)|^2$ and $|\Psi_{\text{a}}(0)|^2$ are the densities of electrons at the nucleus in the emitter and absorber, respectively.

Different oxidation states or different ligands lead to different values of δ. Low-spin and high-spin complexes can be distinguished. If either the emitting or the absorbing nucleus has angular momentum $I \geq 1/2$, it will also have a magnetic moment; in the presence of a magnetic field, the energy of the nucleus will depend on its orientation with respect to that magnetic field with $(2I + 1)$ values of ΔE_{M}, where the effect of ΔE_{M} is not merely to shift the transition energy but to split it into several components. If either the emitting or the absorbing nucleus has an angular momentum $I \geq 1$ and is in an inhomogeneous electric field, the transition energy may be additionally split by ΔE_{Q} into several lines because the interaction between the quadrupole moment and the inhomogeneous electric field causes the

energy of the nucleus to depend on its orientation. Thus, the transition energy $E = \Delta E_{\text{nucl}} + \Delta E_{\text{elec}} + \Delta E_{\text{M}} + \Delta E_{\text{Q}}$ depends on three Mössbauer parameters ΔE_{elec}, ΔE_{M}, and ΔE_{Q} corresponding together to a Doppler velocity on the order of 1 cm s^{-1}.

Application of Mössbauer spectrometry depends on the availability of suitable sources with half-lives of excited states between about 10^{-9} and 10^{-7} seconds. The photon energy must not exceed 100 keV and conversion must not be too high to ensure recoilless emission and absorption. As already mentioned, ^{57}Fe, the daughter of ^{57}Co, see Figure 14.6, is the most frequently used Mössbauer nuclide. ^{57}Co is used as a Mössbauer source and iron of natural isotopic composition (2.17% ^{57}Fe) or enriched ^{57}Fe as the absorber. The emitter is usually prepared by diffusing ^{57}Co into stainless steel in which there are no magnetic fields that will split the $3/2^-$ or $1/2^-$ states in ^{57}Fe produced in the EC of ^{57}Co. In the absorber, on the other hand, ^{57}Fe nuclei may be used to probe local electric and magnetic fields through the observed splitting patterns. The effects of magnetic field and of an inhomogeneous electric field on the ground state ($1/2^-$) and the first excited state ($3/2^-$) of ^{57}Fe are shown schematically in Figure 14.9. Note that the center of gravity of the four levels into

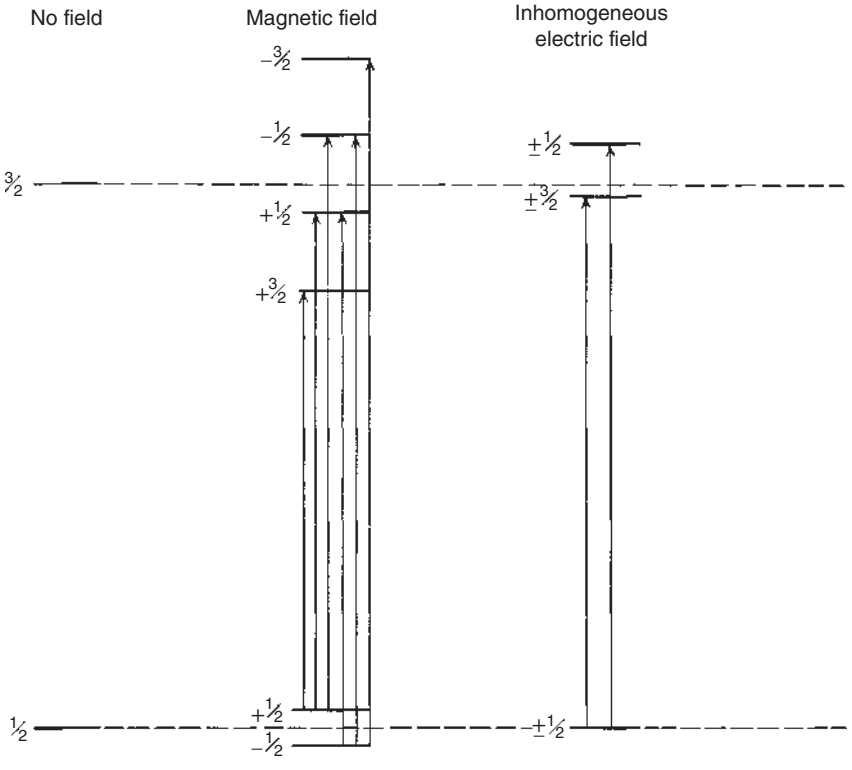

Figure 14.9 The splitting of the $I = 1/2$ ground state and of the $I = 3/2$ excited state in ^{57}Fe in a magnetic field (as in Fe_2O_3) and in an inhomogeneous electric field (as in $FeSO_4 \cdot 7H_2O$). The lines between energy levels represent allowed transitions for γ-ray absorption. Each level is characterized by the projection of its angular momentum on the direction of the field. The spacings of the energy levels are not to scale. Source: Friedlander et al. (1981), figure 04 (p. 50)/John Wiley & Sons.

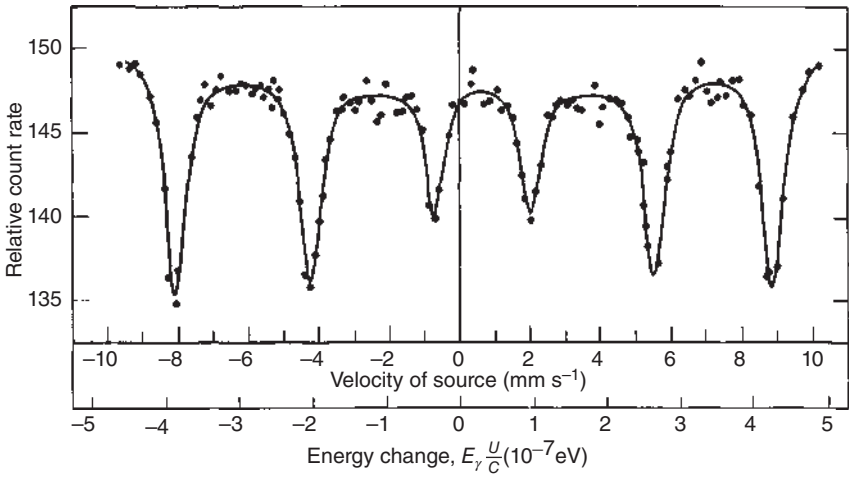

Figure 14.10 The absorption in ^{57}Fe (bound in Fe_2O_3) of the 14.4 keV γ-ray emitted in the decay of ^{57m}Fe (bound in stainless steel) as a function of the relative source–absorber velocity. Positive velocity indicates motion of the source toward the absorber. Source: Kistner and Sunyar (1960), figure 07 (p. 55)/American Physical Society.

which the $3/2^-$ state is split by the magnetic field and of the two levels in the inhomogeneous electric field does not coincide with the unsplit $3/2^-$ state in stainless steel. Experimental observations made with an Fe_2O_3 absorber are shown in Figure 14.10. The six lines expected from the magnetic splitting, as well as the lack of symmetry about zero velocity that is caused by the chemical shift, can be seen. From this spectrum, it was deduced that the splitting is $2.9 \cdot 10^{-7}$ eV for the $1/2^-$ state and $1.6 \cdot 10^{-7}$ for the $3/2^-$ state. From the known magnetic moments of the two states, the splitting corresponds to a field of $5.2 \cdot 10^5$ oersted at the iron nucleus in Fe_2O_3 caused by the magnetic moments of the unpaired electrons in the Fe^{3+} ions. The two lines that are expected from quadrupolar interactions can be seen in Figure 14.11, which shows the spectrum obtained with $FeSO_4 \cdot 7H_2O$ as absorber. The splitting is a consequence of the inhomogeneous electric field provided by the sixth 3d electron accommodated in the lowest 3d orbital of the non-cubic $[Fe(H_2O)_6]^{2+}$ ion. The other five give a spherically symmetric electric field at the nucleus. Also here, the chemical shift causes a lack of symmetry about zero velocity. The Mössbauer effect, then, can serve as a sensitive probe for atomic wave functions, magnetic fields, and electric field gradients at the location of nuclei that are part of solid compounds. It can also yield information about the chemical consequences of nuclear processes that immediately precede the recoilless γ-ray.

About 70 other Mössbauer pairs have also been applied, including Mössbauer nuclides such as ^{61}Ni, ^{67}Zn, ^{83}Kr, ^{99}Tc, ^{99}Ru, ^{101}Ru,^{107}Ag, ^{117}Sn, ^{119}Sn, ^{123}Sb, ^{125}Te, ^{127}I, ^{129}Xe, ^{133}Cs, ^{139}La, ^{151}Eu, ^{161}Dy, ^{169}Tm, ^{181}Ta, ^{182}W, ^{187}Re, ^{189}Os, ^{190}Os, ^{191}Ir, ^{193}Ir, ^{195}Pt, ^{197}Au, ^{199}Hg, and ^{237}Np.

^{237}Np is formed in α decay of ^{241}Am via an excited state at 59.6 keV (Mössbauer level) which decays with a half-life of 68 ns into the ground state. This transition

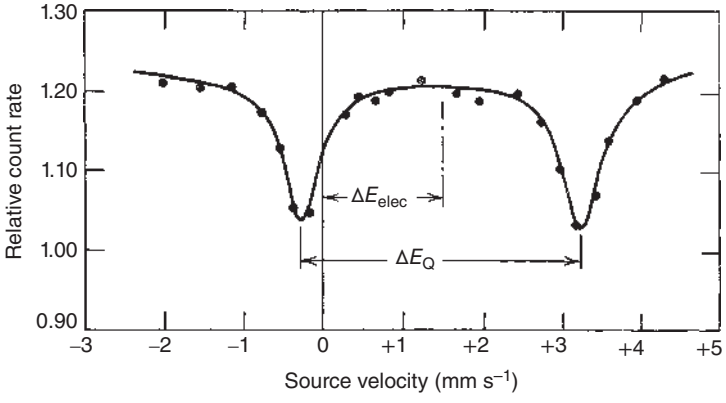

Figure 14.11 Mössbauer spectrum of the Fe^{2+} in an absorber of $FeSO_4 \cdot 7H_2O$ at liquid-nitrogen temperature, taken with a room-temperature stainless steel source. The pattern exhibits the chemical shift ΔE_{elec} and the electric quadrupole splitting ΔE_Q of the excited state of the ^{57}Fe nucleus. The velocity is positive for the source approaching the absorber. Source: DeBenedetti et al. (1961), figure 05 (p. 65)/American Physical Society.

exhibits an exceptionally wide range of isomer shifts for the various oxidation states of Np from about $+70\,mm\,s^{-1}$ for Li_5NpO_6 (Np(VII)) to about $+47\,mm\,s^{-1}$ for $K_3NpO_2F_5$ (Np(VI)), about $+18\,mm\,s^{-1}$ for $NpO_2(OH)\cdot H_2O$ (Np(V)), about $+5\,mm\,s^{-1}$ for NpF_4; and about $-41\,mm\,s^{-1}$ for NpF_3. This wide range allows unambiguous identification of the oxidation state of Np in solid compounds.

Mössbauer spectrometry gives information about the chemical environment of the Mössbauer nuclide in the excited state at the instant of emission of the photon. It does not necessarily reflect the normal chemical state of the daughter nuclide because of the after-effects that follow the decay of the mother nuclide (recoil and excitation effects, including emission of Auger electrons). At very short lifetimes of the excited state, ionization and excitation effects may not have attained relaxation at the instant of emission of the γ-ray photon; this results in a time-dependent pattern of the Mössbauer spectrum.

References

DeBenedetti, S., Lang, G., and Ingalls, R. (1961). Electric quadrupole splitting and the nuclear volume effect in the ions of ^{57}Fe. *Phys. Rev. Lett.* 6: 60.

Friedlander, G., Kennedy, J.W., Macias, E.S., and Miller, J.M. (1981). *Nuclear and Radiochemistry*, 3e. New York: Wiley.

Garwin, R., Lederman, L., and Weinrich, M. (1957). Observation of the failure of conservation of parity and charge conjugation in meson decay: the magnetic moment of the free muon. *Phys. Rev.* 105: 1415.

Kistner, O.C. and Sunyar, A.W. (1960). Evidence for quadrupole interaction of Fe57m. *Phys. Rev. Lett.* 4: 412.

Percival, P.W. (1979). Muonium chemistry. *Radiochim. Acta* 26: 1.

Further Reading

Mössbauer Spectrometry

Mössbauer, R.L. (1958). Kernresonanzfluoreszenz von Gammastrahlen in ^{191}Ir. *Z. Angew. Phys.* 151: 124.

Mössbauer, R.L. (1962). Recoilless nuclear resonance absorption. *Annu. Rev. Nucl. Sci.* 12 (1).

Greenwood, N.N. and Gibb, T.C. (1971). *Mössbauer Spectroscopy*. London: Chapman and Hall.

Bancroft, G.M. (1973). *Mössbauer Spectroscopy*. New York: Wiley.

Gütlich, P. (1975). Mössbauer spectroscopy in chemistry. In: *Topics in Applied Physics*, vol. 5 (ed. U. Gonser). Berlin: Springer-Verlag.

Cohen, R.L. (ed.) (1976). *Applications of Mössbauer Spectroscopy*. New York: Academic Press.

Gibb, T.C. (1976). *Principles of Mössbauer Spectroscopy*. New York: Halsted.

Gütlich, P., Link, R., and Trautwein, A. (1978). *Mössbauer Spectroscopy and Transition Metal Chemistry*, Inorganic Chemistry Concepts, vol. 3. Berlin: Springer-Verlag.

Shenoy, G.K. and Wagner, F.E. (eds.) (1978). *Mössbauer Isomer Shifts*. Amsterdam: North-Holland.

Kuzmann, E., Homonnay, Z., Nagy, S., and Nomura, K. (2011). Mössbauer spectroscopy. In: *Handbook of Nuclear Chemistry*, 2e, vol. 3 (eds. A. Vértes, S. Nagy, Z. Klenczár, et al.), 1379. Berlin: Springer-Verlag.

Other Effects

Deutsch, M. (1951). Evidence for the formation of positronium in gases. *Phys. Rev.* 82: 455.

Green, J.H. and Lee, J. (1964). *Positronium Chemistry*. New York: Academic Press.

Johlige, H.W., Aumann, D.C., and Born, H.-J. (1970). Determination of the relative electron density at the Be nucleus in different chemical combinations, measured as changes in the electron-capture half-life of ^{7}Be. *Phys. Rev. C: Nucl. Phys.* 2: 1616.

Vargas, J.I. (1971). The chemical applications of angular correlation and half-life measurements. In: *Radiochemistry, International Review of Sciences, Inorganic Chemistry, Series One*, vol. 8 (ed. A.G. Maddock). London: Butterworths.

Hughes, V.H. and Wu, C.S. (eds.) (1975). *Muon Physics*, Chemistry and Solids, vol. III. New York: Academic Press.

Keller, C. (1975). Zum Einfluss der chemischen Bindung auf die Halbwertzeit von Radionukliden. *Chem. Ztg* 99: 365.

Adloff, J.P. (1978). Application to chemistry of electric quadrupole perturbation of γ–γ angular correlations. *Radiochim. Acta* 25: 57.

Brewer, J.H. and Crowe, K.M. (1978). Advances in muon spin rotation. *Annu. Rev. Nucl. Part. Sci.* 28: 239.

Ache, H.J. (ed.) (1979). *Positronium and Muonium Chemistry*, Advances in Chemistry Series, vol. 175. Washington, DC: American Chemical Society.

Hautojärvi, P. (ed.) (1979). *Positrons in Solids*, Topics in Current Physics, vol. 12. Berlin: Springer-Verlag.

Matsuura, T. (ed.) (1984). *Hot Atom Chemistry*. Tokyo: Kodansha.

Pyper, N.C. and Harston, M.R. (1988). Atomic effects on β decay. *Proc. R. Soc. London, Ser. A* 420: 277.

Yoshihara, K. (1990). Chemical nuclear probes using photon intensity ratios. In: *Topics in Current Chemistry*, vol. 157. Berlin: Springer-Verlag.

Burke, J.F., Archer, C.M., Wei Chu, K. et al. (1991). A study of core electron binding energies in technetium-99m complexes by internal conversion spectroscopy. *Appl. Radiat. Isot.* 42: 49.

Ohtsuki, T., Yuki, H., Muto, M. et al. (2004). Enhanced electron-capture decay rate of ^{7}Be encapsulated in C_{60} cages. *Phys. Rev. Lett.* 93: 112501.

Ohtsuki, T., Ohno, K., Morisato, T. et al. (2007). Radioactive decay speedup at T = 0.5 K: electron-capture decay rate of ^{7}Be encapsulated in C_{60}. *Phys. Rev. Lett.* 98: 252501.

Horváth, D. (2011). Exotic atoms and muonium. In: *Handbook of Nuclear Chemistry*, 2e, vol. 3 (eds. A. Vértes, S. Nagy, Z. Klenczár, et al.), 1485. Berlin: Springer-Verlag.

Süvegh, K. and Marek, T. (2011). Positron annihilation spectroscopy. In: *Handbook of Nuclear Chemistry*, 2e, vol. 3 (eds. A. Vértes, S. Nagy, Z. Klenczár, et al.), 1461. Berlin: Springer-Verlag.

Yoshihara, H.K. and Sekine, T. (2011). Hot atom chemistry. In: *Handbook of Nuclear Chemistry*, 2e, vol. 3 (eds. A. Vértes, S. Nagy, Z. Klencsár, et al.), 1333. Berlin: Springer-Verlag.

15

Nuclear Energy, Nuclear Reactors, Nuclear Fuel, and Fuel Cycles

15.1 Energy Production by Nuclear Fission

For the production of energy by nuclear fission, the following features are decisive:

- The Q value released in nuclear fission of heavy nuclei is very high (Section 12.7.6).
- As several neutrons are liberated by fission of heavy nuclei ($\overline{\nu} = 2 - 3$), a chain reaction is possible if at least one of these neutrons induces another fission reaction.

The Q value can be assessed from the mean binding energy per nucleon (Figure 3.4) to amount to roughly 200 MeV. In the case of fission of ^{235}U and ^{239}Pu, the energy set free per fission is shared as given in Table 12.2. The sum of the kinetic energy of the fission products (FPs) and the energy of β^- decay can be determined calorimetrically. The energy of the neutrons and the γ-rays is usable only inasmuch as neutrons, and γ-rays are absorbed in the medium considered. The energy of the neutrinos is lost because of their small interaction with matter.

The greatest proportion of fissile nuclides loaded into a nuclear reactor undergoes fission, but another part of these nuclides is transformed by nuclear reactions, in particular (n, γ) reactions, such as ^{238}U(n, γ)^{239}U or ^{235}U(n, γ)^{236}U, into other nuclides that are, at least partly, less fissile. The fraction of nuclides suffering fission is given by Σ_f/Σ_a, the ratio of the macroscopic cross sections for fission and for neutron absorption, where Σ_a comprises (n, f) as well as (n, γ) reactions. For ^{235}U and thermal neutrons, this ratio is 0.855. Consequently, from 1 kg of ^{235}U up to $1.98 \cdot 10^7$ kWh could be produced, provided that the energy of the γ-rays could be used. In practice, however, about 60% of the energy of the γ-rays is lost, which reduces the energy producible from 1 kg of ^{235}U to a maximum value of $1.85 \cdot 10^7$ kWh ($7.70 \cdot 10^5$ MWd per ton of ^{235}U).

A comparison of energy production by nuclear fission and by burning of coal leads to the following result: by burning 1 kg of carbon or coal, energy of 9.4 kWh is set free, and the ratio of the energies producible from 1 kg of ^{235}U and from 1 kg of coal is $\approx 2 \cdot 10^6$. This is the stimulus for the use of nuclear energy. Comparing the energies set free by explosives leads to the result that fission of 1 kg of ^{235}U or ^{239}Pu gives the same energy as the explosion of $20 \cdot 10^6$ kg of trinitrotoluene (TNT). This provided the impetus to develop nuclear weapons.

Nuclear and Radiochemistry: Fundamentals and Applications,
Fourth Edition. Jens-Volker Kratz.

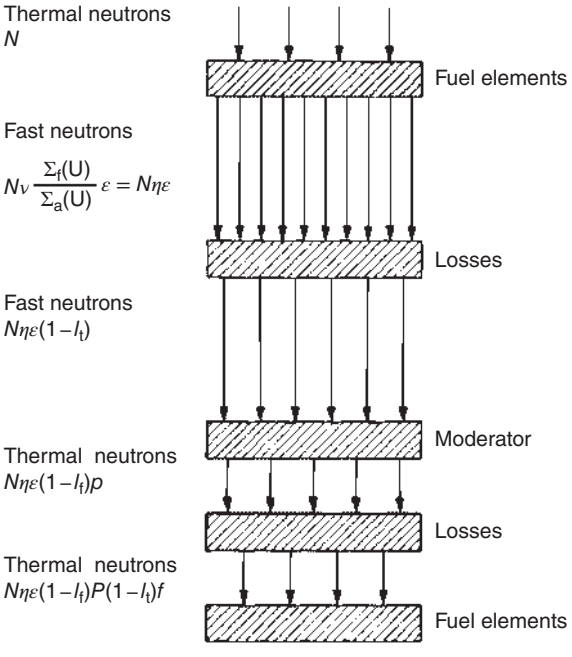

Figure 15.1 Effective multiplication factor k_{eff} for neutrons (schematically).

The possibility of operating nuclear fission in the form of a chain reaction is governed by the effective multiplication factor k_{eff}, the ratio of the number of neutrons in the second generation to that in the first generation:

$$k_{eff} = \bar{\nu}\,\varepsilon\,(1 - l_f)p(1 - l_t)f\frac{\Sigma_f}{\Sigma_a} = \eta\varepsilon(1 - l_f)p(1 - l_t)f \tag{15.1}$$

This is illustrated in Figure 15.1. Fission of ^{235}U may be taken as an example: $\bar{\nu}$ is the average number of neutrons liberated in nuclear fission of ^{235}U by thermal neutrons and Σ_f/Σ_a is the ratio of the "macroscopic" cross sections, σN, for fission and for absorption of neutrons where N is the number of nuclei per cubic centimeter and σ is the (ordinary) cross section. The fission factor $\eta = \bar{\nu}\Sigma_f/\Sigma_a$ is the number of fission neutrons relative to the number of thermal neutrons absorbed in uranium; ε, also called the *fast fission factor*, takes into account the production of neutrons by fission of $^{238}U(1.0 < \varepsilon < 1.1)$. The fraction l_f of neutrons is lost, whereas the remainder is slowed down to low energies in a moderator. Suitable moderators are materials with low absorption cross section for neutrons and low mass, such as H_2O, D_2O, or graphite. The fraction p of neutrons escaping capture while slowing down is referred to as the resonance escape probability. The fraction $(1 - p)$ of neutrons is captured by ^{238}U, inducing the reaction $^{238}U(n, \gamma)^{239}U$ followed by β^- decay into ^{239}Np and ^{239}Pu. From the remaining neutrons, the fraction l_t escapes from the system, the fraction f is captured by uranium atoms, and the fraction $(l - f)$ is captured by other atoms; f is called the *thermal utilization*. Both p and f depend on the nature and the arrangement of fuel and moderator.

To make the losses of fast and thermal neutrons (l_f and l_t, respectively) as small as possible, the reactor core is surrounded by a reflector, preferably made of graphite or beryllium.

The fission cross section σ_f for ^{235}U, ^{239}Pu, and ^{238}U, the ratio σ_f/σ_a for ^{235}U and ^{238}U, and the values of $\eta = \overline{\nu}\sigma_f/\sigma_a$ for ^{235}U and ^{238}U are plotted in Figures 15.2–15.4, respectively, as a function of the neutron energy.

The following operational conditions are distinguished:

Thermal neutrons ($E_n \leq 1\,eV$): Fission of ^{235}U and ^{239}Pu prevails ($\sigma_{n,f} > \sigma_{n,\gamma}$). Although $\sigma_{n,\gamma}$ for ^{238}U is small, (n, γ) reactions play an important role if large amounts of ^{238}U are present.

Epithermal neutrons ($1\,eV \leq E_n \leq 0.1\,MeV$): The influences of neutron capture and fission resonances increase. Heavier isotopes of U and Pu are formed by (n, γ) reactions, such as $^{235}U(n, \gamma)^{236}U$, $^{238}U(n, \gamma)^{239}U$, $^{239}Pu(n, \gamma)^{240}Pu$.

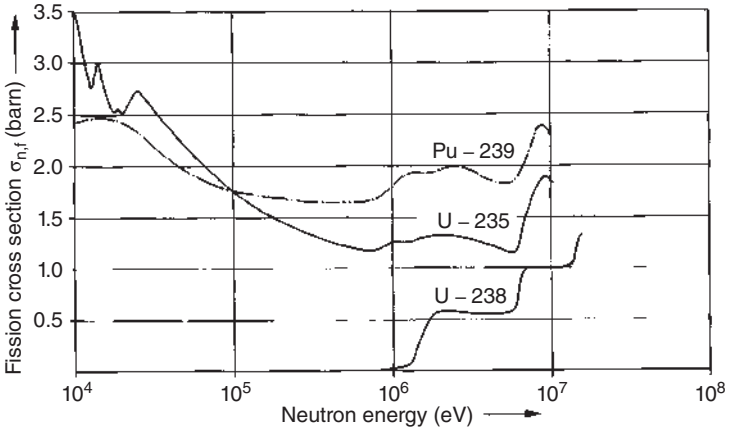

Figure 15.2 Fission cross section $\sigma_{n,f}$ for ^{235}U, ^{238}U, and ^{239}Pu as a function of the neutron energy.

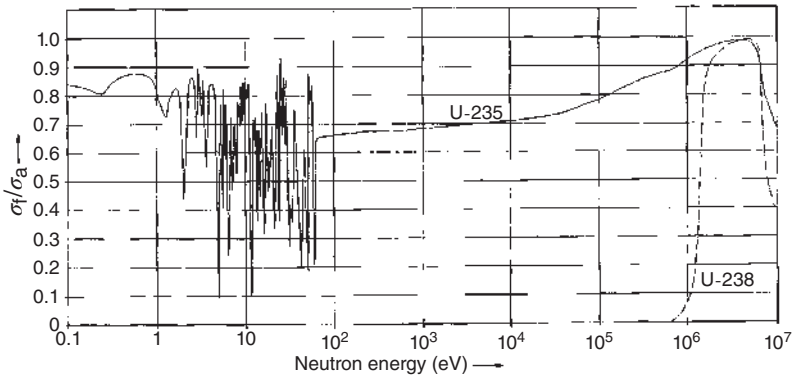

Figure 15.3 The ratio σ_f/σ_a for ^{235}U and ^{238}U as a function of the neutron energy.

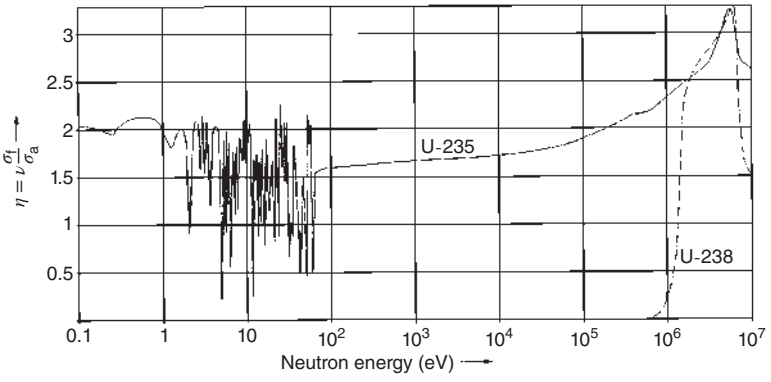

Figure 15.4 $\eta = \nu\sigma_f/\sigma_a$ as a function of the neutron energy for ^{235}U and ^{238}U.

Fast neutrons ($E_n > 0.1$ MeV): Fission prevails ($\sigma_{n,f} > \sigma_{n,\gamma}$). ^{238}U also becomes fissile at $E_n \approx 0.6$ MeV, reaching a constant value of ≈0.5 barn at $E_n \geq 2$ MeV.

The multiplication factor k_{eff} can be appreciably increased by the heterogeneous arrangement of uranium and moderator because resonance absorption of the neutrons by ^{238}U is low after the neutrons have been slowed down in the moderator. Then, p becomes markedly higher, f somewhat lower, and pf becomes higher than in the case of homogeneous arrangement of fissile material and moderator. The following possibilities are distinguished:

$k_{eff} < 1$: The reactor is subcritical; a chain reaction cannot occur.
$k_{eff} = 1$: The reactor is critical; a chain reaction is possible.
$k_{eff} > 1$: The reactor is supercritical.

The term $k_{eff} - 1$ is called *excess reactivity*, and $(k_{eff} - 1)/k_{eff}$ is called *reactivity*. Because the fissile material is continuously used up by fission and because the fission products absorb neutrons, a certain excess reactivity is necessary to operate a nuclear reactor. This excess reactivity is compensated by control rods that absorb the excess neutrons. These control rods contain materials of high neutron absorption cross section, such as boron, cadmium, or rare earth elements. The excess reactivity can also be balanced by adding the coolant of neutron-absorbing substances such as boric acid.

In a medium of infinite extent, the neutron losses l_f and l_t become negligible and the multiplication factor is given by

$$k_\infty = \eta\varepsilon pf \tag{15.2}$$

While ε is somewhat >1, both p and f are somewhat smaller than 1. Therefore, for approximate calculations, εpf can be set ≈1. The fission factor η varies appreciably with the energy of the neutrons, as shown in Figure 15.4 for ^{235}U.

The neutron losses in a reactor of finite dimensions can be taken into account approximately by the sum $L_s^2 + L^2$, where L_s is the mean slowing-down length of the fission neutrons in the moderator and L is the mean diffusion length in the

fuel–moderator mixture. For a spherical reactor of radius R, the approximate relation is

$$k_\infty - k_{\text{eff}} = \pi^2 \frac{L_s^2 + L^2}{R^2} \quad \text{or} \quad R = \pi \left(\frac{L_s^2 + L^2}{k_\infty - k_{\text{eff}}} \right)^{1/2} \tag{15.3}$$

L_s is on the order of 10 cm (H_2O: 5.7 cm; D_2O: 11.0 cm; Be: 9.9 cm; C: 18.7 cm); furthermore, in most cases of practical interest, $L^2 \ll L_s^2$. Using Eqs. (15.2) and (15.3), the critical size of spherical nuclear reactors, given by $k_{\text{eff}} = 1$, can be assessed.

For the operation of nuclear reactors, the β^- delayed neutrons (Section 6.4) play an important role because they cause an increase in the time available for control. The multiplication factor due to the prompt neutrons alone is $k_{\text{eff}}\,(1-\beta)$, β being the contribution of the delayed neutrons, and as long as $k_{\text{eff}}\,(1-\beta) < 1$, the delayed neutrons are necessary to keep the chain reaction going. In the fission of ^{235}U, 0.65% of the fission neutrons are emitted as delayed neutrons from some neutron-rich fission fragments such as ^{87}Kr or ^{137}Xe. That delayed neutrons are necessary to safely operate a nuclear reactor which can be shown in the following way.

As one neutron is necessary to keep the chain reaction going, the number of neutrons N increases with $(k_{\text{eff}} - 1)$ in each generation. Thus, the simplest form of a reactor equation is

$$\frac{dN}{dt} = \frac{N(k_{\text{eff}} - 1)}{\tau}$$

where τ is the average time between successive neutron generations. Integration yields

$$N = N_0 \exp(k_{\text{eff}} - 1)t/\tau$$

k_{eff} is set by mechanically movable control rods. Let us assume that k_{eff} has been set at 1.001 and $\tau = 10^{-3}$ seconds (the lifetime of a thermal neutron in graphite or D_2O). Then, we have

$$N = N_0 \exp t$$

which means that the neutron flux increases every second by $f = e$, that is, $f = 2 \cdot 10^4$ in 10 seconds. This is much too fast for mechanical control of the reactor. However, with the delayed neutrons,

$$\tau = \tau_0 + \sum_i \frac{f_i}{\lambda_i}$$

where τ_0 is the lifetime without delayed neutrons and f_i is the fractional abundance of a delayed neutron emitter i with decay constant λ_i. Measurements yield $\sum_i f_i/\lambda_i =$ 0.08 seconds which is long compared to τ_0. With $k_{\text{eff}} = 1.001$, this gives for the time in which $N = N_0 \cdot e$ a time of ~80 seconds which is sufficient for mechanical control of the reactor.

The ratio Σ_f/Σ_a and correspondingly also the value of η change continuously with the consumption of nuclear fuel, and in practice, it is not possible to use up the fuel quantitatively. The fraction that can be used depends on the composition of the fuel and the operating conditions of the reactor. The widely used boiling water reactor

(BWR) or pressurized water reactor (PWR) contain enriched uranium with a content of about 3% of ^{235}U as fuel, which can be burned up until a residual concentration of about 0.8% ^{235}U is obtained. About half of the energy gained during the time of operation is produced by fission of ^{235}U and the remainder by fission of ^{238}U and of ^{239}Pu formed by neutron capture and β^- decay from ^{238}U.

15.2 Nuclear Fuel and Fuel Cycles

For the use of nuclides as nuclear fuel, their fissionability is the most important aspect. High fission yields by thermal neutrons are obtained if the binding energy of an additional neutron is higher than the fission barrier. Fission barriers, neutron binding energies, and fission cross sections are listed for some nuclides in Table 15.1. The fission cross sections are high for ^{233}U, ^{235}U, and ^{239}Pu, as already mentioned in Section 12.7.6. These nuclides are fissile with high yields by thermal neutrons (thermal reactors). Fission of the even–even nuclides ^{232}Th and ^{238}U requires the use of high-energy (fast) neutrons (fast reactors).

^{233}U, ^{235}U, and ^{239}Pu are most suitable as nuclear fuel in reactors operating with thermal neutrons. ^{235}U is present in natural uranium with an isotopic abundance of 0.72%. Because of this low concentration, use of natural uranium as a nuclear fuel is only possible if the neutron losses are kept as low as possible. For this purpose, D_2O or graphite may be used as moderators. Graphite was applied in the first nuclear reactors. D_2O is still used as a moderator and coolant in heavy-water reactors (HWRs).

^{239}Pu and ^{233}U are produced from ^{238}U and ^{232}Th, respectively, by the following reactions:

$$^{238}U(n,\gamma)^{239}U \xrightarrow[\beta^-]{23.5\ \text{minutes}} {}^{239}Np \xrightarrow[\beta^-]{2.35\ \text{days}} {}^{239}Pu \tag{15.4}$$

$$^{232}Th(n,\gamma)^{232}Th \xrightarrow[\beta^-]{22.3\ \text{minutes}} {}^{233}Pa \xrightarrow[\beta^-]{27.0\ \text{days}} {}^{233}U \tag{15.5}$$

By reaction (15.4), ^{239}Pu is produced in all reactors operated with uranium. Special types of reactors are designed with the aim of producing larger amounts of ^{239}Pu or

Table 15.1 Fission barriers, binding energies of an additional neutron, and fission cross sections for some heavy nuclides.

Nuclide	Fission barrier (MeV)	Binding energy of an additional neutron (MeV)	Fission cross section $\sigma_{n,f}$ (barn)
^{232}Th	7.5	5.4	0.000 04
^{233}U	6.0	7.0	531
^{235}U	6.5	6.8	582
^{238}U	7.0	5.5	<0.000 5
^{239}Pu	5.0	6.6	743

Table 15.2 Some data on nuclear fuel.

	^{233}U	^{235}U	^{239}Pu
Half-life (yr)	$1.59 \cdot 10^5$	$7.038 \cdot 10^8$	$2.411 \cdot 10^4$
$\sigma_{n,\gamma}$ for thermal neutrons (barn)	48	99	269
$\sigma_{n,f}$ for thermal neutrons (barn)	531	582	743
Average number of neutrons liberated in thermal neutron fission	3.13	2.43	2.87

^{233}U. The concept of these reactors is to use one of the neutrons released by fission to initiate another fission, and a second one to produce another fissile atom. The ratio of the number of fissile atoms produced to the number of atoms used up by fission is called the *conversion factor c*. If $c > 1$, the reactor is called a breeder reactor; if $c < 1$, it is called a converter.

Some properties of ^{233}U, ^{235}U, and ^{239}Pu are summarized in Table 15.2. The following kinds of fuel are distinguished:

natural uranium;
weakly enriched uranium ($\approx$3% ^{235}U);
highly enriched uranium (>90% ^{235}U);
mixtures of uranium and plutonium;
mixtures of uranium and thorium.

The energy output of a nuclear reactor is characterized by the "burn up" which is usually given in megawatt days (MWd) per ton of fuel. By use of natural uranium, a burn up of about 10^4 MWd per ton is achieved. This corresponds to fission of about 13 kg of fissile nuclides per ton of fuel, the greatest part being ^{239}Pu produced by reaction (15.4). The fission of ^{235}U leads to a decrease in its concentration below the natural isotopic abundance of 0.72%. From an economic point of view, only the recovery of plutonium is of interest.

Weakly enriched uranium, containing about 3% ^{235}U, is most widely used in nuclear power stations. The usual burn up is about $3.4 \cdot 10^4$ MWd per ton of fuel, corresponding to fission of about 45 kg of the fuel. About half of this is ^{235}U, and the abundance of this nuclide in the fuel decreases from about 3.0% to about 0.8%. The concentration of long-lived isotopes of plutonium increases to about 0.9% and that of fission products to about 3.4%.

Highly enriched uranium containing more than 90% ^{235}U is, in general, only used in research reactors. The production of fissile nuclides is negligible, and the maximum burn up is on the order of 10^5 MWd per ton of fuel, corresponding to the consumption of about 13% of the fuel. Recovery of the remaining ^{235}U is of economic interest.

Mixtures of uranium and plutonium may be used instead of weakly enriched uranium in thermal reactors and are applied in fast breeder reactors, which are operated with the aim of producing more fissile material than is consumed

by fission. The main fissile nuclide is ^{239}Pu, which is continuously reproduced according to reaction (15.4) from ^{238}U. In fast breeder reactors operating with about 6 tons of Pu and about 100 tons of U, a net gain of fissile ^{239}Pu may be obtained. The burn up is about 10^5 MWd per ton of fuel, and reprocessing with the aim to recover the plutonium is expedient.

Mixtures of enriched uranium and thorium are preferably used in high-temperature reactors operating as thorium converters. This means that ^{233}U is produced according to reaction (15.5) and serves as nuclear fuel. The conversion factor, given by the ratio of ^{233}U produced by reaction (15.5) to the amount of nuclides used up by fission, varies between about 0.65 and 0.95. Mixtures of highly enriched uranium (>90% ^{235}U) and thorium in a ratio on the order of 1 : 10 are preferably applied. The burn up is also on the order of 10^5 MWd per ton of fuel. Reprocessing is carried out with the aim of separating U, Th, and the relatively small amounts of Pu. The uranium fraction contains ^{238}U, ^{235}U, and ^{233}U.

High-temperature reactors may also be operated with enriched uranium containing about 10% ^{235}U. As in the case of weakly enriched uranium, ^{235}U is the only fissile material at the beginning and is supplemented by the production of ^{239}Pu according to reaction (15.4).

The reactions taking place with ^{238}U in a nuclear reactor are summarized in Figure 15.5, those occurring with ^{232}Th in Figure 15.6. The main products are the long-lived nuclides ^{239}Pu and ^{233}U. However, other isotopes of Pu and isotopes of Am and Cm are also produced from ^{238}U, and isotopes of U and Pa from ^{232}Th. The relative amounts of these radionuclides increase with the time of irradiation.

The process route of uranium as nuclear fuel is shown in Figure 15.7. It begins with processing of uranium ores, from which pure uranium compounds are produced. These may be used in the natural isotopic composition or transformed into other compounds suitable for isotope separation. The next step is the production of fuel elements for the special requirements of reactor operation. Solutions of uranium compounds are applied only in homogeneous reactors.

Besides the fuel elements, the other main components in a nuclear reactor are the moderator and the coolant. They may be identical.

In general, the fuel elements remain in the reactor for several years. During this time, the chemical composition and the properties of the fuel change markedly. By burning up, a great variety of fission products is produced. The multiplication factor k_{eff} decreases due to the decrease of the concentration of fissile material, and the generation of fission products leads to an increasing absorption of neutrons. Absorption cross sections for thermal neutrons are exceptionally high for some fission products, such as ^{135}Xe (fission yield 6.647% in $^{235}\mathrm{U}(\mathrm{n_{th}}, \mathrm{f})$, $\sigma_{\mathrm{a}} = 2.65 \cdot 10^6$ barn) and many lanthanides. This high neutron absorption must be compensated by an excess of fissile material. However, at a certain burn up, further use of the fuel elements becomes uneconomic and the fuel elements are exchanged for new ones.

After burn up, the fuel elements are stored under water for radiation protection and cooling, for at least several months and generally for about one year. Afterward, they may be either disposed of or reprocessed in order to separate the fuel into three fractions: uranium, plutonium, and fission products including the remainder of the

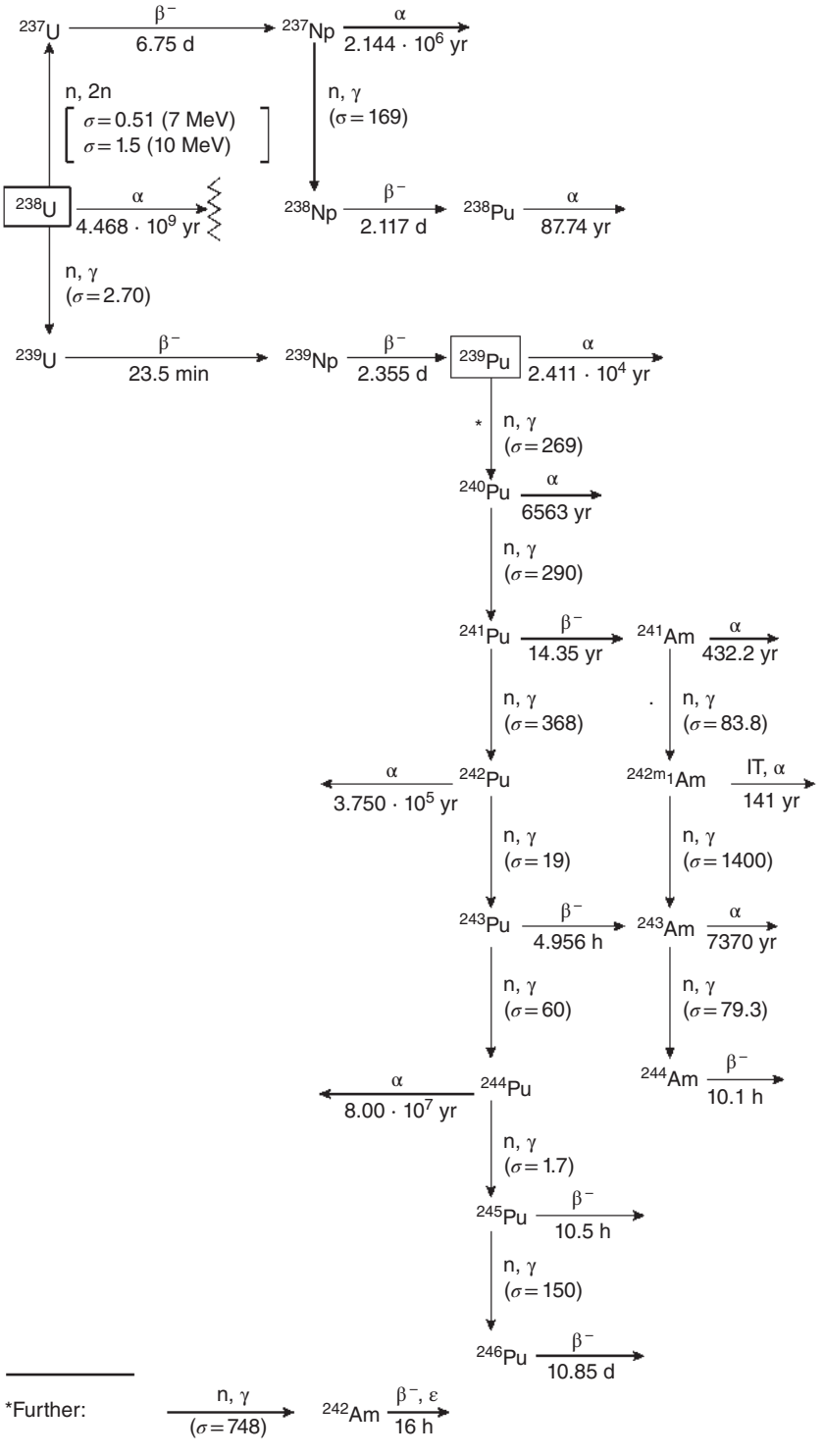

Figure 15.5 Nuclear reactions with ^{238}U (σ [barn] for thermal neutrons).

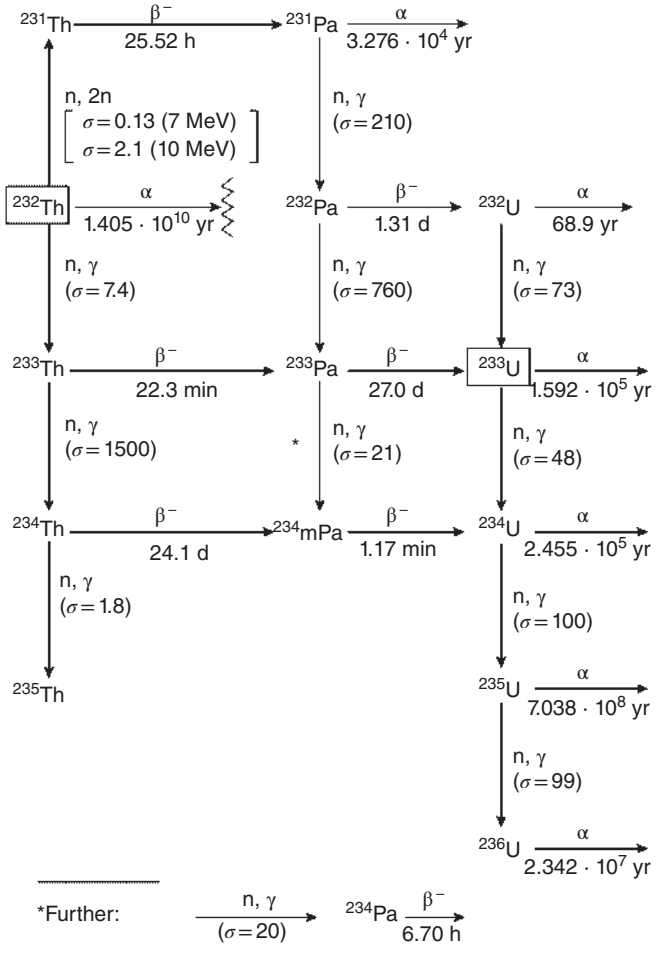

Figure 15.6 Nuclear reactions with ^{232}Th (σ [barn] for thermal neutrons).

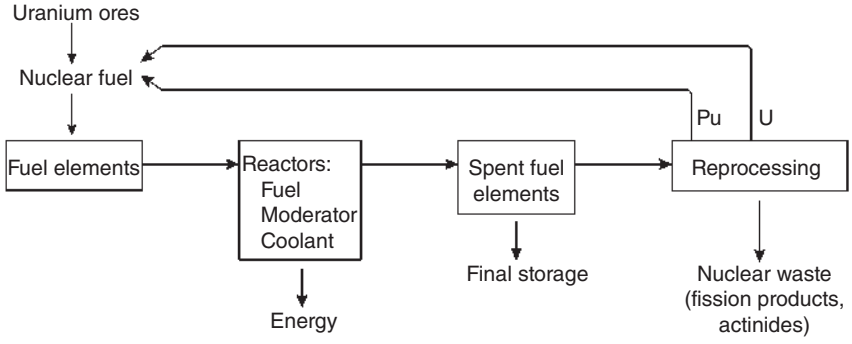

Figure 15.7 Process route of uranium as a nuclear fuel.

actinides ("minor actinides"). Uranium and plutonium may be reused as nuclear fuel, thus closing the U/Pu fuel cycle. The fission products and the remainder of the actinides are converted into chemical forms that are suitable for long-term storage.

In the case of fuel elements containing ^{232}Th, uranium and thorium may be recycled (U/Th fuel cycle).

Handling of fissile material (plutonium and enriched uranium) requires strict observance of criticality conditions. As elucidated in Section 15.1, criticality depends on the properties and mass of fissile material in the system, its concentration (including local concentrations), and the presence of a moderator such as water. In all operations with Pu and enriched U, only limited amounts are permitted to be handled and samples of these materials have to be stored in portions of limited mass and at appropriate distances from each other.

The process route of nuclear fuel will be considered in more detail in Sections 15.3–15.8, mainly for uranium, but also for other kinds of fuel.

15.3 Production of Uranium and Uranium Compounds

The route from uranium ores to uranium concentrates is summarized in Figure 15.8. The mean concentration of U in the Earth's crust is only about 0.0003%. Ores containing high percentages of U are rare. Many uranium ore deposits contain only about 0.1–1% U. Relatively high amounts of U are dissolved in the oceans (about $4 \cdot 10^9$ tons), but in rather low concentrations ($\approx 3\ \mathrm{mg\ m^{-3}}$).

In the course of processing uranium ores, appreciable amounts of long-lived radioactive decay products of U are obtained, as listed in Table 15.3. With respect to radiation hazards, they have to be handled carefully. Some of them, such as ^{230}Th, ^{231}Pa, ^{226}Ra, or ^{210}Pb, may be isolated for practical use.

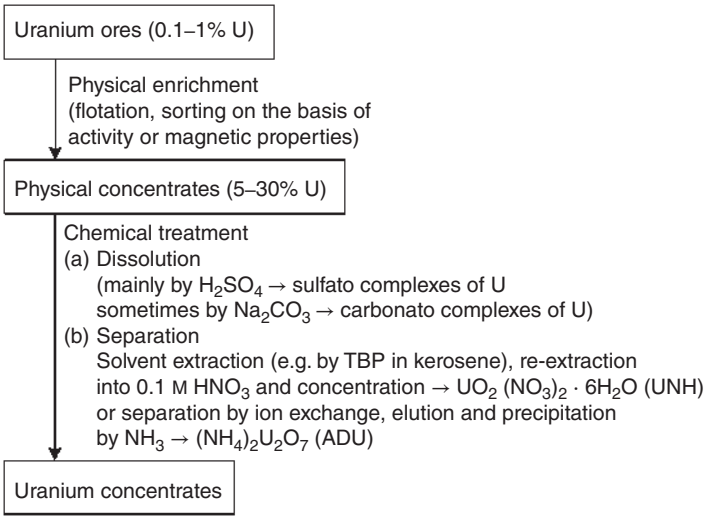

Figure 15.8 The route from uranium ores to uranium concentrates.

Table 15.3 Long-lived members of the ^{238}U and ^{235}U decay series in secular radioactive equilibrium.

		Mass number *A*		
Atomic number *Z*	**Element**	**Uranium family $4n + 2$**	**Actinium family $4n + 3$**	Half-life
92		238		$4.468 \cdot 10^9$ yr
	U		235	$7.038 \cdot 10^8$ yr
		234		$2.455 \cdot 10^5$ yr
91	Pa		231	$3.276 \cdot 10^4$ yr
		234		24.10 d
90	Th	230 (ionium)		$7.54 \cdot 10^4$ yr
			227	18.72 d
89	Ac		227	21.77 yr
88	Ra	226		1600 yr
			223	11.43 d
86	Rn	222		3.825 d
84	Po	210		138.38 d
83	Bi	210		5.013 d
82	Pb	210		22.3 yr

For the production of uranium compounds suitable for use in nuclear reactors or for isotope separation, further chemical procedures are applied, as indicated in Figure 15.9. Nuclear purity means that the compounds are free of nuclides with high neutron absorption cross section, that is, free of boron, cadmium, and rare earth elements. Selective extraction procedures are most suitable for this purpose. Uranyl nitrate hexahydrate ($UO_2(NO_3)_2 \cdot 6H_2O$; UNH) is obtained by concentration of solutions of $UO_2(NO_3)_2$, and ammonium diuranate ($(NH_4)_2U_2O_7$; ADU) by precipitation with ammonia. From UNH or ADU, UO_2 is obtained in two steps:

$$\text{UNH or ADU} \xrightarrow{350\,^\circ\text{C}} UO_3 \xrightarrow{H_2/600\,^\circ\text{C}} UO_2 \tag{15.6}$$

UO_2 may be used as nuclear fuel or transformed into metallic uranium or into UF_6:

$$UO_2 \xrightarrow{\text{HF/450 °C}} UF_4 \begin{cases} \xrightarrow{\text{Ca (or Mg, Na)}} U_2 \\ \xrightarrow{F_2 \text{ (or } ClF_3)} UF_6 \end{cases} \tag{15.7}$$

Uranium metal was used as fuel in early types of reactors. UF_6, sublimating at 56 °C, is used to separate the isotopes ^{235}U and ^{238}U. For enrichment in ^{235}U, physical procedures are applied that make use of the small mass difference between ^{235}U

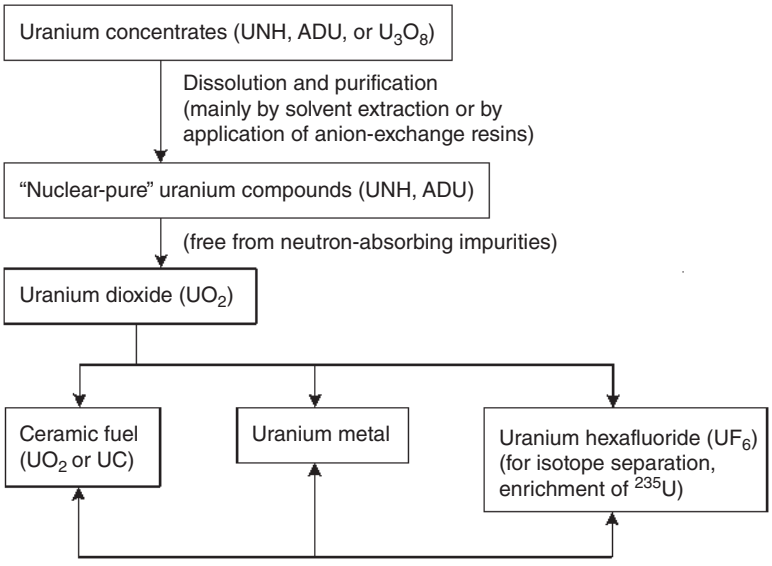

Figure 15.9 The route from uranium concentrates to nuclear fuel.

and ^{238}U. These include gas diffusion, gas centrifugation, electromagnetic separation, and laser ionization and mass separation.

In gas diffusion, one uses the fact that, at a given temperature, the lighter isotope has a higher velocity. We can assume that the average kinetic energy of all gas molecules is the same, so that for $^{235}UF_6$ and $^{238}UF_6$, we have $m_{235}v_{235}^2 = m_{238}v_{238}^2$. From this, we obtain

$$\frac{v_{235}}{v_{238}} = \left(\frac{m_{238}}{m_{235}}\right)^{1/2} = \left(\frac{352}{349}\right)^{1/2} = 1.0043$$

If a gaseous stream of UF_6 is sent into a diffusion cell with porous walls, the lighter $^{235}UF_6$ passes the pores slightly more frequently than the heavier $^{238}UF_6$ due to its higher number of impacts on the walls per unit time. In practice, the separation factor 1.0043 is not reached so that more than 1000 enrichment stages are needed to arrive at an enrichment of 3%. Special membranes have been developed with millions of pores $\leq 100\,\text{nm}\,\text{cm}^{-2}$. The process must be conducted at elevated temperatures in chemically inert vessels that withstand the strongly fluorinating UF_6. This is the most frequently used technique. In gas centrifuges, the centrifugal force pushes the heavier $^{238}UF_6$ to the periphery of the centrifuge, while the lighter $^{235}UF_6$ is enriched near the center. The separation is more efficient than gas diffusion thus requiring only about 10 stages to achieve an enrichment of 3%. In electromagnetic separators, the material to be separated is ionized, accelerated electrostatically, and transmitted through a dipole magnet depositing the different isotopes in different collector positions. In laser enrichment, the isotope shifts of the atomic levels are used to excite and ionize resonantly the ^{235}U atoms in a multi-step excitation scheme using several lasers emitting different wavelengths and by separating the

ions electromagnetically. The feasibility of this approach has been demonstrated, but there has not been a large-scale industrial application.

After isotope separation by gas diffusion and/or gas centrifuges, UO_2 may be obtained from UF_6 by hydrolytic decomposition, precipitation of U as ADU and heating, and uranium metal may be produced by reduction with hydrogen to UF_4 and further reduction with Ca. The handling of enriched uranium compounds requires small-scale operations with amounts on the order of 1–10 kg, depending on the conditions, to exclude criticality.

15.4 Fuel Elements

The design of fuel elements depends on the type of reactor and on the operating conditions. Fabrication of fuel elements does not apply for homogeneous reactors in which the fuel is used in the form of a solution of uranyl sulfate or uranyl [^{15}N] nitrate. In heterogeneous reactors, the fuel is applied in the form of metals or alloys or in the form of ceramic substances, such as UO_2, UC, or mixtures with other components.

In order to prevent corrosion of the fuel and escape of fission products, the fuel is tightly enclosed in fuel rods. Good heat transfer and low neutron absorption are important properties of the cladding. Generally, the fuel rods are assembled to fuel elements to make their exchange easier.

If metallic uranium is used as fuel, the modifications of the metal and their properties have to be taken into account (Table 15.4). The anisotropic thermal expansion of α-U leads to plastic deformations which restrict the use of metallic uranium considerably. Furthermore, from the difference in the density of α-U and β-U, the application of uranium metal is limited to temperatures up to about 660 °C. By adding Mo, the γ-phase can be stabilized down to room temperature, but the negative influence of the high neutron absorption of Mo must be compensated by a higher content of ^{235}U. For these reasons, metallic uranium is not used in modern reactors. It is applied in gas-cooled, graphite-moderated reactors operating with natural uranium (Calder Hall type). In some research reactors, alloys of U and Al or Zr are used, containing up to about 20% U.

The metallurgical properties of metallic plutonium are even more unfavorable than those of U. The melting point of Pu is 639 °C, and six solid phases are known.

Table 15.4 Modifications of uranium metal.

	Temperature range (°C)	Crystal lattice	Density (g cm^{-3})
α-U	Up to 668	Orthorhombic	19.04 (25 °C)
β-U	668–774	Tetragonal	18.11 (720 °C)
γ-U	774–1132	Cubic (b.c.)[a)]	18.06 (805 °C)

a) Body-centered.

Table 15.5 Properties of uranium dioxide and uranium carbide.

	UO_2	UC
Density at 20 °C ($g\,cm^{-3}$)	10.96	13.63
Melting point (°C)	2750	2375
Thermal conductivity ($J\,cm^{-1}\,s^{-1}\,K^{-1}$)	0.036	0.213
Specific heat ($J\,g^{-1}\,K^{-1}$)	0.239 (at 25 °C)	0.201 (at 100 °C)
Coefficient of thermal expansion (K^{-1})	$9.1 \cdot 10^{-6}$	$10.4 \cdot 10^{-6}$
Crystal lattice type	Cubic (b.c.)[a] (CaF_2 type)	Cubic (f.c.)[b] (NaCl type)

a) Body-centered.
b) Face-centered.

Furthermore, the critical mass of a reactor operating with pure Pu as fuel is below 10 kg, and it would be very difficult to take away the heat from such a small amount of material. A great number of Pu alloys have been investigated with respect to their possible use as nuclear fuel, but they have not found practical application.

Some properties of the ceramic fuels UO_2 and UC are summarized in Table 15.5. UO_2 is preferably used as nuclear fuel in all modern light-water reactors (LWRs) of the BWR type as well as of the PWR type. The main advantages of UO_2 are the high melting point and the resistance to H_2, H_2O, CO_2, and radiation. The main disadvantage is the low thermal conductivity, which has to be compensated by application of thin fuel rods.

UO_2 is a non-stoichiometric compound. Freshly reduced with hydrogen, it has the composition $UO_{2.0}$, but in air it takes up oxygen and the composition varies with the partial pressure of O_2 between $UO_{2.0}$ and $UO_{2.25}$. For use as nuclear fuel, pellets of UO_2 about 1 cm in diameter and 1 cm in height are produced. By sintering at 1600–1700 °C in hydrogen, the content of excess oxygen in UO_{2+x} is reduced to $x < 0.03$ and about 98% of the theoretical density is obtained.

The behavior of UO_2 pellets in a nuclear reactor is determined by the high temperature gradient in the pellets. Recrystallization takes place, and hollow spaces are formed in the center. However, up to a burn up of about 20 000 MWd per ton, these effects are of little importance and UO_2 is the most favorable fuel for LWRs.

PuO_2 is also well suited as a nuclear fuel. It is often used in the form of a UO_2/PuO_2 mixture ("mixed oxides"; MOXs) containing up to about 20% PuO_2. UO_2/PuO_2 mixtures may be applied in thermal reactors instead of enriched uranium, or in fast breeder reactors. Pellets of ThO_2 can be used in thermal converters for the production of ^{233}U.

The main advantage of UC is the high thermal conductivity. On the other hand, the low chemical resistance is a major disadvantage: UC is decomposed by water below 100 °C, which is prohibitive for its use in water-cooled reactors. However, UC may be applied in gas-cooled reactors (GCRs) or in the form of UC/PuC mixtures in fast sodium-cooled breeder reactors.

Table 15.6 Properties of some metals considered as cladding materials for nuclear fuel.

Element	Atomic number Z	Absorption cross section for thermal neutrons σ_a (barn)	Melting point (°C)	Thermal conductivity at 20 °C (J cm^{-1} s^{-1} K^{-1})	Specific heat (J g^{-1} K^{-1})	Coefficient of thermal expansion (K^{-1})	Density at 20 °C (g cm^{-3})
Be	4	0.009	1285	1.591	1.800 (20 °C)	$11.6 \cdot 10^{-6}$	1.848
Mg	12	0.063	650	1.574	1.047 (25 °C)	$25.8 \cdot 10^{-6}$	1.74
Zr	40	0.185	1845	0.209	0.335 (200 °C)	$6.11 \cdot 10^{-6}$	6.51
Al	13	0.232	660.2	2.106	0.871 (0 °C)	$23.8 \cdot 10^{-6}$	2.699
Nb	41	1.15	2468	0.553	0.272 (0 °C)	$7.2 \cdot 10^{-6}$	8.57
Fe	26	2.55	1539	0.754	0.473 (20 °C)	$11.7 \cdot 10^{-6}$	7.866
Mo	42	2.65	2622	1.340 (0 °C)	0.247 (0 °C)	$5.1 \cdot 10^{-6}$	10.22
Cr	24	3.1	1875	0.670	0.465 (25 °C)	$6.2 \cdot 10^{-6}$	7.19
Ni	28	4.43	1455	0.670	0.448 (25 °C)	$13.3 \cdot 10^{-6}$	8.90
V	23	5.04	1710	0.310 (100 °C)	0.502 (0 °C)	$8.3 \cdot 10^{-6}$	6.11
W	74	18.5	3410	1.675 (0 °C)	0.137 (20 °C)	$4.98 \cdot 10^{-6}$	19.30
Ta	73	21.1	2996	0.544	0.151 (20 °C)	$6.5 \cdot 10^{-6}$	16.6

The properties of some metals that have been considered as cladding materials for the manufacture of fuel rods are listed in Table 15.6. Al has many advantages, but it reacts with U at higher temperatures to intermetallic phases such as UAl_3. Mg was applied in the first reactor of the Calder Hall type, starting operation in 1956. However, the use of Mg limits the maximum temperature of operation to 400 °C. Be is not corrosion resistant to water. Zr is very resistant to corrosion as well as to temperature. However, it must be carefully refined to separate it from Hf, which exhibits high neutron absorption. Zr and its alloys zircaloy-2 and zircaloy-4 are preferably used in modern nuclear reactors. Steel has favorable mechanical properties, but it can only be used in the form of thin sheets because of its relatively high neutron absorption cross section. The other metals listed in Table 15.6 are also unfavorable because of the relatively high values of σ_a. Coated particles have been designed and developed as a special form of nuclear fuel for use in high-temperature gas-cooled reactors (HTGRs). These particles have a diameter of about 100 µm. They consist of a core of UO_2,UC, or UO_2/ThO_2 coated with layers of graphite and silicium carbide (Figure 15.10). Fuel elements are obtained by filling the coated particles into hollow spheres of graphite of about 6 cm outer diameter and 0.5 cm wall thickness, or by filling the fuel into graphite rods.

Another form of fuel element is the matrix elements in which the fuel is dispersed in a matrix of non-fissile material such as Al. Some combinations of ceramic fuel in a metallic matrix ("cermets") have found interest because of the high thermal conductivity. On the other hand, the metallic matrix causes relatively high neutron

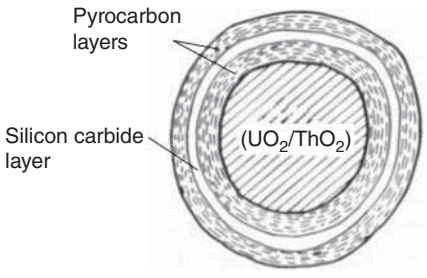

Figure 15.10 Coated particles.

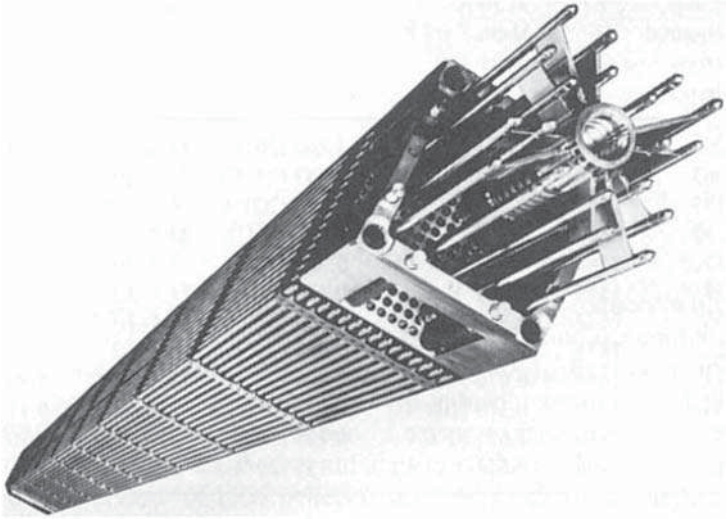

Figure 15.11 Fuel element used in pressurized water reactors (16 × 16 positions for 236 fuel rods and 20 control rods).

absorption and therefore matrix elements including cermets have only found very limited application.

As an example, a fuel element of the type used in a PWR is shown in Figure 15.11. The fuel element has 16 × 16 positions for 236 fuel rods and 20 control rods.

15.5 Nuclear Reactors, Moderators, and Coolants

Several types of nuclear reactors have already been mentioned in the previous section with respect to the use of nuclear fuel and the manufacture of fuel elements. The various types of nuclear reactors are distinguished on the basis of the following aspects:

- the kind of fuel used (e.g. natural U, enriched U, Pu, U/Pu mixtures);
- the energy of the neutrons used for fission (thermal or fast reactors);
- the kind of moderator (e.g. graphite, light water, heavy water);

- the combination of fuel and moderator (homogeneous or heterogeneous);
- the kind of coolant (e.g. gas, water, sodium, organic compounds, molten salts);
- the operation of the coolant (boiling water, pressurized water); and
- the application (e.g. research reactors, test reactors, power reactors, breeder reactors, converters, plutonium production, ship propulsion).

The first nuclear reactor was built by E. Fermi and co-workers, beneath the stand of a football stadium in Chicago, by using natural uranium and bars of graphite, and reached criticality in December 1942. It looked like a pile, the thermal power was 2 W, and cooling and radiation protection were not provided. The next nuclear reactor began operation in 1943 at Oak Ridge (USA) by using 54 tons of uranium metal in the form of fuel rods inserted into a block of graphite 5.6 m long, shielded by concrete. Several reactors of a similar type (graphite-moderated, water-cooled, natural uranium reactors) were built in 1943 and in the following years at Hanford (USA) for the production of plutonium to be used as a nuclear explosive.

The concept of energy production by nuclear reactors has found greater interest since about 1950. The first nuclear power station (graphite-moderated, gas-cooled [CO_2], natural uranium) began operation in 1956 at Calder Hall (UK). Today, PWRs and BWRs are the most widely used power reactors (Table 15.7). They contain about 100 tons of weakly enriched U (about 3.0–3.5% ^{235}U). Fast breeder reactors contain about 100 tons of natural U and about 6 tons of Pu, but no moderator. They exhibit several advantages: the high burn up is due to the fact that large amounts of ^{238}U are transformed into the easily fissile ^{239}Pu. In this way, the energy production from U is increased by a factor of about 100 and enrichment of ^{235}U by isotope separation is not needed. Some problems are caused by use of liquid sodium as a coolant due to its high reactivity. HTGRs have some advantages also because the high temperature of the coolant gives high efficiency, but they have not found broad application. The operation of GCRs, BWRs, PWRs, and HTGRs is shown schematically in Figures 15.12–15.15, respectively. Power reactors have also been developed and installed for ship propulsion, for instance, in submarines (e.g. *Nautilus*, USA) or icebreakers (e.g. *Lenin*, Russia).

Worldwide in 2008, 438 nuclear power plants produced 2600 TWh (14%) of electricity. Thereby, compared to the production of electricity by burning coal, 2 billion tons of CO_2 are avoided. Worldwide, 10 500 tons of spent nuclear fuel per year are discharged from the nuclear power plants of which about two-thirds is stored without reprocessing and about one-third (3900 ton a^{-1}) is reprocessed. On the other hand, the problems with respect to the storage of radioactive waste (fission products and actinides) have not yet been solved in a satisfactory way. Research and test reactors are designed for special purposes, such as the development of new reactor concepts, materials testing, or use as neutron sources. Generally, the energy production and the operating temperature are low. For materials testing, high neutron flux densities are required. Various irradiation facilities are installed in research reactors for neutron irradiation, such as irradiation channels, pneumatic dispatch systems, neutron windows, thermal columns, or uranium converters. The neutron fluxes vary between about 10^{11} and 10^{15} cm^{-2} s^{-1}, and the power varies between about 10 kW

Table 15.7 Most widely used power reactors.

Reactor type	Percentage[a)]	Fuel[b)]	Canning	Moderator	Coolant	Coolant temperature (°C)	Coolant pressure (MPa)	Power (MW_e)	Burn up (MWd per kg)
Pressurized water reactor (PWR)	≈64	UO_2 pellets (2.2–3.2%)	Zircaloy	H_2O	H_2O	300–320	14–16	1000–1300	30–35
Boiling water reactor (BWR)	≈22	UO_2 pellets (2.2–3.2)	Zircaloy	H_2O	H_2O	280–290	≈7	1000–1300	30–35
Pressurized heavy water reactor (PHWR)	≈5	UO_2 pellets (natural U)	Zircaloy	D_2O	D_2O	280–310	8–11	700–800	8–10
Pressurized-tube boiling water reactor (RBMK) (Russian design)	≈4	UO_2 (≈2%)	Zr (1% Nb)	Graphite	H_2O	280–300	7–8	1000	18–19
Gas-cooled reactor (GCR)	≈1.5	U metal (natural U)	Magnox	Graphite	CO_2	340–420	2.8–3.5	600–700	3–4
Advanced gas-cooled reactor (AGR)	≈2.5	UO_2 pellets (≈2%)	Stainless steel	Graphite	CO_2	400–680	3–4	620–930	17–19
Liquid-metal fast breeder reactor (FBR)	≈1	UO_2/PuO_2 pellets (≈1.5% PuO_2)	Stainless steel	—	Na	530–560	≈0.1	1200–1300	70–100
High-temperature gas-cooled reactor (HTGR)	<0.1	UO_2 (90–95%) + ThO_2 for example, coated particles	Graphite	Graphite	He	750–850	1–4	≥300	70–100

a) Percentage of the total nuclear power capacity in the world in 1994.
b) In parentheses: enrichment.

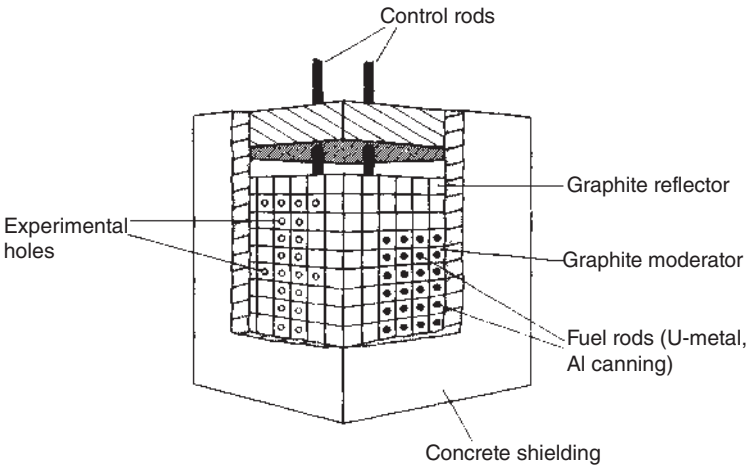

Figure 15.12 Gas-cooled reactor (GCR) operating with natural uranium (schematically).

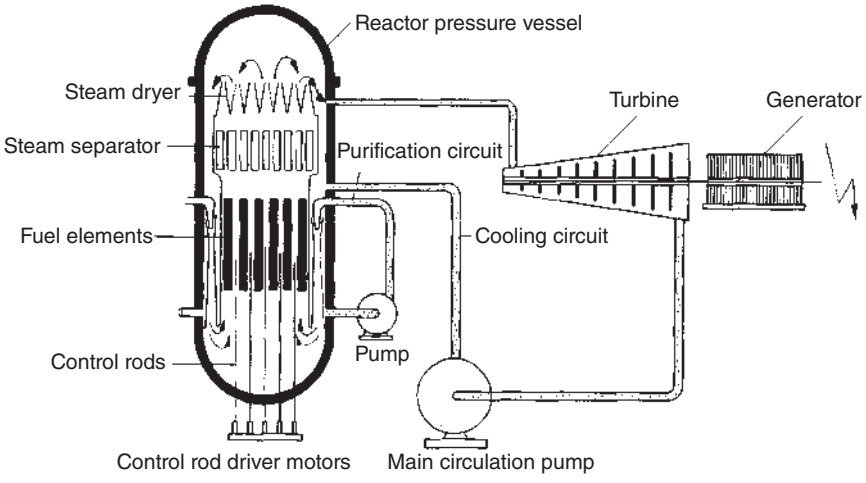

Figure 15.13 Boiling water reactor (BWR) (schematically).

and 100 MW. Reactors of the swimming pool type (Figure 15.16) are often used for research purposes. In the relatively small TRIGA reactors, mixtures of enriched uranium (20% ^{235}U) and zirconium hydride serve as fuel and moderator simultaneously. With increasing temperature, the moderation properties of zirconium hydride decrease, resulting in a prompt negative temperature coefficient of the reactivity which gives the reactor an inherent safety. Furthermore, taking out the control rods leads within about 0.1 seconds to a sudden increase in the neutron flux by a factor of about 1000 for a period of about 30 ms. These pulses can be used to advantage for the investigation of short-lived radionuclides or for the production and storage of ultracold neutrons. Homogeneous reactors containing solutions of enriched uranium (e.g. 20% ^{235}U) as sulfate in a small tank have also been designed for research

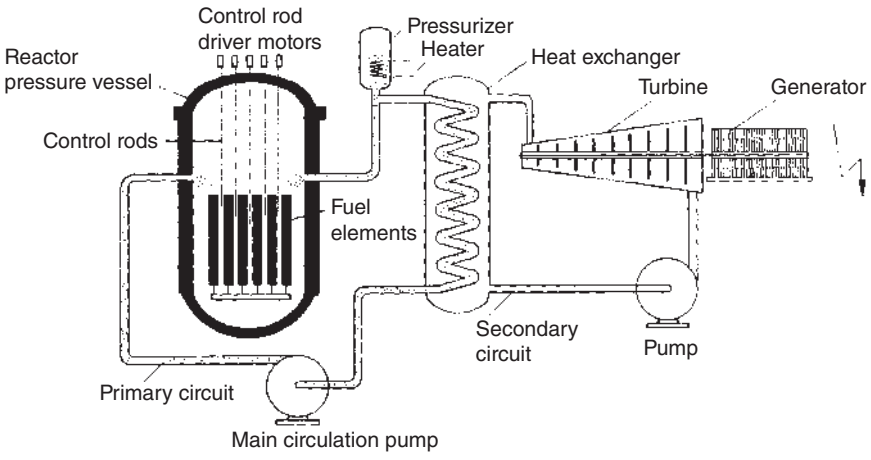

Figure 15.14 Pressurized water reactor (PWR) (schematically).

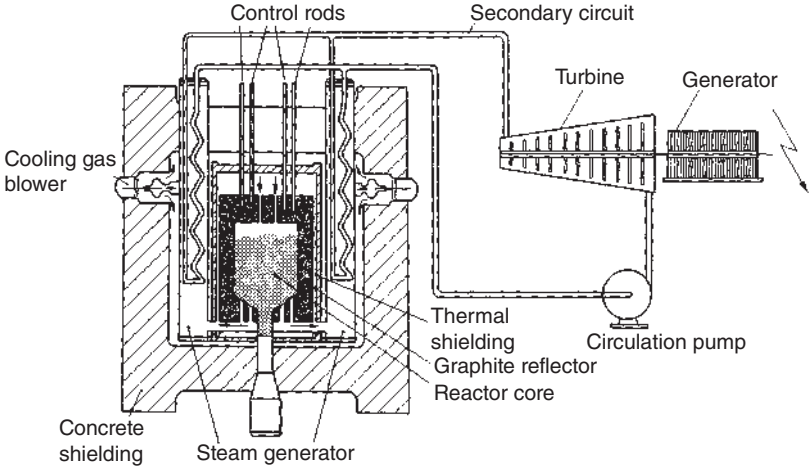

Figure 15.15 High-temperature gas-cooled reactor (HTGR) (schematically).

purposes. The properties of some moderators and coolants are listed in Table 15.8. As already mentioned, the purpose of the moderator is to take away the energy of the fission neutrons by collisions, without absorbing appreciable amounts of the neutrons. The dependence of the fission cross section σ_f of ^{235}U on the neutron energy is illustrated in Figure 15.17. The absorption cross section σ_a is relatively low for graphite, D_2O, CO_2, and He (Table 15.8). The relatively high absorption cross sections of H_2O and liquid metals require use of enriched U or of Pu as fuel. Thermal conductivity is of special importance in power reactors. Application of the same materials as coolant and moderator is desirable in the case of thermal reactors.

The disadvantages of water as a coolant are the low boiling temperature and the influence of corrosion. For operation at high temperatures, gases are preferable as coolants. As the ratio of heat transfer to pumping power is proportional to

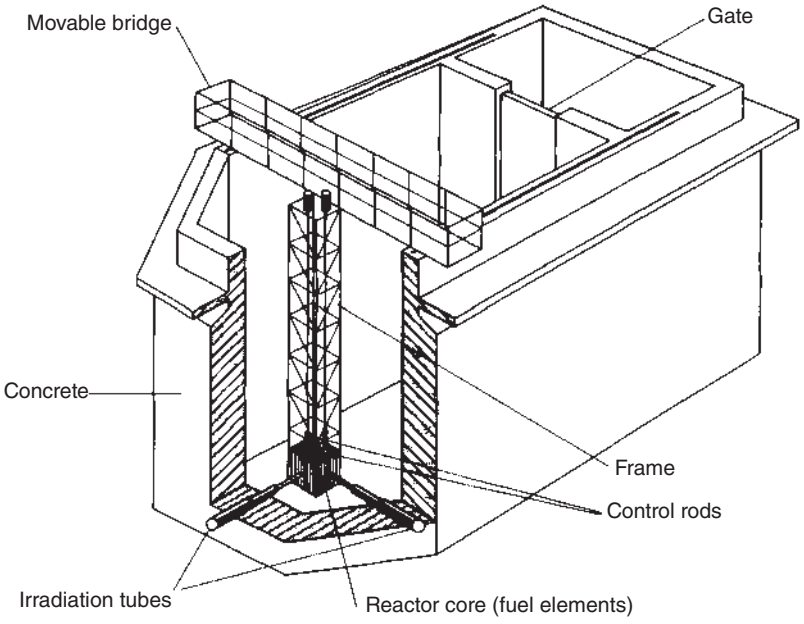

Figure 15.16 Swimming pool reactor (schematically).

Table 15.8 Properties of some moderators and coolants.

	Absorption cross section for thermal neutrons σ_a (barn)	Density at 20 °C (g cm^{-3})	Melting point (°C)	Boiling point (°C)	Thermal conductivity at 20 °C (J cm^{-1} s^{-1} K^{-1})	Specific heat at 20 °C (J g^{-1} K^{-1})
Graphite	0.004 5	2.256	Sublimation	3650	1.674	0.720 (25 °C)
D_2O	0.001 1	1.105	3.8	101.42	0.005 86	4.212
H_2O	0.66	0.998	0	100.0	0.005 86	4.183
CO_2	0.003 8	$1.977 \cdot 10^{-3}$	Sublimation	−78.5	0.000 184 (30 °C)	0.833 (15 °C)
He	0.007	$0.177 \cdot 10^{-3}$	−272.2	−268.6	0.000 611 (50 °C)	5.200
Na	0.53	0.928 (100 °C)	97.7	883	0.863 (100 °C)	1.386 (100 °C)

$M^2 c_p^2$ (M = molecular mass, c_p = specific heat), hydrogen would be the most favorable coolant at high temperatures. However, because of its reactivity, use of hydrogen is prohibitive. Helium is rather expensive; CO_2 is suitable as a coolant for graphite-moderated reactors, but at high temperatures, the instability of graphite due to the equilibrium $C(s) + CO_2(g) \Leftrightarrow 2CO(g)$ has to be taken into account. Liquid

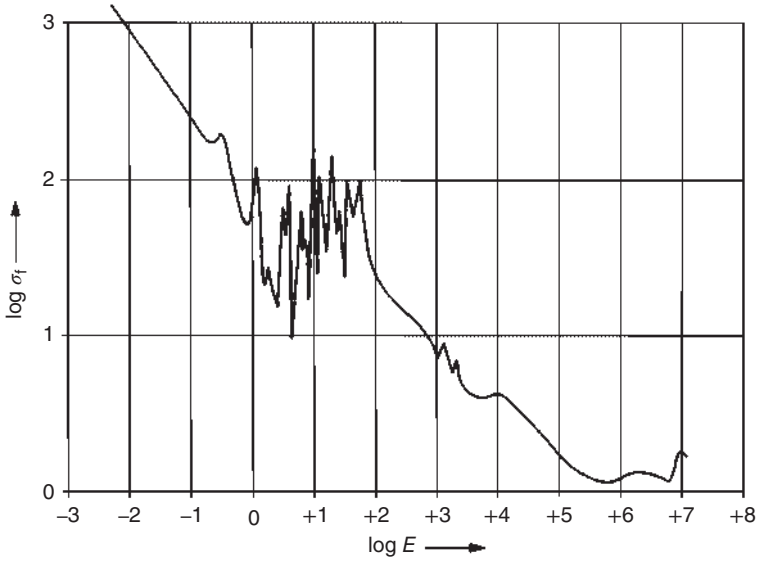

Figure 15.17 Fission cross section σ_f (barn) for the fission of ^{235}U as a function of the neutron energy E (eV). Source: According to Hughes and Harvey (1955).

metals exhibit high thermal conductivity, but because of their reactivity, special precautions are necessary.

All other materials used in nuclear reactors for construction or as tubes should exhibit low neutron absorption, low *activation*, no change in properties under the influence of the high neutron and γ-ray fluxes, and high corrosion resistance. These requirements are best met by zirconium, which has found wide application in nuclear reactors. Al, Be, and Mg have limited applicability. Steel and other heavy metals are only applicable if their relatively high neutron absorption is acceptable.

The range of fission products is small (about 5–10 μm in solids and about 25 μm in water), but their specific ionization is high. This leads to high temperatures in solid fuel, in particular in UO_2 (up to several thousand degrees Celsius). Furthermore, lattice defects and deformations are produced in solids, and gaseous fission products migrate under the influence of the temperature gradient into hollow spaces formed in the central part of the solids. Volatile fission products may escape if there are leaks in the canning material. This makes continuous control of the activity in the coolant and purification of the latter by passage through ion exchangers necessary.

Neutrons also produce lattice defects in solid fuel, but in lower local concentrations. (n, γ) reactions lead to activation products and contribute to the secondary γ radiation in the reactor.

The intense primary γ radiation due to deexcitation of the fission fragments, the β^- radiation from the fission products, and the secondary γ radiation emitted by the fission and activation products give rise to radiation-induced chemical reactions. The most important reaction is the radiation decomposition of water in water-cooled reactors, leading to the formation of H_2, H_2O_2, and O_2. Many substances dissolved

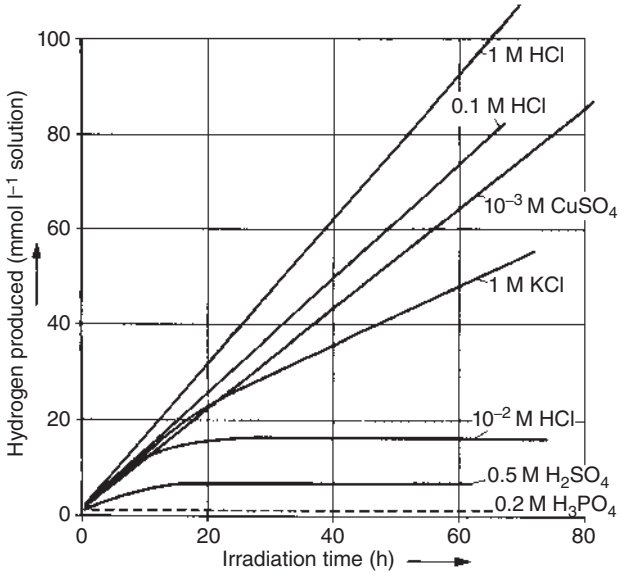

Figure 15.18 Influence of various components on the formation of hydrogen by radiolysis. Source: Dawson and Sowden (1963), figure 03 (p. 51)/Elsevier.

in the water influence the formation of H_2 (Figure 15.18). In most closed coolant systems, equipment for catalytic recombination of H_2 and O_2 is installed. In PWRs, H_2 is added to suppress the radiolytic effects.

As long as the reaction $^{\bullet}OH + H_2 \rightarrow H_2O + H\bullet$ is faster than the reaction $^{\bullet}OH + {}^{\bullet}HO_2 \rightarrow H_2O + H_2$, net decomposition of water does not occur, although all water molecules present in the cooling system are turned over at least once per day.

In order to compensate the excess reactivity (Section 15.1), in water-cooled reactors, boric acid is added to the coolant in concentrations up to about 0.2%. The concentration is reduced with increasing burn up. The pH is adjusted to $\approx$9 by the addition of 1–2 mg of ^{7}LiOH per liter of water to lower the solubility of the metal oxides and hydroxides, respectively, produced by corrosion on the walls of the cooling system.

15.6 The Chernobyl and Fukushima Accidents

It would be inappropriate at this point not to mention the Chernobyl and Fukushima accidents in 1986 and 2011, respectively. Both have caused great psychological problems of anxiety and stress with respect to the safety of nuclear energy in general.

In the following, we cite a passage from the "Historical Portrayal" contained in the Appendix of the Report "The Chernobyl Project – An Overview – Assessment of the Radiological Consequences and Evaluation of the Protective Measures – Report of an

International Advisory Committee" published by the International Atomic Energy Agency (IAEA), Vienna. There, we read:

> In the early hours of Saturday 26 April 1986, an accident which was to have global repercussions occurred at Unit 4 of the Chernobyl nuclear power plant in the USSR. Seconds past 01:23 Moscow time, two explosions in quick succession blew the roof off the Unit 4 reactor building. Concrete, graphite, and debris escaped through a hole which exposed the reactor core. Smoke and fumes along with a large amount of radioactive material rose in a hot plume almost 2 km high to be carried throughout the western portions of the USSR, to eastern and western Europe, and – in much smaller amounts – through the Northern Hemisphere. Heavier debris and particles fell near the site while lighter particles were carried west and north of the plant to the surrounding areas and neighboring Soviet Republics. Fire broke out on the roof of the adjoining turbine building. Fire, along with clouds of steam and dust, filled the Unit 4 building. Alarms went out to fire units in the region and, within minutes, plant firemen arrived. None of the firemen had been trained in fighting fires involving radioactive materials. Some set to work with plant personnel in the turbine hall and the Unit 4 building while others climbed to the roof of Unit 3, where they had to deal with burning graphite from the exploded core. By dawn on Saturday all but the graphite fire in the core had been extinguished.
>
> An explosion of this nature had not been considered possible by many Soviet nuclear experts and the initial reports of core destruction by workers who entered the Unit 4 building were not believed. Operators continued to direct water into the reactor building in a vain attempt to cool the reactor core and this contaminated water flowed to building levels that crossed to other units causing later contamination problems.
>
> Rescue workers, firemen, and operating personnel were generally unaware of the seriousness of the radiation risk. The high radiation levels could not be measured with available monitoring equipment and in some areas must have exceeded 100 Gy h^{-1}. Personnel had no dosimeters to measure their radiation dose and many were seriously irradiated. Less than an hour into the emergency, the first case of acute radiation syndrome was evident. The number of persons present at the reactor site in the early hours of 26 April who showed clinical effects due to radiation exposure or burns was 203.
>
> Signals indicating a serious accident involving an explosion, fire, and radiation from Chernobyl were transmitted automatically to the State Committee on the Utilization of Atomic Energy in Moscow moments after the accident. As the information accumulated even though the magnitude of the accident had not yet been fully established, it was decided to send key people from Moscow to direct operations. Top officials were called together as a Governmental Commission to provide the authority to mobilize resources. The plant management did not have the resources or authority to manage the response to an accident of this scale and it was the Governmental Commission itself

that directed operations. Unit 3 was shut down around 03:00, an hour and a half after the accident, while Units 1 and 2 were not shut down until the following night about 24 hours later.

Army forces were asked to carry out the first radiological assessments and to assist in controlling the fires. Early measurements showed neutron emissions, indicating continuing nuclear reactions in the destroyed Unit 4 core. As the accident would be more devastating if it spread to the other units, the Governmental Commission gave first priority to graphite fires.

The plant emergency plan was not suitable for an accident with large and continuous releases of radioactive material. Emergency facilities and emergency equipment were insufficient. There were no individual dosimeters for the emergency response units and no automatic radiation monitoring stations in the environs. Civil defense authorities specified possible shelters and proposed that the Pripyat town executive committee inform the population by radio of the radiation danger, but this was only done on Sunday just before the evacuation.

High radiation levels forced the Governmental Commission to move its headquarters from the town of Pripyat, 3 km from the reactor, to the town of Chernobyl, 15 km south-southeast of the plant, on 4 May. There were now thousands of people working on the site and organizational responsibility to provide them with equipment and food was transferred to the Deputy President of the Council of Ministers of the USSR, who set up an operations management center.

With the destroyed core open to the atmosphere, it was decided to cover the crater with heat absorbent and filtering materials. Air force pilots flew hundreds of hazardous missions over the core, from 27 April to 10 May, in helicopters rigged to drop tons of boron, lead, sand, and dolomite.[1] A growing concern was the possibility that molten fuel would reach the water in the pressure suppression pools below the core, causing steam explosion and further releases. Under extremely difficult conditions and in a radioactive environment, military volunteers managed to rig up temporary piping to pump out water that had filled the normally dry second level. The command team also undertook the installation of a concrete slab underneath the damaged reactor to prevent any molten fuel from damaging the floor structure and leaking into the ground below.

Thus, the citation from the above-mentioned report. The radioactivity set free was on the order of $5 \cdot 10^{17}$ Bq d^{-1} on 27 April decreasing to $1.5 \cdot 10^{17}$ Bq d^{-1} on 28 April, decreasing slowly to $1 \cdot 10^{17}$ Bq d^{-1} until 2 May, whereupon it increased again to reach $3 \cdot 10^{17}$ Bq d^{-1} on 6 May. On 7 May, the situation got half-way under control. The short-term and long-term radiological situation of the affected areas in the

1 Namely, 40 tons of boron carbide to absorb neutrons and prevent the reactor from becoming critical again, 800 tons of dolomite to give off carbon oxide to reduce the flow of oxygen to the graphite fire, 1800 tons of loam and sand to filter out radioactive particles, and 2400 tons of lead to absorb heat and to act as shielding.

USSR was dominated by the release of iodine (mostly ^{131}I), cesium (^{134}Cs and ^{137}Cs), strontium (primarily ^{90}Sr), and plutonium (^{239,240}Pu). In addition, highly radioactive fuel fragments (hot particles) were released. The Chernobyl accident was the largest short-term release from a single source of radioactive material to the atmosphere ever recorded. Heavy rainfall combined with local conditions created pockets ("hot spots") of exceptionally high surface radioactivity levels resulting in external dose rates that were as much as 5000 times the dose rate due to the natural background. Surface contamination maps were published in 1989.

The question is how such an accident could happen. The reason is related to the insufficient security culture in the USSR. In the years before 1986, there were precursor events that demonstrated the RBMK reactor-specific weaknesses in the technical design of this type of graphite-moderated BWR. In 1975, a reactivity accident happened in the nuclear power plant in Leningrad that damaged the reactor core, but the consequences were much less severe than in Chernobyl due to other circumstances. Measures taken to avoid the influence of the positive void coefficient of the RBMKs remained insufficient. Also, the positive shutdown effect of the RBMKs occurred in 1983 during the commissioning of the reactor in Ignalina. In summary, the technical reasons for the Chernobyl accident were known beforehand. Western BWRs and PWRs have a reactor pressure vessel around the core, a pressure-resistant safety vessel surrounding the latter, and both are mounted inside a solid steel concrete housing. This multi-barrier concept did not exist in the RBMKs, which allowed the exchange of fuel elements during operation (this facilitates plutonium production for weapons). The occasion when the Chernobyl accident happened was during a test that the operating crew had conducted a year ago, which failed. Therefore, there was a given pressure for success. In this test, it was planned, after an emergency shutdown, to use the decreasing rotational energy of the turbogenerator for about 40 seconds, to supply electricity for the operation of the pumping system circulating the water inside the reactor until the starting emergency Diesel engines were able to supply the necessary electric current for the pumping system. The test was categorized as an electrotechnical test only. It was worked out by an electrical engineer who considered the reactor as a steam producer for the turbine. Reactor safety aspects were not considered. The test was not harmonized with the supervising authority in charge of the power plant. At 01:00 on 25 April, the test was initiated by slowly reducing the thermal power of the reactor from 3200 MW downward. At 03:47, when the power was reduced to 1600 MW, the power distributor in the capital Kiev requested continued operation at this power until 23:00 in the late evening of 25 April, which was fulfilled. Before that time, the operating crew's shift ended and a new, inexperienced crew continued operation. At 23:10, that crew started the required further reduction of the power of the reactor with the aim of reaching a level between 700 and 1000 MW which was planned for the test. However, due to the incompetence of the operators, the power reduced to almost zero (30 MW). Running the reactor below 30% of its nominal power was prohibited. In order to regain power, most of the control rods were pulled out of the core (which was prohibited), resulting at 01:00 on 26 April in a presumably stable reactor power of 200 MW. At 01:23:04, the test was initiated. Because of increasing power, an emergency shutdown was

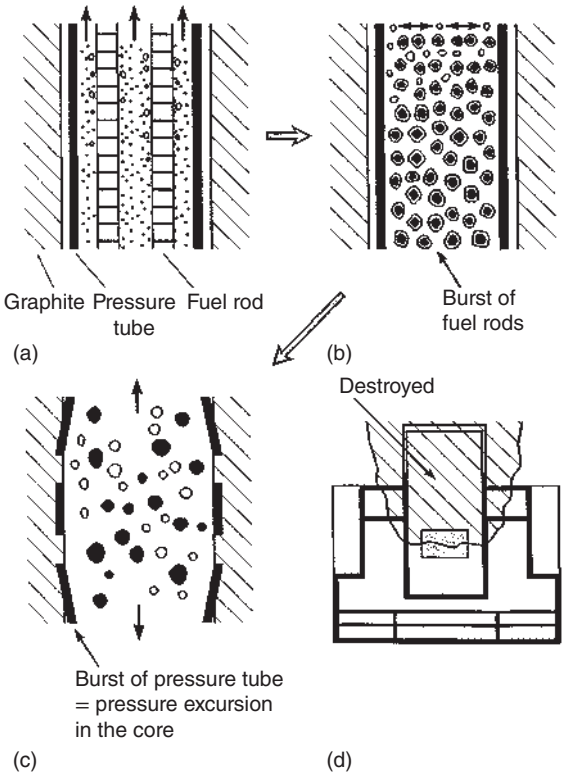

Figure 15.19 Consequences of a power excursion in a pressure tube of a RBMK boiling water reactor. (a) Intact pressure tube surrounded by the graphite moderator. The tube contains the fuel elements and the boiling water. (b) Burst of the fuel elements and production of excessive pressure. (c) Burst of the pressure tube and pressure release into the core. (d) Destruction of the core and the reactor building by explosion of the reactor core.

initiated by introducing all the control rods. Within seconds, a power excursion a hundred times the nominal reactor power developed and destroyed the reactor core, see Figure 15.19.

The reasons for the accident are manifold. First, a power reactor is principally not suited for experiments. Second, there are major deficits in the RBMK design – a positive void coefficient (the opposite of the prompt negative temperature coefficient of the TRIGA reactors). This was known to some experts, but not to the operating crew. Further, there is a positive shutdown effect at fully removed control rods, resulting in an insufficient effectivity of the fast shutdown system. Further, safety regulations were continuously disregarded, and existing safety interlocks were disabled.

On 11 March 2011, an earthquake of magnitude $M_w = 9.0$ (momentum magnitude scale) occurred at 14:46 local time (5:46 UTC) about 120 km east of the main island Honshu. It produced a tsunami which, apart from the direct effects of the earthquake, contributed considerably to the balance of defects of the event in the affected regions (15.592 dead persons, 5.070 missed). In the Japanese trench, the pacific plate dives under the Eurasian plate. The center of the earthquake was at a depth of 30 km and caused a horizontal shift of 23 m at the seafloor and a vertical shift of 9 m which produced the tsunami. In Honshu, the largest ground acceleration measured had a horizontal component of 27.0 m s^{-2} and a vertical component of 18.8 m s^{-2}. The horizontal component was in Sendai 15.2 m s^{-2} and in Tokyo 1.9 m s^{-2}. In many

locations on the east shore of Honshu, the defects caused by the vibrations of the earthquake were by large surpassed by the impact of the tsunami. The tsunami reached the nearest point at the Japanese coast to the center of the earthquake in about 30 minutes, the US-American Pacific coast in 9 hours, and Chile after 22 hours. At the location of the nuclear power station Fukushima Dai-ichi, the main wave arriving at 15:41 had a height of 14 m. (It was planned to withstand a breakwater height of 5.7 m.) The nearby nuclear power stations Fukushima Dai-ni and Onagawa reported heights of 10 and 15 m, respectively. In total, an area of 561 km^2 was flooded by the Tsunami.

The location of the Fukushima Dai-ichi Nuclear Power Station is at the east coast of the Pacific 250 km north of Tokyo. Here are six BWR blocks with powers of 460 (1), 784 (2–5), and 1.100 (6) MW_e. The operator of the installations is Tokyo Electric Power Company (TEPCO). As a consequence of the earthquake, the electrical power supply in northern Japan broke down completely. This caused the fast shutdown of the Fukushima blocks 1–3. The blocks 4–6 were in the stage of revision. In block 4, the reactor core was completely unloaded into the fuel element storage pool. Until the arrival of the tsunami, all blocks were supplied with electrical power by the emergency diesel engines including the additional cooling of the reactor cores and of the fuel element storage pools. As a consequence of the flooding of the power station by the tsunami, the emergency diesel engines, the auxiliary cooling water supplies, and the seawater pumps failed completely. Also, the emergency core cooling system (ECCS) was out of operation. As a consequence of the loss of cooling in the reactor pressure containers of blocks 1–3, the cooling water evaporated and steam was released into the condensation chamber, but there was no back supply of water into the reactor pressure container. As a consequence, the fuel elements melted and a Zr-water reaction, $Zr + 2H_2O \rightarrow ZrO_2 + 2H_2$, occurred. The pressure excursion in the safety container had to be released by venting into the building. Hydrogen explosions occurred in the buildings of blocks 1, 3, and 4, the latter being connected to the same exhaust line as used by block 3, so that hydrogen from the damaged reactor 3 could enter block 4. In addition, a damage occurred in the safety container of block 2. On 12 April 2011, the Nuclear and Industrial Safety Agency (NISA) published estimates of the release of radioactivity into the atmosphere, e.g. $1.6 \cdot 10^{17}$ Bq of ^{131}I and $1.5 \cdot 10^{16}$ Bq of ^{137}Cs, which correspond to roughly 10% of the release in the Chernobyl accident. On 11 March 2011, 20:50, the governor of the Fukushima prefecture decided to evacuate the population living in close vicinity to the nuclear power station within a radius of 2 km and widened the radius to 3 km half an hour later. On 12 March, 05:44, he increased this to 10 km, and at 18:25, after the explosion in block 1, to 20 km. Later this was finally fixed to 30 km.

A large part of the water used for external cooling of the reactors and the fuel element storage pools collected itself in the reactor and machine buildings. The amount was estimated to 100 000 tons of highly contaminated water with up to 1000 $mSv\,h^{-1}$. Part of it ran uncontrolled into the Pacific. According to estimates of TEPCO, between 1 April 2011 and 6 April 2011, these were 500 tons of water of a total of $5 \cdot 10^{15}$ Bq running out of block 2 into the Pacific. Further, TEPCO

released in a controlled way between 4 April 2011 and 10 April 2011 10 000 tons of contaminated water with a total activity of $1.5 \cdot 10^{11}$ Bq into the Pacific. With detectors positioned offshore in the Pacific, TEPCO could show that the activity in the seawater decreased to the detection limit by the end of April. NISA, in an evaluation of the events following 11 March 2011, noted, among others, the following lessons learned from the Fukushima accident:

- In the design of a power plant, the complete spectrum of possible external influences on the installation has to be considered. For this, all existing sources and methods are to be evaluated, which, with respect to the endangerment of the Fukushima Dai-ichi plant by tsunamis, has not been the case.
- One of the decisive reasons for the severe accident in Fukushima Dai-ichi was the long-term disruption of the electricity supply. To avoid such a power failure, the safety of the external power supply to earthquakes must be strengthened and a sufficient and diversified emergency power supply must be planned and realized.
- Even after a power failure, the cooling of the fuel inventory in the reactor pressure container as well as in the storage pools for spent nuclear fuel must be guaranteed by robust emergency provisions.
- There were several weak points discovered in the protocols of the periodic safety assessments (PSAs) of the Fukushima blocks. Neither in the normal nor in the earthquake PSAs, all possible effects of a tsunami on the plant were considered. Furthermore, no long-term station blackout was considered because a fast restoration of the external power supply and a high availability of the Diesel generators were assumed.
- As a plan ahead for the future, emergency measures can no longer be voluntary provisions by the operating company, but have to be integral part of a general safety concept supervised and approved by the responsible board of control.

This assessment shows that the safety margins realized by the power producer TEPCO against earthquakes and tsunamis were surpassed in Fukushima, that is, they were by far insufficient.

The necessary conclusion is that nuclear energy production is potentially dangerous. It can be managed safely, if a number of **safety functions** are guaranteed: (i) sufficient safety margins against external and environmental influences; (ii) reactivity control by an intelligent reactor design, and by efficient control rods and shutdown systems; (iii) reactor cooling by a robust multistage cooling system; and (iv) activity confinement in a pressure-resistant multi-barrier construction according to the defense-in-depth concept. This must be accompanied by a sophisticated, high-quality **safety concept**: (i) regulatory systems with interlocks that cannot be disabled; (ii) automatic shutdown and feed-in systems in case safely designed parameter limits are exceeded; and (iii) clear administration and strict technical rules for measures in case of irregular system conditions at several levels. Several of these fundamentals were disregarded in Fukushima and, moreover, in Chernobyl. Humankind will have to decide whether it is willing to continue to rely on nuclear energy production with the aim of reducing global warming by CO_2 emissions.

15.7 Reprocessing

Mastery of the handling of spent nuclear fuel, including safe disposal of the radioactive waste, is another prerequisite for the use of nuclear energy.

The main effects of the fission products are:

- radiation defects in the fuel elements which may lead to damage;
- poisoning of the reactor by neutron-absorbing fission products.

An example of the effect of poisoning is the series of isobars with mass number $A = 135$:

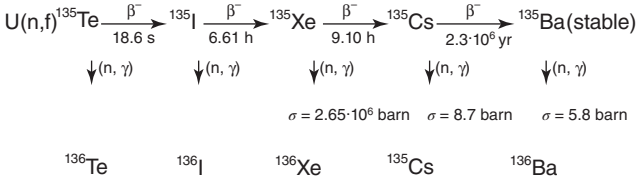

(15.8)

The neutron absorption of ^{135}Xe is extremely high. The ratio of the number of atoms transmuted by β^- decay to the number transformed by (n, γ) reactions depends on the neutron flux density Φ:

$$\frac{(dN/dt)_\beta}{(dN/dt)_{n,\gamma}} = \frac{N\lambda}{N\sigma\Phi} = \frac{\lambda}{\sigma\Phi} \tag{15.9}$$

At a neutron flux density $\Phi = 10^{14}\,cm^{-2}\,s^{-1}$, 93% of ^{135}Xe undergoes (n, γ) reactions.

The fission products that are mainly responsible for neutron absorption are listed in Table 15.9. With respect to the mass, the lanthanides represent the greatest fraction, but with regard to neutron absorption, the noble gases are most important due to the high value of σ_a for ^{135}Xe ($2.65 \cdot 10^6$ barn).

The effect of poisoning can be compensated to a certain extent by an excess reactivity or by installation of a breeder blanket (an outer layer of ^{232}Th) in which new

Table 15.9 Most important long-lived fission products.

Element	Relative abundance in the fission products (%)	Relative neutron absorption (%)
Noble gases	7	72
Samarium	70	14
Other lanthanides		11
Technetium	10	1
Cesium	4	0.5
Molybdenum	1	0.2
Other elements	8	1.3

fissile material is produced. In fast reactors, the effect of poisoning is less important because fast neutrons exhibit a lower absorption cross section. However, in all cases, fuel elements have to be exchanged for new ones after 10–80% of the fissile nuclides have been used up.

Further handling of nuclear fuel is determined by its activity and the heat production due to radioactive decay. The relation between energy production by fission and the number of fissions per second is given by

$$1\,\mathrm{MW} = 6.25 \times 10^{18}\,\mathrm{MeV\,s^{-1}} \approx 3.3 \times 10^{16}\,\mathrm{fissions\,s^{-1}} \tag{15.10}$$

As the *disintegration rate* of the fission products with $t_{1/2} > 1$ second is about five times the rate of fission, the activity of the fuel several seconds after shutting off the reactor is $\approx 17 \cdot 10^{16}$ Bq ($\approx 5 \cdot 10^{6}$ Ci) per MW of thermal energy produced. The β^- activity per MW and the heat production of the fission products are plotted in Figure 15.20 as a function of the time after shutting off the reactor. The heat

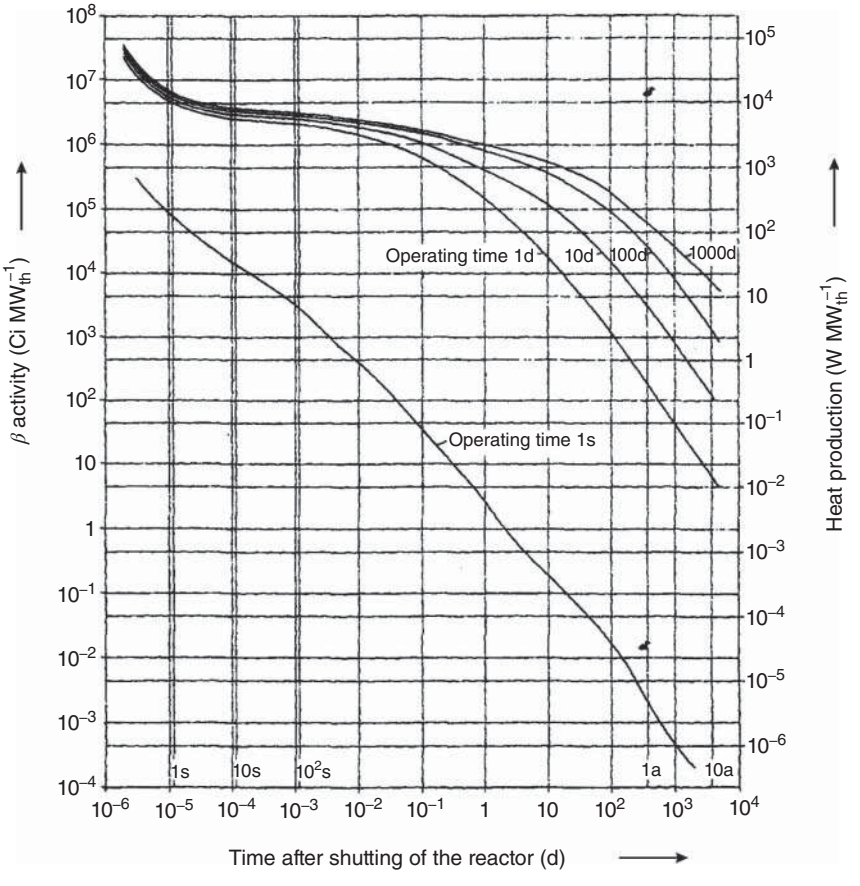

Figure 15.20 β^- activity and heat production of spent fuel as a function of the time after shutting off the reactor. (The γ activity amounts to about half of the β^- activity; the heat production is calculated for an average β^- energy of 0.4 MeV and quantitative absorption.)

production requires cooling of the fuel elements because melting of the fuel and volatilization of fission products may occur under unfavorable conditions. ^{237}U produced by the nuclear reactions ^{235}U(n, γ)^{236}U(n, γ)^{237}U and ^{238}U(n, 2n)^{237}U causes a relatively high initial activity of U. As ^{237}U decays with a half-life of 6.75 days,

$$^{237}\mathrm{U} \xrightarrow[\beta^-,\gamma]{6.75\ \text{days}} {}^{237}\mathrm{Np} \tag{15.11}$$

storage of the fuel elements for about 100 days is necessary before further handling.

The composition of spent nuclear fuel from LWRs after storage of one year is given in Table 15.10. The following options are possible:

(a) final disposal of the spent fuel elements;
(b) long-term intermediate storage with the aim of later reprocessing;
(c) short-term interim storage and reprocessing.

After interim storage for at least several months under water for cooling and radiation protection, the choice has to be made between options (a)–(c).

Table 15.10 Composition of spent nuclear fuel from a light water reactor at an initial enrichment of 3.3% ^{235}U, a burn up of 34 000 MWd per ton, and a storage time of one year.

Nuclide	Weight percent	
Uranium and transuranic elements		
^{235}U	0.756	95.4
^{236}U	0.458	
^{237}U	$3 \cdot 10^{-9}$	
^{238}U	94.2	
^{237}Np	0.05	
^{238}Pu	0.018	0.98
^{239}Pu	0.527	
^{240}Pu	0.220	
^{241}Pu	0.105	
^{242}Pu	0.038	
Americium isotopes	0.015	
Curium isotopes	0.007	
Fission products		
Stable fission products	3.00	3.62
^{85}Kr	0.038	
^{90}Sr	0.028	
^{129}I	0.09	
^{134}Cs + ^{137}Cs	0.275	
Others	0.19	

The main aim of reprocessing is the recovery of fissile and fertile material. If U or U–Pu mixtures are used as fuel, the fissile nuclides are ^{235}U and ^{239}Pu and the fertile nuclide is ^{238}U. Reprocessing of these kinds of fuel closes the U–Pu fuel cycle. The U–Th fuel cycle is closed by reprocessing spent fuel containing mixtures of U and Th. In the case of final storage of the spent fuel elements, the fuel cycle is not closed; fissile and fertile nuclides are not retrieved for further use.

Reprocessing is started after about six months to several years of cooling time, depending on the aim of reprocessing (e.g. recovery of Pu), the storage costs of unprocessed fuel, the reprocessing capacity, and the advantages of lower activities after longer interim storage.

In the case of the U–Pu fuel cycle (the plutonium and uranium recovery by extraction [PUREX] process), the main steps of reprocessing are the separation of U, Pu, and fission products including the other actinides. U and Pu are to be recovered in high purity and free from fission products and other actinides, in order to make further use possible. Pu causes problems because it may be used for the production of nuclear weapons. With respect to non-proliferation, strict controls of Pu input and output are necessary to avoid its misuse. Reprocessing of U–Th mixtures comprises the separation of U, Pu, Th, and the fission products, including the other actinides.

The details of reprocessing depend on the kinds of fuel and fuel elements. In the "head-end" process, the fuel elements are taken apart and the fuel is chopped if necessary. Canning material and fuel may be separated mechanically by using special machines or by chemical means. The chemical "head end" may consist of the dissolution of the canning, but more favorably fuel and canning are separated by dissolving the fuel after chopping the fuel elements ("chop–leach" process).

The result of the separation of U and Pu from the fission products and other actinides is characterized by the decontamination factor, given by the ratio of the activity of the fission products and actinides in the fuel to that in U and Pu after separation. The decontamination factors should be on the order of 10^6–10^7, and the recoveries of U and Pu should be near to 100%. These requirements are best met by solvent extraction procedures. With respect to the high activity of the fuel, remote control of all operations is necessary.

In general, 11 M HNO_3 is used for the dissolution of uranium metal and 7.5 M HNO_3 for dissolution of UO_2. After dissolution in HNO_3, U is present in the form of $UO_2(NO_3)_2$ and Pu mainly as $Pu(NO_3)_4$.

Gaseous or volatile fission products such as ^{85}Kr, ^{129}I (mainly as I_2, HI, and HOI), ^{106}Ru (as RuO_4), and a part of T are liberated in the course of chopping and dissolution of the fuel and are found in the off-gas. Another part of T is oxidized to tritiated water and is found mainly in the dissolver. ^{129}I and ^{106}Ru are retained in the off-gas scrubbers and filters containing silver-impregnated zeolite or charcoal for the fixation of iodine. ^{85}Kr may be separated from the off-gas by low-temperature rectification. After dissolution, the solution is adjusted to 1–2 M HNO_3, and by adding $NaNO_2$, quantitative transformation of Pu into Pu(IV) is secured.

In the first separation procedure operated on a technical scale, Pu was separated as Pu(IV) from U and fission products by coprecipitation with $BiPO_4$ (bismuth

Table 15.11 Extraction procedures used for reprocessing of spent nuclear fuel.

Process	Organic phase	Aqueous phase
PUREX	≈30% TBP (tri-*n*-butyl phosphate) in kerosene or in dodecane	HNO_3 (0.1–3 M)
Redox	Hexon (methyl isobutyl ketone)	HNO_3 (0.1–3 M) containing $Al(NO_3)_3$
Butex	Dibutylcarbitol	HNO_3 (0.1–3 M)
Eurex	TLA (trilaurylamine)	HNO_3 (0.1–3 M)
THOREX	≈40% TBP (tri-*n*-butyl phosphate) in kerosene	HNO_3 (0.1–3 M) containing $Al(NO_3)_3$

phosphate process). Today, solvent extraction is applied because it leads to higher decontamination factors and can be operated as a continuous process.

Solvent extraction can be carried out in pulsated extraction columns, in mixer-settlers, or in centrifuge extractors. Organic compounds such as esters of phosphoric acid, ketones, ethers, or long-chain amines are applied as extractants for U and Pu. Some extraction procedures are listed in Table 15.11. The PUREX process has found wide application because it may be applied for various kinds of fuel, including that from fast breeder reactors. The THOREX process is a modification of the PUREX process and has been developed for reprocessing fuel from thermal breeders.

In the first extraction cycle, U, Pu, and fission products (including other actinides) are separated in the following steps:

- Extraction of U(VI) and Pu(IV) from 1 to 2 M HNO_3 into the organic phase consisting of 20–30% tributylphosphate (TBP) in kerosene (extractor 1). The major part of the fission products and other actinides remains in the aqueous phase.
- Reduction of Pu to Pu(III) by the addition of Fe(II) or U(IV) and separation of Pu(III) from U by extraction into 1–2 M HNO_3 (extractor 2). U remains in the organic phase.
- Back-extraction of U into the aqueous phase (≈0.01 μ HNO_3). The organic phase is refined and recycled.

In the following extraction cycles, U and Pu, respectively, are refined:

Uranium cycle: U is extracted from 1 to 2 M HNO_3 into the organic phase and back-extracted into ≈0.01 M HNO_3. The organic phase is refined and recycled.

Plutonium cycle: Pu is oxidized to Pu(IV), extracted into the organic phase, reduced to Pu(III), and back-extracted into the aqueous phase. The organic phase is refined and recycled. Further purification of Pu is obtained by application of anion-exchange resins.

Refinement of the organic phase is necessary because of the formation of radiolysis products. The main product of radiolysis of TBP is dibutylphosphoric acid (DBP) which forms very stable complexes with Pu(IV) and prohibits quantitative reduction

to Pu(III). DBP is separated by washing the organic phase with an aqueous solution of Na_2CO_3.

The last step of reprocessing ("tail end") is the production of compounds of U and Pu suitable for further use, for example, UNH or a concentrated solution of $UO_2(NO_3)_2$, and PuO_2 or a solution of $Pu(NO_3)_4$, respectively.

An additional advantage of reprocessing may be seen in the possibility of converting the radioactive waste into chemical forms that are more suitable for long-term disposal, thus minimizing possible hazards. In this context, separation of long-lived radionuclides from the rest of the waste and their transformation into chemical forms of high stability have also been discussed. The recovery of actinides other than U and Pu (e.g. ^{237}Np and transplutonium elements) and of fission products such as metals of the platinum group, ^{85}Kr, ^{90}Sr, and ^{137}Cs is only of secondary interest because of the limited practical use of most of these radionuclides. The elements of the platinum group have a certain value as noble metals. ^{85}Kr, ^{90}Sr, ^{137}Cs, and long-lived isotopes of transplutonium elements may be applied as radiation sources, and ^{237}Np may be transformed by neutron irradiation into ^{238}Pu, which has found application as an energy source in *radionuclide generators*.

Dry reprocessing procedures, such as volatilization of U as UF_6, fusion with $Na_2S_2O_7$ or $NaOH/Na_2O_2$, chemical reactions in molten salts, or pyrometallurgical procedures, have also been proposed, but have not yet found practical application. The concept of pyrometallurgy with metallic fuel electrodes in molten LiCl–KCl at 450 °C is attractive because it comes with a large electrochemical window of 3.7 V between the reduction of $Li^+ \rightarrow Li^0$ at the cathode and the oxidation of $Cl^- \rightarrow Cl_2(g)$ at the anode, see Figure 15.21, to be compared to the narrow electrochemical window of only 1.2 V in water between the reduction of $H^+ \rightarrow H_2(g)$ and the oxidation of $H_2O \rightarrow O_2(g)$ making the reduction of lanthanides and actinides impossible in aqueous solution. If Al cathodes are used, the potentials for the electrodeposition of actinides are all more than −1.3 V, while those for the lanthanides are <−1.4 V, which is attractive for *partitioning* to be discussed in Section 15.8. Furthermore, the deposited actinides form stable alloys with the Al so that no reoxidation of the actinides is possible. The scenario of the pyrometallurgical electrodeposition of the actinides is shown schematically in Figure 15.22.

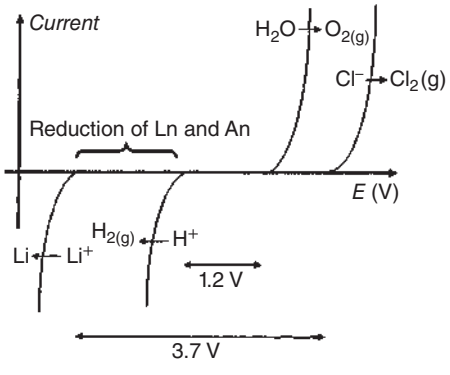

Figure 15.21 Electrochemical windows: LiCl–KCl vs. water.

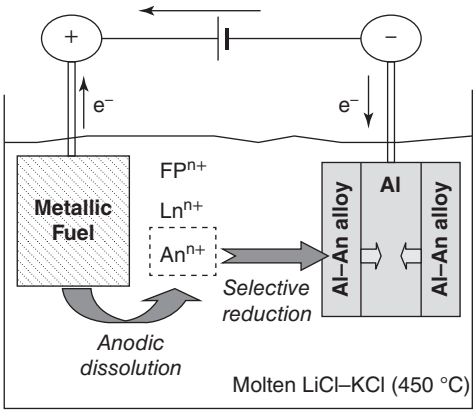

Figure 15.22 Pyrometallurgical electrodeposition of actinides from a molten LiCl–KCl eutectic at a metallic Al cathode. Source: J.-P. Glatz.

15.8 Radioactive Waste

In Table 15.3, the daughters of the uranium present in the original uranium ore were listed. The tailings from uranium mining and milling contain ≈70% of the original activity of the ore. This activity decays with the half-life of ^{230}Th, $\approx 7.5 \cdot 10^4$ year. In spite of the radiological hazard associated with the mill tailings, these were often simply dumped near the uranium mine in nature as, for example, in the former German Democratic Republic. The inert gas ^{222}Rn can escape from these tailings and can create a radiological inhalation risk. Also, ^{230}Th and ^{226}Ra can be leached from the tailings by acidic rain and transferred to the biosphere. The tailing material is finely divided sand that can be dispersed by the wind. Thus, remediation of sites containing mill tailings is necessary and involves coverage by clay or earth more than 3 m thick to reduce the release of Rn, and to minimize leaching and wind dispersal.

The radioactive wastes originating from the operation of nuclear reactors and reprocessing plants are classified according to the activity level:

- low-level waste (LLW or LAW, low-active waste);
- medium-level waste (MLW or MAW, medium-active waste);
- high-level waste (HLW or HAW, high-active waste);
- and according to the state of matter (gaseous, liquid, or solid).

In nuclear reactors, radionuclides are produced by nuclear reactions in the coolant and in various solid materials in the reactor vessel. Furthermore, fission products or actinides may leak into the cooling system from faulty fuel elements. T, ^{14}C, ^{13}N, ^{16}N, ^{19}O, ^{18}F, and ^{41}Ar are produced by a multitude of nuclear reactions with various nuclides in the coolant, for example, ^{2}H(n, γ)^{3}H, ^{10}B(n, 2α)^{3}H, ^{13}C(n, γ)^{14}C, ^{14}N(n, p)^{14}C, ^{13}C(n, p)^{13}N, ^{14}N(n, 2n)^{13}N, ^{16}O(n, p)^{16}N, ^{18}O(n, γ)^{19}O, ^{18}O(n, p)^{18}F, and ^{40}Ar(n, γ)^{41}Ar. Other radionuclides are produced by nuclear reactions with metals and their corrosion products (^{51}Cr, ^{54}Mn, ^{59}Fe, ^{58}Co, ^{60}Co, ^{65}Zn, ^{124}Sb). Corrosion products may dissolve in ionic form, or they may be carried in the form of ionic particles with the coolant. The dominating radionuclides released from faulty fuel elements are ^{3}H, ^{85}Kr, ^{131}I, ^{133}I, ^{133}Xe, ^{135}Xe, ^{134}Cs, and ^{137}Cs.

Off-gas and coolant are purified continuously in the nuclear power stations. The off-gas passes a catalytic hydrogen–oxygen combiner and a delay system allowing short-lived radionuclides to decay. The remaining radionuclides are retained in charcoal filters. Under normal operating conditions, only limited amounts of radionuclides are given off into the air. Part of the coolant is branched off from the primary circuit and passed through a filter and an ion exchanger to retain particulates and ionic species, respectively. Other radioactive wastes are produced by decontamination and various purification procedures.

The amounts of wastes produced from a 1000 MW_e power station per year are on the order of 5000 m^3 LLW and 500 m^3 MLW. Liquid wastes may be reduced in volume by purification or concentration, combustible solid wastes by incineration. The general tendency is to transform larger volumes of LLW into smaller volumes of MLW. The latter are enclosed in blocks of concrete or mixed with bitumen and loaded into steel drums.

Dismantling of decommissioned nuclear reactors requires special procedures. The outer parts can be handled like normal industrial waste, whereas the inner parts, mainly the reactor vessel and some core components, exhibit high radioactivity due to activation. Radioactive deposits on the inner surface of the reactor vessel may be removed by chemical decontamination. All-together, the relatively large volumes of LLW and MLW which are obtained by dismantling are further processed and then preferably enclosed in concrete or bitumen.

The largest amounts of radioactivity are in the spent fuel elements, which represent HLW. For final disposal, the spent fuel elements may be taken apart and the fuel rods may either be canned and put into casks, or be cut into pieces and loaded into canisters and casks.

Reprocessing of nuclear fuel by the PUREX process leads to the following amounts of waste per ton of U: $\approx$1 m^3 HLW (fission products and actinides in HNO_3 solution), $\approx$3 m^3 MLW as organic solution, $\approx$17 m^3 MLW as aqueous solution, $\approx$90 m^3 LLW (aqueous solution). By further processing, a volume reduction is achieved: $\approx$0.1 m^3 HLW, $\approx$0.2 m^3 MLW (organic), $\approx$8 m^3 MLW (aqueous), $\approx$3 m^3 LLW (aqueous).

The HLW solutions obtained by reprocessing are collected in tanks near the reprocessing plants. They contain relatively high concentrations of HNO_3, which can be decomposed by the addition of formaldehyde or formic acid. At low acid concentrations, however, hydrolysis and precipitation of elements of groups III and IV occur. Concentration by heating may lead to the volatilization of fission products, such as Ru isotopes in the form of RuO_4.

After one year of intermediate storage of spent nuclear fuel and reprocessing, the initial activity of the HLW solutions is on the order of 10^{14} Bq l^{-1}. The activity due to the presence of ^{90}Sr and ^{137}Cs is about 10^{13} Bq l^{-1}, and after 10 years, the activity of the HLW solution decreases approximately with the half-life of these radionuclides (28 and 30 years, respectively). After about 1000 years of storage, the activity is on the order of 10^4 Bq l^{-1}, determined by long-lived fission products (e.g. ^{99}Tc and ^{129}I) and the minor actinides.

The high initial activity of the HLW solutions causes heating and radiation decomposition. If no countermeasures are taken, the solutions are self-concentrating by

evaporation, strong corrosion occurs, nitrous gases and gaseous fission products are given off, and hydrogen and oxygen are formed by radiolysis. These effects require extensive precautions, such as cooling, continuous supervision of the tank, ventilation, filtering, and control of the air.

After various times of storage, the HLW solutions are processed with the aim of transforming the waste into a stable form suitable for long-term disposal and to reduce the volume as far as possible. Most suitable chemical forms are ceramics or glasses obtained by calcination or vitrification, respectively, of the waste. Solutions containing large amounts of $Al(NO_3)_3$ due to the dissolution of Al canning may be calcinated by spraying them into a furnace. By adding silicates or SiO_2, leaching of the products by water can be suppressed. Glasses are obtained by the addition of borax or phosphates. The liquid drops of glass formed in the furnace can be collected in steel containers.

Final disposal of HLW is planned and in some places performed in underground repositories. Several kinds of geological formations have been discussed or used, for example, tuff (USA), salt domes (Germany), granite (Sweden), or clay (Switzerland, Belgium, France). The geological formations should remain unchanged for long periods of time ($>10^4$ years), and access of water should be excluded.

In safety assessments, the following scenario is discussed: access of water, corrosion of the containers, leaching of the waste, and migration of the radionuclides to upper layers of the Earth where they may enter the biosphere.

Besides the HLW solutions, various other kinds of waste are obtained by reprocessing. Dismantling and chopping of the fuel elements give rise to solid MLW and LLW. Finely dispersed particles of undissolved metals or metal oxides (e.g. Ru, Rh, Mo, Tc) are separated as MLW from the dissolver solution by filtering or centrifugation. Chopping and dissolution of the fuel lead to volatilization of T (as T_2 or HTO), ^{14}C (as CO_2), ^{85}Kr, ^{129}I, and ^{106}Ru (as RuO_4). The amount of T is relatively high. To avoid release into the air, T may be oxidized to T_2O by treating the fuel after chopping and before dissolution at elevated temperature (500–700 °C) with oxygen ("voloxidation"). HTO formed by dissolution may be condensed and led back into the dissolver. ^{14}C formed by the reaction $^{14}N(n, \gamma)^{14}C$ from nitrogen impurities in the fuel is oxidized in the dissolver to $^{14}CO_2$.

The off-gas passes scrubbers containing NaOH solution and filters with silver-impregnated zeolite or charcoal in which Ru and I are retained. Kr may be separated by condensation or adsorption on charcoal at liquid-nitrogen temperature.

The extraction cycles lead to the production of various aqueous and organic waste solutions, mainly from solvent clean-up and washing. Some of the aqueous LLW solutions may be released directly into the environment if their activity is low enough. Others are decontaminated by precipitation, coprecipitation, ion exchange, or sorption procedures. The general tendency is to reduce the volume as far as possible and to transform the LLW into MLW, as already mentioned. Liquid organic wastes are incinerated, or the radionuclides contained therein are separated by precipitation or other procedures. Solid wastes containing long-lived α emitters (^{239}Pu and other actinides), including wastes from handling these radionuclides in the laboratory, require the application of special procedures such as wet oxidation

by a mixture of H_2SO_4 and HNO_3 followed by solvent extraction and isolation of the α emitters.

Several concepts have been developed to avoid or to minimize the risks of long-term storage of HLW. An interesting concept is that of "burning" long-lived waste by nuclear transmutation, thus reducing the time necessary for storage from "geological time periods" (10^5 years) to "historical time periods" (330 years), after which the *radiotoxicity* has decreased to the level of natural uranium. This accelerator-driven transmutation technology (ADTT) proposed, for example, by Bowman (1995) at Los Alamos, USA, is based on the production of neutrons by spallation of heavy nuclei. A high-intensity proton beam of 1 GeV from a linear accelerator is directed onto a target of molten Pb–Bi eutectic surrounded by a graphite moderator in which the neutrons produced by spallation of Pb and Bi nuclei are slowed down. The waste to be "burned" is dissolved in D_2O or in a molten salt and circulated within the moderator, where it is transmuted by fission (minor actinides) and/or neutron capture followed by β^- decay (fission products). In this way, a great part of the waste is transformed into stable or short-lived products. The heat generated by fission is converted into electricity by the usual techniques. It is estimated that about 20% of this electricity is sufficient to power the accelerator. The "furnace" is surrounded by a cylindrical fuel element containing ^{233}U which, by thermal neutron-induced fission, increases the total neutron flux density to $10^{16}\,n\,cm^{-2}\,s^{-1}$. The ^{233}U reactor is undercritical ($k_{eff} < 1$) when the accelerator is shut down. The assembly is surrounded by another cylinder containing ^{232}Th which is used to produce ^{233}U according to Eq. (15.5), making the total assembly a breeder reactor at the same time. The effective lifetime of ^{239}Pu in the waste inside the "furnace" is less than one day.

A prerequisite for the transmutation of the HLW is the highly efficient chemical separation (partitioning) of the lanthanides from the minor actinides because the lanthanides would jeopardize the transmutation due to their extremely high neutron capture cross sections. In Europe, the strategy being developed is to modify the PUREX process and to link it subsequently with a (DIAmide EXtraction) DIAMEX and a (Selective ActiNide EXtraction) SANEX process. By this partitioning and transmutation strategy (P + T) one aims at the goal that after a few hundred years ("historical time periods"), the radiotoxicity of the inventory of the waste disposal has decreased to the level of natural uranium, thus reducing its long-term risk considerably. Figure 15.23a shows the radiotoxicity of 1 ton of burned nuclear fuel as a function of time after discharge from the reactor. It is shown separately for the fission products, the minor actinides, and for Pu. It is evident that for the first hundred years, the fission products are delivering the largest contribution, then until about 1000 years the minor actinides take over, and afterward, up to 100 000 years ("geological time periods"), the contribution of the Pu is dominant. As discussed in Section 15.7, the separation of U and Pu in the PUREX process is a nuclear technological standard. Industrial reprocessing plants are operated in LaHague (France), Sellafield (England), and Rokkasho (Japan). By separation of 99% of the plutonium, the radiotoxicity of the remainder of the waste reaches the level of natural uranium after about 16 000 years, see Figure 15.23b.

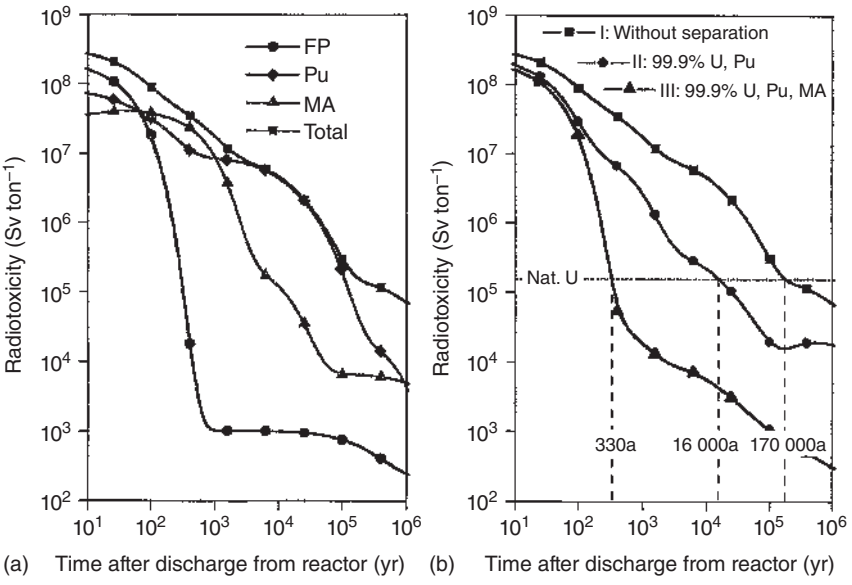

Figure 15.23 Radiotoxicity inventory of 1 ton of spent nuclear fuel from a pressurized water reactor (4.2% ^{235}U, burn up 50 GWd ton^{-1}) vs. time after discharge from the reactor in years. (a) Contribution of plutonium (Pu), minor actinides (MA), and fission products (FP) to the radiotoxicity. (b) Influence of the separation of the actinides on the radiotoxicity. Reference value is the amount of natural uranium that is needed for the fabrication of 1 ton of fuel.

The transmutation of the minor actinides reduces the time until the radiotoxicity has reached the level of natural uranium significantly below 1000 years. However, the separation of the minor actinides must be extremely efficient. It must reach 99.9% in order for the radiotoxicity to fall below the level of natural uranium after 330 years (Figure 15.23b). For the light actinides, the 5f electrons are delocalized, see Chapter 17, and they thus show a rich redox chemistry. This enables these elements to be separated by a marked selection of the oxidation state. By oxidation of the Np to Np(VI), this minor actinide can be separated in a modified PUREX process. In the partitioning concept developed in Europe (Figure 15.24), the modified PUREX process is linked with the *DIAMEX* process. Ligands that have been proven to be suitable in semi-technical processes include DMDOHEMA *N,N′*-dimethyl-*N,N′*-dioctyl-2-(2-hexyloxy-ethyl) malonamide, see Figure 15.25. With that, see Figure 15.24, the fission products are separated from the lanthanides, Am, and Cm. The SANEX process is subsequently applied to separate Am and Cm from the lanthanides. For these heavier actinides, the 5f electrons are again localized closer to the nucleus because of the actinide contraction and influence the chemical properties only negligibly like the 4f electrons in the lanthanides. Ionic radii and oxidation states of the lanthanides and of Am and Cm are very similar. Therefore, separation is extremely difficult; in addition, the lanthanides occur in a large surplus. With hard donor ligands such as oxygen, for example, DMDOHEMA, the Ln^{3+} and An^{3+} complexes are thermodynamically very similar

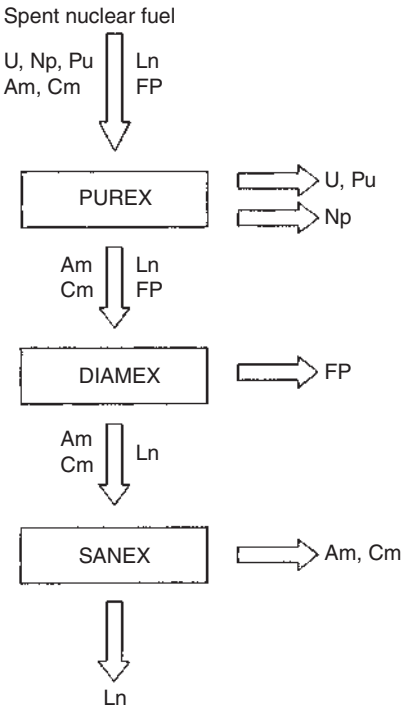

Figure 15.24 Representation of the separation scheme of uranium, neptunium, plutonium, americium, curium, lanthanides, and fission products in the PUREX, DIAMEX, and SANEX processes.

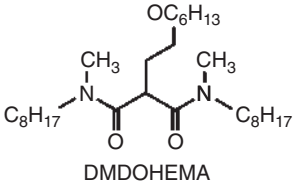

Figure 15.25 Structure of DMDOHEMA.

and no separation is achieved. As the actinides have a larger ability to form covalent bindings, they form, in particular with soft donor ligands (weak Lewis bases) such as N, stronger complexes than the lanthanides. With the bis-triazine-pyridine ligands (BTP and BTBP, Figure 15.26) developed in Karlsruhe (Germany), for the first time, it was possible to separate Am and Cm from the lanthanides up to 1 M HNO_3 (PUREX raffinate) with a separation factor over 100. First experiments uncovered the instability of the BTPs of the first generation against hydrolysis. That was overcome with the $CyMe_4$-BTBP (Figure 15.26) which proved to be sufficiently stable. In hot tests of the process in the laboratory, a recovery of Am^{3+} and Cm^{3+} of over 99.9% was achieved. With extended X-ray absorption fine structure (EXAFS) spectroscopy, see Section 22.6, it was shown that the coordination number of the complexes is 9, that is, three BTP ligands are bound to the An^{3+} ion through three nitrogen atoms each ($AnL_3(NO_3)_3$).

Work is continuing to improve the separation processes and to develop improved nitrogen donor ligands. However, P + T will not be able to replace the geological

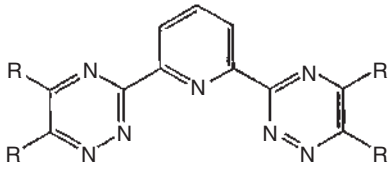

BTP
(bis(5,6-dialkyl-1,2,4-triazin-3-yl)-pyridin)

(a)

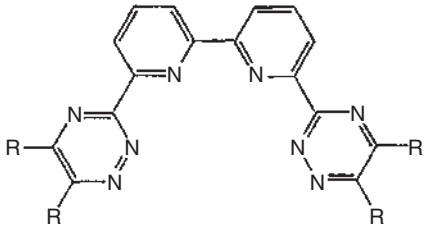

BTBP
(6,6′-bis(5,6-dialkyl-1,2,4-triazin-3-yl)-2,2′-bipyridin)

(b)

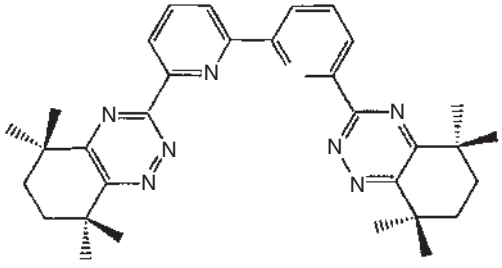

$CyMe_4$-BTBP
(6,6′-bis(5,5,8,8-tetra-methyl-5,6,7,8-tetrahydro-benzo-1,2,4-triazin-3-yl)-2,2′-bipyridin)

(c)

Figure 15.26 Structure of (a) BTP, (b) BTBP, and (c) $CyMe_4$-BTBP.

repositories. The latter are also needed for the remaining highly radioactive waste, which will, however, represent a reduced long-term risk potential.

A new separation process suitable for homogenous reprocessing of major (U, Pu) and minor (Np, Am, Cm) actinides in future closed fuel cycles has successfully been demonstrated with irradiated fast reactor fuel. This process involves two solvent extraction cycles, a first one to recover uranium and a second one to recover the transuranium elements (TRU: Np, Pu, Am, Cm).

The so-called GANEX (grouped actinides extraction) process was initially developed at the CEA (Commissariat a l'energie atomique et aux energies alternatives) in France. It consists of two cycles; the first cycle removes the large mass of uranium

and the second cycle is to recover the transuranium elements. The first cycle process is based on a selective U(VI) extraction from an aqueous phase of approximately 5 mol l^{-1} HNO_3 into DEHiBA (*N*,*N*-di(2-ethylhexyl) isobutyramide), dissolved in TPH (hydrogenated tetrapropylene),an industrial aliphatic diluent. Co-extracted Tc and Np are reduced and scrubbed by hydrazine in a scrubbing section at 1.5 mol l^{-1} HNO_3 and thereby routed together with the TRU and the fission products (FP) to the high-level raffinate (HAR). U(VI) is efficiently stripped from the organic phase into 0.01 mol l^{-1} HNO_3. The first GANEX cycle has been demonstrated in the ATLANTE facility at the CEA using a highly active feed solution from dissolved irradiated fuel. The raffinate from the first cycle is the feed for the second GANEX cycle, where TRU (present as tri-, tetra-, and hexavalent actinides) are separated and selectively recovered: TRU, lanthanides, Y, Mo, Tc, Zr, and Fe are coextracted into a solvent containing DMDOHEMA (*N*,*N*′-dimethyl-*N*,*N*′-dioctyl-2-(2-hexyloxy-ethyl) malonamide and HDEHP (di(2-ethylhexyl)phosphoric acid) diluted in TPH. Several selective stripping stages are implemented. First, Mo, Ru, and Tc are stripped with 0.4 mol l^{-1} citric acid at pH of 2.7, and then TRU are stripped into a solution containing 0.5 mol l^{-1} *N*-(2-hydroxyethyl) ethylenediaminetriacetic acid (HEDTA) and 0.5 mol l^{-1} citric acid at pH = 3 with 0.1 mol l^{-1} hydroxyurea, acting as a reducing agent for neptunium(VI). Finally, Ln, Zr, and Fe are recovered by 0.5 mol l^{-1} oxalic acid and 0.2 mol l^{-1} TEDGA (tetraethyl diglycolamide). The second GANEX cycle has also been demonstrated in the ATLANTE facility at the CEA using the highly active raffinate from the first cycle test. Although excellent results were obtained, it was generally recognized that there is a need to simplify the rather complicated and pH-sensitive stripping section.

Therefore, an alternative GANEX second cycle concept was developed, the EURO-GANEX process. The approach for selective TRU stripping is based on the selectivity of a novel water-soluble BTP molecule for complexation with trivalent actinides compared to the trivalent lanthanides. This enables stripping at higher acidities and thereby removes the need to control pH. The EURO-GANEX solvent is 0.2 mol l^{-1} TODGA (*N*,*N*,*N*′,*N*′-tetra-*n*-octyl diglycolamide; see Figure 15.27), +0.5 mol l^{-1} DMDOHEMA in Exxsol D80 (a kerosene diluent). This solvent co-extracts Np(VI), Pu(IV), Am(III), Cm(III), and Ln(III) from the GANEX first cycle raffinate and is capable of high Pu(IV) loading capacity, up to 40 g l^{-1}. DMDOHEMA extracts An(IV) much more efficiently than An(III). Hence, DMDOHEMA may also contribute to Pu(IV) extraction. Zr(IV) and Pd(II) are masked using CDTA (*trans*-1,2-cyclohexanediaminetetraacetic acid; see Figure 15.28); co-extracted Sr(II) and Fe(III) are scrubbed using 0.5 mol l^{-1} HNO_3. TRU is stripped from the loaded solvent using a strip solution containing SO_{3-}-Ph-BTP (2,6-bis(5,6-di(3-sulphophenyl)-1,2,4-triazin-3-yl) pyridine tetrasodium salt, and AHA (acetohydroxamic acid), while Ln(III) is kept in the solvent by a sufficiently high concentration of HNO_3 in the strip phase. A first "Pu-active" test proved the principle. Excellent results regarding hydrodynamics and Pu and Am recovery were obtained. However, approximately 30% of Np was routed to the raffinate, and approximately 7% of Eu (representing the Ln) was routed to the TRU product. A slightly modified flow sheet was later developed at the UK National Nuclear

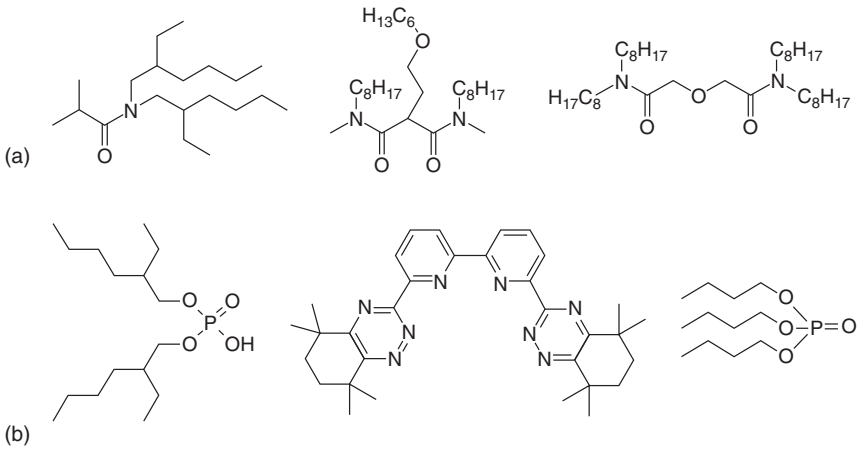

Figure 15.27 Extracting agents used in various GANEX flowsheets: (a) DEHiBA, DMDOHEMA, TODGA; (b) HDEHP, $CyMe_4$-BTBP, TBP. Source: Malmbeck et al. (2019)/De Gruyter.

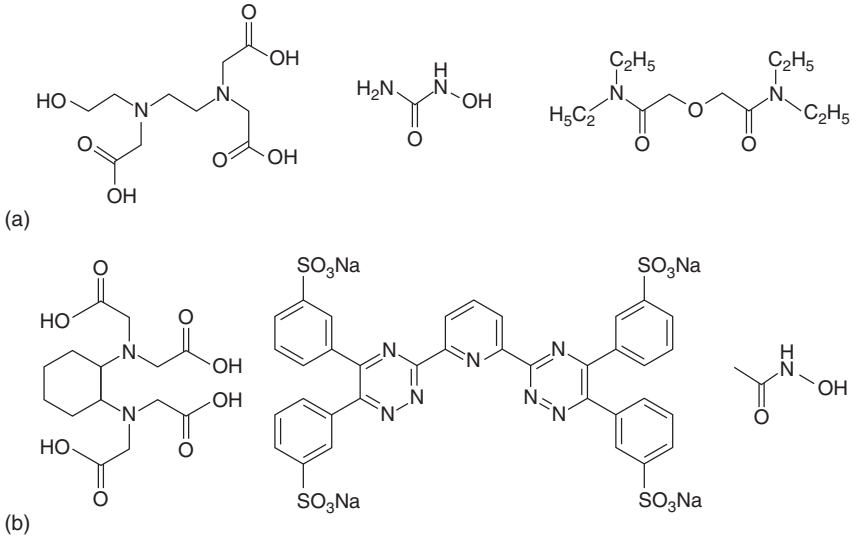

Figure 15.28 Water-soluble complexing and reducing agents used in various GANEX flowsheets: (a) HEDTA, hydroxyurea, TEDGA; (b) CDTA, SO_3-Ph-BTP, AHA. Source: Malmbeck et al. (2019)/De Gruyter.

Laboratory, producing separate Np + Pu and Am + Cm product solutions for potential applications in the heterogeneous recycling of actinides.

Based on the experience gained with the Pu-active test, the EURO-GANEX process was finally "hot tested" using genuine dissolved spent fuel as the feed solution. This solution was obtained by performing a GANEX first cycle run on a feed solution prepared by dissolving irradiated fast reactor fuel ($U_{80}Pu_{20}$). The related paper by Malmbeck et al. (2019) is a full report on the development and execution of the

hot test. It reports on the adapted first and second cycle flow sheets, feed solution preparation, and results from the hot first and second cycle process tests.

To conclude, a new separation process suitable for homogenous reprocessing of major (U, Pu) and minor (Np, Am, Cm) actinides in future closed fuel cycles has successfully been demonstrated with irradiated fast reactor fuel. This process involves two solvent extraction cycles, a first one to recover uranium and a second one to recover the TRU. As expected from experience with an earlier test, U removal in the first cycle process proved to be highly efficient with <0.1% U routed to the aqueous raffinate containing the TRU actinide fraction. Pu, MA, and Ln were not extracted and routed together with 97% of the Np to the raffinate. Compared to the earlier test, this hot test has extended experience with the GANEX first cycle by reprocessing fast reactor fuel with a much higher plutonium concentration and by running the test in short residence time centrifugal contactors. TRU was recovered in the second cycle process with high efficiency (99.9%), together with only 0.06% of the lanthanides inventory and the major fraction of Zr and Mo. The sum of the TRU fractions lost to the first cycle solvent, the second cycle raffinate, second cycle lanthanide product, and second cycle solvent is 3.3% (Np), 0.26% (Pu), and 0.11% (Am), i.e. overall decontamination factors of $DF_{Np} = 30$, $DF_{Pu} = 380$, and $DF_{Am} = 910$. The TRU product decontamination factors for U and lanthanides are $DF_U = 3300$ and $DF_{Ln} = 1700$, respectively.

The EURO-GANEX process has thus been successfully demonstrated with high plutonium content irradiated fast reactor fuel ($10\,g\,l^{-1}$ Pu in the HA feed) and in centrifugal contactors for the first time.

15.9 The Natural Reactors at Oklo

In 1972, it was found that uranium in ore deposits at Oklo, Gabon, contained significantly smaller concentrations of ^{235}U than other deposits of natural uranium (<0.5% compared to 0.72%). At these places, the isotopic composition of other elements is also different from the mean composition in nature. For instance, natural Nd contains ≈27% of ^{142}Nd and ≈12% of ^{143}Nd, whereas Nd at Oklo contains <2% of ^{142}Nd and up to 24% of ^{143}Nd. Comparison to the yields of nuclear fission leads to the result that Nd produced by fission contains ≈29% of ^{143}Nd, but practically no ^{142}Nd. From the high isotope ratio $^{143}Nd/^{142}Nd$ and the low isotope ratio $^{235}U/^{238}U$, it must be concluded that chain reactions have occurred. The age of the Oklo deposits was found by $^{87}Rb/^{87}Sr$ analysis to be $\approx 1.7 \cdot 10^9$ year. At that time, the concentration of ^{235}U in natural uranium was ≈3%. The presence of water in the sedimentary ore deposits led to high values of the resonance escape probability p (Eq. (15.1)) and to criticality of the systems ($k_{eff} > 1$).

The natural reactors at Oklo have been in operation for about 10^6 years, probably with intermissions, depending on the presence of water. The neutron flux density, the power level, and the temperature were relatively low ($\leq 10^9\,cm^{-2}\,s^{-1}$, $\leq 10\,kW$, and about 400–600 °C, respectively). About 6 tons of ^{235}U have been consumed, and about 1 ton of ^{239}Pu has been produced. Since then, the latter has decayed into ^{235}U.

It can be assumed that natural nuclear reactors were in operation about $1–3 \cdot 10^9$ years ago at many other places containing uranium-rich ore deposits in the presence of water.

Analysis of the natural reactors at Oklo gives valuable information about the migration behavior of fission products and actinides in the geosphere. Uranium and the lanthanides have been redistributed locally. Plutonium produced in the Oklo reactors did not move during its lifetime from the site of its formation; 85–100% of the lanthanides, 75–90% of the Ru, and 60–85% of the Tc were retained within the reactor zones. Small amounts of U, lanthanides, Ru, and Tc moved with the water over distances up to 20–50 m.

15.10 Controlled Thermonuclear Reactors

Controlled thermonuclear reactors (CTRs), also referred to as fusion reactors, are in the development stage. Operation on an industrial scale before the year 2050 is unlikely.

The ignition temperature for the D–D reaction is $3 \cdot 10^8$ K, that for the D–T reaction $3 \cdot 10^7$ K. These reactions are most important for the operation of CTRs. Because of the lower ignition temperature, the D–T reaction is more attractive, at least for the first generation of these reactors, although it requires handling large amounts of T. The ignition temperature for the D–^{3}He reaction is similar to that of the D–D reaction, whereas it is appreciably higher for the H–H reaction (about 10^{10} K).

The preferred concept is the magnetic confinement of the plasma of D^+ or T^+, and free electrons at temperatures on the order of 10^8 K. Because no material is able to withstand a plasma of this temperature, it must be kept away from the walls. This can be done by strong magnetic fields. The torus design is most promising, and the experimental reactors based on this design are called "Tokamaks." The Joint European Torus (JET) is operated at Abingdon (UK); another machine, International Thermonuclear Reactor Experiment (ITER), will have an appreciably higher power output.

For a controlled nuclear fusion reaction, the following parameters are important:

- The fusion reaction rate parameter σ_{υ}, where σ is the reaction cross section, which depends on the particle energy, and υ is the velocity of the ions, averaged over the Maxwell velocity distribution and proportional to the temperature.
- The Lawson limit $n\tau$, where n is the particle density and τ is the confinement time (confinement quality) indicating the ability of the plasma to retain the heat.
- The triple product $n\tau T$, where T is the average ion temperature.

The temperature must be $\geq 10^8$ K, and $n\tau$ must be $\geq 10^{21}$ s m^{-3} for the D–D reaction and $\geq 10^{20}$ s m^{-3} for the D–T reaction. The triple product $n\tau T$ must be $\geq 5 \cdot 10^4$ s eV m^{-3}. Since two particles are involved in each collision, the fusion power density increases with the square of the particle density. At 1 Pa ($n = 3 \cdot 10^{20}$ m^{-3}), the power density is several tenths of a megawatt per cubic meter and the required confinement time would be 0.1–1 seconds. Best results have been obtained so

far with central ion temperatures on the order of $\approx 4 \cdot 10^8$ K, particle densities of $\approx 5 \cdot 10^{19}$ m^{-3}, and confinement times of ≈2 seconds.

Steady-state machines may be operated in a pulsed or continuous mode. In both cases, the fuel gases D and T, respectively, must be injected and the fusion products ^{4}He and ^{3}He must be withdrawn. Up to now, this has been done by shutting down, emptying the torus, and filling it with a fresh D–T mixture. Suitable technical solutions for continuous operation of the machines have to be developed.

To meet the Lawson criterion, the plasma density is increased by increasing the magnetic field. This also results in an increase of temperature. The ignition temperature may be obtained by injection of D^+ and T^+ of high kinetic energy or by high-frequency heating. After ignition, the high kinetic energy of $^4He^{2+}$ ions produced by fusion leads to a rapid rise of the plasma temperature. The high magnetic field strength necessary to confine and to compress the plasma requires high currents (≥30 000 A) and the use of superconducting magnets.

A thermonuclear reactor operating on the basis of the D–T reaction will contain several kilograms of T. This requires a well-developed tritium technology comprising production and safe handling, taking into account diffusion through metals and chemical reactions, including exchange reactions.

In the D–T reaction, about 80% of the energy is given off in the form of kinetic energy of the neutrons (14 MeV). In most steady-state concepts, a blanket is provided containing Li in the form of lithium metal or a lithium salt (e.g. Li_2BeF_4) to capture these high-energy neutrons by the reactions

$$^6\mathrm{Li}(7.4\%) + n \rightarrow {}^3\mathrm{H} + {}^4\mathrm{He}\ (\Delta E = 4.78\ \mathrm{MeV}) \tag{15.12}$$

$$^7\mathrm{Li}(92.6\%) + n \rightarrow 2\,{}^4\mathrm{He}\ (\Delta E = 18.13\ \mathrm{MeV}) \tag{15.13}$$

By these reactions, most of the energy of the fusion process is transferred to the blanket, which is heated to high temperatures. The heat is given off in a cooling cycle by pumping the molten Li metal or salt through a heat exchanger in which the heat is transferred to a secondary circuit for the production of steam and operation of a turbine. By reaction (15.12), additional amounts of T are produced (breeding effect) which must be recovered and recycled. For this purpose, the Li metal or salt is treated continuously or intermittently to recover the T.

Bremsstrahlung and synchrotron radiation emitted during operation are absorbed in the walls of the vessel, which must be cooled. Very good heat insulation is required between the hot walls of the vessel (≈1000 °C) and the superconducting coils of the magnets (≈5 K).

A major problem is the proper choice of construction materials, which must be heat- and radiation-resistant and exhibit low neutron absorption. The following components are under discussion:

(a) a vacuum chamber of 10 cm stainless steel, lined on the inside with reinforced carbon shielding to protect the steel, and water cooled on the outside;
(b) a water-cooled blanket about 1.5 cm thick, made of a Va alloy and containing the Li or lithium compound;

(c) a water-cooled shield to absorb neutrons and γ-rays. The vacuum chamber and the blanket are exposed to high radiation intensities leading to radiation damage and activation. Hydrogen atoms escaping from the magnetic confinement react with the walls, which will be loaded with D and T. On the other hand, atoms are emitted from the walls, polluting the plasma.

With respect to the operation of thermonuclear reactors, laser-induced fusion and heavy-ion-induced fusion are also discussed. In these concepts, compression of T or D–T mixtures to high density and heating to high temperatures are achieved by irradiation with a laser beam of very high intensity or with a beam of high-energy heavy ions.

Compared to fission reactors, the operation of fusion reactors is more complicated because of the high ignition temperatures, the need to confine the plasma, and problems with the construction materials. On the other hand, the radioactive inventory of fusion reactors is appreciably smaller. Fission products are not formed, and actinides are absent. The radioactivity in fusion reactors is given by the T and the activation products produced in the construction materials. This simplifies the waste problems considerably. Development of thermonuclear reactors based on the D–D reaction would reduce the radioactive inventory even further because T would not be needed. The fact that the energy produced by fusion of the D atoms contained in 1 l of water corresponds to the energy obtained by burning 120 kg coal is very attractive.

15.11 Nuclear Explosives

The large amounts of energy liberated by nuclear fission and fusion led very early to the production of nuclear explosives, as already mentioned in Section 15.1. ^{235}U, ^{239}Pu, and ^{233}U can be used as nuclear explosives because they have sufficiently high cross sections for fission by fast neutrons. Using the equations in Section 15.1, it can be assessed that, in the absence of a reflector, a sphere of about 50 kg uranium metal containing 94% ^{235}U or a sphere of about 16 kg plutonium metal (^{239}Pu) is needed to reach criticality. If a reflector is provided, the critical masses are about 20 kg for ^{235}U and about 6 kg for ^{239}Pu. The critical masses for ^{233}U are similar to those for ^{239}Pu.

For use in nuclear weapons, the concentration of ^{240}Pu in the Pu should be low because the presence of this nuclide leads to the production of appreciable amounts of neutrons by spontaneous fission; if the concentration of ^{240}Pu is too high, the neutron multiplication would start too early with a relatively small multiplication factor and the energy release would be relatively low. Higher concentrations of ^{241}Pu also interfere because of its transmutation into ^{241}Am with a half-life of only 14.35 years. To minimize the formation of ^{240}Pu and ^{241} Pu, for use in weapons is, in general, produced in special reactors by low burn up (<20 000 MW_{th}d per ton), that is, relatively short irradiation times.

Criticality can be reached by shooting one subcritical hemisphere onto another one by normal explosives (gun type) or by compressing a subcritical spherical shell into a supercritical sphere (implosion type). The bomb dropped on Hiroshima (energy release corresponding to ≈15 kilotons of TNT) was of the gun type and made from ^{235}U, whereas that dropped on Nagasaki was of the implosion type and made from ^{239}Pu (energy release corresponding to ≈22 kilotons of TNT). Nuclear weapons have been made with explosive forces corresponding to about 0.01–500 kilotons of TNT, sometimes with very low efficiency.

Without application of special measures, it would take about 0.2 μs to increase the number of neutrons to that required to fission all fissile atoms. However, the energy released would blow apart the material much earlier, resulting in a very low efficiency. In order to reach a high neutron flux within the short duration of supercritical configuration, a few microseconds before maximum criticality a large number of neutrons are injected by a special neutron source, triggering a rapid neutron multiplication.

Generally, the fissile core is surrounded by a heavy material, in order to reflect the neutrons and to increase the inertia and consequently the time in which the supercritical configuration is held together.

The explosion of fissile material leads to temperatures of about 10^8 K which are sufficient to initiate D–T fusion. This is the basis of the development of hydrogen bombs, in which the energy of fission is used for the ignition of fusion. LiD serves as a source of D and T, the latter being produced by thermal neutrons (^{6}Li(n, α)t) and by fast neutrons (^{7}Li(n, αn)t). If the temperature is high enough, the D–D reaction can contribute to the energy production. The fast neutrons released by the fusion reactions react very effectively with natural or depleted U initiating fission of ^{238}U. In these kinds of weapons, large amounts of fission products are formed ("dirty weapons"). If a surrounding non-fissile heavy material is used, fission products are released only by the ignition process ("clean weapons").

Between 1960 and 1963, hydrogen bombs with explosive forces of up to 60 megatons of TNT were discharged into the atmosphere and underground.

References

Bowman, C.D. (1995). Basis and Objectives of the Los Alamos Accelerator-Driven Transmutation Technology Project. *Los Alamos National Laboratory Report LA-UR-95-206*.

Dawson, J.K. and Sowden, R.D. (1963). *Chemical Aspects of Nuclear Reactors*, vol. 3. London: Butterworths.

Hughes, D.J. and Harvey, J.A. (1955). *Neutron Cross Sections, United States Atomic Energy Commission*. New York: McGraw-Hill.

Malmbeck, R., Magnusson, D., Bourg, S. et al. (2019). Homogenous recycling otransuranium elements fro irradiated fast reactor fuel by the EURO-GANEX solvent extraction process. *Radiochim. Acta* 107: 917.

Further Reading

General

Stephenson, R. (1958). *Introduction to Nuclear Engineering*. New York: McGraw-Hill.
Liverhout, S.E. (1960). *Elementary Introduction to Reactor Physics*. New York: Wiley.
Stoller, S.M. et al. (eds.) (1960–1964). *Reactor Handbook*, 2e. New York: Interscience.
Tipton, C.R. (1960). *Reactor Handbook: Materials*, vol. 1. London: Interscience.
Kouts, H. (1963). Nuclear reactors. In: *Nuclear Physics*, Methods of Experimental Physics, vol. 3B (eds. L.C.L. Yuan and C.S. Wu). New York: Academic Press.
Peterson, S. and Wymer, R.G. (1963). *Chemistry in Reactor Technology*. Oxford: Pergamon.
Glasstone, S. (1967). *Source Book on Nuclear Energy*, 3e. Princeton, NJ: Van Nostrand.
Benedict, M., Pigford, T., and Levi, H.W. (1981). *Nuclear Chemical Engineering*, 2e. New York: McGraw-Hill.
Glasstone, S. and Sesonke, A. (1981). *Nuclear Reactor Engineering*, 3e. London: Van Nostrand.
International Atomic Energy Agency (1982). *Nuclear Power, the Environment and Man*. Vienna: IAEA.
McKay, A. (1984). *The Making of the Atomic Age*. Oxford: Oxford University Press.
Patterson, W.C. (1985). *Nuclear Power*. Hardmondsworth: Penguin (more popular).
Lieser, K.H. (1991). *Einführung in die Kernchemie*, 3e. Weinheim: Wiley-VCH.
Choppin, G., Rydberg, J., and Liljenzin, J.O. (1995). *Radiochemistry and Nuclear Chemistry*, 2e. Oxford: Butterworth–Heinemann.

More Specialized

United Nations (1955, 1958, 1965, 1972). *UN Conferences on Peaceful Uses of Atomic Energy*. Geneva.
International Atomic Energy Agency (1960). *Disposal of Radioactive Wastes*, vols. 1 and 2. Vienna: IAEA.
Amphlett, C.B. (1961). *Treatment and Disposal of Radioactive Wastes*. Oxford: Pergamon.
Bruce, F.R., Fletcher, J.M., Hyman, H.H., and Katz, J.J. (1961). *Process Chemistry*, Progress in Nuclear Energy, Series III, vols. 1–3. Oxford: Pergamon.
Flagg, J. (ed.) (1961). *Chemical Processing of Reactor Fuels*. New York: Academic Press.
Stoller, S.M. and Richards, R.B. (1961). *Reactor Handbook: Fuel Reprocessing*, vol. II. London: Interscience.
Lamarsh, J.R. (1966). *Introduction to Nuclear Reactor Theory*. Reading, MA: Addison-Wesley.
Long, J.T. (1967). *Engineering for Nuclear Fuel Reprocessing*. New York: Gordon and Breach.
Smith, C.O. (1967). *Nuclear Reactor Materials*. Reading, MA: Addison-Wesley.
Wills, J.G. (1967). *Nuclear Power Plant Technology*. New York: Wiley.
Bell, G.I. and Glasstone, S. (1970). *Nuclear Reactor Theory*. London: Van Nostrand.
Häfele, W., Faude, D., Fischer, E.A., and Laue, H.J. (1970). Fast breeder reactors. *Annu. Rev. Nucl. Sci.* 20: 393.
Pocock, R.F. (1970). *Nuclear Ship Propulsion*. London: Ian Allan.

Flagg, J.F. (1971). *Chemical Processing of Reactor Fuels, Nuclear Science and Technology Series*, vol. 1. New York: Academic Press.
Perry, A.M. and Weinberg, A.M. (1972). Thermal breeder reactors. *Annu. Rev. Nucl. Sci.* 22: 317.
Pigford, T.H. (1974). Environmental aspects of nuclear energy production. *Annu. Rev. Nucl. Sci.* 24: 515.
Ahrland, S., Liljenzin, J.O., and Rydberg, J. (1975). *(Actinide) Solution Chemistry, Comprehensive Inorganic Chemistry*, vol. 5. Oxford: Pergamon.
Lamarsh, J.R. (1975). *Introduction to Nuclear Engineering*. Reading, MA: Addison-Wesley.
International Atomic Energy Agency (1976). *Management of Radioactive Wastes from the Nuclear Fuel Cycle*, vols. 1 and 2. Vienna: IAEA.
Guéron, J. (1977). *Les Materiaux Nucléaires*. Paris: Presse Universitaire de France.
International Atomic Energy Agency (1977). *International Conference on Nuclear Power and its Fuel Cycle, Salzburg*. Vienna: IAEA.
Rydin, R.A. (1977). *Nuclear Reactor Theory and Design*. PBS Publications.
Baumgärtner, F. (ed.) (1978). *Chemie der Nuklearen Entsorgung*, vol. 2. München: Thieme.
Lyon, W.S. (1978). *Analytical Chemistry in Fuel Reprocessing*. Princeton, NJ: Science Press.
Grawes, H.W. Jr., (1979). *Nuclear Fuel Management*. New York: Wiley.
Syndicat CFDT de l'énergie atomique (1980). *Le Dossier Electronucléaire*. Paris: Editions du Seuil (data on nuclear energy production).
Wymer, R.G. and Vondra, B.L. (1980). *Technology of the Light Water Reactor Fuel Cycle*. Boca Raton, FL: CRC Press.
Baumgärtner, F., Ebert, K., Gelfort, E., and Lieser, K.H. (eds.) (1981, 1983, 1986, 1988). *Nuclear Fuel Cycle*, vol. 4. Weinheim: Wiley-VCH.
Judd, A. (1981). *Fast Breeder Reactors*. Oxford: Pergamon.
Wymer, R.G. and Vondra, B.L. (eds.) (1981). *Light Water Reactor Nuclear Fuel Cycle*. Boca Raton, FL: CRC Press.
Dlouhy, Z. (1982). *Disposal of Radioactive Wastes*. Amsterdam: Elsevier.
Guéron, J. (1982). *L'Energie Nucléaire*. Paris: Presse Universitaire de France.
Kessler, G. (1983). *Nuclear Fission Reactors, Potential Role and Risks of Converters and Breeders*. Berlin: Springer-Verlag.
International Atomic Energy Agency (1989). *Uranium, Resources, Production and Demand*. Vienna: OECD/NEA and IEAE.
Steinberg, E.P. (1989). Radiochemistry of the fission products. *J. Chem. Educ.* 66: 367.
International Atomic Energy Agency (1991). *The International Chernobyl Project – An Overview – Assessment of the Radiological Consequences and Evaluation of the Protective Measures – Report by An International Advisory Committee*. Vienna: IAEA.
The Uranium Institute (1991). *The Management of Radioactive Waste*. London: The Uranium Institute.
Bowman, C.D., Arthur, E.D., Lisowski, P.W. et al. (1992). Nuclear energy generation and waste transmutation using an accelerator-driven intense thermal neutron source. *Nucl. Instrum. Methods Phys. Res.* A320: 336.

World Nuclear Industry Handbook (1992). *Nuclear Engineering Specialty Publications Nucl. Eng. Spec. Publ.* Oxford.

Rydberg, J., Musika, C., and Choppin, G. (eds.) (1992). *Principles and Practices of Solvent Extraction*. New York: Marcel Dekker.

Miller, W.F. (1993). Present and future nuclear reactor designs, weighing the advantages and disadvantages of nuclear power with an eye of improving safety and meeting future needs. *J. Chem. Educ.* 70: 109.

Kernkraftwerke (1994, 1995). Weltübersicht, atw. *Int. Z. Kernenerg.* 40 (3).

Röthemeyer, H. and Warnecke, E. (1994). Radioactive waste management – the international approach. *Kerntechnik* 59 (1): 7.

Various authors (1994). *Proceedings of the 4th International Conference on Nuclear Fuel Reprocessing and Waste Management*, April 1994, London: British Nuclear Industry Forum.

Koch, L. (1995). Radioactivity and fission energy. *Radiochim. Acta* 70/71: 397.

Neeb, K.-H. (1997). *The Radiochemistry of Nuclear Power Plants with Light Water Reactors*. Berlin: Walter de Gruyter.

Knebel, J.U., Cheng, X., Müller, G. et al. (2000). Thermalhydraulic and Material Specific Investigations into the Realization of an Accelerator Driven System (ADS) to Transmute Minor Actinides. 1999 Status Report, Forschungszentrum Karlsruhe, Wissenschaftliche Berichte FZKA 6506.

Madic, C., Lecomte, M., Baron, P., and Boullis, B. (2002). Separation of long-lived radionuclides from high active nuclear waste. *C.R. Phys.* 3: 797.

International Atomic Energy Agency (2004). Implication of Partitioning and Transmutation in Radioactive Waste Management. *Technical Series No. 435*. Vienna: IAEA.

Ekberg, C., Fermvik, A., Retegan, T. et al. (2008). An overview and historical look back at the solvent extraction using nitrogen donor ligands to extract and separate An(III) from Ln(III). *Radiochim. Acta* 96: 225.

Geist, A. and Gompper, K. (2008). Miniature DIAMEX processes in a hollow fibre module mini-plant: process development and optimization. *Radiochim. Acta* 96: 211.

Hill, C., Desreux, J.-F., Ekberg, C. et al. (2008). Assessment of the ligand extraction properties: an intercomparison campaign amongst EUROPARTners. *Radiochim. Acta* 96: 259.

Koyama, T., Kinoshita, K., Inoue, T. et al. (2008). Equilibrium distribution of actinides including Cm between molten LiCl-KCl eutectic and liquid cadmium. *Radiochim. Acta* 96: 311.

Narbutt, J. and Krejzler, J. (2008). Neutral bidentate *N*-heterocyclic ligands – phase transfer reagents improving the kinetics of solvent extraction of Am(III) and Eu(III) iIons with tetradentate 6,6′-bis-(diethyl-1,2,4-triazin-3-yl)-2,2′-bipyridine. *Radiochim. Acta* 96: 219.

Souček, P., Cassayre, L., Malmbeck, R. et al. (2008). Electrorefining of U-Pu-Zr-aAlloys fuel onto solid aluminium cathodes in molten LiCl-KCl. *Radiochim. Acta* 96: 315.

Adamov, E.O. and Fuji-ie, Y. (2011). Developments and tendencies in fission reactor concepts. In: *Handbook of Nuclear Chemistry*, 2e, vol. 6 (eds. A. Vertés, S. Nagy, Z. Klencsár, et al.), 2663. Berlin: Springer-Verlag.

Borghoff, S., Brück, B., Kilian-Hülsmeyer, Y. et al. (2011). Der Unfall in Fukushima. Report on request of Bundesministerium für Umwelt, Naturschutz und Reaktorsicherheit (BMU), Gesellschaft für Anlagen- und Reaktorsicherheit GRS, GRS-293.

Denschlag, J.O. (2011). Technical applications of nuclear fission. In: *Handbook of Nuclear Chemistry*, 2e, vol. 6 (eds. A. Vertés, S. Nagy, Z. Klencsár, et al.), 2615. Berlin: Springer-Verlag.

Bhattacharyya, A. and Mohapatra, P.K. (2019). Separation of trivalent actinides and lanthanides using various 'N', 'S' and mixed 'N, S' donor ligands: a review. *Radiochim. Acta* 107: 931.

Lan, J.-H., Jiang, S.-L., Liu, Y.-L. et al. (2019). Separation of actinides from lanthanides associated with spent nuclear fuel reprocessing in China: current status and future perspectives. *Radiochim. Acta* 107: 951.

Qaim, S.M., Kratz, J.V., and Simoni, E. (eds.) (2019). Special issue: International year of the periodic table of chemical elements. Editorial: 150 years of the periodic table of chemical elements. *Radiochim. Acta* 107: 767.

Natural Reactors

International Atomic Energy Agency (1975). *The Oklo Phenomenon*. Vienna: IAEA.

International Atomic Energy Agency (1978). *The Natural Fission Reactors*. Vienna: IAEA.

Kuroda, P.K. (1982). *The Origin of the Chemical Elements and the Oklo Phenomenon*. Berlin: Springer-Verlag.

Fusion Technology

Gruen, D.M. (1970). *The Chemistry of Fusion Technology*. New York: Plenum Press.

Post, R.F. (1970). Controlled fusion research and high energy plasmas. *Annu. Rev. Nucl. Sci.* 20: 509.

Ache, H.J. (1989). Chemical aspects of fusion technology. *Angew. Chem. Int. Ed. Engl.* 28: 1.

Conn, R.W., Chuyanov, V.A., Inoue, N., and Sweetman, D.R. (1992). The international thermonuclear experimental reactor. *Sci. Am.* 75.

Cordey, J.G., Goldston, R.J., and Parker, R.R. (1992). Progress toward a tokomak fusion reactor. *Phys. Today*: 22.

Jensen, T.H. and Fusion, A. (1994). Potential power source. *J. Chem. Educ.* 71: 820.

Kudo, H. (1995). Radioactivity and fusion energy. *Radiochim. Acta* 70/71: 403.

Nuclear Explosives

Smith, H.D. (1946). *Atomic Energy for Military Purposes*. Princeton, NY: Princeton University Press.

Teller, E., Talley, W.K., Higgins, G.H., and Johnson, G.W. (1968). *The Constructive Uses of Nuclear Explosives*. New York: McGraw-Hill.

United Nations (1981). *Nuclear Weapons, Report of the Secretary-General of the United Nations*. New York: Autumn Press.

Rhodes, R. (1986). *The Making of the Atomic Bomb*. New York: Simon & Schuster.

16

Sources of Nuclear Bombarding Particles

16.1 Neutron Sources

Radionuclide neutron sources are based on either (α, n) reactions or spontaneous fission. Older (α, n) sources used the 4.78/4.60 MeV α particles of 1600 years ^{226}Ra. The recipe for their production was to mix 100 mg of $RaCl_2$ with 500 mg of finely divided Be powder with a small amount of water to produce a paste. The latter was dried at 150 °C, powdered, and pressed into a small Ni tube that was subsequently hermetically sealed. More modern sources utilize ^{238}Pu, ^{239}Pu, ^{241}Am, and ^{242}Cm. In these sources, the reaction ^{9}Be(α, n)^{12}C produces neutrons having a broad energy spectrum because the α particles can react with the Be at any point in the stopping process. For Ra/Be sources, the shielding must be larger than for other sources. In photoneutron sources, the reaction ^{9}Be(γ, n) is utilized. The energy of the γ quanta must be more than 1.665 MeV. A suitable source is ^{124}Sb produced by neutron irradiation of antimony in a nuclear reactor. Table 16.1 gives a survey of the neutron yield dN/dt (neutrons per second and Ci) that can be achieved with these sources. The neutron flux decreases with the square of the distance from the source. If we consider the source as a point source, we have for the flux density ϕ at distance R

$$\Phi = \frac{1}{4\pi R^2} \cdot \frac{dN}{dt} \tag{16.1}$$

In order to thermalize the neutrons, the neutron source is positioned in the center of a block of paraffin, see Figure 16.1, where the distance between the source and the sample is a few centimeters. For a neutron yield $dN/dt = 10^6\ s^{-1}$, according to Eq. (16.1), $\phi = 10^4\ cm^{-2}\ s^{-1}$. This flux density is sufficient for simple experiments, for example, in a radiochemistry laboratory course, but it is practically too low for radionuclide production.

Table 16.1 also lists the neutron yield of a ^{252}Cf source. ^{252}Cf decays with a half-life of 2.638 years by α decay (96.9%) and by spontaneous fission (3.1%). In its sf decay, 3.8 neutrons are set free per fission; 1 Ci of ^{252}Cf produces $4.3 \cdot 10^9$ neutrons per second. As 1 mg of ^{252}Cf corresponds to an activity of 0.539 Ci, the neutron yield per milligram is $2.3 \cdot 10^9\ s^{-1}$. This makes the use of ^{252}Cf very attractive.

Nuclear and Radiochemistry: Fundamentals and Applications,
Fourth Edition. Jens-Volker Kratz.

Table 16.1 Neutron yields of various neutron sources.

Neutron source		Half-life	Neutron yield (s^{-1} Ci^{-1})
^{210}Po/Be	(α, n)	138.4 d	$2.5 \cdot 10^6$
^{210}Pb/Be	(α, n)	22.3 yr	$2.3 \cdot 10^6$
^{226}Ra/Be	(α, n)	1600 yr	$1.3 \cdot 10^7$
^{227}Ac/Be	(α, n)	21.6 yr	$1.5 \cdot 10^7$
^{228}Th/Be		1.9 yr	$2.0 \cdot 10^7$
^{238}Pu/Be		87.74 yr	$2.2 \cdot 10^6$
^{239}Pu/Be		$2.4 \cdot 10^4$ yr	$1.4 \cdot 10^6$
^{241}Am/Be		433 yr	$2.2 \cdot 10^6$
$^{226}RaBeF_4$		1600 yr	$2.4 \cdot 10^6$
^{242}Cm/Be		162.8 d	$2.5 \cdot 10^6$
^{124}Sb/Be	(γ, n)	60.2 d	$1–5 \cdot 10^6$
^{252}Cf	(sf)	2.64 yr	$4.3 \cdot 10^9$

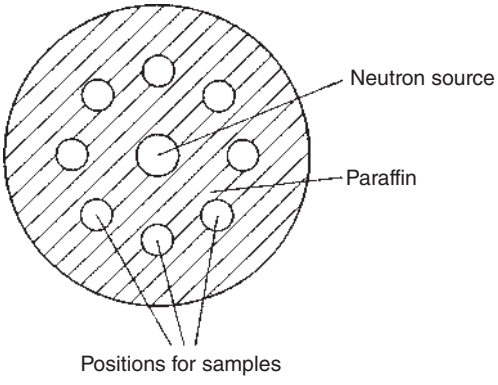

Figure 16.1 Location of the samples during irradiation by a neutron source.

16.2 Neutron Generators

The most common nuclear reactions used in neutron generators are

^{2}H(d, n) $Q = 3.25$ MeV

^{3}H(d, n) $Q = 17.6$ MeV

^{7}Li(p, n) $Q = -1.646$ MeV

^{9}Be(d, n) $Q = 3.79$ MeV

Among these, the second one is most widely used. Here, deuterons are accelerated to ~600 keV with currents of a few milliamps and bombard a tritium target made of

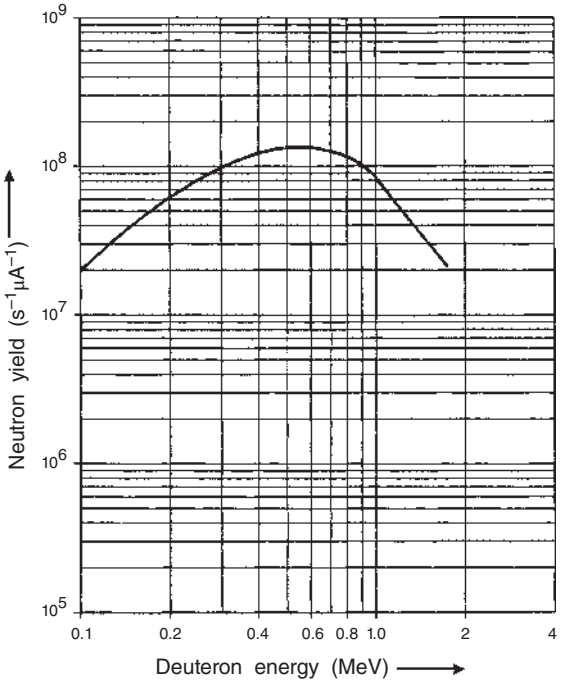

Figure 16.2 Neutron yield of the reaction $t(d, n)\alpha$ as a function of the energy of the deuterons incident on a titanium–tritium target with 1 Ci of tritium.

Ti metal loaded with tritium (titanium tritide). They can have tritium activities of up to 20 Ci. These produce up to 10^{11} 14 MeV neutrons s^{-1}. The neutron yield as a function of deuteron energy is shown in Figure 16.2. The accelerators are usually small Cockcroft–Walton machines. The neutrons produced are used for fast neutron activation analyses for the determination of light elements.

The most powerful accelerator-based neutron sources are the spallation neutron sources, cf. Section 15.8. Neutrons are produced by the spallation reaction induced by 1 GeV protons in a heavy target. The proton beams and the resulting spallation neutrons are pulsed, allowing the use of time-of-flight techniques to determine the energy of the neutrons. Neutron flux densities exceeding the neutron yields of reactors by orders of magnitude are achievable. They are being used for neutron scattering experiments in materials science and biology.

16.3 Research Reactors

The general characteristics of nuclear chain reactors were discussed in Chapter 15, mostly with an emphasis on energy production. Here, we concentrate on the role of reactors as neutron sources. Several hundred research reactors of various designs are in operation worldwide spanning a range of power levels from 0.1 W to about 100 MW. Most of these reactors are fueled with uranium enriched to various degrees in ^{235}U. The vast majority of research reactors use thermal neutrons for the propagation of the chain reaction. Ordinary water, D_2O, and graphite are the favored

moderator materials. The most economical designs are those in which the same substance serves as both moderator and coolant, for example, H_2O or D_2O. Most widespread are so-called swimming pool reactors that have the entire reactor core suspended in the bottom of an open pool with some 5–7 m of water above the core for shielding and with water also serving as moderator, coolant, and reflector. Pool-type reactors give neutron fluxes up to several times 10^{13} neutrons cm^{-2} s^{-1} MW^{-1} and have been built with power levels up to about 50 MW. Higher fluxes can be achieved if the reactor core is enclosed in a sealed tank, with H_2O or D_2O under pressure serving as moderator and coolant. Maximum neutron fluxes range up to several times 10^{15} cm^{-2} s^{-1}. Some reactors such as the popular TRIGA reactors are designed so that they can be pulsed to give brief (~30 ms) bursts with fluxes of the order of 10^{17} neutrons cm^{-2} s^{-1}. Some representative research reactors and their properties are listed in Table 16.2.

Table 16.2 Some representative research reactors.

Reactor type	Fuel, moderator, coolant	Power	Maximum neutron flux (cm^{-2} s^{-1})
Aerojet general corporation's teaching reactor AGN-201	20% ^{235}U as U_3O_8 homogeneously dispersed in polyethylene; uncooled	0.1 W	$5 \cdot 10^6$
Argonaut reactor (Argonne nuclear assembly for university teaching)	80–93% ^{235}U as U_3O_8 dispersed in aluminum; graphite moderator; H_2O cooling	10 kW	$1.7 \cdot 10^{11}$
General atomic's TRIGA reactor mark II	20% ^{235}U as uranium zirconium hydride (solid homogeneous fuel-moderator system); H_2O cooled	250–2000 kW steady; up to $6.4 \cdot 10^3$ MW pulsed	$(1–8) \cdot 10^{13}$ steady; $\sim 2 \cdot 10^{17}$ pulsed
Pool-type reactors	10–93% ^{235}U as U–Al alloy or UO_2 pellets; H_2O moderated and cooled	10 kW–40 MW	$(0.5–2) \cdot 10^{13}$ MW
Brookhaven HFBR	93% ^{235}U as U–Al alloy; D_2O moderated and cooled	60 MW	$1 \cdot 10^{15}$
Grenoble ILL-HFR	93.5% ^{235}U as U–Al alloy; D_2O moderated and cooled	58 MW	$1.5 \cdot 10^{15}$
Munich FRM II	93% ^{235}U as U_3Si_2 + Al powder embedded in Al matrix; D_2O moderated and cooled	20 MW	$8 \cdot 10^{14}$

In principle, two different types of reactors for neutron production can be distinguished: one focuses on facilities for the irradiation of samples including pneumatic tube systems; the other emphasizes beam tubes and channels for bringing neutron beams outside the reactor for structure studies by neutron diffraction, capture γ-ray spectroscopy (prompt gamma activation analysis [PGAA]), or fundamental physics experiments. Pool-type reactors have the flexibility for all kinds of irradiations but are less suited for the installation of beam tubes. On the other hand, tank-type reactors have been especially designed to provide multiple, high-intensity neutron beams. In Table 16.2, we list as an example the high-flux beam reactor (HFBR) at Brookhaven National Laboratory (BNL) fueled with 93% ^{235}U and moderated and cooled with D_2O, a similar reactor at the Institut Laue-Langevin at Grenoble (www.ill.fr) and the FRM II at Munich (www.FRMII.de). Figure 16.3 shows horizontal and vertical sections through the FRM II. Its design is such that the maximum thermal neutron fluxes are in the D_2O tank where the beam tubes originate and where the facilities for the highest-intensity irradiations are located. By tangential arrangements of the beam tubes relative to the core axis, direct view from the instrument back to the core is avoided. As a result, contamination of the neutron beam by fast neutrons and γ-rays is significantly reduced. Twelve beam tubes (10 horizontal, 2 inclined) are arranged around the core with their noses in close proximity to the maximum flux of thermal neutrons or to one of the secondary sources. There will be one through-going beam tube to house the target for a fission fragment accelerator. Two beam tubes are inclined at about 45° to open additional areas in the experimental hall above the ground-floor instruments. The spectrum of the neutrons delivered by these tubes is determined by the source temperature in front of the nose, which will be thermal with respect to the D_2O, cold with respect to the liquid D_2 source, or hot with respect to the graphite source (2900 K). The beam tubes are made of aluminum alloys to minimize losses from the passage of neutrons through the walls. For safety reasons, all guide tubes are filled with helium gas.

A different concept is realized in the high-flux isotope reactor (HFIR) at Oak Ridge, Tennessee. It produces one of the highest fluxes anywhere, that is $5 \cdot 10^{15}\,cm^{-2}\,s^{-1}$, and has the fuel element arranged in an annulus surrounding a central region called a flux trap. The HFIR uses 93% ^{235}U, H_2O as moderator and coolant, and Be as a reflector. One of its main functions is to produce ^{252}Cf and other transplutonium nuclides that are precious target materials for the production of superheavy elements, see Chapter 17.

16.4 Charged-Particle Accelerators

Since the first nuclear transmutation in 1919 until the invention of the Cockcroft–Walton accelerator in 1932, the only sources of particles that could induce nuclear reactions were natural α emitters and, consequently, the only nuclear reaction known in that period was the (α, p) reaction. Today, this is of historical interest only, because of the much higher intensities and energies

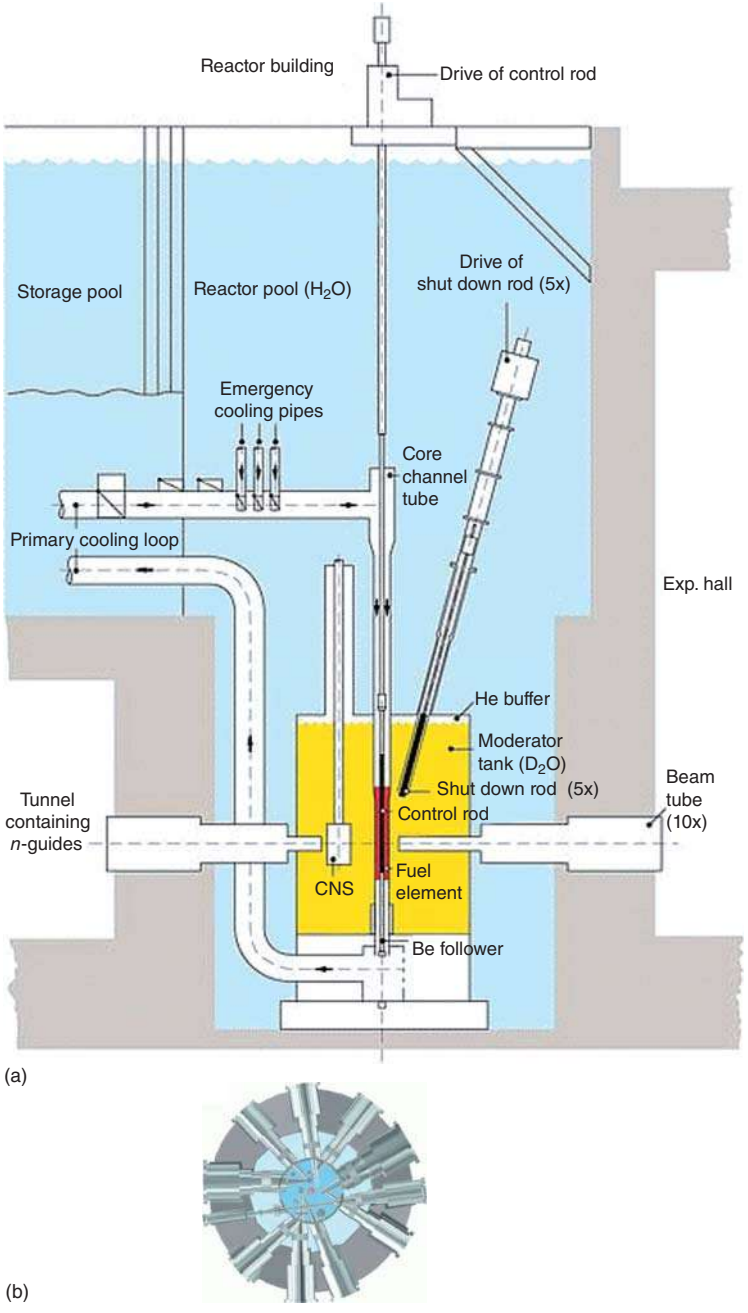

Figure 16.3 (a) Vertical section through the Munich FRM II. (b) Horizontal section through the Munich FRM II. The fuel element is in the center of the D_2O tank. Several beam tubes reach into the central tank with their noses in close proximity to the maximum flux of thermal neutrons or to one of the secondary sources. http://www.FRMII.de.

available from charged-particle accelerators. These all apply electric fields for the acceleration; however, the manner in which these fields are applied differs widely.

16.4.1 Direct Voltage Accelerators

The most obvious application is the direct voltage between two terminals. However, to obtain more than about 200 kV of accelerating voltage, one has to use several stages of voltage-doubling circuits. J.D. Cockcroft and E.T.S. Walton were the first to realize a voltage-multiplying rectifier for nuclear reactions with accelerated protons in 1932. Cockcroft–Walton accelerators are still in use to provide the bias voltages for ion sources for large accelerator complexes or as neutron generators via the d + t reaction. Voltages up to 4 MV and direct currents of 10 mA of protons have been achieved. A schematic diagram of a Cockcroft–Walton accelerator is shown in Figure 16.4.

The adaptation of the electrostatic machine for the production of high potentials for the acceleration of positive ions was pioneered by R.J. van de Graaff. In that machine, a high voltage is built up and maintained on a smooth conducting surface by the continuous transfer of charges from a moving belt to the surface. This is shown in Figure 16.5 where the surface is a sphere. In modern van de Graaff generators, nearly cylindrical shapes are used. The belt, made of a suitable insulator, is driven by a motor. It passes through the gap *AB* which is connected to a high-voltage source (∼30 kV DC) such that a continuous discharge from the point *B* is maintained. Positive charges are sprayed from *B* to the belt which transports them to the interior of the insolated metal sphere where a sharp-toothed comb *C* connected to the sphere strips them off. The sphere charges up until corona discharges and leakage along its insulating support balance the rate of charge transfer from the belt. An ion source is located inside the high-voltage terminal and the ions are guided through focusing

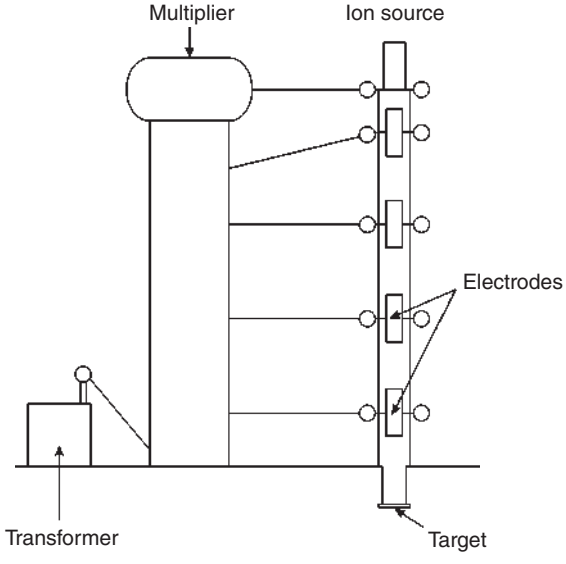

Figure 16.4 Schematic diagram of a Cockcroft–Walton accelerator. Source: Segre (1977). Hachette Book Group.

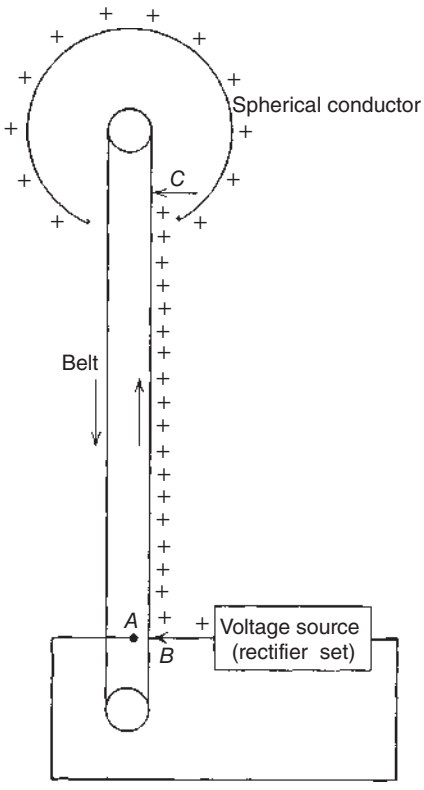

Figure 16.5 Schematic representation of the charging mechanism of a van de Graaff generator. Source: Friedlander et al. (1981). John Wiley & Sons.

electrodes into an accelerating tube along which the electric field is applied. In order to reach as high a potential as possible, electrostatic generators are enclosed in steel tanks pressurized with an isolating gas such as SF_6. Terminal voltages up to 15 MV have thus been attained (Blewett 1963).

An accelerating tube, Figure 16.6, is built of porcelain sections *S*. Inside, sections of metal tube *T* define the path of the ions. Each metal section is supported on a disk that passes between two sections of insulator out into the gas-filled space to a corona ring *R* equipped with corona points *P*. They carry the corona discharge from the high-voltage end of the tube to the low-voltage end and distribute the voltage drop uniformly along the tube. The ions travel along the electric lines of force, the pattern of which is indicated between a pair of sections in Figure 16.6. When entering the gap, the ions are focused and when leaving the gap they are defocused, but the focusing effect is stronger than the defocusing effect. Cross-sectional areas of $\leq 0.1\ cm^2$ can be obtained.

An ingenious idea is the use of the "tandem" principle. In the two-stage tandem van de Graaff accelerator, negative ions are produced by electron bombardment and are accelerated toward the positive high-voltage terminal located in the center of the pressure tank. Inside the terminal, the negative ions, having an energy in megaelectronvolts reflecting the magnitude of the terminal voltage in megavolts, pass through a stripper foil or a gas stripper and are thus stripped of electrons. The

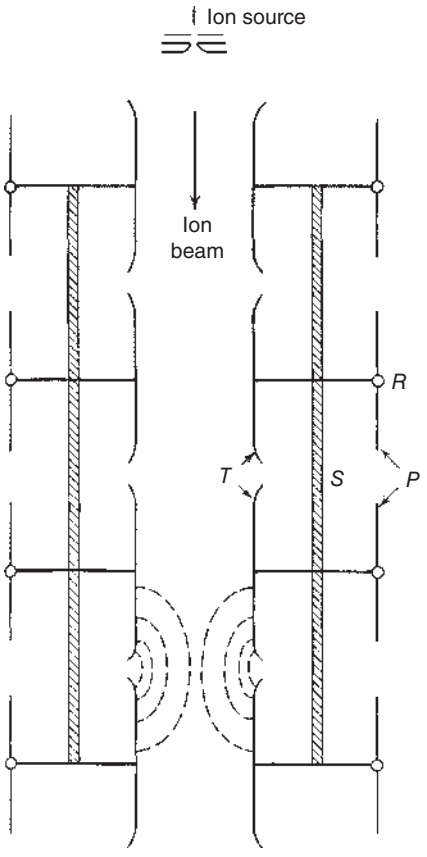

Figure 16.6 Schematic cross-sectional diagram of a portion of an accelerating tube. Source: Friedlander et al. (1981). John Wiley & Sons.

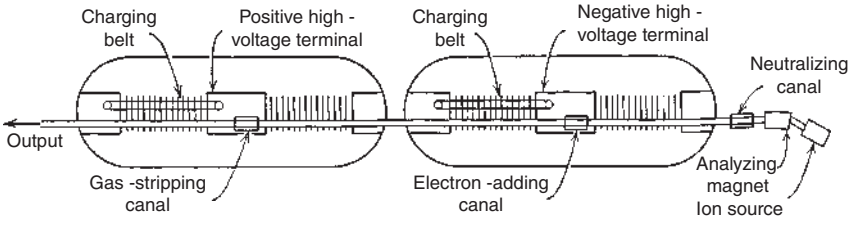

Figure 16.7 Schematic sketch of a three-stage tandem van de Graaff generator. Source: Friedlander et al. (1981). John Wiley & Sons.

positive ion beam so produced is further accelerated toward ground potential. A further increase in energy can be achieved in the three-stage tandem van de Graaff accelerators. They consist of two separate tanks, one with a negative, the other with a positive, high-voltage terminal. Figure 16.7 shows this schematically. Ions are produced in a positive ion source, magnetically analyzed, and subsequently neutralized by electron bombardment. They drift to the negative high-voltage electrode in the first tank where further electron addition produces negative ions that are accelerated to ground potential. The negative ion beam passes from the

first to the second tank and receives two additional stages of acceleration analogous to the two-stage tandem operation. Maximum proton energies up to 45 MeV have been achieved. Tandem van de Graaff machines have been important tools for precise nuclear physics research also with heavy ions.

16.4.2 Linear Accelerators

The limitations of direct voltage accelerators in which the full high potential corresponds to the final energy of the ions are introduced by the insulation problems. The latter are very much reduced in machines that employ repeated acceleration of ions through relatively small potential differences. A beam of ions from an ion source is injected into an accelerating tube containing a number of coaxial, tubular electrodes, see Figure 16.8. Alternate electrodes are connected and a high-frequency alternating voltage from a radio frequency oscillator is applied between the two groups of electrodes. An ion traveling down the tube will be accelerated at each gap between the electrodes if the voltage is in the proper phase. By choosing the frequency and the lengths of the hollow electrodes correctly, one can arrange the system such that the ions arrive at each gap at the proper phase for acceleration across the gap. A given electrode has the polarity that will first attract a bunch of particles toward it and later repel the same bunch of particles after they have passed through the electrode. The potential follows a sine function $V = V_0 \sin(\omega t)$ where V_0 is the peak voltage and ω is the frequency. The beam will drift while in the field-free region inside the tubular electrodes, hence their name drift tubes. The alternating power supply can change the polarity while the beam pulse is inside a drift tube. The amount of time

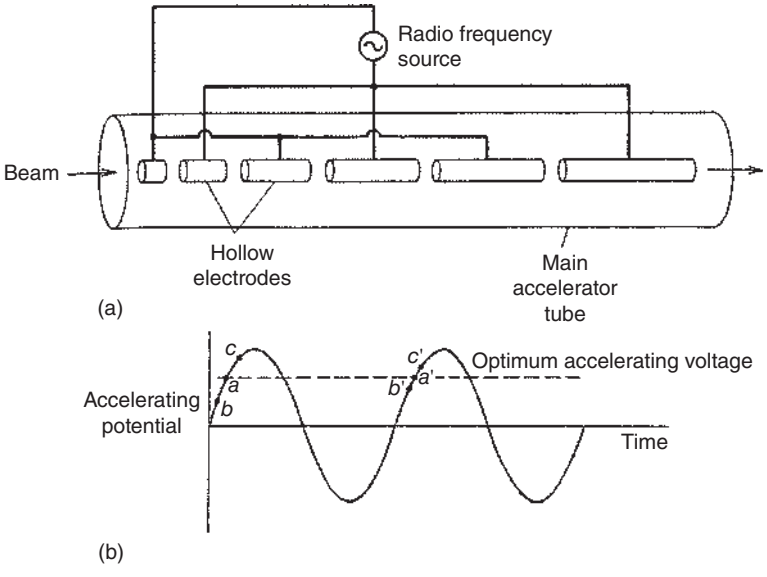

Figure 16.8 (a) Basic design of a linear accelerator. (b) Phase stability in a linear accelerator. Source: Krane (1988), p. 589. John Wiley & Sons

that the beam pulse is inside the drift tubes must be constant to provide a uniform acceleration. The beam pulse must reach the next gap at a time $t = 2\pi/\omega$ thus the length of each drift tube must increase in proportion with the increasing velocity, $L = v_i t/2$, where v_i is the velocity inside the ith drift tube. The dimensions of the drift tubes have a finite acceptance range in velocities, and so linear accelerators are designed for specific velocities. The phasing of the arrival of the particles with respect to the radio frequency has two effects. One might imagine that the arrival of the particles should coincide with the maximum accelerating voltage at the top of the sine wave, but then particles arriving slightly earlier or slightly later will be less accelerated and the bunch will spread out in velocity, arriving at the next electrode at different times. If the center of the pulse arrives at the electrode gap while the voltage is increasing nearly linearly, the faster particles will receive a lower acceleration (point *b* in Figure 16.8b) than that applied to the average particles (point *a* in Figure 16.8b) and the slower particles will receive a larger acceleration (point *c* in Figure 16.8b). These small differences in acceleration will minimize the velocity distribution in the beam pulse. This phase stability is a good feature of linear accelerators. However, tuning the arrival of the beam pulse to coincide with the increasing portion of the accelerating field has the bad feature that the field across the gap is asymmetric. A symmetric field provides the focusing in the accelerator tube of electrostatic machines as discussed in the previous section. In an asymmetric field, the particles will not be focused toward the center of the tube. Thus, the drift tubes must contain quadrupole lenses to focus the beam.

The first linear accelerator on record was built in 1928 by R. Wideröe (1928); it accelerated positive ions to about 50 keV. The Wideröe linac with fixed drift tubes has a rather limited velocity acceptance. A much more flexible linac design, the Alvarez structure, relies on creating a standing electromagnetic wave in a resonant cavity. Most heavy-ion accelerators utilize resonant cavities to provide accelerating voltages. Early designs used copper surfaces to reflect the power, but significant power was still dissipated in the walls. More recent designs have used superconducting niobium surfaces with much lower dissipation. The radio frequency is usually in the megahertz region (radio wave region) so that the pulses are separated by tens of nanoseconds. This time structure is called the beam microstructure. The beam from a linac with standing wave cavities is pulsed on the millisecond time scale in order to allow time to dissipate heat in the walls. This is the macrostructure of the beam. The fraction of the time that the macrostructure of the beam is "on" is called the duty factor. For the UNILAC accelerator at GSI in Darmstadt, this number is 25% (5 ms). The UNILAC is the most advanced linear accelerator for heavy ions in operation. It can accelerate any ion up to uranium to a maximum energy of 11.4 MeV amu^{-1}. In this machine, injection from one of two 300 kV DC generators was followed by acceleration to 1.4 MeV amu^{-1} in a Wideröe section in which radio frequency (rf) power was delivered to the drift tubes by conductors rather than by means of resonant cavities. At this time, the Wideröe section is replaced by an rf quadrupole structure for acceleration and focusing. At 1.4 MeV amu^{-1}, the ions are stripped to increase their charge state, for example, $^{238}U^{9+}$ is stripped to $^{238}U^{27+}$, followed by magnetic analysis to select a single charge state that is further

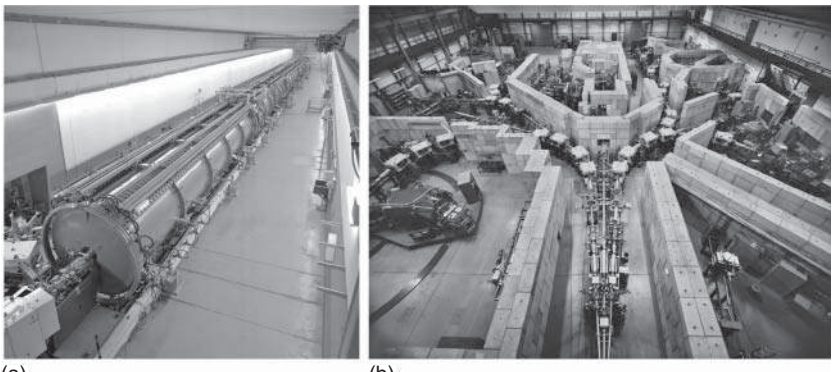

Figure 16.9 Two views of the UNILAC linear accelerator. (a) The Alvarez section. (b) Experimental area as seen from the end of the accelerator. Source: Courtesy GSI Helmholtzzentrum für Schwerionenforschung. Photo A. Zschau.

accelerated in Alvarez tanks. Subsequently, single-gap resonators are used to achieve an almost continuously variable energy. An alternative injection system makes use of an electron cyclotron resonance (ECR) ion source. Views of the post-stripper accelerator (Alvarez tanks) and of the experimental area are shown in Figure 16.9.

16.4.3 Cyclotrons

One of the most successful charged-particle accelerators is the cyclotron invented in 1929 by E.O. Lawrence at Berkeley. The development from the first working model, which produced 80 keV protons in 1930, to the large synchrocyclotrons was breathtaking.

In the cyclotron, as in the linac, multiple acceleration by an rf potential is used. However, instead of traveling in a straight line, the ion trajectories are bent by a magnetic field and move in a spiral path consisting of a series of semicircles with increasing radii as sketched in Figure 16.10. Ions are produced in a PIG ion source *P* near the center of the gap between two hollow semicircular electrode boxes *A* and *B*, called "dees." The dees are positioned in a vacuum tank and are positioned between the circular pole faces of an electromagnet. An rf potential is applied between the dees. A positive ion starting from the ion source is accelerated toward the dee that is at negative potential. In the field-free interior of the dee, the ion is no longer acted

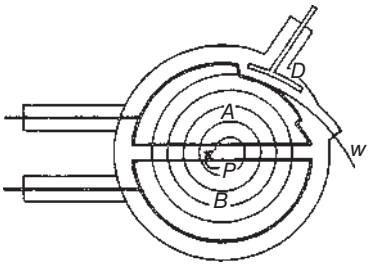

Figure 16.10 Schematic sketch of the operation of a cyclotron. The ions originate at the ion source *P* and follow a spiral path. The "dees" *A* and *B*, the deflector *D*, and the exit window *W* are indicated. Source: Pollard and Davidson (1951). John Wiley & Sons.

on by electric forces, but the magnetic field perpendicular to the plane of the dees keeps the ion on a semicircular path. If the frequency of the rf potential is such that the field has reversed its direction just at the time when the ion again reaches the gap between the dees, the ion is accelerated, now toward the other dee. As its velocity has increased, it moves in a semicircle of larger radius. As will be shown below, the transit time for each semicircle is independent of velocity. Although the ion describes larger and larger semicircles, it continues to arrive at the gap when the oscillating potential is at the right phase for acceleration. When crossing the gap, the ion gains additional kinetic energy equal to the product of the ion charge and the voltage difference between the dees. When the ion reaches the periphery of the cyclotron, it is removed from its circular path by a charged deflector D and exits the cyclotron through a vacuum window W. The equation of motion of an ion of mass M, velocity v in a vector magnetic field B is given by the equality of the centripetal magnetic force Bqv and the centrifugal force Mv^2/r where r is the radius of the orbit:

$$Bqv = \frac{Mv^2}{r} \tag{16.2}$$

Solving for the radius,

$$r = \frac{Mv}{Bq} \tag{16.3}$$

we see that the time t_{cycl} for an ion to complete one orbit given by the circumference divided by the velocity

$$t_{\text{cycl}} = \frac{2\pi r}{v} = \frac{2\pi Mv}{Bqv} = \frac{2\pi M}{Bq} \tag{16.4}$$

is independent of the ion's velocity. The resulting constant angular velocity $\omega = v/r = Bq/M$ is called the cyclotron resonance frequency. Thus, for a standard fixed-frequency cyclotron, the frequency has to be chosen such that its period equals the time it takes for the ion to make one revolution. For $B = 15\,\text{kG}$ and q/M for a proton, the cyclotron resonance frequency $\omega/2\pi$ is 23 MHz. For deuterons or He^{2+} ions at the same B, the frequency is half that value. By squaring and rearranging Eq. (16.3), we see that the maximum energy attainable for a given ion is given by the radius, ρ_{max}, of the vacuum chamber and the dees and is for a nonrelativistic particle

$$T_{\text{max}} = \frac{1}{2}Mv^2 = \frac{(Bq\rho_{\text{max}})^2}{2M} = \frac{(B\rho_{\text{max}})^2}{2} \cdot \left(\frac{q^2}{M}\right) \tag{16.5}$$

We see that the maximum kinetic energy is given by the machine parameters B and ρ_{max} times the ratio of the square of the charge to mass of the ions. The term in Eq. (16.5), $(B\rho_{\text{max}})^2/2$, is the K value of the cyclotron and is given in MeV. Typical cyclotron resonance frequencies of present-day cyclotrons are around 15–30 MHz. Small cyclotrons used to produce isotopes for radiopharmaceuticals have $K = 30\,\text{MeV}$ typically and can produce 30 MeV protons. The highest-energy cyclotron in the world developed at Michigan State University has $K = 1200\,\text{MeV}$ and produces heavy ions up to $E/A = 200\,\text{MeV}$ and is limited by the relativistic mass increase of the accelerated heavy ions.

An ion beam crosses the gap twice per revolution so that it requires $T_{max}/(q \cdot \Delta V \cdot 2)$ turns. For a voltage difference $\Delta V = 100$ kV, a 30 MeV proton beam therefore needs $30/(1 \cdot 0.1 \cdot 2) = 150$ revolutions. This is why it is very important for vertical focusing to be provided for the beam so that it remains on the central plane of the cyclotron. A weak focusing occurs in the case of a magnetic field between two flat and finite pole faces because the magnetic field is only exactly perpendicular in the center and increasingly curves as one moves out radially. This curved shape of the magnetic field provides a weak restoring force for ions that are off the central plane. Stronger vertical focusing can be achieved by dividing the flat poles into sectors with higher (hills) or lower (valleys) field strengths. Then the magnetic field will curve from the hill into the valley and provides restoring toward the center plane each time the ion crosses the borders between sectors. The vertical focusing can even be increased by using spiraled pole sectors, Figure 16.11, rather than straight sectors. Such sector-focused cyclotrons are extensively used and can provide high-energy beams of heavy ions. Strong focusing is also achieved if the hill regions are made from separate wedge-shaped electromagnets and if the valley regions are left open. Of course, there has to be a common vacuum chamber in which the ions can circulate and which houses the dees. The open sectors facilitate the installation of auxiliary equipment, for example, an ECR ion source as an external injector.

The maximum beam energy delivered by cyclotrons is limited by the relativistic increase in the mass of the accelerated ion with increasing velocity, see Eq. (1.16). There are isochronous cyclotrons in which the increasing mass is compensated by increasing the strength of the magnetic field with increasing radius. This is achieved by adding extra, concentric coils to the magnet poles that are called trim coils. The field could also be increased by decreasing the gap between the pole faces. However, the field lines in a cyclotron with increasing field strength with increasing radius will curve in toward the center (opposite to what was discussed above) thus producing a weak defocusing effect. In summary, fixed-frequency cyclotrons cannot produce very high-energy beams.

16.4.4 Synchrocyclotrons, Synchrotrons

Another way of overcoming the relativity limitation in cyclotrons is by modulation of the oscillator frequency. Although this was an obvious solution that followed from

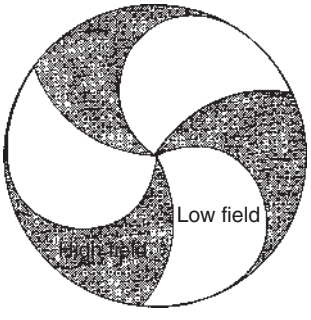

Figure 16.11 Top view of the sectors in a sector-focused cyclotron with spiraled sectors. The particles travel counterclockwise in this figure.

the cyclotron equations, it was not seriously attempted until 1945 because of the difficulty in maintaining synchronism between the oscillator frequency and the revolution frequency. The discovery of the principle of phase stability independently by V. Veksler in the USSR and by E.M. McMillan in the United States removed this formidable difficulty. A plausible discussion of how phase stability in a circular resonance accelerator comes about in a qualitative way may be as follows. Suppose an ion crossing the accelerating gap receives more than its proper amount of energy, so its orbit will have a larger radius than if the ion had just the right amount of energy, and the transit time for that revolution will be too long, that is, longer than one rf wavelength. If the accelerator is designed such that the ions cross the gap when the sinusoidal rf voltage is in the 90–180° phase – decreasing with time(!) – the ion that has previously received too much energy and therefore arrives late at the gap now receives less energy. Conversely, an ion with too little energy follows an orbit of less than the equilibrium radius, arrives at the gap early, and is given more energy than before. Thus, the ions will perform phase oscillations, also called synchrotron oscillations, around the stable phase. The frequency of these phase oscillations is much lower – perhaps several hundred times lower – than the revolution frequency.

Based on this concept, frequency modulation was applied to cyclotrons and a number of frequency-modulated (FM) cyclotrons, or synchrocyclotrons, were built worldwide in the 1940s and 1950s. Many of them have since been shut down; others have been upgraded to deliver both higher energies and higher beam intensities. In most synchrocyclotrons, frequency modulation was achieved by use of a rotating condenser in the oscillator circuit. For successful acceleration, ions have to start their spiral path at the time of maximum frequency. And because they are accepted into stable orbits only during 1% of the FM cycle, the beam consists of successive pulses, thus decreasing the beam currents relative to those of sector-focused cyclotrons. Synchrocyclotrons could accelerate a single pulse of ions up to high energies but would have to be reset to start the next pulse and thus would have a low duty factor. The size of their magnets became extremely large and costly. Therefore, the mechanical design was changed in the 1970s to be just one ring of individual smaller magnets. The set of individual magnets necessary to construct a ring requires much less iron than that of a very large synchrocyclotron magnet. This synchrotron design proved to be extremely robust and is now used in all machines built to produce the highest-energy nuclear beams.

Synchrotrons use the concept that the ions are confined to move in a circular orbit with a constant radius regardless of their energy. Thus, synchrotrons operate in a cycle in which a modest energy beam is injected into the ring at an appropriately chosen low magnetic field. After a sufficiently large number of particles have been fed into the ring, one or more accelerating resonant cavities are turned on and the beam gains energy. The energy gain per turn is on the order of 100 kV and during the acceleration, the magnetic field is ramped up synchronously to the maximum value. The frequency of the accelerating structure has to increase as well. Thus, both the magnetic field and the accelerating structure have to be synchronized with the energy of the particles. The particles can be extracted from the ring, providing a single macrocycle beam pulse. The magnetic field is then returned to

the initial low value for another injection. The time for a single macrocycle is a few seconds. The principle of phase stability is used in synchrotrons to maintain a narrow energy distribution. A variation of the strong focusing obtained with hills and valleys in sector-focused cyclotrons can be applied in synchrotrons. Instead of providing hills and valleys, though, one divides the ring into sections in which the poles of the magnets are wedge shaped. The thinner side of the wedge is alternately on the inside or the outside of the ring. The ions encounter a vertical focusing region with the thin edge inside and a vertical defocusing region with the thin edge outside, which produces a net vertical restoring force. Dipole magnets with tilted poles to provide focusing are called combined-function magnets. Synchrotrons with that type of focusing are called alternating-gradient synchrotrons *(AGS)*. More modern synchrotrons use dipole magnets to bend the beam and quadrupole magnets to focus the beam in straight sections between the dipoles. Such independently functioning magnets are easier to construct and allow for more flexible tuning.

Synchrotrons are used to accelerate protons and heavy ions to the highest energies. These are at this time 0.95 TeV for protons at Fermilab's TEVATRON, 100 GeV amu^{-1} for heavy ions, for example, 20 TeV for ^{197}Au, in RHIC at BNL. The Large Hadron Collider (LHC) (http://lhc-milestones.web.cern.ch) at CERN (www.cern.ch) is designed to collide 7 TeV protons and heavy ions with a total collision energy in excess of 1250 TeV. The maximum energy scales according to Eq. (16.5) as in a cyclotron and the value for the ring is given in units of the magnetic rigidity, namely, tesla meters, T m. The main ring of the AGS at BNL is a 100 T m machine with 240 combined function magnets in a ring of 85 m radius. The rings of the RHIC have 839.5 T m and contain 1740 separated function superconducting magnets in a ring of 3.8 km circumference. An even larger, very versatile accelerator complex has been established successively at CERN. The complex includes several injectors for protons and heavy ions, a booster synchrotron, and the proton synchrotron (PS) that can accelerate these ions, for example, 26 GeV protons, a high-energy synchrotron (SPS) that can further accelerate these ions, for example, 400 GeV protons, 170 GeV amu^{-1} heavy ions in a 1.1 km radius ring, and the largest ring for colliding electrons and positrons (LEP) with a 27 km circumference and that operated in 1989–2000 and has been replaced by the LHC with superconducting magnets operated at −271.3 °C to accelerate and collide these particles, for example, 7 TeV protons.

In a collision in the laboratory between a moving ion and a target at rest, a large fraction of the energy goes into kinematic motion of the center of mass (Eq. (12.6)) and will not be available for new particle production. Second, a majority of the projectiles will pass through the target without colliding with another nucleus. Both of these disadvantages can be removed if counterrotating beams of particles are created that circulate in synchrotron rings. Then, the net momentum of the center of mass is zero and all of the energy is available for the nuclear reaction. It is obviously more cost effective to double the available energy in a collider than to double the radius of the synchrotron. Moreover, if the counterrotating particles miss each other, they continue on their orbit and come back for another try. These features are part of all modern high-energy accelerator complexes.

16.4.5 Radioactive Ion Beams

The production of radioactive beams relies on the creation of exotic nuclei in high-energy spallation reactions followed by the separation of the unstable nuclei with half-lives as short as a few milliseconds and by provision of the exotic nuclei as radioactive beams with energies sufficient to induce secondary nuclear reactions. We introduced the two physical techniques in Section 11.9, namely, ISOL facilities and projectile fragmentation facilities. These physical techniques differ in that the products are the residues of either target or projectile nuclei, the most successful of the former being the ISOLDE facility at CERN. In the latter, fast radioactive ion beams are separated from the primary beam and from other reaction products by a combination of separated function dipole bending magnets and focusing quadrupole magnets acting on the distribution of radioactive ions emerging from the target at high velocities. If fragment recoil separators like the FRS at GSI are operated in the achromatic mode, there is an initial bend for momentum-to-charge ratio selection, an energy-loss degrader for atomic number selection, and a second bend for momentum-to-charge selection of a specific ion. The FRS has a solid angle acceptance of 0.7–2.5 msr and a momentum acceptance of $\Delta p/p = 2\%$, accepts a magnetic rigidity of 9–18 T m, achieves a mass-to-charge resolution of 240–1500, and has a length of 73 m. The existing accelerator complex at GSI consists of the UNILAC linear accelerator injecting beams of 11.4 MeV amu^{-1} into the heavy-ion synchrotron SIS 18. The projectiles leaving the SIS 18 at a maximum energy per nucleon of $E/A = 2$ GeV are fragmented in a Be target 2 g cm^{-2} thick, are separated in the FRS, and then the separated radioactive beams can be subject to decay spectroscopy in the focal plane of the FRS, or stored in the experimental storage ring, for example, for precise mass measurements, Section 3.5, or can be transported to one of the experimental caves, for example, to the LAND-ALADIN facility for nuclear structure investigations by breakup spectroscopy, as discussed in Section 11.10. There is an approved upgrade program, the international Facility for Antiproton and Ion Research (FAIR), in which the existing accelerator complex will be extended by a large synchrotron SIS 100.

16.4.5.1 FAIR – The Universe in the Lab

Currently, the international accelerator facility FAIR, one of the largest research projects worldwide, is being built in Darmstadt, Germany. At FAIR, matter that usually only exists in the depth of space will be produced in a lab for research. Scientists from all over the world will be able to gain new insights into the structure of matter and the evolution of the universe from the Big Bang to the present. FAIR is under construction at GSI Helmholtzzentrum für Schwerionenforschung. Its existing accelerator facilities will become part of FAIR and will serve as first acceleration stage. For the realization of FAIR, accelerator experts, scientists, and engineers of FAIR and GSI are working closely together in teams all over the world. In close cooperation with astronomers, who use telescopes to view the Universe at a distance, the scientists at FAIR will directly create and examine cosmic matter in the laboratory. In giant planets, stars, and also during stellar explosions and collisions, matter is subject to extreme conditions such as very high temperatures, pressures, and densities.

Figure 16.12 Anticipated view upon GSI/FAIR after its completion.

FAIR will enable scientists to create such conditions in the laboratory. To do so, they will bombard small samples of matter with ions. These collisions will, for very short periods of time, create the cosmic matter at the tiny impact points (Figure 16.12).

16.4.5.2 Research at FAIR

In giant planets, stars, and during stellar explosions and collisions, matter is subject to extreme conditions such as very high temperatures, pressures, and densities. FAIR will enable scientists to create such conditions in the laboratory. To do so, they will bombard small samples of matter with particles. The FAIR research is subdivided into the four experiment pillars: NUSTAR, CBM, PANDA, APPA. NUSTAR stands for Nuclear Structure Astrophysics and Reactions. Experiments with atomic nuclei produced as radioactive beams are the key to understanding stars. CBM stands for compressed Baryonic matter. The collision of atomic nuclei at high speeds can simulate the conditions inside supermassive objects for a split second. PANDA stands for antiproton annihilation at Darmstadt. How can antimatter help us understand the mass of matter and the strong force? And APPA stands for atomic, plasma physics, and applications. From the investigation of atoms and macroscopic effects in materials or tissues all the way to engineering and medical applications.

The Particle Accelerator Facility of FAIR and GSI

FAIR will generate particle beams of a previously unparalleled intensity and quality. The variety of these particles will be unique: Ions of all the natural elements in the periodic table, as well as antiprotons, can be accelerated. The key component of FAIR is a ring accelerator, SIS 100, with a circumference of 1100 m. Connected to this is a complex system of storage rings such as the high-energy storage ring (HESR), the collector ring (CR), the superconducting fragment separator (Super-FRS), and

several experimental stations. The existing GSI accelerators will serve as the first acceleration stage. FAIR will be one of the largest and most complex accelerator facilities in the world. The particles will be accelerated to 99% of the speed of light in the FAIR accelerator facility and made available for scientific experiments. FAIR will generate particle beams of a previously unparalleled intensity and quality. There are also additional experimental rings and experimental stations with several kilometers of beam lines in total. SIS 100 will achieve several hundred times higher primary-beam intensities than possible today, and the intensity of the secondary radioactive ion beams will be even higher, from 1000 to 10 000 times due to the higher acceptances of the subsequent separators and storage rings. Furthermore, energies 20 times higher than in the present SIS 18 synchrotron can be achieved (Figure 16.13).

The SIS 100 ring accelerator runs along an underground tunnel whose floor lies as deep as 17 m under the earth's surface. The magnets that keep the ions in their paths are superconducting and are cooled to −269 °C by means of liquid helium. The FAIR facility offers researchers a special opportunity through the fact that the particles, such as antiprotons and special isotopes, which are created when the accelerated ions hit a production target can be captured in storage rings. This capture prevents

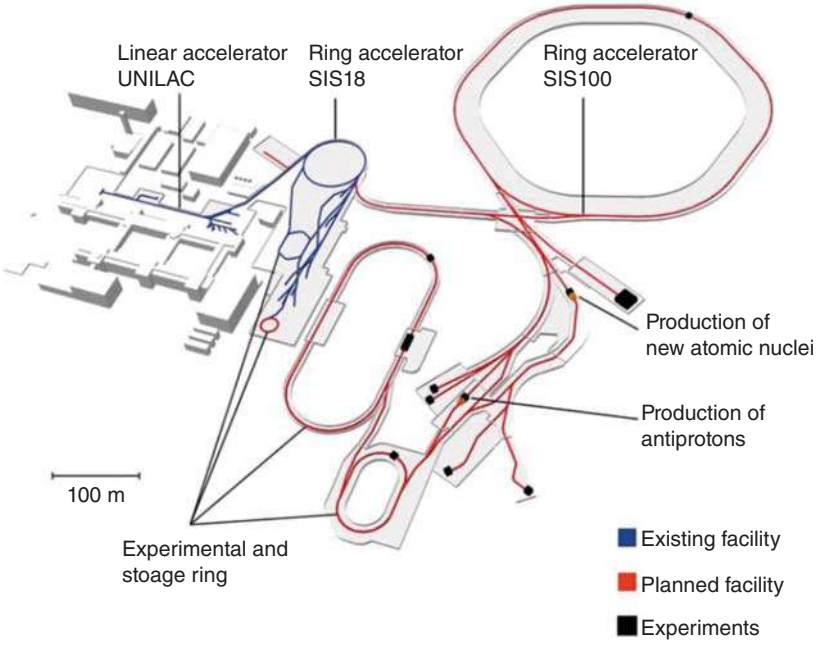

Figure 16.13 Accelerator complex of GSI/FAIR with the UNILAC, the heavy-ion synchrotron SIS 18, the fragment separator FRS, the experimental storage ring ESR, and two experimental halls. SIS 18 beams are injected into the large synchrotron SIS 100, which provides high-energy beams to the high-energy storage ring HESR, to the superconducting fragment separator Super-FRS, to the collector ring CR, and to several experimental stations for NUSTAR, CBM, PANDA, and APPA, and for the production of antiprotons. Source: Picture: GSI/FAIR.

these rare and valuable particles from being lost. On the contrary, the researchers can conduct new experiments with these particles every time they fly past. This is a clever trick, because the repeated use of a particle is indirectly equivalent to a further increase in intensity, but this increase does not require the use of the accelerator facility. The Helmholtz Institute Mainz (HIM) with an annual budget of € 6 million will provide additional personnel and technical resources to foster the operation with the new FAIR facility. Among these resources is a large assembly hall containing a clean room in which parts of the superconducting structures of FAIR, e.g. for the HESR, will be constructed. It will also be used to assemble cavities of the superconducting cw multigap CH accelerator which will replace the UNILAC linear accelerator in attempts to produce new superheavy elements that we will discuss in Chapter 17.

16.4.5.3 Construction of FAIR

The FAIR particle accelerator facility in Darmstadt is one of the world's biggest and most complex construction projects for international cutting-edge research. On a site of approximately 20 ha, unique buildings are being constructed in order to house and operate newly developed high-tech research facilities. This multinational and highly complex mega construction project has entailed the development of integrated construction workflow planning that closely coordinates building, civil and construction engineering, accelerator development and construction, and scientific experiments.

16.4.5.4 International Partners

The FAIR project is being realized in international collaboration. International scientific and technical institutes of the shareholder countries and many more partner countries are cooperating. Roughly 3000 scientists from more than 50 countries are already working on the planning and realization of the scientific program and the experiment facilities. For the realization of FAIR, the FAIR GmbH, an international company under German law, was founded. Therefore, on 4 October 2010, a dedicated contract under international law was signed. The shareholders of FAIR come from the following countries: Finland, France, Germany, India, Poland, Romania, Russia, Slovenia, and Sweden. The United Kingdom is associated, and the Czech Republic is aspirant partner. The cost of FAIR, estimated to be about €1.3 billion, is shared internationally with the largest share contributed by Germany.

16.4.5.5 High Tech for FAIR

Cutting-edge technologies and extremely innovative measuring methods and techniques are being developed for the unique FAIR particle accelerator facility. In order to create the facilities for acceleration and experiments, high-level scientists, engineers, and other experts are working in international partnership to advance new technological developments in many areas such as information and superconductor technology.

16.4.6 Photon Sources

Photons for nuclear research are produced in electron accelerators as secondary beams. Two schemes have been applied for producing monochromatic beams from bremsstrahlung (German for "slowing-down radiation"). In the first, most common scheme, the bremsstrahlung photons are produced by electrons in a thin target of high Z and the degraded electrons are analyzed in an electron spectrometer. Bremsstrahlung photons in coincidence with electrons in a particular energy bin can then be selected and are called "tagged" photons. This type of monochromator is useful for experiments that can be gated by a coincidence pulse, but not for activation experiments.

In a less common, alternative technique, monoenergetic photons are created by in-flight annihilation of positrons. Accelerated electrons interact in a thick, high-Z target producing not only bremsstrahlung but also electron–positron pairs. The positrons may be further accelerated in a linac and are then allowed to strike a thin target of low Z where positron annihilation produces a beam of monoenergetic photons in a forward direction contaminated by a small amount of bremsstrahlung. The latter is minimized by the low Z of the target and can be determined by a separate experiment with electrons instead of positrons hitting the same target. In this way 10^7 photons s^{-1} with 1% energy resolution have been produced with energies up to 30 MeV.

A continuous spectrum of synchrotron radiation is emitted whenever relativistic electrons are bent in a magnetic field. Large circular electron accelerators can therefore be used to produce brilliant synchrotron radiation which is emitted tangentially in the plane of the electron orbit. The spectrum is described in terms of a characteristic wavelength given by

$$\lambda_C = \frac{5.59R}{E^3} = \frac{18.64}{BE^2}$$

where λ_C is in angstroms, R is the orbit radius in meters, E is the electron energy in GeV, and B is the magnetic field in T. Toward the short-wavelength side of λ_C the intensity drops rapidly, whereas it rises slightly to a peak at about $4\lambda_C$ and then decreases slowly toward longer wavelengths. In present-day light sources with electron energies of a few gigaelectronvolts and orbit radii of tens of meters, λ_C values are on the order of 1–10 Å corresponding to photon energies between 12 and 1 keV. Thus, synchrotron radiation is of no interest for nuclear research, but has become a very important tool in other fields including solid-state physics, photoelectron spectroscopy, and X-ray crystallography. We shall focus on X-ray absorption spectroscopy in Chapter 22, that is, on XANES and EXAFS spectroscopy for chemical speciation of radionuclides in the environment. Sources of synchrotron radiation with typically 10^{13} photons s^{-1} $Å^{-1}$ $mrad^{-1}$ per milliampere of circulating current are being achieved. The fact that photons are emitted tangentially all around the azimuth of a machine makes it possible to perform many experiments simultaneously.

References

Blewett, M.H. (1963). The electrostatic (Van de Graaff) generator. In: *Methods of Experimental Physics*, vol. 5B, Nuclear Physics (eds. L.C.L. Yuan and C.S. Wu), 584. New York: Academic Press.

Friedlander, G., Kennedy, J.W., Macias, E.S., and Miller, J.M. (1981). *Nuclear and Radiochemistry*, 3e. New York: Wiley.

Krane, K.S. (1988). *Introductory Nuclear Physics*. New York: Wiley.

Pollard, E. and Davidson, W.L. (1951). *Applied Nuclear Physics*, 2e. New York: Wiley.

Segre, E. (1977). *Nuclei and Particles*, 2e. Reading, MA: Benjamin.

Wideröe, R. (1928). Über ein Neues Prinzip zur Herstellung Hoher Spannungen. *Arch. Elektrotech.* 21: 387.

Further Reading

Thomas, L.H. (1938). The paths of ions in the cyclotron. *Phys. Rev.* 54: 580.

Courant, E.D., Livingston, M.S., and Snyder, H.S. (1952). The strong-focusing synchrotron – a new high-energy accelerator. *Phys. Rev.* 88: 1190.

McMillan, E.M. (1959). Particle accelerators. In: *Experimental Nuclear Physics*, vol. III (ed. E. Segre), 639. New York: Wiley.

Livingston, M.S. and Blewett, J.P. (1962). *Particle Accelerators*. New York: McGraw-Hill.

Kouts, H. (1963). Nuclear reactors. In: *Methods of Experimental Physics*, vol. 5B, Nuclear Physics (eds. L.C.L. Yuan and C.S. Wu), 590. New York: Academic Press.

O'Kelley, G.D. (1963). Radioactive sources. In: *Methods of Experimental Physics*, vol. 5B, Nuclear Physics (eds. L.C.L. Yuan and C.S. Wu), 555. New York: Academic Press.

Livingston, M.S. (1966). *The Development of High-Energy Accelerators*. New York: Dover.

Blewett, M.H. (1967). Characteristics of typical accelerators. *Annu. Rev. Nucl. Sci.* 17: 427.

Courant, E.D. (1968). Accelerators for high intensities and high energies. *Annu. Rev. Nucl. Sci.* 18: 435.

Pellegrini, C. (1972). Colliding beam accelerators. *Annu. Rev. Nucl. Sci.* 22 (1).

Allen, K.W. (1974). Electrostatic accelerators. In: *Nuclear Spectroscopy and Reactions, Part A* (ed. J. Cerny), 3. New York: Academic Press.

Berman, B.L. (1974). Photonuclear reactions. In: *Nuclear Spectroscopy and Reactions, Part C* (ed. J. Cerny), 377. New York: Academic Pree.

Bock, R. (1974). Heavy ion accelerators. In: *Nuclear Spectroscopy and Reactions, Part A* (ed. J. Cerny), 79. New York: Academic Press.

Harvey, B.G. (1974). The cyclotron. In: *Nuclear Spectroscopy and Reactions, Part A* (ed. J. Cerny), 36. New York: Academic Press.

Sanford, J.R. (1976). The fermi national accelerator laboratory. *Annu. Rev. Nucl. Sci.* 26: 151.

Goldsmith, M. and Shaw, E. (1977). *Europe's Giant Accelerator: The Story of the CERN 400 GeV Proton Synchrotron*. London: Taylor & Francis.

Grunder, H.A. and Selph, F.B. (1977). Heavy ion accelerators. *Annu. Rev. Nucl. Sci.* 27: 353.

Clark, D.J. (1985). Positive heavy-ion sources. In: *Treatise on Heavy-Ion Science*, vol. 7 (ed. D.A. Bromley), 3. New York: Plenum Press.

Gallant, J.L. (1985). Stripping foils for heavy-ion beams. In: *Treatise on Heavy-Ion Science*, vol. 7 (ed. D.A. Bromley), 91. New York: Plenum Press.

Middleton, R. (1985). A review of negative heavy-ion sources. In: *Treatise on Heavy-Ion Science*, vol. 7 (ed. D.A. Bromley), 53. New York: Plenum Press.

Tanihata, I. (1989). On the possible use of secondary radioactive beams. In: *Treatise on Heavy-Ion Science*, vol. 8 (ed. D.A. Bromley), 443. New York: Plenum Press.

Csikai, J. and Dóczi, R. (2011). Applications of neutron generators. In: *Handbook of Nuclear Chemistry*, 2e, vol. 3 (eds. A. Vertés, S. Nagy, Z. Klencsár, et al.), 1673. Berlin: Springer-Verlag.

Koltay, E., Pászti, F., and Kiss, Á.Z. (2011). Chemical applications of ion accelerators. In: *Handbook of Nuclear Chemistry*, 2e, vol. 3 (eds. A. Vertés, S. Nagy, Z. Klencsár, et al.), 1695. Berlin: Springer-Verlag.

Barth, W., Aulenbacher, K., Basten, M. et al. (2018). First heavy ion beam tests with a superconducting multigap CH cavity. *Phys. Rev. Accel. Beams* 21: 020102.

For an overview of the FAIR project. see https://www.gsi.de/forschungbeschleuniger/fair/die_maschine; https://www.gsi.de/start/aktuelles/detailseite/2021/06/02/ringschluss-fuer-grossen-fair-beschleuniger-rohbauarbeiten-sind-vollendet.

17

Radioelements

17.1 Natural and Artificial Radioelements

Radioelements are elements existing only in the form of radionuclides, but not as stable isotopes, as already mentioned in Section 3.1.

The natural radioelements are listed in Table 17.1. Isotopes of these elements are members of the uranium, actinium, and thorium families (Table 2.2 and Figures 2.2–2.4). In the ores of U and Th, the concentrations of natural radioelements are relatively high and proportional to the half-life. The average concentration of U in the Earth's crust is about 2.9 mg kg^{-1} (ppm) and that of Th about 11 mg kg^{-1} (ppm). The concentration of U in seawater is about 3 mg m^{-3}, corresponding to a total amount of about $4 \cdot 10^9$ tons of U in the oceans.

All natural radioelements with atomic numbers $Z = 84$–89 and $Z = 91$ have been identified as decay products of U and Th, but the first isotope of astatine (from the Greek "unstable"; $Z = 85$) was obtained in 1940 by the nuclear reaction.

$$^{209}\mathrm{Bi}(\alpha, 2\mathrm{n})^{211}\mathrm{At} \xrightarrow[\epsilon,\alpha,\gamma]{7.22\,\mathrm{hours}} \tag{17.1}$$

The half-life is somewhat shorter than that of ^{210}At ($t_{1/2} = 8.3$ hours), which has the longest half-life of all astatine isotopes. Three years later, At was also identified in nature. ^{219}At produced in the α branching of ^{223}Fr is the longest-lived natural isotope of At ($t_{1/2} = 5.4$ seconds). The very short-lived isotopes ^{218}At and ^{215}At are present in small concentrations as members of the uranium and actinium families (Figures 2.2 and 2.4). Because the main importance of At is as a natural radioelement, it is included in this group.

Many natural radioelements are of great practical importance, in particular U with respect to its application as nuclear fuel, but also Th, Ra, and Rn. ^{226}Ra ($t_{1/2} = 1600$ years) is found in many springs, and the noble gas Rn is the main source of natural radioactivity in the air.

The artificial radioelements are listed in Table 17.2. Their number is now 28, and hopefully, it will continue to increase in the future. Note that, at present, one-third of the total number of known elements is radioelements.

The discovery of technetium ($Z = 43$) in 1937 and of promethium ($Z = 61$) in 1947 filled the two gaps in the periodic table of the elements. These gaps had

Nuclear and Radiochemistry: Fundamentals and Applications,
Fourth Edition. Jens-Volker Kratz.

Table 17.1 The natural radioelements.

Atomic number Z	Name of the element (symbol)	Longest-lived nuclide (half-life)	Discovery	Remarks
84	Polonium (Po)	^{209}Po (102 yr)	1898 Pierre and Marie Curie	Similar to Te
85	Astatine (At)	^{210}At (8.3 h)	1940 Corson, McKenzie, and Segrè	Halogen; volatile
86	Radon (Rn)	^{222}Rn (3.825 d)	1900 Rutherford and Soddy	Noble gas
87	Francium (Fr)	^{223}Fr (21.8 min)	1939 Perey	Alkali metal; similar to Cs
88	Radium (Ra)	^{226}Ra (1600 yr)	1898 Pierre and Marie Curie	Alkaline earth metal; similar to Ba
89	Actinium (Ac)	^{227}Ac (21.773 yr)	1899 Debierne	Similar to La; more basic
90	Thorium (Th)	^{232}Th ($1.405 \cdot 10^{10}$ yr)	1828 Berzelius	Only in the oxidation state IV; similar to Ce(IV), Zr(IV), and Hf(IV); strongly hydrolyzing; many complexes
91	Protactinium (Pa)	^{231}Pa ($3.276 \cdot 10^{4}$ yr)	1917 Hahn and Meitner	Preferably in the oxidation state V; very strongly hydrolyzing; many complexes
92	Uranium (U)	^{238}U ($4.468 \cdot 10^{9}$ yr)	1789 Klaproth	Preferably in the oxidation states IV and VI; in solution UO_2^{2+} ions; many complexes

been the reason for many investigations. Application of Mattauch's rule (stating that neighboring stable isobars do not exist; exception $A = 50, 180$) leads to the conclusion that stable isotopes of elements 43 and 61 cannot exist. The report by I. Noddak and W. Tacke concerning the discovery of the elements rhenium and "masurium" (1925) was only correct with respect to Re ($Z = 75$). The concentration of element 43 (Tc) in nature due to spontaneous or neutron-induced fission of U is several orders of magnitude too low to be detectable by emission of the characteristic X-rays of element 43, as had been claimed in the report.

Many artificial radioelements have gained great practical importance. Production of ^{99}Tc in nuclear reactors has already been mentioned. It is found in all steps of reprocessing nuclear fuel and in all kinds of nuclear waste. In the environment, it

Table 17.2 Artificial radioelements.

Atomic number *Z*	Name of the element (symbol)	Longest-lived nuclide (half-life)	Discovery	Remarks
43	Technetium (Tc)	^{98}Tc ($4.2 \cdot 10^6$ yr)	1937; Perrier and Segrè	Similar to Re; preferred oxidation states IV and VII
61	Promethium (Pm)	^{145}Pm (17.7 yr)	1947; Marinsky, Glendenin, and Coryell	Only in the oxidation state III
93	Neptunium (Np)	^{237}Np ($2.144 \cdot 10^6$ yr)	1940; McMillan and Abelson	Oxidation states III to VII; Np(V) in aqueous soln.
94	Plutonium (Pu)	^{244}Pu ($8.00 \cdot 10^7$ yr)	1940; Seaborg et al.	Oxidation states III to VIII
95	Americium (Am)	^{243}Am (7370 yr)	1944; Seaborg et al.	Oxidation states III to VI
96	Curium (Cm)	^{247}Cm ($1.56 \cdot 10^7$ yr)	1944; Seaborg et al.	Analogous to Gd; can be oxidized to Cm(IV)
97	Berkelium (Bk)	^{247}Bk (1380 yr)	1949; Thompson et al.	Analogous to Tb
98	Californium (Cf)	^{251}Cf (898 yr)	1950; Thompson et al.	Analogous to Dy
99	Einsteinium (Es)	^{252}Es (471.7 d)	1952; Thompson et al.	Analogous to Ho
100	Fermium (Fm)	^{257}Fm (100.5 d)	1953; Thompson et al.	Analogous to Er
101	Mendelevium (Md)	^{258}Md (51.5 d)	1955; Ghiorso et al.	Analogous to Tm
102	Nobelium (No)	^{259}No (58 min)	1958; Ghiorso et al.	Oxidation state 2^+ preferred
103	Lawrencium (Lr)	^{262}Lr (3.6 h)	1961; Ghiorso et al.	Analogous to Yb
104	Rutherfordium (Rf)	^{261}Rf (68 s)	1969; Ghiorso et al.	Tetravalent

(Continued)

Table 17.2 (Continued)

Atomic number Z	Name of the element (symbol)	Longest-lived nuclide (half-life)	Discovery	Remarks
105	Dubnium (Db)	^{262}Db (34 s)	1970; Ghiorso et al.	Pentavalent
106	Seaborgium (Sg)	^{271}Sg (2.4 min)	1974; Ghiorso et al., Flerov et al.	Similar to Mo and W
107	Bohrium (Bh)	^{267}Bh (17 s)	1981; Münzenberg et al.	Homolog of Re
108	Hassium (Hs)	^{270}Hs (30 s)	1984; Münzenberg et al.	Homolog of Os
109	Meitnerium (Mt)	^{276}Mt (0.72 s)	1982; Münzenberg et al.	Homolog of Ir
110	Darmstadtium (Ds)	^{281}Ds (9.6 s)	1995; Hofmann et al.	Homolog of Pt
111	Roentgenium (Rg)	^{280}Rg (4.3 s)	1995; Hofmann et al.	Homolog of Au
112	Copernicium (Cn)	^{285}Cn (34 s)	1996; Hofmann et al.	Homolog of Hg
113	Nihonium (Nh)	^{284}113 (0.92 s)	2004; Morita et al.	Homolog of Tl
114	Flerovium (Fl)	^{289}114 (2.6 s)	2000; Oganessian et al.	Homolog of Pb
115	Moscovium (Mc)	^{288}115 (0.18 s)	2004; Oganessian et al.	Homolog of Bi
116	Livermorium (Lv)	^{293}116 (61 ms)	2000; Oganessian et al.	Homolog of Po
117	Tennessine (Ts)	^{294}117 (78 ms)	2010; Oganessian et al.	Homolog of At
118	Oganesson (Og)	^{294}118 (0.9 ms)	2006; Oganessian et al.	Homolog of Rn

is very mobile under oxidizing conditions, as TcO_4^-. The short-lived isomer ^{99m}Tc is one of the most widely used radionuclides in nuclear medicine (Chapter 22). ^{237}Np is produced in nuclear reactors in amounts of about 0.5 kg/ton of spent fuel after burn up of 35 000 MWd/ton. In general, it goes with the high-level waste (HLW). Special steps have been developed to separate ^{237}Np in the course of reprocessing, for instance, for the production of ^{238}Pu by the reaction

$$^{237}Np(n,\gamma)^{238}Np \xrightarrow[\beta^-]{2.117\ \text{days}} {}^{238}Pu \tag{17.2}$$

The latter is used as an energy source in radionuclide batteries, for instance, in satellites. Pu is the most important radioelement produced in nuclear reactors. About 9 kg of Pu is generated per ton of spent fuel after a burn-up of 35 000 MWd/ton. The main part is ^{239}Pu (about 5.3 kg) produced via

$$^{238}U(n,\gamma)^{239}U \xrightarrow[\beta^-]{23.5\ \text{minutes}} {}^{239}Np \xrightarrow[\beta^-]{2.355\ \text{days}} {}^{239}Pu \xrightarrow[\alpha]{2.411\cdot10^4\ \text{years}} \tag{17.3}$$

^{240}Pu (about 2.2 kg), ^{241}Pu (about 1.1 kg), and ^{242}Pu (about 0.4 kg) are generated by (n, γ) reactions from ^{239}Pu. ^{239}Pu is a valuable nuclear fuel and may also be used for the production of nuclear weapons. The global production rate of ^{239}Pu in nuclear power reactors is on the order of 100 tons/year contained in spent fuel elements. Non-proliferation agreements should prevent uncontrolled distribution of Pu. Moreover, Pu is highly toxic. Am and Cm are generated in smaller amounts in nuclear reactors by (n, γ) reactions (about 0.15 kg Am and about 0.07 kg Cm per ton of spent fuel after a burn-up of 35 000 MWd/ton).

17.2 Technetium and Promethium

^{99}Tc was isolated as the first isotope of technetium (the "artificial" element) in 1937 from neutron-irradiated Mo where it was formed by the reactions

$$^{98}Mo(n,\gamma)^{99}Mo \xrightarrow[\beta^-]{66\ \text{hours}} {}^{99m}Tc \xrightarrow[\text{IT}]{6\ \text{hours}} {}^{99}Tc \xrightarrow[\beta^-]{2.1\cdot10^5\ \text{years}} \tag{17.4}$$

Because of the small cross section (0.13 b), the yield of the (n, γ) reaction is low. Relatively large amounts of ^{99}Tc are produced by nuclear fission of ^{235}U (fission yield 6.2%). After a burn-up of 35 000 MWd/ton of U with an initial enrichment of 3% ^{235}U, the spent fuel contains about 1 kg of ^{99}Tc per ton. The longest-lived isotope of Tc is ^{98}Tc ($t_{1/2} = 4.2 \cdot 10^6$ years); in contrast to ^{99}Tc, it has no practical significance.

Although ^{99}Tc is present in uranium ores in extremely small concentrations, the main importance of Tc is that of a human-made element and counted as an artificial radioelement, due to its production in nuclear reactors and by nuclear explosions.

With respect to chemical behavior, Tc is more closely related to Re than to Mn and exhibits some similarities to the neighboring elements Mo and Ru. Under oxidizing conditions, the stable oxidation state is Tc(VII) as TcO_4^- in aqueous solution or as volatile Tc_2O_7 in the absence of water. Under reducing conditions, Tc(IV) is the most stable oxidation state, strongly hydrolyzing in aqueous solutions and very stable as

TcO_2 in the absence of water. Relatively stable complexes of Tc(V) are formed in the presence of suitable complexing agents. Fluorination leads to the volatile TcF_6. For the separation of Tc, various methods may be used, for example, distillation of Tc_2O_7 from concentrated H_2SO_4 or coprecipitation with Re_2S_7 or with CuS, followed by dissolution in HCl and selective separation of TcO_4^-.

Element 61 (Pm) could not be found in nature, and the gap in the periodic table of the elements remained until 1947 when the element was discovered by Marinsky et al. (Marinsky et al. 1947) in the fission products of U after separating the rare earth fraction by oxalate precipitation. ^{147}Pm is produced with a fission yield of 2.27%. The longest-lived isotope of Pm is ^{145}Pm ($t_{1/2} = 17.7$ years), followed by ^{146}Pm ($t_{1/2} = 5.53$ years). Isotopes of Pm can also be produced by neutron irradiation of Nd

$$\begin{aligned}
&^{146}\mathrm{Nd}(\mathrm{n},\gamma)^{147}\mathrm{Nd}\xrightarrow[\beta^-]{10.98\ \text{days}}{}^{147}\mathrm{Pm}\xrightarrow[\beta^-]{2.62\ \text{years}}\\
&^{148}\mathrm{Nd}(\mathrm{n},\gamma)^{149}\mathrm{Nd}\xrightarrow[\beta^-]{1.73\ \text{hours}}{}^{149}\mathrm{Pm}\xrightarrow[\beta^-]{53.1\ \text{hours}}\\
&^{150}\mathrm{Nd}(\mathrm{n},\gamma)^{151}\mathrm{Nd}\xrightarrow[\beta^-]{12.4\ \text{hours}}{}^{151}\mathrm{Pm}\xrightarrow[\beta^-]{28.4\ \text{hours}}
\end{aligned} \tag{17.5}$$

The element was named promethium in memory of Prometheus who, according to Greek mythology, brought fire to humankind.

Promethium is a typical element of the lanthanide series. The relative abundances of the lanthanides are plotted in Figure 17.1 as a function of atomic number. Figure 17.1 illustrates Harkin's rule: the abundance of elements with even atomic numbers is appreciably higher than that of elements with odd atomic numbers.

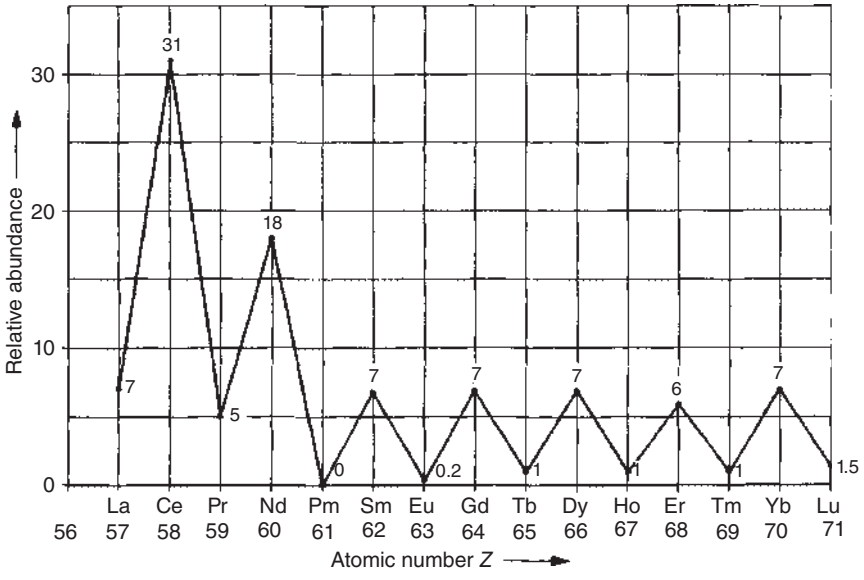

Figure 17.1 Relative abundances of the lanthanides. Source: After V.M. Goldschmidt.

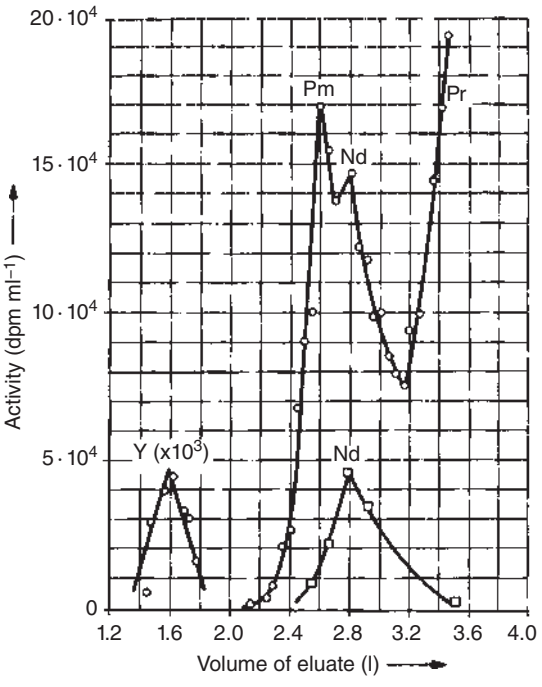

Figure 17.2 Separation of Pm from fission products of uranium on a cation exchange column by elution with citrate solution: o, β activity; □, γ activity. Source: Marinsky et al. (1947), figure 2 (p. 2782)/American Chemical Society.

For element 61, the natural abundance is zero. Usually, Pm is separated from other lanthanides by ion exchange in the presence of complexing agents in solution. This method was also applied by Marinsky et al. (1947): after oxalate precipitation of the rare earth fraction, the precipitate was treated with carbonate solution to remove the main part of Y, dissolved, and passed as 5% citrate solution (pH 2.5) through a cation exchange column. The result is shown in Figure 17.2.

The valence states of the lanthanides are plotted in Figure 17.3 as a function of the atomic number. The most stable electron configurations are $4f^0$ (La^{3+}), $4f^7$ (Gd^{3+}), and $4f^{14}$ (Lu^{3+}). These configurations are also favored by neighboring elements. The colors of the lanthanide ions show a similar variation with the electron configuration: whereas La^{3+}, Gd^{3+}, and Lu^{3+} are colorless, the color intensity of the other Ln^{3+} ions (Ln stands for lanthanides) increases with increasing distance from the atomic numbers of these three elements, with maxima halfway between La^{3+} and Gd^{3+} and between Gd^{3+} and Lu^{3+}. The ionic radii of the lanthanide ions

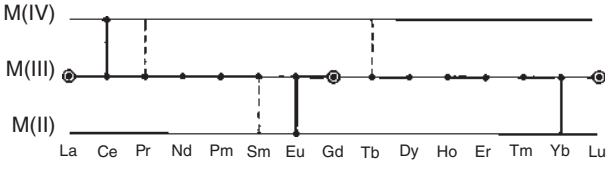

Figure 17.3 Oxidation states of the lanthanides.

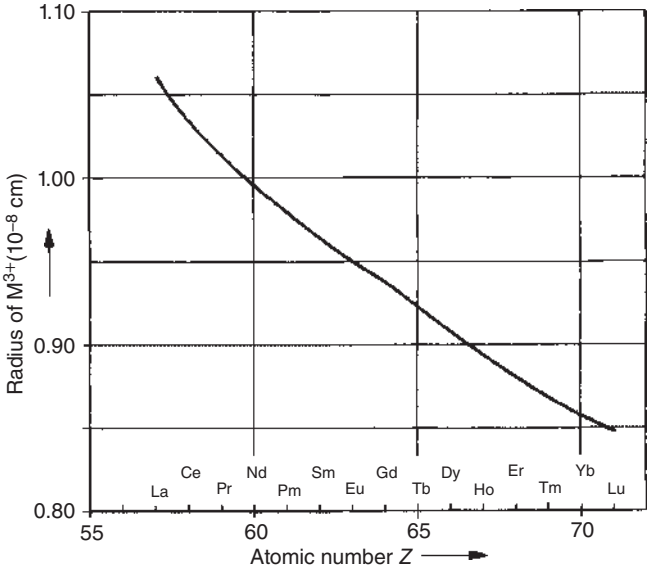

Figure 17.4 Ionic radii of lanthanide ions in the oxidation state +3. Source: Based on Templeton and Dauben (1954).

decrease continuously with increasing atomic numbers, as shown in Figure 17.4, due to the increasing charge on the nucleus at constant outer electron shell. This effect is known as lanthanide contraction.

17.3 Production of Transuranic Elements

The various methods of production of transuranic elements are:

- irradiation with neutrons;
- irradiation with deuterons or α particles; and
- irradiation with heavy ions.

The most important method of production of the first transuranic elements is neutron irradiation of U. After the discovery of the neutron by Chadwick in 1932, this method was applied from 1934 by Fermi in Italy and by Hahn in Berlin. The method is based on the concept that absorption of neutrons by nuclides with atomic number Z leads to the formation of neutron-rich nuclides that decay by β^- decay into nuclides with atomic numbers $Z+1$. Unexpectedly though, the experiments carried out by O. Hahn and F. Strassmann led to the discovery of nuclear fission in 1938.

The production of transuranic elements by neutron irradiation can be described by

$$^{A}Z(\mathrm{n},\gamma)^{A+1}Z \xrightarrow{\beta^-} {}^{A+1}(Z+1) \tag{17.6}$$

After long irradiation times, elements with atomic numbers $Z+2$, $Z+3$, etc. are generated in amounts that increase with irradiation time. The formation of

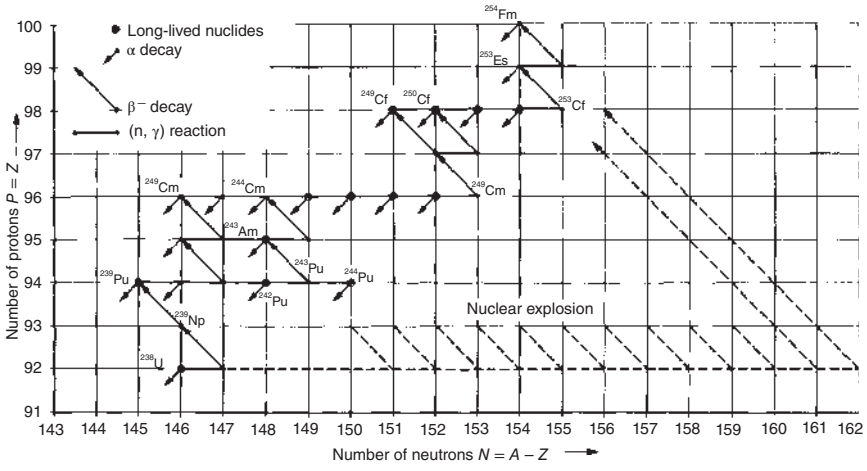

Figure 17.5 Production of transuranic elements by neutron irradiation of ^{238}U.

transuranic elements by neutron irradiation of ^{238}U is illustrated in Figure 17.5; (n, γ) reactions and radioactive decay compete with each other. The formation of heavier nuclides is favored if

$$\sigma_{n,\gamma}\Phi_n > \Lambda \tag{17.7}$$

where $\sigma_{\eta,\gamma}$ is the (n, γ) cross section and Φ_n is the neutron flux density. $\Lambda = \lambda + \Sigma\sigma_i$ Φ_i is the sum of the decay constant λ and all products $\sigma_i\Phi_i$ of nuclear reactions (e.g. nuclear fission) also leading to a decrease in the radionuclide considered. (17.7) is fulfilled in a nuclear reactor at $\sigma_{\eta,\gamma} = 1$ b and $\Phi_n = 10^{14}$ cm^{-2} s^{-1}, if $\Lambda < 10^{-10}$ s^{-1} or, neglecting the contribution of $\Sigma\sigma_i\Phi_i$, if $t_{1/2} > 200$ years. That means that under these conditions, heavier nuclides are only produced in greater amounts if the half-lives of all intermediate nuclides are longer than about 100 years.

At the extremely high fluxes of a thermonuclear explosion, fast multiple neutron capture leads to very neutron-rich isotopes of U or Pu, respectively, changing rapidly into elements of appreciably higher atomic numbers by a quick succession of β^- transmutations. This method of formation of heavier elements is also indicated in Figure 17.5. The elements can be found in the debris of nuclear explosions.

By irradiation with deuterons, one proton is introduced into the nucleus and (d, n), or (d, 2n) reactions lead to the production of elements with $Z + 1$, for instance,

$$^AZ(d, n)^{A+1}(Z + 1) \tag{17.8}$$

For the formation of heavier elements, irradiation with α particles is preferable because by (α, n) or (α, 2n) reactions, the atomic number increases by two units:

$$^AZ(\alpha, n)^{A+3}(Z + 2) \tag{17.9}$$

The most important method of production of elements with $Z > 100$, however, is irradiation with heavy ions of elements that are available in sufficient amounts.

Fusion of projectiles (atomic number Z') with target nuclei (atomic number Z) may lead to elements with atomic number $Z + Z'$:

$$ {}^{A}Z + {}^{A'}Z' \rightarrow {}^{A+A'-x}(Z + Z') + x\mathrm{n} \tag{17.10} $$

The energy needed to surmount the Coulomb barrier increases with Z and Z', whereas the cross section decreases. That is why, in general, only small amounts of heavier elements can be produced by heavy-ion reactions. Elements with $Z \geq 104$ are often obtained with a yield of only one atom at a time.

The first transuranic element, neptunium ($Z = 93$), was first observed by McMillan (McMillan 1939) in February 1939 in Berkeley while investigating the products of the neutron irradiation of a thin uranium target. The range of the ejected radioactive products was measured by observing the distribution of the activity with depth in a layer of cigarette papers placed next to the U during irradiation. After bombardment, fission product activity was found on the first three sheets with parallel decay curves. But the decay curve of the uranium sample showed a strong additional component of about 25 minutes half-life which was likely the substance identified by Hahn, Meitner, and Strassmann as ^{239}U, and also a long period ($\approx$2 days) that was strong compared to the fission product samples. In May 1939, Segrè (Segrè 1939) investigated the "non-recoiling" 2.3 day period chemically and found that this activity did not precipitate with hydrogen sulfide using rhenium as a carrier. According to the erroneous placement of Th, Pa, and U in groups IV through VI in the periodic table, the first transuranic element was believed to be an eka-rhenium. Instead, the "non-recoiling" 2.3 day period behaved like a rare earth. The conclusion published in the *Physical Review* (Segrè 1939) was "that transuranic elements have not yet been observed." In 1940, McMillan and Abelson continued to work with the 2.3 day substance from thin uranium layers and a very characteristic difference from the rare earths was soon found: the substance did not precipitate with HF in the presence of an oxidizing agent (bromate in strong acid). In the presence of a reducing agent (SO_2), it precipitated quantitatively with HF. Cerium was used as a carrier. The final proof that the 2.3 day substance is the daughter of the 23 minutes U was the demonstration of its growth from the latter. A purified solution of neutron-irradiated U in HF was saturated with SO_2, and equal quantities of Ce were added subsequently at 20 minutes intervals and the precipitates filtered out. The initial activities of the 2.3 day substance plotted against the time of separation gave a decay curve with a half-life of 23 minutes.

Thus, the neptunium isotope first identified was ^{239}Np produced by the reaction

$$ {}^{238}\mathrm{U}(\mathrm{n},\gamma){}^{239}\mathrm{U} \xrightarrow[\beta^-]{\text{23.5 minutes}} {}^{239}\mathrm{Np} \xrightarrow[\beta^-]{\text{2.355 days}} \tag{17.11} $$

It was named in analogy to U after the planet Neptune. The Np isotope with the longest half-life ($t_{1/2} = 2.144 \cdot 10^6$ years) is ^{237}Np, the mother nuclide of the (artificial) decay series with $A = 4\mathrm{n} + 1$. It is produced in nuclear reactors:

$$ {}^{238}\mathrm{U}(\mathrm{n},2\mathrm{n}){}^{237}\mathrm{U} \xrightarrow[\beta^-]{\text{6.75 days}} {}^{237}\mathrm{Np} \quad (\approx 70\%) \tag{17.12} $$

$$ {}^{235}\mathrm{U}(\mathrm{n},\gamma){}^{236}\mathrm{U}(\mathrm{n},\gamma){}^{237}\mathrm{U} \xrightarrow[\beta^-]{\text{6.75 days}} {}^{237}\mathrm{Np} \quad (\approx 30\%) $$

Very small amounts of ^{237}Np are present in uranium ores, where this nuclide is produced by neutrons from cosmic radiation. The ratio ^{237}Np/^{238}U in uranium ores is on the order of 10^{-12}.

Plutonium ($Z = 94$) was discovered in 1940 by Glenn T. Seaborg and coworkers. It was also named in analogy to U, after the planet Pluto. The first isotope of Pu was produced by cyclotron irradiation of U with 16 MeV deuterons:

$$^{238}\mathrm{U(d, 2n)}^{238}\mathrm{Np} \xrightarrow[\beta^-]{2.117\ \text{days}} {}^{238}\mathrm{Pu} \xrightarrow[\alpha]{87.74\ \text{years}} \tag{17.13}$$

The discovery of Pu has been described in detail by Seaborg (1958) in his "Plutonium Story" (Chapter 1 of the book *The Transuranium Elements*, 1958). First, the separation of Pu from Th caused some difficulties because both elements were in the oxidation state +4. After oxidation of Pu(IV) by persulfate in the presence of Ag(II) to Pu(VI), separation became possible. ^{239}Pu was produced in a sample of $UO_2(NO_3)_2{\cdot}6H_2O$ weighing 1.2 kg and placed in a large paraffin block positioned directly behind the beryllium target of the 60 in. Berkeley cyclotron. It was bombarded over a period of two days with 3500 μAh neutrons from Be plus 16 MeV deuterons. After bombardment, the uranyl nitrate was dissolved in 2 l ethylether. The ^{239}Np was isolated from the aqueous phase with rare earth fluoride carrier by the method of McMillan and Abelson. This sample had an activity of 125 mCi as determined with an ionization chamber. During the decay of the ^{239}Np, α-particle activity was observed to grow with a half-life of about 2.3 days to be expected for growth from ^{239}Np. A rough half-life of ^{239}Pu of $3 \cdot 10^4$ years was measured. After the discovery of ^{239}Pu, plutonium gained great practical importance because of the high fission cross section of ^{239}Pu by thermal neutrons. Very small amounts of ^{239}Pu are present in uranium ores, due to the (n, γ) reaction of neutrons from cosmic radiation with ^{238}U. The ratio ^{239}Pu/^{238}U is on the order of 10^{-11}. In 1971, the longest-lived isotope of plutonium, ^{244}Pu ($t_{1/2} = 8.00 \cdot 10^7$ years), was found by Hoffman et al. (1971) in the Ce-rich rare earth mineral bastnaesite, in a concentrations on the order of 10^{-15} g kg^{-1}.

Curium was discovered in 1944 by Seaborg et al. by bombarding 10 mg of ^{239}Pu with 40 μAh, 32 MeV He ions in the Berkeley 60-in. cyclotron:

$$^{239}\mathrm{Pu}(\alpha, \mathrm{n})^{242}\mathrm{Cm} \tag{17.14}$$

It was carried quantitatively by lanthanum fluoride, even in the presence of oxidizing agents such as dichromate or silver persulfate, indicating that this substance cannot be oxidized to a +6 oxidation state. Curium was named in analogy to the element gadolinium (having the same number of f electrons) in memory of research scientists – in this case in honor of Marie and Pierre Curie.

Contrary to the impression that curium was discovered before americium, the early publications on the synthesis of element 95 report that a sample of α-irradiated uranium was produced in the 60-in. cyclotron in Berkeley just 2 days prior to the sample that produced element 96. The ^{238}U(α, n) reaction produced the β^- decaying ^{241}Pu followed by the first observation of ^{241}Am in July 1944 by Seaborg, James, and

Morgan. However, one often reads that americium was discovered by Seaborg et al. (1945) after longer neutron irradiation of ^{239}Pu:

$$^{239}\mathrm{Pu(n,\gamma)}^{240}\mathrm{Pu(n,\gamma)}^{241}\mathrm{Pu} \xrightarrow[\beta^-]{14.35\ \mathrm{y}} {}^{241}\mathrm{Am} \tag{17.15}$$

The neutron irradiations were carried out in the Clinton and Hanford reactors. The produced α activity was composed of two components where the lower energy was assigned to ^{241}Am and the higher energy to ^{242}Cm from β-decaying ^{242}Am according to

$$^{241}\mathrm{Am(n,\gamma)}^{242}\mathrm{Am} \xrightarrow[\beta^-]{16\ \mathrm{hours}} {}^{242}\mathrm{Cm} \tag{17.16}$$

Similar to curium, americium could be oxidized to a state where its fluoride is soluble. It was named in analogy to the element europium, which has the same number of f electrons. The observation of a rare-earth-like behavior of the transplutonium elements in their reduced states was the basis for Seaborg's actinide hypothesis. He formulated:

> Although the first members ($_{90}$Th, $_{91}$Pa) of the group 90 to 94 show a great resemblance in chemical properties to the first members ($_{72}$Hf, $_{73}$Ta) in the 5d transition series and to the first members ($_{40}$Zr, $_{41}$Nb) in the 4d transition series, the later members ($_{93}$Np, $_{94}$Pu) show practically no resemblance to $_{75}$Re and $_{76}$Os and to $_{43}$Tc and $_{44}$Ru. This suggests that it is the 5f electron shell which is being filled, although it is not possible to deduce from this chemical evidence alone whether uranium is the first element in the series for which this is the case. While it is beyond the scope of this discussion to give all the supporting evidence, we would like to advance the attractive hypothesis that this rare-earth-like series begins with actinium in the same sense that the "lanthanide" series begins with lanthanum. On this basis it might be termed "actinide" series and the first 5f electron might appear in thorium. Thus, the characteristic oxidation state – that is, the oxidation state exhibited by those members containing seven 5f and fourteen 5f electrons – for this transition series is III.

The elements with the atomic numbers 97 and 98 (berkelium and californium, respectively) at first could not be produced by irradiation with neutrons because isotopes of Cm exhibiting β^- transmutation were not known. After milligram amounts of ^{241}Am had been produced by (17.15), ^{244}Bk was obtained in 1949 by S.G. Thompson et al. (1950) by irradiation with α particles:

$$^{241}\mathrm{Am}(\alpha,\mathrm{n})^{244}\mathrm{Bk} \tag{17.17}$$

The chemical separation of element 97 from the target material and other reaction products was made by combinations of precipitation and ion exchange. Berkelium was named in analogy to terbium after a city (Berkeley).

Californium ($Z = 98$) was discovered in 1950, by Thompson et al., by irradiation of ^{242}Cm with α particles:

$$^{242}\mathrm{Cm}(\alpha,\mathrm{n})^{245}\mathrm{Cf} \tag{17.18}$$

The chemical identification was accomplished through ion exchange employing the resin Dowex 50. It preceded berkelium and curium off the column just as dysprosium precedes terbium and gadolinium. The elution position and a new α-decay energy made the discovery of element 98 unique. It was named after the state of its discovery (California).

Einsteinium ($Z = 99$) and fermium ($Z = 100$) were identified in 1952 and 1953, respectively, by Ghiorso and others in the radioactive debris of the first "Mike" thermonuclear explosion. Hints of the formation of these elements were found in dust samples from the remotely controlled aircraft used in this test. Then, the elements were isolated by processing larger amounts of the radioactive coral material from the test site and named in honor of Einstein and Fermi. The elements had been formed by multi-neutron capture,

$$^{238}\mathrm{U} \overset{15\times(\mathrm{n},\gamma)}{\rightarrow} {}^{253}\mathrm{U} \overset{7\times\beta^-}{\rightarrow} {}^{253}\mathrm{Es} \tag{17.19}$$

$$^{238}\mathrm{U} \overset{17\times(\mathrm{n},\gamma)}{\rightarrow} {}^{255}\mathrm{U} \overset{8\times\beta^-}{\rightarrow} {}^{255}\mathrm{Fm} \tag{17.20}$$

The identification again made use of the cation exchange resin Dowex 50 in elutions at 87 °C with ammonium citrate solution. These experiments showed the elution in a transcalifornium position of a new 6.6 MeV α activity and hence proved conclusively that a new element had been found. Further measurements led to the observation of a 7.1 MeV α activity at an intensity of about 4% of that of the 6.6 MeV activity and the elution position proved that this was due to element 100. Later, einsteinium was synthesized by bombarding U with ^{14}N:

$$^{238}\mathrm{U}(^{14}\mathrm{N}, x\mathrm{n})^{252-x}\mathrm{Es} \tag{17.21}$$

and fermium was isolated as a product of reactor irradiation of Es.

Mendelevium ($Z = 101$) was produced in 1955 by Ghiorso et al. by irradiation of ^{253}Es with α particles:

$$^{253}\mathrm{Es}(\alpha, \mathrm{n})^{256}\mathrm{Md} \tag{17.22}$$

The amount of ^{253}Es available at this time was very small: about $N = 10^9$ atoms ($\approx 4 \cdot 10^{-13}$ g). At a flux of α particles $\Phi_\alpha = 10^{14}\,\mathrm{s}^{-1}$, a cross section $\sigma_{\alpha,\mathrm{n}} = 1$ mb, and an irradiation time of 10^4 seconds, a yield $N\Phi_\alpha\sigma_{\mathrm{n},\alpha}t$ of about one atom per experiment was expected. In order to detect these single atoms, the recoil technique was applied. Es was electrolytically deposited on a thin gold foil. The recoiling atoms of ^{256}Md were sampled on a catcher foil. After irradiation, the catcher foil was dissolved and Md was eluted from a Dowex 50 cation exchange column with ammonium α-hydroxy-isobutyrate, Figure 17.6. In eight experiments, 17 atoms of ^{256}Md were detected and identified by their ε decay into the spontaneously fissioning ^{256}Fm, the properties of which were known:

$$^{256}\mathrm{Md} \xrightarrow[\epsilon]{1.3\ \mathrm{hours}} {}^{256}\mathrm{Fm} \xrightarrow[\mathrm{sf}]{2.63\ \mathrm{hours}} \tag{17.23}$$

Mendelevium was named in honor of Mendelejev.

For the production of elements with atomic numbers $Z > 101$, irradiation with ions of atomic numbers $Z > 2$ is necessary because for irradiation with α particles,

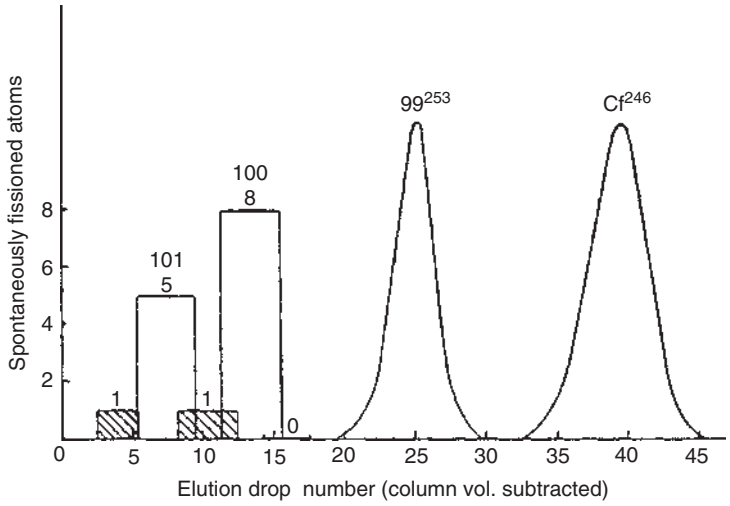

Figure 17.6 Original elution data corresponding to the discovery of mendelevium at Berkeley, 18 February 1955. Dowex 50 ion-exchange resin was used, and the eluting agent was ammonium alpha-hydroxy-isobutyrate. Source: Ghiorso et al. (1955), figure 1 (p. 1518)/American Physical Society.

actinides with adequate half-lives which can be used as targets are not available. Two concepts for the synthesis of new, heavy nuclides can be distinguished.

First, irradiation of actinides with ions of relatively low atomic numbers (e.g. $Z = 5$–22). In general, these reactions lead to excitation energies of the compound nuclei on the order of 40–50 MeV giving rise to 4n to 5n reactions ("hot fusion").

Second, irradiation of spherical closed-shell nuclei, like ^{208}Pb and ^{209}Bi, with ions of medium atomic numbers (e.g. $Z = 18$–30). In these reactions, the excitation energy of the compound nuclei is relatively low because, in the fusion process, the shell structure of the target nuclei is destroyed leading to low excitation energies of the compound nuclei and giving rise to 1n and 2n reactions ("cold fusion").

17.3.1 Hot-Fusion Reactions

The first reports of the discovery of element 102 came from Stockholm in 1957. The element was named nobelium after Alfred Nobel. However, the results could not be confirmed, and the new element was identified in 1958 by Ghiorso and others by the reaction

$$^{246}\mathrm{Cm}(^{12}\mathrm{C}, 4\mathrm{n})^{254}\mathrm{No} \xrightarrow[\alpha]{55\ \text{seconds}} {}^{250}\mathrm{Fm} \tag{17.24}$$

In these experiments, the recoil technique was modified into a double recoil technique by application of a conveyer belt (Figure 17.7). The recoiling atoms generated by the heavy-ion reaction (first recoil) are deposited on the belt and transported along a catcher foil on which the recoiling daughter nuclei from α decay (second recoil) are collected. After bombardment, the catcher foil was cut into five subsequent sections that were counted in five ionization chambers. From the activity

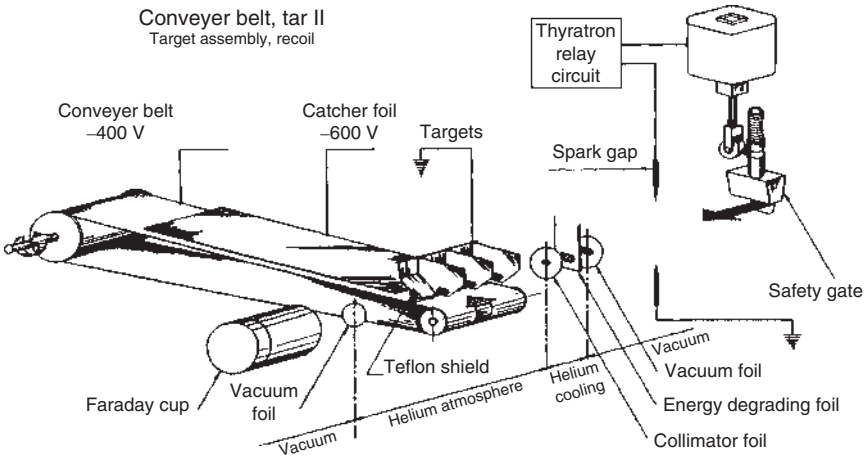

Figure 17.7 Schematic diagram of the conveyer-belt experiment used in the original Berkeley experiments on element 102. Source: Ghiorso et al. (1958), figure 1 (p. 19)/American Physical Society.

recorded as a function of the distance from the target, the half-life can be determined. The spatial distribution of the α activity of 30 minutes ^{250}Fm resulted in a half-life for the mother, ^{254}No, of 55 seconds. By 1966, all isotopes from ^{251}No through ^{258}No had been discovered at Berkeley. In 1967, the first chemical identification of nobelium was conducted with 3.1 minutes ^{255}No. In 1971, at Oak Ridge, Fm K X-rays in coincidence with α particles in the decay of ^{255}No were detected, thus constituting conclusive identification of the atomic number of No. At the 3 m cyclotron at Dubna, in the reaction $^{238}\mathrm{U} + {}^{22}\mathrm{Ne}$, the isotope ^{256}No was identified in 1963 also by using a double recoil technique.

By using the same technique, lawrencium ($Z = 103$) was discovered and identified in 1961 by Ghiorso and others. ^{258}Lr was produced by bombarding 3 μg of a mixture of californium isotopes with both ^{10}B and ^{11}B ions:

$$^{250,251,252}\mathrm{Cf}\left(^{10,11}\mathrm{B}, (2-5)\mathrm{n}\right)^{258}\mathrm{Lr} \xrightarrow[\alpha]{3.9\ \text{seconds}} \tag{17.25}$$

In this case, the recoiling products of the heavy-ion reaction were transported on the moving belt to an array of energy-sensitive Si surface barrier detectors. The half-life of ^{258}Lr was too short to allow chemical separation, and Lr was the first element to be identified by purely instrumental methods. It was named in honor of E.O. Lawrence, the inventor of the cyclotron.

Subsequently, the importance of instrumental methods for the identification of new elements or new radionuclides increased because of the short half-lives on the order of seconds or less.

The first report concerning the discovery of element 104 (named Kurtchatovium, Ku) came from Dubna (Flerov et al. 1964). By irradiating ^{242}Pu with ^{22}Ne, a radionuclide exhibiting a spontaneous fission half-life of about 0.3 seconds was found and attributed to ^{260}Ku. From 1966, I. Zvara made attempts to chemically separate the 0.3 seconds sf isotope by volatilization as tetrachloride using $NbCl_5$ and

$ZrCl_4$ as chlorinating agents and by detecting fission tracks in glass detectors. These authors made a strong point, arguing that the spontaneously fissioning isotope with a half-life of 0.3 seconds was creating the fission tracks and that the half-life could not be 3.7 seconds in order to exclude that the fission tracks could stem from a sf branch in ^{256}No. From 1971, it was argued by Flerov et al. that the fission tracks were due to 3.0 seconds ^{259}Ku. Over 21 years, there was considerable conflict between Dubna and Berkeley concerning the isotope ^{260}104. Ghiorso et al. could not reproduce the 0.3 seconds sf activity and, after 1 year, they gave up. However, using a vertical wheel (VW) equipped with four Si detector stations (Ghiorso et al. 1969) was able to produce element 104 by other, more favorable reactions and to measure the half-lives of two isotopes of this element and the energy of their α decay:

$$^{249}\mathrm{Cf}\,(^{14}\mathrm{C}, 4\mathrm{n})^{257}\mathrm{Rf} \xrightarrow[\alpha]{4.0\ \text{seconds}} {}^{253}\mathrm{No} \tag{17.26}$$

$$^{249}\mathrm{Cf}\,(^{13}\mathrm{C}, 3\mathrm{n})^{259}\mathrm{Rf} \xrightarrow[\alpha]{3.0\ \text{seconds}} {}^{255}\mathrm{No} \tag{17.27}$$

Subsequently, the VW was equipped with "shuttle" detector systems allowing the system to be run in the mother mode and in the daughter mode in which ^{253}No and ^{255}No were identified as daughters. Afterward, the same group applied other reactions for the production of element 104:

$$^{248}\mathrm{Cm}(^{18}\mathrm{O}, 5\mathrm{n})^{261}\mathrm{Rf} \xrightarrow[\alpha]{78\ \text{seconds}} {}^{257}\mathrm{No} \tag{17.28}$$

$$^{248}\mathrm{Cm}(^{16}\mathrm{O}, 5\mathrm{n})^{259}\mathrm{Rf} \xrightarrow[\alpha]{3.0\ \text{seconds}} {}^{255}\mathrm{No} \tag{17.29}$$

In 1970, the Berkeley group conducted an aqueous chemistry experiment with ^{261}Rf showing that its tetravalent ion elutes much earlier from a cation exchange column in 0.1 M ammonium α-hydroxy-isobutyrate at pH 4.0 than the trivalent actinides. Consequently, in 1970, the Berkeley group proposed the name rutherfordium, Rf, for element 104 in honor of Rutherford. In 1973, the Oak Ridge group successfully applied their α K X-ray technique for unambiguous identification of ^{257}Rf.

In between, Ghiorso et al. returned to a search for sf isotopes of rutherfordium. With a drum system, in the $^{12}\mathrm{C} + {}^{249}\mathrm{Cf}$ reaction, they observed a 13 ms sf activity assigned to ^{258}Rf. In the $^{15}\mathrm{N} + {}^{249}\mathrm{Bk}$ reaction, ^{260}Rf was identified as sf activity of 23 ms. Later, starting in 1981 and using a tape of 1 km length and much reduced background from ^{256}Fm, they observed the same isotope with half-lives of 20 ± 1.2 ms in the $^{15}\mathrm{N} + {}^{249}\mathrm{Cf}$ reaction, 21 ± 1.1 ms in the $^{16}\mathrm{O} + {}^{248}\mathrm{Cm}$ reaction, and 19.3 ± 1.4 ms in the $^{16}\mathrm{O} + {}^{249}\mathrm{Cf}$ reaction involving the evaporation of an α particle. In 1985, Ter Akopian et al., in an internal Dubna report, conveyed that they had found a half-life for ^{260}Rf of 28 ± 6 ms in the $^{15}\mathrm{N} + {}^{249}\mathrm{Cf}$ reaction, thus ending the 21-year-long controversy between Dubna and Berkeley.

The Dubna group (Flerov et al. 1968; this citation and the following ones that have no details can be found in Mann and Waber (1970)) was also the first to announce the discovery of element 105 (dubnium) by bombardment of ^{243}Am with ^{22}Ne. α energies of 9.4 and 9.7 MeV with half-lives of 0.1–0.3 seconds and ≥10 ms were

reported, respectively, and $^{260,261}105$ were suggested as candidates. At Berkeley, element 105 was produced by the reaction (Ghiorso et al. 1970)

$$^{249}\mathrm{Cf}(^{15}\mathrm{N}, 4\mathrm{n})^{260}\mathrm{Db} \xrightarrow[\alpha]{1.5\ \text{seconds}} {}^{256}\mathrm{Lr} \tag{17.30}$$

With a mother–daughter recoil-milking technique, the group was able to show that the lawrencium daughter was ^{256}Lr. Since they felt that they had unambiguously identified element 105, the group suggested the name hahnium with the symbol Ha in honor of Otto Hahn. Somewhat later, the reactions

$$^{249}\mathrm{Bk}(^{16}\mathrm{O}, 4\mathrm{n})^{261}\mathrm{Db} \xrightarrow[\alpha]{1.5\ \text{seconds}} {}^{257}\mathrm{Lr} \tag{17.31}$$

$$^{249}\mathrm{Bk}(^{18}\mathrm{O}, 5\mathrm{n})^{262}\mathrm{Db} \xrightarrow[\alpha]{34\ \text{seconds}} {}^{258}\mathrm{Lr} \tag{17.32}$$

were used to produce two more α-emitting isotopes, of which the longer-lived one became a very important isotope for chemistry experiments. The International Union of Pure and Applied Chemistry (IUPAC) Commission on Nomenclature in Inorganic Chemistry (CNIC) surprisingly did not accept the name hahnium, but decided on 30 August 1997 that element 105 be named dubnium with the symbol Db.

Element 106 (seaborgium) was produced and identified in 1974 at Berkeley (Ghiorso et al.) and, seemingly, at Dubna (Flerov et al.) by the reactions

$$^{249}\mathrm{Cf}\,(^{18}\mathrm{O}, 4\mathrm{n})^{263}\mathrm{Sg} \xrightarrow[\alpha]{0.9\ \text{seconds}} {}^{259}\mathrm{Rf} \xrightarrow[\alpha]{3.0\ \text{seconds}} {}^{255}\mathrm{No} \tag{17.33}$$

and

$$^{207,208}\mathrm{Pb}(^{54}\mathrm{Cr}, 2\mathrm{n})^{259,260}\mathrm{Sg} \tag{17.34}$$

respectively. By the Berkeley group, the recoiling atoms of ^{263}Sg were transported by a helium jet to a vertically turning wheel (VW) and passed to an array of solid-state detectors by which α decay was measured, see Figure 17.8. The α decays of $^{263}106$ with a half-life of 0.9 ± 0.2 seconds were mostly at 9.06 MeV with a small group at 9.25 (Figure 17.9). The cross section was only 0.3 nb, but it was possible to demonstrate the genetic connection between $^{263}106$, $^{259}104$, and $^{255}102$. To this end, the group looked at the shuttled detectors where they found daughter atoms that were kicked off the wheel whenever an element 106 α particle was emitted into the wheel. The set of seven detectors monitoring the wheel was shuttled away every six seconds to a low-background position facing seven stationary detectors, while another set of movable detectors took over the job of monitoring the wheel. Whenever an α particle of ^{259}Rf was detected in the shuttled position, that particular detector was not shuttled back into the wheel position until 10 minutes had elapsed to allow the ^{255}No granddaughter to be observed. In this manner, an excellent genetic linkage could be established to prove the atomic number of element 106.

17.3.2 Cold-Fusion Reactions

At about the same time, Yu. Oganessian pointed out that it was possible to conduct "cold fusion" of two elements to make transuranic elements, see Figure 17.10.

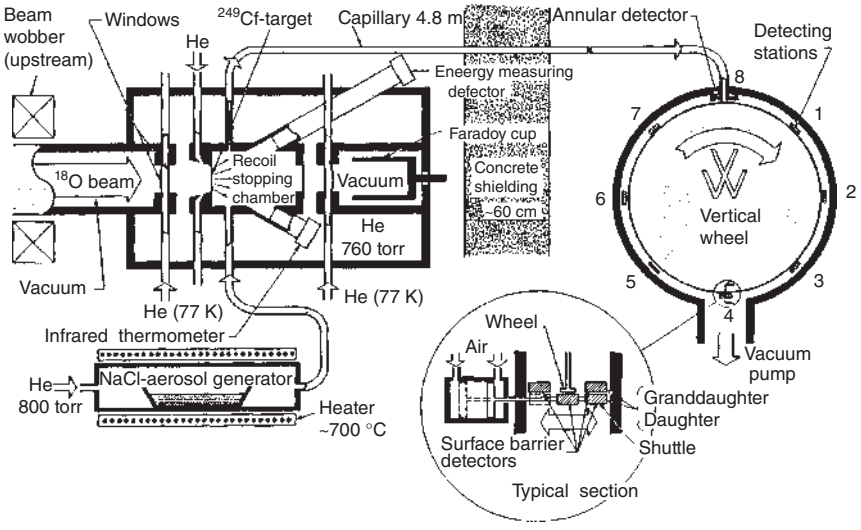

Figure 17.8 Schematic diagram of the apparatus used in the discovery of element 106 at Berkeley. Source: Ghiorso et al. (1974), figure 1 (p. 1491)/American Physical Society.

The basic idea is to use medium-heavy projectiles and fuse them with nuclei with closed shells, like ^{208}Pb or ^{209}Bi, as target nuclei. This was proposed by Oganessian with the argument that an appreciable amount of the energy of the projectiles will be used to destroy the closed shells of the target nucleus and will therefore not appear in the form of excitation energy. This "cold fusion" was demonstrated at Dubna in 1974 by the reaction of ^{40}Ar with ^{208}Pb and then by (17.34): the small number of two neutrons emitted was proof of the low excitation energy of the compound nucleus. Using this new cold-fusion technique, Oganessian et al. reported finding a 4–10 ms sf emitter in the bombardment of ^{207}Pb and ^{208}Pb with ^{54}Cr ions. They attributed the activity to ^{259}106 on the basis of reaction systematics. Was the sf activity found by the Dubna group due to element 106? Later work by a GSI group questioned the assignment because they found that ^{259}106 is a 0.48 ms α emitter. They also discovered that ^{260}106 is a 3.6 ms α emitter which leads to the 6.7 ms sf emission in ^{256}Rf. Their findings suggested that the Dubna group was actually detecting the daughter of element 106 in the 1974 experiment. In 1984, Demin et al. performed new experiments using one of the same reactions, $^{208}\text{Pb} + {}^{54}\text{Cr}$, this time accumulating eight times as many events as were observed in 1974. From the growth and decay of sf activity, it was concluded that the ^{260}106 formed in the 2n reaction was an α emitter with $t_{1/2} = 2.5 \pm 1.5$ ms and that most of the sf events were attributable to its daughter, 6.7 ms ^{256}104.

In 1994, Gregorich et al. at the Berkeley 88 in. cyclotron reproduced the 1974 work by Ghiorso et al. on ^{263}106. Subsequent to this, the Ghiorso group suggested the name seaborgium, symbol Sg.

The main features of cold-fusion reactions with the spherical nuclei of ^{208}Pb or ^{209}Bi as targets are: low excitation energies of the compound nuclei with the consequent emission of only one or two neutrons; low probability of fission, and

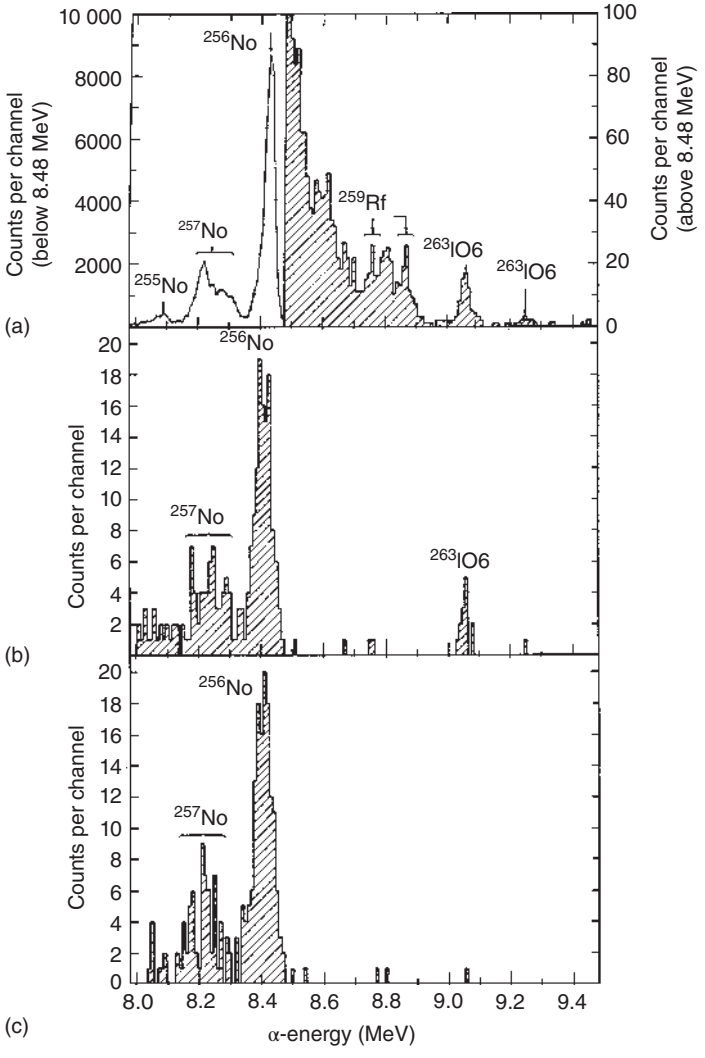

Figure 17.9 (a) Sum of α spectra from stations 1 through 7 using the apparatus of Figure 17.8 in the discovery of element 106. The integrated beam intensity was $1.34 \cdot 10^{18}$ ^{18}O ions. (b) α events in the 0–12 seconds interval preceding ^{259}Rf events (8.65–8.91 MeV). The 12 seconds time interval represents four ^{259}Rf half-lives. (c) α events in the 50–62 seconds interval preceding ^{259}Rf events. A 50 seconds time displacement was chosen to determine the accidental spectrum. Only one α event was found within the ^{263}106 energy region, as had been expected from Poisson statistics. Source: Ghiorso et al. (1974), figure 2 (p. 1492)/American Physical Society.

relatively high fusion cross sections σ_{fus}. On the other hand, the reaction products have relatively small neutron numbers and short half-lives. Suitable projectiles are neutron-rich stable nuclei, such as ^{48}Ca, ^{50}Ti, ^{54}Cr, ^{58}Fe, ^{64}Ni, and ^{70}Zn.

At GSI in Darmstadt, the velocity filter SHIP (Separator for Heavy-Ion reaction Products), Figure 17.11, was developed in order to separate the products of the

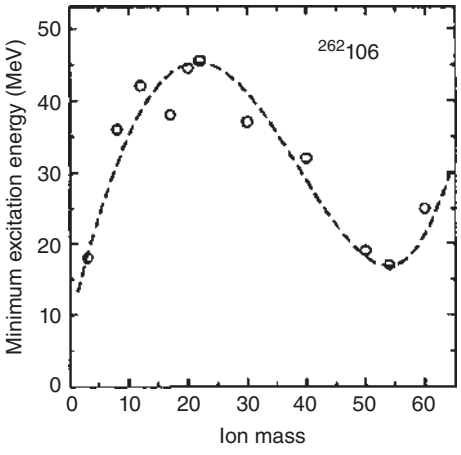

Figure 17.10 Minimum excitation energies of various fusion reactions, all resulting in the compound nucleus ^{262}106. Excitation energies not less than about 45 MeV are obtained in reaction using actinide targets and projectiles with mass numbers $A \approx 20$ (hot fusion). Minimum excitation energy of about 18 MeV is obtained with ^{208}Pb target and ^{54}Cr projectiles (cold fusion). Source: Oganessian et al. (1974)/Elsevier.

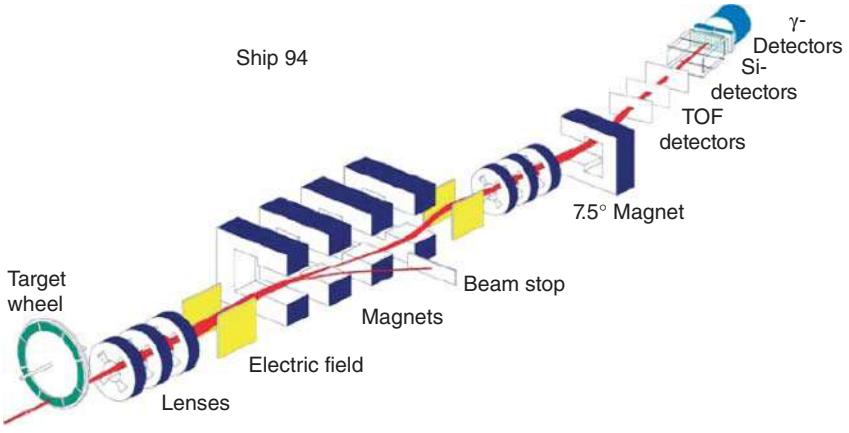

Figure 17.11 The velocity filter SHIP and its detections system. The drawing is approximately to scale, while the target wheel and the detectors are enlarged by a factor of 2. The length of SHIP from the target to the detector is 11 m, and the flight time of the evaporation residues through SHIP is 1–2 μs. The target wheel has a radius of 155 mm and rotates synchronously with the beam macrostructure at 1125 rpm. The target thickness is about 450 μg cm^{-2}. The detector system consists of three large area secondary-electron time-of-flight detectors and a position-sensitive silicon detector array. The filter, consisting of two electric and four magnetic dipole fields plus two quadrupole triplets, was extended by a fifth deflection magnet allowing for positioning the detectors away from the 0° beam line for further reduction of background. Source: Hofmann (2011), figure 5 (p. 409)/De Gruyter.

heavy-ion reactions, which were then identified by α spectrometry of the radionuclides and their decay products. The heavy ions hit the target, which is put on a rotating wheel to avoid overheating. The reaction products enter the velocity filter, which consists of an arrangement of focusing devices and "crossed" electric and magnetic fields, in which the heavy nuclei are separated in flight. The velocity of the separated products and their activities is measured, the α activities by means of solid-state Si detectors and the γ activities by Ge detectors. Actually, the evaporation

residues are implanted in a position-sensitive focal-plane Si detector where the position of the implanted atom is registered. α-decay chains are reconstructed by requiring that α particles are registered at the same position. In addition, their times and energies are recorded.

Two periods of detection of new elements at GSI can be distinguished: elements 107, 108, and 109 from 1981 to 1984 and, after new target and detector arrangements, elements 110, 111, and 112 from 1994 to 1996.

Element 107 (bohrium) was synthesized by the GSI group (Münzenberg, Armbruster et al.) in 1981 by the reactions

$$^{209}\mathrm{Bi}(^{54}\mathrm{Cr}, \mathrm{n})^{262}\mathrm{Bh} \xrightarrow[\alpha]{102\ \mathrm{ms}/8.0\ \mathrm{ms}} {}^{258}\mathrm{Db} \xrightarrow[\alpha]{4.4\ \mathrm{seconds}} {}^{254}\mathrm{Lr} \tag{17.35}$$

and

$$^{209}\mathrm{Bi}(^{54}\mathrm{Cr}, 2\mathrm{n})^{261}\mathrm{Bh} \xrightarrow[\alpha]{11.8\ \mathrm{ms}} {}^{257}\mathrm{Db} \xrightarrow[\alpha]{\approx 1.3\ \mathrm{seconds}} {}^{253}\mathrm{Lr} \tag{17.36}$$

The name bohrium was proposed in honor of Niels Bohr.

Element 108 (hassium) was produced by the same group in 1984 by the reactions

$$^{207}\mathrm{Pb}(^{58}\mathrm{Fe}, \mathrm{n})^{264}\mathrm{Hs} \underset{0.45\ \mathrm{ms}}{\rightarrow} {}^{260}\mathrm{Sg} \underset{0.45\ \mathrm{ms}}{\rightarrow} {}^{256}\mathrm{Rf} \tag{17.37}$$

and

$$^{208}\mathrm{Pb}(^{58}\mathrm{Fe}, \mathrm{n})^{265}\mathrm{Hs} \underset{0.8\ \mathrm{ms}/2.0\ \mathrm{ms}}{\rightarrow} {}^{261}\mathrm{Sg} \underset{0.23\ \mathrm{ms}}{\rightarrow} {}^{257}\mathrm{Rf} \tag{17.38}$$

Three of the decay chains of ^{265}Hs observed in the 1984 experiment are depicted in Figure 17.12. The element is named hassium, symbol Hs, after "Hassia" for Hessen, the state in which Darmstadt is situated.

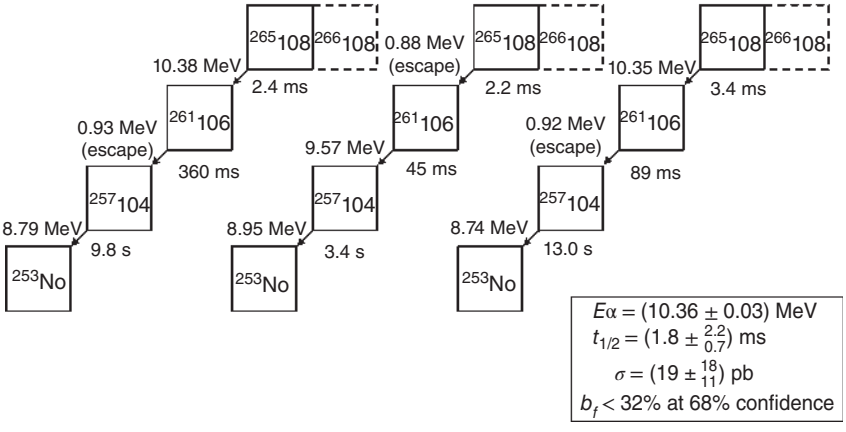

Figure 17.12 Decay chains of the three atoms of ^{265}108 observed in the 1984 experiment of Münzenberg et al.

Element 109 (meitnerium) was synthesized in 1982 by the GSI group by the reaction

$$^{209}\mathrm{Bi}(^{58}\mathrm{Fe},\mathrm{n})^{266}\mathrm{Mt} \xrightarrow[\alpha]{1.7\ \mathrm{ms}} {}^{262}\mathrm{Bh} \xrightarrow[\alpha]{102\ \mathrm{ms}/8.0\ \mathrm{ms}} {}^{258}\mathrm{Db} \tag{17.39}$$

The name meitnerium was given to element 109 in honor of Lise Meitner.

After a major upgrade of SHIP, elements 110 and 111 were synthesized and identified in November and December 1994 by the GSI group (Hofmann et al.) by the reactions

$$^{208}\mathrm{Pb}(^{62}\mathrm{Ni},\mathrm{n})^{269}110 \xrightarrow[\alpha]{0.17\ \mathrm{ms}} {}^{265}\mathrm{Hs} \xrightarrow[\alpha]{2.0\ \mathrm{ms}} {}^{261}\mathrm{Sg} \xrightarrow[\alpha]{0.23\ \mathrm{seconds}} {}^{257}\mathrm{Rf} \tag{17.40}$$

$$^{208}\mathrm{Pb}(^{64}\mathrm{Ni},\mathrm{n})^{271}110 \xrightarrow[\alpha]{1.1\ \mathrm{ms}} {}^{267}\mathrm{Hs} \xrightarrow[\alpha]{59\ \mathrm{ms}} {}^{263}\mathrm{Sg} \xrightarrow[\alpha]{0.9\ \mathrm{seconds}} {}^{259}\mathrm{Rf} \tag{17.41}$$

and

$$^{209}\mathrm{Bi}(^{64}\mathrm{Ni},\mathrm{n})^{272}111 \xrightarrow[\alpha]{1.5\ \mathrm{ms}} {}^{268}\mathrm{Mt} \xrightarrow[\alpha]{70\ \mathrm{ms}} {}^{264}\mathrm{Bh} \xrightarrow[\alpha]{\approx 0.44\ \mathrm{seconds}} {}^{260}\mathrm{Db} \xrightarrow[\alpha]{1.5\ \mathrm{s}} {}^{256}\mathrm{Lr} \xrightarrow[\alpha]{25.9\ \mathrm{s}} {}^{252}\mathrm{Md} \tag{17.42}$$

About 1 year later (in February 1996), the same group announced the discovery of element 112 by the reaction

$$^{208}\mathrm{Pb}(^{70}\mathrm{Zn},\mathrm{n})^{277}112 \xrightarrow[\alpha]{0.24\ \mathrm{ms}} {}^{273}110 \xrightarrow[\alpha]{118\ \mathrm{ms}} {}^{269}\mathrm{Hs} \xrightarrow[\alpha]{9.3\ \mathrm{seconds}} {}^{265}\mathrm{Sg} \xrightarrow[\alpha]{7.4\ \mathrm{s}} {}^{261}\mathrm{Rf} \xrightarrow[\alpha]{78\ \mathrm{seconds}} {}^{257}\mathrm{No} \xrightarrow[\alpha]{26\ \mathrm{seconds}} {}^{253}\mathrm{Fm} \tag{17.43}$$

Most of the new nuclides have been identified by their α-decay chains, as indicated in Eqs. (17.35)–(17.43). The formation of $^{277}112$ has been proven by six successive α decays leading to ^{253}Fm (Eq. (17.43)). In the second GSI decay chain of $^{277}112$, four successive α decays lead to an isomeric state in ^{261}Rf mostly decaying by sf, which has also been observed in chemistry experiments with ^{269}Hs. In 2004, the reaction $^{70}\mathrm{Zn} + {}^{208}\mathrm{Pb}$ irradiation was repeated at RIKEN, Japan, where two more decay chains were detected. The RIKEN decay chains also verify the sf branch in ^{261}Rf. The four decay chains of $^{277}112$ are depicted in Figure 17.13.

The names for elements 110, 111, and 112 proposed by the GSI group have meanwhile been approved by IUPAC. Element 110 is named darmstadtium for obvious reasons, element 111 is named roentgenium in honor of G. Roentgen, and element 112 is named copernicium in honor of Copernicus.

In 1998, a 46-day experiment was performed at SHIP to create element 113 in the irradiation of ^{209}Bi with ^{70}Zn. The integral beam dose was $7.5 \cdot 10^{18}$ particles. In a second experiment in 2003, a beam dose $7.4 \cdot 10^{18}$ was accumulated. No decay which could be assigned to element 113 was observed corresponding to a cross-sectional limit of 160 fb which has to be compared to the value of 19 fb for the successful experiments at RIKEN.

Since 2002, isotopes of the heaviest elements, ^{271}Ds, ^{272}Rg, ^{277}Cn, and $^{278}113$, were produced by Morita et al. in $^{208}\mathrm{Pb}(^{64}\mathrm{Ni},\mathrm{n})$, $^{209}\mathrm{Bi}(^{64}\mathrm{Ni},\mathrm{n})$, $^{208}\mathrm{Pb}(^{70}\mathrm{Zn},\mathrm{n})$, and $^{209}\mathrm{Bi}(^{70}\mathrm{Zn},\mathrm{n})$ reactions, and subsequent decays were studied using the gas-filled

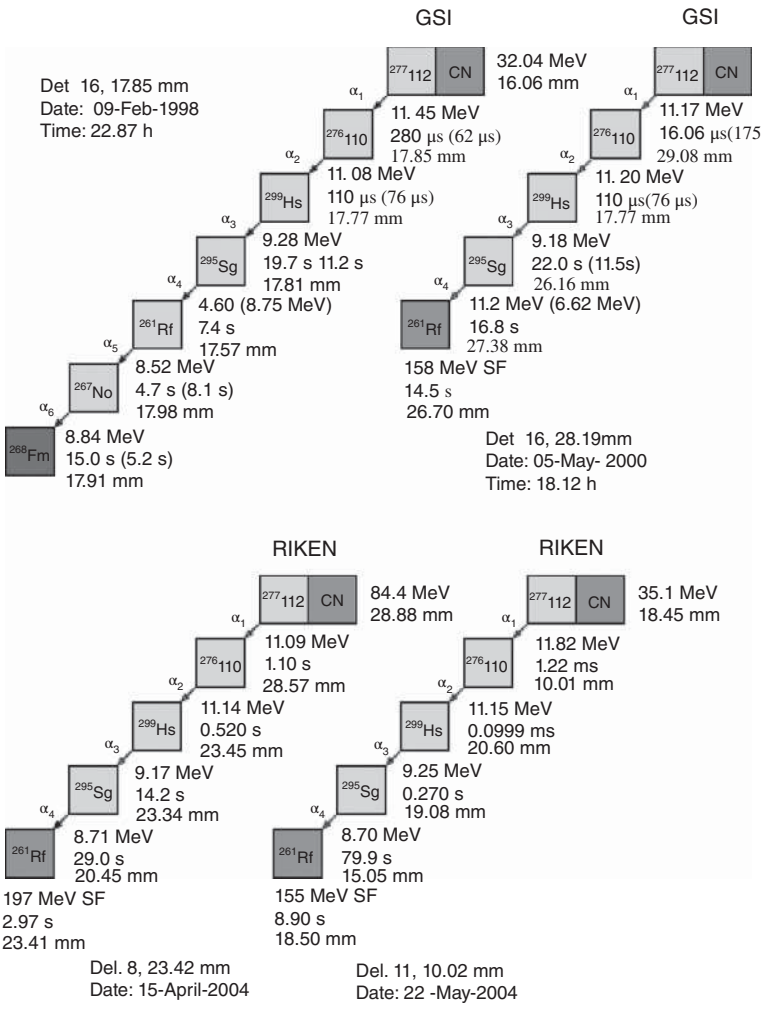

Figure 17.13 Decay chains measured in the cold-fusion reaction $^{70}Zn + {}^{208}Pb \rightarrow {}^{278}112^{*}$. To the left, the two decay chains measured in 1996 and 2000 at SHIP are shown; to the right, those measured in 2004 at RIKEN. The chains were assigned to the isotope $^{277}112$ produced by evaporation of one neutron from the compound nucleus. The lifetimes given in parentheses were calculated using the measured α energies. In the case of escaped α particles, the α energies, given in parentheses, were calculated based on the measured lifetimes. Source: Hofmann (2011), figure 12 (p. 416)/De Gruyter.

recoil ion separator (GARIS) at the RIKEN Linear Accelerator Facility RILAC in Wako-shi, Saitama, Japan. For the first three reactions, the results confirmed the ones previously obtained at SHIP. An isotope of the 113th element, $^{278}113$, was produced at RIKEN for the first time by the $^{209}Bi(^{70}Zn, n)$ reaction since September 2003 until October 2012. Chain 1 starting with $\alpha_1 = 11.68$ MeV was published in 2004, chain 2 with $\alpha_1 = 11.52$ MeV in 2007, and chain 3 with $\alpha_1 = 11.82$ MeV in 2012.

The total beam dose was $1.39 \cdot 10^{20}$. Combining all three events, the production cross section of $^{278}113$ resulted as 19^{+19}_{-10} fb with a 1σ error. This is the lowest cross section ever measured in a heavy-ion fusion reaction.

17.3.3 ^{48}Ca-Induced Fusion Reactions

The discovery and investigation of a new region of superheavy nuclei at the Dubna gas-filled recoil separator (DGFRS) were based on systematic studies of fusion reactions of ion beams of ^{48}Ca ions with ^{233,238}U, ^{237}Np, ^{242,244}Pu, ^{243}Am, ^{245,248}Cm, ^{249}Bk, and ^{249}Cf target nuclei producing evaporation residues of six elements with atomic numbers 113–118. These elements filled the seventh period of the Table of Chemical Elements whose 150th anniversary was celebrated in 2019. In these investigations by Oganessian et al., more than 50 new nuclides, isotopes of elements 104–118 having the largest numbers of neutrons, were produced and their decay properties were determined. The chart of nuclei was extended up to $Z = 118$ and $N = 177$. The heaviest nuclides with mass number 294 were synthesized in the ^{249}Cf + ^{48}Ca and ^{249}Bk + ^{48}Ca reactions producing the even–even isotope $^{294}118$ ($t_{1/2} = 0.69$ ms) and the odd–odd isotope $^{294}117$ ($t_{1/2} = 51$ ms), see Figure 17.14. This way, the border of bound nuclei was shifted from the limit predicted by the liquid-drop model to regions of heavier masses predicted by the microscopic theory to be stabilized by shell effects. For the identification of the atomic number of element 115, the fluoride complexing chemistry (Section 17.8) of element 105 was applied, thus establishing the genetic link between $^{288}115$ and its descendant ^{268}Db. The latter is the final product of five subsequent α-decays of $^{288}115$ to ^{268}Db ($t_{1/2} \sim 1$ day), which was chemically separated with its well-known chemistry. The correlation of the measured half-lives with the measured decay

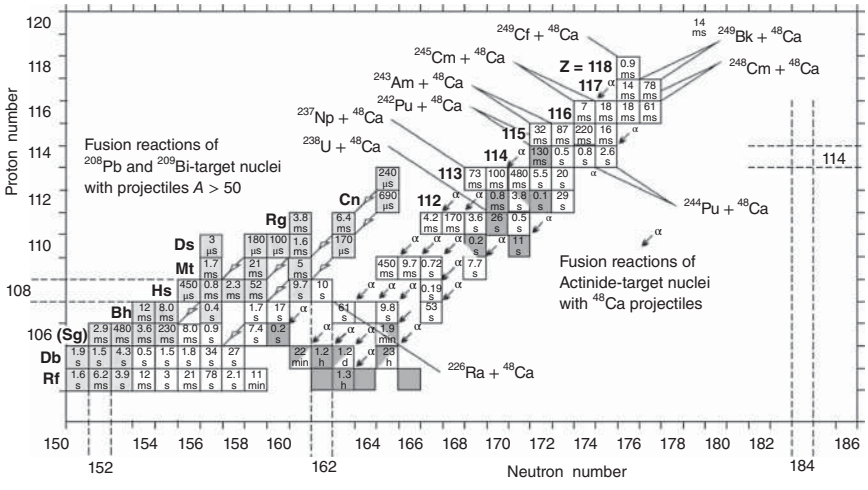

Figure 17.14 Chart of the heaviest nuclides with $Z \geq 104$ and $N = 151$. In order to avoid making the figure too complicated, the squares contain the half-lives only. Source: Oganessian (2011), figure 5 (p. 435)/De Gruyter.

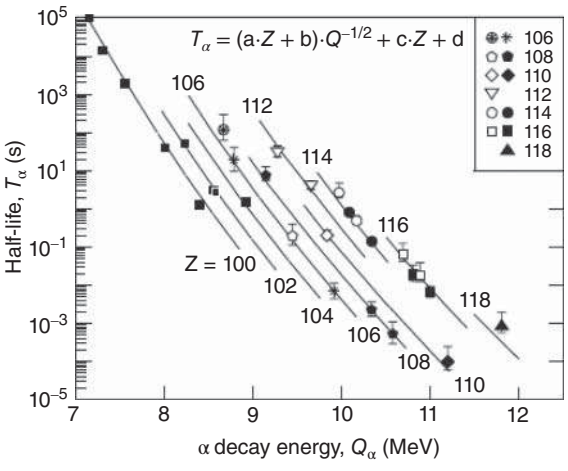

Figure 17.15 α decay half-lives as a function of the α-decay energy Q_α for nuclei with even atomic number $Z \geq 100$. The solid lines represent calculations using the Viola–Seaborg formula given in the figure with parameters $a = 1.787$, $b = -21.40$, $c = -0.2549$, $d = -28.42$. Source: Oganessian (2011), figure 6 (p. 436)/De Gruyter.

energies is depicted in Figure 17.15 for ground-to-ground state transitions. The deviations of the experimental Q_α values from theoretical ones calculated in the macroscopic–microscopic model of Muntian et al. for even Z nuclei with $Z = 106$–118 and $A = 271$–294, and for nuclei with even as well as odd numbers of neutrons, do not exceed 0.5 MeV; for odd Z nuclei, the deviations are ≤ 1 MeV.

For 11 out of the 47 synthesized nuclei, sf is the predominant mode of decay. In two more nuclei, ^{271}Sg and ^{286}114, sf competes with α decay. Four isotopes of element 112 with $N = 170$–173 are located in a region where a steep rise in the sf half-lives is expected. Indeed, in the even–even isotopes ^{282}112 and ^{284}112, the difference of two neutrons increases the partial sf half-life by two orders of magnitude. The neighboring odd isotopes ^{283}112 and ^{285}112 undergo α decay. For them, only lower limits for the sf half-lives can be determined. From the measured sf half-lives for the even–even isotopes ^{282}112 and ^{184}112, it follows that the odd neutron in ^{283}112 imposes a hindrance to sf on the order of $\geq 3 \cdot 10^3$. Given such a large hindrance factor, it cannot be excluded that one or two decay events registered as evaporation residue implantation followed by sf can be attributed to sf of the even–odd isotope ^{283}112. A similar situation is encountered for the even–even isotopes of element 114: the additional two neutrons in the nucleus ^{286}114 ($t_{1/2} \approx 0.13$ seconds) result in a significant increase in the stability of ^{288}114 ($t_{1/2} \approx 0.8$ seconds) for which 17 out of 18 decay events registered at the DGFRS were α decays. In a confirmatory experiment at the new gas-filled separator TransActinide Separator and Chemistry Apparatus (TASCA) at GSI in Darmstadt, nine α decays of ^{288}114 and no sf were observed.

The DGFRS results have been confirmed several times, e.g. at SHIP (Hofmann, 112), at the Berkeley Gas-Filled Separator (BGS) (Stavsetra, 114), at the BGS (Ellison, 114), at TASCA (Düllmann, 114), at SHIP (Hofmann, 116), at TASCA (Rudolph, 113/115), and again at TASCA (Khuyagbaatar, 117). However, there was also an urgent need to question an interpretation of DGFRS results by Oganessian et al. proposing a genetic link of ^{293}117 with ^{289}115. This was sold as a convincing case in cross reactions producing ^{289}115 and ^{293}117 from both ^{48}Ca + ^{243}Am and ^{48}Ca + ^{249}Bk

to the Joint Working Party (JWP) of a collaboration of IUPAC with IUPAP (International Union of Pure and Applied Physics) on the priority claims to the discovery of new elements 113, 115, and 117. The JWP ASSESSMENT upon this reads: "*The 2010 jointly with the 2013 collaboration of Oganessian et al. have met the* Criteria *for the discovery of the element with the atomic number Z = 115 in as much as the reproducibility of chain energies and lifetimes* of $^{289}115$ *in a cross reaction comparison is very convincing*". It also reads: "*A convincing case in cross reaction producing* $^{289}115$ *and* $^{293}117$ *from both* $^{48}Ca + {}^{249}Bk$ *and* $^{48}Ca + {}^{243}Am$ *is demonstrated. Thus, the 2010, 2012 and jointly with 2013 collaboration of Oganessian have met the Criteria for the discovery of elements with atomic numbers 115 and 117*".

At the Nobel Symposium NS160, Chemistry and Physics of heavy and superheavy elements, Bäckaskog Castle, Sweden, 29 May to 03 June 2016, after the talk of Jan Reedijk, in which he reported on the IUPAC decision and announced that the new elements 113, 115, 117, and 118 will officially be recognized and given the names nihonium (Nh), moscovium (Mc), tennessine (Ts), and oganesson (Og), respectively, by the end of the year 2016. Cecilia Jarlskog, representative of IUPAP, in her subsequent talk, complained vehemently against the fact that IUPAC had made this decision without consulting IUPAP. "In my opinion, the collaboration turned out to be a failure. … I could not imagine that there would be 'political' aspects in it. It turned out that the managerial staff of IUPAC cared primarily about getting credit than being fair and giving credit to those who deserved it. This behavior is, in my opinion, **old-fashioned, wrong, bad, and immoral**. … especially the managerial staff of IUPAC, who were in addition arrogant and didn't answer emails." She further criticized "The Chair (of the JWP, Paul Karol) was reluctant to communicate". As an example, at the end of his report to the 2014 IUPAP General Assembly in Singapore … he added: 'Disclosure: This informal progress statement has been prepared entirely by the Chair of the JWP and has not been reviewed by the membership.' "The great surprise was that IUPAC, unexpectedly and without consultation with us, released the results of 'our' JWP on 30 December 2015. In my opinion, if there is going to be a new Joint Working Group, it is essential that IUPAP should insist on a well-defined mandate for the group. IUPAP should insist on openness. The referee reports should be ordered by IUPAP and be available for scrutiny … It is irritating when IUPAC 'proudly announces' the discovery of new elements. What have they done to be proud of? They should congratulate the discoverers. The articles in the non-scientific journals do not help either. They give the credit to IUPAC, by making statements such as 'The International Union for Pure and Applied Chemistry, which verified their existence, announced the entry of the four elements…'. Well, I am sorry to have to say that those who made the announcement did not have the competence to verify their existence".

Also, in complete disagreement with the recommendations by the JWP and by the IUPAC Division of Inorganic Chemistry, Ulrika Forsberg et al., based on two scientific publications (Forsberg et al. 2016a,b), argue that a rigorous statistical analysis of lifetimes in the relevant decay chains implies that the hitherto proposed cross-reaction link between α-decay chains associated with the isotopes $^{293}117$ and $^{289}115$ is highly improbable. The ten element 117 chains together with the four

element 115 chains from Dubna do not, on a close to 100% confidence level, form a congruent ensemble. That this was ignored by the JWP and subsequently by the IUPAC Inorganic Chemistry Division is unbelievable since an early version of the article in Nucl. Phys. A953 (arXiv1502.03030v1 [February 2015]) was available to the JWP. The author of this textbook had the opportunity, after the talks by Reedijk and Jarlskog at the Nobel Symposium NS160, to sit at lunch next to Reedijk, and he asked Reedijk whether he had read the article in Nucl. Phys. A953 and why he, in view of this controversial analysis, had not returned the issue to the JWP asking them to reconsider the case. The answer was that he, Reedijk, had read it, but he found it too complicated and did not confront the JWP with this case again. Because this situation is quite embarrassing, and because, in Section 10.6, we had presented the statistical assessments of lifetimes in decay chains of odd-Z heavy elements, we want here to come back the work by Forsberg et al. that deals with two recoil-α-SF chains denoted T1, T2 (T standing for TASCA) and five recoil-α-α-SF chains (T3–T7). These are summarized in Table 17.3, together with the four recoil-α-α-SF chains published by Oganessian et al. (D1–D4) (D standing for Dubna) and the three recoil-α(-α)-SF chains published by Gates et al. (B1–B3) (B standing for Berkeley), together a total of 14 chains.

The focus lies now on the interpretation of the 14 short chains in Table 17.3. At first glance, there seems to be very little, if any, difference in the distribution of these lifetimes compared with the distributions of the 96 five-α long chains associated with the decay of $^{288}115$. All five-α long chains observed at low excitation energies of the compound nucleus $^{291}115$, $E^* \leq 37$ MeV, were associated with the decay of the 3n evaporation channel $^{288}115$. However, chains D1–D4 were interpreted by Oganessian et al. (2013) to originate exclusively from the previously unknown 2n evaporation channel $^{289}115$. The interpretation that all short chains originate from $^{289}115$ is one unproven explanation of the data. The σ_θ values (Chapter 10) for the three decay steps in the set of 14 short chains are 1.20, 1.75, and 1.84 and should be compared with the intervals $[\sigma_{\theta,\text{low}},\ \sigma_{\theta,\text{high}}]$ being [0.73, 1.77], [0.73, 1.77], and [0.65, 1.82], respectively. All but the last step fit within the intervals. The similarities between the short chains and the 96 decay chains from $^{288}115$ suggest another possibility. Adding the short chains to this data set, giving a total of 110 chains yields σ_θ values of 1.39, 1.43, and 1.08 for the first three decay steps. All three fall within the respective 90% confidence intervals [1.06, 1.49], [1.06, 1.49], and [1.05, 1.50] giving a strong indication that the 110 chains could form a set in which all members follow the same decay sequence. What has not been discussed previously is the fact that the D3 chain is compatible neither with the 3n reference values nor with the remaining 13 short chains. All of the three decay times of D3 are approximately ten times larger than the respective reference time distribution. The α energy E_2 is also significantly lower than that of the remaining short chains. If one excludes D3 from the set of short chains, all the α_θ values are now within the respective interval. Having examined the data set this way, it seems inevitable to assign chain D3 to another decay sequence than the other short chains. Two possible scenarios where the D3 chain forms a separate decay sequence are presented in Figure 17.16.

Table 17.3 Mid-target laboratory-frame beam energies, energies of the implanted recoils E_{rec}, α-energies E_1, E_2, and E_3, together with the associated correlation times of recoil-α-SF and recoil-α–α-SF decay chains observed in the $^{48}Ca + {}^{243}Am$ reaction.

No.	E_{lab} (MeV)	E_{rec} (MeV) pixel (*x*,*y*)	E_1 (MeV) Δt_1 (s)	E_2 (MeV) Δt_2 (s)	E_3 (MeV) Δt_3 (s)	N_γ(SF)	N_{random}
T1	245.0	12.3	**10.51(1)**	**242**[a]		**6**	$<2 \cdot 10^{-5}$
		268(8,12)	**0.227**	**0.378**			
T2	242.1	16.2	**1.45(1)**[b]	**211**		**4**	$<6 \cdot 10^{-2}$
		425(13,9)	**0.0645**	**0.366**			
T3	242.1	13.9	10.54(4)[c]	**9.95(5)**[c]	**196**	**8**	$<2 \cdot 10^{-6}$
		681 (21,9)	0.261	**1.15**	**0.343**		
T4	242.1	14.5	10.34(1)	**9.89(1)**	**218**[a]	**>5**	$<2 \cdot 10^{-6}$
		344(10,24)	1.46	**0.0262**	**0.432**		
T5	242.1	13.8	**10.49(4)**[c]	**9.97(1)**	**135**	**9**	$<3 \cdot 10^{-9}$
		554(17,10)	**0.345**	**0.369**	**14.4**		
T6	245.0	14.5	**10.53(1)**	**9.89(5)**[c]	**230**[a]	**9**	$<3 \cdot 10^{-9}$
		205(6,13)	**0.210**	**1.05**	**8.27**		
T7	245.0	11.9	**0.541(3)**[b]	3.12(1)[b]	**230**[a]	**>4**	$<1 \cdot 10^{-1}$
		128(4,0)	**0.815**	2.33	**2.89**		
D1	240.5	11.38	10.377(26)	**9.886(26)**	**215.7**		
			0.2562	**1.4027**	**1.9775**		
D2	241.0	15.18	10.540(52)[c]	9.916(31)	**214.9**[a]		
			0.0661	1.5500	**2.3638**		
D3	241.0	9.04	10.373(21)	9.579(21)	141.1		
			2.3507	22.5822	60.185		
D4	241.0	13.35	10.292(72)[c]	10.178(23)	**182.2**[a]		
			0.0536	0.4671	**0.0908**		
B1	242	11.65	10.49(5)	9.82(2)	**107**	**6**	
			0.214	1.54	**7.57**		
B2	242	11.18	10.49(2)	**187**		**8**	
			0.0501	**0.824**			
B3	242	13.72	10.22(2)	**128**		**2**	
			0.0455	**0.0142**			

Entries in bold were recorded during beam-off periods. The number of γ-rays detected in prompt coincidence with SF events, N_γ(SF), is also specified. N_{random} corresponds to the number of chains of a given type expected to arise from random background. Uncertainties in decay energies are given as σ_E.

a) Fission event registered by both implantation and box detector.
b) Escaped α particle registered solely by the implantation detector.
c) Reconstructed energy of an α particle registered by both implantation and box detector.

Source: Elsevier.

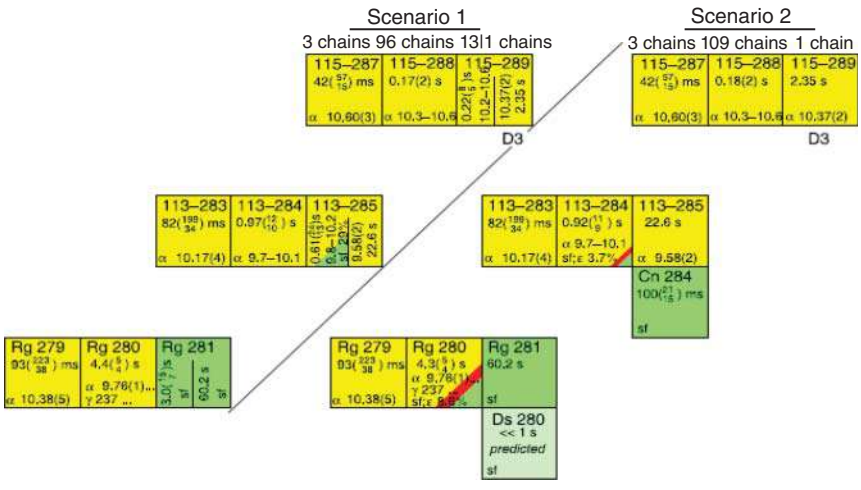

Figure 17.16 Representation of the scenarios 1 and 2 in the chart of nuclides. Source: Elsevier.

Scenario 1: The short chains are all assigned to $^{289}115$, with D3 forming a separate decay sequence. It can be noted that the decay times of D3 look similar to the chain $^{289}\text{Fl} \rightarrow {}^{285}\text{Cn} \rightarrow {}^{281}\text{Ds}$. This decay chain can be entered by electron-capture (EC) decay of $^{289}115$ or $^{285}113$. The remaining 13 short chains that are assigned to $^{289}115$ in this scenario have half-lives very similar to those in the $^{288}115$ chains. The resulting cross sections tell another interesting story, see below.

Scenario 2: Here, D3 is left being the only chain possibly starting from $^{289}115$, while the other 13 chains start with $^{288}115$ and end with either SF or EC decay branches in $^{284}113$ or ^{280}Rg. Then, the short chains have FoM_{geom} values that are comparable with those of the $^{288}115$ chains, which support this scenario. The extremely low FoM_{geom} of D3 supports its exclusion. This assignment of the 13 chains to $^{288}115$ implies formally SF branching ratios of $b_{\text{SF}} = 4/109 = 3.7\%$ for $^{284}113$ and $b_{\text{SF}} = 9/105 = 8.6\%$ for ^{280}Rg. Other options are EC decay branches of $^{284}113$ or ^{280}Rg into even–even ^{284}Cn or ^{280}Ds. As large hindrance factors for SF of the odd–odd nuclei $^{284}113$ and ^{280}Rg are expected, EC preceding SF of the respective even–even daughters is more probable. Their SF half-lives are either known (e.g. Düllmann et al. 2010) or expected to be very short (Smolanczuk 1995). SF or EC branches are theoretically predicted in this region of the nuclear chart (Karpov 2012).

These scenarios can be propagated into cross sections: Scenario 1 implies a ratio of maximum cross sections $\sigma(2n)/\sigma(3n)$ of 0.5 which is in severe conflict with expectations from nuclear reaction theory. In scenario 2, the cross section for the 2n reaction channel is about 1 pb in line with theoretical expectations.

In summary, there is considerable evidence for the view that the IUPAC acceptance of the proposed link between decay chains of elements $^{293}117$ and $^{289}115$ as convincing was incompetent. Much too late, IUPAC seems to have recognized

that its judgment in this case was superficial and brought itself into disrepute. As a consequence, IUPAC negotiated with IUPAP and the JWP was replaced by a new one, whose members were selected in half by IUPAC and in the other half by IUPAP. The new JWG under its chairman S. Hofmann got together and worked out newly defined, strict rules for their future work that were published in Pure and Applied Chemistry.

17.3.4 Other Disciplines

In the special issue on Superheavy Elements (2015) in Nucl. Phys. **A944,** there are also articles related to this topic that come from other disciplines. One comes from the Oak Ridge National Laboratory and its High Flux Isotope Reactor where actinide target materials for the syntheses of superheavy elements are produced in large quantities and are chemically separated. The primary production isotope, ^{252}Cf, is produced in a two-year irradiation in amounts up to 200 mg per campaign. This process also produces 20 mg of ^{249}Bk, micrograms of ^{254}Es, and pictograms of ^{257}Fm. The Am/Cm source material was produced nearly 40 years ago via multi-stage irradiation of plutonium in the decommissioned K-reactor at Savannah River. It was reserved for heavy actinide production at ORNL, and through decades of recycling became rich in ^{246}Cm, and to a lesser extent ^{248}Cm. The ^{252}Cf production process begins with conversion of the Am/Cm source material to oxide microspheres that are blended with aluminum powder and pressed to form cermet pellets. These are loaded into long, finned aluminum tubes that are closure-welded and then hydrostatically compressed to provide good heat transfer between the pellets and target tubes. A final aluminum jacket is wrapped around the target tube to channel the coolant flow around the target during irradiation. Each target contains up to 8 g of Am/Cm. The target rods are inserted into the flux trap of HFIR, where they are exposed to a thermal neutron flux of $3 \cdot 10^{15}$ n cm^{-2}. The Am/Cm is transmuted into heavier isotopes by a series of neutron captures and beta decays with losses due to fission and decay. A typical ^{252}Cf irradiation plan involves placement of targets in positions of maximum neutron flux for three to five 24-day reactor cycles. Under these conditions, ^{252}Cf precursors ^{249}Bk, ^{250}Cf, and ^{251}Cf reach their maximum accumulation rate after one cycle and ^{252}Cf reaches its maximum rate during the second cycle. Further irradiation results in additional accumulation of ^{252}Cf, but at an ever-decreasing rate. For the production of, e.g. ^{249}Bk, a typical irradiation plan would place targets in positions of maximum epithermal-to-thermal flux ratio for a single cycle. This is followed by the chemical processing of the irradiated targets.

Since 2000, six new elements with atomic numbers $Z = 113$–118 have been produced using these target materials in bombardments with ^{48}Ca ions. These elements were first produced at Dubna, with successive experiments at Berkeley confirming element 114 and GSI, Darmstadt, confirming elements 114, 115, 116, and 117.

Another article comes from nuclear astrophysics and deals with the question whether certain stellar r-processes are able to produce superheavy elements. We will touch this question in Chapter 18 by asking whether supernova explosions

are candidates and referring to the recent observation of merging neutron stars that are developing r-processes. Goriely and Martinez-Pinedo report about their related theoretical research in which they study the r-process nucleosynthesis in material that is dynamically ejected by tidal and pressure forces during the merging of binary neutron stars. Neutron star mergers could potentially be the dominant r-process site in the Galaxy, but also due to the extreme neutron richness found in such environment, could potentially synthesize superheavy elements. R-process nucleosynthesis during the decompression is known to be largely insensitive to the detailed astrophysical conditions because of efficient fission recycling, producing a composition that closely follows the solar r-abundance distribution for nuclei with mass numbers $A > 140$. During the neutron irradiation, nuclei up to charge numbers $Z = 110$ and mass number $A = 340$ are produced, with a major peak production at the $N = 184$ shell closure, i.e. around $A = 280$. Superheavy nuclei with $Z > 110$ can hardly be produced due to the efficient fission taking place along those isotopic chains. Long-lived transuranium nuclei are inevitably produced by the r-process. The predictions concerning the production of transuranium nuclei remain however very sensitive to the predictions of fission barrier heights for such superheavy nuclei. More nuclear predictions within different microscopic approaches are needed.

The other article comes from Zagrebaev and Greiner and explores theoretical predictions of cross sections to be expected in syntheses of superheavy elements in different reactions, cold-fusion reactions, hot fusion reactions in particular with ^{48}Ca projectiles, and multinucleon transfer reactions. We have presented their work in Section 12.8.3.

Direct measurements of mass numbers of the transactinide isotopes $^{284}113$ ($t_{1/2} = 0.97$ seconds) and $^{288}115$ ($t_{1/2} = 171$ ms) produced in the ^{243}Am(^{48}Ca, 3n) reaction have been successfully conducted at Berkeley as reported by J.M. Gates et al. (2018). The isotopes were separated by the BGS, and their mass-to-charge ratio was measured by the newly developed FIONA. FIONA consists of a radiofrequency (rf) gas catcher, rf quadrupole (RFQ), RFQ trap, acceleration region, trochoidal spectrometer (mass analyzer), and detector station. Upon entering FIONA, the 115 ions were stopped in 13 kPa of He inside the rf gas catcher. Then, rf and dc electric field gradients directed the ions toward the exit orifice. The average drift time through the gas catcher is estimated to be 28 ms. The ions were then radially confined in the segmented RFQ, while the He gas was differentially pumped to a pressure of 30 Pa. An axial dc gradient applied along the RFQ axis, directed the ions downstream, where they were captured in the RFQ trap, which was configured with an axial dc gradient profile to create a three-dimensional ion trap. Differential pumping on this RFQ trap maintained a He pressure of ∼2 Pa in this region. Collisions with the He buffer gas in the trap cooled the ions further and confined them to within ∼1 mm^3. Every 20 ms, the dc voltages on the RFQ trap segments were changed to eject the cooled ions into a region containing acceleration electrodes, steering electrodes, and Einzel lenses. The 115^{1+} ions were accelerated to 3319 eV. The ions were then separated by their A/q using the trochoidal spectrometer (mass analyzer). Here, the A/q separation is based on the trochoid-phase differences

of ions with different A/q when they exit the magnetic and electric fields, which results in different exit angles in the plane defined by the beam and electric field directions. After exiting the trochoidal spectrometer, the ions were implanted in the focal plane detector. The first decay chain was assigned to $^{284}113$, the second one to $^{288}115$. Thus, the first direct experimental measurements of the mass numbers of $^{288}115$ and $^{284}113$ anchor most of the previously reported superheavy element A assignments, suggesting that most (not all) of the indirectly assigned mass numbers are correct.

17.4 Cross Sections

In Section 12.8.1, we introduced the phenomenon of dynamically hindered fusion for massive systems with $Z_1Z_2 \geq 1600$ and the resulting exponential decrease of the fusion probability at the Bass model fusion barrier, Eq. (12.114). Thus, it is no surprise that the cross sections for the production of superheavy elements decrease systematically as the atomic number of the compound nucleus increases. Cross-sectional data measured in heavy-ion fusion reactions producing heavy elements are plotted in Figure 17.17. The 1n, 2n, and 3n channels in cold-fusion reactions with ^{208}Pb and ^{209}Bi targets result from low excitation energies of about 10–15, 15–25, and 25–35 MeV, respectively, whereas hot-fusion reactions with actinide targets result in excitation energies of 35–55 MeV populating 3n, 4n, and

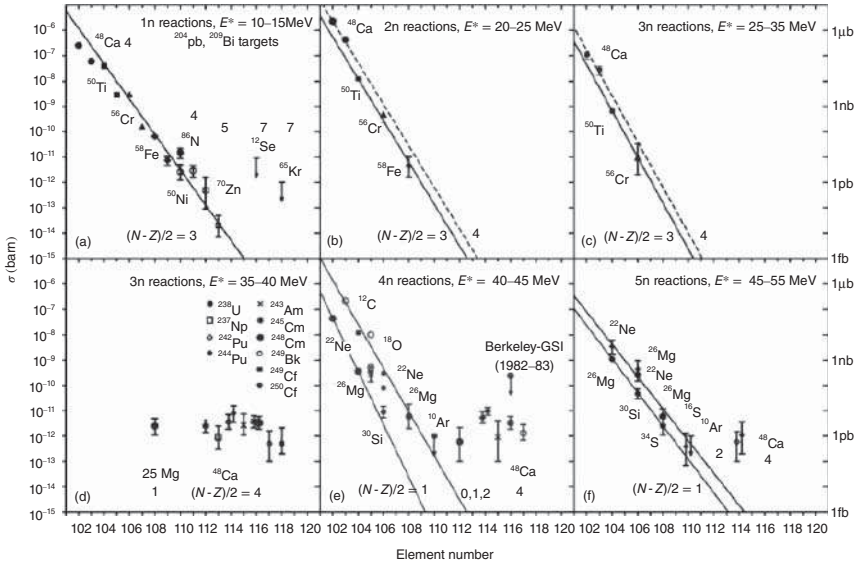

Figure 17.17 Measured cross sections for fusion reactions with ^{208}Pb and ^{209}Bi targets and evaporation of one (a), two (b), and three (c) neutrons and for fusion reactions with actinide targets and evaporation of three (d), four (e), and five (f) neutrons. Values $(N - Z)/2$ characterize the neutron excess of the projectile. The straight lines are fits to data points drawn to guide the eye. Source: Hofmann (2011), figure 16 (p. 419)/De Gruyter.

5n channels. The cross sections for elements up to 113 decrease by a factor of 4 per element in the case of cold fusion (1n channel) and those for elements lighter than 110 by a factor of 10 in the case of hot fusion (4n channel). The decrease of cross sections for cold-fusion reactions is clearly linked to decreasing fusion probabilities due to the dynamical hindrance of fusion. Hot-fusion cross sections suffer from this to a lesser extent, but mainly drop because of strong losses due to fission in the multiple neutron evaporation steps.

There are strong odd–even effects in the 1n cold-fusion data. The decrease of cross sections for the synthesis of elements 105, 107, and 109 using ^{209}Bi targets is about a factor of 10 compared to the cross sections of the next lighter even elements 104, 106, and 108 produced with ^{208}Pb targets in both cases with ^{50}Ti, ^{54}Cr, and ^{58}Fe projectiles. The combination of odd-element projectiles ^{51}V, ^{55}Mn, ^{59}Co, and ^{65}Cu with targets of ^{208}Pb for the synthesis of the odd elements 105, 107, 109, and 111 results in similar cross sections as in reactions with even-element projectiles and ^{209}Bi targets. This shows that the presence of an odd proton, independent of whether it is in the projectile or in the target nucleus, reduces the cross section by an amount which is similar to the increase in the fissility when the projectile Z is increased by 2 units. In Section 12.8.1, we pointed at an odd-particle hindrance in fusion reactions.

Extremely small cross-sectional values result from an extrapolation of the hot-fusion data into the region of element 114 and beyond, while the experimental data reveal an opposite trend. Beyond element 112, the cross sections increase again and reach values on the order of 5 pb for elements 114 and 116 for both 3n and 4n channels. Even higher values of $8.0^{+7.4}_{-4.5}$ pb and $9.8^{+3.9}_{-3.1}$ pb were measured at TASCA by Düllmann et al. in the reaction $^{48}\mathrm{Ca} + {}^{244}\mathrm{Pu} \rightarrow {}^{292}114^{*}$ for the 3n and 4n channel, respectively. We shall return to these increased cross sections below.

Before we do, we have to discuss some features of fusion reactions that are pertinent to the survival probability of excited compound nuclei. The probability $W(Z)$ of surviving fission depends on the partial probabilities Γ_n and Γ_f to deexcite by neutron emission (survival) or by fission (destruction), on the excitation energy of the compound nucleus E^*, and the number of deexcitation steps until the ground state of the evaporation residue is reached:

$$W^{\mathrm{survival}}(Z) = \prod_{i=1}^{\nu} \left(\frac{\Gamma_\mathrm{n}}{\Gamma_\mathrm{n} + \Gamma_\mathrm{f}} \right)_{(i,E^*)} \approx \left(\frac{1}{1 + \Gamma_\mathrm{f}/\Gamma_\mathrm{n}} \right)^{\nu} \tag{17.44}$$

The ratio $\Gamma_\mathrm{n}/\Gamma_\mathrm{f}$, given an excitation energy $E^*$and temperature T, depends on the ratio of level densities above the neutron separation energy B_n and the fission barrier B_f:

$$\Gamma_\mathrm{n}/\Gamma_\mathrm{f} = K \frac{\exp(E^* - B_\mathrm{n})/T}{\exp(E^* - B_\mathrm{f})/T} = K \, \exp[-(B_\mathrm{n} - B_\mathrm{f})/T] \tag{17.45}$$

with $K = 1.4A^{2/3}T$ and A the mass number of the compound system. This holds for "actinide-based" 4n and 5n reactions, that is, for $E^* > B_\mathrm{n} > B_\mathrm{f} > T$. For 50 MeV excitation energy, the value of $\Gamma_\mathrm{n}/(\Gamma_\mathrm{n} + \Gamma_\mathrm{f})$ is close to 0.4. For small excitation energies, the value becomes smaller; for 12 MeV, the value sinks to 10^{-2}. The latter is a question of time scales. The time for fission is typically $3 \cdot 10^{-20}$ seconds; the time for neutron emission at 12 MeV excitation energy is 10^{-17} seconds.

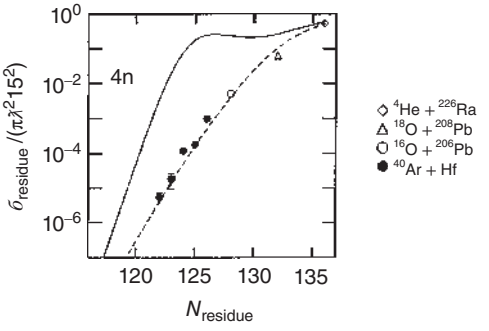

Figure 17.18 Maxima of the 4n excitation functions vs. neutron number for Th evaporation residues. A factor $1/(\pi\lambda^2 \cdot 15^2)$ was applied in order to remove trivial entrance channel effects for different target–projectile combinations and to make the ordinate scale approximately equal to the survival probability $\Pi(\Gamma_n/\Gamma_{tot})$ times the transmission coefficient of the fusion barrier for a low angular momentum. Calculated survival probability for zero angular momentum: standard evaporation calculation (solid line); evaporation calculation without shell effect (dashed line). Source: Sahm et al. (1985), figure 3 (p. 330)/Elsevier.

According to the macroscopic–microscopic model, Section 5.9, the fission barrier $B_f = B_{LDM} + \delta U$, and Γ_n/Γ_f therefore depends on the shell correction energy:

$$\Gamma_n/\Gamma_f = K \exp[-(B_n - B_{LDM})/T] \cdot \exp(\delta U/T) \tag{17.46}$$

For superheavy elements, B_{LDM} is smaller than the zero-point vibrational energy and can completely be ignored. According to A.V. Ignatyuk, δU is damped by excitation energy:

$$\delta U = \delta U_0 \exp(-\gamma E^*) \quad \text{with} \quad \gamma^{-1} = 5.48A^{1/3}/(1 + 1.3A^{-1/3}) \tag{17.47}$$

For deformed evaporation residues, the 1/e damping energy is 27 MeV for hot-fusion reactions. For spherical heavy nuclei, this is different. For Th isotopes from 1n to 4n reactions close to the spherical neutron shell $N = 126$, as models for spherical superheavy elements, Figure 17.18 shows that for the 4n reactions, there is no gain in cross sections due to the shell closure. Only for the lowest excitation energies (Zr isotopes on ^{124}Sn), that is, for the 1n channel, is there an indication for a small gain in cross sections at $N = 126$. The mechanism that reduces Γ_n/Γ_f for spherical nuclei has been called *collective enhancement of level densities* and was introduced by T. Ericson in 1958; it was further worked on by S. Bjørnholm and B. Mottelson in 1974. The enhancement factor K_{coll} of the level densities is different for ground-state level densities that determine Γ_n, and for saddle point level densities that determine Γ_f. At the saddle point, the finite deformation of the nucleus causes a high-level density due to rotational excitations, which is not the case for the spherical ground state.

We are now in a position to discuss the work by Armbruster (Armbruster 2008) in 2008 with his attempt to explain the rise of the cross sections near $Z = 114$. In Section 5.10, we introduced the interacting boson approximation (IBA) and the periodicity of nuclear structure resulting from IBA systematics. According to this systematics, the cornerstone in the superheavy element region should be $^{306}_{184}122$.

The region of spherical nuclei in analogy to the ^{208}Pb region, where it covers the elements between Hg ($Z = 80$) and Po ($Z = 84$), should be expected at $Z = 122 \pm 3$. On traversing the $\overline{X}(5)$ symmetry point at $Z = 119$ toward lower values of Z, a region of oblate-shaped nuclei in analogy to the Os region below ^{208}Pb should be entered. It might cover nuclides of the elements $Z = 115 \pm 3$ in the neutron range $N = 174 \pm 4$ centered around ^{289}115. Accordingly, all the isotopes discovered at Dubna would have ($\beta_2 < 0$) deformed oblate shapes.

For the cross sections, Armbruster suggested a four-factor formula (note that, originally, the independence hypothesis led to a two-factor formula, Eq. (12.78)). The factors follow the sequence of stages during the formation process of the evaporation residues:

$$\sigma(Z) = \sigma_{\text{capture}} \cdot p^{\text{hindrance}} \cdot p^{\text{shape}} \cdot W^{\text{survival}}(Z) \tag{17.48}$$

σ_{capture} and $W(Z)$ allowed for a presentation of fusion induced by α particles and light ions on actinide targets. Elements up to $Z = 106$ were synthesized and correctly described. Cross sections down to 10 nb were reached. The excitation energy of the compound system in nearly symmetric collision systems is $E^* \approx 0$, and for $B_f > B_n$, production of evaporation residues seemed possible without fission losses, that is, by capture alone at $W(Z) \to 1$. First estimates in 1967 by T. Sikkeland to produce superheavy elements gave cross sections of 100 mb. These were the times when the elements Rf and Db were discovered, and the synthesis of superheavy elements became a major goal of nuclear chemistry.

In the first SHIP experiments, the production of superheavy elements at the closed neutron shell $N = 184$ was envisaged. The nearly symmetric reactions ^{136}Xe + ^{170}Er $\to$ $^{306}_{184}122^*$ and ^{65}Cu + ^{238}U $\to$ $^{303}_{182}121^*$ were investigated in 1976–1977 by Armbruster et al. Instead of cross sections in the 100 mb range, a limit below 1 nb was established. The discrepancy between expectation and the observed result by 8 orders of magnitude showed that fusion is governed by more physical processes than capture and deexcitation. New processes, that is, deep inelastic collisions and quasi-fission, were discovered to take the missing flux toward fusion, see Sections 12.8.2 and 12.8.3. Recent calculations by Swiatecki et al. in 2005 confirm the exponential decrease of the reaction flux (Eq. (12.114)). Armbruster used the formula

$$p^{\text{hindrance}}(Z) = C \cdot \exp[-(0.5/\log e)(Z - Z_0)] \tag{17.49}$$

and assumed that Eq. (17.49) is valid for all mass asymmetries of the collision system. Hindrance sets in at a certain value of Z_0 which is smallest for symmetric fusion.

The factor p^{shape} in Eq. (17.48) takes into account the dependence of the fission probabilities on the shape of the nuclei to be produced. Nearly everything that is known about fission concerns nuclei with prolate deformations in the ground state, and these pass over a prolate saddle point toward scission. For these nuclei, p^{shape} is set equal to 1. For oblate nuclei, Armbruster discusses a possible stabilization against fission because these must also pass over a prolate saddle point. This is taken care of by a common gain factor of 10 for all the oblate isotopes of the elements concerned. For spherical nuclei, on the other hand, collective enhancement of level

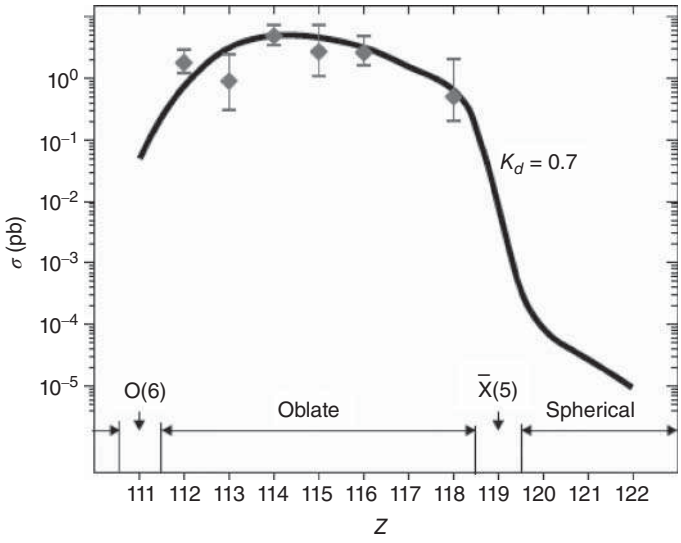

Figure 17.19 Cross sections $\sigma(Z)$ measured at the DGFRS (symbols with error bars) and calculated by Armbruster 19 (solid line) on a log scale to demonstrate the decrease of $\sigma(Z)$ reaching a value of 10^{-5} pb at $Z = 122$. Besides the steady decrease introduced by the hindrance factor $p^{\text{hindrance}}$, the transition from oblate to spherical nuclei between 118 and 120, introduced by the shape factor p^{shape}, is demonstrated. Whether the breakdown by three orders of magnitude is realistic remains to be proven. Even without this breakdown, $\sigma(Z)$ would reach a limit of 10 fb for $Z = 122$ which is not accessible by today's experimental methods. Source: Armbruster (2008), figure 6 (p. 166)/Springer Nature.

densities at the saddle point, as discussed above, reduces the survival of the compound system. The spherical nuclei neighboring the closed shell $N = 126$ for the elements 87–91 were found to show that fission probabilities increased by a factor of 100 compared to their deformed neighbors. In the range of superheavy elements $Z = 119$–126, close to the neutron shell $N = 184$, the same behavior is expected. At least the same loss factor 10^{-2} should be introduced in p^{shape} for the spherical superheavy nuclei.

The Ignatyuk formula, Eq. (17.47), is used in the form $K_{\text{D}} = \exp(-\gamma E^*)$, where K_{D} may take values between no damping, $K_{\text{D}} = 1$, and the Ignatyuk value. Armbruster fixed the value at $K_{\text{D}} = 0.7$ by adjusting the calculated cross sections to the DGFRS values. Thus, by staying within well-known physics, Armbruster was able to reproduce the DGFRS cross sections as shown in Figure 17.19. The increase in the range $Z = 111$ to $Z = 115$ is connected not only with the gain factor for all the oblate isotopes in this range but also with the fact that the foot of the ascent to the doubly closed-shell nucleus $^{306}_{184}122$ at the top has been traversed. With $B_{\text{f}} > B_{\text{n}}$, $Z = 118$ is reached with a survival close to 1. The factor p^{shape} has been set to 10^{-2} for the spherical nuclides above $Z = 118$ which causes the precipitous decrease of the cross sections beyond. Collective enhancement of level densities destroys these nuclei as has been shown for their $N = 126$ partners. Figure 17.19 suggests that it will be very challenging to try to go beyond $Z = 118$.

17.5 Nuclear Structure of Superheavy Elements

The properties of the transactinide nuclei show two remarkable features:

- Spontaneous fission, dominating in the region close to Rf, becomes the relatively weaker decay branch for the heavier elements. Even the heaviest known even–even isotopes exhibit strong α-decay branches.
- The half-lives of the transactinide isotopes grow significantly toward the neutron number $N = 162$.

The fission properties of the heaviest elements are of great importance because fission will finally determine the limits of existence. In the macroscopic description, the fission properties are characterized by the fissility parameter which is normalized to the critical fissility, beyond which nuclei disintegrate promptly, Eq. (6.21). In Figure 17.20, the partial half-lives of the doubly even isotopes of U and beyond are plotted logarithmically against the fissility parameter. They decrease from U to Hs over more than 20 orders of magnitude from the age of the Universe to milliseconds. Besides the overall decrease of the fission half-lives from U to Hs, there is a significant variation within the half-lives of the isotopes of an element. The isotopes with the longest half-lives are those with neutron number $N = 152$. This enhanced stability can be attributed to the deformed neutron shell stabilization. A similar effect is observed for another deformed shell at $N = 162$. The relatively long half-lives of the isotopes of Rf through Hs can be attributed to this shell stabilization.

The fission half-lives calculated within the macroscopic liquid-drop model, see Figure 17.20, are much shorter than the experimental values. In the extreme, the

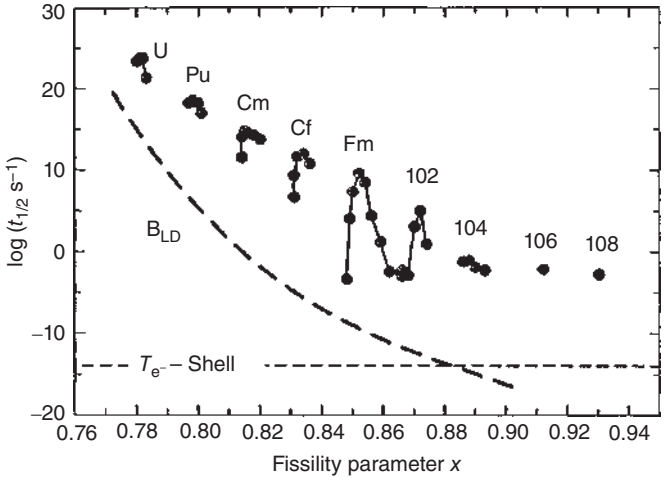

Figure 17.20 Partial half-lives for spontaneous fission of even–even isotopes of the transuranic elements. The dashed line shows the spontaneous fission half-lives calculated in the macroscopic liquid-drop model. The horizontal line marks the time necessary for the formation of electron shells. Source: Münzenberg and Hofmann (1999) / World Scientific Publishing.

difference is almost 20 orders of magnitude, as in the case of ^{252}Fm, ^{260}Sg, and ^{264}Hs. For the heaviest elements, the liquid-drop half-life is so short that these elements can exist only due to shell effects. In the macroscopic–microscopic model, their fission barriers are entirely due to the shell correction energies, as we discussed in Section 5.9. It is impressive to note that, near rutherfordium, the liquid-drop half-lives fall below 10^{-14} seconds. This is the time needed for the formation of an electron shell and is the lower time limit beyond which an element with chemical properties cannot exist. Thus, the shell correction energies exclusively give life to the heaviest elements.

The shell correction landscape for the elements above Pb is shown in Figure 17.21 together with the landing places in the cold-fusion reactions (crosses) and in the hot-fusion reactions (circles). Apart from the shell correction energies of −5 MeV at the deformed $N = 152$ shell (quadrupolar deformation), there are shell correction energies of −6 MeV at the deformed $N = 162$ shell (quadrupolar plus hexadecapolar deformation). Modern theoretical approaches disagree on the size and position of the next spherical proton shell gap. The macroscopic–microscopic models with various parameterizations of the nuclear potential predict $Z = 114$ and $N = 184$ as shown in Figure 17.21. Calculations using self-consistent mean-field approaches have been performed by several authors and broadly fall into two categories, namely, relativistic and non-relativistic approaches. In both cases, the splitting between the $2f_{7/2}$–$2f_{5/2}$ spin–orbit partners which, in the macroscopic–microscopic models opens the single-particle proton gap at $Z = 114$, is not sufficient to open a gap. Most non-relativistic mean-field calculations favor $Z = 124$, $Z = 126$, and $N = 184$, while the relativistic mean-field models show that the effects of magic numbers of single nucleonic configurations valid in lower mass magic nuclei (Sn, Pb) are dissolved in favor of more extended regions of additional shell stabilization, centered mainly around $Z = 120$, $N = 172$, 184 or $Z = 126$, $N = 184$. Thus, various models consistently predict $N = 184$ as the next spherical neutron-shell closure, but disagree in the prediction of the next spherical proton-shell closure. In this connection, it is interesting to look at an exercise performed by Armbruster (Armbruster 2008) with the α-decay chains for pairs of even–even nuclei measured in the DGFRS experiments. They give access to Q_α values between the ground states of the isotopes

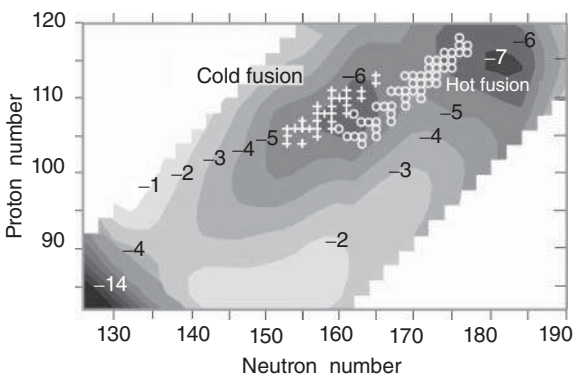

Figure 17.21 Shell corrections to the nuclear macroscopic potential energy. The numbers at the contour lines correspond to the amplitude of the shell correction in MeV. Crosses denote nuclei produced in cold-fusion reactions; circles denote products from ^{48}Ca + actinides reactions. Source: Oganessian (2011), figure 2a (p. 431)/De Gruyter.

involved. The isospin values $(N-Z)/2$ characterizing the chains are 29 and 30 and cover the elements between $Z = 118$ and $Z = 112$. They cross the proposed proton shell $Z = 114$ at $N = 172$ and $N = 174$. The next neutron shell at $N = 184$ is 12 or 10 neutrons away. Q_α values in decay chains decrease steadily, descending the chain to smaller Z values. Passing a shell is well documented in nuclear data tables by a jump from higher Q_α values above the shell to lower values below the shell. The size of the jump becomes smaller going away from the doubly magic nucleus. Armbruster examined by means of a comparison to the well-established shell at $Z = 82$ at equivalent distances in the neutron numbers whether, for a shell at $Z = 114$, a jump should still be observed at a distance of 12 or 10 neutrons from $N = 184$. As the distances between closed shells are 44 neutrons between $N = 82$ and $N = 126$, but 58 neutrons between $N = 126$ and $N = 184$, this difference, taken into account, fixes the point of comparison to $N = 118$ for the Pb shell. The Pb shell crossed at $N = 119–116$ by the chains passing from Po via Pb to Hg manifests a jump of (1.21 ± 0.02) MeV at the shell crossing. The exercise presented in Figure 17.22 demonstrates that the $Z = 82$ shell is still clearly visible at ^{200}Pb, and the shell at $Z = 114$ should be manifested in the α-decay chains $(N-Z)/2 = 29$, 30 measured at the DGFRS. An analysis of the 11 Q_α values published for the even elements between $Z = 118$ and $Z = 112$ was performed. They cover the chains $(N-Z)/2 = 58$ to 61. The off-shell decays were compared to the on-shell decays. A shell closure at $Z = 114$ would be seen not only in the Q_α values but also in the two-proton separation energies S_{2p}. The differences between consecutive Q_α values, δQ_α, and pairs of neighboring isotonic nuclei, δS_{2p}, were selected and compared for off-shell and on-shell decays. For the on-shell transitions between $Z = 116–114$, six differences are compared to five off-shell differences between $Z = 118–116$ and $Z = 114–112$ shown in Figure 17.22. The 11 isotopes chosen for the analysis of the Pb shell gap are referred to ^{200}Pb in identical positions to those observed in the ^{48}Ca experiments referred to ^{288}114. A jump at $Z = 114$ of (0.02 ± 0.07) MeV follows. Within statistical error, there is no shell gap at $Z = 114$. The potential energy surface around ^{288,286}114 is smooth, showing no closed-shell structure. The α-decay chain analysis of the DGFRS experiments does not support the shell at $Z = 114$ which has accompanied superheavy element research since 1966. Thus, a thrilling task remains to identify the location of the next proton-shell closure.

More direct experimental evidence for a missing proton shell-closure at $Z = 114$ was recently presented by Såmark–Roth et al. (2021). They conducted a nuclear spectroscopy experiment to study α-decay chains starting from isotopes of $Z = 114$ using an upgraded multi-coincidence TASISpec decay station in the focal plane of the gas-filled separator TASCA at GSI, see Sections 11.6 and 17.8.3. Eleven decay chains were firmly assigned to ^{286}Fl and ^{288}Fl. In the decay of ^{286}Fl ($Q_\alpha = 10.33(3)$ MeV), a prompt coincidence between a 9.60-MeV α-particle and a 0.36-MeV conversion electron marked the first observation of an excited state in an even-even isotope of one of the heaviest elements, namely ^{282}Cn. Spectroscopy of ^{288}Fl decay chains fixed $Q_\alpha = 10.06$ MeV for this isotope. In one case, a $E_\alpha = 9.46$ MeV decay from ^{284}Cn into ^{280}Ds was observed with ^{280}Ds after 518 μs. The impact of these findings, aggregated with existing data on Fl decay chains, on the size of the long-predicted shell gap

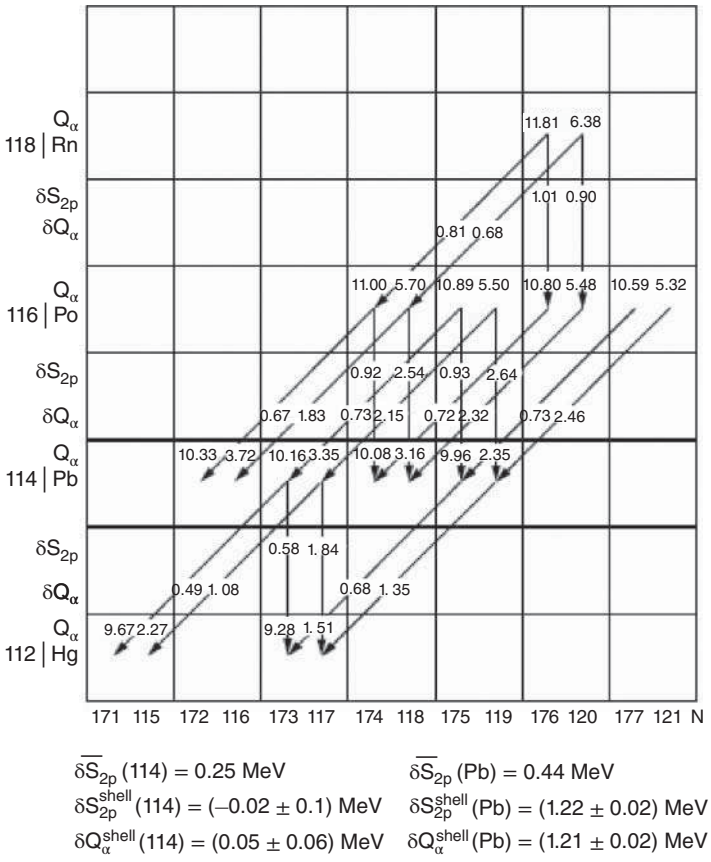

Figure 17.22 The 11 measured Q_α values in the four decay chains with $(N - Z) = 58–61$ of even elements $Z = 118–112$ centered at $^{288}_{174}114$ are compared to 11 known Q_α values of elements Rn, Po, Pb, and Hg in the chains with $(N - Z) = 34–37$ centered at $^{200}_{118}$Pb. The jump in the values of Q_α and S_{2p} (two-proton separation energy) crossing the shell $Z = 82$ between Po and Hg is analyzed and compared to the corresponding jump at $Z = 114$ between $Z = 116$ and $Z = 112$. Comparing on-shell and off-shell values, the $Z = 82$ shell manifests itself in the $\delta Q_\alpha^{\text{shell}}$ values and $\delta S_{2p}^{\text{shell}}$ values by an energy difference of 1.21 ± 0.02 MeV at the shell crossing. At $Z = 114$, the identical analysis gives for the difference of the $\delta Q_\alpha^{\text{shell}}$ values (0.05 ± 0.06) MeV and (-0.02 ± 0.1) MeV for $\delta S_{2p}^{\text{shell}}$, respectively. This analysis shows a smooth transition between the Z values and no indication of a shell closure at $Z = 114$. Source: Armbruster (2008), figure 1 (p. 160)/Springer Nature.

at $Z = 114$, was discussed (Såmark–Roth et al., 2021) in light of theoretical predictions from beyond-mean-field calculations (Gogny-force BMF) of triaxial deformation in these nuclei (Rodriguez and Egido, 2010). A novel type of shape-coexistence, namely, fluctuations between triaxial prolate and triaxial oblate shapes, was predicted to occur in the isotope ^{290}Fl (Egido and Jungclaus, 2020). The existence of the low-energy excited states provided by the observation of a conversion electron in ^{282}Cn and reduced α-decay energies E_α below the Q_α-values of ^{282,284}Cn are anchor

points for nuclear science that definitely rule out the shell closure at $Z = 114$. For excited states in ^{282}Cn, at 0.62(4) MeV (0^+) and at 0.22(4) MeV (2^+), tentative values, notably in the keV regime, are proposed. Consistently, also the measured Q_α-values of the α-decay sequence ^{292}Lv, ^{288}Fl, and ^{284}Cn pass smoothly through $Z = 114$ showing no kink at ^{288}Fl at variance with macroscopic-microscopic (MM) descriptions.

17.6 Spectroscopy of Actinides and Transactinides

For the latter, the early successful explanation of the magic numbers $Z = N = 2$, 8, 20, 28, 50, 82, $N = 126$ via a large spin–orbit splitting led to the 1963 Nobel Prize in Physics for M. Goeppert-Mayer and J.H.D. Jensen. In MM theories for superheavy nuclei, the spin–orbit interaction can open substantial shell gaps – for instance, between the proton $2f_{7/2}$–$2f_{5/2}$ spin–orbit partners. A nucleus with 114 protons will fill all orbitals including the $2f_{7/2}$ shell, and it is the strength of the spin–orbit interaction that determines the size of the $Z = 114$ gap, as schematically shown in Figure 17.23. We have mentioned the macroscopic–microscopic models as well as relativistic and non-relativistic mean-field approaches with their various predictions of the location of the next proton-shell closure. Exploring the single-particle structure of superheavy nuclei is a challenge because experimental data for superheavy elements are scarce due to low production cross sections. With cross sections on the level of 1 pb, only a few atoms per month of beam time can be produced. This means that the majority of data available yield integral quantities such as half-lives, decay modes, and Q_α values, but are insensitive to the details of the nucleonic shell structure. However, recently, it has become possible to perform spectroscopic studies in nuclei approaching the "island of stability" such as ^{254}No

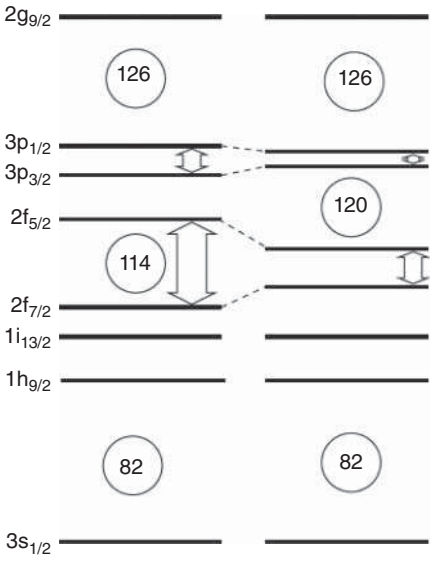

Figure 17.23 Schematic illustration of the spherical single-proton orbital energies of superheavy elements. The strength of the spin–orbit splitting determines the size of the gaps at $Z = 114$ and $Z = 120$. Left, large spin–orbit coupling; right, weak spin–orbit coupling. The spherical levels are labeled in the standard spectroscopic form. The circled numbers indicate the resulting energy gaps. Source: Herzberg et al. (2006), figure 1 (p. 896)/Springer Nature.

($Z = 102, N = 152$). Nuclei in this region are deformed, and the degenerate spherical single-particle orbitals split in a well-defined and adequately understood manner (Section 5.7) into components according to the projection of the angular momentum onto the symmetry axis of the nucleus, the K quantum number. Orbitals originating above the relevant spherical proton shells (such as the $2f_{5/2}$ orbital) come close to the Fermi level in a deformed nucleus near $Z = 102$ and play a key role in the formation of excited states. In even–even nuclei, the ground state always has $K = 0$. Configurations with larger values of K thus require a decay path to the ground state that changes this projection gradually. If such intermediate configurations do not exist, the high K state becomes isomeric. This gives a very clear and unique experimental signature because the isomeric states can readily be identified from their lifetimes and decay paths. In this chapter, we have chosen the nucleus ^{254}No as an example because it provides an ideal laboratory for these studies. It is produced with a reasonable cross section of 2 μb which allows a production rate of several hundred atoms per hour, sufficient for detailed spectroscopic studies. We here refer to experiments performed at the Accelerator Laboratory of the University of Jyväskylä, Finland. The ^{254}No ions were produced via the ^{208}Pb(^{48}Ca, 2n) reaction at a beam energy of 219 MeV. They were separated from the beam and unwanted reaction products in the gas-filled recoil separator RITU before being implanted in a double-sided position-sensitive Si detector (DSSD) at the heart of the GREAT spectrometer. Long-lived isomeric nuclei then decayed to the ground state emitting γ-rays, X-rays, and conversion and Auger electrons. The latter were detected in the same pixel of the DSSD where they summed to a total deposited energy of 600 keV. This provided a clean signal for the decay of the isomer. The γ-rays and X-rays were detected in prompt coincidence with this electron signal in a large segmented planar Ge detector in close proximity to the DSSD and a large Clover Ge detector outside the detector chamber. Finally, the ground state of ^{254}No was detected via its characteristic 8.1 MeV α decay with a half-life of 51.2 seconds and was recorded in the same DSSD pixel. It is this characteristic sequence of implanted recoil, one or more isomeric decays followed by the characteristic α decay, all in the same detector pixel, that allows us to firmly assign the observed isomeric decays to ^{254}No.

Figure 17.24 shows the resulting level scheme of ^{254}No. The 266 ms isomer decays via a 53 keV E1 transition into an excited two-quasi-particle band feeding the 7^+ rotational band member. The E1 character of this transition is deduced from the observed very small internal conversion coefficient. From the γ-ray intensity ratios between stretched E2 and mixed E2/M1 transitions, R(81 keV)/(150 keV) and R(69 keV)/(126 keV), a value of the g factor of the band can be extracted within the rotational model. This g factor is sensitive to the nucleonic configuration. The value is $g_K = 0.87 \pm 0.14$. This band in turn decays via low-energy magnetic dipole and electric quadrupole transitions to the 3^+ band head before decaying to the ground-state band via two prominent transitions at 841 and 943 keV. The M1 character of these transitions firmly establishes the band head angular momentum and parity as 3^+. As the full decay path is known, the isomer can be placed at an excitation energy of 1293 keV. From the single-particle orbitals predicted around the Fermi surface, both a two-neutron structure $[7/2^+[624]_\nu \times 1/2^+[620]_\nu]^{(3+)}$ and

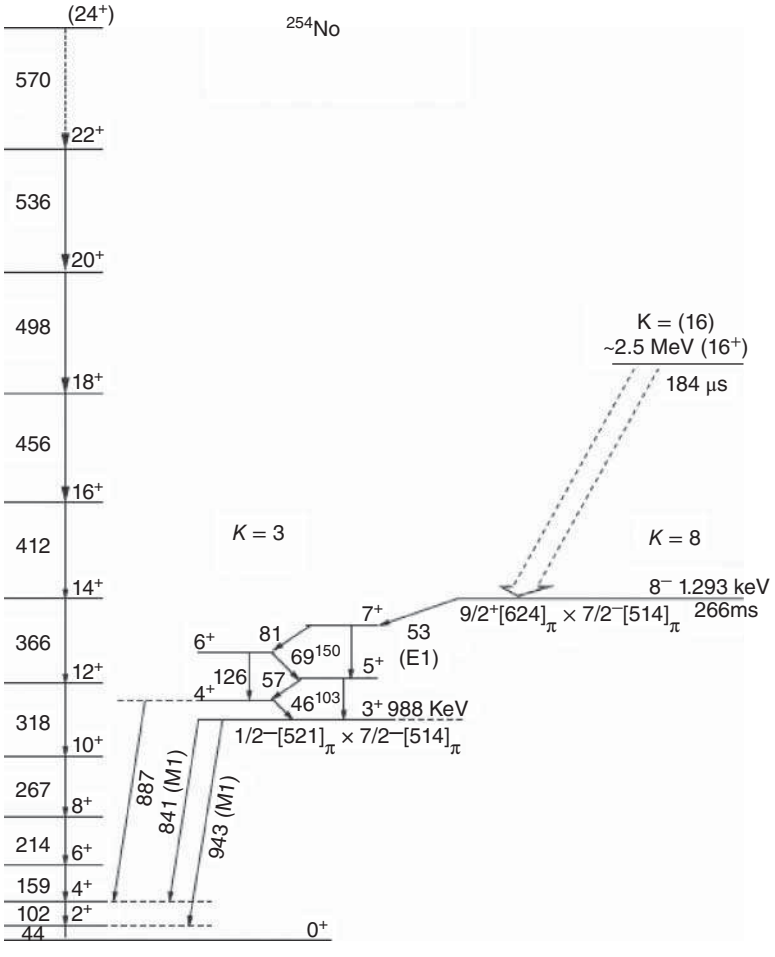

Figure 17.24 Level scheme of ^{254}No. The 266 ms 8^- K isomer is connected to the ground state via an excited 3^+ two-quasi-particle $[1/2^-[521]_\pi \times 7/2^-[514]_\pi]^{(3+)}$ band. Note that the 3^+ state involves the $1/2^-[521]_\pi$ Nilsson orbital stemming from the spherical $2f_{5/2}$ orbital above the $Z = 114$ shell gap. The 184 μs 16^+ K isomer populates the 8^- isomer band. Transitions are labeled by their energies in keV. Levels are grouped according to the projection of the total angular momentum on the symmetry axis of the nucleus (K quantum number). Source: Herzberg et al. (2006), figure 3 (p. 898)/Springer Nature.

a two-proton structure $[1/2^-[521]_\pi \times 7/2^-[514]_\pi]^{(3+)}$ with angular momentum and parity 3^+ can be formed. To distinguish between these configurations, the g factor of both of them can be calculated from the g factors of the individual orbitals to give $g_K^{\nu\nu} = 0.530$ and $g_K^{\pi\pi} = 0.824$. The experimental value of $g_K^{\exp} = 0.87 \pm 0.14$ clearly identifies the $K = 3$ band head as two-proton excitation involving the $1/2^-[521]_\pi$ Nilsson orbital stemming from the spherical $2f_{5/2}$ orbital just above the $Z = 114$ shell gap and from the $1h_{9/2}$ orbital. The message is that any theoretical calculation that gets the 3^+ energy right also has the $2f_{5/2}$ and $1h_{9/2}$ spherical orbitals in the right place. Thus, it is now possible for theoretical models to use this firm assignment as

a "stepping stone" to constrain the parameterizations used in the prediction of the location of the next spherical proton-shell closure. This is especially challenging for the self-consistent models where the high-l orbitals are systematically shifted to too high energies, that is, the proton $1i_{13/2}$ ends up between the $f_{7/2}$ and the $f_{5/2}$ ones, removing 114 as a gap.

As for the structure of the 184 μs isomer, it is proposed that this state is built on a two-proton, two-neutron, four-quasi-particle configuration. One attractive choice is the

$$\left\{[7/2^-[514]_\pi \times 9/2^+[624]_\pi]^{(8-)} \times [7/2^+[624]_\nu \times 9/2^-[734]_\nu]^{(8-)}\right\}^{(16+)}$$

state calculated to lie at 2.75 MeV, that is, the product of the two-proton and two-neutron choices for the 8^- isomer, analogous to the well-known 16^+ isomer in ^{178}Hf.

Today, spectroscopic information exists on a large number of nuclei with $Z \geq 100$: $^{246,\,248,\,250}$Fm, ^{251}Md, $^{252,\,253,\,254}$No, ^{255}Lr, $^{256,\,257}$Rf, ^{261}Sg, and ^{270}Ds. These are rife with K isomers. Such isomers are built on two-quasi-particle configurations and, being isomeric, tend to be very pure configurations indeed. Thus, structure assignments of the isomers and other two-quasi-particle structures found have become a major tool to investigate the single-particle structure of the heavy elements which is driven by the question of the location and extent of the "island of stability."

17.7 Properties of the Actinides

All actinides are radioelements and only Th and U have half-lives long enough to justify neglecting their radioactivity in some special chemical or technical applications. Ac and Pa are present in small amounts as decay products of U and Th (see Table 15.3). Extremely small amounts of Np and Pu are produced in U by neutrons from cosmic radiation: $^{237}\text{Np}/^{238}\text{U} \approx 10^{-12} : 1$, $^{239}\text{Pu}/^{238}\text{U} \approx 10^{-11} : 1$. Harkin's rule is also observed with the actinides, if the half-lives of the longest-lived isotopes of the elements are plotted as a function of the atomic number Z (Figure 17.25). A characteristic feature of the heaviest, most neutron-rich actinides is the tendency to decay by spontaneous fission. The ratio of the cross sections of thermal neutron fission ($\sigma_{n,f}$) and of (n, γ) reactions ($\sigma_{n,\gamma}$) is plotted in Figure 17.26 for various nuclides as a function of the difference between the binding energy of an additional neutron and the threshold energy of fission. The longest-lived actinide isotopes suitable for physical and chemical studies are listed in Table 17.4.

The electron configurations of the f-block atoms and ions are listed in Table 17.5. Whereas, in the case of the lanthanides, generally only one f electron is available for chemical bonding, in the case of the actinides, more f electrons may be engaged in chemical bonds (e.g. all the f electrons in compounds of U(VI) and Np(VII)). This is due to the relatively low differences in the binding energies of the 5f and 6d electrons up to $Z \approx 95$ (Am). However, these differences increase with Z, and the chemistry of elements with $Z \geq 96$ becomes similar to that of the lanthanides. The fact that the actinides up to and including Np keep a 6d electron in their ground-state electron

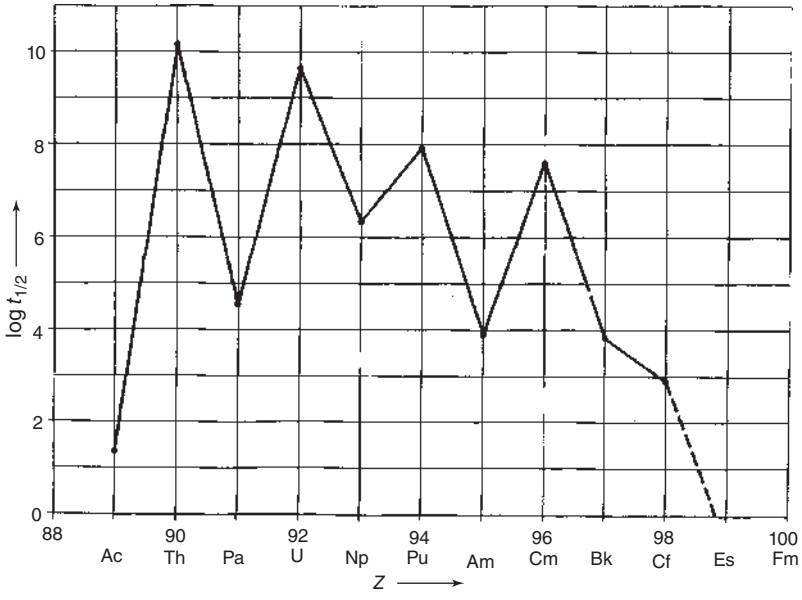

Figure 17.25 Logarithm of the half-life (yr) of the longest-lived isotopes of the actinides as function of the atomic number Z.

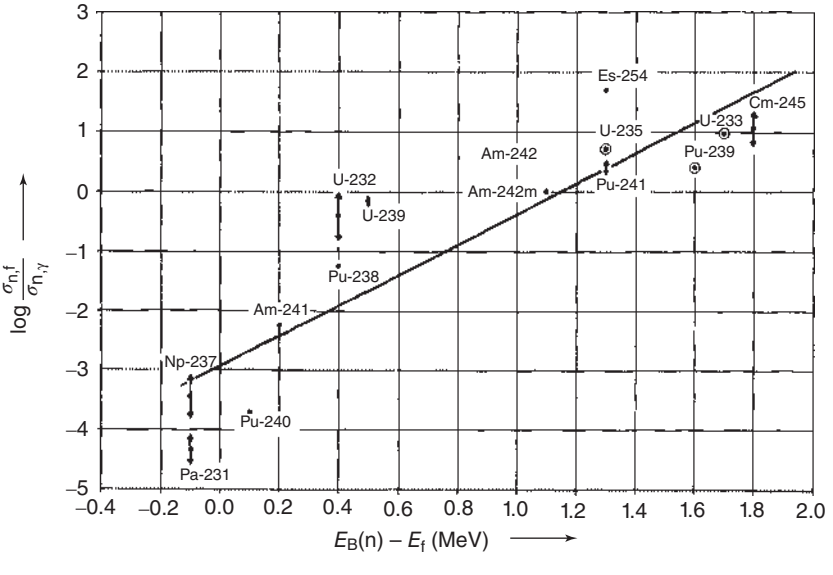

Figure 17.26 Logarithm of the ratio of the cross sections $\sigma_{n,f}$ and $\sigma_{n,\gamma}$ for various nuclides of the actinides as a function of the difference between the neutron binding energy $E_{B(n)}$ and the energy barrier of fission E_f. Source: Seaborg (1958)/Yale University Press.

Table 17.4 Longest-lived actinide isotopes suitable for physical and chemical studies.

Actinium	^{227}Ac	21.8 yr
Thorium	^{232}Th	$1.41 \cdot 10^{10}$ yr
Protactinium	^{231}Pa	$3.28 \cdot 10^{4}$ yr
Uranium	^{238}U[a)]	$4.47 \cdot 10^{9}$ yr
Neptunium	^{236}Np[b)]	$1.55 \cdot 10^{5}$ yr
	^{237}Np	$2.14 \cdot 10^{6}$ yr
Plutonium	^{239}Pu	24 150 yr
	^{240}Pu	6570 yr
	^{242}Pu	$3.76 \cdot 10^{5}$ yr
	^{244}Pu	$8.1 \cdot 10^{7}$ yr
Americium	^{241}Am	433 yr
	^{243}Am	7380 yr
Curium	^{244}Cm	18.1 yr
	^{245}Cm	8540 yr
	^{246}Cm	4700 yr
	^{247}Cm	$1.6 \cdot 10^{7}$ yr
	^{248}Cm	$3.4 \cdot 10^{5}$ yr
	^{250}Cm[b)]	$1.1 \cdot 10^{4}$ yr
Berkelium	^{247}Bk[c)]	1380 yr
	^{249}Bk	320 d
Californium	^{249}Cf	350 yr
	^{252}Cf	2.6 yr
Einsteinium	^{253}Es	20.5 d
	^{254}Es	277 d
	^{255}Es	39.8 d
Fermium	^{257}Fm	100 d

a) Natural mixture (99.3% of ^{238}U, 0.72% of ^{235}U, and 0.006% of ^{234}U). Half-life given is for the major constituent ^{238}U.
b) Available only in very small amounts from neutron irradiations in thermonuclear explosions.
c) Available so far only in tracer quantities from charged particle irradiations.

configuration makes the early actinides "pseudo-d elements". This is impressively reflected in their atomic volumes, see Figure 17.27. The shapes of the three s and d electrons are broad and overlap strongly so that these elements are metals, d metals. The atomic volumes of d-transition metals exhibit a bathtub-like behavior with increasing numbers of electrons with a broad minimum in the middle, a shape that is also exhibited by the early actinides Th through Pu. In principle, f electrons are more localized or atomic-like. The lanthanide metal cerium having one 4f electron

Table 17.5 Electron configurations of f-block atoms and ions.

Element	Lanthanide series				Actinide series			
	Gaseous atom	M^{3+} (g)	Element	Gaseous atom	M^{+} (g)	M^{2+} (g)	M^{3+} (g)	M^{4+} (g)
La	$5d6s^2$		Ac	$6d7s^2$	$7s^2$	7s		
Ce	$4f5d6s^2$	4f	Th	$6d^27s^2$	$6d7s^2$	5f6d	5f	
Pr	$4f^36s^2$	$4f^2$	Pa	$5f^26d7s^2$	$5f^27s^2$	$5f^26d$	$5f^2$	5f
Nd	$4f^46s^2$	$4f^3$	U	$5f^36d7s^2$	$5f^37s^2$	$5f^36d$	$5f^3$	$5f^2$
Pm	$4f^56s^2$	$4f^4$	Np	$5f^46d7s^2$	$5f^57s$	$5f^5$	$5f^4$	$5f^3$
Sm	$4f^66s^2$	$4f^5$	Pu	$5f^67s^2$	$5f^67s^2$	$5f^6$	$5f^5$	$5f^4$
Eu	$4f^76s^2$	$4f^6$	Am	$5f^77s^2$	$5f^77s$	$5f^7$	$5f^6$	$5f^5$
Gd	$4f^75d6s^2$	$4f^7$	Cm	$5f^76d7s^2$	$5f^77s^2$	$5f^8$	$5f^7$	$5f^6$
Tb	$4f^96s^2$	$4f^8$	Bk	$5f^97s^2$	$5f^97s$	$5f^9$	$5f^8$	$5f^7$
Dy	$4f^{10}6s^2$	$4f^9$	Cf	$5f^{10}7s^2$	$5f^{10}7s$	$5f^{10}$	$5f^9$	$5f^8$
Ho	$4f^{11}6s^2$	$4f^{10}$	Es	$5f^{11}7s^2$	$5f^{11}7s$	$5f^{11}$	$5f^{10}$	$5f^9$
Er	$4f^{12}6s^2$	$4f^{11}$	Fm	$5f^{12}7s^2$	$5f^{12}7s$	$5f^{12}$	$5f^{11}$	$5f^{10}$
Tm	$4f^{13}6s^2$	$4f^{12}$	Md	$5f^{13}7s^2$	$5f^{13}7s$	$5f^{13}$	$5f^{12}$	$5f^{11}$
Yb	$4f^{14}6s^2$	$4f^{13}$	No	$5f^{14}7s^2$	$5f^{14}7s$	$5f^{14}$	$5f^{13}$	$5f^{12}$
Lu	$4f^{14}5d6s^2$	$4f^{14}$	Lr	$5f^{14}7s^27p_{1/2}$	$5f^{14}7s^2$	$5f^{14}7s$	$5f^{14}$	$5f^{13}$

undergoes a phase transition under a pressure and temperature in which the localized 4f electron becomes delocalized. All the other lanthanide solids have localized (atomic-like) f electrons. In the actinide series, however, the lightest solids have, due to a secondary relativistic effect (see below), delocalized (metallic-like) f electrons, whereas the heavier actinides have localized (atomic-like) f electrons. As the atomic number of the nucleus increases, the attraction between the electrons and the positively charged nucleus increases pulling the f electrons closer to the nucleus. This causes the shape of the 5f orbitals to change from overlapping (delocalized) to non-overlapping (localized), and the transition occurs mid-way in the series: Pu in its ground state has delocalized f electrons and Am has localized f electrons. As pointed out by Albers (2001), the 25% increase in volume seen when the room-temperature α phase of Pu is heated to reach the δ phase has been a puzzle in condensed matter physics. It is now clear that the f electrons in the δ phase of Pu are half-localized, suggesting that the transition from delocalized f electrons to localized f electrons (from metal to insulator) occurs between the different lattice symmetries of Pu. From Am to the heaviest actinides, the atomic volumes follow the continuous, almost linear decrease known as the lanthanide or actinide contraction.

The special properties of the actinides are also evident from their oxidation states, given in Table 17.6 as a function of the atomic number. In contrast to the lanthanides, a tendency to form high oxidation states (Th(IV), Pa(V), U(VI),

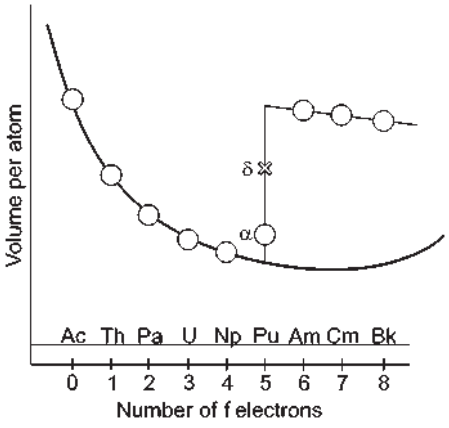

Figure 17.27 Atomic volumes (between 8 and 23 cm^3 g^{-1} per atom) as a function of the number of electrons. For d transition metals, the volumes per atom exhibit a bathtub-like behavior with a broad minimum. The volumes of Th though Pu follow the trend of the d transition metals due to the presence of a 6d electron in their ground-state electron configuration and due to the delocalization of their 5f electrons contributing to metallic bonding. The huge volume increase between plutonium and americium is due to the localization of the f electrons because atomic-like electrons no longer contribute to chemical bonding. The transition occurs between the different phases of solid plutonium where the δ phase has been arrested mid-way in the transition from metal-like to insulator-like behavior. Source: Modified from Nagame (2019).

Table 17.6 The oxidation states of the actinide elements.

Atomic number	**89**	**90**	**91**	**92**	**93**	**94**	**95**	**96**	**97**	**98**	**99**	**100**	**101**	**102**	**103**
Element	Ac	Th	Pa	U	Np	Pu	Am	Cm	Bk	Cf	Es	Fm	Md	No	Lr
Oxidation states							(2)			(2)	(2)	2	2	**2**	
	3	(3)	(3)	3	3	3	**3**	**3**	**3**	**3**	**3**	**3**	**3**	3	**3**
		4	4	4	4	**4**	4	4	4	(4)					
			5	5	**5**	5	5								
				6	6	6	6								
					7	(7)									

Bold type = most stable; ( ) = unstable.

Np(VII)) is observed in the first half of the actinides. Starting with Am, the trivalent oxidation state becomes the most stable one in aqueous solution except for No, where the early closure of the 5f shell with 14 electrons stabilizes the divalent oxidation state. Divalent ions are also known for Am, Cf, Es, Fm, and Md preferably in the solid state but also in aqueous solutions after pulse radiolysis or in the presence of strongly reducing agents. Relatively stable M(IV) ions are observed for Th through Bk where the latter is stabilized by the $5f^7$ configuration. M(IV) for Cm

and Cf exist only in the solid state as CmO_2 and CfO_2. The MO_2^+ and MO_2^{2+} ions are very stable and exhibit a linear O=M=O structure. MO_5^{3-} ions exist only in alkaline solution; in acidic solution, they are strongly oxidizing.

With respect to the chemical properties of the actinides, a new effect becomes central importance: with increasing atomic number Z, the action of the positive nuclear charge on the electrons with radially symmetric s and $p_{1/2}$ orbitals increases in such a way that their velocity approaches the velocity of light. The resulting relativistic mass increase leads to their increasing localization and energetic stabilization, which is termed primary relativistic effect. The resulting larger screening of the nuclear charge for the non-spherical $p_{3/2}$, d, and f electron orbitals leads to their expansion (delocalization) and energetic destabilization, termed the secondary relativistic effect. The third relativistic effect is the strong spin–orbit splitting between, for example, the $p_{1/2}$ and the $p_{3/2}$ or the $d_{3/2}$ and the $d_{5/2}$ electrons with a strong energetic stabilization of the state with the lower angular momentum. In the early actinides, it is the secondary relativistic effect that leads to the delocalization of the 5f electrons, making them available for chemical bonding (Table 17.6) and causing a wealth of "unusual" oxidation states. As relativistic effects increase approximately with Z^2, we anticipate that their influence on the chemical properties of the transactinides will become of utmost importance.

The analogy between the 4f and 5f elements is obvious from Figure 17.28, in which the ionic radii of actinide and lanthanide 3^+ ions in aqueous solution are plotted as a function of the atomic number: the contraction of the actinide ions runs parallel to that of the lanthanide ions except for No^{3+} and Lr^{3+} where the $5f^{14}$ shell closure is associated with an unusually large ionic radius.

It has long been known that ionic radii of the trivalent actinide ions decrease with increasing atomic number and this tendency is called the actinide contraction similar to the lanthanide contraction. This contraction is due to the increasing nuclear charge which can only partially screened by the added f electrons. Therefore, their elution from a cation-exchange column by using the eluting agent α-hydroxy iso-butyric acid (α-HIB) occurs in the inverse order of atomic number for both lanthanides and actinides. The elution sequence depends on a balance between the adsorption of the ionic species to the resin and the relative stability of the aqueous complexes formed with the eluting agent which is correlated with the variation of ionic radius with atomic number; stability of complexes between the smaller size of cations (hard ions) and α-HIB is larger than that between the larger size of cations and the eluting agent.

The determination of the ionic radii of the heaviest actinides is of particular interest to experimentally assess the magnitude of the contraction influenced by relativistic effects on valence electrons. The investigation to deduce the ionic radii of Md^{3+} and Lr^{3+} by using cation-exchange chromatography was conducted in the work of Brüchle et al. (1988). The isotopes ^{260}Lr ($t_{1/2}$ = 3 mintues) and ^{255}Md ($t_{1/2}$ = 27 minutes) were produced in the bombardment of a ^{249}Bk target with ^{18}O beams, and distribution coefficients (K_d) in 0.05 M α-HIB solution at pH = 4.85 were measured. This is based on the fact that ionic radii of aquo ions of the same charge and coordination number undergoing the same type of chemical

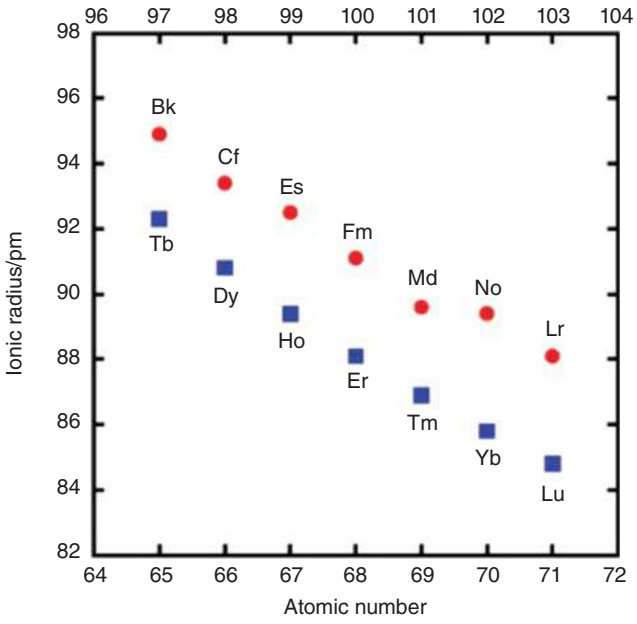

Figure 17.28 Ionic radii of trivalent lanthanide (blue) and actinide ions (red) based on the crystallographic radii for lanthanide ions with CN = 6 by Templeton and Dauben (Templeton and Dauben 1954). The well-known lanthanide contraction finds its analogy in the actinide contraction. The ionic radii of the heaviest actinides are based on their elution positions from cation exchange columns with α-hydroxi isobutyrate calibrated with the elution positions of the lanthanides and the known ionic radii of these trivalent ions. Source: Modified from Nagame (2019).

process are correlated linearly with the logarithm of K_d in a given chromatographic system. From the elution positions of Md and Lr, ionic radii of Md^{3+} and Lr^{3+} were evaluated to be 89.6 ± 0.1 pm and 88.1 ± 0.1 pm, respectively. The ionic radius of Fm^{3+} was also measured from the K_d value determined in the separate very similar experiments: ≈91.1 pm. The measurement of the ionic radius of No^{3+} has been essential to understand the contraction. However, because of the strong stability of the completely filled 5f electron shell, the divalent state is most stable for No in aqueous solution. To determine the ionic radius of No^{3+}, the No^{2+} ion has to be oxidized to No^{3+} that should be held in the 3+ oxidation state during the experiment. A new experimental approach was undertaken by Bilewicz using strong oxidizing agent H_2IO_6 to measure the ionic radius of No^{3+}. The isotope ^{259}No ($t_{1/2}$ = 58 minutes) was produced in the reaction of $^{248}Cm(^{18}O, \alpha 3n)$. Produced No^{2+} was oxidized by H_2IO_6 and loaded together with some lanthanide tracers on a chromatographic column packed with the cryptomelane MnO_2 inorganic ion exchanger. Cryptomelane MnO_2 shows excellent ion-exchange selectivity toward cations, and in acidic solutions, it exhibits strong oxidizing properties. Thus, No^{3+} was expected to be held in the column. From the elution curve in 0.5 M HNO_3, the K_d value of No^{3+} was determined and the radius was evaluated to be

Table 17.7 Ionic radii of lanthanide and actinide elements.[a)]

Lanthanide series			Actinide series		
Element	**M^{3+} (nm)**	**M^{4+} (nm)**	**Element**	**M^{3+} (nm)**	**M^{4+} (nm)**
La	0.1061		Ac	0.119	
Ce	0.1034	0.092	Th	(0.108)	0.0972
Pr	0.1013	0.090	Pa	(0.105)	0.0935
Nd	0.0995		U	0.1041	0.0918
Pm	(0.0979)		Np	0.1017	0.0903
Sm	0.0964		Pu	0.0997	0.0887
Eu	0.0950		Am	0.0982	0.0878
Gd	0.0938		Cm	0.0970	0.0871
Tb	0.0923	0.084	Bk	0.0949	0.0860
Dy	0.0908		Cf	0.0934	0.0851
Ho	0.0894		Es	0.0925	
Er	0.0881		Fm	0.0911	
Tm	0.0869		Md	0.0896	
Yb	0.0858		No	0.0894	
Lu	0.0848		Lr	0.0881	

a) Suggested values in parentheses.

89.4 ± 0.7 pm that was in between radii of Md^{3+} and Lr^{3+}, and closer to that of Md^{3+}.

Table 17.7 gives reported ionic radii of lanthanide and actinide elements, and Figure 17.28 shows the ionic radii of the trivalent lanthanide and actinide ions as a function of atomic number. The contraction of the actinide ions runs parallel to that of the lanthanide ions, although the radii of No^{3+} and Lr^{3+} are slightly larger than the systematic trend.

The first ionization potential (IP_1) most sensitively reflects the outermost electronic configuration of every atom. Laser spectroscopy and resonance ionization mass spectroscopy (RIMS) of weighable amounts of actinides up to einsteinium (Es), including actinium (Ac) and protactinium (Pa), have been extensively performed to measure IP_1 values (Köhler et al. 1997, Chapter 20). However, IP_1 values of heavy actinides with $Z \geq 100$ have not been measured experimentally due to the limitation of one atom-at-a-time condition. Sato et al. successfully measured the IP_1 of heavy actinides from Fm through Lr using a surface ionization technique coupled to a mass separator (Chapter 20). The surface ion source installed at the JAEA-ISOL (Japan Atomic Energy Agency-isotope separator on-line) was applied for measuring the ionization of the short-lived isotopes ^{249}Fm ($t_{1/2} = 2.6$ minutes), ^{251}Md ($t_{1/2} = 4.27$ minutes), ^{257}No ($t_{1/2} = 24.5$ seconds), and ^{256}Lr ($t_{1/2} = 27$ seconds) that were produced in the $^{243}Am + {}^{11}B$, $^{243}Am + {}^{12}C$, $^{248}Cm + {}^{13}C$, and $^{249}Cf + {}^{11}B$

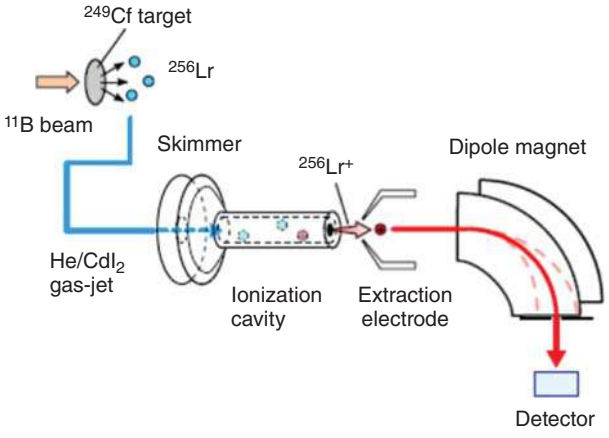

Figure 17.29 Experimental setup for the surface ionization technique with ^{256}Lr coupled to a mass separator. Source: Nagame (2019)/De Gruyter.

reactions, respectively, at the JAEA tandem accelerator. The number of ions collected after the mass separation was determined by α-spectrometry to evaluate ionization efficiencies. The obtained IP_1 values were in good agreement with those predicted by state-of-the-art relativistic calculations (Figures 17.29 and 17.30).

Laser resonance ionization spectroscopy of No, using ^{254}No ($t_{1/2} = 51.2$ seconds) produced in the reaction of ^{208}Pb with ^{48}Ca, was also performed. The IP_1 has been measured with extreme precision to be $6.626\,21 \pm 0.000\,05$ eV (Block 2019) from the convergence of measured Rydberg series. Both results on IP_1 of No obtained by the RADRIS method (Chapter 20) and surface ionization are in good agreement with each, thus providing independent validation. The new technical approaches give hope to be extended into the transactinides.

Table 17.8 shows the first ionization potentials of lanthanide and actinide elements. In the light actinides, significant deviations of the IP_1 from a smooth trend are observed due to complex configurations of valence electronic states because of the close energy differences between the 5f and 6d orbitals. Similar to the well-established behavior for the lanthanides, values of the heavy actinides up to No increase with filling up the 5f orbital. That of Lr is the lowest among the actinides in very good agreement with theoretical calculations which predict the $7s^2 7p_{1/2}$ configuration. These results clearly demonstrate that the 5f orbital is fully filled at No with the $[Rn]5f^{14}7s^2$ configuration and that Lr has a weakly bound electron, a $7p_{1/2}$ electron, see Table 17.5. In analogy to the lanthanide series, the results unequivocally verify that the actinide series end with Lr (Sato et al. 2018).

The colors of the various oxidation states of the actinides Ac to Cf are listed in Table 17.9. Similar to the lanthanides, the color intensity of the M^{3+} ions increases with the distance from the electron configurations f^0 and f^7. The analogy between actinides and lanthanides is also valid for the magnetic susceptibilities, for example, $U(VI) \approx Pa(V) \approx Th(IV) \approx Ac(III) \approx La(III)$ or $Pu(VI) \approx Np(V) \approx U(IV) \approx Pa(III) \approx Pr(III)$. The redox potentials of the actinide ions in 1 M $HClO_4$ vs. the

Table 17.8 First ionization potentials (IP_1) of lanthanide and actinide elements.

Element	IP_1 (eV)	Element	IP_1 (eV)
La	5.5769	Ac	5.3802
Ce	5.5386	Th	6.3067
Pr	5.4703	Pa	6.0753
Nd	5.5250	U	6.1940
Pm	5.5800[a)]	Np	6.2655
Sm	5.6437	Pu	6.0258
Eu	5.6704	Am	5.9738
Gd	6.1498	Cm	5.9914
Tb	5.8638	Bk	6.1978
Dy	5.9391	Cf	6.2817
Ho	6.0215	Es	6.3676
Er	6.1077	Fm	6.52[b)]
Tm	6.1843	Md	6.59[b)]
Yb	6.2542	No	6.62[b)]/6.62621[c)]
Lu	5.4259	Lr	4.96[b)]

The data are from the NIST data base, while those for the heavy actinides Fm through Lr are recently measured values (see text).
a) Suggested value.
b) Measured values by the surface ionization method.
c) Measured value by the laser resonance ionization method.

Table 17.9 Colors of the actinide ions.

	M^{3+}	M^{4+}	MO_2^+	MO_2^{2+}	MO_5^{3-}
Actinium	Colorless	—	—	—	—
Thorium	—	Colorless	—	—	—
Protactinium	—	Colorless	—	—	—
Uranium	Reddish-brown	Green	—	Yellow	—
Neptunium	Blue to crimson	Yellowish green	Green	Pink	Dark green
Plutonium	Violet	Orange	Reddish	Orange	Dark green
Americium	Pink	Pink[a)]	Yellow	Yellowish	—
Curium	Pale green	Pale yellow[a)]	—	—	—
Berkelium	Green	Yellow	—	—	—
Californium	Green	—	—	—	—

a) Fluoro complexes.

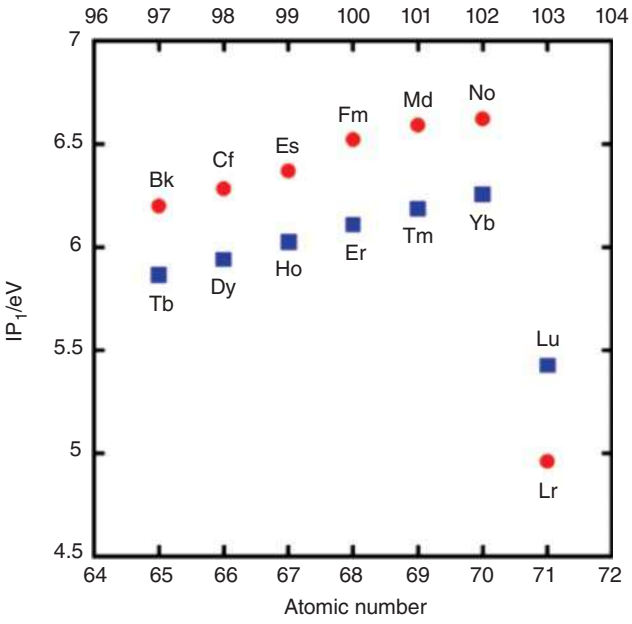

Figure 17.30 Variation of the experimental IP_1 values of heavy actinides and heavy lanthanides with atomic numbers. The ^{256}Lr atoms recoiling from a ^{249}Cf target were promptly transported to the ionization site (ionization cavity) by a He/CdI_2 gas-jet transport system. The transported products were surface-ionized, then, the ionized ^{256}Lr atoms were extracted and mass-separated. The number of ^{256}Lr ions after the mass-separation was determined by α-spectrometry. Source: Nagame (2019).

standard $H_2/2H^+$ potential are shown in Figure 17.31. The redox reactions M^{4+}/M^{3+} are fast and reversible; there is only one electron involved and no break in the binding structure. The same holds for the pairs MO_2^{2+}/MO_2^+. Redox reactions MO_2^{2+}/M^{4+}, MO_2^{2+}/M^{3+}, and MO_2^+/M^{4+} are slow and not reversible because of a break in the binding structure. Ions such as Pu^{4+} and AmO_2^+ show disproportionation. The aqueous chemistry of Pu is one of the most complicated ones because Pu(III), Pu(IV), Pu(V), and Pu(VI) can coexist in the same solution.

The hydrolysis reaction,

$$M(OH_2)_x^{n+} \rightarrow M(OH_2)_{x-1}(OH)^{(n-1)+} + H^+ \tag{17.50}$$

in which the aquo cations M^{5+}, M^{4+}, and M^{3+} are involved, indicates that the latter are acids. Th^{4+} in 1 M acid exists as $Th(OH)^{3+}$. $Pu^{4+}(aq)$ exists only in strong acid. $Pa^{5+}(aq)$ exists as $Pa(OH)_2^{3+}$ with continuing hydrolysis and polymerization. Polymerization involves polynuclear complexes with M–OH–M or M–O–M bridges. For example, one is familiar with the species $U_6(OH)_{15}^{9+}$ and $U_6O_4(OH)_4^{12+}$. Pu(IV) tends extremely strongly to polymerization, and molecular weights up to 10^{10} have been detected. The tendency toward hydrolysis is $M^{4+} > MO_2^{2+} > M^{3+} > MO_2^+$. UO_2^{2+} forms dimers in acidic solution and precipitates with ammonia as yellow $(NH_4)_2U_2O_7$.

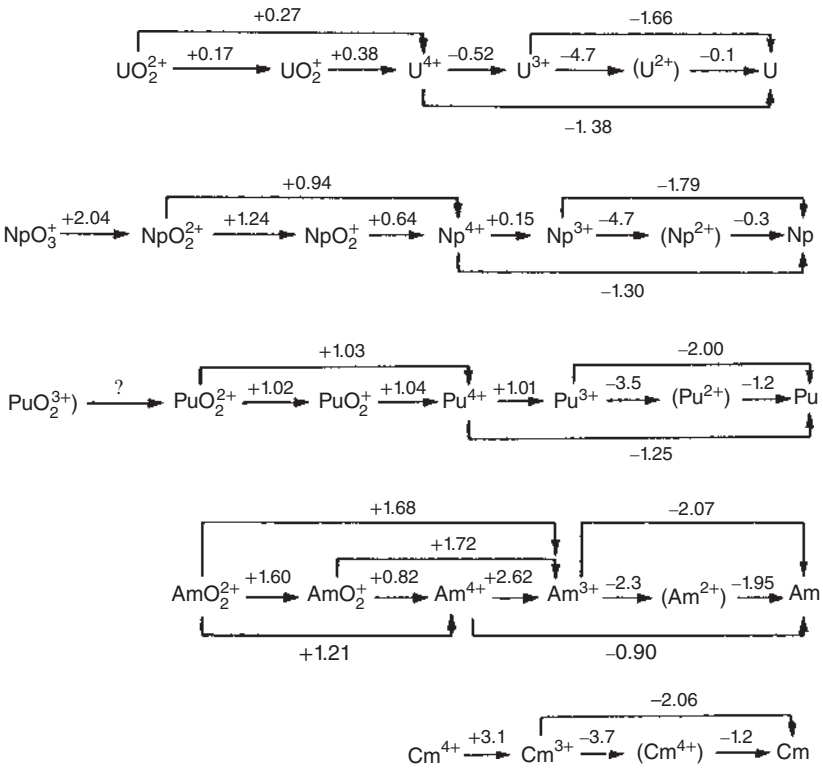

Figure 17.31 Redox potentials for the actinides U through Cm in 1 M $HClO_4$ vs. standard $H_2/2H^+$ potential.

The tendency for complex formation runs parallel to the tendency for hydrolysis. The complexing ligand replaces part of the water molecules in the inner hydration sphere. The sequences are

$$M^{4+} > MO^{2+} > M^{3+} > MO_2^+$$

$$F^- > NO_3^- > Cl^- > ClO_4^- \tag{17.51}$$

$$CO_3^{2+} > \text{oxalate}^{2-} > SO_4^{2-}$$

For similar ions, the tendency for complexation increases with decreasing ionic radius: the actinide ions are hard acceptors. PO_4^{3-} and organic phosphates form strong complexes with MO_2^{2+} and M^{4+}. This is made use in the PUREX process with tri-butyl phosphate $(n\text{-but})_3P{=}O$. The actinide ions prefer O compounds with free electron pairs which are present in the chelating agents such as β-diketones, EDTA, TTA, and α-HiB. Complexation of the actinides by inorganic and organic ligands is very important for their chemical separation and their behavior in the environment. Examples are the separation of trivalent actinides by complexation with α-hydroxy

acids and the high solubility of U(VI) due to complexation with carbonate ions to give the *tris*-carbonato complex $[UO_2(CO_3)_3]^{4-}$ found in seawater.

Similar to the lanthanides, actinides in the elemental state are reactive electropositive metals, pyrophoric, and react with water vapor, oxygen, and nitrogen in finely dispersed form. This often necessitates working in glove boxes under an Ar atmosphere. For the heaviest actinides, shielding against fission neutrons is required. Strong reducing agents are necessary to prepare the metals from their compounds, for instance, in small amounts (≤milligrams) by reduction of the halides by Li or Ba at 1200 °C (e.g. $2PuF_3 + 3Ba \rightarrow 2Pu + 3BaF_2$). In large amounts, for example, the oxides of Th, U, and Pu are reduced with La or Th metal. The actinides are distilled off and cleaned simultaneously. Cleanest samples are obtained in the Van Arkel process in which the metal iodides are formed and decomposed on a hot filament.

S. Fried et al. (1958) wrote a historical survey of the methods used in the Metallurgical Laboratory during World War II in the first preparations of Pu metal. The first synthesis in November 1943 yielded an amount of 3 μg of Pu metal. The apparatus used in this experiment is depicted in Figure 17.32. The reduction according to the above equation was performed in a double-crucible system inside an oven at 10^{-6} mm Hg. The beryllia outer crucible containing the reductant metal and, below, a refractory crucible containing the PuF_3 pellet were produced beforehand from a paste of finely milled BeO with 6 M HNO_3, formed and burned at 1000 °C and subsequently outgassed at 1600 °C in vacuum by applying 12 V and 14 A to the tantalum wire coil, Figure 17.32. At the optimum temperature of 1150 °C, the Ba evaporated

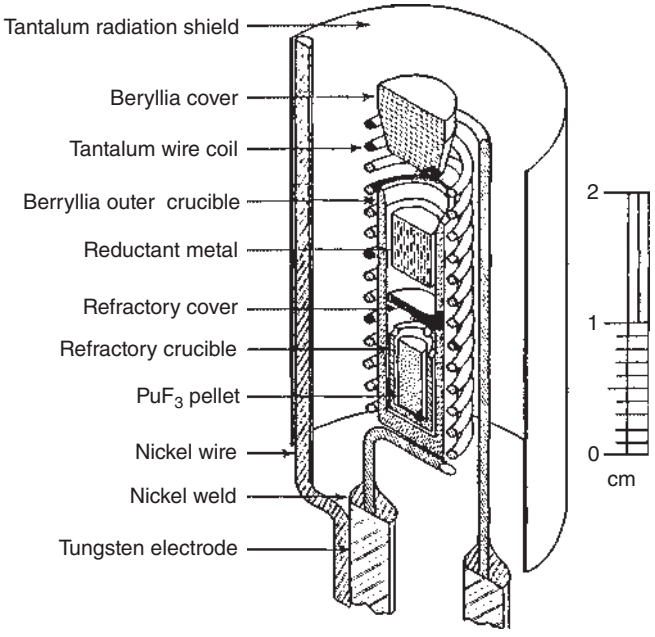

Figure 17.32 Double crucible system for the reduction of PuF_3 with Ba to obtain Pu metal. Source: Fried et al. (1958), figure 1 (p. 184)/Elsevier.

and reduced the PuF_3 to Pu metal, while the BaF_2 slag was sucked up by the porous BeO crucible. Subsequently, the metal density was determined.

Metal densities and some other properties of the actinides in the metallic state are listed in Table 17.10. The number of metallic modifications and the densities are remarkably high for U, Np, and, in particular, Pu. The lattice symmetries of

Table 17.10 Properties of the actinide metals.

Element	Melting point (°C)	Enthalpy of vaporization at 25 °C (kJ mol^{-1})	Lattice symmetry	Temp. range of stability (C°)	X-ray density (g cm^{-3})	Atoms per unit cell	Metallic radius CN 12 (10^{-8} cm)
Actinium	1050	418	f.c.c.		10.01	4	1.878
Thorium	1750	598	α, f.c.c.	<~1360	11.724	4	1.798
			β, b.c.c.	~1360–1750	11.10	2	1.80
Protactinium	1572	660	α, b.c. tetragonal	Below 1165	15.37	2	1.642
			β, b.c.c.	1165–1572	13.87	2	1.775
Uranium	1133	536	α, orthorhombic	Below 668	19.16	4	1.542
			β, tetragonal	668–775	18.11	30	1.548
			γ, b.c.c.	775–1133	18.06	2	1.548
Neptunium	637	465	α, orthorhombic	Below 280	20.45	8	1.503
			β, tetragonal	280–576	19.36	4	1.511
			γ, b.c.c.	576–637	18.04	2	1.53
Plutonium	640	342	α, monoclinic	Below 122	19.86	16	1.623
			β, monoclinic	122–207	17.70	34	1.571
			γ, othorhombic	207–315	17.14	8	1.588
			δ, f.c.c.	315–457	15.92	4	1.640
			δ′, b.c. tetragonal	457–479	16.00	2	1.640
			ε, b.c.c.	479–640	16.51	2	1.592
Americium	1173	284	α, hexagonal	Below 658	13.6	4	1.730
			β, f.c.c.	793–1004	13.65	4	1.730
			γ	~1050–1173			
Curium	1345	387	α, hexagonal	Below ~ 1277	13.5	4	1.743
			β, f.c.c.	1277–1345	12.9	4	1.782
Berkelium	1050	310	α, hexagonal	Below 930	14.79	4	1.704
			β, f.c.c.	930–986	13.24	4	1.767
Californium	900	196	α, hexagonal	Below 600	15.10	4	1.694
			β, f.c.c.	>725	18.74	4	2.030
Einsteinium	860	133	α, hexagonal	Below 860		4	
			β, f.c.c.		8.84	4	2.03

f.c.c. = face-centered cubic, b.c.c. = body-centered cubic, b.c. = body-centered.

the light actinides resemble rather those of the d-transition elements, not those of the lanthanides. They end up in body-centered cubic (b.c.c.) symmetry close to the melting point. Some modifications of these elements are of low symmetry; this is an exception for metals that is explained by the properties of the 5f electrons. The properties of Am and the following elements (double hexagonal close-packed (d.h.c.p.), at low temperatures) correspond to those of the lanthanides. The properties of the actinide metals are unique in that they are not only different from the properties of the lanthanides but also different from other elements. They are important objects for the study of metals in a general sense. To be complete, we mention briefly that some actinide metals, for example, Cm, Bk, and Cf, can be compacted by high pressures of 30–40 GPa ($3–4 \cdot 10^5$ atm) whereby the non-binding (localized) electrons are transformed into binding (delocalized) electrons. This is accompanied by a collapse of the atomic volume $\Delta V/V$ of 20% and a transition into the low-symmetry orthorhombic structure which is normal for U and Np with their binding 5f electrons. Another feature is the superconductivity of actinides with delocalized 5f electrons. For example, Pa becomes superconducting at 0.42 K. The localization of the 5f electrons in the higher actinides leads to paramagnetism. Pu behaves anomalously: it does not exhibit superconductivity or paramagnetism. The study of conductivity at low temperatures is a challenge because the radioactivity is heating.

Actinide(III) compounds are similar to lanthanide(III) compounds. Th(III) is unstable. In aqueous solution, U(III) liberates hydrogen, whereas Np(III) and Pu(III) are oxidized in the presence of air. The properties of actinides(IV) are similar to those of Ce(IV) and Zr(IV). Th(IV) is very stable; U(IV) and Np(IV) are stable in aqueous solution, but are oxidized slowly in the presence of air to U(VI) and Np(V). Pu(IV) is stable at high concentrations of acid or of complexing agents, otherwise it disproportionates to Pu(III) and Pu(VI). In moist air and at temperatures up to 350 °C, PuO_2 is slowly oxidized to PuO_{2+x} and hydrogen is set free. PuO_{2+x} contains Pu(VI) on the cationic sites of the fluorite structure and additional oxygen ions on octahedral interstices. In solution, Am(IV) and Cm(IV) are known only as fluoro complexes. Bk(IV) behaves similarly to Ce(IV). All actinides form sparingly soluble iodates and arsenates. The basicity decreases in the order $Th^{4+} > U^{4+} \approx Pu^{4+} > Ce^{4+} > Zr^{4+}$. In the oxidation state V, Pa shows distinct differences from U and the following elements. Hydrolysis of Pa(V) in aqueous solutions can only be prevented by the presence of concentrated acids (e.g. 8 M HCl) or of complexing agents such as F^-. In contrast to Pa(V), U(V), Np(V), and Pu(V) form dioxocations MO_2^+ in which oxygen is strongly bound by the metal. Obviously, the formation of these dioxocations depends on the availability of a sufficient number of f electrons. In aqueous solution, UO_2^+ exists in small amounts in equilibrium with U^{4+} and UO_2^{2+}. NpO_2^+ is quite stable, whereas PuO_2^+ and AmO_2^+ disproportionate easily.

The oxidation state VI is preferred by U, but it is also found with Np, Pu, and Am. In aqueous solution, this oxidation state always exists in the form of "yl" ions MO_2^{2+}. These ions are not formed by hydrolysis and are also stable at high acid concentrations. In a linear arrangement, the oxygen atoms are firmly bound by the metals and the interatomic distance is in agreement with the formation of double bonds.

Four to six ligands are coordinated in the equatorial plane perpendicular to the linear MO_2^{2+} group.

By application of strongly oxidizing agents, for example, by melting with alkali peroxides, Np and Pu can be transformed into the oxidation state VII.

Actinide metals react with hydrogen at about 300 °C to form non-stoichiometric metallic hydrides of composition MH_2 to MH_3. The formation of uranium hydride is reversible at higher temperatures and can be used to store tritium. The formation of non-stoichiometric compounds is very pronounced for the oxides. These contain mixed valencies to compensate for defects at the cation and anion lattice positions in order to achieve electrical neutrality. The phenomenon is pronounced between U and Cm. When Pa_2O_5 is reduced with H_2, one obtains $PaO_{2.19}$, $PaO_{2.33}$, $PaO_{2.41}$, and $PaO_{2.43}$, which are distinguishable roentgenographically. The U–O system is extremely complex; between UO_2 and UO_3, there exist about 10 phases, some even in various modifications. By statistically building in excess oxygen into UO_2, the CaF_2 structure of UO_2 is weakened until $UO_{2.4}$ is reached and, from thereon until UO_3, six phases with new structures show up. For Np, the situation is simpler, exhibiting the phases NpO_2 through $NpO_{2.5}$ by subsequently building in Np(V). Pu has oxides of Pu(III) until Pu(IV) with $PuO_{1.6}$ in between. There is no oxide of Pu(VI). Beginning with americium, the stoichiometric An_2O_3 is dominant with CmO_2 and CfO_2 as exceptions.

An interesting class of compounds are the metal–organic compounds of the actinides. Here, derivatives of 1,3 cyclopentadiene are mentioned in the first place, where the cyclopentadienyl anion (Cp^-, $Cp = C_5H_5$) has aromatic character with three π-electron pairs that can contribute to the electron budget of the complex-forming central atom. In 1956, G. Wilkinson synthesized the first metallacyclopentadienyl complex of an actinide, Cp_3UCl, having a red–brown color and a sublimation temperature of 260 °C. In 1965, F. Baumgärtner synthesized Cp_3NpCl and $PuCp_3$, the latter being a green compound with a sublimation temperature between 140 and 165 °C. Later, compounds with indenyl- and cyclooctatetraenyl-π donors were also synthesized, for example, uranocene, $U(C_8H_8)_2$. The binding character of these compounds is ionic through σ covalent. They are of theoretical interest for the study of chemical bonds in the 5f series. The synthesis of metallacyclopentadienyl complexes is carried out by mixing KCp with an actinide compound AnX_n in tetrahydrofurane, extraction of the metal–organic complex by the solvent, and sublimation.

The behavior of the minor actinides in the environment will be covered separately in Chapter 22.

17.8 Chemical Properties of the Transactinides

The chemical properties of the transactinides have been repeatedly reviewed by the present author. Two approaches have to go hand in hand to investigate these properties and to understand their origin. These are:

- Theoretical predictions of the electronic structure of the elements and the energy levels of the electrons in the atoms and in their compounds by relativistic quantum-chemical calculations.
- Ultrasensitive chemical investigations with the microamounts of the elements available on-line at a heavy-ion accelerator down to one atom-at-a-time chemistry.

Both of these are most informative if they are also carried out for the lighter homologs of the transactinides under exactly the same conditions and to the pseudo-homologs in the early actinides, for example, Th for group IV elements, Pa for group V elements, U for group VI elements. Straightforward extrapolations in the periodic table for an assessment of the chemical properties have also been done on occasion; however, precise information about the properties cannot be obtained in this way because of the relativistic effects in the electron shells, mentioned in the previous section, particularly as these effects increase nonlinearly with Z^2.

Relativistic atomic calculations provide information about expected electron configurations in the ground state. The relativistic effects lead to the energetic stabilization of the s and $p_{1/2}$ orbitals and to their spatial contraction, and indirectly to the destabilization and expansion of the $p_{3/2}$, d, and f orbitals. Furthermore, subshells split due to the relativistic spin–orbit coupling. These have an appreciable influence on the properties of these elements, such as electron configurations, ionization potentials, and ionic radii. The atomic wave functions have to be inserted into suitable relativistic molecular orbital calculations that describe the properties of various compounds of the transactinides that can be compared to experimental observations. Methodical developments in both fields, theoretical and experimental over decades, have brought substantial advances such that, at this time, theoretical studies of the chemical properties of superheavy elements are done with fully relativistic, four-component, density functional theory calculations implementing the non-collinear spin-polarized (SP) approximation and large optimized sets of basis functions, while experimental studies are being carried out fully automatically on atoms with half-lives of less than a second that are being produced with cross sections on the picobarn level.

17.8.1 Prediction of Electron Configurations and the Architecture of the Periodic Table of the Elements

Electronic configurations and oxidation states predicted for the transactinide elements 104–120 on the basis of relativistic Hartree–Fock calculations are listed in Table 17.11. An important result of these calculations is the splitting of the p levels into a $p_{1/2}$ sublevel for two electrons and a $p_{3/2}$ sublevel for four electrons.

Elements 104–112 are transition elements ($6d^2s^2$ to $6d^{10}s^2$). For the first half of these elements, high oxidation states are predicted. Elements 112 and 114 are of special interest because of the relativistic stabilization of the filled $7s^26d^{10}$ level of 112 and the filled $7s^2$ level and $7p_{1/2}^2$ sublevel of 114, which give these elements a noble character, and it has long been hypothesized whether these elements exhibit a noble-gas-like chemical behavior. The relativistic stabilization of the $7p_{1/2}^2$

Table 17.11 Predicted electron configurations and some other predicted properties of the superheavy elements 104 through 120.

Element	Electrons in the outer orbitals	Preferred oxidation state	Ionization potential (eV)	Ionic radius in the metallic state (10^{-8} cm)	Density (g cm^{-3})
104	$6d^2 7s^2$	IV	5.1	1.66	17.0
105	$6d^3 7s^2$	V	6.2	1.53	21.6
106	$6d^4 7s^2$	VI	7.1	1.47	23.2
107	$6d^5 7s^2$	VII	6.5	1.45	27.2
108	$6d^6 7s^2$	VIII	7.4	1.43	28.6
109	$6d^7 7s^2$	VI	8.2	1.44	28.2
110	$6d^8 7s^2$	IV	9.4	1.46	27.4
111	$6d^9 7s^2$	III	10.3	1.52	24.4
112	$6d^{10} 7s^2$	0	11.1	1.60	16.8
113	$7s^2 7p^1$	I	7.5	1.69	14.7
114	$7s^2 7p^2$	0	8.5	1.76	15.1
115	$7s^2 7p^3$	I	5.9	1.78	14.7
116	$7s^2 7p^4$	II	6.8	1.77	13.6
117	$7s^2 7p^5$	III	8.2	—	—
118	$7s^2 7p^6$	0	9.0	—	—
119	$8s^1$	I	4.1	2.6	4.6
120	$8s^2$	II	5.3	2.0	7.2

sublevel is also expected to influence the oxidation states of elements 115–117. With increasing atomic number, the energy difference between the $p_{1/2}$ and $p_{3/2}$ sublevels increases, with the result that only the $p_{3/2}$ electrons will be available as valence electrons. Element 118 should be a noble gas, but, due to its low ionization energy, compounds should easily be formed in which this element has preferentially the oxidation state IV.

The most stable electron configurations of elements 122 through 155 from the atomic calculations by Mann and Waber (1970) are listed in Table 17.12. They form the so-called superactinide series. In this series, the 8s and $8p_{1/2}$ shells are filled: beginning with element 123, a 6f shell is filled; beginning with element 125, a 5g shell is subsequently filled with 18 electrons. There is a competition between the filling of the 6f levels by the bonding of $7d_{3/2}$ electrons so that the full $6f^{14}$ configuration is only achieved in element 154. In particular, the 5g, 6f, and 7d orbitals are energetically so close to each other that these electrons are not filled in separate series such as a separate 6f series, a separate 5g series, and a separate 7d series, but are mixed into a common superactinide series. The expected electron configurations of elements 156–172 are contained in Table 17.13. The resulting architecture of the periodic table is shown in Figure 17.33.

Table 17.12 Expected electron configurations of the superactinides $Z = 121–155$.

Element	Electron configurations from Mann and Waber (plus $Z = 118$ core)						
Z	$8s_{1/2}$	$8p_{1/2}$	$5g_{7/2}$	$5g_{9/2}$	$6f_{5/2}$	$6f_{7/2}$	$7d_{3/2}$
122	2	1					1
123	2	1			1		1
124	2	1			3		
125	2	1	1		3		
126	2	2	2		2		
127	2	2	3		2		
128	2	2	4		2		
130	2	2	6		2		
132	2	2	8		2		
134	2	2	8		4		
136	2	2	8	2	4		
138	2	2	8	4	3		1
140	2	2	8	6	3		1
141	2	2	8	7	2		2
142	2	2	8	8	2		2
144	2	2	8	10	1		3
145	2	2	8	10	3		2
146	2	2	8	10	4		2
149	2	2	8	10	6		3
150	2	2	8	10	6		4
152	2	2	8	10	6	3	3
154	2	2	8	10	7	7	
155	2	2	8	10	7	7	1

Source: Modified from Mann and Waber (1970).

17.8.2 Methods to Investigate the Chemistry of the Transactinides

For a chemical reaction

$$aA + eE \Leftrightarrow xX + zZ \tag{17.52}$$

the change in the Gibbs free energy is

$$\Delta G = \Delta G_0 + RT\frac{[X]^x \cdot [Z]^z}{[A]^a \cdot [E]^e} \tag{17.53}$$

where the square brackets indicate activities (concentrations, partial pressures) of the substances involved. According to the law of "mass action,"

$$\frac{[X]^x \cdot [Z]^z}{[A]^a \cdot [E]^e} = K \tag{17.54}$$

Table 17.13 Expected electron configurations of the elements $Z = 156–172$.

Element Z	$7d_{3/2}$	$7d_{5/2}$	$8p_{1/2}$	$8p_{3/2}$	$9s_{1/2}$	$9p_{1/2}$
156	2		2			
157	3		2			
158	4		2			
159	4	1	2			
160	4	2	2			
161	4	3	2			
162	4	2	2			
163	4	5	2			
164	4	6	2			
165	4	6	2		1	
166	4	6	2		2	
167	4	6	2		2	1
168	4	6	2		2	2
172	4	6	2	4[a)]	2	

a) It should be noted that in the calculations by Fricke and Waber (1971), after filling the $9p_{1/2}$ orbital in elements 167 and 168, the $8p_{3/2}$ orbital is filled in elements 169 through 172 rather than the $9p_{3/2}$ orbital.

Source: Modified from Fricke et al. (1971).

where K is the equilibrium constant. In equilibrium, $\Delta G = 0$, and

$$\Delta G_0 = RT \ln K \tag{17.55}$$

This is well established for macroscopic quantities where, for example, ions of the metal M are constituents of A and X at the same time, and Eq. (17.52) characterizes a dynamical, reversible process in which reactants and products are continuously transformed into each other back and forth even at equilibrium. If only one atom of M is present, it cannot be a constituent of A and X at the same time, and at least one of the activities on the left- or right-hand side of Eq. (17.52) is zero. Consequently, an equilibrium constant can no longer be defined, and the same holds for the thermodynamic function ΔG_0. Does it make sense, then, to study chemical equilibria with one atom?

Guillaumont et al. (1989, 1991), in view of this dilemma, pointed out that chemical speciation of atoms at the tracer scale is usually feasible with partition methods in which the species to be characterized is distributed between two phases. This can be an aqueous phase or a solid phase and the gas phase. According to Guillaumont et al. (1989), single-atom chemistry requires the introduction of a specific thermodynamic function, the single-particle Gibbs free energy. An expression equivalent to the law of "mass action" is derived by Guillaumont et al. in which activities (concentrations or partial pressures) are replaced by a probability of finding the species in the appropriate phase. According to this law, an equilibrium constant,

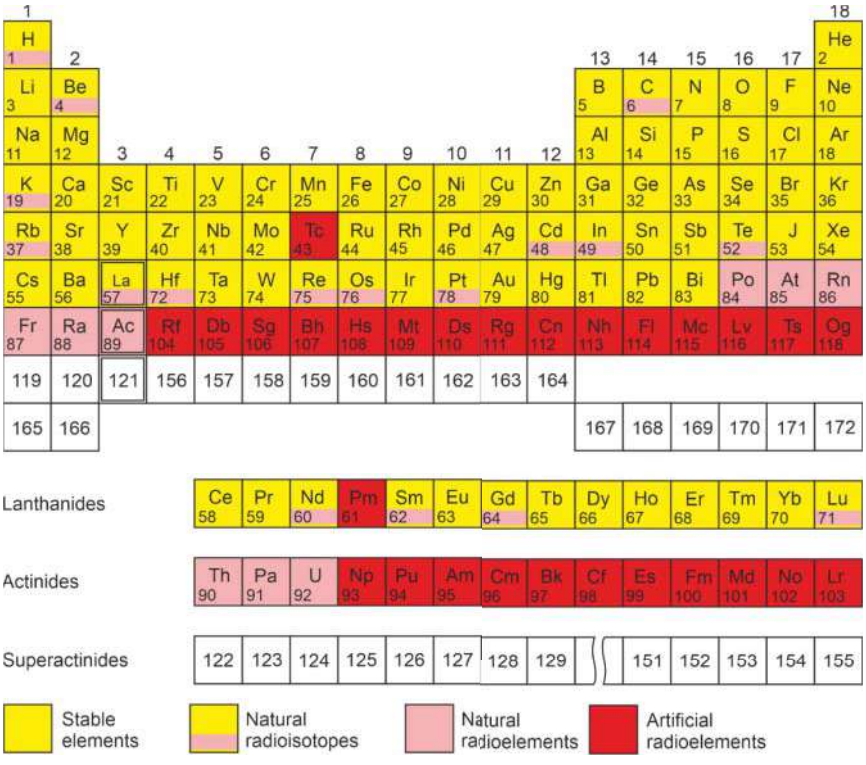

Figure 17.33 Extended periodic table of the elements.

that is, the distribution coefficient K_d of M between two phases, is correctly defined in terms of the probabilities of finding M in one phase or the other. If a static partition method is used, this coefficient must be measured many times in repetitive experiments. Since dynamical partition methods (chromatographic experiments) can be considered as spatially repetitive static partitions, the displacement of M along the chromatographic column itself is a statistical result and only one experiment is necessary, in principle. This underlines the validity of partition experiments with single atoms and the particular attractiveness of chromatographic methods in single-atom chemistry.

For short-lived atoms, additional considerations with regard to the kinetics are in order. The partition equilibrium must be reached during the lifetime of the atom, which requires high reaction rates. Consider a single-step exchange reaction

$$\mathrm{MX + Y} \underset{k_2}{\overset{k_1}{\longleftrightarrow}} \mathrm{MY + X} \tag{17.56}$$

Here, M is the single atom that can bind with either X or Y, and k_1 and k_2 are the rate constants for the reaction forth and back, respectively. The rate of a chemical reaction depends on the height of the reaction barrier between the states MX + Y and MY + X because, in between, there is a state of high potential energy (the transition state [Y…M…X], see Figure 17.34).

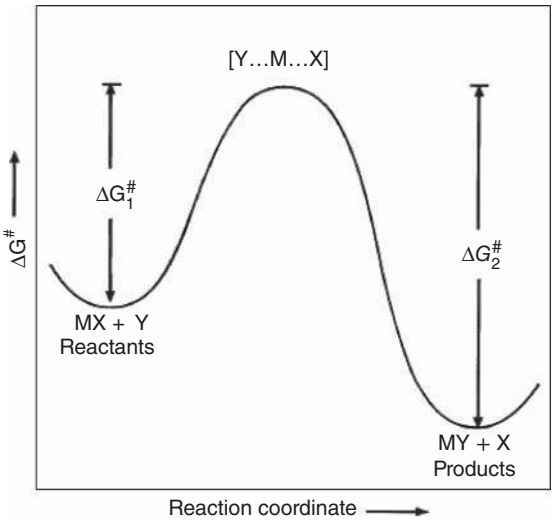

Figure 17.34 The reaction barrier between two chemical states MX + Y and MY + X. The metastable transition state [Y…M…X] has a higher potential energy than the reactants and the products. The energy differences $\Delta G_1^{\#}$ and $\Delta G_2^{\#}$ are the activation energies for the reactions from left to right and from right to left, respectively. Source: Adapted from Borg and Dienes (1981).

This state is unstable because the old chemical bond is not completely disrupted and the new one not yet completely formed. If the Gibbs free energies of activation $\Delta G_1^{\#}$ and $\Delta G_2^{\#}$ are high, the reaction proceeds very slowly. The transitions from left to right and from right to left do not occur with sufficient frequency, and the system is far from thermodynamic equilibrium. Borg and Dienes 29 found that if $\Delta G^{\#}$ is <15 kcal (60 kJ), then the residence time of M in either state (MX or MY) is rather short (<1 seconds) and an equilibrium is rapidly reached (in comparison to the nuclear half-lives of the transactinides). Borg and Dienes point out that the average time that M spends as MX or MY is proportional to the equilibrium constant. Thus, a measurement of the partition of M between the states MX and MY with very few atoms of M will already yield an equilibrium constant close to the "true" value, provided that both states are rapidly sampled. This again shows that chromatographic systems with fast kinetics are ideally suited for single-atom separations as there is rapid, multiple sampling of the absorbed or mobile species. The fractional average time that M spends as the absorbed species (which is proportional to the equilibrium constant, see above) is closely related to the chromatographic observable, the retention time.

Recent reviews of chemical separation techniques developed for transactinide studies can be found in Schädel (1995), Trautmann (1995), and Kratz (1999, 2011). A scheme of a target and recoil chamber arrangement is shown in Figure 17.8. Heavy-ion beams pass through a vacuum isolation window, a volume of He cooling gas, and a target backing before interacting with the target material. Reaction products recoiling out of the target are thermalized in a volume of He gas loaded with aerosol particles of 10–200 nm size and densities on the order of 10^7 particles cm^{-3} to which the reaction products attach. At a flow rate of about 2 l min^{-1}, the transport gas with the aerosols is transported through capillary tubes of about 2 mm inner diameter over distances of 5, 10, 20 m or even more to the chemistry apparatus where it deposits the reaction products. Transport times are

on the order of 2–5 seconds. Aerosol materials are selected so as to minimize their influence on the chemical procedures. Separations in the aqueous phase often use KCl as aerosol, while MoO_3 and carbon clusters are preferred in gas-phase separations. The aerosols are separated from the transport gas by passing the latter through a quartz-wool filter or by depositing them by impaction. The transactinides so deposited are then transformed into volatile species at elevated temperatures by reactive gases or are dissolved in aqueous solutions. Volatile species can also be produced "in situ" directly behind the target and transported without aerosols to a gas chromatography system. In the early frontal gas chromatography experiment with element 104 by I. Zvara in 1966 and 1969, the target and recoil chamber were bombarded by the internal beam inside the cyclotron. The recoils were stopped by nitrogen heated to 300 °C (flow rate 18–20 l min^{-1}) and transported into an outlet tube (i.d. 3.5 mm) where, at a distance of 3 cm from the target, a stream of nitrogen (0.5–1.0 l min^{-1}) containing the chlorinating reactive gases $NbCl_5$ and $ZrCl_4$ was introduced. The resulting volatile $RfCl_4$ was transported through the 4 m long outlet tube to mica fission-track detectors outside the cyclotron. The experiment was based on the difference in volatility of the chlorides MCl_4 (M = Zr and element 104) and MCl_3 (M = lanthanides). This in-situ production of volatile compounds directly behind the target without the use of an aerosol transport was later used in the investigation of the volatility of OsO_4 and HsO_4. Also, the investigations of the volatile metals copernicium, element 112, and element 114 were performed without a cluster jet. Recent important developments in the field of target and transport systems are the use of (i) rotating target wheels; (ii) pre-separation of the fusion–evaporation residues in an electromagnetic separator such as the BGS or the newly commissioned TASCA at GSI, by coupling the chemistry apparatus to the separator via a recoil transfer chamber (RTC) in the focal plane; and (iii) avoiding vacuum windows by differential pumping in the target area.

Vapor pressure curves (P [mm Hg] vs. temperature [°C]) give a measure of the volatility of volatile compounds. For macroscopic quantities, these curves are calculated using standard sublimation enthalpies $\Delta H_s^{o(298\ K)}$ and standard sublimation entropies $\Delta S_s^{o(298\ K)}$ relevant for the desorption of a volatile species from the surface of a solid composed of the same molecules. Since in the experiments with transactinide elements, only single molecules can be studied, $\Delta H_s^{o(298\ K)}$of, for example, $RfCl_4$ cannot be determined directly. The quantity deduced from gas chromatography experiments is then $\Delta H_a^{o(T)}$, the adsorption enthalpy on the chromatographic surface (usually quartz glass) at zero coverage. As was demonstrated by Zvara et al. (1970), there exists a linear relationship between $\Delta H_a^{o(T)}$ and $\Delta H_s^{o(298\ K)}$. By measuring $\Delta H_a^{o(T)}$ of chlorides of 24 elements on quartz glass surfaces, Eichler et al. (1976) established the empirical relation

$$-\Delta H_a^{o(T)} = (0.655 \pm 0.042)\cdot\Delta H_s^{o(298K)} + (18.0 \pm 8.8)\ \text{kJ mol}^{-1}. \qquad (17.57)$$

Thus, $-\Delta H_a^{o(T)}$ is the quantity used to judge the volatility of transactinide compounds relative to the volatility of their lighter homologs also determined for weightless samples.

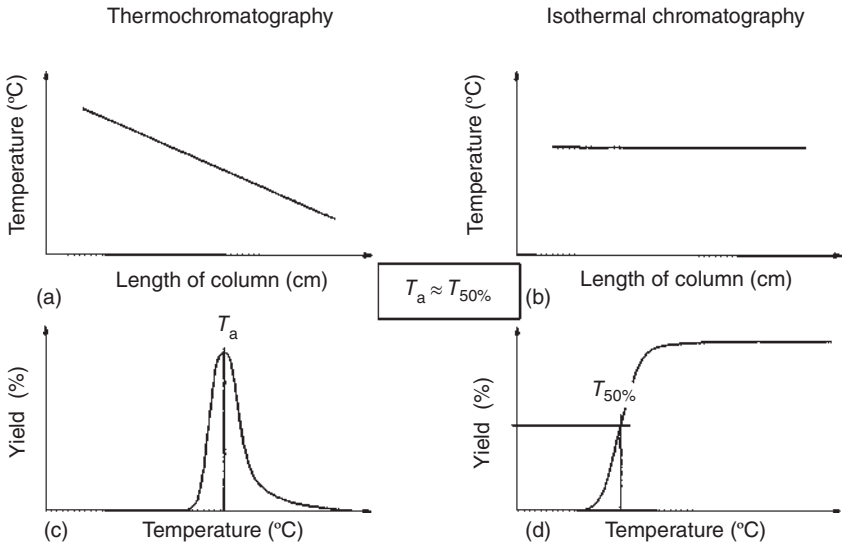

Figure 17.35 (a, b) temperature profiles in thermochromatography and isothermal gas chromatography. (c, d) deposition peak and yield versus temperature curve resulting from thermochromatography and isothermal chromatography, respectively.

There are two experimental approaches to determine $\Delta H_a^{o(T)}$, thermochromatography (TC) and isothermal gas chromatography (IC), both being depicted in Figure 17.35. In thermochromatography, a longitudinal, negative temperature gradient is established along the chromatography column in the flow direction of the carrier gas. Volatile species are deposited inside the column according to their volatility in a characteristic adsorption peak defining the adsorption temperature T_a. In the radiochemical laboratory classes at the University of Bern, a thermochromatographic separation of $^{212}PbCl_2$ and $^{212}BiCl_3$ in an open quartz glass column is studied, see Figure 17.36. In this experiment, a ^{232}U source is continuously flushed with a stream of nitrogen gas containing KCl aerosols transporting 10.64 hours ^{212}Pb and its daughter, 60.6 minutes ^{212}Bi, continuously through a capillary to the hot section of the chromatography tube containing a quartz wool plug where the aerosols are deposited. ^{212}Pb and ^{212}Bi react here with gaseous $SOCl_2$ and form the volatile $^{212}PbCl_2$ and the more volatile $^{212}BiCl_3$ that are transported in the column. After two hours, the gas flow is stopped and the deposition zones of $PbCl_2$ and $BiCl_3$ are detected from outside by scanning the column in steps 1 cm wide with a Geiger–Müller counter that can only detect the 2.3 MeV β^- particles emitted in the decay of ^{212}Bi through the wall of the column. In the deposition zone of $^{212}PbCl_2$, the ingrowing activity of ^{212}Bi is detected, whereas in the deposition zone of $BiCl_3$, the primary ^{212}Bi is decaying with a half-life of 60 minutes. Two separate thermochromatography peaks are observed and assigned as shown in Figure 17.36. In Figure 17.36, the result of a Monte Carlo simulation (MCS) (dashed line), based on the model of ideal linear gas chromatography to be discussed below, is compared to the actual experiment (histogram). In the lower panel, the integrated activity of

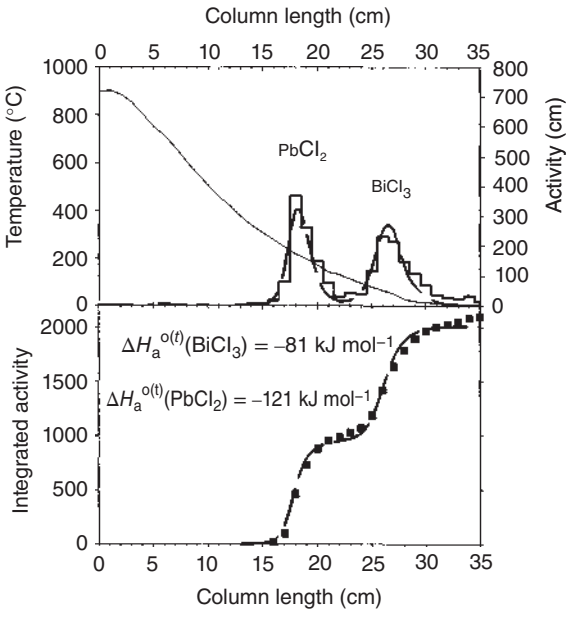

Figure 17.36 Upper panel: thermochromatographic separation of $^{212}PbCl_2$ and $^{212}BiCl_3$ in an open quartz glass column. The histogram represents the experimentally determined β^- activity of ^{212}Bi in steps 1 cm wide after completion of the experiment. The dashed line represents the result of a Monte Carlo simulation using the microscopic model of Zvara (1985). Lower panel: the integrated activity of ^{212}Bi and the integral results of the Monte Carlo simulation as a function of the column length. Source: Türler (1999)/University of Bern.

^{212}Bi is shown as a function of the column length for the experimental (squares) and for the simulated data (dashed line). The free parameters in the model are $\Delta H_a^{o(T)}(^{212}PbCl_2)$ and $\Delta H_a^{o(T)}(^{212}BiCl_3)$. The values that are in best agreement with the experimental data are -121 and -81 kJ mol^{-1}, respectively, characterizing $BiCl_3$ as the more volatile species. In the model of ideal linear gas chromatography, a relationship between the experimental parameters and the thermochemical properties, $\Delta H_a^{o(T)}$ and $\Delta S_a^{o(T)}$, is derived:

$$t = -\frac{T_0}{g u_0} \cdot \ln \frac{T_a}{T_s} + \frac{a \cdot T_0 (V/A) \cdot \exp(\Delta S_a^{o(T)}/R)}{v g u_0} \times \left(\mathrm{Ei}^* \left(\frac{-\Delta H_a^{o(T)}}{R T_a} \right) - \mathrm{Ei}^* \left(\frac{-\Delta H_a^{o(T)}}{R T_s} \right) \right) \quad (17.58)$$

where

t = duration of the experiment
T_0 = standard temperature (298 K)
g = temperature gradient
u_0 = linear velocity of the gaseous phase at standard conditions (cm s^{-1})
T_a = deposition temperature of the compound (K)
T_s = temperature of the starting position (K)
a = open surface per unit length (1 cm) of the column (cm^2 cm^{-1})
v = open volume per unit length (1 cm) of the column (cm^3 cm^{-1})
A = standard molar area
V = standard molar volume
$\Delta H_a^{o(T)}$ = standard enthalpy of adsorption

$\Delta S_a^{o(T)}$ = standard entropy of adsorption
R = gas constant
Ei^* = integral exponential function

As the standard enthalpy and standard entropy of adsorption determine the chromatographic behavior, the simultaneous determination of both quantities requires at least two experiments with grossly different parameters (e.g. variation of the flow rate of the carrier gas and duration of the experiment). The resulting values of $\Delta S_a^{o(T)}$ are in good agreement with theoretical estimates according to Eichler et al. (1979). As the uncertainties in the determination of $\Delta S_a^{o(T)}$, even in a series of carefully conducted experiments, are not smaller than 10%, $\Delta H_a^{o(T)}$ is often determined experimentally by using a calculated value for the standard adsorption entropy based on

$$\Delta S_a^{o(T)} = R \cdot \ln \left[\frac{1}{(1\ \mathrm{cm}) \cdot \nu_B} \left(\frac{kT}{2\pi M} \right)^{1/2} \right] + \frac{1}{2} R \tag{17.59}$$

with

R = gas constant
ν_B = characteristic frequency of the adsorbent (for quartz glass, $5 \cdot 10^{12}\ \mathrm{s}^{-1}$)
k = Boltzmann's constant
T = temperature (K)
M = molar mass

In isothermal gas chromatography experiments, the chromatography is performed at a constant temperature that is varied systematically in subsequent experiments and the activity that leaves the column is determined as a function of the isothermal temperature, right part of Figure 17.35. This gives a curve of yield that rises at a certain temperature and reaches saturation at high temperature; that is, at temperatures where the retention time of the volatile species in the chromatography tube is negligible compared to the nuclear half-life. The characteristic quantity to be determined is the temperature, $T_{50\%}$, at which the retention time equals the nuclear half-life. Thus, one is using the nuclear half-life as an internal clock. In IC, this retention time, t_r, is related to $\Delta H_a^{o(T)}$ and $\Delta S_a^{o(T)}$ by

$$\Delta H_a^{o(T)} = -RT \ln \left[\left(\frac{t_r \overline{v}_0 T}{(z_1 - z_2) T_0 \Phi} - 1 \right) \frac{\nu}{a} \frac{A}{V} \exp \left(\frac{-\Delta S_a^{o(T)}}{R} \right) \right] \tag{17.60}$$

by using a calculated $\Delta S_a^{o(T)}$. Here,

$\Delta H_a^{o(T)}$ = standard enthalpy of adsorption
R = gas constant
T = temperature (K)
t_r = retention time
$\overline{v}_0$ = gas flow rate at standard conditions ($\mathrm{cm}^3\ \mathrm{s}^{-1}$)
$z_1 - z_2$ = length of the isothermal chromatography column

T_0 = standard temperature (298 K)
Φ = cross section of the chromatography column (cm^2)
a = open surface per unit length (1 cm) of the column ($cm^2\ cm^{-1}$)
v = open volume per unit length (1 cm) of the column ($cm^3\ cm^{-1}$)
A = standard molar area
V = standard molar volume
$\Delta S_a^{o(T)}$ = standard entropy of adsorption

To measure the decay of the separated species, they are – after leaving the chromatographic column and entering a water-cooled "recluster chamber" – attached to new aerosols and transported through a capillary to a detection system, a rotating wheel, or a moving tape system that positions the deposited activity in front of successive PIPS detectors (Passivated Ion-implanted Planar Silicon detectors), which register α particles and sf events. The most advanced version of the Online Gas Chemistry Apparatus, OLGA III, is shown in Figure 17.37.

From a theoretical point of view, the dependence of the retention time in IC or the deposition temperature in TC on experimental parameters for uniform surfaces and ideal IC or linear TC temperature profiles is well understood. In the actual experiments, however, ideal temperature profiles are mostly not realized. Also, in TC, the deposition peaks are broad and often asymmetric. Therefore, Zvara (1985) developed a microscopic model that describes the downstream migration of a single molecule as a series of adsorption–desorption events followed by a rather

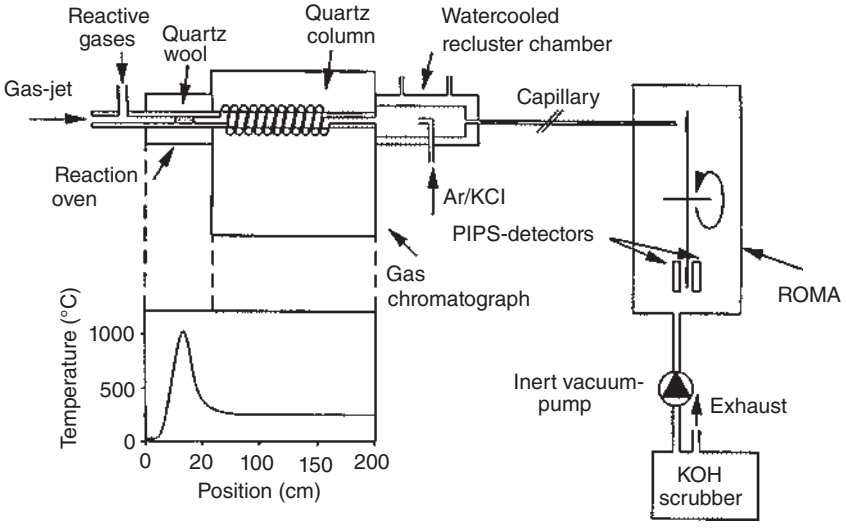

Figure 17.37 The OLGA III system used in the study of seaborgium. The gas jet transports the seaborgium atoms attached to graphite particles in He gas to the reaction oven where the reactive gas $Cl_2/SOCl_2/O_2$ is added to form volatile oxychlorides and to convert the graphite particles into CO_2. Behind the isothermal chromatography section, the gaseous molecules are attached to new aerosol particles and transported to the rotating wheel counting device ROMA. Source: Gäggeler (1998)/Elsevier.

long downstream displacement before the next adsorption–desorption sequence takes place. The relevant probability density distributions for the residence time of an adsorption–desorption event as well as for the downstream displacement were derived. Based on this model, a MCS procedure was proposed and has been made available by Türler (1996). It is very versatile and experimental conditions such as high carrier gas flow rates, actual temperature profiles, radioactive decay, and transmutation of chemical species can be adopted. It allows the results to be expressed in terms of probabilities, which is of special interest in single-atom chemistry. For example, for IC, these calculations result in a curve of yield against temperature for each value of the adsorption enthalpy. The curve for the particular $\Delta H_a^{o(T)}$ which best fits the measured data is chosen by a least-squares method.

As can be seen in the example shown in Figure 17.38, the experimental data are perfectly reproduced by the MCSs based on the microscopic model with $\Delta H_a^{o(T)} = -94\,\mathrm{kg\,mol^{-1}}$. If, on the other hand, the yield curve is calculated using the model of ideal gas chromatography, the best fit to the data is obtained with $\Delta H_a^{o(T)} = -88\,\mathrm{kg\,mol^{-1}}$ and the differences between the two approaches become apparent. Due to the slower diffusion across the column diameter at low temperatures, the mean jump length increases at low temperatures, that is, the probability for long jumps increases with decreasing temperature. If the mean jump length is on the order of the length of the isothermal section of the column, a not negligible fraction of the molecules pass this part of the column without ever "seeing" the wall. This is pronounced in the experiment displayed in Figure 17.38 which was performed using a very high gas flow rate of $1\,\mathrm{l\,min^{-1}}$.

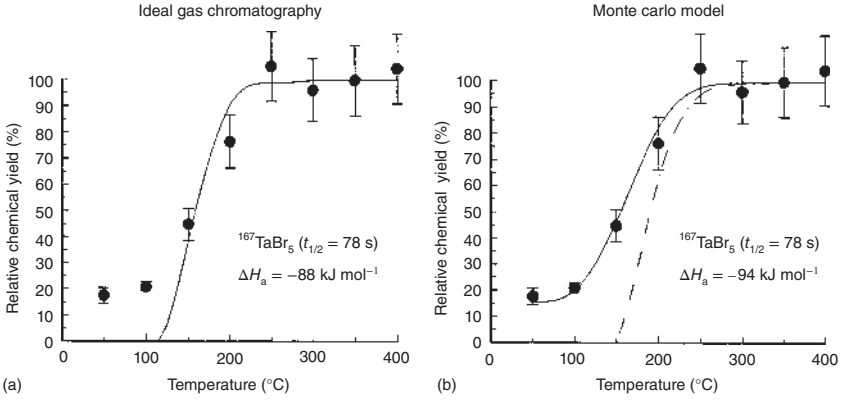

Figure 17.38 Yield curve of $^{167}TaBr_5$ ($t_{1/2}$ = 78 seconds) measured with OLGA II by Gäggeler et al. (1992). In (a), the solid line shows the best fit to the data with $\Delta H_a^{o(T)} = -88\,\mathrm{kJ\,mol^{-1}}$ using the model of ideal linear gas chromatography. In (b), a much better fit to the experimental data is obtained with the Monte Carlo simulation based on the microscopic model of Zvara (1985) with $\Delta H_a^{o(T)} = -94\,\mathrm{kJ\,mol^{-1}}$ (solid line). The difference between the two models becomes apparent by comparing the dot-dashed line resulting from the model of ideal linear gas chromatography and $\Delta H_a^{o(T)} = -94\,\mathrm{kJ\,mol^{-1}}$ with the solid line resulting from the Monte Carlo simulation based on the microscopic model with the same adsorption enthalpy. Source: Türler (1999)/University of Bern.

The recently developed in-situ volatilization and on-line detection technique IVO makes use of a narrow chromatography channel ~40 cm long consisting of pairs of Positive Intrinsic Negative (PIN) diode detectors to which a negative temperature gradient from room temperature down to ~−180 °C is applied. This powerful cryodetection technique has been instrumental in thermochromatography with the highly volatile OsO_4 and HsO_4 and in studies of the volatility of elements 112 and 114.

While gas-phase chemistry is generally carried out continuously as an on-line process, aqueous chemistry has been performed mostly in a discontinuous batch-wise manner. It is then necessary, in order to get statistically significant results, to repeat the same experiment several hundred or even several thousand times with a cycle time of typically 1 min^{-1}. These have mostly been performed with the Automated Rapid Chemistry Apparatus, ARCA II, developed at GSI/Mainz or with the further advanced Automated Ion-exchange separation apparatus coupled with the Detection system for Alpha spectroscopy, AIDA, developed at Tokai in Japan. Automated separations with these devices incorporating high-performance liquid chromatography (HPLC) separations were conducted with elements 104, 105, and 106. A schematic representation of ARCA II is shown in Figure 17.39.

ARCA II consists of a central catcher-chemistry part incorporating the sliders SL1–SL3, and two movable magazines containing 20 of the chromatographic columns C1, C2 (1.6 mm i.d. × 8 mm) each, and peripheral components, that is, three chemically inert HPLC pumps, P1–P3, and a number of pneumatically driven four-way slider valves, S1–S4. Each pump pumps one eluent, in the case of the

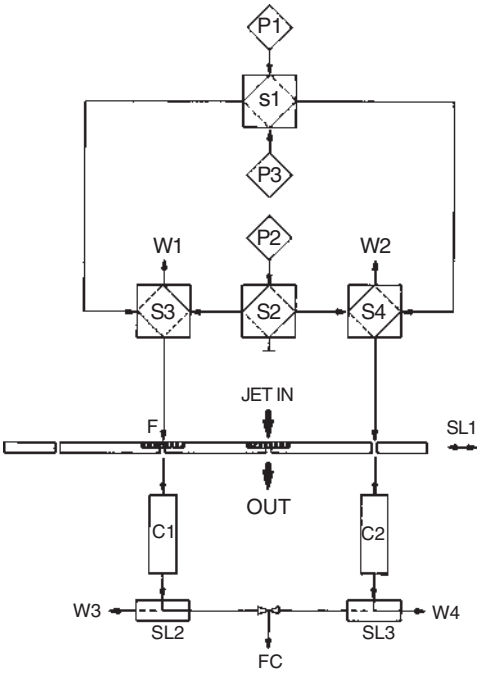

Figure 17.39 Schematic representation of the computer-controlled HPLC system ARCA II (for details see text). Source: Schädel et al. (1989), figure 2 (p. 173)/De Gruyter.

separations of element 105 in mixed HCl/HF solutions (Kratz et al. 1989), one 12 M HCl/0.02 M HF, another 4 M HCl/0.02 M HF, and the third 6 M HNO_3/0.015 M HF, through Teflon tubing of 0.3 mm i.d. to the central catcher-chemistry unit. The He(KCl) gas jet deposits the transported reaction products continuously onto one of two polyethylene frits F. After collection for one minute, the frit is moved on top of one of the microcolumns C1 and washed with 12 M HCl/0.02 M HF, whereby the reaction products are dissolved, complexed, and extracted into the organic phase (the columns are filled with Teflon grains coated with tri-isooctyl amine, TiOA), while the non-extractable species (notably the actinides) run through into the waste, W3. The column is then washed with 4 M HCl/0.02 M HF, and the effluent (containing Nb, Pa, and element 105) is directed through SL2 to the fraction collector FC where it is collected on a Ta disk and quickly evaporated to dryness by intense IR light and hot He gas. Next, the Ta fraction is eluted with 6 M HNO_3/0.015 M HF, collected on a Ta disk, and evaporated to dryness. The Ta disks are inserted into the counting chambers about 55 seconds after the end of collection. Then, five seconds later, the next one minute collection on the twin frit is completed. That frit is moved on top of the column C2 contained in the opposite magazine, and the next separation cycle is carried out. After each separation, the magazine is moved by one step, thus introducing a new column into the elution position. In this way, the time-consuming reconditioning of used columns and cross-contaminations from previous separations are avoided. After 40 minutes of continuous collection and separation cycles, the program is stopped, the used magazines are removed, two new magazines are introduced, and another 40 cycles are started. More than 7800 of such ARCA II experiments have been conducted in the study of element 105 so far.

Figure 17.40 shows an example for such a separation (Schädel et al. 1989). The upper part is the result of a manually operated HPLC separation on a TiOA/Teflon column (1.7 mm i.d. × 11 mm). Radioactive tracers of lanthanides (Ln), actinides (An), Zr, Hf, Pa, Nb, and Ta are introduced into the system through a sample loop in 12 M HCl/0.02 M HF. Under these conditions, halide complexes of Pa, Nb, and Ta are extracted into the amine, while Ln, An, Zr, and Hf pass the column (fraction A). Pa and Nb are then eluted together with 4 M HCl/0.02 M HF (fraction B), and, finally, Ta is stripped from the column in 6 M HNO_3/0.015 M HF (fraction C). The manually performed separation takes about 75 seconds. This time does not include the times required for rinsing the tubings when the eluent is changed. The lower part of Figure 17.7 shows the same separation performed automatically with ARCA II. A volume of 50 µl of 12 M HCl/0.02 M HF is used to precondition each column before the tracer activities are loaded onto the column in 25 µl 12 M HCl/0.02 M HF. The complete extraction and elution cycle is complete in ≤35 seconds. This is achieved by reducing the void volumes to a minimum.

A schematic diagram of the Automated Ion-exchange separation apparatus coupled with the Detection system for Alpha spectroscopy AIDA is shown in Figure 17.41. In the modified ARCA, there are two different paths to supply solutions: the first eluent goes through the collection port to the microcolumn, while the other is directed to the column without going through the collection port.

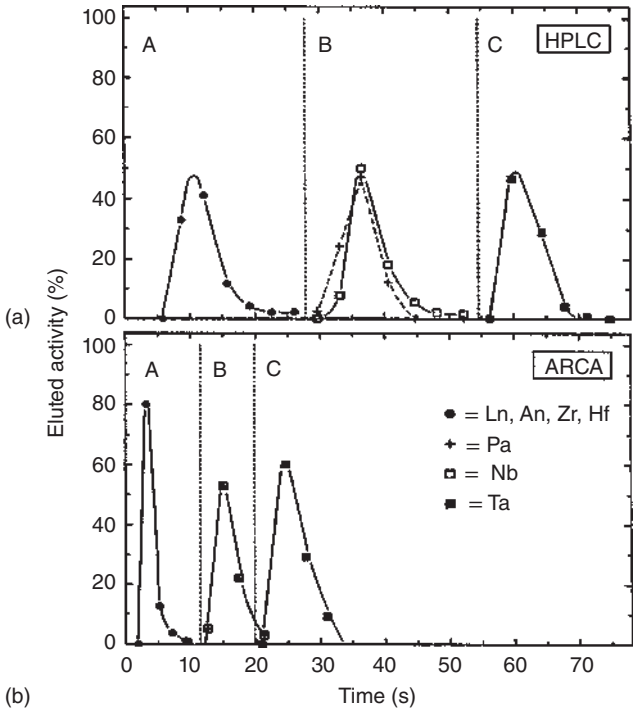

Figure 17.40 Separation of trivalent lanthanides (Ln) and actinides (An), Zr, Hf, Nb, Ta, and Pa in an extraction chromatographic system with TiOA (tri-isooctyl amine) on an inert support as stationary phase and 12 M HCl/0.02 M HF (A), 4 M HCl/0.02 M HF (B), and 6 M HNO_3/0.015 M HF (C) as eluents. In (a) HPLC, the chromatogram of a manually performed separation with standard HPLC techniques on a 1.7×11 mm column is shown. (b) shows a fully automated separation in ARCA II on a 1.6×8 mm column at a flow rate of 1.0 ml min^{-1}. Source: Schädel et al. (1989), figure 3 (p. 175)/De Gruyter.

This minimizes contamination of the strip fraction. A drawing of AIDA is given in Figure 17.42. The Ta disks with the evaporated samples are automatically inserted into the eight vacuum chambers for α spectroscopy.

In an ion-exchange experiment with transactinides, these are transported by a He(KCl) gas jet and are collected for typically 60 seconds by impaction inside ARCA II or AIDA. The deposit is dissolved in typically 200 µl of an aqueous solution containing complexing ions such as the fluoride anion and fed onto the column at a flow rate of 1 ml min^{-1}. The effluent from the column is evaporated to dryness as sample 1 containing the activity A_1. In order to elute the remaining transactinide activity from the column, a second fraction is collected by using a suitable stripping solution. This fraction is also evaporated to dryness and is referred to as sample 2 containing the activity A_2. From the activities A_1 and A_2 observed in samples 1 and 2, the percentage %ads is evaluated using the equation

$$\%\text{ads} = 100A_2/(A_1 + A_2) \tag{17.61}$$

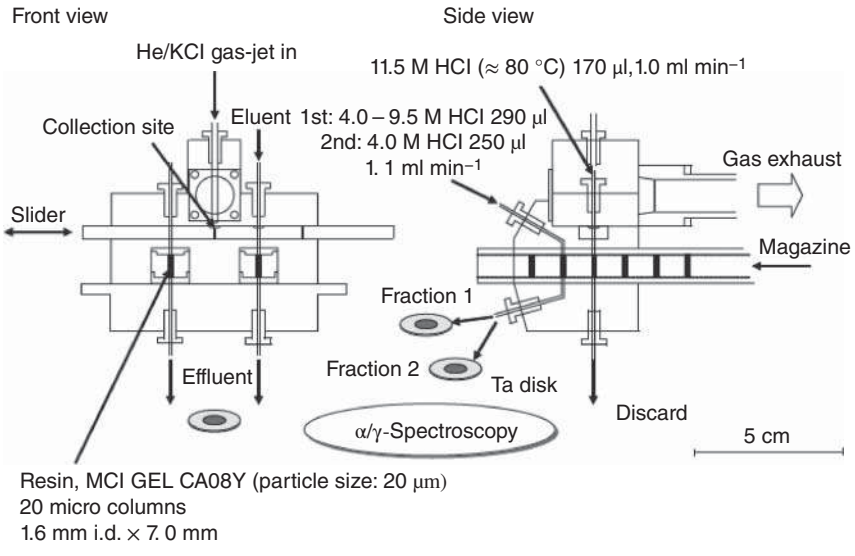

Figure 17.41 Schematic diagram of the modified ARCA in AIDA. Source: Nagame et al. (2005), figure 4 (p. 521)/De Gruyter.

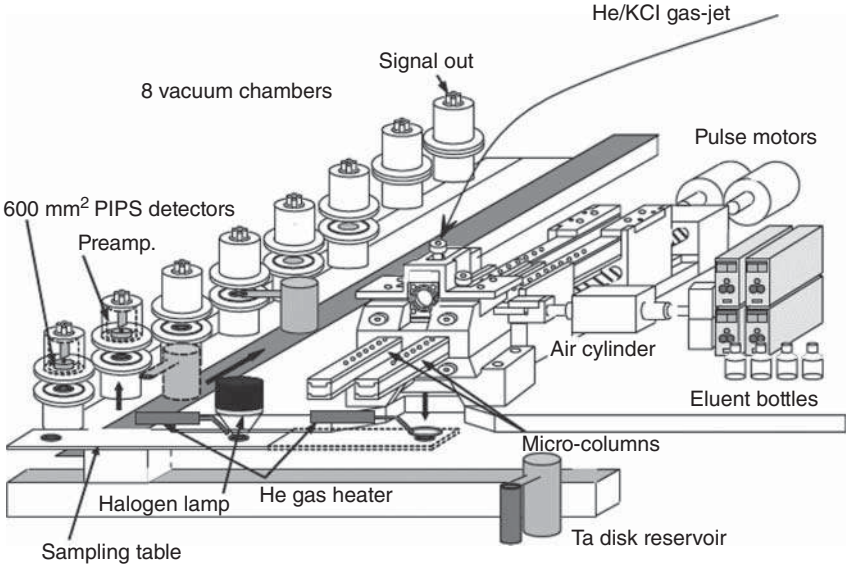

Figure 17.42 Drawing of AIDA. Source: Nagame et al. (2005), figure 3 (p. 521)/De Gruyter.

In order to demonstrate how this quantity can be related to the distribution coefficient $K_d = A_{resin}/A_{liquid}$, we use as an example the anion exchange chromatographic behavior of Rf as investigated by Haba et al. (2004) in 1.9–13.9 M HF and compare it to that of Zr and Hf. As HF is a weak acid, equilibration among HF, H^+, F^-, and

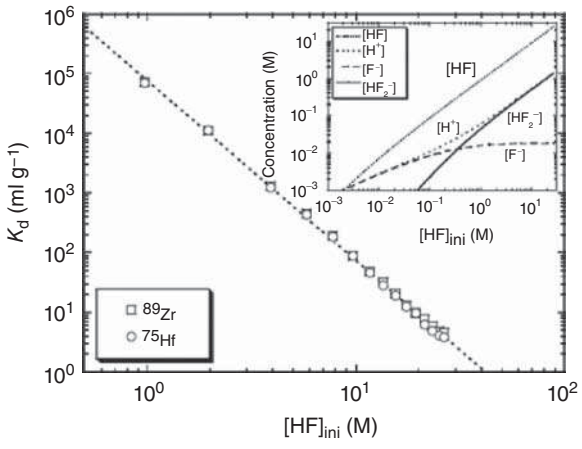

Figure 17.43 Variation of the distribution coefficient K_d of Zr and Hf on the anion exchange resin CA08Y as a function of the initial HF concentration. The linear relation with a slope of -3.0 ± 0.1 is indicated by a dotted line. The inset shows the variation of [HF], [H^+], [F^-], and [HF_2^-] as a function of [HF]$_{ini}$. Source: Haba et al. (2004), figure 1 (p. 5221)/American Chemical Society.

HF_2^- in aqueous solution is established by the chemical equations

$$H^+ + F^- \Leftrightarrow HF \tag{17.62}$$

$$HF + F^- \Leftrightarrow HF_2^- \tag{17.63}$$

with $K_1 = 935\,M^{-1}$ and $K_2 = 3.12\,M^{-1}$ for the first (Eq. (17.62)) and the second (Eq. (17.63)) equilibria, respectively. The inset of Figure 17.43 shows the variation of [HF], [H^+], [F^-], and [HF_2^-] as a function of the initial [HF]$_{ini}$. Above 1 M HF, the concentration of the HF_2^- anion is more than one order of magnitude higher than that of F^- and [HF_2^-] increases linearly with increasing [HF]$_{ini}$. Thus, the decrease in the K_d values of Zr and Hf with increasing [HF]$_{ini}$ as determined in batch experiments and shown in Figure 17.43 is explained as the displacement of the metal complex from the binding sites of the anion exchange resin by HF_2^- as the dominant anionic species in solution. In Figure 17.44, elution curves for Zr and Hf produced simultaneously are shown with (i) a 1.6 mm i.d. × 7.0 mm column in 17.4 and 7.7 M HF; and (ii) a 1.0 mm i.d. × 3.5 mm column in 9.7 and 5.8 M HF. The percentages of the eluted activities are depicted and are nearly the same as expected from the same K_d values in the batch experiment, see Figure 17.43. According to the Glückauf equation of chromatography, the eluted activity $A(v)$ with the effluent volume v is

$$A(v) = A_{max} \exp[-N/2(v_{peak} - v)^2/v_{peak}v] \tag{17.64}$$

where A_{max}, N, and v_{peak} are the maximum peak height, the number of theoretical plates, and the peak volume, respectively. The results of the fit of Eq. (17.64) are shown as solid or dotted curves in Figure 17.44. In the dynamic chromatographic system, the K_d value is

$$K_d = v_{peak}/m_r \tag{17.65}$$

where m_r is the mass of the dry resin. In Figure 17.45, the K_d values of Zr and Hf calculated with Eq. (17.65) are shown. The K_d values of the different column sizes are consistent with each other.

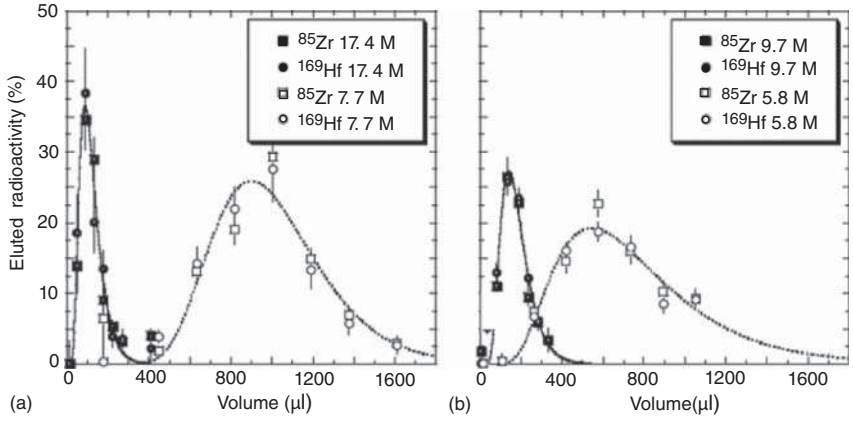

Figure 17.44 Elution curves of Zr and Hf from (a) 1.6 mm i.d. × 7.0 mm columns in 17.4 and 7.7 M HF and from (b) 1.0 mm i.d. × 3.5 mm columns in 9.7 and 5.8 M HF. The solid and dotted curves are fitted by the Glückauf equation. The number of theoretical plates results as (a) 4.8 ± 0.5 and (b) 4.6 ± 0.5. Source: Haba et al. (2004), figure 2 (p. 5222)/American Chemical Society.

Figure 17.45 Variation of the K_d of Zr and Hf on the anion exchange resin CA08Y obtained in chromatographic experiments as a function of the initial HF concentration. The dotted line indicates the results obtained from batch experiments. Source: Haba et al. (2004), figure 3 (p. 5222)/American Chemical Society.

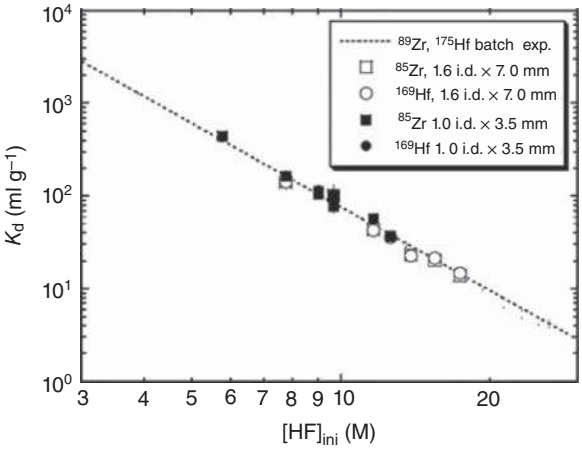

From the radioactivities A_1 and A_2 observed in fractions 1 and 2, respectively, the percentages %ads were evaluated using Eq. (17.61). The %ads values of Zr, Hf, and Rf are shown in Figure 17.46 as a function of $[HF]_{ini}$ for the 1.6 mm i.d. × 7.0 mm columns (i) and for the 1.0 mm i.d. × 3.5 mm columns (ii). The %ads values of Zr and Hf obtained by the on-line experiments decrease steeply with increasing $[HF]_{ini}$ above 8 M for the larger columns and above 5 M for the smaller ones, while the %ads of Rf decrease at much smaller $[HF]_{ini}$. In Figure 17.47, the correlations between the %ads values shown in Figure 17.46 and the K_d values from Figure 17.43 are plotted with the same symbols as used in Figure 17.44 and are fitted (solid curves) by

$$\%\text{ads} = 100 \exp\{-a \exp[-b(K_d - c)]\} \tag{17.66}$$

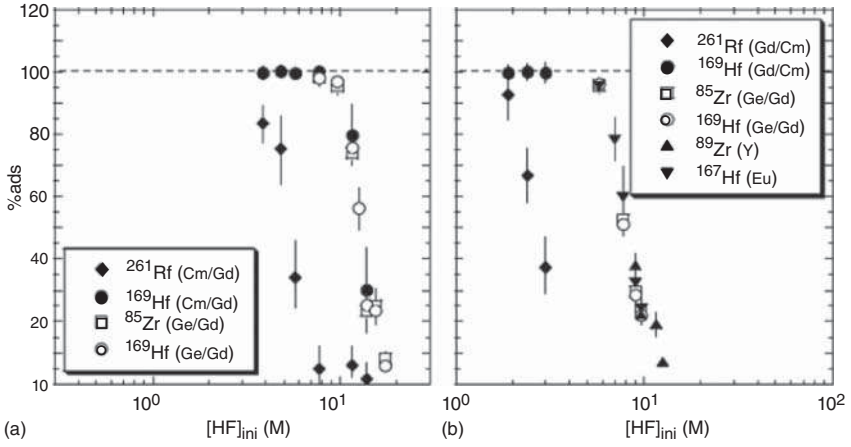

Figure 17.46 %ads of Zr, Hf, and Rf on the anion exchange resin CA08Y as a function of the initial HF concentration with (a) the 1.6 mm i.d. × 7.0 mm columns and with (b) the 1.0 mm i.d. × 3.5 mm columns. Source: Haba et al. (2004), figure 4 (p. 5223)/American Chemical Society.

Assuming that the kinetics in the complexation and ion-exchange processes of Rf are as fast as those for Zr and Hf, the %ads of Rf from the dynamic column method have been transformed into K_d values using Eq. (17.66). This assumption has subsequently been verified by measuring the elution curve for Rf in 5.4 M HF and by deducing the K_d value according to Eq. (17.65) by Toyoshima et al. (2004). The results from Haba et al. (2004) for Rf are shown as diamonds in Figure 17.48, together with those of Zr and Hf by the same symbols as used in Figure 17.45. As shown by a solid line, the K_d values of Rf decrease linearly with increasing $[HF]_{ini}$ and are much smaller than those of Zr and Hf for the same $[HF]_{ini}$. The slope of -2.0 ± 0.3 of log K_d vs. log$[HF]_{ini}$ for Rf differs from the slope of -3.0 ± 0.1 for Zr and Hf, indicating that different anionic fluoride complexes are formed, that is, RfF_6^{2-} and ZrF_7^{3-} and HfF_7^{3-}. This example indicates the amount of information that one can extract from dynamical column experiments.

The centrifuge system SISAK III allows for the continuous separation of nuclides with half-lives down to one second. The separation is based on multistage liquid–liquid extractions using static mixers and specially designed mini-centrifuges for subsequent phase separation. SISAK was successfully applied to a large number of γ-spectroscopic studies of lighter elements. Recently, a new detection system based on liquid scintillation counting (LSC) has been developed for on-line α spectroscopy and sf detection in the flowing organic phase behind SISAK. Suppression of interfering β and γ radiation is done by pulse-shape discrimination and pile-up rejection. However, in experiments with ^{261a}Rf, due to a high level of interfering β and γ radiation, the number of random αα mother–daughter correlations due to pile-up was too large to allow for the unambiguous identification of ^{261a}Rf decay chains. Two solutions of this problem have been pursued recently. (i) The BGS was used as a pre-separator for ^{257}Rf produced in the ^{208}Pb(^{50}Ti, 1n) reaction followed

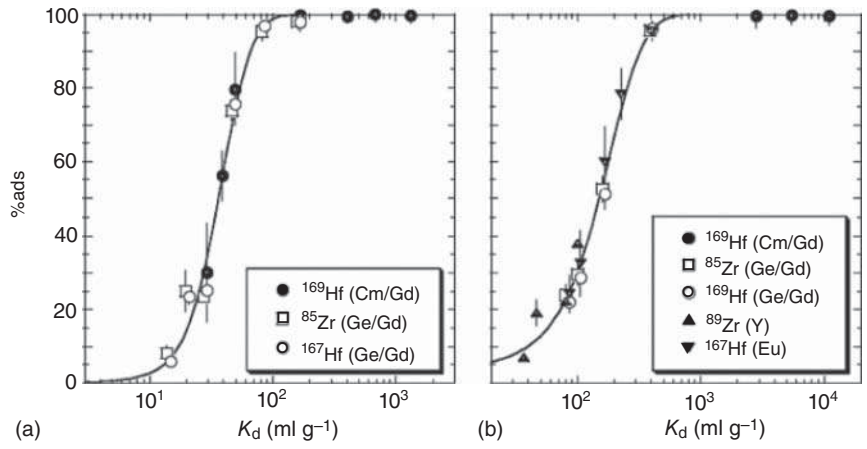

Figure 17.47 Variation of the %ads of Zr and Hf on the anion exchange resin CA08Y with (a) the 1.6 mm i.d. × 7.0 mm columns and with (b) the 1.0 mm i.d. × 3.5 mm columns as a function of the distribution coefficient K_d. The solid lines are a fit of Eq. (17.66) to the data. Source: Haba et al. (2004), figure 5 (p. 5224)/American Chemical Society.

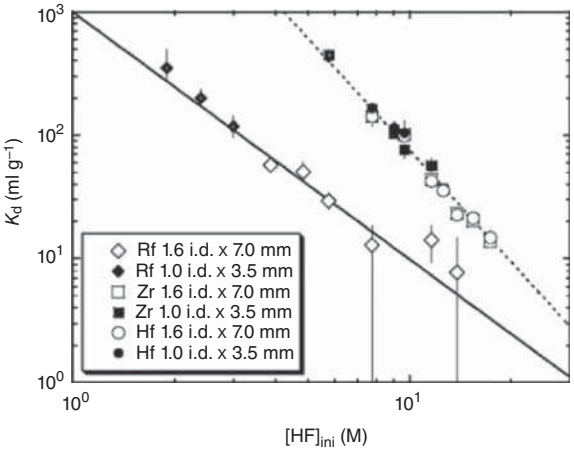

Figure 17.48 Variation of the distribution coefficient K_d of Zr, Hf, and Rf on the anion exchange resin CA08Y as a function of the initial HF concentration. The linear relationships with slopes -2.0 ± 0.3 for Rf and -3.0 ± 0.1 for Zr and Hf are indicated by the solid and dotted lines, respectively. Source: Haba et al. (2004), figure 6 (p. 5224)/American Chemical Society.

by the transfer of ^{257}Rf to a gas jet delivering the activity to the SISAK system (Omtvedt et al. 2002). This reduced the interfering β and γ radiation by more than three orders of magnitude, thus enabling the unambiguous detection of ^{257}Rf by LSC. (ii) A fast transient recorder was introduced into the data acquisition in order to digitally record the pulse shapes, and a neural network was trained to recognize true α events and to distinguish these from ββ pile-up and βγ pile-up events.

As we indicated above, it is important that the experimental investigations are accompanied by theoretical investigations. The most appropriate quantum chemistry methods for the heaviest elements are those that treat both relativity and electron correlations at the highest level of theory. Most of them are described by Barysz and Ishikawa (2010). Presently, the highest theoretical level in atomic codes is the

Dirac–Coulomb–Breit (DCB) Hamiltonian

$$h_{\mathrm{DCB}} = \sum_i h_{\mathrm{D}}(i) + \sum_{i<j} (1/r_{ij} + B_{ij}) \tag{17.67}$$

where the one-electron Dirac operator is

$$h_{\mathrm{D}}(i) = c\boldsymbol{\alpha}_i \mathbf{p}_i + c^2(\beta_i - 1) + V^n(i) \tag{17.68}$$

Here, $\boldsymbol{\alpha}$ and $\boldsymbol{\beta}$ are four-dimensional Dirac matrices, and V^n is the nuclear attraction operator. The Breit term in the low-photon frequency limit is

$$B_{ij} = -\frac{1}{2}[(\boldsymbol{\alpha}_i \boldsymbol{\alpha}_j) r_{ij}^{-1} + (\boldsymbol{\alpha}_i \mathbf{r}_{ij})(\boldsymbol{\alpha}_j \mathbf{r}_{ij}) r_{ij}^{-3}] \tag{17.69}$$

The operators of the Dirac equation (Eq. (17.67)) are 4×4 matrix operators, and the corresponding wave function is therefore a four-component (4c) spinor. The V^n includes the effect of the finite nuclear size, while some finer effects, like quantum electrodynamics (QED), can be added to h_{DCB} perturbatively. The DCB Hamiltonian in this form (no-pair approximation) contains all effects through the second order in α, the fine-structure constant. Correlation effects are taken into account by configuration interaction (CI), many-body perturbation theory (MBPT) or, presently at the highest level of theory, coupled cluster theory with single–double (and perturbative triple) (CCSD(T)) excitations.

The Fock–Space (FS) DCB CC method by Kaldor et al. (2002) is one of the most powerful methods applied for accurate atomic calculations. The DC FS CCSD method incorporated into the DIRAC program package has a slightly lower accuracy than the former one, as Breit interactions are not implemented at the coupled-cluster level. A practical instrument for many-electron systems is the multi-configuration Dirac–Fock (MCDF) method by Desclaux (1973). In the past, predictions of ground-state electron configurations of the heaviest elements were made with single-configuration Dirac–Fock and Dirac–Slater methods (Fricke 1975). Figure 17.49 shows radial distributions of the *n*s electrons in Nb, Ta, and Db as a result of the atomic (at) DS relativistic (solid line) and non-relativistic (dashed line) calculations. The dot–dashed lines (mol) are from relativistic molecular calculations of the metal ions for the electronic configuration obtained for MCl_5. It is interesting to note that the non-relativistic $R_{\max}$ of (6s) Ta is smaller than $R_{\max}$ of (5s) Nb, which is a result of the lanthanide contraction. The non-relativistic $R_{\max}$ of (7s) Db is larger than $R_{\max}$ of (6s) Ta due to the orbital effect (expansion), while the relativistic contraction moves the maximum much closer to the core, so one can clearly see that orbital and relativistic effects act in opposite directions. The associated relativistic stabilization of the *n*s and destabilization of the $(n-1)$d electron binding energies is demonstrated in Figure 17.50. There is a drastic increase in the binding energy for the relativistic 7s orbital of Db in comparison to the non-relativistic case. On the other hand, both the $d_{3/2}$ and $d_{5/2}$ electrons show increasing destabilization from Nb to Db. Thus, the analysis of the atomic functions shows that the properties of Nb and Ta should be close in both relativistic and non-relativistic schemes, while Db should behave differently due to strong relativistic effects, but in the opposite direction than in the non-relativistic case.

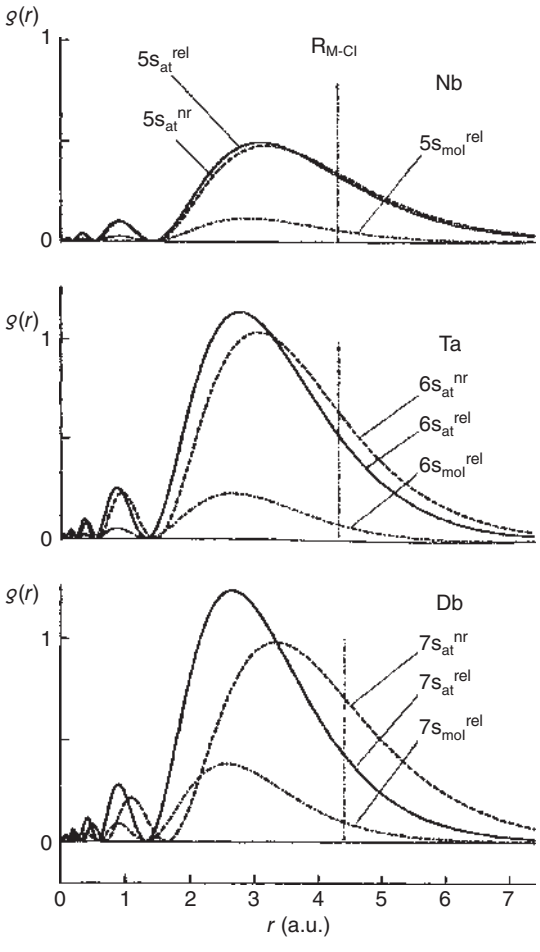

Figure 17.49 Radial distribution of the *ns* electrons in Nb, Ta, and Db as a result of the atomic (at) DS relativistic (solid line) and non-relativistic (dashed line) calculations. The dot-dashed lines (mol) are relativistic molecular calculations of the metal ions for the electronic configurations of MCl_5. The vertical line gives the bond distance. Source: Pershina and Fricke (1993), figure 1 (p. 9721)/American Institute of Physics.

Among the molecular methods, due to the high accuracy and efficiency, relativistic density functional theory (DFT) is most important in theoretical chemistry. It is based on knowledge of the ground-state electron density or current which uniquely determines the Hamiltonian and, hence, the ground-state energy of a system. In principle, DFT is exact, but the accuracy depends on an adequate choice of the exchange correlation potential functional E_{ex} whose exact form is not known. In the past, the simplest local density approximation was used extensively. The DS discrete variational method (DS-DVM) by Rosen and Ellis (1975), the predecessor of the modern relativistic DFT methods, was based on this approximation. One of the most advanced versions used for the heaviest elements is the non-collinear SP 4c-DFT method by Anton et al. (2004). The method, particularly the embedded cluster procedure by Jacob et al. (2003), makes it suitable for modeling adsorption on large solid surfaces, for example, adsorption of elements 112 and 114 on gold surfaces.

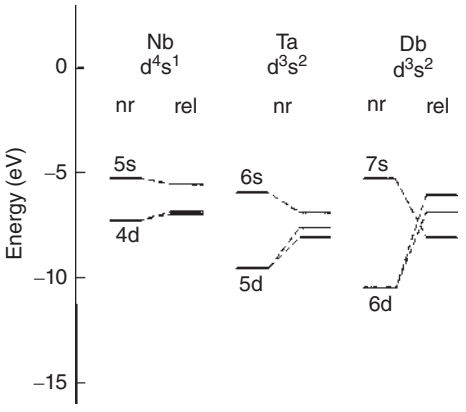

Figure 17.50 Binding energies of Nb, Ta, and Db as a result of the DF relativistic and HF non-relativistic calculations. Source: Pershina and Fricke (1993)), figure 3 (p. 9722)/American Institute of Physics.

17.8.3 Selected Experimental Results

A selection of species studied in chemical investigations of elements 104–114 is contained in Table 17.14 together with the methods applied, the sequences of elution (or the sequences in volatility), and the relevant references. In the following, we comment on a few exemplary cases. Toyoshima et al. (2008) have examined the fluoride complexation of Rf in mixed HNO_3/HF solutions by determining %ads values on an anion exchange resin and correlating them with the relationship between K_d and %ads for Zr and Hf as in Haba et al. (2004).The variation of the K_d values of Zr and Hf under static conditions and K_d values of Rf from column chromatography as a function of the equilibrated concentration of free F^- ($[F^-]_{eq}$) is shown in Figure 17.51a. It is obvious that with increasing $[NO_3^-]$, the K_d values of the anionic Zr, Hf, and Rf fluoride complexes decrease; obviously, the nitrate ion acts as a counterion competing for the binding sites on the anion exchange resin. The solid, dashed, and dotted curves in Figure 17.51a are the results of theoretical calculations to be discussed below. A typical exchange reaction of an anionic complex A with charge c, A^{c-}, with a counterion L^- between the solution and the resin is

$$A^{c-} + cRL \Leftrightarrow R_cA + cL^- \tag{17.70}$$

where R denotes the anion exchange resin. The equilibrium constant of the exchange reaction D_c is described as

$$D_c = \frac{[R_cA][L^-]^c}{[A^{c-}][RL]^c} \tag{17.71}$$

The K_d value can be expressed as

$$K_d = \frac{[R_cA]}{A^{c-}} = D_c \frac{[RL]^c}{[L^-]^c}. \tag{17.72}$$

Taking logarithms of both sides of Eq. (17.72) results in

$$\log K_d = \log D_c - c \log \frac{[L^-]}{[RL]} \tag{17.73}$$

This indicates that the slope c in the log K_d vs. log$[L^-]$ plot is equivalent to the charge of the anionic complex. The concentration of the counterion in the resin can

Table 17.14 Chemical species studied with elements 104 through 114, applied methods, elution sequences, and references.

Element	Species	Method	Elution sequence	References[a)]
104	$Rf^{4+} + \alpha$HiB	CIX	Rf ≫ Ln	Silva et al. (1970)
	$RfCl_4$	TC	Rf ≈ Hf	Zvara et al. (1971b)
	$RfCl_6^{2-}$	Aliquat 336	Rf ≈ Hf	Hulet et al. (1980)
	$RfCl_4$	IC	Rf ≈ Zr > Hf	Türler (1996)
	$Rf(NO_3)_4$	TBP	Hf ≈ Rf > Zr	Günther et al. (1998)
	RfF_6^{2-}	CIX	Zr ≥ Hf > Rf > Th	Strub et al. (2000)
	$RfCl_6^{2-}$	AIX	Hf > Zr > Rf	Haba et al. (2002)
	RfF_6^{2-}	AIX	Rf > Zr ≈ Hf	Haba et al. (2004)
	RfF_6^{2-}	AIX	Rf > Zr ≥ Hf	Toyoshima et al. (2008)
	$Rf(HSO_4)_6^{2-}$	CIX	Zr > Hf > Rf > Th	Li et al. (2011)
105	$DbBr_5$	TC	Nb > Db ≥ Hf	Zvara et al. (1976)
	$DbBr_5$	IC	Nb ≈ Ta > Db	Gäggeler et al. (1992)
	$DbCl_6^-$	Aliquat 336	Ta > Db ≥ Nb > Pa	Paulus et al. (1999)
	DbF_6^-	Aliquat 336	Pa > Db ≈ Nb ≈ Ta	Paulus et al. (1999)
	DbF_6^-	AIX	Pa > Db > Ta ≈ Nb	Tsukada et al. (2009)
	$DbBr_5$	IC	Db > Nb > Ta	Qin et al. (2012)
106	SgO_2Cl_2	IC	Mo > W > Sg	Türler (1999)
	$SgO_2(OH)_2$	IC		Hübener et al. (2001)
	$SgO_2F_3^-$	CIX		Schädel et al. (1997)
	$SgO(OH)_3(H_2O)_2^+$	CIX	Mo > W > Sg	Schädel et al. (1998)
107	BhO_3Cl	IC	Tc > Re > Bh	Eichler et al. (2000b)
108	HsO_4	IC	Os > Hs	Düllmann et al. (2002b)
	$Na_2[HsO_4(OH)_2]$	IC	Hs > Os	von Zweidorf et al. (2004)
112	E112 (Cn)	TC	Rn > Cn > Hg	Eichler et al. (2008)
114	E114	TC	Rn > E114 ≥ Cn > Hg	Eichler et al. (2010)
	E114	IC/TC	Rn > Cn > E114 > Hg	Yakushev et al. (2012)

CIX = cation exchange chromatography, AIX = anion exchange chromatography, for reversed-phase extraction chromatography the extractant is given, TC = thermochromatography, IC = isothermal gas chromatography.
a) The references are those given in Kratz (2011).

be regarded as a constant value that is given by the exchange capacity of the anion exchange resin, [RL] = constant. In order to understand the slopes in the log K_d vs. $\log[NO_3]_{eq}$ plot, one has to consider potential other counterions, that is, F^- and HF_2^- present in mixed HNO_3/HF solutions. One can show that the contributions of F^- and HF_2^- are negligible at $[F^-]_{eq} < 5 \cdot 10^{-3}$ M. The slope of the log K_d vs. $\log [NO_3^-]_{eq}$ plot at $[F^-]_{eq} < 5 \cdot 10^{-3}$ M, therefore, represents the charge of the anionic complex, and

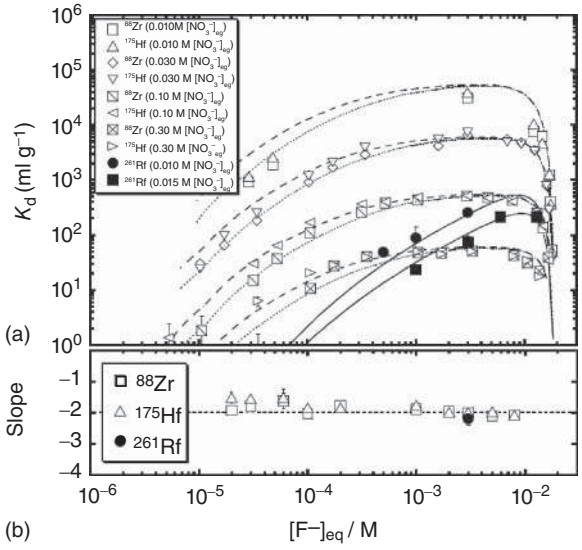

Figure 17.51 (a) Variation of the K_d values of Zr and Hf under static conditions and of Rf in column chromatography on an anion exchange resin (CA08Y) as a function of the equilibrated concentration of free F^- ($[F^-]_{eq}$). Values for Zr and Hf are shown for$[NO_3^-]_{eq}$ = 0.01, 0.03, 0.1, and 0.3 M. Values for Rf are shown for $[NO_3^-]_{eq}$ = 0.01 and 0.015 M. The solid, dashed, and dotted curves represent theoretical calculations of K_d values, see text. (b) Variation of the slopes in the log K_d vs. log$[NO^-]_{eq}$ plots as a function of $[F^-]_{eq}$. Source: Toyoshima et al. (2008), figure 5 (p. 130)/De Gruyter.

the −2 slopes shown in Figure 17.52 and in Figure 17.51b mean that anionic complexes of Zr, Hf, and Rf with a charge of −2 are replaced by NO_3^- ions on the resin in an equilibrium between resin and solution. On the other hand, the increasing K_d values of Zr, Hf, and Rf with increasing $[F^-]_{eq}$ at constant $[NO_3^-]_{eq}$ in Figure 17.51a indicate that the anionic complexes with the charge of −2 are increasingly formed in chemical reactions with the fluoride ion. The consecutive formation reactions of fluoride complexes are

$$[MF_{n-1}]^{4-(n-1)} + F^- \Leftrightarrow [MF_n]^{4-n} \quad (n = 1 - 6) \tag{17.74}$$

where M indicates Zr, Hf, and Rf and n denotes the coordination number in the products. The equilibrium constants of the formation reactions, K_n, are described as

$$K_n = \frac{[MF_n^{4-n}]}{[MF_{n-1}^{4-(n-1)}][F^-]} \quad (n = 1 - 6) \tag{17.75}$$

The anionic fluoride complexes $[MF_5]^-$ and $[MF_6]^{2-}$ in Eq. (17.74) participate in the adsorption–desorption process on the anion exchange resin. However, the exchange of $[MF_6]^{2-}$ is dominant over that of $[MF_5]^-$ because of the −2 slope. Therefore, A^{c-} in Eq. (17.72) is replaced by $[MF_6]^{2-}$, and Eq. (17.72) is modified to

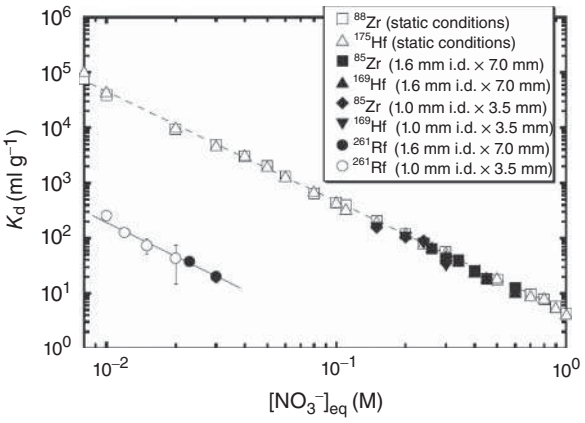

Figure 17.52 Distribution coefficients, K_d, of Zr and Hf under static conditions and those of Zr, Hf, and Rf from column chromatography with the anion exchange resin CA08Y as a function of the nitrate ion concentration at fixed $[F^-]_{eq} = 3 \times 10^{-3}$ M. Linear relationships of log K_d vs. log $[NO_3^-]_{eq}$ for Rf and the homologs are indicated by the solid and dashed lines, respectively. Source: Toyoshima et al. (2008), figure 4 (p. 129)/De Gruyter.

the form containing Eq. (17.74) as

$$K_d = \frac{[R_2MF_6]}{\sum_{n=0}^{6}[MF_n^{4-n}]} \tag{17.76}$$

Substituting Eq. (17.71) with $c = 2$ and Eq. (17.75) into Eq. (17.76) yields

$$K_d = \frac{D_2\beta_6[F^-]^6[RL]^2}{\left(1 + \sum_{n=1}^{6}\beta_n[F^-]^n\right)[L^-]^2} \tag{17.77}$$

where the symbols β_n (n = 1–6) denote the stability constants represented as $\beta_n = \prod_{i=1}^{n} K_i$. Taking logarithms of both sides of Eq. (17.77), log K_d becomes

$$\log K_d = \log D_2 - 2\log\frac{[L^-]}{[RL]} + \log\frac{\beta_6[F^-]^6}{1 + \sum_{n=1}^{6}\beta_n[F^-]^n} \tag{17.78}$$

which has an additional term compared to Eq. (17.73). Under the condition of a constant $[F^-]_{eq}$, the last term in Eq. (17.78) is constant and the slope in the log K_d vs. log$[L^-]$ plot also gives the charge of the anionic complex. In Figure 17.48a, the results of the calculations for Zr and Hf with Eq. (17.78) are shown by the dotted and dashed curves, respectively. In these calculations, values of K_n (n = 1–6) from the literature were used and the contribution of HF_2^- as counterion was also considered; the abrupt increase in $[HF_2^-]_{eq}$ for $[F^-]_{eq} > 5 \cdot 10^{-3}$ M causes a sudden decrease in the K_d values of Zr and Hf. Obviously, the exchange reactions between $[ZrF_6]^{2-}$ and $[HfF_6]^{2-}$ and the counterions NO_3^- and HF_2^- are well described. The results of the calculations for Rf using the values of $K_5 = 4 \cdot 10^3$, $K_6 = 2$, and $D_2 = 5 \cdot 10^5$ are

shown as solid lines in Figure 17.51a. The equilibrium constant of exchange reactions D_2 was assumed to be equal to that of the homologs Zr and Hf. Under this assumption, the value of K_5 is one order of magnitude smaller and the value of K_6 is three orders of magnitude smaller than those of the homologs. This shows that the chemical properties of the transactinides can deviate markedly from those of their lighter homologs.

For element 105, dubnium, we have selected the investigations of the volatility of the dubnium bromides as an example to be discussed in some detail. The first experiments on the volatility of Db halides were performed in gas thermochromatography experiments by Zvara et al. (1970) in a chlorinating atmosphere. Later studies (1976) also investigated Db bromide. Its volatility was observed to be lower than that of Nb bromide. However, only sf events were detected in this experiment; thus, the assignment of the observed fission tracks to an isotope of Db was not unambiguous. In 1992, Gäggeler et al. (1992) performed the first on-line isothermal gas chromatography of the bromides of Db using 34 seconds ^{262}Db. Detection of ^{262}Db was performed via sf detection corroborated by the analysis of the half-life. In this experiment, they observed a rather similar volatility in the bromides of Nb and Ta. The volatile Ta bromide was only formed when HBr was saturated with BBr_3 vapor. For Nb bromide, pure HBr was sufficient for its formation. Db bromide was found to be less volatile than those of Nb and Ta; hence, the sequence in volatility Nb $\approx$ Ta > Db was deduced. This sequence is in agreement with the data of Zvara et al. (1976) but in conflict with the theoretical expectations of Pershina et al. (1992). Gäggeler et al. (1992) therefore stated that formation of the less volatile Db oxybromide instead of the more volatile pure pentabromide could not be excluded. In an additional on-line isothermal experiment, the volatility of chlorides of the group 5 elements was investigated by Türler (1996). The volatility of pure Db pentachloride could not be determined, only that of Db oxychloride. Therefore, in the most recent work by Qin et al. (2012), concentrating on a determination of the volatility of Nb, Ta, and Db bromides at the highest feasible level of chemical purity of the reactive gas to ensure the formation of the pure pentabromides instead of the oxybromides, a liquid-nitrogen trap and a high-temperature (1000 °C) tantalum getter were used to remove trace amounts of water or oxygen in the carrier gas prior to entering OLGA (Figure 17.37). Volatile bromide compounds of the type MBr_5 (M = Nb, Ta, and Db) were formed with the reactive gas HBr at 900 °C. Without purification, Nb formed both the oxybromide and the pentabromide. Only after careful purification of the carrier gas did Nb, Ta, and Db form the pure pentabromides and the adsorption enthalpies $\Delta H_a^{o(T)}$ of -89 ± 5 kJ mol^{-1} for $NbBr_5$, -101 ± 5 kJ mol^{-1} for $TaBr_5$, and -71 ± 5 kJ mol^{-1} for $DbBr_5$, see Figure 17.53, determined. The sequence in volatilities $DbBr_5 > NbBr_5 > TaBr_5$ is now in agreement with the theoretical calculations of Pershina et al. (1992) where the high volatility of the $DbBr_5$ was predicted due to relativistic effects resulting in the lowest effective charge on Db and the highest covalence of the $DbBr_5$ among the homologs. Thus, it is suggested that the species investigated in the work by Gäggeler et al. (1992) and Zvara et al. (1976) was $DbOBr_3$ instead of $DbBr_5$.

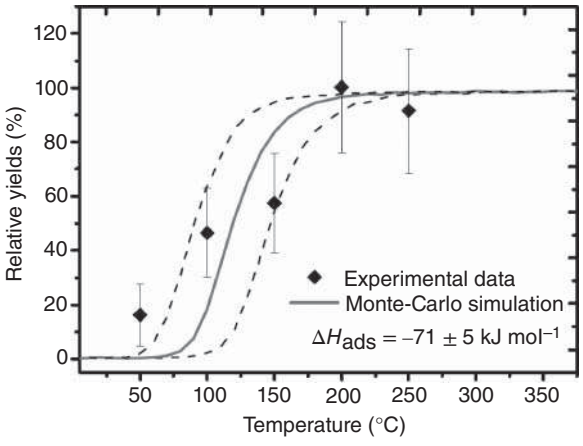

Figure 17.53 Relative chemical yield for $DbBr_5$ with HBr as reactive gas as a function of the temperature of the isothermal part of the quartz glass chromatography column. A Monte Carlo simulation based on the microscopic model of Zvara (1985) shows that an adsorption enthalpy $\Delta H_a^{o(T)} = -71 \pm 5$ kJ mol^{-1} is in best agreement with the data. Source: Qin et al. (2012).

For the discussion of the chemical properties of element 105, we return to the aqueous-phase chemistry. First studies of the aqueous chemistry of element 105 have provided expected results as well as surprises (Pitzer 1975; Kratz et al. 1989). The sorption of 34-seconds ^{262}Db on glass surfaces after fuming with nitric acid was compared with tracers of the group 4 elements Zr and Hf and the group 5 elements Nb and Ta produced under similar conditions (Pitzer 1975). Even after washing with 1.5 M HNO_3, Db was found to adhere to the glass, a property characteristic of the group 5 elements. Experiments to investigate, whether Db is extracted into methyl isobutyl ketone (MIBK) under conditions in which the lighter homolog Ta extracts but the next lighter homolog Nb does not, were also conducted (Pitzer 1975). It was expected that Db would behave more like Ta than Nb but, surprisingly, Db did not extract from mixed nitric acid/hydrofluoric acid solutions, although Ta did. The formation of polynegative anions is a possible explanation.

Later, a large number of automated anion exchange chromatography separations using triisooctyl amine (TIOA) on an inert support was performed (Kratz et al. 1989) in order to compare the halide complexation of Db in detail with the lighter group 5 elements Nb and Ta, and with Pa. Complete extraction-elution cycles were performed on a one-minute time scale with Db, and Nb, Ta, and Pa, produced under similar conditions. It was found (Kratz et al. 1989) that Db sorbs on the columns from either 12 M HCl/0.02 M HF or 10 M HCl like its homologs Nb, Ta, and Pa. In elutions with 4 M HCl/0.02 M HF (Pa–Nb fraction), and with 6 M HNO_3/0.015 M HF (Ta fraction), the Db activity was found in the Pa–Nb fraction, showing that the anionic halide complexes of Db are different from those of Ta and are more like those of Nb and Pa, indicating a reversal in the trend in going from Nb via Ta to Db. In another series of experiments, after the extraction into TIOA from 10 M HCl, elutions were performed with 10 M HCl/0.025 M HF (Pa fraction) and 6 M HNO_3/0.015 M HF (Nb Strip). The Db activity was divided almost equally between these two fractions, showing again a behavior very different from Ta, and close to Nb and Pa (Kratz et al. 1989). It was suggested (Kratz et al. 1989) that the non-tantalum like halide complexation of Db is indicative of the formation of oxohalide or hydroxohalide complexes

like $[NbOCl_4]^-$ and $[PaOCl_4]^-$ or $[Pa(OH)_2Cl_4]^-$, in contrast to the pure halide complexes of Ta, such as $[TaCl_6]^-$.

Stimulated by the previously observed similarity of the aqueous-phase chemistry of element 105 to that of Nb and Pa, further automated extraction chromatography experiments (Gober et al. 1992) were conducted in the system HBr/HCl-diisobutylcarbinol (DIBC). The extraction, from concentrated HBr, was followed by the elution of a Nb fraction in 6 M HCl/0.0002 M HF, and a Pa fraction in 0.5 M HCl. Some Db activity was observed in the Nb fraction but with an apparent cross section which indicated that <45% of the Db was extracted into the DIBC from concentrated HBr. It was concluded that, under these conditions, the bromide complexing of Db is closer to that of Nb than to that of Pa, indicating a greater tendency to form non-extractable polynegative anions in the sequence Pa < Nb < Db.

In subsequent work (Schädel et al. 1992), studies of the complexation of element 105 by unbuffered α-hydroxy-isobutyric acid (α-HiB) and its elution from strongly acidic cation exchange resin were performed on Db, Nb, Ta, and Pa activities. The motivation for these experiments was (i) to provide another, definitive verification that pentavalent Db is the most stable state in aqueous solution, (ii) to provide a faster chemical separation of element 105 than in previous experiments, (iii) to search, with this faster chemistry, for the previously undiscovered isotope ^{263}Db. Complexation of metal ions by α-hydroxy-carboxylate anions, such as $(CH_3)_2COH–COO^-$, depends strongly on the charge of the ion. For cation exchange separations of pentavalent species (Nb, Ta, Pa, Ha) from tetravalent (Zr, Hf, Rf) and trivalent actinide ions, rather low α-hydroxycarboxylate concentrations are sufficient: α-HiB complexes of the group 5 elements are immediately eluted from the resin, while tetravalent ions are retained on the column and retention on the column is even more pronounced for the trivalent actinides. 0.05 M α-HiB was selected because at this concentration the narrowest elution curve was observed. Higher molarities did not notably improve the elution and were disregarded as they might decrease the retention of tetravalent and trivalent metal ions on the columns. After collection of the transported activities on the polyethylene frit in ARCA II for one minute, the frit was washed with about 100 nl of unbuffered 0.05 M α-HiB solution (6.5 seconds). This solution was passed through one of 38 cation exchange columns contained in two magazines and was collected on a Ta disk and quickly evaporated to dryness by intense infrared light and a stream of hot He gas. After flaming and cooling, the Ta disk was inserted into one of ten detector stations for α-particle spectroscopy. Start of counting was 39 seconds after the end of collection. After three separations each, a new column was positioned below the collection frit. Thus, 114 continuous collection and separation cycles were conducted before the program was stopped; the used magazines were removed, and two new magazines were introduced for the next 114 one-minute cycles.

The α-HiB separations in the bombardment of a ^{249}Bk target with ^{18}O-ions were started at 99 MeV (center of target, cot). Compared to the earlier studies of halide complex formation and extraction of element 105 into triisooctyl amine (Kratz et al. 1989), decontamination from the Fm/Md activities was improved by more than 2 orders of magnitude. The spectrum contained 41 α events attributable to element

105, among them 9 correlated pairs of parent–daughter decays. Also, 23 fissions attributable to Db decays were detected. These event rates were consistent with the detection efficiency and the known production cross section at 99 MeV (Kratz et al. 1989). This demonstrates that element 105, in 0.05 M α-HiB, is eluted with very high yield from cation exchange columns as are Nb, Pa, and Ta. This furnishes further proof that pentavalent Db is the most stable state in aqueous solution.

The α-HiB procedure involving evaporation to dryness of the effluent and pulse-height analyses in vacuum with ten 300 mm^2 PIPS detectors was also applied to the products of bombardment at a lower projectile energy of 93 MeV (cot), thought to be optimum for the production of the hitherto undiscovered isotope ^{263}Db in this reaction. In a total of 374 experiments, nine α-particles, with energies between 8.3 and 8.5 MeV as well as 18 SF events were registered (Kratz et al. 1992). The absence of a-particles above 8.5 MeV indicated that the pair ^{262}Db/^{258}Lr was no longer present (<1.3 nb) in agreement with evaporation calculations. Instead, groups at 8.355 and 8.445 MeV were detected that were assigned (Kratz et al. 1992) to ^{263}Db and its daughter, ^{259}Lr, respectively. ^{263}Db decays with a half-life of 27 seconds and has a 43% α branch and a 57% SF branch. The average post-neutron emission total kinetic energy is 207 MeV. The assignment to mass number 263 is consistent with α-decay energy systematics in that region. The mass assignment is also consistent with the measured production cross section of 10 ± 6 nb at 93 MeV which is on the same order of magnitude as the 5n cross section at 99 MeV as predicted by evaporation calculations. The mass assignment is also supported by the observation of the 8.45 MeV α-particles of the daughter ^{259}Lr in the 93 MeV ^{18}O bombardment of ^{249}Bk. The cross section for production of ^{262}Db at 99 MeV and the SF branch in the decay of ^{262}Db, as reported earlier (Kratz et al. 1989), must be revised because it became clear now that both isotopes, 34-seconds ^{262}Db and 27-seconds ^{263}Db, are produced at this energy. This is suggested by evaporation calculations as well as by the data themselves. Of the total of 41 α-events attributable to Db decays, two events around 8.35 MeV must be assigned to ^{263}Db. A comparable number of daughter α-decays at $E_\alpha = 8.45$ MeV must have been present, too, but these are masked by the 8.45 MeV α-decay branch in ^{262}Db. Based on the 57% fission branch in the decay of ^{263}Db, we conclude that these 4 α events should have been accompanied by 6 or 7 SF events. Subtracting these from the total of 23 SF events observed at 99 MeV, leaves about 16 SF events associated with the decay of ^{262}Db. After these subtractions, the new value for the fission branch in ^{262}Db is 33%. The cross sections at 99 MeV from the α-HiB separations are 6 ± 3 nb for ^{262}Db and 2 ± 1 nb for^{263}Db, respectively.

At about the same time, K.R. Czerwinski (1992) had searched for ^{263}Rf in the ^{248}Cm(^{18}O, 3n) reaction at 92.5 MeV using liquid–liquid extraction of rutherfordium from 0.05M HCl into 0.5 M thenoyltrifluoroacetone in benzene. In 300 three-minute collections and separations, 7 SF events were observed with a half-life of 500^{+300}_{-200} seconds corresponding to a cross section of 140 ± 50 pb. No α particles attributable to the decay of ^{263}Rf were found. As presented above, Kratz et al. (Schädel et al. 1992; Kratz et al. 1992) had discovered the isotope 27-seconds ^{263}Db in the ^{249}Bk(^{18}O, 4n) reaction at 93 MeV by eluting element 105 from cation

exchange columns in unbuffered 0.05 M α-HiB (Kratz et al. 1992). ^{263}Db decays predominately by SF (57%) and by α decay (43%) and was produced with a cross section of 10 ± 6 nb. An EC decay branch could not be excluded. Therefore, a search for an EC-branch in the decay of 27-seconds ^{263}Db was performed in a milking experiment: ^{263}Db was again produced in the ^{249}Bk(^{18}O, 4n) reaction and transported to the ARCA (Schädel et al. 1989) by a He/KCl jet. After one minute collections, the activity was dissolved in 0.05 M α-HiB and eluted in that solution from a cation exchange column. The same column was used for five subsequent collection-elution cycles with ^{263}Db. After the fifth elution, an elution of tetravalent ions including those of rutherfordium, if present, was performed with 0.1 M HF. In 155 of such rutherfordium fractions, a total of 22 SF events were observed. From the known α/SF ratio for Fm isotopes and from the Fm contained in the measured α-particle spectra, 8.8 of these SF events had to be attributed to ^{256}Fm. A two-component fit with the ^{256}Fm fixed yielded a half-life of 600^{+300}_{-200} seconds for ^{263}Rf. Based on the effective production cross section and on the known cross section for the production of ^{263}Db at 93 MeV, 10 ± 6 nb, an EC-branch in the decay of ^{263}Db on the order of 5% was deduced. Two α particles at 7.9 MeV with lifetimes compatible with a half-life of about 10 minutes were discussed as possibly being associated with the decay of ^{263}Rf giving an upper limit for the α-decay branch of 30%. The effective production cross section for ^{263}Rf via EC decay of ^{263}Db is thus significantly higher than that in the ^{248}Cm(^{18}O, 3n) reaction. Kratz et al. (Schädel et al. 1992; Kratz et al. 1992) have attempted to add further evidence for an EC branch in the decay of ^{263}Db and for ^{263}Rf in a new series of experiments producing again ^{263}Db in the ^{249}Bk(^{18}O, 4n) reaction at 93 MeV (Kratz et al. 2003). A two-step chemical separation scheme was used consisting of the successful cation exchange separation with α-HiB and a liquid–liquid extraction of the group-4 elements from 9 M HCl into tributylphosphate (TBP)/cyclohexane yielding an improved decontamination of the rutherfordium fraction from actinides. The activity delivered by a He/KCl gas jet was collected for 15 minutes (sufficiently long for 27-seconds ^{263}Db to decay) on a Ta disc by impaction. The KCl spot was dissolved by 2×20 µl of unbuffered 0.5 M α-HiB containing ^{88}Zr tracer and pipetted on top of a 3×50 mm glass column thermostated at 50 °C containing the cation-exchange resin AG 50 W × 8, minus 400 mesh. The column was previously preconditioned with 0.5 M α-HiB. The group-4 elements were eluted from the column in 2×500 µl 0.5 M α-HiB and collected in a centrifuge cone. The eluate (1 ml) was combined with 3 ml concentrated HCl to yield a solution being 9 M in HCl. This was contacted for about 20 seconds with 200 µl of a 20 vol% TBP/cyclohexane solution for liquid–liquid extraction. The phases were separated, and the organic phase was evaporated to dryness on a Ta disc. The Ta discs were assayed for α and SF activity starting about eight minutes after the end of collection. The chemical yields were determined via the ^{88}Zr activity by γ-ray spectroscopy for each sample and were 65% on the average. The decontamination factor from trivalent metal ions determined with lanthanide tracers was on the order of 15 000. ^{263}Db was produced in the reaction ^{249}Bk(^{18}O, 4n) at the Philips Cyclotron of the Paul Scherrer Institute (PSI) Villigen, Switzerland. The 478 µg cm^{-2} target was prepared by electrodeposition of $Bk(NO_3)_3$

on Be. After the plating process, the nitrate was converted into the oxide by heating. It was bombarded with average $^{18}O^{5+}$ beam intensities of $2.7 \times 10^{12}\,s^{-1}$ with a projectile energy of 93 MeV. The target contained 80–100 $\mu g\,cm^{-2}$ Tb as upper layer to simultaneously produce Ta isotopes (notably ^{172}Ta) that was used to perform yield checks by γ-spectroscopy. Reaction products recoiling out of the target were stopped in He gas containing KCl aerosols. The aerosols together with the recoil products were transported through a steel capillary (2 mm inner diameter, length 50 m) to the collection site. The transport plus deposition yield was $38 \pm 11\%$ on the average at a He flow of about $2\,l\,min^{-1}$.

A total of 9 SF events were registered of which 2 have to be considered a long-lived electronic background. The remaining 7 events are compatible with a half-life of 24^{+19}_{-7} minutes and an effective production cross section of 290^{+140}_{-50} pb. With the measured production cross section for ^{263}Db at 93 MeV of 10 ± 6 nb, this results in an EC-branching the decay of ^{263}Db of $3^{+4}_{-1}\%$ (Kratz et al. 2003).

In the work by Paulus et al. (1999), a systematic study of the extraction of the group-5 elements from pure HF, HCl, and HBr solutions into aliphatic amines was performed. Based on these results, chromatographic separations of the group-5 elements and element 105 with ARCA II were carried out in the HF and HCl systems. From the respective elution positions of element 105, its distribution coefficients were determined and compared to new theoretical predictions (Paulus et al. 1999) in which the competition between hydrolysis and halide complex formation was explicitly taken into account.

The sequence of extraction from 1 M to 8 M HCl into the organic phase was Pa > Nb > Ta > Zr, Hf, which is the complete inversion of the known sequence Ta > Nb > Pa in the TiOA/HCl system containing 0.03 M HF (Kratz et al. 1989), This reversal is independent of the choice of a particular amine and is clearly associated with the presence or absence of HF in the aqueous phase. In the column experiments, most of the amines tested in the HCl system showed slow kinetics for extraction into the aqueous phase, resulting in elution peaks with an unacceptable tailing of the activities into the subsequent fraction, a feature that is absent in the mixed HCl/HF system (Kratz et al. 1989). Only with the quaternary amine Aliquat 336 could an acceptable chromatographic separation be achieved at the flow rate of the mobile aqueous phase of $1\,ml\,min^{-1}$. Carrier-free tracers of Eu, Nb, Ta, Pa, Zr, and Hf were fed onto the column from 10 M HCl. Zr, Hf, and Ta were eluted in 6 M HCl, Nb in 4 M HCl, and Pa in 0.5 M HCl. Thus, this system provides conditions for extracting all relevant elements from one HCl solution.

Similarly, new partition experiments and chromatographic separations were performed with the fluoride salt of Aliquat 366/HF and the bromide salt of Aliquat 336/HBr. The K_d values in the HBr system show the same sequence Pa > Nb > Ta as in the HCl system. However, the threshold HBr concentrations above which an appreciable extraction is observed are shifted to higher HBr molarities, i.e. to 6 M for Pa, 9 M for Nb, while Ta is not extracted even from 12 M HBr. The fact that Ta does not extract from HBr solutions makes this system the least attractive for an application to element 105. With the fluoride salt of Aliquat 336, K_d values on the order of 10^3 are observed for all elements even at low HF concentrations in

the aqueous phase. The same extraction sequence Pa > Nb > Ta as in the HCl- and HBr-systems is observed at 0.5 M HF. For increasing HF concentrations above 1 M, the K_d values stay high for Nb and Ta up to 12 M HF, while they decrease for Pa, Zr, and Hf due to the formation of polynegative fluoro complexes. In chromatographic separations, after feeding the activities onto the 1.6×8 mm columns, 930 experiments were conducted with element 105 in ARCA II in the Aliquat 336/HCl system with a 50 seconds cyclic collection time of the aerosol on a Kel-F™ slider. The reaction products were fed onto the columns in 167 µl of 10 M HCl followed by elution with 183 µl of 6 M HCl (Ta fraction, $75 \pm 3\%$ elution) and elution of a strip fraction with 167 µl of 6 µ $HNO_3$3/0.015 M HF (Nb, Pa fraction). The effluents were continuously sprayed through a nozzle onto Ta disks on which they were evaporated to dryness by hot He gas and infrared light. Start of measurement of the *a*- and SF-activities was 60 seconds (Ta fraction) and 76 seconds (Nb, Pa fraction) after the end of collection. Six α singles in the Ta fraction and 12 in the Nb, Pa fraction were observed.

The resulting K_d – values were compared with the results of theoretical calculations by V. Pershina (1998) showing that the extraction behavior of the group-5 elements is primarily the result of their complex formation in acidic solutions which is in competition with the hydrolysis of the formed complexes. In pure HCl solutions, at concentrations above 2–4 M HCl, all the elements, Nb, Ta, Pa, and presumably 105, form the same type of complexes, $M(OH)_2Cl_4^{2-}$, $MOCl_4^-$, $MOCl_5^{2-}$, and MCl_6^- with increasing HCl concentration. The reactions which must be considered here are

$$M(OH)_yL_a{}^{(z-y-a)-} + bH^+ + bL^- \leftrightarrow M(OH)_{y-b}L_{a+b}{}^{(z-y-a-b)-} + bH_2O + \Delta E \tag{17.79}$$

Pershina (1998) has made estimates of the free energy change, ΔE, of the complex formation (17.79) using results of relativistic calculations of the electronic structures of the molecules $M(OH)_6^-$, $M(OH)_2Cl_4^{2-}$, $MOCl_4^-$, $MOCl_5^{2-}$, and MCl_6^- for Nb, Ta, 105, and Pa with the DS–DV code. Due to changes in the electrostatic part of the interaction energy which is the dominant contribution, the total energy differences, ΔE, for (17.79) with the formation of all types of the above-mentioned complexes have been shown to decrease in the order Ta > 105 > Nb > Pa. This means that the complex formation changes in the following way

$$Pa \gg Nb > 105 > Ta \tag{17.80}$$

Thus, for the same type of complexes, those of Pa are formed in more dilute HCl solutions (starting with $Pa(OH)_2Cl_4^{2-}$; at 2–4 M), than those of the other elements. The complexes of Nb start to form next (above 4–5 M), while those of Ta are formed at even higher HCl molarities (above 6 M). This result is in agreement with the complex formation data on Nb, Ta, and Pa. The results of the solvent extraction experiments for Nb, Ta, and Pa confirm sequence (17.80) of the complex formation. Accordingly, hydrolysis of the complexes changes in the opposite direction to (17.80). Comparison (Paulus et al. 1999) of the calculated ΔE values for $M(OH)_2Cl_4^{2-}$, $MOCl_4^-$, and MCl_6^- shows that, in agreement with experiment,

the $M(OH)_2Cl_4^{2-}$ species are formed at lower HCl concentration, while MCl_6^- forms at the highest concentrations. The complex formation develops in the order $M(OH)_2Cl_4^{2-} > MOCl_4^- > MCl_6^-$ with increasing HCl concentration. By combining sequence (17.80) with theoretical considerations about the partition of the complexes between the organic and aqueous phases the following trend in the K_d values for the group-5 elements has been predicted (Pershina and Fricke 1993) as

$$Pa \gg Nb > 105 > Ta \tag{17.81}$$

This holds particularly for concentrations of HCl between 4 and 8 M, where the rising K_d values are indicative of the formation of chloro-complexes. Sequence (17.81) is exactly the sequence obtained in the experiments. According to the theoretical predictions, the calculated values of the free energy change, ΔE, are on the order of 12 eV for the fluorides, 20 eV for the chlorides, and 22 eV for the bromides (not taking into account the enthalpy of formation of H_2O which is 3 eV). This means that the most exothermic reaction occurs with the fluorides. This is in excellent agreement with the experimental findings: For the fluorides, the equilibrium is always on the right-hand side of Eq. (17.79) even at low HF concentrations; for the chlorides, it takes >3 M HCl to form extractable chloride complexes, and for the bromides, the threshold is shifted to >6 M HBr. For HBr solutions where complexes of Nb, Ta, Pa, and 105 are analogous to those formed in HCl solutions, the theoretically predicted sequence of extraction is the same as (17.81), with the onset of extraction being shifted to higher acid concentrations. For HF solutions, the situation is more complicated which hinders the interpretation of the experimental results. The fluoride complexes of the metals of interest are formed very early (at very low HF concentrations) due to the very weak competition of hydrolysis. Accordingly, no rising slopes are observed on the extraction curves. This means that the complex formation might compete with the other steps of the extraction process and the entire picture becomes more complicated.

For the discussion of the chemical properties of element 106, seaborgium, we return to cation exchange chromatography in 0.1 M HNO_3/5 · 10^{-4} M HF. Under these conditions, the homologs Mo and W are eluted within 10 seconds, presumably as $MoO_2F_3^-$ and $WO_2F_3^-$, respectively. No trivalent metal ions or group IV ions are eluted under these conditions. Also, the pseudo-homolog U, in the form UO_2^{2+}, is completely retained on the column. A total of 3900 identical separations were conducted with a collection and cycle time of 45 seconds. Counting of the evaporated samples started 38 seconds after the end of collection of the activity. The chemical yield for W was 80% (Schädel et al. 1997, see Table 17.14). Three correlated αα mother–daughter decays were observed that were assigned to the decay of the descendants of ^{265}Sg, ^{261}Rf, and ^{257}No. As the mother decays were not observed (due to the short half-life of ^{265}Sg), it is important to note that ^{261}Rf and ^{257}No can only be observed if ^{265}Sg passed through the column because group 4 elements and No are strongly retained on the cation exchange resin. Presumably, Sg forms $SgO_2F_3^-$ anions or the neutral SgO_2F_2, but due to the low fluoride concentration used, the anionic SgO_4^{2-} (seaborgate in analogy to molybdate MoO_4^{2-} and tungstate WO_4^{2-}) formed by hydrolysis could not be excluded.

In order to get experimental information on this latter question, a new series of seaborgium experiments with ARCA II was performed in which 0.1 M HNO_3 without HF was used as the mobile aqueous phase and the cation exchange resin Aminex A6 as the stationary phase (Schädel et al. 1998, see Table 17.14). If the "seaborgate" ion was what was isolated in the previous experiment, it was supposed to show up here again. A 691 $\mu g\,cm^{-2}$ ^{248}Cm target containing 22 $\mu g\,cm^{-2}$ enriched ^{152}Gd was bombarded with 123 MeV ^{22}Ne ions. The simultaneously produced ^{169}W served as a yield monitor. Cycles of 45 seconds were run in which the effluent was evaporated on thin ($\sim$500 $\mu g\,cm^{-2}$) Ti foils mounted on Al frames. These were thin enough to be counted in close geometry by pairs of PIPS detectors, thus increasing the efficiency for αα correlations by a factor of 4 compared to the previous experiment. A beam dose of $4.32 \cdot 10^{17}$ beam particles was collected in 4575 separations. Only one αα correlation possibly attributable to the ^{261}Rf–^{257}No pair was observed. With an expected number of random correlations of 0.5, this is likely (the probability is 30%) to be a random correlation. From the beam integral and the overall yield as measured simultaneously for ^{169}W, a total of five correlated events were to be expected. This tends to indicate that, in the absence of fluoride ion, there is sorption of Sg on the cation exchange resin.

This non-tungsten-like behavior of Sg under the given conditions may be attributed to its weaker tendency to hydrolyze:

$$(M(H_2O)_6)^{6+} \rightleftarrows M(OH)(H_2O)_5^{5+} + H^+ \tag{17.82}$$

$$\vdots$$

$$MO(OH)_3(H_2O)_2^+ \rightleftarrows MO_2(OH)_2(H_2O)_2 + H^+ \tag{17.83}$$

$$MO_2(OH)_2(H_2O)_2 \rightleftarrows MO_3(OH)^- + 2H_2O + H^+ \tag{17.84}$$

$$MO_3(OH)^- \rightleftarrows MO_4^{2-} + H^+ \tag{17.85}$$

The measured equilibrium constants for this step-wise deprotonation scheme for Mo and W have been collected from the literature. They show that Mo is more hydrolyzed than W and that the deprotonation sequence for Mo and W at pH 1 reaches the neutral species $MO_2(OH)_2(H_2O)_2$. Assuming the deprotonation processes for Sg to be similar to those of Mo and W, Eqs. (17.82)–(17.85), Pershina and Kratz (2001) predicted that, by performing fully relativistic molecular density functional calculations of the electronic structure of hydrated and hydrolyzed species in group 6, the hydrolysis of the cationic species decreases in the order Mo > W > Sg, which is in agreement with the experimental data on the hydrolysis of Mo and W and with the results for Sg (Schädel et al. 1998, see Table 17.14) for which the deprotonation sequence ends earlier with a cationic species such as $SgO(OH)_3(H_2O)_2^+$ which sorbs on a cation exchange resin.

Looking back at the experiments by Schädel et al. (1997) where fluoride ions were present having a strong tendency to replace OH^- ligands, it appears plausible that,

in this preceding experiment, neutral or anionic species were formed:

$$MO_2(OH)_2(H_2O)_2 + 2HF \rightleftarrows MO_2F_2(H_2O)_2 + 2H_2O \tag{17.86}$$

$$MO_2F_2(H_2O)_2 + F^- \rightleftarrows MO_2F_3(H_2O)^- + H_2O \tag{17.87}$$

Thus, the presence of fluoride ions seems to be an important prerequisite for further aqueous-phase studies of Sg.

We continue with a new project, the study of volatile carbonyl complexes of Sg (Even et al. 2012, 2014). This project started at the TRIGA Mainz reactor by chance, when it was observed that fission products of refractory transition metals such as Mo can be easily transformed into volatile carbonyl complexes by stopping them in a gas volume containing carbon monoxide (CO). The reaction takes place at pressures of around 1 bar at room temperature. The formed complexes are highly volatile and can be transported within a gas stream. The rapid synthesis appeared to hold promise for radiochemical purposes and was immediately thought to be useful for studying chemical properties of superheavy elements.

More than 100 years after pioneering the synthesis of metal carbonyl complexes, this compound class is still of high interest in various areas of fundamental and applied chemistry. Classically, most highly coordinated metal carbonyl complexes (with more than three CO ligands) are synthesized by treating finely powdered metals under high CO pressure and high temperatures. These challenging technical aspects restricted their broad application. In radiopharmaceutical chemistry, e.g. higher coordinated carbonyl complexes are deemed powerful lung perfusion agents, but their potential could not yet be exploited, mainly because of limits in their synthesis. Because these complexes are generally volatile, they would be ideal for gas-phase transport of short-lived isotopes of refractory metals for the production of radioactive-ion beams. In the fundamental sciences, the study of carbonyl complexes of transactinide elements ($Z \geq 104$; superheavy elements, SHE) has raised interest in theoretical chemistry. A prominent example is the prediction that relativistic effects, which scale with Z^2 and are thus most pronounced and best studied in SHEs, would be expressed in a stronger π-back-bonding in $Sg(CO)_6$ compared to $Mo(CO)_6$.

In the first publication, Even et al. (2012) reported on the syntheses and gas chromatographic studies of single transition-metal carbonyl complexes with short-lived isotopes of Mo, W, and Os. Short-lived Mo isotopes ($t_{1/2}$: a few seconds to several minutes) were produced in the neutron-induced fission of ^{249}Cf at the TRIGA Mainz reactor. Fission products (4d elements) recoiling from the ^{249}Cf target (e.g. on the order of 10^4 atoms per second of ^{104}Mo) were thermalized in a gas volume flushed with a N_2/CO mixture. Short-lived nuclides of the 5d elements W and Os were produced in the nuclear fusion reactions ^{144}Sm(^{24}Mg, 4–5n)^{163,164}W ($t_{1/2}$ = 2.75 and 6.0 seconds) and ^{152}Gd(^{24}Mg, 5–6n)^{170,171}Os ($t_{1/2}$ = 7.3 and 8.0 seconds) at the UNILAC accelerator at GSI Darmstadt. The nuclides of interest were isolated in the TASCA and guided into a gas-filled volume, the RTC where they were thermalized in a 0.8 bar CO/He gas mixture. On the order of 10^3 ions per second of the isotopes of interest entered the RTC. During thermalization of nuclear reaction

products, their charge states decrease. The thermalized ions or atoms of refractory metals interact with CO present in the gas phase during diffusion, yielding neutral carbonyl complexes. They found that these can be rapidly (within a few seconds, as follows from the observation of, e.g. short-lived ^{108}Mo and ^{163}W) transported with high yields (over 50%) with a gas stream over several meters through capillaries to, e.g. a collection station or gas chromatography setup. With this method, γ-ray emitting fission products of Se, Mo, Tc, Ru, and Rh as well as α- or γ-decaying nuclides of W, Re, Os, and Ir were identified. Kratz et al. (2003) presents the results on Mo, W, and Os. A more detailed report involving the other elements was also given elsewhere. Indirect arguments given below lead to assign the transported species to $Mo(CO)_6$, $W(CO)_6$, and $Os(CO)_5$. They were found to be volatile at 22 °C, which was exploited for studies by two gas chromatography techniques: isothermal chromatography (IC) and thermochromatography (TC). These allow determination of the adsorption enthalpy, $-\Delta H_{ads}$, of the species on the column material. IC experiments with $Mo(CO)_6$ were conducted on a SiO_2 surface. The relative yield vs. the column temperature is shown in Figure 17.54, along with the results of MCSs of the migration of the complexes through the isothermal chromatography (IC) column. The only free parameter in these simulations was $-\Delta H_{ads}$. The best fit to the experimental data set was obtained with $-\Delta H_{ads} = 42.5 \pm 2.5$ kJ mol^{-1}.

The adsorption of $Os(CO)_5$ and $W(CO)_6$ on quartz was also studied with the thermochromatography (TC) detector channel cryo-online multidetector for physics and chemistry of the transactinoides (COMPACT), which is suitable to register α-decaying species deposited inside the TC column. To evaluate these experiments, the MCS procedure was adapted to take into account the rectangular cross section of the COMPACT column by using a modified Golay equation. Typical

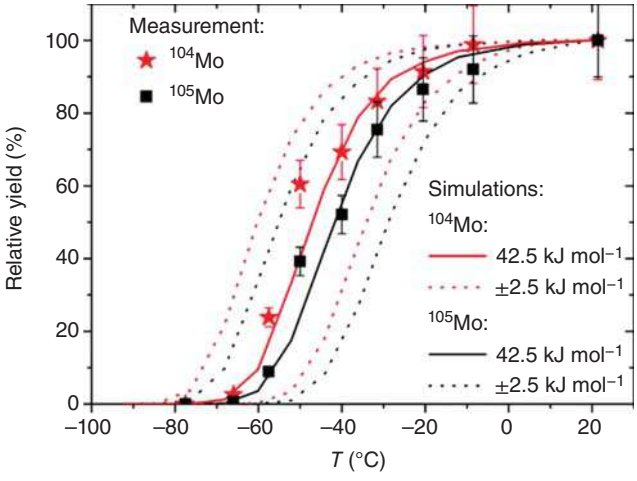

Figure 17.54 Isothermal chromatograms of ^{104}Mo and ^{105}Mo. The gas flow rate was 600 ml min^{-1} (40% N_2 and 60% CO). Symbols: experimental values. Solid lines: result of MCS with $-\Delta H_{ads} = 42.5$ kJ mol^{-1}. Dotted lines: uncertainties of ±2.5 kJ mol^{-1}. Source: Even et al. (2012)), figure 3 (p. 6432)/American Chemical Society.

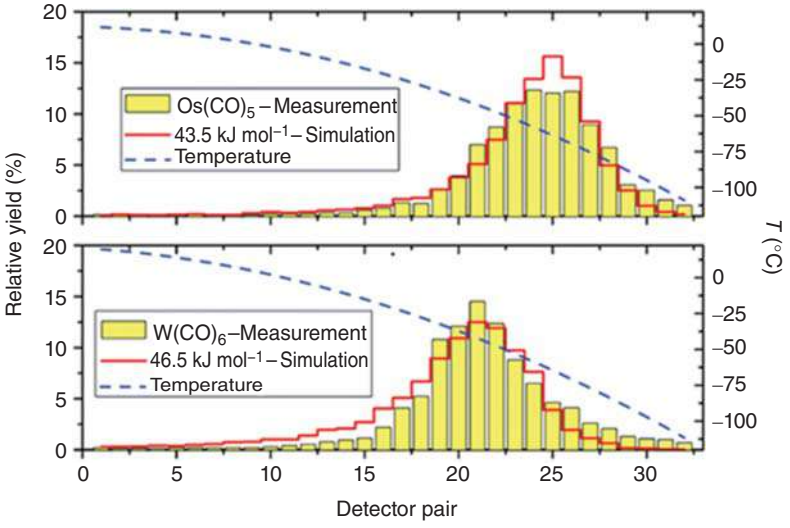

Figure 17.55 Combined thermochromatogram of $^{170}Os(CO)_5$ and $^{171}Os(CO)_5$. Combined thermochromatogram of $^{163}W(CO)_6$ and $^{164}W(CO)_6$. The data refer to a SiO_2 surface. Dashed blue lines: temperature gradient (right-hand *y* axis). Yellow bars: relative yields per detector pair using $-\Delta H_{ads}$ values as given in the Figure. Red solid lines: results of MCS. The gas mixture was 50% He and 50% CO. The total gas flow rates were 0.73 l min^{-1} [$Os(CO)_5$] and 0.85 l min^{-1} [$W(CO)_6$]. The pressure inside the RTC was 0.8 bar. Source: Even et al. (2012), figure 4 (p. 6433)/American Chemical Society.

thermochromatograms along with the results of MCS are shown in Figure 17.55. The peak of the deposition of $Os(CO)_5$ on the SiO_2 surfaces in COMPACT was found at -64 ± 10 °C. Similar experiments with $W(CO)_6$ yielded an adsorption temperature of -42 ± 10 °C. From the deposition patterns of W and Os, $-\Delta H_{ads}$ for $W(CO)_6$ of 46.5 ± 2.5 kJ mol^{-1} and $43.5^{+3.5}_{-2.5}$kJ mol^{-1} for $Os(CO)_5$ were deduced. Such values for $-\Delta H_{ads}$ are comparable to those reported for OsO_4, 39.6 ± 1.3 kJ mol^{-1}, and indicative of physisorption processes.

On the basis of these results, fast chemical and nuclear spectroscopy studies of the transactinide elements seaborgium (Sg, $Z = 106$) and hassium (Hs, $Z = 108$) appear to be possible. The method developed in Even et al. (2012) promises to find applications also in other fields, such as nuclear medicine, or the production of radioactive-ion beams, where fast and efficient synthesis of carbonyl complexes is of interest.

Subsequent work by Even et al. (2014) has been looking deeper into the in situ synthesis of metal carbonyl complexes with short-lived isotopes of transition metals. Complexes of molybdenum, technetium, ruthenium and rhodium were synthesized by thermalization of products of neutron-induced fission of ^{249}Cf in a carbon monoxide/nitrogen mixture. Complexes of tungsten, rhenium, osmium, and iridium were synthesized by thermalizing short-lived isotopes produced in ^{24}Mg-induced fusion-evaporation reactions in a carbon monoxide containing atmosphere. The chemical reactions took place at ambient temperature and pressure

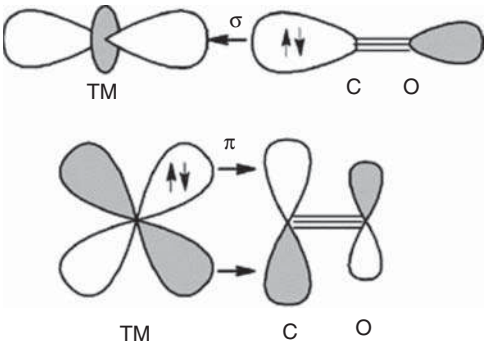

Figure 17.56 Schematic drawing of the σ-donation bond (upper picture) from the HOMO of the carbonyl ligand to the atomic orbitals of the transition metal in σ-symmetry, and π-back-donation bond (bottom) from the d-orbital of the transition metal to the LUMO of the carbonyl ligand.

conditions. The complexes were rapidly transported in a gas stream to collection setups or gas-phase chromatography devices. The physisorption of the complexes on Au and SiO_2 surfaces was studied. Also studied was the thermal stability of some of the complexes, showing that these start to decompose at temperatures above 300 °C in contact with a quartz surface.

In Even et al. (2014), a closer look is directed on the carbon monoxide which is a very strong ligand, a good σ-donor, and π-acceptor. The dominant interactions in the bonding between the transition metal and the ligand are (i) the interaction of the Highest Occupied Molecular Orbital (HOMO) of the CO molecule with an empty σ-symmetric atomic orbital of the metal and (ii) the interaction between occupied π-type d-orbitals of the metal and the $2\pi^*$ orbital Lowest Unoccupied Molecular Orbital (LUMO) of CO. The σ-donor bond strengthens the C—O bond. The π-backbonding, on the other hand side, weakens the C—O bond, as electron density is donated to the antibonding LUMO (Figure 17.56).

For adsorption studies, a spiral-shaped quartz tube was connected to the gas loop. The quartz tube had an inner diameter of 2 mm and was placed over a length of 191 cm in a cooling bath, the temperature of which was varied for the different IC measurements. An activated charcoal trap was placed behind the spiral and monitored by a HPGe γ-detector.

In the experiments aiming at studying the thermal stability of the carbonyl complexes, a quartz tube placed in a tube furnace was installed in the gas loop. In the middle of the quartz tube, a quartz wool plug was inserted, which provided an efficient surface contact of the gas to the quartz. The temperature of the quartz wool was varied between room temperature and 600 °C. The transport yield achieved through the quartz tube was determined for different temperatures. An activated charcoal trap was placed behind the quartz tube and monitored by a HPGe γ-detector.

The experiments with α-particle emitting isotopes were performed by thermochromatography TC with the COMPACT detector array. Two different COMPACT detector arrays were used: one with a SiO_2 surface covering the PIN diode detectors (COMPACT SiO_2), the other one with a gold surface on the detectors (COMPACT Au). A COMPACT array consists of two Invar^{TM} panels. On each panel, 32 PIN diodes of (1×1) cm^2 are mounted, forming a 32-cm long, 1-cm wide detector array. The active detection surface of each PIN diode

in COMPACT SiO_2 is (9.3×9.3) mm^2. In COMPACT Au, the active detection surface of the PIN diodes is (9.7×9.9) or (9.7×9.7) mm^2. Two panels are assembled such that the active surfaces of PIN diodes face each other at a distance of 0.6 mm. With this detector assembly, a detection efficiency for registering α particles emitted from species inside the channel of 76% is reached. The gas and the volatile carbonyls collided with the detector surfaces. The detector channel was placed in a vacuum box made of steel covered with nickel. The down-stream end of the detector panel is contacted by a copper cold finger, which is cooled with liquid nitrogen. This way, a temperature gradient is established along the chromatography column. Temperatures are monitored with type K thermocouples. At the COMPACT SiO_2 detector array, four thermocouples are mounted along the array at equal distances. At the COMPACT Au detector array, three sensors are mounted, one at each end of the array and one in the center. In the following, we show examples for thermochromatograms with COMPACT with a gold surface, followed by isothermal chromatograms with "exotic" radioisotopes on SiO_2 surfaces (Figures 17.57–17.59).

The example with a short-lived iridium radionuclide is interesting because its heavy homologue is meitnerium (element 109) for which, so far, there were no realistic ideas for a chemical separation. Among the studied transition metal carbonyl complexes, the group 6 hexacarbonyl complexes are the best studied ones. The absorption enthalpies of the group 6 hexacarbonyl complexes including seaborgium hexacarbonyl on a quartz surface have been calculated (Even et al. 2012), and trends in $-\Delta H_{ads}$ have been predicted. The adsorption enthalpy $-\Delta H_{ads}$ is related to the binding energy $E_{(x)}$ by

$$E_{(x)} = -\Delta H_{ads} + 0.5 \cdot RT \tag{17.88}$$

In the case of physisorption, the binding energy can be calculated with

$$E_{(x)} = -\left(\frac{\pi}{6}\right) \cdot N \cdot C_1 \cdot \frac{1}{x^3} \tag{17.89}$$

where N is the number of atoms per one cubic centimeter and x is the interaction distance in centimeters. The van der Waals constant C_1 can be expressed as

$$C_1 = \frac{3}{2} \cdot \alpha_A \cdot \alpha_B \cdot \frac{E_A \cdot E_B}{E_A + E_B} \tag{17.90}$$

Here, α_A and α_B are the polarizabilities of the adsorbed molecule A and the surface B. E_A and E_B are the average dipole transition energies. The average dipole energies can be replaced by the reciprocal of the first ionization potential. The physisorption energy can thus be written as

$$E_{(x)} = -\frac{\pi}{4} \cdot N \cdot \frac{1}{x^3} \cdot \frac{\alpha_A \cdot \alpha_B}{\frac{1}{IP_A} + \frac{1}{IP_B}} \tag{17.91}$$

The polarizability can be calculated as

$$\alpha_B = \frac{3}{4 \cdot \pi \cdot N} \cdot \frac{(\varepsilon - 1)}{(\varepsilon + 3)} \tag{17.92}$$

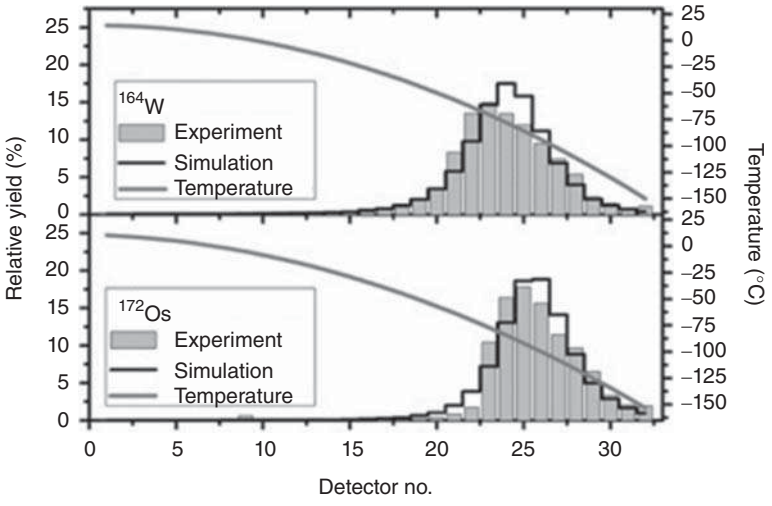

Figure 17.57 Thermochromatograms with the COMPACT with a gold surface. The gas mixture was 50% He and 50% CO. The total gas flow rate was 0.73 l min^{-1}. The pressure inside the RTC was 0.8 bar. thermochromatogram of $^{172}Os(CO)_5$ thermochromatogram of $^{164}W(CO)_6$ Grey solid lines: temperature gradient (right-hand y- axis). Grey bars: relative yields per detector pair (left-hand y-axis). Black lines: results of Monte Carlo simulations (left-hand *y*-axis). Source: Even et al. (2014), figure 13 (p. 1103)/De Gruyter.

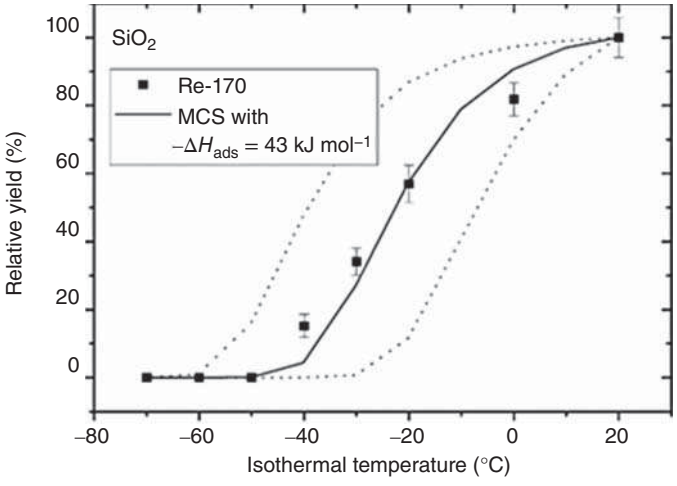

Figure 17.58 Isothermal chromatogram measured with ^{170}Re ($t_{1/2} = 9.2$ seconds). The gas mixture was He:CO 4 : 1. The gas flow rate was 0.54 l min^{-1}. Black symbols: measured values normalized to the measurement at 20 °C. Solid lines: result of a Monte Carlo simulation MCS with $-\Delta H_{ads} = 43$ kJ mol^{-1}, Dashed lines: uncertainty limits of ± 3 kJ mol^{-1}. Source: Even et al. (2014), figure 15 (p. 1104)/De Gruyter.

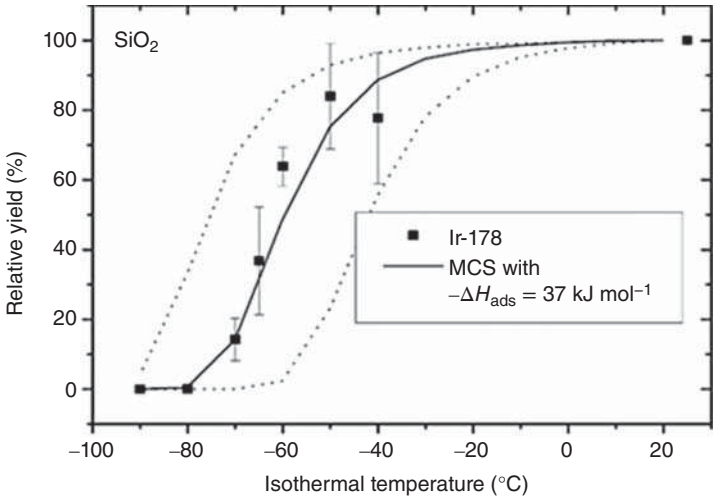

Figure 17.59 Isothermal chromatogram measured with ^{178}Ir ($t_{1/2} = 12$ seconds). The gas mixture was 4 : 1 He:CO. The gas flow rate was 0.54 l min^{-1}. Black symbols: experimental data normalized to the measurement at 25 °C. Solid line: result of a Monte Carlo simulation with $-\Delta H_{ads} = 37$ kJ mol^{-1}. Dashed lines: uncertainty limits of ± 3 kJ mol^{-1}. Source: Even et al. (2014), figure 16 (p. 1104)/De Gruyter.

where ε is the dielectrical constant of the surface material. For the calculation of the adsorption energy on a surface material for which no data on the polarizability are available, the following equation can thus be applied

$$E_{(x)} = \frac{3}{16} \cdot \frac{(\varepsilon - 1)}{(\varepsilon + 2)} \cdot \frac{\alpha_A}{\left(\frac{1}{IP_A} + \frac{1}{IP_B}\right) \cdot x^3} \tag{17.93}$$

according to Eqs. (17.88) and (17.93). The dielectrical constant of silicon dioxide is 3.81, and the ionization potential is 11.7 eV. For the calculation of the adsorption enthalpies on gold, Eqs. (17.88) and (17.91) are used. The ionization potential of gold is 9.2 eV, and the polarizabilty is 5.8×10^{-24} cm.

In summary, the experiments showed that in situ carbonyl chemistry is a very effective and fast method. Additionally, carbonyl chemistry can be combined with gas-phase chromatography. Adsorption studies of several carbonyl complexes on silicon dioxide or gold surfaces showed these complexes to physisorb at temperature below −40 °C. This allows studies with on-line thermochromatography detectors like COMPACT. It was also shown that the carbonyl complexes decompose at temperatures around 300–400 °C in contact with a quartz surface. Here, the interactions of the surface material with the complexes may play an important role. Therefore, further decomposition studies with different hot surfaces will be required to allow for an improved understanding. Studying the formation and adsorption of seaborgium hexacarbonyl appeared to be the next most promising step. The synthesis of this compound would result in the first volatile transactinide complex with the met metal in oxidation state zero. Sg is expected to form stable hexacarbonyl complexes (Even et al. 2012) like its lighter homologs. Relativistic effects, however,

lead to enhanced contraction of the $p_{1/2}$ orbital in Sg, weakening the σ-donation bond. Consequently, because of the relativistic contraction of s and $p_{1/2}$ orbitals, the d-orbitals are better shielded from the atomic nucleus and expand. The overlap with the LUMO of the CO ligand becomes stronger. This may lead to a stronger contribution of π-back-donation relative to σ-donation in comparison with the corresponding ratio in the complexes of the lighter members of group 6. Overall, the first bond dissociation energy (FBDE) should remain similar to that of $W(CO)_6$. Also, the calculated bond lengths are similar (Even et al. 2012). Theory predicts a lower ionization potential and a higher polarizability of $Sg(CO)_6$ compared with $W(CO)_6$ (Even et al. 2012). Both properties influence the interaction with a surface in a way that, for example, equal values for the adsorption enthalpies of $Sg(CO)_6$ and $W(CO)_6$ on silicon dioxide (SiO_2) are predicted (Even et al. 2012). This promises to facilitate identification of $Sg(CO)_6$ through a direct comparison with the behavior of $W(CO)_6$, if both elements are studied under identical conditions. The successful synthesis of $Sg(CO)_6$ would then present a crucial step toward more detailed studies of the metal–carbon bond involving transactinide elements.

Among the known isotopes of seaborgium, ^{265}Sg is sufficiently long-lived and can be produced in the nuclear fusion reaction of a ^{22}Ne beam with ^{248}Cm targets. Two long-lived, α-decaying states have been identified in this isotope with half-lives of $8.5^{+2.6}_{-1.6}$ and $14.4^{+3.7}_{-2.5}$ seconds (Haba et al. 2012). The experiments were performed at the GARIS at RIKEN, Japan. The $Mo(CO)_6$ and $W(CO)_6$ complexes were produced in the nuclear fusion of ^{24}Mg with Zn nuclei at 85 MeV, forming ^{87,88}Mo in the ^{nat}Zn(^{24}Mg, xn) reaction. W isotopes were produced in the nuclear reaction ^{144}Sm(^{24}Mg, 4–5n)^{163,164}W at 144 MeV energy. For the synthesis of Sg, 264 μg cm^{-2} of ^{248}Cm, deposited in oxidic form on a 2-μm thick Ti foil, was irradiated with $1.5 \cdot 10^{19}$ ^{22}Ne beam particles of 122 MeV energy.

The ions were thermalized behind GARIS in a RTC. The RTC was flushed with a He/CO mixture at 500–750 mbar. Volatile species were transported to the COMPACT. The isotopes ^{163}W ($t_{1/2} = 2.75$ seconds) and ^{164}W ($t_{1/2} = 6.0$ seconds) were identified in COMPACT by their α-particle energies. In the experiments with Mo isotopes, signals from β-decay were recorded. β-particles feature a continuous energy spectrum. Hence, isotopes emitting the β-particles cannot be identified according to registered energies. Therefore, Mo was accumulated for 15 minutes in the COMPACT detector. Afterward, the irradiation of the target was stopped, and the decay of the activity deposited on the detectors was monitored. The decay curves of every single detector pair of COMPACT were then recorded, revealing in the detector pairs around detector number 25 a component with a half-life of ∼13 seconds to be present, which was assigned to ^{87}Mo. In the detector pairs around detector number 27, a component with a half-life of ∼8 minutes was dominant, which agrees with the half-life of ^{88}Mo. Small contributions of a species with a half-life of ∼2 minutes have also been observed, which we assigned to ^{89}Mo. Thus, ^{87}Mo and ^{88}Mo as well as small amounts of ^{89}Mo were identified by their half-lives. The deposition pattern of Mo shows a double-peak structure. We assign the first one, peaking in detector number 25, to the 14.5-seconds isotope ^{87}Mo, and the second one, peaking at detector 27, to 8.2-minutes ^{88}Mo. Because of its longer

half-life, the latter is transported to lower temperatures before its decay occurs. The maximum of shorter-lived ^{164}W ($t_{1/2} = 6.0$ seconds) was registered in detector 24.

From comparison with the MCS, the adsorption enthalpies were deduced (Even et al. 2014) to be (-50 ± 2) kJ mol^{-1} for $Mo(CO)_6$ and (-49 ± 2) kJ mol^{-1} for $W(CO)_6$. A statistical analysis was applied to extract ΔH_{ads} of the $Sg(CO)_6$ from the results obtained at different experimental conditions. Thus, a probability distribution of the adsorption enthalpies was deduced, yielding a value for ΔH_{ads} of (-50 ± 4) kJ mol^{-1} (Even et al. 2014). Within the statistical error limits, this is equivalent to the values for the $Mo(CO)_6$ and $W(CO)_6$ complexes as deduced in the present experiment. Fully relativistic quantum chemical calculations predict adsorption properties of the $Sg(CO)_6$ complex on SiO_2 to be very similar to those of $W(CO)_6$ (Pershina and Anton 2013). This corroborates the interpretation that Sg forms a volatile hexacarbonyl complex. Thus, the experimental adsorption enthalpies are in good agreement with those predicted (Pershina and Anton 2013) for the group 6 hexacarbonyl complexes.

Thus, owing to advanced techniques, the unequivocal detection of a carbonyl complex of element Sg belonging to a new compound class which was unknown for the transactinides was a success. Sg is a full homolog of Mo and W (Even et al. 2015), and the results are in agreement with theoretical predictions. Studies of the thermal stability of $Sg(CO)_6$ appear feasible, as do syntheses of carbonyl complexes of Bh, Hs, and meitnerium (Mt, $Z = 109$). Furthermore, the combination of physical and chemical separation techniques bears potential for background-free nuclear decay spectroscopy because purified transactinde samples can be prepared.

A focus of ongoing and future research is the thermal stability of the group-6 hexacarbonyls which might be different for $Mo(CO)_6$, $W(CO)_6$, and $Sg(CO)_6$, depending on their different FBDE (Lewis et al. 1984) which was calculated to be, e.g. 179 ± 8 kJ mol^{-1} for $Sg(CO)_6$, i.e. 4 kJ mol^{-1} higher than that for $W(CO)_6$. Following this idea, Usoltsev et al. (2016) have set up an experiment devoted to the production and thermal decomposition of $Mo(CO)_6$ and $W(CO)_6$. They constructed a tubular flow reactor for assessing differences in the thermal stability of $Mo(CO)_6$ and $W(CO)_6$. Their approach proved to be effective in discriminating between the thermal stabilities of $Mo(CO)_6$ and $W(CO)_6$ in order to demonstrate an experimental verification of the predicted bond dissociation energies in this way. Figure 17.60 shows that the decomposition reaction of $W(CO)_6$ starts consistently at around 350 °C, which is 100 °C higher compared to that of $Mo(CO)_6$. Therefore, they concluded that a difference in the first bond dissociation energies of 23 kJ mol^{-1} (Lewis et al. 1984) leads to a 100 °C shift in the decomposition temperatures. An attempt to extend this to Sg has been undertaken, but the result suffers from low statistics (Eichler et al. 2016).

For element 108, hassium, the in situ production of volatile tetroxides directly behind the target by adding oxygen (typically 10%) to the carrier gas that contains no aerosol particles is an extremely attractive approach. Typically, the reaction products are transported with the carrier gas through a quartz column containing a quartz wool plug heated to some 600 °C at the exit of the recoil chamber providing a hot surface on which oxidation of the group VIII elements to their tetroxides is

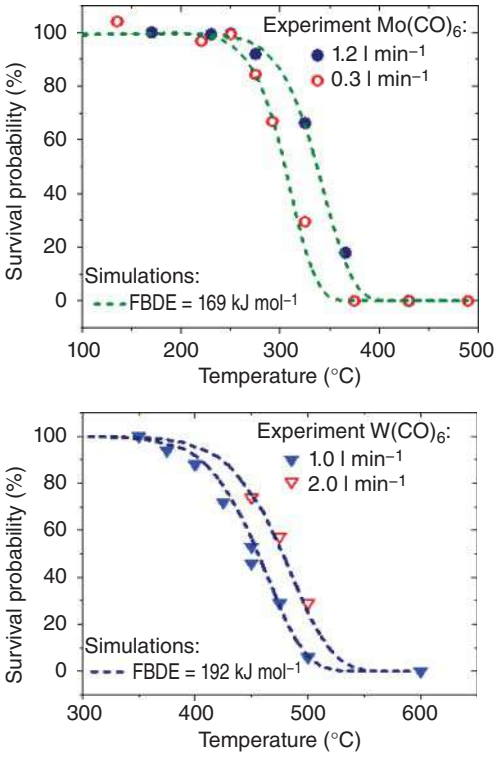

Figure 17.60 Experimental decomposition curves of the Mo (symbols left) and W (symbols right) carbonyl complexes, respectively, at different gas flow rates together with simulated decomposition curves (lines) using for the $Mo(CO)_6$ decomposition (top): FBDE = 169 kJ mol^{-1}, and for $W(CO)_6$ decomposition (bottom): FBDE = 192 kJ mol^{-1}. Note the sensitivity of the model to the changed gas flows at otherwise same experimental conditions. Source: Courtesy of Y. Usoltsev.

completed. The latter are further transported through a Teflon capillary to the detection system. Using thermochromatography at low temperatures, Düllmann et al. (2002) measured the temperature at which HsO_4 deposits with their cryo on-line detector (COLD), which also served as the detection system for the isotopes ^{269,270}Hs. COLD consists of 12 pairs of silicon PIN diodes of $1 \times 3\,cm^2$ mounted at a distance of 1.5 mm inside a copper bar. A temperature gradient from −20 to −170 °C was established along the detector array. The efficiency for detecting a single α particle was 77%. The experimental setup involved three banana-shaped ^{248}Cm targets mounted on a rotating target wheel that was bombarded with up to $8 \cdot 10^{12}$ $^{26}Mg^{5+}$ ions per second, delivered by the UNILAC accelerator at GSI, Darmstadt. The projectile energy was ∼146 MeV inside the ^{248}Cm targets. The functioning of the entire experiment was checked at the beginning and after the Hs experiment by mounting a ^{152}Gd target and by producing 19.2 seconds ^{172}Os which has an α-decay branch of 1%. The experiment to produce Hs lasted 64.2 hours during which a total of $1.0 \cdot 10^{18}$ ^{26}Mg ions passed through the targets. Seven correlated decay chains were observed, two representatives of which are shown in Figure 17.61.

As depicted in Figure 17.62, the α decay of one Hs atom was registered in detector 2, the decay of four atoms in detector 3, and the decay of two atoms in detector 4. The maximum of the Hs distribution was found at a temperature of -44 ± 6 °C, that for the Os distribution at -82 ± 7 °C. The adsorption enthalpy was extracted from the data by a MCS with the value of ΔH_a being a free

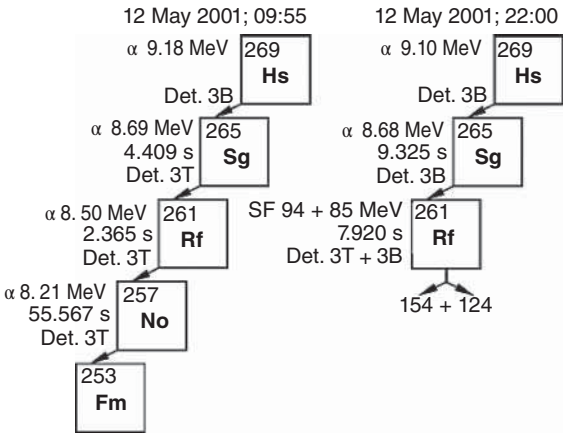

Figure 17.61 Two of seven nuclear decay chains originating from Hs isotopes (Düllmann et al. 2002b). Indicated are the energies of α particles and fission fragments in MeV and the lifetimes in s. In the detector in which the decay was registered T stands for top detector and B for bottom detector. The two selected chains are typical in the sense that both show 3 s ^{261b}Rf as granddaughter of ^{269}Hs decaying either by the emission of an 8.5 MeV α particle or by sf. Source: Düllmann et al. (2002).

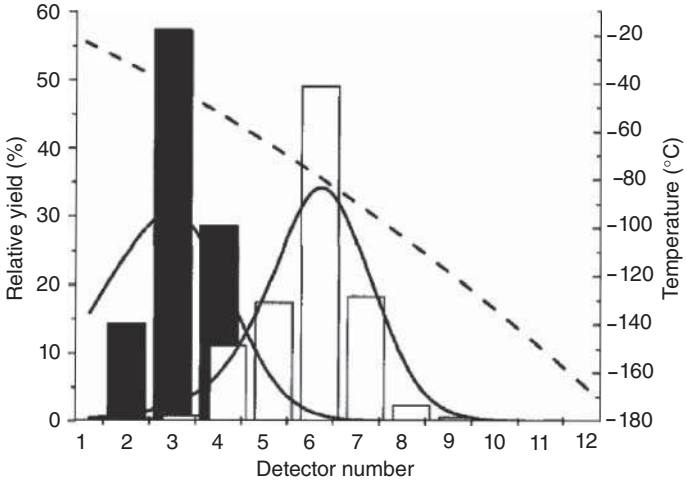

Figure 17.62 Thermochromatograms of HsO_4 and OsO_4. Measured values are presented by bars (HsO_4 black, OsO_4 white). The dashed line represents the temperature profile. The maxima of the deposition zones are -44 ± 6 °C for HsO_4 and -82 ± 7 °C for OsO_4. Solid lines represent the results of Monte Carlo simulations with standard adsorption enthalpies of -46 kJ mol^{-1} for HsO_4 and -39 kJ mol^{-1} for OsO_4. Source: Düllmann et al. (2002).

parameter. The results that best reproduce the experimental data are shown in Figure 17.62 (solid lines) and suggest a value of the standard adsorption enthalpy of -46 ± 2 kJ mol^{-1} for HsO_4 and -39 ± 1 kJ mol^{-1} for OsO_4 on the silicon nitride surface of the detectors. For OsO_4, the value is in good agreement with that using quartz glass surfaces. Therefore, a direct analogy between theory and experiment

is expected because a comparable adsorption interaction of OsO_4 is ascertained for quartz and silicon nitride surfaces. The significantly lower volatility of HsO_4 compared to that of OsO_4 was a surprise as a similar or slightly higher volatility for HsO_4 had been predicted theoretically. The apparent discrepancy between experiment and theory has triggered new theoretical efforts by Pershina et al. (1992); in this work, fully relativistic, four-component, DFT calculations were performed on MO_4 (M = Ru, Os, and Hs). Implementation of the non-collinear SP approximation in the method and the use of large optimized sets of numerical basis functions resulted in a high accuracy of the calculated molecular properties, especially the molecular polarizabilities. The latter have fully reproduced the experimental values for RuO_4 and OsO_4 and showed a dramatic increase in the polarizability, by 8.95 a.u., for HsO_4 in comparison to the old value. This led to a new value of $\Delta H_a^{o(T)} = -45.4 \pm 1$ kJ mol^{-1} for HsO_4, now in perfect agreement with experiment.

It is noteworthy that the decay properties of ^{261}Rf in Figure 17.61 are consistent with those observed in the decay chains of ^{277}112 but deviate from experimental data where ^{261}Rf was produced directly. In the latter case, a half-life of 68 seconds and an α-particle energy of 8.28 MeV are observed. Apparently, when ^{261}Rf is formed by the α decay of precursors, the α-decay energy is 8.5 MeV, the half-life is about three seconds, and a sf branch of 91% is evident. In the work of von Zweidorf et al. (2004), ^{269}Hs was also produced in the ^{248}Cm(^{26}Mg, 5n) reaction. In the CALLISTO (Continuously working Arrangement for cLuster-Less transport of In-SiTu produced volatile Oxides) experiment, an admixture of ^{152}Gd to one of the three banana-shaped rotating target segments simultaneously produced α-emitting 19.2 seconds ^{172}Os and 22.4 seconds ^{173}Os. The evaporation residues were oxidized in situ behind the target in a mixture of He and O_2 and transported to a deposition and detection system. The latter consisted of 16 PIN diode detectors facing in close geometry a layer of NaOH which served, in the presence of a certain partial pressure of water in the transport gas, as a reactive surface for the deposition of the volatile tetroxides. For OsO_4, the deposition involves the formation of a salt, an osmate(VIII). In analogy, the deposition of HsO_4 is likely to involve the reaction

$$2\,NaOH + HsO_4 \rightarrow Na_2[HsO_4(OH)_2] \tag{17.94}$$

Thus, CALLISTO has shown that HsO_4, like OsO_4, is an acid anhydride and forms with NaOH a hassate(VIII) in analogy to the known osmate(VIII), that is, a salt. Figure 17.63 shows the distribution of the deposited amount of OsO_4 and HsO_4 as a function of the detector position. While the majority of the Os activity is centered in front of detector 1 and tails into the subsequent positions, the five α-decay chains of ^{269}Hs are centered in front of detector position 3. In the work by von Zweidorf et al., it was not claimed that this indicates a lower reactivity of HsO_4 with respect to moisturized NaOH compared to OsO_4; however, theoretical work by V. Pershina (2005) predicts interestingly that the hassate(VIII) should be more covalent than the osmate(VIII) and HsO_4 should react slightly weaker with NaOH (by <52 kJ mol^{-1}) than OsO_4.

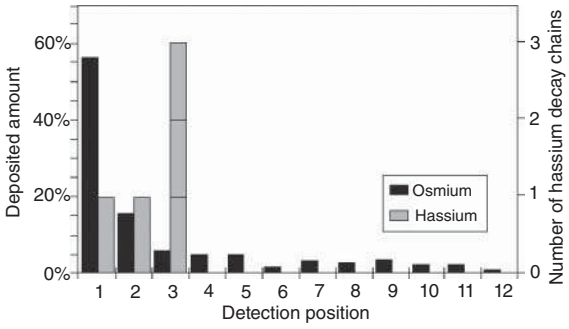

Figure 17.63 Distribution of the deposited amount of OsO_4 and HsO_4 on the surface of NaOH facing a phalanx of PIN diode detectors. While the ^{172,173}Os α activity is centered in front of detector 1, the ^{269}Hs decays are centered around position 3. Source: von Zweidorf et al. (2004) / Walter de Gruyter.

In three runs at the U-400 cyclotron at FLNR Dubna, a stationary grid supporting a $^{242}PuO_2$ target was irradiated with a beam of ^{48}Ca ions. The goal was to use the indirect production path ^{242}Pu(^{48}Ca, 3n)^{287}114 ($t_{1/2}$ = 0.48 seconds, E_α = 10.02 MeV) → ^{283}Cn to produce element 112, copernicium, and to study its chemical properties in the elemental state. Neodymium was added to the target to simultaneously produce 49 seconds ^{185}Hg. Additionally, several isotopes of radon, for example, 3.96 seconds ^{219}Rn, were produced in multi-nucleon transfer reactions. The recoiling reaction products were stopped in He/Ar (1 : 1) and swept with the carrier gas (1500 ml min^{-1}) through an oven heated to 850 °C and containing a quartz glass column with a quartz wool filter to remover aerosol particles and Ta metal to remove traces of O_2 and H_2O. Non-reactive volatile products were transported through a PFA capillary 8 m long to chemical apparatus based on the thermochromatographic in-situ volatilization and on-line detection technique (IVO), in combination with the COLD containing 32 sandwiched pairs of PIPS detectors forming a rectangular chromatographic column with an opening of 11.6 × 1.5 mm with 80% active detector area. One side was covered with a gold layer. A spontaneous, diffusion-controlled deposition of ^{185}Hg was observed in the first detectors. ^{219}Rn deposited at the cold end of the thermochromatography channel. In the first experiment performed in 2006, one decay chain of ^{283}Cn (compatible with the known properties, $t_{1/2}$ = 3.8 seconds, E_α = 9.54 MeV, followed by sf of ^{279}Ds with a lifetime of 200 ms) was detected in the second detector (−28 °C) together with ^{185}Hg. In the second experiment performed in 2006, with a steeper temperature gradient, ^{283}Cn was observed in the seventh detector (−5 °C). In the third experiment performed in 2007 with an increased gas flow rate, chains 3 and 5 were detected in detectors 11 (−21 °C) and 14 (−39 °C). Chain 4 was detected in detector 26 (−124 °C). From dew point measurements in the carrier gas, it has to be concluded that the detector surfaces held below −95 °C were covered by a thin ice layer (Figure 17.64a–c, vertical lines). Thus, it was concluded that four events (chains 1–3 and 5) are attributable to atoms of element 112 deposited on the gold surface, while chain 4 represents an atom of element 112 deposited on ice (on an inert surface).

MCS following (Zvara 1985) were applied to determine the most probable standard adsorption enthalpy on gold surfaces at zero coverage from the chromatographic deposition of Hg, Rn, and element 112 (Pershina and Kratz 2001).

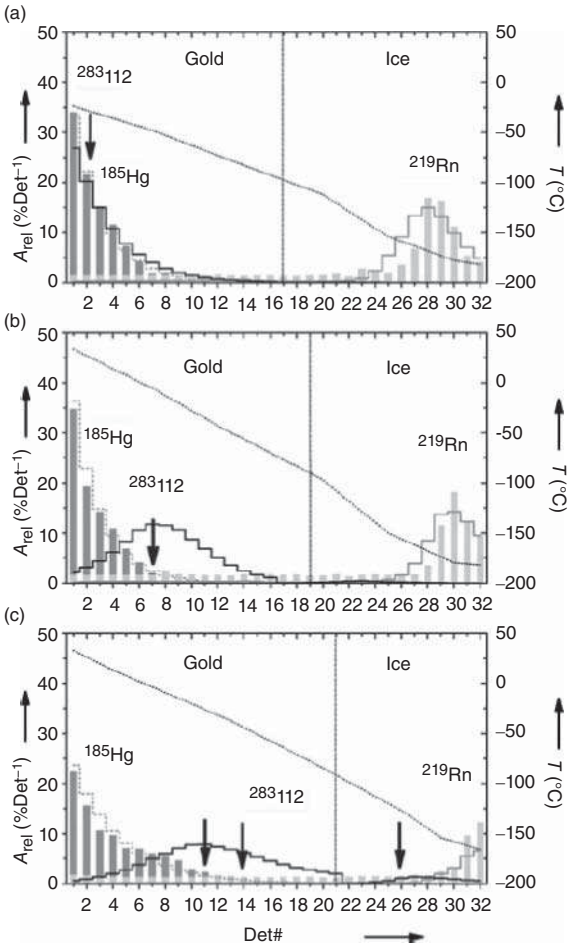

Figure 17.64
Thermochromatographic deposition patterns of ^{185}Hg, ^{219}Rn, and ^{283}Cn in the COLD, dependent on experimental parameters. The measured relative activity per detector (A_{rel}, left hand axis) of ^{185}Hg (dark-gray bars, MCS: gray dashed line) and ^{219}Rn (gray bars, MCS: gray solid line) is shown. The positions of the detected ^{283}Cn atoms are indicated (black arrows, MCS: black solid lines). The temperature gradient is shown (black dashed line, right hand axis). Experimental parameters: (a) gas flow 860 ml min^{-1}, temperature gradient from −24 to −184 °C; (b) gas flow 890 ml min^{-1}, temperature gradient from 35 to −180 °C; (c) gas flow 1500 ml min^{-1}, temperature gradient from 32 to −164 °C. The beginning of ice coverage of the detectors at −95 °C is indicated by the vertical lines. Source: Eichler et al. (2008)), figure 2 (p. 3263)/John Wiley & Sons.

The diffusion-controlled deposition of Hg (Figure 17.64, gray dashed lines) yielded a lower limit for $-\Delta H_a^{Au}(\mathrm{Hg}) > 65\,\mathrm{kJ\,mol^{-1}}$, in agreement with data from the literature. The deposition of ^{219}Rn (Figure 17.64, gray solid lines) gave an adsorption enthalpy of $-\Delta H_a^{ice}(\mathrm{Rn}) = 19 \pm 2\,\mathrm{kJ\,mol^{-1}}$ in agreement with a value of $-20 \pm 2\,\mathrm{kJ\,mol^{-1}}$ measured for Rn on ice. The MCS of the deposition of ^{283}112 (Figure 17.64, black arrows) resulted in an adsorption enthalpy of element 112 on gold surfaces of $-\Delta H_a^{Au}(112) = 52^{+4}_{-3}\,\mathrm{kJ\,mol^{-1}}$ (68% confidence interval). Using this value, the calculated deposition pattern (Figure 17.64, black lines) indicates for the highest gas flow a probability of 15% for atoms of element 112 to reach detector 21 and to continue the chromatographic process on ice. This explains the observation of chain 4 by detector 26. The expected number of random correlations during the entire experiment was calculated to be 0.05. The enhanced adsorption enthalpy of element 112 on gold compared to a prediction using a physisorption model indicates a metallic bond character of the interaction of element 112 with gold. The calculations of the 112–Au interaction potential using DFT by Pershina et al.

predict a metallic bond character but seem to overestimate somewhat the energetic content of this interaction. In summary, element 112 is chemically not as inert as a noble gas as suggested by Pitzer (1975).

An empirical link between the single-atom quantity ΔH_a and the volatility of macroscopic amounts of an element or compound, determined by the standard sublimation enthalpy ΔH_{aubl}, reveals linear relationships for various elements and compound classes on various surfaces. A similar correlation was established between ΔH_a^{Au} values of elements and their ΔH_{subl} values. By using this correlation, the standard sublimation enthalpy can be estimated as $\Delta H_{subl}(112) = 38^{+10}_{-12}$ kJ mol^{-1}, indicating that element 112 is more volatile than its lighter homologs Zn, Cd, and Hg, reflecting an increasing stabilization of the atomic state due to relativistic effects in group 12 of the periodic table up to element 112.

In the 2007 experiments by Eichler et al. studying the volatility of element 112 in the indirect production path ^{242}Pu(^{48}Ca, 3n)^{287}114 ($t_{1/2}$ = 0.48 seconds, E_α = 10.02 MeV) → ^{283}Cn, the measured mean transport time of volatile reaction products through the 8 m long capillary to the COLD thermochromatography detector was 2.2 seconds, resulting in an efficiency of seeing ^{283}Cn ($t_{1/2}$ = 3.8 seconds) of 67%. Due to the much shorter half-life of the mother nuclide, the efficiency of seeing a possibly volatile ^{287}114 was 5% only. Surprisingly, one decay chain of ^{287}114 decaying with a 10.04 MeV α particle (detector 19, top) into ^{283}Cn that decayed 10.93 seconds later by emission of a 9.53 MeV α particle (detector 19, bottom), followed 0.242 seconds later by sf of ^{279}Ds (detector 19, top and bottom), was detected. More surprising was the observation of this decay chain on detector 19, held at a temperature of −88 °C. This is because the prediction by Pershina et al. (2007) using their fully relativistic 4c DFT code is that element 114 should absorb much stronger on transition metal surfaces than Cn. In a continuation of the experiment by Eichler et al., the production of ^{288}114 ($t_{1/2}$ = 0.8 seconds, E_α = 9.94 MeV) in the ^{244}Pu(^{48}Ca, 4n) reaction was attempted. One additional decay chain attributed to ^{288}114 was observed decaying with an α particle of 9.95 MeV (detector 19, top) followed 0.109 seconds later by sf of ^{284}112 (detector 18, bottom). Detector 19, in this experiment, was held at −90 °C. Another interesting event was observed with an α decay of 9.81 MeV in detector 3 (top, −4 °C) and tentatively assigned to ^{288}114 with a sf decay followed 104 ms later at three detectors downstream in detector 6 (bottom). This was explained by the recoil of the daughter ^{284}Cn into the gas phase and its subsequent sorption at −19 °C. From the observation of three atoms of element 114 adsorbed on a gold surface, using the Monte Carlo model, a standard adsorption enthalpy $-\Delta H_a^{Au}$(E114) = 34^{+54}_{-11} kJ mol^{-1} (95% confidence level) was deduced (Eichler et al. 2010). A value of −34 kJ mol^{-1} corresponds to a weak physisorption which is in conflict with the theoretical prediction of an even stronger metal–metal interaction of element 114 with gold than that of element 112 with gold.

In 2009, after having detected 15 decay chains of ^{288,289}114 from the ^{244}Pu(^{48}Ca, 3–4n) reactions in the focal-plane detector of the gas-filled separator TASCA at GSI, of which two decay chains were detected in the small image mode (SIM), another

chemistry experiment with element 114 was conducted by Yakushev et al. using pre-separation of the evaporation residues. The magnets of TASCA were set to focus ions with a magnetic rigidity, $B\rho$, of 2.27 T m into an area of about 3 cm diameter in TASCA's focal plane. MCS indicate that 35% of the produced element 114 nuclei reached the focal plane. There, they penetrated a Mylar window 3.3 ± 0.1 µm thick and entered the RTC where they were thermalized in a He/Ar gas mixture. Volatile species were flushed with this carrier gas mixture to a series of two COMPACT detector arrays consisting of 32 pairs each of PIN diodes covered with Au. The first array was kept at room temperature, while a temperature gradient from +20 to −162 °C was applied along the second detector. Using short-lived Hg isotopes as model species, the most probable transport time to COMPACT I was measured to be 0.81 ± 0.06 seconds. The only materials that transported species encountered downstream of the RTC were PTFE and Au. A search for correlated decay chains as observed in the preparatory experiment revealed two decay chains that were assigned to $^{288}114 \rightarrow {}^{284}$Cn (chain 1) and $^{289}114 \rightarrow {}^{285}\text{Cn} \rightarrow {}^{281}$Ds (chain 2), produced in 4n and 3n evaporation channels. Chain 1, starting with the 9.65 MeV α decay of the mother nucleus and followed 0.65 seconds later by sf of the daughter, was observed in detector pair 9 in COMPACT I, which was kept at room temperature (21 °C). Chain 2 was distributed over both COMPACT arrays: the 9.78 MeV α particle of the mother nucleus initiating the chain was detected in detector 9 (top) in COMPACT I. The rest of the chain occurred in detector pair 52 in COMPACT II (9.11 MeV α decay of ^{285}Cn after 11.6 seconds in detector 9 (bottom) followed 25.3 seconds later by sf of ^{281}Ds in 52 (top + bottom)).

Both decays from E114 were found in the IC section, where Pb and Hg were deposited (Yakushev et al. 2014). These elements interact strongly with Au, and their deposition temperatures on Au are well above room temperature. Therefore, when passing a Au surface kept at room temperature, adsorption occurs upon first contact with the surface and the deposition pattern reflects the diffusion-controlled nature of this process. This produces the exponentially decaying intensity along COMPACT I. In the first decay chain originating from $^{288}114$, the sf decay from ^{284}Cn was registered in the same detector pair as the α decay of the mother nuclide $^{288}114$, after a lifetime of 650 ms. The chemical interaction of Cn with Au at this temperature is weak, and a Cn atom adsorbed on the Au surface would be released quickly and transported toward COMPACT II. Instead, ^{284}Cn remained at this position during its whole lifetime, which points to an implantation of the recoiling daughter nucleus, ^{284}Cn, into the detector after the α decay of $^{288}114$, rather than to adsorption on the detector surface. As the recoil range of this daughter, ^{284}Cn, is very small, the mother nucleus had to be adsorbed on the detector surface at the moment of its decay. Its measured deposition temperature thus reflects its chemical interaction with Au. In the second decay chain originating from $^{289}114$, the remainder of the decay chain, starting from the daughter nucleus ^{285}Cn, was found in the detector pair 52 at a temperature of −32 °C. In this case, following α decay of the mother nucleus, the daughter ^{285}Cn recoiled into the open volume flushed with gas. The ^{285}Cn atom was thus transported along the detector channel into COMPACT II, where it was deposited. This agrees well with the calculated

deposition peak of ^{285}Cn at the adsorption enthalpy $-\Delta H_a^{Au}(Cn) = 52\,kJ\,mol^{-1}$. Considering confidence intervals for experiments with background and small numbers of events, the observation of two atoms of element 114 in COMPACT I and zero atoms in COMPACT II corresponds to a deposition of more than 38% in COMPACT I at a confidence level (c.l.) of 95%. From this, a lower limit for $-\Delta H_a^{Au}$(E114) that yields such a distribution in COMPACT was obtained by MCS. The determined limit is $-\Delta H_a^{Au}(E114) > 48\,kJ\,mol^{-1}$ (95% c.l.). The adsorption enthalpy of element 114 on Au is therefore at least as strong as that of Cn, which clearly points to the formation of metallic bonds between element 114 and Au. This is in contrast to the noble-gas-like behavior predicted by Pitzer and claimed by the previous experiment. Instead, calculations that take the influence of relativistic effects on the shell structure of superheavy elements into full account are in good agreement with the observed behavior of element 114 in the TASCA experiment. Thus, superheavy element 114 is a volatile metal due to a relativistic subshell closure of the $7p_{1/2}^2$ configuration, which is the new feature in the periodic table of the elements.

Thus, even though the absorption enthalpy of Fl on Au appeared at least as strong as that of Cn, pointing to the formation of a metallic bond between Fl and Au (Yakushev et al. 2014), there was a broad band of values for the absorption enthalpies that was covered in both experiments (Eichler et al. 2010; Yakushev et al. 2014), so that the interpretation concerning the nature of the interaction differed substantially, leaving the chemical nature of Fl an open question. In light of the low statistics of these experiments, further investigations were performed at TASCA in 2014/2015 using three COMPACT detectors in line where the detectors in COMPACT 1 had a SiO_2 surface, COMPACT 2 a Au surface operated at room temperature, and COMPACT 3 a Au surface operated with a negative temperature gradient. No Fl decays were registered in the SiO_2– covered detectors. Operation of COMPACT 2 and 3 led to the observation of additional six Fl atoms. These were evaluated together with the two events reported in (Eichler et al. 2016). All eight events formed two deposition zones. The first one was located near the deposition zone of Hg. This suggested that Fl forms metallic bonds with Au. The second zone overlapped with the Rn deposition zone, indicative of weak interaction of the Fl–Au system. Therefore, this experiment was complemented by an analysis of the structure of the Au surface present in the experiments, an aspect that was neglected in both previous works on Fl chemistry. The production of the Au-covered COMPACT detectors involved the thermal evaporation of a thin Au film onto the surface of the PIN diodes that was analyzed by several analytical methods showing polycrystalline, inhomogeneous Au films. They consisted of Au grains of different sizes with different orientations. They included well-ordered epitaxial Au(111) crystallites. The retention times of an adatom are different (i) on the regular surface of Au(111) grains and (ii) at defects, depending on the corresponding adsorption enthalpy values. The observation of two Fl deposition zones indicates that a fraction of Fl atoms reached a grain boundary where they were energetically trapped for longer than their nuclear lifetime. The other fraction of Fl atoms always desorbed back into the gas phase before reaching a trapping site.

These atoms were transported by the gas flow to the cold end of the COMPACT 3 with the temperature gradient, where the retention time even on weakly interacting sites became longer than the residual nuclear lifetime. To conclude: There are two scenarios for the single adsorption–desorption step on an inhomogeneous Au surface; an adatom approaches the well-ordered Au(111) surface and diffuses randomly by hopping across this surface being shortly in a number of weakly absorbing states before it desorbs back into the gas phase (case 1). For the hopping from one weakly absorbing site to the next one, an adatom needs to overcome the energy barrier equal to the activation energy. An adatom finds during the random walk a surface defect, an energetically more favorable place, where its retention time is significantly extended (case 2). This is incorporated in MCSs for diffusive mobile absorption. This way, both the experimentally observed Fl distributions in the COMPACT (Yakushev et al. 2014) and the COLD (Eichler et al. 2010) arrays are both well described by the new MCSs for the diffusive mobile adsorption, and the contradictory interpretations of previous Fl studies (Eichler et al. 2010; Yakushev et al. 2014) become complementary by considering the absorption mechanism on the inhomogeneous Au surface. The new TASCA experiments have demonstrated that due to the strong relativistic contraction of the fully occupied 7s and $7p_{1/2}$ (sub-)orbitals, Fl is a very volatile and inert element (no sorption on SiO_2) forming metallic bonds with Au. A paper is in the final stage of preparation for submission.

The neighbors of Fl, element 113, nihonium (Nh), and element 115, moscovium (Mc), are members of groups 13 and 15, placed below Tl and Bi, respectively. From their position, an electronic ground state configuration $7s^2 7p_{1/2}{}^1$ is expected for Nh and $7s^2 7p_{1/2}{}^2 7p_{3/2}{}^1$ for Mc. The presence of an unpaired $7p_{1/2}$ or $7p_{3/2}$ electron implies a higher reactivity than that of the neighbors Cn and Fl, having closed $6d^{10}7s^2$ and quasi-closed $7s^2 7p_{1/2}{}^2$ valence electron shells. Because of the availability of a single valence p-electron outside the (quasi)closed-shell, both elements are expected to be monovalent. However, due to the relativistic effects, i.e. a stabilization of the $7p_{1/2}$ electron sub-shell compared to corresponding $6p_{1/2}$ electron sub-shell, an enhanced volatility is expected for Nh and Mc compared to Tl and Bi, respectively. The bond strength in dimers and in compounds with Au is predicted to be the strongest for Mc among all 7p elements, see Figure 17.65.

In the course of the Fl experiments in 2014/2015, the residence time of the reaction products in the RTC was several times improved (shortened) so that a yield of 50% for short-lived Hg-radioisotopes at the entrance of COMPACT was reached within 0.4 seconds, thus improving the survival probability of 0.66 s-^{288}Fl and 1.9 s-^{289}Fl significantly. The cross section and the half-life of ^{284}Nh which is best produced indirectly via the reaction ^{243}Am(^{48}Ca, 3n)^{288}Mc are very similar to the corresponding values in experiments with Fl rendering ^{284}Nh the ideal isotope for chemical studies of Nh. The improved setup was commissioned in 2018/2019 in test experiments with parasitic beams. In the following, a Nh experiment was conducted in April–May 2020 leading to the observation of 7 decay chains. The detection system consisted of a first COMPACT section with SiO_2 surfaces followed by Au surfaces on the following detectors. In two cases, also the α-decay precursor ^{288}Mc was observed

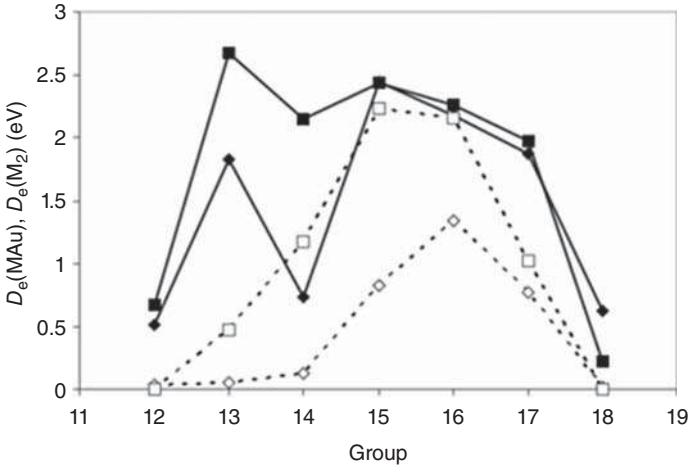

Figure 17.65 Calculated dissociation energies (D_e) of Mau and M_2 (M are elements Hg/Cn through Rn/118). Filled and open squares are D_e(Mau) and D_e(M_2) of the 6p elements, while filled and open rhomboids are D_e(MAu) and D_e(M_2) of the 7p elements. Source: Pershina et al. (2010), figure 2 (p. 104304-3)/American Institute of Physics.

for the first time in a chemistry experiment despite of its half-life of only 170 ms. Except for one decay chain of ^{284}Nh, all ^{284}Nh decay chains were found on the SiO_2 surface. This observation is in agreement with the predicted reactivity of Nh, see Figure 17.65. The observation of ^{288}Mc suggests to collect more data on the chemical properties of Mc. The comparative study of all three elements, Nh, Fl, and Mc, at TASCA would provide the direct observation of the influence of relativistic effects in SHE chemistry. To reach even the heaviest elements Lv, Ts, and Og, the existing RTC will be exchanged by a universal high-pressure gas stopping cell named Uni-Cell (Varentsov and Yakushev 2019) allowing for an even faster ($\approx$ 1 ms) and highly efficient (up to 100%) extraction of ions for gas-phase chemical studies and studies of nuclear properties. It consists of a DC cage and (RF + DC) funnel; a RF-only ejector serves as an interface between the extraction hole in the funnel of the stopping cell and the entrance in the narrow detector channel. The extraction time from Uni-Cell will be measured by using the macropulse structure of the UNILAC beam.

References

Albers, R.C. (2001). An expanding view of plutonium. *Nature* 410: 759.

Anton, J., Fricke, B., and Engel, E. (2004). Noncollinear and collinear relativistic density-functional program for electric and magnetic properties of molecules. *Phys. Rev.* A69: 012505.

Armbruster, P. (2008). Shifting the closed proton shell to Z = 122 – a possible scenario to understand the production of superheavy elements Z = 112–118. *Eur. Phys. J. A* 37: 167.

Barysz, M. and Ishikawa, Y. (eds.) (2010). *Relativistic Methods for Chemists*. Berlin: Springer-Verlag.

Block, M. (2019). Direct mass measurements and ionization potential measurements of the actinides. *Radiochim. Acta* 107: 821.

Borg, R.J. and Dienes, G.J. (1981). On the validity of single atom chemistry. *J. Inorg. Nucl. Chem.* 43: 1129.

Brüchle, W., Schädel, M., Scherer, U.W. et al. (1988). The hydration enthalpies of Md^{3+} and Lr^{3+}. *Inorg. Chim. Acta* 146: 267.

Czerwinski, K.R. (1992). PhD thesis, LBL-32 233/UC-413. University of California, Berkeley.

Desclaux, J.-P. (1973). Relativistic Dirac-Fock expectation values for atoms with Z = 1 to Z = 120. *At. Data Nucl. Data Tables* 12: 311.

Düllmann, C. et al. (2002). Chemical investigation of hassium (element 108). *Nature* 418: 859–862.

Düllmann, Ch.E. et al. (2010). Production and decay of element 114, high cross sections and the new nucleus ^{277}Hs. *Phys. Rev. Lett.* 104: 252701.

Egido, J.L. and Jungclaus, A. (2020). Predominance of triaxial shapes in transitional super-heavy nuclei: ground-state deformation and shape coexistence along the Flerovium ($Z = 114$) chain of isotopes. *Phys. Rev. Lett.* 125: 192504.

Eichler, B., Domanov, V.P., and Zvara, I. (1976). *JINR Dubna Report P12-9454*.

Eichler, B., Gäggeler-Koch, H., and Gäggeler, H. (1979). Thermochromatography of carrier-free elements: polonium in copper columns. *Radiochim. Acta* 26: 193.

Eichler, R., Aksenov, N.V., Belozerov, A.V. et al. (2008). Thermochemical and physical properties of element 112. *Angew. Chem. Int. Ed.* 47: 3262.

Eichler, R., Aksenov, N.V., Albin, Yu.V. et al. (2010). Indication for a volatile element 114. *Radiochim. Acta* 98: 133.

Eichler, R. et al. (2016). Complex chemistry with complex compounds. *Nobel Symposium NS160 – Chemistry and Physics of Heavy and Superheavy Elements. EPJ Web of Conferences 131*, 07005.

Even, J., Yakushev, A., Düllmann, Ch.E. et al. (2012). Rapid synthesis of radioactive transition-metal carbonyl complexes at ambient conditions. *Inorg. Chem.* 51: 6431.

Even, J., Yakushev, A., Düllmann, Ch.E. et al. (2014). In-situ formation, thermal decomposition, and adsorption studies of transition metal carbonyl complexes with short-lived radioisotopes. *Radiochim. Acta* 102: 1093.

Even, J., Yakushev, A., Düllmann, Ch.E. et al. (2014). Synthesis and detection of a seaborgium carbonyl complex. *Science* 345: 1491.

Even, J., Ackermann, D., Asai, M. et al. (2015). In-situ synthesis of volatile carbonyl complexes with short-lived nuclides. *J. Radioanal. Nucl. Chem.* 303: 2457.

Flerov, G.N., Oganesyan, Yu.Ts., Lobanov, Yu.V. et al. (1964). Synthesis and physical identification of the isotope of element 104 with mass number 260. *Phys. Lett.* 13: 73.

Forsberg, U., Rudolph, D., Andersson, L.-L. et al. (2016a). Recoil-α-fission and recoil-α-α-fission events observed in the reaction ^{48}Ca + ^{243}. *Am. Nucl. Phys. A* 953: 117.

Forsberg, U., Rudolph, D., Fahlander, C. et al. (2016b). A new assessment of the alleged link between element 115 and element 117 decay chains. *Phys. Lett. B* 760: 293.

Fricke, B. (1975). Superheavy elements. In: *Structure and Bonding*, vol. 21 (eds. W.L. Jörgensen et al.), 89. Berlin: Springer-Verlag.

Fricke, B. and Waber, J.T. (1971). Theoretical predictions of the chemistry of superheavy elements, continuation of the periodic table up to Z = 184. *Actinides Lanthanides Rev.* 1: 433.

Fricke, B., Greiner, W., and Waber, J.T. (1971). The continuation of the periodic table up to *Z* = 172. *Theor. Chim. Acta* 21: 235.

Fried, S., Westrum, E.F., Baumbach, H.L., and Kirk, P.L. (1958). The microscale preparation and micrometallurgy of plutonium metal. *J. Inorg. Nucl. Chem.* 5: 182.

Gäggeler, H., Jost, D.T., Kovacs, J. et al. (1992). Gas phase chromatography experiments with bromides of tantalum and element 105. *Radiochim. Acta* 57: 93.

Gäggeler, H.W. (1998). Chemistry gains a new element: Z = 106. *J. Alloys Compd.* 271: 277.

Gates, J.M., Pang, G.K., Pore, J.L. et al. (2018). First direct measurement of superheavy-element mass numbers. *Phys. Rev. Lett.* 121: 222501.

Ghiorso, A., Harvey, B.G., Choppin, G.R. et al. (1955). New element mendelevium, atomic number 101. *Phys. Rev.* 98: 1518.

Ghiorso, A. et al. (1958). Element No. 102. *Phys. Rev. Lett.* 1: 18.

Ghiorso, A., Nurmia, M., Harris, J. et al. (1969). Positive identification of two alpha-particle-emitting isotopes of element 104. *Phys. Rev. Lett.* 22: 1317.

Ghiorso, A. et al. (1974). Element No. 106. *Phys. Rev. Lett.* 33: 1490.

Gober, M.K., Kratz, J.V., Zimmermann, H.P. et al. (1992). Chemical properties of element 105 in aqueous solution: extraction into diisobutylcarbinol. *Radiochim. Acta* 57: 77.

Guillaumont, R., Adloff, J.P., and Peneloux, A. (1989). Kinetic and thermodynamic aspects of tracer-scale and single atom chemistry. *Radiochim. Acta* 46: 169.

Guillaumont, R., Adloff, J.P., Peneloux, A., and Delamoye, P. (1991). Sub-tracer scale behaviour of radionuclides, application to actinide chemistry. *Radiochim. Acta* 54: 1.

Qin, Z., Lin, M.S., Fan, F.L. et al. (2012). On-line gas chromatographic studies of Nb, Ta, and Db bromides. *Radiochim. Acta* 100: 285.

Haba, H., Tsukada, K., Asai, M. et al. (2004). Fluoride complexation of element 104, rutherfordium. *J. Am. Chem. Soc.* 126: 5219.

Haba, H., Kaji, D., Kudou, Y. et al. (2012). Production of ^{265}Sg in the ^{248}Cm(Ne,5n)^{265}Sg reaction and decay properties of two isomeric states in ^{265}Sg. *Phys. Rev. C* 85: 024611.

Herzberg, R.D. et al. (2006). Nuclear isomers in superheavy elements as stepping stones towards the island of stability. *Nature* 442: 896.

Hoffman, D.C., Lawrence, F.U., Mewherter, J.L., and Rourke, F.M. (1971). Detection of plutonium-244 in nature. *Nature* 234: 132.

Hofmann, S. (2011). Synthesis of superheavy elements by cold fusion. *Radiochim. Acta* 99: 405.

Jacob, T., Anton, J., Sarpt-Turodan, C. et al. (2003). Embedded cluster approach to simulate single atom adsorption on surfaces: Cu on Cu surface. *Surf. Sci.* 536: 45.

Kaldor, U., Eliav, E., and Landau, A. (2002). Accurate relativistic Fock-Space calculations for many-electron atoms. In: *Relativistic Electronic Structure Theory, Parts 1 and 2*, vol. 2 (ed. P. Schwerdtfeger), 81. Amsterdam: Elsevier.

Köhler, S., Deißenberger, R., Eberhardt, K. et al. (1997). Determination of the ionization potential of actinide elements by resonance ionization mass spectrometry. *Spectrochim. Acta* B52: 717.

Kratz, J.V. (1999). Chemical properties of the transactinide elements. In: *Heavy Elements and Related New Phenomena*, vol. I (eds. W. Greiner and R.K. Gupta), 129. Singapore: World Scientific.

Kratz, J.V. (2011). Chemistry of transactinides. In: *Handbook of Nuclear Chemistry*, 2e, vol. 2 (eds. A. Vértes, S. Nagy, Z. Klencsár, et al.), 925. Berlin: Springer-Verlag.

Kratz, J.V., Zimmermann, H.P., Scherer, U.W. et al. (1989). Chemical properties of element 105 in aqueous solutions: halide complex formation and anion exchange into triisooctyl amine. *Radiochim. Acta* 48: 121.

Kratz, J.V., Gober, M.K., Zimmermann, H.P. et al. (1992). The new nuclide ^{263}Ha. *Phys. Rev. C* 45: 1064.

Kratz, J.V., Nähler, A., Rieth, U. et al. (2003). An EC-branch in the decay of 27-s ^{263}Db: evidence for the isotope ^{263}Rf. *Radiochim. Acta* 91: 59.

Lewis, K.E., Golden, D.M., and Smith, G.P. (1984). Organometallic bond dissociation energies: laser pyrolysis of $Fe(CO)_5$, $Cr(CO)_6$, Mo(CO), and $W(CO)_6$. *J. Am. Chem. Soc.* 106: 3905.

Mann, J.B. and Waber, J.T. (1970). SCF relativistic Hartree-Fock calculations on the superheavy elements 118–131. *J. Chem. Phys.* 53: 2397.

Marinsky, J.A., Glendenin, L.E., and Coryell, C.D. (1947). *J. Am. Chem. Soc.* 69: 2781.

McMillan, E. (1939). Radioactive recoils from uranium activated by neutrons. *Phys. Rev.* 55: 510.

McMillan, E. and Abelson, P.H. (1940). Radioactive element 93. *Phys. Rev.* 57: 1185.

Münzenberg, G. and Hofmann, S. (1999). Discovery of the heaviest elements. In: *Heavy Elements and Related New Phenomena*, vol. I (eds. W. Greiner and R.K. Gupta), 9. Singapore: World Scientific.

Nagame, Y. (2019). Nuclear and chemical characterization of heavy actinides. *Radiochim. Acta* 107: 803.

Nagame, Y., Tsukada, K., Asai, M. et al. (2005). Chemical studies on rutherfordium (Rf) at JAERI. *Radiochim. Acta* 93: 519.

Oganessian, Y. (2011). Synthesis of the heaviest elements in ^{48}Ca-induced reactions. *Radiochim. Acta* 99: 429.

Oganessian, Y.T., Abdullin, F.S., Dmitriev, S.N. et al. (2013). Investigation of the ^{243}Am + ^{48}Ca reaction products previously observed in the experiments on elements 113, 115 and 117. *Phys. Rev.* C87: 014302.

Oganessian, Y.T. et al. (1974). *JETP Lett.* 20: 265.

Paulus, W., Kratz, J.V., Strub, E. et al. (1999). Chemical properties of element 105 in aqueous solution: extraction of the fluoride-, chloride-, and bromide complexes of the group-5 elements into an aliphatic amine. *Radiochim. Acta* 84: 69.

Pershina, V. (1998). Solution chemistry of element 105 Part II: hydrolysis and complex formation of Nb, Ta, Ha, and Pa in HCl solutions. *Radiochim. Acta* 80: 75.

Pershina, V. (2005). Theoretical investigations of the reactivity of MO_4 and the electronic structure of $Na_2[MO_4(OH)_2]$, where M = Ru, Os, and Hs (element 108). *Radiochim. Acta* 93: 373.

Pershina, V. and Anton, J. (2013). Theoretical predictions of properties and gas-phase chromatography behaviour of carbonyl complexes of group-6 elements Cr, Mo, W, and element 106, seaborgium. *J. Chem. Phys.* 138: 174301-6.

Pershina, V. and Bastug, T. (1999). Solution chemistry of element 105 Part III: hydrolysis and complex formation in HF and HBr solutions. *Radiochim. Acta* 84: 79.

Pershina, V. and Fricke, B. (1993). Relativistic effects in physics and chemistry of element 105. Their influence on the electronic structure and related properties. *J. Chem. Phys.* 99: 9720.

Pershina, V. and Kratz, J.V. (2001). Solution chemistry of element 106: theoretical prediction of hydrolysis of group 6 cations Mo, W, and Sg. *Inorg. Chem.* 40: 776.

Pershina, V., Sepp, W.-D., Fricke, B. et al. (1992). Relativistic effects in physics and chemistry of element 105, electronic structure and properties of group 5 elements bromides. *J. Chem. Phys.* 97: 1116.

Pershina, V., Anton, J., and Fricke, B. (2007). Intermetallic compounds of the heaviest elements and their homologs: the electronic structure and bonding of MM′, where M = Ge, Pb, and element 114, and M′ = Ni, Pd, Pt, Cu, Ag, Au, Sn, Pb, and element 114. *J. Chem. Phys.* 127: 134310.

Pershina, V., Borschevsky, A., Anton, J., and Jacob, T. (2010). Theoretical predictions of trends in spectroscopic properties of gold containing dimers of the 6p and 7p elements and their adsorption on gold. *J. Chem. Phys.* 133: 104304.

Pitzer, K.S. (1975). Are elements 112, 114, and 118 relatively inert gases? *J. Chem. Phys.* 63: 1032.

Qin et al. (2012). *On-line Gas Chromatographic Studies of Nb, Ta, and Db Bromides*. Walter de Gruyter.

Rosen, A. and Ellis, D.E. (1975). Relativistic molecular calculations in the Dirac–Slater model. *J. Chem. Phys.* 62: 3039.

Sahm, C.-C. et al. (1985). *Nucl. Phys. A* 44: 316.

Såmark–Roth, A., Cox, D.M., Rudolph, D. et al. (2021). Spectroscopy of Flerovium decay chains: Discovery of ^{280}Ds and an Excited state in ^{282}Cn. *Phys. Rev. Lett.* 126: 032503.

Sato, T.K., Asai, M., Borschevsky, A. et al. (2018). First ionization potentials of Fm, Md, No, and Lr: verification of filling-up the 5f electrons and confirmation of the actinide series. *J. Am. Chem. Soc.* 140: 14609.

Schädel, M. (1995). Chemistry of the transactinide elements. *Radiochim. Acta* 70/71: 207.

Schädel, M., Brüchle, W., Jäger, E. et al. (1989). ARCA II – a new apparatus for fast, repetitive HPLC separations. *Radiochim. Acta* 48: 171.

Schädel, M., Brüchle, W., Schimpf, E. et al. (1992). Chemical properties of element 105 in aqueous solution: cation exchange separations with α-hydroxyisobutyric acid. *Radiochim. Acta* 57: 85.

Seaborg, G.T. (1958). *The Transuranium Elements*. New Haven, CT: Yale University Press.

Seaborg, G.T., James, R.A., and Ghiorso, A. (1944). Heavy Isotopes by Bombardment of ^{239}Pu. *Metallurgical Laboratory Report CS-2135*. University of Chicago, p. 26.

Seaborg, G.T., James, R.A., Morgan, L.O., and Ghiorso, A. (1945). Search for New Heavy Isotopes. *Metallurgical Laboratory Report CS-2741*. University of Chicago, p. 9.

Segrè, E. (1939). An unsuccessful search for transuranic elements. *Phys. Rev.* 55: 1104.

Templeton, D.H. and Dauben, C.H. (1954). Atomic number *Z*. *J. Am. Chem. Soc.* 76: 5237.

Ter Akopian, G.M., Sagaidak, R.N., Pleve, A.A. et al. (1985). Measurements of the Half-Life of a Short-Lived Spontaneously Fissioning Nuclide Formed in the Nuclear Reaction ^{249}Bk + ^{15}N. *JINR Dubna Report P7-85-634*.

Thompson, S.G., Ghiorso, A., and Seaborg, G.T. (1950). Element 97. *Phys. Rev.* 77: 838.

Toyoshima, A., Haba, H., Tsukada, K. et al. (2004). Elution curves of rutherfordium (Rf) in anion-exchange chromatography with hydrofluoric acid solution. *J. Nucl. Radiochem. Sci.* 5: 45.

Toyoshima, A., Haba, H., Tsukada, K. et al. (2008). Hexafluoro complex of rutherfordium in mixed HF/HNO_3 solutions. *Radiochim. Acta* 96: 125.

Trautmann, N. (1995). Fast radiochemical separations for heavy elements. *Radiochim. Acta* 70/71: 237.

Türler, A. (1996). Gas phase chemistry experiments with transactinide elements. *Radiochim. Acta* 72: 7.

Türler, A. (1999). *Habilitationsschrift*. Universität Bern.

Usoltsev, Y., Eichler, R., Wang, Y. et al. (2016). Decomposition studies of group 6 hexacarbonyl complexes Part 1. Production and decomposition of $Mo(CO)_6$ and $W(CO)_6$. *Radiochim. Acta* 104: 141.

Varentsov, V. and Yakushev, A. (2019). Concept of a universal high density gas stopping cell setup for the study of gas-phase chemistry and nuclear properties of superheavy elements (UniCell). *Nucl. Instrum. Methods Phys. Res.* 940: 206.

Yakushev, A., Gates, J.M., Türler, A. et al. (2014). Superheavy element Flerovium (element 114) is a volatile metal. *Inorg. Chem.* 53: 1624.

Zvara, I. (1985). Simulation of thermochromatographic processes by the Monte Carlo method. *Radiochim. Acta* 38: 95.

Zvara, I., Belov, V.Z., Korotkin, Y.S. et al. (1970). *JINR Dubna Report P12-5120*.

Zvara, I., Belov, V., Domanov, V.P., and Shalaevski, M.R. (1976). Chemical isolation of nilsbohrium as ekatantalum in the form of the anhydrous bromide. *Sov. Radiochem.* 18: 371.

von Zweidorf, A. et al. (2004). *Evidence for the Formation of Sodium Hassate(VIII)*. Walter de Gruyter.

Further Reading

General and Historical

Hahn, O. (1948). *Künstliche Neue Elemente*. Verlag Chemie: Weinheim.

Bagnall, K.W. (1957). *Chemistry of the Rare Radioelements (Polonium, Actinium)*. London: Butterworths.

Hyde, E.K. and Seaborg, G.T. (1957). *The Transuranium Elements, Handbuch der Physik*, vol. XLII. Berlin: Springer-Verlag.

Seaborg, G.T. (1963). *Man-Made Transuranium Elements*. Englewood Cliffs, NJ: Prentice Hall.

Haissinsky, M. and Adloff, J.P. (1965). *Radiochemical Survey of the Elements*. Amsterdam: Elsevier.

Keller, C. (1971). *The Chemistry of the Transuranium Elements*. Verlag Chemie: Weinheim.

Bagnall, K.W. (ed.). *International Review of Science, Inorganic Chemistry*, vol. 7. Series One and Two, Butterworths, London: Lanthanides and Actinides.1972 and 1975

Freeman, A.J. and Darby, J.B. Jr., (eds.) (1974). *The Actinides: Electronic Structure and Related Properties*. New York: Academic Press.

Seaborg, G.T. (ed.) (1978). *Transuranium Elements – Products of Modern Alchemy*. Stroudsburg, PA: Dowden, Hutchinson & Ross.

Edelstein, N.M. (ed.) (1980). *Lanthanide and Actinide Chemistry and Spectroscopy*, ACS Symposium Series, vol. 131. Washington, DC: American Chemical Society.

Edelstein, N.M. (ed.) (1982). *Actinides in Perspective*. Oxford: Pergamon.

Katz, J.J., Seaborg, G.T., and Morss, L.R. (eds.) (1986). *The Chemistry of the Actinide Elements*, 2e, vol. 2. London: Chapman and Hall.

Seaborg, G.T. and Loveland, W.D. (1990). *The Elements Beyond Uranium*. New York: Wiley.

Morss, L.R. and Fuger, J. (eds.) (1992). *Transuranium Elements: A Half Century*. Washington, DC: American Chemical Society.

Seaborg, G.T. (1995). Transuranium elements: the synthetic actinides. *Radiochim. Acta* 70/71: 69.

Münzenberg, G. and Schädel, M. (1996). *Die Jagd nach den schwersten Elementen*. Braunschweig: Vieweg.

Schädel, M. (ed.) (2003). *The Chemistry of Superheavy Elements*. Dordrecht: Kluwer Academic.

Morss, L.R., Edelstein, N.M., Fuger, J., and Katz, J.J. (2006). *The Chemistry of Actinide and Transactinide Elements*, 3e. Dordrecht: Springer.

Gregorich, K.E., Henderson, R.A., Lee, D.M., et al. (1988). Aqueous chemistry of element 105. *Radiochim. Acta* 43: 223.

Pershina, V., Anton, J., and Jacob, T. (2008). Fully relativistic density-functional-theory calculations of the electronic structures of MO_4 (M = Ru, Os, and element 108, Hs) and prediction of physisorption. *Phys. Rev. A* 78: 032518.

Handbooks

Gmelin, L. *Gmelins Handbook of Inorganic Chemistry, Transuranium Elements*, vols. 7a, 7b, 8, 31, 8e. Weinheim: Verlag Chemie.1973–1976

Freeman, A.J. and Keller, C. (eds.) (1984 onward). *Handbook on the Physics and Chemistry of the Actinides*, vols. III, IV. Amsterdam: North-Holland.

Freeman, A.J. and Lander, G.H. (eds.) (1984 onward). *Handbook on the Physics and Chemistry of the Actinides*, vols. I, II, V. Amsterdam: North-Holland.

Vertés, A., Nagy, S., Klencsár, Z. et al. (eds.) (2011). *Handbook of Nuclear Chemistry*, 2e, vol. 6. Berlin: Springer.

More Specialized, Actinides

Seaborg, G.T. (1945). The chemical and radioactive properties of the heavy elements. *Chem. Eng. News* 23: 2190.

Kennedy, J.W., Seaborg, G.T., Segrè, E., and Wahl, A.C. (1946). Properties of 94(239). *Phys. Rev.* 70: 555.

Seaborg, G.T., McMillan, E.M., and Kennedy, J.W. (1946). Radioactive element 94 from deuterons on uranium. *Phys. Rev.* 69: 366.

Thompson, S.G., Street, K., Ghiorso, A., and Seaborg, G.T. (1950). Element 98. *Phys. Rev.* 78: 298.

Asprey, L.B., Stephanou, S.E., and Penneman, R.A. (1951). Hexavalent americium. *J. Am. Chem. Soc.* 73: 5715.

Asprey, L.B. (1954). New compounds of quadrivalent americium, AmF_4, $KAmF_5$[1]. *J. Am. Chem. Soc.* 76: 2019.

Ghiorso, A., Thompson, S.G., Higgins, G.H. et al. (1955). New elements einsteinium and fermium, atomic numbers 99 and 100. *Phys. Rev.* 99: 1048.

Maly, J., Sikkeland, T., Silva, R., and Ghiorso, A. (1968). Nobelium: tracer chemistry of the divalent and trivalent ions. *Science* 160: 1114.

Cordfunke, E.H.P. (1969). *The Chemistry of Uranium*. Amsterdam: Elsevier.

Milyukova, M.S., Gusev, N.I., Sentyurin, I.G., and Sklyarenko, I.S. (1969). *Analytical Chemistry of Plutonium*. Ann Arbor, MI: Ann Arbor–Humphrey.

Ryabchikov, D.I. and Golbraikh, E.K. (1969). *Analytical Chemistry of Thorium*. Ann Arbor, MI: Ann Arbor–Humphrey.

Cleveland, J.M. (1970). *The Chemistry of Plutonum*. New York: Gordon and Breach.

Lavrukhina, A.K. and Podznyakov, A.A. (1970). *Analytical Chemistry of Technetium, Astatine and Francium*. Ann Arbor, MI: Ann Arbor–Humphrey.

Palei, P.N. (1970). *Analytical Chemistry of Uranium*. Ann Arbor, MI: Ann Arbor–Humphrey.

Palshin, E.S. and Myasoedov, B.F. (1970). *Analytical Chemistry of Protactinium*. Ann Arbor, MI: Ann Arbor–Humphrey.

Ryabchikov, D.I. and Ryabukhin, V.A. (1970). *Analytical Chemistry of Yttrium and the Lanthanide Elements*. Ann Arbor, MI: Ann Arbor–Humphrey.

Baybarz, R.D., Asprey, L.B., Strouse, C.E., and Fukushima, E. (1972). Divalent americium: the crystal structure and magnetic susceptibility of AmI_2. *J. Inorg. Nucl. Chem.* 34: 3427.

Peterson, J.R. and Baybarz, R.D. (1972). The stabilization of divalent californium in the solid state: californium dibromide. *Inorg. Nucl. Chem. Lett.* 8: 423.
Silva, R.J. (1972). Transcurium elements. In: *International Review of Science, Inorganic Chemistry Series One: Radiochemistry*, vol. 8 (ed. A.G. Maddock), 71. London: Butterworths.
Mikhailov, V.A. (1973). *Analytical Chemistry of Neptunium*. New York: Halsted Press.
Myasoedov, B.F., Guseva, L.I., Lebedev, I.A. et al. (1974). *Analytical Chemistry of Transplutonium Elements*. New York: Wiley.
Silva, R.J., McDowell, W.J., Keller, O.L., and Tarrant, J.R. (1974). Comparative solution chemistry, ionic radius, and single ion hydration energy of nobelium. *Inorg. Chem.* 13: 2235.
Blank, H. and Lindner, R. (eds.) (1976). *Plutonium and Other Actinides*. Amsterdam: North-Holland.
Müller, W. and Blank, H. (eds.) (1976). *Heavy Element Properties*. Amsterdam: North-Holland.
Müller, W. and Lindner, R. (eds.) (1976). *Transplutonium Elements*. Amsterdam: North-Holland.
David, F. (1981). Radiochemical studies of transplutonium elements. *Pure Appl. Chem.* 53: 997.
Carnall, W.T. and Choppin, G.R. (eds.) (1983). *Plutonium Chemistry*, ACS Symposium Series, vol. 216. Washington, DC: American Chemical Society.
Hulet, E.K. (1983). Chemistry of the elements einsteinium through-105. *Radiochim. Acta* 32: 7.
Sinha, S.P. (ed.) (1983). *Systematics and the Properties of the Lanthanides*. Dordrecht: Kluwer Academic.
Stein, L. (1983). The chemistry of radon. *Radiochim. Acta* 32: 163.
Choppin, G.R., Navratil, J.D., and Schulz, W.W. (eds.) (1985). *Actinides–Lanthanides Separation*. Singapore: World Scientific.
Narayama, R.K. and Arnikar, H.J. (eds.) (1985). *Artificial Radioactivity*. New Delhi: Tata McGraw-Hill.
Hopke, P.K. (ed.) (1987). *Radon and Its Decay Products: Occurrence, Properties and Health Effects*. Washington, DC: American Chemical Society.
Zvara, I. (1990). Thermochromatographic method of separation of chemical elements in nuclear and radiochemistry. *Isotopenpraxis* 26: 251.
Choppin, G.R. and Nash, K.L. (1995). Actinide separation science. *Radiochim. Acta* 70/71: 225.
Kuroda, P.K. (1995). Formation of heavy elements in nature. *Radiochim. Acta* 70/71: 229.
Peterson, J.R., Erdmann, N., Nunnemann, M. et al. (1998). Determination of the first ionization potential of einsteinium by resonance ionization mass spectrometry. *J. Alloys Compd.* 271–273: 876.
Haschke, J.M., Allen, T.H., and Morales, L.A. (2000). Reaction of plutonium dioxide with water: formation and properties of PuO_{2+x}. *Science* 287: 285.
Bilewicz, A. (2002). The ionic radius of No^{3+}. *J. Nucl. Radiochem. Sci.* 3: 147.
Griffin, H.C. (2011). Radioelements. In: *Handbook of Nuclear Chemistry*, 2e, vol. 2 (eds. A. Vértes, S. Nagy, Z. Klencsár, et al.), 689. Berlin: Springer-Verlag.

Nagame, Y., Hirata, M., and Nakahara, H. (2011). Production and chemistry of the transuranium elements. In: *Handbook of Nuclear Chemistry*, 2e, vol. 2 (eds. A. Vértes, S. Nagy, Z. Klencsár, et al.), 817. Berlin: Springer-Verlag.

Sato, T.K., Asai, M., Borschevsky, A. et al. (2015). Measurement of the first ionization potential of lawrencium, element 103. *Nature* 520: 209.

Chhetri, P., Ackermann, D., Backe, H. et al. (2018). Precision measurement of the first ionization potential of nobelium. *Phys. Rev. Lett.* 120: 3003–3001.

Laatiaoui, M., Lauth, W., Backe, H. et al. (2018). Atom-at-a-time laser resonance ionization spectroscopy of nobelium. *Nature* 538: 495.

Transactinides

Zvara, I., Chuburkov, Y.T., Caletka, R. et al. (1966). Chemical properties of element 104. *Sov. J. At. Energy* 21: 709.

Zvara, I., Chuburkov, Y.T., Caletka, R., and Shalaevsky, M.R. (1969). Experiments on the chemistry of element 104 – kurchatovium, II. Chemical investigation of the isotope which undergoes spontaneous fission with a half-life of 0.3 sec. *Sov. Radiochem.* 11: 161.

Zvara, I., Chuburkov, Y.T., Zvarova, T.S., and Caletka, R. (1969). Experiments on the chemistry of element 104 – kurchatovium, I. Development of a method for studying short-lived isotopes. *Sov. Radiochem.* 11: 153.

Fricke, B., Greiner, W., and Waber, J.T. (1971). The continuation of the periodic table up to Z = 172. The chemistry of superheavy elements. *Theor. Chim. Acta* 21: 235.

Herrmann, G. (1975). Superheavy elements. In: *International Review of Science: Radiochemistry*, Inorganic Chemistry Series Two, vol. 8 (ed. A.G. Maddock), 221. London: Butterworths.

Keller, O.L.Jr. and Seaborg, G.T. (1977). Chemistry of the transactinide elements. *Annu. Rev. Nucl. Sci.* 27: 139.

Herrmann, G. (1979). Superheavy element research. *Nature* 280: 543.

Pyykkö, P. and Desclaux, J.-P. (1979). Relativity and the periodic table of the elements. *Acc. Chem. Res.* 12: 276.

Eichler, B. and Zvara, I. (1982). Evaluation of the enthalpy of adsorption from thermochromatographical data. *Radiochim. Acta* 30: 233.

Oganessian, Yu.Ts., Hussonnois, M., Demin, A.G. et al. (1984). Experimental studies on the formation and radioactive decay of isotopes with $Z = 104–109$. *Radiochim. Acta* 37: 113.

Vermeulen, D., Clerc, H.-G., Sahm, C.-C. et al. (1984). Cross sections for evaporation residue production near the N = 126 shell closure. *Z. Phys. A: At. Nucl.* 318: 157.

Armbruster, P. (1985). On the production of heavy elements by cold fusion; the elements 106 to 109. *Annu. Rev. Nucl. Part. Sci.* 35: 113.

Hyde, E.K., Hoffman, D.C., and Keller, O.R. Jr., (1987). A history and analysis of the discovery of elements 104 and 105. *Radiochim. Acta* 42: 57.

Seaborg, G.T. (1987). Superheavy elements. *Contemp. Phys.* 28: 33.

Herrmann, G. (1988). Synthesis of heaviest elements. *Angew. Chem. Int. Ed. Engl.* 27: 1417.

Kumar, K. (1989). *Superheavy Elements*. Bristol: Adam Hilger.

Ghiorso, A. (1990). The discovery of elements 95–106. *Proceedings of the Robert A. Welch Foundation Conference on Chemical Research XXXIV "Fifty Years with Transuranium Elements"*, Houston, TX (22–23 October 1990).

Bock, R., Herrmann, G., and Siegert, G. (1993). *Schwerionenforschung*. Darmstadt: Wiss. Buchgesellschaft.

Münzenberg, G. (1995). Discovery, synthesis and nuclear properties of the heaviest elements. *Radiochim. Acta* 70/71: 193.

Ghiorso, A. (1997). The techniques and instrumentation used for the discoveries of the transuranium elements. *Proceedings of the Robert A. Welch Foundation Conference XXXI on Chemical Research "The Transactinide Elements"*, Houston, TX (27–28 October 1997).

Rosen, A. (1997). Twenty to thirty years of DV-Xα calculations: a survey of accuracy and applications. *Adv. Quantum Chem.* 29: 1.

Cwiok, S. and Magierski, P. (1999). Skyrme-Hartree-Fock theory for shell structure of superheavy elements. In: *Heavy Elements and Related New Phenomena*, vol. I (eds. W. Greiner and R.K. Gupta), 277. Singapore: World Scientific.

Pershina, V. and Fricke, B. (1999). Electronic structure and chemistry of the heaviest elements. In: *Heavy Elements and Related New Phenomena*, vol. I (eds. W. Greiner and R.K. Gupta), 194. Singapore: World Scientific.

Reinhard, P.-G. and Maruhn, J.A. (1999). Superheavy nuclei in deformed mean-field calculations. In: *Heavy Elements and Related New Phenomena*, vol. I (eds. W. Greiner and R.K. Gupta), 332. Singapore: World Scientific.

Sobiczewski, A. (1999). New islands of stability using the finite-potential approach to superheavy elements. In: *Heavy Elements and Related New Phenomena*, vol. I (eds. W. Greiner and R.K. Gupta), 374. Singapore: World Scientific.

Kratz, J.V. (2003). Critical evaluation of the chemical properties of the transactinide elements. *Pure Appl. Chem.* 75: 103.

Omtvedt, J.P., Alstad, J., Breivik, H. et al. (2003). SISAK liquid–liquid extraction experiments with preseparated ^{257}Rf. *J. Nucl. Radiochem. Sci.* 3: 121.

Jensen, H.J.A. and Visscher, L. (2008). DIRAC package: DIRAC, a Relativistic ab initio Electronic Structure Program, Release DIRAC08.0. http://dirac.chem.sdu.dk (accessed 26 March 2013).

Zvara, I. (2008). *The Inorganic Radiochemistry of Heavy Elements: Methods for Studying Gaseous Compounds*. Berlin: Springer-Verlag.

Hoffman, D.C. and Shaughnessy, D.A. (2011). Superheavy elements. In: *Handbook of Nuclear Chemistry*, 2e, vol. 2 (eds. A. Vértes, S. Nagy, Z. Klencsár, et al.), 1005. Berlin: Springer-Verlag.

Münzenberg, G. and Gupta, M. (2011). Production and identification of transactinide elements. In: *Handbook of Nuclear Chemistry*, 2e, vol. 2 (eds. A. Vértes, S. Nagy, Z. Klencsár, et al.), 877. Berlin: Springer-Verlag.

Fusion reactions with ^{48}Ca beams

Oganessian, Yu.Ts. et al. (2000). Observation of the decay of ^{292}116. *Phys. Rev. C* 63: 011301(R).

Oganessian, Yu.Ts. et al. (2000). Synthesis of superheavy nuclei in the $^{48}Ca + ^{244}Pu$ reaction: $^{288}114$. *Phys. Rev. C62*: 041604(R).

Morita, K. et al. (2004). Experiment on the synthesis of element 113 in the reaction $^{209}Bi(^{70}Zn,n)^{278}113$. *J. Phys. Soc. Jpn.* 73: 2593.

Oganessian, Yu.Ts. et al. (2004). Measurements of cross sections and decay properties of the isotopes of elements 112, 114 and 116 produced in the fusion reactions $^{233, 238}U$, ^{242}Pu and $^{248}Cm + ^{48}Ca$. *Phys. Rev. C* 70: 064609.

Oganessian, Yu.Ts. et al. (2006). Synthesis of isotopes of elements 118 and 116 in the ^{249}Cf and $^{248}Cm + ^{48}Ca$ fusion reactions. *Phys. Rev. C* 74: 044602.

Eichler, R. et al. (2007). Chemical characterization of element 112. *Nature* 447: 72–75.

Hofmann, S. et al. (2007). The reaction $^{48}Ca + ^{238}U \rightarrow ^{286}112^*$ studied at the GSI SHIP. *Eur. Phys. J. A* 32: 251–260.

Morita, K. et al. (2007). Observation of the second decay chain from $^{278}113$. *J. Phys. Soc. Jpn.* 76: 045001.

Stavsetra, L. et al. (2009). Independent verification of element 114 production in the $^{48}Ca + ^{242}Pu$ reaction. *Phys. Rev. Lett.* 103: 132502.

Ellison, P.A. et al. (2010). New superheavy element isotopes: $^{242}Pu(^{48}Ca,5n)^{285}114$. *Phys. Rev. Lett.* 105: 182701.

Oganessian, Yu.Ts. et al. (2010). Synthesis of a new element with atomic number 117. *Phys. Rev. Lett.* 104: 142502.

Hofmann, S. et al. (2012). The reaction $^{48}Ca + ^{248}Cm \rightarrow ^{296}116^*$ studied at the GSI SHIP. *Eur. Phys. J. A* 48: 62.

Morita, K. et al. (2012). New result in the production and decay of an isotope, $^{278}113$, of the 113th element. *J. Phys. Soc. Jpn.* 81: 103201.

Oganessian, Yu.Ts., Abdullin, F.Sh., Alexander, C. et al. (2013). Experimental studies of the $^{249}Bk + ^{48}Ca$ reaction including decay properties and excitation function for isotopes of element 117, and discovery of the new isotope ^{277}Mt. *Phys. Rev. C* 87: 054621.

Oganessian, Yu.Ts., Abdullin, F.Sh., Dmitriev, S.N. et al. (2013). Investigation of the $^{243}Am + ^{48}Ca$ reaction products previously observed in the experiments on elements 113, 115 and 117. *Phys. Rev. C* 87: 014302.

Rudolph, D., Forsberg, U., Golubev, P. et al. (2013). Spectroscopy of element 115 decay chains. *Phys. Rev. Lett.* 111: 112502.

Khuyagbaatar, J. et al. (2014). $^{48}Ca + ^{249}Bk$ fusion reaction leading to element 117: long-lived α-decaying ^{270}Db and discovery of ^{266}Lr. *Phys. Rev. Lett.* 112: 172501.

Yakushev, A., Gates, J.M., Türler, A. et al. (2014). Superheavy element flerovium (element 114) is a volatile metal. *Inorg. Chem.* 53: 1624–1629.

Oganessian, Yu.Ts. and Utyonkov, V.K. (2015). Super-heavy element research. *Rep. Prog. Phys.* 78: 036301.

Jarlskog, C. (2016). Procedure around naming new elements. *Nobel Symposium NS160, Chemistry and Physics of Heavy and Superheavy Elements*, Bäckaskog Castle, Sweden (May 29–June 03, 2016).

Karol, P.J., Barber, R.C., Sherrrill, B.M. et al. (2016). Discovery of the elements with atomic numbers $Z = 113$, 115 and 117 (IUPAC Technical Report). *Pure Appl. Chem.* 88: 139 and 155.

Öhrström, L. and Reedijk, J. (2016). Names and symbols of the elements with atomic numbers 113, 115, 117 and 118. (IUPAC Recommendation 2016). *Pure Appl. Chem.* 88: 1225.

Hofmann, S., Dmitriev, S.N., Fahlander, C. et al. (2018). On the discovery of new elements. Provisional Report of the 2017 Joint Working Group of IUPAC and IUPAP. *Pure Appl. Chem.* 90: 1773.

Khuyagbaatar, J., Yakushev, A., Düllmann, Ch.E. et al. (2019). Fusion reaction $^{48}Ca + {}^{249}Bk$ leading to formation of the element Ts (Z = 117). *Phys. Rev. C* 99: 054306.

Special Issues

Düllmann, Ch.E. (2011). Superheavy element studies with preseparated isotopes. *Radiochim. Acta* 99: 515.

Gäggeler, H.W. (2011). Gas chemical properties of heaviest elements. *Radiochim. Acta* 99: 503.

Herzberg, R.-D. and Cox, D.M. (2011). Spectroscopy of actinide and transactinide nuclei. *Radiochim. Acta* 99: 441.

Hofmann, S. (2011). Synthesis of superheavy elements by cold fusion. *Radiochim. Acta* 99: 405.

Kratz, J.V. (2011). Aqueous-phase chemistry of the transactinides. *Radiochim. Acta* 99: 477.

Kratz, J.V. (ed.) (2011). Special issue: international year of chemistry 2011. Editorial: heavy elements. *Radiochim. Acta* 99: 375.

Nagame, Y. and Hirata, M. (2011). Production and properties of the transuranium elements. *Radiochim. Acta* 99: 377.

Oganessian, Yu.Ts. (2011). Synthesis of the heaviest elements in ^{49}Ca-induced reactions. *Radiochim. Acta* 99: 429.

Pershina, V. (2011). Relativistic electronic structure studies on the heaviest elements. *Radiochim. Acta* 99: 459.

Rodriguez, T.R. and Egido, J.L. (2010). Triaxial angular momentum projection and configuration mixing calculations with the Gogny force. *Phys. Rev.* C81: 064323.

Sobiczewski, A. (2011). Theoretical description of superheavy nuclei. *Radiochim. Acta* 99: 395.

Düllmann, Ch.E., Herzberg, R.-D., Nazarewicz, W., and Oganessian, Yu.Ts. (eds.) (2015). Special issue on superheavy elements. Editorial. *Nucl. Phys. A* 944: 1.

Goriely, S. and Martinez-Pinedo, G. (2015). The production of transuranium elements by the r-process nucleosynthesis. *Nucl. Phys. A* 944: 158.

Morita, K. (2015). SHE research at RIKEN/GARIS. *Nucl. Phys. A* 944: 30.

Münzenberg, G. (2015). From bohrium to copernicium and beyond SHE research at SHIP. *Nucl. Phys. A* 944: 5.

Münzenberg, G. and Morita, K. (2015). Synthesis of the heaviest nuclei in cold fusion reactions. *Nucl. Phys. A* 944: 3.

Oganessian, Yu.Ts. and Utyonkov, V.K. (2015). Superheavy nuclei from ^{48}Ca-induced reactions. *Nucl. Phys. A* 944: 62.

Zagrebaev, V.I. and Greiner, W. (2015). Cross sections for the production of superheavy nuclei. *Nucl. Phys. A* 944: 257.

Block, M. (2019). Direct mass measurements and ionization potential measurements of the actinides. *Radiochim. Acta* 107: 821.

Chemey, A.T. and Albrecht-Schmitt, T.E. (2019). Evolution of the periodic table through the synthesis of new elements. *Radiochim. Acta* 107: 771.

Eichler, R. (2019). The periodic table – an experimenter's guide to transactinide chemistry. *Radiochim. Acta* 107: 865.

Hofmann, S. (2019). Synthesis and properties of isotopes of the transactinides. *Radiochim. Acta* 107: 879.

Pershina, V. (2019). Relativity in the electronic structure of the heaviest elements and its influence on periodicities in properties. *Radiochim. Acta* 107: 833.

Qaim, S.M., Kratz, J.V., and Simoni, E. (eds.) (2019). Special issue: international year of the periodic table of chemical elements. Editorial: 150 years of the periodic table of chemical elements. *Radiochim. Acta* 107: 767.

18

Radionuclides in Geo- and Cosmochemistry

18.1 Natural Abundances of the Elements and Isotope Variations

A main concern of geochemistry is the investigation of the abundance and the distribution of the elements on the surface and in deeper layers of the Earth, and of transport processes. The components of the geosphere are the lithosphere, the hydrosphere, and the atmosphere. The relative abundance of the elements on the surface of the Earth is plotted in Figure 18.1 as a function of the atomic number. This relative abundance is similar within the Solar System. The elements H, O, Si, Ca, and Fe exhibit the highest abundances and maxima are observed at the magic numbers $Z = 8$, 20, 50, and 82. The abundances of the elements and their isotopes are determined by the nuclear reactions by which they have been produced and by their nuclear properties, whereas the chemical properties of the elements are only responsible for distribution and fractionation processes.

The abundances of the isotopes of the elements in the geosphere show some variations caused by their formation, by isotope effects, or by transport processes. A certain isotope ratio (IR) is taken as standard and the relative deviation from this standard is expressed as the δ value:

$$\delta = \frac{\text{IR(sample)} - \text{IR(standard)}}{\text{IR(standard)}} \cdot 1000 \tag{18.1}$$

High variations of the isotope ratio are observed for the isotopes of hydrogen, H and D, because of their high relative mass difference. The average isotope ratio D:H in the oceans ($\text{IR} = 1.56 \cdot 10^{-4}$) is taken as standard. In natural waters, δ(D) varies between +6 and −200. Evaporation of water leads to appreciable isotope effects, and high isotope effects are also found in the water of hydrates.

Some values of the isotope ratios ^{16}O:^{18}O, ^{12}C:^{13}C, and ^{32}S:^{34}S are listed in Table 18.1. Because oxygen is the most abundant element on the Earth, determination of the ^{18}O:^{16}O ratio is of great interest in geochemistry. For instance, ^{18}O is strongly enriched in silicates containing only Si—O—Si bonds, whereas the ^{18}O:^{16}O ratio is lower in Si—O—Al bonds and particularly low in Si–OH groups. As the *isotope exchange* equilibria between minerals and water depend on temperature, information about the temperature of formation of the minerals is obtained by

Nuclear and Radiochemistry: Fundamentals and Applications,
Fourth Edition. Jens-Volker Kratz.

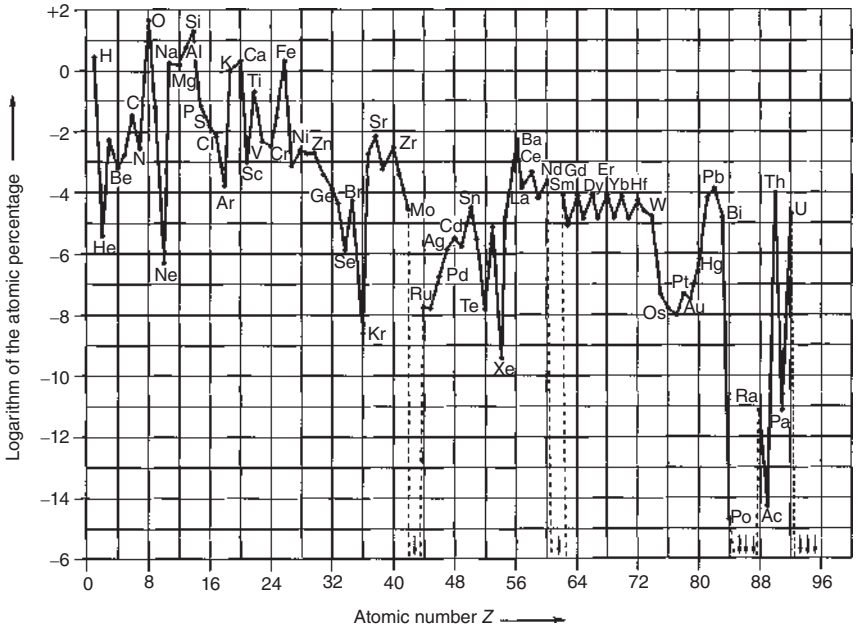

Figure 18.1 Abundance of the elements on the surface of the Earth (lithosphere, hydrosphere, and atmosphere).

measuring the isotope ratio ^{18}O:^{16}O (geochemical isotope thermometry). The same holds for the exchange equilibrium between carbonates and water:

$$Ca^{16}O_3 + H_2^{18}O \Leftrightarrow Ca^{16}O_2^{18}O + H_2^{16}O \tag{18.2}$$

From the isotope ratio ^{18}O:^{16}O in carbonates, the temperature of their formation can be obtained.

In the case of the stable isotopes of carbon, ^{13}C and ^{12}C, two isotope effects are noticeable: the kinetic isotope effect in photosynthesis, leading to an enrichment of ^{12}C in plants, and the equilibrium isotope effect in the exchange reaction:

$$^{13}CO_2 + H^{12}CO_3^- \Leftrightarrow {}^{12}CO_2 + H^{13}CO_3^- \tag{18.3}$$

causing an enrichment of ^{13}C in hydrogen carbonate. The equilibrium constant K of reaction (18.3) depends on the temperature ($K = 1.009$ at 10 °C and 1.007 at 30 °C) and the ratio $CO_2 : HCO_3^-$ strongly on pH. In seawater of pH 8.2, 99% of the dissolved CO_2 is present in the form of HCO_3^-, whereas at lower pH, CO_2 prevails. From the measurement of δ (^{12}C) values, conclusions can be drawn with respect to the conditions of formation of carbonates.

The isotope ratios of the sulfur isotopes are also affected by kinetic and equilibrium isotope effects. Kinetic isotope effects are marked in the reduction of sulfates to hydrogen sulfide by bacteria (enrichment of the lighter isotopes in H_2S). The equilibrium isotope effect in the reaction:

$$^{32}SO_4^{2-} + H_2^{34}S \Leftrightarrow {}^{34}SO_4^{2-} + H_2^{32}S \tag{18.4}$$

Table 18.1 Isotope ratios of oxygen, carbon, and sulfur isotopes in various samples.

Sample	$^{16}O/^{18}O$
Fresh water	488.95
Ocean water	484.1
Water from the Dead Sea	479.37
Oxygen in the air	474.72
Oxygen from photosynthesis	486.04
CO_2 in the air	470.15
Carbonates	470.61
$^{12}C/^{13}C$	
CO_2 in the air	91.5
Limestone	88.8–89.4
Shells of sea animals	89.5
Ocean water	89.3
Meteorites	89.8–92.0
Coal, wood	91.3–92.2
Petroleum, pitch	91.3–92.8
Algae, spores	92.8–93.1
$^{32}S/^{34}S$	
Sulfates in the oceans	21.5–22.0
Volcanic sulfur	21.9–22.2
Magmatic rocks	22.1–22.2
Meteorites	21.9–22.3
Living things	22.3
Petroleum, coal	21.9–22.6

Source: Adapted from Silverman (1951), Murphey and Nier (1941), and Vinogradov (1954).

leads also to an enrichment of ^{32}S in H_2S (equilibrium constant $K = 1.075$ at 25 °C). Isotope exchange reactions between sulfidic minerals also lead to a shift of the isotope ratios. For example, ^{34}S is enriched in relation to ^{32}S in the order pyrite > sphalerite > galerite. Measurement of the ^{34}S:^{32}S ratio gives information about the conditions of formation of sulfidic minerals (e.g. magmatic or hydrothermal, and temperature). Sulfates precipitated in seawater exhibit ^{34}S:^{32}S ratios that are characteristic of the geological era in which they were formed.

For special geochemical investigations, isotope ratios of other elements, such as B, N, Si, K, and Se, are also determined. The measurement of the distribution of the natural radioelements U and Th and their daughter nuclides in minerals, sediments, oil, water, and the air gives information about the genesis of the minerals, sediments,

and oils, and about the processes taking place in the lithosphere, hydrosphere, and atmosphere. The nuclear methods of dating will be discussed in Chapter 19.

18.2 General Aspects of Cosmochemistry

The concern of cosmochemistry is the investigation of extraterrestrial matter (Sun, Moon, planets, stars, and interstellar matter) and their chemical changes. Meteorites are objects of special interest in cosmochemistry because of the nuclear reactions induced by high-energy protons in cosmic radiation (E(p) up to about 10^9 GeV) and by other particles, such as α particles and various heavy ions. Measurement of the radionuclides produced in meteorites by cosmic radiation gives information about the intensity of this radiation in interstellar space and about the age and the history of meteorites.

With the exception of a few special cases, the isotope ratios in meteorites are the same as on the Earth, which means that during the formation of the various parts of the Solar System, only some fractionation of the elements occurred, but no isotope fractionation. Differences in the isotope ratios in meteorites and on the Earth can be explained by radioactive decay, nuclear reactions induced by cosmic radiation, and some isotope fractionation of light elements.

For the investigation of meteorites, various experimental methods are applied, in particular mass spectrometry, neutron activation analysis, measurement of natural *radioactivity* by low-level counting, and track analysis. The tracks can be caused by heavy ions in cosmic radiation, by fission products from spontaneous or neutron-induced fission, and by recoil due to α-decay. Etching techniques and measurement of the tracks give information about the time during which the meteorites have been in interstellar space as individual particles (irradiation age).

Lunar samples have been investigated by similar methods, with the result that many details have been learned about the chemical composition of the surface of the Moon and the nuclear reactions occurring there under the influence of the cosmic radiation that hits the Moon's surface without hindrance by an atmosphere.

The first elements were formed in the early stage of the Universe and their production continued by subsequent nuclear reactions, in particular nuclear fusion (thermonuclear reactions), (n, γ) reactions, and radioactive transmutations. The most probable and generally accepted concept of the beginning of the Universe is that of a single primordial event, called the "Big Bang," at time zero. Since then, the Universe has been continuously expanding and the galaxies are moving away from each other. If this expansion is extrapolated back to the stage when the galaxies were close to each other, a value of $(14 \pm 1) \cdot 10^9$ years is obtained for the age of the Universe. This is called the Hubble time.

18.3 Early Stages of the Universe

According to the concept of the Big Bang, a mixture of fundamental particles and energy existed at time zero at an extremely high temperature (on the order of

about 10^{30} K) and an extremely high density (on the order of about 10^{50} g cm^{-3}) in an extremely small volume. The unified theory of fundamental particles and forces assumes that only one elementary constituent of matter and only one force existed at that time, but the origin of the Big Bang is not clear. Within 10^{-32} seconds, space expanded by a factor of 10^{50} with a velocity $\upsilon = H_0 xr$, where H_0 is today's Hubble constant and r is the distance. The well-known red shift of the spectral lines is directly connected to this expansion. Quantum fluctuations in the energy density were amplified and build the basis for future galaxy formation. Until 10^{-10} seconds, quarks, gluons, and exchange bosons were constantly interacting, thereby cooling off by further spatial expansion and modification of the coupling strength.

Primordial matter was eventually merged into mesons and baryons. Matter and antimatter annihilated, thereby creating a tiny (1 in 10^{-9}) excess of matter over antimatter. Below 10^{10} K, neutrinos stopped exchanging energy and momentum with other particles, for example, $\mathrm{n} + \nu \Leftrightarrow \mathrm{p} + \mathrm{e}^-$ and $\mathrm{p} + \nu \Leftrightarrow \mathrm{n} + \mathrm{e}^+$. Subsequently, electroweak processes such as $\mathrm{p} + \mathrm{e}^- \rightarrow \mathrm{n} + \nu$ and $\mathrm{n} + \mathrm{e}^+ \rightarrow \mathrm{p} + \nu$ prevailed. Because of the larger mass of the neutron, in thermal equilibrium, $N_\mathrm{n}/N_\mathrm{p} = \exp[-(m_\mathrm{n} - m_\mathrm{p})c^2/kT]$, and because electron–positron pairs annihilated and ceased to be created at $kT < 1.02$ MeV, a freeze-out resulted at $N_\mathrm{n}/N_\mathrm{p} = 0.2$. But for times >1 second, neutron decay changed this ratio to 0.135. At this time, 86.5% of the nucleons were protons and 13.5% were neutrons. The early stages of the Universe are listed in Table 18.2.

Synthesis of nuclei heavier than protons started after about 100 seconds at a temperature of about 10^9 K by the merging of a proton with a neutron into a deuteron:

$$\mathrm{p} + \mathrm{n} \rightarrow \mathrm{d} + \gamma \tag{18.5}$$

initiating primordial nucleosynthesis. At this temperature, $kT = 0.1$ MeV, the energy of most of the protons was not high enough to split deuterons into nucleons, and the deuterons were able to combine with more nucleons to give nuclei with mass numbers up to 7:

$$\begin{aligned}
&\mathrm{d} + \mathrm{n} \rightarrow {}^3\mathrm{H} + \gamma \qquad && \mathrm{d} + \mathrm{d} \rightarrow {}^4\mathrm{He} + \gamma \\
&{}^3\mathrm{H} + \mathrm{p} \rightarrow {}^4\mathrm{He} + \gamma \qquad && \mathrm{d} + \mathrm{d} \rightarrow {}^3\mathrm{H} + \mathrm{p} \\
&\mathrm{d} + \mathrm{p} \rightarrow {}^3\mathrm{He} + \gamma \qquad && {}^3\mathrm{H} + \mathrm{d} \rightarrow {}^4\mathrm{He} + \mathrm{n} \\
&{}^3\mathrm{He} + \mathrm{n} \rightarrow {}^4\mathrm{He} + \gamma \qquad && {}^3\mathrm{He} + \mathrm{d} \rightarrow {}^4\mathrm{He} + \mathrm{p} \\
&{}^3\mathrm{He} + {}^3\mathrm{He} \rightarrow {}^4\mathrm{He} + \mathrm{d} + \gamma \\
&{}^3\mathrm{He} + {}^4\mathrm{He} \rightarrow {}^7\mathrm{Be} + \gamma \\
&{}^7\mathrm{Be} + \mathrm{e}^- \rightarrow {}^7\mathrm{Li} + \gamma
\end{aligned} \tag{18.6}$$

Heavier masses could not be created because there are no stable isotopes with $A = 5, 8$. Complete conversion of protons into ^{4}He was not possible because of the lack of neutrons. After about 250 seconds, the mass of the Universe consisted of about 73% hydrogen nuclei, about 27% helium nuclei, and traces of ^{7}Be and ^{7}Li nuclei. The mass fractions relative to protons as a function of time are shown in

Table 18.2 Evolution of the Universe.

Time	Universe
0	$T \approx 10^{30}$ K, density $\approx 10^{50}$ g cm^{-3}; primordial matter (quark–gluon plasma)
↓	Beginning of rapid expansion, merging of primordial matter into mesons, nucleons, neutrinos, photons, and electrons
1 s	$T \approx 10^{10}$ K
↓	Freeze-out of the neutron-to-proton ratio
100 s	$T \approx 10^{9}$ K
↓	Synthesis of d, ^{3}H, ^{3}He, ^{4}He, ^{7}Be, and ^{7}Li nuclei
$3 \cdot 10^{5}$ yr	$T \approx 3 \cdot 10^{3}$ K; about 73% of the matter consists of H and about 27% of the He nuclei
↓	Formation of atoms (H and He) by combination of nuclei and electrons
	Before, there were continuous interactions of the photons with the charged particles
	After the formation of neutral atoms, decoupling of the photons giving rise to the 3 K cosmic microwave background radiation
	Formation of first molecules
$1 \cdot 10^{9}$ yr	—
↓	Beginning of formation of galaxies and stars, gravitational contraction of the stars → increase in temperature, thermonuclear reactions (hydrogen burning and helium burning)
$5 \cdot 10^{9}$ yr	—
↓	Further gravitational contraction (depending on the mass of the stars) → further increase in temperature → carbon burning, oxygen burning, liberation of neutrons → (n, γ) reactions
$14 \cdot 10^{9}$ yr	Present

Figure 18.2. The whole chain lasted for a few minutes, and these light nuclei existed in an environment of photons, electrons, and neutrinos for several thousand years. The ambient temperature decreased slowly to the order of about 10^4 K, but it was too low for further nucleosynthesis and too high for the formation of atoms and molecules.

After about $3 \cdot 10^5$ years, the temperature was about $3 \cdot 10^3$ K and by a combination of nuclei and electrons the first atoms of hydrogen and helium were formed. Previously, there were continuous interactions of photons with the charged particles. After the formation of neutral atoms, the photons decoupled and gave rise to the $T = 3$ K cosmic microwave background radiation predicted by the Big Bang theory. The best data ($T = 2.728 \pm 0.004$ K) confirm this prediction. At further stages of expansion and cooling, the first H_2 molecules became stable. Due to gravitation, the matter began to cluster and the formation of galaxies and stars began after about 10^9 years. Further individual development of the stars depended and still depends mainly on their mass.

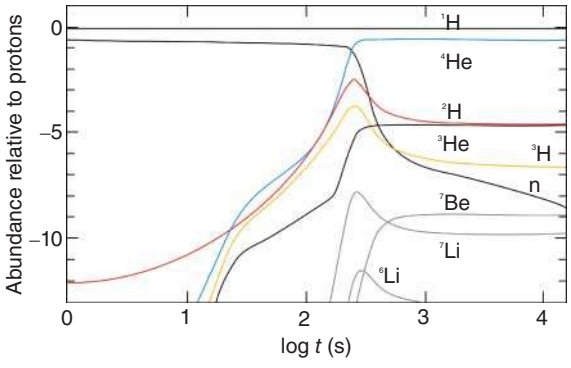

Figure 18.2 Mass fractions of neutrons, protons, ^{2}H, ^{3}H, ^{3}He, ^{4}He, ^{6,7}Li, and ^{7}Be nuclei relative to protons as a function of time after the Big Bang.

The density of the photons in the Universe was always appreciably higher than that of the nucleons. At present, the average densities are about $5 \cdot 10^8$ photons and only about 0.05–5 nucleons per cubic meter. However, because of the low mass equivalent of the photons, their mass is small compared to that of the nucleons.

18.4 Synthesis of the Elements in the Stars

With the aggregation of matter in the stars under the influence of gravitation, new processes begin to dominate:

- Gravitational contraction of the stars causes an increase in temperature associated with the emission of light and other kinds of electromagnetic radiation.
- If the temperature in the core of the stars becomes sufficiently high, thermonuclear reactions give rise to new phases of nucleogenesis, and the energy produced by these reactions leads to further emission of radiation, including visible light.

The influences of gravitational contraction and thermonuclear reactions depend primarily on the mass of the stars. The phases of contraction and thermonuclear reactions overlap and determine nucleogenesis as well as the fate of the stars.

18.4.1 Evolution of Stars

The gravitational energy associated with the collapse of matter is stored in the interior of a forming star rather than being radiated into space. At some stage, a radiative equilibrium is established in a protostar which continues to shrink under the influence of gravity with continued heating of its interior. At a temperature of $\sim 10^7$ K, thermonuclear reactions between protons start to occur due to barrier penetration. Three generations of stars formed in this way and are distinguished by the following historical nomenclature. Population III stars are the first generation of stars consisting of the Big Bang material; they were massive and are now extinct. The debris from these stars was incorporated into later generations of stars. Population II stars are the second generation of stars consisting of hydrogen, helium, and ~1% of heavier elements such as carbon. Population I stars are members of a

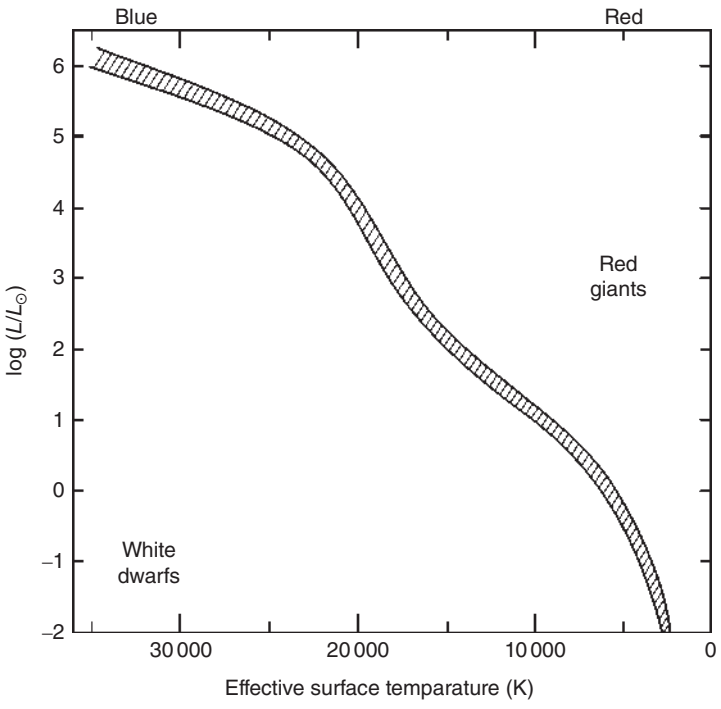

Figure 18.3 Schematic H–R diagram. The ordinate is luminosity relative to that of the Sun, on a logarithmic scale. The diagonal band marks the position of the main sequence. The positions of the red giants and the white dwarfs are also indicated.

third generation of stars consisting of hydrogen, helium, and 2–5% of the heavier elements such as carbon, nitrogen, and oxygen. Our Sun is a population I star. Its mass is $2 \cdot 10^{30}$ kg, its average density is $1.4 \cdot 10^3$ kg m^{-3}, and its radius is $7 \cdot 10^6$ m, and it has a surface temperature of ~6000 K, a luminosity of $3.8 \cdot 10^{26}$ W, and an age of $4.5 \cdot 10^9$ years. The Danish astronomer E. Hertzsprung and his American collegue H.N. Russell observed a clear correlation between the luminosity and the surface temperature of stars. That correlation, the Hertzsprung–Russell (HR) diagram, is shown schematically in Figure 18.3. A large number of stars including our Sun form a narrow band in the H–R diagram, called the *main sequence*. Main-sequence stars have luminosities L roughly proportional to $T_{\text{surface}}^{5.5}$. Eventually, stars may leave the main sequence depending on the reaction rates in their interior. In the upper right corner of the H–R diagram, stars that have very large radii and are relatively cool (~3000–5000 K) are clustered. This is why they are called *red giants*. These are former main-sequence stars whose energy production by helium burning is insufficient to sustain main-sequence luminosities. Our Sun is expected to belong to this category in about $7 \cdot 10^9$ more years. In the lower left corner of the H–R diagram, there is a cluster of small, dense stars of high surface temperature (>10^4 K), the *white dwarfs*. They are remnants of red giants with masses between 0.1 and 1.5 solar masses whose helium has been burned and which have become unstable, ejecting their envelopes as planetary nebula, and move down the main

sequence in luminosity to become white dwarfs. On the other hand, red giants with >8 solar masses experience a more spectacular development with increasing temperatures allowing for carbon–oxygen burning, silicon burning until producing iron, followed by an explosive death in a supernova. Type I supernovae represent the final evolutionary stage of old, relatively small stars (1.2–1.5 solar masses) in which the entire star disintegrates in a giant thermonuclear explosion. The timescale for this phase is seconds and the temperature reached in various regions of the star is between 10^9 and 10^{10} K. Type II supernovae, by contrast, occur only in stars with initial masses at least 10 times that of the Sun. In such stars, elements build up until the core consists almost entirely of iron-group elements. At that point, gravitational contraction must continue and with it further heating. At about $5 \cdot 10^9$ K, the iron and nickel nuclei are suddenly photodisintegrated into protons and neutrons and a gravitational collapse occurs leading to central densities of 10^{14} g cm^{-3} associated with an immediate transmutation of the protons by electrons into neutrons according to

$$p + e^- \rightarrow n + \nu_e \tag{18.7}$$

The core collapse on a timescale of seconds into a neutron star is accompanied by the explosive ejection of the outer layers of the star in which it was believed (Section 18.4.7) that an extremely high neutron flux causes the rapid neutron capture process (r-process) to occur, which is responsible for the formation of heavy elements. Supernova explosions are rather rare events. The flash of the explosion is brighter than the Sun by several orders of magnitude, fading away within a few days or weeks, while the cloud of dust ejected by the star in the form of a nebula expands continuously. Later generations of stars aggregate the debris of these burned-out stars, which is evident, for example, in the atomic abundances of the elements in the Solar System. One recent observation of a supernova explosion in the Large Magellanian Cloud (LMC), which was observed by the Kamiokande detector in Japan, with its directional resolution, on 23 February 1987, at 7:35 universal time, produced within 12 seconds a burst of 7–50 MeV electron neutrinos, corroborating Eq. (18.7).

18.4.2 Evolution of the Earth

Stages of the evolution of the Earth are listed in Table 18.3. The evolution of the Sun and the planets from solar nebula began about $4.6 \cdot 10^9$ years ago. Materials of this age are not found on the Earth because most primordial solids on the Earth went through one or several metamorphoses. However, the material of meteorites which were formed simultaneously with the Earth make it possible to date the age of the Earth at $4.5 \cdot 10^9$ years. The oldest minerals on the Earth have an age on the order of $4.3 \cdot 10^9$ years and underwent metamorphoses about $3.8 \cdot 10^9$ years ago. The age of the oldest rock formations is in the range $(3.8–3.5) \cdot 10^9$ years. The first indications of life are dated back to about $3.5 \cdot 10^9$ years ago.

Several proposals have been made about the origin of the matter from which the Earth and the Solar System were formed. These proposals are mainly based on the isotopic composition. The supernova hypothesis explains the presence of

Table 18.3 Stages of the evolution of the Earth.

Time before present	Stage
$5 \cdot 10^9$ yr	Solar nebula
$4.6 \cdot 10^9$ yr	Formation of the Solar System
$4.5 \cdot 10^9$ yr	Formation of the Earth, the Moon, and of meteorites
$4.3 \cdot 10^9$ yr	First stages of the Earth's crust, formation of the oldest minerals found on the Earth, formation of hydrosphere and atmosphere
$3.9 \cdot 10^9$ yr	End of major meteoritic impacts
$3.8 \cdot 10^9$ yr	Beginning of formation of rocks
$(3.8–3.5) \cdot 10^9$ yr	Formation of oldest rocks
$3.5 \cdot 10^9$ yr	First traces of life (stromatolites)

Table 18.4 Ratio of the activities of some long-lived radionuclides at the time of birth of the Earth to those present at this time.

Radionuclide	Activity ratio A/A_0
^{40}K	11.4
^{87}Rb	1.07
^{232}Th	1.02
^{235}U	84.1
^{238}U	2.01

heavy nuclei in the Solar System by a supernova explosion some time before the evolution of the Solar System. This hypothesis is supported by the isotopic analysis of meteorites, which shows an anomaly in the ^{129}Xe content. This anomaly is attributed to the decay of ^{129}I ($t_{1/2} = 1.57 \cdot 10^7$ years) which must have been present during the evolution of the Solar System.

In any case, the primordial radioactivity on the Earth was appreciably higher than at present. The ratios of the activities at the time of birth of the Earth to those at present are listed in Table 18.4 for some long-lived radionuclides that represent the main radioactive inventory on the Earth. The relatively high activity of ^{235}U about $2 \cdot 10^9$ years ago is the reason for the operation of the natural nuclear reactors at Oklo at that time (Section 15.9).

18.4.3 Thermonuclear Reaction Rates

In thermonuclear reactions, as opposed to charged-particle nuclear reactions studied with accelerators, the energy of the colliding nuclei is thermal energy. Both reacting particles are moving, thus it is their relative velocity (or cm energy) that is important. In nuclear reactions in the laboratory, we have

$$R = N{\cdot}\sigma{\cdot}\phi$$

where R is the reaction rate in reactions s^{-1}, σ is the cross section in cm^2, φ is the incident beam intensity in particles s^{-1}, and N is the number of target atoms cm^{-2}. For thermonuclear reactions, we write

$$R = N_i N_j \int_0^\infty \sigma(\upsilon)\upsilon \, d\upsilon = N_i N_j \langle \sigma\upsilon \rangle \tag{18.8}$$

where υ is the relative velocity between nuclei i and j, each present at a concentration of N particles cm^{-3}, and the expectation value $\langle \sigma\upsilon \rangle$ is the temperature-averaged reaction rate per particle pair. To exclude double counting of collisions of identical particles, Eq. (18.8) is rewritten as:

$$R = \frac{N_i N_j \langle \sigma\upsilon \rangle}{1 + \delta_{ij}} \tag{18.9}$$

where δ_{ij} is the Kronecker delta being 0 when $i \neq j$ and 1 when $i = j$. The mean lifetime of nuclei i is then $1/N_i\langle \sigma\upsilon \rangle$. This means that the mean lifetime is inversely proportional to the reaction rate. The thermal velocity distribution of each particle component will be a Maxwell–Boltzmann distribution:

$$P(\upsilon) = \left(\frac{m}{2\pi kT}\right)^{3/2} \exp\left(-\frac{m\upsilon^2}{2kT}\right) \tag{18.10}$$

Here, m is the particle mass, k is Boltzmann's constant, and T is the temperature. Integration over all velocities of particles i and j gives

$$\langle \sigma\upsilon \rangle = \left(\frac{8}{\pi\mu}\right)^{1/2} \frac{1}{(kT)^{3/2}} \int_0^\infty \sigma(E) E \, \exp\left(-\frac{E}{kT}\right) dE \tag{18.11}$$

where μ is the reduced mass.

For slow neutron-induced reactions below the resonance region (Section 12.7.2), we recall that $\sigma_n(E) \propto 1/\upsilon_n$ making $\langle \sigma\upsilon \rangle$ constant. For charged-particle reactions, there is a Coulomb barrier. For the p + p reaction, the Coulomb barrier is 0.55 MeV, but kT is on the order of 1 keV (in the Sun). For a proton–proton cm energy of 1 keV, the barrier penetration probability is $\sim 2 \cdot 10^{-10}$. The latter can be approximated as:

$$P = \exp\left(-\frac{2\pi Z_i Z_j e^2}{\hbar\upsilon}\right) = \exp\left(-\frac{b}{E^{1/2}}\right) \tag{18.12}$$

where $b = 0.989 Z_i Z_j \mu^{1/2}$ $(\text{MeV})^{1/2}$, E is in keV, and μ is in amu. This is referred to as the Gamow factor. The cross section is also proportional to $\pi\lambda^2 \propto 1/E$ so that the cross section can be written as:

$$\sigma(E) = \frac{1}{E} \exp\left(-\frac{b}{E^{1/2}}\right) S(E) \tag{18.13}$$

where $S(E)$ is the so-called astrophysical S factor containing all constants and terms related to the nuclei involved. In order to express the overlap between the high-energy tail of the Maxwell–Boltzmann distribution and the low-energy part of

the cross section from barrier penetration, we substitute Eq. (18.13) into Eq. (18.11) and obtain

$$\langle \sigma v \rangle = \left(\frac{8}{\pi \mu} \right)^{1/2} \frac{1}{(kT)^{3/2}} \int_0^\infty S(E) \exp\left(-\frac{E}{kT} - \frac{b}{E^{1/2}} \right) \mathrm{d}E \tag{18.14}$$

The product of these two expressions produces a peak in the overlap region of these two functions which is known as the Gamow peak. It occurs at an average energy $(bkT/2)^{2/3}$.

18.4.4 Hydrogen Burning

The first stage of nucleogenesis in the stars is the fusion of protons into ^{4}He by the net reaction:

$$4\mathrm{p} \rightarrow {}^4\mathrm{He} + 2\mathrm{e}^+ + 2\nu_\mathrm{e} + \Delta E \quad (\Delta E = 26.7\,\mathrm{MeV}) \tag{18.15}$$

This process is called *hydrogen burning*. The temperature in the core of the stars must be $\sim 1.5 \cdot 10^7$ K ($kT \sim 1$ keV) in order to populate the Gamow peak. (To convert temperature in K to energy kT in eV, note that $kT\,(\mathrm{eV}) = 8.6 \cdot 10^{-5}\,T\,(\mathrm{K})$.) The neutrinos escape into outer space due to their small interaction with matter. Hydrogen burning is the longest stage of the stars. It involves the reactions:

$$\begin{aligned}
\mathrm{p} + \mathrm{p} &\rightarrow \mathrm{d} + \mathrm{e}^+ + \nu_\mathrm{e} && 99.6\% \\
\mathrm{p} + \mathrm{e}^- + \mathrm{p} &\rightarrow \mathrm{d} + \nu_\mathrm{e} && 0.4\% \\
\mathrm{d} + \mathrm{p} &\rightarrow {}^3\mathrm{He} + \gamma \\
{}^3\mathrm{He} + {}^3\mathrm{He} &\rightarrow {}^4\mathrm{He} + 2\mathrm{p} && 86\% \\
{}^3\mathrm{He} + {}^4\mathrm{He} &\rightarrow {}^7\mathrm{Be} + \gamma && 14\% \\
{}^7\mathrm{Be} + \mathrm{e}^- &\rightarrow {}^7\mathrm{Li} + \nu_\mathrm{e} \\
{}^7\mathrm{Li} + \mathrm{p} &\rightarrow {}^8\mathrm{Be}^* + \gamma \\
{}^7\mathrm{Be} + \mathrm{p} &\rightarrow {}^8\mathrm{B} + \gamma && 0.02\% \\
{}^8\mathrm{B} &\rightarrow {}^8\mathrm{Be}^* + \mathrm{e}^+ + \nu_\mathrm{e} \\
{}^8\mathrm{Be}^* &\rightarrow {}^4\mathrm{He} + {}^4\mathrm{He}
\end{aligned} \tag{18.16}$$

The p + p reaction is a weak interaction process and has a very small cross section of about 10^{-47} cm^2 at $kT = 1$ keV, resulting in a reaction rate of $5 \cdot 10^{-18}$ reactions s^{-1} per proton. The d + p reaction leading to ^{3}He has a reaction rate $\sim 10^{16}$ times greater than that of the weak p + p reaction. The p + p, d + p, and ^{3}He + ^{3}He reactions, called the ppI chain, produce 91% of the Sun's energy. In 14% of the cases, the side reaction of ^{3}He with ^{4}He takes place. Note that the subsequent EC decay of ^{7}Be does not involve the capture of an orbital electron of ^{7}Be, since it is fully ionized in the Sun but rather involves the capture of a free electron. The consequence is that the half-life is on the order of 120 days compared to the terrestrial half-life of 77 days. The ^{8}Be* is unbound and decays into two α particles. The p + p, d + p, ^{3}He + ^{4}He, ^{7}Be EC, ^{7}Li(p, α) reactions constitute the ppII chain which produces about 7% of the Sun's energy. A small fraction of the ^{7}Be from the ^{3}He + ^{4}He reaction experiences proton capture leading

to ^{7}B. This sequence, p + p, p + d, ^{3}He + ^{4}He, ^{7}Be(p, γ), ^{8}B → ^{8}Be* → 2α, constitutes the ppIII chain which produces 0.015% of the Sun's energy.

Our Sun is a typical population I star (see Section 18.4.1). It is a third-generation star that has accumulated some debris of earlier generation stars. Thus, it consists of hydrogen and helium plus 2–5% of carbon, nitrogen, and oxygen leading to another set of nuclear reactions, the CNO cycle. The net effect of these reactions is again the conversion $4p \rightarrow {}^{4}He + 2e^{+} + 2\nu_{e}$ where the heavy nuclei act as catalysts according to

$$\begin{aligned} {}^{12}C + p &\rightarrow {}^{13}N + \gamma \\ {}^{13}N &\rightarrow {}^{13}C + e^{+} + \nu_{e} \\ {}^{13}C + p &\rightarrow {}^{14}N + \gamma \\ {}^{14}N + p &\rightarrow {}^{15}O + \gamma \\ {}^{15}O &\rightarrow {}^{15}N + e^{+} + \nu_{e} \\ {}^{15}N + p &\rightarrow {}^{12}C + {}^{4}He \end{aligned} \tag{18.17}$$

and this cycle adds about 4% to the energy production of the Sun. In the Sun, hydrogen burning lasts for about 10^{10} years.

18.4.5 Helium Burning

Toward the end of the stage of hydrogen burning, the concentration of hydrogen in the core of the stars and the energy production decrease, and the helium-rich core continues to contract, until the densities and the temperature in the core increase to about 10^{4} g cm^{-3} and 10^{8} K, respectively. Under these conditions, the ^{4}He nuclei accumulated by hydrogen burning are able to undergo further thermonuclear reactions, namely, helium burning. One might think that $^{4}He + {}^{4}He \rightarrow {}^{8}Be$ is the first reaction, but ^{8}Be is unstable ($t_{1/2} = 6.7 \cdot 10^{-17}$ seconds) so this reaction is hindered by a low transient population of the product nuclei. Instead, the so-called 3α process proceeds

$$3\,{}^{4}He \rightarrow {}^{12}C + \gamma \tag{18.18}$$

This three-body reaction proceeds through a 0^{+} resonance at 7.65 MeV in ^{12}C which has a more favorable nuclear structure than the ground state for allowing this reaction to occur. After a significant amount of ^{12}C has been accumulated, α-capture reactions occur such as:

$$\begin{aligned} {}^{12}C + {}^{4}He &\rightarrow {}^{16}O + \gamma \\ {}^{16}O + {}^{4}He &\rightarrow {}^{20}Ne + \gamma \\ {}^{20}Ne + \gamma &\rightarrow {}^{16}O + {}^{4}He \\ {}^{20}Ne + {}^{4}He &\rightarrow {}^{24}Mg + \gamma \end{aligned} \tag{18.19}$$

The stage of helium burning is reached earlier at higher mass. Hydrogen burning continues in the outer zones of these stars, which become brighter and red. If the mass is similar to or greater than that of the Sun, the stars expand in the outer zones

to red giants with diameters that are greater than before by a factor of 10^2–10^3. On the cosmic scale, helium burning is a relatively short stage.

The mean lifetimes for these various nucleosynthesis reactions are inversely related to the reaction rates.

18.4.6 Synthesis of Nuclei with $A < 60$

Gravitational contraction continues with increasing concentration of ^{12}C and ^{16}O, and in stars with masses more than three times that of the Sun, the temperature and the density rise from about $6 \cdot 10^8$ to $2 \cdot 10^9$ K and about $5 \cdot 10^4$ g cm^{-3}, respectively. Under these conditions, fusion of two ^{12}C isotopes becomes possible and reactions such as:

$$\begin{aligned} {}^{12}C + {}^{12}C &\rightarrow {}^{20}Ne + {}^{4}He \\ {}^{12}C + {}^{12}C &\rightarrow {}^{23}Na + p \\ {}^{12}C + {}^{12}C &\rightarrow {}^{23}Mg + n \\ {}^{12}C + {}^{12}C &\rightarrow {}^{24}Mg + \gamma \\ {}^{16}O + {}^{16}O &\rightarrow {}^{24}Mg + 2{}^{4}He \\ {}^{16}O + {}^{16}O &\rightarrow {}^{28}Si + {}^{4}He \end{aligned} \tag{18.20}$$

$$\begin{aligned} {}^{16}O + {}^{16}O &\rightarrow {}^{31}P + p \\ {}^{16}O + {}^{16}O &\rightarrow {}^{31}Si + n \\ {}^{16}O + {}^{16}O &\rightarrow {}^{32}S + \gamma \end{aligned}$$

occur. Of these, the reactions leading to ^{28}Si and ^{32}S are the most important. These are followed at even higher temperatures of about $5 \cdot 10^9$ K by photodisintegration and radiative capture reactions in equilibrium (silicon burning) such as:

$$\begin{aligned} {}^{28}Si + \gamma &\rightarrow {}^{24}Mg + {}^{4}He \\ {}^{28}Si + {}^{4}He &\rightarrow {}^{32}S + \gamma \end{aligned} \tag{18.21}$$

In these equilibrium processes, the yields of product nuclei are related to their nuclear stability with greater yields for even–even nuclei. This way, nuclei up to $A = 60$ are produced. The timescales are again inversely proportional to the reaction rates. For a star of one solar mass, typical times for H burning are 10^{10} years, for He burning 10^5 years, for C burning 100 years, for Ne burning 1 year, for O burning months, and for Si burning days.

18.4.7 Synthesis of Nuclei with $A > 60$

With increasing temperature caused by gravitational contraction, more and more excited states of the nuclei are populated, the photon intensities increase, and neutrons are liberated by (γ, n) reactions induced by high-energy photons. These neutrons trigger further nucleosynthesis by (n, γ) reactions. Three processes are distinguished.

18.4.7.1 The s- (Slow) Process

The key to the synthesis of nuclides beyond the iron peak, which is not possible by exoergic charged-particle reactions, is to be found in neutron-induced reactions. In a second- or later-generation star that already contained debris from previously evolved stars, this makes possible not only the CNO cycle operative in the hydrogen burning phase, but also, at about 10^8 K, a number of exoergic neutron-producing reactions, in particular $^{13}C(\alpha, n)^{16}O$, $^{17}O(\alpha, n)^{20}Ne$, $^{21}Ne(\alpha, n)^{24}Mg$, and $^{25}Mg(\alpha, n)^{28}Si$. These reactions are important in red giants. The neutrons furnished by these reactions will now continue the element-building process beyond iron by successive (n, γ) reactions. This process is slow and is therefore called the s-process. At low neutron flux densities, neutron absorption is slower than β^- decay, and unstable nuclides formed by (n, γ) reactions have enough time to change by β^- decay into stable nuclides. The whole process may last for more than 10^7 years. The abundance of the nuclides produced by the s-process can be calculated by use of the cross sections of the (n, γ) reactions. However, the formation of neutron-rich nuclides next to other β^--unstable nuclides and the nucleosynthesis of heavy nuclides such as ^{232}Th and ^{238}U cannot be explained by the s-process. It follows a zigzag path up the stability line in the nuclide chart as illustrated in Figure 18.4. Qualitatively, the s-process accounts for the prevalence of the heavier isotopes in the even-*Z* elements, the lighter isotopes being depleted by neutron captures. It also accounts for the flat abundance distribution as (n, γ) cross sections are not a strong function of *Z*, for the abundance peaks at magic neutron numbers where (n, γ) cross sections are low because of low-level densities in these compound nuclei. They hold up the mass and charge flow in the s-process and act as "waiting points." The s-process also accounts for the odd–even alterations in the abundances because of lower level densities in even-*N* and even-*Z* compound nuclei. Both these latter effects are clearly visible in Figure 18.5. In the calculations that entered into Figure 18.5, it is assumed that the appropriate "thermal" energy was 25 keV, and that there is an equilibrium between the production and loss of *adjacent* nuclei. Stable nuclei are destroyed by neutron capture. For the rate of change of a nucleus with mass number *A*, we can write

$$\frac{dN_A}{dt} = \sigma_{A-1}N_{A-1} - \sigma_A N_A \tag{18.22}$$

where σ_i and N_i are the capture cross sections and number of nuclei. At equilibrium,

$$\frac{dN_A}{dt} = 0$$

so that

$$\sigma_{A-1}N_{A-1} = \sigma_A N_A \tag{18.23}$$

These calculations have been very successful in accounting for the abundance distribution of the majority of nuclides up to bismuth.

18.4.7.2 The r (Rapid) Process

At high neutron flux densities, as in supernova explosions, neutron absorption becomes faster than β^- decay, and many successive (n, γ) reactions may occur

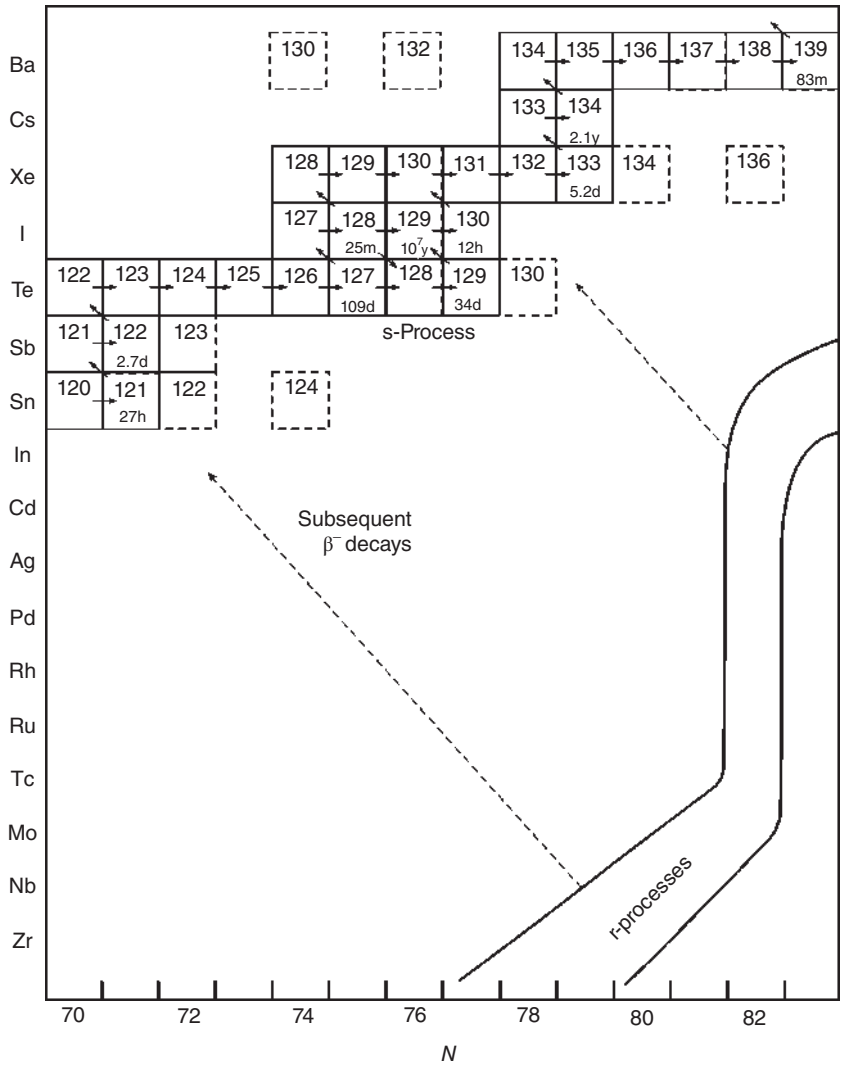

Figure 18.4 Portion of the s- and r-process paths. The s-process path involves (n, γ) reactions, indicated by horizontal arrows, and β^- decays, shown by diagonal arrows. The squares with only mass numbers are stable nuclei. The β^- emitters have the half-lives shown. The squares with dashed borders are stable nuclides not reached by the s-process. The r-process path is indicated schematically, with the prominent effect of the $N = 82$ neutron shell shown. Source: Friedlander et al. (1981)/John Wiley & Sons.

before the nuclides undergo β^- decay (multineutron capture). Formation of ^{232}Th and ^{238}U as well as the abundance peaks at $A = 80$, 130, and 194 and some other abundance features not accounted for by the s-process and p-process (see below), for example, the most neutron-rich isotopes not reached by the s-process, such as ^{122,124}Sn, ^{123}Sb, ^{130}Te, and ^{134,136}Xe in Figure 18.4, have led to the postulation of a much more rapid neutron capture chain than the s-process. It is called the r-process. In an enormous neutron flux, successive neutron captures can take place

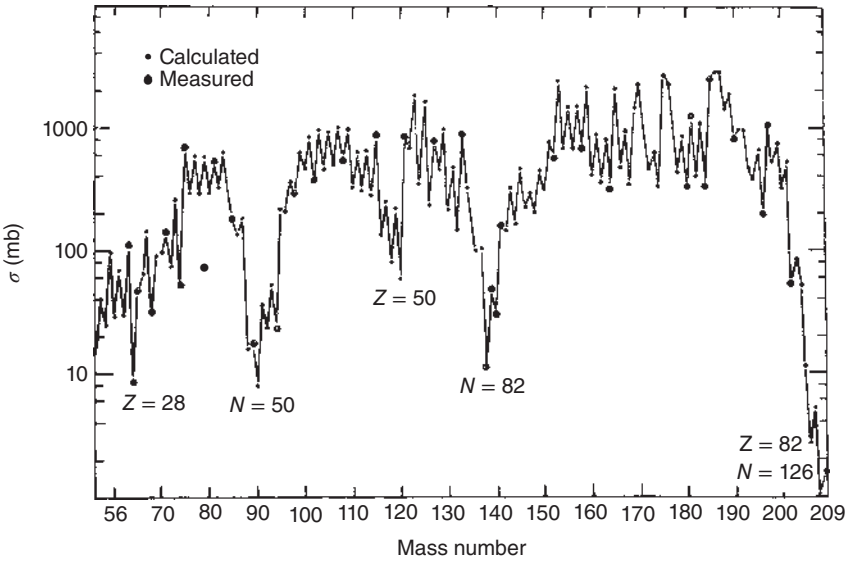

Figure 18.5 Neutron capture cross sections at 25 keV for nuclei on the s-process path. The odd–even alteration and strong shell effects are evident. Source: Clayton (1968)/McGraw-Hill Inc.

in milliseconds to seconds without intermediate β^- decays. Such processes have in fact been observed terrestrially as a result of thermonuclear explosions and have produced the first einsteinium and fermium through rapid multiple neutron captures in uranium followed by successive β^- decays. The r-process path follows a band approximately parallel to the valley of β-stability, but far on the neutron-excess side, where β^- half-lives become comparable to the neutron capture times of milliseconds. A portion of the path is schematically indicated in Figure 18.4. Where the r-process reaches magic neutron numbers, it climbs up in atomic number in single neutron capture – β^- steps (waiting points) leading to a pile-up of the mass and charge flow in this region. This magic-number effect far from stability is reflected, after subsequent β^- decays, in the abundance peaks at $A = 80$, 130, and 194, that is, roughly 10 mass units below the mass numbers where the magic neutron numbers cross the β-stability line (the location of the s-process abundance peaks). The Solar System abundances and their association with specific processes are shown in Figure 18.6.

Quantitative calculations of the r-process depend on knowledge of the properties of neutron-rich nuclei far from β-stability. Extension of experimental information to nuclides further and further out from the stability valley is therefore of great interest to astrophysics, and we have given examples of such investigations in Section 11.10. The evidence cited earlier for the existence of ^{244}Pu in the early Solar System shows that the r-process did not stop at uranium. It is interesting to note that most of the nuclides used in geo- and cosmochronology – ^{244}Pu, ^{238}U, ^{235}U, ^{232}Th, ^{129}I, and ^{87}Rb – are produced entirely or largely by the r-process.

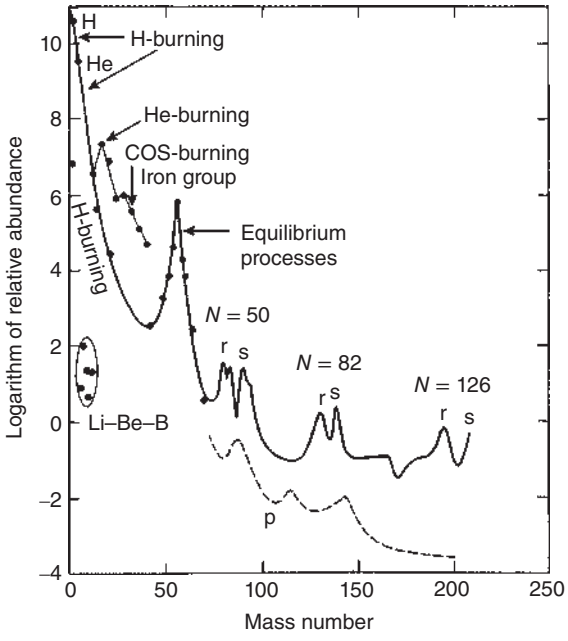

Figure 18.6 Schematic representation of the Solar System abundances as a function of mass number. Features due to specific processes are indicated. Source: Rolfs and Trautvetter (1978), figure 2 (p. 117)/Annual reviews, Inc.

It has long been discussed that supernovae might provide the necessary conditions for the r-process; however, the contribution of core-collapse supernova ejecta to neutron-rich heavy elements seems to be too scarce, to explain measured values of these elements in the interstellar matter. After the core-collapse supernova explosion, the proto-neutron star in the center of the event cools by emitting neutrinos. The energy transported by the neutrinos accelerates a "wind" of baryonic particles, e.g. protons and neutrons. This front of particles escapes with more than the speed of sound from the center of the explosion and has long been guessed to be the locus of the r-process. However, actual simulations show that in neutrino-driven supernovae, there cannot be an r-process because the density of neutrinos is so overwhelmingly high that the neutrinos in a weak interaction transfer neutrons into protons: $\nu_e + n \rightarrow p + e^-$. The surviving neutrons are abundant enough for a nucleosynthesis of lighter elements up to silver, but heavier elements are not formed.

Some supernova explosions set free not only large amounts of energy but are also involving strong magnetic fields and fast rotational motions. This can result in a γ-ray burst (GRB) that lasts a few seconds. In extremely strong magnetic fields, the magnetic pressure can push matter to the exterior. It leaves the center along the rotational axis so that a jet-like supernova results that is driven by neutrinos and the high magnetic field. Due to the high velocity of the emitted matter, the neutrinos transfer only a few neutrons into protons, so that, in this type of supernova, the r-process can produce the heaviest elements.

Alternatively, kilonovae are considered as an important source for heavy elements of the r-process. On 17 August 2017, there was the observation of light from the source of gravitational waves GW170817 of two merging neutron stars whose

electromagnetic radiation was enhanced by the radioactive decay of elements produced in the r-process. And 1.7 seconds later, the Fermi Gamma-ray Space Telescope registered the γ-ray burst GRB170817A, and both observations could be brought in connection with an optical transient in the Galaxy NGC4993 130 light years far from the Earth. In this merger, the smaller neutron star was destroyed by the bigger one with the largest part of the shreds being swallowed by the bigger neutron star, but $(2–2.5) \cdot 10^{-2}$ solar masses of the destroyed neutron star were emitted isotropically with a velocity of 0.25 times the speed of light. The neutron-rich matter transformed in a few seconds into elements that are produced in the r-process. The newly synthesized radioactive elements decayed and the emitted radiation could be detected as an outburst with a brightness of 10^{34}–$10^{35.5}$ W. The spectrum changed within a few days from blue to red. After one week, the kilonova emitted most of the electromagnetic radiation in the infrared. The emitted matter interacted with existing interstellar material associated with the emission of Roentgen radiation. The fusion of two compact stars is the reason for the GRB of less than two seconds duration. The fusion of two compact stars also emits gravitational waves that were detected by the Laser Interferometer Gravitational-Wave Observatory (LIGO) in the United States and the Virgo Interferometer in Italy.

The kilonova GW170817 is considered as a direct proof that heavy elements formed in the r-process are produced in the collision of neutron stars.

18.4.7.3 The p (Proton) Process

Synthesis of proton-rich nuclides such as ^{130,132}Ba in Figure 18.4 and others cannot be explained by the s- or r-process. It is assumed that these nuclides are formed by photonuclear reactions (γ, p), (γ, α), and (γ, n) on seed nuclei from the s- or r-process in the so-called p-process. Previously, it was believed that it involves successive (p, γ) reactions and can take place when already synthesized heavy elements are mixed with high concentrations of hydrogen in the outer shell of supernovae at $\sim 3 \cdot 10^9$ K. However, it was found that the proton densities are too low to explain the observed abundances. Instead, blackbody radiation is believed to cause the above-mentioned photonuclear reactions. The p-process abundances of most elements are very modest as shown in Figure 18.6.

Another important process leading to the synthesis of proton-rich nuclei is the rp-process, the rapid proton capture process. This process makes proton-rich nuclei with $Z \leq 50$ involving a set of (p, γ) reactions and β^+ decays that populate proton-rich nuclei. It starts as a breakout of the CNO cycle that produces proton-rich nuclei such as ^{18}Ne and ^{21}Na and which form the basis for further proton captures. The process follows a path analogous to the r-process but on the proton-rich side of the stability line. The sources of the protons for this process are double-star systems in which a neutron star accretes matter from a partner star, leading to X-ray bursts. The nuclear processes in accreting neutron stars occur under extreme density and temperature conditions due to high gravitational fields. Therefore, the nuclear reactions are quite different from those occurring in usual stars (the Coulomb barrier is not overcome by temperature but by pressure) and involve exotic, very short-lived, neutron-deficient nuclei close to the proton drip line.

18.5 The Solar Neutrino Problem

Several of the nuclear reactions involved in the hydrogen burning of the Sun also result in the emission of electron neutrinos, see Eqs. (18.16) and (18.17). Because of the very small absorption cross sections for neutrinos, these are not generally absorbed in the Sun. The loss of neutrinos corresponds to a loss of 2% of the solar energy. Thus, the solar neutrinos observable on the Earth are a microscope allowing one to look into the stellar interior. Much attention has been devoted to the "solar neutrino problem" and its solution. The 2002 Nobel Prize in Physics awarded to R. Davis and M. Koshita for their solar neutrino work reflects this. Of special interest is the role of nuclear and radiochemistry in the work of Davis, who is a nuclear chemist. The observation and solution of this problem is one of the major scientific achievements of recent years.

The Sun emits $\sim 1.8 \cdot 10^{38}$ electron neutrinos s^{-1} which, after eight minutes transport time, reach the Earth at a rate of $6.07 \cdot 10^{10}$ neutrinos $cm^{-2}\ s^{-1}$. The predictions of the standard solar model for the neutrino fluxes at the surface of the Earth due to the various nuclear reactions are given in Table 18.5. The associated energy spectra are depicted in Figure 18.7. The source labeled pp in Table 18.5 and in Figure 18.7 refers to the reaction:

$$p + p \rightarrow d + e^+ + \nu_e$$

which is the most abundant source of solar neutrinos. The source labeled pep refers to the

$$p + e^- + p \rightarrow d + \nu_e$$

reaction which produces monoenergetic neutrinos. The source labeled hep refers to the reaction:

$$^3He + p \rightarrow {}^4He + e^+ + \nu_e$$

Table 18.5 Predicted solar neutrino fluxes at the surface of the Earth according to the standard solar model.

Source	Flux (particles s^{-1} cm^{-2})
pp	$5.94 \cdot 10^{10}$
pep	$1.40 \cdot 10^{8}$
hep	$7.88 \cdot 10^{3}$
^{7}Be	$4.86 \cdot 10^{7}$
^{8}B	$5.82 \cdot 10^{6}$
^{13}N	$5.71 \cdot 10^{8}$
^{15}O	$5.03 \cdot 10^{8}$
^{17}F	$5.91 \cdot 10^{6}$
Sum	$6.07 \cdot 10^{10}$

Source:Modified from Bahcall and Pena-Garay (2004).

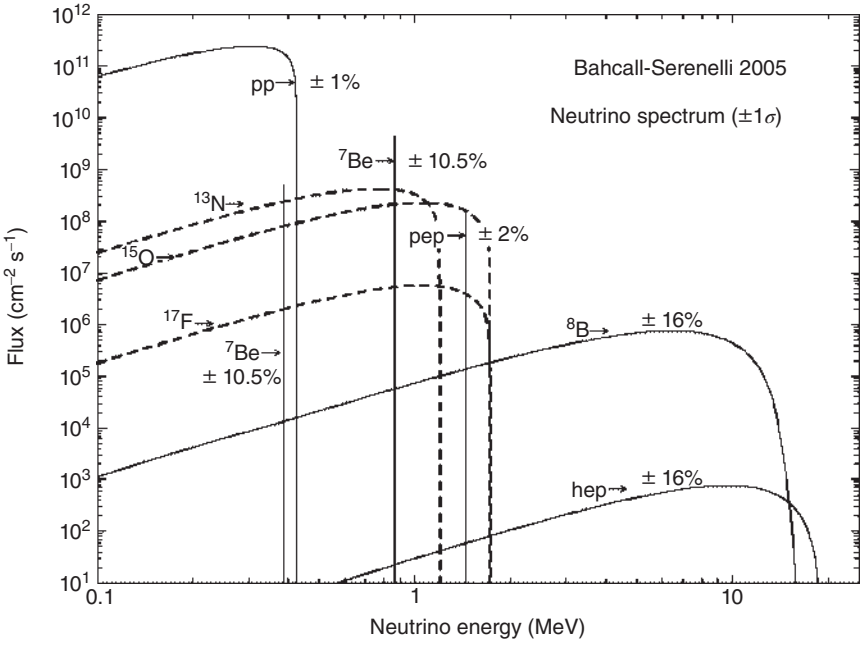

Figure 18.7 Solar neutrino energy spectra for the various sources $\pm 1\sigma$ uncertainties. Source: John Bahcall et al. (2005)/IOP Publishing. From Bahcall website www.sns.ias.edu/~jnb. Exact figure taken from source, hence permission required. Source link: https://iopscience.iop.org/article/10.1086/428929

which produces the highest-energy neutrinos of 18.77 MeV. However, the intensity of this source is 7 orders of magnitude lower than that of the pp source. The ^{7}Be source in the pp chain refers to the EC decay:

$$^{7}\mathrm{Be} + \mathrm{e}^{-} \rightarrow {}^{7}\mathrm{Li} + \nu_{\mathrm{e}}$$

which produces two monoenergetic neutrinos, one in which the ground state of ^{7}Li is formed (90%) and one associated with the formation of the excited state at 0.477 MeV (10%). The source labeled ^{8}B refers to the positron decay:

$$^{8}\mathrm{B} \rightarrow {}^{8}\mathrm{Be}^{*} + \mathrm{e}^{+} + \nu_{\mathrm{e}}$$

populating the first excited state at 3.04 MeV in ^{8}Be. The sources labeled ^{13}N, ^{15}O, and ^{17}F refer to β^{+} decays in the CNO cycle, that is,

$$^{13}\mathrm{N} \rightarrow {}^{13}\mathrm{C} + \mathrm{e}^{+} + \nu_{\mathrm{e}}$$
$$^{15}\mathrm{O} \rightarrow {}^{15}\mathrm{N} + \mathrm{e}^{+} + \nu_{\mathrm{e}}$$
$$^{17}\mathrm{F} \rightarrow {}^{17}\mathrm{O} + \mathrm{e}^{+} + \nu_{\mathrm{e}}$$

The predicted neutrino fluxes as a function of the neutrino energy are shown as a log–log plot in Figure 18.7. Obviously, detectors with different energy thresholds are sensitive to different energy regions of these neutrino spectra. Two types of detectors have been used to detect the weakly interacting neutrinos: radiochemical detectors

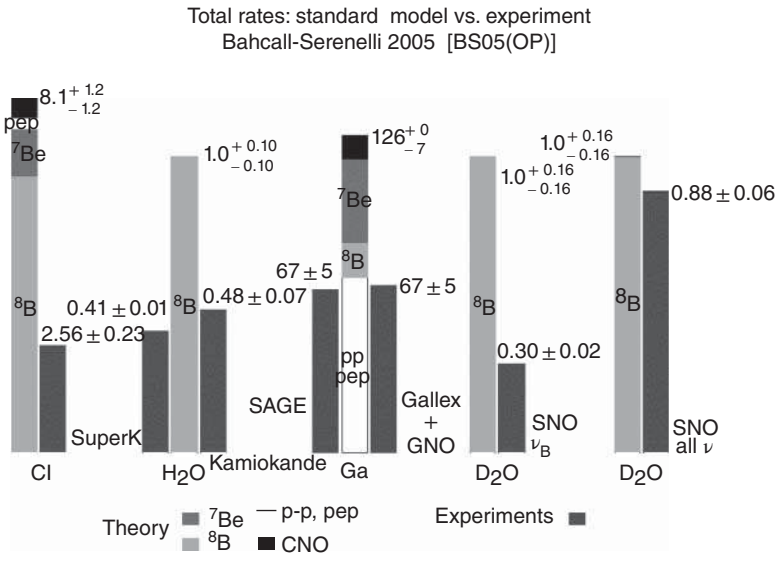

Figure 18.8 Total detected rates of solar neutrinos in the various detectors. Source: John Bahcall (1934–2005)/IOP Publishing.

and Cerenkov detectors. Radiochemical detectors rely on detecting radioactive product nuclei produced in inverse β-decay reactions in huge amounts of target material. Cerenkov detectors observe the light produced by the neutrino-induced scattering of charged particles. The pioneering radiochemical detector constructed by R. Davis et al. in the Homestake gold mine in South Dakota 1500 m below the surface of the Earth made use of 615 tons ($4 \cdot 10^5$ l) of perchloroethylene (C_2Cl_4) to observe the nuclear reaction:

$$^{37}\mathrm{Cl}(\nu_e, e^-)^{37}\mathrm{Ar}$$

having an energy threshold of 813 keV and producing the 35-day EC decaying ^{37}Ar. After the C_2Cl_4 had been exposed to the solar neutrinos for a suitable period of time, the accumulated ^{37}Ar atoms were flushed out of the tank with He gas and transferred into a proportional counter detecting the 2.8 keV Auger electrons from the EC decay. This detector was sensitive to the ^{8}B, hep, pep, and ^{7}Be ground-state decay neutrinos with the ^{8}B decay delivering the highest flux. The detector was placed deep underground to shield against cosmic-ray background-producing protons that could also produce ^{37}Ar in the ^{37}Cl(p, n) reaction. About three atoms of ^{37}Ar were detected per week, corresponding to ∼2.6 SNUs (Solar Neutrino Units, 1 SNU = 10^{-36} neutrino captures per target atom per second). The expected rate according to the standard solar model, see Figure 18.8, is ∼8.1 SNUs. The discrepancy defined the "Solar Neutrino Problem" which caused intensive discussion since the first results of the Cl experiment were announced in 1968. Over the next 20 years, many different possibilities were examined by hundreds, perhaps thousands, of scientists:

- The rate of production of ^{8}B in the Sun depends approximately upon the 20th power of the central temperature in the Sun. Is the standard solar model wrong?

- Is the experiment wrong?
- Is there a neutrino spin-flip in the magnetic fields of the Sun?
- Does something unknown happen to the neutrinos after they were created in the Sun?

In 1986, Japanese physicists led by Masatoshi Koshiba re-instrumented a huge tank of pure water designed to measure the possible decay of the proton. The experimentalists increased the sensitivity of their detector so that it could also serve as a large underground observatory of solar neutrinos. The new experiment, called Kamiokande, in a mine at Kamioka 1600 m beneath Mt. Ikena Yama, confirmed that the neutrino rate from the ^{8}B decay was less than predicted by the standard solar model, see Figure 18.8, and demonstrated, by its ability to detect the orientation of the Cerenkov cone of light produced by scattered electrons, that the detected neutrinos came from the Sun.

In the sense that detectors essentially sensitive to the ^{8}B neutrinos can be seen as thermometers of the Sun, being sensitive to its central temperature, radiochemical experiments using the reaction $^{71}\mathrm{Ga}(\nu_e, e^-)^{71}\mathrm{Ge}$ due to the low-energy threshold of 232 keV allowing for the detection of much of the dominant pp neutrinos, Figure 18.7, can be seen as the calorimeter of the Sun as long as the pp flux is fixed at the known luminosity of the Sun. An experiment in Baksan/USSR (called SAGE, led by V. Gavrin) and in the Gran Sasso underground laboratory in Italy (GALLEX and later GNO, led by T. Kirsten) again measured a large deficit in the neutrino rate, see Figure 18.8, which no longer could be blamed on possible deficiencies in the standard solar model. In GALLEX, in HCl containing an aqueous solution of 30 tons of Ga in a tank 8 m high, solar neutrinos produced 11.4 days ^{71}Ge in the form of volatile $GeCl_4$ that was periodically flushed out of the tank, collected in H_2O containing scrubbers, transformed into GeH_4 (a chemical homolog of methane which is commonly used as counting gas) with KBH_4 and transferred with Xe into a 0.63 cm^3 proportional counter where the K X-rays (10.4 keV) and the L X-rays (1.2 keV) were detected. The mini proportional counter was operated inside the well of an NaI(Tl) scintillation crystal used as an anticoincidence counter. The muon-induced rate of ^{71}Ge from the ^{71}Ga(p, n) reaction was reduced in the Gran Sasso underground laboratory to 1% of the rate for solar neutrinos. This made it definitely clear that the "Mystery of the Missing Neutrinos" or the "Solar Neutrino Problem" was not to be found in an understanding of the burning processes in the Sun, but in new physics.

As early as 1969, B. Pontecorvo and V. Gribov, working in Russia, proposed that the discrepancy could be due to an inadequacy in the textbook description of particle physics rather than in the standard solar model. They suggested that neutrinos oscillate back and forth between different mass eigenstates, which requires that $m_\nu \neq 0$. As the electron neutrinos ν_e travel from the Sun to the Earth, they oscillate between easier-to-detect ν_e and difficult-to-detect ν_μ and ν_τ; in fact, the Cl and Ga experiments are blind for the latter flavors.

Building upon this idea, Wolfenstein (1978) and Mikheyev and Smirnov (1985) showed that the effects of matter on neutrinos moving through the Sun might

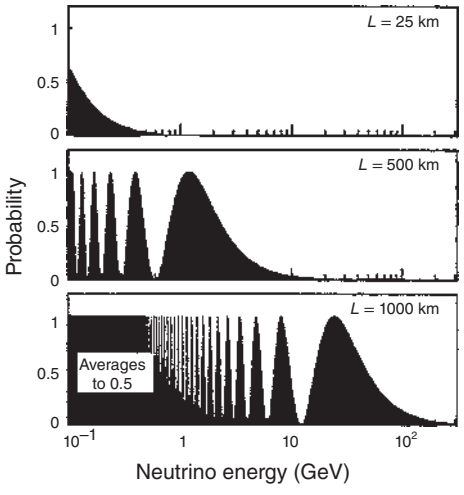

Figure 18.9 Probability that an electron neutrino is not an electron neutrino after traveling a distance *L*.

increase the oscillation probability of the neutrinos (the Mikheyev–Smirnov–Wolfenstein effect). In the absence of matter, the oscillation probability is

$$P(\nu \rightarrow \nu') = (\sin\ 2\Theta_{12})^2 \sin^2 \left[\frac{(m_2^2 - m_1^2)L}{4E} \right] \tag{18.24}$$

where Θ_{12} is the mixing angle, Δm_{12}^2 is the quadratic mass difference between two mass eigenstates, L is the distance between source and detector (oscillation length), and E is the neutrino kinetic energy. Thus, a detector that is sensitive only to ν_e sees intensity fluctuations as a function of L as demonstrated in Figure 18.9.

Neutrinos are also produced by collisions of cosmic-ray particles with other particles in the Earth's atmosphere:

$$\begin{aligned} p + X &\rightarrow \pi^- \\ \pi^- &\rightarrow \mu^- + \bar{\nu}_\mu \\ \mu^- &\rightarrow e^- + \bar{\nu}_e + \nu_\mu. \end{aligned}$$

The half-life of the pions is $2.6 \cdot 10^{-10}$ seconds, that of the muons $1.5 \cdot 10^{-6}$ seconds. A negative pion decays into a left-handed muon and a right-handed muon antineutrino. Likewise, a negative muon decays into a left-handed electron, a right-handed electron antineutrino, and a left-handed muon neutrino. The muons from pion decay are polarized in the emission direction. In the β-decay of the muons, there are more electrons (positrons) emitted under the angle θ than under $(180° - \theta)$. In 1998, the Super-Kamiokande, consisting of a tank 41 m high with 50 000 tons of H_2O surrounded by 13 000 phototubes, looked at atmospheric muon and electron neutrinos that can be distinguished from solar neutrinos by their much higher energy on the order of 10 GeV compared to the maximum energy of the solar neutrinos of 20 MeV. Depending on their flavor, a small fraction of the neutrinos produces in a collision with a quark in the atomic nuclei of water molecules either electrons or muons. These particles move in the direction of the original neutrinos with a velocity faster

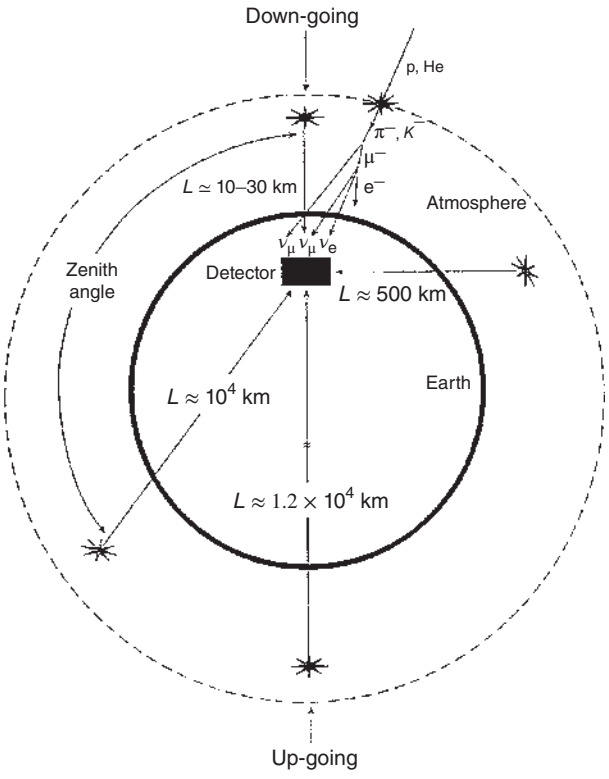

Figure 18.10 The decays of particles produced in the atmosphere by cosmic rays give muon neutrinos and electron neutrinos observed in the Super-Kamiokande detector. The large range of distances through which the neutrinos propagate allows a sensitive measure of neutrino oscillation effects. Note that the depth of the atmosphere and size of the detector are greatly exaggerated.

than the velocity of light in water. They produce Cerenkov light cones from which the direction of the original neutrino and its energy can be deduced. In this process, electrons are scattered more than muons, leading to a more washed-out signal. Tau neutrinos would create tau leptons with a quark; these are so heavy and short-lived that this process is very rare, and the produced tau lepton would be too slow to produce Cerenkov radiation. The direction of the original neutrino determines the zenith angle under which the atmospheric neutrinos were created and this defines the propagation distance L that the neutrinos traveled through the Earth to reach the detector, as illustrated in Figure 18.10. Figure 18.11 shows the ratio of observed to expected neutrino events vs. the ratio of the propagation distance L to the neutrino energy E_ν indicating oscillation effects for the muon neutrinos. At a distance of 20 km, the expected number of muon neutrinos relative to the number of electron neutrinos is observed. At a distance of 12 700 km (diameter of the Earth), only half the expected number of muon neutrinos is observed. This finding provided indirect support for the suggestion that solar neutrinos oscillate among different states. But we do not yet know whether the change of identity occurs while the

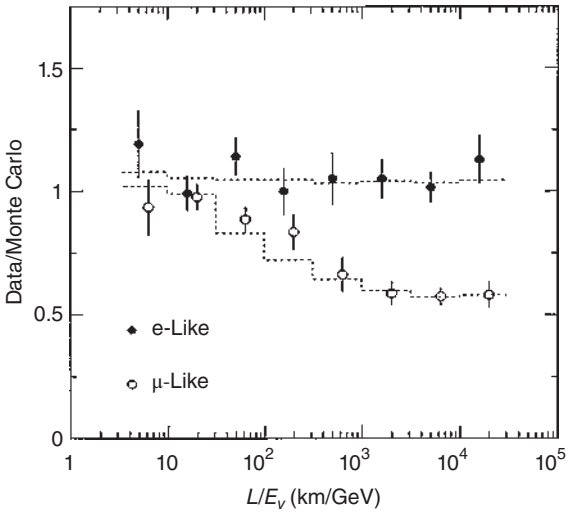

Figure 18.11 The ratio of observed to expected neutrino events vs. the ratio of the propagation distance L to the neutrino energy E_ν provides a measure of neutrino oscillation effects. The Super-Kamiokande data from 848 days of operation show oscillation effects for muon neutrinos but not for electron neutrinos. The dashed lines show expectations for ν_μ oscillations with mass-squared difference of $3.5 \cdot 10^{-3}$ eV^2 and no ν_e oscillations.

neutrinos are traveling to the Earth from the Sun, or whether matter does cause the solar neutrino oscillation.

Before the work with atmospheric neutrinos, the Kamiokande Collaboration (Hirata et al.) had detected solar ^{8}B neutrinos whose flux obtained was 0.46 ± 0.13 (stat) ± 0.08 (syst) of the value predicted by the standard solar model in agreement with the value obtained in the ^{37}Cl radiochemical detector. Later, solar ^{8}B neutrino measurements were continued by Hosaka et al. in Super-Kamiokande determining allowed regions in the $\Delta m^2 - \tan^2 \Theta$ plane delivering thereby the first direct evidence for solar electron neutrino oscillations on their way from the Sun to the Earth: $5 \cdot 10^{-5} < \Delta m^2 < 12 \cdot 10^{-5}$ and $\tan^2 \Theta = 0.44$. This agrees with the KamLAND analysis, see below.

A new generation of solar neutrino experiments worldwide was now again attempting to determine the cause of the oscillations of solar neutrinos. Among these was the Sudbury Solar Neutrino Observatory (SNO) in Ontario, Canada, placed 2 km underground in a nickel mine. It consists of 1000 tons of D_2O (the former moderator-coolant of the early Canadian nuclear power reactors), now contained in a spherical acryl vessel of 12 m diameter surrounded by high-purity light water in a vessel of 22 m diameter and 34 m height containing 9456 photomultipliers (PMTs). These 7000 tons of light water shield against neutrons from radioactivity in the rock. In the heavy water, the reactions:

$$\nu_e + {}^2H \rightarrow p + p + e^- \quad \text{charged current reaction (CC)}$$
$$\nu_x + {}^2H \rightarrow p + n + \nu_x \quad \text{neutral current reaction (NC)}$$
$$\nu_x + e^- \rightarrow e^- + \nu_x \quad \text{elastic scattering (ES)}$$

occur. The latter two detect all types of neutrinos. In the neutral current reaction, the emitted neutron is detected by a (n, γ) reaction, where the γ quantum is detected by scintillation detectors. The current status of the SNO results is also indicated in Figure 18.8. In the charged current reaction, 30% of the ^{8}B ν_e above 8 MeV are

detected, clearly indicating neutrino oscillations, as the other two reactions, being sensitive to all neutrino flavors, are compatible, within the uncertainties, with the rate predicted by the standard solar model.

In detail, the early SNO results published by Ahmad, Q.R. et al. were

$$\varphi(\nu_{\mu\tau}) = 3.69 \pm 1.13 \cdot 10^6 \text{ cm}^{-2} \text{ s}^{-1}$$

$$\varphi(\nu_x) = 5.44 \pm 0.99 \cdot 10^6 \text{ cm}^{-2} \text{ s}^{-1}$$

with the difference leadingto

$$\varphi(\text{CC}) \approx 1.75 \cdot 10^6 \text{ cm}^{-2} \text{ s}^{-1}$$

This is the rate depicted in Figure 18.8.

In a final joint analysis of phase I and phase II data from SNO above a kinetic energy threshold of 3.5 MeV for ^{8}B decay by Aharmim et al.:

$$\varphi(\text{NC}) = 5.140 - 0.158 + 0.160\,(\text{stat}) - 0.117 + 0.132\,(\text{syst}) \cdot 10^6 \text{ cm}^{-2} \text{ s}^{-1}$$

These uncertainties are more than a factor of 2 smaller than previously published. The total flux of ^{8}B neutrinos from recoil electrons from the charged current reaction and the elastic scattering of electrons is now:

$$\varphi(\nu_x) = 5.046 - 0.152 + 0.159\,(\text{stat}) - 0.123 + 0.107\,(\text{syst}) \cdot 10^6$$

For the detection of direct evidence for neutrino flavor oscillations, requiring finite neutrino masses, the 2015 Nobel Prize in Physics was awarded to Takaaki Kajita (Tokyo, Japan) and Arthur B. McDonald (Kingston, Canada).

The BOREXINO detector in the Gran Sasso underground laboratory in Italy is a large volume liquid scintillator detector whose primary purpose is the real-time measurement of low-energy solar neutrinos. Its primary goal is the detection of monochromatic neutrinos that are emitted in the electron-capture decay of ^{7}Be in the Sun. It also aims at the spectral study of other solar neutrino components, such as the CNO, pep, and possibly pp neutrinos. Neutrinos of all flavors are detected by means of their elastic or, in the case of electron anti-neutrinos, by means of their inverse β-decay on protons or carbon nuclei. The electron (positron) recoil energy is converted into which is collected by photomultipliers. The low-energy neutrino detection is possible because of the high light yield that allows the energy threshold to be set down to a few tens of kiloelectronvolts.

The inner part of Borexino is an unsegmented stainless-steel sphere (SSS) that is both the container of the scintillator and the mechanical support of the PMTs. Within this sphere, two nylon vessels separate the scintillator volume in three shells of radii 4.25, 5.50, and 6.85 m, the latter being the radius of the SSS itself. The inner nylon vessel contains the scintillator solution, namely PC (pseudocumene, 1,2,4-trimethylbenzene) as a solvent and the fluor PPO (2,5-dimethyloxazole) as the solute. The second and third shell contain PC with a small admixture of DMP (dimethylphtalate) that is added as a light quencher in order to reduce the scintillaztion yield of pure PC.

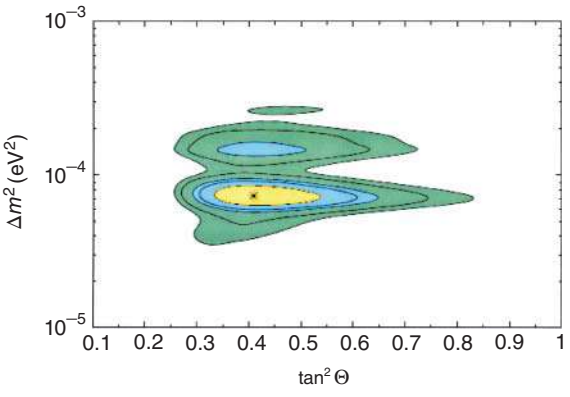

Figure 18.12 Allowed regions in the Δm^2 vs. $\tan^2\Theta$ plane from a combined analysis of the solar neutrino data and the KamLAND spectrum of reactor neutrinos. Contour lines for 1σ, 90%, 95%, 99%, and 3σ confidence levels are depicted. The best fit point is marked by an asterisk. Source: de Holanda and Smirnov (2003), figure 4 (p. 9)/IOP Publishing.

During phase I (2007–2010), Borexino first detected and then precisely measured the flux of the ^{7}Be solar neutrinos via the rate of neutrino–electron elastic scattering of the 862 keV ^{7}Be solar neutrinos and yielded an electron–neutrino survival probability of 0.51 ± 0.07 at 862 keV. Thus, the energy dependence of the survival probability (≈57% for the pp neutrinos, ≈50% for the 862 keV ^{7}Be neutrinos, and ≈30% for the high-energy ^{8}B neutrinos) favors the Mikheyev–Smirnov–Wolfenstein large mixing angle model (LMA MSW solution).

Borexino also made the first direct observation of the pep neutrinos and set the highest upper limit on the flux of solar neutrinos produced in the CNO cycle where carbon, nitrogen, and oxygen serve as catalysts in the fusion process. The measurement of the annual modulation of the ^{7}Be neutrino interaction rate caused by the eccentricity of the Earth's rotational trajectory around the Sun is also reported. The period, the amplitude, and the phase of the modulation are consistent with the solar origin of these events, and the absence of their annual modulation is rejected at >99% C.L.

There is also a detector studying reactor neutrino oscillations, called KamLAND. It contributes to the game by favoring the LMA MSW solution as well (de Holanda and Smirnov 2003). In a χ^2 analysis of the KamLAND spectrum and of the solar neutrino data, an absolute minimum in the Δm^2 vs. $\tan^2\Theta$ plane at a high confidence level of 96.3% is found at

$$\Delta m^2 = 7.32{\cdot}10^{-5}(\text{eV})^2 \text{ and } \tan^2\Theta = 0.409$$

The presently allowed regions in the $\Delta m^2 - \tan^2\Theta$ plane are depicted at 1σ, 90%, 95%, 99%, and 3σ by the contour lines in Figure 18.12. The new generation of solar neutrino experiments will further confine the LMA parameter space. It is remarkable that the "Mystery of the Missing Solar Neutrinos" has provided a clue to physics behind the standard model of particle physics.

18.6 Absolute Neutrino Masses

Experiments devoted to neutrino oscillations deliver only quadratic neutrino mass differences but not the absolute masses. Till today, evidence for finite neutrino

masses and for oscillations between the fluctuating mass eigenstates are the only evidence for physics behind the standard model of elementary particles. Also, for cosmology, the large number of neutrinos produced in the Big Bang plays a key role in the understanding of large structures in the universe. Exactly how large this role is depends on the absolute value of the neutrino mass.

The existence of neutrino mixing tells us that the neutrino eigenstates ν_e, ν_μ, and ν_τ are certain superpositions of mass eigenstates m_i. Therefore, one can only obtain upper limits for $m(\nu_e)$, $m(\nu_\mu)$, and $m(\nu_\tau)$ that correspond to the weighted average of the neutrino mass eigenstates contributing to the given flavor. Here, U is a unitary 3×3 mixing matrix:

$$m^2(\nu_e) = \sum_{i=1}^{3} \left| U_{ei}^2 \right|^2 m_i^2 \quad m^2(\nu_\mu) = \sum_{i=1}^{3} \left| U_{\mu i}^2 \right|^2 m_i^2 \quad m^2(\nu_\tau) = \sum_{i=1}^{3} \left| U_{\tau i}^2 \right|^2 m_i^2$$

18.6.1 $m(\nu_\mu)$ from Pion Decay

The muon neutrino mass $m(\nu_\mu)$ has been investigated in the two-body decay of pions:

$\pi^+ \rightarrow \mu^+ + \nu_\mu$ or $\pi^- \rightarrow \mu^- + \bar{\nu}_\mu$

Energy and momentum conservation require $p(\mu) = p(\nu)$ from which follows:

$$m^2(\nu_\mu) = (m^2(\pi) + m^2(\mu)) - 2m(\pi)\sqrt{m^2(\mu) + p^2(\mu)}$$

according to the relativistic invariant for the total energy E_{tot} and the momentum p:

$$m^2 = E_{tot}^2 - p^2$$

In a precision experiment at the Paul Scherrer Institute, the muon momentum was determined to be $p(\mu) = 29.792$ MeV. Using input parameters $m(\mu) = 105.658$ MeV and $m(\pi) = 139.570$ MeV, the authors obtained from the energy and momentum conservation an upper limit for the muon neutrino mass:

$$m(\nu_\mu) < 190 \text{ keV (90\%C.L.)}$$

18.6.2 $m(\nu_\tau)$ from Tau Decay

The most sensitive information on the mass of the tau neutrino $m(\nu_\tau)$ comes from the investigation of the tau pairs which are produced at electron–positron colliders and decay into pions. The quantity to be looked at is the invariant mass of the multiple pions M_π. In the rest frame of the decaying tau, the respective relations are

$$M_\pi^2 = \left(\sum_j E_{totj}(\pi), \sum_j p_{j(\pi)} \right)^2 = (m(\tau) - E_{tot}\ (\nu_\tau), -p(\nu_\tau))^2 \leq (m(\tau) - m(\nu_\tau))^2$$

The most precise result was obtained at LEP, restricting the tau neutrino mass to

$$m(\nu_\tau) < 18.2 \text{ MeV (95\%C.L.)}$$

18.6.3 $m(\nu_e)$ from Nuclear β-Decay

The phase space region of low-energy neutrinos, where the highest sensitivity to the neutrino mass is achieved, corresponds to the very upper end of the β-spectrum. Several arguments favor tritium, endpoint energy $E_0 \approx 18.6$ keV, as the isotope suited best for a neutrino mass search experiment:

- Tritium allows a specific activity large enough for an experimental setup with a β-source and a separated β-electron spectrometer.
- Tritium β-decay is a super-allowed decay having a nuclear matrix element which does not show any dependence on the energy of the β-electron.
- T_2 is the simplest molecule allowing quantitative calculation of its final-state spectrum.

Very detailed considerations and their solutions concerning

(i) Q value and endpoint of β-spectrum
(ii) Nuclear β-spectrum, and
(iii) Final-state spectrum

can be found in the work by Otten and Weinheimer. Their results are roughly summarized as follows:

(i) For the decay of gaseous T_2 into the ground state of the molecular daughter ion $(^3HeT)^+$, the endpoint energy is $E_0(T_2) = 18\,571.8 \pm 1.2$ eV.
(ii) The two-particle phase space density of β and ν is given by the product:

$$P_2(E_{tot}, E_{tot\,\nu}) = \frac{dn}{dE_{tot}d\Omega}\,\frac{dn_\nu}{dE_{tot\,\nu}\;d\Omega_\nu} = \frac{V^2\,E_{tot}\sqrt{E_{tot}^2 - m^2}}{(2\pi)^6}\cdot\frac{V^2 E_{tot\,\nu}\sqrt{E_{tot\,\nu}^2 - m_\nu^2}}{(2\pi)^6}$$

which in contrast to Eq. (6.39) is containing separately the variables for β and ν.
(iii) The recoil energy of the daughter system $^3He + T^+$, for example, is 1.72 eV, so that the endpoint energy is lowered to $E_0 = Q - 1.72$ eV.

The resulting upper limit for the mass is $m(\nu_e) < 2$ eV at 95% C.L.

The experiment by Otten et al. at Mainz used a solid T_2 target coupled to a magnetic adiabatic collimation applied to an electrostatic filter (MAC-E-Filter). The flight pass had a length of 6 m. The source was a film of up to 140 monolayers of T_2 condensed onto a substrate of highly oriented pyrolytic graphite at 1.8 K.

18.6.4 The Karlsruhe Tritium Experiment on the Neutrino Mass KATRIN

Members from earlier neutrino mass experiments at Los Alamos, Mainz, and Troitsk together with the Forschungszentrum Karlsruhe succeeded to get a design report approved in 2004 for the construction of an experiment that aims at an improvement of the sensitivity limit of the leading Mainz experiment by an order of magnitude to $m(\nu_e) < 0.2$ eV. This requires improvement of tritium β-spectroscopy by

a factor of 100. It was decided to build a MAC-E-Filter much larger than that of the Mainz experiment with a diameter of 10 m, corresponding to a 100 times larger analyzing plane. A decay rate of 10^{11} Bq is aimed for from a windowless gaseous T_2 source (WGTS) with a column density of $5 \cdot 10^{17}$ molecules cm^{-2} corresponding to a thickness of 500 monolayers. The WGTS consists of a 16-m-long cryostat. The electrons from the source are guided by strong magnets to the giant main spectrometer. The latter was transported in 2006 from the producer in Bavaria not on motorways but by boat on the Danube River into the Black Sea, the Mediterranean Sea, the Atlantic Ocean, the North Sea, and on the Rhine River over nearly 9000 km to Karlsruhe. There, it was inaugurated in June 2018. After data taking, the first publication announced in December 2019 that the limit of the Mainz experiment had been reduced by almost a factor of 2 reaching a limit of $m(\nu_e) < 1.1$ eV (90% C.L.).

18.7 Interstellar Matter and Cosmic Radiation

18.7.1 Interstellar Matter

In interstellar space, matter is distributed very unevenly. As already mentioned in Section 18.4, some stars are ejecting their matter in the form of nebulas of dust and gas. These nebulas contain various elements (mainly H, C, O, Si, and others) at temperatures between about 10^2 and 10^3 K. Far away from the stars, the density of interstellar matter is on the order of 0.1 atoms cm^{-3}, mainly H and C. In some regions, however, matter is condensed in the form of big interstellar clouds, the mass of which may exceed the mass of the Sun by a factor of 10^3 or more. Two types of interstellar clouds are distinguished: optically transparent, diffuse clouds containing $<10^3$ atoms cm^{-3} (mainly H, but also some compounds such as CO or HCHO) at temperatures on the order of 100 K, and opaque, dense clouds containing 10^4–10^6 molecules cm^{-3} (mainly H_2, but also a variety of compounds) at temperatures varying between about 10 and 10^3 K. Densities and temperatures increase from the outer parts to the core of the clouds.

Dense interstellar clouds have been investigated by microwave spectroscopy, and many compounds have been identified, comprising simple molecules such as H_2, H_2O, CO, NH_3, HCHO, HCN, SO_2, CH_3OH, and C_2H_5OH, radicals such as OH and CN, and more complex compounds containing many carbon atoms. Interstellar space can be looked upon as a big chemistry laboratory, where chemical reactions take place at extremely low pressures and temperatures under the influence of electromagnetic and cosmic radiation, including light and charged particles. Radiation-induced reactions play a predominant role.

Altogether, the mass of the interstellar matter consists of ≈70% H_2, ≈28% He, and ≈2% other elements. The heavier elements such as C and S are assumed to be incorporated in the interstellar dust, and the mass of this dust is estimated to amount to about 1% of the total interstellar matter or about 10^8–10^{10} tons. The dust grains may adsorb molecules from the gas phase and catalyze chemical reactions. The average residence time of dust grains in interstellar space is assumed to be on the order of

10^8 years. By aggregating interstellar matter under the influence of gravitation, dust grains may be incorporated into a new star. The probability of the presence of biologically important compounds in the dust grains is also being discussed. However, our knowledge of interstellar dust is very limited because no samples are available.

The present state of knowledge about invisible dark matter (nonbaryonic matter) indicates that it represents the predominant part (94%) of the total mass of the Universe. Dark matter is not discernible by any kind of electromagnetic radiation in the region from γ-rays to radio waves, but its gravitational effects on other kinds of matter are observable. For example, the rotation of spiral galaxies such as our Milky Way can only be explained if about 90% of the matter is invisible in the sense mentioned above. The question of the nature of the dark matter was still open, but there is fascinating news.

On 6 October 2020, the Royal Swedish Academy of Sciences has decided to award the Nobel Prize in Physics 2020 with one half to Roger Penrose, University of Oxford, United Kingdom, "*for the discovery that black hole formation is a robust prediction of the general theory of relativity*," and the other half jointly to Reinhard Genzel, Max Planck Institute for Extra-terrestrial Physics, Garching, Germany, and University of California, Berkeley, United States, and Andrea Ghez, University of California, Los Angeles, United States, "*for the discovery of a supermassive compact object at the centre of our galaxy*." Roger Penrose used ingenious mathematical methods in his proof that black holes are a direct consequence of Albert Einstein's general theory of relativity. Einstein did not himself believe that black holes really exist, these super-heavyweight monsters that capture everything that enters them. Nothing can escape, not even light. In January 1965, 10 years after Einstein's death, Roger Penrose proved that black holes really can form and described them in detail; at their heart, black holes hide a singularity in which all the known laws of nature cease. His groundbreaking article is still regarded as the most important contribution to the general theory of relativity since Einstein. Reinhard Genzel and Andrea Ghez each lead a group of astronomers that, since the early 1990s, has focused on a region called Sagittarius A* at the center of our galaxy. The orbits of the brightest stars closest to the middle of the Milky Way have been mapped with increasing precision. The measurements of these two groups agree, with both finding an extremely heavy, invisible object that pulls on the jumble of stars, causing them to rush around at dizzying speeds. Around 4 million solar masses are packed together in a region no larger than our solar system. Using the world's largest telescopes, Genzel and Ghez developed methods to see through the huge clouds of interstellar gas and dust to the center of the Milky Way. Stretching the limits of technology, they refined new techniques to compensate for distortions caused by the Earth's atmosphere, building unique instruments and committing themselves to long-term research. Their pioneering work has given us the most convincing evidence yet of a supermassive black hole at the center of the Milky Way.

It is tempting to conclude this fascinating news with a speculation: if normal baryonic matter of millions of solar masses giving rise to a black hole can be formed by gravitation, is it possible that several of these super-heavyweight monsters, sitting in the centers of numerous other galaxies, attract themselves over very

large distances? Could this, over extremely long periods of time, give an end to the expansion of the universe? and could the universe then shrink and collapse giving rise to the next time zero, at an extremely high temperature, an extremely high density in an extremely small volume, causing the next Big Bang?

18.7.2 Cosmic Radiation

An important proportion of the matter in interstellar space appears in the form of cosmic rays consisting of high-energy particles and photons. The intensity of cosmic radiation (about 10 particles $cm^{-2}\ s^{-1}$) is relatively weak compared to the intensity of radioactive sources, but the energy of the particles in cosmic radiation is extremely high (from about 10^2 to about 10^{14} MeV). Potential sources of primary cosmic radiation are supernova explosions and pulsars. Furthermore, particles may be accelerated in interstellar space by shock waves and cosmic magnetic fields. It is assumed that most of the particles are not able to escape from the galaxy in which they are produced. Primary cosmic rays consist mainly of protons with ~1% of electrons. About 15% of the primaries are helium nuclei and electrons, and atomic numbers up to ~90 and perhaps beyond have been identified, with an abundance distribution roughly matching that in the Universe. The energy spectra per nucleon for protons and heavier nuclei have the same shape at least above 500 MeV/u.

The cosmic radiation incident on the Earth is generated in our galaxy. It is largely absorbed in the atmosphere, and the flux density is reduced from about 20 to about 1 $cm^{-2}\ s^{-1}$ at the surface of the Earth. By interaction with the atoms and the molecules in the atmosphere, showers of mesons (mostly π mesons) and nucleons are produced, making up the secondary cosmic radiation. Many of these undergo further nuclear reactions. Muons produced in flight by π mesons are found lower in the atmosphere, and they constitute most of the hard component of the cosmic radiation on the Earth's surface. With energies of many gigaelectronvolts, these muons are very penetrating and may still be observed (at largely reduced intensity) in underground laboratories.

At the surface of the Sun, high-temperature bursts are observed as particularly bright areas (flares) at certain intervals (≈11 years, corresponding to the intervals between sunspot activity). With these flares, the Sun ejects great amounts of protons, called the solar wind. The flux of these protons may be several orders of magnitude higher than the flux of cosmic rays, but the energy of the solar protons is lower than in cosmic rays (on average 10–100 keV, at maximum 10^2 MeV). These protons are absorbed in the atmosphere and do not reach the surface of the Earth.

Part of the solar wind is trapped in the magnetic field of the Earth, forming the outer Van Allen radiation belt, whereas more energetic solar protons are accumulated in narrow zones above the magnetic field of the Earth, producing the auroral displays.

18.7.3 Radionuclides from Cosmic Rays

The impact of primary and high-energy secondary cosmic rays near the top of the atmosphere results in spallation reactions in which many neutrons, protons, α

particles, and other fragments are created. These secondary particles react with nuclei in the lower part of the atmosphere (mostly nitrogen, oxygen, and argon), and many radioactive products resulting from these nuclear reactions are observed, such as ^{3}H, ^{7}Be, ^{26}Al, ^{32}Si, and ^{39}Ar. Most of the neutrons are slowed down to thermal energies and, by (n, p) reaction with ^{14}N, produce ^{14}C, the 5730 years β^- emitter. From cosmic-ray data, the production rate averaged over the whole atmosphere is calculated to be $\sim 2\,s^{-1}\ cm^{-2}$. The lifetime of ^{14}C is long enough for the radioisotope to be thoroughly mixed with all the carbon in the so-called exchangeable reservoirs: atmospheric CO_2 (1.4%), ocean (95%, mostly as dissolved bicarbonate), and biosphere (3.2%). The total carbon content of these reservoirs is estimated as $9.66\,g\,cm^{-2}$ on the Earth's surface. Therefore, the *specific activity* of ^{14}C in all of this carbon is estimated to be $14.9\,min^{-1}\ g^{-1}$. This is a readily measurable activity level and is the basis for radiocarbon dating, see Chapter 19.

18.7.4 Cosmic-Ray Effects in Meteorites

Unshielded bodies in interplanetary space are bombarded by cosmic rays, and their interaction produces stable and radioactive spallation products. Since the ranges of galactic cosmic-ray (GCR) protons in solids are on the order of 1 m, the amounts of spallation products detected give information on the length of time the material investigated has been near the surface – the so-called exposure age. The spallation products can also give information on the time dependence of the cosmic-ray flux in the past. Interpretation of the data depends very much on measurements of cross sections for nuclear reactions by multi-gigaelectronvolt protons at accelerators and is aided by the fact that these are hardly energy-dependent above ~1 GeV, so that details of the cosmic-ray spectrum need not to be known. Many spallation products with half-lives ranging from days to millions of years as well as some stable products have been identified in meteorites and in lunar samples. Provided the cosmic-ray flux has been constant for a time that is long compared to the half-life, the radioactive product should be at saturation. Typical saturation activities of radionuclides in meteorites are on the order of $10–100\,min^{-1}\ kg^{-1}$. The saturation activity of a radioactive spallation product depends on the cosmic-ray flux averaged over time on the order of the half-life, whereas the mass of a stable spallation product that has accumulated is a measure of the total flux throughout the exposure. If it is assumed that the cosmic-ray flux has been constant in time, see below, and if the relative cross sections for production of a stable and a radioactive product are known from accelerator data, the ratio of their concentrations in a meteorite at the time of fall gives immediately the exposure age. Isobaric pairs such as ^{36}Cl–^{36}Ar, ^{3}H–He, and ^{22}Na–^{22}Ne serve this purpose most reliably, but concentration ratios of other pairs such as ^{26}Al–^{21}Ne, ^{39}Ar–^{38}Ar, and ^{40}K–^{41}K have also been used. Here, the stable nuclide is determined mass spectrometrically, and it must be known to have had a negligible primordial concentration. Preferably, exposure ages are determined by more than one method. Exposure ages of meteorites range from $2 \cdot 10^4$ to $8 \cdot 10^7$ years for stone meteorites and from $4 \cdot 10^6$ to $2 \cdot 10^9$ years for iron meteorites. For particular types of meteorites, there is clustering around certain ages. These meteorites

were presumably formed by the breakup of larger extraterrestrial bodies, that is, asteroids with diameters <500 km, through collisions. The clustering of exposure ages probably dates the breakup of their parent bodies.

The ratios of saturation activities of products of different half-lives in iron meteorites are supposed to equal the ratios of their production cross sections in iron/nickel spallation reactions, if the GCR fluence was indeed constant for times on the order of the half-lives. Comparisons for suitable pairs, for example, ^{39}Ar(269 years)–^{36}Cl($3 \cdot 10^5$ years) and ^{54}Mn(312 days)–^{53}Mn($3.7 \cdot 10^6$ years), have indicated little variation in GCR flux over the respective time periods. Deviations of the activity ratio for the shorter-lived ^{37}Ar(35 days)–^{39}Ar(269 years) from that resulting from the measured cross sections have been interpreted as hints of a gradient in cosmic-ray flux with distance from the Sun due to its magnetic field. This comes about because meteorite orbits are quite eccentric: the shorter-lived ^{37}Ar is formed while the meterorite is close to the Earth, while the ^{39}Ar integrates the GCR flux over the entire orbit.

18.7.5 Abundance of Li, Be, and B

As was discussed in Section 18.3, the Big Bang nucleosynthesis produces hydrogen, helium, and a trace of ^{7}Li. In stars of the main sequence in the H–R diagram, hydrogen burning transforms ~7% of the hydrogen into ^{4}He. Due to the relative fragility of the isotopes of Li, Be, and B with respect to decay or nuclear reactions that lead to the much more stable ^{4}He, neither of these processes is able to produce the observed, although low, abundances of Li, Be, and B in the Solar System, see Figure 18.5. However, the observed abundances of Li, Be, and B in the Solar System are supplied by spallation reactions in which interstellar nuclei such as ^{12}C and ^{16}O react with GCR. Cross sections for these spallation reactions are 1–100 mb and the duration of the bombardment is on the order of 10^{10} years. The product nuclei have low excitation energies and can survive. This view is corroborated by the high relative abundance of Li, Be, and B in the secondary cosmic-ray flux with a pattern resembling the yield distributions of these fragments in high-energy reactions.

References

Cosmochemistry

Bahcall, J.N. and Pena-Garay, C. (2004). Solar models and solar neutrino oscillations. *New J. Phys.* 6: 63.

Clayton, D.D. (1968). *Principles of Stellar Evolution and Nuclear Synthesis*. New York: McGraw-Hill.

Friedlander, G., Kennedy, J.W., Macias, E.S., and Miller, J.M. (1981). *Nuclear and Radiochemistry*, 3e. New York: Wiley.

de Holanda, P.C. and Smirnov, A.Y. (2003). LMA MSW solution of solar neutrino problem and first KamLAND results. *J. Cosmol. Astropart. Phys.* 02: 1.

Mikheyev, S.P. and Smirnov, A.Y. (1985). Resonance enhancement of oscillations in matter and solar neutrino spectroscopy. *Sov. J. Nucl. Phys.* 42: 913.
Murphey, B.F. and Nier, A.O. (1941). *Phys. Rev.* 59: 772.
Rolfs, C. and Trautvetter, H.P. (1978). Experimental nuclear astrophysics. *Annu. Rev. Nucl. Sci.* 28: 115.
Silverman, S.R. (1951). The isotope geology of oxygen. *Geochim. Acta* 2: 26.
Vinogradov, A.P. (1954). *Bull. Acad. Sci. USSR. Ser. Geol.* 3: 3.
Wolfenstein, L. (1978). Neutrino oscillations in matter. *Phys. Rev.* D17: 2369.

Further Reading

General

Hahn, O. (1936). *Applied Radiochemistry*. Ithaca, NY: Cornell University Press.
Haissinsky, M. (1964). *Nuclear Chemistry and Its Applications*. Reading, MA: Addison-Wesley.
Evans, E.A. and Muramatsu, M. (1977). *Radiotracer Techniques and Applications*. New York: Marcel Dekker.
Draganic, I.G., Draganic, Z.D., and Adloff, J.P. (1990). *Radiation and Radioactivity on the Earth and Beyond*. Boca Raton, FL: CRC Press.

Geochemistry

Faul, H. (1954). *Nuclear Geology*. New York: Wiley.
Kohman, T.P. and Saito, N. (1954). Radioactivity in geology and cosmology. *Annu. Rev. Nucl. Sci.* 4: 401.
Suess, H.E. (1965). *Abundances of the Elements in the Universe, Landolt-Börnstein, Physical Tables*, New Series VI/1, 83. Berlin: Springer-Verlag.
Rutten, M.G. (1971). *The Origins of Life by Natural Causes*. Amsterdam: Elsevier.
Hoefs, J. (1973). *Stable Isotope Geochemistry*. Berlin: Springer-Verlag.
Miller, S.L. and Orgel, L.E. (1974). *The Origins of Life on the Earth*. Englewood Cliffs, NJ: Prentice Hall.
Trimble, V. (1975). The origin and abundances of the chemical elements. *Rev. Mod. Phys.* 47: 877.
Windley, B.F. (ed.) (1976). *The Early History of Earth*. New York: Wiley.
Faure, G. (1977). *Principles of Isotope Geology*. New York: Wiley.
Ponnamperuma, C. (ed.) (1977). *Chemical Evolution of the Early Earth*. New York: Academic Press.
Rydberg, J. and Choppin, G. (1977). Elemental evolution and isotopic composition. *J. Chem. Educ.* 54: 742.
Ozima, M. (1981). *The Earth, Its Birth and Growth*. Cambridge: Cambridge University Press.
Kuroda, P.K. (1982). *The Origin of the Chemical Elements and the Oklo Phenomenon*. Berlin: Springer-Verlag.
Mason, B. and Moore, C.B. (1982). *Principles of Geochemistry*. New York: Wiley.

Durrance, E.M. (1986). *Radioactivity in Geology: Principles and Applications*. Chichester: Ellis Horwood.
Cox, P.A. (1989). *The Elements*. Oxford: Oxford University Press.

Cosmochemistry

Hubble, E. (1929). A relation between distance and radial velocity among extragalactic nebulae. *Proc. Natl. Acad. Sci. U.S.A.* 15: 168.
Gamow, G. (1946). Expanding universe and the origin of the elements. *Phys. Rev.* 70: 572.
Alpher, R.A., Bethe, H.A., and Gamov, G. (1948). The origin of chemical elements. *Phys. Rev.* 73: 803.
Burbridge, E.M., Burbridge, G.R., Fowler, W.A., and Hoyle, F. (1957). Synthesis of the elements in stars. *Rev. Mod. Phys.* 29: 547.
Schaeffer, O.A. (1962). Radiochemistry of meteorites. *Annu. Rev. Phys. Chem.* 13: 151.
Craig, H., Miller, S.L., and Wassenburg, G.J. (eds.) (1963). *Isotopic and Cosmic Chemistry*. Amsterdam: North-Holland.
Fowler, W.A. and Hoyle, F. (1965). *Nucleosynthesis in Massive Stars and Supernovae*. Chicago: University of Chicago Press.
Arnold, J.R. and Suess, H.E. (1969). Cosmochemistry. *Annu. Rev. Phys. Chem.* 20: 293.
Fruchter, J.F. (1972). Chemistry of the noon. *Annu. Rev. Phys. Chem.* 23: 485.
Manolescu, O. (1974). Geochemistry and cosmochemistry. *Rev. Fiz. Chim. A* 226.
Nagy, B. (1975). *Carbonaceous Meteorites*. Amsterdam: Elsevier.
Bahcall, J.N. and Davis, R. Jr., (1976). Solar neutrinos: a scientific puzzle. *Science* 191: 246.
Ross, J.E. and Aller, L.H. (1976). The chemical composition of the sun. *Science* 191: 1223.
Schramen, D. and Wagoner, R.V. (1977). Element production in the early universe. *Annu. Rev. Nucl. Sci.* 27: 1.
Weinberg, S. (1977). *The First Three Minutes*. New York: Bantam.
Clayton, R.N. (1978). Isotopic anomalies in the early solar system. *Annu. Rev. Nucl. Sci.* 28: 501.
Dermott, S.F. (ed.) (1978). *Origin of the Solar System*. New York: Wiley.
Galant, R.A. (1980). *Our Universe*. Washington, DC: National Geographic Society.
Sagan, C. (1980). *Cosmos*. New York: Random House.
Barnes, C.A., Clayton, D.D., and Schramm, D.N. (eds.) (1982). *Essays in Nuclear Astrophysics*. Cambridge: Cambridge University Press.
Wolfendale, A.W. (ed.) (1982). *Progress in Cosmology*. Dordrecht: Reidel.
Clayton, D.D. (1983). *Principles of Stellar Evolution and Nuclear Synthesis*. Chicago: University of Chicago Press.
Dullet, W.W. and Williams, D.A. (1984). *Interstellar Chemistry*. New York: Academic Press.
Taube, M. (1985). *Evolution of Matter and Energy on a Cosmic and Planetary Scale*. Berlin: Springer-Verlag.
Wood, J.A. and Chang, S. (eds.) (1985). *The Cosmic History of the Biogenic Elements and Compounds*. Washington, DC: NASA Scientific and Technical Information Branch.

Rolfs, C.E. and Rodney, W.S. (1988). *Cauldrons in the Cosmos*. Chicago: Chicago University Press.

Hirata, K.S. (1989). Observation of 8B solar neutrinos in the Kamiokande-II detector. *Phys. Rev. Lett.* 63: 16.

Viola, V.E. (1990). Formation of the chemical elements and the evolution of our universe. *J. Chem. Educ.* 67: 723.

Norman, E.B. (1994). Stellar alchemy: the origin of the chemical elements. *J. Chem. Educ.* 71: 813.

Hahn, R.L. (1995). The physics and (radio)chemistry of solar neutrino experiments. *Radiochim. Acta* 70/71: 177.

Käppeler, F., Thielemann, F.-K., and Wiescher, M. (1998). Current quests in nuclear astrophysics and experimental approaches. *Annu. Rev. Nucl. Part. Sci.* 48: 175.

Reddy, S., Prakkash, M. and Lattimer, J.M. (1998). Neutrino interactions in hot and dense matter. *Phys. Rev.* D58: 013009.

Hampel, W. and the GALLEX Collaboration (1999). GALLEX solar neutrino observations: results for GALLEX IV. *Phys. Lett.* B447: 127.

Viola, V.E. (2000). LiBeB nucleosynthesis and clues to the chemical evolution of the universe. In: *Origin of Elements in the Solar System: Implications of Post-1957 Observations* (ed. O. Manuel), 189. New York: Kluwer Academic.

Ahmad, Q.R. and the SNO Collaboration (2001). Measurement of the rate of interactions produced by 8B solar neutrinos at the Sudbury neutrino observatory. *Phys. Rev. Lett.* 87: 071301.

Bahcall, J.N. (2001). Neutrinos reveal split personalities. *Nature* 412: 29.

Ahmad, Q.R. and the SNO Collaboration (2002). Direct evidence for neutrino flavor transformation from neutral-current interactions in the Sudbury neutrino observatory. *Phys. Rev. Lett.* 89: 011301.

Eguchi, K. and the KamLAND Collaboration (2002). First Results from KamLAND: Evidence for Reactor Anti-Neutrino Disappearance, hep-ex/0212021.

Fukada, S. and the SUPER-KAMIOKANDE Collaboration (2002). Determination of the solar neutrino oscillation parameters using 1496 days of super-Kamiokande I data. *Phys. Lett.* B539: 179.

Hosaka, J. et al. (2006). Solar neutrino measurements in Super-Kamiokande-I. *Phys. Rev.* D73: 112001.

Craens, J.P. and the SUPER-KAMIOKANDE II Collaboration (2008). Solar neutrino measurements in Super-Kamiokande II. *Phys. Rev.* D78: 032002.

Abdurashitov, J.N. and the SAGE Collaboration (2009). Measurement of the solar neutrino capture rate with gallium metal III. Results for the 2002–2007 data taking period. *Phys. Rev.* C80: 015807.

Alimonti, G. et al. (2009). The Borexino detector at the Laboratori del gran Sasso. *Nucl. Instrum. Methods Phys. Res.* A600: 568.

Aharmim, B. and the SNO Collaboration (2010). Low-energy-threshold analysis of the phase I and phase II data sets of the Sudbury neutrino observatory. *Phys. Rev.* C81: 055504.

Kaether, F., Hampel, W., Heusser, G. et al. (2010). Reanalysis of the GALLEX solar neutrino flux and source experiments. *Phys. Lett.* B685: 47.

Bellini, G. and the BOREXINO Collaboration (2011). Precision measurement of the 7Be solar neutrino interaction rate in Borexino. *Phys. Rev. Lett.* 107: 141302.

Rauscher, T. and Patkós, A. (2011). Origin of the chemical elements. In: *Handbook of Nuclear Chemistry*, 2e, vol. 2 (eds. A. Vértes, S. Nagy, Z. Klencsár, et al.), 613. Berlin: Springer-Verlag.

Kelley, L.Z. et al. (2012). Electromagnetic transients as triggers in searches for gravitational waves from compact binary mergers. *Phys. Rev.* D87: 123004, arxiv; 1209.3027....

Martinez-Pinedo, G. et al. (2012). Charged-current weak interaction processes in hot and dense matter. *Phys. Rev. Lett.* 109: 251104.

Tanvir, N.R. et al. (2013). A kilonova associated with the short-duration ϒ-ray burst GRB170817A. *Nature* 599: 547, arxiv: 1306.4971.

Bellini, G. et al. (2014). Final results of Borexino phase-I on low-energy solar neutrino spectroscopy. *Phys. Rev.* D89: 112007.

Rosswog, S. et al. (2014). The longterm evolution of neutron star merger remnants I: The impact of r-process nucleosynthesis. *Mon. Not. R. Astron. Soc.* 439: 744.

Zanaka, M. et al. (2017). Kilonova from post-merger ejecta as an optical and near-infrared counterpart of GW170817. *Astrophysics. Solar and Stellar Astrophysics*, arxiv: 1710.05850v1.

Evans, P.A. et al. (2017). Swift and NuSTAR observations of GW170817: detection of a blue kilonova. *Astrophysics. Solar ans Stellar Astrophysics*, arxiv: 1710.05437v1.

information@eso.org (2017). ESO-Teleskope beobachten erstes Licht einer Gravitationswellen-Quelle – Verschmelzende Neutronensterne verstreuen Gold und Platin im Weltraum. Recorded October 17, 2017.

Martinez-Pinedo, G. et al. (2017). Der Beginn einer Multi-Messenger Ära. *Phys. J.* 12: 200.

Smartt, S.J. (2017). A kilonova as the electromagnetic counterpart to a gravitational-wave source. *Astrophysics. Solar and Stellar Astrophysics*, arxiv: 1710.05841v2.

Horowitz, C.J. et al. (2019). R-process nucleosynthesis: connecting rare-isotope beam-facilities with the cosmos. *J. Phys. G: Nucl. Part. Phys.* 46: 083001.

19

Dating by Nuclear Methods

19.1 General Aspect

The laws of radioactive decay are the basis of geo- and cosmochronology by nuclear methods. From the variation of the number of atoms with time due to radioactive decay, time differences can be calculated almost exactly. This possibility was realized quite soon after the elucidation of the natural decay series of uranium and thorium. Rutherford was the first to stress the possibility of determining the age of uranium minerals from the amount of helium formed by radioactive decay. Dating by nuclear methods is applied with great success in many fields of science, but mainly in archeology, geology, mineralogy, and cosmochemistry, and various kinds of "chronometers" are available. Two kinds of dating by nuclear methods can be distinguished:

- dating by measuring the radioactive decay of cosmogenic radionuclides, such as ^{3}H or ^{14}C;
- dating by measuring the daughter nuclides formed by the decay of primordial mother nuclides (various methods, e.g. K/Ar, Rb/Sr, U/Pb, Th/Pb, Pb/Pb).

All naturally occurring radionuclides can be used for dating. The timescale of applicability depends on the half-life. With respect to the accuracy of the results, it is most favorable if the age to be determined and the half-life $t_{1/2}$ of the radionuclide are on the same order of magnitude. In general, the lower limit is about $0.1 \cdot t_{1/2}$ and the upper limit about $10 \cdot t_{1/2}$. Therefore, the long-lived mother nuclides of the uranium, thorium, and actinium decay series, and other long-lived naturally occurring radionuclides such as ^{40}K and ^{87}Rb, are most important for application in geology and cosmology.

The attainment of *radioactive equilibria* in the decay chains depends on the longest-lived daughter nuclides in the series. These are ^{234}U ($t_{1/2} = 2.455 \cdot 10^5$ years), ^{228}Ra ($t_{1/2} = 5.75$ years), and ^{231}Pa ($t_{1/2} = 3.276 \cdot 10^4$ years) in the uranium ($4n + 2$), thorium ($4n$), and actinium ($4n + 3$) series, respectively. After about 10 half-lives of these radionuclides, equilibrium is practically established (Sections 7.3 and 7.4), and dating on the basis of radioactive equilibrium is possible.

On the other hand, the concentration of stable decay products, such as ^{4}He, ^{206}Pb, ^{208}Pb, ^{207}Pb, ^{40}Ar (daughter of ^{40}K), and ^{87}Sr (daughter of ^{87}Rb), increases

Nuclear and Radiochemistry: Fundamentals and Applications,
Fourth Edition. Jens-Volker Kratz.

continuously with time. If one stable atom (subscript 2) is formed per radioactive decay of the mother nuclide (subscript 1), the number of stable radiogenic atoms is

$$N_2 = N_1^0 - N_1 = N_1^0(1 - e^{-\lambda t}) = N_1(e^{\lambda t} - 1) \tag{19.1}$$

(N_1^0 is the number of atoms of the mother nuclide at $t = 0$.) For dating, N_2 and N_1 have to be determined. If several stable atoms are formed per radioactive decay of the mother nuclide, as in the case of ^{4}He formed by radioactive decay of ^{238}U, ^{232}Th, ^{235}U, and their daughter nuclides, the number of stable radiogenic atoms is

$$N_2(\mathrm{He}) = n(N_1^0 - N_1) = nN_1^0(1 - e^{-\lambda t}) = nN_1(e^{\lambda t} - 1) \tag{19.2}$$

where n is the number of ^{4}He atoms produced in the decay series.

The following methods of dating by nuclear methods can be distinguished: Measurements of

- cosmogenic radionuclides;
- terrestrial mother/daughter nuclide pairs;
- members of the natural decay series;
- isotope ratios of stable radiogenic isotopes;
- radioactive disequilibria;
- fission tracks.

The main problems with the application of cosmogenic radionuclides are knowledge of the production rate during the time span of interest and the possibility of interferences (e.g. by nuclear explosions). For the other methods, it is important whether the systems are closed or open, that is, whether nuclides involved in the decay processes (mother nuclides, daughter nuclides, or α particles in the case of measurement of He) are lost or enter the system during the time period of interest.

The methods will be discussed in more detail in the following sections. Nonnuclear methods of dating such as thermoluminescence and electron spin resonance (ESR) will not be dealt with.

19.2 Cosmogenic Radionuclides

Cosmogenic radionuclides applicable for dating are listed in Table 19.1. The radionuclides are produced at a certain rate by the interaction of cosmic rays with the components of the atmosphere, mainly in the stratosphere. If the intensity of cosmic rays (protons and neutrons) can be assumed to be constant, the production rate of the radionuclides listed in Table 19.1 is also constant. The cosmogenic radionuclides take part in the various natural cycles on the surface of the Earth (water cycle, CO_2 cycle) and are incorporated in various organic and inorganic products of these cycles, such as plants, sediments, and glacial ice. If no exchange takes place, the activity of the radionuclides is a measure of the age.

The tritium atoms formed in the stratosphere are transformed into HTO and enter the water cycle as well as the various water reservoirs, such as surface waters, groundwaters, glaciers, and polar ice. This offers, in principle, the possibility of

Table 19.1 Cosmogenic radionuclides applicable for dating.

Radio-nuclide	Production	Decay mode and half-life (yr)	Production rate (atoms m^{-2} yr^{-1})	Range of dating (yr)	Application
^{3}H (T)	$^{14}N(n, t)\,^{12}C$	β^-, 12.323	$\approx 1.3 \cdot 10^{11}$	0.5–80	Water, ice
^{14}C	$^{14}N(n, p)\,^{14}C$	β^-, 5730	$\approx 7 \cdot 10^{11}$	$2.5 \cdot 10^{2}$–$4 \cdot 10^{4}$	Archeology, climatology, geology (carbon, wood, tissue, bones, carbonates)
^{10}Be	Interaction of p and n with ^{14}N and ^{16}O	β^-, $1.6 \cdot 10^{6}$	$\approx 1.3 \cdot 10^{10}$	$7 \cdot 10^{4}$–10^{7}	Sediments, glacial ice, meteorites
^{26}Al	Interaction of cosmic rays with ^{40}Ar	β^+, $7.16 \cdot 10^{5}$	$\approx 4.8 \cdot 10^{7}$	$5 \cdot 10^{4}$–$5 \cdot 10^{6}$	Sediments, meteorites
^{32}Si	Interaction of cosmic rays with ^{40}Ar	β^-, 172	$\approx 5 \cdot 10^{7}$	10–10^{3}	Hydrology, ice
^{36}Cl	Interaction of cosmic rays with ^{40}Ar	β^-, $3.0 \cdot 10^{5}$	$(4.5–6.5) \cdot 10^{8}$	$3 \cdot 10^{4}$–$2 \cdot 10^{6}$	Hydrology, water, glacial ice
^{39}Ar	Interaction of cosmic rays with ^{40}Ar	β^-, 269	$\approx 4.2 \cdot 10^{11}$	10^{2}–10^{4}	—

determining the age of samples of various kinds, for example, groundwaters, polar ice, or old wine. However, from the thermonuclear explosions carried out in the atmosphere, mainly in 1958 and in 1961–1962, large quantities of T have been set free into the atmosphere causing an increase in the T:^{1}H ratio in the atmosphere from the natural value of several 10^{-18} up to about 1000 times this natural value at some places in the northern hemisphere. In the meantime, the concentration of T in the atmosphere has decreased considerably due to radioactive decay and transfer into the water reservoirs; however, it is still higher than the natural value. This restricts reliable tritium dating appreciably. However, the tritium method is successfully applied for the dating of glacier and polar ice in layers in which the influence of nuclear explosions is negligible. T may be measured either directly, preferably after preconcentration by multistage electrolytic decomposition of water samples, or by sampling the ^{3}He formed by the decay of T.

Formation of ^{14}C by the interaction of cosmic rays with the nitrogen in the atmosphere was proved in 1947 by W.F. Libby, who also demonstrated the applicability of ^{14}C dating in the following years. The half-life of ^{14}C is very favorable for dating archeological samples in the range of about 250–40 000 years. The ^{14}C atoms are rather quickly oxidized in the atmosphere to CO_2, which is incorporated by the

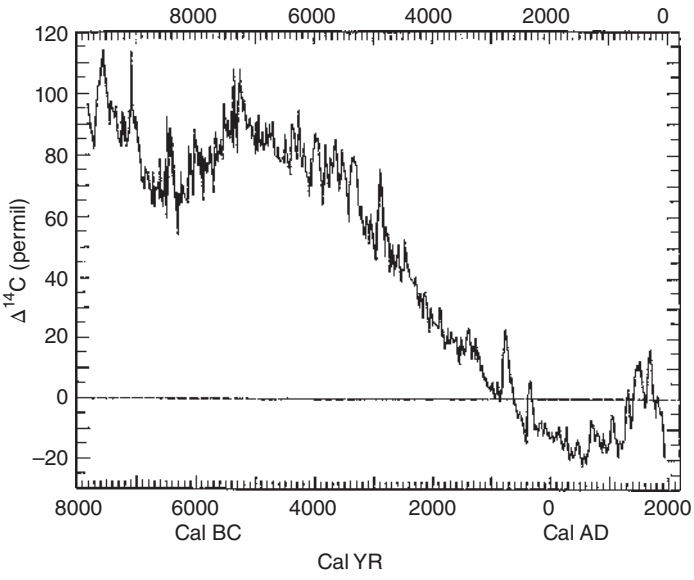

Figure 19.1 Atmospheric $\Delta^{14}C$ during the past 10 000 years. $\Delta^{14}C$ is the deviation of the actual ^{14}C specific activity (in permil) from the ^{14}C specific activity based on a constant production rate (Stuiver et al. 1986). Source: von Gunten (1995), figure 2 (p. 307)/De Gruyter.

process of assimilation into plants and via the food chain into animals and humans. With the death of living things, the uptake of ^{14}C ends, and its activity decreases with the half-life, provided that no exchange of carbon atoms with the environment takes place. ^{14}C dating is based on the assumption that the ^{14}C:^{12}C ratio in living things is identical with that in the atmosphere and that this ratio has been constant in the atmosphere during the period of time considered. The second assumption, however, is not strictly correct. A periodic variation of the ^{14}C:^{12}C ratio with a period of about $9 \cdot 10^3$ years, and an amplitude of about $\pm 5\%$ is correlated with the variation of the magnetic field of the Earth causing changes in the intensity and composition of cosmic radiation and consequently in the production rate of ^{14}C. Furthermore, the $^{14}CO_2$ concentration in the atmosphere is also changing with temperature and climate on the Earth, because the exchange equilibria between the atmosphere and the various CO_2 reservoirs in the biosphere and the oceans vary with temperature. Calibrations of the ^{14}C dating method, Figure 19.1, have been done by dendrochronology (tree-ring counting) establishing a variation in the ^{14}C production rate of about 10% during the past 10 000 years (Stuiver et al. 1986). Based on these calibration data, a Swiss research team under M. Schwikowski, using carbonaceous particles ($\mu g\, l^{-1}$) from biogenic emissions contained in a glacier ice core, was able to date, using ^{14}C accelerator mass spectrometry (AMS), the oldest alpine ice from Colle Gnifetti (Monte Rosa) to over 10 000 years.

Of the total amount of exchangeable ^{14}C, about 1.5% is in the atmosphere, 2% in the terrestrial biosphere, 3% in humus, 4% in the form of dissolved organic matter, and the remainder (about 90%) in the form of carbonate and hydrogen carbonate

in the oceans. Whereas the equilibration of ^{14}C between the atmosphere and the terrestrial components takes about 30–100 years, equilibration with the deep layers of the oceans takes up to about 2000 years. The determination of the ^{14}C:^{12}C ratio allows the calculation of the residence time of ^{14}C in the various reservoirs.

Drastic changes in the ^{14}C:^{12}C ratio have been caused by human activities since the beginning of the industrial age. On the one hand, by the combustion of fossil fuels, such as carbon, oil, petrol, and natural gas, large amounts of ^{14}C-free CO_2 are set free leading to a dilution of $^{14}CO_2$ in the atmosphere and a decrease in the ^{14}C:^{12}C ratio by about 2%. On the other hand, an opposite and much greater change in the ^{14}C:^{12}C ratio in the atmosphere was caused by nuclear explosions. The neutrons liberated by these explosions led to a sharp increase of the ^{14}C production in the upper layers of the atmosphere, and the ^{14}C:^{12}C ratio increased by a factor of about 2 in the northern hemisphere in 1962–1963. With respect to these effects, the relatively small amounts of $^{14}CO_2$ liberated from nuclear power stations and reprocessing plants can be neglected. In the meantime, the ^{14}C:^{12}C ratio decreased to a value that is about 20% higher than the original value. Large amounts of the $^{14}CO_2$ produced by nuclear explosions have been transferred to the reservoirs, with the result that the ^{14}C:^{12}C ratio in the surface layers of the oceans has increased by about 20%. These changes, however, have no influence on dating by the ^{14}C method, because samples suitable for application of this method are more than 100 years old.

For the measurement of ^{14}C, proportional counters and liquid scintillation techniques are most suitable. The samples are oxidized in a stream of air or oxygen to CO_2, which is carefully purified, stored to allow decay of ^{222}Rn, and introduced into a proportional counter. CO_2 may also be converted into CH_4 by reaction with hydrogen at 475 °C or into C_2H_2 by reaction with Li to Li_2C_2 at 600 °C, followed by decomposition of Li_2C_2 by water to C_2H_2. By transformation into CH_4 or C_2H_2, the purification procedures necessary in the case of CO_2 are avoided. For measurement in a liquid scintillation counter, CO_2 is usually transformed into an organic compound, for instance, by reaction to C_2H_2 as described earlier and catalytic trimerization of C_2H_2 to C_6H_6. The measuring times are usually rather long, on the order of many hours, in order to keep the statistical errors low. Various kinds of samples can be dated by the ^{14}C method (Table 19.1). Depending on the carbon content, samples weighing from about ten to several hundred grams are needed. In order to obtain reliable results, it is very important that the samples are free from impurities containing carbon of recent origin.

The ratio of the carbon isotopes ^{14}C:^{13}C:^{12}C in samples of recent origin is about $1 : 0.9 \cdot 10^{10} : 0.8 \cdot 10^{12}$. This ratio cannot be measured by classical mass spectrometry (MS), because, by this method, ions of the same mass such as $^{14}C^+$, $^{14}N^+$, $^{13}CH^+$, and $^{12}CH_2^+$ are found at practically the same position. This restricts the measurement of isotope ratios in the case of ^{14}C to about 10^{-9}. However, in recent years, new developments in mass spectrometry have made it possible to measure isotope ratios down to the order of about 10^{-15}. In AMS, the samples are bombarded with ions (e.g. Cs^+) from an ion source, negative ions such as $^{14}C^-$ and $^{12}C^-$ are formed and pass an accelerator (usually of the tandem type), and there are several separation steps in which ions of the same mass containing different elements are sorted.

By application of AMS, ^{26}Al, ^{32}Si, ^{36}Cl, ^{41}Ca, and ^{129}I were identified in 1979–1980 as cosmogenic radionuclides.

^{10}Be is found in concentrations of about $(3–7) \cdot 10^4$ atoms g^{-1} of Antarctic ice. Because of the longer half-life compared to that of ^{14}C, dating for a longer period of time (up to about 10^7 years) is possible. On the other hand, determination of ^{10}Be is more difficult, because its production rate is lower (Table 19.1).

The rate of cosmogenic production of ^{26}Al is still lower than that of ^{10}Be, and in fresh sediments, the ratio ^{26}Al:^{27}Al is on the order of 10^{-14}, whereas the ratio ^{10}Be:^{9}Be is on the order of 10^{-8}. This makes the determination of ^{26}Al in terrestrial samples very difficult. On the other hand, the production rate of ^{26}Al in meteorites and samples from the surface of the Moon is comparable to that of ^{10}Be, because, in these samples, low-energy protons from the Sun contribute appreciably to the production of ^{26}Al. Measurement of the ^{26}Al:^{10}Be ratio in extraterrestrial samples provides information about their history.

^{32}Si is produced in the atmosphere by the reaction ^{40}Ar(p, p2α)^{32}Si. It is oxidized to SiO_2 and stays in the atmosphere for some time in the form of fine particles, until it comes down with the precipitations. It is found in surface waters, glaciers, polar ice, and marine sediments. Due to the low production rate of ^{32}Si (Table 19.1), the measurement of its radioactivity in water samples requires the processing of large amounts of water or ice on the order of tons, from which hydrous $SiO_2 \cdot xH_2O$ has to be separated. ^{32}Si changes into stable ^{30}S by a sequence of two transformations:

$$^{32}\mathrm{Si} \xrightarrow{\beta^- (0.2\ \mathrm{MeV};172\ \mathrm{years})} {}^{32}\mathrm{P} \xrightarrow{\beta^- (1.7\ \mathrm{MeV};14.26\ \mathrm{days})} {}^{32}\mathrm{S}$$

^{32}P is most suitable for activity measurements, because of the relatively high energy of the β^- particles. However, application of AMS is much more favorable for the determination of ^{32}Si, because smaller samples can be used, but elaborate separation techniques are also required. ^{32}Si is applicable for dating groundwater, ocean water, glacier ice, polar ice, and sediments. Its half-life of 172 years offers some advantages over other radionuclides with respect to dating of ages up to about 10^3 years.

^{36}Cl is produced in the atmosphere by the (n, p) reaction with ^{36}Ar and (p, nα) reaction with ^{40}Ar. It also comes down with the precipitations. Appreciable amounts of ^{36}Cl have been formed in the atmosphere by the neutrons liberated by nuclear explosions. Consequently, the ^{36}Cl deposition by precipitations increased from about 20 to about 5000 atoms m^{-2} s^{-1} in the years 1955–1962, and since then it has decreased slowly to the original value.

Because ^{36}Cl stays predominantly in the aqueous phase, it is mainly applied for hydrological studies, for example, on the time of transport of water within deep layers, the rate of erosion processes, and the age of deep groundwaters. In the case of groundwaters without access to cosmogenic ^{36}Cl, the production of ^{36}Cl by the reaction ^{35}Cl(n, γ) ^{36}Cl induced by neutrons from spontaneous fission of uranium contained in granite has to be taken into account.

^{39}Ar is produced in the atmosphere by the nuclear reaction ^{40}Ar(n, 2n)^{39}Ar. Due to its properties as a noble gas, about 99% of the cosmogenic ^{39}Ar stays in the atmosphere and the applicability of this radionuclide for dating purposes is very limited.

The amounts of ^{41}Ca ($t_{1/2} \approx 10^5$ years) produced in the atmosphere are extremely small. Only at the surface of the Earth is some ^{41}Ca formed by the reaction ^{40}Ca(n, γ)^{41}Ca; however, the ratio ^{41}Ca:^{40}Ca is only on the order of $0.8 \cdot 10^{-14}$. Because of this low concentration, measurement of ^{41}Ca is very difficult. It is of some interest for the dating of bones in the interval between about $5 \cdot 10^4$ and 10^6 years.

19.3 Terrestrial Mother/Daughter Nuclide Pairs

Terrestrial mother/daughter nuclide pairs suitable for dating are given in Table 19.2. Dating by means of these nuclide pairs requires evaluation of Eq. (19.1). In doing this, it has to be taken into account that, in general, at time $t = 0$, stable nuclides identical with the radiogenic nuclides are already present. This leads to the equation

$$N_2 = N_2^0 + N_1(e^{\lambda t} - 1) \tag{19.3}$$

where N_2 is the total number of atoms of the stable nuclide (2), N_2^0 is the number of atoms of this nuclide present at $t = 0$, and $N_1(e^{-\lambda t} - 1)$ is the number of radiogenic atoms formed by decay of the mother nuclide (1).

In practice, two approaches are used: independent determination of N_2 and N_1 or simultaneous determination of N_2 and N_1 by mass spectrometry (MS). The second approach is not applicable if the properties of the mother nuclide and the daughter nuclide are very different, for example, in the case of dating by the ^{40}K/^{40}Ar method or by measuring ^{4}He formed by radioactive decay. Both methods require additional determination of the unknown number N_2^0; however, in special cases N_2^0 can be neglected.

N_2 and N_1 can be determined independently by various analytical methods. Isotopic dilution (addition of a known amount of an isotope followed by MS) is often applied.

Table 19.2 Terrestrial pairs of nuclides applicable for dating.

Nuclide pair	Decay mode of the mother nuclide	Half-life of the mother nuclide (yr)	Range of dating (yr)	Application
^{40}K/^{40}Ar	β^- (89%)	$1.28 \cdot 10^9$	10^3–10^{10}	Minerals
	$\varepsilon + \beta^+$ (11%)			
^{87}Rb/^{87}Sr	β^-	$4.8 \cdot 10^{10}$	$8 \cdot 10^6$–$3 \cdot 10^9$	Minerals, geochronology, geochemistry
^{147}Sm/^{143}Nd	α	$1.06 \cdot 10^{11}$	10^8–10^{10}	Minerals, geochronology, geochemistry
^{176}Lu/^{176}Hf	β^- (97%)	$3.8 \cdot 10^{10}$	10^7–10^9	Geochemistry
	ε (3%)			
^{187}Re/^{187}Os	β^-	$5 \cdot 10^{10}$	10^6–10^{10}	Minerals

In the $^{40}K/^{40}Ar$ method, the samples are heated to melting in order to drive out all Ar and a measured quantity of ^{38}Ar (>99% enriched) is added (method of isotope dilution). After purification, the isotope ratios ^{40}Ar:^{38}Ar and ^{38}Ar:^{36}Ar are measured by means of MS. From the isotope ratios ^{40}Ar:^{38}Ar and ^{38}Ar:^{36}Ar in the added sample and in the air, the number of radiogenic ^{40}Ar atoms is calculated. The concentration of K in the sample is determined independently by the usual analytical methods. The main problem with the $^{40}K/^{40}Ar$ method is the possibility that some ^{40}Ar may have escaped or that additional amounts of ^{40}Ar may have entered the system in the course of time.

Simultaneous determination of N_2 and N_1 is conveniently performed by use of a stable non-radiogenic nuclide as the reference nuclide (r) and measurement of the ratios N_2/N_r and N_1/N_r. Division of Eq. (19.3) by N_r gives

$$\frac{N_2}{N_r} = \frac{N_2^0}{N_r} + \frac{N_1}{N_r}(e^{\lambda t} - 1) \tag{19.4}$$

The value of N_2^0/N_r can be assessed or found by iterative application of Eq. (19.4). For constant values of t (the same age of samples), the plot of N_2/N_r as a function of N_1/N_r gives a straight line with slope $(e^{\lambda t} - 1)$ intersecting the ordinate at N_2/N_r. Such a plot is called an *isochron* and is used for evaluation, in particular for identification of samples of the same age.

According to Eq. (19.4), the age of the sample is

$$t = \frac{t_{1/2}}{\ln 2} \ln \left[1 + \frac{N_2/N_1/ - N_2^0/N_r}{N_1/N_r} \right] \tag{19.5}$$

where $t_{1/2}$ is the half-life of the radioactive mother nuclide.

Simultaneous determination of mother and daughter nuclide by MS is applied in the $^{87}Rb/^{87}Sr$ method. The stable Sr isotope ^{86}Sr serves as the reference nuclide. $^{87}Rb/^{87}Sr$ dating has been used for many kinds of minerals, magmatic rocks, and sedimentary rocks of various origins. An example is shown in Figure 19.2 with the Rb/Sr isochron for a gneiss sample from Greenland. The slope of the isochron shows an age of $3.66 \pm 0.09 \cdot 10^9$ years. The intercept with the ordinate indicates the $^{87}Sr/^{87}Rb$ ratio at $t = 0$.

In the $^{147}Sm/^{143}Nd$ method, mother and daughter nuclides are also determined simultaneously by MS. ^{144}Nd serves as the reference nuclide. The method has also found application in geochronology, mainly for dating very old minerals.

Applications of the $^{176}Lu/^{176}Hf$ method and of the $^{187}Re/^{187}Os$ method have no advantages over the methods mentioned previously. For simultaneous determination of the mother and daughter nuclide by MS, suitable non-radiogenic nuclides have to be selected as reference nuclides. In the case of Hf, the use of ^{177}Hf is preferred for this purpose. However, the main drawbacks of the $^{176}Lu/^{176}Hf$ method are the low concentration of Lu in minerals ($<1\ mg\ kg^{-1}$) and the difficulties in measuring Hf by MS due to the low ionization yield. In the $^{187}Re/^{187}Os$ method, ^{186}Os is used as the reference nuclide. As in the case of dating by the $^{176}Lu/^{176}Hf$ method, the low concentration of Re in minerals (on average $\approx 1\ ng\ kg^{-1}$) is a basic drawback with respect to broad application. The method has been used for dating meteorites and

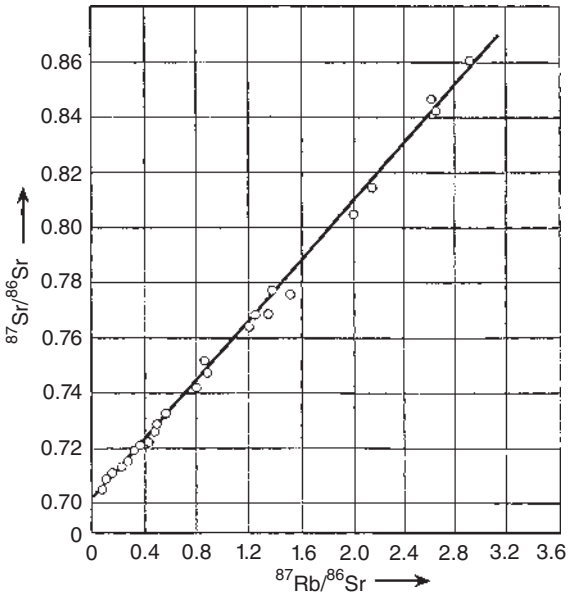

Figure 19.2 Rb/Sr isochron for a gneiss sample from Greenland. The slope of the isochron gives an age of $3.66 \pm 0.09 \cdot 10^9$ years. The intercept with the ordinate indicates the $^{87}Sr/^{87}Rb$ ratio at $t = 0$ (from Moorbath et al. 1972). Source: von Gunten (1995), figure 8 (p. 310)/De Gruyter.

minerals containing higher amounts of Re. For both systems, independent determination of mother and daughter nuclides is also applied. Because of the low concentrations, elaborate instrumental techniques are required.

19.4 Natural Decay Series

The atomic ratios ^{206}Pb:^{238}U, ^{207}Pb:^{235}U, and ^{208}Pb:^{232}Th due to radioactive decay of the mother nuclides are plotted in Figure 19.3 as a function of the age, provided that no losses have occurred. Application of the natural decay series for dating is summarized in Table 19.3. The $^{238}U/^{206}Pb$ method and the $^{232}Th/^{208}Pb$ method offer the possibility of determining the ages of many minerals in the range of 10^6–10^{10} years with rather high precision. Taking into account the long-lived radionuclides, radioactive equilibrium is established after about 10^6 years in the case of the uranium and actinium series, and after about 10 years in the case of the thorium series. ^{235}U decays faster than ^{238}U, and the ratio of the production rates of ^{207}Pb and ^{206}Pb decreases appreciably with time. Therefore, variations in the ratio ^{207}Pb:^{206}Pb indicate geological processes. In contrast to ^{208}Pb, ^{207}Pb, and ^{206}Pb, ^{204}Pb is not radiogenic. This is the reason why Pb isotope ratios are usually related to ^{204}Pb as the reference nuclide.

Three kinds of systems can be distinguished:

a) Systems losing parts of the members of the decay chains or the radiogenic Pb by diffusion or recrystallization processes (open systems). These losses may be pronounced if the half-lives of the intermediates are relatively long, as in the case of the uranium decay series ($t_{1/2}(^{226}Ra) = 1600$ years, $t_{1/2}(^{222}Rn) = 3.825$ days) or if the incorporation of Pb into the lattice of the mineral is hindered with the

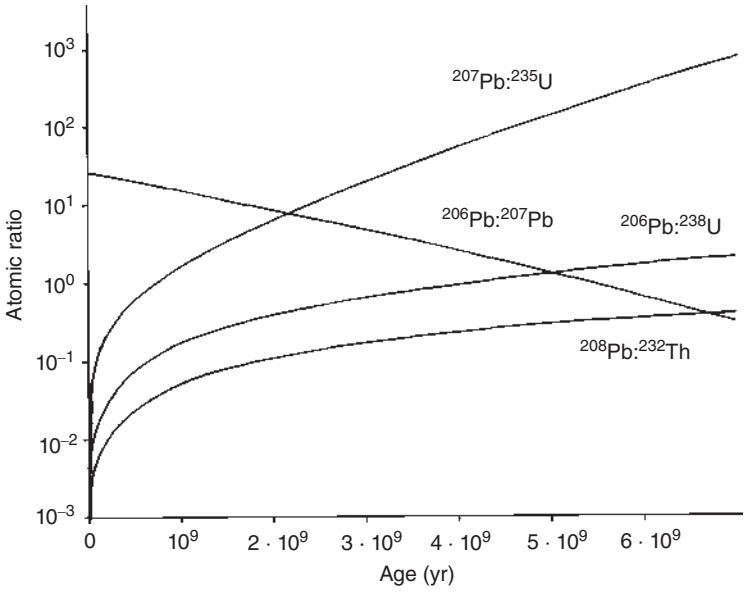

Figure 19.3 Radiogenic Pb isotopes: atomic ratios as a function of age.

Table 19.3 Natural decay series applicable for dating.

Decay series	Decay mode of the mother nuclide	Half-life of the mother nuclide (yr)	Range of dating (yr)	Application
$^{238}U\ldots^{226}Ra\ldots^{206}Pb$	α	$4.468 \cdot 10^9$	10^6–10^{10}	Minerals, geology, geochemistry
$^{235}U\ldots^{207}Pb$	α (sf: $3.7 \cdot 10^{-7}$%)	$7.038 \cdot 10^8$	10^6–10^{10}	Minerals, geology, geochemistry
$^{232}Th\ldots^{208}Pb$	α	$1.405 \cdot 10^{10}$	10^6–10^{10}	Minerals, geology, geochemistry
$^{210}Pb\ldots^{206}Pb$	β^-	22.3	20–150	Ice, exchange with the atmosphere

consequence of migration of Pb out of the crystals. An example is zircon, in which U^{4+} ions form solid solutions by substituting Zr^{4+}, whereas Pb^{2+} ions leave the lattice. Dating of these open systems encounters severe difficulties. Special correction methods have been proposed.

b) Systems for which the loss of members of the decay chains can be neglected and in which the concentration of the mother nuclide can be taken as a measure of the age. For these systems, Eq. (19.4) can be applied in the forms

$$\left(\frac{^{206}Pb}{^{204}Pb}\right) = \left(\frac{^{206}Pb}{^{204}Pb}\right)_0 + \left(\frac{^{238}U}{^{204}Pb}\right)(e^{\lambda(238)t} - 1) \tag{19.6}$$

$$\left(\frac{^{207}\mathrm{Pb}}{^{204}\mathrm{Pb}}\right) = \left(\frac{^{207}\mathrm{Pb}}{^{204}\mathrm{Pb}}\right)_0 + \left(\frac{^{235}\mathrm{U}}{^{204}\mathrm{Pb}}\right)(\mathrm{e}^{\lambda(235)t} - 1) \tag{19.7}$$

$$\left(\frac{^{208}\mathrm{Pb}}{^{204}\mathrm{Pb}}\right) = \left(\frac{^{208}\mathrm{Pb}}{^{204}\mathrm{Pb}}\right)_0 + \left(\frac{^{232}\mathrm{Th}}{^{204}\mathrm{Pb}}\right)(\mathrm{e}^{\lambda(232)t} - 1) \tag{19.8}$$

c) Systems for which the loss of members of the decay chains can be neglected, but in which the concentration of the mother nuclide cannot be taken as a measure of the age, because of loss of U due to oxidation to UO_2^{2+} and dissolution. For these systems, the Pb/Pb method of dating is applied; this will be discussed in more detail in Section 19.5.

A practical application of Eqs. (19.6)–(19.8) is the calculation of the age of the Solar System. MS analysis of meteorites containing negligible amounts of U gives the following values for the isotope ratios of the Pb isotopes: ^{206}Pb:^{204}Pb = 9.4 and ^{207}Pb:^{204}Pb = 10.3. If these values are assumed to be the initial isotope ratios at the time of formation of the Solar System, the age is obtained from the present isotope ratios of the Pb isotopes in the Solar System and the ratios of the present abundances of U and Pb, for example, by application of Eq. (19.6):

$$t = \frac{1}{\lambda(238)} \ln\left[1 + \frac{(^{206}\mathrm{Pb}/^{204}\mathrm{Pb}) - (^{206}\mathrm{Pb}/^{204}\mathrm{Pb})_0}{(^{238}\mathrm{U}/^{204}\mathrm{Pb})}\right] \tag{19.9}$$

Dating by means of ^{210}Pb is of special interest with respect to ages in the range between about 20 and 150 years, in particular for dating glacier and polar ice, lake sediments, and climatology. The activity of ^{210}Pb in fresh snow is on the order of 10^{-2} Bq kg^{-1}, and the detection limit is on the order of 10^{-4} Bq kg^{-1}. The source of ^{210}Pb is ^{222}Rn emitted into the air in amounts of about $2 \cdot 10^3$ to $2 \cdot 10^4$ atoms m^{-2} s^{-1}. Some ^{222}Rn is also emitted from volcanoes. In the air, ^{210}Pb is sorbed on aerosols and found in the precipitations (rain or snow), wherein the average activity of ^{210}Pb is about 0.08 Bq kg^{-1}. The concentration of ^{210}Pb in the air and in the precipitations varies considerably within short periods of time and with the seasons; however, the annual amount deposited with the precipitations is relatively constant. It has been found that the concentration of ^{210}Po, the daughter of ^{210}Pb, in the air is appreciably higher than that expected for radioactive equilibrium with ^{210}Pb. This is explained by the emission of relatively large amounts of ^{210}Po, together with sulfur, by volcanoes.

Measurement of the β^- radiation of ^{210}Pb is difficult, because of its low energy, but the α activity of ^{210}Po is easily measurable by α spectrometry (detection limit $\approx 10^{-4}$ Bq) after attainment of radioactive equilibrium and chemical separation. An example of a ^{210}Pb depth profile in sediments of Lake Zurich is presented in Figure 19.4. ^{210}Pb entering lake sediments by settling particles eventually forms a closed system, that is, no exchange with the surrounding environment, in which ^{210}Pb decays with its half-life. The measured ^{210}Pb activity must be corrected to a background activity resulting from ^{210}Pb ("supported ^{210}Pb") directly produced by the decay of radium in the sample. Figure 19.4 also shows the depth profile of a radioactive time marker, ^{137}Cs, from the fallout of atmospheric testing of very large

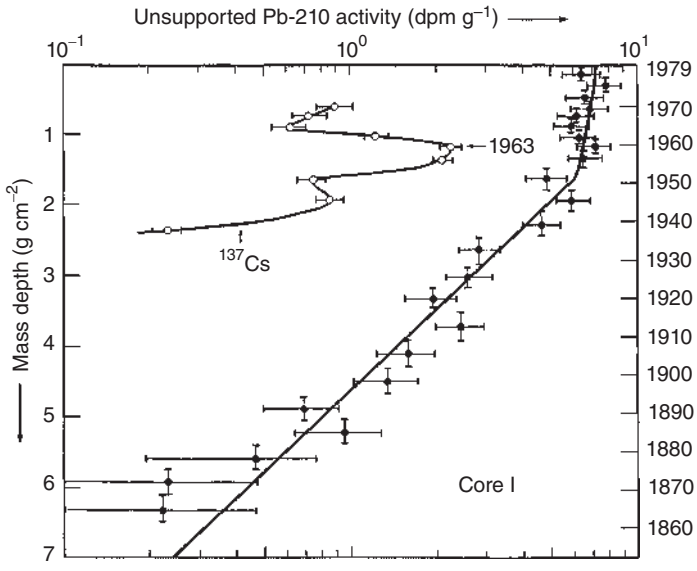

Figure 19.4 Activities of "unsupported" ^{210}Pb and ^{137}Cs from a sediment core of Lake Zurich, Switzerland (Erten et al. 1985). The ^{137}Cs peak enables an absolute dating with ^{210}Pb. Source: von Gunten (1995), figure 1 (p. 307)/De Gruyter.

H-bombs by the USSR around 1962. The relatively narrow ^{137}Cs peak allows the assignment of an absolute timescale to the ^{210}Pb data.

In the early stages of dating by nuclear methods, the measurement of ^{4}He formed by α decay in the natural decay series (nine, six, and seven ^{4}He atoms in the uranium series, the thorium series, and the actinium series, respectively) has been applied. The preferred method was the U/He method, which allows the dating of samples with very low concentrations of U on the order of 1 mg kg^{-1}. Helium produced by α decay is driven out by heating and measured by sensitive methods, for example, by MS. However, it is difficult to ensure the prerequisites of dating by the U/He method: neither ^{4}He nor α-emitting members of the decay series must be lost and no ^{4}He atoms must be produced by other processes such as decay of ^{232}Th and spallation processes in meteorites.

19.5 Ratios of Stable Isotopes

Lead has four stable isotopes, ^{204}Pb, ^{206}Pb, ^{207}Pb, and ^{208}Pb. The stability of ^{204}Pb has been debated, but the half-life is $>10^{17}$ years and, with respect to the age of the Earth and the Universe, ^{204}Pb can be considered to be stable. In the course of the genesis of the elements, certain amounts of the aforementioned four stable isotopes of Pb were formed (primordial Pb). Additional amounts of ^{206}Pb, ^{207}Pb, and ^{208}Pb (radiogenic Pb) were produced by the decay of ^{238}U, ^{235}U, and ^{232}Th, respectively.

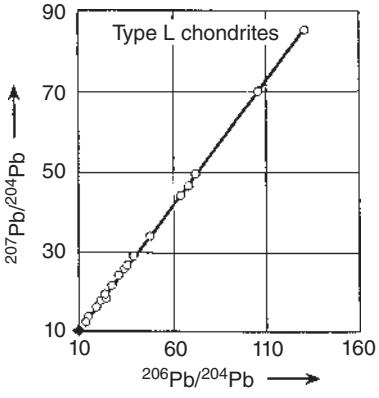

Figure 19.5 $^{206}Pb/^{207}Pb$ isochron of meteorites of L type (○) and a troilite from Canion Diablo (⧫) showing an age of $4.555 \pm 0.014 \cdot 10^9$ years. Source: von Gunten (1995), figure 9a (p. 311)/De Gruyter.

On average, the relative percentages of the Pb isotopes in the Earth's crust are: $^{204}Pb \approx 1.4\%$, $^{206}Pb \approx 24.1\%$, $^{207}Pb \approx 22.1\%$, $^{208}Pb \approx 52.4\%$. These ratios vary considerably with the concentrations of U and Th in the samples and with the age of the samples. For dating minerals, ^{204}Pb is taken as the reference nuclide, and the isotope ratios ^{206}Pb:^{204}Pb, ^{207}Pb:^{204}Pb, and ^{208}Pb:^{204}Pb are determined by MS. If the contents of U or Th are known and losses can be neglected, Eqs. (19.6)–(19.8) can be applied.

However, measurement of the ratios of the Pb isotopes alone (Pb/Pb method) offers the possibilities of dating without knowledge of the contents of U and Th and of taking into account possible losses of U due to oxidation of U^{4+} to UO_2^{2+} by leaching of the latter, by simultaneous application of two or even three of the chronometers $^{238}U/^{206}Pb$, $^{235}U/^{207}Pb$, $^{232}Th/^{208}Pb$. The basis for the Pb/Pb method is given by Eqs. (19.6)–(19.8), knowledge of the ratio ^{235}U:^{238}U as a function of time, and the fact that the ratio Th:U is practically constant for minerals of the same genesis. By this method, additional information about the history of the sample, in particular about losses of U, can also be obtained. Figure 19.5 depicts the $^{206}Pb/^{207}Pb$ isochron of a type L chondrite and a troilite from Canyon Diablo showing an age of 4.555 ± 0.014 years and providing an estimate of the age of the Solar System.

The $^{39}Ar/^{40}Ar$ method is a variant of the $^{40}K/^{40}Ar$ method. For determining the amount of K present in the sample, neutron activation is applied. The sample and a standard of known age (i.e. containing a known ratio ^{40}Ar:^{40}K) are irradiated under the same conditions at a neutron flux of about 10^{14} cm^{-2} s^{-1} for about one day. ^{39}Ar is produced by the nuclear reaction $^{39}K(n, p)^{39}Ar$ and the ratio ^{39}Ar:^{40}Ar is measured by MS. Because the half-life of ^{39}Ar is rather long ($t_{1/2} = 269$ years), its decay after the end of irradiation can be neglected. From the relation

$$\left(\frac{N(39)}{N(40)}\right)_x = \left(\frac{N(39)}{N(40)}\right)_s \frac{\exp(\lambda t_s) - 1}{\exp(\lambda t_x) - 1} \tag{19.10}$$

the age of the sample can be calculated. $N(39)/N(40)$ are the measured isotope ratios ^{39}Ar:^{40}Ar of the sample (x) and the standard (s), λ is the decay constant of ^{39}Ar, and t_s is the known age of the standard. Corrections for the presence of atmospheric ^{40}Ar, for the production of ^{39}Ar by the reaction $^{42}Ca(n, \alpha)^{39}Ar$, for the production of ^{40}Ar by the reaction $^{40}K(n, p)^{40}Ar$, and for losses of ^{39}Ar may be necessary.

19.6 Radioactive Disequilibria

Mother and daughter nuclides of decay series are often separated by natural processes. Such separations are very common if the mother nuclide is dissolved in water (e.g. in the oceans); however, they may also occur in solids. By measuring the decay of the separated daughter nuclide or the growth of the daughter nuclide in the phase containing the mother nuclide, the time can be determined when the separation took place. This provides information about separation processes in minerals and ores and about the formation of sediments in oceans or lakes. The prerequisite of application of radioactive disequilibria is that mother and daughter nuclide exhibit different chemical behavior under the given conditions.

Radioactive disequilibria may be caused by different solubilities of mother and daughter nuclides, by different probabilities of escape, or by different leaching rates due to recoil effects. Examples of different solubilities are U/Th and U/Pa. The probability of escape may be very high in radioactive equilibria with Rn. Recoil effects due to α decay lead to displacement and local lattice defects and may cause higher leaching rates. For instance, a change in the ratio ^{234}U:^{238}U caused by leaching is often observed.

An example of the application of radioactive disequilibria for dating is the $^{234}U/^{230}Th$ method. The chemical properties of U(VI) differ appreciably from those of Th(IV). Whereas UO_2^{2+} ions are found in natural waters, in particular in the oceans, in the form of $[UO_2(CO_3)_3]^{4-}$ ions, Th^{4+} ions are completely hydrolyzed and easily sorbed on particulates. With these, they settle down in the sediments. On the other hand, corals and other inhabitants of the oceans form their skeletons by the uptake of elements dissolved in the sea, for example, U together with Ca, but not Th. In this way, ^{234}Th (daughter of ^{238}U) and the long-lived ^{230}Th are separated, and if the skeletons can be considered to be closed systems, the in-growth of ^{230}Th is a measure of the age.

The $^{235}U/^{231}Pa$ method is based on the same principles. The chemical properties of U(VI) and Pa(V) differ even more than those of U(VI) and Th(IV).

Radioactive disequilibria are applied in geochemistry for dating crystallization processes by measuring the ratio ^{238}U:^{230}Th. Excess ^{230}Th or ^{231}Pa found in marine sediments allows the dating of these sediments and determination of the sedimentation rate. In archeology, the $^{234}U/^{230}Th$ method is applied for dating carbonates used by humans or for dating bones or teeth. U is taken up from natural waters during formation of the bones, and the content of ^{230}Th gives information about the age.

19.7 Fission Tracks

Fission tracks are observed in solids due to spontaneous or neutron-induced fission of heavy nuclei. The primary tracks can be made visible under an optical microscope by etching, from which track diameters on the order of 0.1–0.5 μm are obtained. The method is the same as that used with track detectors (Section 9.11). The length

of the fission tracks depends on the nature of the minerals and varies between about 10 and 20 μm. With respect to dating, the only important source of fission tracks is spontaneous fission of ^{238}U. Spontaneous fission of other naturally occurring heavy nuclides gives no measurable density of fission tracks; neutron-induced fission is, in general, negligible; and the tracks of recoiling atoms due to α decay are very short (on the order of 0.01 μm).

The track density (number of fission tracks per square centimeter) in a mineral is a function of the concentration of U and the age of the mineral. For the purpose of dating, a sufficient number of tracks must be counted, which means that the concentration of U or the age (or both) should be relatively high. Usually, first the fission track density due to spontaneous fission of ^{238}U is counted, then the sample is irradiated at a thermal neutron flux density Φ_n in order to determine the concentration of U in the sample by counting the fission track density due to neutron-induced fission of ^{235}U. The age t of the mineral is calculated from the formula

$$t = \frac{1}{\lambda(238)} \ln \left[1 + 7.252 \cdot 10^{-3} \frac{D(\mathrm{sf})}{D(\mathrm{n,f})} \frac{\lambda(238)}{\lambda(\mathrm{sf},238)} \sigma_{\mathrm{n,f}} \Phi_n t_i \right] \tag{19.11}$$

where $\lambda(238)$ is the decay constant of ^{238}U, $7.252 \cdot 10^{-3}$ is the isotope ratio ^{235}U:^{238}U, D(sf) and D(n, f) are the fission track densities due to spontaneous fission of ^{238}U and neutron-induced fission of ^{235}U, respectively, $\sigma_{\mathrm{n,f}}$ is the cross section of fission of ^{235}U by thermal neutrons, and t_i is the irradiation time. In the case of homogeneous distribution of U in the sample, the values of D(sf) and D(n, f) can be determined in different aliquots of the sample. In the case of heterogeneous distribution of U, D(sf) and the sum $D(\mathrm{sf}) + D(\mathrm{n,f})$ must be counted in the same sample. D(n, f) may also be determined by an external detector, for example, a plastic foil that is firmly pressed onto a polished surface of the sample. After irradiation of the combination of sample plus detector, the fission tracks are counted in the detector and multiplied by the factor 2 to obtain D(n, f). The factor 2 takes into account the different geometric conditions: 2π for the detector and 4π for the sample.

Fission tracks are influenced by recrystallization processes in the solids (aging), the rate of which increases appreciably with temperature. At higher temperatures, fission tracks may anneal quantitatively, but recrystallization processes may also be effective at normal temperatures, for example, under the influence of pressure or of water. By comparing the ages calculated on the basis of fission track densities to those obtained by other methods, information can be obtained about the temperatures to which the minerals have been exposed in the course of time.

Unusually high fission track densities are found in the vicinity of nuclear explosions and at the natural reactors at Oklo.

References

More Specialized

von Gunten, H.R. (1995). Radioactivity: a tool to explore the past. *Radiochim. Acta* 70/71: 305.

Moorbath, S., O'Nions, R.K., Parkhurst, R.J. et al. (1972). Further rubidium strontium age determinations on the very early precambrian rocks of Godthaab District West Greenland. *Nat. Phys. Sci.* 240: 78.

Stuiver, M., Kromer, B., Becker, B., and Ferguson, C.W. (1986). Radiocarbon age calibration back to 13.300 years BP and the ^{14}C age matching of German oak and US Bristlecone pine chronologies. *Radiocarbon* 28: 969.

General

Erten, H.N., von Gunten, H.R., Rössler, E., and Sturm, M. (1985). Dating of sediments from Lake Zürich (Switzerland) with ^{210}Pb and ^{137}Cs. *Schweiz. Z. Hydrol.* 47: 11.

Further Reading

General

Hahn, O. (1936). *Applied Radiochemistry*. Ithaca, NY: Cornell University Press.

Wahl, A.C. and Bonner, N.A. (1951). *Radioactivity Applied to Chemistry*. New York: Wiley.

Faul, H. (1954). *Nuclear Geology*. New York: Wiley.

Aldrich, L.T. and Wetherill, G.W. (1958). Geochronolgy by radioactive decay. *Annu. Rev. Nucl. Sci.* 8: 257.

International Atomic Energy Agency (1963). *Symposium on Radioactive Dating*. Vienna: IAEA.

Haissinsky, M. (1964). *Nuclear Chemistry and its Applications*. Reading, MA: Addison-Wesley.

Hamilton, E.I. and Ahrens, L.H. (1965). *Applied Geochronology*. New York: Academic Press.

Roth, E. (1968). *Chimie Nucléaire Appliquée*. Paris: Masson.

York, D. and Farquhar, R.M. (1972). *The Earth's Age and Geochronology*. Oxford: Pergamon.

Harper, C.T. (1973). *Geochronology*. Stroudsburg, PA: Dowden, Hutchinson and Ross.

Faure, G. (1977). *Principles of Isotope Geology*. New York: Wiley.

Roth, E. and Poty, B. (eds.) (1985). *Méthodes de Datation par les Phénomènes Nucléaires Naturels – Applications*. Paris: Masson.

Durrance, E.M. (1986). *Radioactivity in Geology: Principles and Applications*. Chichester: Ellis Horwood.

Geyh, M.A. and Schleicher, H. (1990). *Absolute Age Determination*. Berlin: Springer-Verlag.

Bowen, R. (2011). Radioactive dating methods. In: *Handbook of Nuclear Chemistry*, 2e, vol. 2 (eds. A. Vértes, S. Nagy, Z. Klencsár, et al.), 761. Berlin: Springer-Verlag.

More Specialized

Libby, W.F. (1955). *Radiocarbon Dating*. Chigaco: University of Chicago Press.

Wetherill, G.W. (1956). Discordant uranium-lead ages I. *Trans. Am. Geophys. Union* 37: 320.

Maddock, A.G. and Willis, E.H. (1961). Atmospheric activities and dating procedures. *Adv. Inorg. Chem. Radiochem.* 3: 287.

Perlam, I., Asaro, I., and Michel, H.V. (1972). Nuclear applications in art and archaeology. *Annu. Rev. Nucl. Sci.* 22: 383.

Muller, R.A. (1979). Radioisotope dating with accelerators. *Phys. Today* 32 (2): 23.

Litherland, A.E. (1980). Ultrasensitive mass spectrometry with accelerators. *Annu. Rev. Nucl. Part. Sci.* 30: 437.

Currie, L.A. (1982). *Nuclear and Chemical Dating Techniques: Interpreting the Environmental Record*, ACS Symposium Series 176. Washington, DC: American Chemical Society.

Aitken, J. (1984). *Physics and Archaeology*, 2e. Oxford: Clarendon Press.

Furlan, G., Cassola Guida, P., and Tuniz, C. (eds.) (1986). *New Paths in the Use of Nuclear Techniques for Art and Archaeology*. Singapore: World Scientific.

Ivanovich, M. and Harmon, R.S. (1992). *Uranium-Series Disequilibrium: Applications to Earth, Marine and Environmental Sciences*, 2e. Oxford: Clarendon Press.

Nierenberg, W.A. et al. (1992). *Encyclopedia of Earth System Science*. New York: Academic Press.

Huber, G., Passler, G., Wendt, K. et al. (2003). Accelerator mass spectrometry (AMS). In: *Handbook of Radioactivity Analysis*, Chapter 10, Radioisotope Mass Spectrometry (ed. M.F. L'Annunziata), 799. San Diego, CA: Elsevier.

20

Radioanalysis

20.1 General Aspects

The low detection limits of radioactive substances are very attractive for use in analytical chemistry. In principle, a single radioactive atom can be detected provided that it is measured at the moment of its decay. In practice, however, a greater number of radioactive atoms is necessary to measure their radioactivity with a sufficiently low statistical error. The mass m of a radionuclide and its activity A are correlated by the half-life $t_{1/2}$:

$$m = A\frac{M}{\ln 2N_{\mathrm{Av}}}t_{1/2} \tag{20.1}$$

where M is the mass of the radionuclide in atomic mass units u and N_{Av} is Avogadro's number. On the assumption that 1 Bq can be measured with sufficient accuracy, the amounts of radionuclides listed in Table 20.1 can be determined quantitatively. From this table, it is evident that short-lived radionuclides can be measured with extremely high sensitivity (extremely low detection limits). Because radioactivity is a property of atoms, radioanalytical methods are primarily applicable to the determination of elements.

The following applications of radionuclides in analytical chemistry can be distinguished:

- analysis on the basis of the inherent radioactivity of the elements to be determined;
- activation analysis, that is, activity measurement after activation by nuclear reactions of the elements to be determined;
- analysis after addition of radionuclides as tracers (isotopic dilution and radiometric methods).

Inherent radioactivity is a property of elements containing radioisotopes, such as K, and of all radioelements, for example, U, Ra, Th, and others. If the daughter nuclides are also radioactive, they can be measured instead of the mother nuclides, provided that radioactive equilibrium is established.

Activation analysis may be applied in many variants. Neutron activation analysis (NAA) is the most widely used, but often charged-particle activation or photon activation is more advantageous. If the energy of the projectiles can be varied,

Nuclear and Radiochemistry: Fundamentals and Applications,
Fourth Edition. Jens-Volker Kratz.

Table 20.1 Detection limits of radionuclides (the amounts correspond to an activity of 1 Bq).

	Detection limit	
$t_{1/2}$	Number of atoms *N*	Mol
1 h	5200	$8.64 \cdot 10^{-21}$
1 d	125 000	$2.08 \cdot 10^{-19}$
1 yr	$4.55 \cdot 10^{7}$	$7.55 \cdot 10^{-17}$
10^5 yr	$4.55 \cdot 10^{12}$	$7.55 \cdot 10^{-12}$
10^9 yr	$4.55 \cdot 10^{16}$	$7.55 \cdot 10^{-8}$

many variations are possible. The application of the manifold methods of activation depends on the availability of research reactors and accelerators. In addition, purely instrumental or radiochemical methods may be used. In instrumental activation analysis, the samples are measured after irradiation without chemical separation, whereas radiochemical activation analysis includes chemical separation.

If a microcomponent is to be determined in the presence of a macrocomponent, the conditions of irradiation are chosen in such a way that the microcomponent is highly activated, whereas the activation of the macrocomponent is as low as possible.

Addition of radioactive tracers for analytical purposes offers additional possibilities of radioanalysis. By isotopic dilution, not only elements but also compounds can be determined quantitatively, provided that these compounds are available in labeled form. Radiometric methods comprise the application of isotopic exchange, release of radionuclides, and radiometric titration.

The various radioanalytical methods will be discussed in more detail in the following chapters.

20.2 Analysis on the Basis of Inherent Radioactivity

The activity of naturally radioactive elements is a measure of their mass. Prerequisites of application of the correlation between mass and activity according to Eq. (20.1) are that the isotopic composition of the element to be determined is constant and that interfering radioactive impurities are absent. If the daughter nuclides are also radioactive, radioactive equilibrium must be established or the daughter nuclides must be separated off quantitatively. Interference of radioactive impurities may be avoided by measuring the α or γ spectrum of the radionuclide considered.

Analytical determination on the basis of natural radioactivity is often used for K, U, Ra, and Th. K contains 0.0117% of ^{40}K ($t_{1/2} = 1.28 \cdot 10^9$ years). The isotopic composition is practically constant and ^{40}K is easily measurable due to the emission of relatively high-energy β^-, β^+, and γ radiation. The natural radioactivity of 1 kg of

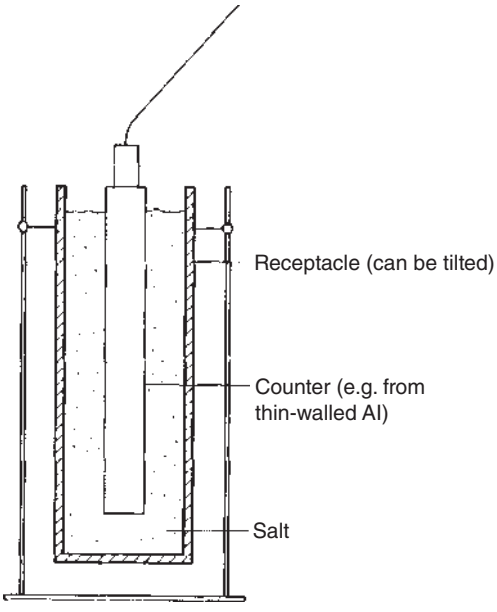

Figure 20.1 Setup for the determination of K in salts.

K is $3.13 \cdot 10^4$ Bq. On the assumption that 0.1 Bq can be measured with an acceptable error, the limit of quantitative determination is 3 mg. For the measurement of the potassium concentration in salts, the arrangement shown in Figure 20.1 is used. High counting efficiency is provided by a counter with a thin wall and a large volume, and by filling the salt into the space surrounding the counter. In this way, the concentration of K in salt mines can be determined directly. Higher concentrations of Rb interfere because of the natural radioactivity of this element.

In natural uranium, the radionuclides of the uranium family and the actinium family are present, and sometimes also radionuclides of the thorium family. Therefore, direct determination of U in ores without chemical separation is difficult, especially since the absorption of the radiation depends on the nature of the minerals. Generally, the samples are dissolved and ^{234}Th is separated, for example, by coprecipitation or by extraction with thenoyltrifluoroacetone (TTA). Radioactive equilibrium between ^{234}Th and the daughter nuclide ^{234m}Pa is rather quickly attained, and the high-energy β^- radiation of the latter can easily be measured. A prerequisite of the determination of U by measuring the activity of either ^{234}Th or ^{234m}Pa is the establishment of radioactive equilibrium. This means that the uranium compound must not have been treated chemically for about eight months.

^{226}Ra can be determined with high sensitivity by measuring ^{222}Rn in radiochemical equilibrium with ^{226}Ra. Ra is loaded into a closed receptacle, and after about six weeks, Rn is transferred into an ionization chamber where its α activity is measured as a function of time. By separating the radon, the influence of radioactive impurities is excluded. In this way, the very low ^{226}Ra content in human bones, on the order of 10^{-12} g, can be determined.

In the case of ^{232}Th, the attainment of radioactive equilibrium with the daughter nuclides is very slow because of the long half-life of ^{228}Ra ($t_{1/2} = 5.75$ years). ^{232}Th

can be determined directly by measuring its α radiation, but the measurement of ^{212}Po is more sensitive (about 10^{-6} g of Th can be determined in this way in 1 g of rock material). Other methods are based on the separation and measurement of ^{228}Ra or ^{220}Rn. In all determinations of Th, the possibility of the presence of radioactive impurities, mainly of members of the uranium and actinium families, has to be taken into account.

20.3 Neutron Activation Analysis (NAA)

Activation analysis is based on the production of radionuclides by nuclear reactions. The specific activity is given by the equation of activation:

$$A_s = \sigma \Phi \frac{N_{Av}}{M} H \left(1 - \left(\frac{1}{2}\right)^{t/t_{1/2}}\right) \tag{20.2}$$

where σ is the cross section of the nuclear reaction in cm^2, Φ is the flux density of projectiles in cm^{-2} s^{-1}, N_{Av} is Avogadro's number, M is the atomic mass of the element (in atomic mass units u), and H is the relative abundance of the nuclide undergoing the nuclear reaction. Introducing 1 barn = 10^{-24} cm^2 for σ and the value $N_{Av} = 6.022 \cdot 10^{23}$ gives

$$A_s = 0.602\sigma[\text{barn}]\cdot\Phi \frac{H}{M} \left(1 - \left(\frac{1}{2}\right)^{t/t_{1/2}}\right) \tag{20.3}$$

From Eqs. (20.2) and (20.3), it is evident that the limits of quantitative determination depend on the cross section σ of the nuclear reaction, the flux density Φ of the projectiles, and the ratio $t/t_{1/2}$ (time of irradiation to half-life).

The following possible modes of neutron activation can be distinguished:

- activation by reactor neutrons (mainly [n, γ] reactions induced by thermal neutrons);
- activation by the neutrons from a spontaneously fissioning radionuclide (mainly [n, γ] reactions);
- activation by high-energy neutrons such as 14 MeV neutrons from a neutron generator (mainly [n, 2n] reactions).

Reactor neutrons are most frequently used for activation analysis because they are available in high flux densities. Moreover, for most elements, the cross section of (n, γ) reactions is relatively high. On the assumption that an activity of 10 Bq allows quantitative determination, the lower limits of determination by (n, γ) reactions at a thermal neutron flux density of 10^{14} cm^{-2} s^{-1} are as given in Table 20.2 for a large number of elements and two irradiation times (one hour and one week). Detection limits on the order of 10^{-14} to 10^{-10} g g^{-1} are, in general, not available by other analytical methods.

Li and B are not listed in Table 20.2, because they undergo (n, α) reactions with high yields. Activation of H, Be, C, and N is negligible, and these elements are therefore also not listed in the table. O exhibits only little activation and is found in the last row. If these elements are present in the form of macrocomponents of a sample, for example, in water or in biological samples, they are practically not

Table 20.2 Detection limits by neutron activation analysis at a thermal neutron flux of 10^{14} cm^{-2} s^{-1} on the assumption that 10 Bq allows quantitative determination.

Detectable in 1 g of sample (g)	Irradiation time 1 h	Irradiation time 1 wk
10^{-14} to 10^{-13}	Dy[a)]	Eu[a)], Dy[a)]
10^{-13} to 10^{-12}	Co, Rh,[b),c)] Ag,[b),c)] In,[a)] Eu,[a)] Ir	Mn, Co, Rh,[a),c)] Ag,[b),c)] In, Sm,[a)] Ho, Re,[a)] Ir, Au
10^{-12} to 10^{-11}	V, Mn, Se,[c)] Br,[a)] I,[a)] Pr, Er,[c)] Yb,[c)] Hf,[c)] Th[a)]	Na, Sc, V, Cu,[b)] Ga,[a)] As, Se,[c)] Br,[a)] Pd, Sb, I,[a)] Cs, La, Pr, Er,[c)] Tm,[a)] Yb,[c)] Lu, Hf,[c)] W, Hg, Th[a)]
10^{-11} to 10^{-10}	Mg, Al, Cl,[a)] Ar, Cu,[a)] Ga,[b)] Nb, Cs, Sm, Ho, Lu, Re, Au, U	Mg, Al, Cl,[a)] Ar, K,[a)] Cr,[a)] Ni,[a)] Ge,[a)] Kr, Y,[d)] Nb, Ru, Gd,[a)] Tb,[a)] Tl,[a)] Os,[a)] U
10^{-10} to 10^{-9}	F,[c)] Na, Ge,[a)] As, Kr, Rb,[a)] Sr, Mo, Ru, Pd, Sb, Te,[a)] Ba, La, Nd,[a)] Gd,[b)] W, Os, Hg, Tl[d)]	F,[c)] P,[d)] Zn, Rb,[a)] Sr, Mo, Te,[a)] Ba, Ce, Nd, Pt, Tl[d)]
10^{-9} to 10^{-8}	Ne,[c)] Si,[d)] K, Sc, Ti, Ni, Y,[d)] Cd, Sn, Xe, Tb,[a)] Tm, Ta, Pt	Ne,[c)] Si,[d)] Ti, Cd, Sn, Xe, Bi[d)]
10^{-8} to 10^{-7}	P,[d)] Cr,[a)] Zn, Ce	S,[d)] Ca,[d)] Fe, Zr
10^{-7} to 10^{-6}	S,[d)] Zr, Pb,[d)] Bi[d)]	Pb[d)]
10^{-6} to 10^{-5}	O,[c)] Ca[d)]	O[c)]

a), b) If the γ radiation is measured by means of a γ-ray spectrometer, the elements are to be transferred into the next group (^{a}) or the next-but-one group (^{b}) because of the relative abundance of the γ transitions.

c) From these elements, radionuclides with half-lives between one second and one minute are obtained. Therefore, 100 Bq is assumed necessary for quantitative determination and the elements are relegated to the next group below.

d) Only β radiation, no γ radiation.

activated and do not interfere. The light elements H, Li, Be, B, C, N, and O can be determined by activation with charged particles or with photons. Charged-particle or photon activation may also be more favorable for other elements listed in the lower rows of Table 20.2.

The spectrum of neutron energies in nuclear reactors is, in general, relatively broad. Furthermore, it varies with the type of reactor, and in the same reactor with the position. As the cross sections of nuclear reactions depend on the energy of the projectiles (excitation functions; Section 12.3), the activity obtained according to Eq. (20.2) or (20.3) varies also with the energy spectrum of the neutrons. Many elements exhibit a high resonance cross section in the range of epithermal neutrons. Therefore, it is necessary to use standards that are irradiated under the same conditions and at the same position as the samples. Some reactors have thermal columns in which only thermal neutrons are available, but at appreciably lower flux densities.

In general, the activity of the radionuclide produced by the nuclear reaction is measured after irradiation, either directly or after chemical separation. However, the prompt γ-ray photons emitted in (n, γ) reactions may also be counted on the site

of their production (prompt gamma activation analysis, PGAA). For that purpose, the samples must be irradiated outside the nuclear reactor or by another neutron source, and the γ-ray photons are recorded by means of a γ-ray spectrometer. The intensity I of the γ-rays produced by the nuclear reaction is proportional to the rate of the nuclear reaction (number of transmutations per unit time):

$$I \propto \frac{\mathrm{d}N}{\mathrm{d}t} = \sigma \Phi N_{\mathrm{A}} \tag{20.4}$$

where N_{A} is the number of atoms of the radionuclide undergoing the nuclear reaction.

Activation by high-energy neutrons is of interest if the cross sections of (n, γ) reactions are too low or if the macrocomponents are too highly activated by thermal neutrons. For the purpose of activation analysis, special neutron generators have been developed. In these generators, protons or deuterons with energies on the order of 0.1–1 MeV are used for the production of neutrons by nuclear reactions. The preferred reactions are

$$\mathrm{t(d, n)}\alpha \tag{20.5}$$

and

$$^{9}\mathrm{Be(d, n)}^{10}\mathrm{B} \tag{20.6}$$

The deuterons are accelerated in a van de Graaff generator and hit a tritium or a beryllium target. The neutron yields of these reactions are plotted in Figure 16.2 and in Figure 20.2.

For application of reaction (20.5), suitable tritium targets have been developed in which T is preferably bound in the form of hydrides such as titanium hydride deposited on copper. The targets must be well cooled to suppress escape of T due to heating by the incident deuterons. Neutron shielding is achieved by a block of paraffin, in which the energy of the neutrons is reduced, and by boron as a neutron absorber.

With tritium targets of 1 Ci ($3.7 \cdot 10^{10}$ Bq) and deuteron fluxes of about 50 mA, neutron yields up to about $5 \cdot 10^{12}\ \mathrm{s}^{-1}$ are obtained. The flux density depends on the distance between the tritium target and the sample. The energy of the neutrons produced by reaction (20.5) is 14 MeV and allows activation by (n, p), (n, γ), or (n, 2n) reactions with relatively high yields. Most cross sections of (n, 2n) reactions are in the range of about 10–100 mb, which means that about 10^{-5} to 10^{-4} g of many elements can be determined quantitatively. Examples are given in Table 20.3.

Spontaneously fissioning radionuclides may be applied as neutron sources in those cases where irradiation in a nuclear reactor is not possible, for example, if manganese nodules at the bottom of the sea are to be analyzed. For that purpose, ^{252}Cf is a suitable neutron source. It has a half-life of 2.645 years and decays in 96.9% by emission of α particles and in 3.1% by spontaneous fission. It may be installed together with a shielded γ-ray detector in the form of a mobile unit. The neutron production of ^{252}Cf is $2.34 \cdot 10^{12}\ \mathrm{s}^{-1}\ \mathrm{g}^{-1}$. The neutron flux density is only on the order of $10^{9}\ \mathrm{cm}^{-2}\ \mathrm{s}^{-1}$, but this is sufficient for applications in which high sensitivity is not needed.

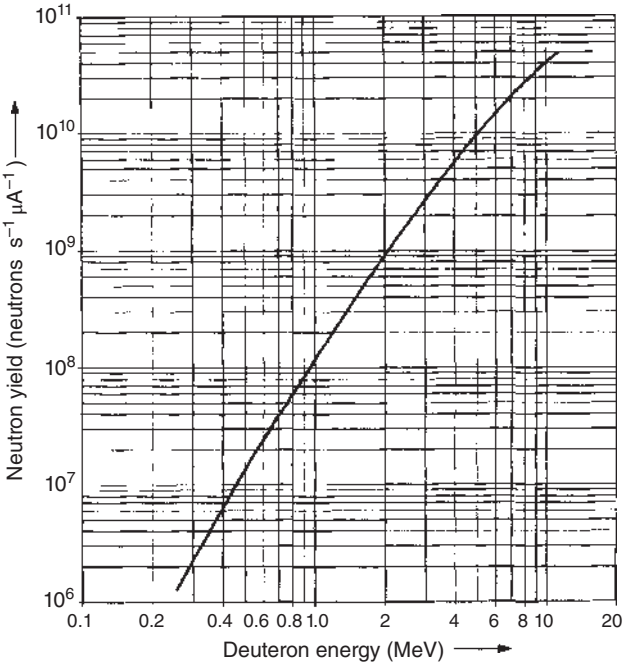

Figure 20.2 Neutron yield of the reaction ^{9}Be(d, n)^{10}B as a function of the deuteron energy (thick Be target).

Table 20.3 Examples of activation by 14 MeV neutrons.

Element determined	Main component of the sample	Nuclear reaction	Detection limit
O	Organic compounds	^{16}O(n, p)^{16}N	$\approx 10\,\mu g\,g^{-1}$
Si	Oil	^{28}Si(n, p)^{28}Al	$\approx 10\,\mu g\,g^{-1}$
Ti	Al	^{48}Ti(n, p)^{48}Sc	$\approx 100\,\mu g\,g^{-1}$
Zn	—	^{68}Zn(n, p)^{68}Cu	$\approx 1\,\mu g\,g^{-1}$
Al	Si	^{27}Al(n, α)^{24}Na	$\approx 1\,\mu g\,g^{-1}$
Na	Organic polymers	^{23}Na(n, α)^{20}F	0.3%
K	—	^{41}K(n, α)^{38}Cl	$6\,\mu g\,g^{-1}$
N	Organic compounds	^{14}N(n, 2n)^{13}N	$\approx 100\,\mu g\,g^{-1}$
F	Organic compounds	^{19}F(n, 2n)^{18}F	$\approx 10\,\mu g\,g^{-1}$
Pb	Petrol	^{208}Pb(n, 2n)^{207m}Pb	$20\,\mu g\,g^{-1}$

20.4 Activation by Charged Particles

Charged particles must have a minimum energy (threshold energy) to surmount the Coulomb barrier (Section 12.1). In general, the excitation functions exhibit maxima in the range of about 0.1–1 barn. For the acceleration of charged particles, van de Graaff generators are often preferred because the energy of the particles can be kept fairly constant and because operation of the generator is less costly.

In contrast to neutrons, the penetration depth of charged particles is relatively small, with the result that only the surface layers of thicker samples are activated. Furthermore, the energy of charged particles decreases drastically with the penetration depth, and consequently the cross section varies with the penetration depth. On the other hand, these properties of charged particles offer the possibility of surface analysis.

For example, oxygen can be determined by the following reactions:

$$^{16}\mathrm{O(p,\alpha)^{13}N} \tag{20.7}$$

$$^{16}\mathrm{O(^{3}He,p)^{18}F} \tag{20.8}$$

$$^{16}\mathrm{O(\alpha,d)^{18}F} \tag{20.9}$$

$$^{16}\mathrm{O(t,n)^{18}F} \quad (\mathrm{t\ produced\ by\ ^{6}Li\ (n,\alpha)t}) \tag{20.10}$$

In all cases, the determination of oxygen is limited by the range of the charged particles. For determination by reaction (20.10), a Li compound is mixed with the sample.

The elements Be, B, and C, which are not activated by irradiation with thermal neutrons, can also be determined by charged-particle activation. Limits of quantitative determination down to the order of about 10^{-9} g g^{-1} can be achieved. The same holds for F which gives a nuclide of short half-life (^{20}F, $t_{1/2} = 11$ seconds).

Heavy ions such as ^{7}Li, ^{10}B, or others may also be used for charged-particle activation, provided that a suitable heavy-ion accelerator is available. Examples of activation analysis by charged particles are given in Table 20.4.

20.5 Activation by Photons

Photons may induce quite a number of nuclear reactions (Section 12.7.5), and photoexcitation (γ, γ') may also be applied to activation analysis. In general, the photons are obtained in the form of bremsstrahlung: high-energy electrons produced in an electron accelerator hit a target of high atomic number such as tungsten. The maximum energy of the photons is given by the energy of the incident electrons. All kinds of electron accelerators may be applied – van de Graaff generators, betatrons, or linear accelerators. Simple electron accelerators of high power such as the "microtrons" are the most suitable.

Table 20.4 Examples of activation by charged particles.

Element determined	Main component of the sample	Nuclear reaction	Projectile energy (MeV)	Detection limit
B	Si	$^{11}B(p, n)^{11}C$	20	$\approx 0.01\,\mu g\,g^{-1}$
Fe	—	$^{56}Fe(p, n)^{56}Co$	12	$6\,\mu g\,g^{-1}$
Cu	—	$^{65}Cu(p, n)^{65}Zn$	12	$3\,\mu g\,g^{-1}$
As	Organic compounds	$^{75}As(p, n)^{75}Se$	12	$3\,\mu g\,g^{-1}$
Mo	—	$^{96}Mo(p, n)^{96}Tc$	12	$2\,\mu g\,g^{-1}$
Pb	—	$^{206}Pb(p, n)^{206}Bi$	12	$11\,\mu g\,g^{-1}$
C	Fe (steel)	$^{12}C(p, \gamma)^{13}N$	0.8	0.04%
F	Si (glass)	$^{19}F(p, \alpha)^{16}O$	1.4	—
B	Si, Ta	$^{10}B(d, n)^{11}C$	6–7	$\approx 0.1\,\mu g\,g^{-1}$
C	Steel	$^{12}C(d, n)^{13}N$	6.7	$\approx 0.1\,\mu g\,g^{-1}$
N	—	$^{14}N(d, n)^{15}O$	>3	$\approx 1\,\mu g\,g^{-1}$
O	—	$^{16}O(d, n)^{17}F$	>3	$\approx 0.01\,\mu g\,g^{-1}$
Si	Al	$^{30}Si(d, p)^{31}Si$	4	0.4%
Ga	Fe	$^{69}Ga(d, p)^{70}Ga$	6.4	$6\,\mu g\,g^{-1}$
Mg	Steel	$^{24}Mg(d, \alpha)^{22}Na$	—	—
S	—	$^{32}S(d, \alpha)^{30}P$	—	$\approx 0.1\,\mu g\,g^{-1}$
Be	—	$^{9}Be(t, p)^{11}Be$	3.5	$1\,\mu g\,g^{-1}$
B	—	$^{10}B(t, 2n)^{11}C$	3.5	$0.1\,\mu g\,g^{-1}$
N	—	$^{14}N(t, 2n)^{15}O$	3.5	$0.1\,\mu g\,g^{-1}$
O	—	$^{16}O(t, n)^{18}F$	3.5	$0.001\,\mu g\,g^{-1}$
O	Metal surfaces	$^{16}O(t, n)^{18}F$	3	$5\,ng\,cm^{-2}$
Mg	—	$^{26}Mg(t, n)^{28}Al$	3.5	$0.02\,\mu g\,g^{-1}$
Si	—	$^{28}Si(t, n)^{30}P$	3.5	$0.01\,\mu g\,g^{-1}$
Fe	Nb, Ta, W	$^{56}Fe(^{3}He, pn)^{57}Co$	14	$\approx 0.1\,\mu g\,g^{-1}$
Mo	W	$^{95}Mo(^{3}He, n)^{97}Ru$	14	$\approx 0.1\,\mu g\,g^{-1}$
B	—	$^{10}B(\alpha, n)^{13}N$	>6	$\approx 100\,\mu g\,g^{-1}$
C	—	$^{12}C(\alpha, n)^{15}O$	>10	—
F	—	$^{19}F(\alpha, n)^{22}Na$	>6	—
Al	—	$^{27}Al(\alpha, n)^{30}P$	>6	—
O	—	$^{16}O(\alpha, d)^{18}F$	40	$<10\,\mu g\,g^{-1}$
O	—	$^{16}O(\alpha, pn)^{18}F$	40	$<10\,\mu g\,g^{-1}$
Fe	—	$^{56}Fe(\alpha, pn)^{58}Co$	15	10^{-12} g
C	—	$^{12}C(\alpha, \alpha n)^{11}C$	>10	—
^{1}H	—	$^{1}H(^{7}Li, n)^{7}Be$	78	$0.1\,\mu g\,g^{-1}$
^{1}H	—	$^{1}H(^{10}B, \alpha)^{7}Be$	60	$0.5\,\mu g\,g^{-1}$
^{2}H	—	$^{2}H(^{7}Li, p)^{8}Li$	78	$0.1\,\mu g\,g^{-1}$
^{2}H	—	$^{2}H(^{11}B, p)^{12}B$	70	$0.1\,\mu g\,g^{-1}$

Table 20.5 Examples of activation by γ-rays.

Element determined	Main components of the sample	Nuclear reaction	γ energy (MeV)	Detection limit
C	Na, AI, Si, Mo, W	$^{12}C(\gamma, n)^{11}C$	35	0.01–0.1 μg g^{-1}
N	Na, Si	$^{14}N(\gamma, n)^{13}N$	35	0.1–1 μg g^{-1}
O	Na, Al, Si, Fe, Cu, Nb, Mo, W	$^{16}O(\gamma, n)^{15}O$	35	0.1–1 μg g^{-1}
F	Al, Cu, organic polymers	$^{19}F(\gamma, n)^{18}F$	35	0.01–0.1 μg g^{-1}
Cl	Organic polymers	$^{35}Cl(\gamma, n)^{34}Cl$	18	≈0.1%
Cu	—	$^{65}Cu(\gamma, n)^{64}Cu$	35	≈1 μg g^{-1}
As	—	$^{75}As(\gamma, n)^{74}As$	35	≈1 μg g^{-1}
Cd	—	$^{116}Cd(\gamma, n)^{115}Cd$	35	≈1 μg g^{-1}
Hg	—	$^{198}Hg(\gamma, n)^{197m}Hg$	35	≈1 μg g^{-1}
Pb	—	$^{204}Pb(\gamma, n)^{203}Pb$	35	≈1 μg g^{-1}

The most important photon-induced nuclear reactions are (γ, n) and (γ, 2n) reactions, but (γ, p) reactions may also be applied. The number of possible reactions increases with the energy of the photons. Photons with energies in the range between about 15 and 40 MeV are preferred, and detection limits between about 1 ng and 1 μg are obtained. Photofission of heavy nuclei is achieved with photons of relatively low energy (about 5–10 MeV). It leads also to detection limits of about 1 ng to 1 μg.

For photoexcitation (γ, γ′), photons with energies between about 1 and 15 MeV are used. The detection limits are in the range of about 0.1–10 μg.

Because high-energy photons exhibit only little absorption, reliable results are obtained with compact samples. Activation by photons is favorable if the sample contains macrocomponents with elements of high neutron absorption cross sections, such as Li, B, Cd, In, or rare earth elements. Furthermore, photon activation is applied for the determination of elements that cannot be determined by (n, γ) reactions, such as Be, C, N, O, and F. These elements can be determined in concentrations down to about 10^{-7} g g^{-1}. Other elements such as Si, Zr, and Pb can also be determined by (γ, n) reactions. Examples are listed in Table 20.5.

If the concentrations of C, N, or O are small (<10 μg g^{-1}), chemical separation after irradiation is recommended. For example, by combustion of the sample, ^{11}C and ^{13}N are transformed into $^{11}CO_2$ and $^{13}N_2$, respectively, and sorbed on a molecular sieve for measurement of their activity.

20.6 Special Features of Activation Analysis

Due to the high sensitivity, activation analysis is one of the most important methods for the determination of microcomponents, in particular trace elements, in materials of high purity (e.g. in semiconductors), in water, in biological samples, and in minerals. The main fields of application are

- geo- and cosmochemistry (terrestrial and lunar samples, meteorites);
- art and archeology (identification of the origin by the trace element pattern in very small samples);
- environmental samples (atmospheric aerosols, fly ash, and water);
- biological samples (blood, organs, body fluids, hair, and food).

Another special feature of activation analysis is the fact that, in contrast to other methods, impurities introduced after irradiation in the course of chemical operations by reagents do not affect the results because these impurities are not activated.

Activation analysis is a blank-free technique. In general, blanks not only determine the limits of detection (LOD), but at low concentrations also cause the main problems with respect to accuracy, because the small amounts to be determined have to be conveyed through all the steps of the chemical procedures, from sampling to detection, without introducing systematic errors. These problems are not encountered in activation analysis because contamination by other radionuclides can, in general, be excluded and losses of the radionuclides to be determined can easily be detected by activity measurements.

For these reasons, activation analysis is preferably applied for certification and calibration purposes in trace element analysis. On the other hand, activation analysis is seldom used as a routine method because the handling of radioactive samples and disposal of the radioactive waste require special precautions.

A great advantage of activation analysis is the possibility of determining a large number of trace elements (up to about 30) simultaneously by γ spectrometry. The γ spectra are preferably recorded by means of Ge(Li) or high-purity Ge detectors in combination with a multichannel analyzer (Section 9.6). By use of these semiconductor detectors, high resolution is obtained, whereas the counting efficiency is relatively low. On the other hand, scintillation detectors such as NaI(Tl) detectors exhibit a relatively high counting efficiency, but low resolution. Radionuclides emitting only β radiation must be measured individually, mostly after selective chemical separation.

An important aim of activation analysis is high activation of the trace elements to be determined and low activation of the main components. In this respect, the ratios of the cross sections of the elements to be determined (σ_x) and of the main components ($\Sigma\sigma_m$) and the half-lives are important. The higher the ratio $\sigma_x/\Sigma\sigma_m$, the more favorable is the application of activation analysis. Furthermore, if the half-lives of the activation products of the main components are shorter than those of the radionuclides to be measured, the activity of the latter is determined some appropriate time after the end of irradiation. If they are relatively long, the time of irradiation is chosen in such a way that activation of the elements to be determined is high, whereas activation of the main components is low.

For example, activation of the elements H, Be, C, N, O, F, Mg, Al, Si, and Ti by thermal neutrons is negligible or low because the products of (n, γ) reactions are stable (^{2}H, ^{13}C, ^{15}N, ^{17}O, ^{18}O, ^{25}Mg, ^{26}Mg, ^{29}Si, ^{30}Si, ^{49}Ti, ^{50}Ti), short-lived (^{20}F, ^{27}Mg, ^{28}Al, ^{31}Si, ^{51}Ti), or very long-lived (^{10}Be). Samples containing these elements as main components are very well suited to the application of NAA.

In cases in which activation by thermal neutrons causes relatively high activity of the main components, the following measures can be taken:

a. Variation of the time of irradiation (t_i) and the time of decay after irradiation (t_d). Optimal conditions can be calculated by means of the equation:

$$\frac{A_x}{A_m} = \frac{\sigma_x}{\sigma_m} \frac{N_A(x)}{N_A(m)} \frac{(1 - e^{-\lambda_x t_i})e^{-\lambda_x t_d}}{(1 - e^{-\lambda_m t_i})e^{-\lambda_m t_d}} \tag{20.11}$$

where A are the activities, σ the cross sections of the (n, γ) reactions, N the number of atoms, and λ the decay constants (subscript x denotes the element to be determined, and subscript m the main component).

b. Shielding of thermal neutrons with the aim of activating only with high-energy neutrons, for example, by wrapping the sample in a cadmium foil.
c. Choice of other projectiles for activation, for instance, activation by 14 MeV neutrons, by charged particles, or by γ-ray photons.

Selection of the time of irradiation and the time of measuring is important. If possible, the time of irradiation should correspond to one or several half-lives of the radionuclide to be measured. Long-term irradiation (days or weeks) and short-term irradiation (seconds or minutes) are distinguished. For short-term irradiation, a fast transport system is needed, for example, a pneumatic tube system.

In general, activation analysis relies on the use of standards that are irradiated under the same conditions and in the same position and are also measured under the same conditions. Monoelement standards contain a known amount of one element. If they are applied to the evaluation of other elements, the ratio of the cross sections σ_x/σ_s under the special conditions of irradiation and the ratio H_x/H_s of the relative abundances of the decay processes that are measured must be known (subscript x is for the sample and subscript s for the standard). Knowledge of the ratio σ_x/σ_s may cause problems because the cross sections may vary drastically with the energy of the projectiles, for instance, in the energy range of epithermal neutrons. These problems are not encountered with multielement standards that contain all the elements to be determined. However, the preparation of such multielement standards may be time-consuming.

As already mentioned, two kinds of activation analysis are distinguished:

- direct activity measurement of the samples after activation (instrumental activation analysis, in particular, instrumental neutron activation analysis [INAA]); and
- chemical separation after irradiation followed by activity measurement of the separated fraction (radiochemical activation analysis, in particular, radiochemical neutron activation analysis [RNAA]).

Chemical separation is unavoidable if the activities of the individual radionuclides cannot be measured by instrumental methods, as in the case of β radiation. In many cases, α and γ radiation can be measured by means of α and γ spectrometry. However, if the resolution of the spectra is insufficient, chemical separation is also necessary. Isotopic dilution (Section 20.7) is often applied because quantitative separation can be avoided by this method.

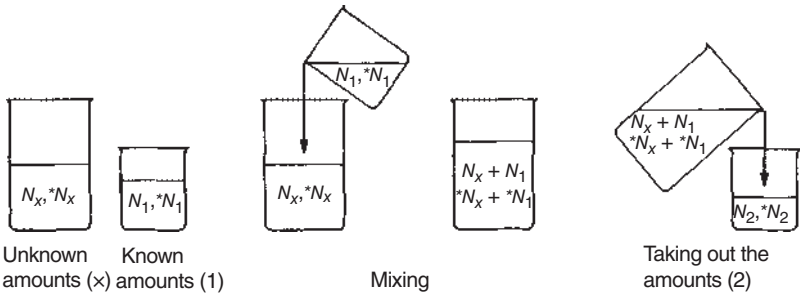

Figure 20.3 Principle of isotope dilution.

20.7 Isotope Dilution Analysis

The principle of isotope dilution analysis (IDA) is illustrated in Figure 20.3. The sample contains an unknown number N_x of atoms or molecules, and it may also contain an unknown number ${}^*N_x$ of labeled atoms or molecules of the same kind. Known numbers N_1 and ${}^*N_1$ are added. These atoms or molecules (subscript 1) must not be identical with the atoms or molecules x, but they must exhibit the same behavior under the given conditions. After mixing to obtain homogeneous distribution, any fraction is taken and the numbers N_2 and ${}^*N_2$ are determined in this fraction.

Due to homogeneous distribution by mixing, the following relation is valid:

$$\frac{{}^*N_2}{N_2} = \frac{{}^*N_x + {}^*N_1}{N_x + N_1} \tag{20.12}$$

Introducing the specific activities A_s and assuming that ${}^*N_i \ll N_i$ gives

$$N_x = N_1 \frac{A_s(1) - A_s(2)}{A_s(2) - A_s(x)} \tag{20.13}$$

In the case of a determination of inactive atoms or compounds (${}^*N_x = 0$), the following relation is valid:

$$N_x = N_1 \frac{A_s(1) - A_s(2)}{A_s(2)} \tag{20.14}$$

This equation can also be applied in the form:

$$m_x = m_1 \frac{A_s(1) - A_s(2)}{A_s(2)} \tag{20.15}$$

According to Eqs. (20.13)–(20.15), the change of specific activity is a measure of the unknown number N_x.

It should be mentioned that the same kind of equations hold if stable isotopes are applied for labeling of the elements or compounds to be determined by IDA. In this application, isotope ratios take the place of specific activities, and they are preferably measured by mass spectrometry.

The main and unique advantage of this method is the fact that quantitative separation of the element or compound to be determined is not necessary. It is substituted

by measuring any fraction. This advantage is most clearly illustrated by an example from biology: if the blood volume of an animal is to be determined, it is obvious that the animal will not survive the extraction of the whole amount of blood to be measured. By application of IDA, a small measured volume V_1 of a solution is injected that contains a measured activity of a radionuclide of low radiotoxicity. Mixing is affected by blood circulation. After some minutes, a small volume of blood is taken and the activity is measured. In analogy to Eq. (20.15), the unknown volume is

$$V_x = V_1 \frac{A_1(1) - A_2(2)}{A_s(2)} \tag{20.16}$$

IDA is a very valuable method for the determination of trace elements in all kinds of samples. The radioactive tracers or *labeled compounds* are added at the beginning of the analysis, and provided that they exhibit the same behavior as the elements or compounds to be determined, losses in the course of chemical separation procedures are without influence on the results. Furthermore, time-consuming quantitative separation procedures can be substituted by simpler, more qualitative methods. An important application of isotope dilution in radiochemistry is the determination of a radionuclide by dilution with an inactive nuclide (inactive compound), also called *reverse isotope dilution*. This application is very valuable if the radionuclide is present in carrier-free form. Again, quantitative separation is avoided; a measured amount m_1 of an inactive isotope of the element to be determined is added and after a nonquantitative separation the amount m_2 is measured. The ratio m_2/m_1 is the yield of the separation procedure and the activity A_x of the carrier-free radionuclide ($N_x = 0$) is obtained from the measured activity A_2:

$$A_x = A_2 \frac{m_1}{m_2} \tag{20.17}$$

Combining isotope dilution with the principle of substoichiometric analysis offers the possibility of avoiding determination either of the chemical yield of the separation procedure or of the specific activity in the isolated fraction. Two identical aliquots of the radiotracer solution are taken, both containing the tracer with mass m_0 and activity A_0. One aliquot is added to the solution to be analyzed and the other is left as such. Then the same amount m of the substance x to be determined is isolated from both solutions. To ensure this, the concentration of the reagent used for the isolation is adjusted, so that it is less than would correspond to quantitative stoichiometric reaction in either solution (substoichiometric principle). The specific activity in the tracer solution is $A_s(0) = A_0/m_0$ and that in the solution to which the tracer solution has been added is $A_s(2) = A_0/(m_0 + m_x)$. The specific activities are not changed by the chemical procedures; in the fractions isolated from the solutions, they are $A_s(0) = A_0/m_0 = A_1/m$ and $A_s(2) = A_0/(m_0 + m_x) = A_2/m$. The resulting relation is

$$m_x = m_0 \left(\frac{A_1}{A_2} - 1 \right) \tag{20.18}$$

where A_1 and A_2 are the activities measured in the isolated fractions.

Equation (20.18) is similar to Eq. (20.15), but the advantage is that the measurement of the relative activities A_1/A_2 is sufficient and the determination of masses is avoided.

Many metals in amounts ranging from micro- to nanograms have been determined by isotope dilution in combination with the substoichiometric principle. Isolation of equal amounts m is usually achieved by solvent extraction of a metal chelate into an organic solvent. It must be certain that the substoichiometric amount of the chelating reagent reacts quantitatively with the metal ions in the concentration range considered.

20.8 Radiometric Methods

Radiometric analysis is also based on the use of *radiotracers*. However, in contrast to IDA, stoichiometric relations are applied in radiometric methods. The substance to be determined is brought into contact with another substance labeled with a radionuclide or containing a radionuclide. Reaction between these two substances yields a radioactive product that either can be separated and measured or can be measured continuously in the course of the reaction. The activity is proportional to the amount of substance to be determined.

The following applications are distinguished:

- radioreagent methods;
- radiorelease methods;
- isotope exchange methods;
- radiometric titration.

In radioreagent methods, the radioactive product of the reaction between the substance to be determined and a radioactive reagent is separated by various methods, such as precipitation or liquid–liquid extraction. For example, Cl^-, Br^-, or I^- in concentrations down to $0.5\,\mu g\,l^{-1}$ can be determined by addition of an excess of phenylmercury nitrate labeled with ^{203}Hg. The complexes formed with the halide ions are extracted into benzene, whereas the phenylmercury nitrate stays in the aqueous phase. From the difference between the activities in the aqueous phase before and after the reaction, the amount of halide ions is calculated. Traces of Hg^{2+} in water can be determined by shaking with a solution of silver dithizonate in CCl_4 labeled with ^{110m}Ag. Due to the displacement of Ag by Hg, ^{110m}Ag is transferred to the aqueous phase, where it can be measured.

Radiorelease methods are based on the same principle: the substance to be determined is brought into contact with another substance containing a radionuclide reagent, and by their interaction a certain amount of the radionuclide is released and measured. For this method, substances loaded with ^{85}Kr (radioactive kryptonates), for example, krypton clathrates, may be applied. By reaction with oxygen, ^{85}Kr is released and can be measured continuously. Oxygen dissolved in water can be measured by reaction with ^{204}Tl deposited on Cu; ^{204}Tl is oxidized and released into the water where it can be measured. Other oxidizing substances in water, such

as dichromate, can be determined in the same way. Further examples are the determination of SO_2 by reaction with IO_3^- labeled with ^{131}I and determination of active hydrogen in organic substances by reaction with $LiAlH_4$ labeled with T.

The isotope exchange method is based on the exchange between two different forms or compounds of the element M to be determined:

$$\underset{(1)}{MX} + \underset{(2)}{M^*Y} \Leftrightarrow \underset{(1)}{M^*X} + \underset{(2)}{MY} \tag{20.19}$$

The labeled species M*Y is added and, after equilibration, the specific activity is the same in (l) and (2):

$$\frac{A_1}{m_1} = \frac{A_2}{m_2} \tag{20.20}$$

After separation of compounds (1) and (2), their activity is measured and the mass m_1 can be calculated from Eq. (20.20). Homogeneous as well as heterogeneous exchange reactions may be applied in analytical chemistry. An example is the determination of small amounts of Bi:Bi is selectively extracted by diethyldithiocarbamate in chloroform, a known amount of BiI_4^- labeled with ^{210}Bi is added, after about 30 seconds BiI_4^- is extracted into water, and the activities in both phases are measured. In the case of heterogeneous exchange reactions, separation of the components is simple.

An advantage of isotope exchange methods is that, in special cases, individual chemical forms (species) can be determined with high sensitivity. The systems applied have to be selected by the following criteria: knowledge of the species between which exchange occurs, relatively rapid attainment of the exchange equilibrium, and exclusion of side reactions.

In radiometric titration, the radioactivity of one component or in one phase is recorded as a function of addition of titrant. The compound formed is separated by precipitation, extraction, or ion exchange in the course of the titration, and the endpoint is determined from the change in the activity in the residual solution. Radiometric titration may be applied in different ways: inactive test solution and active titrant (activity in the solution is low at the beginning and begins to rise at the endpoint); active test solution and inactive titrant (activity in the solution decreases continuously, until the endpoint is reached); both the test solution and the titrant active (activity in the solution decreases until the endpoint is reached and then increases again). Many applications of radiometric titration based on precipitation or complex formation have been described.

20.9 Other Analytical Applications of Radiotracers

Radiotracer techniques have proven to be indispensable with respect to the examination of the individual steps of an analytical procedure, in particular with the aim of revealing the sources of systematic errors. Actually, tracer techniques have contributed essentially to the development of the present state of trace element analysis.

The most significant sources of error in trace element analysis are contamination or losses by adsorption or volatilization. The key property of radiotracers with respect to the investigation of the accuracy of analytical techniques is the emission of easily detectable radiation in any stage of an analytical procedure with extraordinary high sensitivity.

Mechanisms and yields of analytical procedures such as precipitation or coprecipitation that are essential for their application can be elucidated. Furthermore, general analytical data can be obtained by the application of tracer techniques, for example, distribution coefficients, stability constants, and solubilities.

20.10 Absorption and Scattering of Radiation

Backscattering of β radiation can be taken as the basis for surface analysis. It is due to electron–electron interaction, which is nearly independent of the atomic number Z of the material, and to scattering by atomic nuclei, which increases with Z. Both effects overlap, and the saturation value of backscattering increases approximately with $\sqrt{Z}$. Because the backscattered radiation originates from the layers near the surface, surface analysis is possible. An example is the determination of heavy elements in a solid or liquid matrix of light elements by use of the β^- radiation of ^{90}Sr.

Backscattering of γ-rays and X-rays depends on the mass per unit area and the effective average atomic number Z. The saturation value of backscattering decreases approximately with this number. For example, the composition of ores can be determined by this method. Elastic scattering of γ radiation ((γ, γ') process) can also be applied for analytical purposes. High selectivity is obtained by resonance absorption, that is, by application of a radionuclide that decays into a stable ground state of the element to be determined. The γ-rays emitted by the (γ, γ') process are measured.

Absorption or moderation of neutrons is used for the detection of elements exhibiting high neutron absorption cross sections, such as B or Cd. For this purpose, mostly neutron sources, for example, ^{252}Cf, or neutron generators are applied (Section 20.3). With neutron generators, B can be determined in steel in concentrations down to about 0.001%.

Neutrons give off energy by collision with protons (moderation). This can be applied for the determination of hydrogen in samples by measuring the thermal neutron flux density either by means of a detector or by activation of a suitable material such as a gold foil. Examples of the application of this technique are the determination of the humidity of soil, coke, coal, iron ores, or food, and determination of the H:C ratio in organic liquids and in oil. By investigating boreholes with a neutron source combined with a detector for thermal neutrons, water and oil can be localized.

Boreholes can also be investigated by measuring the prompt γ radiation emitted by (n, γ) reactions. Examples are the investigation of the C:O or the Ca:Si ratio in order to find layers containing oil or coal. Measurement of the backscattering of γ-rays allows localization of different layers and gives information about their composition, density, and ore content.

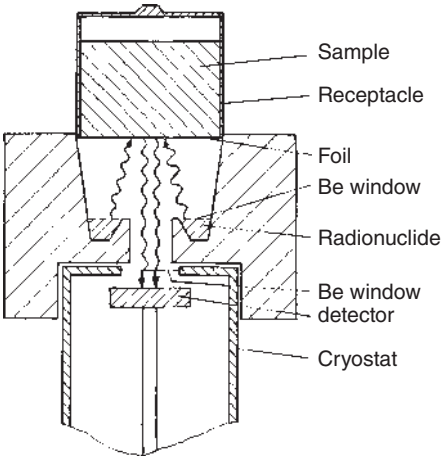

Figure 20.4 Setup for X-ray fluorescence.

20.11 Radionuclides as Radiation Sources in X-ray Fluorescence Analysis (XFA)

The application of radionuclides as radiation sources in X-ray fluorescence analysis (XFA) is illustrated in Figure 20.4. The X-rays or γ-rays emitted by a radionuclide are absorbed in the sample and the X-rays emitted by the sample are measured by means of a semiconductor in combination with a multichannel analyzer. Quantitative evaluation of the spectra is possible by use of suitable standards. In comparison to excitation by means of X-ray tubes, the main advantages of radionuclides are

- monoenergetic radiation;
- the possibility of measuring the K rays of heavy elements by excitation with γ-ray emitters;
- no need for a high-voltage installation.

The detection limits obtained by excitation with radionuclides are on the order of several micrograms per gram. Appreciably higher intensities and lower detection limits are, in general, achieved by X-ray tubes. Monoenergetic radiation may also be obtained with X-ray tubes in combination with a secondary target, and the intensity of the secondary radiation is on the same order as that obtained with radionuclide sources.

Radionuclides suitable for use as X-ray sources for XFA are listed in Table 20.6. ^{109}Cd is applied most frequently. The use of γ emitters such as ^{57}Co, ^{133}Ba, or ^{192}Ir offers the possibility of exciting heavy elements, for example, Au, Pb, Th, and U, to emit K radiation with high yield. Furthermore, heavy elements can also be measured in thick samples or within tubes or vessels, due to the high energy of their K radiation. These are distinct advantages in comparison to X-ray tubes.

The independence from high-voltage supply and the small amounts of technical equipment required allow the construction of mobile units for multielement analysis of mineralogical or geological samples in the field.

Table 20.6 Radionuclides suitable as excitation sources for X-ray fluorescence analysis (XFA).

Radionuclide	Half-life	Decay mode	Energy of the emission lines used (keV)
^{55}Fe	2.73 yr	ε	5.9 (Mn K)
^{238}Pu	87.74 yr	α	12–17 (U L)
^{109}Cd	462.6 d	ε	22.1 (Ag K)
^{125}I	59.41 d	ε	27.4 (Te K); 35.4 (γ)
^{210}Pb	22.3 yr	β^-	46.5 (γ)
^{241}Am	432.2 yr	α	59.6 (γ)
^{170}Tm	128.6 d	β^-	84.4 (γ)
^{153}Gd	239.47 d	ε	103.2 (γ); 97.4 (γ); 69.7 (γ)
^{57}Co	271.79 d	ε	136 (γ); 122 (γ)

20.12 Analysis with Ion Beams

Sensitive methods of online elemental analysis have been developed using energetic charged-particle beams. Ion beams for these analyses are often produced in cyclotrons and van de Graaff generators (see Chapter 16). The techniques described in this chapter have in common the detection of radiation from a target stimulated by ion bombardment, during the bombardment itself. This is in contrast to activation analysis techniques which detect radiation from radionuclides after the end of the irradiation. In Section 20.3, we mentioned the measurement of prompt γ-rays following neutron capture, PGAA. Analysis of γ-rays following inelastic scattering of protons has been used for simultaneous analysis of low-Z elements such as C, N, O, F, Na, Si, and S at microgram levels. The technique, called proton-induced gamma emission (PIGME), has been applied in atmospheric pollution studies by irradiating particles deposited on filters with 7 MeV protons by Macias et al. (1978). Characteristic γ-rays from the (p, p′γ) reaction such as the 4.43 and 6.6 MeV γ-rays of C and O, respectively, are easily detected in a Ge detector without the need for sample absorption corrections.

The emission of characteristic X-rays induced by charged-particle beams (particle-induced X-ray emission [PIXE]) has been used for elemental analyses of thin samples (≤1 mg) and small areas. The technique, shown schematically in Figure 20.5, involves the observation of characteristic X-rays emitted when atomic inner-shell vacancies created by particle bombardment are filled from outer shells. This method is fundamentally different from others described in this chapter in that purely atomic *transitions* are involved. The technique takes advantage of the excellent resolution of semiconductor detectors which allow the identification of virtually all elements whose X-rays are detected. A major advantage is to focus the ion beam to achieve high lateral resolution and great excitation density for

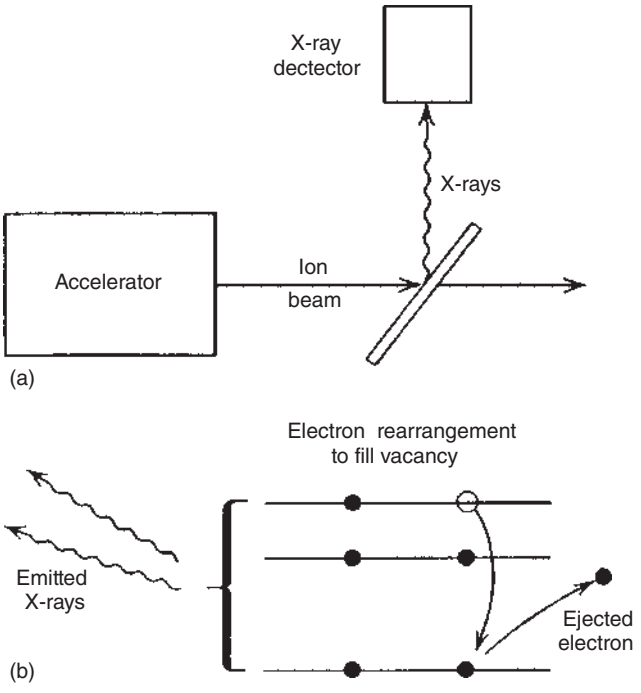

Figure 20.5 Schematic diagrams of (a) the experimental arrangement for PIXE and (b) the physical process that leads to the production of characteristic X-rays. Source: Friedlander et al. (1981)/John Wiley & Sons.

near-surface elements. Typical operating conditions within thin targets are irradiations with 10 μC (microcoulombs) of 4 MeV protons and detection of the X-rays with a 10 mm^2 Si(Li) detector of 3 mm thick equipped with a thin Be window (10^{-3} cm). The method is generally sensitive to elements with $Z \geq 11$. A typical proton-induced X-ray spectrum is shown in Figure 20.6. An application of the PIXE method that takes advantage of the unique features of the technique is the trace element analysis of particles (diameter < 20 μm). This is important in studies of air pollution, mining problems, and porous catalysts. Porous catalysts are distributed on substrates with large surfaces in order to have maximum interaction with liquids or gases forced through under pressure. When poisons deposited from the carrier stream stop catalytic activity, it is interesting to determine what reduced its effectiveness. For analysis, the catalyst is pulverized, and a few milligrams, deposited on thin Mylar, are analyzed by PIXE. Protons of a few megaelectronvolts can penetrate 20 μm particles and lose less than 10% of their energy, which minimizes cross-section changes. Therefore, this analysis is nearly independent of particle size.

Another method that is more sensitive but that requires very thin samples (<1 mg cm^{-2}) is the measurement of elastically scattered particles (generally p or α) in the forward direction (40°–50° from the beam axis). The forward-scattering geometry provides increased sensitivity to low-Z elements. This can be seen from

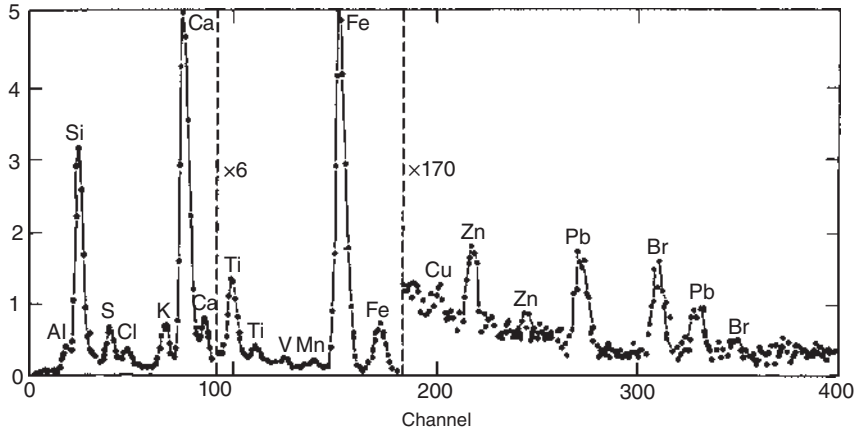

Figure 20.6 Proton-induced X-ray spectrum of an atmospheric particulate sample. The abscissa scale corresponds to approximately 35 eV per channel. Each X-ray peak is labeled with the element it represents. The lead X-rays are Lα and Lβ, and all others are K X-rays. Where there are two K peaks for an element, the left-hand one is the Kα and the right-hand one is the Kβ peak. Source: Friedlander et al. (1981)/John Wiley & Sons.

the equation for the energy loss of the scattered projectile determined from the kinematics of elastic scattering:

$$\frac{E'}{E_0} = \left(\frac{m\cos\theta + \sqrt{M^2 - m^2\sin^2\theta}}{m + M} \right)^2 \tag{20.21}$$

Here, E_0 and E' are the projectile energies before and after scattering, m and M are the projectile and target masses in amu, and θ is the scattering angle. Elements with Z between 2 and 13 are usually seen as isolated peaks in thin targets, making this a complement to PIXE analysis. Nuclear backscattering was first described by Geiger and Marsden (1909) and explained by Rutherford (1911). The scattering is due to Coulomb repulsion, described in Section 12.1, which degrades the energy of the incident beam due to conservation of momentum. The energy of the backscattered projectile is used to mass-analyze the elements in the target surface as given in Eq. (20.21). Scattering from a light element results in more energy transferred to the target nucleus than scattering from a heavier element. The process is summarized in Figure 20.7. Because the cross section for scattering is proportional to Z^2 of the target, the method is most sensitive to heavy elements. Bombarding particles are typically protons of a few hundred kiloelectronvolts or α particles of a few megaelectronvolts. With these energies, the top micrometer of the surface can be analyzed for individual elements. Rutherford backscattering (RBS) can be used for determining the bulk composition of the sample surface without the need for external standards. A historical example was the first elemental analysis of the Moon by Surveyor 5, the first vehicle to make a soft landing on the Moon. In this experiment, designed by Turkevich et al. (1967), the 5-MeV α particles from a 100 mCi ^{242}Cm source irradiated the lunar surface and protons (from the [α, p] reaction), and backscattered α particles were measured with semiconductor detectors. Pulse-height analysis of the

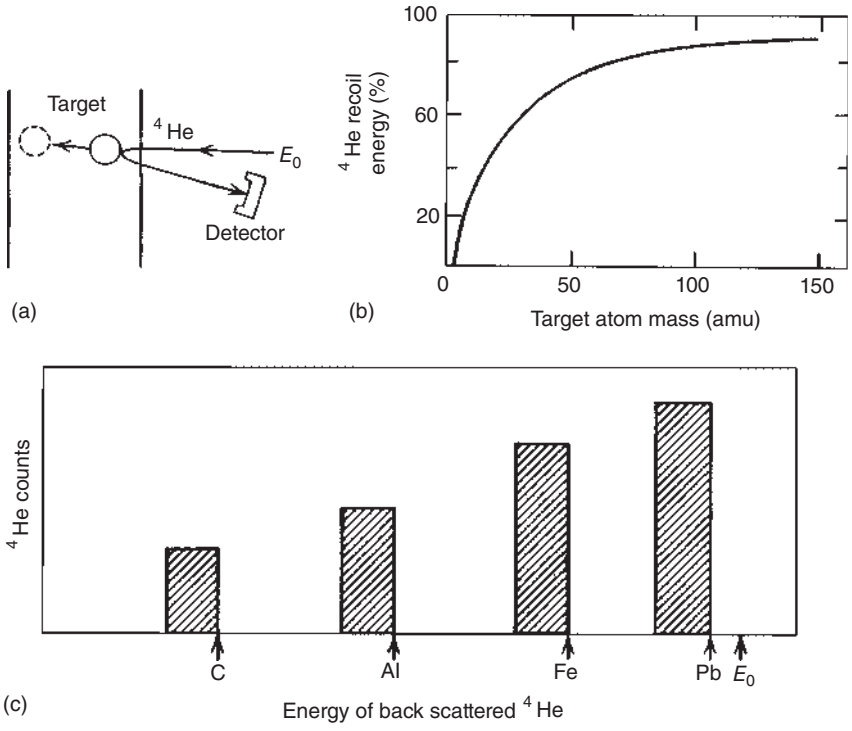

Figure 20.7 Arrangement for a Rutherford backscattering experiment (a); the fraction of energy retained by a backscattered α particle vs. the mass of the target atom (b); spectrum of energies of backscattered α particles for various scatterers (c). Here, E_0 is the incident energy. Each peak corresponds to a depth profile of target element concentration with the highest-energy α particles coming from the surface. Source: Friedlander et al. (1981)/John Wiley & Sons.

energy spectra was used to determine C, O, Na, Mg, Al, and Si, and two groups of unresolved heavier elements. The results agreed, within rather large uncertainties, with later analyses of Moon rocks brought to the Earth.

The success of the above-mentioned ion beam analysis methods has triggered further methodical developments making use of scattered ions, sputtered atoms and light emission, secondary ions, Auger electrons, and so forth. On this basis, sputter-induced photon spectrometry (SIPS), secondary-ion mass spectrometry (SIMS), and Auger electron spectroscopy (AES) were developed, to name but a few. The number of sputtered atoms per incoming ion in the kiloelectronvolt range is 1–100 and alters periodically, correlating with the filling of the electron shells in the target atoms. In SIPS, the photons pass a monochromator and are counted by a photomultiplier. The rate is typically 1 photon per 100 sputtered atoms. The sensitivity is two orders of magnitude less than that for SIMS. SIMS makes use of the fact that 0.1–1% of the sputtered atoms are ionized. The mass analyzer is usually a quadrupole spectrometer followed by a particle counter, mostly a channel plate detector. The sensitivity is on the order of nanograms per gram. AES

involves the use of solenoids or semiconductor detectors. As these methods are nondestructive, they are often applied in the scientific departments of museums where they are devoted to archeology and art. Examples are the local origin of pottery reflecting geochemical signatures, the technical development of metal alloys (archeometallurgy), pigments in paintings, the characterization of historical coins, and so forth.

20.13 Radioisotope Mass Spectrometry

Radioisotope mass spectrometry has been reviewed by Huber et al. (2003). It has gained increasing importance recently because radiometric methods used as the standard approach for the determination of radionuclides has some disadvantages for ultratrace analysis of long-lived nuclides because the detection limit depends on the half-life and the decay mode of the isotope to be measured. Further, for β measurements, as applied for trace analysis of pure β emitters like ^{89,90}Sr or ^{99g}Tc, careful and time-consuming chemical separations are needed to remove other β emitters, while for α spectroscopy with surface barrier detectors, carrier-free samples are a prerequisite for good energy resolution, and even then an unambiguous isotope assignment is difficult, such as, for example, for ^{239}Pu/^{240}Pu due to the very similar α particle energies. Here, mass spectrometric techniques which apply direct atom counting and different experimental setups and ionization methods to achieve a good sensitivity, and isotopic as well as isobaric selectivity, are superior. The sensitive and fast determination of long-lived radioisotopes is of great interest in areas such as risk assessment, low-level surveillance of the environment, radioactive waste control, or investigations of the migration behavior of actinides, etc. The most important radioisotope mass spectrometric techniques are thermal ionization mass spectrometry (TIMS), glow discharge mass spectrometry (GDMS), inductively coupled plasma mass spectrometry (ICP-MS), laser ablation inductively coupled plasma mass spectrometry (LA-ICP-MS), resonance ionization mass spectrometry (RIMS), and accelerator mass spectrometry (AMS). RIMS and AMS are used for sensitive monoelemental ultratrace analysis and precise determination of isotope ratios, whereas the other methods represent sensitive multielement techniques permitting the determination of the concentrations and isotopic abundances of trace elements. Their LOD are in the range of nanograms per gram for solids and subpicograms per liter for aqueous solutions. A precision as low as 0.02% relative standard deviation for isotope ratios can be obtained. The detection limits for RIMS and AMS are 10^6 and 10^4 atoms per sample, respectively. In the following, we shall select RIMS and AMS and their applications for the determination of long-lived radionuclides and isotope ratio measurements as representative examples.

20.13.1 Resonance Ionization Mass Spectrometry (RIMS)

Generally, the various traditional mass spectrometric methods are limited by isobaric interferences and neighboring masses, due to their finite abundance sensitivity.

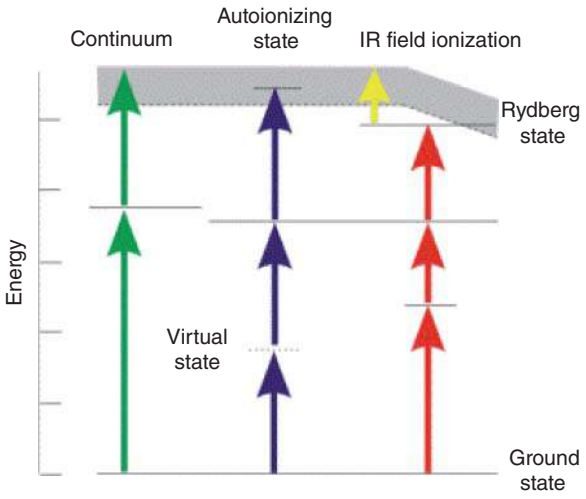

Figure 20.8 Principle of two- or three-step resonant excitation and ionization of an atom by laser light. Besides photon absorption, other ionizing mechanisms also may be exploited for the ionization step. Source: Modified from Wendt et al. (2000).

This is because the common types of ion sources feature only limited or even negligible elemental and no isotopic selectivity at all. Using resonant excitation and ionization of the analyte by laser light, RIMS achieves the highest elemental and, if needed, even very high isotopic selectivity in the ionization process. In order to apply this selective laser ionization, the analyte needs to be volatilized in form of neutral atoms.

RIMS offers outstanding properties, which may be summarized as follows:

- Almost complete suppression of atomic and molecular isobaric interferences.
- Very good overall sensitivity in the femtogram range ($\sim 10^6$ atoms).
- Feasibility of ultrahigh isotope selectivity by taking advantage of the isotope shift in the atomic transitions in addition to the abundance sensitivity of the mass spectrometer.

However, in contrast to other mass spectrometric methods, RIMS is dedicated to single-element determination and not suitable for multielement analysis.

The principle of resonant ionization (RIS) is shown in Figure 20.8. Starting from the ground state or from a thermally populated low-lying excited state, the sample atom is excited to a high-lying excited state by resonant photon absorption. Finally, the highly excited atom is ionized by another photon, which nonresonantly raises the electron energy beyond the ionization limit to the continuum (Figure 20.8, left) or resonantly populates an autoionizing state (Figure 20.8, middle), that is, a bound state above the first ionization potential. Such an autoionizing state immediately decays under emission of the electron and formation of an ion. Alternatively, high-lying Rydberg states may be resonantly populated (Figure 20.8, right) and subsequently ionized by, for example, application of an electric field, far-infrared photons, or by any other state-selective ionization method.

Due to the high cross section for the photon–atom interaction, an efficiency of the optical excitation and ionization near 100% can be realized with laser light.

Total photon fluxes of $\geq 10^{15}$ to 10^{18} photons per second from cw lasers or per pulse ($\sim$10 ns) from pulsed laser systems are easily achievable, while the cross section for optical excitation from the ground state is on the order of $\lambda^2/2\pi$, that is, $\sim 10^{-10}$ to 10^{-9} cm^2 or $\sim 10^{14}$ to 10^{15} barn, respectively. The bottleneck of the RIS process is the ionizing step with a cross section of only 10^{-17} to 10^{-19} cm^2 for the nonresonant process to the continuum. If an autoionizing state is populated, the efficiency is increased by 2–3 orders of magnitude. Nearly, the same holds if a Rydberg state is involved. Thus, power and bandwidth of the lasers are crucial factors in order to achieve highest possible ionization efficiency. The bandwidth of the lasers compared to the line widths of the excited transitions determines both the optical selectivity and the laser power needed for the saturation of these transitions.

The most outstanding property of RIMS is its extremely high elemental selectivity; that is, the suppression of isobars and neighboring masses from other elements is almost complete. This is due to the fact that in an atom, the density of levels which are accessible via electric dipole transitions is on the order of $\sim 1\ \text{eV}^{-1}$ for low-lying levels and $\sim 100\ \text{eV}^{-1}$ around $n = 20$, while the typical natural line width is around $7 \cdot 10^{-8}$ eV (for $\sim$10 ns lifetime). The line width of a common-type, pulsed tunable laser is around 10^{-4} eV, and even far less for cw lasers. Thus, the probability of accidentally matching a transition of an unwanted atomic species is negligible, especially for a two- or three-step excitation. The only contribution from other elements or molecules may stem from thermal ionization in the atomic beam source or from nonresonant photoionization. Particularly, the latter may be of some importance, if high-power ultraviolet light is used in the RIS process.

A detailed review of RIMS is given by Payne et al. (1994). RIMS has been widely used in fundamental research as well as in analytical applications since it was first proposed in 1972 (Ambartzumian and Letokhov 1972). The studies range from atomic physics and quantum optics to nuclear physics or trace detection. Highlights in fundamental research are the measurements on isotope shift and nuclear moments of very short-lived, neutron-deficient gold, platinum, and iridium isotopes produced online at ISOLDE/CERN (Hilberath et al. 1992), or fission isomers of americium (Backe et al. 2001) in order to study nuclear properties. Also, the determination of the ionization potentials of the actinides up to einsteinium (Peterson et al. 1998) with samples of only $\sim 10^{12}$ atoms per element as well as the first atomic spectroscopy on fermium (Sewtz et al. 2003a,b) show the outstanding possibilities that RIMS offers.

One particular field for the analytical application of RIMS is the ultratrace determination of very long-lived radioisotopes (Wendt et al. 2000). Many long-lived α and β emitters belong to the most important hazardous radioisotopes. Depending on their half-life, decay type, and individual interferences with other radioisotopes, like, for example, ^{239}Pu/^{240}Pu, ^{238}Pu/^{241}Am, or ^{89}Sr/^{90}Sr, the determination via radiometric techniques suffers from comparably high LOD and often insufficient selectivity for some of these isotopes. However, for effective surveillance of the environment and a rapid risk assessment in case of a nuclear accident, fast determination of the most hazardous isotopes at low detection limits, that is, in the femtogram range

(10^6–10^7 atoms) is indispensable and, in some cases, the isotopic composition provides valuable information on the source of such a contamination, see below. Beyond that, ultratrace determination of long-lived radioisotopes is also applied in biomedical tracer investigations, for radiodating, and in cosmochemistry (Willis et al. 1991; Müller et al. 2001).

If the demands on isotope selectivity are moderate (i.e. the resolution of the used mass spectrometer is sufficient), usually pulsed lasers are used for RIMS. In this way, saturation of the optical excitation steps is normally achieved, and the ionization process is easily combined with a mass separation by a time-of-flight mass spectrometer, where the laser pulse delivers the start signal. For good sensitivity, the temporal and spatial overlap of the evaporized sample and the laser beams need to be considered. If the sample is vaporized continuously by resistive heating, the use of high-repetition-rate pulsed lasers (5–25 kHz) is mandatory. Such a system is routinely used for ultratrace determination of actinides, primarily plutonium, in environmental and biological samples (Passler et al. 1997; Grüning et al. 2004)

After chemical separation of the plutonium from the sample, plutonium hydroxide is electrolytically deposited on a tantalum backing. Subsequently, the plutonium hydroxide is covered with a thin layer (~1 μm) of titanium by sputtering. Thus, when such a so-called sandwich filament is heated to about 1000 °C inside the vacuum recipient, the plutonium hydroxide is converted to the oxide, which then is reduced to the metallic state during diffusion through the titanium layer. On reaching the titanium surface, the plutonium is efficiently evaporated. Subsequently, the atoms are ionized near the filament surface by a three-step, three-color laser excitation. The ions are then accelerated in an electric field and mass selectively detected with a multichannel plate detector behind a time-of-flight drift tube equipped with an ion reflector to improve the mass resolution ($m/\Delta m = 600$ at $A = 240$). In order to obtain quantitative results, a known amount of a tracer isotope – usually ^{244}Pu in the case of environmental samples – is added to the sample, prior to the chemical treatment. Additionally, in most cases, a very small amount of ^{236}Pu is added for monitoring the chemical yield by α spectroscopy.

As mentioned above, a high-repetition-rate laser system is used for maximum temporal overlap. Until recently, three dye lasers pumped by two powerful copper vapor lasers were in operation. The repetition rate was 6.6 kHz, the pulse length ~10–20 ns, and the line width of the dye lasers varied from 1 to 8 GHz, depending on the wavelength and the mode of operation. As copper vapor lasers suffer from high maintenance efforts and costs, a new, full solid-state laser system has been established, consisting of three Ti-sapphire lasers pumped by a high-power, high-repetition-rate Nd:YAG laser (1–25 kHz) with an average output power of up to 50 W at 532 nm. Though the pulse duration of the pump laser exceeds 400 ns, the Ti-sapphire lasers provide pulses of ~70 ns. The tuning range of the lasers is 725–895 nm, while the line width is 2–5 GHz. Each laser delivers up to 3 W output power. The tuning range can be extended by frequency doubling in a nonlinear crystal. This is done for one of the lasers, as the ionization energy of ~6 eV for the actinides must be provided by the sum of the corresponding three photons. Figure 20.9 shows the setup as used in Mainz for sensitive and

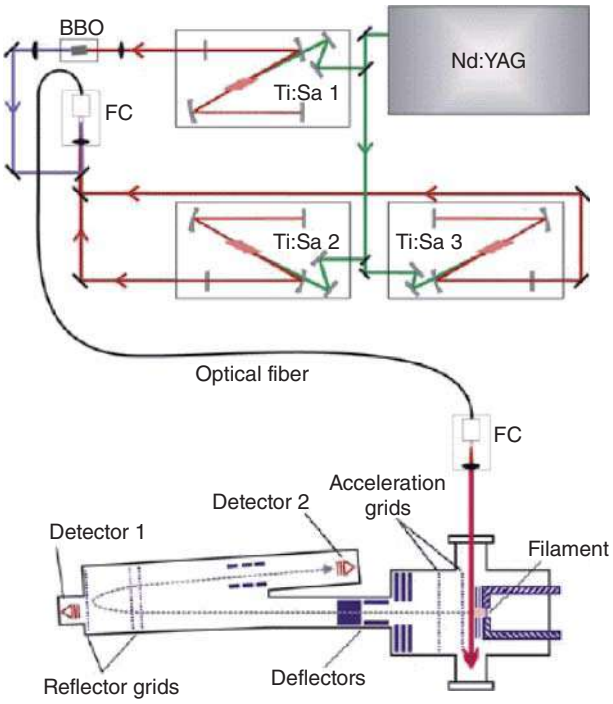

Figure 20.9 Sketch of the setup for pulsed laser RIMS as used at Mainz for sensitive and isotope-selective determination of plutonium and other actinides. Frequency doubling of laser 1 is achieved with a β-barium borate (BBO) crystal. Source: Trautmann et al. (2004), figure 1 (p. 350)/Springer Nature.

isotope-selective determination of plutonium and other actinides. Figure 20.10 shows as an example the threefold excitation scheme for plutonium. Starting from the ground state $^7F_0$, $J = 0$, frequency-doubled laser light with wavelength $\lambda_1 = 420.76\,\text{nm} = 23\,766\,\text{cm}^{-1}$ populates the state $^7D_1$, $J = 1$, and, subsequently, light with wavelength $\lambda_2 = 847.28\,\text{nm} = 11\,803\,\text{cm}^{-1}$ leads to a state with $J = 2$. From there, a high-lying Rydberg state is populated with $\lambda_3 = 767.53\,\text{nm} = 13\,029\,\text{cm}^{-1}$. This state is only $7\,\text{cm}^{-1}$ below the ionization potential of plutonium, IP = 6.0261(1) eV = 48 604(1) cm^{-1}, and, therefore, an electric field of $1.3\,\text{V cm}^{-1}$ is sufficient for the field ionization of the highly excited plutonium. For isotope composition measurements, due to isotope shifts, the wavelengths of lasers 1 and 2 must be readjusted, while laser 3 can be maintained at the same wavelength, Figure 20.10.

Figure 20.11a shows relative isotopic abundances of a plutonium sample from the Chernobyl area exhibiting the typical pattern of the fuel of a power reactor (66.2% ^{239}Pu, 26.1% ^{240}Pu, 5.5% ^{241}Pu, and 1.8% ^{242}Pu in agreement with the published reactor parameters). Figure 20.11b shows for comparison the typical isotopic composition of weapons plutonium from the French test site (^{240}Pu:^{239}Pu ≤ 0.05). Fallout plutonium, in contrast, exhibits a ratio ^{240}Pu:^{239}Pu = 0.18. As stated above, the isotopic composition provides information on the source of the contamination.

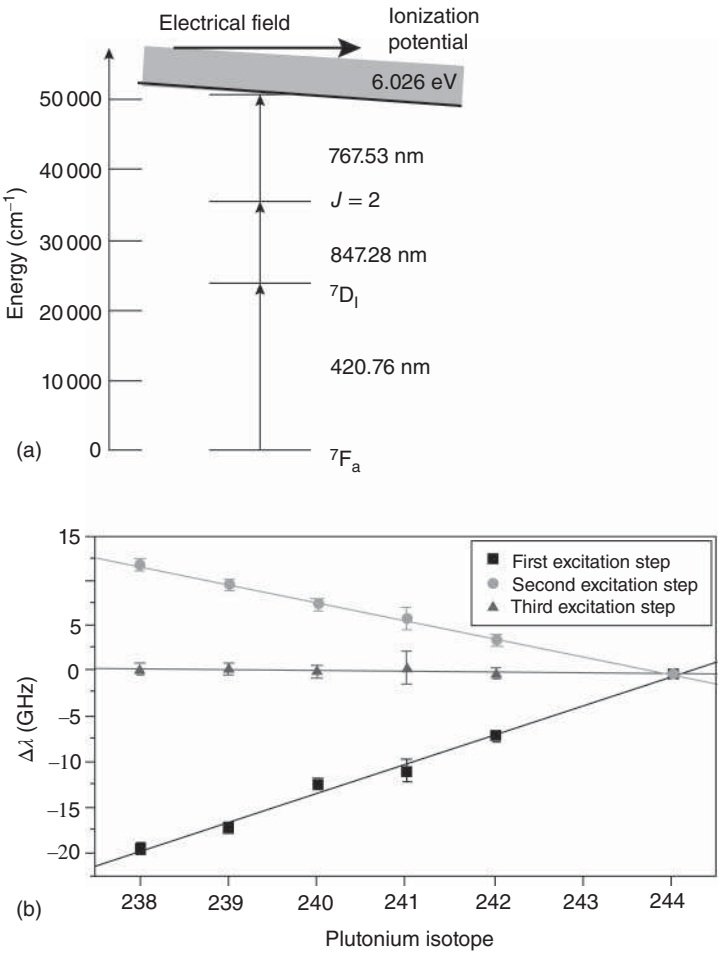

Figure 20.10 Excitation scheme for plutonium using wavelengths produced by three Ti-sapphire solid-state lasers. For isotopic composition measurements, lasers 1 and 2 must be readjusted, while laser 3 can be maintained at the same wavelength. Source: Modified from Grüning et al. (2004).

20.13.2 Accelerator Mass Spectrometry (AMS)

AMS is a modern and sophisticated mass spectrometric technique, specialized to provide the highest selectivity with respect to isobaric and isotopic contaminations. This feature is realized by identifying and counting individual atoms with special detection techniques after acceleration to energies in the megaelectronvolt range. Any interferences from atomic or molecular species are efficiently suppressed in the AMS. Thus, it permits the determination of ultrarare radioisotopes with abundances far below 10^{-9} of a dominant neighboring isotope and surpasses the usual selectivity limits in isotopic ratio measurements of conventional mass spectrometric techniques by far (Purser et al. 1981). The development of this technique has been

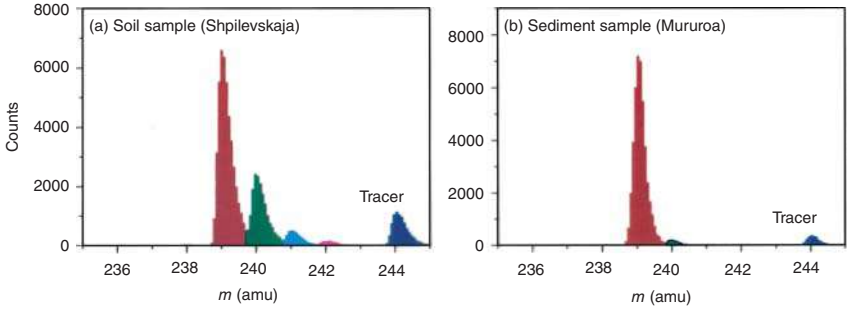

Figure 20.11 (a) Relative isotopic abundances of a plutonium sample from the Chernobyl area. (b) Typical isotopic composition of weapons plutonium from the Mururoa Atoll. Source: Passler et al. (1997)/International Atomic Energy Agency.

boosted primarily in connection with the determination of the cosmogenic radioisotope ^{14}C, which has a unique status offering numerous applications, for example, for radiodating, atmospheric and oceanographic circulation studies, determination of anthropogenic *radioactive contamination* levels, or in biomedicine for studies of cancer prevention using ^{14}C-labeled compounds. Many of these fields of ^{14}C determination have just become possible by AMS, which has replaced the formerly used technique of low-level radiometric counting, as by W.F. Libby in 1955, due to its higher sensitivity, smaller sample size requirement, and faster response. Radiocarbon dating, carried out on ^{14}C isotopic levels as low as 10^{-15}, is the broadest field of application of AMS with thousands of samples per year, but further applications on other radioisotopes have been discovered, which contributes to the value and acceptance of the technique (Michel 1999).

Following a suggestion by Williams et al. (1969), which was triggered by a first, very early mass spectrometric experiment at an accelerator by Alvarez and Cornog (1939), it was realized in the late 1970s that isobaric contaminations can often be eliminated very efficiently by performing mass spectrometry with high-energy (MeV) ion beams (Suter et al. 2000). In this regime, a variety of experimental techniques can be applied and quantitative and highly selective counting of the species of interest with unrivaled background suppression is enabled:

- Already in the ion source of the mass spectrometer, atomic isobars can be expelled by exploiting the stability property of negative ions most often used for AMS in the first acceleration stage of a tandem accelerator. For example, $^{14}N^-$, the only abundant atomic isobar of $^{14}C^-$, is not stable and consequently is not produced or accelerated.
- Molecular isobars can be efficiently removed by passing the accelerated beam through a stripping foil or a gas jet. Here negative ions are efficiently converted into positive ions by stripping off some electrons, while molecules are forced to disintegrate.
- Finally, versatile and discriminatory ion detection techniques, for example, elemental-selective energy loss measurements in segmented ionization chambers,

can be applied on high-energy ions (MeV) to identify the species via its mass and charge number and further reduce the influence of isobaric interferences.

Examples of those interferences in the case of the $^{14}C^{+}$ ion are $^{28}Si^{2+}$, $^{14}N^{+}$, or $^{13}CH^{+}$. Other limiting effects include background effects originating from gas kinetics, wall scattering, and charge-exchange collisions. Nevertheless, these contributions can be strongly suppressed by optimizing the experimental conditions. A typical AMS system is based on a tandem accelerator with a terminal voltage of 2.5–10 MV, usually involving a beam line length of several tens of meters. On the side of the ion source, the so-called low-energy side, intense beams of negative atomic or molecular ions of the species to be analyzed are produced. This is accomplished usually by sputtering, applying Cs^{+} ion bombardment with about 10 keV energy, focused onto the target of the analyte. The latter is introduced in the form of about 10 mg of material, fixed within a target wheel or a sample exchange mechanism with several positions, which enables rapid changing between analytical sample, blank, and standard. The importance of proper chemical pretreatment of the sample, including removal of extraneous material, separation of the element of interest, and conversion into the most suitable form for the sputtering process, must be pointed out. Negative target ions from the sputtering process are accelerated toward a first low-energy (typically $\sim$ 50 keV) mass separator for the first mass selection. By varying the electric potential applied at the magnet chamber, a rapid change from one mass to another is possible. Subsequently, acceleration to the high terminal voltage of several megavolts takes place within the first half of the tandem accelerator. On the high positive potential of the terminal, the ions undergo a stripping process in a thin foil ($\sim$5 μg cm^{-2}) or a gas jet, and a distribution of positive charge states is populated. Now positively charged, these ions are accelerated a second time, this time from the terminal voltage down to ground, for example, in the case of carbon, typically charge states between C^{2+} and C^{7+} are populated, depending on the ion velocity. For the case of the C^{5+} ion, this leads to a total beam energy of 15 MeV on the high-energy side, when a typical 2.5 MV tandem accelerator is used. All molecular ions are dissociated during the stripping process and remaining fragments have significantly altered mass-to-charge ratios and can easily be separated afterward. For this purpose, the high-energy ion beam undergoes another mass-selective step in the second sector field magnet as well as a charge state and energy filtering within an electrostatic deflector before reaching the detectors. Due to the high energy of the incoming ions, some kind of species identification with respect to charge number Z and mass number A is possible by measuring the energy and specific energy loss in a sensitive semiconductor telescope or an energy-sensitive, segmented ionization chamber. A typical layout of an AMS machine, which shows these individual components, is given in Figure 20.12.

Generally, AMS determines the concentration of the rare radioisotope under study by comparing its count rate to the ion current of an abundant stable isotope of the same element as reference. The measured quantity is therefore, in most cases, an isotope ratio, which might cover many orders of magnitude. In most applications, a high accuracy on the order of $\leq$ 1% for this value is required. Such precise isotope

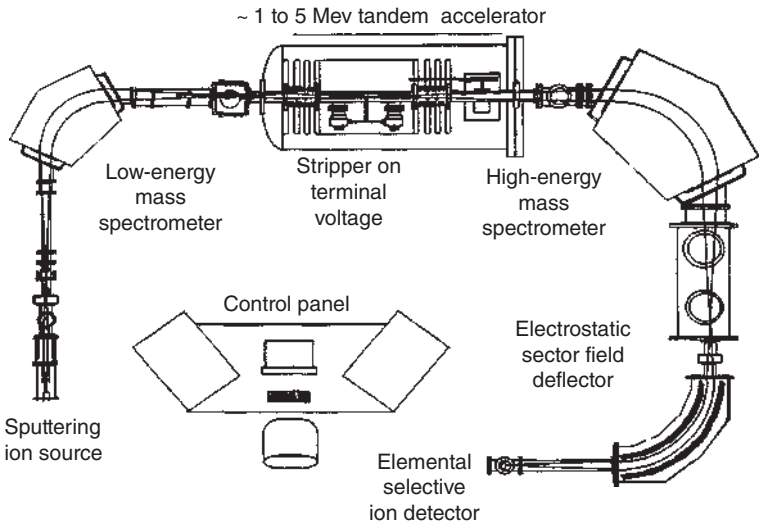

Figure 20.12 Schematic of a modern, compact AMS machine. Source: Huber et al. (2003), p. 799/Elsevier.

ratio measurements with unrivaled dynamical range of up to 15 orders of magnitude are accomplished experimentally by accelerating both isotopes alternately in a fast cyclic mode. While the transmitted atoms of the rare ultratrace isotope are counted individually as ion counts in a Z–A plane, the reference isotope, which typically is up to a factor of 10^{12} more abundant, is measured as electric current using a Faraday cup. Thus, each measurement is accompanied by measurements of blanks and calibration samples for background control and proper quantification. For the heavier isotopes, the energy resolution of semiconductor detectors or ionization chambers is not sufficient for a proper species identification and suppression of isobars and/or neighboring isotopes. A better background suppression is possible by combining the energy determination in the detector with a velocity analysis of the incoming ions by a time-of-flight measurement. In a different approach, a gas-filled magnet in front of the detector leads to a spatial separation of projectiles with different Z and hence significantly increases the selectivity with respect to those isobars which have not been filtered out sufficiently during the stripping process. Recently, enormous effort has been made within the AMS community to reduce the size and costs of AMS systems. By incorporating well-matched technical features like gas strippers and state-of-the-art silicon detectors, low-voltage (300 kV to 1 MV) and very compact AMS machines have been developed (Tuniz et al. 1998). So far, these systems have demonstrated their broad range of applicability not only for ^{14}C measurements but also in analyzing other radioisotopes like ^{3}H, ^{26}Al, ^{41}Ca, ^{129}I, and Pu isotopes with selectivities close to that of a standard large-frame AMS machine (Suter et al. 2000).

AMS has become a standard method for investigations on a variety of long-lived radioisotopes. Commonly investigated isotopes are ^{10}Be, ^{14}C, ^{26}Al, ^{36}Cl, ^{41}Ca, and ^{129}I. Many other isotopes, such as ^{3}H, ^{3}He, ^{7}Be, ^{22,24}Na, ^{32}Si, ^{39}Ar, ^{44}Ti, ^{53}Mn, ^{55,60}Fe, ^{59,63}Ni, ^{79}Se, ^{81}Kr, ^{90}Sr, ^{93}Zr, ^{93}Mo, ^{99}Tc, ^{107}Pd, ^{151}Sm, ^{205}Pb, ^{236}U, ^{237}Np, and

$^{238-244}$Pu, have also been investigated by AMS during the last few years. Most of the radioisotopes mentioned in both categories have natural abundances in the range of 10^{-9} down to 10^{-18}. Several of these are of primordial origin or produced by cosmic radiation, neutron capture, or as fission products. More details about AMS and a compilation of the different AMS versions for individual radioisotopes can be found in the textbook on AMS (Tuniz et al. 1998). The application of AMS in various fields has increased rapidly since the late 1970s. As of the year 2000, there were approximately 50 uniquely dedicated AMS facilities in use around the world, while also nuclear physics accelerators have been adapted to perform AMS measurements. Typical applications include radiodating in archeology with ^{14}C (Chapter 19) with thousands of samples per year, applications in geo- and cosmochemistry, in the life sciences, and in environmental studies of anthropogenic long-lived radionuclides from the nuclear fuel cycle.

20.13.3 Measurements of Ionization Potentials

The RIMS, in which the ionization step can also be done from a high-lying Rydberg state by applying a static electrical field of a few V cm^{-1}, see Figure 20.10, has been shown to be useful in the precise determination of the first ionization potentials of actinides up to einsteinium (Peterson et al. 1998; Willis et al. 1991) that are available in weighable amounts. Even for fermium ($Z = 100$), resonance ionization spectroscopy has been applied (Müller et al. 2001) with the first observation of excited atomic levels of the element.

The method is based on the determination of photoionization thresholds in the presence of a static electric field. According to the classical saddle point model, Figure 20.13, the excitation energy $W(r)$ relative to the electronic ground state of an atom with one highly excited electron, located in an external electric field F, is – in a one-dimensional approximation – given by:

$$W(r) = \mathrm{IP} - \frac{Z_{\mathrm{eff}}\, e^2}{4\pi\varepsilon_0 r} - eFr$$

where e is the electric charge of the electron, Z_{eff} is the effective charge number of the core, r is the distance of the excited electron from the nucleus, e_0 is the permittivity of the vacuum, and IP is the first ionization potential. The ionization threshold W_{th}, which is the maximum of $W(r)$, see Figure 20.13, depends on the electric field strength as follows:

$$W_{\mathrm{th}} = \mathrm{IP} - 2 \cdot \sqrt{\frac{Z_{\mathrm{eff}}\, e^3}{4\pi\varepsilon_0}} \cdot \sqrt{F} = \mathrm{IP} - \mathrm{const} \cdot \sqrt{F}$$

For the determination of photoionization thresholds, a highly excited level of the atom is populated by a two-step or a one-step (Np) resonant excitation. The ionizing laser is scanned across the ionization threshold W_{th} in the presence of F. W_{th} is indicated by a sudden increase in the ion count rate, Figure 20.14. This procedure is repeated for various electric field strengths. Extrapolation of W_{th} to zero field strength leads directly to the first IP (Figure 20.15).

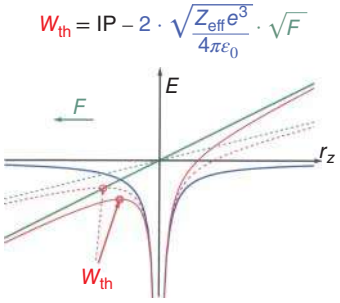

Figure 20.13 Classical saddle point model in which an electrical field gradient F (green) deforms the undisturbed atomic potential (blue) resulting in ionization thresholds W_{th} that depend on the square root of the electric field strength.

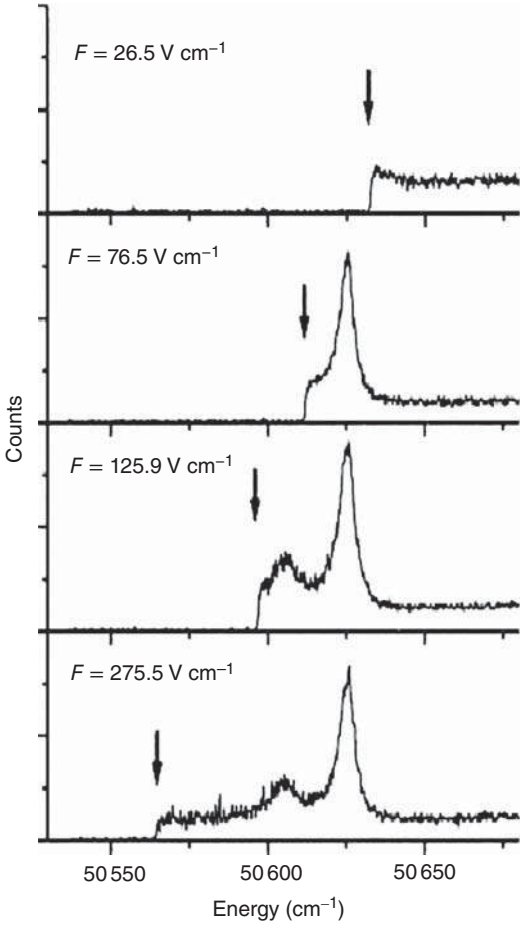

Figure 20.14 Ionization thresholds of ^{252}Cf for four different electric field strengths F. Source: Elsevier.

First ionization potentials (IP_1) of heavier elements with $Z \geq 100$, however, could not be determined experimentally because production rates are drastically decreasing for elements with increasing atomic number. This requires studying these elements with new techniques on an atom-at-a-time scale. Sato et al. have produced ^{256}Lr ($t_{1/2} = 27$ seconds) in the fusion evaporation reaction of a ^{149}Cf target with a ^{11}B beam. A highly efficient experimental setup based on the surface ionization process

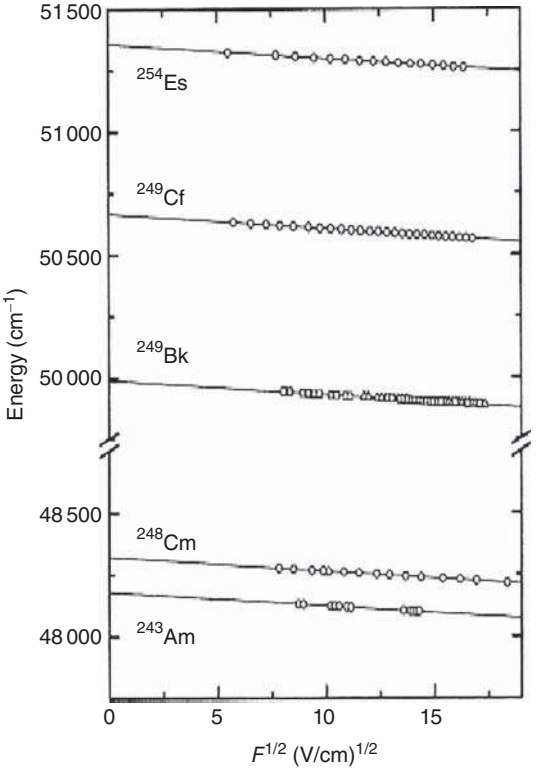

Figure 20.15 Extrapolation of the thresholds W_{th} as a function of the square root of the electric field strength F to zero field strength for the determination of the first ionization potentials IP_1 for five actinide elements. Source: Elsevier.

on a solid surface kept at high temperature coupled to an online mass separator has been implemented to determine the IP_1 value of Lr. The ground-state electronic configuration of Lr is predicted to be $[Rn]5f^{14}\ 7s^2\ 7p_{1/2}$, in contrast to that of its lanthanide homolog Lu, $[Xe]4f^{14}\ 6s^2\ 5d$, as the $7p_{1/2}$ orbital is expected to be stabilized below the 6d orbital in Lr by strong relativistic effects. The determination of the IP_1 sheds light on the important role of relativistic effects in heavy elements by comparison with theoretical predictions. For Lr, theory predicts an exceptionally low IP_1 value.

Based on the Saha–Langmuir equation, an analytical model by Kirchner (1990) describes the surface ionization in a hollow-tube (cavity)-type ion source. The ionization efficiency I_{eff} can be expressed as:

$$I_{\text{eff}} = \frac{N \exp\left(\frac{\phi - IP_1^*}{kT}\right)}{1 + N \exp\left(\frac{\phi - IP_1^*}{kT}\right)} \tag{20.22}$$

where ϕ is the material-dependent work function, T is the temperature of the ionizing surface, N is a parameter depending on the number of atom–surface interactions in the cavity, and k is the Boltzmann constant, and IP_1^*, the effective IP_1, is directly related to the IP_1 as:

$$IP_1^* = IP_1 - kT \ln\left(\frac{Q_i}{Q_0}\right) \tag{20.23}$$

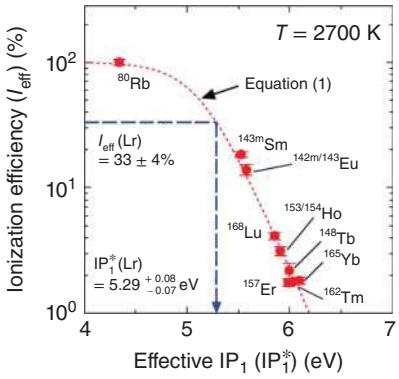

Figure 20.16 Correlation of measured values of I_{eff} at 2700 K for various isotopes with values of IP_1^* (Eq. (20.22)) applied to Lr (lawrencium). Source: Sato et al. (2015)/Springer Nature.

where Q_i and Q_o are the partition functions at a given temperature for the ion and the atom, respectively, which can be calculated using excitation energies and statistical weights of their ground and excited states. As the cavity material, tantalum (Ta) was chosen. The ionization experiments were conducted at $T = 2700$ and 2800 K. For ^{256}Lr, the I_{eff} values of $(33 \pm 4)\%$ and $(36 \pm 7)\%$, respectively, were determined. The following procedure was applied to determine the value of the free parameter N in Eq. (20.22): short-lived lanthanide and alkali isotopes ^{142143}Eu, ^{143}Sm, ^{148}Tb, ^{153154}Ho, ^{157}Er, ^{162}Tm, ^{165}Yb, ^{168}Lu, and ^{80}Rb were produced in bombardments of ^{136}Ce/^{141}Pr/^{159}Tb, ^{142}Nd/^{148}Sm/^{159}Tb, ^{162}Dy, and Ge targets with ^{11}B, and their I_{eff} values were experimentally determined at $T = 2700$ and 2800 K. Figure 20.16 shows the I_{eff} values at 2700 K as a function of IP_1^*. The IP_1^* value for each element was calculated with Eq. (20.23). Energies and statistical weights of low-lying states in the ion and the atom of each element were taken from the National Institute of Standards and Technology (NIST) atomic database. The I_{eff} values determined for all isotopes were best-fitted with Eq. (20.22) using N values of 43 ± 3 and 50 ± 3 at $T = 2700$ and 2800 K, respectively. The Lr IP_1^* values of $5.29^{+0.08}_{-0.07}$ eV and $5.33^{+0.11}_{-0.10}$ eV were determined from Eq. (20.22) at $T = 2700$ and 2800 K, respectively. The result at 2700 K is illustrated in Figure 20.16. The Lr IP_1 can be calculated from the IP_1^* using Eq. (20.23) with Q_i and Q_o. No experimental data on excited states of the Lr atom and ion are available. Thus, the energies and statistical weights for calculating Q_i and Q_o were taken from relativistic Fock-space coupled cluster (FSCC) calculations by Borschevsky et al. (2007).

The average absolute error for the 20 lowest excitation energies of Lu (where comparison with experimental data are possible) was 0.05 eV using the same approach of Borschevsky et al. A similar accuracy for the predicted transition energies of Lr was expected. The resulting values of $kT \ln(\frac{Q_i}{Q_o})$ for Lr at $T = 2700$ and 2800 K are $-0.34^{+0.06}_{-0.04}$ and $-0.36^{+0.06}_{-0.04}$, respectively. The errors include uncertainties in the calculated excitation energies of 0.087 eV (700 cm^{-1}) for each state, and in the temperatures. From this, IP values of $4.95^{+0.10}_{-0.08}$ eV and $4.97^{+0.12}_{-0.11}$ eV were obtained at $T = 2700$ and 2800 K, respectively. Based on these results, the experimental value for the first ionization potential of Lr is $4.96^{+0.08}_{-0.07}$ eV.

The calculated $7s^2\ 7p_{1/2}$ level of Lr is lower by ~180 meV than the $7s^2\ 6d_{3/2}$ level, confirming earlier identification of the former as the atomic ground state. This is due to relativistic effects; a nonrelativistic calculation puts the energy of the $7s^2$ 6d configuration about 2.2 eV below that of $7s^2\ 7p_{1/2}$.

The experimental result on the first ionization potential of Lr of $4.96^{+0.08}_{-0.07}$ eV is in excellent agreement with the theoretical value of 4.963(15) eV also obtained by Borschevsky et al. Thus, it was shown that the first ionization potential of Lr is significantly lower than that of Lu. Lr has the lowest IP_1 value of all lanthanides and actinides. For the last actinide element, this reflects quantitatively and confirms the theoretically predicted situation of closed $5f^{14}$ and $7s^2$ shells with an additional weakly bound electron in the valence orbital. The surface ionization method, successfully applied by Sato et al. to determine the IP_1 of Lr, can provide experimental data which can benchmark quantum chemical calculations of the heaviest elements.

With the successful application of the surface ionization method to determine the IP_1 of Lr, it was obvious that one would like to apply it equally to the elements Fm, Md, and No, for which ionization potentials were not yet known. Thus, the efforts of Sato et al. were extended to this goal. According to the systematic variation of the IP_1 values of heavy actinides, an increasing trend is anticipated up to No due to filling electrons up in the 5f orbital. Nobelium is expected to have the highest IP_1 among the actinides due to the closed-shell structure of $[Rn]5f^{14}7s^2$. To verify this, short-lived isotopes ^{249}Fm ($T_{1/2}$ = 2.6 minutes), ^{251}Md ($T_{1/2}$ = 4.27 minutes), ^{257}No ($T_{1/2}$ = 24.5 seconds), and ^{256}Lr ($T_{1/2}$ = 27 seconds) were produced in nuclear fusion reactions. The produced atoms, recoiling from the target, were transported via a Teflon capillary to a surface ion source installed at the JAEA-ISOL (Isotope Separator Online) by the He/CdI_2 gas-jet transport system. Transported products were injected into the ionization cavity of the ion source. The products were surface-ionized on the hot surface of the Ta cavity kept at a temperature between 2550 and 3000 K. Produced ions were extracted and mass-separated in the ISOL. The number of collected ions after the mass separation was determined by α spectrometry. The I_{eff} value was calculated from a ratio of the number of mass-separated ions to that of directly collected atoms transported by the gas-jet system. The IP_1^* values for ^{249}Fm, ^{251}Md, ^{257}No, and ^{256}Lr were determined on the basis of Eqs. (20.22) and (20.23). To confirm the correlation between I_{eff} and IP_1^* in the present system, I_{eff} values of short-lived lanthanides, an alkali metal, and a chromium isotope were measured. The short-lived isotopes, ^{143m}Sm, ^{142m,143}Eu, ^{148m}Tb, ^{153154}Ho, ^{157}Er, ^{162}Tm, ^{165}Yb, ^{168}Lu, ^{80}Rb, and ^{49}Cr were employed. Figure 20.17 shows the typical plot of the measured I_{eff} values vs. IP_1^* of these elements at T = 3000 K. The IP_1^* values of the above elements were calculated via Eq. (20.23) using their known IP_1 values compiled in the NIST atomic spectra database (ASD). Low-lying excited states for the calculation of Q_i and Q_0 were also taken from NIST ASD. Values of the parameter N were obtained by a best-fit with Eq. (20.22) to the measured I_{eff} values for the isotopes. As an example, the determination of IP_1^* = 6.45 eV for No from I_{eff} = 0.77% at T = 3000 K is depicted in Figure 20.17.

The experiments (Williams et al. 1969; Alvarez and Cornog 1939) described hereafter were carried out behind the velocity filter SHIP at the linear accelerator

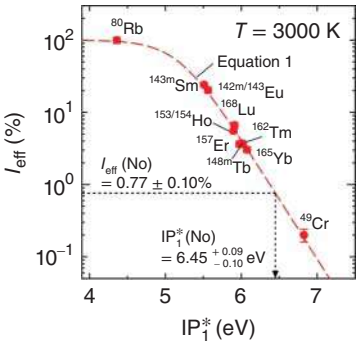

Figure 20.17 Correlation of measured values of I_{eff} for various isotopes with values of IP_1^* (Eq. (20.22) applied to, e.g. No (nobelium). Source: Sato et al. (2018)/American Chemical Society.

(UNILAC) of GSI Helmholtzzentrum für Schwerionenforschung in Darmstadt. The isotopes ^{252254}No were produced in the complete fusion evaporation reactions ^{206}Pb(^{48}Ca,2n)^{252}No and ^{208}Pb(^{48}Ca,2n)^{254}No at UNILAC beam energies of 217 MeV with cross sections of 515 + 80 nb and 2050 + 46°nb. For laser spectroscopy experiments, the beam was chopped in accordance with user-defined measurement cycles. In the case of ^{254}No, the implantation rate of the fusion products delivered to the experiment was repeatedly checked by a retractable position-sensitive 16-strip silicon detector placed at the focal plane of SHIP.

The fusion evaporation residues with a mean kinetic energy of about 41 MeV were separated from the ^{48}Ca primary beam by the velocity filter SHIP and subsequently thermalized inside a buffer gas stopping cell filled with 95-mbar argon of ultrahigh purity. The cell was separated from the vacuum of the SHIP by a 3.5-pm-thick entrance foil (Mylar) on a support grid. A substantial fraction of the stopped fusion products remained in a positive charged state and was collected during the accumulation time of every measurement cycle onto a catcher filament, a tantalum wire with a diameter of 125 p.m. The filament was heated for 300 ms to a temperature of about 1350 K, triggering the evaporation of neutral nobelium atoms for subsequent two-step laser ionization. Ions produced during this process were promptly guided by suitable electric fields to a particle detector, a passivated implanted planar silicon (PIPS) detector. The two-step laser ionization took place during a 5-second time window every cycle, while the primary ion beam was switched off. Correspondingly, 3-second beam-on and 3-second beam-off periods were chosen for the short-lived isotope ^{252}No ($T_{1/2} = 2.42$ seconds). Waiting cycles were introduced by interrupting the data acquisition while changing the laser frequencies necessary especially in the case of ^{254}No, to minimize residual ^{254}No α-decay events that might lead to counts not belonging to the chosen laser frequency.

The extended level search in nobelium was carried out using four tunable excimer laser-pumped dye lasers and an optical oscillator (OPO) system pumped by a frequency-tripled Nd:YAG laser. The dye lasers were set up to scan in the range 25 000–31 000 cm^{-1}. For efficient use of beam time, the lasers were operated simultaneously in different wavelength ranges. They were synchronized with excimer laser synchronization units with respect to the ionizing eximer laser delivering an average pulse energy of 45 mJ of broadband laser light in the wavelength range of

349–353 nm at the optical cell. The total photon energy available for ionization was much higher than all theoretical predictions and extrapolations of the ionization potential of nobelium. The scans near the ionization potential were performed by replacing the excimer ionizing laser with a tunable dye laser scanning in the blue range of the optical spectrum. Only two dye lasers were operated simultaneously. In addition, the dye lasers enabled the use of intracavity etalons and thus a narrowing of the laser bandwidth down to 1.2 GHz.

The overall efficiency of the setup was defined as the ratio of the nobelium decay count rate measured with the PIPS detector at the maximum of a resonance to the implantation rate of nobelium ions delivered to the optical cell, both normalized to the intensity of the primary beam. On average, decay rates in the PIPS detector of 0.39 ± 0.05 and 0.048 ± 0.006 per second per particle microampere ($6.2 \cdot 10^{12}$ ^{48}Ca projectiles per second) were obtained for ^{254}No and ^{252}No, respectively. With these numbers, an overall efficiency of the apparatus of $6.4\% \pm 1\%$ and $3.3\% \pm 1\%$ was calculated for ^{254}No and ^{252}No, respectively, demonstrating the high efficiency of the applied spectroscopy technique. The difference in the quoted numbers is mainly due to the half-lives of the isotopes under investigation. In the spectroscopy of ^{252}No, a shortest possible beam-off period of three seconds was applied. Even though the measurement cycle was optimized to minimize the impact of the half-life on the overall efficiency, the spectroscopy of ^{252}No turned out to be less efficient than that of ^{254}No.

In summary, a robust and efficient two-step excitation scheme with a resonant first excitation step to an intermediate excited state (that is scanned) and a nonresonant second excitation step into the continuum was developed by Block et al. Achieving a high efficiency in the second step requires a laser power with pulse energies of tens of millijoules. This is called the RADRIS method which was successfully applied for nobelium laser spectroscopy. In the experiments, more than 30 atomic states were identified in the isotopes ^{252254}No. The nobelium atom is favorable for atomic spectroscopy due to its relatively simple atomic ground state [Rn] $5f^{14}$ $7s^2$. In addition, it can be produced with relatively high rates in comparison to neighboring elements. The strongest transition in nobelium is from the ground state to the excited $^1P_1$ state, which was identified by a wavelength of 333 nm. This way, the first ionization potential of nobelium was determined with a very high precision from the convergence of measured Rydberg series to be $6.626\,21 \pm 0.000\,05$ eV. This work provides a stringent benchmark for state-of-the-art many-body atomic modeling that considers relativistic and quantum electrodynamic effects and paves the way for high-precision measurements of atomic properties of elements only available from heavy-ion accelerator facilities.

References

General

Friedlander, G., Kennedy, J.W., Macias, E.S., and Miller, J.M. (1981). *Nuclear and Radiochemistry*, 3e. New York: Wiley.

Macias, E.S., Radcliffe, C.D., Lewis, C.W., and Sawicki, C.R. (1978). Proton induced γ-ray analysis of atmospheric aerosols for carbon, nitrogen, and sulfur composition. *Anal. Chem.* 50: 1120.

Sato, T.K., Asai, M., Borschevsky, A. et al. (2015). Measurement of the first ionization potential of lawrencium, element 103. *Nature* 520: 209.

Sato, T.K., Asai, M., Borschevsky, A. et al. (2018). First ionization potentials of Fm, Md, No, and Lr: verification of filling-up the 5f electrons and confirmation of the actinide series. *J. Am. Chem. Soc.* 140: 14609.

Sewtz, M., Backe, H., Dong, C.Z. et al. (2003a). Resonance ionization spectroscopy of fermium (Z = 100). *Spectrochim. Acta B* 58: 1077.

Sewtz, M., Backe, H., Dretzke, A. et al. (2003b). Resonance ionization spectroscopy of fermium (Z = 100) first observation of atomic levels for the element of fermium (Z = 100). *Phys. Rev. Lett.* 90: 163002.

More Specialized

Geiger, H. and Marsden, E. (1909). Diffuse reflection of the α particle. *Proc. R. Soc.* 82: 495.

Rutherford, E. (1911). The scattering of α and β particles by matter and the structure of the atom. *Philos. Mag.* 21: 669.

Turkevich, A., Franzgrote, E., and Patterson, J. (1967). Chemical analysis of the moon at the surveyor 5 landing site. *Science* 158: 635.

Radionuclide Mass Spectrometry

Alvarez, L.W. and Cornog, R. (1939). ^{3}He in helium. *Phys. Rev.* 56: 379.

Ambartzumian, R.V. and Letokhov, V.S. (1972). Selective two-step (STS) photoionization of atoms and photodissociation of molecules by laser radiation. *Appl. Opt.* 11: 354.

Backe, H., Dretzke, A., Habs, D. et al. (2001). Stability of superdeformation for americium fission isomers as function of the neutron number. *Nucl. Phys.* A690: 215C.

Grüning, C., Huber, G., Klopp, P. et al. (2004). Resonance ionization mass spectrometry for ultratrace analysis of plutonium with a new solid-state laser system. *Int. J. Mass spectrom.* 235: 171.

Hilberath, T., Becker, S., Bollen, G. et al., and the ISOLDE Collaboration (1992). Ground-state properties of neutron-deficient platinum isotopes. *Z. Phys.* A342: 1.

Huber, G., Passler, G., Wendt, K. et al. (2003). Radioisotope mass spectrometry. In: *Handbook of Radioactivity Analysis*, Chapter 10, 2e (ed. M.F. L'Annunziata), 799. San Diego, CA: Elsevier.

Michel, R. (1999). Long-lived radionuclides as tracers in terrestrial and extraterrestrial matter. *Radiochim. Acta* 87: 47.

Muller, R.A. (1977). Radioisotope dating with a cyclotron. *Science* 196: 489.

Müller, P., Bushaw, B.A., Blaum, K. et al. (2001). ^{41}Ca ultratrace determination with isotopic selectivity > 10^{12} by diode-laser-based RIMS. *Fresenius J. Anal. Chem.* 370: 508.

Passler, G., Erdmann, N., Hasse, H.-U. et al. (1997). Application of laser mass spectrometry for trace analysis of plutonium and technetium. *Kerntechnik* 62: 85.
Payne, M.G., Deng, L., and Thonnard, N. (1994). Applications of resonance ionization mass spectrometry. *Rev. Sci. Instrum.* 65: 2433.
Peterson, J.R., Erdmann, N., Nunnemann, M. et al. (1998). Determination of the first ionization potential of einsteinium by resonance ionization mass spectroscopy (RIMS). *J. Alloys Compd.* 271–273: 876.
Purser, K.H., Williams, P., Litherland, A.E. et al. (1981). Isotopic ratio measurement at abundance sensitivities greater than $1{:}10^{15}$: A comparison between mass spectrometry at keV and MeV energies. *Nucl. Instrum. Methods Phys. Res.* 186: 487.
Suter, M., Jacob, S.W.A., and Synal, H.-A. (2000). Tandem AMS at sub-MeV energies – status and prospects. *Nucl. Instrum. Methods Phys. Res.* B172: 144.
Synal, H.-A., Jacob, S., and Suter, M. (2000). The PSI/ETH small radiocarbon dating system. *Nucl. Instrum. Methods Phys. Res.* B172: 1.
Trautmann, N., Passler, G., and Wendt, K. (2004). Ultratrace analysis and isotope ratio measurements of long-lived radioisotopes by resonance ionization mass spectrometry (RIMS). *Anal. Bioanal. Chem.* 378: 348.
Tuniz, C., Bird, J.R., Fink, D., and Herzog, G.F. (1998). *Accelerator Mass Spectrometry*. Boca Raton, FL: CRC Press.
Wendt, K., Trautmann, N., and Bushaw, B.A. (2000). Resonant laser ionization mass spectrometry: an alternative to AMS? *Nucl. Instrum. Methods Phys. Res.* B172: 162.
Williams, P.M., Oeschger, H., and Kinney, P. (1969). Natural radiocarbon activity of the dissolved organic carbon in the north-East Pacific Ocean. *Nature* 224: 256.
Willis, R.D., Thonnard, N., Eugster, O. et al. (1991). *Resonance Ionization Spectroscopy 1990Inst. Phys. Conf. Ser*, vol. 114 (eds. J.E. Parks and N. Omenetto), 275. Bristol: IOP Publishing.

Measurements of ionization potentials

Borschevsky, A., Eliav, E., Vikas, M. et al. (2007). Transition energies of atomic lawrencium. *Eur. Phys. J.* D45: 115.
Kirchner, R. (1990). On the thermoionization in hot cavities. *Nucl. Instrum. Methods A* 292: 203.

Further Reading

General

Hahn, O. (1936). *Applied Radiochemistry*. Ithaca, NY: Cornell University Press.
Wahl, A.C. and Bonner, N.A. (1951). *Radioactivity Applied to Chemistry*. New York: Wiley.
Haissinsky, M. (1964). *Nuclear Chemistry and its Applications*. Reading, MA: Addison-Wesley.
Duncan, J.F. and Cook, G.B. (1968). *Isotopes in Chemistry*. Oxford: Clarendon Press.
Tölgyessy, J., Varga, S., Krivan, V. (vols. I, II), Kyrs, M. (vol. II), and Krtil, J. (vol. III). *Nuclear Analytical Chemistry*, vols. I, II, III. Baltimore, MD: University Park Press.1971, 1972, 1974

Comber, D.I. (1975). *Radiochemical Methods in Analysis*. London: Plenum Press.
Elving, P.J., Krivan, V., and Kolthoff, I.M. (eds.) (1986). Treatise on analytical chemistry, Part I theory and practice. In: *Section K, Nuclear Activation and Radioisotopic Methods of Analysis*, 2e, vol. 14. New York: Wiley.
Ehmann, W.D. and Vance, D.E. (1991). *Radiochemistry and Nuclear Methods of Analysis*. New York: Wiley.
Tölgyessy, J. and Bujdosó, E. (1991). *CRC Handbook of Radioanalytical Chemistry*, vols. I, II. Boca Raton, FL: CRC Press.

More Specialized

Braun, T. and Tölgyessy, J. (1967). *Radiometric Titrations*. Oxford: Pergamon.
Ruzicka, J. and Stary, I. (1968). *Substoichiometry in Radiochemical Analysis*. Oxford: Pergamon.
Lenihan, J.M. and Thomson, S.J. (eds.). *Advances in Activation Analysis*. New York: Academic Press.1969, 1972
Hoste, J., Op de Beeck, J., Gijbels, R. et al. (1971). *Activation Analysis*. London: Butterworths.
de Soete, D., Gijbels, R., and Hoste, J. (1972). *Neutron Activation Analysis*. New York: Wiley.
Tölgyessy, J., Braun, T., and Kyrs, M. (1972). *Isotope Dilution Analysis*. Oxford: Pergamon.
Cooper, J.A. (1973). Comparison of particle and photon excited X-ray fluorescence applied to trace element measurements on environmental samples. *Nucl. Instrum. Methods* 106: 525.
Ziegler, J.F. (ed.) (1975). *New Uses of Ion Accelerators*. New York: Plenum.
Erdtmann, G. (1976). *Neutron Activation Tables* (ed. K.H. Lieser). Weinheim: Verlag Chemie.
Ziegler, J.F. (1976). Material analysis with ion beams. *Phys. Today* 29 (11): 52.
Various authors (1977). Proceedings of the International Conference on Modern Trends in Activation Analysis, Munich, (1976). *J. Radioanal. Chem*. 37 (1982) Toronto, (1981). *J. Radioanal. Chem*., 69 and 70.
Chu, W.-K., Mayer, J.W., and Nicolet, M.-A. (1978). *Backscattering Spectrometry*. New York: Academic Press.
Erdtmann, G. and Petri, H. (1986). Nuclear activation analysis: fundamentals and techniques. In: *Treatise on Analytical Chemistry*, Part I, 2e, vol. 14 (ed. P.J. Elving). New York: Wiley.
Pilz, N., Hoffmann, P., and Lieser, K.H. (1989). In-line determination of heavy elements by gamma-ray induced energy-dispersive K-line XRF. *J. Radioanal. Chem.* 130: 141.
Parry, S.J. (1991). *Activation Spectrometry in Chemical Analysis*. New York: Wiley.
Yonezawa, C. (1993). Prompt γ-ray analysis of elements using cold and thermal reactor neutrons. *Anal. Sci.* 9: 185.
Csikai, J. and Dóczi, R. (2011). Application of neutron generators. In: *Handbook of Nuclear Chemistry*, 2e, vol. 3 (eds. A. Vértes, S. Nagy, Z. Klencsár, et al.), 1673. Berlin: Springer-Verlag.

Koltay, E., Pászti, F., and Kiss, Á.Z. (2011). Chemical applications of accelerators. In: *Handbook of Nuclear Chemistry*, 2e, vol. 3 (eds. A. Vértes, S. Nagy, Z. Klencsár, et al.), 1695. Berlin: Springer-Verlag.

Révay, Z., Lindstrom, R.M., Mackey, E.A., and Belgya, T. (2011). Neutron-induced prompt gamma activation analysis (PGAA). In: *Handbook of Nuclear Chemistry*, 2e, vol. 3 (eds. A. Vértes, S. Nagy, Z. Klencsár, et al.), 1619. Berlin: Springer-Verlag.

Zeisler, R., Vajda, N., Kennedy, G. et al. (2011). Activation analysis. In: *Handbook of Nuclear Chemistry*, 2e, vol. 3 (eds. A. Vértes, S. Nagy, Z. Klencsár, et al.), 1619. Berlin: Springer-Verlag.

Radionuclide Mass Spectrometry

Bennett, C.L., Beukens, R.P., Clover, M.R. et al. (1977). Radiocarbon dating using electrostatic accelerators: negative ions provide the key. *Science* 198: 508.

Betti, M., Giannarelli, S., Hiernaut, T. et al. (1996). Detection of trace radioisotopes in soil, sediment and vegetation by glow discharge mass spectrometry. *Fresenius J. Anal. Chem.* 355: 642.

Fifield, L.K., Cresswell, R.G., di Tada, M.L. et al. (1996). Accelerator mass spectrometry of plutonium isotopes. *Nucl. Instrum. Methods Phys. Res.* B117: 295.

Erdmann, N., Betti, M., Stetzer, O. et al. (2000). Production of monodisperse uranium oxide particles and their characterization by scanning electron microscopy and secondary ion mass spectrometry. *Spectrochim. Acta* B55: 1565.

Grüning, C., Huber, G., Kratz, J.V. et al. (2001). Determination of trace amounts of plutonium in environmental samples by RIMS using a high repetition rate solid state laser system. In: *Resonance Ionization Spectroscopy 2000*, AIP Conference Proceedings, vol. 584 (eds. J.E. Parks and J.P. Young), 255. Melville, NY: AIP Press.

Measurements of ionization potentials

Maeda, H., Mizugai, Y., Matsumoto, Y. et al. (1989). Highly excited even Rydberg series of Lu I studied by two-step laser photoionization spectroscopy. *J. Phys.* B22: L511.

Eliav, E., Kaldor, U., and Ishikawa, Y. (1995). Transition energies of ytterbium, lutetium, and lawrencium by the relativistic coupled-cluster method. *Phys. Rev. A* 52: 291.

Erdmann, N., Nunnemann, M., Eberhardt, K. et al. (1998). Determination of the first ionization potential of nine actinide elements by resonance ionization mass spectroscopy (RIMS). *J. Alloys Compd.* 271–273: 837.

Liu, W., Küchle, W., and Dolg, M. (1998). Ab initio pseudopotential and density-functional all-electron study of ionization and excitation energies of actinide atoms. *Phys. Rev.* A58: 1103.

Peterson, J.R., Erdmann, N., Nunnemann, M. et al. (1998). Determination of the first ionization potential of einsteinium by resonance ionization mass spectroscopy (RIMS). *J. Alloys Compd.* 271–273: 876.

Backe, H., Dretzke, A., Eberhardt, K. et al. (2002). First determination of the ionization potential of actinium and first observation of optical transitions in fermium. *J. Nucl. Sci. Technol.* (Suppl. 3): 86.

Cao, X., Dolg, M., and Stoll, H. (2003). Valence basis sets for relativistic energy-consistent small-core actinide pseudopotentials. *J. Chem. Phys.* 118: 487.

Indelicato, P., Santos, J.P., Boucard, S., and Desclaux, J.-P. (2007). QED and relativistic corrections in superheavy elements. *Eur. Phys. J.* D45: 155.

Pershina, V. (2010). Electronic structure and chemistry of the heaviest elements. In: *Relativistic Methods for Chemists*, Challenges and Advances in Computational Chemistry and Physics, vol. 10 (eds. M. Barysz and Y. Ishikawa), 451. Dordrecht: Springer.

Kramida, A., Ralchenko, Y., Reader, J., and Team, N.A. (2013). NIST atomic spectra database (version 5.1). http://physics.nist.gov/asd (accessed July 2014).

Sato, T.K. et al. (2013). First successful ionization of Lr ($Z = 103$) by a surface-ionization technique. *Rev. Sci. Instrum.* 84: 023304(5).

Visscher, L. et al. (2013). DIRAC, A relativistic ab initio electronic structure program, Release DIRAC13. see www.diracprogram.org (accessed 09 February 2021).

Stora, T. (2014). Radioactive ion sources. *CERN Yellow Report* CERN-2013-007, 331. http://cds.cern.ch/record/1693046 (accessed 09 February 2021).

Backe, H., Lauth, W., Block, M., and Laatiaoul, M. (2015). Prospects for laser spectroscopy, ion chemistry and mobility measurements of superheavy elements in buffer-gas traps. *Nucl. Phys.* A944: 492.

Block, M. (2015). Direct mass measurements of the heaviest elements with penning traps. *Nucl. Phys.* A944: 471.

Eliav, E., Fritzsche, S., and Kaldor, U. (2015). Electronic structure theory of the superheavy elements. *Nucl. Phys.* A944: 518.

Schwerdtfeger, P., Pasteka, L.F., Punnett, A., and Bowman, P.O. (2015). Relativistic and quantum electrodynamic effects in superheavy elements. *Nucl. Phys.* A944: 551.

NIST ASD Team (2016). Atomic Spectra Database version 5.3. http://physics.nist.gov ASD (NIST, accessed March 2016).

Chhetri, P., Ackermann, D., Backe, H. et al. (2018). Precision measurement of the first ionization potential of nobelium. *Phys. Rev. Lett.* 120: 3003–3001.

Laatiaoui, M., Lauth, W., Backe, H. et al. (2018). Atom-at-a-time laser resonance ionization spectroscopy of nobelium. *Nature* 538: 495.

21

Radionuclides in the Life Sciences

21.1 Survey

Application of radionuclides in life sciences is of the greatest importance, and the largest single user of radionuclides is nuclear medicine. Shortly after the discovery of radium in 1898 by Marie Curie and its subsequent isolation from pitchblende in amounts of 0.1–1 g, the finding that this element was useful as a radiation source led to the first application of radionuclides in medicine. In 1921, G. de Hevesy investigated the metabolism of lead in plants by use of natural radioisotopes of Pb.

The spectrum of radionuclides available for application in the life sciences broadened appreciably with the invention of the cyclotron by E.O. Lawrence in 1930 and the possibility of producing radionuclides on a large scale in nuclear reactors in the late 1940s. By the application of T and ^{14}C, important biochemical processes, such as photosynthesis in plants, could be elucidated.

Nowadays, nuclear medicine has become an indispensible section of medical science, and the production of radionuclides and labeled compounds for application in nuclear medicine is an important branch of nuclear and radiochemistry. The development of radionuclide generators made short-lived radionuclides available at any time for medical application. New imaging devices, such as single-photon emission computed tomography (SPECT) and positron emission tomography (PET), made it possible to study local biochemical reactions and their kinetics in the living human body.

It is an attractive object of research to synthesize labeled compounds that are taking part in specific biochemical processes or are able to pass specific barriers in the body, with the aim of detecting malfunctions and of localizing the origin of diseases. Complexes of short-lived, no-carrier-added radionuclides and high yields of the syntheses are of special interest. In the case of short-lived radionuclides, such as ^{11}C, the synthesis must be fast and as far as possible automated. Labeled organic molecules can also be used to transport radionuclides to special places in the body for therapeutic application, that is, as specific internal radiation sources.

Nuclear and Radiochemistry: Fundamentals and Applications,
Fourth Edition. Jens-Volker Kratz.

The following fields of application of radionuclides in the life sciences can be distinguished:

- ecology (uptake of trace elements and radionuclides from the environment by plants, animals, and humans);
- analysis (determination of trace elements or compounds in plants, animals, and humans);
- physiology and metabolism (reactions and biochemical processes of elements and compounds in plants, animals, and humans);
- diagnosis (identification and localization of diseases);
- therapy (treatment of diseases).

In ecological and metabolic studies, and in diagnosis, radioactive tracers are applied (radiotracer techniques). Analytical applications in the life sciences are based either on activation or on tracer techniques, whereas for therapeutic purposes, relatively high activities of radionuclides are used.

21.2 Application in Ecological Studies

The uptake of trace metals from the soil by plants and animals can be studied with high sensitivity by radiotracer techniques. In these applications, it is important that the chemical form of the radiotracer is identical with that of the trace element to be studied. For example, in agriculture, the uptake of trace elements necessary for plant growth can be investigated. Essential trace elements, such as selenium, are of special interest. By using radioactively labeled selenium compounds, the transfer of this element from the soil to plants and animals can be measured. For the investigation of the transfer of radionuclides (radioecology), the addition of tracers is, in general, not needed.

In radioecology, transfer factors for relevant radionuclides in various systems (e.g. soil → plant, plant → animal, plant → human, animal → human) have been determined. These transfer factors are used for the assessment of radiation doses received by animals or humans because of the presence of natural radionuclides or of *radioactive fallout*.

21.3 Radioanalysis in the Life Sciences

Two radioanalytical methods described in Chapter 20 are applied preferentially in the life sciences, namely, activation analysis and isotope dilution, the latter mainly in combination with the substoichiometric principle.

Activation analysis can be used for the determination of trace elements, in particular heavy metals and essential elements, in various parts or organs, respectively, of plants or animals and humans. Making use of the high sensitivity of activation analysis, small samples on the order of several milligrams taken from selected places give information about the concentration of the elements of interest. The results

of activation analysis of trace elements also allow conclusions to be drawn about diseases or malfunctions and are valuable aids to diagnosis. Examples are the determination of selenium in humans or of trace element concentrations in bones or other body parts, with respect to the sufficient supply of essential elements and metabolism. In vivo irradiation has also been proposed.

Isotope dilution in combination with the substoichiometric principle is applied in various ways. The most important examples are radioimmunoassay for protein analysis and DNA analysis. In radioimmunoassay, radionuclides are used as tracers and immunochemical reactions for isolation. Radioimmunoassay was first described in 1959 by R.S. Yalow and S.A. Berson and since then has found very broad application in clinical medicine, in particular for the measurement of serum proteins, hormones, enzymes, viruses, bacterial antigens, drugs, and other substances in blood, other body fluids, and tissues. Only one drop of blood is needed, and the analysis can be performed automatically. Today more than 10^7 immunoassays are done annually in the USA. The most important advantages of the method are the high sensitivity and the high specificity. In favorable cases, quantities down to 10^{-13} g can be determined and, in general, only the components of interest are detected. Since measurement of absolute quantities is not necessary, the accuracy is excellent. Difficulties may arise if the immunochemical reactions fail or if they are not selective.

The general procedure of radioimmunoassay is as follows. Two aliquots each containing a known mass m_0 of a labeled protein *P are taken. One aliquot is mixed with a much smaller (substoichiometric) mass of an antibody B which forms the complex *PB. The latter is isolated and its radioactivity A_1 is measured. The other aliquot of the labeled protein *P is mixed with the unknown mass m_x of the protein to be determined, and this mixture is also allowed to react with the same amount of antibody B as before. Again, the complex *PB is isolated, and its radioactivity A_2 is measured. The unknown mass m_x is calculated by the application of Eq. (20.18).

A large number of variations of radioimmunoassay are possible: competitive or non-competitive binding assays and different antibodies may be applied, and various radionuclides may be used for labeling (preferably T, ^{14}C, ^{35}S, ^{32}P, ^{125}I, and ^{131}I).

The base sequence of DNA is determined in the following way. The cell walls are broken up by osmosis or other methods and the double-stranded DNA is denaturized to single-stranded pieces, which may be concentrated by centrifugation. By the application of different restriction enzymes, the nucleotide chains are sectioned further into different sets of smaller fragments. To these sets labeled compounds are added that attach selectively to the different fragments. The compounds are labeled with radionuclides, such as T, ^{14}C, or ^{32}P. On the other hand, the original DNA chain is directly labeled (e.g. by ^{32}P) in a cloning process, and the cloned DNA is also split into fragments by the application of restriction enzymes. All samples obtained by treatment with different restriction enzymes are subjected to electrophoresis in a gel, such as agarose or polyacrylamide, by which the fragments are separated according to their migration velocities. By means of autoradiography, characteristic patterns of spots or bands are obtained which give information about the individual from which the DNA was taken.

Table 21.1 Examples of trace element determination in biological samples by isotope dilution in combination with substoichiometric isolation.

Species	Conditions
Ca^{2+}	2-Thenoyltrifluoroacetone in CCl_4
Sr^{2+}	8-Quinolinol in $CHCl_3$
Sn(IV)	*N*-Benzoyl-*N*-phenylhydroxylamine in $CHCl_3$
PO_4^{3-}	Extraction of phosphomolybdate formed with molybdate into methyl isobutyl ketone
F^-	$(CH_3)_3SiCl$ in C_6H_6
Ag^+	Dithizone in CCl_4
Au(III)	Cu diethyldithiocarbamate in $CHCl_3$
Cd^{2+}	Dithizone in $CHCl_3$
Hg^{2+}	Thionalide in $CHCl_3$
$(C_6H_5)_2Hg$	Dithizone in $CHCl_3$
Cr(VI)	Diethylammonium diethyldithiocarbamate in C_6H_6
Fe^{3+}	8-Quinolinol in $CHCl_3$
Ni^{2+}	Diacetyldioxime in $CHCl_3$

DNA analysis is of growing importance for various purposes, such as transplantation of organs, detection of genetic diseases, investigation of the evolution of species, or identification of criminals in forensic science.

The substoichiometric principle is also applied for the determination of trace elements in biological systems. Some examples are listed in Table 21.1. The detection limits are usually below $1\,mg\,l^{-1}$ and in some cases (e.g. $(C_6H_6)_2Hg$) below $10^{-3}\,mg\,l^{-1}$.

21.4 Application in Physiological and Metabolic Studies

For investigating physiological or metabolic processes in plants, animals, and humans, radiotracer techniques are very useful because of their high sensitivity and the possibility of labeling at certain positions of the molecules. In plant physiology, important biochemical processes can be elucidated by the application of radiotracers. An illustrative example is photosynthesis in plants. Plants growing in an atmosphere containing $^{14}CO_2$ synthesize ^{14}C-labeled sugars and cellulose in a sequence of chemical reactions. By measuring the ^{14}C-labeled intermediates and products, it is possible to trace the steps of photosynthesis and to identify the intermediates.

Labeled species taken up by animals are incorporated in various amounts and may be accumulated in certain organs where they undergo chemical reactions, in particular biochemical synthesis and degradation. Finally, products of metabolism

are removed from the body. The distribution of the radionuclides in the body gives significant information about normal and abnormal processes. The radionuclides may be measured by direct counting or by autoradiography. Examples are the investigation of the metabolism of amino acids, vitamins, drugs, or other compounds in animals by means of labeled compounds.

The position of labeling must be chosen in such a way that the products of metabolism can be identified, for example, by labeling with T or ^{14}C in the side chain of an aromatic compound if the fate of the side chain is of interest or labeling in the aromatic part of the molecule if this is the main object of the investigation. Double labeling, for instance, by T and ^{14}C at different positions, is often very helpful.

New drugs developed in the laboratories of the pharmaceutical industry must be investigated with respect to their metabolism, before they are admitted for general use. Labeling of the drugs with radionuclides at certain positions of the molecule is the most appropriate method for detailed examination of the metabolism.

The metabolism of trace elements, their possible accumulation in certain organs or parts of the body, and their excretion can also be studied with high sensitivity by the application of radiotracers.

21.5 Radionuclides Used in Nuclear Medicine

The production of radionuclides, among others particularly those used in nuclear medicine, has been covered in Section 11.5. Many of these radionuclides are also applied in biochemical and agricultural studies with animals and plants.

For diagnostic applications in medicine, four aspects are of major importance:

- the radiation exposure of the patients;
- the measurability of the radionuclide from outside;
- the availability of the radionuclide and of suitable labeled compounds; and
- the radionuclide purity.

The radiation exposure of the patients depends on the activity of the radionuclide, the kind of radiation emitted, the half-life of the radionuclide, and its residence time in the body. With respect to radiation exposure, α emitters are not suitable for diagnostic applications because of the high-energy doses transmitted locally to organs or tissues.

However, radiation exposure is low if only γ-rays are emitted, as in the case of isomeric transition (IT) or electron capture (ε). γ-ray emitters are easily measurable from outside, and γ-ray energies in the range between about 50 and 500 keV are most favorable with respect to penetration through tissues and counting efficiency.

The lower limit of half-lives of radionuclides for diagnostic applications is on the order of minutes. It is determined by the time needed for the synthesis of suitable compounds and for transport in the body to the place of application. On the other hand, half-lives >1 day are less favorable because of the longer radiation exposure of the patients and the risk of environmental contamination.

For the application of radionuclides with half-lives <10 hours, radionuclide generators or suitable accelerators must be available in the hospital or nearby. Radionuclide generators are described in Section 11.5.4. They offer the significant advantage that the radionuclides are available at any time for direct application. The ^{99}Mo/^{99m}Tc generator is used most frequently because of the favorable properties of ^{99m}Tc: only γ-rays are emitted, the half-life is very suitable for diagnostic application, and the 141 keV rays can be measured from outside with high counting efficiency. Furthermore, the activity of the ground state ^{99}Tc can be neglected because of its relatively long half-life; the activity ratio of ^{99}Tc formed by the decay of ^{99m}Tc to the initial activity of the latter is only $A(^{99}\text{Tc}):A(^{99m}\text{Tc}) \approx 3 \cdot 10^{-9}$. Because of its favorable properties, ^{99m}Tc is the most frequently used radionuclide in nuclear medicine. After elution from the generator as $^{99m}TcO_4^-$, it is transformed into or attached to suitable compounds for specific applications. For this purpose, kits are used that guarantee high yields, good reproducibility, and good performance by people not skilled in radiochemistry.

The production of short-lived positron emitters has been described in Chapter 11. By interacting with electrons, the positrons are annihilated and two γ-ray photons of 511 keV each are emitted simultaneously in opposite directions. By measuring these photons by means of a suitable array of detectors, exact localization of the radionuclides in the body is possible. This is the basis of PET, which has found broad application in nuclear medicine. The most frequently used positron emitters were presented in Section 11.5.2. They are preferably produced by small cyclotrons in the hospitals or nearby.

For therapeutic purposes, natural radionuclides, mainly ^{226}Ra and ^{222}Rn, were the first to be applied as external and internal radiation sources. For example, encapsulated samples of ^{226}Ra have been attached to the skin or introduced into the body, and ^{222}Rn has been recommended for the treatment of the respiratory tract by inhalation in radon galleries, or it has been encapsulated in small, thin-walled gold tubes and introduced into the body for the treatment of cancer.

Various artificial radionuclides were originally applied in relatively large amounts for external and internal irradiation, and some of these radionuclides are still used in radiotherapy, either as external radiation sources (e.g. ^{60}Co and ^{137}Cs for the treatment of cancer) or for internal application. Examples are ^{131}I in amounts of about 200–1000 MBq for the treatment of hyperthyroidism or thyroid cancer, ^{32}P for the treatment of bone cancer or leukemia, and ^{198}Au for the treatment of ovarian cancer.

A fascinating aspect of radiotherapy is the development of monoclonal antibodies that are labeled with α or β emitters and able to seek out particular types of cancer cells, to which they deliver large absorbed doses, whereas neighboring tissues receive only small doses.

For all internal medical applications, in particular for diagnostic purposes, radionuclide purity is of the highest importance. The absence of long-lived radioactive impurities, in particular α emitters, such as actinides, or high-energy β emitters, such as ^{90}Sr, must be guaranteed. The main problem in checking the radionuclide

purity of short-lived radionuclides is that many impurities, for example, pure β emitters, can only be detected after decay of these short-lived radionuclides or after chemical separation. This makes the checking of purity before application difficult, and the development of suitable and reliable procedures for the control of radionuclide purity is of great importance.

21.6 Single-Photon Emission Computed Tomography (SPECT)

In computed tomography (CT) with radionuclides, one or several radiation detectors, a computer, and a display are used. The detector array is moved in relation to the patient, and the variations in counting rates with the absorbancies of the radiation in the body as a function of the geometry are processed by the software of the computer to give an image on the screen. This procedure is repeated in subsequent sections (slices) of the body, thus providing a three-dimensional picture. The resolution of the scan is on the order of 1 mm. The method is similar to that used in X-ray CT, but in the latter, both the radiation source and the detector array can be moved in relation to the patient.

The application of compounds labeled with suitable radionuclides as radiation sources makes it possible to measure the incorporation and removal of these substances in certain organs of the body, thus providing information about the metabolism and the function of organs of interest. In this way, malfunction and disorder can be detected at very early stages.

Radionuclides applied for SPECT should preferably decay by emission of a single γ-ray photon, and the best resolution is obtained at relatively low γ energies. The γ-rays are usually measured by means of NaI(Tl) crystals to obtain high counting efficiencies. Crystals and collimators are combined with a so-called gamma camera which may be used as a stationary detector system to give a single two-dimensional picture. Several cameras at fixed positions or rotating around the patient are used for scanning, to obtain a three-dimensional picture and to study the dynamical behavior of the radionuclides or labeled compounds in certain organs.

SPECT is primarily used for cardiovascular and brain imaging. For example, brain tumors can be located after intravenous injection of $Na^{99m}TcO_4$ because such tumors exhibit high affinity for and slow release of Tc. On the other hand, in the case of brain infarcts, the uptake of Tc is low and its release is fast, whereas the release is still faster from healthy parts of the brain.

The radionuclide most frequently used in SPECT is ^{99m}Tc, either for static investigations (e.g. secondary spread of malignancy in bones and liver, pulmonary embolism, thyroid function, occult metastases) or for dynamical investigations (e.g. pulmonary emphysema, renal function, liver function, motion of the cardiac wall, brain drainage, vascular problems). More than 20 different compounds of Tc are commercially available for the diagnosis of diseases and disorders in bones, thyroid, liver, kidneys, heart, and brain.

21.7 Positron Emission Tomography (PET)

In PET, the two 511 keV γ-ray photons emitted simultaneously in opposite directions are registered by γ-ray detectors, indicating that the positron decay must have occurred somewhere along the line between these two detectors. The patients are positioned inside a ring of about 50–100 scintillation detectors, and the ring is rotated and moved in a programmed manner. As in SPECT, the results are evaluated by computer software to give a three-dimensional picture of the distribution of the radionuclide in the organ of interest. The resolution is also on the order of 1 mm.

Positron emitters most frequently used for PET were introduced in Section 11.5.2. As already mentioned in Section 21.5, production of these positron emitters requires the availability of a suitable cyclotron, fast chemical separation techniques, and fast syntheses.

PET is primarily used for kinetic investigations of the brain, heart, and lungs. For example, ^{11}C-labeled glucose has been applied extensively for the study of brain metabolism. Because glucose is the only energy source used in the brain, the rate of glucose metabolism provides information about the brain's viability. By the application of PET, valuable new information about various forms of mental illness, such as epilepsy, manic depression, and dementia, has also been obtained. The development of new radiopharmaceuticals that are able to pass the blood–brain barrier will contribute to a better understanding of normal and abnormal functioning of the brain.

21.8 Labeled Compounds

Labeled compounds have found broad application in various fields of science and technology. A great variety of labeled compounds are applied in nuclear medicine. The compounds are produced on a large scale as radiopharmaceuticals in cooperation with nuclear medicine, mainly for diagnostic purposes and sometimes also for therapeutic applications. The study of metabolism by means of labeled compounds is also of great importance in biology. For completeness, we mention that, in chemistry, labeled compounds are used to elucidate reaction mechanisms and to investigate diffusion and transport processes. Other applications are the study of transport processes in the geosphere, in the biosphere, and in special ecological systems and the investigation of corrosion and transport processes in industrial plants, in pipes, or in motors.

Organic or inorganic compounds may be labeled at various positions and by various nuclides. For that purpose, certain atoms in a molecule are substituted by isotopic radionuclides, by stable isotopes, or even by non-isotopic radionuclides. To illustrate the great variety of possibilities, acetic acid is taken as an example: it may be labeled at the methyl or carboxyl group with ^{14}C, ^{13}C, or ^{11}C, and the hydrogen atoms of the methyl group or the acidic hydrogen on the carboxyl group may be labeled with ^{2}H (D) or ^{3}H (T). Finally, the oxygen atoms in the carboxyl group may be labeled with ^{15}O, ^{17}O, or ^{18}O. Sometimes, double labeling with two different

nuclides is of interest, to track the different pathways of certain groups. In the case of non-isotopic labeling, it must be checked whether the different properties of the resulting compound are acceptable. The following discussion is restricted to labeling with radionuclides.

For the preparation of labeled compounds, the following parameters have to be considered:

- the kind of nuclide (isotopic or non-isotopic, half-life);
- the position of labeling (labeling at a certain position in a molecule or labeling of all atoms of a certain element at random);
- the specific activity (activity per unit mass of the element);
- the chemical purity (fraction of the compound in the desired chemical form);
- the radionuclide purity (fraction of the total radioactivity present as the specified radionuclide);
- the radiochemical purity (fraction of the radionuclide present in the desired chemical form and in the specified position in the molecule).

The choice of the parameters depends on the application of the labeled compound. Labeled compounds may be prepared in various ways:

- simple compounds are obtained by the selection of suitable targets (e.g. ^{11}CO and $^{11}CO_2$ by irradiation of nitrogen containing traces of oxygen with protons);
- chemical synthesis (most widely applied);
- biochemical methods (which allow labeling of complex organic compounds);
- exchange reactions (which offer the possibility of introducing radionuclides or stable nuclides into inactive compounds);
- recoil labeling and radiation-induced labeling (based on recoil and radiation-induced reactions, see Section 13.7; in general, a spectrum of labeled compounds is obtained).

Some points of view with respect to the synthesis of labeled compounds should be emphasized:

- In most cases, the masses of the radionuclides to be handled in the synthesis are very small (on the order of a milligram or less), in particular if high specific activities are required.
- Adequate methods are to be selected with regard to confinement of the radioactive substances (e.g. use of small closed apparatus).
- The problem of waste production, in particular in the case of long-lived radionuclides, or the cost of the radionuclides, for example, in the case of ^{14}C, makes it necessary to select simple chemical reactions with high yields. Reactions proceeding in one stage and in one receptacle are to be preferred to multistage reactions and use of different kinds of glassware.

In consideration of these points, known procedures of chemical synthesis have been modified. Special techniques have been developed for the preparation of a large number of ^{14}C-labeled organic compounds. Some reactions starting from $Ba^{14}CO_3$ are summarized in Figure 21.1, in which, as an example, various preparation routes

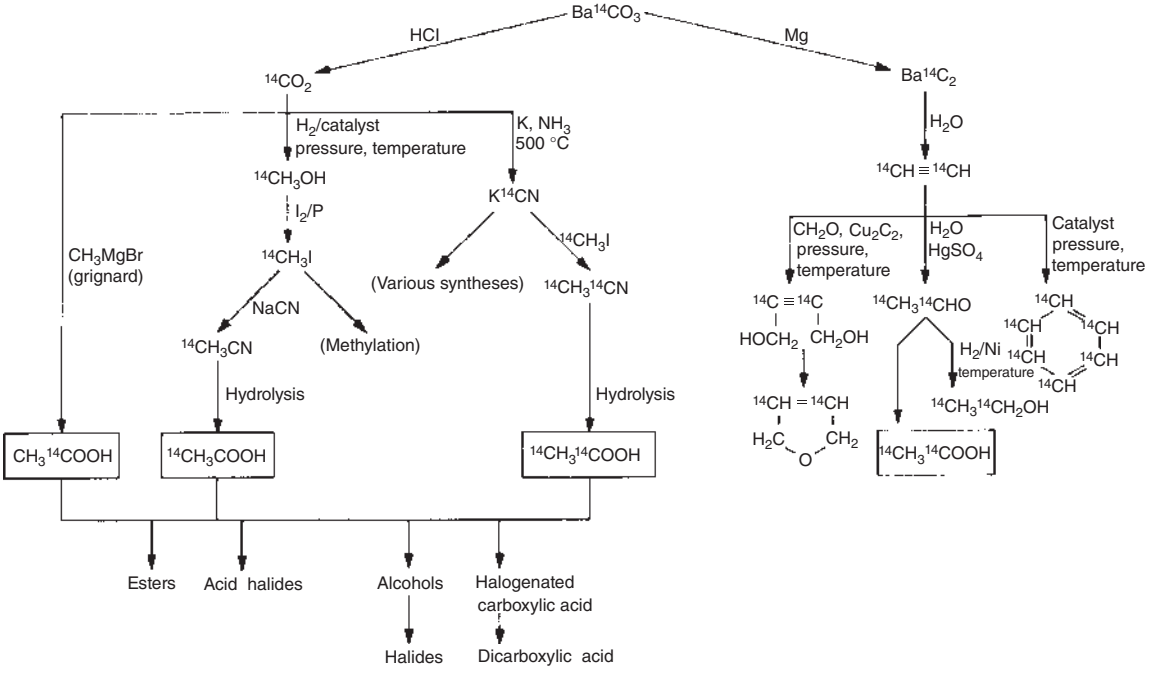

Figure 21.1 Preparation of ^{14}C-labeled compounds (example acetic acid) from $Ba^{14}CO_3$.

to labeled acetic acid are shown. Labeling of medically relevant compounds with various other radionuclides is exemplified in the following paragraphs.

For labeling with ^{11}C, the most important primary precursor is $^{11}CO_2$. Irradiation of high-purity nitrogen-containing traces of oxygen, Section 11.5.2, leads to the formation of ^{11}CO and $^{11}CO_2$, because of hot-atom reactions (recoil labeling). $^{11}CO_2$ can easily be separated cryogenically. In the presence of small amounts of hydrogen (≈5%), $^{11}CH_4$ and NH_3 are formed. $^{11}CH_4$ is another primary precursor. $^{11}CH_4$ and NH_3 react on heated Pt to give $H^{11}CN$. Various methods are also available for introducing ^{11}C into organic compounds by means of $H^{11}CN$, for example,

$$R\text{–}CH_2Cl \xrightarrow{Na^{11}CN} R\text{–}CH_2{}^{11}CN \xrightarrow{H_2/Pd} R\text{–}CH_2{}^{11}CH_2NH_2$$

Several reactive molecules have been prepared by simple on-line or one-pot procedures from $^{11}CO_2$. Some of the most important secondary precursors obtained from $^{11}CO_2$ are shown in Figure 21.2, which also shows the preparation of more reactive labeling reagents starting from the other main primary precursor, $^{11}CH_4$. $^{11}CH_3I$ has been the most versatile among the secondary precursors. It can be prepared by reduction of $^{11}CO_2$ with lithium aluminum hydride in tetrahydrofuran followed by reaction with hydroiodic acid

$$^{11}CO_2 \xrightarrow{LAH} {}^{11}CH_3OH \xrightarrow{HI} {}^{11}CH_3I \xleftarrow{I_2} {}^{11}CH_4$$

On the other hand, target production of $^{11}CH_4$ followed by iodination is often the method of choice. Further synthetic routes involve ^{11}C—C bond formation, transition metal-mediated reactions, cyanations, cross-couplings, carbonylations, and enzymes as catalysts and lead to a large variety of ^{11}C-labeled compounds such as amino acids, carbohydrates, steroids, fatty acids, nucleosides, and compounds for the study of enzymes and receptors. A comprehensive review is given by Antoni et al. (2011). In all syntheses with ^{11}C, the time needed is a decisive factor because of the rather short half-life (20.38 minutes).

^{13}N ($t_{1/2} = 9.96$ minutes) is the longest-lived radioisotope of nitrogen. It has found limited application in biological studies, mainly as $^{13}NH_3$ or $^{13}NO_3^-$. Both compounds are obtained by use of a water target. If ethanol is added as a scavenger for

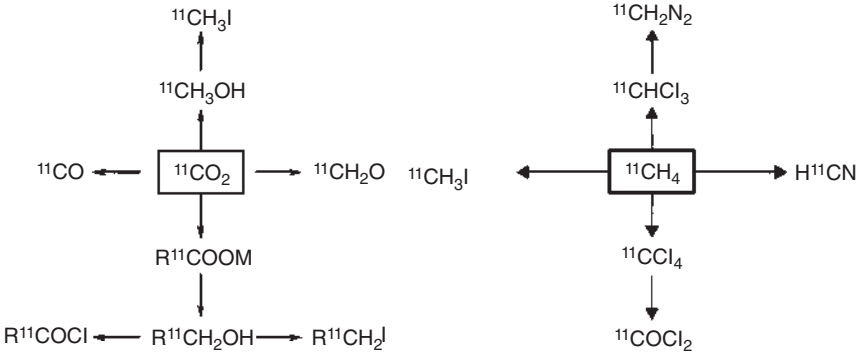

Figure 21.2 Examples of secondary precursors obtained from [^{11}C]CO_2 and from [^{11}C]CH_4.

oxidizing radicals, the main product is $^{13}NH_3$ (forming $^{13}NH_4^+$ in aqueous solution), which can be separated on a cation exchange resin followed by elution with NaCl solution. Under oxidizing conditions, $^{13}NO_3^-$ and $^{13}NO_2^-$ are the predominant products. The by-product $^{13}NH_3$ can be separated on a cation exchanger and $^{13}NO_2^-$ can be decomposed by the addition of acid. After expelling the nitrogen oxides by heating, a solution of $^{13}NO_3^-$ is obtained. The mixture of $^{13}NO_3^-$ and $^{13}NO_2^-$ may also be reduced by Devarda's alloy to $^{13}NH_3$.

^{15}O ($t_{1/2} = 2.03$ minutes) is produced by proton irradiation of nitrogen containing small amounts (0.2–0.5%) of oxygen. From ^{15}O-labeled oxygen, $H_2{}^{15}O$ is obtained by reaction with H_2 on Pd and $C^{15}O$ is produced by reaction with graphite at 1000 °C. ^{15}O-labeled organic compounds may be synthesized by rapid chemical reactions. An example is the reaction of ^{15}O-labeled O_2 with tri-*n*-butylborane to ^{15}O-labeled butanol for use as a lipophilic substance in nuclear medicine. If a mixture of nitrogen with about 2% CO_2 is irradiated with protons, ^{15}O-labeled CO_2 is obtained by reaction of the recoiling ^{15}O atoms with CO_2.

^{18}F ($t_{1/2} = 109.7$ minutes) is preferably produced by the nuclear reactions $^{18}O(p, n)^{18}F$ and $^{20}Ne(d, \alpha)^{18}F$, Section 11.5.2, because of the relatively high yields at moderate projectile energies. If O_2 or Ne gas is used, the chemical form of ^{18}F obtained after irradiation depends on the impurities in the target gas and on the inner walls of the target. Application of traces of F_2 leads to the formation of electrophilic $[^{18}F]F_2$. Proton irradiation of ^{18}O-enriched water is most effective for the production of non-carrier-added (n.c.a.) ^{18}F. From aqueous solution, nucleophilic $^{18}F^-_{aq}$ can be separated by sorption on an anion exchange resin, and the eluted ^{18}O-enriched water can be recycled. By nucleophilic substitution or electrophilic fluorination, a great variety of ^{18}F-labeled compounds are synthesized for application in nuclear medicine, such as 2-[^{18}F]fluoro-2-deoxy-D-glucose, l-6-[^{18}F]fluoro-3,4-dihydroxyphenylalanine (l-6-[^{18}F]fluoro-DOPA), 3-*N*-[^{18}F]fluoroethylpiperone, and many others. For labeling by nucleophilic substitution, ^{18}F must be applied free of water in a polar aprotic solvent. For that purpose, water is removed by distillation in the presence of large counter-ions (e.g. Rb^+, Cs^+, Bu_4N^+, or K^+-Kryptofix), which enable subsequent dissolution in an aprotic organic solvent. An overview of the scope and limitations of the ^{18}F labeling chemistry and labeled compounds is given by Ross and Wester (2011).

Radioisotopes of iodine have been used for some time in medicine, mainly for diagnosis of thyroid diseases. From the various radioisotopes available, ^{123}I has the most favorable properties. It decays by electron capture and emission of 159 keV γ-rays into ^{123}Te. The radiation dose is relatively low and the γ radiation can easily be measured from outside. Labeling of organic compounds with ^{123}I is performed by exchange of halogen atoms or by iodination. The decay of ^{123}Xe, see Section 11.5.2, in the presence of organic compounds also leads to the formation of labeled compounds (recoil labeling). The radioiodination of organic compounds, of peptides and proteins, and the clinical applications are surveyed by Eisenhut and Mier (2011).

^{75}Br ($t_{1/2} = 1.6$ hours) is applied as a positron emitter in nuclear medicine. The most suitable reactions for the production of this radionuclide are $^{76}Se(p, 2n)^{75}Br$

and $^{75}As(^{3}He, 3n)^{75}Br$. Irradiation of highly enriched ^{76}Se with 30 MeV protons leads to yields of about 4 GBq μAh^{-1}. The ^{76}Br impurity is about 0.9%. Elemental Se or selenides such as Ag_2Se or Cu_2Se may be used as targets. After irradiation, ^{75}Br can be separated from elemental Se by thermochromatography at 300 °C and taken up in a small volume of water. In the case of reaction with ^{75}As, enrichment is not necessary because ^{75}As is the only stable nuclide of As. Cu_3As may be used as the target, and, after irradiation, ^{75}Br can be separated by thermochromatography at 950 °C.

α-emitting radionuclides may be used for therapeutic purposes if they can be transported in the form of labeled compounds to those places in the body where their action is desired. With respect to this application, ^{211}At has found interest because it can be introduced into organic compounds and has a half-life suitable for medical application ($t_{1/2}$ = 7.22 hours). It can be produced by the nuclear reaction $^{209}Bi(\alpha, 2n)^{211}At$ (threshold energy 22 MeV) and separated from Bi in a gas stream at elevated temperature or by wet chemical procedures. Labeled compounds are obtained by methods similar to those used for iodine.

Generator-produced radionuclides are also introduced into compounds suitable for specific applications, in particular in medicine. For instance, $^{99m}TcO_4^-$ eluted from a $^{99}Mo/^{99m}Tc$ radionuclide generator can be introduced into organic compounds by various chemical procedures that can be performed by use of special "kits", which allow easy handling. A variety of ^{99m}Tc radiopharmaceuticals are also commercially available, such as myocardial imaging agents, cerebral blood flow agents, and agents for renal function. ^{99m}Tc labeling chemistry and labeled compounds are reviewed by Alberto and Abram (2011).

For routine syntheses of labeled compounds, automated procedures have been developed that enable fast, safe, reproducible, and reliable production. Automation has found broad application for the synthesis of radiopharmaceuticals. All steps must be as efficient as possible. For that purpose, target positioning and cooling, irradiation, removal of the target after irradiation, addition of chemicals, temperature, and reaction time, purification of the product, and dispensing are remotely controlled. Automation is done by computer control, and robotics are being applied.

Most biochemical methods are based on the assimilation of $^{14}CO_2$ by plants and the feeding of various kinds of microorganisms or animals with labeled compounds. Afterward, the compounds synthesized in the plants, microorganisms, or animals are isolated. In this way, glucose, amino acids, adenosine triphosphate, proteins, alkaloids, antibiotics, vitamins, and hormones can be obtained that are labeled with ^{14}C, ^{35}S, or ^{32}P. Cultures of various microorganisms such as *Chlorella vulgaris* may be applied and operated as "radionuclide farms." The labeled compounds produced by biochemical methods are, in general, labeled at random, that is, not at special positions.

Exchange reactions have the advantage that long routes of synthesis with radionuclides or radioactive compounds are avoided. This is of particular interest if the chemical yields of the syntheses are low. Homogeneous exchange reactions may be applied for the labeling of compounds with halogens, for example,

$$\underset{(1)}{RCl} + \underset{(2)}{Li^{36}Cl} \leftrightarrow \underset{(1)}{R^{36}Cl} + \underset{(2)}{LiCl} \tag{21.1}$$

RCl and LiCl are dissolved in polar organic solvents, and exchange proceeds quickly at elevated temperature. Instead of isotopic exchange according to Eq. (21.1), non-isotopic exchange may also be applied, for example,

$$RCl + Li^{131}I \Leftrightarrow R^{131}I + LiCl \tag{21.2}$$

The compounds can be separated by distillation or by chromatography. Aromatic compounds RX (X = halogen) may be labeled in the presence of catalysts such as $AlCl_3$. In the isotope exchange equilibrium (21.1), the specific activity of (1) is given by

$$A_s(1) = \frac{n_1}{n_1 + n_2} A_s(2) \tag{21.3}$$

where n_1 and n_2 are the mole numbers of (1) and (2) and $A_s(2)$ is the initial specific activity of (2). In the non-isotopic exchange (21.2), the equilibrium constant has to be taken into account.

Heterogeneous exchange reactions are applicable for labeling in the batch mode or in a continuous mode. Labeling in a continuous mode may be carried out by use of exchange columns loaded with radionuclides. For example, volatile compounds containing acidic hydrogen atoms may be passed through a gas chromatography column loaded with tritium in the form of T-labeled sorbite as the stationary phase, where they are labeled by multistage isotope exchange and may approach the initial specific activity of the sorbite. In a similar way, volatile halides can be labeled with radioactive halogens.

Radiation-induced exchange may be applied instead of thermal exchange, if thermal exchange does not occur below the decomposition temperature, whereas the chemical bonds involved in the exchange reaction are easily split under the influence of radiation. An example is the labeling of aromatic halogen compounds.

Recoil labeling and radiation-induced labeling (self-labeling) are described in Section 13.7. Examples of recoil-induced labeling of simple compounds such as CO, CO_2, or HCN with ^{11}C, NH_3 with ^{13}N, and CO, CO_2, or H_2O with ^{15}O have been described in the previous paragraphs. For the production of larger compounds, recoil labeling and radiation-induced labeling are relatively seldom applied because, generally, a greater number of different labeled compounds are produced, which must be separated from each other. Radiation decomposition and the number of degradation products increase with the size of the molecules, whereas the yields and the specific activities of individual labeled compounds decrease markedly.

References

Labeled Compounds

Alberto, R. and Abram, U. (2011). ^{99m}Tc: labeling chemistry and labeled compounds. In: *Handbook of Nuclear Chemistry*, 2e, vol. 4 (eds. A. Vértes, S. Nagy, Z. Klencsár, et al.), 2073. Berlin: Springer-Verlag.

Antoni, G., Kihlberg, T., and Långström, B. (2011). ^{11}C: labeling chemistry and labeled compounds. In: *Handbook of Nuclear Chemistry*, 2e, vol. 4 (eds. A. Vértes, S. Nagy, Z. Klencsár, et al.), 1977. Berlin: Springer-Verlag.

Eisenhut, M. and Mier, W. (2011). Radioiodination chemistry and radioiodinated compounds. In: *Handbook of Nuclear Chemistry*, 2e, vol. 4 (eds. A. Vértes, S. Nagy, Z. Klencsár, et al.), 2121. Berlin: Springer-Verlag.

Ross, T.L. and Wester, H.J. (2011). ^{18}F: labeling chemistry and labeled compounds. In: *Handbook of Nuclear Chemistry*, 2e, vol. 4 (eds. A. Vértes, S. Nagy, Z. Klencsár, et al.), 2021. Berlin: Springer-Verlag.

Further Reading

General

Hevesy, G. (1948). *Radioactive Indicators: Application to Biochemistry, Animal Physiology and Pathology*. New York: Interscience.

Calvin, M., Heidelberger, C., Reid, J.C. et al. (1949). *Isotopic Carbon*. New York: Wiley.

Kamen, M.D. (1949). *Radioactive Tracers in Biology*. New York: Academic Press.

Siri, W.E. (ed.) (1949). *Isotopic Tracers*. New York: McGraw-Hill.

Wolf, G. (1964). *Isotopes in Biology*. New York: Academic Press.

International Atomic Energy Agency (1974). *Radiopharmaceuticals and Labelled Compounds*, vol. I. Vienna: IAEA.

Wang, C.H., Willis, D.H., and Loveland, W.D. (1975). *Radiotracer Methodology in the Biological, Environmental and Physical Sciences*. Englewood Cliffs, NJ: Prentice Hall.

Lawrence, J.H. and Budinger, T.F. (eds.) (1978). *Recent Advances in Nuclear Medicine*. New York: Grune and Stratton.

Boyd, R.E. (1982). Radiochemistry related to the life sciences. *Radiochim. Acta* 30: 123 and 34: 1 (1983).

Lambrecht, R.M. and Morcos, N.A. (eds.) (1982). *Applications of Nuclear and Radiochemistry, Part I, Radio-Pharmaceutical Chemistry*. Oxford: Pergamon.

International Atomic Energy Agency (1985). *Radiopharmaceuticals and Labelled Compounds*. Vienna: IAEA.

Cox, P.H., Mather, S.J., Sampson, C.B., and Lazarus, C.R. (eds.) (1986). *Progress in Radiopharmacy*. Dordrecht: Martinus Nijhoff.

Van Rijk, P.P. (ed.) (1986). *Nuclear Techniques in Diagnostic Medicine*. Dordrecht: Martinus Nijhoff.

Deckart, H. and Cox, P.H. (eds.) (1987). *Principles of Radiopharmacology*. Jena: G Fischer.

Baillie, T.A. and Jones, J.R. (eds.) (1989). *Synthesis and Application of Isotopically Labelled Compounds*. Amsterdam: Elsevier.

Theobald, A. (ed.) (1989). *Radiopharmaceuticals Using Radioactive Compounds in Pharmaceutics and Medicine*. Chichester: Ellis Horwood.

Nias, A.H.W. (1990). *An Introduction to Radiobiology*. New York: Wiley.

Nunn, A.D. (ed.) (1992). *Radiopharmaceuticals: Chemistry and Pharmacology*. New York: Marcel Dekker.

Schubiger, P.A. and Westera, G. (eds.) (1992). *Progress in Radiopharmacy*. Dordrecht: Kluwer Academic.

Stöcklin, G., Qaim, S.M., and Rösch, F. (1995). The impact of radioactivity on medicine. *Radiochim. Acta* 70/71: 249.

Labeled Compounds

Murray, A. and Williams, D.L. (1958). *Organic Synthesis with Isotopes*, 2 vols. New York: Interscience.

Wolf, A.P. (1960). Labeling of organic compounds by recoil methods. *Annu. Rev. Nucl. Sci.* 10: 259.

Catch, J.R. (1961). *Carbon-14 Compounds*. London: Butterworths.

Herber, R.H. (ed.) (1962). *Inorganic Isotopic Synthesis*. New York: Benjamin.

Wenzel, M. and Schulze, P.E. (1962). *Tritium-Markierung, Darstellung, Messung und Anwendung nach Wilzbach ^{3}H-markierter Verbindungen*. Berlin: Walter de Gruyter.

Yaffe, L. (1962). Preparation of thin films, sources and targets. *Annu. Rev. Nucl. Sci.* 12: 153.

Feinendegen, L.E. (1967). *Tritium-Labeled Molecules in Biology and Medicine*. New York: Academic Press.

Rasen, V.F., Ropp, G.A., and Raaen, H.P. (1968). *Carbon-14*. New York: McGraw-Hill.

Thomas, A.F. (1971). *Deuterium Labeling in Organic Chemistry*. New York: Appleton-Century-Crofts.

Evans, E.A. (1974). *Tritium and its Compounds*. London: Butterworths.

Clark, J.C. and Buckingham, P.D. (1975). *Short-Lived Radioactive Gases for Clinical Use*. London: Butterworths.

Silvester, D.J. (1976). Preparation of radiopharmaceuticals and labelled compounds using short-lived radionuclides. In: *Radiochemistry, Specialist Periodical Reports*, vol. 3. London: The Chemical Society.

Abraham, G.E. (1977). *Handbook of Radioimmunoassay*. New York: Marcel Dekker.

Welch, W.M. (ed.) (1977). Radiopharmaceuticals and other compounds labelled with short-lived nuclides. *Int. J. Appl. Radiat. Isot.* 28 (Special Issue): 1.

Ott, D.G. (1981). *Synthesis with Stable Isotopes of Carbon, Nitrogen and Oxygen*. New York: Wiley.

Eckelman, W.C. (ed.) (1982). *Receptor-Binding Radiotracers*, vols. I, II. Boca Raton, FL: CRC Press.

Qaim, S.M. (1982). Nuclear data relevant to cyclotron produced short-lived medical radioisotopes. *Radiochim. Acta* 30: 147.

Waters, S.L. and Silvester, D.J. (1982). Inorganic cyclotron radionuclides. *Radiochim. Acta* 30: 163.

Muccino, R.R. (1983). *Organic Syntheses with Carbon-14*. New York: Wiley.

O'Brien, H.A. Jr. (1983). *Radioimmunoimaging and Radioimmunotherapy*. Amsterdam: Elsevier.

Pochin, E. (1983). *Nuclear Radiation: Risks and Benefits*. Oxford: Clarendon Press.

Sharp, J.R. (ed.) (1983). *Guide to Good Pharmaceutical Manufacturing Practice*. London: HMSO.

L'Annunziata, M.F. and Legg, J.O. (eds.) (1984). *Isotopes and Radiation in Agricultural Sciences*. New York: Academic Press.
Sharp, P.F., Dendy, P.P., and Keyes, W.I. (1985). *Radionuclide Imaging Technique*. New York: Academic Press.
Deckart, H. and Cox, P.H. (eds.) (1987). *Principles of Radiopharmacology, Developments in Nuclear Medicine*, vol. 11. Dordrecht: Kluwer Academic.
Guillaume, M. and Brihaye, C. (1987). Generators of ultra-short-lived radionuclides for routine clinical applications. *Radiochim. Acta* 41: 119.
Hundeshagen, H. (ed.) (1988). *Spezielle Syntheseverfahren mit kurzlebigen Radionukliden und Qualitätskontrolle. Emissions-Computertomographie mit kurzlebigen Zyklotron-produzierten Radio-pharmaka*. Berlin: Springer-Verlag.
Srivastava, S.C. (ed.) (1988). *Radiolabeled Monoclonal Antibodies for Imaging and Therapy*. New York: Plenum Press.
Swenberg, C.E. and Conklin, J.J. (1988). *Imaging Techniques in Biology and Medicine*. New York: Academic Press.
Webb, S. (ed.) (1988). *The Physics of Medical Imaging*. Bristol: Adam Hilger.
Beckers, C., Goffinet, A., and Bol, A. (eds.) (1989). *Positron Emission Tomography in Clinical Research and Clinical Diagnosis: Tracer Modelling and Radioreceptors*. Dordrecht: Kluwer Academic.
Bryant, R. (1989). *The Pharmaceutical Quality Control Handbook*. Eugene, OR: Aster.
European Commission (1990). *The Rules Governing Medical Products in the European Community*. Brussels: Commission of the European Communities.
Kilbourn, M.R. (1990). *Fluorine-18 Labeling of Radiopharmaceuticals*, Nuclear Science Series NAS-NS. Washington, DC: National Academy Press.
Baum, R.P., Cox, P.H., Hör, G., and Burragi, G.L. (eds.) (1991). *Clinical Use of Antibodies, Tumors, Infection, Infarction, Rejection, and in the Diagnosis of AIDS*. Dordrecht: Kluwer Academic.
Biersack, H.J. and Cox, P.H. (eds.) (1991). *Nuclear Medicine in Gastroenterology*. Dordrecht: Kluwer Academic.
Dewanjee, M.K. (1991). *Radioiodination:, Theory, Practice and Biomedical Applications*. Dordrecht: Kluwer Academic.
Kuhl, D. (ed.) (1991). *Frontiers in Nuclear Medicine: In Vivo Imaging of Neurotransmitter Functions in Brain, Heart and Tumors*. Washington, DC: American College of Nuclear Physics.
Mazoyer, B.M., Heuss, W.D., and Comar, D. (eds.) (1993). *PET Studies on Aminoacid Metabolism and Protein Synthesis*. Dordrecht: Kluwer Academic.
Meares, C.F. (1993). *Perspectives in Bioconjugate Chemistry*. Washington, DC: American Chemical Society.
Stöcklin, G. and Pike, V.W. (eds.) (1993). *Radiopharmaceuticals for Positron Emission Tomography*. Dordrecht: Kluwer Academic.
McCarthy, T.J., Schwarz, S.W., and Welch, M.J. (1994). Nuclear medicine and positron emission tomography. *J. Chem. Educ.* 71: 830.
Jones, A.G. (1995). Technetium in nuclear medicine. *Radiochim. Acta* 70/71: 289.
Weiner, R.E. and Thakur, M.L. (1995). Metallic radionuclides: applications in diagnostic and therapeutic nuclear medicine. *Radiochim. Acta* 70/71: 273.

Fani, M., Good, S., and Maecke, H.R. (2011). Radiometals (non-Tc, non-Re) and bifunctional labeling chemistry. In: *Handbook of Nuclear Chemistry*, 2e, vol. 4 (eds. A. Vértes, S. Nagy, Z. Klencsár, et al.), 2143. Berlin: Springer-Verlag.

Ferrier, M.G., Radchenko, V., and Scott Wilbur, D. (2019). Radiochemical aspects of alpha emitting radionuclides for medical applications. *Radiochim. Acta* 107: 1065.

Lapi, S.E. and Engle, J.W. (2019). Radiochlorine: an underutilized halogen tool. *Radiochim. Acta* 107: 1027.

Okoye, N.C., Baumeister, J.E., Khosroshahi, F.N. et al. (2019). Chelators and metal complex stability for radiopharmaceutical applications. *Radiochim. Acta* 107: 1087.

Qaim, S.M., Kratz, J.V., and Simoni, E. (eds.) (2019). International year of the periodic table of chemical elements. Editorial: 150 years of the periodic table of chemical elements. *Radiochim. Acta* 107 (Special Issue): 767.

Qaim, S.M., Scholten, B., Spahn, I., and Neumaier, B. (2019). Positron-emitting radionuclides for applications, with special emphasis on their production methodologies for medical use. *Radiochim. Acta* 107: 1011.

Wilbur, D.S. and Adam, M.J. (2019). Radiobromine and radioiodine for medical applications. *Radiochim. Acta* 107: 1033.

Radionuclide Therapy and Therapy with Ion Beams

Kraft, G. (1990). The radiobiological and physical basis for radiotherapy with protons and heavier ions. *Strahlenther. Onkol.* 166: 10.

Amaldi, U. and Larsson, B. (eds.) (1994). *Hadrontherapy in Oncology*. Amsterdam: Elsevier.

Zalutsky, M.R. (2011). Radionuclide therapy. In: *Handbook of Nuclear Chemistry*, 2e, vol. 4 (eds. A. Vértes, S. Nagy, Z. Klencsár, et al.), 2179. Berlin: Springer-Verlag.

Radioanalytical Methods

Heydorn, K. (ed.) (1984). *Neutron Activation Analysis for Clinical Trace Element Research*, vols. I, II. Boca Raton, FL: CRC Press.

Wieland, D.M., Tobes, M.C., and Mangner, T.J. (1986). *Analytical and Chromatographic Techniques in Radiopharmaceutical Chemistry*. Heidelberg: Springer-Verlag.

22

Radionuclides in the Geosphere and the Biosphere

22.1 Sources of Radioactivity

Two groups of radioactivity sources on the Earth are to be distinguished, natural and anthropogenic. Natural sources such as ^{40}K, ^{232}Th, ^{235}U, and ^{238}U have been produced in the course of nucleogenesis (primordial radionuclides; Chapter 18) and have been present on the Earth from the beginning. Further sources of natural radioactivity are the cosmogenic radionuclides, such as T and ^{14}C; they are produced continuously by the interaction of cosmic rays with the atmosphere.

By mining ores and minerals, appreciable amounts of natural radionuclides, in particular ^{40}K, ^{232}Th, ^{235}U, ^{238}U, and the members of the thorium, uranium, and actinium decay series, are brought up to the surface of the Earth and contribute to the radioactivity in the environment. In nuclear power stations, artificial radionuclides, mainly fission products and transuranic elements, are produced, and great care is usually taken in handling the resulting radioactive waste safely and to localize it to selected places inaccessible to humans. The optimal conditions of final storage of high-level waste (HLW) are still a subject of discussion and research. On the other hand, from the use of nuclear weapons, nuclear weapon tests, and nuclear accidents, considerable amounts of fission products and radioelements have been set free and distributed via the atmosphere as radioactive fallout over large areas, in particular in the northern hemisphere.

Radionuclides of major importance in the geosphere and the biosphere are listed in Table 22.1. Not taken into account are radionuclides with half-lives $t_{1/2} < 1$ day (in the case of activation products of materials used in nuclear reactors, $t_{1/2} < 1$ year) and with half-lives $t_{1/2} > 10^{11}$ years; radionuclides with fission yields <0.01%; radioisotopes of elements that are not members of the natural decay series; and radionuclides produced solely for medical or technical applications. The radionuclides are arranged according to their position in the periodic table of the elements, in order to facilitate the discussion of their chemical behavior. Radionuclides with half-lives >10 years are underlined, because their behavior over long periods of time is of special importance.

With respect to radiation doses and possible hazards, the local concentrations and the radiotoxicities of the radionuclides have to be taken into account. Local concentrations of fission products and transuranic elements are high in

Nuclear and Radiochemistry: Fundamentals and Applications,
Fourth Edition. Jens-Volker Kratz.

Table 22.1 Radionuclides of major importance in the geosphere and biosphere (radionuclides with half-lives >10 years and present in relatively high concentrations are underlined).

Element	Group of the periodic table	Radionuclide (half-life)	Source
H		^{3}H (12.323 yr)	Cosmic radiation and nuclear fission
C		^{14}C (5730 yr)	Cosmic radiation and nuclear fission
K	1	^{40}K ($1.28 \cdot 10^{9}$ yr)	Potassium salts
Rb		^{87}Rb ($4.80 \cdot 10^{10}$ yr)	Rubidium salts; fission
Cs		^{134}Cs (2.06 yr); ^{135}Cs ($2.0 \cdot 10^{6}$ yr)	Nuclear fission
		^{137}Cs (30.17 yr)	
Sr	2	^{89}Sr (50.5 d); ^{90}Sr (28.64 yr)	Nuclear fission
Ba		^{140}Ba (12.75 d)	Nuclear fission
Ra		^{223}Ra (11.43 d); ^{224}Ra (3.66 d)	Ores/minerals
		^{225}Ra (14.8 d); ^{226}Ra (1600 yr)	
		^{228}Ra (5.75 yr)	
Sn	14	^{121}Sn (1.125 d); ^{121m}Sn (≈50 yr);	Nuclear fission
		^{123}Sn (129.2 d); ^{125}Sn (9.64 d)	
Pb		^{210}Pb (22.3 yr)	Ores/minerals
Sb	15	^{125}Sb (2.77 yr); ^{126}Sb (12.4 d) ^{127}Sb (3.85 d)	Nuclear fission
Bi		^{210}Bi (5.013 d)	Ores/minerals
Se	16	^{79}Se ($4.8 \cdot 10^{5}$ yr)	Nuclear fission
Te		^{127m}Te (109 d); ^{129m}Te (33.6 d)	Nuclear fission
		^{131m}Te (1.25 d); ^{132}Te (3.18 d)	
Po		^{210}Po (138.38 d)	Ores/minerals
I	17	^{129}I ($1.57 \cdot 10^{7}$ yr); ^{131}I (8.02 d)	Nuclear fission
Kr	18	^{85}Kr (10.76 yr)	Nuclear fission
Xe		^{133}Xe (5.25 d); ^{133m}Xe (2.19 d)	Nuclear fission
Rn		^{222}Rn (3.825 d)	Ores/minerals
Ag	11	^{111}Ag (7.45 d)	Nuclear fission
Cd	12	^{109}Cd (1.267 yr); ^{113m}Cd (14.6 yr) ^{115}Cd (2.224 d); ^{115m}Cd (44.8 d)	Activation; fission
Y	3	^{90}Y (2.671 d); ^{91}Y (58.5 d)	Nuclear fission
La		^{140}La (1.678 d)	Nuclear fission

(*continued*)

Table 22.1 (Continued)

Element	Group of the periodic table	Radionuclide (half-life)	Source
Ce		^{141}Ce (32.5 d); ^{143}Ce (1.375 d)	Nuclear fission
		^{144}Ce (284.8 d)	
Pr		^{143}Pr (13.57 d)	Nuclear fission
Nd		^{147}Nd (10.98 d)	Nuclear fission
Pm		^{147}Pm (2.623 yr); ^{149}Pm (2.212 d)	Nuclear fission
		^{151}Pm (1.183 d)	
Sm		^{151}Sm (93 yr); ^{153}Sm (1.928 d)	Nuclear fission
Eu		^{155}Eu (4.761 yr); ^{156}Eu (15.2 d)	Nuclear fission
Ac		^{225}Ac (10.0 d)	Decay of ^{237}Np
		^{227}Ac (21.773 yr)	Ores/minerals
Th		^{227}Th (18.72 d); ^{228}Th (1.913 yr)	Ores/minerals
		^{229}Th (7880 yr)	Decay of ^{237}Np
		^{230}Th ($7.54 \cdot 10^4$ yr) ^{232}Th ($1.405 \cdot 10^{10}$ yr); ^{234}Th (24.10 d)	Ores/minerals
Pa		^{231}Pa ($3.276 \cdot 10^4$ yr)	Ores/minerals
		^{233}Pa (27.0 d)	Decay of ^{237}Np
U		^{233}U ($1.592 \cdot 10^5$ yr)	Decay of ^{237}NP
		^{234}U ($2.455 \cdot 10^5$ yr); ^{235}U ($7.038 \cdot 10^8$ yr)	Ores/minerals
		^{236}U ($2.342 \cdot 10^7$ yr); ^{237}U (6.75 d)	Nuclear reactors
		^{238}U ($4.468 \cdot 10^9$ yr)	Ores/minerals
Np		^{236}Np ($1.54 \cdot 10^5$ yr); ^{237}Np ($2.144 \cdot 10^6$ yr)	Nuclear reactors
		^{238}Np (2.117 d)	
Pu		^{239}Pu ($2.411 \cdot 10^4$ yr); ^{240}Pu (6563 yr)	Nuclear reactors
		^{241}Pu (14.35 yr); ^{242}Pu ($3.750 \cdot 10^5$ yr)	
Am		^{241}Am (432.2 yr); ^{242m}Am (141 yr)	Nuclear reactors
		^{243}Am (7370 yr)	
Cm		^{242}Cm (162.9 d); ^{243}Cm (29.1 d) ^{244}Cm (18.10 yr); ^{245}Cm (8500 yr) ^{246}Cm (4730 yr); ^{247}Cm ($1.56 \cdot 10^7$ yr) ^{248}Cm ($3.40 \cdot 10^5$ yr)	Nuclear reactors

(*continued*)

Table 22.1 (Continued)

Element	Group of the periodic table	Radionuclide (half-life)	Source
Bk		^{249}Bk (320 d)	Nuclear reactors
Cf		^{249}Cf (350.6 yr); ^{250}Cf (13.08 yr)	Nuclear reactors
		^{251}Cf (898 yr); ^{252}Cf (2.645 yr)	
Zr	4	^{93}Zr ($1.5 \cdot 10^6$ yr); ^{95}Zr (64.02 d)	Fission and activation
Nb	5	^{94}Nb ($2.0 \cdot 10^4$ yr)	Activation
		^{95}Nb (34.97 d); ^{95m}Nb (3.61 d)	Nuclear fission
Mo	6	^{99}Mo (2.75 d)	Nuclear fission
Tc	7	^{99}Tc ($2.13 \cdot 10^5$ yr)	Nuclear fission
Re		^{187}Re ($5 \cdot 10^{10}$ yr)	Rhenium compounds
Fe	8	^{55}Fe (2.73 yr)	Activation
Co	9	^{60}Co (5.272 yr)	Activation
Ni	10	^{59}Ni ($7.5 \cdot 10^4$ yr): ^{63}Ni (100 yr)	Activation
Ru	8	^{103}Ru (39.35 d); ^{106}Ru (1.023 yr)	Nuclear fission
Rh	9	^{105}Rh (1.475 d)	Nuclear fission
Pd	10	^{107}Pd ($6.5 \cdot 10^6$ yr)	Nuclear fission

anthropogenic sources, such as nuclear reactors, reprocessing plants, and HLW. Local concentrations of radionuclides are also high in natural sources, such as uranium or thorium ores. On the other hand, local concentrations are generally low in the case of fallout (with the exception of the regions of the Chernobyl and Fukushima accidents) and off-gas and effluents from nuclear installations. They are also low for dispersed natural radionuclides, such as T, ^{14}C, and other widespread natural sources containing K, U, or Th and daughter nuclides. The radiotoxicities of T, ^{14}C, and K are also low, whereas they are high for many fission products, and for the actinides.

22.2 Mobility of Radionuclides in the Geosphere

Gaseous species, aerosols, and species dissolved in aquifers are mobile and easily transported by air or water, respectively. Mobility of solid particles, on the other hand, may be caused by dissolution or suspension in water or spreading by wind.

Solubility and leaching of solids depend on the properties of the solid containing the radionuclide and the properties of the solvent, in general water, in which the various components are dissolved. The radionuclide may be present as a micro- or macrocomponent, and dissolution and solubility may vary considerably with the composition, the degree of dispersion, and the influence of radiation (radiolytic

decomposition). In the case of solid solutions (mixed crystals) the solubility of the components is, in general, different from that of the pure compounds. Eh, pH, and complexing agents may be of significant influence.

The inventory of radionuclides on the surface of the Earth, including surface waters, is mobile, provided that the species are soluble in water. A large proportion of the relevant radionuclides is of natural origin. ^{40}K is widely distributed in nature and easily soluble in the form of K^+ ions, which are enriched in clay minerals by sorption. Th, present as a major or minor component in minerals, is immobile, because chemical species of Th(IV) are very sparingly soluble in natural waters. However, some of the decay products of ^{232}Th, such as ^{228}Ra, ^{224}Ra, and ^{220}Rn, are mobile. In contrast to Th(IV), U(IV) is oxidized by air to U(VI), which is easily soluble in natural waters containing carbonate or hydrogencarbonate, respectively. The triscarbonato complex $[UO_2(CO_3)_3]^{4-}$ is found in all rivers, lakes, and oceans in concentrations on the order of 10^{-6} to 10^{-5} g l^{-1}. The daughters of ^{238}U, the long-lived ^{226}Ra and ^{222}Rn, are also mobile. ^{226}Ra is found in relatively high concentrations in mineral springs, and ^{222}Rn contributes considerably to the radioactivity in the air. ^{222}Rn and the daughters ^{218}Po, ^{214}Pb, ^{214}Bi, ^{214}Po, ^{210}Pb, ^{210}Bi, and ^{210}Po are the major sources of the radiation dose received by humans under normal conditions.

In the atmosphere, T and ^{14}C are generated continuously by the impact of cosmic radiation (Section 19.2). The natural concentration of T in the air is about $1.8 \cdot 10^{-3}$ Bq m^{-3} and that of ^{14}C is about $5 \cdot 10^{-4}$ Bq m^{-3}.

From near-surface layers, radionuclides are brought to the surface by natural processes and by human activities. ^{222}Rn produced by decay of ^{238}U in uranium ores is able to escape into the air through crevices. Its decay products are found in the air mainly in the form of aerosols. Ions, such as Ra^{2+} and $UO_2{}^{2+}$, are leached from ores or minerals by groundwater and may come to the surface. Volcanic activities also lead to the distribution of radionuclides on the surface, where they may be leached out and enter the water cycle.

The mining of uranium ores and of other ores and minerals (e.g. phosphates) brings up to the surface appreciable amounts of U, Th, and members of their decay series, and initiates mobilization of relevant radionuclides. Large amounts of Rn are released into the air. The residues of mining and processing are stockpiled and slag heaps as well as waste waters contain significant amounts of radionuclides. The isotopes of Ra continue to emit Rn: about 1 GBq of ^{222}Rn is released per ton of ore containing 1% U_3O_8. Ra and its daughters migrate to natural oil and gas reservoirs and constitute the major radioactive contaminants of crude oil. The global activity of Ra isotopes brought to the surface by oil production is on the order of 10^{13} Bq yr^{-1}.

Mining potassium salt deposits for use of K as a fertilizer brings additional amounts of ^{40}K to the surface of the Earth, where it enters the surface waters.

Radionuclides are also liberated by the burning of coal in thermal power stations. Depending on its origin, coal contains various amounts of U and Th, and these as well as their daughters are released by combustion. Volatile species, in particular Rn, are emitted with the waste gas, ^{210}Pb and ^{210}Po are emitted with the fly ash, and

the rest, including U and Th, are found in the ash. The global release of Rn is on the order of 10^{14} Bq yr^{-1}.

Other human activities have led to the distribution of appreciable amounts of radionuclides in the atmosphere and on the Earth's surface. In the first place, nuclear explosions and nuclear weapons tests have to be mentioned, by which Pu and fission products have been deposited on the Earth, either directly or via the atmosphere in the form of fallout. The amount of Pu released by nuclear weapons tests between 1958 and 1981 is estimated at 4.2 tons, of which 2.8 tons was dispersed in the atmosphere and 1.4 tons deposited locally. From underground nuclear explosions about 1.5 tons of Pu have been liberated. Radionuclides released into the air are mainly present in the form of aerosols.

Nuclear reactors and reprocessing plants are constructed and operated in such a way that the radioactive inventory is confined to shielded places. Only limited amounts of radionuclides are allowed to enter the environment. The amounts of T and ^{14}C produced in nuclear reactors vary with the reactor type, between about 10^{12} and 10^{13} Bq of T and about 10^{12} Bq of ^{14}C per GWe per year. Tritium is released as HTO and about one-third of the ^{14}C is in the form of $^{14}CO_2$. Under normal operating conditions, very small amounts of fission products and radioelements are set free from nuclear reactors and reprocessing plants. In this context, the actinides and long-lived fission products, such as ^{99}Tc, ^{129}I, and ^{137}Cs, are of greatest importance.

Despite the safety regulations, accidents have occurred with nuclear reactors and reprocessing plants, primarily due to mistakes by the operators. From these accidents, parts of the radioactive inventory have entered the environment. Mainly gaseous fission products and aerosols have been emitted, but solutions have also been given off. In the Chernobyl accident, gaseous fission products and aerosols were transported through the air over large distances. Even molten particles from the reactor core were carried by the wind over distances of several hundred kilometers.

The behavior of radionuclides in the environment depends primarily on their chemical and physicochemical form (species). Alkali and alkaline earth ions, such as $^{137}Cs^+$ or $^{90}Sr^{2+}$, are easily dissolved in water, independently of pH. Their mobility is limited if they are bound to clay minerals or incorporated into ceramics or glass. ^{129}I forms quite mobile species and reacts easily with organic substances. ^{85}Kr and ^{133}Xe stay predominantly in the air. The lanthanides, for example, ^{144}Ce, ^{147}Pm, and ^{151}Sm, are only sparingly soluble in water, because of the hydrolysis of the cations. However, colloids may be formed – either intrinsic colloids or carrier colloids – with natural colloids as the main components. The solubility of the actinides in the oxidation states III and IV is similar to that of the lanthanides, but hydrolysis is more pronounced in the oxidation state IV. On the other hand, the dioxocations MO_2^+ and MO_2^{2+} exhibit relatively high solubility in water in the presence of carbonate or hydrogencarbonate, respectively, as already mentioned for UO_2^{2+}. In general, these species are rather mobile. The mobility of Zr(IV) and Tc(IV) is similar to that of actinides in the oxidation state IV. The influence of the redox potential is very pronounced in the case of Tc, whereas Tc(IV) is not dissolved in water and immobile, Tc(VII) is easily dissolved in the form of TcO_4^+, and very

mobile. The oxidation of PuO_2 to PuO_{2+x} in moist air leads to an unexpected solubility of PuO_2 and has a marked influence on the migration behavior of Pu.

Large amounts of ores and minerals with considerable contents of U, Th, and their daughter nuclides are still buried deep under the surface. They can be considered to be immobile as long as they are not brought up to the surface by geological or human activities, and as long as contact with water is excluded. The concept behind the storage of radioactive waste is to put it down into layers deep underground, in order to confine it there safely (Section 15.8).

Investigations of the migration behavior of natural radionuclides in geomedia (natural analog studies) provide valuable information about the mobility of radionuclides over long periods of time. Examples are the migration of U, Ra, and Th in the neighborhood of natural ore deposits and of nuclides produced by nuclear fission at the natural reactors at Oklo (Section 15.9) and the investigation of radioactive disequilibria (Section 19.6).

22.3 Reactions of Radionuclides with the Components of Natural Waters

In aqueous solutions, the majority of the radionuclides listed in Table 22.1 are present in cationic forms, for which primarily the following reactions have to be taken into account:

- hydration (formation of aquo complexes),
- hydrolysis (formation of hydroxo complexes),
- condensation (formation of polynuclear hydroxo complexes),
- complexation (formation of various complexes with inorganic or organic ligands),
- formation of radiocolloids (intrinsic or carrier colloids).

Inorganic anions such as Cl^-, CO_3^{2-}, SO_4^{2-}, and HPO_4^{2-} and organic compounds containing functional groups compete with the formation of aquo and hydroxo complexes, depending on their chemical properties and their concentrations. Cations of transition elements are known to form relatively strong covalent bonds with ligands containing donor atoms, and chelate complexes exhibit high stability. Formation of radiocolloids has been discussed in Section 11.1.4.

Groundwaters, rivers, lakes, and the oceans contain a great variety of substances that may interact with radionuclides. Besides the main component (water), other inorganic compounds have to be considered:

- dissolved gases, such as oxygen and carbon dioxide, which influence the redox potential Eh and the pH;
- salts, such as NaCl, $NaHCO_3$, and others, which affect pH and complexation and are responsible for the ionic strength;
- inorganic colloids, such as polysilicic acid, iron hydroxide, or hydrous iron oxide, and finely dispersed clay minerals giving rise to the formation of carrier colloids;
- inorganic suspended matter (coarse particles).

Organic components in natural waters comprise:

- compounds of low molecular mass, for example, organic acids, amino acids, and other metabolites;
- compounds of high molecular mass, such as humic and fulvic acids, and colloids formed by these substances or by other degradation products of organic matter;
- suspended coarse particles of organic matter;
- microorganisms.

The concentrations of these compounds in natural waters vary over a wide range. Coarse particles are observed only in agitated waters and settle down as soon as agitation stops. Even though many of the components listed above may be present in rather low concentrations (microcomponents), their concentration is usually still many orders of magnitude higher than that of the radionuclides in question and therefore cannot be neglected.

The aspect of low concentration is of special importance for short-lived isotopes of radioelements, the concentration of which is, in general, extremely low. In the case of radioisotopes of stable elements, on the other hand, the ubiquitous presence of these elements leads to measurable concentrations of carriers, with the consequence that these radionuclides show the normal chemical behavior of trace elements.

Due to the large number of components, natural waters are rather complex systems. The relative concentrations of many components, as well as the pH and Eh, are controlled by chemical equilibria. However, there are also components, in particular colloids and microorganisms, for which thermodynamic equilibrium conditions are not applicable. The complexity of the chemistry in natural waters and the non-applicability of thermodynamics are the main reasons for the fact that calculations are very difficult and problematic. The same holds for laboratory experiments with model waters; results obtained with a special kind of water are, in general, not applicable for other natural waters of different origin.

The redox potential, Eh, has a great influence on the behavior of radionuclides in geomedia, if different oxidation states have to be taken into account. In this context, the presence of oxygen (aerobic, oxidizing conditions) or of hydrogen sulfide (anaerobic, reducing conditions) in natural waters is significant. H_2S is produced by weathering of sulfidic minerals or by decomposition of organic compounds in the absence of air. It indicates reducing conditions and leads to the formation of sparingly soluble sulfides. The redox potential is of special importance for the behavior of I, U, Np, Pu, and Tc. Elemental iodine is volatile and reacts with organic compounds, in contrast to I^- or IO_3^- ions. U(IV) does not form soluble species in natural waters, in contrast to U(VI). But under aerobic conditions, U(IV) is oxidized to $UO_2{}^{2+}$ and dissolved; the latter is reduced again if the water enters a reducing zone and is redeposited as UO_2. The most important feature of Np in water is the great stability range of Np(V) in the form of NpO_2^+; in this respect Np differs markedly from the neighboring elements U and Pu. Under reducing conditions, Np(IV) is formed and resembles U(IV) and Pu(IV). The chemical form of Tc also depends on the redox potential. Under anaerobic conditions, the stable oxidation state is IV, whereas under aerobic conditions Tc is easily oxidized to TcO_4^-.

The pH in natural waters varies between about 6 and 8 (apart from acid rainwater) and strongly influences the chemical behavior of elements that are sensitive to hydrolysis (elements of groups 3, 4, 5, and 8, 9, 10 of the periodic table). Relevant radionuclides belong to the lanthanide and actinide groups. The tendency of the actinides to hydrolyze increases in the order $MO_2^+ < M^{3+} < MO_2^{2+} < M^{4+}$. In the presence of complexing agents, the formation of other complexes competes with that of hydroxo complexes, as already mentioned. Complexes exhibiting the highest stability under the given conditions are formed preferentially.

Polynuclear hydroxo complexes may be formed by condensation of mononuclear hydroxo complexes of the same kind, provided that the concentration of the latter is high enough. Otherwise, condensation with reactive species of other origins, such as polysilicic acid or hydrous SiO_2, iron(III) hydroxide, or hydrous Fe_2O_3, and finely dispersed (colloidal) clay minerals, is preferred. Accordingly, either intrinsic colloids (*Eigenkolloide*) or carrier colloids (*Fremdkolloide*) may be formed. Due to hydrolysis and the interaction of hydroxo complexes with other components, actinides are not found as monomeric species in natural waters in the absence of complexing agents, whereas in the presence of carbonate or hydrogencarbonate, respectively, monomeric carbonato or hydrogencarbonato complexes prevail.

Inorganic salts affect the behavior of radionuclides in natural waters in various ways. At high salinity (high ionic strength), the formation of colloids is hindered and colloids already present are coagulated if salt water enters the system. For instance, precipitation of colloids carried by rivers occurs on a large scale in estuaries. Moreover, dissolved salts influence pH, hydrolysis, and complexation. They may act as buffers, for example, in seawater, where the pH is kept constant at about 8.2 by the presence of $NaHCO_3$. Finally, anions in natural waters form ion pairs and complexes with cationic radionuclides and affect solubility, colloid formation, and sorption behavior. Mobility may be enhanced by complexation; Cl^- ions, for example, are relatively weak complexing agents, but they are able to substitute OH^- ions in hydroxo complexes and to suppress hydrolysis, if they are present in relatively high concentrations.

The logarithms of the stability constants β_1 for the formation of 1 : 1 complexes of the actinide ions M^{3+}, M^{4+}, MO_2^+, and $MO_2{}^{2+}$ with various inorganic ligands are plotted in Figure 22.1. Carbonato complexes of alkaline earth elements, lanthanides, actinides, and other transition elements play an important role in natural waters and may stabilize oxidation states.

The formation of intrinsic colloids in natural waters can be excluded for radioisotopes of elements of groups 1, 17, and 18, and the probability that they may be formed is small for radioisotopes of elements of other groups as long as the concentration of the elements is low. In general, formation of carrier colloids by the interaction of radionuclides with colloids already present in natural waters is most probable. Thus, clay particles have a high affinity for heavy alkali and alkaline earth ions, which are bound by ion exchange. This leads to the formation of carrier colloids with ^{137}Cs, ^{226}Ra, and ^{90}Sr. The formation of radiocolloids with hydrolyzing species has already been discussed (Section 11.1.4). Aluminosilicate colloids are well known to form pseudocolloids with actinide ions.

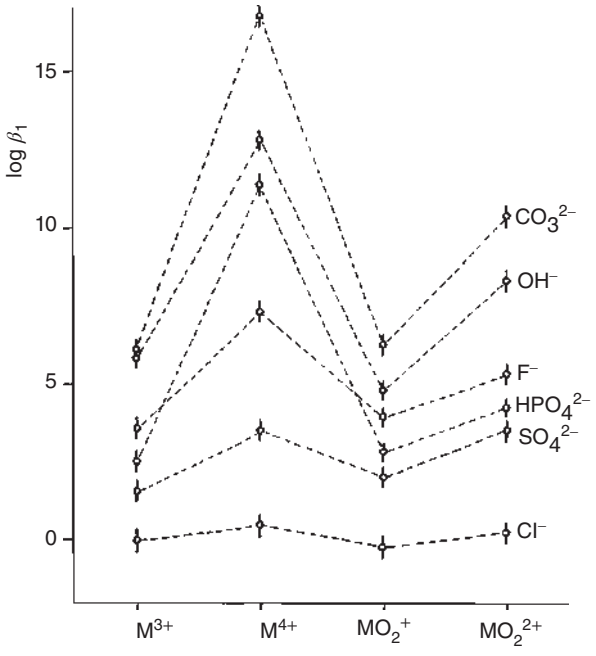

Figure 22.1 Logarithm of the stability constant β_1 of 1 : 1 complexes of the actinide ions M^{3+}, M^{4+}, MO_2^+, and MO_2^{2+} with various inorganic ligands.

Organic compounds are found primarily not only in surface waters but also in groundwaters, if these are or have been in contact with organic substances. Compounds of low molecular mass may be of natural origin (e.g. metabolites, such as organic acids, amines, or amino acids) or anthropogenic (e.g. detergents, aromatic sulfonic acids). Many of these organic compounds are strong complexing agents and well soluble in water. They are able to form stable complexes with radioisotopes of nearly all elements.

The most important representatives of organic compounds of high molecular mass in natural waters are humic and fulvic acids, both degradation products of organic matter. They are polyelectrolytes and contain carboxylic and phenolic hydroxyl groups which make these compounds hydrophilic and enable them to form quite stable complexes. Other compounds of high molecular mass are proteins, lipids, and carbohydrates. The concentration of dissolved organic matter in natural waters varies considerably. It may be as low as $0.1\,mg\,l^{-1}$ DOC (dissolved organic carbon) in deep groundwaters, it ranges from 0.5 to $1.2\,mg^{-1}$ in the oceans, and it may go up to about $50\,mg\,l^{-1}$ in swamp waters. Relatively high stability constants have been measured for complexes of actinides with humic substances.

Complexation of actinides by organic compounds may also cause an increase in solubility. For example, NpO_2^+ ions exhibit strong complexation by organic complexing agents, even in high salt concentrations. The influence of hydrolysis increases in the order $MO_2^+ < M^{3+} < MO_2^{2+} < M^{4+}$. Whether the formation of hydroxo complexes or of other complexes prevails depends on the stability constants of the complexes, the concentration of the complexing agents, and the pH.

With increasing mass of the organic compounds, colloidal properties may prevail and a pronounced difference between noncolloidal and colloidal species no longer exists. Radiocolloids containing organic substances may be formed by sorption or ion exchange of radionuclides on macromolecular organic compounds or by sorption of organic complexes of the radionuclides on inorganic colloids. In all cases, the surface properties determine the behavior (Section 11.1.4).

Microorganisms may also influence the fate of radionuclides in natural waters, in particular in surface waters and near-surface ground waters. Depending on the metabolism of the microorganisms and their preference for certain elements, they incorporate radionuclides which then migrate with the microorganisms. From uptake by microorganisms, the radionuclides may enter the food chain.

The migration behavior of radionuclides may also be affected by precipitation and coprecipitation. In the range of low concentrations, coprecipitation is generally the most important process. Radionuclides may be coprecipitated by isomorphous substitution or by adsorption (Section 11.1.3). Precipitation reactions often observed in natural waters are the precipitation of $CaCO_3$ caused by a shift in the equilibrium between $Ca(HCO_3)_2$ and $CaCO_3$ due to the escape of CO_2 and precipitation of iron(III) hydroxide due to oxidation of iron(II), dissolved as $Fe(HCO_3)_2$, from the access of air. Depending on the conditions and the properties of the compounds, precipitation may stop at an intermediate stage with the formation of a colloid (e.g. formation of a sol of colloidal iron(III) hydroxide in water). Coprecipitation of trace elements with iron(III) hydroxide is used as an effective procedure in the preparation of drinking water. Generally, coprecipitation of microcomponents is to be expected if these would also precipitate under the given conditions, provided they were present in higher concentrations. However, actinides(IV) and actinides(III) are also coprecipitated with $BaSO_4$ and $SrSO_4$ by the formation of anomalous solid solutions. Coprecipitation may influence considerably the mobility of radionuclides in natural waters, in particular that of lanthanides and actinides.

22.4 Interactions of Radionuclides with Solid Components of the Geosphere

Mobility and transport of radionuclides in the geosphere are influenced markedly by their interaction with solids. Migration is retarded, or even stopped, if the interaction is strong, in particular if the radionuclides are incorporated into the solids. Sorption of radionuclides on solids has been investigated extensively for materials in the neighborhood of planned HLW repositories. Various kinds of interaction have to be taken into account:

- fixation by predominantly ionic bonds (ion exchange);
- sorption by mainly covalent bonds (chemisorption);
- sorption by weak (van der Waals) bonds (physisorption);
- interaction at the outer surface of solids;
- interaction at inner surfaces of porous substances;

- ion exchange at positions within the solids (e.g. clay minerals);
- incorporation into solids by the formation of solid solutions.

Reactions of hydroxo complexes or anionic forms of radionuclides with hydroxyl groups at the surface of solids (≡SiOH, =AlOH, or =FeOH) are frequently observed, for example,

$$\equiv\mathrm{SiOH(s)} + \mathrm{HO{-}M^{(n-1)+}} \Leftrightarrow \equiv \mathrm{Si{-}O{-}M^{(n-1)+}(s)} + \mathrm{H_2O} \tag{22.1}$$

(additional water molecules are omitted). In this way, the complex of the metal M in solution is converted into a complex at the surface of the sorbent ("surface complex") with a partly changed coordination sphere. The bonds formed are of a predominantly covalent nature. This type of reaction has been described in the older literature as hydrolytic adsorption. It is very common and has been applied in analytical chemistry for selective separations.

Exchange of nonhydrolyzed cationic species of radionuclides at the outer surface or within the layer structure of solids plays an important role in the case of $^{137}Cs^{+}$, $^{90}Sr^{2+}$, and $^{226}Ra^{2+}$. It is very effective if clay minerals are present that exhibit high exchange capacity. The predominant type of interaction is ion exchange. Exchange of cationic or anionic forms of radionuclides on the surface of ionic compounds such as $CaCO_3$ or $BaSO_4$ may also contribute to sorption, in particular if the radionuclides are incorporated in the course of recrystallization.

Adsorption of complexes of radionuclides with inorganic or organic ligands (in particular, complexes with humic substances) and of colloidal species of radionuclides may also markedly influence the migration behavior. The predominant kind of interaction is physical adsorption.

The solids in the geosphere are of a very different kind and composition. With respect to the interaction with radioactive species, the surface properties are of special interest. Keeping this aspect in mind, the following main components of the geosphere can be distinguished:

- consolidated rocks (magmatic rocks, such as basalt, granite, feldspar, quartz, olivine, plagioclases, and pyroxenes, and sedimentary rocks, for example, sandstone, limestone, or dolomite);
- unconsolidated rocks (more or less loose packed, consisting mainly of glacial deposits of gravel, sand, and clay);
- sediments in rivers, lakes, and oceans;
- soils (mainly sand, clay, humus with plant residues, small animals, and plenty of microorganisms).

Besides the main components, many other minerals have to be taken into account:

- oxides and hydroxides (e.g. hydrargillite, diaspore, corundum, spinels, hematite, magnetite, perovskites);
- halides (e.g. rock salt, cryolite, carnallite);
- sulfides (e.g. pyrite);
- sulfates (e.g. gypsum, anhydrite, alum);

- phosphates (e.g. apatites, monazites – some phosphates contain exchangeable protons);
- carbon and carbonaceous material.

Of special significance with respect to their properties as sorbents are the clay minerals (e.g. kaolinite, montmorillonite, vermiculite, illite, chlorite), mainly due to their high exchange capacity.

The surfaces of silicate rocks alter in the course of time. Cations such as Na^+, K^+, Mg^{2+}, and Ca^{2+} that are integral components of the silicates are leached and hydroxyl groups are formed at the surface that may add or give off protons, depending on the pH. The resulting sorption sites are of a different nature and quality. ≡SiOH, =AlOH, and =FeOH groups are found most frequently. In neutral media radionuclides present as hydroxo complexes or divalent anions are sorbed preferentially. Most investigations with consolidated rocks have been made with granites, because they are possible host rocks for HLW repositories.

With sedimentary rocks, radionuclides may also interact in different ways. They may be sorbed on sandstone, limestone, and other sedimentary rocks. Heterogeneous exchange may contribute to the sorption, for example, exchange of $^{14}CO_3^{2-}$(aq) for $^{12}CO_3^{2-}$(s) or exchange of $^{90}Sr^{2+}$ (aq), $^{210}Pb^{2+}$ (aq), or $^{226}Ra^{2+}$ (aq) for Ca^{2+} (s) at the surface of calcite, limestone, or dolomite. In addition, incorporation into the inner parts of the crystals due to recrystallization and formation of solid solutions may take place. Interaction of radionuclides with consolidated volcanic tuffs has been investigated intensively because the deposits in the Yucca Mountains, United States, have been under investigation as potential repositories for HLW.

The loose-packed material of unconsolidated rocks consists mainly of sand and clay. Clay minerals are the most important components, because of their high sorption capacity and their selectivity for heavy alkali and alkaline earth ions. Compared to clay minerals, sand is a rather poor sorbent, although hydrated silica also exhibits exchange properties due to the presence of ≡SiOH groups. The exchange capacity of clay minerals with a layer structure (e.g. montmorillonite, vermiculite) goes up to about 1–2 meq g^{-1}. Clay minerals with high charge densities, like illite and the micas, exhibit a marked preference for monovalent cations ($Cs^+ > Rb^+ > K^+$), which are bound more or less irreversibly. Divalent cations ($Ra^{2+} \geq Ba^{2+} > Sr^{2+}$) are also firmly bound. Mica-type clay minerals play an important role in nature, because they are present in all fertile soils. ^{137}Cs, ^{90}Sr, and ^{226}Ra are fixed very strongly in positions between the layers. Hydroxo complexes of lanthanides and actinides are mainly bound at the outer surfaces by interaction with ≡SiOH or =AlOH groups. In Germany, layers of unconsolidated rocks above salt domes proposed for the storage of HLW have been investigated in great detail with respect to the migration behavior of radionuclides. In other countries, clay is discussed as a host for HLW repositories, because of the favorable sorption properties of clay minerals.

Compounds present in relatively small amounts are often decisive for the sorption behavior of natural solids. Examples are small amounts of clay in association with large amounts of sand with respect to sorption of ^{137}Cs, and small amounts of carbonaceous material with respect to sorption of ^{129}I.

Heterogeneous exchange of radionuclides on carbonates has already been mentioned. Exchange on other sparingly soluble minerals (e.g. halides, sulfates, phosphates) may lead to rather selective separation of radionuclides. Following the exchange at the surface, ions may be incorporated into the solids in the course of recrystallization, which is a very slow but continuous process. Anomalous solid solutions with radioactive ions of different charges may also be formed.

Aquatic sediments are formed in all surface waters by the settling of coarse and fine inorganic and organic particles. They are present in rivers, in lakes, and in the oceans, and radionuclides deposited on the surface of the Earth will sooner or later come into contact with these sediments. They may enter the sediments by sorption of molecularly dispersed species (ions, molecules), by precipitation or coprecipitation, by coagulation of colloids (in particular carrier colloids) followed by sedimentation of the particles formed, or by sedimentation of coarse particles (suspended matter). By desorption, the radionuclides may be remobilized and released again into the water.

The main components of these sediments are similar to those in the sediments formed at earlier times: sand and clay minerals. However, river and lake sediments also contain relatively large amounts of organic material and microorganisms. Appreciable fractions of radionuclides present in rivers and lakes are sorbed in sediments, but usually it is difficult to discriminate between the influences of the various processes taking place and to correlate the fixation in the sediments with certain components. As far as the inorganic components are concerned, clay minerals play the most important role.

With respect to components and chemistry, soils are even more complex than river or lake sediments. On the other hand, large areas of the continents are covered with soils of various compositions, and therefore interest in the behavior of radionuclides in soils is justified. Furthermore, radionuclides are easily transferred from soils to plants and animals, and in this way they enter the biosphere and the food chain.

The main components of soils are sand, clay, and humus. Whereas interaction between radionuclides and sand is rather weak, as in the case of sediments, sorption by clay minerals and reactions with the organic compounds in humus are most important for the migration behavior of radionuclides. $^{137}Cs^{+}$ ions are quite strongly bound in clay particles, as already mentioned. $^{90}Sr^{2+}$, $^{226}Ra^{2+}$, and $^{210}Pb^{2+}$ are also retained by clay particles or bound on chalky soil via precipitation or ion exchange. $^{129}I^{-}$ ions are oxidized, and I_2 reacts easily with organic compounds that take part in the metabolism of microorganisms. Lanthanides and actinides are present either as hydroxo complexes or as organic complexes. These species are rather firmly bound to the components of soils, but organic compounds may also stay in solution, possibly in the form of colloids. TcO_4^{-} reacts with proteins and may thus be incorporated into organic matter.

Besides the composition of the soils, other factors have a major influence on the migration of radionuclides: rainfall, the thickness of the soil layers, their permeability to water, and the nature of the layers underneath. For example, ^{137}Cs is washed down quickly through layers of sand, but it will stay in layers of clay. ^{239}Pu is sorbed

by clay more strongly than by sand and may stay in soils for rather long times, if it is not dissolved by complexation or displaced by other compounds.

The large number of measurements in various systems lead to the result that the interaction of radionuclides with solids is rather complex and depends on many parameters: the species of the radionuclides in the solution, their properties and their dispersion, the components of the solid, the surface area of the particles, the nature of the sorption sites, the presence of organic substances and of microorganisms, and the interference or competition of other species. Therefore, an investigation of the behavior of the radionuclides in the specific system of interest is unavoidable, if reliable information about their migration behavior is required.

We present here an example for detailed work by Marsac et al. (2015) that goes beyond the measurement of simple surface sorption data and their interpretation in a surface complexation model. Plutonium with its particularly complex redox chemistry may be thermodynamically stable in the states +III to +VI depending on the redox conditions in the environment. Mineral surfaces can also affect Pu redox speciation. Therefore, the interpretation of Pu sorption data becomes particularly challenging, even for simplified laboratory experiments. The selected study focuses on Pu sorption to kaolinite. Am(III), Th(IV), Np(V), and U(VI) literature sorption data are used as analogues for the corresponding Pu redox states to construct and superimpose two independent pH–pe diagrams, one for the kaolinite surface and another for the aqueous phase. This allows visualization of the prevalent Pu redox state in both phases. The model suggests that the stability field of the most strongly adsorbing redox state is larger at the surface than in solution. Because Pu(V) weakly sorbs to kaolinite, it never prevails at the surface. Within the stability field of Pu(V) in 0.1 M $NaClO_4$ solution, Pu(VI) and Pu(IV) prevail at the kaolinite surface under oxidizing and slightly reducing conditions, respectively. By contrast, the Pu(IV)/Pu(III) boundary is hardly affected because both redox states strongly sorb to kaolinite, especially for pH > 6. The method is applied to literature data for Pu sorption to kaolinite vs. pH where a steady state was reached but showing a very uncommon pattern. By estimating the pe from a Pu redox state analysis in solution, overall Pu uptake could be predicted. Generic equations were derived that are applicable to minerals and actinides other than kaolinite and Pu, where thermodynamic models are particularly necessary to predict Pu mobility.

To determine the stability fields of different Pu redox states at a mineral surface, the sorption behavior of all redox states must be known separately. It appears that for Pu such experimental data will hardly ever become available because a mixture of redox states is found in most experimental studies. Fortunately, lanthanides/actinides (Ln/An) exhibit similar chemical behavior for the same redox state. Therefore, the use of these elements as chemical analogues might help to unravel the complex geochemical behavior of Pu in a first approach. The study (Marsac et al. 2015) focuses on kaolinite because experimental sorption data for americium(III) (Am^{3+}), thorium(IV) (Th^{4+}), neptunium(V) (NpO_2^+), and uranium(VI) (UO_2^{2+}) on kaolinite are available by Buda et al. (2008), Banik et al. (2007), Schmeide and Bernhard (2010), and Křepelová (2007). These data are assumed to be representative for sorption of Pu(III, IV, V, VI), respectively, and are

used for each redox state of Pu to calibrate a simple surface complexation model. By merging Pu redox chemistry with sorption processes, the resulting model is used to construct a predominance (pH–pe) diagram for Pu redox speciation at the kaolinite surface. The modeling results are compared with experimental data in order to test the capacity of the model to predict Pu sorption to kaolinite as a function of pH and pe. The present approach is subsequently tested on metal sorption on other minerals.

PHREEQC (version 2; Parkhurst and Appelo 1999) is a computer code that can perform speciation (including surface complexation) and saturation-index calculations in water. Predominance (pH–pe) can be obtained using PhreePlot (Kinniburgh and Cooper 2009) which contains an embedded version of PHREEQC. In Marsac et al. (2015), thermodynamic constants for Pu aqueous speciation and solubility are taken from the Nuclear Energy Agency (NEA) thermodynamic database. Reactions and corresponding thermodynamic constants at 25 °C and zero ionic strength are given in Marsac et al. (2015). In case of gaps in the Pu database, data for analogues were chosen and are included in the database. A redox reaction involving aqueous Pu^{4+} and PuO_2^{2+} or PuO_2^{+} is not given. They were calculated based on the reaction $PuO_{2(am,\,hyd)} = PuO_2^{2+} + e^-$ with $K = -19.78$ at zero ionic strength (NEA thermodynamic database). The specific ion interaction theory (SIT) accounts for ionic strength effects and the corresponding parameters for Pu (or the chosen analogue) from NEA are used.

Use of distribution coefficients (K_d) to express An uptake by kaolinite is particularly convenient for the present purpose. K_d is defined as

$$K_d = \frac{[An]_{surf}}{[An]_{aq}} \times \frac{V}{S} \tag{22.2}$$

where $[An]_{surf}$ and $[An]_{tot,aq}$ refer to the total amount (i.e. the sum of all the species including various redox states) at the surface and in solution, respectively, and V/S is the liquid to solid ratio. S can be either expressed as the mass of solid (K_d in $l\,kg^{-1}$) or as the surface area (K_d in $l\,m^{-2}$) in contact with a given solution volume. K_d is a highly conditional parameter that depends on the physico-chemical conditions (e.g. pH, I, T, ligands in solution, surface loading). Study (Marsac et al. 2015) focused on data obtained at room temperature, for 0.1 M $NaClO_4$, in the absence of complexing ligands other than OH^- and assuming ideal sorption behavior. Therefore, the evolution of K_d with pH can be calculated using the simple surface complexation model. K_d is commonly experimentally determined to quantify actinide sorption to minerals. In the case of redox sensitive elements like Pu, several redox states (Pu(X); X = III, IV, V, or VI) might occur simultaneously both at the surface and in the aqueous phase, depending on the redox conditions. The overall (measured) K_d will be ultimately affected by the Pu redox state distribution. For a mixture, K_d is denoted $K_{d,tot}$ and can be written as follows:

$$K_d = \frac{\sum_X [Pu(X)]_{surf}}{\sum_X [Pu(X)]_{aq}} \times \frac{V}{S} = \frac{\sum_X K_d(X) \times [Pu(X)]_{aq}}{\sum_X [Pu(X)]_{aq}} \tag{22.3}$$

$K_d(X)$ is the K_d in an ideal case where only one redox state X is present both at the surface and in solution, when $K_{d,tot} = K_d(X)$:

$$K_d(X) = \frac{[Pu(X)]_{surf}}{[Pu(X)]_{aq}} \times \frac{V}{S} \tag{22.4}$$

$$Pu(X)^{n+} + iH_2O = Pu(X)(OH)^{n-i} + iH^+ \tag{22.5}$$

$${}^{OH}K_{X,i} = \frac{\left[Pu(X)(OH)_i^{n-i}\right]}{[Pu(X)^{n+}]} \tag{22.6}$$

With these equations, a predominance (pH–pe) diagram can be constructed that shows the predominance field of the different redox states as well as the predominance field of the different hydrolyzed species of a given redox state. Here, a simplified diagram is preferred based on total aqueous concentrations, which does not show the speciation of a given redox state. This way, only the boundaries between redox states are visible. The total aqueous concentration of Pu in the redox state X ($[Pu(X)]_{aq}$) can be related to the concentration of the free cation ($[Pu(X)^{n+}]$) when taking into account its hydrolysis:

$$\begin{aligned}[Pu(X)]_{aq} &= \left[Pu(X)^{n+}\right] + \sum_i \left[Pu(X)(OH)_i^{n-i}\right] \\ &= \left[Pu(X)^{n+}\right] \times \left(1 + \sum_i \frac{{}^{OH}K_{X,i}}{\left[H^+\right]^i}\right) = \left[Pu(X)^{n+}\right] \times a_x\end{aligned} \tag{22.7}$$

where a_x is the side reaction coefficient for the Pu redox state X. Introducing Eq. (22.7) into the Nernst equation yields

$$pe = \log K_{ox/red}/q + \log\left(\frac{[Pu(Ox)]}{Pu(Red)} \times \frac{a_{Red}}{a_{Ox}}\right) \Big/ q - m \times pH \tag{22.8}$$

And the pe representing the borderline between two redox states in solution $(Ox/Red)_{aq}$ is found for

$$(Ox/Red)_{aq} = pe = \log K_{Ox/Red}/q + \log\left(\frac{a_{Red}}{a_{Ox}}\right) \Big/ q - m \times pH \tag{22.9}$$

$(Ox/Red)_{aq}$ develops as a function of pH and ionic strength. The redox state with the strongest hydrolysis enlarges its predominance field with increasing pH. To account for sorption processes in the Nernst equation, $K_d(Ox)$ and $K_d(Red)$ can be included in Eq. (22.8) yielding

$$pe = \log K_{Ox/Red}/q + \log\left(\frac{[Ox]_{surf}}{[Red]_{surf}} \times \frac{a_{Red}}{a_{Ox}} \times \frac{K_d(Red)}{K_d(Ox)}\right) \Big/ q - m \times pH \tag{22.10}$$

It is this equation that allows us to construct the predominance field of different Pu redox states selectively at the surface of a mineral. Because the compartments are distinguished, the resulting plot is independent of the one in solution and both of them must be superimposed to realize the differences: the predominance area of the state having the strongest tendency to be sorbed at the mineral surface is enlarged compared to that in solution.

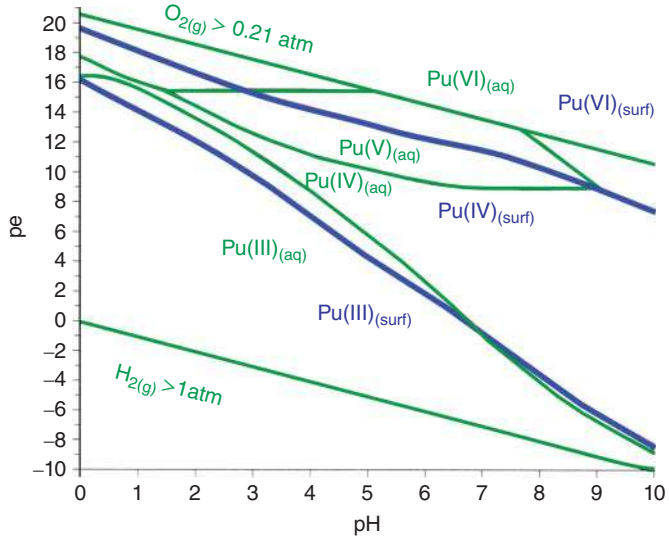

Figure 22.2 Superposition of Pu predominance plot in solution (green) and at the kaolinite surface (blue). Only the predominance field of each redox state is shown, not the detailed speciation (e.g. hydrolyzed species). Source: Data from author's Notebook.

Based on the large database contained in Marsac et al. (2015) and on the above developed equations, predominance diagrams for aqueous species and for sorbed species at the kaolinite surface can be constructed. Figure 22.2 shows the superposition of the Pu predominance plot in solution (green) and at the kaolinite surface (blue). Pu redox speciation at the kaolinite surface is interpreted based on the thermodynamic stability of the respective Pu redox state at the surface. To overcome difficulties in the interpretation of results related to the sensitivity of Pu to redox conditions, uptake data on kaolinite of the more redox-stable Am(III), Th(IV), Np(V), and U(VI) – chemical analogues for Pu(III,IV,V,VI) – have been used to calibrate a surface complexation model. To fully understand Pu redox chemistry in the aqueous kaolinite suspension, the system is treated separately for the aqueous solution and the kaolinite surface, and the two resulting Pu predominance diagrams are superimposed. This method visualizes how the prevailing Pu redox states can differ between solution and surface for given pH/pe conditions. Notably, the kaolinite surface has no impact on the Pu(IV)/Pu(III) distribution in neutral to alkaline conditions, in the absence of aqueous ligands other than OH^-. Therefore, the study of Pu(III) sorption to minerals is relevant for the reducing conditions encountered in deep geological nuclear waste repository sites. Under slightly oxidizing conditions, Pu(IV) can be stabilized at the kaolinite surface within the stability field of Pu(V) in solution, which significantly increases the overall Pu uptake. The model predicts overall experimental Pu uptake when the Pu(V)/Pu(IV) redox couple is involved. This suggests that Pu–mineral interaction is strong, even under slightly oxidizing condition. Also Pu(VI) can be stabilized at the kaolinite surface within the stability field of Pu(V) in solution, under oxidizing conditions. Its impact on

overall Pu uptake is limited to redox conditions in equilibrium with ambient air atmosphere (O_2), by the weak Pu(VI) sorption to kaolinite for pH < 5 and the strong Pu(VI)–carbonate (due to atmospheric CO_2) complexation in alkaline conditions. Independent experimental data for other minerals with Pu and with Np corroborate this approach. The derived equations are of rather generic form making them easily applicable to other adsorbant/adsorbat systems.

Based on the thermodynamic stability of the sorbed Pu species, the exact redox mechanism does not need to be explicitly considered, but the redox potential of the system must be known. Measurement of redox potential is rarely simple and often bears large uncertainties, but the pe (or Eh) strongly affects overall Pu uptake by kaolinite. A redox state analysis of aqueous Pu can provide information on pe, when a steady state is reached. The determination of pe from Pu redox state analysis heavily relies on the accuracy of the available thermodynamic database for aqueous complexes, i.e. their capability to describe the speciation of the different Pu redox states in presence of various ligands. This fact becomes more important for natural samples that are more complex than the systems considered in Marsac et al. (2015).

22.5 Radionuclides in the Biosphere

Radionuclides in the atmosphere, in surface waters, and on the surface of the Earth have immediate access to the biosphere. From surface waters as well as from near-surface groundwaters, from soils, and from the air, radionuclides may be taken up by microorganisms, plants, fish, and other animals, thus also entering the various pathways of the food chain. The fractions of radionuclides transferred to living things depend on the chemical form (species) of the radionuclide considered and the metabolism of the microorganisms, plants, and animals and may differ by several orders of magnitude. The study of the behavior of radionuclides in ecosystems comprising air, water, soil, microorganisms, plants, animals, and humans is the field of radioecology. Various ecosystems, such as aquatic, agricultural, forest, and alpine, are distinguished.

The pathways of radionuclides in ecosystems are illustrated schematically in Figure 22.3. Plants may take up radionuclides from the air by deposition on the

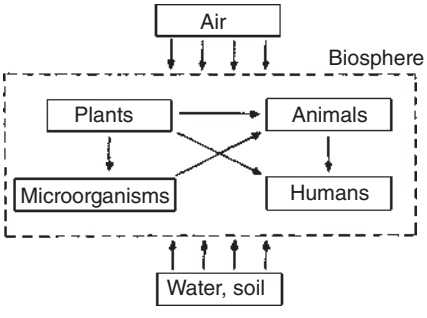

Figure 22.3 Pathways of radionuclides in ecosystems.

leaves, or from the soil by the roots with water and minerals. In this step, the species of the radionuclides and their solubility are most important. Microorganisms incorporate radionuclides present in water or in the soil. Animals and humans may be contaminated by radionuclides from the air (gases, aerosols, dust) by inhalation or deposition on the skin, or by uptake of water and via the food chain by digestion. Animals may also be contaminated by ingestion of contaminated soil particles.

The metabolism of radionuclides in plants, animals, and humans can be compared to that of trace elements. Radioisotopes of essential trace elements, such as T, ^{14}C, ^{55}Fe, ^{54}Mn, ^{60}Co, and ^{65}Zn, show the same behavior as the stable isotopes of these elements. Other radionuclides behave in a similar way to other elements (e.g. ^{90}Sr ≈ Ca, ^{137}Cs ≈ K), and radioisiotopes of heavy elements are comparable to other heavy elements.

Metabolism in humans, animals, and plants comprises the following steps:

- resorption in the lung or in the gastrointestinal tract (humans and animals) or by the leaves or roots (plants);
- distribution in the body or in the plant;
- retention in the body or in the plant, often in special organs or places.

Resorption depends on the chemical properties and the chemical form (species) of the element. Biologically inert and bioavailable species are distinguished. For example, mono- and divalent cations are easily resorbed, whereas elements of higher valency are, in general, not able to pass the intestinal walls or the membranes, respectively, and to enter the body fluids or the plants. The presence of other substances may diminish the resorption of radionuclides. For example, resorption of ^{137}Cs is reduced if cows take up soil particles together with grass, because this radionuclide is bound quite firmly on the clay particles in soil. The resorption factor f_R is given as

$$f_R = \frac{A}{A_0} \tag{22.11}$$

where A_0 is the activity taken up and A the activity resorbed.

In most cases, the concentration of radionuclides in animals and humans decreases with excretion and decay. In the ideal case, decrease of activity A due to excretion can be described by an exponential law

$$A = A_0 \exp(-\lambda_b t) = A_0 \left(\frac{1}{2}\right)^{t/t_{1/2}(b)} \tag{22.12}$$

where $\lambda_b A$ is the rate of excretion, and $t_{1/2}$(b) is the biological (ecological) half-life of the radionuclide in the animal or human. In general, the decay, given by the physical decay constant λ_p, must also be considered, and the effective rate constant of decrease of activity in the body or in the plant is

$$\lambda_{eff} = \lambda_b + \lambda_p \tag{22.13}$$

Accordingly, the time dependence of the activity in the body or the plant is

$$A = A_0 \exp(-\lambda_{eff} t) \tag{22.14}$$

Effective, biological (ecological), and physical half-lives ($t_{1/2}$(eff), $t_{1/2}$(b), and $t_{1/2}$(p), respectively) may also be distinguished, where

$$t_{1/2}(\text{eff}) = \frac{\ln 2}{\lambda_{\text{eff}}} = \frac{t_{1/2}(\text{b})t_{1/2}(\text{p})}{t_{1/2}(\text{b}) + t_{1/2}(\text{p})} \tag{22.15}$$

In the case of short-lived radionuclides, λ_{eff} is mainly determined by the physical decay constant, and in the case of long-lived radionuclides mainly by the rate constant of excretion.

In general, radionuclides are often not distributed evenly in the body or in plants, but enriched in certain organs or parts, as illustrated in Figure 22.4. For example, in humans and animals, Sr and Pu are enriched in bones, and I in the thyroid gland. Considering a single uptake of a radionuclide in a certain organ or part X of a body or plant, respectively, the activity in that organ or part after the time t is

$$A_{\text{X}} = A_0 f_{\text{R}} f_{\text{X}} \exp(-\lambda_{\text{eff}} t) \tag{22.16}$$

Continuous uptake of a radionuclide at a certain rate R leads to an increase in the activity in the body, organ, plant, or part of the plant which is given by

$$A = \frac{R}{\lambda_{\text{eff}}}[1 - \exp(-\lambda_{\text{eff}} t)] \tag{22.17}$$

In animals and humans, the activity A often approaches a saturation value in which the rates of decrease in the body (by excretion and decay) and of ingestion are the same:

$$A = \frac{R}{\lambda_{\text{eff}}} \tag{22.18}$$

R is usually measured in Bq d^{-1} and λ_{eff} in d^{-1}.

Resorption and metabolism in plants vary with the composition and pH of the soils and with the seasons; in animals and humans they vary with age, sex, health, diet, and other factors. In cases in which radionuclides are resorbed selectively and accumulated in certain organs of animals or humans, or in certain parts of plants, or in which the rate of excretion in animals or humans is small compared to the rate of sorption, these radionuclides will be enriched in the body or in the plant (bioaccumulation), with the result that the activity may reach high values.

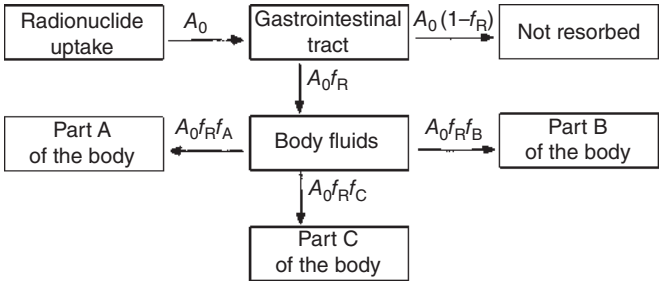

Figure 22.4 Distribution of radionuclides in an animal. f_A, f_B, and f_C are the fractions transferred to different parts of the body.

In radioecology, the transfer of radionuclides from water, soil, or food to animals, humans, or plants is described in various ways. In aquatic ecosystems, concentration factors (CFs) are determined, given by the concentration $c_i(2)$ of a certain radionuclide i in microorganisms or animals in relation to the concentration $c_i(1)$ of that radionuclide in water at the same time: $\mathrm{CF} = c_i(2)/c_i(1)$. Some typical CFs for ^{137}Cs and ^{90}Sr measured in fresh water and marine ecosystems are listed in Table 22.2. The influence of the competition of K and Na with ^{137}Cs, and of Ca with ^{90}Sr, in marine ecosystems is obvious.

The transfer from soil to vegetation is described by transfer factors (TFs), given by the activity in Bq kg^{-1} of dry plants, divided by the activity in Bq m^{-2} of the soil (m^2 kg^{-1}). In agricultural ecosystems the transfer of radionuclides from grass to agricultural products, such as meat or milk, is characterized by various factors, which are listed in Table 22.3.

CFs, TFs, and transfer coefficients depend on the radionuclide considered, its chemical form (species), the conditions in the soil, and the kind of vegetation and animal; they may vary appreciably with the seasons.

The concentration of many elements, such as C, K, or Ca, in animals or plants is often regulated in such a way that it remains constant or nearly constant. Because radioisotopes (subscript i) and stable isotopes (subscript s) of these elements exhibit

Table 22.2 Typical concentration factors in freshwater and marine ecosystems.

Radionuclide	Ecosystem	Molluscs	Crustaceans	Fish muscle
^{137}Cs	Freshwater	600	4000	3000
	Marine	8	23	15
^{90}Sr	Freshwater	600	200	200
	Marine	1	3	0.1

Table 22.3 Factors used to characterize the transfer of radionuclides to meat (or milk).

Factor	Definition	Unit
Concentration factor (CF)	Activity (Bq) per kilogram of meat (per liter of milk) divided by the activity (Bq) per kilogram of grass	kg kg^{-1} (l kg^{-1})
Transfer factor T (also called transfer coefficient)	Activity (Bq) per kilogram of meat (per liter of milk) divided by the activity (Bq) taken up with the food per day	d kg^{-1} (d l^{-1})
Transfer factor (TF) (also called aggregated transfer factor T_{ag})	Activity (Bq) per kilogram of meat (per liter of milk) divided by the activity (Bq) per m^2 of the soil	m^2 kg^{-1} (m^2 l^{-1})

the same behavior, their ratios in the substance taken up and in the plants or animals are the same:

$$\frac{c_i(2)}{c_s(2)} = \frac{c_i(1)}{c_s(1)} \tag{22.19}$$

This relationship is called the specific activity model. Its main advantage is its independence of the kind of animal or plant. The model can also be applied if the radionuclides show a similar behavior to stable isotopes of other elements, for example, $^{90}Sr^{2+}$ and Ca^{2+}. Different behavior can be taken into account by a correction factor (called the observed ratio OR):

$$c_i(2) = \frac{c_i(1)}{c_s(1)} c_s(2) \cdot OR \tag{22.20}$$

For radionuclides for which values of OR are not known, the specific activity model is not applicable.

Natural radionuclides are present in all plants and animals and in humans. The activity of ^{40}K is 31 Bq g^{-1} of K, and the average activities in meat and in milk are about 120 Bq kg^{-1} and 50 Bq l^{-1}, respectively. The inventory of ^{40}K in a living human of 75 kg weight is 4000 Bq, that of ^{14}C is 3000 Bq, that of ^{228}Ra 4 Bq, and that of ^{226}Ra 2 Bq. The human inhales 220 000 Bq yr^{-1} of ^{222}Rn and 320 000 Bq yr^{-1} of its decay products. The transfer of U and Th to plants and animals is very small due to the low solubility and the low resorption of these elements. Their activities in milk are on the order of 10^{-4} Bq l^{-1} and in meat and fish $5 \cdot 10^{-3}$ Bq kg^{-1}. Ra has better access to the food chain and, due to its similarity to Ca, Ra is enriched in bones, where it is found in amounts on the order of 10^{-12} g g^{-1}. The activity of ^{226}Ra in other parts of animals and humans is about 10^{-2} Bq kg^{-1}. ^{210}Pb and ^{210}Po, decay products of ^{222}Rn, are present in aerosols and deposited with precipitations on plants. Their uptake from the air is much higher than that by the roots. They enter the food chain and are found in concentrations of 1–10 Bq kg^{-1} in meat. In reindeer livers values above 100 Bq kg^{-1} have been measured.

The activity of cosmogenic T in ecosystems is negligible, because of the dilution of T in the water cycle and its short residence time in all living things. The specific activity of cosmogenic ^{14}C in the biosphere is 0.23 Bq g^{-1} of carbon. As the average carbon content of organisms is about 23% (w/w), the average activity of ^{14}C in organisms is about 50 Bq kg^{-1}.

Artificial radionuclides released by nuclear explosions, weapons tests, and accidents have been deposited from the air as fallout on soil and vegetation. In 1963, values up to 0.8 Bq l^{-1} of ^{90}Sr and up to 1.2 Bq l^{-1} of ^{137}Cs were measured in precipitations in Central Europe. In 1964, the concentration of ^{137}Cs in beef reached values of about 36 Bq kg^{-1}. Consequently, the concentration of ^{137}Cs in humans went up to about 11 Bq kg^{-1}.

Much higher activities of radionuclides were found after the reactor accident at Chernobyl, for example, in Bavaria up to $\approx 10^4$ Bq of ^{131}I and up to $\approx 3 \cdot 10^3$ Bq of ^{137}Cs per kg of grass. In the following days, the activity of these radionuclides in

milk increased quickly to values of ≈400 Bq of ^{131}I and ≈60 Bq of ^{137}Cs per liter. The local activities varied considerably, depending on the local deposition with the precipitations. Whereas the activity of ^{131}I in the biosphere decreased quite rapidly with the half-life of this radionuclide, that of ^{137}Cs decreased slowly and varied with the agricultural activities. For example, by plowing, radionuclides may be moved from the surface to deeper layers and vice versa.

After the Chernobyl accident, the behavior of ^{137}Cs and ^{90}Sr in ecosystems was investigated in detail in many countries. The resorption factor for ^{137}Cs in cows is $f_R \approx 0.6$, and its biological half-life in animals varies between about 40 and 150 days, increasing with the size of the animal. ^{137}Cs is quite evenly distributed in the body and shows some similarity to K. TFs (soil–grass) in the range between 0.0005 and 0.1 m^2 kg^{-1}, CFs between 0.3 and 0.7, and aggregated TFs T_{ag} (soil–meat) between 0.0001 and 0.1 m^2 kg^{-1} have been measured. The aggregated soil–milk TFs varied between 0.0001 and 0.005 m^2 l^{-1}. High TFs were observed for moose (0.01–0.3 m^2 kg^{-1}) and in particular for fungi (1–2 m^2 kg^{-1}). Consequently, aggregated TFs were high for roe deer and reindeer (T_{ag} = 0.03–0.2 m^2 kg^{-1}). Typical transfer coefficients are $T \approx 0.06$ d kg^{-1} for beef, ≈0.3 d kg^{-1} for pork, ≈0.6 d kg^{-1} for lamb, and ≈0.01 d kg^{-1} for milk. Very little or no decrease in the activity of ^{137}Cs was found in many plants, which means that in these plants the ecological half-life is given mainly by the physical half-life.

For ^{90}Sr the resorption factor in cows is f_R = 0.05–0.4 (in young animals f_R = 0.2–1.0). About 90% of the resorbed ^{90}Sr is deposited in the bones. The biological half-life in domestic animals is of the order of 100–500 days for the skeleton and 20–100 days for the rest of the body. In humans the biological half-life of ^{90}Sr is in the range 200–600 days. Aggregated TFs (soil–meat) vary between 0.01 and 0.06 m^2 kg^{-1}, and typical transfer coefficients (food–product) are $T \approx 0.0003$ d kg^{-1} for beef, ≈0.002 d kg^{-1} for pork, and ≈0.002 d kg^{-1} for milk.

In ecosystems, Pu is present mainly in the form of sparingly soluble Pu(IV) dioxide or hydroxide and is therefore rather immobile. It stays mainly in the upper layers of the soil and its uptake by roots is very small (soil–plant TFs <0.001 d kg^{-1}). However, plants may be contaminated with Pu by deposition from the air. Resorption factors in the gastrointestinal tract of animals are also very small ($f_R < 10^{-4}$). On the other hand, up to 5% of inhaled Pu is found in blood and up to 15% in the lymph glands. About 80% of resorbed Pu is deposited in bones, the rest in the kidneys and liver. Biological half-lives reported in the literature vary between 500 and 1000 days for the lymph glands and between 1 and 100 years for the skeleton.

22.6 Speciation Techniques with Relevance for Nuclear Safeguards, Verification, and Applications

Until 2020, the spent nuclear fuel discharged from nuclear power plants worldwide totals 445 000 tons. One ton of uranium spent fuel has a radiotoxicity of 10^8 Sv, which exceeds the toxicity of the same amount of natural uranium by a factor of 10^5. The spent fuel can either be reprocessed in order to be able to reuse the U and Pu, or

be disposed of directly as high level radioactive waste (HLRW) in deep underground repositories. While the technical questions associated with building and operating such repositories are well in hand, the long-term safety of a repository depends not just on these technical systems. It depends moreover on the long-term behavior of long-lived radionuclides from the nuclear fuel cycle under geochemical conditions, and these need to be studied and understood on a molecular level in order to provide the tools for a long-term safety assessment. Fission products account for the largest fraction of radiotoxicity for the first few hundred years. Thereafter, the minor actinides and Pu pose the biggest risk for environmental contamination as was illustrated in Figure 15.23a where the radiotoxicity of 1 ton of spent fuel of a pressurized light-water reactor (enrichment 4.2% ^{235}U) after a burn-up of 50 GWd was shown as a function of time. This makes it immediately clear that a profound knowledge of the chemistry of the minor actinides and of Pu under geochemical conditions is indispensable for a critical risk assessment. While early work on the solution chemistry of Pu was driven by the requirement to separate and purify Pu in highly acidic solutions, it was of less relevance to understand other basic mechanisms of plutonium chemistry, for example, the polymerization of Pu(IV). Even though polymerization was recognized, emphasis lay on avoiding it because of its interference with the process chemistry. In contrast, the assessments of the safety of nuclear waste repositories where the low acidity of groundwaters favors the formation of colloids and thus provides a doorway for migration of Pu away from the repository, today requires a profound understanding of the complex thermodynamics and redox chemistry of Pu in aqueous media. The concentration of Pu in solution is controlled by the solubility and precipitation of Pu(IV) hydroxide phases which, like the Pu colloids, span a wide range of structural features, crystallinities, and stabilities. Freshly formed colloids dissolve easily upon dilution at constant pH or acidification. Aging leads to irreversible elimination of water, that is, the transformation of hydroxide bonds to oxygen bonds. These aged colloids are less soluble and are termed insoluble Pu(IV) colloids. Studies on Pu compounds including colloids by Conradson et al. (2004, 2005) have revealed an astonishing variety of structures and provided evidence for deprotonation of aging species and a contribution of higher oxidation states in aged "Pu(IV) solid phases." The presence of Pu(V) in these solid phases helps to understand why Pu(IV) colloids are in equilibrium with Pu(V) and why the disproportionation of Pu(V) cannot be understood without the involvement of Pu(IV) colloids as intermediate complexes. Recent results underline that Pu(IV) colloids play an important role in the Pu redox chemistry and link Pu(III) and Pu(IV) with the pentavalent and hexavalent species PuO_2^+ and $PuO_2{}^{2+}$, as is shown in Figure 22.5. Here, the black arrows mark equilibria where the equilibrium constants are known. Blue arrows indicate where equilibrium constants are unknown. There is by now increasing evidence for the fact that a solid phase of $Pu(OH)_3$ (s) does not exist. Red arrows mark those equilibrium constants that were derived in the work by Neck et al. (2007). Pu(IV), Pu(VI), Pu(III), and Pu(V) have effective ionic charges of +4, +3.3, +3, and +2.3, respectively, resulting in their tendency toward hydrolysis to decrease in the order $Pu^{4+} > PuO_2{}^{2+} > Pu^{3+} > PuO^+$. Formation constants for $Pu(OH)_y^{4-y}$ are $\log \beta^o_{1,1} = 0.6 \pm 0.5$, $\log \beta^o_{1,2} = 0.6 \pm 0.3$,

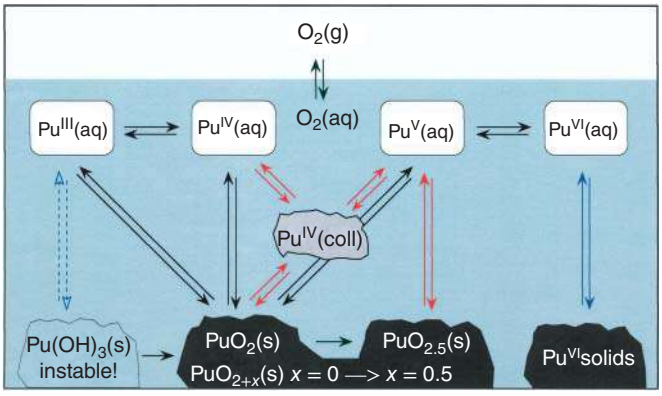

Figure 22.5 Solid–liquid and redox equilibria of Pu in the presence of oxygen. Polymeric and colloidal Pu species are in equilibrium with $Pu(IV)_{aq}$, PuO_2^+, and, if present, with precipitates such as PuO_{2+x} (s, hyd). There is evidence that $Pu(OH)_3$ (s) does not exist. The double arrows in black, blue, and red are explained in the text. Source: Neck et al. (2007), figure 6 (p. 203)/De Gruyter.

$\log \beta^{o}_{1,3} = -2.3 \pm 0.4$, and $\log \beta^{o}_{1,4} = -8.5 \pm 0.5$. The high tendency for hydrolysis is associated with the small ionic radius of Pu^{4+} due to the actinide contraction: $r(Th^{4+}) = 1.0\,Å$, $r(U^{4+}) = 0.93\,Å$, $r(Pu^{4+}) = 0.90\,Å$. The first hydrolysis species, $Pu(OH)^{3+}$, accounts for roughly half of the $Pu(IV)_{aq}$ in 0.5 M HCl. Further hydrolysis with increasing pH leads to the formation of mononuclear $Pu(OH)_y^{4-y}$ and, at $[Pu(IV)] > 10^{-6}$ M, polynuclear $Pu_x(OH)_y^{4x-y}$ complexes are formed and grow into nanometer-sized colloids.

Understanding the aqueous chemistry of the minor actinides is a necessary prerequisite, but this information alone does not suffice to conduct a safety assessment of a repository. Complex formation of the radionuclides with various inorganic and organic ligands needs to be considered in addition, as well as interactions with the corroding container material, backfill material, and the host rock. Moreover, the sorption to aquatic colloids (1 nm to 1 μm) that are suspended in water needs to be characterized. Of highest relevance for transport phenomena are colloids smaller than 50 nm due to their high mobility and large surface-to-volume ratio. These are hard to characterize by standard methods such as transmission electron microscopy (TEM) or scanning electron microscopy (SEM), which require sample preparation and are thus destructive. Methods based on light scattering are nondestructive. They are sensitive for detecting particles >100 nm, but due to the λ^{-6} decrease in the amplitude of Rayleigh scattering, they are limited to particles larger than one-quarter of the wavelengths of visible light. The very sensitive laser-induced breakdown detection (LIBD) instrument was developed in the 1980s by T. Kitamori and colleagues and subsequently improved continuously by Scherbaum et al. (1996), Bundschuh et al. (2001a,b,c), and Walther et al. (2002, 2006). It is schematically depicted in Figure 22.6. The light of a pulsed laser is focused into the sample cell where it induces a so-called breakdown and ignites a plasma. Within nanoseconds, the plasma is heated to temperatures of more than 20 000 K and expands rapidly

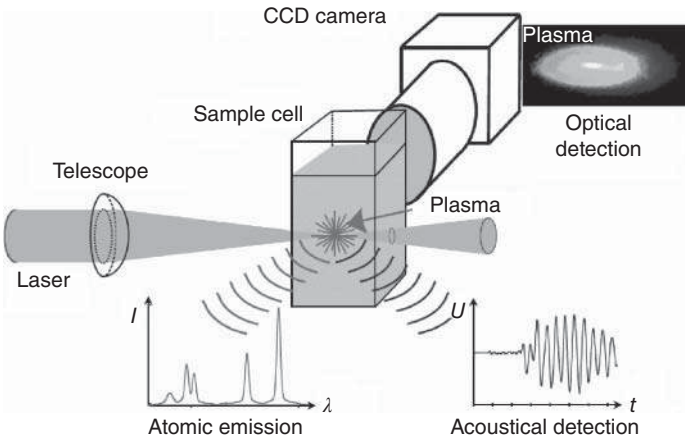

Figure 22.6 Schematic illustration of LIBD detection. The plasma created by a pulsed laser causes an acoustic wave which is detected by a piezoelectric receiver. Alternatively, the emitted light can be detected by a spectrometer or spatially resolved by a microscope lens and a CCD camera. Source: Modified from Walther (2007).

causing a shock wave. This can be detected by an acoustic receiver (piezodetector or microphone). The second detection method makes use of plasma cooling by emission of radiation. For the first several hundred nanoseconds, the plasma emits blackbody radiation. Thereafter, the lower temperature allows the recombination of ions and electrons which is accompanied by the emission of characteristic atomic line spectra. The emitted light can be imaged on a CCD camera, and from the spatial distribution of plasma events, the mean size of the colloids can be deduced. Plasma ignition is possible in pure liquids as well, but in LIBD, plasma formation occurs in the solid colloids at several orders of magnitude lower power density than in liquids. LIBD allows the detection of very dilute (10^4–10^5 particles ml^{-1}) suspensions of inorganic colloids down to ≈5 nm. Considerable effort was put into understanding the fundamentals, modeling the LIBD data, and extending the capabilities of LIBD to measure even particle-size distributions over orders of magnitude.

Obviously, complex formation, polymerization, solubility, and formation of precipitates depend strongly on the oxidations state of Pu. Therefore, monitoring and controlling its redox state is indispensable. For rather concentrated solutions ($[Pu] > 10^{-5}$ M), visible absorption spectroscopy (UV–vis) is a convenient speciation method. Due to electronic intraband transitions in the 5f shell, each oxidation state exhibits several unique absorption bands. In the following chapter, among others, a paper on the effect of hydrolysis on spectral absorption of $Pu(IV)_{aq}$ will be discussed, paying attention also to the influence of polymerization and colloid formation. A sensitive decrease in the detection limit can be achieved by extending the optical absorption path length by use of liquid capillary waveguides of 1 m length (Neck et al. 2007; Scherbaum et al. 1996). Of similar sensitivity is laser-induced photoacoustic spectroscopy (LIPAS) (Neck and Kim 2001). Light from a tunable laser is absorbed by the solvated ions and locally heats the sample which expands

and causes an acoustic wave which is detected by a piezoreceiver. In the following chapter, we describe how LIPAS was used to observe the dissolution of Pu(IV) colloids at low concentrations. Fairly recently, detection limits for redox speciation below $[Pu] = 10^{-7}$ M were achieved by Kuczewski et al. (2003) combining capillary electrophoresis with inductively-coupled plasma mass spectrometry (CE-ICP-MS), and even further down to $[Pu] = 10^{-10}$ M for hyphenated CE-RIMS (Bürger et al. 2007). In the past, speciation at such ultratrace concentrations was reserved for solvent extraction, ion exchange, or coprecipitation methods, which, however, involve the risk of shifting chemical and redox equilibria.

A nanoelectrospray mass spectrometry technique (ESI-MS) for the investigation of polynuclear hydroxide complexes has been developed by Walther et al. (2007). It is equipped with a spray capillary made of borosilicate with an inner tip diameter of 1 µm and a thick outer metal coating. It can be operated in positive or negative ion mode. After passing differential pumping stages involving a skimmer and apertures, the ions are injected orthogonally into a time-of-flight mass spectrometer of up to $m/\Delta m \leq 26\,000$. The extraction voltage is 42 V. Nitrogen is used as a gas curtain at a flow rate of 0.1 l min^{-1}. The sample flow rate is 15 nl min^{-1}, and the ESI current is between 50 and 100 nA. The technique has been used for the investigation of the homologs Th(IV) and Zr(IV) with emphasis on the formation of their oxihydroxide colloids and the stability of the latter in equilibrium with ionic species.

The application of advanced X-ray techniques at synchrotron radiation facilities has entered the speciation methods for long-lived radionuclides over a number of years. At energies close to the absorption edge (L_I, L_{II}, or L_{III} for a heavy element), transitions may occur into unfilled bound, nearly bound resonance states, or unbound states close to the binding energy. These processes yield the absorption near edge structure (XANES) from which the oxidation state and coordination (e.g. octahedral or hexahedral) of the chosen central atom can be deduced. At energies ≥30 eV above the absorption edge, transitions always lead into the continuum. In this energy region, the extended X-ray absorption fine structure (EXAFS) is observed, which is modulated by the distances of neighboring atoms, coordination number, and atomic number of the neighbors. The core hole is filled by an electron from a higher-lying level, accompanied by the emission of a fluorescent photon with the energy difference of the two levels, which is detected by a semiconductor detector. As the energy of the incident X-ray is varied, the kinetic energy of the photoelectron, its momentum, and its wavelength change, whereby the absorption probability is altered. The probability of absorption oscillates due to constructive and destructive interference of initial and scattered waves. The XANES analysis is a qualitative approach lacking a suitable quantitative description, and it is used as a fingerprint that is compared to the spectra of known phases. In EXAFS analyses, interpretation in terms of the wave number k (Å^{-1}) of these oscillations, denominated $\chi(k)$, is done using the classical EXAFS equation. Different frequencies present in the signal can be assigned to separate neighboring coordination spheres. $\chi(k)$ is proportional to the amplitude of the scattered photoelectron at the central absorbing atom. In the next step, a Fourier transform of the unsmoothed data within a suitable k window is calculated and yields transform magnitudes as a

function of *R*-space. Both XANES and EXAFS yield valuable structural information of solid or liquid samples.

In a few exceptional cases, nature provides particularly elegant tools for speciation: UO_2^{2+}, Cm^{3+}, and, to some extent, Am^{3+} exhibit fluorescence properties similar to those of the lanthanide ions Ce^{3+}, Sm^{3+}, Eu^{3+}, Gd^{3+}, Tb^{3+}, Dx^{3+}, and Yb^{3+}. For the three actinide ions, a rather large energy gap between the ground state and first excited state within the 5f electronic configuration causes narrow and, because of parity prohibition of the transition, long-lived fluorescence bands (Cm^{3+}: $\tau = 4.8$ ms; Am^{3+}: $\tau = 1.9\,\mu s$). The method is very sensitive and mere detection is possible for $>10^{-10}$ M. The electric field produced by ligand molecules shifts the energy levels of Cm^{3+} and affects the emission wavelength. Thus, by observing the fluorescence, one obtains direct information on the chemical neighborhood of the central metal ion. To these ligands, including the hydration sphere of water molecules, energy can be transferred from the excited state. This decreases the lifetime. This is used to advantage in time-resolved laser-induced fluorescence spectroscopy (TRLFS). Excitation by a pulsed laser is followed by detection of the fluorescence emission, and from the lifetime one concludes on the number of quenchers (Kimura equation, Kimura and Choppin 1994). In the example to be introduced below, the complexation and hydrolysis of Pa(IV) have been investigated by TRLFS. In the chapter to follow, a few representative examples for applications of the speciation methods briefly introduced above will be presented. They are from C. Walther (2007).

22.6.1 Redox Reactions, Hydrolysis, and Colloid Formation of Pu(IV)

Due to the very similar redox potentials of the couples Pu(III)/Pu(IV) ($E^0 = -1.047$ V), Pu(IV)/Pu(V) ($E^0 = -1.031$ V), and Pu(V)/Pu(VI) ($E^0 = -0.936$ V), an equilibrium of two or more oxidation states in solutions which contained only one oxidation state in the beginning is possible. Here, Pu is both oxidizing and reducing agent at the same time, which is called disproportionation. The formation of Pu(III), Pu(V), and Pu(VI) from Pu(IV) in solutions exposed to air is commonly ascribed to the disproportionation of Pu(IV) into Pu(III) and Pu(V)

$$2\,Pu^{4+} + 2\,H_2O \Leftrightarrow Pu^{3+} + PuO_2^+ + 4H^+ \tag{22.21}$$

followed by the disproportionation of Pu(V) into Pu(IV) and Pu(VI)

$$2\,PuO_2^+ + 4\,H^+ \Leftrightarrow Pu^{4+} + PuO_2^{2+} + 2\,H_2O \tag{22.22}$$

Combining reactions (22.21) and (22.22) leads to the equation

$$3\,Pu^{4+} + 2\,H_2O \Leftrightarrow 2\,Pu^{3+} + PuO_2^{2+} + 4\,H^+ \tag{22.23}$$

The equilibrium constant at zero ionic strength of reaction (22.23) at an acidity close to $[H^+] = 1$ M is reported to range from $\log K^{\circ}_{IV} = 2.38$ to 2.43. As the measured oxidation state distributions led to doubts on this reaction path, Cho et al. (2005) revisited this topic and studied 10^{-5} to $5 \cdot 10^{-4}$ M Pu(IV) solutions at $pH_c = 0.3$–2.1 in 0.5 M HCl/NaCl as a function of time. A Pu(IV) stock solution was prepared electrochemically. Most of the various solutions obtained by dilution were kept under air

in closed vials. Parts of the experiments were also performed in an Ar glove box. The concentrations of Pu(IV)aq, Pu^{3+}, PuO_2^+, and $PuO_2{}^{2+}$ were determined by UV–vis absorption spectroscopy using a capillary cell 1 m long. The fraction of colloidal Pu(IV) was calculated from the difference $[Pu]_{tot} - ([Pu(IV)aq] + [Pu^{3+}] + [PuO_2^+] + [PuO_2{}^{2+}])$.

According to reactions (22.21) and (22.23), independent of whether an equilibrium is reached, the balance for Pu(III), Pu(V), and Pu(VI) resulting from the disproportionation of Pu(IV) must be

$$[Pu(III)] = [Pu(V)] + 2[Pu(VI)] \tag{22.24}$$

However, none of the solutions fulfilled this balance, and the formation of Pu(III) was always found to be close to the simultaneous decrease of Pu(IV)aq, as is shown for four examples in Figure 22.7. Thus, the experiments suggested that

$$d[Pu(III)] \Big/ dt = -d[Pu(IV)aq] \Big/ dt \tag{22.25}$$

that is, $[Pu(IV)aq] + [Pu(III)] = \text{const}$, and consequently

$$d([Pu(V)] + [Pu(VI)]) \Big/ dt = -d[Pu(IV)coll] \Big/ dt\sqrt{b^2 - 4ac} \tag{22.26}$$

This demonstrates that the "disproportionation of Pu(IV)" in reality is a two-step process in which the presence of Pu(IV) colloids is an integral part of the Pu redox equilibrium system. The first step is the formation of PuO_2^+ either by the redox equilibrium with the Pu(IV) colloids

$$PuO_2(coll, hyd) \Leftrightarrow PuO_2^+ + e^- \tag{22.27}$$

or by the oxidation of the colloidal Pu(IV) species by O_2 followed by the dissolution of the oxidized Pu(V)

$$\begin{aligned} &PuO_2(coll, hyd) + (x/2)O_2 + xH_2O \\ &\quad \rightarrow PuO_{2+x}(coll, hyd) + xH_2O \\ &\quad \rightarrow 2x(PuO_2^+ + OH^-) + (1 - 2x)PuO_2(coll, hyd) \end{aligned} \tag{22.28}$$

The second step is the simultaneous equilibration of the redox couples Pu(V)/Pu(VI) and Pu(IV)/Pu(III) which are related by pe (and by pH because of the Pu(IV) hydrolysis equilibria):

$$PuO_2^+ \Leftrightarrow PuO_2{}^{2+}e^- \tag{22.29}$$

$$Pu(OH)_n^{4-n} + nH^+ + e^- \Leftrightarrow Pu^{3+} + nH_2O \tag{22.30}$$

This mechanism explains that the sum $[Pu(III)] + [Pu(IV)aq]$ always remains constant. It also explains the different behavior of a colloid-free solution at pH = 0.3 (Figure 22.7a) and at pH = 1.0 (Figure 22.7b) where colloidal Pu(IV) is formed. In the experiment at $[Pu(IV)_{tot}] = 1.0 \cdot 10^{-5}$ M and $pH_c = 2.1$ (Figure 22.7c), Pu(V) is evidently formed faster than Pu(III) and not simultaneously as required by the disproportionation reaction (22.21).

The presence of O_2 is not necessary for reaction (22.27), but it is for reaction (22.28). That analogous experiments under air and in an inert-gas box gave similar

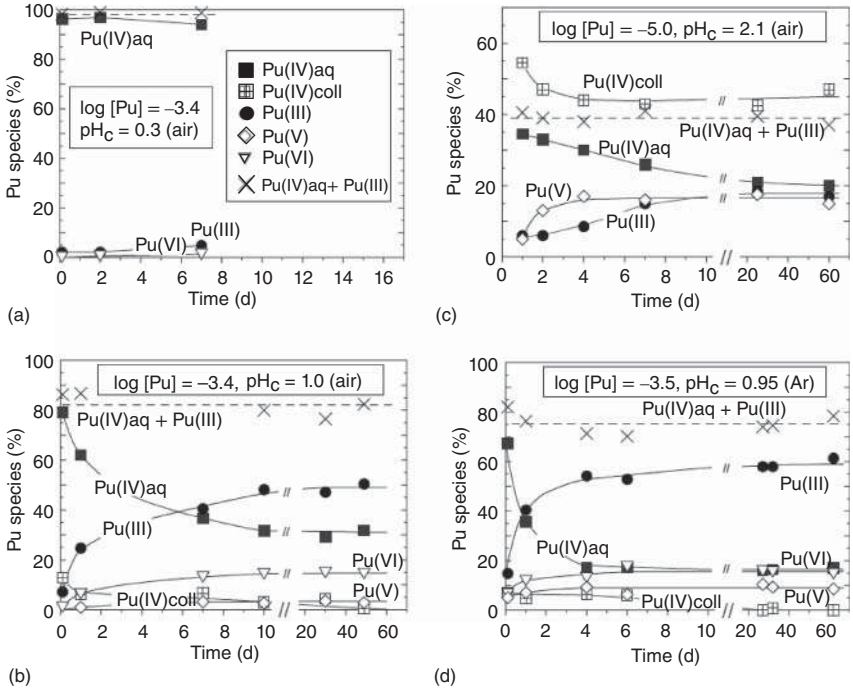

Figure 22.7 Oxidation state distributions of initially Pu(IV) solutions as a function of time: (a–c) solutions exposed to air; (d) solution kept in an Ar glove box containing about 10 ppm of O_2. Source: Modified from Cho et al. (2005).

results (Figure 22.7b,d) favors reaction (22.27). However, the Ar box used had an O_2 contamination of about 10 ppm, possibly sufficient to produce Pu(V) from colloidal Pu(IV), so that a final conclusion is not yet possible.

The oxidation-state distributions and pe values ($pe = -\log a_{e^-}$ analogous to $pH = -\log a_{H^+}$; $Eh = -(RT/F)a_{e^-} = (RT\ \ln(10)/F)pe$; $pe = 16.9Eh$ [at 25 °C]) measured after equilibration times of >20 days were consistent with the redox equilibria (22.27), (22.29), and (22.30). The "disproportionation" reactions (22.21)–(22.23) describe correctly the equilibrium-state thermodynamics, but not the underlying reaction mechanism.

Next, we want to introduce a novel approach to determine the solubility of Pu(IV) by Walther et al. (2003). Most conventional solubility measurements on Pu were performed from undersaturation by contacting a Pu solid with the aqueous phase. The amount of Pu in solution after a given contact time is measured by spectrophotometry, liquid scintillation counting, solvent extraction, or a combination of several techniques. However, measurements from undersaturation can only be meaningful if the solid phase PuO_2 (s, hyd) is free of a more soluble phase such as Pu(III) or Pu(VI) that may lead to an apparent increase in solubility. The same is true for the homogeneity of the solid. Small particles of the same solid have a higher solubility than larger ones, hence the presence of minute amounts of nanometer-sized particles can increase the apparent solubility by orders of magnitude 1 up to

solubilities of amorphous $Pu(OH)_4$. Radiolytic effects may go in the same direction. Therefore, Walther et al. (2003), instead of starting from undersaturation, started from oversaturation. An acidic solution with a well-defined concentration of Pu(IV) was titrated to higher pH. Since the solubility decreases as the pH increases, the solution becomes oversaturated and the amount of Pu(IV) exceeding the solubility begins to form colloids. These have been detected by LIBD. A ^{242}Pu stock solution in 0.5 M $HClO_4$ was prepared electrolytically and fumed with HCl several times under control by UV–vis spectrometry. From this stock solution, several batch samples of constant ionic strength (HCl/NaCl) but different Pu(IV) concentration and different pH were prepared by dilution with 0.5 M HCl and subsequent pH increase by slow (10 µl min^{-1}) titration with 0.5 M NaCl. Pu concentration and acidity were lowered simultaneously, indicated by the light arrow in Figure 22.8. The pH increase led to the formation of Pu(IV) colloids at a critical pH observed by a sharp increase in the LIBD signal, indicating that the solubility limit has been exceeded. The critical pH was determined for four different Pu concentrations between $[Pu]_{tot} = 10^{-3}$ and $2 \cdot 10^{-6}$ M visualized by the crosses in Figure 22.8. For the higher concentrations, the fraction of Pu(IV) was determined by UV–vis or LIPAS. The essential result of this work is that the solubility curve has a slope $d[Pu(IV)]/dpH = -2$ which requires the dominant species in solution to be twofold charged. This is $Pu(OH)_2^{2+}$, which forms amorphous $Pu(OH)_4$ precipitate leading to Pu(IV) oxyhydroxo colloids via

$$Pu(OH)_2^{2+} + 2H_2O \Leftrightarrow Pu(OH)_{4(coll)} + 2H^+ \qquad (22.31)$$

The solubility product, extrapolated to zero ionic strength using published hydrolysis constants and SIT coefficients (specific ion interaction theory by Grenthe et al. 1997), agrees well with the literature value of

$$K_{sp}^0 = (\log[Pu^{4+}](\gamma_{Pu})) + 4(\log[OH^-](\gamma_{OH})) = -58.7 \pm 0.9$$

In another UV–vis study by Walther et al. (2007), it was shown that hydrolysis of Pu(IV) has no effect on the absorption spectra of mononuclear Pu(IV) species in

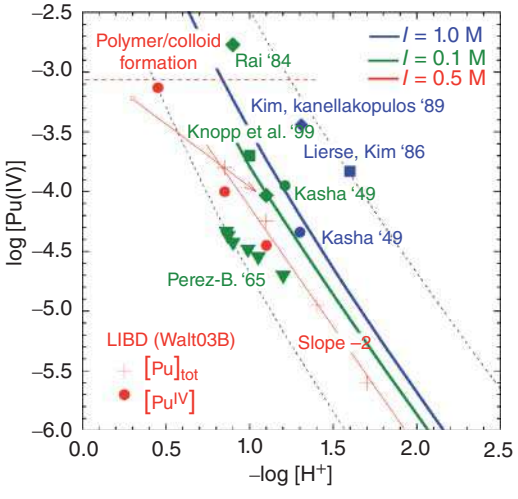

Figure 22.8 Solubility of amorphous Pu(IV) hydroxide $Pu(OH)_4$(am). The data of the LIBD study of Walther et al. (2003) are given by the red crosses. For higher concentrations (red points), the fraction of Pu(IV) was determined by UV–vis or LIPAS. The data are compared to literature values and calculations for $I = 0.1$ M and $I = 1.0$ M using $\log K_{sp}^0 = -58.7$. (Neck and Kim 2001; the formation constants of mononuclear hydrolysis complexes are from Metivier and Guillaumont 1972.) Source: Based on Walther et al. (2003).

solution. In the work by Yun et al. (2007), hydrolysis constants for the mononuclear Pu(IV)–hydroxide complexes were determined by UV–vis measurement of the oxidation-state distribution and the redox potential Eh. The values obtained and extrapolated to zero ionic strength are $\log \beta^0_{1,1} = 14.0 \pm 0.2$, $\log \beta^0_{1,2} = 26.8 \pm 0.6$, and $\log \beta^0_{1,3} = 38.9 \pm 0.9$.

With increasing evidence for the relevance of polynuclear Pu(IV) complexes and small colloids for the Pu redox chemistry, the need for more detailed investigations of their formation mechanisms and structure became evident. In the work by Rothe et al. (2004), samples within $0.2 < [\mathrm{Pu}]_{\mathrm{tot}} < 1.2$ mM were prepared at acidities (HCl) of $0 < -\log [\mathrm{H}^+] < 1.75$ by dilution of a Pu(IV) stock solution with the addition of appropriate amounts of milli-*Q* water and solutions of HCl and NaCl. After equilibration of two to four days, the samples were measured by EXAFS and a second set of samples at $0.3 < -\log [\mathrm{H}^+] < 0.75$ was probed for the presence of colloids by LIBD. The LIBD data confirm the slope of −2 of the solubility plot, see above, and, furthermore, indicate an increase in the weighted mean colloid size with increasing degree of oversaturation from 12 nm at $-\log [\mathrm{H}^+] = 0.45$–25 nm at $-\log [\mathrm{H}^+] = 0.73$.

Evaluation of the EXAFS data yields direct information on the structure of Pu solution species. In order to obtain data of the Pu(IV) mononuclear species, samples at high acidity were measured and the structure of colloids was inferred from highly oversaturated solutions, where colloids account for the largest fraction of Pu(IV). In the former case, no Pu–Pu backscattering was detected, which complies with the expectation that only mononuclear species are present at high acidity. Eight to nine water molecules coordinate the Pu(IV) at a 2.38 ± 0.02 Å Pu—O bond distance. At higher pH, different Pu—O bond lengths indicate the formation of Pu(–O, OH, OH_2) coordination species. The shorter Pu–O distance of 2.22 Å is assigned to hydroxyl groups and a coordination number $N_{\mathrm{OH}} > 2$ is found for all colloidal samples. With decreasing acidity, that is, formation of larger colloids, the samples show a trend toward increasing Pu–Pu coordination number ($N_{\mathrm{Pu}} = 4.9$ at $-\log [\mathrm{H}^+] = 1.75$). The Pu–Pu distance is rather constant at 3.86–3.89 Å and is hardly affected by the O-peak splitting, supporting the hypothesis of a rather rigid Pu–O–Pu backbone. This rules out that the Pu(IV) colloids are composed of purely amorphous Pu(IV) hydroxide in line with the result by Rothe et al. (2004) that an amorphous Pu(IV) hydroxide precipitate has $N_{\mathrm{Pu}} = 2.4$. It suggests that polymerization proceeds via agglomeration of ordered polymers from the mononuclear dihydroxo complex $\mathrm{Pu(OH)_2(H_2O)_6^{2+}}$. Based on a model by Fujiwara et al., Rothe et al. proposed that polymerization proceeds via the formation of edge-sharing dimers and trimers followed by the release of protons for charge compensation, see Figure 22.9. While, according to the model by Fujiwara et al., polymerization should culminate in the formation of crystalline PuO_2 which is incompatible with the solubility measurements, the Rothe et al. model suggests the formation of a hydrated Pu oxide hydroxide phase with the general stoichiometry $\mathrm{Pu}_n\mathrm{O}_p(\mathrm{OH})_{4n-2p}(\mathrm{H_2O})_z$.

A concluding comment is in order concerning the formation of PuO_{2+x}. All samples containing colloids showed a small feature in the Fourier Transform spectra at $R - \Delta = 1.9$ Å. Since a Pu–O distance of less than 2 Å appears to be unphysical at first

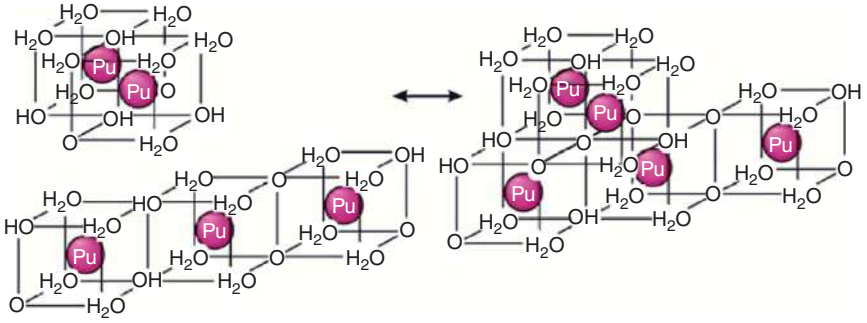

Figure 22.9 Model for polymerization of Pu(IV) hydroxides from Rothe et al. (2004). Dimers and trimers form via edge sharing from $Pu(OH)_2^{2+}$. These subunits agglomerate and eventually form nanometer-sized colloids. During this process, the cubic subunits are preserved and form a distorted fluorite-like Pu lattice. With increasing size of the colloids, the disorder decreases, but even at the highest pH investigated (pH 1.75) a high number of defect sites leads to a mean Pu–Pu coordination number of only $N_{Pu} = 4.9$. Source: Modified from Rothe et al. (2004).

sight, the authors attributed this peak to multielectron excitations. However, two detailed XANES and EXAFS studies by Conradson et al. on various PuO_{2+x} solids and aged colloids revealed that, in a $PuO_{2.26}$ solid, the small shoulder indicating the interatomic distance at 1.9 Å evolves into the dominant spectral feature. Thus, the small shoulder in the Rothe FT spectra might indicate a small contribution of Pu(V) in the colloids. Hence, it is desirable to investigate the polymerization process further using direct speciation of the polynuclear complexes as is now possible, for example, by using the ESI-TOF MS.

22.6.2 Investigation of the Homologs Th(IV) and Zr(IV)

Speciation of radionuclides is often preceded by experiments with their chemical homologs with the aim of validating new techniques, reducing radiation risks, and saving rare and expensive material. In the case of Pu(IV), suitable homologs are the stable element zirconium and the extremely long-lived isotope ^{232}Th ($t_{1/2} = 1.4 \cdot 10^{10}$ years). Both form exclusively tetravalent ions in solution and thus offer the attractive possibility of studying complexation and solubility without interference from the complex redox chemistry that we have to deal with in the case of plutonium. The present chapter gives some examples of such studies that address the characterization of Th(IV) and Zr(IV) colloids.

The paper by Walther et al. (2003) on single-particle analytical techniques for the characterization of aquatic colloids contains discussions of various techniques used for colloid characterization and comparison of the respective advantages and limitations. The investigation of Th(IV) colloids is treated as a case study. Earlier investigations on the solubility of amorphous Th hydroxide and crystalline Th dioxide suggested that the structure of the colloids strongly depends on the pH and concentrations of oversaturated solution. Upon pH increase at $[Th]_{tot} \approx 0.1$–10 mM, colloid formation was observed between pH 1 and 2 (A in Figure 22.10). The critical pH

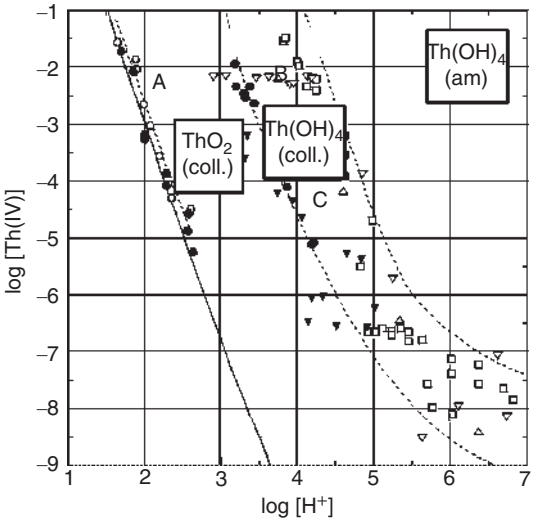

Figure 22.10 Solubility diagram of Th(IV). When the solubility is exceeded, colloids are formed: thorium dioxide at pH 1.5–2.5 (lower curve) and thorium hydroxide at pH > 3 (between two dashed curves). Three samples A, B, and C have been further investigated in Walther (2003). Source: Walther (2003), figure 1 (p. 83)/Elsevier.

values of colloid formation coincided with the solubility curve of crystalline ThO_2, thus the colloids were considered to have microcrystalline composition. If the pH is further increased, a second domain of colloid formation is reached around pH 4–5 close to the solubility curve of amorphous $Th(OH)_4$ (B, C in Figure 22.10). Colloids from both domains were investigated by SEM and TEM, transmission electron diffraction (TED), atomic force microscopy (AFM), and LIBD.

For the colloids of sample A, a mean size of 10 nm was found by AFM, SEM, and LIBD ($[Th]_{tot} \approx 2.5 \cdot 10^{-3}$ M, pH 1.9, twofold oversaturated [vertical distance to the solubility curve] with respect to ThO_2); however, the LIBD s-curve, Figure 22.11, showed that the size distribution extended to somewhat larger colloids. This was confirmed by the observation of colloids up to 50 nm size by TEM, which exhibited a core–layer structure. TED on single particles showed diffraction patterns of a fluorite structure with spacing of 3.1 Å in the (111) plane, slightly smaller than the spacing of crystalline ThO_2 which is 3.23 Å. It was concluded that the particles consisted of a crystalline ThO_2 core layered by amorphous Th hydroxide. Sample B ($[Th]_{tot} = 3 \cdot 10^{-3}$ M, pH 3.8, >50-fold oversaturated with respect to $Th(OH)_4$) contained larger colloids of 50–100 nm. TED showed that these particles were amorphous. TEM data indicated smaller subunits of about 2 nm. The subunits must have been amorphous themselves, or, if they were crystalline, lattice distortion caused destructive interference on the diffraction patterns.

In sample A, colloid formation represents the *upper limit* of the solubility curve of crystalline ThO_2. Conversely, in samples B, C, the colloids detected by LIBD represent the *lower limit* of the solubility curve of amorphous $Th(OH)_4$. This could reflect the particle size effect: large particles have a lower solubility than small particles. If applied to Th, both solubility curves could perhaps be explained by assuming the same material (ThO_2) but bigger colloids for ThO_2(mycrocryst.) and 2 nm for ThO_2(am,hyd) = $Th(OH)_4$(am). In the case of a precipitate, different solubilities might result from the inclusion of particulates. A perfect crystal yields the known

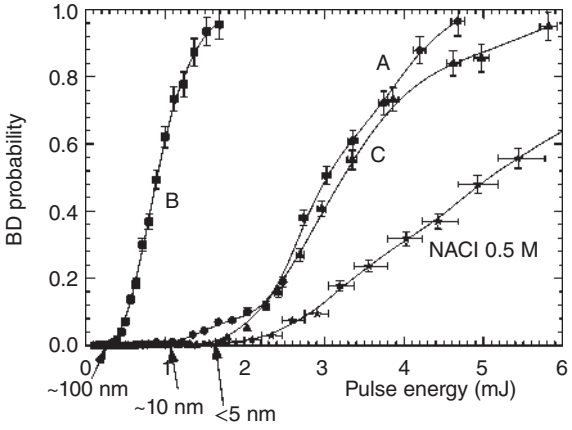

Figure 22.11 All three samples are measured by LIBD without preparation or prefractionation and the breakdown (BD) probability as a function of the laser pulse energy, so-called s-curves, are plotted. The energy threshold allows the weighted mean particle size (arrows below *x* axis) to be determined. While B and C show a narrow size distribution, the saddle of A at low BD probability indicates a higher polydispersivity. Source: Walther (2003), figure 7 (p. 87)/Elsevier.

solubility product of ThO_2 (K_{sp}^0(cryst.) $= -54.2 \pm 1.1$). With inclusions of 20 nm colloids, the solubility product would increase to K_{sp}^0(mycrocryst.) $= 53 \pm 0.5$. The amorphous, hydrated Th oxide would then be a solid including 2 nm small particles (K_{sp}^0(am, hyd) $= -47.8 \pm 0.6$), and truly amorphous $Th(OH)_4$ would be the most soluble phase (K_{sp}^0(am) $= -46.7 \pm 0.9$).

In a second paper by Bitea et al. (2003), it was investigated whether the Th colloids are in thermodynamic equilibrium with the ionic Th(IV) species. This study started from a slightly oversaturated suspension, A in Figure 22.12, containing $[Th]_{coll} \approx 1 \cdot 10^{-3}$ M colloids. One aliquot was diluted by adding an HCl/NaCl solution such that acidity and ionic strength remained constant (B in Figure 22.12). The colloids dissolved completely within about 30 days which led to a pH increase due to

$$Th(OH)_{4(coll)} \rightarrow ThOH^{3+} + 3\,OH^- \tag{22.32}$$

assuming the first hydrolysis species $ThOH^{3+}$ to be the dominant ion in solution. Subsequently, the sample was diluted by the addition of pH neutral NaCl solution (C in Figure 22.12) until the solubility was exceeded and $Th(OH)_{4(coll)}$ colloids formed (D in Figure 22.12). Complementary to reaction (22.32), the formation was accompanied by H^+ release and acidification of the sample

$$ThOH^{3+} + 3H_2O \rightarrow Th(OH)_{4(coll)} + 3H^+ \tag{22.33}$$

The second aliquot was diluted along a different path in the solubility plot (A, E, F, G in Figure 22.12) which never left the region of oversaturation, that is, the Th(IV) colloids never completely dissolved. The total dilution of both aliquots was chosen in such a way as to give equal $[Th]_{tot}$ concentrations in the final solutions. After

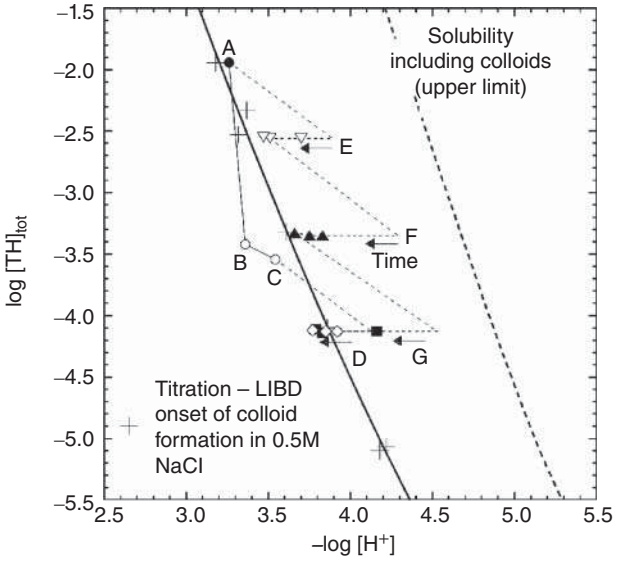

Figure 22.12 Thorium and H^+ concentrations of solutions B and C and colloidal suspensions D, E, F, and G prepared by dilution of suspension A at constant pH and with 0.5 M NaCl. In suspensions D–G, the pH value is shifted with time to the solubility curve determined by titration combined with LIBD. Source: Bitea et al. (2003), figure 4 (p. 67)/Elsevier.

equilibration for more than 140 days, both samples adjusted to equal acidity and very similar total colloid content, supporting the conclusion of colloids being in thermodynamic equilibrium with the ionic Th(IV) species.

Another finding in Bitea et al. (2003) concerns the size of the Th(IV) colloids. By that time, the group was not yet able to extract the particle-size distribution from the LIBD data. Nevertheless, the thresholds of the s-curves are a measure of the weighted mean size of the colloids. This breakdown threshold is plotted as a function of the degree of oversaturation (defined by the ratio of the amount of Th(IV) in solution over the equilibrium concentration of ionic Th(IV) species $[Th]_{tot}/[Th]_{eq}$) in Figure 22.13. There is a clear correlation between the mean colloid size and the degree of oversaturation. With increasing oversaturation, the threshold decreases, which corresponds to increasing mean colloid size ranging from a few nanometers close to the solubility curve to ≈200 nm in a 10-fold oversaturated solution where the eigencolloids contribute the main fraction of Th(IV) concentration. At near neutral pH, Th(IV) eigencolloids are expected to show strong sorption to solids and will experience significant retention in human-made or natural barriers around a repository and will not contribute significantly to the intake in the biosphere. Ionic $Th(IV)_{aq}$, however, will sorb to natural colloids and form so-called pseudocolloids and will migrate over considerable distances.

Similar investigations on the solubility of $Zr(OH)_4(am)$ (hydrated Zr(IV) oxyhydroxide) were performed by Cho et al. (2005) by coulometric titration (CT), and colloids were detected when the solubility limit was exceeded. The results

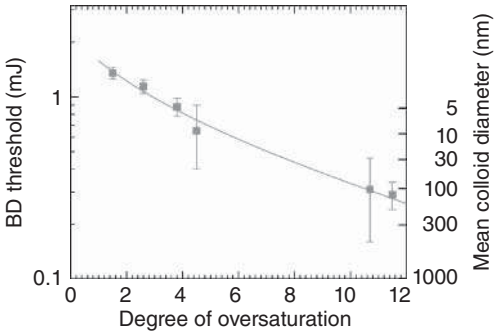

Figure 22.13 Mean Th(IV) colloid size as a function of oversaturation. Source: Modified from Walther (2007).

at pH 3–8 demonstrate that the solubility of $Zr(OH)_4(am)$ is several orders of magnitude higher than reported classical solubility data for acidic solutions, determined from undersaturation with the less soluble microcrystalline Zr(IV) oxide precipitate. EXAFS data show that the microcrystalline colloids in 0.1 M aqueous solution at pH 0.2 contain tetrameric units, similar to those present in the structure of $ZrOCl_2 \cdot 8H_2O$. Characterization of the CT solutions by EXAFS shows that oligomeric species, polynuclear hydroxide complexes ($Zr_x(OH)_y^{4x-y}$) in equilibrium with the mononuclear ionic species, form as the solubility limit is approached. The current lack of data on equilibrium constants for polynuclear hydroxide complexes prohibits the use of a realistic speciation model to describe the solubility of pH-dependent $Zr(OH)_4(am)$. However, the solubility curve was obtained using the mononuclear hydrolysis constants estimated by Cho et al. along with the solubility constant $\log K'_{sp} = -49.9 \pm 0.5$ in 0.5 M NaCl from which $\log K^0_{sp} = -53.1 \pm 0.5$ results at $I = 0$.

In the work by Walther (2003), it is shown that nano-electrospray mass spectrometry is suited for the direct detection of the species distribution of metal hydroxide complexes in aqueous solutions. Starting from solutions of ultrapure $ZrOCl_2$, the size (number of metal ions), number of ligands, and charge of the complex are unambiguously determined. Different species that are present simultaneously are well resolved down to contributions of only 0.2% of the total metal-ion concentration. High mass resolution is required as, for example, the masses of the first and second monomeric hydrolysis complex $m([^{90}Zr(OH)^{35}Cl^{37}Cl \cdot 9H_2O]^+) = 340.937$ amu and $m([^{90}Zr(OH)_2^{37}Cl \cdot 10H_2O]^+) = 340.981$ amu differ by less than 1/20th of a mass unit ($m/\Delta m = 7750$) are well resolved by the nano-ESI reflectron time-of-flight mass spectrometer. For direct proof that the species distribution is not altered by the electrospray process, EXAFS measurements were performed on selected samples. Though no species distribution can be deduced from the EXAFS FT spectra, the Zr–Zr and Zr–O distances and the coordination numbers can be confronted with the size distribution measured by ESI-TOF.

Typical mass spectra are displayed in Figures 22.14 and 22.15. The large number of peaks originates from the natural isotope distribution of Zr (five stable isotopes) and Cl (two stable isotopes) dividing the signal of each polymer $Zr_x(OH)_y^{z+}$ into many peaks according to the binomial distribution. Figure 22.14a shows a portion of a mass spectrum corresponding to mononuclear complexes of Zr^{4+}. The natural

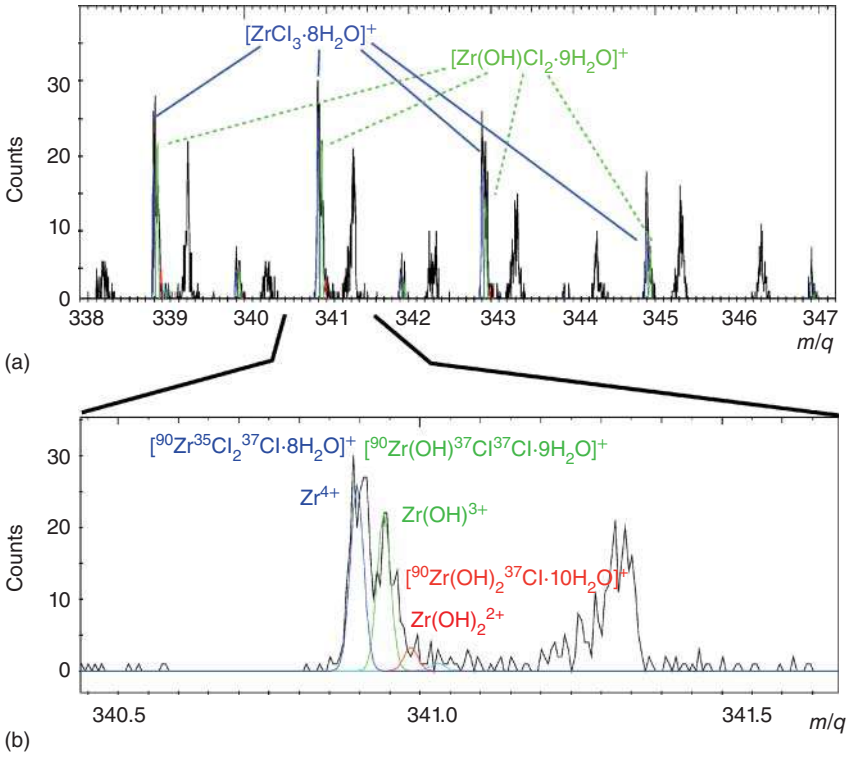

Figure 22.14 Portion of the mass spectrum of Figure 22.15 for the solution with [Zr] = 2.5 mM, pH_c = 0.2. (a) Isotopic distributions of the complexes $[ZrCl_3 \cdot 8H_2O]^+$ and $[Zr(OH)Cl_2 \cdot 9H_2O]^+$ due to the natural isotopic abundances of Cl and Zr. (b) The isobars $[^{90}Zr^{35}Cl_2^{37}Cl \cdot 8H_2O]^+$ (blue) and $[^{90}Zr(OH)^{35}Cl^{37}Cl \cdot 9H_2O]^+$ (green) are well resolved and can be evaluated separately. The peaks slightly above each mass unit (e.g. at 341.3 amu) are due to organic contaminants which are clearly separated from the Zr signals due to the high mass resolution. Source: Walther et al. (2007), figure 3 (p. 413)/Springer Nature.

isotopic compositions of $^{90,91,92,94,96}Zr$ and $^{35,37}Cl$ result in a unique isotopic pattern for each complex in the mass spectrum. In Figure 22.14b, the region around m = 341 amu is magnified. The metal ion is embedded in a solvation shell of eight water molecules in the case of the blue peak. The charge of the Zr^{4+} ion is partly compensated by three chloride ions, in the present example by two $^{35}Cl^-$ and one $^{37}Cl^-$, which results in a singly charged complex. The second peak that occurs 0.05 amu above this (green) corresponds to the first hydroxide complex $[Zr(OH)^{35}Cl^{37}Cl \cdot 9H_2O]^+$. The dihydroxo complex (red curve) is not present in significant amounts. The peaks slightly above each mass unit (e.g. at 341.3 amu) are due to an organic contamination and are, however, clearly discriminated from the signals of the Zr species due to the high mass resolution.

Monomers account for less than 20% of the mass fraction of the Zr species in solution. The full mass spectrum ([Zr] = 2.5 mM, pH_c = 0.2) is shown in Figure 22.15a and shows that the abundance of tetramers far exceeds the fraction of monomers

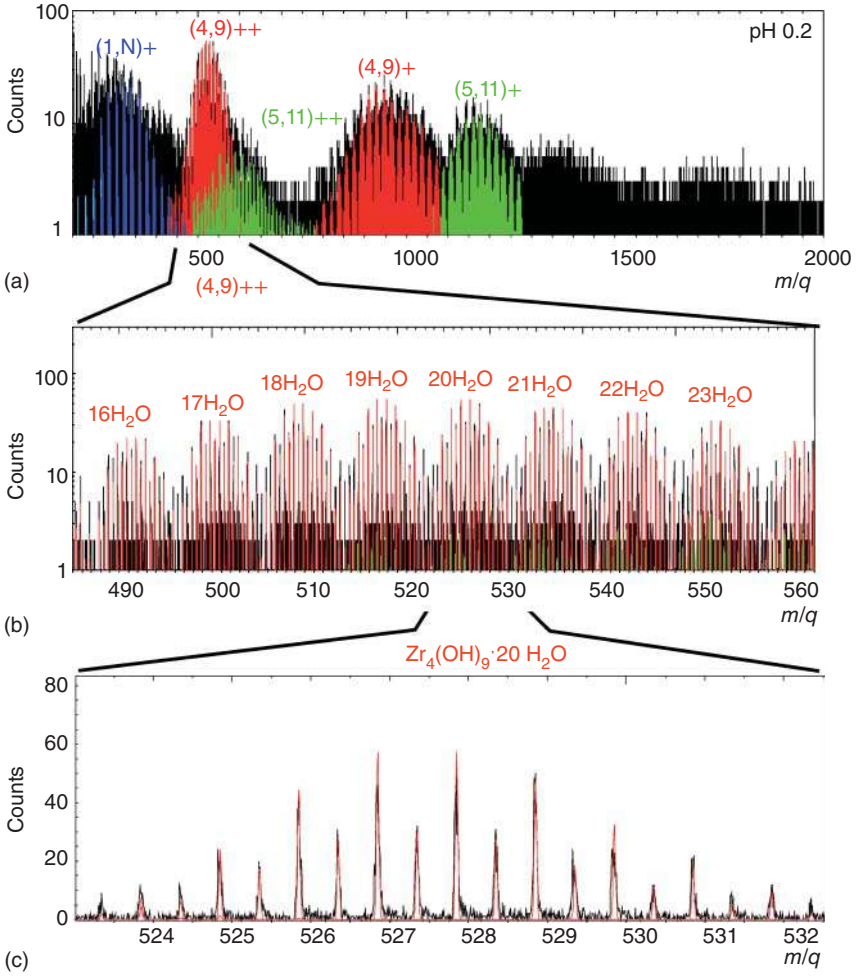

Figure 22.15 Total mass spectrum of a solution with [Zr] = 2.5 mM, pH_c = 0.2. (a) The full spectrum shows the monomers (blue), tetramers (red), and pentamers (green). (b) Magnification of the peak cluster between m/q = 490 and 560 (doubly charged tetramers) reveals that this cluster is composed of peak clusters representing different numbers of water molecules. (c) The isotopic distribution of $[Zr_4(OH)_9Cl_5]^{2+}\cdot 20H_2O$ is shown by further magnification. The measured spectrum (black) agrees excellently with the theoretical distribution (red). Source: Walther et al. (2007), figure 4 (p. 414)/Springer Nature.

(note the logarithmic scale of the ordinate). The polymers in Figure 22.15 are the tetramers $[Zr_4(OH)_9Cl_6]^{+}\cdot nH_2O$, $[Zr_4(OH)_9Cl_5]^{2+}\cdot nH_2O$ (red) and the pentamers $[Zr_5(OH)_{11}Cl_8]^{+}\cdot nH_2O$, $[Zr_5(OH)_{11}Cl_7]^{2+}\cdot nH_2O$ (green), respectively. These "peak clusters" consist of groups of peaks with different numbers n of water molecules in the solvation shells. Such a sequence of peak clusters is shown for the doubly charged tetramer in Figure 22.15b. Further magnification of the peak group representing $[Zr_4(OH)_9Cl_5]^{2+}\cdot 20H_2O$ shows almost 20 peaks (Figure 22.15c) due to the isotope distribution of chlorine and zirconium. The measured spectrum is shown

in black, the theoretical distribution convoluted with the mass resolution is plotted in red, and these show excellent agreement. Although the large number of isotopes complicates the spectrum, the isotope distribution is a fingerprint that can be used for the unequivocal identification of the polynuclear species.

While tetramers and monomers account for over 80% of the species at molar acidity, larger polymers form with increasing pH. Polymers up to $x = 21$ were identified and most likely even larger species form at lower acidity, eventually reaching the size of colloids. The EXAFS measurements consistently corroborate the ESI-TOF results. The mean Zr–Zr distances of all samples for [Zr] ≈ 10 mM, pH < 1 are in good agreement with the dominance of tetramers. With increasing variety of polymers, the FT peaks broaden and eventually vanish due to destructive interference. Further evidence for the correctness of this explanation comes from the EXAFS measurement at pH 1.8: the Zr–Zr signal reappears ($d = 3.66(3)$ Å with a mean coordination number of 2) in accordance with the ESI spectra showing that about 80% of the polymers are octamers. The lower concentrated samples show a slightly larger mean Zr–Zr distance attributed to the pentamer which is then dominant. The good correlation of the EXAFS results with the species distributions obtained by ESI-TOF suggests again that the species were not significantly disturbed by the electrospray process.

Looking back at the work by Cho et al. (2005) where broadening of the Zr–Zr backscattering peak suggested that, for [Zr] = 1 mM at pH > 2, several species with different Zr–Zr distances coexist in solution, ESI unravels these as the pentamer, the octamer, and the decamer. Colloid formation was detected by LIBD between pH 2.8 and 3.0 explaining the clogging of the nano-ESI capillary at pH > 2.7. Close to the solubility limit, the charge of the dominating complex in solution must equal the slope of the solubility curve. The ESI-TOF confirms this expectation: as the solubility limit is approached, the charges of the dominating complexes decrease toward $z = 2$ (pentamer and octamer). Charge compensation proceeds via step-wise hydrolysis of the complexes; in addition, chloride ions coordinate to the complex, presumably in an outer shell. It must be noted that no measurements can be performed in oversaturated solutions since immediate formation of a precipitate clogs the capillary. In fact, ESI-TOF and LIBD complement each other, since colloids are detected by LIBD only in oversaturated solutions.

Walther et al. (2007) have demonstrated that the hydrolysis of polynuclear Zr(IV) complexes is a continuous process. The charge of the polymers is compensated through sequential substitution of H_2O by OH ligands. While tetramers account for the majority of the Zr(IV) at high acidity, pentamers and octamers dominate at increasing pH. From the ESI-TOF mass spectra, no evidence for the formation of dimers and trimers is found.

22.6.3 Time-Resolved Laser-Induced Fluorescence

As the name implies, atoms are excited by absorption of photons from a short laser pulse. The favorite example is the Cm^{3+} ion in aqueous solution. Following excitation, the ion decays radiation less to the lowest excited level, for Cm^{3+} the $^6D_{7/2}$ state. It decays to the $^8S_{7/2}$ ground state by emitting fluorescent light of 593.8 nm,

see Figure 22.16a. This is detected time resolved by a gated intensified CCD camera following a spectrometer. The interaction of the Cm^{3+} ion with ligands alters the outer orbitals (ligand field) causing a spectral shift of the fluorescence emission line, Figure 22.16b. If the excitation energy of the Cm^{3+} ion ($^6D_{7/2} \rightarrow {}^8S_{7/2} \approx 16\,900\,cm^{-1}$) equals an integer multiple of the energy of a vibronic mode of the ligand, the energy may rapidly be transferred to the ligand. This quenching by overtone excitation shortens the lifetime of the emitting state considerably. H_2O is a particularly strong quencher of Cm^{3+}. The fifth overtone excitation of the symmetric O–H stretching vibration (3400 cm^{-1}, width $\pm 250\,cm^{-1}$) almost perfectly matches the $^6D_{7/2} - {}^8S_{7/2}$ energy difference. For a Cm^{3+} ion with nine H_2O ligands in the first coordination sphere, the lifetime is reduced to $\tau = 69 \pm 4\,\mu s$ as compared to $\tau = 1/\Gamma \approx 4\,ms$ in vacuum. A decreasing number of coordinated H_2O ligands, for example, in the case of inner sphere surface sorption to a solid, causes a decreasing decay rate as the number of quenching ligands is linearly related to k_Q (Kimura equation). Moreover, the number of nonequivalent complexes can be determined from the time dependence of the fluorescence: a mono-exponential decay with a characteristic lifetime $\tau = 1/k_T = 1/(\Gamma + k_Q)$ indicates the presence of only one metal–ligand complex, whereas the simultaneous presence of two complexes with different coordination numbers (quench rates) results in a biexponential decay, Figure 22.16c.

The triple selectivity, excitation wavelength, emission wavelength, and time resolution make TRLFS a sensitive and element-selective speciation method. Typical applications are speciation of different complexes, measurement of formation constants, determination of the thermodynamic quantities ΔG, ΔH, and ΔS, and the effects of the chemical environment on the metal ion.

The selected application returns to the tetravalent actinide ions – here to protactinium. Interest in Pa chemistry arose from its role in ^{232}Th breeder reactors and accelerator-driven transmutation reactors (Section 15.8) where it is an intermediate product in the reaction

$$^{232}Th + n \longrightarrow {}^{233}Th \xrightarrow{\beta^-} {}^{233}Pa \xrightarrow{\beta^-} {}^{233}U$$

The related development of separation schemes requires fundamental knowledge of its chemical behavior in aqueous and organic liquids. Previous investigations focused on Pa(V) which is known for its high tendency to hydrolyze and to form polymers. Much less work was devoted to Pa(IV) due to the low stability of this oxidation state: Pa(IV) is readily oxidized to Pa(V) by traces of oxygen or by absorption of UV light, but the rate of oxidation can be reduced by exclusion of oxygen. Absorption spectroscopy on Pa(IV) in acidic solutions has been reported, revealing absorption bands in perchloric acid at 225, 256, and 278 nm. However, fluorescence spectroscopy has so far not been performed with $Pa(IV)_{aq}$. Two recent papers have been published focusing on complexation of Pa(IV) in acidic aqueous media and on hydrolysis: Marquardt et al. (2004) and Lindqvist-Reis et al. (2005). Purified ^{231}Pa was used to prepare a $[Pa]_{tot} = 3.3 \cdot 10^{-4}$ M stock solution in 9.5 M HCl. Samples were diluted to a final protactinium concentration of about $1 \cdot 10^{-5}$ M and, finally, Pa(V) was reduced to Pa(IV) in an inert-gas box by adding Zn amalgam. The resulting solution was characterized by UV–vis spectroscopy and, for the first

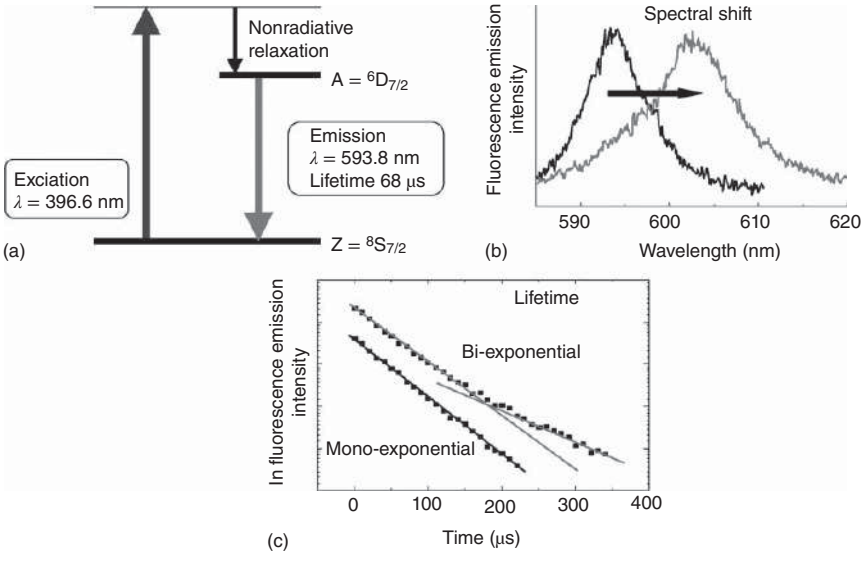

Figure 22.16 (a) Excitation scheme of Cm^{3+}; (b) bathochromic shift of the fluorescence wavelength caused by a change of the ligand field; (c) the lifetime of the emitting state is determined by the number of coordinated quenching ligands. A biexponential decay curve indicates the simultaneous presence of two species with different numbers of quenching ligands. Source: Modified from Beitz (1991).

time, by TRLFS using the $5f^1$–$6d^1$ transition of Pa(IV) in contrast to the f–f intraband transition in Cm^{3+}. The f–d inter-band transitions are short lived and strong, but featureless and spectrally broad. Excitation at 308 nm by an excimer laser and at 278 nm by a frequency-doubled dye laser, respectively, lead to fluorescence light emission around $\lambda = 450$ nm. In contrast to the large number of transitions reported by the Edelstein group in the early 1990s for Pa^{4+}-doped crystals, only one broad fluorescence band with FWHM = 60 nm is being observed for the aquo ion.

Depending on the type and concentration of the acid, peak shifts to shorter wavelengths upon complexation (hypsochromic shifts) were observed, whereas for Cm^{3+} always a bathocromic shift is observed. The shift is strongest for SO_4^{2+} complexation, less pronounced for Cl^-, and almost no shift is observed for ClO_4^- which reflects the decreasing complexation strength of the respective ligands. No parity forbiddance hinders the f–f transition, which leads to a short lifetime of 16 ± 2 ns. The measurement of such short lifetimes involves two technical complications. First, the pulse length of the excimer pumped laser system is approximately 26 ns so that the temporal pulse profile must be deconvoluted from the measured decay curve. Second, another obstacle arose from the photooxidation by the UV light of Pa(IV). A continuous scan of the time delay between laser and fluorescence detection would have overestimated the decay rate because the Pa(IV) concentration decreased with increasing illumination. Therefore, the measurement cycles were alternated with reference cycles at fixed delay times which were used for off-line normalization. The lifetime remained constant independent of the ligands, which is in line with expectations: for such short lifetimes, no significant energy transfer to the ligands is possible and no quenching occurs.

In continuation of the work by Marquardt et al. (2004), the complexation of Pa(IV) by fluoride was also investigated by Marquardt et al. (2005). A solution containing $[Pa(IV)] = 1.5 \cdot 10^{-5}$ M in 1 M $HClO_4$ was titrated with a NaF solution. With increasing fluoride concentration from $[F^-] = 0$ to 0.11 M, the formation of the complexes PaF_y^{4-y} up to $PaF_{4(aq)}$ and finally dispersed crystallite $PaF_{4(s)}$ lead to distinct changes in the absorption spectra which were well explained by a species distribution based on the formation constants of Guillaumont. However, in none of the samples was a change in the fluorescence emission band at $\lambda = 469$ nm observed; only the intensity increased with increasing fluoride concentration up to $[F^-] = 0.025$ M and decreased strongly for higher fluoride concentration. This fall is due to the formation of $PaF_{4(s)}$ colloids.

The second part of Marquardt et al. (2005) focused on the hydrolysis of Pa(IV). This was associated with a strong "blue shift" of the emission band of Pa(IV) in a sample of $[Pa(IV)] = 1.4 \cdot 10^{-5}$ M in 1 M $HClO_4$ when the pH was increased by step-wise addition of NaOH. From pH 0 to 1.6, the peak position of the fluorescence band remained constant but the intensity increased up to pH 0.38 and decreased continuously thereafter. Further increase of the pH led to the pronounced spectral shift from 469 to 422 nm at pH 3.6. The intensity variation correlates with the relative abundance of the $Pa(OH)^{3+}$ complex and the peak shift coincides with the formation and dominance of the third hydrolysis complex $Pa(OH)_3^+$ at pH 1.6 as calculated using the formation constants for mononuclear hydroxide complexes from

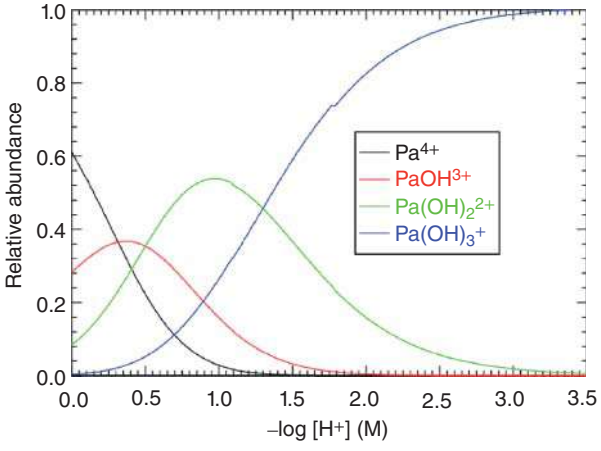

Figure 22.17 Calculated distribution of mononuclear hydroxide complexes ($HClO_4/NaClO_4$ solutions at $I = 3$ M) in the absence of polynuclear species, for example, at very low metal-ion concentrations. Hydrolysis constants from R. Guillaumont.

Guillaumont and displayed in Figure 22.17. The most plausible explanation of this observation is that structural changes in the first hydration sphere and associated changes in the ligand field upon the third hydrolysis step cause the large peak shift. Further pH increase led to a strong decrease of Pa in solution, as measured by liquid scintillation counting, which was either due to sorption onto the walls of the quartz cuvette or due to precipitation. The authors refrained from giving an estimate of the solubility products since data from the literature scattered considerably. Using the experimental value of Duplessis and Guillaumont (1977), $\log K^0_{sp} = -53.4$ one estimates that up to pH 4, $[Pa(IV)] = 10^{-4}$ M should be soluble and precipitation should not play a role for $[Pa(IV)] = 1.4 \cdot 10^{-5}$ M. In conclusion, this work demonstrated that TRLFS lends itself to the investigation of the tetravalent actinide ion Pa(IV) in solution. Hydrolysis that affects the absorption spectra only weakly causes a strong shift of the fluorescence emission and can be observed with high selectivity. The most important advantage of TRLFS over UV–vis is its superior sensitivity, which allows speciation at $[Pa(IV)] = 10^{-7}$ M.

22.7 Conclusions

Formation constants and chemical properties for polynuclear tetravalent actinides and colloids are needed in order to develop realistic models for the prediction of potential radionuclide release from underground repositories in case of accidents. The first direct observation of the continuous hydrolysis of polynuclear metal hydroxide complexes of the homologs Zr(IV) and Th(IV) opens up a novel approach of determining formation constants by ESI-TOF. Furthermore, the work discussed above contributes precise data on the solubility of Pu(IV), the formation constants of mononuclear Pu(IV) hydrolysis complexes, and new insights into the formation

processes of Pu(IV) colloids. Plutonium redox chemistry has been reformulated by including polymeric plutonium as a link between trivalent and tetravalent plutonium on the one hand and the plutonyl ions PuO_2^+ and PuO_2^{2+} on the other. The new insights need to be included in databases such as the NEA database, in order to contribute to the continuous improvement of radionuclide transport modeling.

References

New Speciation Techniques with Relevance for Nuclear Safeguards, Verification, and Applications

Banik, N.L., Buda, R.A., Bürger, S. et al. (2007). Sorption of tetravalent plutonium and humic substances onto kaolinite. *Radiochim. Acta* 95: 569.

Beitz, J.V. (1991). *Radiochim. Acta* 52/53: 35.

Bitea, C., Müller, R., Neck, V. et al. (2003). Study of the generation and stability of thorium(IV) colloids by LIBD combined with ultrafiltration. *Colloids Surf.* A217: 63.

Buda, R.A., Banik, N.L., Kratz, J.V., and Trautmann, N. (2008). Studies of the ternary systems humic substances – kaolinite – Pu(III) and Pu(IV). *Radiochim. Acta* 96: 657.

Bundschuh, T., Knopp, R., and Kim, J.I. (2001a). Laser-induced breakdown detection (LIBD) of aquatic colloids with different laser systems. *Colloids Surf.* A177: 47.

Bundschuh, T., Hauser, W., Kim, J.I. et al. (2001b). Determination of colloid size by two-dimensional optical detection of laser induced plasma. *Colloids Surf.* A180: 285.

Bundschuh, T., Knopp, R., Winzenbacher, R. et al. (2001c). Quantification of aquatic nano particles after different steps of Bodensee water purification with laser-induced breakdown detection (LIBD). *Acta Hydroch. Hydrob.* 29: 7.

Bürger, S., Banik, N.L., Buda, R.A. et al. (2007). Speciation of the oxidation states of plutonium in aqueous solutions by UV/VIS spectroscopy, CE-ICP-MS, and CE-RIMS. *Radiochim. Acta* 95: 433.

Cho, H.R., Walther, C., Rothe, J. et al. (2005). Combined LIBD and XAFS investigation of the formation and structure of Zr(IV) colloids. *Anal. Bioanal. Chem.* 383: 28.

Conradson, S.D., Abney, K.D., Begg, B.D. et al. (2004). Higher order speciation effects on plutonium L-3 X-ray absorption near edge spectra. *Inorg. Chem.* 43: 116.

Conradson, S.D., Begg, B.D., Clark, D.L. et al. (2005). Charge distribution and local structure and speciation in the UO_{2+x} and PuO_{2+x} binary oxides for $x \leq 0.25$. *J. Solid State Chem.* 178: 521.

Duplessis, J. and Guillaumont, R. (1977). Hydrolyse du neptunium tetravalant. *Radiochem. Radioanal. Lett.* 31: 293.

Grenthe, I. et al. (1997). *Modelling in Aquatic Chemistry*. Paris: OECD/NEA.

Kimura, T. and Choppin, G.R. (1994). Luminescence study on determination of the hydration number of Cm(III). *J. Alloys Compd.* 213: 313.

Kinniburgh, D.G. and Cooper, D.M. (2009). PhreePlot: creating graphical output with PHREEQC. http://www.phreeplot.org (accessed 09 February 2021).

Křepelová, A. (2007). Influence of humic aciid on the sorption of uranium(VI) and americium(III) onto kaolinite. PhD thesis. Germany: Faculty of Mathematics and Natural Scirnces, University of Dresden.

Kuczewski, B., Marquardt, C.M., Seibert, A. et al. (2003). Separation of plutonium and neptunium species by capillary-electrophoresis-ICP-MS and application to natural groundwater samples. *Anal. Chem.* 75: 6769.

Lindqvist-Reis, P., Klenze, R., Schubert, G., and Fanghänel, T. (2005). Hydration of Cm^{3+} in aqueous solution from 20 to 200 °C. A time-resolved laser fluorescence spectroscopy study. *J. Phys. Chem.* B109: 3077.

Marquardt, C.M., Panak, P.J., Apostolidis, C. et al. (2004). Fluorescence spectroscopy on protactinium(IV) in aqueous solution. *Radiochim. Acta* 92: 445.

Marquardt, C.M., Panak, P.J., Walther, C. et al. (2005). Fluorescence spectroscopy of protactinium(IV). In: *Recent Advances in Actinide Science* (eds. I. May, R. Alvarez and N. Bryan), 776. London: Royal Society of Chemistry.

Marsac, R., Banik, N.L., Lützenkirchen, J. et al. (2015). Modeling plutonium sorption to kaolinite: accounting for redox equilibria and the stability of surface species. *Chem. Geol.* 400: 1.

Metivier, H. and Guillaumont, R. (1972). Hydrolyse du plutonium tetravalant. *Radiochem. Radioanal. Lett.* 10: 27.

Neck, V. and Kim, J.I. (2001). Solubility and hydrolysis of tetravalent actinides. *Radiochim. Acta* 89: 1.

Neck, V., Altmaier, M., Seibert, A. et al. (2007). Solubility and redox reactions of Pu(IV) hydrous oxide: evidence for the formation of PuO_{2+x}(s, hyd). *Radiochim. Acta* 95: 193.

Parkhurst, D.L. and Appelo, C.A.J. (1999). User's Guide to PHREEQC (Version 2) – A Computer Program for Speciation, Batch Reaction, One-Dimensional Transport and Inverse Geochemical Calculation. *Water-resources Investigation Report 99-4259*. Denver, CO: USGS, p. 312.

Rothe, J., Walther, C., Denecke, M.A., and Fanghänel, T. (2004). XAFS and LIBD investigation of the formation and structure of colloidal Pu(IV) hydrolysis products. *Inorg. Chem.* 43: 4708.

Scherbaum, F.J., Knopp, R., and Kim, J.I. (1996). Counting of particles in aqueous solutions by laser-induced photoacoustic breakdown detection. *Appl. Phys.* B63: 299.

Schmeide, K. and Bernhard, G. (2010). Sorption of Np(V) and Np(VI) onto kaolinitr: effects of pH, ionic strength, carbonate and humic acid. *Appl. Geochem.* 25: 1238.

Walther, C. (2003). Comparison of colloid investigations by single particle analytical techniques – a case study on thorium-oxohydroxides. *Colloids Surf.* A217: 81.

Walther, C. (2007). *Habilitationsschrift*, "From hydrolysis to the formation of colloids – polymerization of tetravalent actinide ions," at the Johannes Gutenberg-Universität Mainz.

Walther, C., Bitea, C., Hauser, W. et al. (2002). Laser-induced breakdown detection for the assessment of colloid mediated radionuclide migration. *Nucl. Instrum. Methods Phys. Res.* B195: 374.

Walther, C., Bitea, C., Yun, J.I. et al. (2003). Nanoscopic approaches to the aquatic plutonium chemistry. *Actinide Res. Q.* 11: 12.

Walther, C., Büchner, S., Filella, M., and Chanudet, V. (2006). Probing particle size distributions in natural surface waters from 15 nm to 2 μm by a combination of LIBD and single particle counting. *J. Colloid Interface Sci.* 301: 532.

Walther, C., Rothe, J., Fuss, M. et al. (2007). Investigation of polynuclear Zr(IV) hydroxide complexes by nanoelectrospray mass-spectrometry combined with XAFS. *Anal. Bioanal. Chem.* 388: 409.

Walther, C., Cho, H.R., Marquardt, C.M. et al. (2007). Hydrolysis of plutonium(IV) in acidic solutions: no effect of hydrolysis on absorption spectra of mononuclear hydroxide complexes. *Radiochim. Acta* 95: 7.

Yun, J.I., Cho, H.R., Neck, V. et al. (2007). Investigation of the hydrolysis of plutonium(IV) by a combination of spectroscopy and redox potential measurements. *Radiochim. Acta* 95: 89.

Further Reading

General

Materials Research Society (1978–1989). *Proceedings of the Conference on the Scientific Basis for Nuclear Waste Management*, vols. I (1978) to XII (1989) and subsequent conferences. Amsterdam: North-Holland.

United Nations (1979). The Environmental Impacts of Production and Use of Energy. *Energy Report Series 2-79*. Nairobi: UNEP.

Hall, E.J. (1984). *Radiation and Life*, 2e. Oxford: Pergamon.

Migration Conferences (1988). Chemistry and migration behaviour of actinides and fission products in the geosphere. *Radiochim. Acta* 44/45; 52/53 (1990); 58/59 (1992); 66/67 (1994); 74 (1996).

Morss, L.R., Edelstein, N.M., Fuger, J., and Katz, J.J. (eds.) (2006). *The Chemistry of Actinide and Transactinide Elements*, 3e. Dordrecht: Springer.

Firestone, R.B. (2011). Table of nuclides. In: *Handbook of Nuclear Chemistry*, vol. 2, Appendix, 2e (eds. A. Vertés, S. Nagy, Z. Klencsár, et al.), 1033. Berlin: Springer-Verlag.

Magill, J., Pfennig, G., Dreher, I.R., and Sóti, Z. (2015). *Karlsruher Nuklidkarte*, 9. Auflage. Nucleonica GmbH, developed under a License of the European Atomic Energy Community.

Radionuclides in the Environment

Junge, C.E. (1963). *Air Chemistry and Radioactivity*. New York: Academic Press.

Lal, D. and Suess, H.A. (1968). The radioactivity of the atmosphere and the hydrosphere. *Annu. Rev. Nucl. Sci.* 18: 407.

National Academy of Sciences (1971). *Radioactivity in the Marine Environment*. Washington, DC: National Academy of Sciences.

International Atomic Energy Agency (1975). *The Oklo Phenomenon*. Vienna: IAEA.

National Academy of Sciences (1975). *Long-term Worldwide Effects of Nuclear-Weapons Detonations*. Washington, DC: National Academy of Sciences.

International Atomic Energy Agency (1976). *Transuranium Nuclides in the Environment*. Vienna: IAEA.
Fritz, P. and Fontes, J.Ch. (eds.) (1980). *Handbook on Environmental Isotope Chemistry*, vol. 1. Amsterdam: The Terrestrial Environment, Elsevier.
International Atomic Energy Agency (1982). *Environmental Migration of Long-lived Radionuclides*. Vienna: IAEA.
International Atomic Energy Agency (1982). *Nuclear Power, the Environment and Man*. Vienna: IAEA.
Stein, L. (1983). The chemistry of radon. *Radiochim. Acta* 32: 163.
Barney, G.S., Navratil, J.D., and Schulz, W.W. (eds.) (1984). *Geochemical Behaviour of Radioactive Waste*, ACS Symposium Series. Washington, DC: American Chemical Society.
Brookins, D.G. (1984). *Geochemical Aspects of Radioactive Waste Disposal*. Berlin: Springer-Verlag.
Kathren, R.L. (1984). *Radioactivity in the Environment; Sources, Distribution and Surveillance*. Chur: Harwood.
American Chemical Society (1986). *Chemical Phenomena Associated with Radioactivity Releases During Severe Nuclear Plant Accidents*, ACS Symposium Series. Washington, DC: American Chemical Society.
Desmet, G. and Myttenaere, C. (eds.) (1986). *Technetium in the Environment*. Amsterdam: Elsevier.
Durrance, E.M. (1986). *Radioactivity in Geology: Principles and Applications*. Chichester: Ellis Horwood.
International Atomic Energy Agency (1986). *Summary Report on the Post-accident Review Meeting on the Chernobyl Accident*, International Nuclear Safety Advisory Group (INSAG), Safety Series No. 75-INSAG-1. Vienna: IAEA.
Tadmor, J. (1986). Radioactivity from coal-fired power plants. *J. Environ. Radioact.* 4: 177.
Eisenbud, M. (1987). *Environmental Radioactivity from Natural, Industrial and Military Sources*, 3e. Orlando, FL: Academic Press.
Desmet, G., Nassimbeni, P., and Belli, M. (eds.) (1990). *Transfer of Radionuclides in Natural and Semi-Natural Environments*. Amsterdam: Elsevier.
International Atomic Energy (1990). *The Environmental Behaviour of Radium*. Vienna: IAEA.
International Atomic Energy Agency (1990). *Proceedings of the International Symposium on Environmental Contamination Following a Major Accident*. Vienna: IAEA.
Chamberlain, A.C. (1991). *Radioactive Aerosols*, Cambridge Environmental Chemistry Series 3. Cambridge: Cambridge University Press.
International Atomic Energy Agency (1992). *The Radiobiological Impact of Hot Beta-Particles from the Chernobyl Fallout: Risk Assessment*. Vienna: IAEA.
Ivanovich, M. and Harmon, R.S. (1992). *Uranium Series Disequilibrium: Applications to Earth, Marine, and Environmental Sciences*, 2e. Oxford: Clarendon Press.
Lieser, K.H. (1993). Technetium in the nuclear fuel cycle, in medicine and in the environment. *Radiochim. Acta* 63: 5.

Sandalls, F.J., Segal, M.G., and Victorova, N. (1993). Hot particles from Chernobyl: a review. *J. Environ. Radioact.* 18: 5.

Strand, P. and Holm, E. (eds.) (1993). Environmental radioactivity in the arctic and antarctic. *Proceedings of the International Conference*, August, Kirkenes, Norway.

Ure, A.M. and Davidson, C.M. (eds.) (1994). *Chemical Speciation in the Environment*. London: Chapman and Hall.

Gäggeler, H.W. (1995). Radioactivity in the atmosphere. *Radiochim. Acta* 70/71: 345.

Lieser, K.H. (1995). Radionuclides in the geosphere: sources, mobility, reactions in natural waters and interactions with solids. *Radiochim. Acta* 70/71: 355.

Silva, R.J. and Nitsche, H. (1995). Actinide environmental chemistry. *Radiochim. Acta* 70/71: 377.

Chemistry and Speciation

Haissinsky, M. (1934). *Les Radiocolloides*. Paris: Hermann.

Cleveland, J.M. (1971). *The Chemistry of Plutonium*. New York: Gordon and Breach.

Keller, C. (1971). *The Chemistry of the Transuranium Elements* (ed. K.H. Lieser). Weinheim: Verlag Chemie.

Stumm, W. and Brauner, P.A. (1975). Chemical speciation. In: *Chemical Oceanography*, 2e (eds. J.P. Riley and G. Skirow). New York: Academic Press.

Gesell, T.F. and Loder, W.M. (eds.) (1980). *Natural Radiation Environment III*. Springfield, IL: NTIS.

Hanson, W.C. (ed.) (1980). *Transuranic Elements in the Environment*. Washington, DC: US Department of Energy, Technical Information Center.

International Atomic Energy Agency (1981). *Transuranic Speciation in Aquatic Environments*. Vienna: IAEA.

Edelstein, N.M. (ed.) (1982). *Actinides in Perspective*. Oxford: Pergamon.

Carnall, W.T. and Choppin, G.R. (eds.) (1983). *Plutonium Chemistry*, ACS Symposium Series, vol. 216. Washington, DC: American Chemical Society.

Stumpe, R., Kim, J.I., Schrepp, W., and Walther, H. (1984). Speciation of actinide ions in aqueous solution by laser-induced pulsed spectrophotoacoustic spectroscopy. *Appl. Phys.* B34: 203.

Bulman, R.A. and Cooper, J.R. (eds.) (1985). *Speciation of Fission and Activation Products in the Environment*. Amsterdam: Elsevier.

Choppin, G.R. and Allard, B. (1985). Complexes of actinides with naturally occurring organic compounds. In: *Handbook on the Physics and Chemistry of the Actinides*, vol. 3 (eds. A.J. Freeman and C. Keller), 407. Amsterdam: Elsevier.

Newton, T.W. and Sullivan, J.C. (1985). Actinide carbonate complexes in aqueous solution. In: *Handbook on the Physics and Chemistry of the Actinides*, vol. 3 (eds. A.J. Freeman and C. Keller), 387. Amsterdam: Elsevier.

Bernhard, M., Brinckman, F.E., and Sadler, P.J. (eds.) (1986). *The Importance of Chemical Speciation in Environmental Processes*. Berlin: Springer-Verlag.

Kim, J.I. (1986). Chemical behaviour of transuranic elements in natural aquatic systems. In: *Handbook on the Physics and Chemistry of Actinides*, vol. 4 (eds. A.J. Freeman and C. Keller), 413. Amsterdam: Elsevier.

Landner, L. (ed.) (1987). *Speciation of Metals in Water, Sediment and Soil Systems*. Berlin: Springer-Verlag.
Kramer, J.R. and Allen, H.E. (eds.) (1988). *Metal Speciation: Theory, Analysis and Application*. Chelsea, MI: Lewis.
Batley, G.E. (ed.) (1989). *Trace Element Speciation: Analytical Problems and Methods*. Boca Raton, FL: CRC Press.
Broekart, J.A.C., Gücer, S., and Adams, F. (eds.) (1990). *Metal Speciation in the Environment*. Berlin: Springer-Verlag.
Lieser, K.H., Ament, A., Hill, R. et al. (1990). Colloids in groundwater and their influence on migration of trace elements and radionuclides. *Radiochim. Acta* 49: 83.
Ahrland, S. (1991). Hydrolysis of the actinide ions. In: *Handbook on the Physics and Chemistry of the Actinides*, vol. 9 (eds. A.J. Freeman and C. Keller). Amsterdam: Elsevier.
International Atomic Energy Agency (1992, 1995). Reports of the VAMP (Validation of Environmental Model Predictions) Terrestrial Working Group, IAEA Tech. Doc. 647; (1994, 1995) Reports of the Urban Working Group, IAEA Tech. Doc. 760, Vienna.
Dozol, M. and Hagemann, R. (1993). Radionuclide migration in groundwaters: review of the behaviour of actinides. *Pure Appl. Chem.* 65: 1081.

Trace Elements in Water

Förstner, U. and Müller, G. (1974). *Schwermetalle in Flüssen und Seen*. Berlin: Springer-Verlag.
Baes, C.F. Jr., and Mesmer, R. (1976). *The Hydrolysis of Cations*. New York: Wiley.
Smith, R.M. and Martell, A.E. (1976). *Critical Stability Constants*. New York: Plenum Press.
Beneš, P. and Majer, V. (1980). *Trace Chemistry in Aqueous Solutions*. Amsterdam: Elsevier.
Kavanough, M.C. and Leckie, J.O. (1980). *Particulates in Water*, ACS Advances in Chemistry Series, vol. 189. Washington, DC: American Chemical Society.
Duursma, E.K. and Dawson, H.J. (1981). *Marine Organic Chemistry*. Amsterdam: Elsevier.
Förstner, U. and Wittmann, G.T.W. (1981). *Metal Pollution in the Aquatic Environment*, 2e. Berlin: Springer-Verlag.
Stumm, W. and Morgan, J.J. (1981). *Aquatic Chemistry*, 2e. New York: Wiley.
Högfeld, E. (1982). *Stability Constants of Metal-Ion Complexes*. Oxford: Pergamon.
Leppard, G.G. (ed.) (1983). *Trace Element Speciation in Surface Waters and Its Geological Implications*. New York: Plenum Press.
Morel, F.M.N. (1983). *Principles of Aquatic Chemistry*. New York: Wiley.
Wong, C.S., Boyle, E., Bruland, K.W. et al. (eds.) (1983). *Trace Metals in Sea Water*. New York: Plenum Press.
Salomons, W. and Förstner, U. (1984). *Metals in the Hydrocycle*. Berlin: Springer-Verlag.
Buffle, J. (1988). *Complexation Reactions in Aquatic Systems: An Analytical Approach*. Chichester: Ellis Horwood.
Bidoglio, G. and Stumm, W. (eds.) (1994). *Chemistry of Aquatic Systems: Local and Global Perspectives*. Dordrecht: Kluwer Academic.

Interaction with Solids

Amphlett, C.B. (1964). *Inorganic Ion Exchangers*. Amsterdam: Elsevier.

Gregg, S.J. and Sing, K.S.W. (1964). *Adsorption, Surface Area and Porosity*. New York: Academic Press.

International Atomic Energy Agency (1965). *Exchange Reactions, Proceedings*. Vienna: IAEA.

Gould, R.F. (1968). *Adsorption from Aqueous Solutions*, ACS Advances in Chemistry Series, vol. 79. Washington, DC: American Chemical Society.

Hauffe, K. and Morrison, S.R. (1974). *Adsorption*. Berlin: Walter de Gruyter.

Bohn, H.L., McNeal, B.L., and O'Connor, G.A. (1979). *Soil Chemistry*. New York: Wiley.

Lindsay, W.L. (1979). *Chemical Equilibria in Soils*. New York: Wiley.

Davies, B.E. (ed.) (1980). *Applied Soil Trace Elements*. New York: Wiley.

Anderson, M.A. and Rubin, A.J. (eds.) (1981). *Adsorption of Inorganics at Solid–Liquid Interfaces*. Ann Arbor, MI: Ann Arbor Science.

Clearfield, A. (1982). *Inorganic Ion Exchange Materials*. Boca Raton, FL: CRC Press.

Sposito, G. (1984). *The Surface Chemistry of Soils*. Oxford: Oxford University Press.

Sibley, T.H. and Myttenaere, C. (eds.) (1985). *Application of Distribution Coefficients in Radiological Assessment Models*. Amsterdam: Elsevier.

Stumm, W. (1987). *Aquatic Surface Chemistry*. New York: Wiley.

Dzombak, D.A. and Morel, F.F.M. (1990). *Surface Complexation Modelling: Hydrous Ferric Oxide*. New York: Wiley.

Hochella, M.F. Jr., and White, A.F. (eds.) (1990). *Mineral–Water Interface Geochemistry, Reviews in Mineralogy*, vol. 23. Washington, DC: Mineralogical Society of America.

Lieser, K.H. (1991). Non-siliceous inorganic ion exchangers. In: *Ion Exchangers* (ed. K. Dorfner), 519. Berlin: Walter de Gruyter.

Weiss, A. and Sextl, E. (1991). Clay minerals as ion exchangers. In: *Ion Exchangers* (ed. K. Dorfner), 492. Berlin: Walter de Gruyter.

Kim, M.A., Panak, P.J., Yun, J.I. et al. (2003). Interaction of actinides with aluminosilicate colloids in statu nascendi Part I: Generation and characterization of actinide(III) – pseudocolloids. *Colloids Surf.* 216: 97.

Panak, P.J., Kim, M.A., Yun, J.I., and Kim, J.I. (2003). Interaction of actinides with aluminosilicate colloids in statu nascendi Part II: Spectroscopic speciation of colloid-borne actinides(III). *Colloids Surf.* 227: 93.

Kim, M.A., Panak, P.J., Yun, J.I. et al. (2005). Interaction of actinides(III)with aluminosilicate colloids in statu nascendi Part III: Colloid formation from monosilanol and polysilanol. *Colloids Surf.* 254: 137.

Radioecology

Russell, R.S. (ed.) (1966). *Radioactivity and Human Diet*. Oxford: Pergamon.

Schultz, V. and Klement, A.W. Jr., (eds.) (1966). *Radioecology of Aquatic Organisms*. Amsterdam: North-Holland.

Åberg, B. and Hungate, F.P. (eds.) (1967). *Radioecological Concentration Processes*. Oxford: Pergamon.

Garner, R.J. (1972). *Transfer of Radioactive Materials from the Terrestrial Environment to Animals and Man*. Boca Raton, FL: CRC Press.

International Commission on Radiological Protection (1972). *The Metabolism of Compounds of Plutonium and Other Actinides*, ICRP Publ. 19. Oxford: Pergamon.
Greenberg, D. (1973). *Radioecology*. New York: Wiley.
International Atomic Energy Agency (1976). *Effects of Ionizing Radiation on Aquatic Organisms and Ecosystems*, Technical Report Series 172. Vienna: IAEA.
Whicker, F.W. and Schultz, V. (1982). *Radioecology, Nuclear Energy and the Environment*, vols. I and II. Boca Raton, FL: CRC Press.
International Atomic Energy Agency (1985). Sediment Kd's and Concentration Factors in the Marine Environment. *Tech. Rep. 247*. Vienna: IAEA.
Nair, S. et al. (1986). Nuclear Power and Terrestrial Environment: The Transport of Radioactivity through Foodchains to Man. *CEGB Research, No. 19*.
Haberer, K. (1989). *Umweltradioaktivität und Trinkwasserversorgung*. Munich: Oldenbourg.
Commission of the European Communities (1992). *Proceedings of the International Symposium on Radioecology*, Znojmo, Brussels.
Dahlgaard, H. (ed.) (1994). *Nordic Radioecology: The Transfer of Radionuclides through Nordic Ecosystems to Man*, Studies in Environmental Science, vol. 62. Amsterdam: Elsevier.
International Atomic Energy Agency (1994). Handbook of Parameter Values for the Prediction of Radio-nuclide Transfer in Temperate Environments. *Tech. Rep. 364*. Vienna: IAEA.

New Speciation Techniques with Relevance for Nuclear Safeguards, Verification, and Applications

Kitamori, T., Yokose, K., Suzuki, K. et al. (1988). Laser breakdown acoustic effect of ultrafine particles in liquids and its application to particle counting. *Jpn. J. Appl. Phys.* 27: L983.
Kim, J.I. and Klenze, R. (1990). Laser-induced photoacoustic spectroscopy for the speciation of transuranic elements in natural aquatic systems. *Top. Curr. Chem.* 157: 129.
Reich, T., Bernhard, G., Geipel, G. et al. (2000). The Rossendorf Beamline ROBL – a dedicated experimental station for XAFS measurements of actinides and other radionuclides. *Radiochim. Acta* 88: 633.
Fujiwara, K., Yamana, H., Fuji, T., and Moriyama, H. (2001). Solubility product of plutonium hydrous oxide. *J. Nucl. Fuel Cycle Environ.* 7: 17.
Walther, C., Cho, H.R., and Fanghänel, T. (2004). Measuring multimodal size distributions of aquatic colloids at trace concentrations. *Appl. Phys. Lett.* 85: 6329.
Denecke, M.A., Rothe, J., Dardenne, K. et al. (2005). The INE-beamline for actinide research at ANKA. *Phys. Scr.* T115: 1001.
Reich, T. (2005). Speciation analysis with synchrotron radiation. *Anal. Bioanal. Chem.* 383: 10.
Reich, T., Reich, T.Y., Amayri, S. et al. (2007). Application of EXAFS spectroscopy to actinide environmental science. Proceedings of the 13th International Conference on X-ray Absorption Fine Structure XAFS13, Stanford, July 9–14, 2006. *AIP Conf. Proc.* 882: 179.

23

Dosimetry and Radiation Protection

23.1 Dosimetry

The units used in radiation dosimetry are summarized in Table 23.1. The energy dose and the ion dose are also used in radiation chemistry, whereas the equivalent dose is only applied in radiation biology and in the field of radiation protection.

The energy dose D is the differential energy $\mathrm{d}E$ transmitted by ionizing radiation to the mass $\mathrm{d}m$ of density ρ in the volume $\mathrm{d}V$:

$$D = \frac{\mathrm{d}E}{\mathrm{d}m} = \frac{\mathrm{d}E}{\rho\,\mathrm{d}V} \tag{23.1}$$

In contrast to the ion dose, the energy dose is independent of the nature of the absorbing substance. The integral energy dose is

$$E = \int D\mathrm{d}m \quad (\text{SI unit 1 J}) \tag{23.2}$$

Because direct determination of the energy dose D is difficult, the ion dose J is measured in radiation dosimeters. This is the charge $\mathrm{d}Q$ of ions of one sign generated by the ionizing radiation in the volume $\mathrm{d}V$ of air containing the mass $\mathrm{d}m$:

$$J = \frac{\mathrm{d}Q}{\mathrm{d}m} = \frac{\mathrm{d}Q}{\rho\,\mathrm{d}V} \tag{23.3}$$

The unit of the ion dose is the roentgen (R). It is used in radiology and defined as the dose of X- or γ-rays that produces in air under normal conditions of temperature and pressure ions and electrons of one electrostatic unit each. From this definition, it follows that $1\,\mathrm{R} = 2.580 \cdot 10^{-4}\,\mathrm{C\,kg^{-1}}$ (1 C [Coulomb] = 1 A s). Because 34 eV is needed to produce one ion pair (ion + electron) in air, 1 R is equivalent to an energy absorption of $0.877 \cdot 10^{-2}\,\mathrm{J\,kg^{-1}}$ of air. At the same ion dose, the energy absorption in various substances can be rather different. However, for substances of interest in radiation protection (aqueous solutions and tissue), the energy absorption is similar to that in air. For example, an ion dose of 1 R of X-rays or γ-rays in the energy range between 0.2 and 3.0 MeV causes an energy absorption of $0.97 \cdot 10^{-2}\,\mathrm{J\,kg^{-1}}$ in water, $0.93 \cdot 10^{-2}\,\mathrm{J\,kg^{-1}}$ in soft tissue, and $0.93 \cdot 10^{-2}\,\mathrm{J\,kg^{-1}}$ in bone. Therefore, in the praxis of radiation protection, the following approximative relation is valid:

$$1\,\mathrm{R} \approx 10^{-2}\,\mathrm{Gy} = 10^{-2}\,\mathrm{J\,kg^{-1}} \tag{23.4}$$

Nuclear and Radiochemistry: Fundamentals and Applications,
Fourth Edition. Jens-Volker Kratz.

Table 23.1 Radiation doses and dose rates.

Dose	Symbol	Unit	Abbreviation	SI unit
Energy dose	D	gray	Gy	$1\,\mathrm{Gy} = 1\,\mathrm{J\,kg^{-1}}$
Formerly		rad	rd	$1\,\mathrm{rd} = 0.01\,\mathrm{J\,kg^{-1}}$
Ion dose	J	roentgen	R	$1\,\mathrm{R} = 2.580 \cdot 10^{-4}\,\mathrm{C\,kg^{-1}}$
Equivalent dose	H	sievert	Sv	$1\,\mathrm{Sv} \approx 1\,\mathrm{J\,kg^{-1}}$
Formerly		rem	rem	$1\,\mathrm{rem} \approx 0.01\,\mathrm{J\,kg^{-1}}$

Dose rate	Unit	SI unit
Energy dose rate $\mathrm{d}D/\mathrm{d}t$	$\mathrm{Gy\,s^{-1}}$ ($\mathrm{Gy\,h^{-1}}$, …)	$1\,\mathrm{Gy\,s^{-1}} = 1\,\mathrm{J\,kg^{-1}\,s^{-1}}$
Formerly	$\mathrm{rd\,s^{-1}}$ ($\mathrm{rd\,h^{-1}}$, …)	$1\,\mathrm{rd\,s^{-1}} = 0.01\,\mathrm{J\,kg^{-1}\,s^{-1}}$
Ion dose rate $\mathrm{d}J/\mathrm{d}t$	$\mathrm{R\,s^{-1}}$ ($\mathrm{R\,h^{-1}}$, …)	$1\,\mathrm{R\,s^{-1}} = 2.580 \cdot 10^{-4}\,\mathrm{C\,kg^{-1}\,s^{-1}}$
Equivalent dose rate $\mathrm{d}H/\mathrm{d}t$	$\mathrm{Sv\,s^{-1}}$ ($\mathrm{Sv\,h^{-1}}$, …)	$1\,\mathrm{Sv\,s^{-1}} \approx 1\,\mathrm{J\,kg^{-1}\,s^{-1}}$
Formerly	$\mathrm{rem\,s^{-1}}$ ($\mathrm{rem\,h^{-1}}$, …)	$1\,\mathrm{rem\,s^{-1}} \approx 0.01\,\mathrm{J\,kg^{-1}\,s^{-1}}$

Table 23.2 Radiation weighting factors w_R 1.

LET in water ($\mathrm{eV\,nm^{-1}}$)	Weighting factor w_R	Type of radiation
0.2–35	1	Photons (X- and γ-rays)
0.2–1.1	1	Electrons and positrons >5 keV
≈20	5	Slow neutrons <10 keV
≈50	20	Intermediate neutrons 0.1–2 MeV
	10	Fast neutrons 2–20 MeV
	5	Protons >2 MeV
≈130	20	α Particles
	20	High-energy ions

In order to take into account the biological effects of different kinds of radiation, radiation weighting factors w_R were introduced by the International Commission on Radiological Protection (ICRP) in 1990 (Table 23.2). The weighting factor w_R indicates the ratio of the degree of a certain biological effect caused by the radiation considered to that caused by X-rays or γ-rays at the same energy absorption. It is based on the experience gained in radiation biology and radiology.

The equivalent dose H is measured in sieverts (Sv) and defined as

$$H = w_R \cdot D \tag{23.5}$$

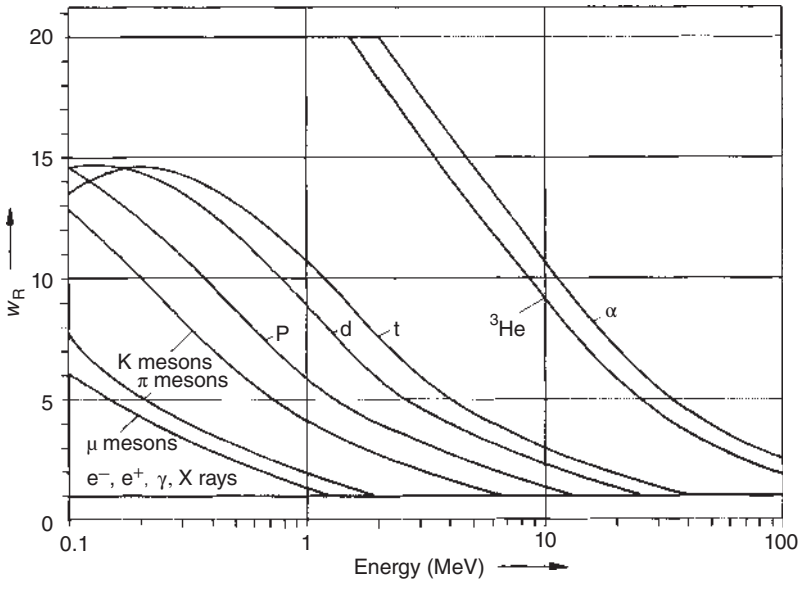

Figure 23.1 Weighting factor w_R for charged particles as a function of their energy.

where D is the absorbed energy dose, measured in Gy. Considering the effects of various radiations R on a special tissue T, the equivalent dose H_T received by this tissue is

$$H_T = \sum w_R \cdot D_{T,R} \tag{23.6}$$

$D_{T,R}$ is the absorbed dose averaged over the tissue T due to the radiation R. The sum is taken over all radiations R. In the case of low linear energy transfer (LET; Section 8.1), w_R is equal to 1 and $H_T = D_{T,R}$. Instead of the weighting factor w_R, the term quality factor Q of relative biological effectiveness f_{RBE} was used before 1990. An earlier, but similar, concept was the rem (radiation equivalent man, 1 rem = 10^{-2} Sv).

The advantages of the equivalent dose are that the biological effectiveness is directly taken into account and that equivalent doses received from different radiation sources can be added. However, the dimension J kg^{-1} is only correct if $w_R = 1$.

Weighting factors are assessed on the basis of the LET value. The influences of spatial ionization density and of temporal distribution of ionization have to be taken into account separately. Weighting factors for various particles and for γ-ray photons are plotted in Figure 23.1 and those for neutrons in Figure 23.2 as a function of the energy.

23.2 External Radiation Sources

Sensitive parts of the body with respect to external radiation sources are the hematogenous organs, the gonads, and the eyes. Less sensitive parts are the arms

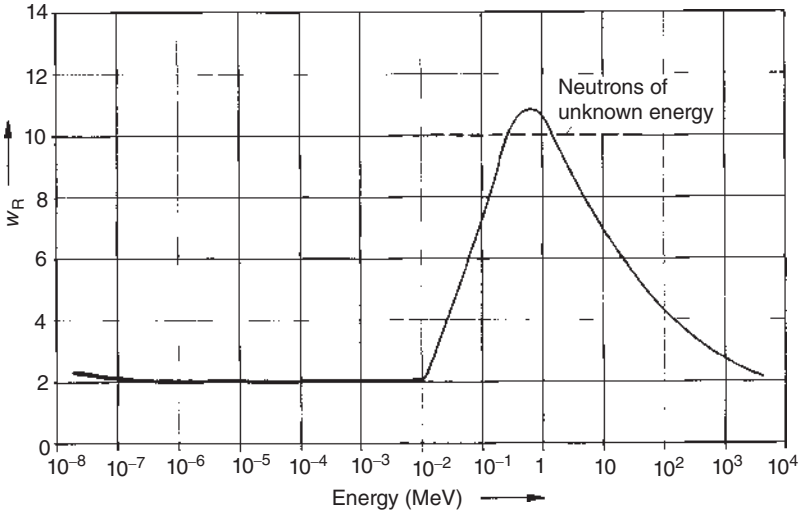

Figure 23.2 Weighting factor w_R for neutrons as a function of their energy.

and hands, the legs and feet, the head (except the eyes), and the neck. The ion dose rate transmitted by a point-like γ-radiation source of activity A at distance r is

$$\frac{dJ}{dt} = k_\gamma \frac{A}{r^2} \tag{23.7}$$

The dose rate constant k_γ for γ radiation depends on the energy of the γ-rays and on the decay scheme of the radionuclide. Values of k_γ for various radionuclides are listed in Table 23.3. For rough estimation, it is useful to know that a point-like radiation source of 1 GBq emitting γ-rays with energies of ≈1 MeV transmits an ion dose rate of about 0.03 R h^{-1} at a distance of 1 m.

The ion dose rate transmitted by a point-like β emitter can be calculated by an equation similar to Eq. (23.7),

$$\frac{dD}{dt} = k_\beta(r) \frac{A}{r^2} \tag{23.8}$$

In contrast to k_γ, however, $k_\beta(r)$ depends strongly on the distance because of the much stronger absorption of β particles in air; $k_\beta(r)$ is higher than k_γ by about 2 orders of magnitude. Below $r \approx 0.3 R_{max}$ (R_{max} = maximum range), a rough estimate is $k_\beta \approx 1$ Rm^2 h^{-1} GBq^{-1}.

The influence of the distance r indicates the importance of remote handling of higher activities.

23.3 Internal Radiation Sources

Internal radiation sources are always more dangerous than external ones because shielding is impossible and the incorporated radionuclides may be enriched in certain organs or parts of the body and affect them over long periods of time.

Table 23.3 Dose rate constants k_γ for various radionuclides (the frequency of the γ transitions is taken into account).

Radionuclide	k_γ (mGy m^2 h^{-1} GBq^{-1})	Radionuclide	k_γ (mGy m^2 h^{-1} GBq^{-1})
^{22}Na	0.32	^{82}Br	0.40
^{24}Na	0.49	^{85}Kr	0.0003
^{42}K	0.038	^{99m}Tc	0.016
^{51}Cr	0.0049	^{110m}Ag	0.40
^{52}Mn	0.48	^{123}I	0.019
^{54}Mn	0.13	^{124}Sb	0.24
^{56}Mn	0.24	^{131}I	0.057
^{59}Fe	0.17	^{132}I	0.31
^{58}Co	0.15	^{137}Cs + ^{137m}Ba	0.086
^{60}Co	0.35	^{140}Ba	0.032
^{64}Cu	0.032	^{144}Ce	0.0065
^{68}Zn	0.081	^{182}Ta	0.18
^{68}Ga	0.15	^{192}Ir	0.14
^{76}As	0.068	^{198}Au	0.062

With respect to radiotoxicity, possible storage in the body and half-lives of radionuclides are therefore most important. Removal from the body is characterized by the biological half-life, and the effective half-life $t_{1/2}$(eff) is given by the relation (Section 22.5)

$$\frac{1}{t_{1/2}(\text{eff})} = \frac{1}{t_{1/2}(\text{b})} + \frac{1}{t_{1/2}(\text{p})} \tag{23.9}$$

where $t_{1/2}$(b) and $t_{1/2}$(p) are the biological and physical half-lives, respectively. Physical half-lives and effective half-lives of some radionuclides in the human body are listed in Table 23.4. The latter half-lives depend largely on the part of the body considered.

Radiotoxicity depends on the radiation emitted by the radionuclide considered, the mode of intake (e.g. by air, water, or food), the size of the ingested or inhaled particles, their chemical properties (e.g. solubility), metabolic affinity, enrichment, effective half-life, and ecological conditions. The radiotoxicity of some radionuclides is listed in Table 23.5. The limits of free handling of radionuclides and the acceptable limits of radionuclides in air, water, and food are also laid down on the basis of their radiotoxicity.

Most of the properties mentioned in the previous paragraph are taken into account in the ALI and DAC concepts (ALI = Annual Limits of Intake; DAC = Derived Air Concentration, based on the ALI value); 1 ALI corresponds to an annual committed equivalent dose of 50 mSv.

Table 23.4 Physical half-lives $t_{1/2}$(p) and effective half-lives $t_{1/2}$(eff) of radionuclides in the human body.

Radionuclide	$t_{1/2}$(p)	Part of the body considered	$t_{1/2}$(eff)
T	12.323 yr	Body tissue	12 d
^{14}C	5730 yr	Fat	12 d
^{24}Na	14.96 h	Gastrointestinal tract	0.17 d
^{32}P	14.26 d	Bone	14 d
^{35}S	87.5 d	Testis	76 d
^{42}K	12.36 h	Gastrointestinal tract	0.04 d
^{51}Cr	27.7 d	Gastrointestinal tract	0.75 d
^{55}Fe	2.73 yr	Spleen	390 d
^{59}Fe	44.5 d	Gastrointestinal tract	0.75 d
^{60}Co	5.272 yr	Gastrointestinal tract	0.75 d
^{64}Cu	12.7 h	Gastrointestinal tract	0.75 d
^{65}Zn	244.3 d	Total	190 d
^{90}Sr	28.64 yr	Bone	16 yr
^{95}Zr	64.0 d	Bone surface	0.75 d
^{99}Tc	$2.1 \cdot 10^5$ yr	Gastrointestinal tract	0.75 d
^{106}Ru	373.6 d	Gastrointestinal tract	0.75 d
^{129}I	$1.57 \cdot 10^7$ yr	Thyroid	140 d
^{131}I	8.02 d	Thyroid	7.6 d
^{137}Cs	30.17 yr	Total	70 d
^{140}Ba	12.75 d	Gastrointestinal tract	0.75 d
^{144}Ce	284.8 d	Gastrointestinal tract	0.75 d
^{198}Au	2.6943 d	Gastrointestinal tract	0.75 d
^{210}Po	138.38 d	Spleen	42 d
^{222}Rn	3.825 d	Lung	3.8 d
^{226}Ra	1600 yr	Bone	44 yr
^{232}Th	$1.405 \cdot 10^{10}$ yr	Bone	200 yr
^{233}U	$1.592 \cdot 10^5$ yr	Bone, lung	300 d
^{238}U	$4.468 \cdot 10^9$ yr	Lung, kidney	15 d
^{238}Pu	87.74 yr	Bone	64 yr
^{239}Pu	$2.411 \cdot 10^4$ yr	Bone	200 yr
^{241}Am	432.2 yr	Kidney	64 yr

Source: Modified from International Commission on Radiological Protection (1993).

Table 23.5 Radiotoxicity of radionuclides and radioelements.

Radiotoxicity	Radionuclides and radioelements
Group I: very high	^{90}Sr, Ra, Pa, Pu
Group II: high	^{45}Ca, ^{55}Fe, ^{91}Y, ^{144}Ce, ^{147}Pm, ^{210}Bi, Po
Group III: medium	^{3}H, ^{14}C, ^{22}Na, ^{32}P, ^{35}S, ^{36}CI, ^{54}Mn, ^{59}Fe, ^{60}Co, ^{89}Sr, ^{95}Nb, ^{103}Ru, ^{106}Ru, ^{127}Te, ^{129}Te, ^{137}Cs, ^{140}Ba, ^{140}La, ^{141}Ce, ^{143}Pr, ^{147}Nd, ^{198}Au, ^{199}Au, ^{203}Hg, ^{205}Hg
Group IV: low	^{24}Na, ^{42}K, ^{64}Cu, ^{52}Mn, ^{76}As, ^{77}As, ^{85}Kr, ^{197}Hg

23.4 Radiation Effects in Cell

With respect to radiation protection, the relation between radiation dose and damage, in particular the effects of radiation in cells, is of the greatest importance.

Cells contain about 70% water, and the radiation is largely absorbed by interaction with the water molecules and the formation of ions, free radicals, and excited molecules. The ions may react at ionizable positions of the DNA (e.g. phosphate groups). Radicals, such as ·OH and ·H, and oxidizing products, such as H_2O_2, may be added at unsaturated bonds, or they may break the bonds between two helices. Excited molecules may transfer the excitation energy to the DNA and also cause breaks. A large number of different products of DNA damage have been identified.

On the other hand, living cells contain natural radical scavengers, and as long as these are present in excess of the radiolysis products, they are able to protect the DNA. However, when the concentration of radiolysis products exceeds that of the scavengers, radiation damage is to be expected. This leads to the concept of a natural threshold for radiation damage which should at least be applicable for low-LET values and low radiation intensities, for example, for low local concentrations of ions and radicals. The scavenging capacity may vary with the age and physical conditions of the individuals concerned.

Furthermore, the cells are protected by various repair mechanisms with the aim of restoring damages. Details of these mechanisms are not known, but most single-strand breaks are correctly repaired. Sometimes, however, repair fails (e.g. by replacement of a lost section by a wrong base pair), which may lead to somatic effects, such as cancer or inheritable DNA defects. Results obtained with cells of living organisms and samples studied in the laboratory indicate that repair mechanisms are more effective in living organisms, that is, in the presence of surrounding cells and body fluids.

γ-Rays exhibit low-LET values and cause only few ionizations in a DNA segment several nanometers in length, corresponding to an energy transmission of up to about 100 eV. If this energy is distributed over a large number of bonds, these will not receive enough energy to break and the DNA segment will not be changed. However, formation of clusters of ions by low-LET radiation will increase the risk

of damage. This risk is appreciably higher in the case of the high-LET values of α particles, for example, of high ionization density. At low-LET values, the ratio of double-strand breaks to single-strand breaks is about 3 : 100, whereas at high-LET values, this ratio is much higher. Repair of double-strand breaks is more difficult and takes more time (on average several hours) than that of single-strand breaks (on average ≈10 minutes). Therefore, the probability of repair errors causing permanent damage or mutation is much higher in the case of double-strand breaks. Consequently, chromosome aberrations are only observed after double-strand breaks.

In the nucleus of a single cell, a γ-ray photon produces up to about 1500 ionizations (on average ≈70), up to 20 breaks of single-strand DNA (on average ≈1), and only up to a few breaks of double-strand DNA (on average ≈0.04). For an α particle crossing a nucleus, the corresponding values are: up to 10^5 ionizations (on average 23 000), up to 400 single-strand breaks (on average 200), and up to 100 double-strand breaks (on average 35).

With respect to the damage, the dose rate (i.e. the time during which a certain dose is transmitted to the body) is of great importance. This is illustrated by the following example. A low-LET dose of 3 Gy produces ≈3000 single-strand breaks and ≈100 double-strand breaks in every cell of a human body. If this dose is transmitted within a short time of several minutes, the damage in the cells cannot be repaired and may result in death. However, if the same dose is spread over a period of about a week, only aberrations in the chromosomes are observed.

With respect to radiation effects, two types of cells are distinguished: those involved in the function of organs (e.g. in bone marrow, liver, and the nervous system) and those associated with reproduction (gonads). In the first group, radiation damage may give rise to somatic effects (e.g. cell death or cancer) and in the second group, to genetic effects (e.g. effects transferred to future generations).

23.4.1 BNCT

A medical strategy against cancer called boron neutron capture therapy (BNCT) is applied since quite some time at nuclear reactors operating an external neutron beamline. It is based on the nuclear reaction $^{10}B(n, \alpha)^7Li$, where the short-lived intermediate nucleus ^{11}B decays into an α-particle and a ^7Li both having a recoil range shorter than the cell dimension, so that the total LET is dissipated completely inside the cell. This leads with high probability to the death of the cell. The highly enriched ^{10}B must be brought into the cell; this is done by binding the ^{11}B to an amino acid (e.g. phenylalanine), and the ^{10}BPA is injected into the body of the patient. Within about an hour's time, the ^{10}BPA penetrates the cell wall and is welcomed by the cell as foodstuff. Cancer cells have a food intake that is about six times higher than healthy cells, so that the tissue surrounding the tumor receives a six times lower LET dose than the tumor. The LET in the tumor cell is so high that breaks of double-strand DNA occur with high probability often leading to the death of the tumor cell. A critical aspect remains, however, because the neutron beam must penetrate the patient's body to arrive at the tumor and this cannot occur without a certain damage of "innocent" tissue. Figure 23.3 illustrates the $^{10}B(n, \alpha)^7Li$ reaction.

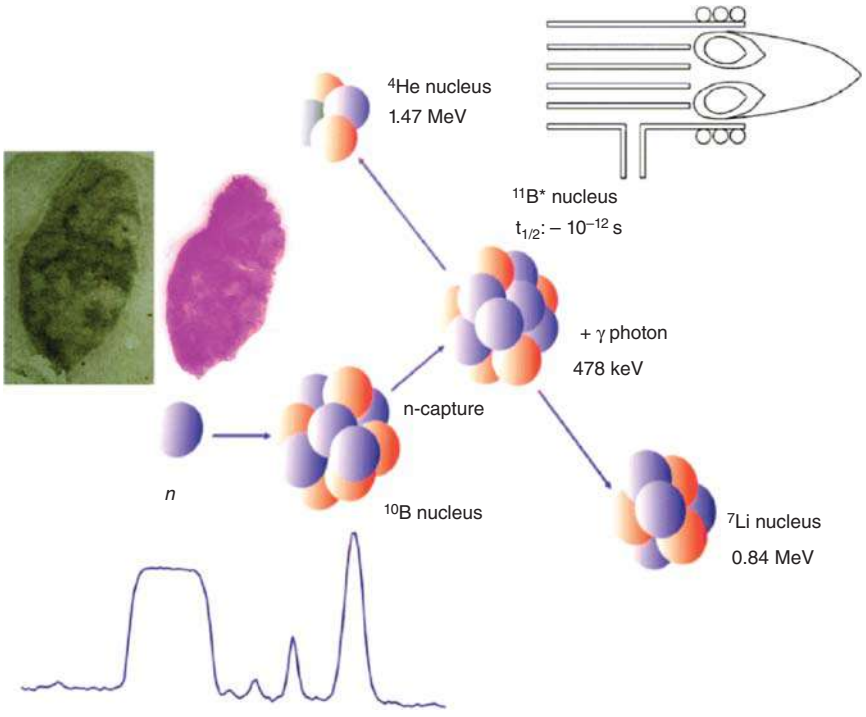

Figure 23.3 Neutron capture on ^{10}B leads to an excited ^{11}B emitting, after $\approx 10^{-12}$ seconds, a Υ-ray photon of 478 keV, an α-particle of 1.47 MeV, and a ^{7}Li nucleus of 0.84 MeV characterized by high linear energy transfer (LET) and very short range (<10 μm). To reconstruct the radiation dose in the malignant cells, (i) the boron concentration in the tissue must be determined, e.g. by ICP-MS (top) after decomposition of the sample matrix (middle) by wet ashing in a microwave, and (ii) the neutron fluence must be known. Bottom: Time spectrum of the incoming neutron bunch followed by the photon, the α-particle, and ^{7}Li.

We now turn to a completely new development in BNCT: About the end of the 1990s, Pinelli and Zonta (Pinelli et al. 1996, 2001) proposed and then, in 2001, performed the first in the world extracorporeal application of BNCT to an isolated liver, suffering from diffuse metastases. This therapeutic project had been conceived some 20 years before and elaborated in detail during several long series of experimental researches (Pinelli et al. 2002). It deals with a new concept from many points of view. In 2001, for the first time, an abdominal organ was treated with BNCT; an extracorporeal irradiation was carried out; the target of thermal neutrons was the liver, which is known to be highly sensitive to radiations. The neutron treatment was performed using not a collimated neutron beam, as in traditional BNCT applications, but in an isotropic neutron field. Moreover, the diseased part of the organ was pre-treated, i.e. (i) deprived of all its blood content through washing and (ii) made hypothermic at a temperature near 4 °C by flushing it with a chilled Wisconsin solution. This modality of neutron irradiation warrants several precious advantages, improving the specificity, selectivity, and efficacy of BNCT. Actually,

in comparison with traditional BNCT applications, the intrinsic specificity of neutron irradiation was enhanced by avoiding the dangerous damage to endothelial cells and lowering to a minimum the background irradiation: these results derive from the removal of blood content before irradiation. Secondly in this project, the selectivity of action was assured because the diseased organ, after being loaded with the boron compound, was extracted, dipped into a homogeneous neutron field and then reconnected. In this way, any interfering effect due to irradiation of other organs or tissues is abolished. Finally, the efficacy of BNCT was exalted because not only a portion but also the whole volume of the diseased organ was exposed to the neutron flux so that the dose of the absorbed radiation was the same in any known or unknown tumor nodule, depending merely on boron concentration reached in its cells.

In December 2001, after the approval of the project as compassionate therapeutic action by the Ethics Committee of Pavia San Matteo Hospital and the Italian Ministry of Health, Pinelli et al. performed the first clinical application of BNCT on an isolated human liver. In 2003, a second patient was submitted to the same procedure. According to the guidelines approved for the clinical protocol, the candidates should be of young age (<55 years), with liver-only metastases of a colon carcinoma already radically excised and should have all vital organs in good health without serious impairment of liver functions.

The adopted procedure consisted basically of three phases. The early surgical phase included the liver perfusion for two hours with a solution of ^{10}BPA, a biopsy of metastatic and normal hepatic tissue after one hour of perfusion and another biopsy at the end of it in order to verify a favorable concentration ratio of ^{10}B between the samples (higher than 4 : 1) and then the hepatectomy. In the radiotherapeutic phase, the isolated liver is washed and chilled, transferred to the thermal column of Triga Mark II nuclear reactor of the University of Pavia and irradiated for about 10 minutes. Then, in the late surgical phase, the liver was reconnected to the patient and the extracorporeal bypass was removed.

The first patient was a man, 48 years old, with 14 liver synchronous metastases of a sigmoid carcinoma, operated 7 months before. The residual liver function, as expressed by galactose elimination capacity (GEC), was 63% (with normal values higher than 70%) and then slightly impaired. The dose of ^{10}BPA was infused through a colic vein afferent to the portal tree. The whole radio-surgical procedure lasted 21 hours. The ratio between the ^{10}B concentrations in tumor and normal liver tissues resulted to be near 6 : 1.

The second patient was a 39 years old male, who was affected by 11 diffuse, small and large, hepatic metastases of a rectum carcinoma already operated. In his pre-operative assessment, three negative features were noteworthy: his residual liver function was poor (GEC = 58%), the vascular anatomy of the liver was abnormal (two arterial peduncles to the liver), and the cardiac function was deficient because of a dilatative cardiomyopathy with a stroke volume of 40% (normal value 70%). ^{10}B concentrations in tumor and normal tissue were comparable to the ones of the first patient, and the duration of the procedure was shorter (18 hours and 40 minutes), in

spite of the difficulties raised by the operative correction of the mentioned vascular anomaly.

The liver irradiation position was built inside the thermal column of the 250 kW TRIGA Mark II of the University of Pavia. The γ-background coming from the reactor core was lowered with two bismuth screens, whose overall thickness was 20 cm. In the irradiation channel, the neutron flux was measured with Au and Cu wires and foils and the γ-dose was measured by BeO thermoluminescence detectors (TLD) dosimeters.

For the boron concentration in hepatic tissues, a method based on the α-particle spectrometry was developed. Thin tissue samples were irradiated in a position of the thermal column and the α-particles emitted from the reaction $^{10}B(n, \alpha)^{7}Li$ were detected. When the boron concentrations were known in the liver (CH) and in the tumor (CT), the respective doses DH and DT produced by the known neutron fluence were calculated. In Table 23.6, the concentrations measured in liver and tumor samples of the two patients are listed together with the doses corresponding to the neutron fluence.

For the irradiation, the liver was located inside two Teflon bags and then positioned in a circular Teflon container. A semi-automatic trolley was used to position the liver inside the irradiation channel. Using a remote control, the cylindrical holder was rotated by 180° halfway through the irradiation time, in order to increase the uniformity of the thermal neutron flux distribution.

The first three weeks after BNCT were very similar in both patients and proved the heavy impact of the procedure on their clinical conditions. The patients, who were admitted after the operation to a surgical intensive care unit, remained in general anesthesia with controlled ventilation for a period of three and four weeks; then, a gradual reversal of anesthetic agents was adopted until the post-operative recovery. During this period, the most evident symptoms were characterized for both patients by rhabdomyolysis, with early brutal elevation of creatine kinase and myoglobin in blood, altered endothelial barrier permeability, with huge imbibition of subcutaneous tissue, especially in the face, and mental confusion. Other signs of this complex derangement were due to liver insufficiency with jaundice and renal failure from a likely acute tubular necrosis with transitory anuria, which required renal replacement therapy (extracorporeal hemodialysis). Laboratory tests showed

Table 23.6 Values of the boron concentrations and of the doses produced by a neutron fluence in the normal liver and in the tumor of the two treated patients.

	Boron concentration (ppm)		Absorbed dose (Gy)	
	First patient	**Second patient**	**First patient**	**Second patient**
Tumor	47 ± 2	45 ± 5	18 ± 1	18 ± 1
Liver	8 ± 1	8 ± 1	6 ± 0.3	6 ± 0.3
Tumor/liver	5.9	5.6	3	3

an early important increase of the values for hepatic microsomal enzymes like aspartate aminotransferase AST and alanine aminotransferase ALT. These clinical and hematochemical aberrations were present in both patients with the same temporal cadence and evolution toward recovery.

In the fourth week after BNCT, the clinical evolution of the two patients became different. The first one kept on improving in health with a progressive return to normal of all altered laboratory values. In particular, neoplastic markers turned negative and also the residual liver function became normal (73% for GEC). The patient was discharged 40 days after BNCT in a good state of health. The second patient was suffering from a dilatative cardiomyopathy and the clinical situation worsened toward the end of the first month: he indeed incurred subsequent circulatory complications consisting in a thrombosis of the hepatic artery and later on a cardiac congestive failure, which caused his death on the 33rd p.o.d.

The subsequent post-operative course in the surviving patient was uneventful until one and a half year after BNCT. A gradual disappearance of the low-density images took place in the liver structure; in their place, apparently normal hepatic tissue showed up again. The patient, who had refused any anti-neoplastic regimen, enjoyed good health and got married too.

Twenty months after BNCT, announced by an increase in blood of the value for carcino-embryonic antigen (CEA; a marker of gastro-intestinal tumors), an image of a recurrence appeared in a CT scan. It was external, but adjacent to the liver left lobe. A new operation was performed in the patient with excision of a nodule 23 mm in width and of a diaphragmatic scar 2 mm in thickness. At the pathological examination, both samples resulted site of focal infiltrations of colon carcinoma cells. After the operation, the value for CEA returned to normal. The patient accepted to start again chemotherapy and another year followed without problems. Thirty-three months after BNCT, there was a new increase of the value for CEA and multiple images of abdominal recurrences appeared at a CT scan. They resulted resistant to new cycles of chemotherapy and immunotherapy. Also, a further operation in February 2005 for debulking the neoplastic masses was ineffective, and the patient died on 04 August (44 months after BNCT).

These are some (not all) informative paragraphs of the publication by Pinelli et al. where many very special medical conclusions are omitted here.

At the TRIGA Mark II Mainz reactor, this news caused much interest, and, under the guidance of the responsible leader of the reactor operation, G. Hampel, a research group was founded with the goal to find out whether a BNCT project similar to the Pavia project could be established at the TRIGA Mainz. This project would also involve the university clinic for transplantation surgery and the clinic for radiology and radiation therapy. The Ethics Committee of the Mainz University Hospital agreed that 15 patients with metastases in part of their liver needing liver surgery could be asked to agree on their free will to accept a ^{10}BPA injection prior to their surgery. This way, after surgery, samples of liver tissue were made available for boron analyses, asking for the ratio between the ^{10}B concentrations in tumor and normal liver tissues and how this could be improved. Monte Carlo simulations of the radiation fields inside the thermal column of the reactor were performed (Hampel et al.

2009). The basic characteristics of the radiation field in the thermal column as beam geometry, neutron and γ ray energies, angular distributions, neutron flux, as well as absorbed γ and neutron doses were determined in a reproducible way. To determine the mixed irradiation field, TLD made of CaF_2:Tm with a newly developed energy-compensation filter system and LiF:Mg,Ti materials with different ^{6}Li concentrations and different thicknesses as well as thin gold foils were used (Nagels et al. 2009). The Monte Carlo code MCNP5 was used to calculate the biologically weighted dose for different ratios of the ^{10}B-concentration in tumor to normal liver tissue. The simulation results showed that the dosimetric goals were only partially met. To guarantee effective BNCT treatment, the organ has to be better shielded from all γ radiation (Blaickner et al. 2012). Boron determinations in blood and tissue samples are a crucial task especially for treatment planning, preclinical research, and clinical application of BNCT. The comparability of inductively coupled plasma mass spectrometry, quantitative neutron capture radiography, and prompt γ activation analysis for the determination of boron in biological samples was addressed. It was possible to demonstrate that three different methods relying on three different principles of sample preparation and boron detection can be validated against each other and yield consistent results for both blood and tissue samples. The samples were obtained during a clinical study for the application of BNCT for liver malignancies and therefore represent a realistic situation for boron analysis. Analyses with local resolution could be compared to hematological images and showed excellent agreement (Schütz et al. 2012). It was found that feeding of the organ with amino acid prior to the BNCT treatment increased the subsequent intake of the ^{10}BPA by the liver malignancies.

In summary, the techniques developed at Mainz were superior to those applied at Pavia. It is all-the-more unfortunate that the leader of the project, G. Hampel, left her position at the TRIGA Mainz. As a consequence, the BNCT project at Mainz fell into sleep and needs an active person to wake it up again.

23.5 Radiation Effects in Humans, Animals, and Plants

The effects of radiation on microorganisms, plants, and animals differ appreciably. From Table 23.7, it is evident that organisms at a low stage of evolution exhibit much higher radiation resistance than those at a higher evolutionary stage.

Two kinds of radiation exposure are distinguished: stochastic exposure (the effects are distributed statistically over a large population) and deterministic exposure (the effects are inevitable or intended, as in the case of deliberate irradiation, e.g. in radiotherapy).

The survivors of the bombs dropped on Japan in 1945 are the most important source of information about human whole-body irradiation. The health of about 76 000 people who had been exposed to doses of up to 7–8 Gy of instantaneous neutron and γ radiation and that of their children has been investigated in detail for 50 years. The frequency of leukemia observed as a function of dose is plotted in Figure 23.4. Following large-dose exposure, leukemia is first observed after a

Table 23.7 Effect of γ irradiation on enzymes, microorganisms, plants, animals, and humans.

Organism	Dose of inactivation (D_i) or 50% lethal dose within 30 d ($D_{50/30}$)	
Enzymes	$D_i > 20\,000$ Gy	
Viruses	$D_i = 300–5000$ Gy	
Bacteria	$D_i = 20–1000$ Gy	
Flowers	$D_i > 10$ Gy d^{-1}	During the growing season
Trees	$D_i > 1$ Gy d^{-1}	
Ameba	$D_{50/30} \approx 1000$ Gy	
Drosophila	$D_{50/30} \geq 600$ Gy	
Shellfish	$D_{50/30} \approx 200$ Gy	
Goldfish	$D_{50/30} \approx 20$ Gy	
Rabbit	$D_{50/30} \approx 8$ Gy	
Monkey	$D_{50/30} \approx 6$ Gy	
Dog	$D_{50/30} \approx 4$ Gy	
Man	$D_{50/30} \approx 4$ Gy	

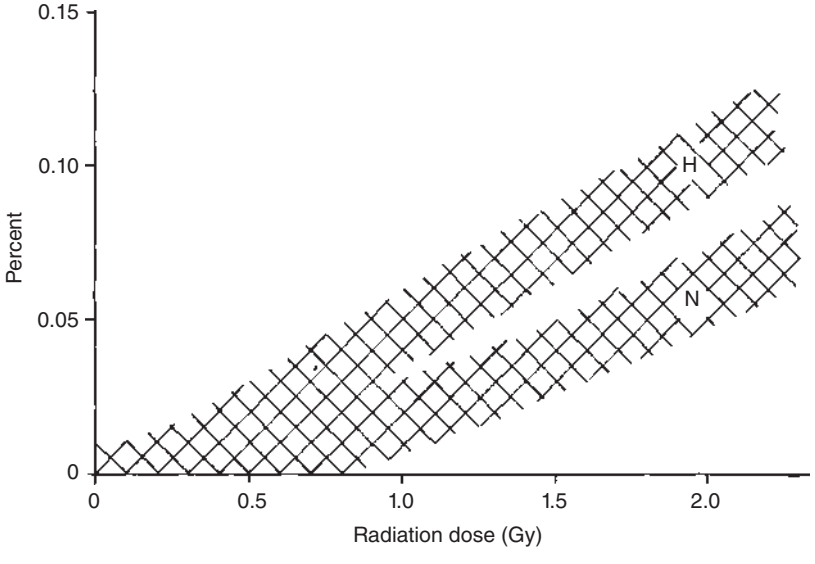

Figure 23.4 Frequencies of leukemia observed in Hiroshima (H) and Nagasaki (N): percentage of people as a function of the radiation dose.

latent period of about 2–3 years, reaches a peak frequency after about 6–8 years, and almost disappears after about 25 years. The large statistical variations are obvious from Figure 23.4. The higher frequency of leukemia after the Hiroshima explosion is explained by the higher neutron flux density of this nuclear explosion. With respect to the influence of γ irradiation, the results obtained from Nagasaki are more meaningful.

For other types of cancer, the excess malignancies are relatively low. They appear usually after a latent period of about 10 years, and their frequency increases with time.

Deterministic irradiation is applied in nuclear medicine for therapeutic purposes (Chapter 22). For tumor treatment, large doses are delivered to selected tissues. γ-Rays emitted by ^{60}Co (up to $2 \cdot 10^{14}$ Bq) or ^{137}Cs (up to $2 \cdot 10^{13}$ Bq) are preferred for irradiation of deeply located organs. The doses transmitted to malignant tumors vary between about 10 and 100 Sv, and the individual responses of patients to certain radiation doses may vary appreciably.

In order to take into account the radiation sensitivity of different tissues, tissue weighting factors w_T are introduced and the effective equivalent dose H_E received by the tissue E is defined by

$$H_E = \sum w_T \cdot H_T \tag{23.10}$$

where H_T is given by Eq. (23.6). H_E is also measured in Sv. For low-LET whole-body irradiation Σw_T is equal to 1 and $H_E = H_T$. The weighting factors w_T are used in nuclear medicine (therapeutic applications of radionuclides).

The possibility of genetic effects has received special attention since radiation-induced mutations were observed for drosophila in 1927. However, the vast majority of changes in the DNA are recessive. In mammals, no radiation-induced hereditary effects have been observed. Irradiation of the genitals of mice with ≈2 Sv for 19 generations did not lead to observable genetic changes, and careful investigations of the 75 000 children born to parents who were exposed to the irradiation released by the nuclear explosions in 1945 did not show any increase in the frequency of cancer or hereditary diseases.

Information about radiation effects due to ingestion or inhalation of radioactive substances is mainly obtained from the following groups:

- workers in uranium mines (inhalation of Rn and ingestion of U and its daughters);
- people living in areas of high Rn concentrations (inhalation of Rn);
- people who were painting luminous watch dials in Europe before 1930 (ingestion of Ra by licking the brushes);
- patients who received therapeutic treatment with ^{131}I or other radionuclides.

Therapeutic treatment of hyperthyroidism with ^{131}I led to large local doses of several hundred sieverts of β radiation, but with respect to leukemia, no significant difference was observed in comparison to untreated people.

Investigation of tumor frequencies in animals after incorporation of ^{90}Sr or ^{226}Ra, or irradiation with X-rays or electrons, indicates a threshold dose of ≤5 Gy, below

Table 23.8 Effects of accidental radiation exposure on humans (approximate values).

Dose	Effects
Whole-body irradiation	
0.25 Sv	No clinically recognizable damage
0.25 Sv	Decrease of white blood cells
0.5 Sv	Increasing destruction of the leukocyte-forming organs (causing decreasing resistance to infections)
1 Sv	Marked changes in the blood picture (decrease of leukocytes and neutrophils)
2 Sv	Nausea and other symptoms
5 Sv	Damage to the gastrointestinal tract causing bleeding and ≈50% death
10 Sv	Destruction of the neurological system and ≈100% mortality within 24 h
Irradiation of the hands	
2 Gy	No proven effects
4 Gy	Erythema, skin scaling
6 Gy	Skin reddening, pigmentation
8.5 Gy	Irreversible degeneration of the skin
50 Gy	Development of non-healing skin cancer (amputation necessary)

which no effects are observed. The effects of large single doses on humans are summarized in Table 23.8.

Large irradiation doses applied to plants cause mutations which either improve the properties of the species or produce disadvantageous effects. Although irradiation of plant seeds results in a ratio of only about 1 : 1000 of advantageous to harmful effects, new plant variations have been obtained by selection and cultivation of the few plants exhibiting improved properties. For example, most of the grain grown today in Scandinavian countries consists of radiation-produced species showing greater resistance to the cold weather conditions.

In the range of low radiation doses, reliable conclusions with respect to radiation effects on humans are difficult because malignancies or mortalities caused by radiation have to be calculated from the difference between those observed under the influence of radiation and those without radiation and are therefore very uncertain. For example, any significant increase in cancer or malignant mortality of the population in the United States, United Kingdom, Canada, France, Sweden, Finland, China, and other countries due to the natural background in the range of dose rates between about 1 and 5 $\mathrm{mSv\,yr^{-1}}$ has not been found. Furthermore, except for uranium miners, a statistically proven relation between the frequency of lung cancer and the concentration of Rn in the air could not be established, although such a relation is assumed to exist.

Because of the uncertainties caused by the impossibility of obtaining statistically significant data, the construction of dose–effect curves is difficult in the range

of small doses <0.1 Sv or small dose rates <0.5 Sv yr^{-1}. This is also evident from Figure 23.4, in which the frequency of leukemia in the populations of Hiroshima and Nagasaki after receiving relatively large doses is plotted as a function of the dose. In the range of doses <0.2 Sv, the statistical errors are appreciably greater than the effects.

Several assumptions are made for the range of small doses:

- a linear increase of the effects with the dose (ICRP, recommendation);
- a threshold at about 50 mSv, below which there is no increase of cancer or other radiation-induced diseases (this assumption is favored by many radiologists);
- a quadratic linear model assuming an initial increase with the square of the dose in the range of small doses, followed by a linear increase.

23.6 Non-occupational Radiation Exposure

Average equivalent dose rates received from natural radiation sources are listed in Table 23.9. The values vary appreciably with the environmental conditions. The influence of cosmic radiation increases markedly with the height above sea level, and terrestrial radiation depends strongly on the local and the living conditions.

The largest contribution to the everyday radiation dose of the population comes from the concentration of Rn and its daughter products in the air, as can be seen from Table 23.9. The concentration of ^{222}Rn is relatively high in regions of high uranium concentration in the ground and in poorly ventilated housing built of materials containing small amounts of U, Ra, or Th. Accordingly, the dose rate varies considerably (e.g. between about 0.3 and 100 mSv yr^{-1} in the United Kingdom, on average 1.2 mSv), but epidemiological investigations have failed to exhibit any statistically significant correlation between these different radiation doses and lung cancer. Only at larger doses is such a correlation evident: for example, for uranium miners working from 1875 to 1912 in the Erzgebirge region, 25–50% of these miners died from lung cancer caused mainly by the decay products of ^{222}Rn present in the form of aerosols in the air.

Some caves in granitic rocks containing relatively high concentrations of Rn are used for radiotherapy of the respiratory tract. At activity levels of Rn in domestic air <400 Bq m^{-3}, carcinogenic effects are not proven, but action is proposed for dwellings containing more than 200–600 Bq of Rn per cubic meter of air.

Average equivalent dose rates due to artificial radiation sources are listed in Table 23.10. These dose rates originate from the application of X-rays and radionuclides for diagnostic and therapeutic purposes, from various radiation sources applied in daily life, and from radioactive fallout.

23.7 Safety Recommendations

The assumption by the ICRP of a linear relation between radiation effects and dose (Section 23.5) implies the highest degree of safety. It may overestimate the risk, but

Table 23.9 Average radiation exposure by natural radiation sources.

	Equivalent dose (mSv yr^{-1})		
Kind of exposure	**Whole body and gonads**	**Bone**	**Lung**
External radiation sources			
Cosmic radiation[a)] (sea level, 50°N)	0.35	0.35	0.35
Terrestrial radiation[b)] (K; U, Th, and decay products)	0.49	0.49	0.49
Internal radiation sources			
Uptake by ingestion			
T	<0.000 02	—	—
^{14}C	0.016	0.016	0.016
^{40}K	0.19	0.11	0.15
^{87}Rb	0.003	—	—
^{210}Po	—	0.14	—
^{220}Rn + ^{222}Rn	0.02	0.02	0.02
^{226}Ra + ^{228}Ra	0.03	0.72	0.05
^{238}U	0.0008	—	—
Uptake by inhalation			
^{220}Rn	—	—	1.75[c)]
^{222}Rn	—	—	1.30[c)]
Sum	≈1.10	≈1.85	≈4.10

a) On the ground, locally up to ≈2 Sv yr^{-1}. Intensity of cosmic radiation increases by a factor of ≈1.6 per 1000 m above sea level.
b) Locally up to ≈4.3 Sv yr^{-1}. On average, in the open air ≈25% less than in buildings. Minimum values ×1/10, maximum values ×10 of the values listed.
c) Values for brick buildings and 3.5-fold exchange of air per hour. In concrete buildings without exchange of air, the values are higher by a factor of 4–7.

for safety reasons, its application is recommended. In the linear ICRP approach, the risk L_c of cancer is assumed to be given by

$$L_c = 0.05 H_E \tag{23.11}$$

In this equation, the risk of cancer is assumed to be 100% for an effective equivalent dose of 20 Sv. The equation is based on the probabilities listed in Table 23.11. In order to take into account that a dose delivered with a relatively low dose rate over a longer period of time has an appreciably smaller effect than a single dose, a dose reduction factor of 2 is recommended for smaller dose rates. However, in the report of the United Nations Scientific Committee on the Effects of Atomic Radiation

Table 23.10 Radiation exposure by artificial radiation sources.

Kind of exposure	Single radiation dose: Local dose	Single radiation dose: Whole-body and gonad dose	Average radiation dose per capita of the population (mSv yr^{-1})
Medical applications			
External radiation sources (medical application of X-rays or radionuclides)			
Diagnosis	1–10 mSv	0.1–1 mSv	≈0.5
Therapy	Up to 50 Sv	50 mSv	≈0.01
Internal radiation sources (medical application of radionuclides such as ^{99m}Tc)			
Diagnosis	1–1000 mSv	0.1–10 mSv	≈0.02
Therapy	10 Sv	50 mSv	<0.01
Other radiations			
Technical applications of radionuclides and ionizing radiation	—	—	<0.02
Luminous dials	—	0.3 mSv yr^{-1}	<0.01
Occupational radiation exposure	500 mSv yr^{-1}	50 mSv yr^{-1}	<0.001
Radioactive fallout	a)	a)	<0.1
Nuclear installations	a)	a)	<0.01
Sum			0.6–0.7

a) In severe accidents, such as the Chernobyl accident, doses up to several sieverts have been transmitted.

Table 23.11 Probability coefficients assessed for stochastic detrimental effects.

Population sector	Probability (% per Sv): Fatal cancer	Non-fatal cancer	Severe hereditary effects
Adult workers	4	0.8	0.8
Whole population	5	1.0	1.2

Source: International Commission on Radiological Protection (1990)/Elsevier.

(UNSCEAR) in 1993, it is noted that a reduction factor between 2 and 10 is more appropriate.

Another dose concept is that of the collective dose. It is based on the assumption that cancer is induced by a stochastic single process, independently of the dose rate and the dose fractionation, and it implies that the detriment is the same whether one person receives 20 Sv or 20 000 persons receive 1 mSv each. In both cases, the

Table 23.12 Recommended dose limits.

Dose	Occupational	Public
Effective dose	20 mSv yr^{-1} a)	1 mSv yr^{-1} b)
Equivalent dose		
In the lens of the eye	150 mSv	15 mSv
In the skin	500 mSv	50 mSv
In the hands and feet	500 mSv	50 mSv

a) Averaged over five years, but in one year, 50 mSv should not be exceeded.
b) May be exceeded as long as the five-year dose does not exceed 5 mSv.
Source: Modified from International Commission on Radiological Protection (1990).

collective dose is 20 man sieverts (man Sv) and there should be a 100% probability of one disease of cancer. The collective dose concept is often applied to assess the effect of the natural radiation background. At an average level of 3 mSv yr^{-1}, 0.015% of the population should die each year due to natural radiation. As the frequency of deaths by cancer is about 0.2% per year, it is not possible to confirm the collective dose concept by epidemiological investigations.

In the committed dose concept, also introduced by the ICRP, the total dose contribution to the population over all future years due to a specific release or exposure is considered. The committed dose is defined as the time integral per capita dose rate between the time of release and infinite time and is measured in Sv

$$H_{\mathrm{comm}}(t) = \int_t^{\infty} \frac{\mathrm{d}H}{\mathrm{d}t}\mathrm{d}t \tag{23.12}$$

Similarly, a collective committed dose is obtained by integrating the collective dose.

Dose limits recommended by the ICRP (International Commission on Radiological Protection 1990) are listed in Table 23.12. With respect to possible genetic damage, an upper limit of 50 mSv in 30 years should not be exceeded. The maximum permissible single dose without consideration of genetic damage is 0.25 Sv. At this dose, clinical injuries are not observed (Table 23.8). To take into account the different sensitivity of various organs and parts of the human body, respectively, coefficients and weighting factors were published in 1991 by the ICRP (International Commission on Radiological Protection 1991).

23.8 Safety Regulations

Special regulations have been established for people working professionally with X-rays or with radioactive substances in radiology, nuclear medicine, in chemical or physical laboratories, technical installations, at accelerators, nuclear reactors, or in reprocessing and other technical plants. With respect to possible damage, in particular genetic damage, dose and dose rate limits are laid down.

Rooms are classified according to the activities permitted, for example, controlled areas and supervised areas, α laboratories and β laboratories.

In rooms in which high activities are handled, the stay should be as short as possible and the operations in these rooms should be restricted to a minimum.

Regular measurements of the dose rates are obligatory in all rooms in which radioactive substances are handled, and the doses received by the people working in these rooms have to be noted down. Furthermore, the rooms have to be checked regularly with respect to contamination. Finally, all people working in these rooms have to be supervised medically.

The radiation doses received by people working in radiochemical laboratories vary appreciably with the conditions. For example, continuous working with 1 GBq of a high-energy γ emitter (1 MeV) without shielding at a distance of 40 cm during eight hours transmits a dose of ≈1 mSv. If the radiation is shielded by 5 cm of lead, the dose is only ≈0.01 mSv and can be neglected. Shielding of β radiation is much simpler because it is largely absorbed in the samples and in the walls of the equipment used. However, bremsstrahlung has to be taken into account, particularly in the case of high-β activities. Because the intensity of bremsstrahlung increases with the energy of the β radiation and with the atomic number of the absorber, materials containing elements of low atomic numbers, such as Perspex, are most suitable absorbers. Generally, a shield of 1 cm thickness is sufficient for quantitative absorption of β radiation. Shielding of α radiation is unproblematic because it is absorbed in several centimeters of air.

Practical experience in handling radioactive substances and safety regulations has led to general rules for radiochemical laboratories concerning the distinction between laboratories, measuring rooms and storage rooms, the equipment used in the laboratories, the handling of radionuclides, radioactive waste, used air and waste water, and the supervision of those people working in the laboratories.

With respect to practical work with radioactive substances, the risk of a hazardous effect should be as low as possible, and below 0.1%. The following measures are recommended to keep radiation exposure to a minimum:

- an adequate distance to the radioactive substance;
- use of shielding, particularly in the handling of high activities;
- control of working place, equipment, hands, and clothing for radioactivity.

Safety regulations and rules for the operation of radiochemical laboratories depend strongly on the activities to be handled and on the kind of radiation emitted. In accordance with the classification by the International Atomic Energy Agency (IAEA), it is useful to distinguish between laboratories for low activities (type C), medium activities (type B), and high activities (type A). This classification is given in Table 23.13. Laboratories for handling higher activities are often classified according to the kind of radiation emitted by the radionuclides (α laboratories, β laboratories, γ laboratories).

Type C laboratories can be fitted out in normal chemical laboratories. The floors, walls, and benches should be free of grooves, and the ventilation should be good. It is recommended that all operations with radionuclides be carried out in tubs and

Table 23.13 Classification of laboratories for open handling of radioactive substances (IAEA recommendations).

	Type of laboratory		
Radiotoxicity of the radionuclide	**Type C (simple equipment)**	**Type B (better equipment)**	**Type A (hot laboratory)**
Very high	<10 μCi	10 μCi to 10 mCi	>10 mCi
High	<100 μCi	100 μCi to 100 mCi	>100 mCi
Medium	<1 mCi	1 mCi to 1 Ci	>1 Ci
Low	<10 mCi	10 mCi to 10 Ci	10 Ci

$1\ \text{Ci} = 3.7 \cdot 10^{10}$ Bq.
Factor 100 for storage in closed ventilated containers.
Factor 10 for simple wet chemical procedures.
Factor 1 for usual wet chemical procedures.
Factor 0.1 for wet chemical procedures with the danger of spilling, and simple dry procedures.
Factor 0.01 for dry procedures with the danger of production of dust.

that suitable containers be provided for solid and liquid waste. Because of the risk of incorporation, all mouth operations (e.g. pipetting with the mouth) are strongly forbidden. For the wiping of pipettes and other equipment, paper tissue is used. Monitors must be available at the working place, to detect radioactive substances on the equipment and to check hands and working clothes for radioactivity.

Type B laboratories require sufficient equipment for radiation protection, such as tongs for remote handling, lead walls constructed of lead bricks, lead-glass windows for handling γ emitters, and Perspex shielding for handling β emitters. The use of gloves is recommended. Dosimeters for the measurement of dose rates must be available. For handling α emitters, glove boxes are used that are equipped for the special chemical operations and may be combined in glove-box lines. Ventilation must be efficient, and people as well as laboratories must be supervised with care. Treatment of waste water and of solid and liquid radioactive waste needs special attention.

Radioactive contamination of the laboratories must be strictly avoided because reliable activity measurements would otherwise become impossible and low activities could no longer be measured. Therefore, careful handling of radioactive substances and regular activity checking in the laboratories are indispensible. Personal danger due to radioactive contamination is, in general, only to be feared in the case of high contamination of the laboratories and great carelessness.

Handling materials of high activity in type A laboratories require special installations, in particular hot cells equipped with instruments for remote handling.

All operations with radionuclides need careful preparation, and the time needed for that preparation increases with the activity to be handled. All operations should be as simple and as safe as possible, which implies the use of small numbers of receptacles. Boiling the solutions containing radioactive substances is to be avoided

because of the risk of spraying. Closed receptacles are preferable whenever possible. Often preliminary experiments with inactive substances are useful, in order to find the optimal conditions.

The cleaning of receptacles and other equipment is recommended immediately after the end of a chemical operation because radionuclides may enter the surface layers of glass and other materials by diffusion, with the result that cleaning becomes very difficult. For the purpose of decontamination, solutions containing carriers are often useful. All the parts used, the working place, the hands, and clothes must finally be checked carefully for radioactivity.

For the supervision of people working in radiochemical laboratories, pocket dosimeters (generally ionization dosimeters) and film dosimeters are used. The lower detection limits of these dosimeters vary between about 1 and 40 mR. Furthermore, hand–foot monitors are installed near the exit of the laboratories, by which external contamination can be detected. In the case of suspected internal contamination, the person is checked by means of a whole-body counter which allows the detection of γ-ray emitters with high sensitivity. The presence of natural ^{40}K contributes essentially to the γ activity in the body. Further, about 100 Bq of ^{137}Cs can be determined quantitatively.

If a radioactive substance is taken up by ingestion or inhalation, attempts are to be made to remove it as quickly as possible, before it might be incorporated into tissue where it could exhibit a relatively long biological half-life. For this purpose, complexing agents forming stable complexes with the radionuclides may be applied.

Monitors in the laboratory are used for control of the working place and the equipment, as well as for control of hands and working clothes. Counters with large sensitive areas (generally flow counters operating with methane) allow more exact control of the working place and the floor for contamination. Wiping tests are also very useful for contamination control. Humid filter papers or other absorbent materials used for wiping benches or floors are measured for α or β activity by means of a suitable counter. In this way, the radionuclide causing the contamination can also be identified.

Radioactive waste solutions can be handled in different ways: the solutions may be collected separately, according to the radionuclides, in labeled bottles. This makes sorting easy and separate processing possible. Alternatively, all radioactive waste solutions may be collected in tanks and processed together.

Waste water from radiochemical laboratories which may contain radioactive substances, for example, by mistake, must be checked for radioactivity. If the condition is such that the activity should not be higher than the acceptable limit for drinking water (e.g. 1 Bq l^{-1}), very sensitive methods are necessary to detect these low concentrations. For comparison, 1 Bq l^{-1} is the activity of 20 mg of natural K per liter, river water contains about 1 Bq l^{-1}, water from natural springs up to several kilobecquerels per liter, and rainwater sampled after test explosions of nuclear weapons contained up to 1 kBq l^{-1}. The safest method for determining concentrations on the order of 1 Bq l^{-1} is evaporation of about 1 l and measurement of the residue by means of a large-area low counter. This method makes it possible to detect several millibecquerels of α or β emitters.

In the off-gas system of radiochemical laboratories, filters are installed which retain aerosols and vapors. These filters have to be checked regularly for radioactivity and exchanged from time to time. Automated supervision of the off-gas is also possible. In this case, the activity is recorded continuously.

Combustible and non-combustible solid radioactive waste is often collected separately. Waste containing only short-lived radionuclides is usually stored until the activity has vanished. Solid waste containing long-lived radionuclides is collected in polyethylene bags, which are closed by welding, filled in drums, and taken to a central collecting station for radioactive waste.

23.9 Monitoring of the Environment

In many countries, radioactivity in the environment is continuously measured by means of monitoring stations, in particular at and in the neighborhood of nuclear power stations and other nuclear facilities. Monitors are installed at elevated positions or on the ground, to measure the radioactivity in the air and on the surface of the Earth, respectively. Furthermore, samples of rainwater and river water are taken at certain intervals.

For automated routine measurements, usually the γ activity is determined by means of Geiger–Müller or scintillation counters. Additional measurements are made by filtering off aerosols from the air and by taking samples of water, soil, or plants. The samples may be dried or processed by chemical methods for more detailed investigations. The α, β, or γ activities on the aerosol filters and in the processed samples are measured by means of proportional counters or α and γ spectrometers, by which the radionuclides can be identified.

The results of routine measurements at various stations are evaluated and can be fed into a computerized network in which all the data are collected. By suitable programs such as IMIS (Integrated Measuring and Information System for the surveillance of environmental radioactivity), the data can be evaluated further to give, at any time, an up-to-date overview of the radioactivity in various regions of the country.

The principal objective of radiation protection and monitoring is the achievement of appropriate safety conditions with respect to human exposure. Consequently, radionuclides in those parts of the environment which are of immediate influence on human life (e.g. air, foodstuffs, or surroundings) are taken into account by safety regulations and monitored. However, the effects of radionuclides in other parts of the environment, particularly in other living things, have not been investigated in detail, and the radioactivity in these parts is not kept under surveillance, even though radioactive fallout has been widely distributed in the natural environment and radioactive waste has been disposed of in remote areas, above all in the deep sea. Consequently, radiological protection and monitoring of the whole natural environment have found increasing interest in recent years.

23.10 Geological Disposal of Radioactive Waste

In 2013, the ICRP published its *Publication* 122 with the title "Radiological Protection in Geological Disposal of Long-lived Solid Radioactive Waste" that it had developed as a joint effort between the radiological protection community and the waste management community. It has brought those two communities closer together by fostering a common understanding of the basic concepts and the language used. Disposal of radioactive waste has been the primary subject of more ICRP publications than any other phase in the nuclear fuel cycle. This reflects not only the importance of the subject but also the unusual and challenging radiological protection considerations entailed.

Radioactive waste was first mentioned, if only in passing, in *Publication* 7 (ICRP 1966). The first ICRP publication dedicated specifically to radioactive waste disposal issues – *Publication* 46 – came two decades later (ICRP 1985). In this publication, two special features of radiological protection for radioactive waste disposal were identified: the probabilistic nature of future exposures, and the long-time scales involved. These challenges remain an important focus in *Publication* 77 (ICRP 1997b), *Publication* 81 (ICRP 1998), and in the publication to be presented here. We will do this by looking at the Executive Summary of *Publication* 122, which

(a) provides advice on application of the Commission's 2007 Recommendations (ICRP 2007) for the protection of humans and the environment against any harm that may result from the geological disposal of long-lived radioactive waste. It illustrates how the key protection concepts and principles of *Publication* 103 (ICRP 2007) should be interpreted, and how they apply over the different time frames a geological disposal facility for long-lived solid radioactive waste would have to provide radiological protection, see Figure 23.5.

(b) The goal of a geological disposal facility is to contain and isolate the waste in order to protect humans and the environment for time scales that are comparable with geological time scales. At large distances from the surface, changes are particularly slow. Given the distance from the surface and the selection of appropriate sites, the potential for human intrusion is limited. Radioactivity is

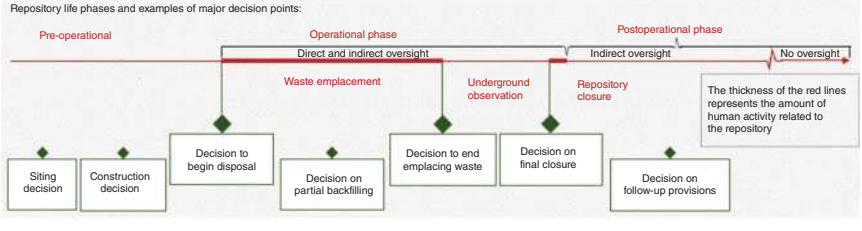

Figure 23.5 Disposal facility phases and relevant oversight periods. (This figure was contained in ICRP *Publication* 122 in miserable quality which was impossible to reproduce. It is simulated here in largely improved clarity.)

increasing with time, and any release will be delayed and further diluted by a properly chosen geological formation. Geological disposal is recognized by international organizations as especially suited for high-level radioactive waste or spent fuel where long-term containment and isolation is required. Geological disposal may also be used for other long-lived wastes, especially when a similar need for long-term protection applies.

(c) One of the important factors that influence application of the protection system over the different phases of the lifetime of a geological disposal facility is the level of oversight or "watchful care" of the disposal facility. The level of oversight directly affects the capability to control the source and to avoid or reduce some exposures. Three main time frames have to be considered: time of direct oversight when the disposal facility is being operated and active control is taking place (operational phase); time of indirect oversight, when the disposal facility is partly (backfilling and sealing of drifts) or fully sealed (postclosure period) where indirect regulatory or societal oversight might be continued for a period and then be supplemented or replaced by indirect oversight (e.g. monitoring the performances of the repository and the pathways for potential radionuclide releases, verification that restrictions on land control use are being met, maintaining records and memory of the facility, etc.); and time of no oversight (postclosure period), when the memory of the disposal facility is lost. In the periods of indirect or no oversight, once the facility is sealed, protection relies on the passive controls built into the facility at the time of its design, licensing, and operation.

(d) The design and associated safety case of a geological disposal facility address a series of evolutions with different probabilities that may be defined by regulation. Besides these design-basis evolutions, the developer/implementer, overseen by the regulator and society, may want to assess evolutions in non-design-basis conditions in order to judge the robustness of the facility.

(e) This report describes the radiological concepts and criteria that should be used by the designer and/or of the facility, the regulator, and the concerned stakeholders. Various dose and risk constraints are used for the assessment of the safety and radiological protection of the geological disposal facility for long-lived radioactive waste. Optimization addresses the main aim of a disposal facility (i.e. the radiological protection of humans and the environment). Optimization of protection is the central element of the stepwise construction and implementation of the geological disposal facility. It has to cover all elements of the system, including the societal component, in an integrated way. Important aspects of optimization of the protection must occur prior to waste emplacement, largely during the siting and design phase. The optimization efforts can be informed by, and construction supplemented with, consideration of Best Available Techniques (BAT) as applied to all stages of disposal facility siting and design. During the implementation phase, some further optimization is possible, but it is accepted that very little can be done to further optimize the performance of the engineered features after waste emplacement has occurred, and more so when galleries have been sealed.

(f) In the distant future, the geological disposal facility might give rise to some releases to the accessible environment and the safety case has to demonstrate that such releases, should they occur, will be within radiological protection criteria specified as part of the regulatory requirements. In application of the optimization principle, the reference radiological impact criterion for the design of a waste disposal facility recommended by ICRP is an annual dose constraint for the population of 0.3 $\mathrm{mSv\,yr^{-1}}$ (ICRP 2007), without any weighting of doses in the distant future. For doses in the future and for less likely events resulting in exposures, both categorized as potential exposures, the Commission continues to recommend a risk (as defined in *Publication* 103 [ICRP 2007]) constraint for the population of $1 \cdot 10^{-5}$ $\mathrm{year^{-1}}$ when applying an aggregated approach combining probability of the exposure scenario and the associated dose. However, *Publication* 103 (ICRP 2007) also warns that effective dose loses its direct connection to health detriment for doses in the future after a time span of a few generations, given the evolution of society, human habits, and characteristics. Furthermore, in the distant future, the geosphere, the engineered system and, even more so, the biosphere will evolve in a less predictable way. The scientific *basis* for assessments of detriment to health at very long times into the future therefore becomes uncertain, and the strict application of numerical criteria may be inappropriate. In the very long term, dose and risk criteria should be used for comparison of options rather than a means of assessing health detriment.

(g) The design-basis evolution of the geological disposal facility includes the expected evolution of the protection provided by the facility, and also events with a low probability of occurrence (less likely evolutions). It does not include either severe disturbing events of very low probability that may disrupt the facility, or inadvertent human intrusion. The exposures arising from the design-basis evolution scenarios are planned exposure situations as defined in *Publication* 103 (ICRP 2007). They include potential exposures from events with low probability, which have to be considered as part of the design basis. More specifically, for exposure to be delivered in the distant future, potential exposures will have to be considered due to the considerable uncertainties surrounding such exposures (ICRP 2007, Para. 265). If severe disturbing events outside the design basis occur, while there is still oversight (direct or indirect) of the disposal facility, the ensuing situation will be considered by the competent authority at that time, and the relevant protection measures will be implemented. If a severe disturbing event occurs when there is no longer oversight of the disposal facility, there is no certainty that a competent authority will be able to understand the source of the exposure; therefore, it is not possible to consider with certainty the implementation of relevant measures to control the source. Inadvertent human intrusion into the geological disposal facility is not a relevant scenario during the period of direct or indirect oversight. In the period of no oversight, inadvertent human intrusion may occur and the consequences considered by the competent authorities at that time may be relevant if and when they understand the source of the exposure.

(h) For the design-basis evolution, the dosimetric criteria relevant to planned exposure situations are considered for assessing the safety and robustness of the disposal facility over the three main time frames. In the design stage, potential impacts of severe disturbing events may be estimated using stylized or simplified calculations. An indication of the robustness of the system could then be obtained by comparing these results with numerical values of dose or risk, if required. If this approach is adopted, the appropriate reference levels should be those for an existing exposure situation (a few millisieverts per year), or for an emergency exposure (in the range of 20–100 mSv for the first year), depending on the specific scenario. If the event actually occurs in the future, the competent authority should apply the relevant protection criteria at the time.

(i) The safety case of a geological disposal facility, by including events of low probability and exposures to be delivered in the distant future, includes consideration of how to deal with potential exposures as defined by *Publication* 103 (ICRP 2007).

(j) ICRP recommends that dose or risk estimates derived from these exposure assessments should not be regarded as direct measures of health effects beyond time scales of around several hundred years into the future. Rather, they represent indicators of the protection afforded by the geological disposal facility.

(k) Application of the three exposure situations and of associated dose limits, constraints, and reference levels as defined in *Publication* 103 (ICRP 2007) during the three main time frames are summarized in a table in IRCP (2013) Radiological protection in geological disposal of long-lived solid radioactive waste (IRCP *Publication* 122). For brevity, we do not reproduce this table here.

References

Health Effects and Radiation Protection

Blaickner, M., Kratz, J.V., Minouchehr, S. et al. (2012). Dosimetric feasability study for an extracorporeal BNCT application on liver metastases at the TRIGA Mainz. *Appl. Radiat. Isot.* 70: 139.

Hampel, G., Wortmann, B., Blaickner, M. et al. (2009). Irradiation facility at the TRIGA Mainz for treatment of liver metastases, 13th International Congress on Neutron Capture Therapy BNCT: a new option against cancer. *Appl. Radiat. Isot.* 67 (7–8, Suppl. 1): 238.

International Commission on Radiological Protection (1990). Recommendations. *Ann. ICRP* 20 (4).

International Commission on Radiological Protection (1991). Risks associated with ionizing radiation. *Ann. ICRP* 22 (1).

International Commission on Radiological Protection (1993). *Protection Against Radon-222 at Home and at Work*, ICRP Publication No. 65. Oxford: Pergamon.

Nagels, S., Hampel, G., Kratz, J.V. et al. (2009). Determination of the radiation field at the research reactor TRIGA Mainz for BNCT, 13th International Congress on

Neutron Capture Therapy: a new option against cancer. *Appl. Radiat. Isot.* 67 (7–8, Suppl. 1): 242.
Pinelli, T., Zonta, A., Altieri, S. et al. (2002, 2002). Taormina: from the first idea to the application to the human liver. Research and development in neutron capture therapy. In: *Proceedings of the 10th International Congress on Neutron Capture Therapy*, Essen, Germany (eds. W. Sauerwein et al.), 1065. Bologna: Monduzzi Editore.
Schütz, C.L., Brochhausen, C., Hampel, G. et al. (2012). Intercomparison of inductively coupled plasma mass spectrometry, quantitative neutron capture radiography, and prompt gamma activation analysis for the determination of boron in biological samples. *Anal. Bioanal. Chem.* 404: 1887.
UNSCEAR (2008). Report, Sources and Effects of Ionizing Radiation, United Nations Scientific Committee on the Effects of Atomic Radiation, Report to the General Assembly, with Scientific Annexes.

Further Reading

Dosimetry

Snell, A.H. (ed.) (1962). *Nuclear Instruments and Their Uses*. New York: Wiley.
Attix, F.H., Roesch, W.C., and Tochilin, E. (eds.) (1966–1972). *Radiation Dosimetry*, vols. I, II, III and Supplement I, 2e. New York: Academic Press.
Cameron, J.R., Suntharalingham, N., and Kenney, G.N. (1968). *Thermoluminescent Dosimetry*. Madison, WI: University of Wisconsin Press.
Holm, N.E. and Berry, R.J. (eds.) (1970). *Manual on Radiation Dosimetry*. New York: Marcel Dekker.
United Nations (1985). *Radiation, Doses, Effects, Risks*. Nairobi: United Nations Environment Programme (UNEP).

Health Effects and Radiation Protection

Price, B.T., Horton, C.C., and Spinney, K.T. (1957). *Radiation Shielding*. Oxford: Pergamon.
Rockley, J.C. (1964). *An Introduction to Industrial Radiology*. London: Butterworths.
Morgan, K.Z. and Turner, J.E. (eds.) (1967). *Principles of Radiation Protection*. New York: Wiley.
Snyder, W.S. et al. (eds.) (1968). *Radiation Protection*, Parts 1 and 2. Oxford: Pergamon.
Cember, H. (1969). *Introduction to Health Physics*. Oxford: Pergamon.
National Council on Radiation Protection (1971). Basic Radiation Protection Criteria. *Report 39*. Washington, DC: NCRP Publications.
Kiefer, H. and Maushart, R. (1972). *Radiation Protection Measurement*. Oxford: Pergamon.
International Commission on Radiological Protection (1977). Recommendations. ICRP Publication No. 26. *Ann. ICRP* 1 (3).
Martin, A. and Harbisson, S.A. (1979). *An Introduction to Radiation Protection*, 2e. London: Chapman and Hall.

Aurand, H., Gans, I., and Rühle, H. (1982). *Radioökologie und Strahlenschutz*. Stuttgart: Erich Schmidt Verlag.

International Atomic Energy Agency (1982). *Nuclear Power, the Environment and Man*. Vienna: IAEA.

United Nations (1982). *Ionizing Radiation: Sources and Biological Effects*. New York: United Nations.

Nygaard, O.F. and Simic, M.G. (eds.) (1983). *Radioprotectors and Anticarcinogens*. New York: Academic Press.

Pochin, E. (1983). *Nuclear Radiation; Risks and Benefits*. Oxford: Clarendon Press.

Hall, E.J. (1984). *Radiation and Life*, 2e. Oxford: Pergamon.

Kraft, G. (1987). Radiobiological effects of very heavy ions: inactivation, induction of chromosome aberrations and strand breaks. *Nucl. Sci. Appl.* 3: 1.

National Council of Radiation Protection (1987). Exposure of the Population in the United States and Canada from Natural Background Radiation. *Report No. 94*; Radiation Exposure of the US Population from Consumer Products and Miscellaneous Sources, Report No. 95. Washington, DC: NCRP Publications.

von Sonntag, C. (1987). *The Chemical Basis of Radiation Biology*. Philadelphia: Taylor & Francis.

Burns, M.E. (ed.) (1988). *Low-Level Radioactive Waste Regulation: Science, Politics and Fear*. Chelsea, MI: Lewis.

Greening, J.R. (1989). *Fundamentals of Radiation Dosimetry*. Bristol: Adam Hilger.

European Commission (1993). Proceedings of the International Symposium on Remediation and Restoration of Radioactive-Contaminated Sites in Europe, Antwerp, October, EC Document XI-5027/94, 1994.

National Council on Radiation Protection and Measurements (1993). Evaluation of Risk Estimates for Radiation Protection Purposes. *Report 115*. Bethesda, MD: NCRP.

UNSCEAR (1993). Report, Sources and Effects of Ionizing Radiation, United Nations Scientific Committee on the Effects of Atomic Radiation, Report to the General Assembly, with Scientific Annexes.

International Atomic Energy Agency (1994). Advances in Reliability Analysis and Probabilistic Safety Assessment for Nuclear Power Reactors, IAEA Technical Document No. 737, Vienna.

International Atomic Energy Agency (1994). Assessing the Radiological Impact of Past Nuclear Activities and Events, IAEA Technical Document No. 755, Vienna.

Kaul, A. (1994). Present and future tasks of the International Commission on Radiological Protection. *Kerntechnik* 59: 238.

Kaul, A., Kraus, W., and Schmitt-Hannig, A. (1994). Exposure of the public from man-made and natural sources of radiation. *Kerntechnik* 59: 98.

Nimmo-Scott, W. and Golding, D.J. (eds.) (1994). *Proceedings of the 17th IRPA Regional Congress on Radiological Protection, Portsmouth, June*. Ashford, Kent: Nuclear Technology Publishing.

van Kaick, G., Karaoglou, A., and Kellerer, A.M. (eds.) (1995). *Health Effects of Internally Deposited Radionuclides: Emphasis on Radium and Thorium*, EUR 15877 EN. Singapore: World Scientific.

International Radiation Protection Association (1996). Standards of Protection against Radiation, Title 10, Code of Federal Regulations, Part 20 (published annually). *Proceedings of the 1996 International Congress on Radiation Protection*, volumes 1–4. Vienna: IRPA.

International Atomic Energy Agency (1997). *One Decade After Chernobyl: Summing up the Consequences of the Accident*. Vienna: IAEA.

International Commission on Radiological Protection (2007). The 2007 recommendations. *Ann. ICRP* 37: 2–4.

Monitoring and Dosimetry

Chieco, N.A. and Bogan, D.C. (eds.) (1992). *Environmental Measurements Laboratory (EML), Procedures Manual (HASL-300)*, 27e, vol. 1. New York: US Department of Energy.

Reaktorsicherheit (1992). *Meßanleitungen für die Überwachung der Radioaktivität in der Umwelt und zur Erfassung radioaktiver Emissionen und kerntechnischer Anlagen*. Stuttgart: Gustav Fischer.

Bayer, A., Leeb, H., and Weiss, W. (1993). Measurement, assessment and evaluation within an integrated measurement and information system for surveillance and environmental radioactivity (IMIS). In: *Proceedings of the Topical Meeting on Environmental Transport and Dosimetry*, Charleston, SC, September, 108.

Weiss, W. and Leeb, H. (1993). IMIS – the German integrated radioactivity information and decision support system. *Radiat. Prot. Dosim.* 50: 163.

Pentreath, R.J. (1999). A system for radiological protection of the environment: some initial thoughts and ideas. *J. Radiol. Prot.* 19: 117.

Schmitz, T., Blaickner, M., Schütz, C. et al. (2010). Dose calculation in biological samples in a mixed neutron-gamma field at the TRIGA reactor of the University of Mainz. *Acta Oncol.* 49: 1165.

Kanyár, B. and Köteles, G.J. (2011). Dosimetry and biological effects of ionizing radiation. In: *Handbook of Nuclear Chemistry*, 2e, vol. 5 (eds. A. Vértes, S. Nagy, Z. Klencsár, et al.), 2213. Berlin: Springer-Verlag.

McLaughlin, W.L., Miller, A., Kovács, A., and Mehta, K.K. (2011). Dosimetry methods. In: *Handbook of Nuclear Chemistry*, 2e, vol. 5 (eds. A. Vértes, S. Nagy, Z. Klencsár, et al.), 2287. Berlin: Springer-Verlag.

Schütz, C., Brochhausen, C., Altieri, S. et al. (2011). Boron determination in liver tissue by combining quantitative neutron capture radiography (QNCR) and histological analysis for BNCT treatment planning at the TRIGA Mainz. *Radiat. Res.* 176: 388.

Weiss, W., Larsson, C.-M., McKenney, C. et al. (2013). The International Commission on Radiological Protection ICRP, Annals of the ICRP, Radiological protection in geological disposal of long-lived solid radioactive waste. ICRP Publication 122. *Ann. ICRP* 42: 3.

Index

Nuclear and Radiochemistry: Fundamentals and Applications,
Fourth Edition. Jens-Volker Kratz.

g

h

i

j

k

l

m

n

q

r

t